NASA/CR—1998-207410 UM-MEAM-98-01

Dryout and Rewetting in the Pool Boiling Experiment Flown on STS-72 (PBE-II B) and STS-77 (PBE-II A)

Herman Merte, Jr., Ho Sung Lee, and Robert B. Keller
University of Michigan, Ann Arbor, Michigan

Prepared under Grant NAG3–1684

National Aeronautics and
Space Administration

Lewis Research Center

June 1998

Trade names or manufacturers' names are used in this report for identification only. This usage does not constitute an official endorsement, either expressed or implied, by the National Aeronautics and Space Administration.

Available from

NASA Center for Aerospace Information
7121 Standard Drive
Hanover, MD 21076
Price Code: A23

National Technical Information Service
5287 Port Royal Road
Springfield, VA 22100
Price Code: A23

Abstract

Experiments were conducted in the microgravity of space in which a pool of liquid (R-113), initially at a precisely defined pressure and temperature, is subjected to a step imposed heat flux from a semi-transparent thin-film heater forming part of one wall of the container such that boiling is initiated and maintained for a defined period of time at a constant pressure level. Transient measurements of the heater surface and fluid temperatures near the surface are made, noting in particular the conditions at the onset of boiling, along with motion photography of the boiling process in two simultaneous views, from beneath the heating surface and from the side. The conduct of the experiment and the data acquisitions are completely automated and self-contained. A total of nine tests were conducted at three levels of heat flux and three levels of subcooling in each of the two space experiments designated as PBE-IIA, -IIB on the STS-77, -72, respectively. These space experiments differed from each other in the levels of subcooling and heat flux used relative to those of three space experiments conducted earlier under essentially identical circumstances and designated as PBE-IA, -IB, -IC on the STS-47, -57,-60, respectively. The subcooling levels in PBE-IIA on STS-77 were identical to those of the latter three identical space experiments referred to above, while the heat flux levels were decreased to a minimum level one-fourth that previously used. The heat flux levels in PBE-IIB on STS-72 were identical to those of the latter three identical space experiments above, while the subcooling levels were increased to a maximum level double that previously used. The physical hardware used in PBE-IIA, -IIB was the same, including the heater surface, as that referred to as the Flight Version, PBE-IB on STS-57.

The basic mechanisms of pool boiling are reviewed, with particular emphasis on the roles of buoyancy, and the experimental concepts and parameters used are given. The hardware and operating procedures followed are described in some detail.

The experimental results for each of the nine (9) runs in each of the space flights, along with those from several post-flight ground tests, are given in sufficient detail that the derived parameters and conclusions can be independently obtained, if desired. Sample images are provided for each Run, following digitizing from the 16 mm film.

The distinct advantage gained by the transient heating of a stagnant liquid in microgravity is that the temperature distribution is known at the moment of nucleation and at the beginning of the growth period of the vapor. The temperature distribution known at nucleation permits the application of the modification of the classical homogeneous nucleation theory to the prediction of the heater surface superheat at nucleation. Successful comparisons with the effects of varying the heat flux and initial bulk liquid subcooling are presented.

As a result of the higher bulk liquid subcoolings and lower heat flux levels used in the present work, three (3) additional modes of propagation of boiling across the heater surface and subsequent vapor bubble growths were observed, in addition to the two (2) modes observed in the previous microgravity pool boiling space flights. Of particular interest were the extremely dynamic or "explosive" growths, which were determined to be the consequence of the large increase in the liquid-vapor interface area associated with the appearance of a corrugated or rough interface, which itself is due to the presence of an instability. The identification and modeling of the source of this instability, including predictions of circumstances for its onset, have been carried out. Assumptions were necessary regarding the character of disturbances necessary for the instabilities to grow, and require future experimentation in the microgravity of space for clarification, in particular about the wave lengths associated with the instabilities.

A new vapor bubble phenomena was observed at the combination of the lower heat flux levels and highest subcooling levels, in which distinct regular migrations of small vapor bubbles took place while remaining in the immediate vicinity of the heater surface, proceeding from their region of origin toward a larger bubble, also on the heater surface, and eventually coalescing with this larger bubble. The heat transfer was enhanced approximately 30% as a result of these migrating bubbles, which is believed to be a vapor bubble manifestation of Marangoni convection and/or molecular momentum effects, sometimes referred to as vapor recoil. No analytical development describing these motions is available yet, but the results of measurements of the bubble velocities and sizes are presented for the well-defined initial conditions employed.

Summaries of the mean heat transfer behavior for each of the experimental variables are given. The circumstances of heat flux and liquid subcooling necessary to produce heater surface dryout for an initially stagnant liquid subjected to an imposed heat flux have been more closely identified.

Table of Contents

List of Figures

List of Tables

List of Appendices

1. INTRODUCTION

1.1 General Background

Nucleate boiling is an important mode of heat transfer in that relatively small temperature differences can provide large rates of heat transfer, which can result in significant economic and other benefits associated with the smaller heat transfer areas necessary to accomplish a given function.

A limitation in the development of more compact power sources using nuclear energy lies in the ability to remove the large heat generation rates possible from the reactor core in a manner that is consistent, reliable and predictable. Nucleate boiling would be a candidate for wide spread use in such an application were the fundamental mechanisms that govern the process sufficiently well understood. Additional important applications of nucleate boiling exist, such as steam generation in conventional power plants, distillation processes in petroleum and other chemical plants, and the boiling of refrigerants in cooling coils, in which the motion of the bulk liquid is generally imposed externally. This is termed forced convection boiling, and the liquid motion moves the vapor formed away from the heated surface so that the vapor may be utilized and/or further processed and the nucleate boiling process can continue.

Other applications exist in which externally forced flow is absent, where buoyancy provides the major mechanism for vapor removal from the vicinity of the heating surface, and is generally designated pool boiling. Even in circumstances where forced convection exists to some extent, the forces associated with flow acting on the vapor bubbles may be sufficiently small that buoyancy or body forces will continue to be responsible for the vapor removal process. It should then be possible to describe the behavior, in terms of basic governing mechanisms, by the pool boiling process. Devices in which pool boiling occurs are two-phase closed thermosyphons, reboilers, and heat pipes, whether gravity assisted or not. Potentially significant applications exist in the cooling of microelectronic circuitry and the internal cooling of gas turbine blades. The latter would involve pool boiling under high gravity fields, and its successful application would permit higher operating temperatures with attendant higher efficiencies, and would also eliminate the need for the development of exotic ceramic materials with the difficulties of thermal stresses and reliability. Another important and as yet poorly understood area incorporated in the mechanism of pool boiling is the breakdown of film boiling into the transition boiling regime. This is of concern in the loss-of -coolant accident in nuclear power plants, and is encompassed in the reflooding and fuel element rewetting processes. A good understanding of this rewetting process in microgravity or in the absence of buoyancy would improve its application with buoyancy.

The effective and enhanced application of both nucleate pool and forced convection boiling requires a sound understanding of the mechanisms governing the processes. The vapor removal

from the vicinity of the heater surface, as understood to this point, occurs primarily by buoyancy in the case of pool boiling and bulk liquid inertia in the case with forced convection. The results of pool boiling experiments in long term microgravity, reported by Merte et al (1996), demonstrated that under certain circumstances the effects of momentum imparted to the liquid by dynamic growing vapor bubbles and of surface tension associated with the coalescence of different size vapor bubbles can serve to remove vapor bubbles from the heater surface. Although the variation of both gravity and forced flow are known to influence the overall heat transfer processes, other forces or potentials are acting as well, and the relative significance's of these are as yet poorly understood.

Requirements for the proper functioning of equipment and personnel in the space environment of reduced gravity and vacuum, as will be necessary in space station modules and space power generation, introduce unique problems in temperature control, power generation, energy dissipation, the storage, transfer, control and conditioning of fluids (including cryogenic liquids), and liquid-vapor separation.

The temperature control in certain locations where internal heat generation takes place as a result of dissipation, as from friction or joulian heating in electronic equipment, or as a consequence of a nuclear or chemical heat source, may require that this energy be transported to other locations of the facility or stored locally for later transport and elimination. The use of the phase changes of vaporization and condensation to transport energy have the advantage of accommodating large variations in heat loads with relatively small temperature gradients and changes in temperature levels, along with the economical use of pumping power. Energy storage might be advantageous for intermittent processes or for processes where momentary surges could not be accommodated by a steady transfer of mass to a remote location, and also could take advantage of the latent heat associated with phase changes.

A distinction must be made between pool boiling and flow boiling when considering applications in the space environment of microgravity, since these two processes may arise in quite different specific technical applications. Pool boiling, for example, would be important for the short term cooling of high power electronic and other devices, and for the long term space storage of cryogens. Flow boiling, on the other hand, occurs in applications where liquid flow is imposed externally, such as in Rankine cycle vapor generation or in thermal energy management using pumped latent heat transport.

Certain effects which can be neglected at normal earth gravity, such as surface tension and vapor momentum, can become quite significant at microgravity conditions. Momentum imparted to the liquid by the vapor bubble during growth tends to draw the vapor bubble away from the surface, depending on the rate of growth, which in turn is governed by the temperature distribution of the liquid. Thermocapillary forces, arising from the variation of the liquid-vapor surface tension

with temperature, on the other hand, tend to move the vapor bubble toward the region of higher temperature. The bubble motion will be governed by which of these two effects prevail. In addition, thermocapillary forces acting at the liquid-vapor interface of vapor bubbles in contact with a heated surface could act to bring cooler liquid to the heater surface, delaying or inhibiting the onset of dryout, or promoting and enhancing the rewetting of the heater surface.

1.2 Objectives of Study

The research as originally proposed was intended to seek to improve the understanding of the fundamental mechanisms that constitute nucleate pool boiling. The vehicle for accomplishing this is an investigation, including experiments conducted in microgravity and coupled with appropriate analyses, of the heat transfer and vapor bubble dynamics associated with nucleation, bubble growth/collapse and subsequent motion, considering the interrelations between buoyancy, momentum and surface tension which will govern the motion of the vapor and surrounding liquid, as a function of the heating rate at the heat transfer surface and the temperature level and distribution in the bulk liquid.

As became clear when the prior results obtained by Merte et al (1996) were examined, a more accurate representation of the objectives would have been a proposal for a general study of pool boiling in microgravity. The circumstances under which nucleate boiling and what is generally termed, to this point, film boiling take place with pool boiling in microgravity is as yet unclear. Both of these processes were observed, sometimes simultaneously, in the prior work.

An adequate understanding of the mechanisms in any process implies that its behavior can be predicted in terms of the governing parameters. The behavior here would include the conditions for the onset of boiling, the dynamics of the vapor bubbles, including both the number density of active nucleating sites and the frequency of formation, and the associated heat transfer. Although a considerable amount of research has been conducted on nucleate boiling over the years, and has been useful with respect to application to various technologies on earth, the ability to predict its behavior is as yet very limited, owing to the involvement and interaction of the many parameters. To this now should be added also the limitations in predicting the onset of dryout or rewetting, whether in earth gravity or microgravity.

For the basic studies proposed and conducted, with further results presented here, it was deemed essential to establish well-defined "bench marks" which could withstand future interrogation. The availability of a long period of quiescence prior to the onset to each test, as a result of the microgravity environment, means that the initial state at the onset of heating and at the onset of boiling (nucleation) will be well-defined. This is not possible in a gravity field. The availability of relatively long test periods permit the use of combinations of low heat flux and subcooling that require more time for the inception of boiling than is available in a drop tower, and

also permit the observing of long-term vapor dynamic behavior following the transient bubble growth.

The components which constitute the nucleate boiling process-nucleation, growth, motion, collapse (if subcooled) of the vapor bubbles - are common to both pool and flow boiling. The study here focuses on the fundamental mechanisms of pool boiling only, under microgravity conditions. This eliminates the complications associated with having an external flow field superimposed on that generated by growing/collapsing vapor bubbles. In addition, this eliminates the possibility of having other effects masked by an external flow field similar to that produced by buoyancy.

The specific objectives of the study represented by the results here from the two space experiments on STS-72, -77 were to examine the phenomena of nucleation and dryout/rewetting in more detail by extending the range of experimental parameters beyond those used previously: The heat flux levels in PBE-IIA on STS-77 were reduced to 2, 1, and 0.5 w/cm^2 in place of 8, 4, and 2 w/cm^2 in all the other space experiments; The initial bulk liquid subcooling levels in PBE-IIB on STS-72 were increased to 40, 30, 20 °F in place of 20, 5, 0 ° F in all the other space experiments. The heating of the liquid which takes place in microgravity then has the effect of varying the temperature distributions in the liquid at the onset of boiling and during the phenomena of dryout and rewetting.

In the experiments as conducted, a pool of liquid, initially at a precisely defined pressure and temperature, is subjected to a step imposed heat flux from a semi-transparent thin-film heater forming part of one wall of the container such that boiling is initiated and maintained for a defined period of time at a constant pressure level. Transient measurements of the heater surface and fluid temperatures near the surface are made, noting in particular the conditions at the onset of boiling, along with motion photography of the boiling process in two simultaneous views, from beneath the heating surface and from the side. The conduct of the experiment and the data acquisitions are completely automated and self-contained. Two space flights were successfully carried out, with each one consisting of a total of nine tests at three levels of heat flux and three levels of subcooling.

Following the successful development work conducted during the ground-based activity under NASA Grant NAG3-663, which included reduced gravity testing in the evacuated 5 second drop tower at the NASA Lewis Research Center, the results of which were reported in Ervin and Merte (1991), Ervin et al (1992), and Lee and Merte (1993), approval was given for a space experiment. An Engineering Model was developed by the NASA Lewis Research Center for testing the feasibility of incorporating the experimental concepts described in the Science Requirements Document by Merte (1989) into the space available in a Get-Away-Special (GAS). Following the successful demonstration of the operation of the Engineering Model, the

construction of a Prototype Version was undertaken. This proved to operate so successfully with full testing in earth gravity that when an opportunity for an unexpected early GAS flight came to light a request was made to fly the Prototype Version. This was justified primarily as an opportunity to further test the heretofore untried engineering concepts in the facility, and to confirm the camera timings which could not be determined in the drop tower testing. The successful acquisition of any experimental measurements was thus viewed to be a bonus. This experiment flew in the STS-47 on September 12, 1992, and was designated as PBE-IA.

The Flight Version of the experimental apparatus was designated as PBE-IB, and flew in the STS-57 on June 21, 1993. Subsequent to this, another opportunity for a space flight with the Prototype Version occurred, which was approved and designated as PBE-IC, and took place in the STS-60 on February 3, 1994.

The experimental parameters in these three flights are identical, with differences only in the length of the individual test runs and the timing of the on-off and speed of the camera, to optimize the use of the fixed film length. When the experimental results are examined in Merte et al (1996), the fortuitous opportunity for conducting the seemingly same experiment three times contributes immensely to authenticating some of the conclusions reached. By using the identical physical facility, as between the STS-47 (PBE-IA) and STS-60 (PBE-IC), the issue of repeatability could be addressed. By using a physical facility with the same design and fabrication techniques, as with PBE-IB on STS-57, the matter of reproducibility could be examined.

The Flight Version of the experimental apparatus flew again as PBE-IIB in the STS-72 on February 5, 1996 and as PBE-IIA in the STS-77 on May 19, 1996, with the results given here.

1.3 Basic Mechanisms of Pool Boiling

As stated above, consideration of any externally imposed flow field on the boiling process, termed as forced convection boiling, is explicitly excluded here in order to:

(a) Eliminate an additional complicating variable from an already complex process at the outset. Pool boiling is the limiting case of forced convection boiling as the imposed velocity is reduced to zero.

(b) Minimize the possibility that certain weak effects would be overshadowed by the kinetic energy associated with the imposed bulk liquid flow. The supposedly weak effects were considered to consist primarily of thermocapillary and molecular momentum forces.

In the general discussion of the basic mechanisms of pool boiling below, reference will be made, as appropriate, to the new understanding of certain elements gained from the first three space experiments conducted and reported in Merte et al (1996) and subsequent other technical publications.

1.3.1 Nucleate Boiling

Nucleate boiling may be characterized by the following:

(i) A liquid-vapor phase change occurs with the formation of discrete bubbles at individual sites.

(ii) The energy transfer rates are large with small temperature difference driving potentials.

(iii) The process is inherently transient, although quasi cyclic repetitions are possible with vapor removal mechanisms acting such as buoyancy.

Before a nucleate pool boiling system can attain the steady periodic behavior normally observed in a gravity field, where buoyancy is the dominant vapor removal mechanism, the process must pass through the transient phase referred to as nucleation, initiation or onset of nucleate boiling. Before understanding the cyclic nature of nucleate boiling, one must first understand the elements of the initial transient process.

To provide a perspective of the relationship between the study conducted here and the overall processes which constitute pool boiling, a qualitative physical description of the sequence of events which occur is presented, beginning with the transient heating of a liquid at a solid-liquid interface.

a. Conduction

With an initially static liquid the heat transfer process can be described by static thermal diffusion alone until buoyancy, thermophorysis, thermocapillary or other forces set the liquid in motion. The rate of temperature rise and the temperature distributions in this early interval depend on the nature of the heat source and the dynamic interactions with the system. The common idealizations taken as limits in analyses are step changes in either temperature or heat flux at the solid-liquid heater interface. The degree and extent to which the liquid becomes superheated above its saturation temperature in a given time also depends on whether and by how much the bulk liquid is subcooled. This temperature distribution will be modified by the onset of liquid motion arising from natural convection or other disturbances. If the motion can be quantified, computation of the temperature distribution will still be possible. Comparisons between transient measured heater surface temperatures and one-dimensional predictions for the short time microgravity in drop towers are given in Ervin and Merte (1993) and in Merte et al (1994), while comparisons with three-dimensional computations for longer microgravity times in space flights are given in Merte et al (1996). By varying the heat flux imposed on the liquid and its initial subcooling it becomes possible to control the temperature distribution in the liquid.

b. Onset of Natural convection

Natural convection is driven by buoyancy, and its onset is described in terms of an instability, in which enervating disturbances are always present. Reducing the buoyancy by reducing the body forces such as to microgravity delays the onset of the convection and reduces the resulting convection velocities. Both of these serve to increase the temperature levels in the liquid adjacent to the heating surface for a given heating time, regardless of whether the bulk liquid is initially saturated or subcooled. The liquid temperature levels and distributions adjacent to the heater surface are thus influenced by buoyancy, and in turn can influence the next two elements of nucleate boiling: the nucleation and bubble growth rates. Comparisons between the predictions and measurements in earth gravity using the techniques of the current experiments are given by Oker and Merte (1978), while the observed consequences on natural convection of disturbances in space flight, on the order of 0.3 milli-g lasting 2 seconds, are presented in Merte et al (1996).

c. Nucleation

Vaporization can take place only at an existing liquid -vapor interface, which then constitutes the growth phase of nucleate boiling. If an interface does not exist it must be formed. The formation of a vapor nucleus is called nucleation, and is classified either homogenous or heterogeneous , depending on the presence of other components or species in the vicinity of the nucleation. The circumstances under which nucleation takes place on a heated surface depends on:

(i) The Heater Surface Microgeometry. This can provide the crevices and intergranular defects which serve as pre-existing interfaces. The temperature levels required to activate these pre-existing nuclei have been modeled in terms of thermodynamic equilibrium at curved liquid-vapor interfaces. Assuming that the pre-existing interface has the form of a hemisphere of the size of the surface defect , the liquid superheat required for subsequent bubble growth can be related to the cavity size. The smaller is the cavity, the larger is the heater surface superheat required for the onset of nucleate boiling, and the larger will be the bulk liquid temperatures at the onset of the next element of the boiling process.

(ii) The Solid-Fluid properties. This governs not only the temperature distributions in both the heater and fluids, related by their respective thermal properties, but also the surface energy relationships between the solid-liquid-vapor, often expressed in terms of a contact angle or wettability.

(iii) The Liquid Temperature Distribution. This includes the solid-liquid interface temperature, since this is one spatial limit of the liquid temperature. As discussed under "b" above, the onset of natural convection governs the

subsequent temperature distributions, as does also the initial imposed heat flux. Once nucleation has occurred, the subsequent bubble growth rates will be governed by the bulk liquid temperature distribution at this time.

As reported in the results of Merte et al (1996) for pool boiling in long-term microgravity, both heterogeneous and what has been termed quasi-homogenous nucleation have been observed from the back side of the same heater surface: Heterogeneous nucleation was defined for the circumstances where repeating the experiment produced nucleation at the identical site on the heater surface, whereas under other circumstances the nucleation took place at different random locations, denoted as quasi-homogeneous nucleation. The latter process was associated with higher heater surface superheats, and the influence of heat flux and system pressure used to produce the bulk liquid subcooling are accounted for by a modification of classical homogeneous nucleation theory. Details are given by Merte and Lee (1997).

d. Vapor Bubble Growth/Collapse

Vapor bubble growth requires that the liquid at the liquid vapor interface be superheated with respect to the saturation temperature corresponding to the interfacial liquid pressure. The rate of vapor formation, and hence bubble growth, depends on this superheat and on the liquid temperature gradient at the interface, and thus on the liquid temperature distribution at the onset of bubble growth. The interfacial liquid superheat governs the internal vapor bubble pressure, which acts to move the bulk liquid away from the vicinity of the heater surface. In the dynamics of the growth process this pressure is balanced in a complex manner by the liquid inertia, liquid viscosity, buoyancy, and surface tensions. If the bulk liquid is subcooled, the pressure difference can reverse with the subsequent collapse of the vapor bubble. The various forces acting in the bubble growth/collapse can be summarized:

(i) Internal Bubble Pressure. This is governed by the liquid temperature distribution, which in turn is influenced by buoyancy.

(ii) Liquid Momentum. This is sometimes referred to as bulk liquid inertia.

(iii) Buoyancy. The pressure differences associated with the liquid-vapor density differences in a body force field act in addition to those natural convection effects which influence the liquid temperature distribution.

(iv) Surface Tension. This includes both that occurring at the liquid - vapor interface and at the liquid-solid-vapor interline.

(v) Viscosity. This refers primarily to the liquid viscosity acting in the vicinity of the solid surface, but could include the viscous normal shear at the liquid vapor interface away from the solid surface in circumstances where the radial

growth rate is very large. Vapor viscosity could also be a factor during the very early periods when surface rates of vapor formation are large.

Since the liquid-vapor interface is deformable, the interfacial shape during growth will be governed by the net balance of the dynamic forces acting at each point on the interface, and the interface will not necessarily be spherical or hemispherical, as has been assumed in the absence of capabilities for dealing with flexible interfaces.

Immediately following the initial nucleation process on transient heating in microgravity, distinct differences in the subsequent propagation of the boiling front over the heater surface were observed, which led to the definitions of six categories of boiling propagation. These are described in Ervin and Merte (1993), Ervin et al (1992), and Ervin and Merte (1991). Three of these categories have been observed only in microgravity, and of these three one gave rise to an energetic vapor bubble growth accompanied by an unstable interface Such a violent or almost explosive growth generally took place following the onset of the quasi-homogeneous nucleation referred to in (c) above, and was associated with superheated boundary layers having the largest energy content. This accompanied the lower levels of heat flux and longer nucleation delay times. The physical appearance of such bubbles during the violent growth process was quite different from that observed heretofore, taking on a roughened appearance over the entire interface. A simple model was developed by Lee and Merte (1993), describing the liquid -vapor interfacial area with roughness present in terms of a circular function to approximate the behavior of the rapid bubble growth by modifying a previous solution developed without the interfacial roughness present. The theoretical basis for the formation of the "rough" liquid-vapor interface is given by Lee and Merte (1996a).

Comparisons of measured vapor bubble growths with computations for bubbles having smooth interfaces are given in Lee and Merte (1996 b,c), where the heating under microgravity conditions provided known temperature distributions around the bubble at the beginning of growth from the critical size nucleus. It was found to be necessary to account for the geometry of the heater surface used, as well as the applied heat flux mode used: In the absence of gravity heating from a flat surface produces a liquid temperature gradient normal to the heater surface. A vapor bubble initiating its growth from the thermodynamic critical size in the immediate vicinity of the heater surface then effectively grows in a uniform superheat environment parallel to the surface, and in a non-uniform superheat environment perpendicular to the surface. In microgravity, it appears that the growth in the early stages observed produces hemispheres, as a consequence of surface tension effects. Based on a relatively limited amount of data to date, given in Merte et al (1996), it appears that the growth during the early hemispherical phase can be described by a constant proportioning of the growth between the two limits described by the initial uniform and non-uniform superheats surrounding the bubble.

(e) Departure

The subsequent motion of the vapor bubble depends on the net effect of the forces listed in "d" above, plus a phenomena associated with simultaneous evaporation and condensation across a vapor bubble, referred to as a molecular momentum effect. This is related to the molecular kinetic energy necessary for vapor molecules to escape or to be retained at a liquid-vapor interface. With thermodynamic equilibrium the net rate of evaporation and condensation is zero, but the normal nucleate boiling process is highly non-equilibrium. The net resulting molecular momentum forces are generally unobservable in the presence of the overwhelming body and other forces which usually exist. The bulk liquid momentum induced by the rapid bubble growth can act to assist in the removal of the bubble from the heater surface. In microgravity, of course, buoyancy effects are reduced significantly.

With slow heating in microgravity, the high liquid superheat at the initial nucleation resulted in a dynamic vapor bubble growth such that sufficient momentum was imparted to the surrounding liquid to cause departure of a large vapor bubble from the heater surface (Merte et al- 1996).

f. Motion Following Departure

If the circumstances of the forces acting on the vapor bubble are such that departure takes place, the subsequent motion depends on the following:

(i) Buoyancy

(ii) Initial velocity upon departure. This velocity induces momentum in the bulk liquid, which must be considered, and can tend to accelerate the vapor bubble if collapse takes place, or will decelerate the bubble if it grows.

(iii) Degree and distribution of liquid superheat and/or subcooling. The bulk liquid temperature distribution can act via the liquid-vapor surface tension or Marangoni-induced effects, via the bulk liquid momentum effects associated with growth or collapse, together with liquid viscosity, and via the molecular momentum effects. In microgravity conditions, only buoyancy will be changed, except for its more indirect influence on the bulk liquid temperature distribution.

1.3.2 Dryout (Film Boiling in Earth Gravity)

Nucleate boiling can take place only in circumstances where the liquid substantially wets the heater surface. This entails two implications. First, the liquid itself must be inherently wetting on the heater surface. As observed and discussed by Merte (1967), it is well known, for example, that mercury is generally non-wetting except for materials with which it forms amalgams. For the operation of power generation plants with mercury boilers it was necessary to add traces of

Magnesium and Titanium to the mercury to promote wetting and nucleate boiling in the boiler tubes. The second implication is that the vapor generation rate and hence the heat flux level is not sufficiently high to reach the critical heat flux, sometimes referred to as the first boiling crisis, the nucleate boiling maximum heat flux, or the burnout heat flux. A specific heater surface temperature is generally related to this heat flux in earth gravity. If the heater surface temperature exceeds this level, the high associated rate of vapor generation inhibits the liquid motion to the heater surface and a decrease in the heat transfer rate takes place, hence the term maximum heat flux. This decrease takes place because of the progressive increase in the dryout of the surface, until finally the liquid is no longer in contact with the heater surface. This condition is then referred to as film boiling, since in the buoyancy of earth gravity the vapor takes on the form of a thin vapor film or boundary layer in contact with the heater, and departure of the vapor from the vicinity of the heater occurs in various ways depending on the heater surface configuration and orientation relative to gravity. The minimum heater surface temperature at which film boiling can be sustained at its corresponding heat flux is referred to as the minimum film boiling heat flux, the Leidenfrost point, or the second boiling crisis.

The so-called transition boiling region between the first and second crises can be considered as a spatially averaged combination of nucleate boiling and film boiling. In the present and prior works, the use of the transparent heater surface permits the direct viewing and assessment of the relative proportions of the dry areas on the heater surface. The circumstances of operation in the transition region taking place during pooling boiling in microgravity are considerably less well-known and less well-defined than in earth gravity, and provided the impetus for expanding the experimental parameters in the present study.

During the initial dynamic vapor bubble growth process in microgravity described briefly above, almost complete dryout of the heater surface generally takes place as a result of the evaporation of the highly superheated liquid in contact with the heater surface. This is invariably followed by an inflow of liquid which causes rewetting of the heater surface. Whether the heater surface remains wet thereafter depends on the combinations of heat flux and initial bulk liquid subcooling.

The first boiling crisis is the maximum heat flux at which nucleate boiling occurs, where the liquid continues to substantially wet the heater surface. The vapor must leave the vicinity of the heater surface and the liquid must be able to flow in toward the heater surface to sustain nucleate boiling. The first hydrodynamic model was proposed by Kutateladze (1952) on the basis of dimensional analysis, and was later given a theoretical foundation by Zuber (1958) and Chang and Snyder (1960). The second boiling crisis is that condition of film boiling in terms of the minimum heater superheat (and the associated heat flux) at which no contact between the liquid and the heater surface takes place. This can also be designated as the point at which dryout of the heater surface

is complete. Based on the hydrodynamic instability theory of Zuber (1958), Berenson (1961) developed a relationship for the heat flux at this point.

As stated above, the so-called transition boiling region between the first and second boiling crises can be considered as a spatially averaged combination of nucleate boiling and film boiling, in which the fractional proportions of film boiling or dryout change from 0 to 1 over this domain. This perspective neglects the contributions of dry areas under individual nucleation sites, if such exit. In an early work (Donald and Haslam - 1958) the fractional dry area under the vapor bubbles boiling on a horizontal wire 0.06 inches in diameter was measured in the nucleate boiling domain, up to the critical heat flux, using liquid electrical conductive measurements between the liquid and the heater surface. For pure water, with a small amount of HCl added to reduce the resistivity, it was found that a linear relationship existed between the fractional dry area under the bubbles and the heat flux, reaching a value of 50% at the critical heat flux. In the opinion of the writer, this large a value at the critical heat flux is a consequence of the departing vapor flow patterns surrounding the small horizontal cylinder heater surface, and would be considerably smaller for a flat horizontal heating surface facing upward.

Electrical impedance measurements have been used extensively since the above work for determination of the fractional wetted area in transition boiling, both for pool and forced convection boiling, primarily with water. Dhuga and Winterton (1985) provide a comprehensive review, as well as introducing the use of a new capacitative impedance procedure. The fraction of wetted area was measured in the transition boiling region for a horizontal flat surface facing upward, using a transient quenching technique with a massive copper heater to pass through this region. The results, presented in the form of fractional wet area as a function of the wall superheat, exhibit highly non-linear behavior, with considerable differences between the water and methanol used. The copper substrate body was anodized with aluminum at the boiling surface in order to have the new technique function, and it can be anticipated that this in itself would influence the boiling process.

The processes of the first and second boiling crisis, including the transition boiling regime between, can be generically designated by a single term as dryout or wetting, depending on the direction in which the inherently transient or dynamic process is taking place. Based on the inability to operate steadily in any of these domains, they are considered to be highly unstable on a local basis, if not on a global basis. These have received considerable attention in the nuclear power industry because of possible loss-of-coolant-accidents (LOCA), some of which can occur without immediate disastrous consequences. One such is described by Becker et al (1990), where considerable effort was expended in trouble-shooting following the discovery of damage to fuel elements during refueling operations. The heat transfer processes were modeled, and this disclosed shortcomings arising from the lack of sufficient understanding of the fundamentals

involved. The understanding of conditions necessary for dryout and rewetting is also important for the reliable operation of heat pipes, as pointed out in Peterson et al (1992).

When rewetting is desired subsequent to dryout, as might take place upon the loss of coolant in the nuclear reactor core, it is set in motion by gravity, either by the downward flow of the cooling medium over the heater surface or by flooding the vessel from the bottom upward. Most prior modeling of rewetting involve solutions of the transient conduction in the heater surface using a variety of presumed boundary conditions at the liquid-vapor-solid contact line. Recent examples may be found in Hewitt and Govan (1990), Duffy and Hughes (1991), and in Johannsen (1991). One frequently used boundary condition is that the wall superheat at the onset of surface rewetting is almost constant. This was observed to be the case in research conducted by Inoue and Tanaka (1991) with R-113, even though the heat transfer characteristics and rewetting mechanisms changed as the flow patters changed with the flow quality.

Unal et al (1992) have attempted to unify the Critical Heat Flux and the "quenching of hot surfaces," which can be rephrased to mean unifying the first and second boiling crisis, by relating both processes to the same governing mechanism - the ability of the liquid to contact a hot surface. The concept of a critical rewetting temperature is introduced in order to justify such a unity. Such a hypothesis based solely on current experimental observations would neglect the influence that body forces or gravity have on these processes. It was demonstrated by Merte and Clark (1964) that both the critical heat flux and the minimum film boiling heat are influenced by body forces. A further indication is given by the measurements of the liquid-solid contact in film boiling by Kikuchi et al (1992), in which such contacts are strongly influenced by both the depth of immersion or hydrostatic pressure and the bulk liquid subcooling. These both also influenced the onset of the boiling into the transition region. In an experimental study of transition boiling with high velocity forced convection by Peng et al (1992), using R-11, it was demonstrated that the length in the flow direction over which transition boiling and hence rewetting takes place decreases as either the velocity or subcooling are increased.

1.3.3 Heat Transfer

From the prior results of the Pool Boiling Experiment (PBE) in the Get Away Special (GAS), given in Merte et al (1996), the mean heat transfer behavior could be categorized as one of the following cases, depending on the mean heat flux level and initial bulk liquid subcooling:

(i) Steady Nucleate Boiling. The heater surface was continuously "wet" by the liquid, providing a continual process of apparent nucleate boiling at discrete sites on the heater surface.

(ii) Dry-Out. The heater surface essentially became completely dried out, except for a narrow region around the edges of the heater. The heater surface

temperature was rising continuously during the length of the test conducted, but a steady temperature at a high level presumably would be reached eventually.

(iii) Partial Dry-out. The heater surface became partially dried out, or partially wet, such that a quasi-steady or slowly changing fractional dry-out took place. The state of dry-out would increase at times, and then decrease, but on a slow basis, hence the term quasi-steady.

By using the mean heat flux over the entire heater surface and the mean heater surface temperature, as computed from the measured mean heater film electrical resistance, the resultant behavior of this latter case can be considered to be in the domain generally termed as transition boiling. This domain is highly unstable, with rapid changes for pool boiling in earth gravity, but appears to be reasonably stable in microgravity. Data in this domain are represented in Figure 15 of Lee et al (1997). With complete dryout in microgravity, corresponding to what is called film boiling in earth gravity, the mean heat flux level would be considerably lower than that represented in the film boiling region of this Figure 15. What is of particular note here, however, is the considerable enhancement of the nucleate boiling process in microgravity over that in earth gravity. This is attributed to the action of the liquid layer underlying the large bubble somewhat removed from the heater surface. It was noted that definite relationships exist between the transient mean heater surface temperatures and the heat transfer coefficients, with the surface temperature decreasing as the heat transfer coefficient increases, and vice versa. These serve to indicate, qualitatively at present, the modes of heat transfer between the heater surface and fluid: conduction to the liquid; nucleate boiling; conduction to the vapor phase (termed dryout); and combinations of the three forgoing mechanisms based on the fractional part of the heater surface over which each is acting. From the photographic data taken through the transparent heating surface from the underside, it is possible to discern quite distinctly those portions of the heater surface on which dryout has taken place.

2. EXPERIMENTAL CONCEPTS AND PARAMETERS

The study conducted here is intended to assist in extending the understanding of the mechanisms of nucleate pool boiling. Because of the complexity associated with the conduct of research in a microgravity environment it is essential to establish a well defined "bench mark" which will not require repeating, insofar as is practicable in view of present understandings. The availability of a reasonably long period of quiescence prior to the onset of each test means that the initial state at the onset of heating and at the onset of boiling (nucleation) can be well-defined. The availability of relatively long test periods for each run, with a maximum value of 4 minutes selected

here as a compromise, permits the combinations of low heat flux and subcooling that require more than the 5 seconds previously available in a drop tower for the inception of boiling, and also permits the observing of long-term vapor dynamic behavior following the transient bubble growth. The 4 minute maximum was deemed necessary as the heat flux levels were reduced below the prior minimum, which heretofore had rendered the 2 minute period as adequate.

The elements of pool boiling for which research conducted under microgravity would advance the basic understanding are stated in brief here:

(i) Nucleation or onset of stated boiling. Prior research has indicated that both heater surface temperature and temperature distribution in liquid are necessary to describe nucleation, in addition to the character of the heater surface itself.

(ii) The dynamic growth of a vapor bubble in the vicinity of the heater surface. This includes the shape as well as motion of the liquid-vapor interface as growth is taking place. These are influenced by the liquid temperature distribution at the initiation of growth.

(iii) The subsequent behavior of the vapor bubble. This includes the motion, whether departure takes place, whether the heater surface remains wetted by the liquid or dries out, and the associated heat transfer.

Each of the specific features of the experiment were selected so as to provide data which will be consistent with and maximize the objectives of improving the basic understanding embodied in these elements. These features are described individually below.

2.1 Geometry and Configuration

(a) Pool boiling. This eliminates the complications associated with having an external flow field superimposed on that generated by a growing/collapsing vapor bubble.

(b) Large flat heater surface. A flat surface avoids poorly defined local surface tension effects associated with curved interfaces, and a transparent substrate can permit viewing from beneath the heater surface. A size as large as possible consistent with other constraints is desirable in order to minimize edge effects, and to permit a reasonable degree of axial symmetry of the vapor bubble as it grows to a quasi-steady condition. Additional considerations associated with large flat heater surfaces are:

(i) With heating from curved surfaces, different liquid flow patterns will occur during bubble growth depending on whether the liquid is on the convex or concave size.

(ii) With flat surfaces, which may also be approximations of curved surfaces, the orientation with respect to the body force vector will affect the flow behavior, down to some (as yet) unknown body force level.

(iii) The fluid motion with large surfaces will differ depending on whether the surface is heated uniformly or locally.

One further facet of vapor bubble nucleation and growth as influenced by surface tension and related to geometry can be mentioned here. The superheat that the liquid acquires in the boundary layer adjacent to the heater surface can be considerable, prior to nucleation. It is thus possible for the vapor formed initially to completely envelope the heater surface. With certain configurations such as small wires or cylinders it is possible that subsequent surface tension effects will maintain a stable "pseudo" film boiling process only because of the particular geometry used. It is expected that even if film boiling becomes suppressed to nucleate boiling on a small wire or cylinder, thermocapillary and surface tension effects and the resulting heat transfer will be quite different than with flat surfaces. Observations made by Weinzierl and Straub (1982) that pool nucleate boiling is uninfluenced by changes from earth gravity to microgravity are believed to be a result of the large surface tension effects associated with the fine wire used, so that buoyancy is indeed relatively unimportant.

(c) Transparent heater surface. This permits the observation of the detailed behavior of the boiling process from beneath the heating surface, including rewetting of the heater surface and possibly the microlayer behavior, without distortions due to intervening liquid-vapor interfaces. Simultaneous viewing of the behavior of the liquid-vapor interfaces from the side provides details otherwise not observable.

(d) Thin-film heater. Using the technique of a thin gold film as a simultaneous heater and resistance thermometer provides a well-defined heat flux and mean temperature at a precise location at the heater surface, as well as a transparent heater surface.

2.2 Fluid

The fluid to be boiled must be non-conducting at present. The fluid is in direct contact with the electrical resistance heat source, and a conducting fluid such as water would quickly destroy the thin film surface. For energy conservation in the conduct of the experiment and convenience in comparing results with ground tests it is desirable that the fluid have a boiling point in the vicinity of earth ambient temperatures at near atmospheric pressures. It is further desirable that the fluid used initially have wetting characteristics with the heater surface such that the contact angle is

relatively small, in order to evaluate fluids expected to be early candidates for space use, such as cryogenic liquids. The fluorocarbon R-113 meets these requirements, and its properties are well established.

2.3 Controlled Variables:

(a) Pressure. This defines the liquid saturation temperature, and maintaining it constant keeps the temperature at the liquid-vapor interface constant at the saturation level during the transient process. The pressure level also defines the initial liquid subcooling.

(b) Initial uniform temperature in the bulk liquid. This permits the precise calculation of the temperature distribution in the liquid at the onset of boiling, in the absence of buoyancy.

(c) Step change in a uniform heat flux. This permits the ready computation of the temperature distribution in the liquid at the time of nucleation. A constant imposed heat flux provides a well-defined temperature gradient in the liquid at the heat transfer surface. Additionally, it is possible to construct all other desired functional behaviors in heat flux from combinations of step changes.

(d) Length of test. Each individual test should be as long as possible consistent with compromises arising between the internal volume of the test vessel, heater surface size and heat flux, so that a reasonably quasi-static condition can be attained when the early dynamic growth transients are completed. Additionally, certain liquid temperature distributions at the time of nucleation will only be possible with low levels of heat flux, which will require relatively long test periods to achieve nucleation. Independent control of the initial liquid subcooling and imposed heat flux permit the independent variation of the transient temperature distribution in the liquid.

2.4 Measured Parameters:

(a) Bulk liquid temperature distribution. This is necessary to be assured of the uniformity of the initial temperatures.

(b) Transient temperature of the thin film heater surface. During the non-boiling phase, this serves as an indication of the presence/absence of natural convection effects. During the boiling phase this provides a means for computing the net mean heat flux to the boiling fluid. It also provides a measure of the effectiveness of the boiling heat transfer process.

(c) Local system acceleration. This is necessary to assess the presence/absence of uncontrolled acceleration forces acting on the experimental vessel.

(d) Precision current/voltage drops across the thin film electrical heater. This permits computation of the heater resistance and hence mean heater surface temperature, as well as the heat flux.

(e) Photography. This enables the determination of the time interval between the onset of heating and boiling, along with the transient growth of the vapor bubble and its subsequent motion, as a function of the initial liquid temperature distribution, governed by the heat flux and initial liquid subcooling.

The specific technical requirements for the experiment, taken from the Addendum to the Science Requirements Document of June 1994, are listed in Table I. These are identical for each of the two flights with the exception of the Test Heat Flux and Nominal Test Temperature levels, both of which are listed. The Test Heat Flux levels in the left hand column were used in PBE-IIB on STS-72, with the Nominal Test Temperature level of 37.8°C; The Test Heat Flux levels in the right hand column were used in PBE-IIA on STS-77, with the Nominal Test Temperature level of 48.9°C.

The vapor-pressure equation and coefficients used for the R-113 are given in Table II. The commercial R-113 was purified and degassed by distallation, filtering, and freezing under a vacuum on stainless steel fins cooled to liquid nitrogen temperatures. The apparatus used is shown schematically in Figure 2.1. The distillation was repeated, and followed by measurement of the vapor-pressure under equilibrium conditions. The R-113 was deemed to be adequately degassed when the measured vapor-pressure corresponded to that given by the equation in Table II to within ±0.025 psia for temperatures measured to within a calibrated accuracy of ±0.1°F in the laboratory.

The Resistance-Temperature relationship for the heater surface was determined by calibration over the anticipated temperature operating range prior to installation in the experiment test vessel. Prior experience had demonstrated that a linear relationship was entirely adequate. Although maximum laboratory absolute measurement uncertainties of ±1°F(±0.6°C) in the mean heater surface temperatures were attained, these were increased to ±3°F (±1.7°C) for the space experiments. However, instrumentation equipment sensitivities were requested to detect changes in heater surface temperatures of ±1°F (±0.6°C), if not the absolute uncertainty. To reduce the uncertainties, a single point calibration was conducted prior to each test run of the test matrix,

using the prevailing equilibrium system temperature as an anchor point of the linear calibration curve. A post-flight calibration was conducted following the STS-77 (PBE-IIA), and included the calibration of the power supply measurements simultaneously. The change in the R-T slope was negligibly small, and the absolute shift was compensated by the procedure of a single-point calibration prior to each run.

Table I

Specific Technical Requirements

Parameter	Requirement
Test Fluid	Fluorocarbon R-113
Heating Surfaces	19.05mm x 38.1 mm (3/4" x 1-1/2") Gold on Quartz (7.25 cm^2) Nominal thickness corresponding to a resistance of 3.8 ± 0.2 ohms (Approximately 400 Angstroms), uniform to ± 5% desired.
Test Heat Flux	2 w/cm^2 (14.5 w) 2 w/cm^2 (14.5 w) 4 w/cm^2 (29.0 w) 1 w/cm^2 (7.3 w) 8 w/cm^2 (58.0 w) 0.5 w/cm^2 (3.6 w)
Test Chamber	15.2 cm (6") Dia. x 10.2 cm (4") High
Temperature Uniformity	± 0.22°C (± 0.4°F)
Nominal Test Temperature	48.9°C (120°F); 37.8°C (100°F)
Pressure Control	± 690 N/m^2 (± 0.1 psi)
Heater Power	Constant voltage ± 1%. Heater calibration current should not raise heater temperature more than 0.11°C (0.2°F).
Temperature Sensor	12 Sensor Locations 3 Vicinity of each Heater Surface 3 in Bulk Liquid 2 on the Rear of Heater Substrate 1 in surrounding area behind substrate
Data Requirements	V, I, Time...(19 parameters).
Heater V & I	± 0.1% Meas. Accuracy, but with a sensitivity of ± 0.03% x a full scale
Temperatures	± 0.06°C (± 0.1°F) Meas. Accuracy
Pressure	± 345 N/m^2 (± 0.05 psi) Meas. Accuracy
Acceleration (3 Axis) Data Requirements	Levels less than 10^{-3}g desired Time correlated to experimental elapsed time Sample Rate - 10 Hz Accuracy - ± 10^{-4} Range - 10^{-2} thru 10^{-4}g Frequency - D.C. thru 2.5 Hz
Photography	100 pps, 10 pps, 0.18 mm (0.007") Resolution
Clock	Nearest 0.01 Sec. Elapsed Time

Table II

Coefficients for the Vapor-Pressure Curve for R-113

(From Mastroianni et al, 1978)

$$\ell n\, p = A + \frac{B}{T} + CT + DT^2 + (E)\left[\frac{(F-T)}{T}\right]\left[\ell n(F-T)\right]$$

where:

p = pressure = psia
T = Temperature in °R = °F + 459.67
A = + 23.428348
B = -9095.6033
C = -0.012548607
D = +5.3391227 x 10^{-6}
E = + 0.14025795
F = 878.48416
ℓnx = Natural logarithm of argument x.

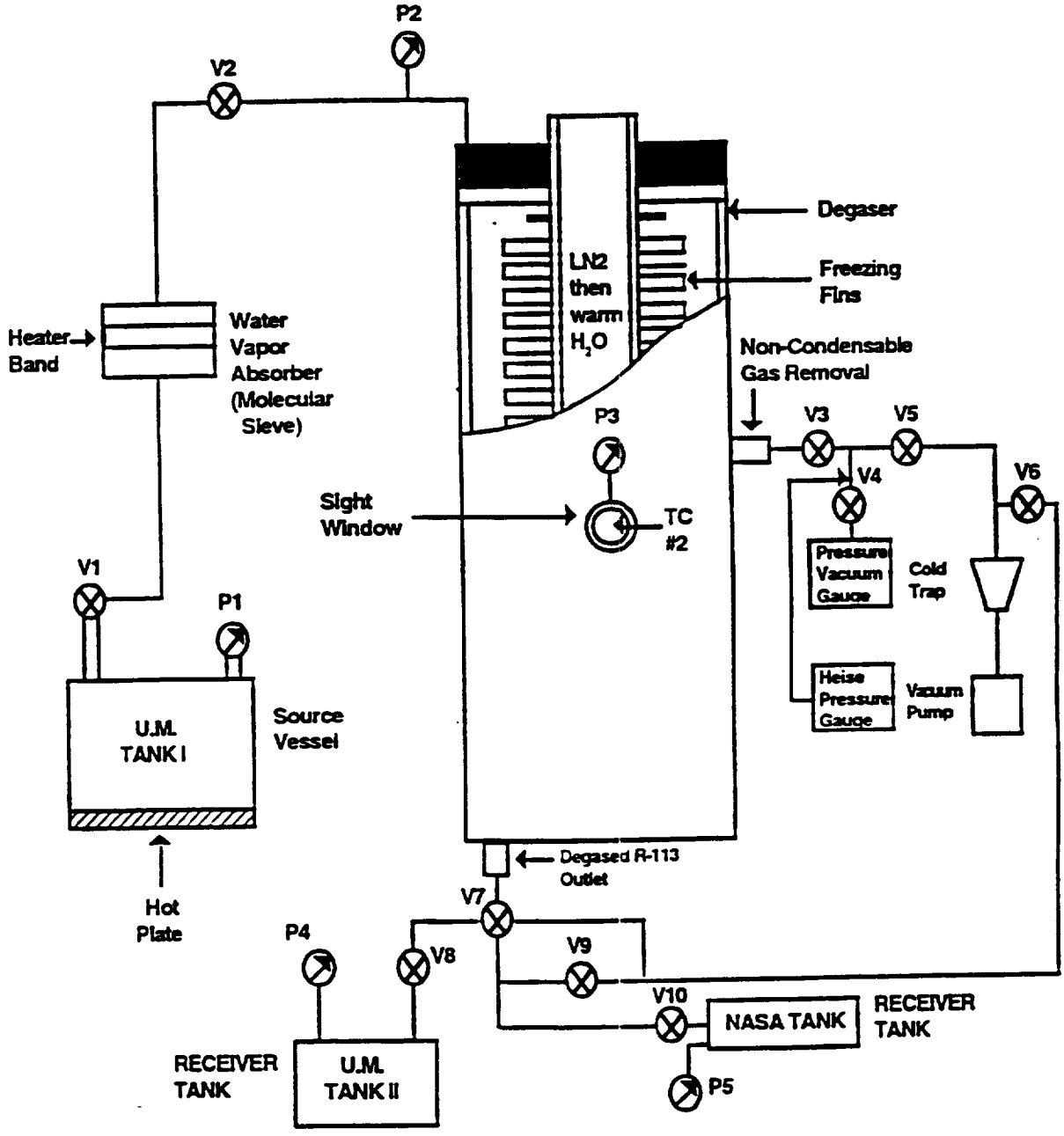

Figure 2.1. R-113 Degassing Unit Schematic.

3. HARDWARE DESCRIPTION

3.1 Heater Surface

A sketch of the transparent gold film heater is shown in Figure 3.1. Two separate heaters are mounted on each surface, identified as the primary and backup heaters, and configured so that should the primary heater fail the backup heater is automatically activated for the next test run of the matrix. A nominal film thickness of 400 Angstroms in the heater section of size 0.75" x 1.50" (19.1 mm x 38.1 mm) corresponds to a nominal resistance of 3.8 ohms, and provides the desired transparency for viewing the boiling process from beneath. Power to the heater is provided by Silver-Zinc batteries, and the voltage is controlled, with the voltage drops across the potential taps and the calibrated shunt resistor (for the current measurement) stored in the data acquisition system. The instantaneous heat flux input and the mean heater surface temperature are computed from the voltage drop across the potential tap and the current.

The backup heater was used in both the PBE-IIB and IIA (STS-72 and -77), which is the same heater used from the onset in the PBE-IB (STS-57) because of the presence of a persistent premature nucleation site on the primary heater, observed during pre-flight testing.

Calibration of both the primary and backup heaters took place prior to installation in the test vessel over temperature ranges of 66°F to 152°F (18.9°C to 66.7°C). Only the heaters used in the flight experiments were calibrated following the completion of the experiment. The electrical resistance - temperature follows a linear relationship within ±1°F (±0.6°C), well within the precision tolerances specified.

A slope - intercept equation of the form:

$$\overline{T} = A + B \times \overline{R} \tag{3.1}$$

is used to compute the mean heater surface temperature $\overline{T}$ from the mean resistance $\overline{R}$ measured. The coefficient B is the slope, while A is the intercept at R=O. A single-point calibration is conducted just prior to each Run of the test matrix, using the bulk liquid temperature measured with a calibrated thermister in the immediate vicinity of the heater surface, 1 mm away. This is used to modify the coefficient A for each Run, using an appropriate value of B, which generally was found to change relatively little with a suitably aged heater surface. The surfaces were calibrated again over the entire temperature range following the experiments, and a new value of B obtained. The single-point calibration procedure significantly reduces the effects of any large changes in B taking place over a period of time. The values of A and B for each of the experiments are given in Table III below. It is noted that a significant change took place in the coefficient B for the Backup Heater in the PBE-IB. This was a consequence of insufficient operation with this heater prior to the space experiment, and so the post-flight value of B was used for data reduction.

It was determined that a difference of only 1.5°F (0.8°C) existed between the single point calibration and the post-flight calibration values. The post-flight calibration of the STS-72 experiment (PBE-IIB) differs from that of the STS-77 experiment (PBE-IIA) because the heater power supply and heater surface are calibrated as integral units, and a different heater power supply was used between these two experiments because of the large differences in power requirements.

Table III. Heater Surface Calibration Coefficients

PBE-IB (STS-57) Pre-Flight	A(°F)	-1489.44
	B(°F/ohm)	460.635
PBE-IB (STS-57) Post-Flight	A(°F)	-1356.92
	B(°F/ohm)	427.32
PEB-IIB(STS-72) Pre-Flight	A(°F)	-1375.38
	B(°F/ohm)	433.58
PBE-IIB(STS-72) Post-Flight	A(°F)	-1322.05
	B(°F/ohm)	420.09
PBE-IIA(STS-77) Pre-Flight	A(°F)	-1369.08
	B(°F/ohm)	430.75
PBE-IIA(STS-77) Post-Flight	A(°F)	-1379.77
	B(°F/ohm)	435.06

3.2 Test Vessel

A schematic of the test vessel is shown in Figure 3.2, together with the hardware concepts necessary to provide a constant pressure and an initially uniform fluid temperature during each Run. Although the stirrer was intended to be activated only between the various runs of the matrix in order to promote the uniformity of temperature of the fluid, it was also activated toward the end of several runs so as to observe its influence on the vapor bubbles and, in some cases, on the heat transfer.

Figure 3.3 shows the locations of the various sensors used to determine the behavior of the boiling process. PRHV and PRHI are the primary heater voltage taps and current readings, while BRHV and BRHI are the respective values for the back up heater, which was used for both PBE-IIB and -IIA. TM01 - TM03 and TM07 - TM09 are thermisters above the primary and back up heaters to measure the respective fluid temperatures, at locations 1 mm, 5 mm, and 10 mm above the center of each heater. The thermister beads have a maximum diameter of 0.6 mm, and are stated by the manufacturer as having a time constant of 23 msec when plunged into water. The respective locations of TM04 - TM05 - TM06 are given in Figure 3.4 as A, B and C, and are provided to check the uniformity of fluid temperatures prior to the beginning of each Run.

Thermisters TM12 and TM11 are cemented to the quartz substrate on the side opposite the gold film, at the center of the primary and back up heaters, respectively, while TM13 is in the canister air space very near the quartz substrate backside.

Figure 3.5 gives the relative locations of the internal components of the test vessel, including the viewing and lighting windows. The lighting is diffused internally for maximum clarity. The maximum internal dimensions of the R-113 chamber are also given, as 14.48 cm diameter by 11.5 cm long, which implies that the maximum diameter of a vapor bubble that can be accommodated without pressing on the heater surface is about 12 cm.

Figures 3.6 and 3.7 present the side and front views of the entire system components within the GAS canister, with the optical path followed to the 16 mm camera, which has a 400 ft. film capacity. This gives a total of approximately 18,000 frames, which must be budgeted among the various Runs.

3.3 Accelerometer System

A Space Acceleration Measurement System (SAMS) type triaxial accelerometer head is included in the payload, shown in Figure 3.7. This provides accelerometer data in the direct vicinity of the test chamber. The use of an internal accelerometer also eliminates the need to correlate experiment data with a remote acceleration measurement system. Three Sunstrand QA2000-030 accelerometers are used. The manufacturer resolution specification for this model is

1 micro-g, and the accuracy is given as $\pm$100 micro-g, found by using the root sum of squares of the various stabilities (thermal, shock and time).

A typical correlation between the accelerometer outputs and the local and vehicle coordinates is given in Figures 3.8 and 3.9, for PBE-IA on the STS-47. The upper right view in Figure 3.9 is taken through the heater surface, viewed from left to right in the right side of Figure 3.5, while the upper lift view is taken from the side, viewed from the bottom side of Figure 3.5. The coordinate directions shown in Figure 3.9 are the same for all the space experiments.

3.4 Optical System

The views in the upper part of Figure 3.9 are obtained by combining the images, as illustrated in Figure 3.6. Also within the camera field of view, seen in Figure 3.9 are LED timing lights for synchronization with the Data Acquisition Unit. The binary code used for time is given in Figure 3.10.

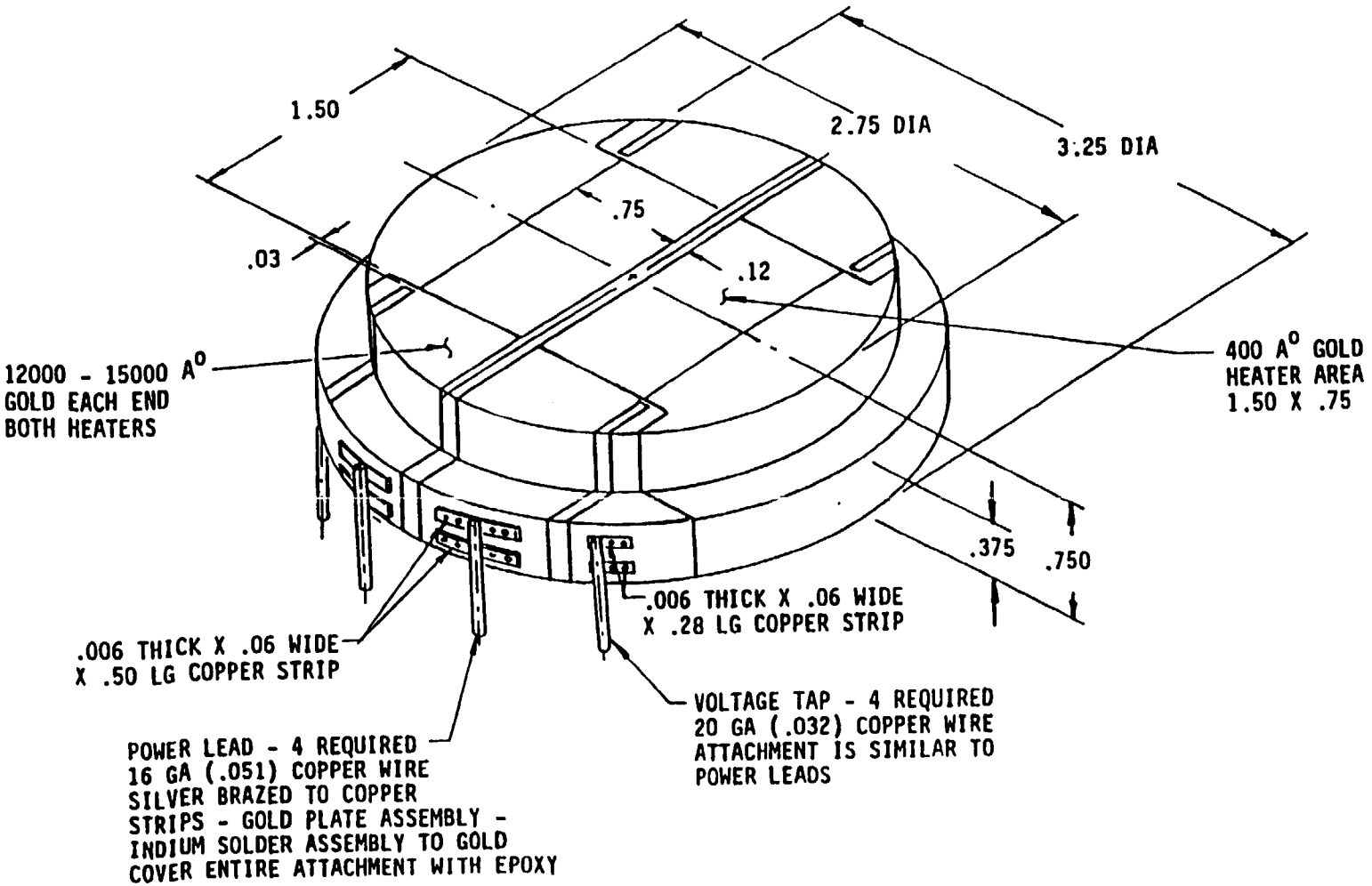

Figure 3.1. Transparent gold film heater/resistance thermometer on quartz substrate.

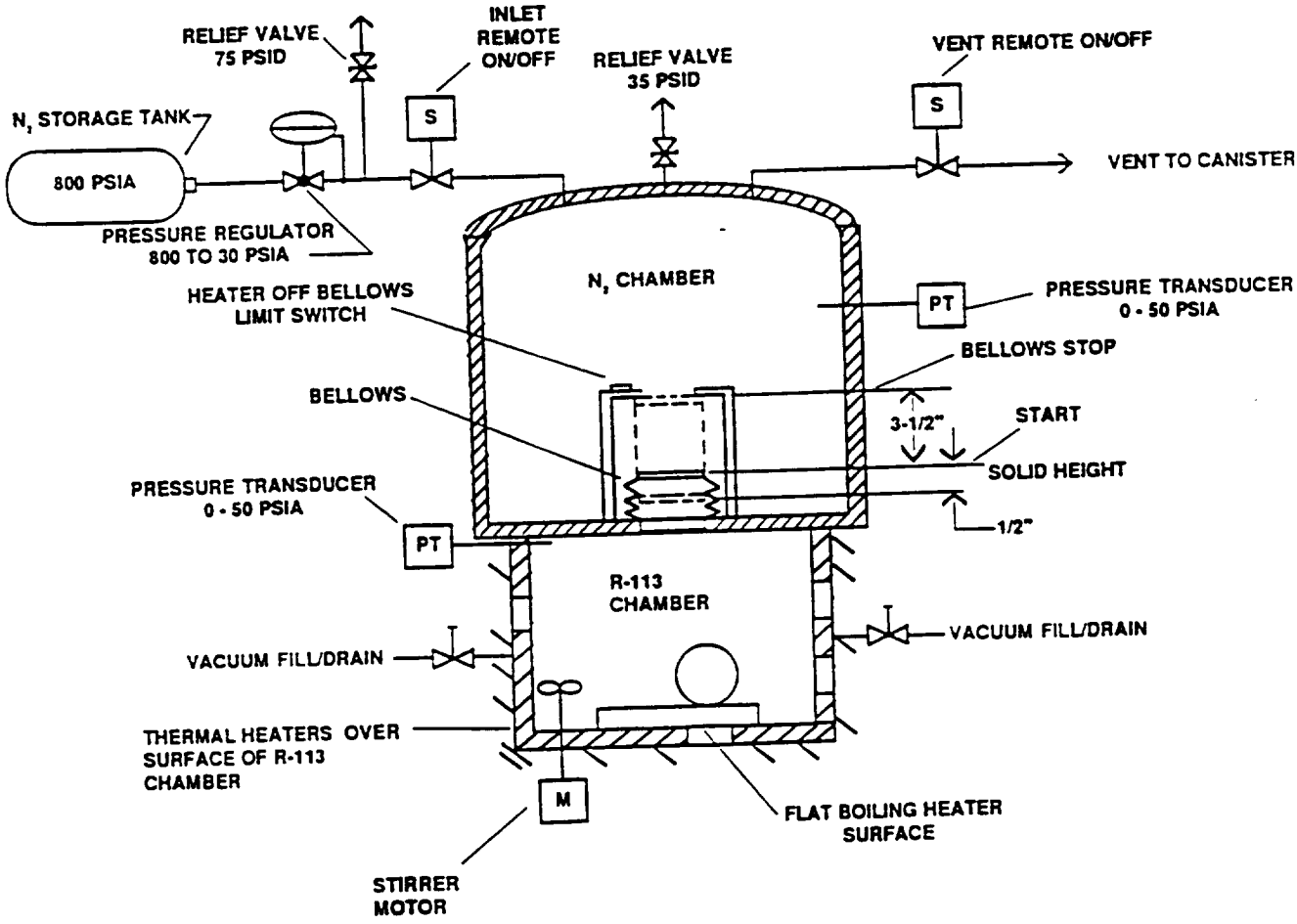

Figure 3.2. Schematic of Test Vessel with concepts to provide constant pressure and initially uniform fluid temperature.

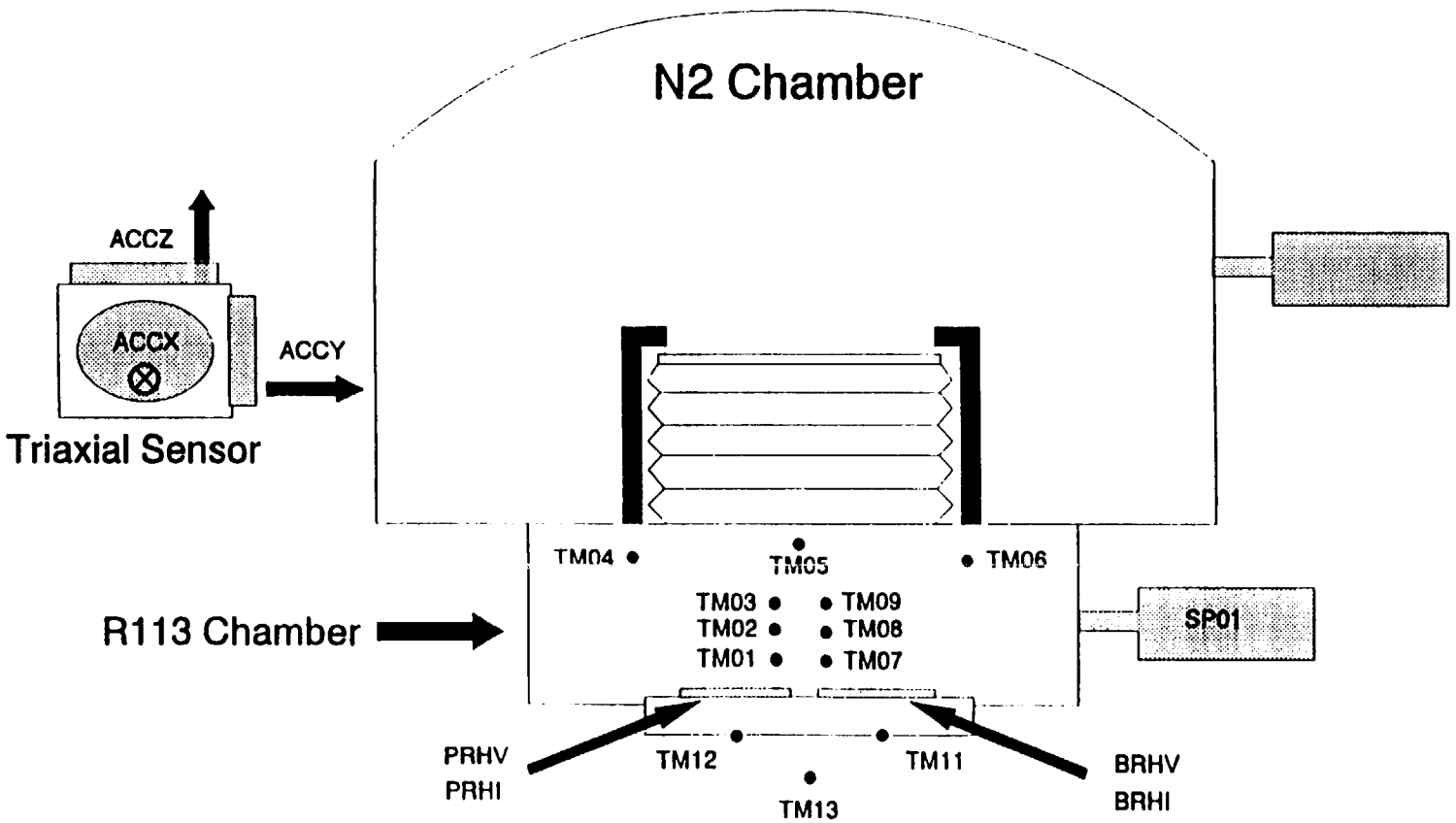

Figure 3.3. Location of Sensors for Scientific Analysis.

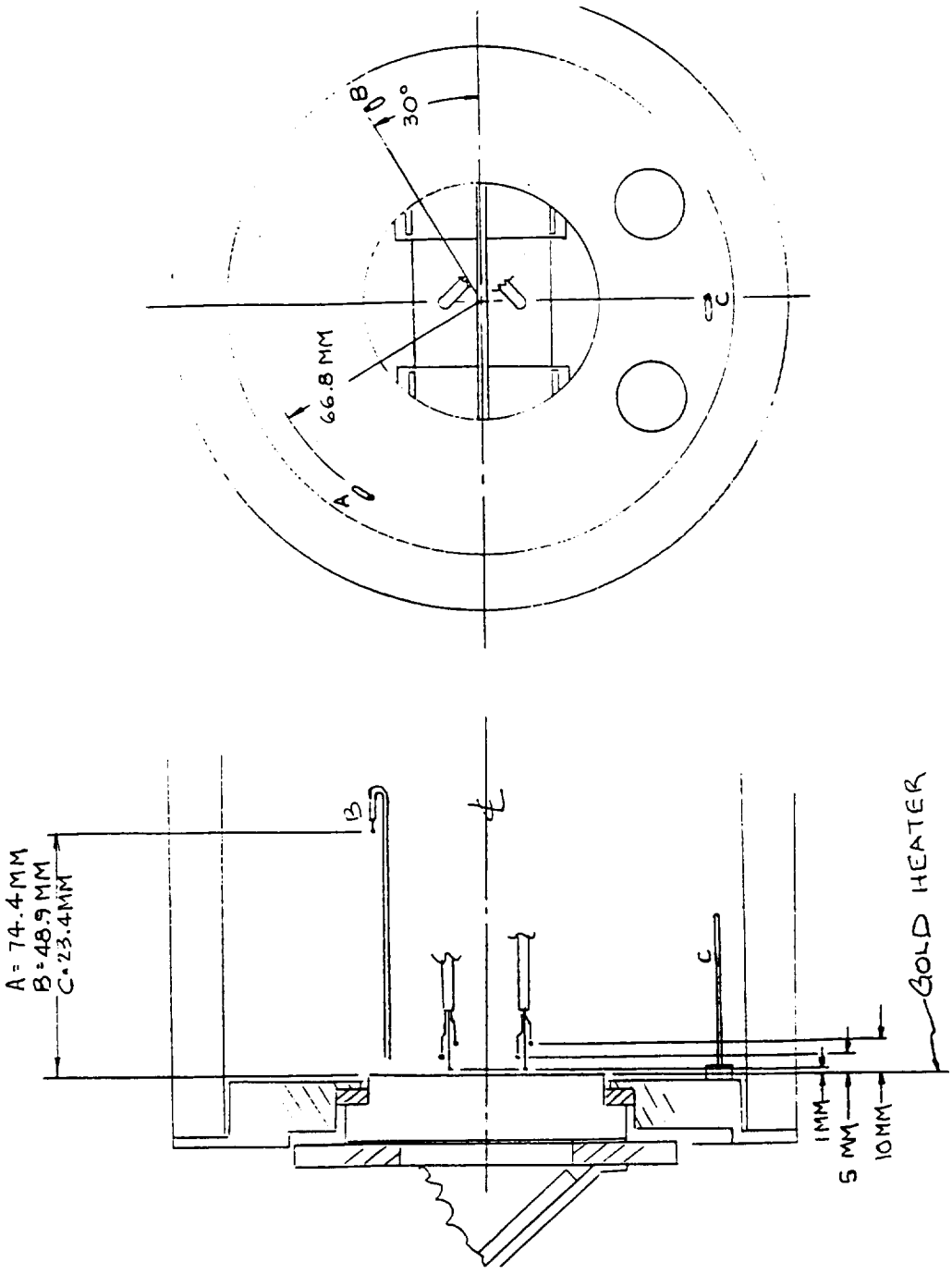

Figure 3.4. Locations of R-113 fluid thermistors in test vessel.

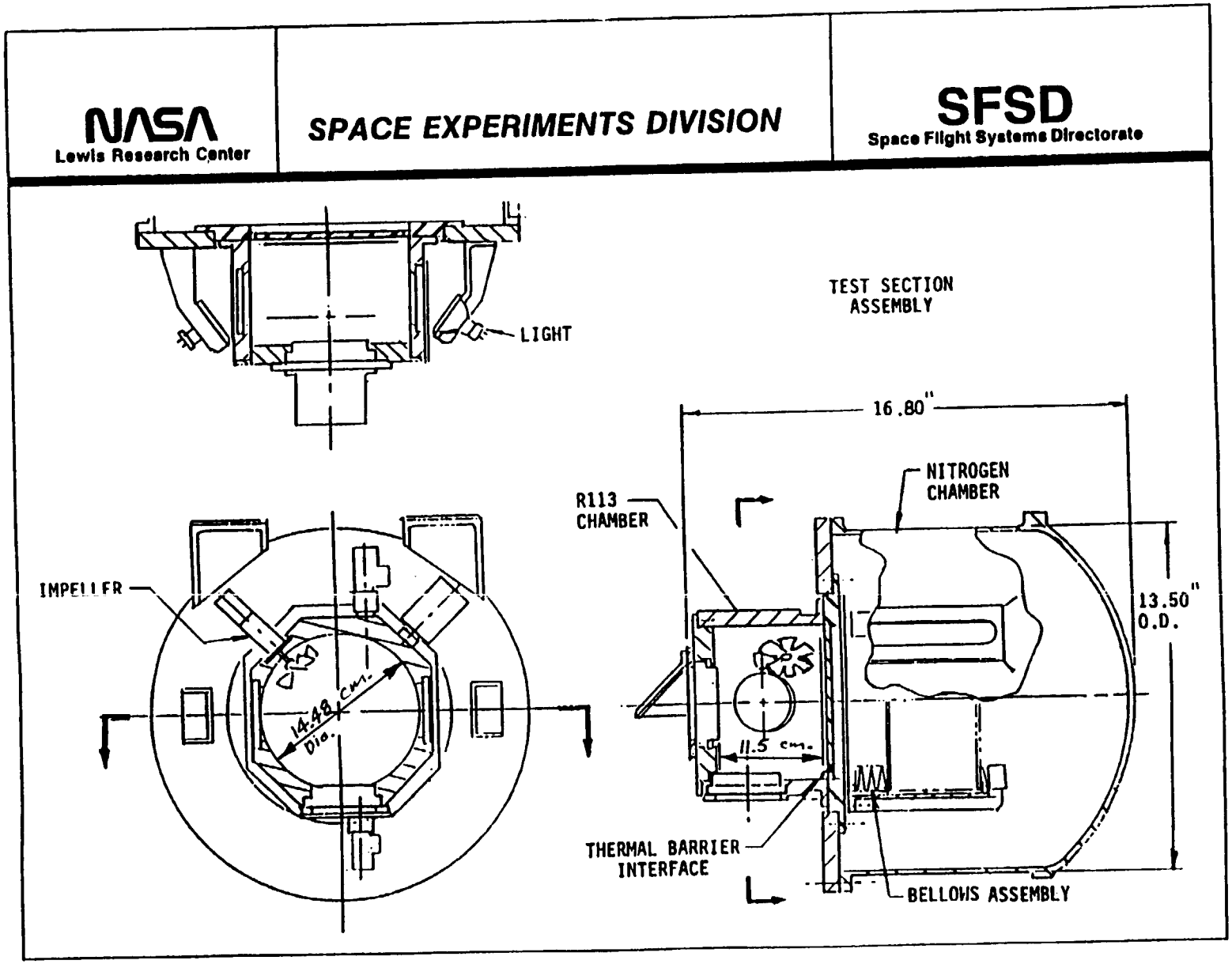

Figure 3.5. Test vessel. Relative locations of internal components, lights and viewing windows.

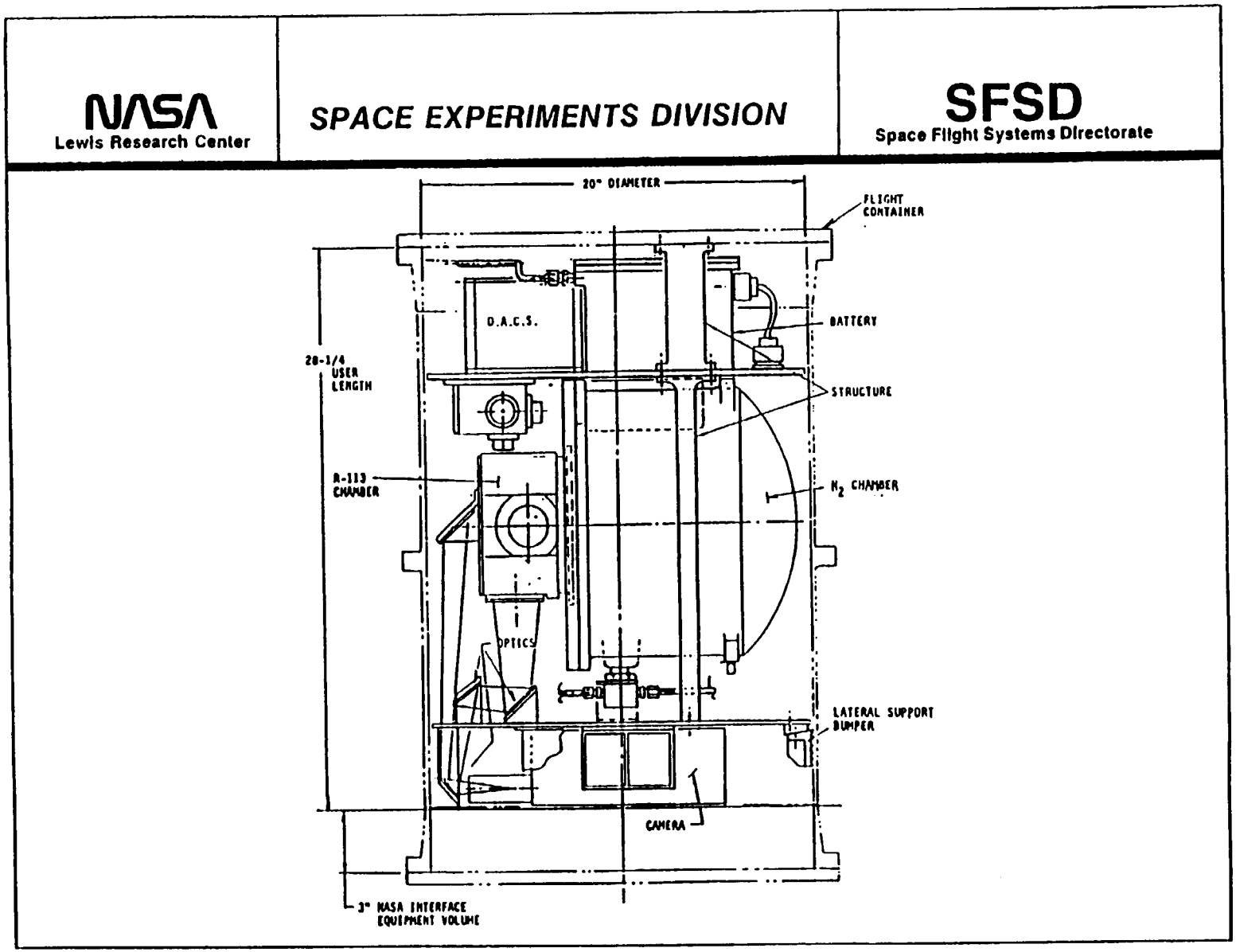

Figure 3.6. PBE components in GAS canister. Side view.

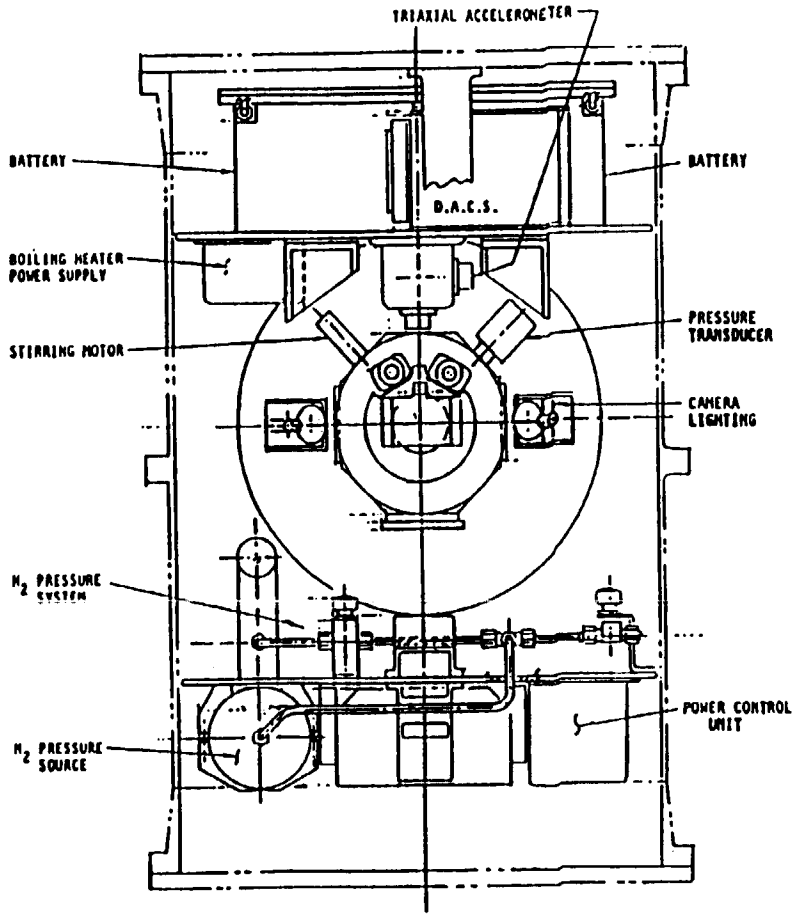

Figure 3.7. PBE components in GAS canister. Front view.

PBE/STS AXIS TRANSLATION

SED-PBE-DOC-028

PBE	STS	SAMS
+Y	+X	+Y
+Z	+Y	-X
+X	+Z	+Z

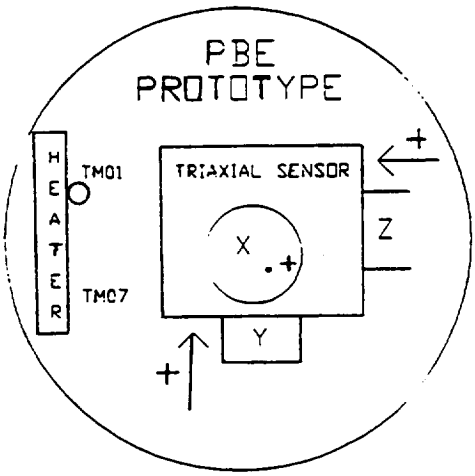

+Z signal indicates that acceleration is in direction indicated above.
e.g., - this decreases buoyancy moving vapor bubble away from heater, or would move the vapor bubble toward heater.

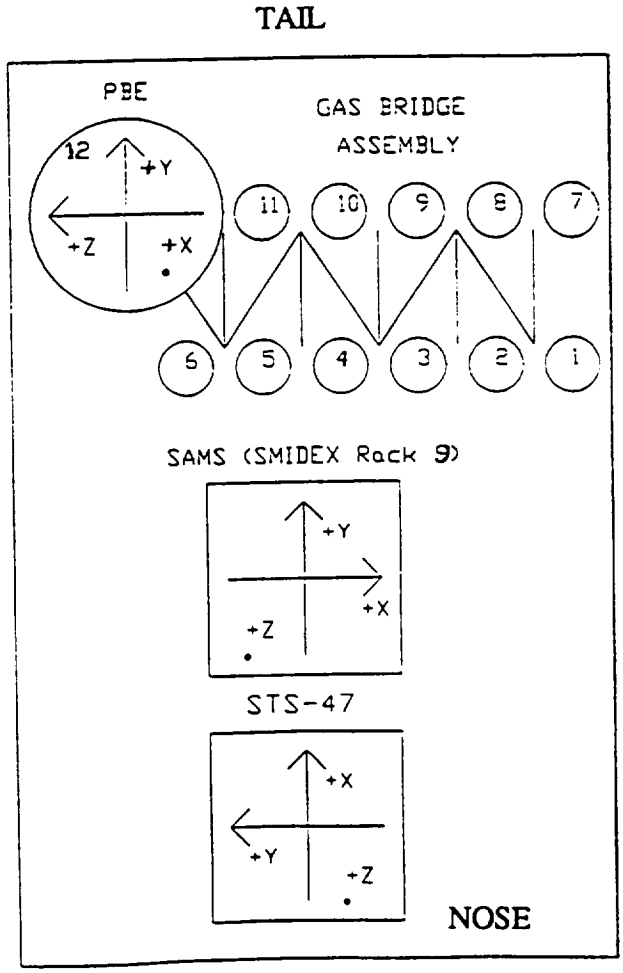

Figure 3.8. Typical correlation between coordinates of the PBE accelerometer and SAMS STS units. Above applies to PBE-IA (STS-47).

Acceleration coordinate for the space experiment

Example

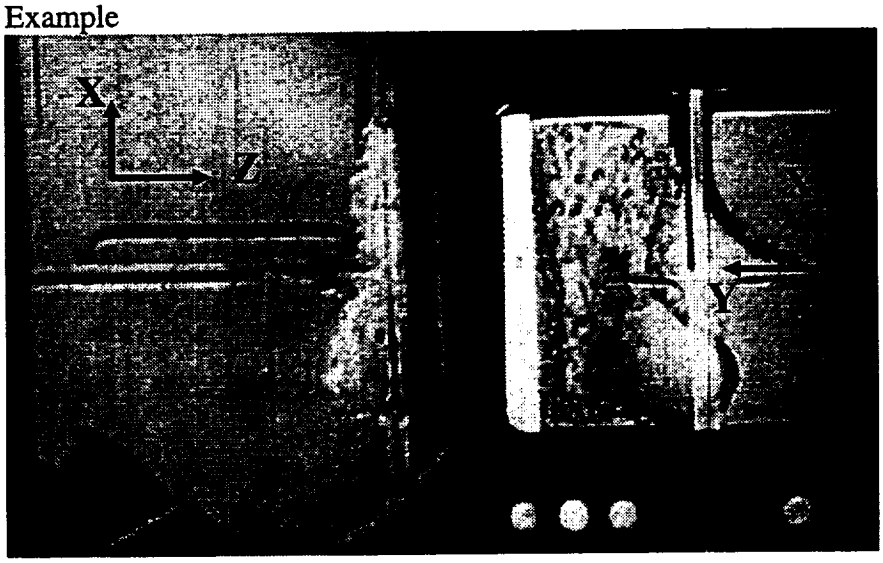

* The above figure shows both side view in left hand side and bottom view in right hand side.

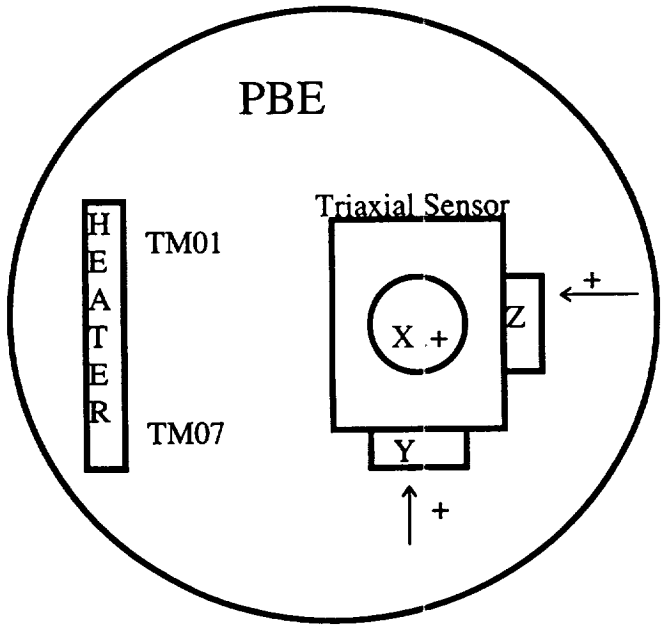

Figure 3.9. Correlation between PBE-1A accelerometer and photographic view on STS-47. Primary heater in use on left side.

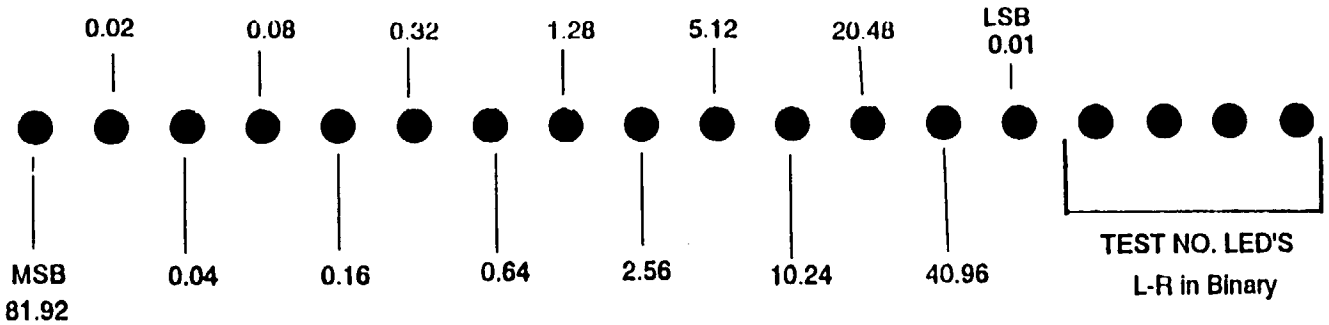

Figure 3.10. Scheme for LED timing lights in camera field of view.

4. TEST MATRICES

The test matrices followed for the PBE-IIB-IIA on the STS-72-77 are given as Tables IV and V, respectively, below. The nominal levels of heat flux input (in w/cm^2) and the initial bulk liquid subcooling (in °F) are given for each Test Run, followed by the timing sequences used. The test is initiated with the heater power at 10 seconds. The camera is operated at the maximum speed of 100 pps in the time domain when nucleation is expected to occur in microgravity, based on the prior drop tower testing and prior space experiments, and then followed by operation at 10 pps during the remainder of each Experiment Run for PBE-IIB. The total number of frames in a 400 ft. roll of 16 mm film is approximately 18,000, so careful consideration was given as to how these were divided amount the various Runs in order to maximize the opportunities for new knowledge. For PBE-IIA, the camera was run only at 10 pps, since the uncertainty of the nucleation time was too large with the low levels of heat flux used here.

The early bubble growth following nucleation was not captured at 100 pps for Run No. 2 of PBE-IIB (STS-72), with nucleation occurring at t* = 25.44 sec. (15.44 +10), while the 100 pps took place during the 15-25 sec. interval, nor was it captured in Run No. 5, with t* =25.02 sec. (15.02 +10), while the 100pps took place during the 15-25 sec. interval. In both of these cases nucleation occurred just following the time when the camera speed was reduced to 10 pps. The subcoolings were considerably larger than that used previously, which increased the heating period more than anticipated. Since these so-called nucleation delay times were considerably longer than the 5 second microgravity period in the NASA-Lewis Research Center vacuum drop tower, it was not possible to confirm the times prior to the space experiments.

The nucleation points were missed by considerably larger margins for the 100 pps camera speed period in Run No's 6 and 9 in PBE-IIB (STS-72). The nucleation in Run No. 6 occurred at t* = 67.64 sec. (57.64 + 10) while the 100 pps photography took place in the interval 30-50 sec. This run had the same larger subcooling of 30°F as Run No. 5, but the nominal input heat flux was only one-half as large, resulting in a magnification of the effect of subcooling, compounded by the effect of pressure on nucleation, unrecognized at that time. This is clarified by the discrepancy in Run No. 9.

Run No's 7, 8, 9 in PBE-IIB (STS-72) are identical to Run No's 1, 2, 3 in PBE-IB (STS-57) in the nominal levels of heat flux and subcooling used, except that the nominal bulk liquid temperature was 100 °F (37.8 °C) instead of 120 °F (48.9 °C) for the latter case, in order to achieve the higher levels of liquid subcooling desired without modifying the pressure control system. This had the effect, of course, of having these two sets of experiments operate at different pressure levels, even though the heat flux and liquid subcoolings were the same. A direct

comparison is given in Table VI below between the corresponding results of Run No. 3 of PBE-IB (STS-57) and Run No. 9 of PBE-IIB (STS-72), in which the identical hardware is used, but the system pressure is different. In reducing the system pressure from 149.26 kPa to 110.66 kPa the nucleation delay time (the interval between the onset of heating and nucleation) increased from 23.63 sec. to 62.39 sec., with a corresponding increase in the heater surface superheat at nucleation from 37.0°C to 59.8 °C. The analysis of the influence of system pressure on nucleation is presented in Merte and Lee (1997), and more detailed results will be given below.

The repressurization in Run No. 6 of Table IV should have taken place in Run No. 5. As a consequence, this repressurization took place before the onset of nucleation, and the system pressure and bulk subcooling were different than originally planned, and is as given in Table IV. Run No. 6 in Table IV is a virtual repeat, although inadvertent, of Run No. 3. Detailed comparisons will be given below.

As can be noted in Table V, the camera speeds for PBE-IIA on STS-77 were all maintained at 10 pps, since the imposed heat flux levels were all at q_t=2 w/cm^2 or lower, and the nucleation delay time uncertainty was too large to warrant the use of higher framing rates. Nucleation did not take place at all for Run No. 3, with the lowest imposed heat flux of q_t = 0.51 w/cm^2 and the large level of subcooling ΔT_{sub} = 11.0°C, in spite of an active heating time of 240 sec. The mean heater surface superheat at the end of the heating time reached only $\Delta T_w^* \cong$ 12 °C. For the same low level of heat flux but lower subcooling levels, the nucleation delay time for Run No. 6 was t* = 190.5 sec., and for Run No. 9 was t* = 215.2 sec. The corresponding bulk liquid subcoolings were ΔT_{sub} = 2.7°C and ΔT_{sub} = 0.2°C, respectively.

The stirrer was activated in a number of cases near the end of the Runs in order to determine the influences of the relatively weak random liquid motion on the vapor bubble behavior in microgravity, initially attached to the heater surface. Qualitative effects on the heat transfer were also obtained. For Runs with subcooled liquids, the stirrer operation produced rapid condensation of the vapor bubbles, which otherwise persisted for long periods of time because of the low thermal conductivity of R-113.

The repressurizations taking place with the initially saturated liquid case in Run Nos. 7-9 of PBE-IIA (STS-77) were planned in order to obtain additional data for vapor bubble collapse in microgravity. However, in these cases the collapse process became chaotic; surface tension forces were not sufficient to provide a reasonably smooth single vapor bubble.

Pre-flight ground tests for PBE-IIB (STS-72) were conducted conforming to the test procedure and matrix given in Table IV with the heater surface in both the inverted position, at

$a/g = -1$, and in the normal upward facing position, at $a/g = +1$, in order to confirm that the system components functioned properly, and to provide normal gravity data with which to compare the microgravity boiling behavior. No post-flight tests were conducted with this matrix because of the time requirements necessary to prepare the same hardware for the subsequent space experiment.

Both pre-flight and post-flight ground tests for PBE-IIA (STS-77) were conducted conforming to the matrix given in Table V, with the heater surface in both the inverted position, at $a/g = -1$, and in the normal upward facing position, at $a/g = +1$, to confirm that the system operated reproducibly following the space flight. The data are included in the Appendix.

PBE Flight-System Matrix (STS-72)

RUN #	HEAT FLUX W/CM^2	SUBCOOLING (^0F)	HEATER POWER ON/OFF (SEC)	10 FPS ON/OFF (SEC)	STIRRER START (SEC)	REPRESS. START (SEC)	TOTAL TEST TIME (SEC)
1	8	40	10 - 70	15 - 80	60	-	80
2	4	40	10 - 100	10 - 15, 25 - 35	-	-	135
3	2	40	10 - 120	20 - 30, 50 - 130	110	-	130
4	8	30	10 - 55	15 - 65	45	-	65
5	4	30	10 - 100	10 - 15, 25 - 105	90	-	110
6	2	40	10 - 95	20 - 30, 50 - 110	-	45	115
7	8	20	10 - 40	15 - 55	-	50	55
8	4	20	10 - 70	10 - 15, 25 - 80	60	-	80
9	2	20	10 - 115	10 - 30, 50 - 125	95	-	125

Table IV. Test matrix for PBE-IIB on STS-72. (Flight Hardware)

PBE Flight-System Matrix (STS-77)

RUN #	HEAT FLUX W/CM^2	SUBCOOLING (^{0}F)	HEATER POWER ON/OFF (SEC)	10 FPS ON/OFF (SEC)	STIRRER START (SEC)	REPRESS. START (SEC)	TOTAL TEST TIME (SEC)
1	2	20	10-180	25-190	170	-	190
2	1	20	10-220	50-230	210	-	230
3	0.5	20	10-250	70-260	240	-	260
4	2	5	10-170	30-180	160	-	180
5	1	5	10-210	60-220	200	-	220
6	0.5	5	10-250	80-260	240	-	260
7	2	0.5	10-110	30-140	-	120	140
8	1	0.5	10-210	60-240	-	220	240
9	0.5	0.5	10-250	80-280	-	260	280

Table V. Test matrix for PBE-IIA on STS-77. (Flight Hardware)

Space Experiment		PBE-IB (STS-57) Run No. 3	PBE-IIB (STS-72) Run No. 9
q_T''	w/cm^2	2.03	2.04
ΔT_{sub}	°C	11.0	11.1
P	Kpa	149.26	110.66
T_{sat}	°C	59.7	50.2
T_{bulk}	°C	48.7	39.1
t^*	Sec. (Nucleation delay time)	23.63	62.39
T_w^*	°C (Mean heater superheat temperature at nucleation)	96.7	110.0
ΔT_w^*	°C (Mean heater superheat at nucleation)	37.0	59.8

Table VI. Comparisons between two experiments identical except for system pressure (saturation temperature) and bulk liquid temperature.

5. EXPERIMENTAL RESULTS

5.1 Measured Parameters

5.1.1 Internal to Test Vessel

Table VII gives the parameters as measured for each of the Runs of PBE-IIB during the pre-flight tests at a/g = -1 and a/g = +1, and during the STS-72 Space Flight. These are identified in each Run No. by the date conducted and the orientation. Following this are the nominal and actual levels of input heat flux, followed by the nominal and actual initial bulk liquid subcooling. The initial bulk liquid temperature is virtually constant, and the subcooling is changed by varying the system pressure, which changes the saturation temperature, as indicated in the succeeding columns of Table VII. T_w^*, T_{sup}^* and t* are the mean heater surface temperature, the mean heater surface superheat, and the time interval from the onset of heating that nucleation or the onset of boiling takes place, respectively. The last column gives the high speed camera on-off times relative to the heater power on.

Table VIII gives the measured parameters for each of the Runs of PBE-IIA (STS-77). Details of the measurements are given in Appendices A and B for PBE-IIB, -IIA on the STS-72, -77 respectively, and Tables VII and VIII are repeated therein for convenience.

5.1.2 Accelerometer

Tables IX and X list a summary of the relatively larger acceleration excursions measured during each of the runs in the PBE-IIB-IIA of STS-72-77 respectively. The accelerometer units here are given as micro-g's, and the heating for each Run begins at 10 seconds. Accelerometer measurements were made prior to the onset of heating to determine if any disturbances might be carried over to the test period. No consistent observable effects were noted at the times indicated in Tables IX and X either in the vapor bubble boiling behavior, from the motion picture films, or in the heat transfer behavior as might be reflected in the heater surface temperature measurements. The interface motions during boiling are reasonably intense, and the relatively large surface tensions acting are believed to mask influences of these residual acceleration levels, having maximum values on the order of 0.2 milli-g's. Any deviations from the background least reading of ± 1, as indicated by the term noise levels were recorded.

Since the system hardware design for these experiments was identical to that for PBE-IA on STS-47, the orientation of the triaxial accelerometer relative to the heater surface is the same as that given in Figure 3.9.

The effect of the larger excursions in acceleration would be detectable only in special circumstances where a particular sensitivity to buoyancy exists, for example parallel to the heater surface with vapor bubbles present.

NASA test Matrix for Pool boiling

a/g -1 experiment based on date 10/5/95
a/g +1 experiment based on date 10/5/95
a/g 0 experiment based on date 2/5/96 STS-72

Run#	Date of Experiment	Flight system	Gravi a/g	Heat Flux (W/cm^2) Nom.	Actual	Subcool,°F Nom	Actual	Tbulk °C	Sys. Press kPa	Tsat °C	T°wall °C	T°sup °C	t° time sec	100fps On-Off	Remark
1	10/5/95	Flight system	-1	8.00	7.15	40	39.40	39.43	157.91	61.32	~	~	~	0~5	
	10/5/95	Flight system	1	8.00	8.10	40	39.87	37.22	147.81	59.37	87.84	28.47	1.70	0~5	
	2/5/96	Flight system	0	8.00	8.09	40	39.83	36.65	145.13	58.78	86.28	27.50	0.81	0~5	not explosive
2	10/5/95	Flight system	-1	4.00	3.82	40	42.16	38.03	158.51	61.45	115.70	54.25	18.20	5~15	
	10/5/95	Flight system	1	4.00	4.01	40	39.86	37.26	147.97	59.40	~	~	~	5~15	no nucleation
	2/5/96	Flight system	0	4.00	4.04	40	39.85	39.11	156.51	61.25	118.86	57.61	15.44	5~15	
3	10/5/95	Flight system	-1	2.00	2.02	40	39.51	38.81	155.27	60.76	~	~	~	20~40	no nucleation
	10/5/95	Flight system	1	2.00	2.06	40	39.92	37.96	151.32	60.14	~	~	~	20~40	no nucleation
	2/5/96	Flight system	0	2.00	2.05	40	39.91	38.13	152.10	60.30	97.99	37.69	36.41	20~40	
4	10/5/95	Flight system	-1	8.00	7.21	30	29.48	38.55	129.69	54.93	~	~	~	0~5	
	10/5/95	Flight system	1	8.00	8.12	30	29.90	37.71	126.35	54.32	84.48	30.16	1.10	0~5	
	2/5/96	Flight system	0	8.00	7.85	30	29.93	38.40	129.21	55.03	83.35	28.32	0.36	0~5	not explosive
5	10/5/95	Flight system	-1	4.00	3.81	30	29.43	38.39	128.93	54.74	113.20	58.46	17.40	5~15	
	10/5/95	Flight system	1	4.00	4.01	30	29.91	37.43	125.28	54.05	~	~	~	5~15	no nucleation
	2/5/96	Flight system	0	4.00	4.03	30	29.88	40.08	136.07	56.68	119.94	63.26	15.02	5~15	
6	10/5/95	Flight system	-1	2.00	2.02	30	35.98	38.63	145.48	58.62	~	~	~	20~40	no nucleation
	10/5/95	Flight system	1	2.00	2.07	30	36.32	37.94	142.24	58.11	~	~	~	20~40	no nucleation
	2/5/96	Flight system	0	2.00	2.04	30	41.13	38.57	157.30	61.42	107.53	46.11	57.64	20~40	

Table VII. Parameters measured at a/g = -1 and a/g = +1 in Pre-Flight tests, and during STS-72 Space Flight.

	Page 2 of 2															
Run#	Date of Experiment	Flight system	Gravi a/g	Heat Flux (W/cm^2) Nom.	Actual	Subcool,oF Nom	Actual	Tbulk °C	Sys. Press kPa	Tsat °C	T°wall °C	T°sup °C	t° time sec	100pps On-Off	
7	10/5/95	Flight system	-1	8.00	7.35	20	21.11	38.53	108.57	50.26	~	~	~	0~5	
	10/5/95	Flight system	1	8.00	8.15	20	21.10	37.81	108.31	49.53	80.32	30.79	1.00	0~5	
	2/5/96	Flight system	0	8.00	7.60	20	19.78	38.60	108.50	49.59	80.82	31.23	0.51	0~5	not explosive
8	10/5/95	Flight system	-1	4.00	3.85	20	19.51	38.41	108.11	49.25	111.15	61.90	16.80	5~15	
	10/5/95	Flight system	1	4.00	4.03	20	19.94	37.38	104.56	48.46	~	~	~	5~15	no nucleation
	2/5/96	Flight system	0	4.00	4.05	20	19.85	38.35	107.76	49.38	109.59	60.21	11.50	5~15	
9	10/5/95	Flight system	-1	2.00	2.02	20	6.84	38.48	108.18	42.28	~	~	~	20~40	no nucleation
	10/5/95	Flight system	1	2.00	2.06	20	19.84	37.96	106.38	48.99	~	~	~	20~40	no nucleation
	2/5/96	Flight system	0	2.00	2.04	20	19.89	39.14	110.66	50.19	109.95	59.76	62.39	20~40	

Table VII. Continued.

NASA test Matrix for Pool boiling

a/g -1 experiment based on date 3/19/96
a/g+1 experiment based on date 3/19/96
a/g 0 experiment based on date 5/19/96 STS-77
a/g -1 experiment based on date 7/18/96
a/g+1 experiment based on date 7/18/96

Run#	Date of Experiment	Flight system	Gravi a/g	Heat Flux (W/cm²) Nom.	Actual	Subcool,°F Nom	Actual	Tbulk °C	Sys. Press kPa	Tsat °C	T°wall °C	T°sup °C	t° time sec	10fps On-Off	Remarks
1	3/19/96	Flight system	-1	2.00	1.95	20	19.79	49.73	154.03	60.73	117.10	56.37	141.40	25-190	
	3/19/96	Flight system	+1	2.00	2.00	20	19.86	47.48	143.96	58.51	~	~	~	25-190	no nucleation
	5/19/96	Flight system	0	2.00	2.01	20	19.85	47.21	142.79	58.24	94.53	36.29	23.80	25-190	
	7/18/96	Flight system	-1	2.00	1.94	20	19.84	50.03	155.55	61.05	113.08	52.03	79.80	25-190	
	7/18/96	Flight system	+1	2.00	2.00	20	19.84	47.64	144.65	58.66	~	~	~	25-190	no nucleation
2	3/19/96	Flight system	-1	1.00	1.00	20	19.88	49.57	153.48	60.61	~	~	~	50-230	no nucleation
	3/19/96	Flight system	+1	1.00	1.00	20	19.84	48.20	147.13	59.22	~	~	~	50-230	no nucleation
	5/19/96	Flight system	0	1.00	1.00	20	19.81	49.67	153.82	60.68	86.00	25.32	68.30	50-230	
	7/18/96	Flight system	-1	1.00	1.00	20	19.90	49.47	153.06	60.52	~	~	~	50-230	no nucleation
	7/18/96	Flight system	+1	1.00	1.01	20	19.89	48.15	147.07	59.20	~	~	~	50-230	no nucleation
3	3/19/96	Flight system	-1	0.50	0.51	20	19.88	49.97	155.34	61.01	~	~	~	70-260	no nucleation
	3/19/96	Flight system	+1	0.50	0.51	20	19.83	48.27	147.48	59.29	~	~	~	70-260	no nucleation
	5/19/96	Flight system	0	0.50	0.51	20	19.85	48.69	149.41	59.72	~	~	~	70-260	no nucleation
	7/18/96	Flight system	-1	0.50	0.51	20	19.90	50.14	156.24	61.20	~	~	~	70-260	no nucleation
	7/18/96	Flight system	+1	0.50	0.51	20	19.86	48.39	148.03	59.42	~	~	~	70-260	no nucleation
4	3/19/96	Flight system	-1	2.00	1.94	5	4.81	49.33	117.35	52.00	114.54	62.54	93.70	30-180	
	3/19/96	Flight system	+1	2.00	2.00	5	4.85	47.98	112.45	50.68	~	~	~	30-180	no nucleation
	5/19/96	Flight system	0	2.00	2.02	5	4.80	48.91	115.76	51.58	96.76	45.18	23.60	30-180	
	7/18/96	Flight system	-1	2.00	1.94	5	4.85	49.37	117.56	52.06	110.25	58.19	70.80	30-180	
	7/18/96	Flight system	+1	2.00	2.01	5	4.87	47.96	112.38	50.66	~	~	~	30-180	no nucleation

Table VIII. PBE-IIA. Parameters measured at a/g = -1 and a/g = +1 in Pre-Flight and Post-Flight tests, and during STS-77 Space Flight.

	Page 2 of 2														
Run#	Date of Experiment	Flight system	Gravi a/g	Heat Flux (W/cm^2) Nom.	Actual	Subcool,°F Nom	Actual	Tbulk °C	Sys. Press kPa	Tsat °C	T°wall °C	T°sup °C	t° time sec	10fps On-Off	Remarks
5	3/19/96	Flight system	-1	1.00	1.00	5	4.86	49.28	117.28	51.98	~	~	~	60-220	no nucleation
	3/19/96	Flight system	+1	1.00	1.01	5	4.80	48.03	112.52	50.70	~	~	~	60-220	no nucleation
	5/19/96	Flight system	0	1.00	1.01	5	4.82	48.97	116.04	51.65	86.29	34.64	79.60	60-220	
	7/18/96	Flight system	-1	1.00	1.00	5	4.86	48.99	116.18	51.69	~	~	~	60-220	no nucleation
	7/18/96	Flight system	+1	1.00	1.01	5	4.91	48.03	112.73	50.76	~	~	~	60-220	no nucleation
6	3/19/96	Flight system	-1	0.50	0.51	5	4.81	49.42	117.69	52.09	~	~	~	80-260	no nucleation
	3/19/96	Flight system	+1	0.50	0.51	5	4.85	48.01	112.52	50.70	~	~	~	80-260	no nucleation
	5/19/96	Flight system	0	0.50	0.51	5	4.81	49.00	116.11	51.67	75.56	23.89	190.50	80-260	
	7/18/96	Flight system	-1	0.50	0.51	5	4.85	49.51	118.11	52.20	~	~	~	80-260	no nucleation
	7/18/96	Flight system	+1	0.50	0.51	5	4.80	48.18	113.07	50.85	~	~	~	80-260	no nucleation
7	3/19/96	Flight system	-1	2.00	1.96	0.5	0.34	49.29	108.11	49.48	111.70	62.22	81.10	30-140	
	3/19/96	Flight system	+1	2.00	2.01	0.5	0.32	47.79	102.87	47.97	~	~	~	30-140	no nucleation
	5/19/96	Flight system	0	2.00	1.99	0.5	0.30	48.86	106.52	49.03	108.47	59.44	39.20	30-140	
	7/18/96	Flight system	-1	2.00	1.97	0.5	0.29	49.34	108.18	49.50	~	~	~	30-140	no nucleation
	7/18/96	Flight system	+1	2.00	2.01	0.5	0.30	47.91	103.21	48.07	~	~	~	30-140	no nucleation
8	3/19/96	Flight system	-1	1.00	1.00	0.5	0.38	49.13	107.63	49.34	~	~	~	60-240	no nucleation
	3/19/96	Flight system	+1	1.00	1.01	0.5	0.33	47.91	103.28	48.09	~	~	~	60-240	no nucleation
	5/19/96	Flight system	0	1.00	1.00	0.5	0.32	49.06	107.28	49.24	84.84	35.60	66.30	60-240	
	7/18/96	Flight system	-1	1.00	1.00	0.5	0.35	48.86	106.59	49.05	~	~	~	60-240	no nucleation
	7/18/96	Flight system	+1	1.00	1.01	0.5	0.30	47.81	102.87	47.97	~	~	~	60-240	no nucleation
9	3/19/96	Flight system	-1	0.50	0.51	0.5	0.36	49.30	108.18	49.50	~	~	~	80-280	no nucleation
	3/19/96	Flight system	+1	0.50	0.51	0.5	0.35	47.89	103.28	48.09	~	~	~	80-280	no nucleation
	5/19/96	Flight system	0	0.50	0.51	0.5	0.36	49.08	107.42	49.28	73.18	23.90	215.20	80-280	
	7/18/96	Flight system	-1	0.50	0.51	0.5	0.39	49.46	108.80	49.67	~	~	~	80-280	no nucleation
	7/18/96	Flight system	+1	0.50	0.51	0.5	0.32	47.83	103.01	48.01	~	~	~	80-280	no nucleation

Table VIII. Continued.

RUN #	Time, sec	Peaks	Maximum Acceleration value			Noise
			x	y	z	
1		no	47	25	51	24
2		no	47	50	77	24
3	70.5	yes	47	25	152	24
3	70.8	yes	24	0	152	24
4		no	47	50	77	24
5	15.9	yes	148	50	0	24
5	16	yes	148	25	25	24
5	16.3	yes	147	25	26	24
5	42.7	yes	47	25	127	24
6		no	47	75	51	24
7		no	50	50	77	24
8	7.9	yes	0	25	178	24
8	8.1	yes	47	50	152	24
8	8.4	yes	47	50	178	24
8	8.7	yes	0	25	153	24
8	9	yes	0	50	177	24
8	9.3	yes	47	50	152	24
8	9.5	yes	0	50	127	24
8	9.9	yes	23	0	152	24
8	34.5	yes	47	0	152	24
8	79.9	yes	0	25	152	24
9	14.9	yes	0	25	127	24
9	15.2	yes	47	0	152	24
9	15.5	yes	0	0	152	24

Notes: (1) Accelerometer units are given as micro-g's.

(2) Heating in each run begins at t = 10 sec.

Table IX. Summary of relatively larger acceleration excursions during PBE-IIB in STS-72 Flight.

RUN #	Time, sec	Peaks	Maximum Acceleration value			Noise
			x	y	z	
1	105.0	yes	6	31	100	24
1	110.2	yes	6	119	24	24
1	110.4	yes	18	119	24	24
1	115.0	yes	18	106	27	24
1	115.1	yes	18	131	1	24
1	115.2	yes	6	106	1	24
1	115.3	yes	18	106	1	24
1	140.4	yes	166	156	75	24
1	140.5	yes	240	181	50	24
1	140.6	yes	18	156	77	24
1	140.7	yes	56	181	128	24
1	140.9	yes	166	19	50	24
1	141.0	yes	166	94	75	24
1	141.3	yes	117	19	100	24
1	183.3	yes	18	69	103	24
1	183.4	yes	43	19	103	24
2	111.9	yes	50	117	26	24
3	70.5	yes	47	25	152	24
3	70.8	yes	24	0	152	24
4		no	47	50	77	24
5	15.9	yes	148	50	0	24
5	16.0	yes	148	25	25	24
5	16.3	yes	147	25	26	24
5	42.7	yes	47	25	127	24
6		no	47	75	51	24
7		no	50	50	77	24
8	7.9	yes	0	25	178	24
8	8.1	yes	47	50	152	24
8	8.4	yes	47	50	178	24
8	8.7	yes	0	25	153	24
8	9.0	yes	0	50	177	24
8	9.3	yes	47	50	152	24
8	9.5	yes	0	50	127	24
8	9.9	yes	23	0	152	24
8	34.5	yes	47	0	152	24
8	79.9	yes	0	25	152	24
9	14.9	yes	0	25	127	24
9	15.2	yes	47	0	152	24
9	15.5	yes	0	0	152	24

Notes: (1) Accelerometer units are given as micro-g's.
(2) Heating in each run begins at t = 10 sec.

Table X. Summary of relatively large acceleration excursions during PBE-IIA in STS-77 Flight.

5.2 Test Matrix Results Organization

The experimental data, including representative photographic views from the films, for each of the nine (9) Runs of PBE-IIB and -IIA conducted in the microgravity of space on the STS-72 and -77 are given, respectively, in Appendices A and B. The organization of these two (2) Appendices are parallel with respect to the Figure Numbers, Titles and Subjects treated, so the contents of only Appendix A will be described in some detail here. Comments on the behavior and special differences observed in the experiments will be deferred to the following discussion section.

The test matrix, measured parameters and summary of relatively large acceleration excursions are repeated in Appendix A as Tables A-I, A-II and A-III, respectively, for convenience in reviewing the results.

Each of the Figures A-1 through A-6 and A-9 through A-13 are subdivided as a - i, corresponding to Run Nos. 1-9, and follow the sequences of Tables A-I, A-II, A-III.

Figures A-la --- A-li include the measured mean heater surface temperature and the heat transfer coefficient computed from a one-dimensional finite difference procedure in the quartz substrate, using the measured surface temperature as a boundary condition. Cubic splines are fitted through successive data points to provide interpolation between the measured points. The procedure is described by Merte (1992). During the conduction phase of heating the heat transfer coefficient is defined in terms of the difference between the heater surface temperature and the initial temperature. This permits a comparison with the well-known analytical solution of conduction in two semi-infinite solids with a step input in heat flux at the plane between the two solids. This is shown by the labeled dotted curves in Figures A-la -- A-li. Once motion takes place in the fluid, comparison with the analytic conduction solution is no longer appropriate. However, it is included in all such plots in order to provide a reference. It becomes obvious that deviations from the one-dimensional conduction behavior takes place because of the finite lateral heater dimensions. This issue will be addressed below. Once nucleation takes place the heat transfer coefficient is appropriately defined in terms of the difference between the measured heater surface temperature and the liquid saturation temperature.

Figures A-2a --- A-2i show the temporal variation of the input heat flux to the thin gold film. The changes measured are a consequence of the increase in resistance of the gold film as it is heated, with the imposed voltage being controlled to remain essentially constant. This variation is relatively small, except when substantial heater surface dryout takes place, and it was not deemed worthwhile to control the power input to remain constant.

The measured system pressures are plotted in Figures A-3a - A-3i, along with the heat flux to the fluid as computed from the measured power input and the heat flux to the substrate, computed in turn from the measured heater surface temperature. This parameter makes it

convenient to determine when steady-state conditions are reached, since the heat flux to the fluid becomes equal to the heat flux input to the film heater. In some cases pressure spikes are observed at the moment of nucleation, associated with the rapid formation of vapor before the pressure control system can respond. The relatively low sample rate of 10 Hz for pressure is responsible for the seemingly random sensing of these pressure spikes.

Figures A-4a --A-4i give the fluid temperatures above the passive so-called primary heater, labeled TM01, TM02 and TM03, at distances of 1 mm, 5 mm and 10 mm above the heater surfaces, as indicated in Figures 3.3 and 3.4. The lower plot shows TM04, TM05 and TM06, the bulk liquid temperatures at the various distances indicated above the heater surfaces, around the perimeter as given in Figures 3.3 and 3.4, and thus gives an indication of the effects of lateral motions of the vapor bubble for the case where the secondary heater is active. The measured active mean heater surface temperature, the so-called secondary heater here, is included at the top in order to provide temporal reference marks for the various temperatures measured. The measured fluid temperatures provide an indication as to the uniformity of temperature at the beginning of each Test Run.

Figures A-5a --A-5i show the changes in liquid temperature above the active secondary heater, labeled TM07, TM08 and TM09, at 1 mm, 5 mm and 10 mm above its center. In the lower part of these Figures, TM11 measures the quartz surface temperature centered under the secondary heater, while TM12 measures the quartz surface temperature under the center of the primary heater. TM13 measures the air space temperature slightly removed from the center of the underside of the quartz substrate. If necessary, this permits estimating the heat loss from the back side of the quartz substrate.

Twelve (12) selected representative frames from the 400 ft. 16 mm motion film are presented for each Run in Figures A-6a --A6i, along with the frame number, counted from an arbitrary initial frame, and with the time, related to the onset of heating, which begins at 10 seconds. Filming took place at either 10 or 100 pps, as indicated in the matrix given in Table A-I for PBE-IIB (STS-72). All films for PBE-IIA (STS-77) were made at 10 pps, as discussed previously. The images were obtained by projecting the film on a large screen, picking it up with a video camera, and using a frame grabber and digitizer for storage on laser discs. The times shown may differ slightly from the frame number because the camera speed may vary, as when changing framing speed. The LED's seen in the bottom of each image provide synchronization with the thermal data, following the time format given in Figure 3.10.

The nucleation delay time here is defined as the time interval between the onset of heating and the moment when the first vapor bubble appears. For a given input heat flux a distinct relationship exists, in the absence of buoyancy, between the nucleation delay time, the heater surface superheat, and the liquid temperature distribution at the onset of boiling. The latter

quantities govern the character of the early bubble dynamics and the spread of the boiling across the heater surface. Such processes are described in detail in Ervin and Merte (1991), Ervin et al (1992), and Lee and Merte (1993), using the results of transient boiling tests in the 5.1 second drop tower at the NASA Lewis Research Center. Based on these tests and space experiments prior to the present results, an optimum correlation was developed, as shown in Figure A-7, in order to estimate the delay times expected in the flight experiment. All nucleation delay times measured with the PBE-IIB, including the pre-flight ground tests, are plotted in Figure A-7. The comparison with the flight data is quite good, while convection effects in earth gravity result in some scattering. The limitations on the lower levels of input heat flux become obvious in such a plot, where nucleation can not take place in a 5.1 second drop tower below a heat flux of about 5.5 w/cm^2.

Figure A-8 is a plot of mean heater surface superheat at nucleation for the same tests plotted in Figure A-7. It is noted that a peak exists in the mean heater surface superheat on nucleation between the high and low levels of heat flux, even with different subcooling levels, and is particularly high in microgravity. In addition, for the most part, as the subcooling level increases the heater surface superheat on nucleation is smaller. These phenomena will be discussed below in terms of heterogeneous and homogeneous nucleation theories, with the influence of the liquid temperature gradients at the heater surface and bulk liquid subcooling incorporated in the latter.

In certain circumstances of the test matrix followed here, it was noted that after the initial nucleation and prior to the spreading of the boiling process across the heating surface, the vapor bubble appeared to be growing spherically or hemispherically. Measurements of size as a function of time were made and reported for such bubbles in earlier space experiments by Merte et al (1996), with the growths compared with predictions of spherically symmetric analytic models, as developed by Lee and Merte (1993). The measurements of growth for a hemispherical bubble have been made in only one case for the experiments here, and will be presented below.

Experiment PBE-IIB (STS-72) was conducted with subcooling levels considerably higher than that used previously. The combination of these higher subcooling levels and the lowest heat flux level resulted in behavior heretofore unseen: Small bubbles formed at certain regions on the heater surface, and then migrated rather consistently to another domain, coalescing with an almost static larger sized vapor bubble. These behaviors could be discerned quite distinctly from the photographic data taken through the transparent heating surface from the underside. Measurements of the migration velocities of certain of such bubbles were made, and are presented below in Figures 6.14-6.25, together with sequences of photographs representative of such motions.

From the photographics data taken through the transparent heating surface from the underside, it is possible to discern quite distinctly those portions of the heater surface on which dryout has taken place. Examples are abundant in Figures A-6a -- A-6i. It is observed that under some circumstances this is a time varying phenomena, and is related in some fashion to both the

transient mean heater surface temperature and heat transfer coefficient. If measurements of the time varying fractional area of the heat transfer surface in contact with vapor, which will be termed the fractional dryout area, can be made with sufficient temporal detail, it is felt that the possibility exists for quantifying the contributions to the total heat transfer of the different modes of heat transfer taking place. Since only mean heater surface temperatures and heat transfer coefficients are measurable at present, only spatial mean parameters can be determined: local measurements in the future would permit determination of these parameters on a spatially local basis.

In order to provide an efficient means for quantifying the time varying fractional dry portion of the heater area from the 16 mm films, an optical processing system was set up in which the 16 mm film is projected on a screen with a motion picture projector; the motion is stopped at the desired frame; the time noted; the image picked up with a video camera, which can then be stored on a VCR and/or immediately digitized with a frame grabber for greater resolution; the digitized data is stored on an optical disc for later processing. The fractional dry area measurements were made from the digitized data for selected portions of each Run, which are indicated on the index, Table A-IV. The fractional dry area and corresponding mean heater surface temperatures are plotted in Figures A-10--i - A-10i--i. A predictable conformity is to be noted in each Run between the fractional dry area and the mean heater surface temperature: As the fractional dry area increases for a given heat flux input, so does the mean heater surface temperature. Sample images showing dryout and rewetting in each of the selected portions of each Run are included as Figures A-10a--iv - A-10i--iv. Discussion of the development of the computational procedures for determining the microgravity boiling heat transfer coefficients are presented in Merte et al (1996).

Figures A-11 - A-20 provide the same experimental results as described for Figures A-1 - A-5 above, except that the former were obtained at a/g = +1 and a/g = -1 during the pre-flight testing of the hardware, following the identical automated matrix cycle as for the space flight. These results proved data by which direct comparisons can be made of behavior between earth gravity and microgravity under otherwise identical circumstances. For the present here it may be stated that at a/g = +1 nucleate boiling only took place at the highest heat flux level for the subcooling levels employed here. Boiling did not take place at a/g = -1 at the combination of the lowest heat flux level and the two higher levels of subcooling.

6. DISCUSSION

6.1 Conduction Effects

In the absence of buoyancy and forced convection, heat transfer in fluids takes place by pure stationary conduction, as in solids. This was confirmed for relatively short periods (up to 5.1 seconds) in microgravity, in solids and in fluids before nucleation takes place, by the measurements of Ervin and Merte (1991) also appearing in Ervin and et al (1992). In this case the physical processes of conduction conformed closely to the analytical solution for two semi-infinite solids, initially at a uniform temperature, with a uniform step in a plane heat source at the interface.

An important consideration in the measurement of the mean heater surface temperature as determined from the measurement of the mean electrical resistance of the thin gold film, from Equation (3.1), is how accurately the mean resistance actually represents the mean temperature. The question was examined analytically in detail in Appendix D of Merte et al (1996), with the conclusion that the maximum discrepancy between the true mean surface temperature and that computed from the mean surface electrical resistance is less than the absolute uncertainty in the heater surface temperature measurement, under the most adverse temperature distribution over the surface.

6.1.1 Conduction in Substrate

The analytic solution for the interface temperature between the two semi-infinite solids, which corresponds to the gold film heater surface temperature in the physical system, is plotted as the 1-D Analytical Surface temperature for reference purposes for each of the Runs of the matrices of PEB-IIB-IIA in Figures 1a-1i of Appendices A, B.

The discrepancy between the analytical and the measured values increase for the lower level of heat fluxes, for which longer periods of conduction heat transfer in both the solid and fluid domains take place before nucleation occurs. This discrepancy is attributed to three dimensional conduction effects during this period, primarily in the quartz substrate domain, which has a larger thermal diffusivity, a=k/ρc=8.34 x 10-7m2/s, compared to a =5.24 x 10-8 m2/s for R-113. Comparisons of the short 5.1 second drop tower ground base testing were excellent with one-dimensional solutions. In this case the quartz substrate was less massive than that in the PBE, and the single heater surface of the substrate was located symmetrically. To confirm that three dimensional effects were operating in the PBE, a 3-D finite element model was developed for the particular geometry of the PBE with the results presented and discussed in Merte et al (1996). As described in this same work, some filtering of the measurements associated with the power input to the thin film heater, taken at 10 Hz, was found to be necessary, and the same techniques were followed in the experimental results presented here: The mean heater surface temperatures and

heater transfer coefficients are obtained by taking three (3) successive heater surface temperatures at 100ms intervals, averaged to provide the temperature at the middle point of the time scale. This procedure was advanced for each 100 ms data point. The results presented in Figures 1a-1i of Appendices A and B were obtained using this three 3 point averaging technique, with a polynomial fit for interpolation between data points.

6.1.2 Conduction in Fluid

The measured mean heater surface temperatures were used to compute the heat flux and heat transfer coefficients to the fluid, with the latter given in Figures 1a-1i of Appendices A and B. The imposed heat flux inputs were taken as constant in the computation of the heat transfer to the fluid. As can be noted in Figures 2a-2i of Appendices A and B, significant variations in the imposed heat flux occurred only where dryout had occurred on large portions of the heater surface, because the current decreased as resistance increased, with a constant voltage input. The detailed descriptions associated with the significant dryouts were relatively unimportant.

The temperature distribution in the liquid at the nucleation sites at the moment of nucleation, including the local temperature at the heater surface itself, are necessary for assessing the vapor bubble nucleation process in microgravity, which will be considered below. These temperature distributions are computed as 1-D transient conduction processes in the liquid, using as boundary conditions, however, the local heater surface temperatures and liquid heat flux computed by the 3-D finite element model for the substrate. This procedure was necessary because the grid spacing of the finite element model was too coarse to provide the special temperature resolution necessary in the liquid. An assessment of the process is presented in Merte et al (1996). The application of this procedure will be made in the analysis of the nucleation process below.

It was originally expected that nucleation and early bubble growth would always occur in that part of the heater having the highest temperature, in the central portion, and not near the edges of the heater where the temperature falls off sharply because of three-dimensional conduction in the substrate. The latter behavior was confirmed by early finite computations of the 3-D substrate temperature distributions, and by recent 3-D finite element transient computations.

Results have indicated that under certain circumstances nucleation does not take place at the domains of highest surface temperature, but sometimes takes place at locations on the heater surface where the temperatures are lower-near the edges, depending on the heat flux level. This is illustrated in the upper part of Figure 6.1, in which the locations of the nucleation sites are indicated for each Run in the five PBE experiments flown to date. The left hand side shows the nucleation sites on the primary heater used with the Prototype Model, for PBE-IA-IC (STS-47-60), while the right hand side shows the nucleation sites on the backup heater (secondary) used with the Flight Model, for PBE-IB-IIB-IIA (STS-57-72-77). It is noted that the highest heat flux

cases, Run Nos. 1,4,7 of both STS-47 and STS-60, identified as (a) on the left, and Run Nos. 1,4,7 of both STS-57 and STS-72, also identified as (a), except on the right, all nucleated at the identical site near an edge on their respective surfaces. Run Nos. 1,4,7 of STS-77 were conducted at a much lower heat flux level, and nucleation took place at random locations over the heater surface, as with all the other Runs at the lower levels of heat flux. Where the nucleation sites in particular Run Nos. are identified as not possible to determine, this corresponds to the cases where the vapor bubble growth was quite energetic, such that no vapor bubble was visible in one film frame but filled the heater surface in the next. It is assumed in these cases that nucleation occurred in the highest superheat domain - in the central part of the heater. This is consistent with the Run Nos labeled as point (b) in both sides of Figure 6.1.

The local heater surface temperatures and heat flux were then used to compute the local temperature distributions in the liquid normal to the heater surface at the moment of nucleation, for each of the nine (9) Runs for each of the two PBE space flights, where appropriate.. These are presented in Figures 6.2 and 6.3 for PBE-IIB (STS-72) and PBE-IIA (STS-77), respectively, as local liquid superheats. It is noted in Figure 6.2 for PBE-IIB (STS-72) that the Runs with the highest heat flux, Nos. 1,4 and 7, have the lowest total superheated liquid content at nucleation, which is related to the subsequent non-dynamic bubble growth rates. The medium heat flux case, Run Nos. 2, 5 and 8, have the highest local surface temperature at nucleation. The Runs with the lowest level of heat flux in Figure 6.3 for PBE-IIA (STS-77), on the other hand, have the lowest heater surface superheat at nucleation, which is also related to the subsequent non-dynamic bubble growth rates. Run No.3 is missing in Figure 6.3 since nucleation did not take place, in spite of the heating period of 4 minutes, a result of the combination of high subcooling and very low heat flux level.

6.2 Convection Effects

Natural convection is driven by buoyancy, and its onset may be described in terms of an instability in which disturbances are always present. Reducing the buoyancy by reducing the body forces delays the onset of convection and reduces the resulting convection velocities. However, acting over a sufficiently long period it can be anticipated that any non-zero level of body force, no matter how small, will produce motion, depending on the stabilizing forces acting in the particular circumstance. An example is given in Merte et al (1996) for PBE-IC (STS-60) Run No. 8, during the single phase transient heating process, in which a disturbance of about 0.3 mg perpendicular to the heating surface at about 16 seconds and lasting approximately 2 seconds induces a slight amount of natural convection. It was noted that this natural convection in turn affects the mean surface temperature and the heat transfer coefficient.

The results of the pre-and post flight tests at a/g= +1, in which non-boiling natural convection took place, provided an opportunity to compare values of the natural convection heat transfer coefficients generated by the procedure followed for the microgravity boiling cases with values from well established natural convection correlations. For example, the correlation of Lloyd and Moran (1974) for a horizontal surface facing upward predicts a heat transfer coefficient of h = 460 w/m2k for R-113 at earth gravity. This is to be compared with measurements over the range h=425-500 w/m2k from Figures 14 in Appendix A for those cases where boiling does not occur, and from Figures 14 and 20 in Appendix B.

6.3 Nucleation

Nucleation delay times, the time interval between the onset of heating and nucleation or the onset of boiling, are necessary for estimating the beginning of high speed photography. Comparison between the correlation based on early drop tower testing, given in Merte et al (1996), and measurements for PBE-IIB (STS-72) at earth gravity $a/g = \pm 1$ and in space, are shown in Figure A-7. It is obvious that absolute uncertainties become quite large as the input heat flux is reduced. Figure B-7 presents the comparisons between the nucleation delay times for the five (5) PBE space experiments only, PBE-IA-IB-IC-IIB-IIA on STS-47-57-60-72-77, respectively, and their best-fit correlation.

Nucleation at earth gravity took place only at $a/g = -1$ in PBE-IIA (STS-77), and then only with the highest input heat flux level of $q" = 2 w/cm^2$. The nucleation delay times for this case were 141.4, 93.7, 81.1 seconds for Run Nos. 1, 4, 7, respectively, and correspond to initial bulk liquid subcooling levels of 11.0, 2.7, 0.2°C, respectively. The heat flux levels were too low to produce nucleation at $a/g = \pm 1$ for the experimental times selected for space operation. As a result, a separate plot of nucleation delay times for PBE-IIA (STS-77) was not provided.

The nucleation delay times in earth gravity were somewhat different for PBE-IIB (STS-72) in which the heat flux levels were the same order as for the prior three (3) space experiments, but in which the subcooling levels were increased significantly to nominal levels of 22.2, 16.7, 11.1°C. At $a/g = +1$ nucleation took place only at the highest nominal heat flux level of $q_T^{"} = 8 w/cm^2$. At $a/g = -1$, on the other hand, nucleation occurred virtually immediately at the highest nominal heat flux level of $q_T^{"} = 8 w/cm^2$, had delay times of 18.2, 17.4, 16.8 seconds for

$q_T'' = 4\,{}^{w}/_{cm^2}$ in run Nos. 2, 5, 8, respectively, and did not occur at all for $q_T'' = 2\,{}^{w}/_{cm^2}$ because of lateral convection combined with the high subcooling.

The mean heater surface superheat at nucleation, or the onset of boiling, are plotted for PBE-IIB and -IIA in Figures 8 of Appendices A and B, respectively, as a function of the input heat flux, which is directly proportional to the heat flux to the fluid in the microgravity non-boiling conduction heat transfer domain. It is noted in Figure A-8 for PBE-IIB (STS-72), which used the same nominal input heat flux levels as the prior three (3) PBE space experiments but with considerably higher liquid subcooling levels, a distinct peak exists in the mean heater surface superheat at nucleation between the high and low levels of heat flux, with one exception: In microgravity this superheat remained as high at the lowest heat flux level as it was at the intermediate level, for the lowest subcooling level here. The heater surface superheat at nucleation is related to both the heat flux levels and the nucleation delay times: For a given heat flux level a longer delay time results in a higher heater surface superheat at nucleation.

The behavior shown in Figure A-8 is quite similar in character to that observed in the three (3) previous space experiments PBE-IA-IB-IC (STS-47-57-60), with the nucleations taking place at the highest heat flux levels designated as heterogeneous nucleation, in that all such nucleations took place at precisely the same locations on the heater surface. The same took place in PBE-IIB (STS-72), as can be noted in the right hand side of Figure 6.1, where the nucleations took place at site "a" for Run Nos. 1, 4, 7. This is the identical site as with PBE-IB (STS-57) two years prior.

The heater surface superheats in Figure B-8, for the lower levels of heat flux input, decrease consistently as the heat flux is reduced, and can be viewed as extensions of the decrease in heater surface superheat as heat flux decreases observed in Figure A-8. The system pressures were identical in PBE-IIB (STS-72) and PBE-IIA (STS-77) for the same Run Nos., and resulted in virtually the same heater surface superheat for the case where the imposed heat was the same, at $q'' = 2\ {}^{w}/_{cm^2}$. Although the initial bulk liquid subcoolings were different at this heat flux, this results only in a difference in the nucleation delay time.

The modification to the homogeneous nucleation theory, presented in Merte et al (1996) and in Merte and Lee (1997), predicts the effects of system pressure and imposed heat flux on the heater surface superheat at nucleation, for a given fluid and the smooth gold film heater on polished quartz used in the present research. Although this type of nucleation is called homogeneous nucleation here, no explicit evidence exists yet that this nucleation did not take place exactly on the heater surface itself. As described above, the indirect evidence that the nucleation was homogeneous, except for the Test Runs taking place at the highest level of heat flux $q_T'' = 8\ {}^{w}/_{cm^2}$, for which the nucleation always occurred at precisely the same location on the

heater surface even after a two (2) year interval between tests, is that the nucleation for each Test Run occurred at different locations on the heater surface, and were generally associated with subsequent dynamic vapor bubble growth rates, to be described below. Because of the lack of explicit evidence at this time, this type of nucleation is called quasi-homogeneous nucleation until appropriate physical measurements demonstrate that the nucleation is indeed not taking place directly on the heater surface. As can be deduced from examining Figures 6.22-6.24 in Merte et al (1996), such measurements, most likely photographic will require great sensitivity to detect the small differences in dimensions involved.

Except for the highest imposed heat flux levels in Figure A-8, for PBE-IIB (STS-72), and the lowest levels in Figure B-8, for PBE-IIA (STS-77), the vapor bubble growths subsequent to nucleation were quite dynamic. The conditions necessary to produce the dynamic vapor bubble growths will be reviewed below. The lack of dynamic vapor bubble growths imply that whatever the nucleation source, whether homogeneous or heterogeneous, the total superheat content in the liquid is insufficient to trigger the dynamic growth phenomena.

The theoretical equation for the prediction of quasi-homogeneous nucleation, developed and presented in Merte et al (1996) and Merte and Lee (1997), is shown in Figure 6.4 for the three levels of system pressure used to vary the initial bulk liquid subcooling for the various Runs. The plot is identical to Figure 6.29 in Merte et (1996), with the addition of the measurements of PBE-IIB-IIA (STS-72-77) for the same physical hardware. The original analysis resulted in one empirical constant, which has not been changed although it was evaluated based on data obtained with different hardware. The estimated superheat limit from classical homogeneous nucleation theory is included, and is on the order of superheats between 105°C-115°C for the pressures used here, and predict imposed heat flux levels on the order of 50 $^{w}/_{cm^2}$. As can be noted in Figure 6.4, heat flux imputs of 8 $^{w}/_{cm^2}$ result in the heterogeneous nucleation referred to earlier. It should be noted here that a time interval of 18 months elapsed between the experiments of PBE-IB (STS-57) and PBE-IIB (STS-72), with 6 months between PBE-IIB (STS-72) and PBE-IIA (STS-77). The apparent "scatter" of the data in Figure 6.4 could be reduced considerably if a different value of K* were determined for each space flight experiment. However, this would result in 3 sets of curves, instead of the one set plotted, with the possibility for some confusion. The significant point to be noted in Figure 6.4 is that for a given space experiment and subcooling, an increase in q" produces an increase in the heater surface superheat at nucleation, while for a given heat flux an increase in bulk liquid subcooling (an hence pressure) results in a decrease in heater surface superheat at nucleation, both of which are consistent with the predictions given by Eq. 6.35 in Merte et al (1996), or Eq. 26 in Merte and Lee (1997).

Figure 6.5 is similar to Figure 6.4, except that a linear scale is used for the imposed heat flux instead of a logarithmic scale, and only the pressure limits are given. Those particular experiments in which the vapor bubble growth following nucleation were quite dynamic are indicated by a special symbol defined in Figure 6.4. The data for the higher heat flux levels in the lower right all correspond to the heterogeneous nucleation described above, and all lack a vigorous bubble growth. It is to be noted in particular that all nucleations falling within the heater surface temperatures as predicted result in the dynamic bubble growths.

6.4 Bubble Dynamics

Based on both observations and measurements conducted in earth gravity at a/g =+ 1, a/g= -1, and in the 5.1 second NASA-Lewis drop tower as part of the pre-spaceflight testing program, once nucleation occurred the propagation of the boiling across the heater surface and the bubble growths could be classified as one of six categories, termed as follows:

A. Advancement of interface by irregular protuberances.

B. Growth of mushroom-like bubble with spreading along heater surface.

C. Orderly growth of bubble with a "smooth" interface.

D. Orderly growth followed by onset of interface instabilities.

E. Energetic growth of bubble with unstable interface.

F. Slow motion of bubbles toward region of higher temperature.

These are described in some detail in Merte et al (1996), and as reported therein, all boiling propagations in PBE-IA-IB-IC (STS - 47 - 57 - 60) were in either categories D or E, depending on the combination of heat flux and subcooling. Because of the extensions of the parameters of subcooling and imposed heat flux for the space experiments reported here, the additional categories A, C, F were present, and are summarized in Table XI. The only category in the above list not observed in any of the space experiments now is "B", which is associated with buoyancy effects.

Run No.	PBE-IIB (STS-72) q " w/cm^2	ΔTsub °C	Category	PBE-IIA STS-77 q " w/cm^2	ΔT sub °C	Category
1	8	22.2	A	2	11.1	E
2	4	"	E	1	"	D+F
3	2	"	D+F	0.5	"	No Nucleation
4	8	16.6	A	2	2.8	E
5	4	"	E	1	"	E
6	2	"	E+F	0.5	"	C
7	8	11.1	A	2	0	E
8	4	"	E	1	"	D
9	2	"	E	0.5	"	C

Table XI. Boiling propagation and bubble growth categories observed in PBE-IIB-IIA (STS-72-77).

It is noted that once nucleation takes place the subsequent propagation and growth should be governed primarily by the levels of heat flux and initial bulk liquid subcooling used, and have been observed to be quite reproducible. This is seen in Table XI above between PBE-IIB (STS-72) Run 9 and PBE-IIA (STS-77) Run 1, which differ only in the system pressure as given in Tables VII and VIII.

Several of the categories will be considered in some detail below, as appropriate. Of particular interest here is category "E", where the vapor growth rates were quite dynamic, and could be termed explosive. This was the most commonly observed category in microgravity, and was most generally associated with what was called "quasi-homogeneous nucleation" in the previous section. The camera speeds and amount of film available were not adequate to capture details of the behavior, although it was evident that such behavior was taking place.

Photographs and measurements of the vapor bubble growth obtained in preliminary testing in the NASA-Lewis R.C. 5.1 second drop tower provide evidence for rates of growth not accountable by conventional models. The photographs, including all of the space experiments in which category growth "E" above took place, reveal that the liquid-vapor interface of the explosive bubbles become wrinkled and corrugated, leading to the conclusion that some type of instability mechanism is acting. Subsequent to the submission of the report of Merte et al (1996), some preliminary success was achieved in modeling the onset of the initial dynamic growth observed, approximating, for the flat heater surface geometry used, the conditions necessary. Further space experimentation is necessary, including the use of high magnification and high framing rate photography, to solidify the basis for the model. Details of the model development are given in Lee and Merte (1996a) and will not be repeated here. However, some of the results of the analysis will be given here to demonstrate the relationship to the present work.

The rapid evaporation rates observed have been described by various terms such as vapor explosion, explosive boiling, thermal explosion, rapid phase transitions (RPTs), and have been discussed by Reid (1983). It has been presumed that potential high pressure water cooled nuclear reactor explosions, LNG spill explosions and high pressure boiler accidents are related to vapor explosions. A current concern that such behavior could arise with liquid metals exists in the use of mercury as a target material for the Spallation Neutron Source being proposed at the Oak Ridge National Laboratory. The model of Lee and Merte (1996a) was adapted to mercury as a working fluid, and some analytical results presented by Lee and Merte (1997).

Figure 6.6, from Lee and Merte (1996a), demonstrates the difference in appearance between growing vapor bubbles of the "dynamic" or "explosive" type (a) and the "normal" type (b). As demonstrated and discussed in Merte et al (1996), the extremely rapid growth of (a) is a consequence of the large increase in liquid-vapor interface area associated with the corrugated or rough interface, which itself is due to the presence of an instability. The identification and modeling of the source of this instability, including predictions of the circumstances for its onset, are treated in the work of Lee and Merte (1996a), as mentioned above. Figure 6.7 compares the growth of the bubble of Figure 6.6(a) with predictions for normal bubbles having smooth interfaces, for the two limits of uniform and non-uniform initial superheat possible for growth on a flat interface, as described in Lee and Merte (1996 b,c). The measurements are below the physically unrealistic model of Rayleigh (1917), which assumes that the internal vapor pressure of the bubble remains constant at the initial saturation pressure corresponding to the heater surface superheat at nucleation, but is significantly above the model for the upper limit. Similar comparisons are given in Figure 6.8 for the normal growing vapor bubble in Figure 6.6(b). The measurements now fall between the two limits, as is expected.

Figure 6.9 presents the results of the instability analysis for Figure 6.6(a), where the intersections of the so-called k-limit and kmax curves represent the predicted unstable domain leading to the growth of disturbances of appropriate sizes, which are assumed to always be present. Experimental evidence regarding the character of these disturbances is still lacking, and will be the subject of proposals for future experimentation in the microgravity of space. Figure 6.10 shows the results of the instability analysis corresponding to Figure 6.6(b), where the k-limit and k-max curves do not intersect but make only a single contact.

The photographic sequence in Figure 6.11 from PBE-IIA (STS-77) Run No. 6, represents the only Run of the last two space PBE-GAS experiments which permitted quantification of the initial vapor bubble growth rates. The imposed heat flux was sufficiently low ($q'' = 0.51$ w/cm^2) that the low camera speed of 10 pps was able to follow the growth. It can be seen in Figure 6.12 that this growth follows the lower limit of the initial non-uniform superheat model quite well.

Figure 6.13 is the corresponding plot of the stability curves, where it is noted again that no intersection exists between the k-limit and k-max curves.

As described earlier, PBE-IIB (STS-72) consisted of the experimental sequences in which the nominal successive heat flux levels were identical to those of the three previous space experiments, PBE-IA-IB-IC (STS-47-57-60), at q" =8,4,2 w/cm^2, but that the nominal subcooling levels were increased to ΔT sub = 22.2, 16.7, 11.1 °C instead of the previous levels of ΔT sub = 11.1, 2.8, 0 °C. A new vapor bubble phenomena was observed at the combination of the lowest heat flux level q" =2 w/cm^2 and the two higher levels of subcooling ΔT sub = 22.2, 16.7 °C, in which distinct regular migrations of small vapor bubbles took place while remaining in the immediate vicinity of the heater surface, proceeding from their region of origin toward a large bubble, also on the heater surface, and eventually coalescing with this larger bubble. This process has been referred to as bubble migration, and is believed to be a vapor bubble manifestation of Marangoni convection and/or molecular momentum effects, sometimes referred to as vapor recoil, taking place in the presence of large liquid temperature gradients associated with the relatively large bulk liquid subcooling now present here.

The migration of gas bubbles in a liquid in which a temperature gradient is imposed is a well-known phenomena (e.g.-Subramanian-1990), and the migration of gas bubbles along a heated wire has been reported by Trefethan (1961), where the gas was the volatile component of a mixture of two liquids. In this case the bubbles were formed at the center of a horizontal wire, and they migrated alternatively in opposite directions. What is believed to be taking place in the present work is a two-dimensional version of the phenomena reported by Trefethan (1961), except that a pure substance is used, and the motion of the bubble is not constrained to a particular direction, although once initiated and in motion the bubbles were observed to move, more or less, consistently in a given direction.

Absent an analytical development of the mechanisms acting to produce the two-dimensional migrations observed here, at the present time, it is deemed desirable to present the results of measurements of bubble velocities and sizes, where possible, for the well-defined initial experimental conditions employed. For each of the bubbles, followed, a sequence of digitized photographs will be shown, with the bubble identification within a sequence, together with the time of each image in order that it can be related to the overall experiment time scale. This sequence will be followed immediately by a time plot of the velocity in the plane of the heater and of the bubble diameter. The various bubble data are presented below as Figures 6.14-6.25 in their temporal order, although the individual bubble identification numbers used will not be correspondingly sequential.

As will be quantified in the following section, the action of the migrating bubbles had the effect of increasing the relative effectiveness of the heat transfer from the heater surface.

6.5 Dryout, Rewetting, Heat Transfer to Fluid

As pointed out in connection with the bubble dynamics for PBE-IA-IB-IC (STS-47-57-60) in Merte et al (1996), the initial bubble growth in certain cases following nucleation was so rapid that the camera speed was not sufficient to capture the motion. Certain of these cases resulted in departures from the heat transfer surface of the large vapor bubbles formed due to the momentum imparted to the liquid, causing rewetting of the heater surface and sustaining the nucleate boiling process even in the absence of buoyancy. Upon examining the photographs and the associated heat transfer coefficients it was noted that such departures took place in Run No. 2 of PBE-IA-IB-IC and also in Run Nos. 5 and 8 of PBE-IB. These all are Runs corresponding to the medium level of heat flux, nominally $q_T^{"} = 4\,{}^{w}/_{cm^2}$, which also produce the largest heater surface superheat at nucleation. To be contrasted with the prior behavior, the dynamic early vapor bubble growth producing a distinct momentum-induced departure took place in only one case with the last two space experiments, PBE-IIB-IIA (STS-72-77), in Run No. 2 of PBE-IIB (STS-72), as can be seen in Figure A-6b. This was also at the medium level of heat flux, $q^{"} = 4\,{}^{w}/_{cm^2}$, but at the higher subcooling of PBE-IIB (STS-72). The high superheats at nucleation necessary to produce the momentum-induced departure were not present in PBE-IIA (STS-77) because of the low levels of heat flux used.

The mean heat transfer behavior for all nine (9) Runs of the test matrix for PBE-IIB (STS-72) are summaried below in Table XII, along with the ${}^{a}/_{g} = +1$ Pre-flight test. Also included for comparison is the microgravity boiling heat transfer behavior for PBE-IB (STS-57), which employed the same hardware and heat flux levels. Only the subcooling levels for the latter case were different, at 11.1, 2.7, 0°C, as indicated in parentheses. For each Run the derived mean heat transfer coefficient is given, followed in parentheses by a mean steady heater surface superheat (when appropriate), followed by brief comments on the general behavior observed.

It is noted in Table XII that nucleate boiling at ${}^{a}/_{g} = +1$ takes place only for the highest levels of heat flux, in Run Nos. 1, 4, 7, with non-boiling convection occuring in all the others. In microgravity, in PBE-IIB (STS-72), on the other hand, dryout takes place at the highest level of heat flux in Run Nos. 4 and 7, but not in Run 1, because of the very high initial subcooling level (22.2 °C) employed here.

It is noted that the lower levels of heat flux, $q^{"} = 2\,{}^{w}/_{cm^2}$, in Run Nos. 3, 6, 9 of PBE-IIB (STS-72) resulted in higher heat transfer coefficients than those with the next higher level of heat

			PBE-IIB	PBE-IIB	PBE-IB
Run No.	q" W/cm^2	ΔT_{sub} °C	$h\ ^{W}/_{m^2}.K$ a/g~0 STS-72 2/5/96	$h\ ^{W}/_{m^2}.K$ a/g = 1 Pre-Flight 10/5/95	$h\ ^{W}/_{m^2}.K$ a/g~0 STS-57 6/2/93
1	8	22.2 (11.1)*	2400 (31) Nucleate Boiling	2800 (26) Nucleate Boiling	700 → 1000 Dry out → Rewet
2	4	22.2 (11.1)	1300 (24) Steady State + Oscillating	500 Non-Boiling Convection	1680 (22) Steady State
3	2	22.2 (11.1)	1500 (12) Steady State + Oscillating	480 (11) Non-Boiling Convection	960 (18) Steady State
4	8	16.7 (2.7)	500 Dry out	2800 (27) Nucleate Boiling	200 Dry Out
5	4	16.7 (2.7)	1000 (35) Nucleate Boiling	550 (43) Non-Boiling Convection	1420 (26) → 250 Steady S. → Dry out
6	2	16.7 (2.7)	1500 (14) Steady State + Bubble Migration	450 (14) Non-Boiling Convection	1080 (20) Steady State
7	8	11.1 (0)	200 Dry out	2600 (28) Nucleate Boiling	200 Dry Out
8	4	11.1 (0)	900 (41) Dry out + Nucleate Boiling	500 (47) Non-Boiling Convection	1340 (29) → 200 Steady S. → Dry out
9	2	11.1 (0)	1200 (18) Steady State + Oscillation	475 (23) Non-Boiling Convection	800 (STS-47-60) Steady-State Boiling

( ) Steady state mean heater surface superheat (°C)
* These subcooling levels correspond to PBE-IB (STS-57)

Table XII. Comparison of measured mean heat transfer coefficients between STS-72 Space Flight and a/g = + 1 Pre-Flight Test, and previous STS-57 Space Flight.

flux, $q^{"} = 4\ ^{w}/_{cm^2}$, in Run Nos. 2, 5, 8, for the same respective levels of subcooling. This is contrary to normal behavior in earth gravity, and is attributed to the presence of the small "migrating vapor bubbles" in the former case, as described previously in connection with Figures 6.14 - 6.25. The data from PBE-IB (STS-57) is included in Table XII to permit a direct comparison between the two series of microgravity tests that are identical, with the same hardware, except that the subcooling levels have been increased in PBE-IIB (STS-72), as indicated. No data

were available for Run No. 9 of PBE-IB (STS-57), so the mean values from PBE-IA-IC (STS-47-60) were inserted here for the sake of completeness. No definitive influence of subcooling is yet possible for pool boiling, since the process is inherently transient in microgravity conditions, except that dryout is inhibited as the subcooling level is increased significantly.

Table XIII provides the corresponding comparisons of the heat transfer coefficients for PBE-IIA (STS-77), in which the subcooling levels were the same as those employed earlier, but the heat flux levels were reduced. Also included are both the Pre- and Post-Flight tests at a/g = + 1, and the consistent reproducibility in the measurements is to be noted, albeit with only non-boiling natural convection present. The heat transfer coefficients in microgravity at these low levels of heat flux are considerably lower than those for the high heat flux levels: As noted from the photographs, the bubble population density, responsible in part for the effectiveness of the boiling process, is quite low in this case.

As described previously, the mean fluid heat transfer coefficients computed from the measured mean heater surface temperatures are plotted in Figures 1a ---- li of Appendices A and B for each of the respective Runs of the matrix. A definite relationship exists between the transient mean heater surface temperature and the heat transfer coefficient. These serve to indicate, qualitatively, the modes of heat transfer between the heater surface and fluid: conduction to the liquid; nucleate boiling; conduction to the vapor phase (termed dryout); and combinations of the three forgoing mechanisms based on the fractional part of the heater surface over which each is acting. For the heat flux levels used to date, nucleation and its propagation across the heater surface take place early in the process, so that the major part of the heat transfer surface is either covered by vapor or influenced by the nucleate boiling phenomenon itself. Where the heat flux levels are sufficiently low that relatively smaller portions of the heater surface are influenced by the presence of either nucleating sites or significant amounts of vapor, as in PBE-IIA (STS-77), the heat transfer to the stagnant liquid regions can then be incorporated, once the heat transfer associated with each nucleation site is determined. This element of the analytical work will be conducted in the future.

For those circumstances where a portion of the heating surface is dry during boiling in microgravity, a procedure is used by which the mean transfer coefficient is computed for that portion of the heater surface on which nucleate boiling is taking place, using measurements of the overall mean heat transfer coefficient and the fractional dry area of the heater surface. The procedure is described in Appendix E of Merte et al (1996), and involve several simplifying assumptions, also included in Appendix E. The most severe one under certain circumstances is that the ratio of the mean superheat over the nucleate boiling portion of the heater surface to that over the entire heater surface is approximately unity. In the process of evaluating the fractional dry heater area from the digitized images, using commercial image analyzing software, it was found

			PBE-IIA	PBE-IIA	PBE-IIA
Run No.	q'' W/cm^2	ΔT_{sub} °C	h $W/m^2.K$ a/g~0 STS-77 5/19/96	h $W/m^2.K$ a/g = + 1 Pre-Flight 3/19/96	h $W/m^2.K$ a/g = + 1 Post-Flight 7/18/96
1	2	11.1	900 (20) Steady-State + Oscillating	450 (26) Non-Boiling Convection	470 (26) Non-Boiling Convection
2	1	11.1	860 (11) Steady State + Oscillating	400 (10) Non-Boiling Convection	420 (9) Non-Boiling Convection
3	0.5	11.1	No Boiling	450 (0) Non-Boiling Convection	450 (0) Non-Boiling Convection
4	2	2.7	1050 (18) Nucleate Boiling	450 (33) Non-Boiling Convection	470 (32) Non-Boiling Convection
5	1	2.7	700 (13) Nucleate Boiling + Oscillating	470 (17) Non-Boiling Convection	410 (19) Non-Boiling Convection
6	0.5	2.7	375 (13) Steady State + Oscillating (rewet)	450 (7) Non-Boiling Convection	450 (7) Non-Boiling Convection
7	2	0	900 (23) Nucleate Boiling	450 (34) Non-Boiling Convection	450 (37) Non-Boiling Convection
8	1	0	700 (16) Nucleate Boiling	450 (20) Non-Boiling Convection	420 (20) Non-Boiling Convection
9	0.5	0	450 (14) Nucleate Boiling (Barely)	500 (10) Non-Boiling Convection	450 (10) Non-Boiling Convection

( ) Steady state mean heater surface superheat (°C)

Table XIII. Comparison of measured mean heat transfer coefficients between STS-77 Space Flight and a/g = + 1 Pre- and Post-Flight Tests.

that defining the dry-out portion of the heater surface requires a certain element of human interpretation, since the automatic measurements based on a defined gray scale in conjunction with the processing software available tended to produce much larger fractional dry areas than was deemed reasonable. Nucleating sites produce light shaded areas similar to dry areas, but make significant contribution to the heat transfer, and must be discounted in the area evaluation.

The time domains within each Run of PBE-IIB-IIA (STS-72-77) over which measurements of the dry fraction of the heater surface were made are tabulated in Table IV of Appendices A and B, respectively. Following these, for each of these time domains the heater surface dry fraction and mean temperature are plotted in Figures 10--i, the wet fraction and mean heat transfer coefficient are plotted in Figures 10--ii, the microgravity boiling heat transfer coefficient computed from Equation (E.12) of Merte et al (1996) is added to these latter two quantities in Figures 10--iii, and sample images are given in Figures 10--iv.

The net results in Figures 10 of Appendices A and B are condensed in Table XIV in terms of the following for each time domain in each Run: Range of mean heater surface temperatures covered; Range of fractional dry heater surface area; Range of mean heat transfer coefficient (w/m^2k); and range of microgravity boiling heat transfer coefficient. For each time domain in each Run the values listed for the ranges are corresponding ones in the order given. All of the results are transient in nature in that variations with time take place, and where single values are given represent short term steady states. These transients, consisting of progressive dry-out or rewetting, can be viewed as taking place in a transition from complete nucleate boiling to complete dry-out, termed the transition boiling domain at $a/g = +1$.

Run		PBE-II-B (STS-72)				PBE-IIA (STS-77)			
No.	Section	T_ω(°C)	x (dry)	h (mean)	h (boil)	T_ω(°C)	x (dry)	h (mean)	h (boil)
1	1	89-92	0-0.16	2100-2450	2100-2800	75-82	.10-.60	600-1100	900-1600
	2					76-82	.1-.5	700-1100	1200
	3					76-84	.1-.4	500-1200	900-1500
	4								
2	1	80-85	.04-.22	2150-1450	2350-1700	70-75	.02-.18	400-1200	400-1400
	2	81-89	0-.35	1200-2050	1600-2200	69-73	.05-.18	600-1300	600-1600
	3								
	4								
3	1								
	2								
4	1	123-144	.38-.57	550-800	1100-1500				
	2								
5	1	84-93	.18-.4	850-1500	1250-2000	61-68	.2-.7	400-1400	1000-3000
	2	89-94	.25-.45	850-1200	1300-1600	63-67	.1-.5	400-1000	600-1600
6	1	77-96	.05-.5	800-1600	1400-1800	63-66	.25-.5	200-600	200-1100
	2								
7	1					72-95	.5-.95	300-1100	1000-4000
	2					70-72	.5-.9	800-1000	2000-4000
8	1	81-88	.35	750-1000	1200-1500	63-67	.1-.6	300-1100	500-2000
	2	89-93	.27-.4	700-850	1050-1300				
9	1	69-73	0-.4	800-1500	1200-2000	62-67	.2-.6	300-600	400-800
	2								

Table XIV. Measurement summary of transient dry-out and rewetting on heater surface in microgravity. PBE-IIB-IIA (STS-72-77).

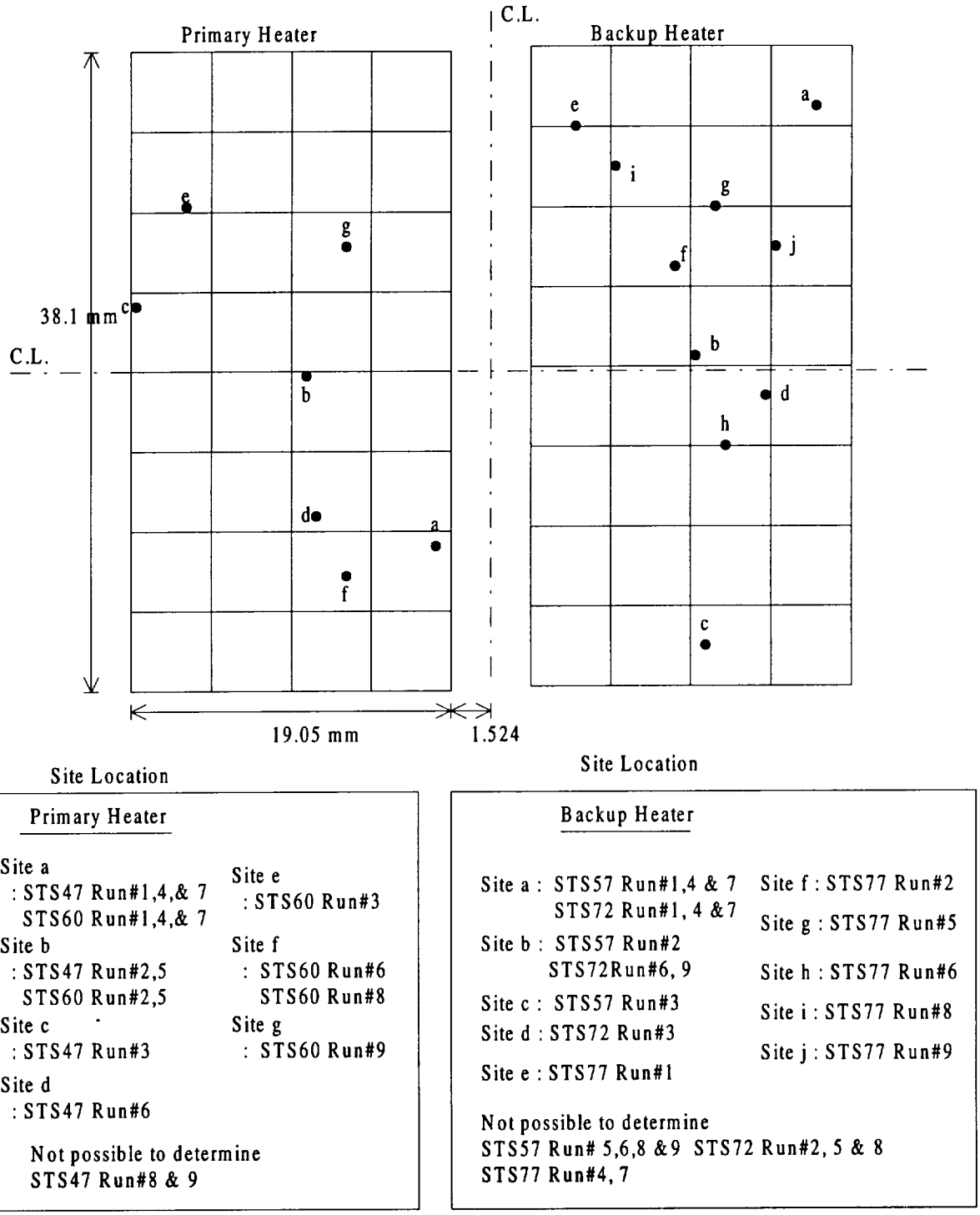

Figure 6.1. Locations of the initial nucleation sites for all Pool Boiling Experiments conducted in microgravity to date. Left side: Primary heater used for PBE-IA-IC (STS-47-60). Right side: Secondary heater used for PBE-IB-IIB-IIA (STS-57-72-77).

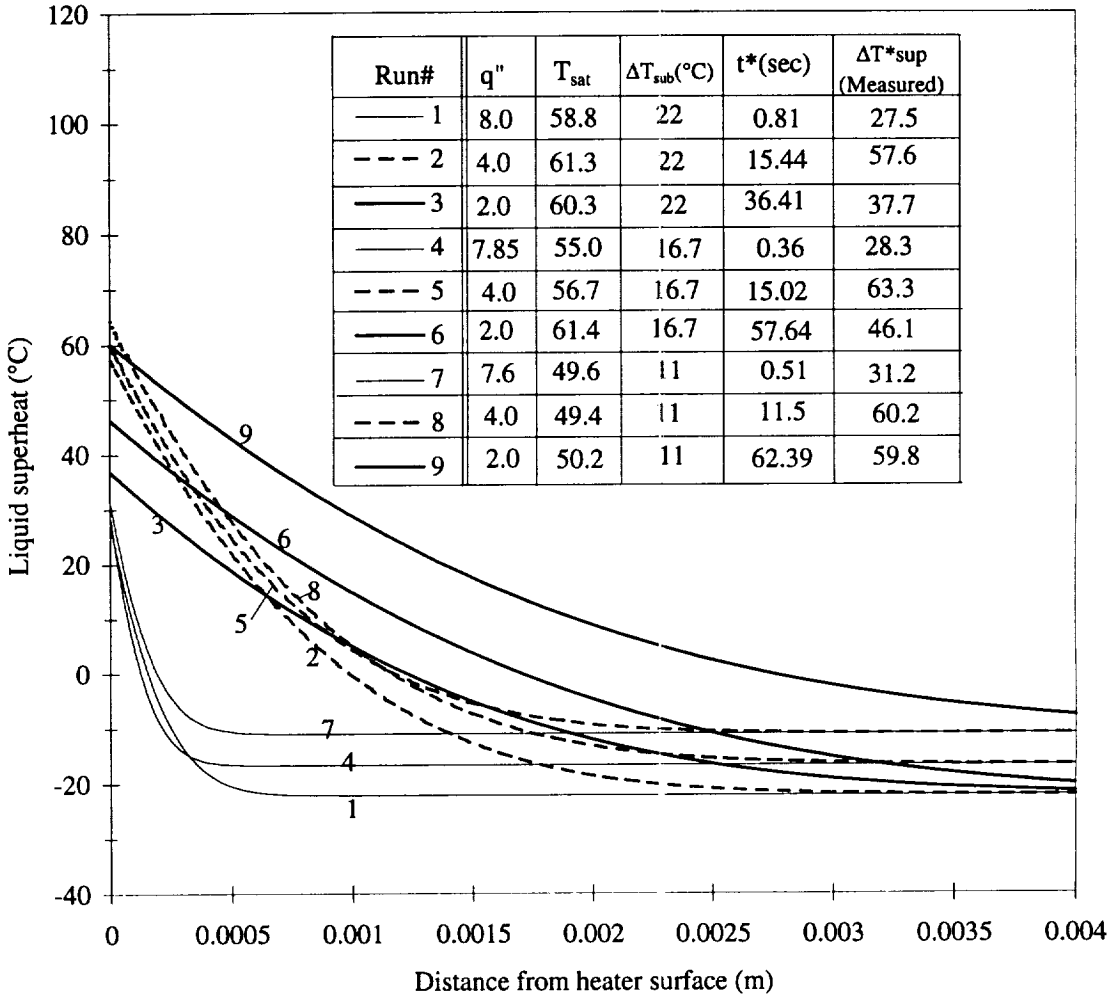

Figure 6.2. Local R-113 temperature distribution at nucleation at heater surface sites indicated on Figure 6.1 PBE-II B (STS-72).

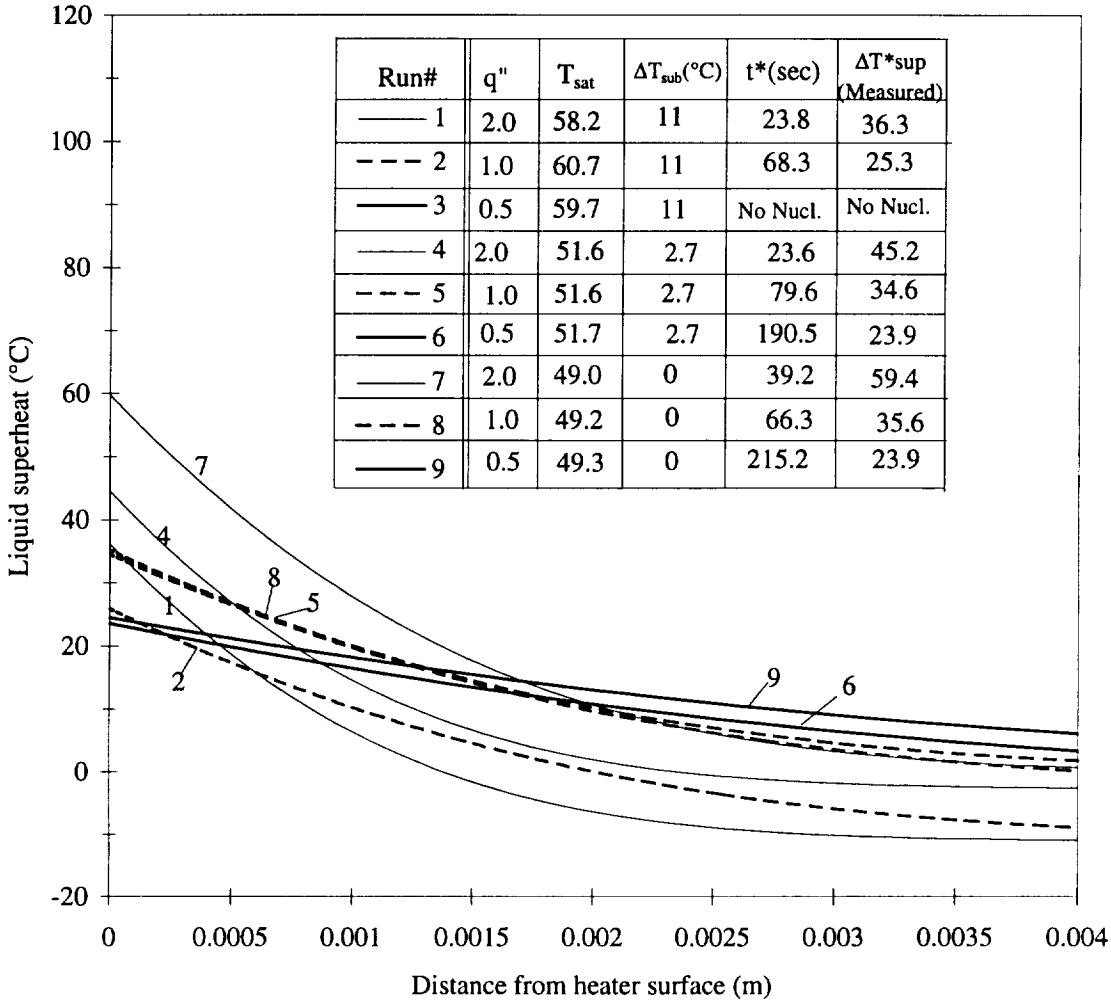

Run#	q"	T_{sat}	ΔT_{sub}(°C)	t*(sec)	ΔT*sup (Measured)
1	2.0	58.2	11	23.8	36.3
2	1.0	60.7	11	68.3	25.3
3	0.5	59.7	11	No Nucl.	No Nucl.
4	2.0	51.6	2.7	23.6	45.2
5	1.0	51.6	2.7	79.6	34.6
6	0.5	51.7	2.7	190.5	23.9
7	2.0	49.0	0	39.2	59.4
8	1.0	49.2	0	66.3	35.6
9	0.5	49.3	0	215.2	23.9

Figure 6.3. Local R-113 temperature distribution at nucleation at heater surface sites indicated on Figure 6.1 PBE-II A (STS-77).

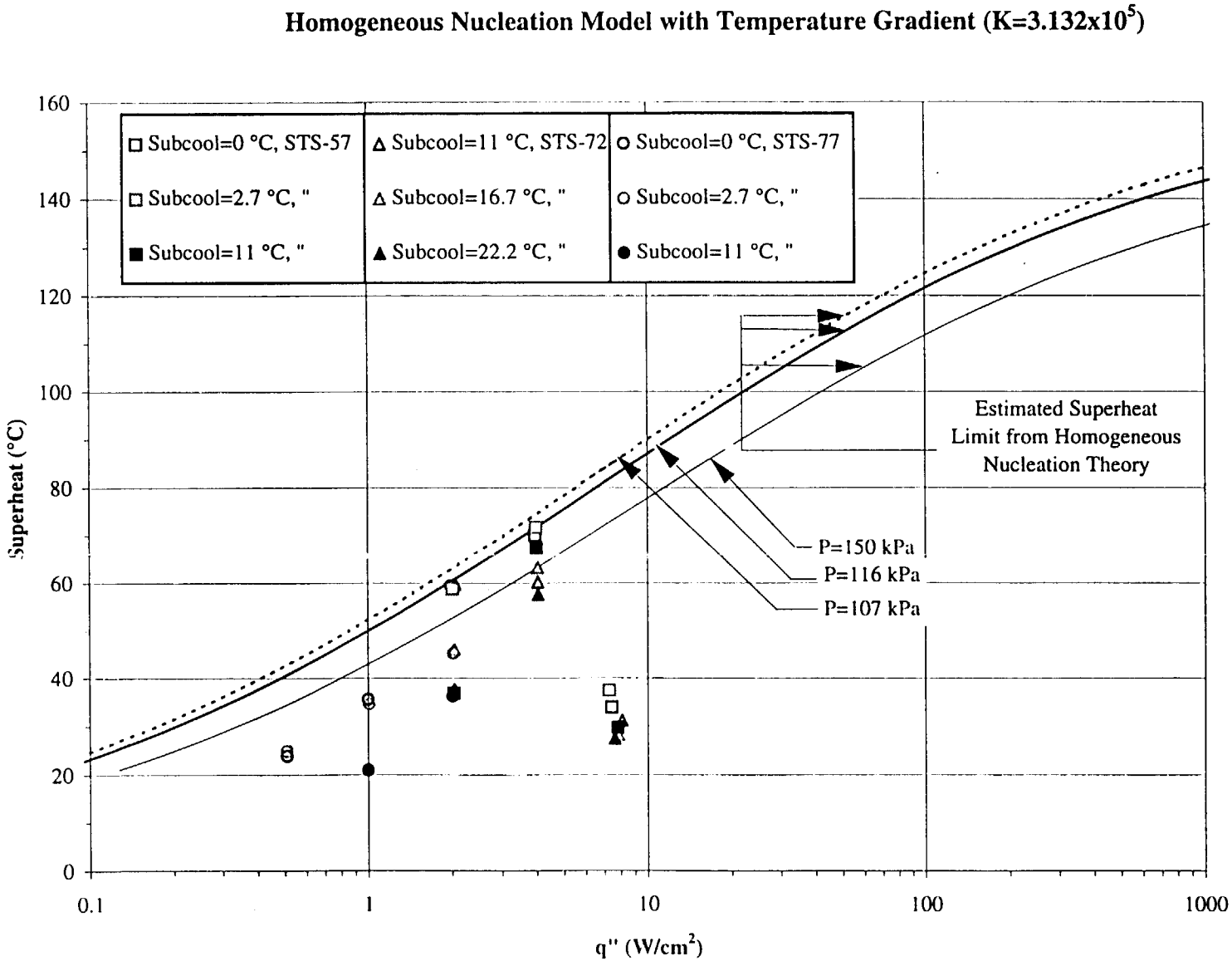

Figure 6.4. Homogeneous nucleation model for R-113 with transient heating in microgravity. Nucleation measurements from PBE-IB (STS-57), PBE-IIB (STS-72), PBE-IIA (STS-77). K* evaluated from PBE-IA (STS-47). Run No. 9.

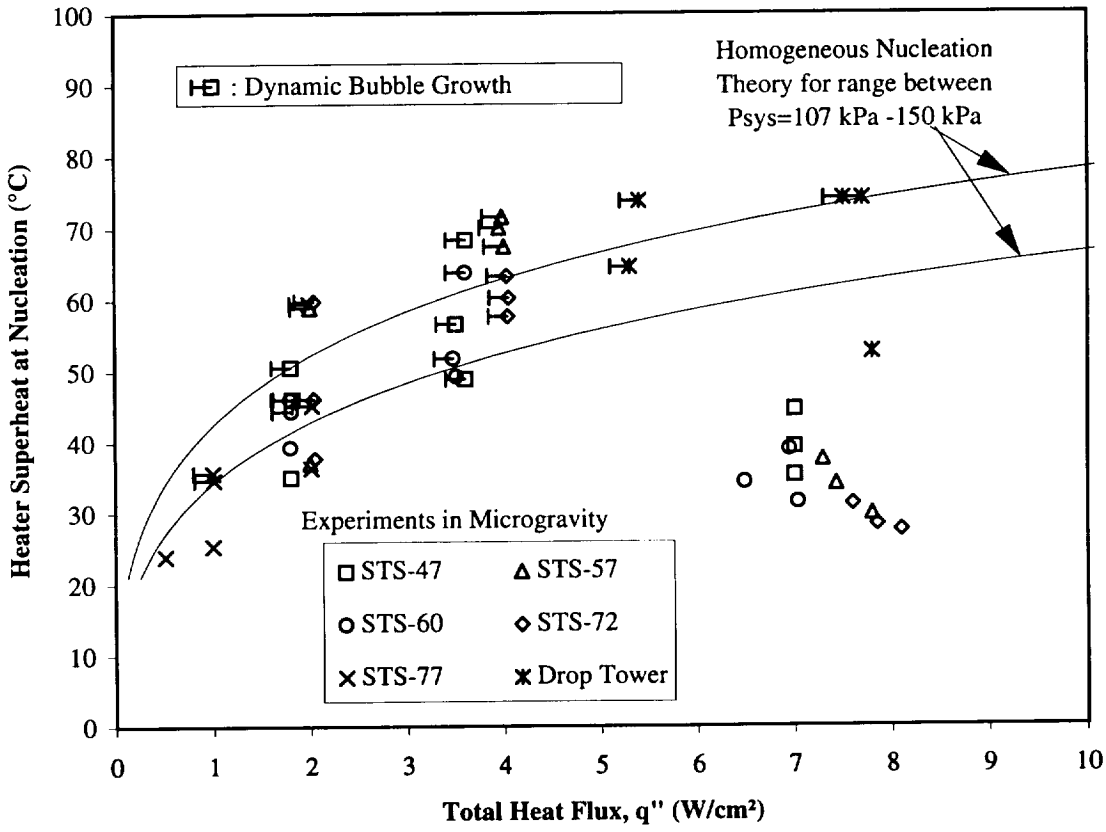

Figure 6.5. Homogeneous nucleation model for R-113 with transient heating in microgravity. Measurements from PBE-IA-IB-IC-IIB-IIA (STS-47-57-60-72-77), plus pre-flight drop tower tests. K* evaluated from PBE-IA (STS-47). Run No. 9.

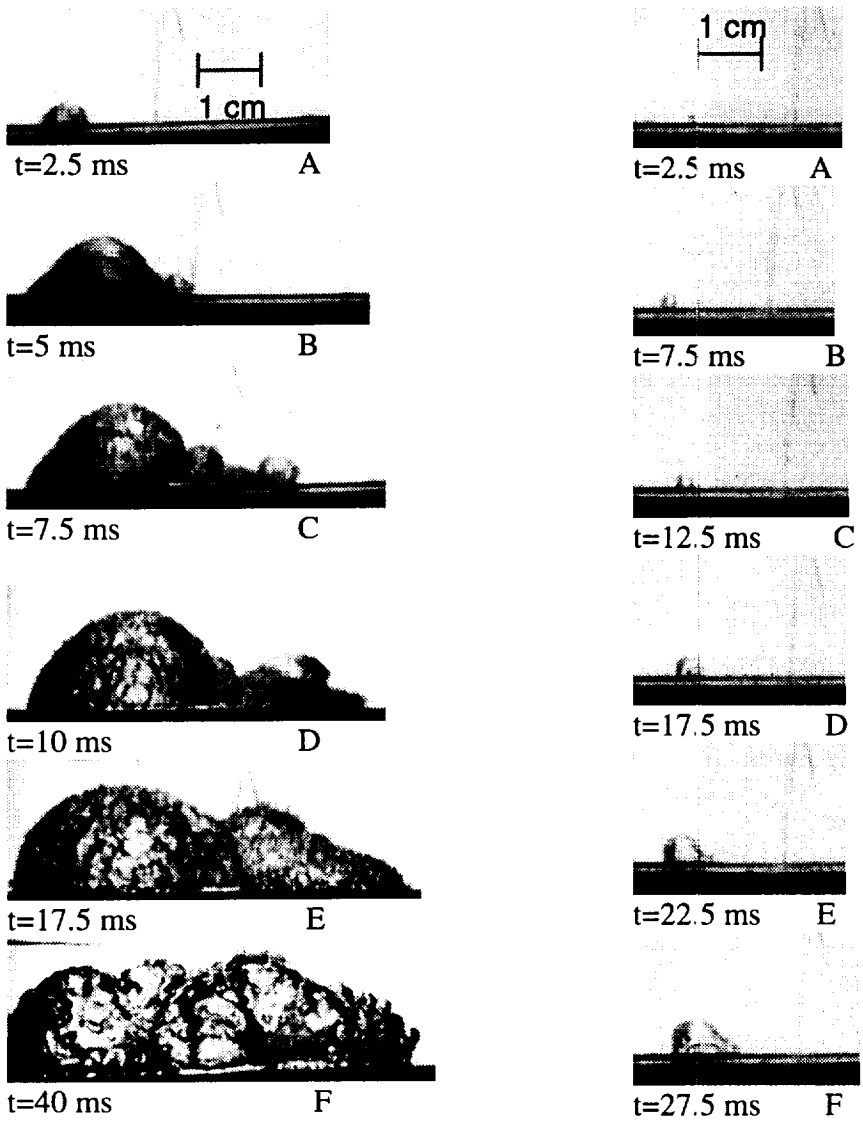

PBMT1102.800
q''_T=7.70W/cm²
t*=2.264 sec
P_{sys}=103.75 kPa,
T_∞ =47.50 °C
T_{sat}=48.27 °C
T_w^*=123.62 °C
ΔT_{wsup}^*=75.35 °C
ΔT_{sub}=0.77 °C
(a)

PBMT1129.820
q''_T=7.87 W/cm²
t*=1.550 sec.
P_{sys}=142.34 kPa
T_∞ =47.06 °C
T_{sat}=58.19 °C
T_w^*=110.60 °C
ΔT_{wsup}^*=52.41 °C
ΔT_{sub}=11.13 °C
(b)

Figure 6.6. Comparisons of early vapor bubble growth behavior under microgravity of drop tower with different levels of heat flux and subcooling. For Lee and Merte (1996a).

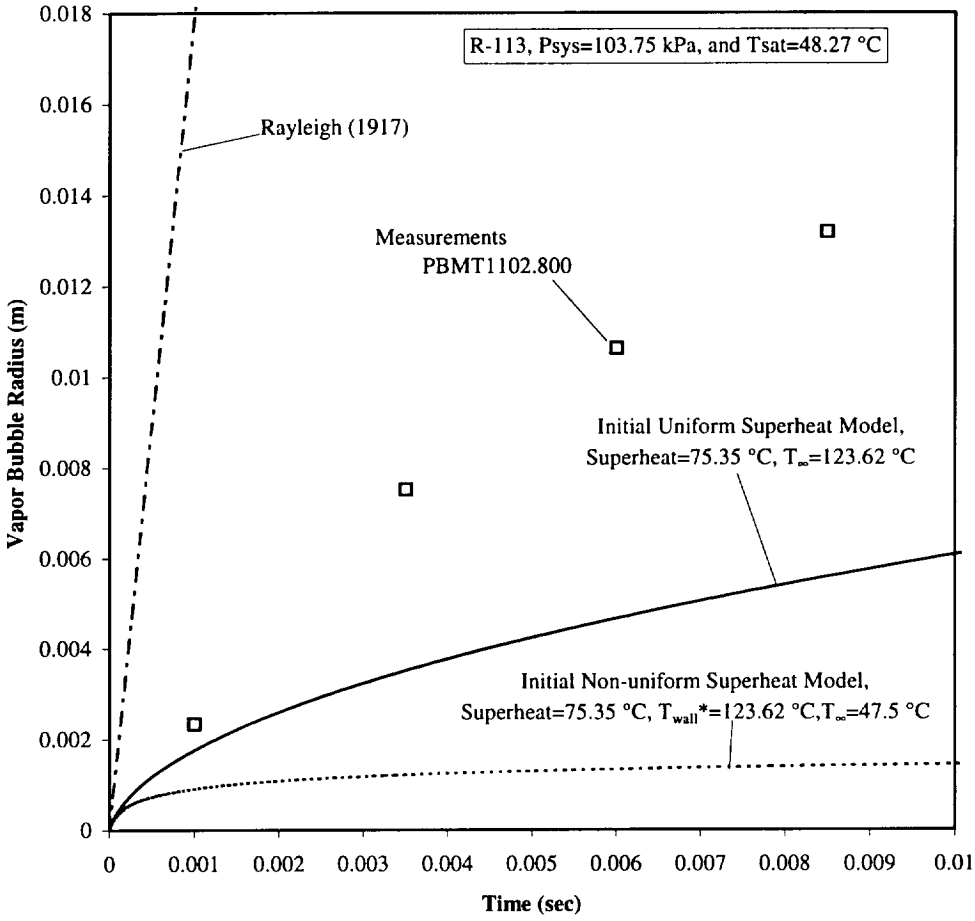

Figure 6.7. Comparisons of experimental bubble growth data with several spherical vapor bubble growth models. Experimental conditions correspond to Figure 6.6 (a).

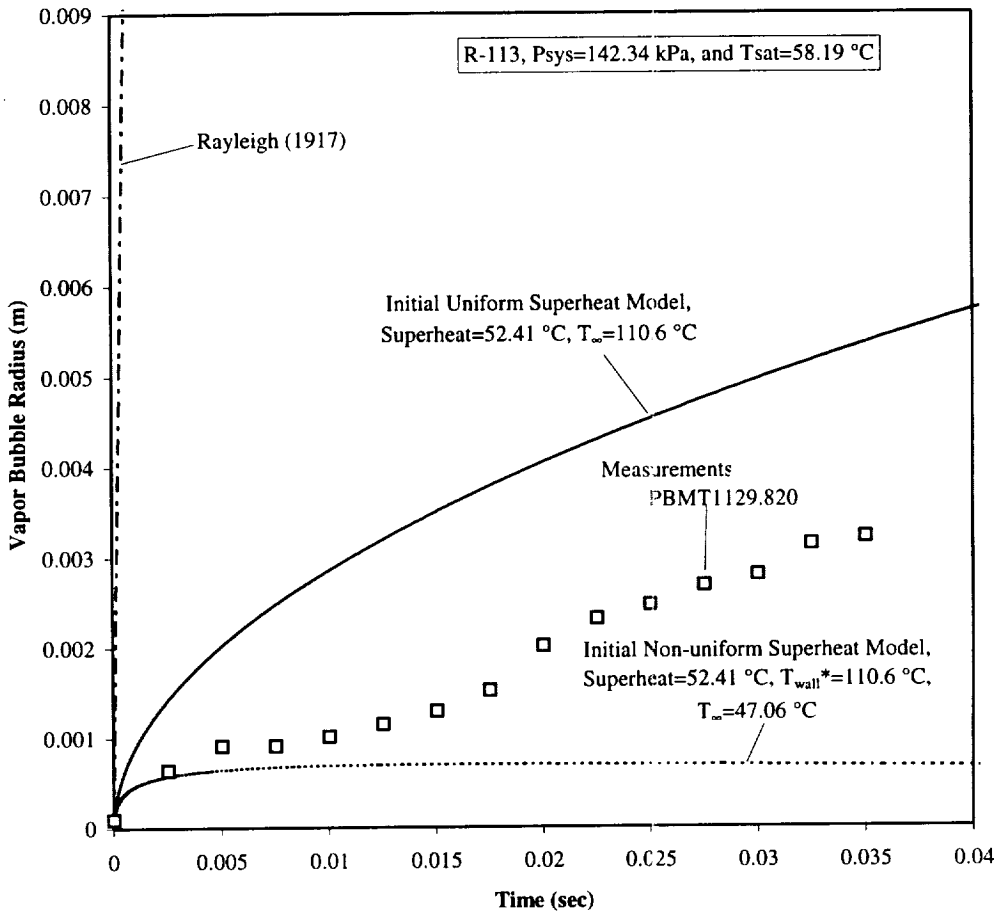

Figure 6.8. Comparisons of experimental bubble growth data with several spherical vapor bubble growth models. Experimental conditions corresponds to Figure 6.6 (b).

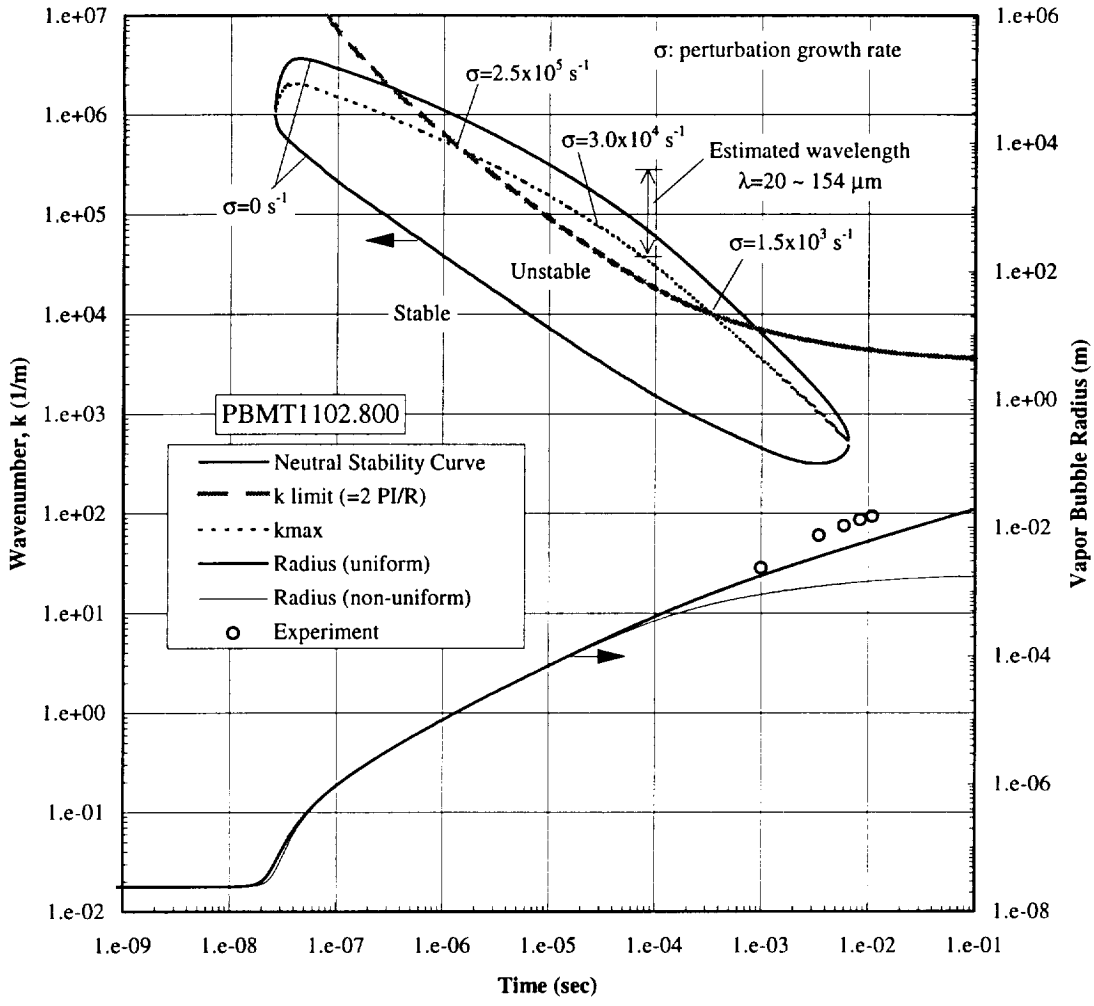

Figure 6.9. Neutral stability diagram and growing bubble radius for R113. Experimental conditions corresponds to Figure 6.6 (a).

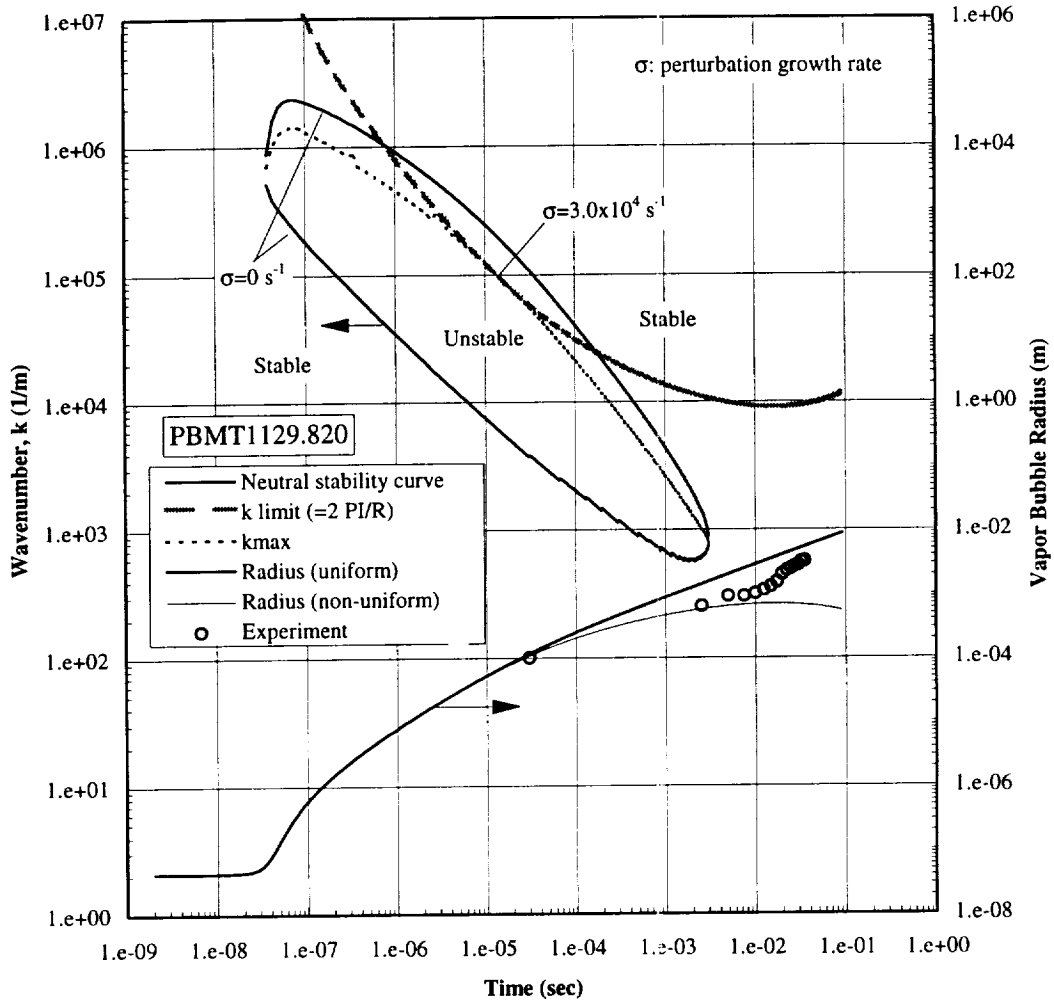

Figure 6.10. Neutral stability diagram and growing bubble radius for R113. Experimental conditions corresponds to Figure 6.6 (b).

STS-77 Run #6

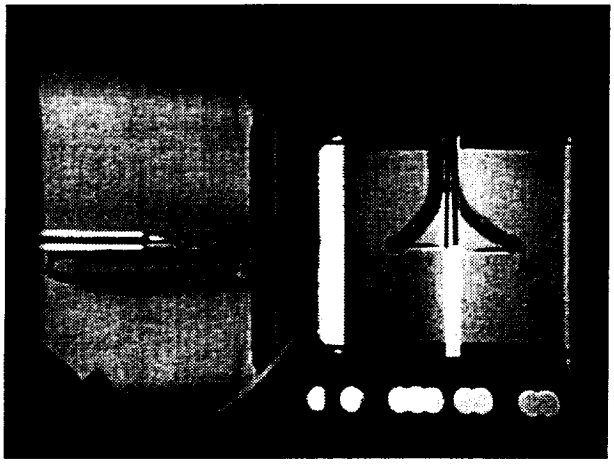

Frame # 0001 time=200.50sec

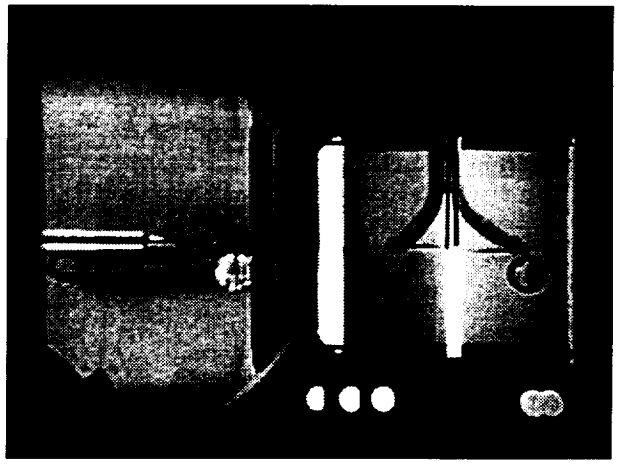

Frame #0002 time=200.60sec

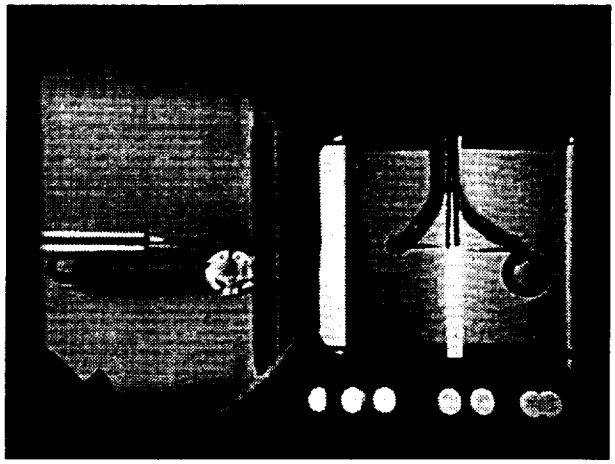

Frame #0003 time=200.70sec

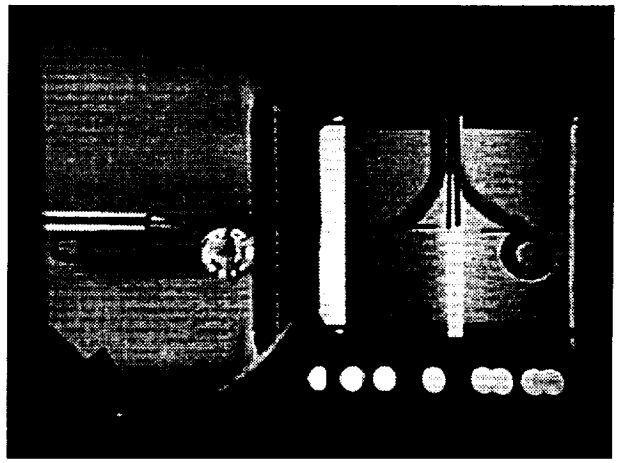

Frame #0004 time=200.80sec

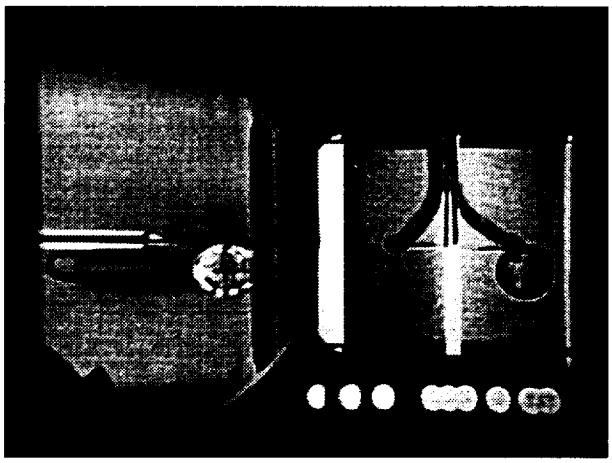

Frame #0005 time=200.90sec

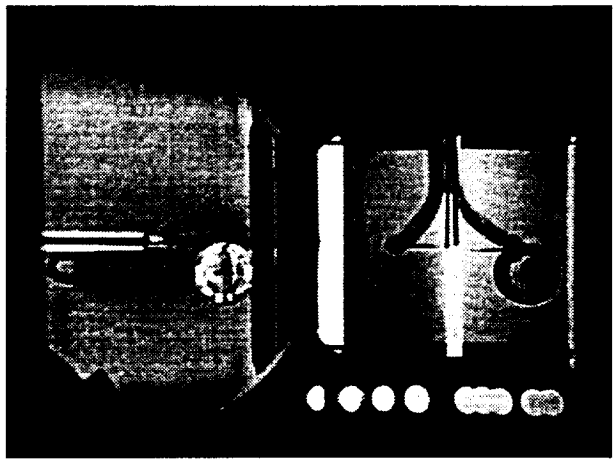

Frame #0006 time=201.00sec

Figure 6.11. Photos of initial "normal" vapor bubble growth obtained in microgravity at 10 pps. PBE-IIA (STS-77). Run No. 6. $q'' = 0.51$ w/cm^2; $T_{sat} = 51.7$°C; P = 116.11 kPa; $\Delta T_{sub} = 2.7$°C; t* = 190.5 sec.

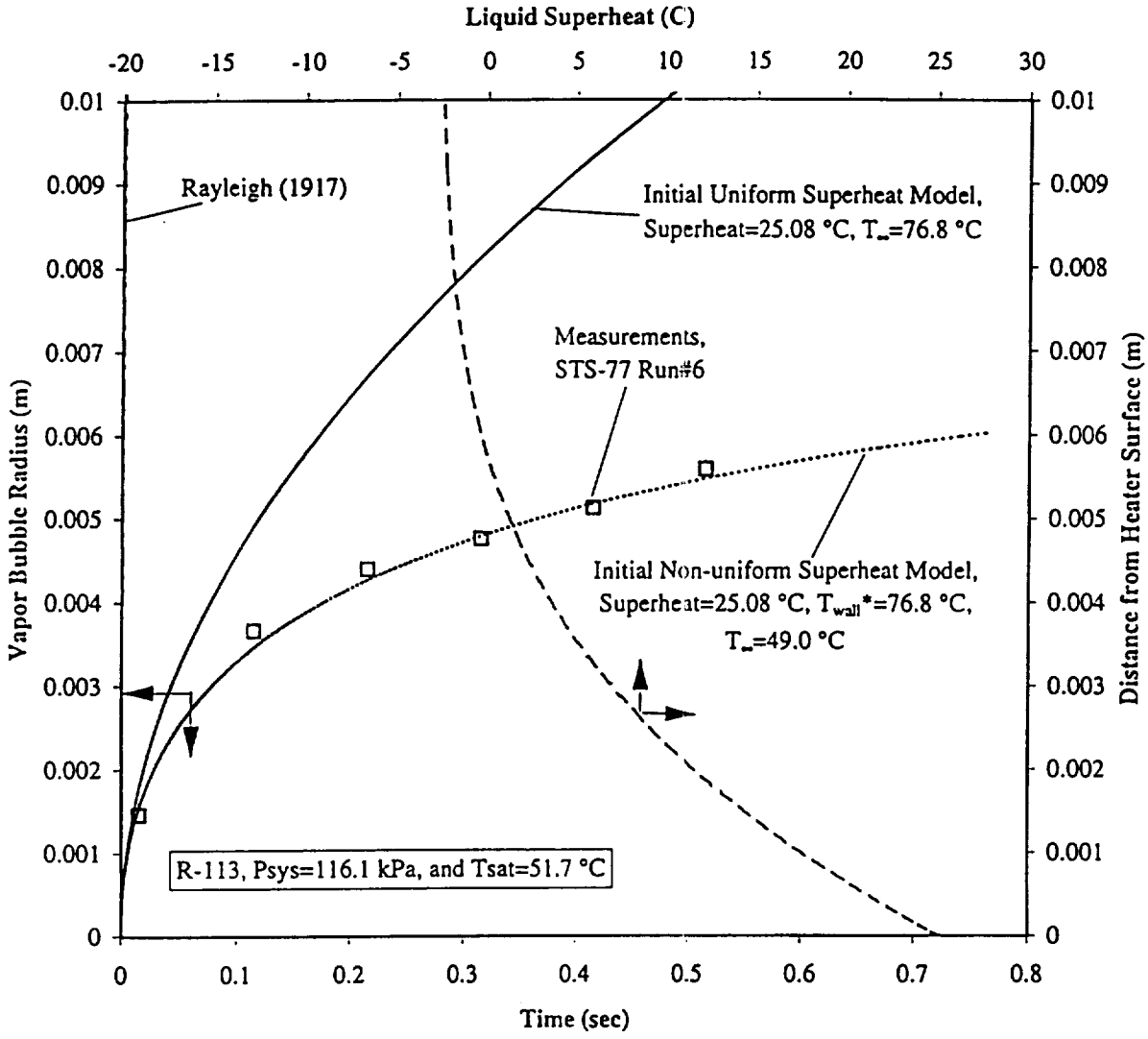

Figure 6.12. Comparison of vapor bubble growth measurements from Figure 6.11 with theoretical model. PBE-IIA (STS-77). Run No. 6. Liquid superheat distribution is that existing at nucleation. q" = 0.51 w/cm^2; T_{sat} = 51.7°C; P = 116.11 kPa; ΔT_{sub} = 2.7°C; t* = 190.5 sec.

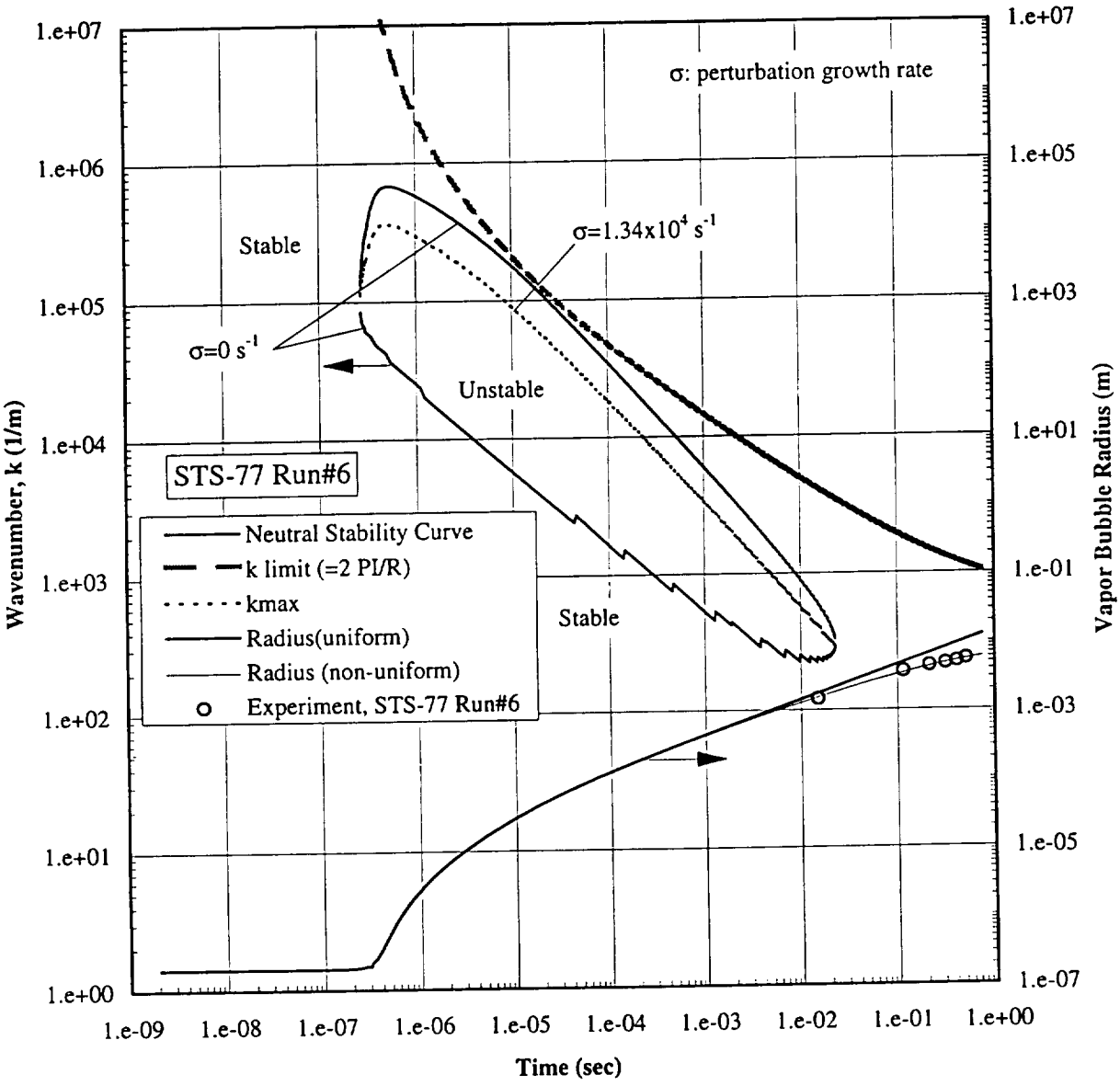

Figure 6.13. Neutral stability diagram and growing vapor bubble radius from Figure 6.11 for R-113 in microgravity. PBE-IIA (STS-77). Run No. 6.

Figure 6.14a. Sequential photographic images of migrating bubbles. PBE-IIB (STS-72). Run No. 3. Bubble #5. See Table VII for parameters. Time interval: 70.7-74.2 seconds.

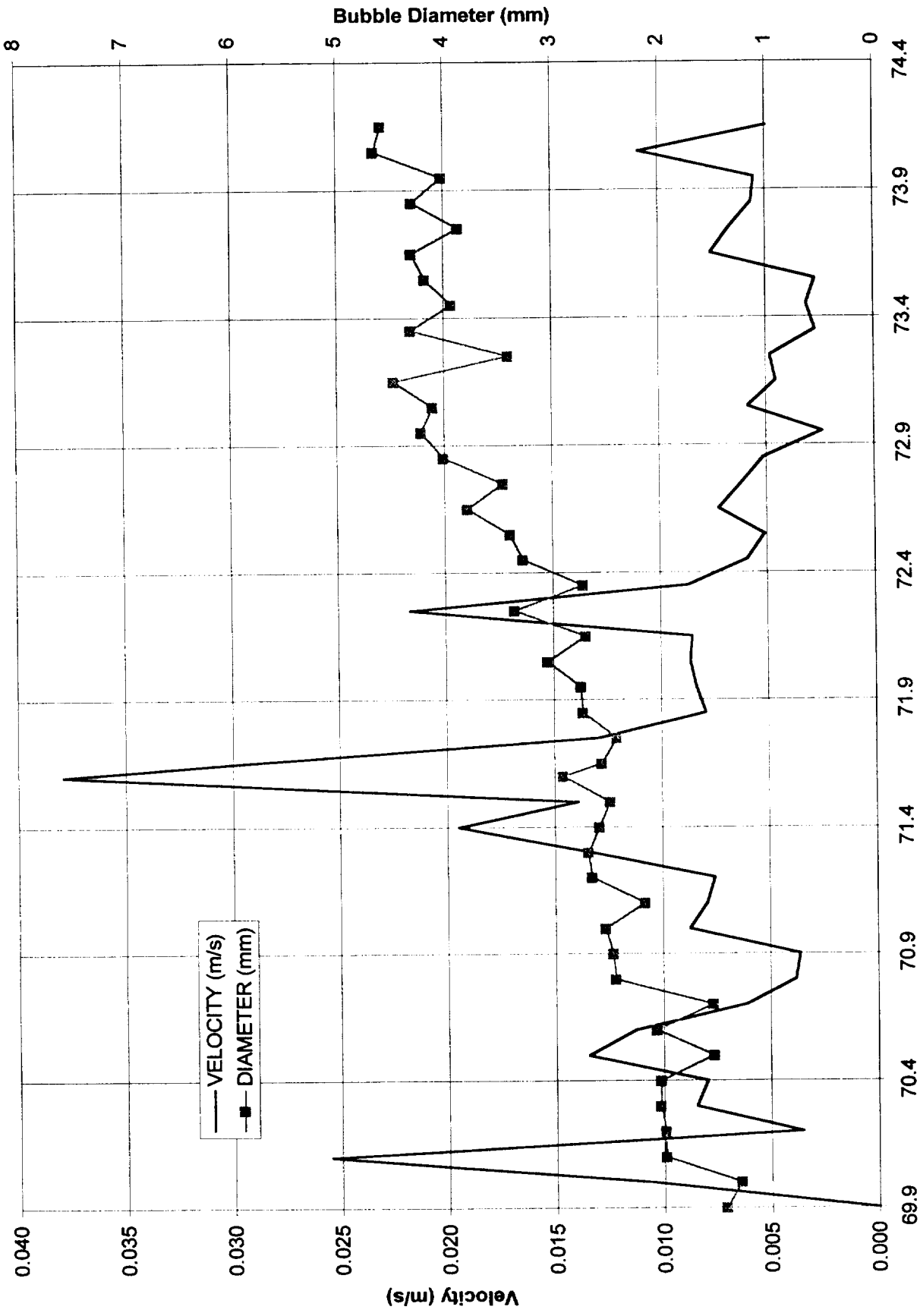

Figure 6.14b. Velocities and diameters for bubble of Figure 6.14a.

STS-72 Run #3, Bubble #6

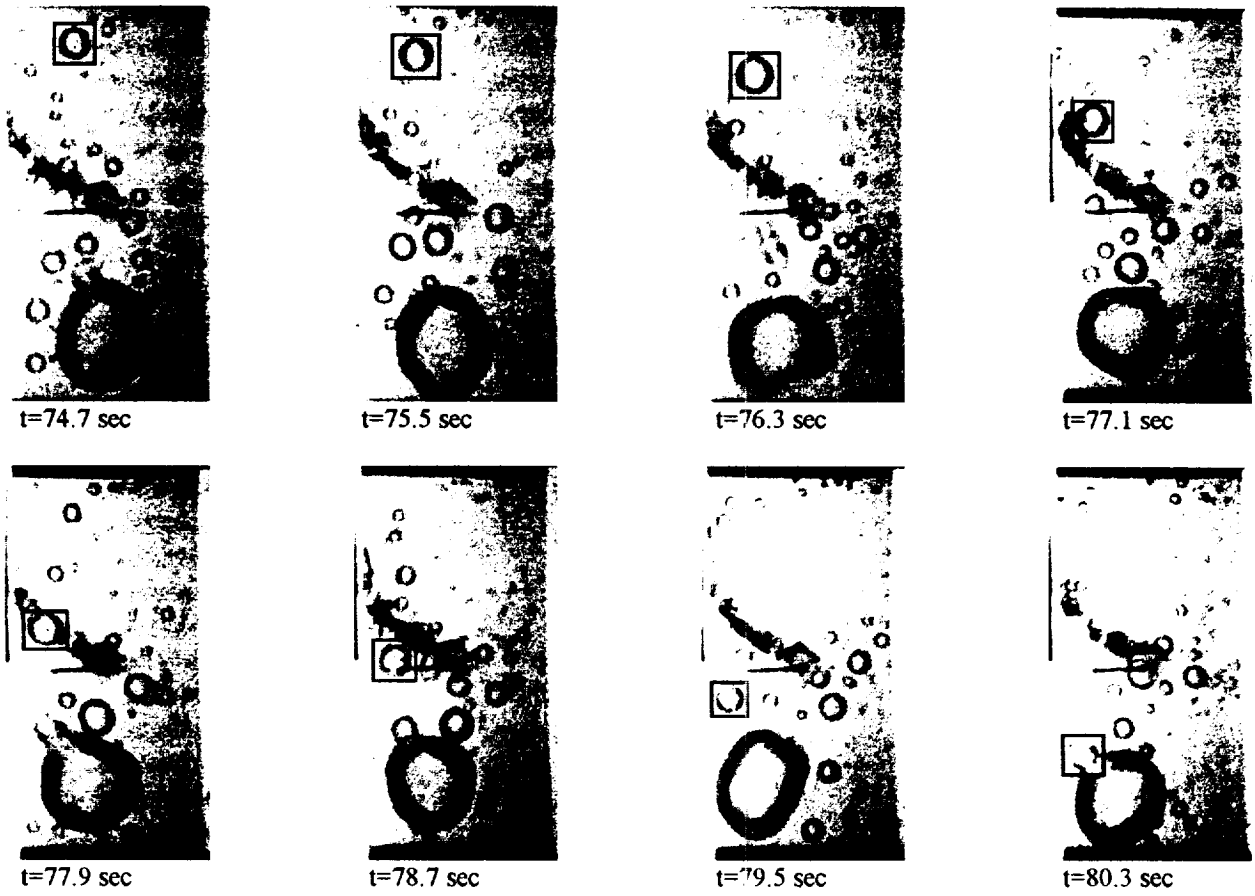

Figure 6.15a. Sequential photographic images of migrating bubbles. PBE-IIB (STS-72). Run No. 3. Bubble #6. See Table VII for parameters. Time interval: 74.7-80.3 seconds.

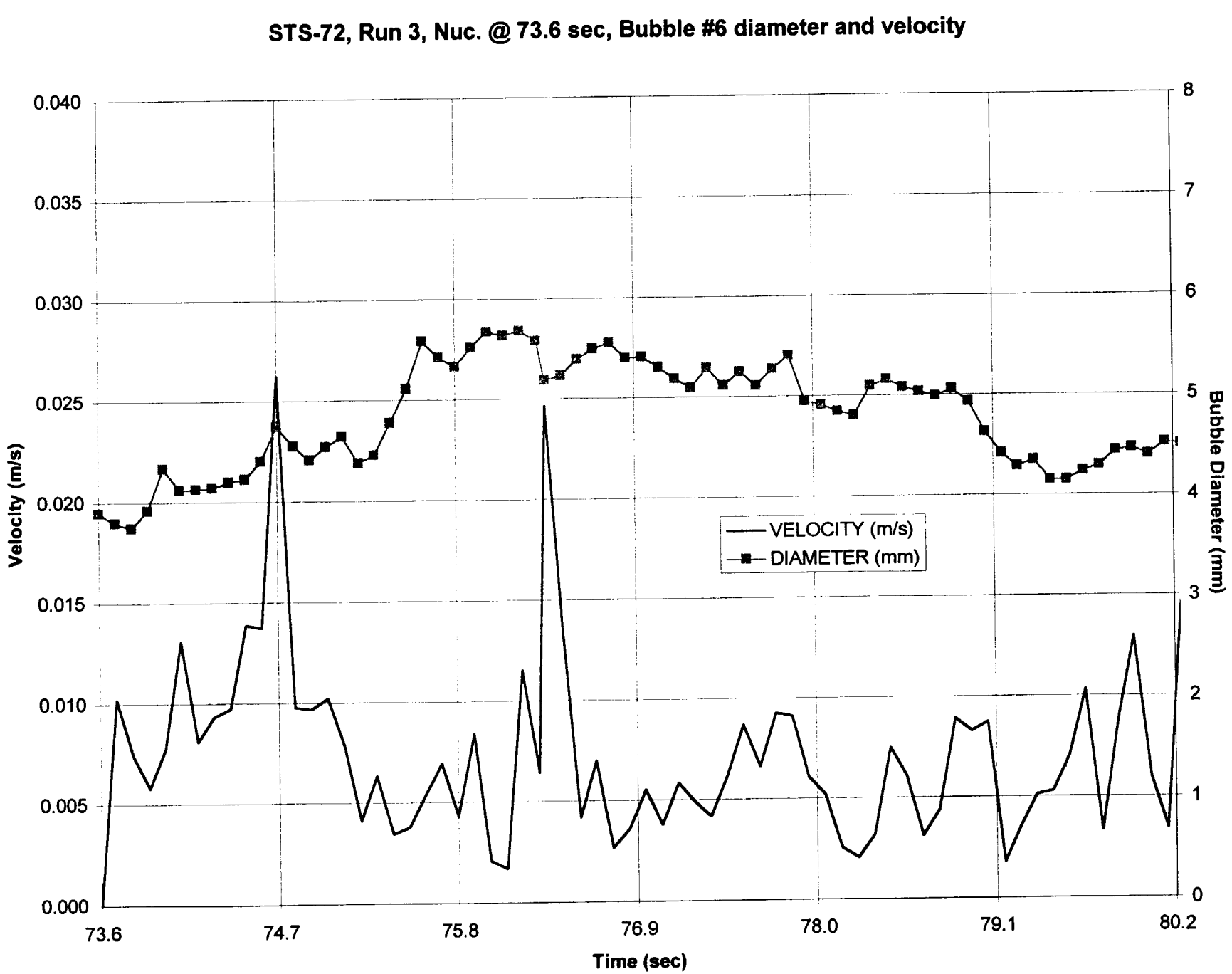

Figure 6.15b. Velocities and diameters for bubble of Figure 6.15a.

STS-72 Run #3, Bubble #4

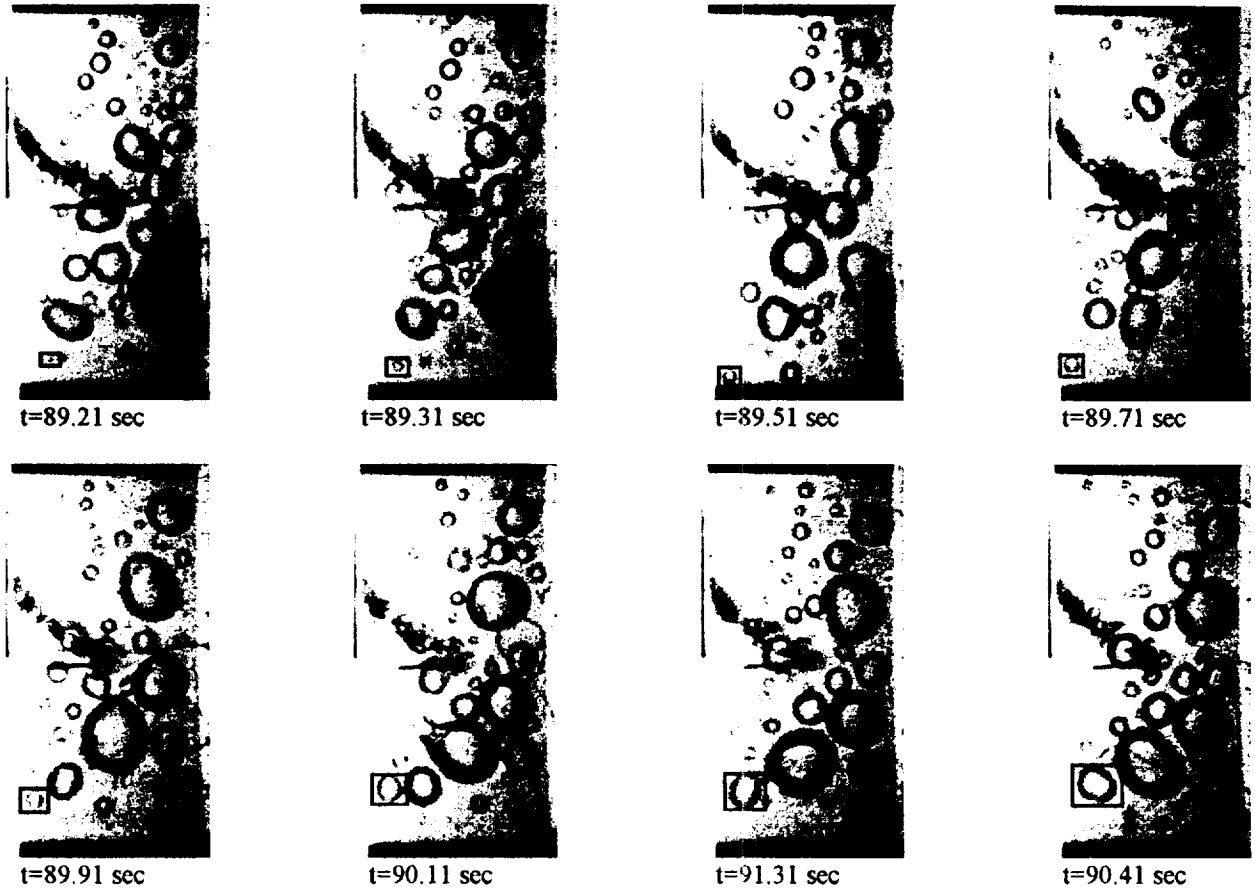

Figure 6.16a. Sequential photographic images of migrating bubbles. PBE-IIB (STS-72). Run No. 3. Bubble #4. See Table VII for parameters. Time interval: 89.21-90.41 seconds.

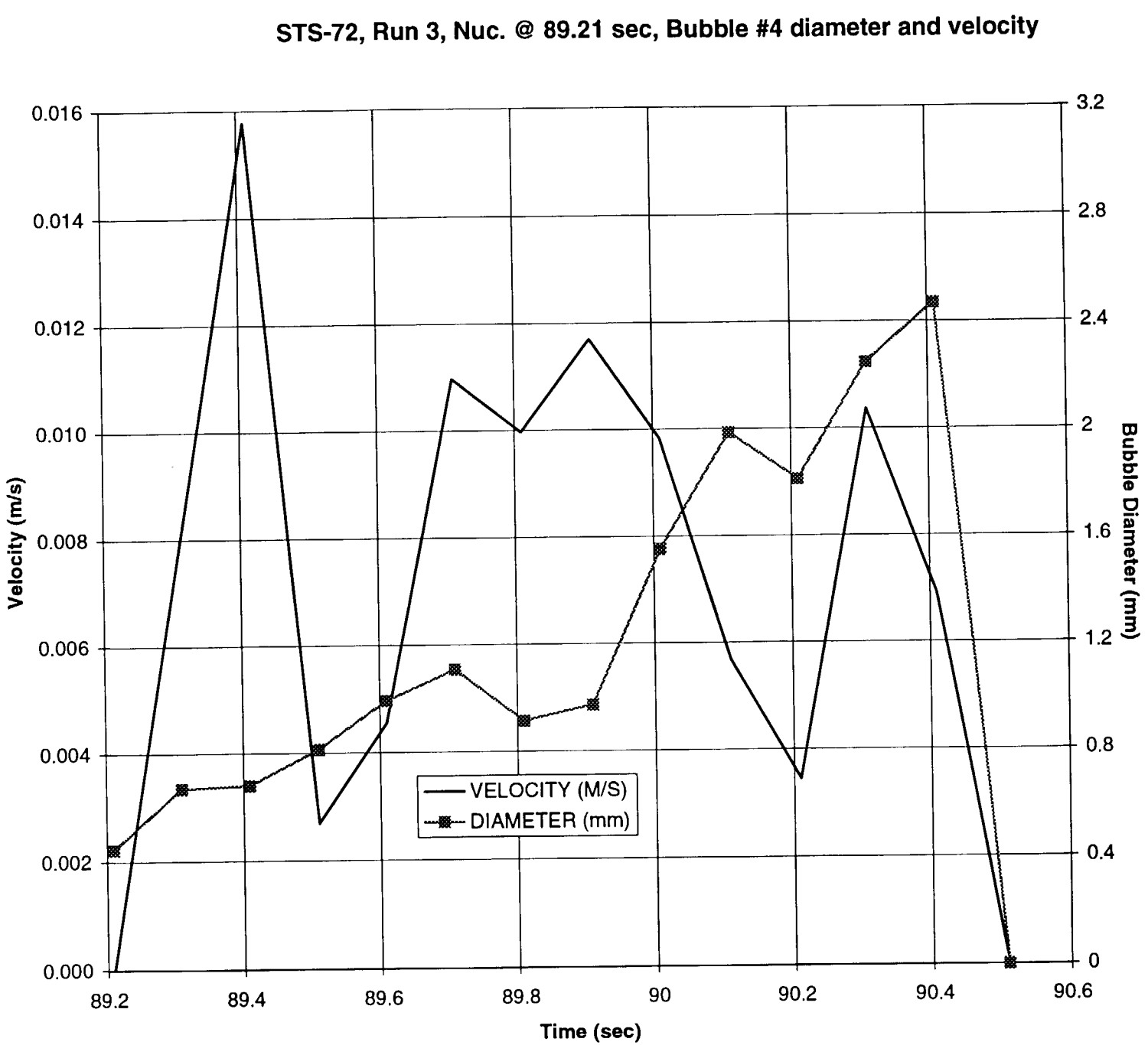

Figure 6.16b. Velocities and diameters for bubble of Figure 6.16a.

STS-72 Run #3, Bubble #1

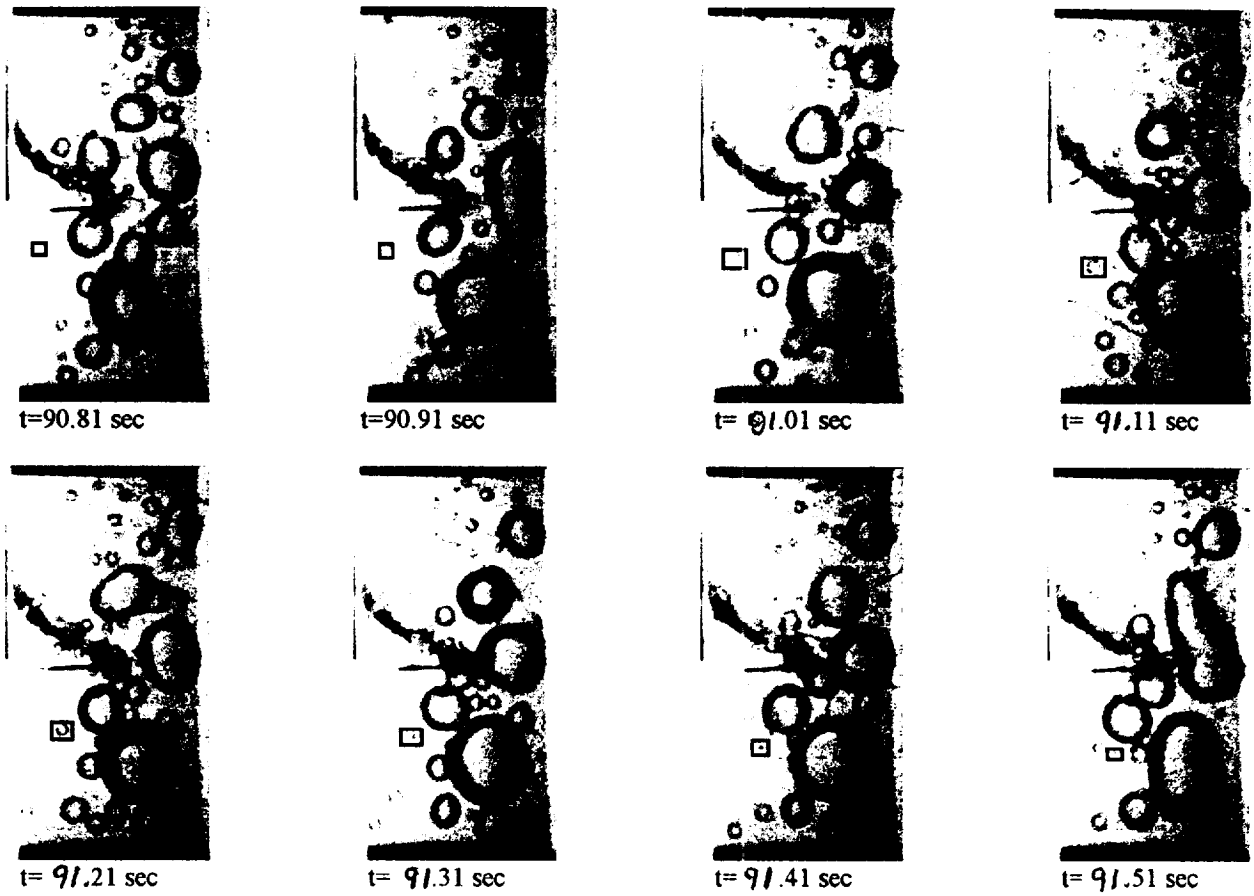

Figure 6.17a. Sequential photographic images of migrating bubbles. PBE-IIB (STS-72). Run No. 3. Bubble #1. See Table VII for parameters. Time interval: 90-81-91.51 seconds.

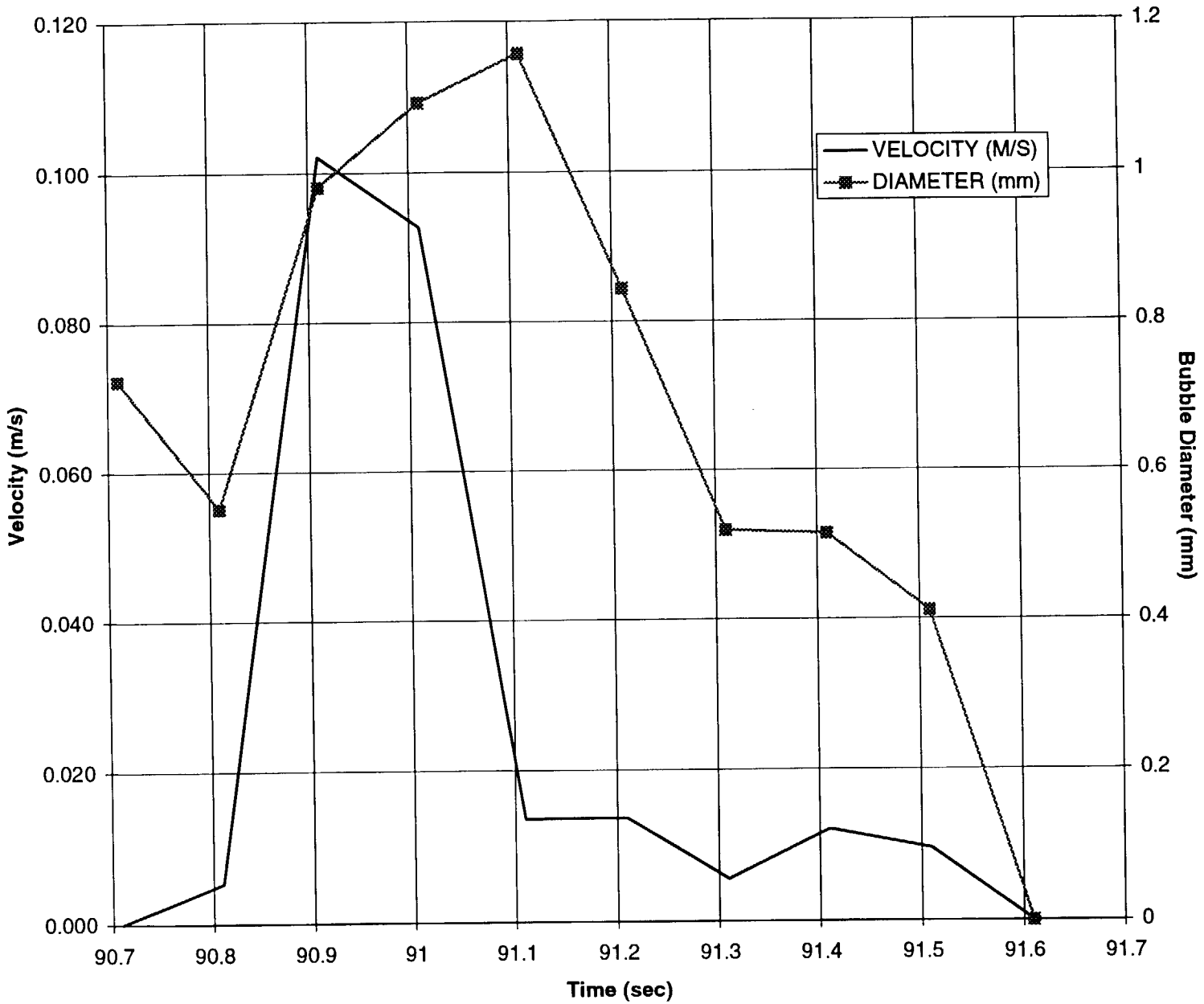

Figure 6.17b. Velocities and diameters for bubble of Figure 6.17a.

STS-72 Run #3, Bubble #2

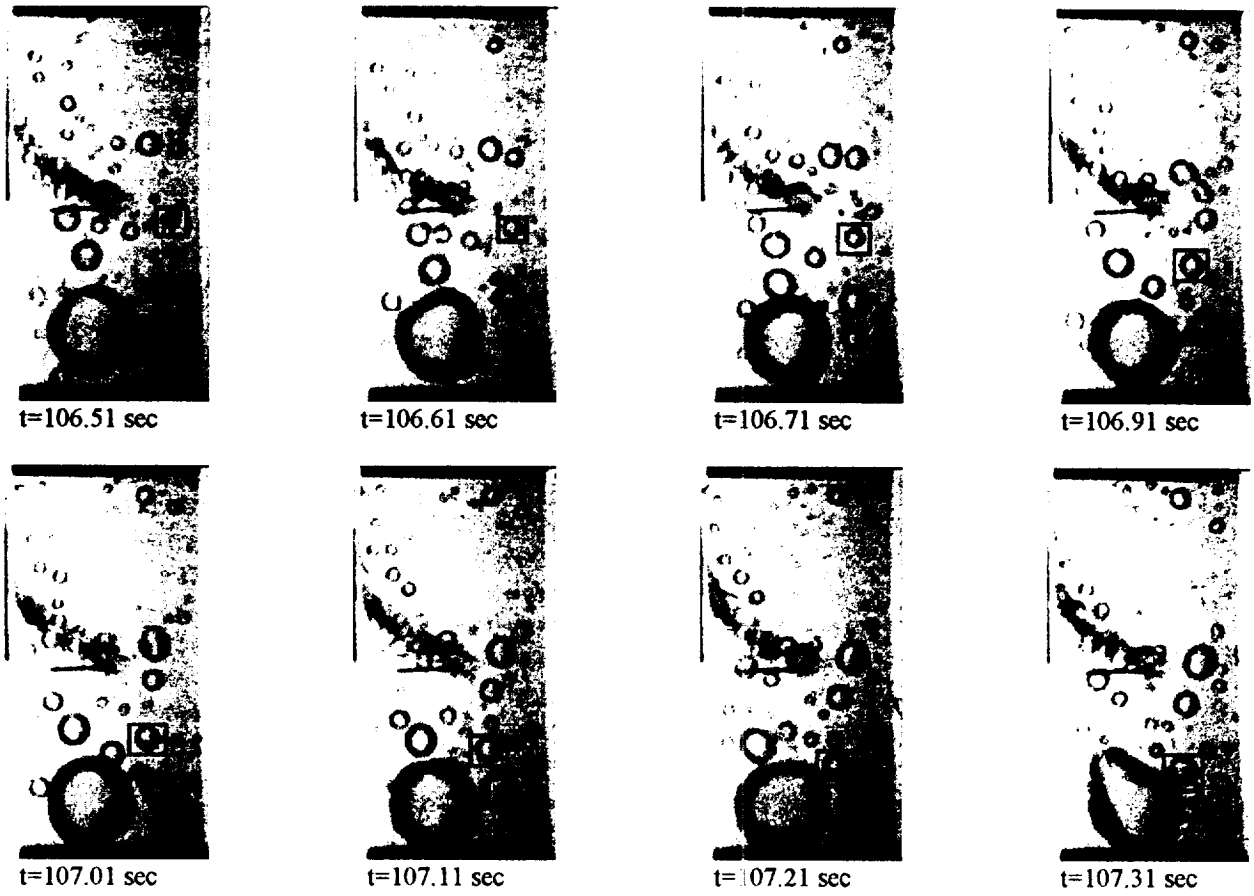

Figure 6.18a. Sequential photographic images of migrating bubbles. PBE-IIB (STS-72). Run No. 3. Bubble #2. See Table VII for parameters. Time interval: 106.51-107.31 seconds.

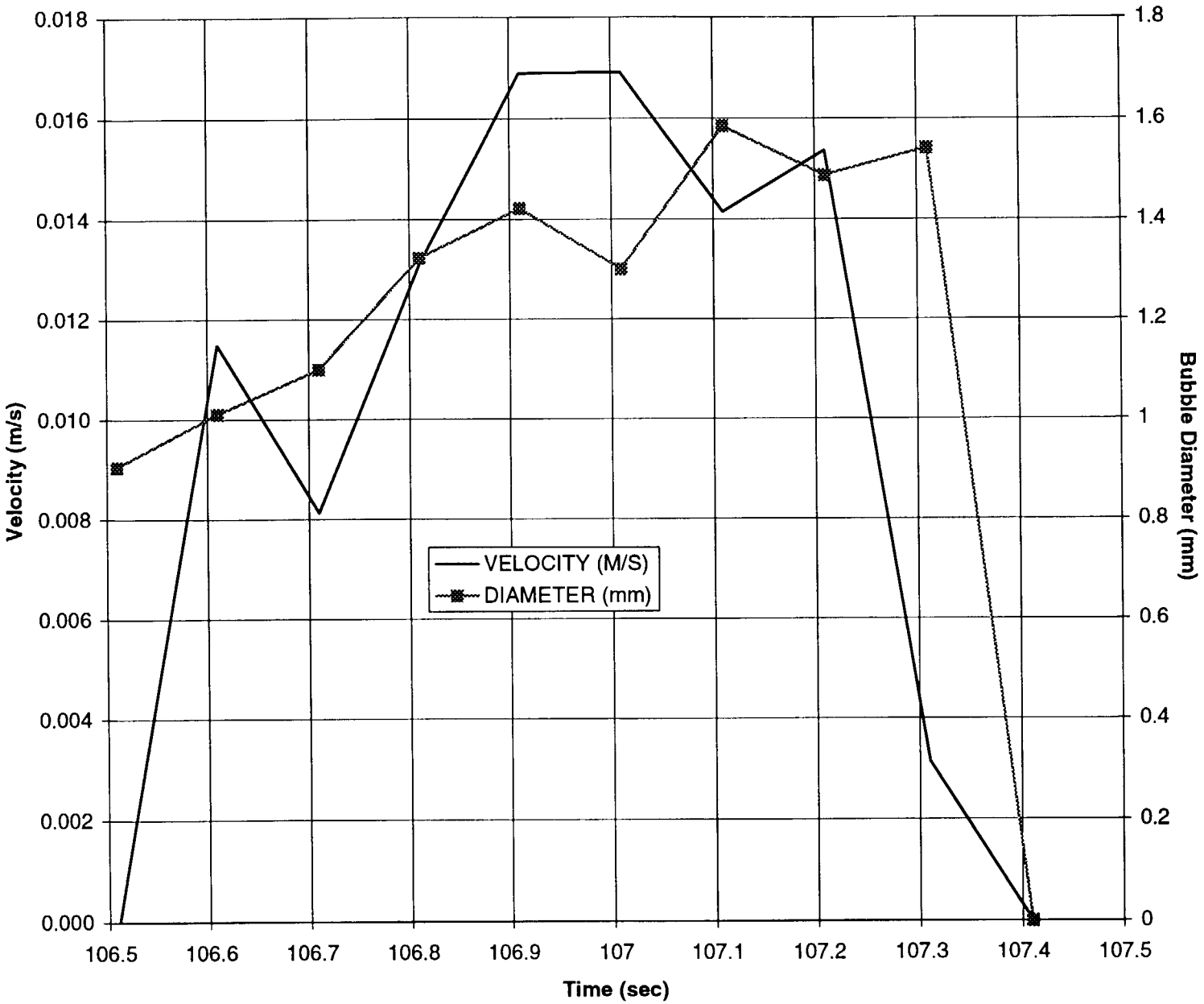

Figure 6.18b. Velocities and diameters for bubble of Figure 6.18a.

STS-72 Run #3, Bubble #3

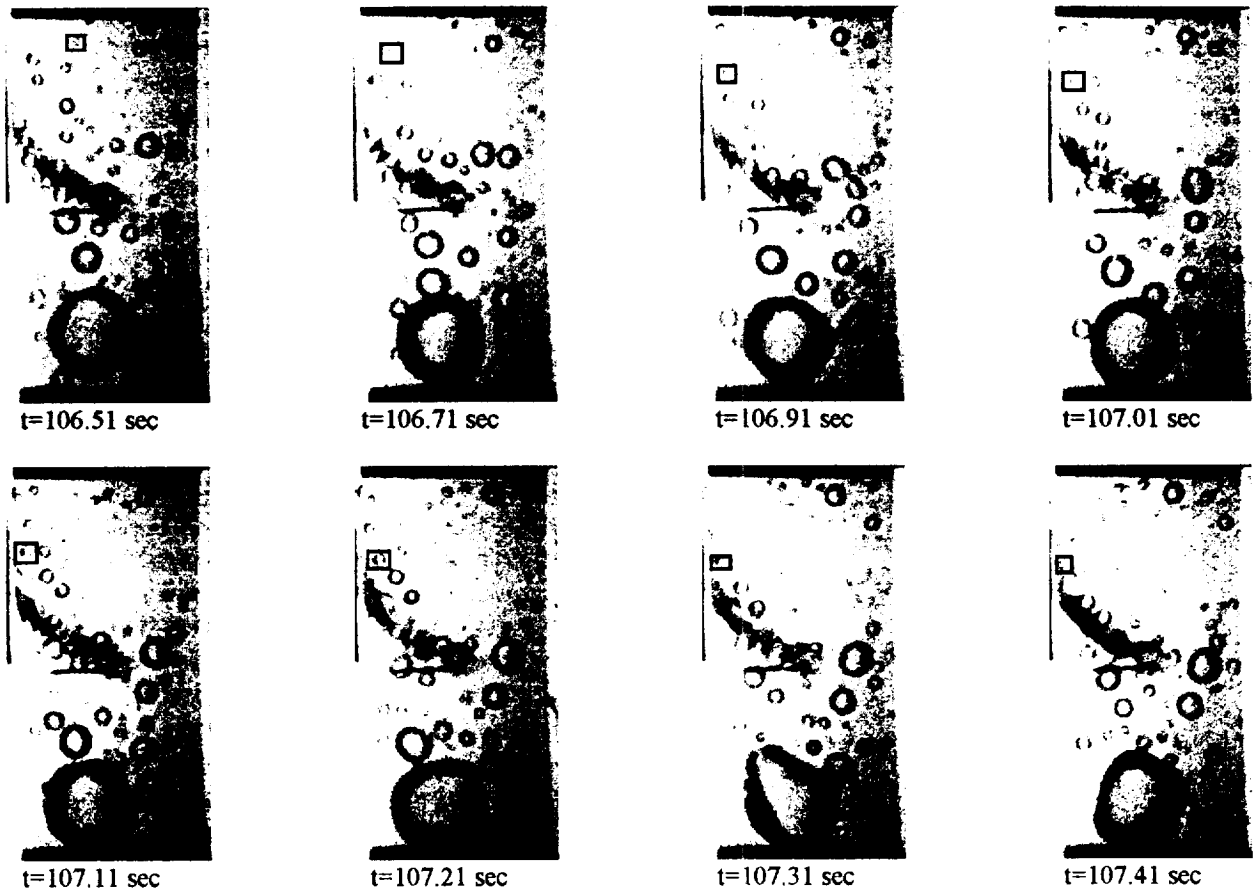

Figure 6.19a. Sequential photographic images of migrating bubbles. PBE-IIB (STS-72). Run No. 3. Bubble #3. See Table VII for parameters. Time interval: 106.51-107.41 seconds.

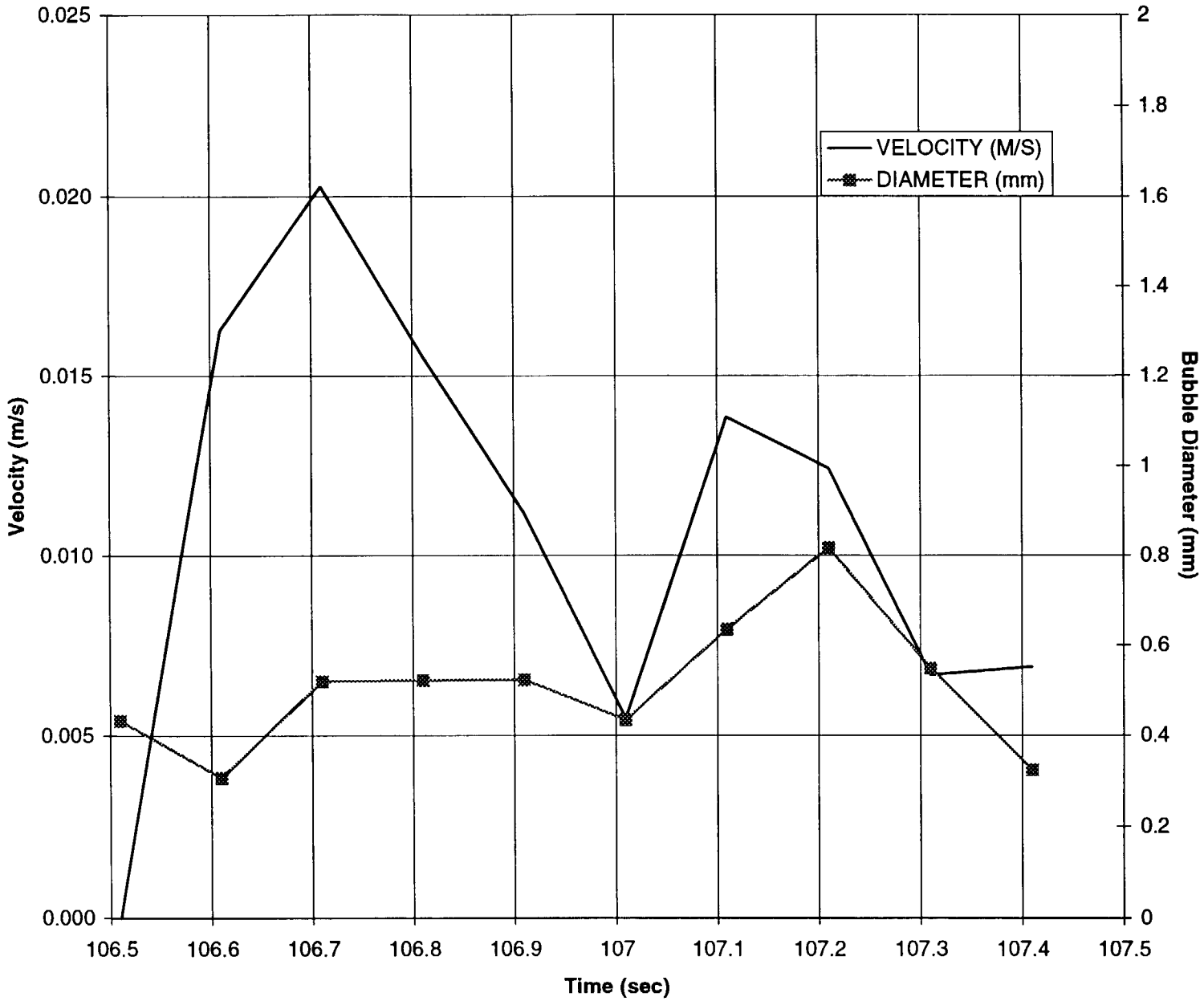

Figure 6.19b. Velocities and diameters for bubble for Figure 6.19a.

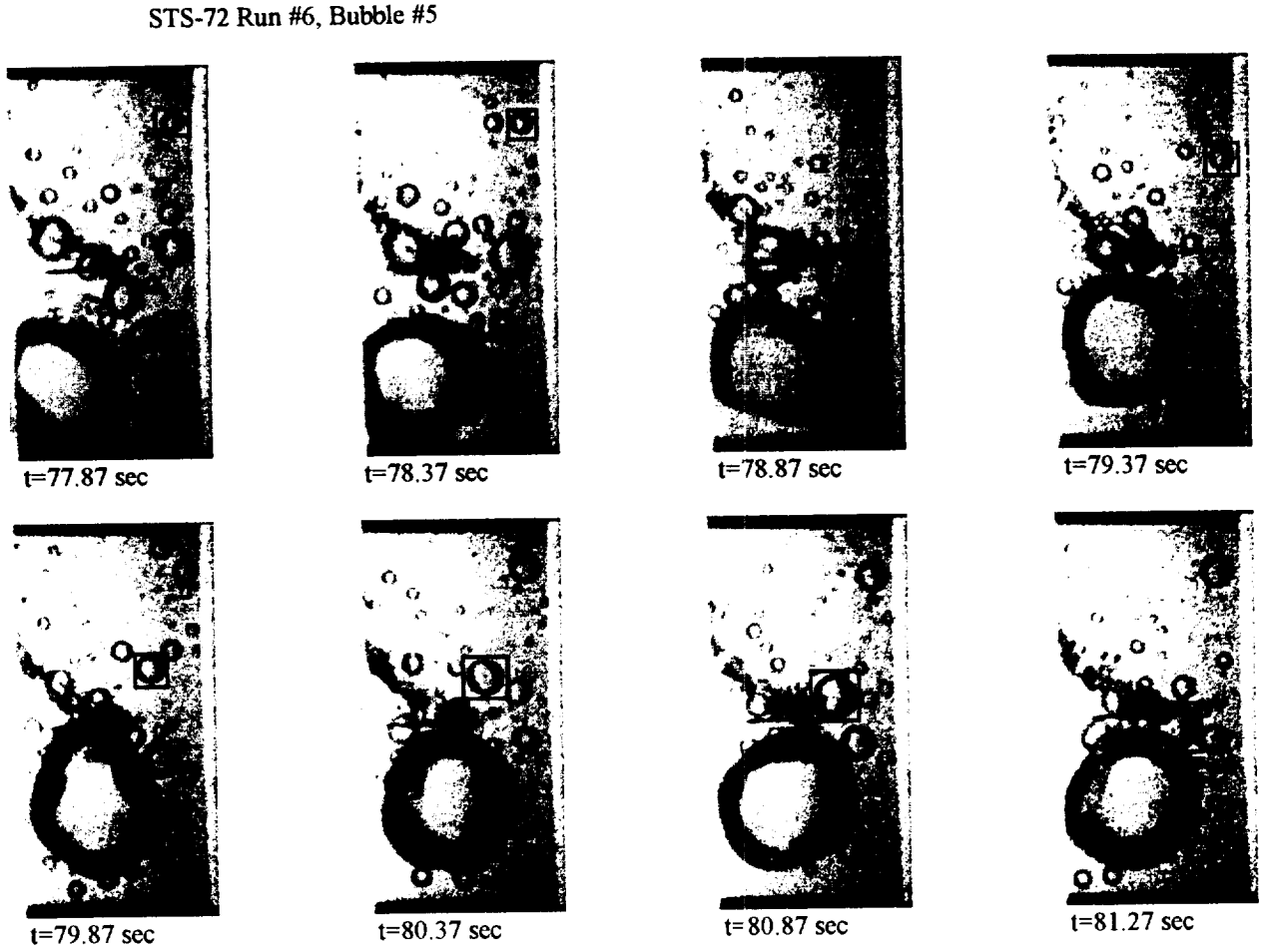

Figure 6.20a. Sequential photographic images of migrating bubbles. PBE-IIB (STS-72). Run No. 6. Bubble No. 5. See Table VII for parameters. Time interval: 77.87-81.27 seconds.

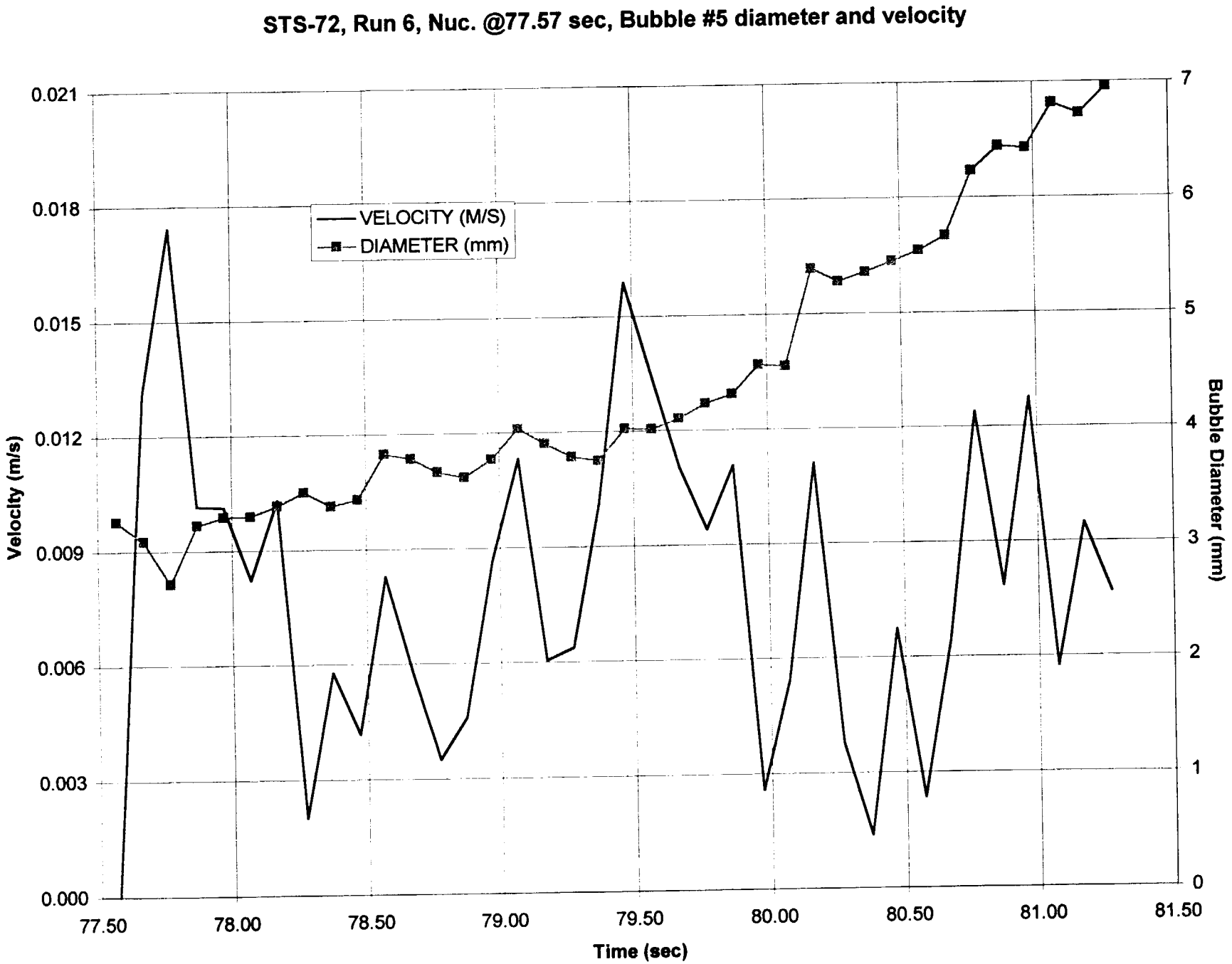

Figure 6.20b. Velocities and diameters for bubble of Figure 6.20a.

STS-72 Run #6, Bubble #3

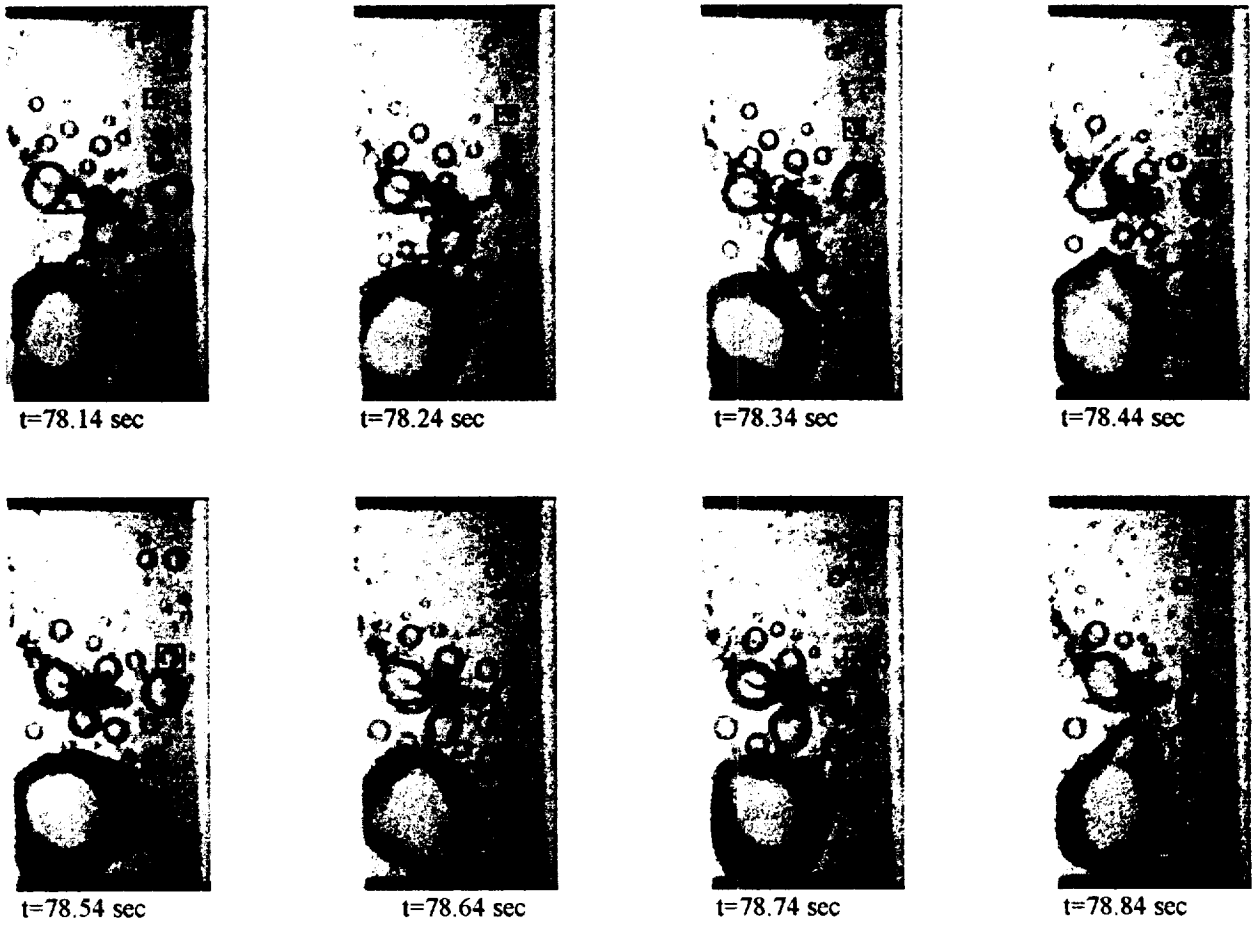

Figure 6.21a. Sequential photographic images of migrating bubbles. PBE-IIB (STS-72). Run No. 6. Bubble #3. See Table VII for parameters. Time interval: 78.14-78.84 seconds.

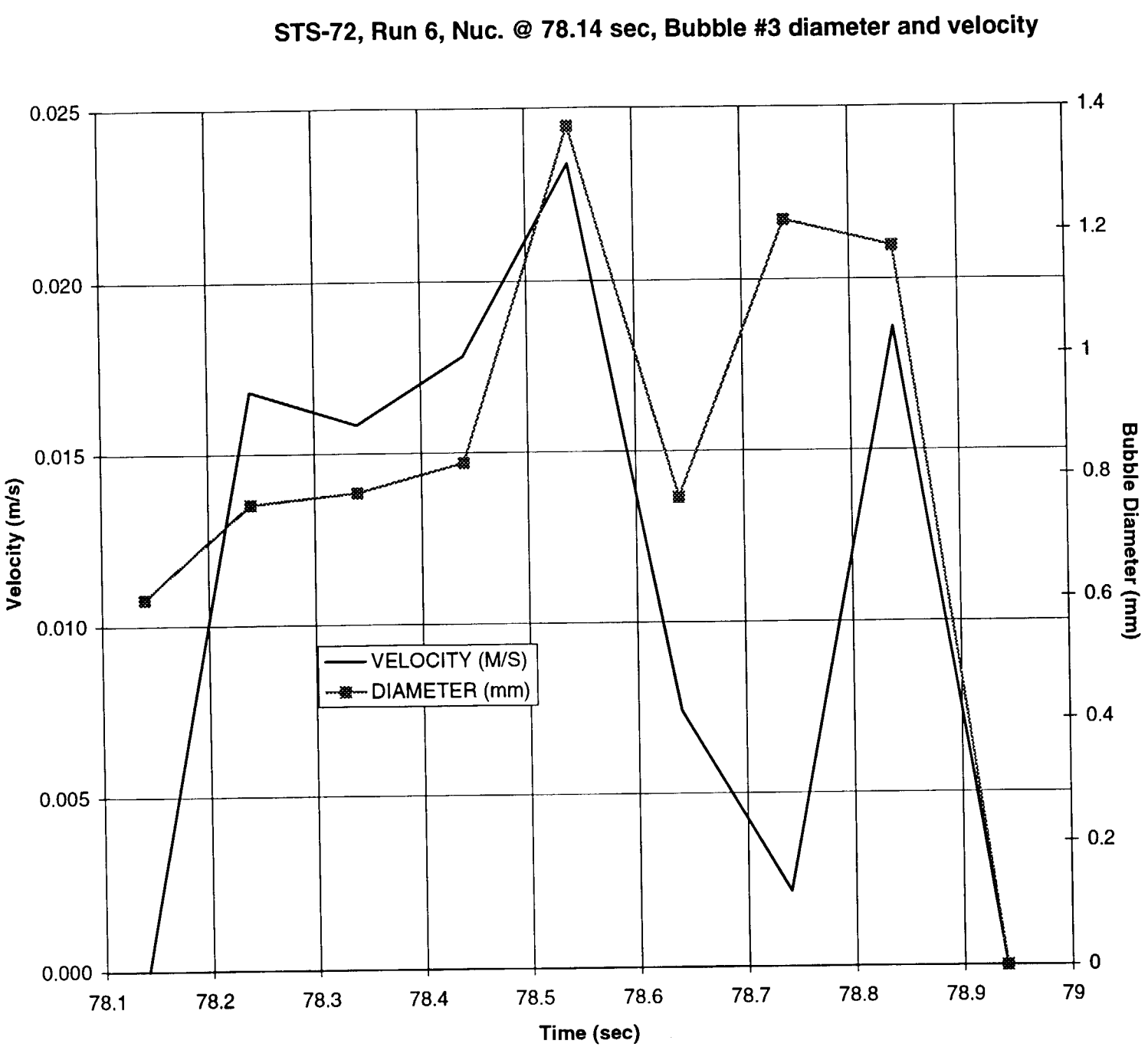

Figure 6.21b. Velocities and diameters for bubble of Figure 6.21a.

STS-72 Run #6, Bubble #4

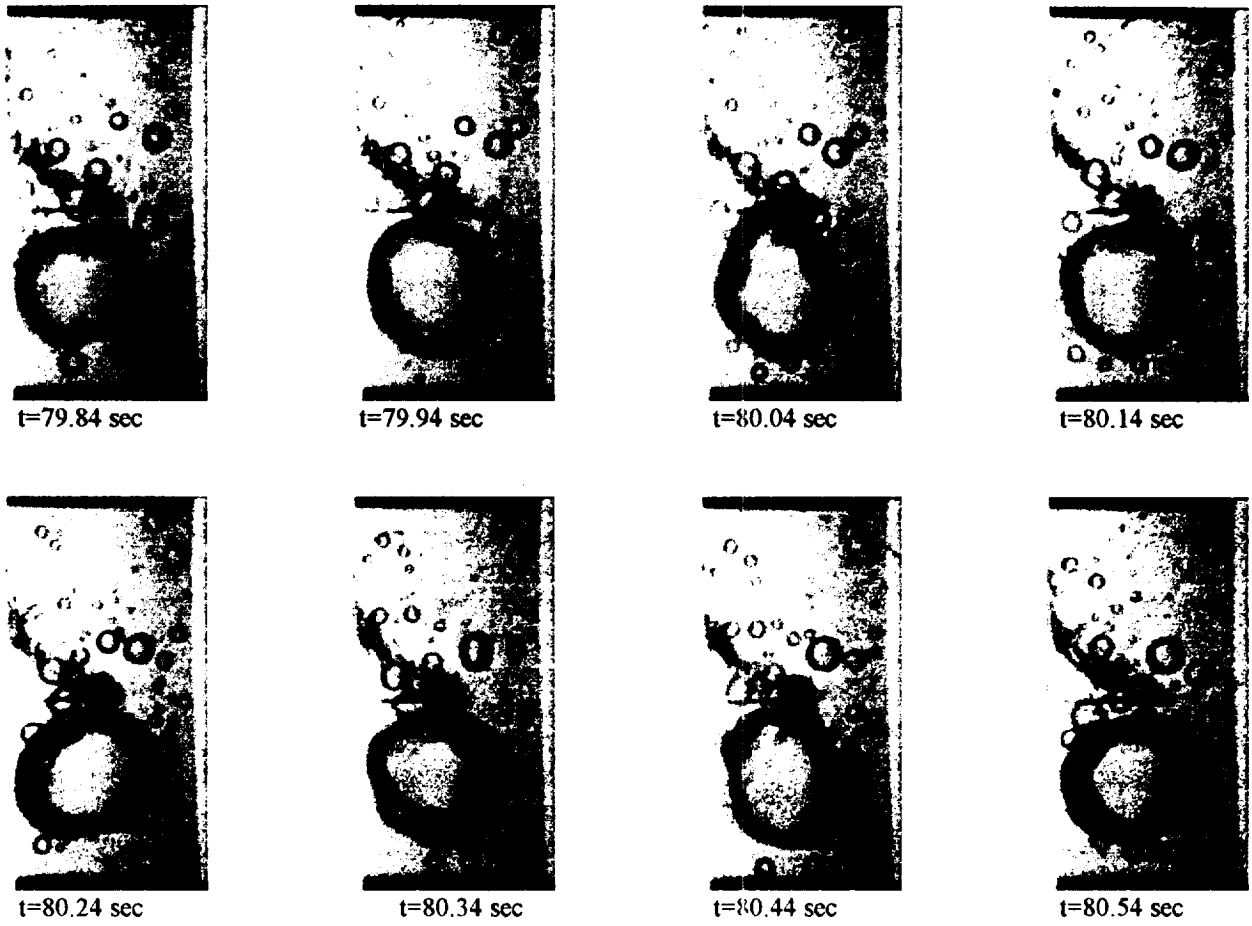

Figure 6.22a. Sequential photographic images of migrating bubbles. PBE-IIB (STS-72). Run No. 6. Bubble #4. See Table VII for parameters. Time interval: 79.84-80.54 seconds.

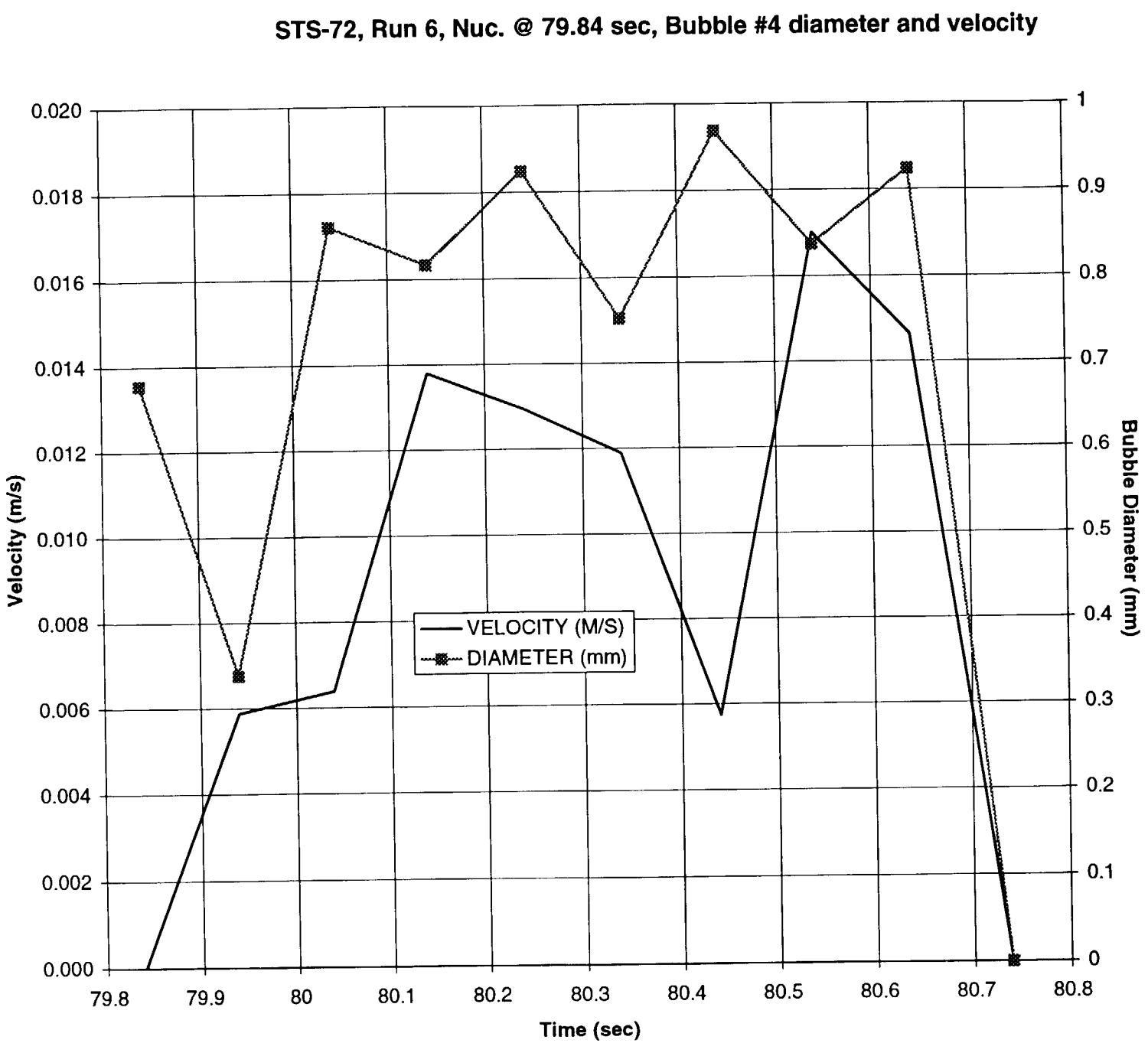

Figure 6.22b. Velocities and diameters for bubble of Figure 6.22a.

STS-72 Run #6, Bubble #6

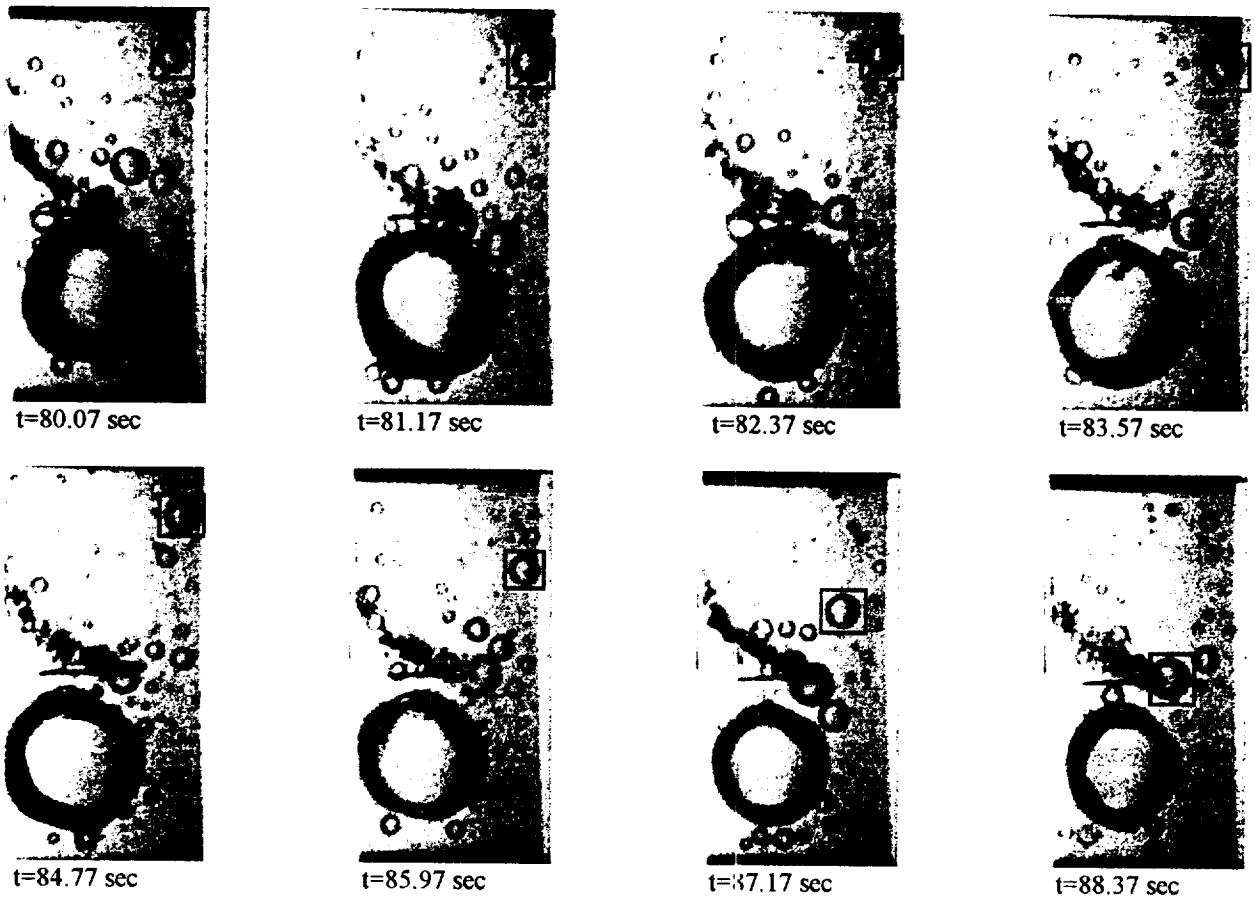

Figure 6.23a. Sequential photographic images of migrating bubbles. PBE-IIB (STS-72). Run No. 6. Bubble #6. See Table VII for parameters. Time interval: 80.07-88.37 seconds.

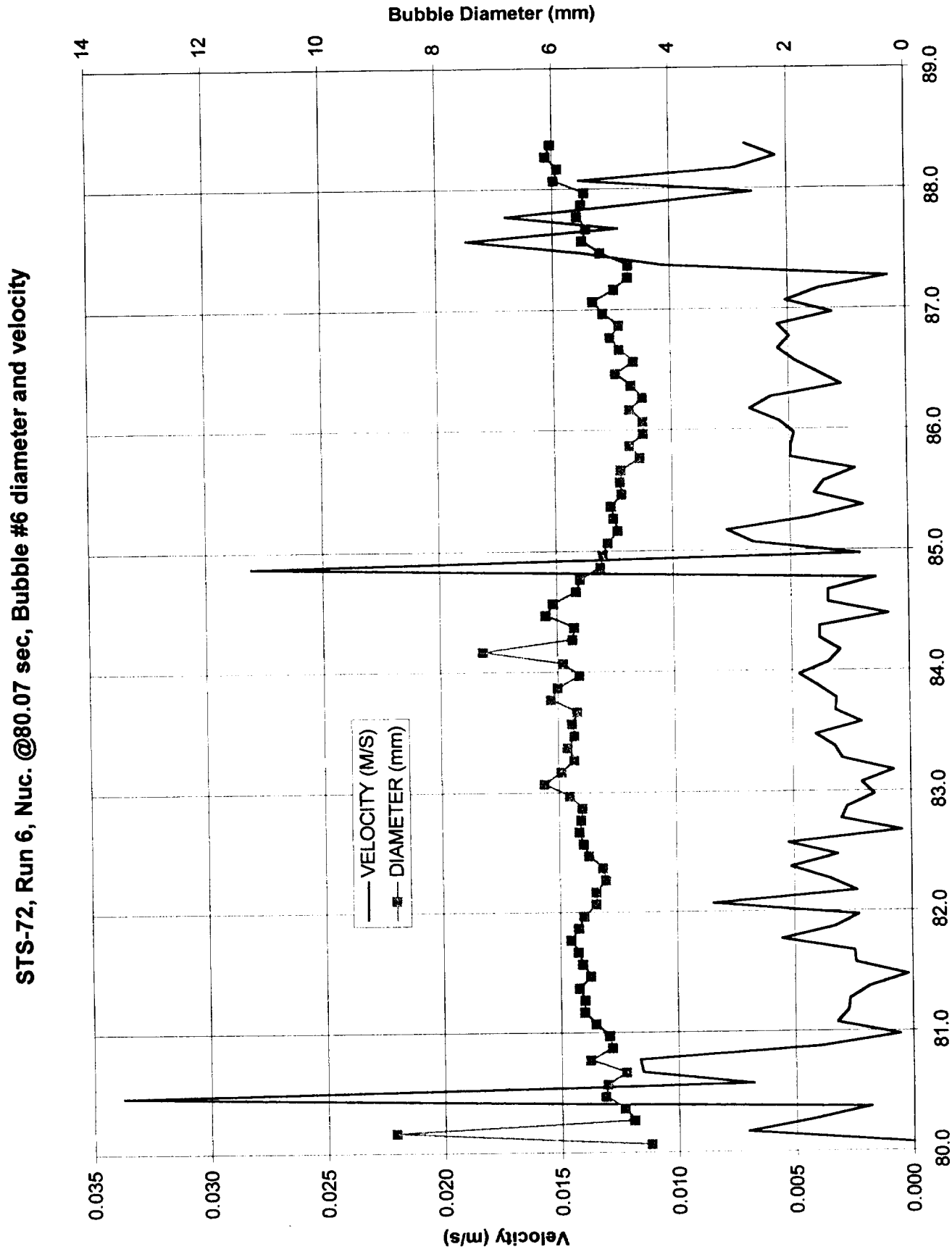

Figure 6.23b. Velocities and diameters for bubble of Figure 6.23a.

STS-72 Run #6, Bubble #1

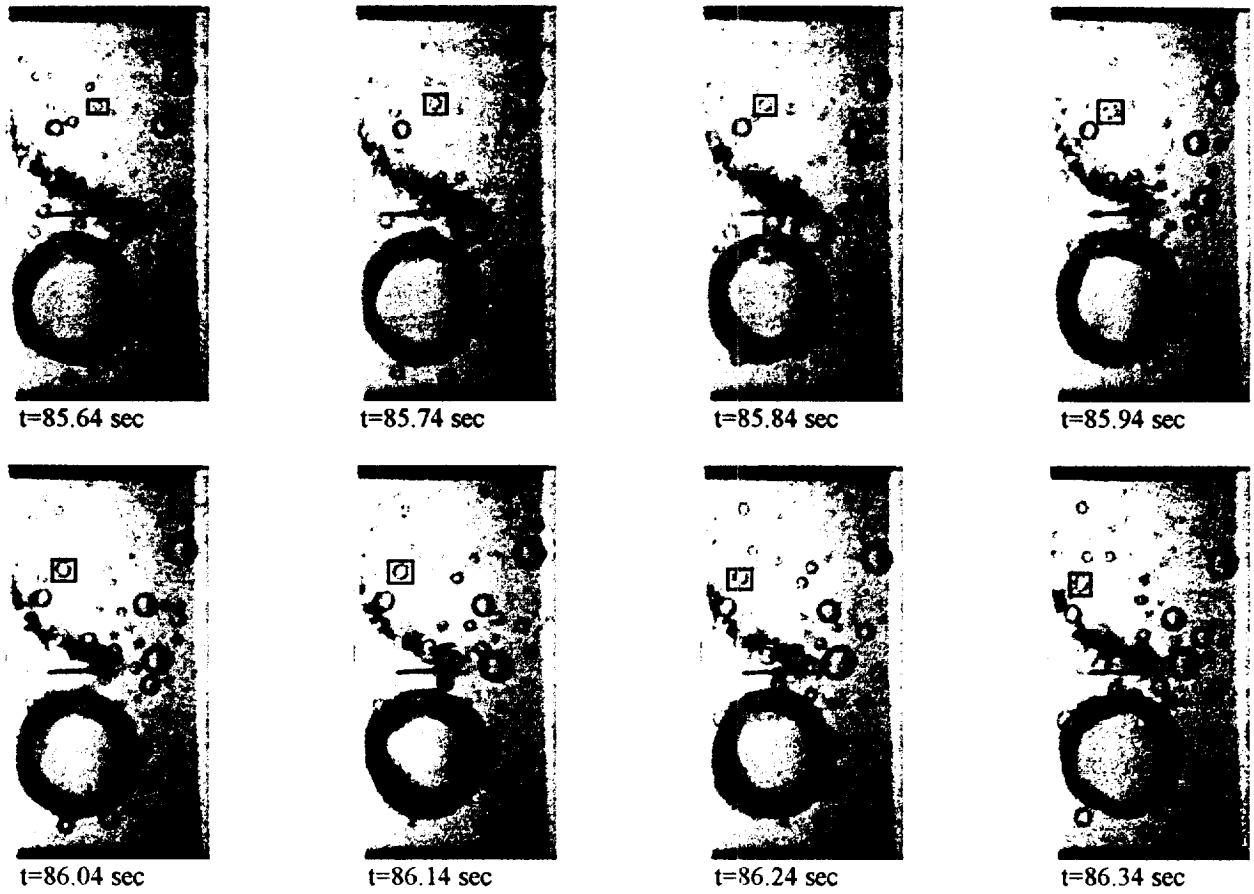

Figure 6.24a. Sequential photographic images of migrating bubbles. PBE-IIB (STS-72). Run No. 6. Bubble #1. See Table VII for parameters. Time interval: 85.64-86.34 seconds.

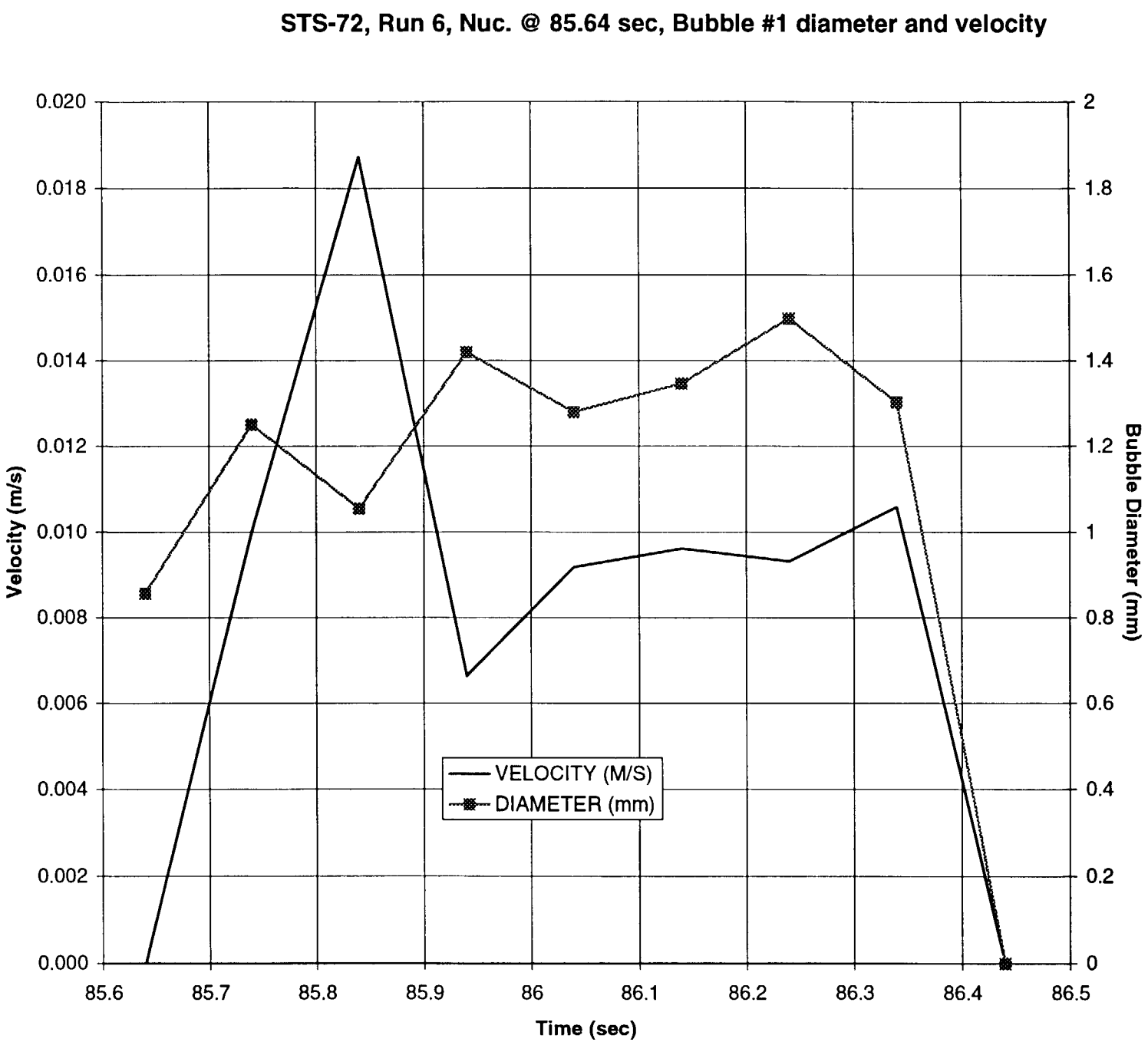

Figure 6.24b. Velocities and diameters for bubble of Figure 6.24a.

STS-72 Run #6, Bubble #2

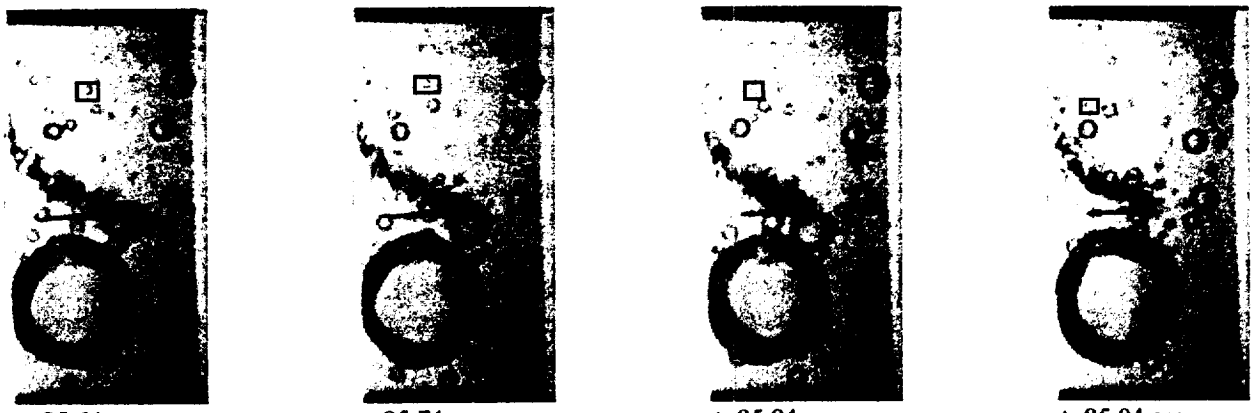

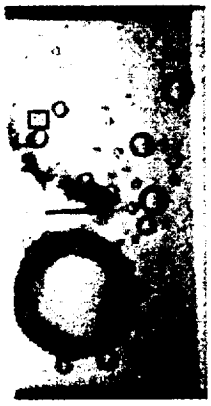

Figure 6.25a. Sequential photographic images of migrating bubbles. PBE-IIB (STS-72). Run No. 6. Bubble #2. See Table VII for parameters. Time interval: 85.64-86.04 seconds.

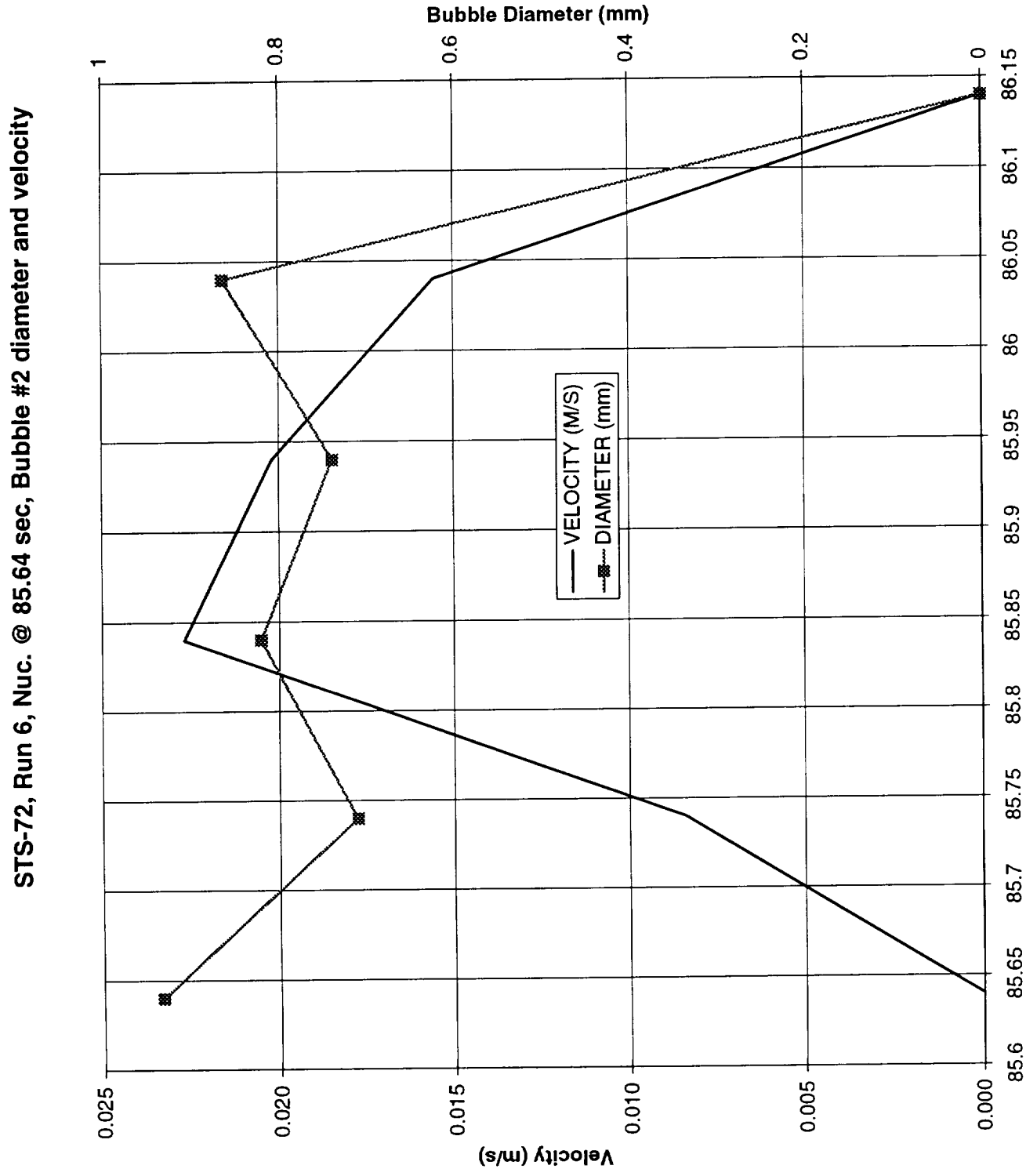

Figure 6.25b. Velocities and diameters for bubble of Figure 6.25a.

7. CONCLUSIONS AND SUMMARY

With the completion of this study of pool boiling in microgravity, statements can be made as to what has been learned and discovered:

a. The absence of buoyancy and the associated single phase natural convection permits the attainment of homogeneous nucleation at low levels of heat flux.

b. The high liquid superheats obtained at nucleation produce an extremely dynamic and unusual initial vapor bubble growth under certain conditions in microgravity which appears to be associated with an instability problem, and which results in an unusual interfacial behavior. An analysis has been developed which predicts the circumstances necessary to produce the instability.

c. In certain circumstances where rapid expansion of the boiling front takes place, vapor bubbles appear to be formed both within the residual liquid microlayer remaining on the surface as this front passes by, and in advance of the boiling front.

d. It appears that long term steady-state nucleate boiling can take place on a flat heater surface in microgravity with a wetting liquid under conditions in which a large vapor bubble somewhat removed from the heater surface is formed, which acts as a thermal sink to remove the nucleating bubbles from the heater surface.

e. The steady nucleate boiling heat transfer is significantly enhanced in microgravity compared to that in earth gravity, under certain conditions.

f. Related to (d) above, surface tension has an important role in producing dryout and/or rewetting on a heated surface. A summary of the circumstances of bulk liquid subcooling and heat flux level which approximately describe the limits at which dryout occurs with R-113 is presented below. The heat flux at which dryout occurs is considerably less in microgravity than in earth gravity.

A visual comparison of typical pool boiling with the same heater surface in both earth gravity and microgravity under a certain subcooling is presented in Figure 7.1 (a) and (b), where the upper half presents the side view and the lower half is the bottom view through the semi-transparent gold film heater. The operating conditions are almost identical for both the normal gravity and reduced gravity. In Figure 7.1 (a) in earth gravity, the numerous small bubbles grow and detach/rise from

the heater surface and collapse in the bulk, inducing agitation and turbulence within the thermal boundary layer on the heater, which is called microconvection. In addition to this nucleate boiling heat transfer mechanism, the microlayer evaporation (or latent heat transport) within the individual vapor bubbles are believed to play a role in enhancing the heat transfer, for which the contribution depends on subcooling levels. Vapor bubbles in microgravity are observed to be quite large, compared to those in earth gravity, since no buoyancy forces are acting to remove them from the vicinity of the heater surface. The bottom view together with a side view provides a clear visual image of the 3-D bubble arrangement. The numerous relatively larger bubbles in Figure 7.1 (b) are uniformly distributed and attached to or in the vicinity of the heater surface.

In order to see the entire picture of the boiling phenomena over the complete operating parameters used here, a matrix of representative photographs over the various levels of heat flux (0.5, 1, 2, 4, 8 W/cm^2) and subcooling (0.3, 2.7, 11.1, and 22.2°C) are presented in Figure 7.2 (a)-(q), with the corresponding operating conditions given in Table XV. The measured heater surface temperature and derived heat transfer coefficient for selected tests in the matrix are shown in Figures 7.3 - 7.7, with summary discussions to be given below.

Table XV. Operating conditions for the matrix in Figure 7.2

Photos	ref. #	Heat Flux q" W/cm^2	Subcool T_{sat} - T∞ (°C)	Pressure kPa	T_{sat} (°C)	S.S. Twall ±2 (°C)	time for the photos (sec)	t* (sec)	h ±50 (W/m^2.K)
(a)	s72rl	8	22.2	145.1	58.8	90	55.47	10.81	2300
(b)	s47rl	8	11.1	149.0	59.7	-	36.98	11.58	-
(c)	s60r4	8	2.7	117.3	52.0	-	21.47	10.74	-
(d)	s47r7	8	0.3	106.9	49.4	-	25.10	11.36	-
(e)	s72r2	4	22.2	156.5	61.3	86	108.26	25.44	1500
(f)	s60r2	4	11.1	145.9	58.9	78	61.47	30.85	1650
(g)	s60r5	4	2.7	117.6	52.1	-	50.98	19.60	-
(h)	s47r8	4	0.3	106.9	49.4	-	22.78	20.63	-
(i)	s72r3	2	22.2	152.1	60.3	73	76.23	46.41	1500
(j)	s72r9	2	11.1	110.7	50.2	67	84.29	72.39	1200
(k)	s77r4	2	2.7	115.8	51.9	70	168.72	33.60	1000
(l)	s60r9	2	0.3	107.7	49.4	67	68.47	40.52	1000
(m)	s77r2	1	11.1	153.8	60.7	72	168.72	78.30	900
(n)	s77r5	1	2.7	116.0	51.7	65	185.04	89.60	750
(o)	s77r8	1	0.3	107.3	49.2	64	132.60	76.30	700
(p)	s77r6	0.5	2.7	116.1	51.7	64	216.30	190.50	350
(q)	s77r.9	0.5	0.3	107.4	49.3	63	240.60	225.20	400

Only seventeen (17) test runs out of the total forty five (45) are represented in Figure 7.2. These are all at significant elapsed times following the onset of heating, which always began at 10 seconds, and are given in Table XV. In general, the higher levels of heat flux are associated with increased tendencies for dryout, seen in Figure 7.2 (b), (c), (d), (g), and (h), as might be anticipated, and depend on the levels of initial subcooling. The large bubble in Figure 7.2 (c), with heat flux of 8 W/cm^2 and subcooling of 2.7°C, almost completely covers the heater surface, causing the mean heater surface temperature to rise continuously, as shown in Figure 7.4. Also included here is the behavior in earth gravity for the same experimental conditions. In contrast to the dryout in Figure 7.4, increasing the level of subcooling to 22°C for the same high heat flux of 8 W/cm^2 results in steady nucleate boiling, as seen in Figure 7.2 (a), with the corresponding heater surface and heat transfer coefficients given in Figure 7.3. What might be termed the most ideal pool boiling observed are Figures 7.2 (a) and (f) where, due to surface tension, the small bubbles formed initially agglomerate to become a large bubble, which is eventually detached slightly from the heater surface. This is attributed to the momentum and coalescence of the small growing bubbles toward the large bubble. The large vapor bubble acts as a reservoir for the vapor bubbles growing on the heater surface. It is noted that the large bubble hovering just above the heater surface tends to maintain its size due to the balance of the dual processes of condensation at the bubble cap and coalescence with the small bubbles. This is believed to be responsible for the steady boiling observed in microgravity, even under saturation conditions. The quantitative evidence of the effective steady boiling for Figure 7.2 (f) is illustrated in Figure 7.6, where the measurement in earth gravity is superimposed. It is note that an enhancement of about 32% occurs in the heat transfer coefficient with microgravity. The oscillations in the heat transfer coefficient observed in Figure 7.6 were measured to have a period of 4 sec/cycle, which has significance in that the small bubbles agglomerate to a certain size, causing the mean heat transfer surface temperature to rise, and then coalesce repeatedly with the large bubble hovering above the heat surface, which in turn produce turbulence in the fluid near the bubbles, leading to a decrease in the mean heater surface temperature.

On close examination of the first three rows (8, 4, an 2 W/m^2) of the matrix in Figure 7.2, it is noted that the vapor bubbles tend to remain more in the vicinity of the heater surface as the subcooling increases and vice versa, as is noted particularly in Figures 7.2 (e) and (i). This phenomenon is attributed to the combination of condensation and Marangoni convection. As a consequence, it often occurs with high subcooling that the large vapor bubble is impelled toward the heater surface, not only serving as a reservoir attracting the small bubbles, which decrease the mean heater surface temperature, but also causes partial dryout beneath the large bubble, which increases the mean heater surface temperature. These opposing effects can occur sequentially, as illustrated in Figure 7.5 for the photograph of Figure 7.2 (e). The large spikes in the heat transfer coefficient at times over the range of 70-95 seconds correspond to the partial dryout area increasing in connection with dual large bubbles formed on the heater surface, which then coalesce to form a single large bubble, and which then become somewhat removed from the heater surface due to the imbalance between surface tension a decrease in size due to condensation. This process repeated itself several times.

A peculiar phenomenon began to occur under the operating conditions of high subcooling (16.7-22.2°C) and a low heat flux of 2 W/cm^2. A scarcity of bubbles on the heater surface is obvious in Figure 7.2 (i) relative to that at lower levels of subccoling. On the other hand, Figure 7.7 shows that the heat transfer coefficient of approximately 1500 $W/m^2.K$ is the same or slightly higher than for the heat flux level of 4 W/cm^2 in Figure 7.5. It also shows an approximate 30% increase in the heat transfer coefficient compared to Figure 7.2 (j), for the same level of heat flux and a lower level of subcooling of 11.1°C. Numerous very small growing bubbles on the heater surface are moving toward the large bubble with a velocity of approximately 2.5 cm/s, and are believed to be responsible for the enhanced heat transfer. This motion, not seen clearly in the figure, is defined here as *bubble migration*. In figure 7.7, the bubble migration increased gradually with time, accompanied by an increase in the heat transfer.

Of the 45 test runs conducted under microgravity in the five separate flights, true steady boiling was present in only 27, whereas the remainder exhibited a quasisteady or transient rise of heater

surface temperature associated with various degrees of dryout. The identical test runs were repeated in earth gravity following the space experiments so that direct comparisons could be obtained between the behavior in microgravity and in earth gravity. All the steady-state data in microgravity and in earth gravity were used for the analysis of the pool boiling.

A plot of the heat transfer coefficient (h) was constructed as a function of the imposed heat flux, using the data described above, and is shown in Figure 7.8. There appears to be a general trend that the heat transfer coefficient is proportional to the heat flux, within the band as shown. The two symbols below this band indicate the deterioration of the heat transfer associated with partial dryout, as described before. The two symbols above the band indicate the enhancement of the heat transfer associated with the strong vapor bubble migration also described above.

An uncertainty exists about the role of subcooling in microgravity pool boiling, but its resolution is not obvious from prior work because of the apparent sensitivity of pool boiling to the magnitude and duration of the microgravity. For example, although the data in Oka et al. (1995), conducted at $a/g \approx 10^{-2}$ showed no indication of significant effects of subcooling for R-113, that in Oka et al (1996) conducted at $a/g \approx 10^{-5}$ showed a considerable effect, in basic agreement with the present results. To make the influence of subcooling on pool boiling in microgravity more clear, the steady-state heat transfer coefficients are plotted as a function of subcooling in Figure 7.9. Since the heat transfer coefficients appear to be proportional to the imposed heat flux, the data are grouped by heat flux, as shown. For the high flux of 8 W/cm^2 in earth gravity, a distinct increase takes place as subcooling increases. For the group with the heat flux of 4 W/cm^2 in earth gravity, only two data points for a subcooling of 11.1°C are available, since no boiling took place above this level of subcooling due to natural convection. Overall, the trend of the influence of subcooling on nucleate pool boiling in microgravity appears similar to that in earth gravity, including heat flux levels of 4, 2, 1, and 0.5 W/cm^2. It is noted that the heat transfer coefficient at the high heat flux level of 8 W/cm^2 in earth gravity is greater than that in microgravity, while the opposite is true at

the medium heat flux level of 4 W/cm^2, also shown in Figure 7.9, This phenomenon was also observed qualitatively by Straub (1994) for R-12.

The comparison of the behavior of pool boiling between microgravity and earth gravity enjoys a high level of validity in the present work since the identical hardware and software were used, as were the identical data reduction techniques. As a result, any ambiguities of uncertainties associated with instrumentation and operating conditions were minimized. Figures 7.3, 7.4, and 7.6 provide examples of the consistency.

The resulting steady-state data available for microgravity and earth gravity are plotted in Figure 7.10. The dark symbols indicate the data in microgravity, while the open symbols indicate the data in earth gravity. It was possible to construct a reference curve in earth gravity for a subcooling of 11.1°C only, including both the nucleate boiling and natural convection regimes. As a result of the influence of subcooling from Figure 7.9, the boiling curve in microgravity are constructed for three different subcooling levels. The solid curves indicate the best fit of the limited data.

The principal mechanism which produces the steady-state pool boiling observed in microgravity is attributed to surface tension effects : A large vapor bubble hovering near the heater surface acts as a reservoir, absorbing the smaller vapor bubbles growing on the heater surface, resulting in a maximum 32% enhancement in heat transfer. An effective enhancement of approximately 30% was observed associated with *bubble migrations*, where numerous every small bubbles nucleate and move in a consistent manner toward a large bubble in the vicinity of the heater.

Three important features concerning the boiling characteristics are noted: Pool boiling heat transfer in microgravity at lower levels of heat flux appears to be enhanced compared to that in earth gravity; The boiling heat transfer in microgravity is enhanced as subcooling increases; The CHF appears to decrease significantly in microgravity.

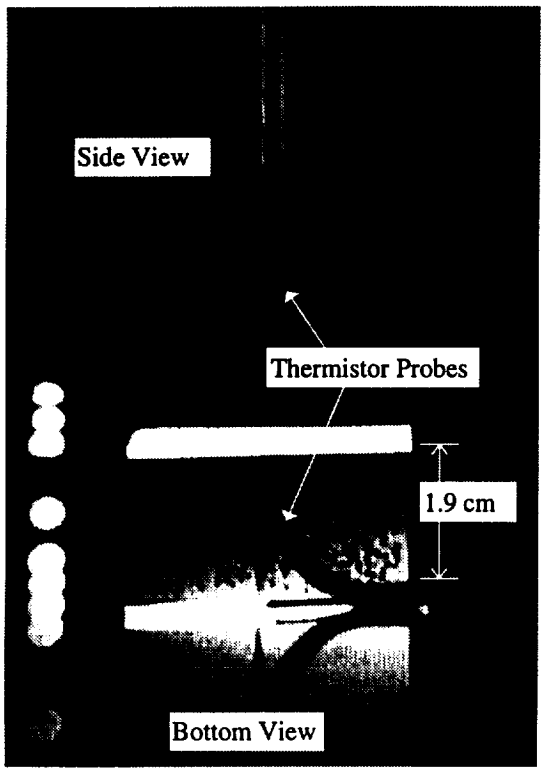

(a) Normal gravity a/g=+1 (t=78.22 sec.)

Post flight (STS-60) Run #2
q''_T=3.6 W/cm^2, Psys=150.1 kPa,
ΔT_w=27 °C, ΔT_{sub}=11.5 °C.

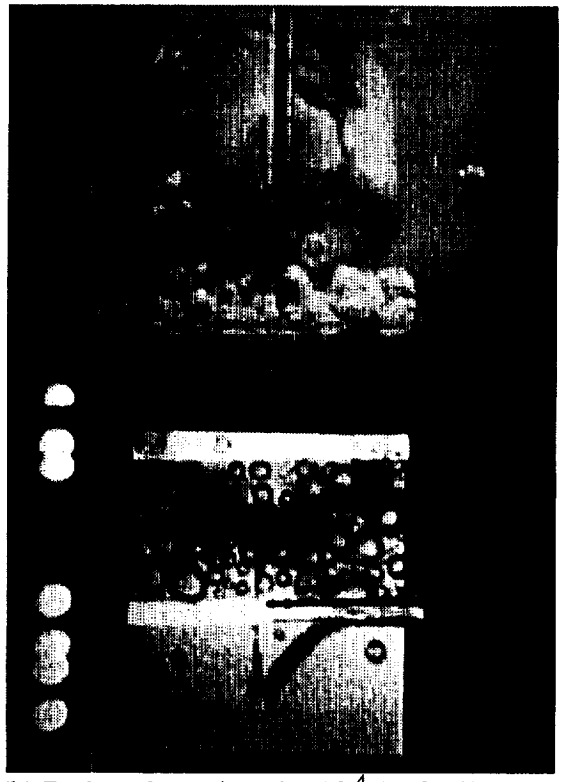

(b) Reduced gravity a/g=10^{-4} (t=61.47 sec)

Space flight (STS-60) Run #2.
q''_T=3.6 W/cm^2, Psys=145.9 kPa,
ΔT_w=18.1 °C, ΔT_{sub}=11.5 °C.

Figure 7-1. Visual comparison of pool boiling with R-113 on earth and during a space shuttle flight under otherwise similar conditions.

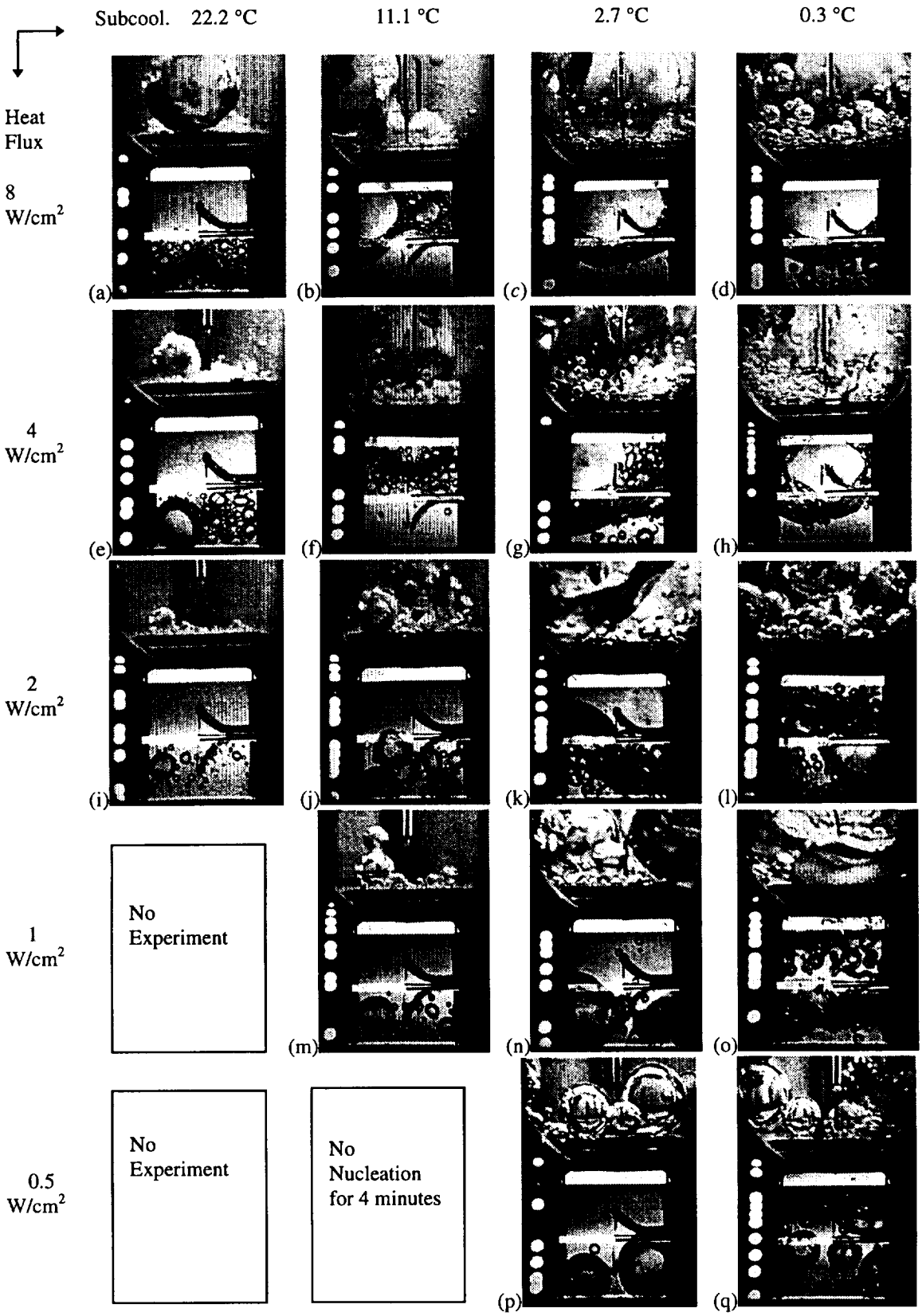

Figure 7.2. A representative photographic matrix for pool boiling conducted in microgravity with R-113 at various levels of heat flux and subcooling.

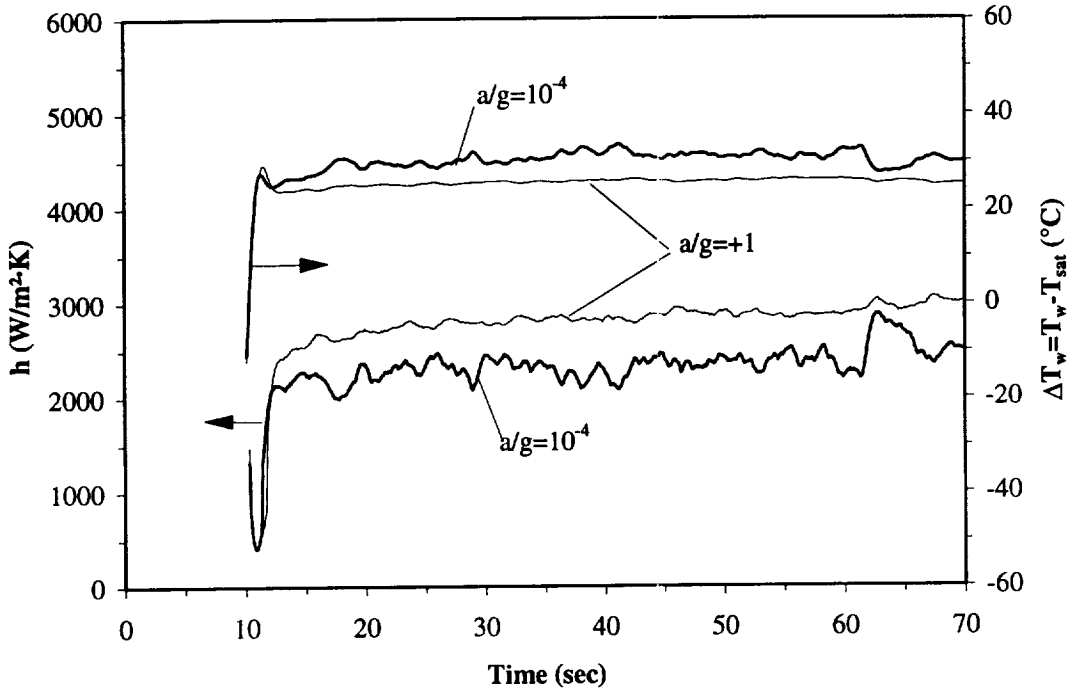

Figure 7.3. Measured mean heater surface temperature and derived heat transfer coefficient for Figure 7.2 (a) and a corresponding run in Earth gravity. Refer to Table XV for the operating conditions.

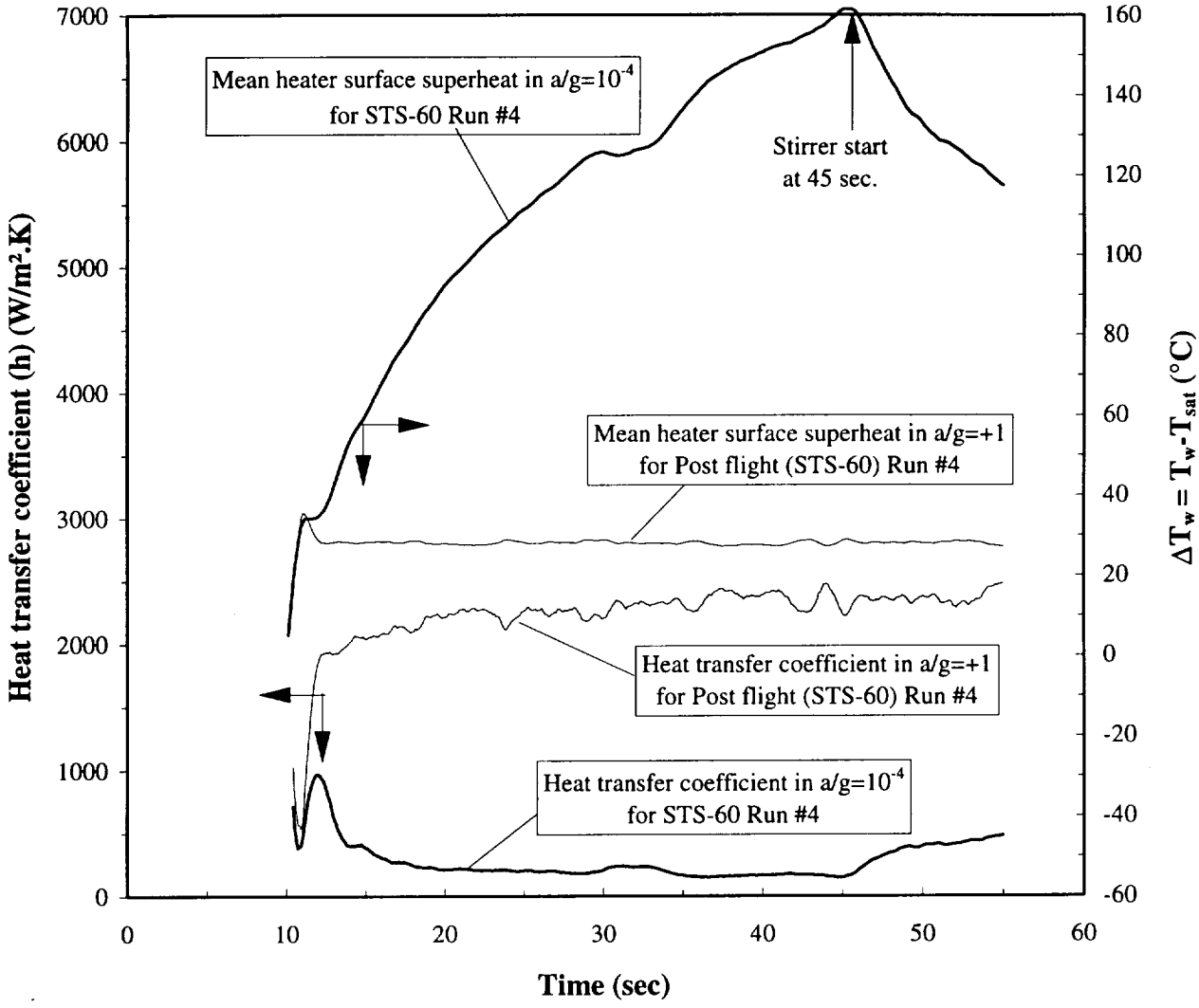

Figure 7.4. Measured mean heater surface temperature and derived heat transfer coefficient for Figure 7.2 (c) and a corresponding run in earth gravity.

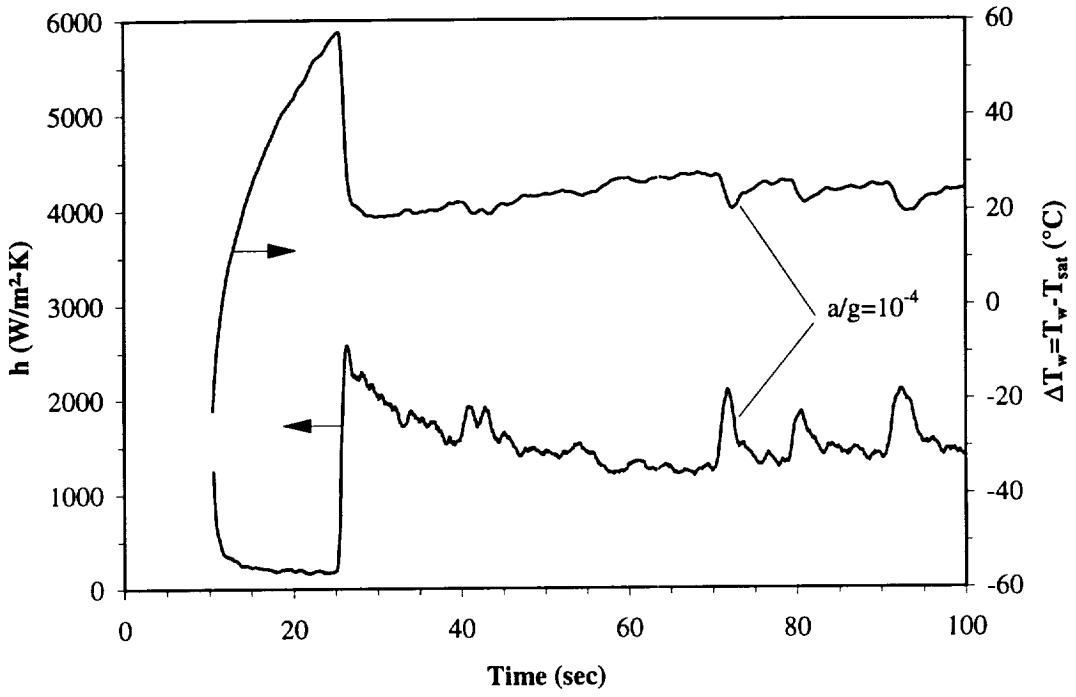

Figure 7.5. Measured mean heater surface temperature and derived heat transfer coefficient for Figure 7.2 (e).

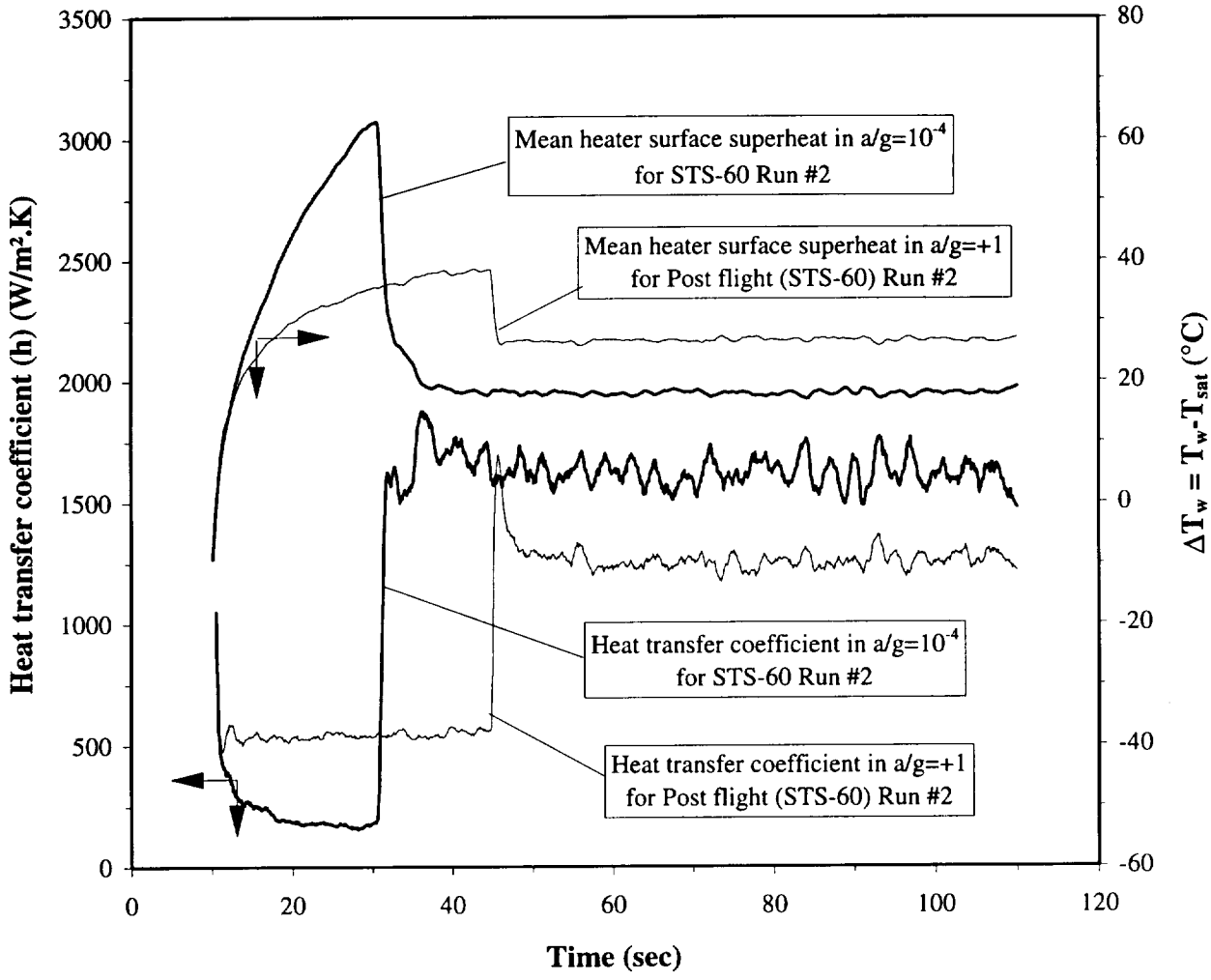

Figure 7.6. Measured mean heater surface temperature and derived heat transfer coefficient for Figure 7.2 (f) and a corresponding run in Earth gravity.

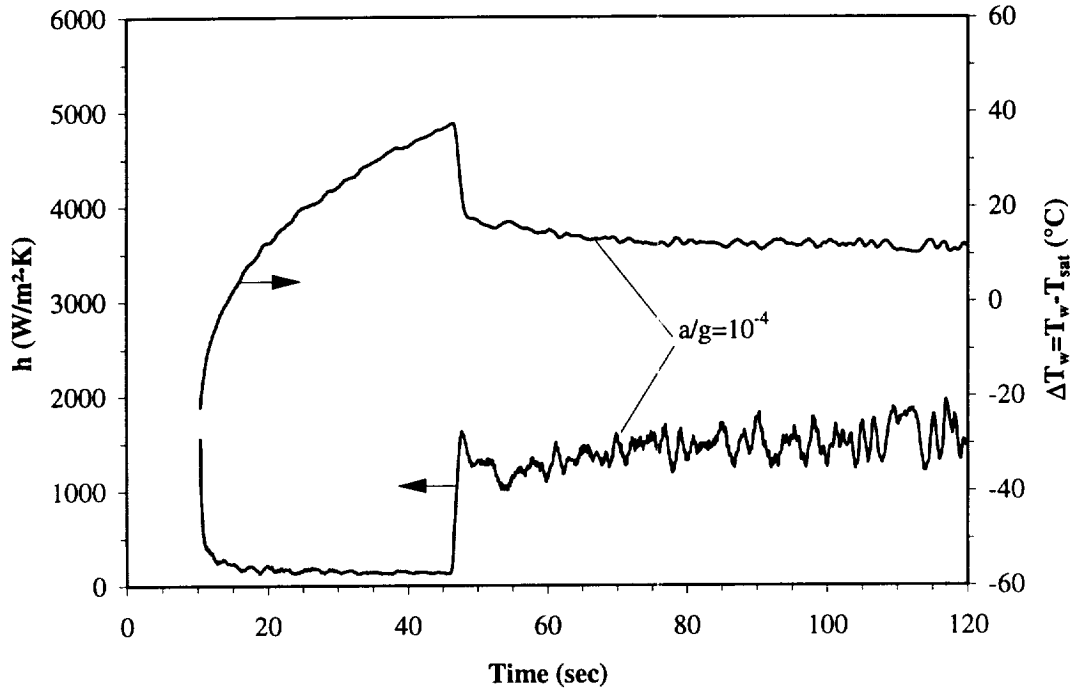

Figure 7.7. Measured mean heater surface temperature and derived heat transfer coefficient for Figure 7.2(i).

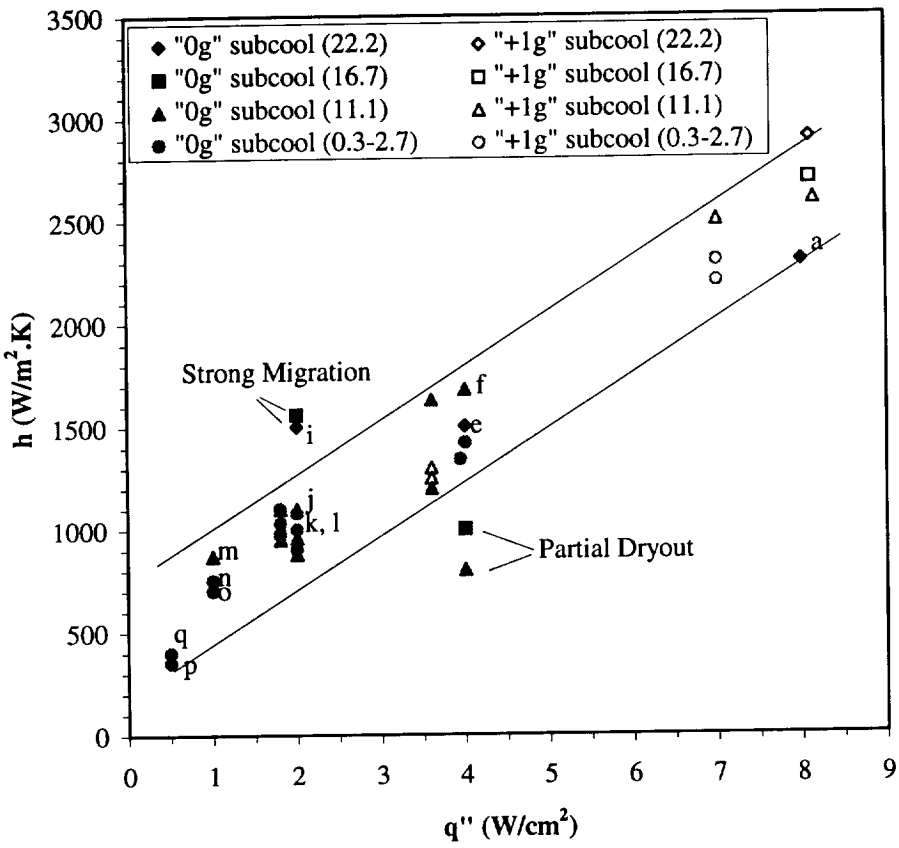

Figure 7.8. Mean heat transfer coefficient as a function of imposed heat flux in microgravity with R-113. Data from b, c, d, g, and h not included because of dryout.

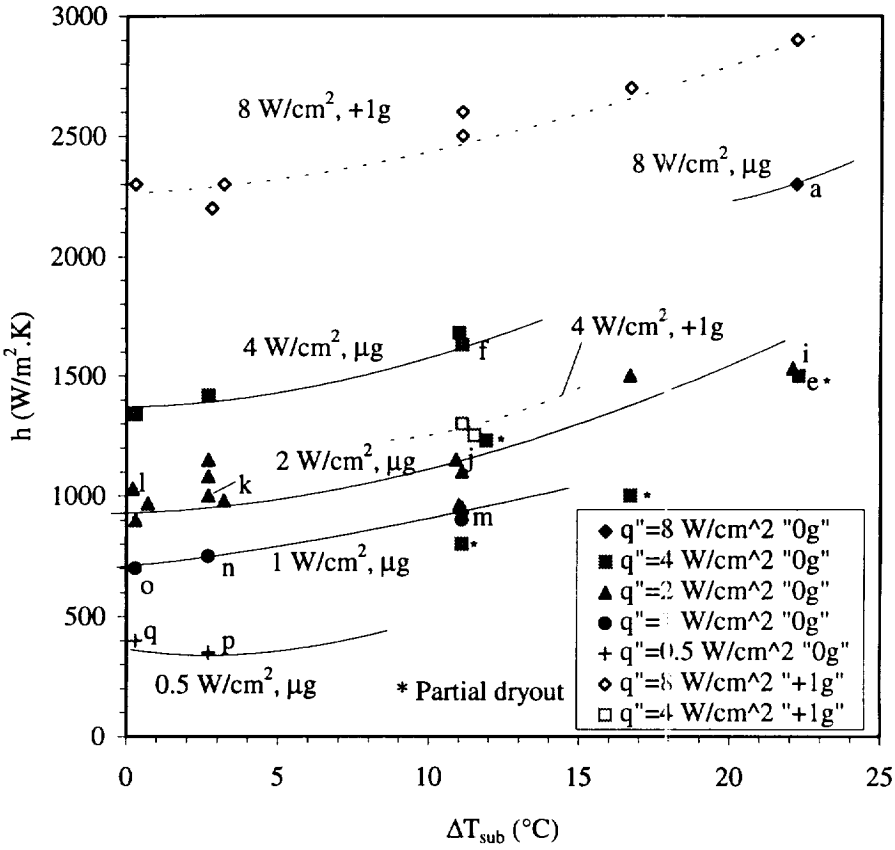

Figure 7.9. Demonstration of the influence of subcooling on the heat transfer coefficient with pool boiling in microgravity for R-113.

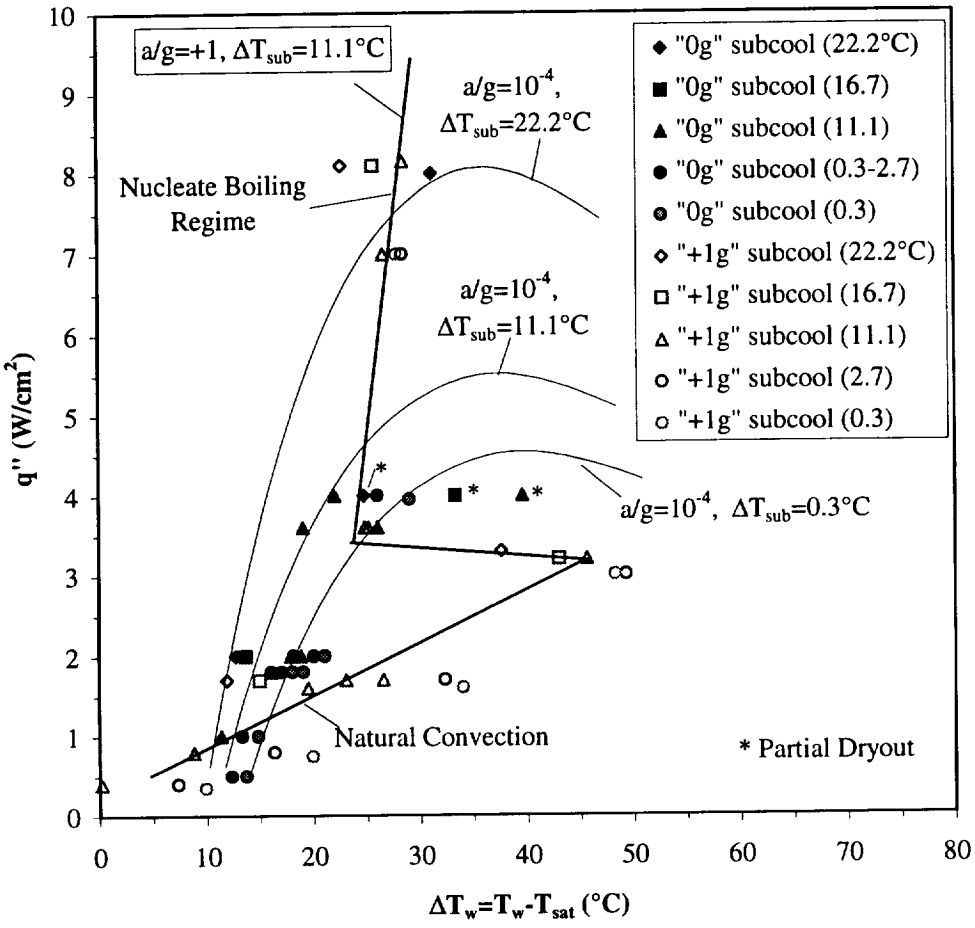

Figure 7.10. Pool boiling curve in microgravity with R-113.

References

Becker, K. M., Engstrom, J., Nylund, O., Scholin, B., (1990), "Analysis of the Dryout Incident in the Oskarshamn 2 Boiling Water Reactor," *Int. J. Multiphase Flow*, 16, No. 6, pp. 959-974.

Berenson, P. J., (1961), "Film Boiling Heat Transfer from a Horizontal Surface," Trans. ASME, *J. Heat Transfer*, 83C, pp. 351-356.

Chang, Y.P. and Snyder, N.W., (1960), "Heat Transfer in Saturated Boiling, " Chem. Eng. Prog. Symp. Ser., 56, No. 30, pp. 25-35.

Dhuga, D.S. and Winterton, R.H.S., (1985), "Measurement of Surface Contact in Transition Boiling," *I.J. Heat and Mass Transf.*, 28, pp 1869-1880.

Donald, M.D. and Haslam, F., (1958), "The Mechanism of the Transition from Nucleate to Film Boiling, "Chem. Eng. Sci., 8, pp. 287.

Duffy, R.B., and Hughes, E.D., (1991), "Dryout Stability and Inception at Low Flow Rates, " *Int. J. Heat Mass Transfer*, 34, No. 2, pp. 473-481.

Ervin, J.S., and Merte, H., Jr., (1991), "A Fundamental Study of Nucleate Pool Boiling under Microgravity," Report No. UM-MEAM-91-08, Department of Mechanical Engineering and Applied Mechanics, University of Michigan, Ann Arbor, MI., Final Report on NASA Grant NAG3-663.

Ervin, J.S., Merte, H., Keller, R.B., Kirk, K., (1992). "Transient Pool Boiling in Microgravity", *Int. J. Heat Mass Transfer*, Vol. 35, pp. 659-674.

Ervin, J.S., and Merte, H., Jr., (1993), "Boiling Nucleation and Propagation in Microgravity", in ASME HTD-Vol. 269, *Heat Transfer in Microgravity*, pp 131-138.

Hewitt, G.F., and Govan, A.H., (1990), "Phenomenological Modeling of Non-Equilibrium Flows with Phase Change,"*Int. J. Heat Mass Transfer*, 33, No. 2, pp. 229-242.

Inoue, M. and Tanaka, H., (1991),"Study on Surface Rewet Caused by Uniform Collapse of Flow Film Boiling," *Int. J. Heat Mass Transfer*, 34, No. 4-5, pp. 1139-1147.

Johannsen, K., (1991), "Low Quality Transition and Inverted Annular Flow Film Boiling of Water: An Updated Review," Exp. Thermal Fluid Sci., 4, No. 5, pp. 497-509.

Kikuchi, Y., Ebisu, T., Michiyoshi, I., (1992), "Measurement of Liquid-Solid Contact in Film Boiling," *Int. J. Heat Mass Transfer*, 35, No. 6, pp. 1589-1594.

Kutateladze, S. S., (1952), "Heat Transfer in Condensation and Boiling. "USAEC Report AEC-tr-3770.

Lee, Ho Sung, and Merte, H., Jr., (1993), "Vapor Bubble Dynamics in Microgravity," Report No. UM-MEAM-93-10, Department of Mechanical Engineering and Applied Mechanics, University of Michigan, Ann Arbor, MI., Pool Boiling Experiment Report on NASA Contract NAS3-25812.

Lee, H.S., and Merte, H., Jr., (1996a), "The Origin of the Dynamic Growth of Vapor Bubbles Associated with Vapor Explosions", ASME HTD-Vol. 332, pp 3-14. To be published in *J. of Heat Transfer*, February, 1998.

Lee, H.S., and Merte, H., Jr., (1996b), "Spherical Vapor Bubble Growth in Uniformly Superheated Liquids", *Int. J. Heat Mass Transfer*, 39, 12, pp 2427-2447.

Lee, H.S., and Merte, H., Jr., (1996c), "Hemispherical Vapor Bubble Growth in Microgravity: Experiments and Model", *Int. J. Heat Mass Transfer*, 39, 12, pp. 2449-2461.

Lee, H.S., Merte, H., Jr., Chiaramonte, F., (1997), "Pool Boiling Curve in Microgravity," AIAA *J. of Thermophysics and Heat Transfer*, Vol. 11, No. 2, pp 216-222.

Lee, H.S., and Merte, H. Jr., (1997), "Mercury Vapor Bubble Dynamics and Vapor Explosions," presented at session "Accelerator Thermal Hydraulics-II". American Nuclear Society 1997 Winter Meeting, Nov. 16-20, 1997, Albuquerque, N.M.

Lloyd, J.R., and Moran, W.R., (1974), "Natural Convection Adjacent to Horizontal Surface of Various Planforms, "Trans. ASME, J. Heat Transfer Transfer 96C, 4, pp. 443-447.

Mastroianni, M.J., Stahl, R.F., and Sheldon, P.N., (1978), "Physical and Thermodynamic Porperties of 1, 1, 2 - Trifluorotrichloroethane (R-113), *J. of Chemical and Engineering Data*, 23, 2, pp. 113-118.

Merte, H., and Clark, J.A., (1964), "Boiling Heat Transfer with Cryogenic Fluids at Standard, Fractional and Near-Zero Gravity", J. Heat Transfer, 86C, 3, pp 351-359.

Merte, H., (1967), "Liquid Metal Boiling in Agravic Fields," in Technical Report AFAPL-TR-66-85," Investigation of Liquid Metal Boiling Heat Transfer", Air Force Contract AF33 (-657) - 11548, January 1967. pp 92-140.

Merte, Herman Jr., (1992), "Pool Boiling Experiment, "Report No. UM-MEAM-91-19, Department of Mechanical Engineering and Applied Mechanics, University of Michigan, Ann Arbor, Michigan, Status Report for period 2/1/91 - 9/30/91 to NASA Lewis Research Center on Contract NAS3-25812.

Merte, H. Jr., Lee, H.S., Ervin, J.S., (1994), "Transient Nucleate Pool Boiling in Microgravity - Some Initial Results, " Microgravity Science and Technology, VII/2, pp 173 -179.

Merte, H. Jr., Lee, H.S., Keller, R.B., (1996), "Report on Pool Boiling Experiment Flown on STS-47 (PBE-IA), STS-57 (PBE-IB), STS-60 (PBE-IC)," NASA Contractor Report CR-198465, March 1996.

Merte, H. Jr., and Lee, H.S., (1997), "Quasi-Homogeneous Nucleation in Microgravity at Low Heat Flux: Experiments and Theory", *J. of Heat Transfer*, 119, May 1997., pp 305-312.

Oka, T., Abe, Y., Mori, Y.H. and Nagashima, A., 1995, "Pool Boiling of N-Pentane, CFC-113, and Water under Reduced Gravity: Parabolic Flight experiments with a Transparent Heater", Journal of Heat Transfer, Vol. 117, pp. 408-417.

Oka, T., Abe, Y., Mori, Y.H. and Nagashima, A., 1996, "Pool Boiling Heat Transfer in Microgravity," JSME International Journal, Series B, Vol.39, No. 4, pp. 798-807.

Oker, E., and Merte, H. Jr., (1978), "A Study of Transient Effects Leading up to Inception of Nucleate Boiling", Proc. 6th Int. Heat Transfer Conf., Vol.I, paper PB-5, Toronto, Canada, Aug. 7-11, 1978, pp 139-144.

Peng, X.F., Wang, B.X., Peterson, G.P., (1992), "Film and Transition Boiling Characteristics of Subcooled Liquid Flowing Through a Horizontal Flat Duct," Int. J. Heat Mass Transfer, 35, No. 11, pp.3077-3083.

Peterson, G.P., Lu, X. J., Peng, X.F., Wang, B.X., (1992), "Analytical and Experimental Investigation of the Rewetting of Circular Channels with Internal V-grooves," Int. J. Heat Mass Transf., 35, No. 11, pp. 3085-3094.

Rayleigh, Lord, (1917), "On the pressure developed in a liquid during the collapse of a spherical cavity", Phil. Mag.34, pp. 94-98.

Reid, R. C., (1983), "Rapid Phase Transitions from Liquid to Vapor", Advances in Chemical Engineering, Vol. 12, pp. 105-208.

Straub, J., (1994), "The Role of Surface Tension for Two-Phase Heat and Mass Transfer in the Absence of Gravity", Experimental Thermal and Fluid Science, Vol. 9, pp, 253-273.

Subramanian, R.S., (1990), "The Motion of Bubbles and Drops in Reduced Gravity", in "Transport Processes in Bubbles, Drops, and Particles" (Eds.-R.P.Chabra and D. Dekee) Hemisphere Publishing Corp., New York.

Trefethen, L., (1961), "On the Jet Propulsion of Bubbles in a Heated Liquid", Mechanical Engineering Report 61-8- 1, Tufts University.

Unal, C., Daw, V., Nelson, R.A., (1992), "Unifying the Controlling Mechanisms for the Critical Heat Flux and Quenching: The Ability of the Liquid to Contact the Hot Surface, "ASME J. Heat Transfer, 114, No.4, pp. 972-982.

Weinzierl, A., and Straub, J., (1982), "Nucleate Pool Boiling in Microgravity Environment", Proceedings of the 7th International Heat Transfer Conference, September 6-10, 1982, Munich.

Zuber, N., (1958), "On the Stability of Boiling Heat Transfer", Trans, ASME 80, pp. 711-720.

Appendix A. PBE-IIB (STS-72). Experimental Results

PBE Flight-System Matrix (STS-72)

RUN #	HEAT FLUX W/CM^2	SUBCOOLING (^{0}F)	HEATER POWER ON/OFF (SEC)	10 FPS ON/OFF (SEC)	STIRRER START (SEC)	REPRESS. START (SEC)	TOTAL TEST TIME (SEC)
1	8	40	10 - 70	15 - 80	60	-	80
2	4	40	10 - 100	10 - 15, 25 - 35	-	-	135
3	2	40	10 - 120	20 - 30, 50 - 130	110	-	130
4	8	30	10 - 55	15 - 65	45	-	65
5	4	30	10 - 100	10 - 15, 25 - 105	90	-	110
6	2	40	10 - 95	20 - 30, 50 - 110	-	45	115
7	8	20	10 - 40	15 - 55	-	50	55
8	4	20	10 - 70	10 - 15, 25 - 80	60	-	80
9	2	20	10 - 115	10 - 30, 50 - 125	95	-	125

Table A-I. Test matrix for PBE-IIB on STS-72. (Flight Hardware)

NASA test Matrix for Pool boiling - STS 72

a/g -1 experiment based on date 10/5/95
a/g +1 experiment based on date 10/5/95
a/g 0 experiment based on date 2/5/96 STS-72

Run#	Date of Experiment	Flight system	Gravi a/g	Heat Flux (W/cm^2) Nom.	Actual	Subcool,°F Nom	Actual	Tbulk °C	Sys. Press kPa	Tsat °C	T*wall °C	T*sup °C	t* time sec	100fps On-Off	Remark
1	10/5/95	Flight system	-1	8.00	7.15	40	39.40	39.43	157.91	61.32	~	~	~	0~5	
	10/5/95	Flight system	1	8.00	8.10	40	39.87	37.22	147.81	59.37	87.84	28.47	1.70	0~5	
	2/5/96	Flight system	0	8.00	8.09	40	39.83	36.65	145.13	58.78	86.28	27.50	0.81	0~5	not explosive
2	10/5/95	Flight system	-1	4.00	3.82	40	42.16	38.03	158.51	61.45	115.70	54.25	18.20	5~15	
	10/5/95	Flight system	1	4.00	4.01	40	39.86	37.26	147.97	59.40	~	~	~	5~15	no nucleation
	2/5/96	Flight system	0	4.00	4.04	40	39.85	39.11	156.51	61.25	118.86	57.61	15.44	5~15	
3	10/5/95	Flight system	-1	2.00	2.02	40	39.51	38.81	155.27	60.76	~	~	~	20~40	no nucleation
	10/5/95	Flight system	1	2.00	2.06	40	39.92	37.96	151.32	60.14	~	~	~	20~40	no nucleation
	2/5/96	Flight system	0	2.00	2.05	40	39.91	38.13	152.10	60.30	97.99	37.69	36.41	20~40	
4	10/5/95	Flight system	-1	8.00	7.21	30	29.48	38.55	129.69	54.93	~	~	~	0~5	
	10/5/95	Flight system	1	8.00	8.12	30	29.90	37.71	126.35	54.32	84.48	30.16	1.10	0~5	
	2/5/96	Flight system	0	8.00	7.85	30	29.93	38.40	129.21	55.03	83.35	28.32	0.36	0~5	not explosive
5	10/5/95	Flight system	-1	4.00	3.81	30	29.43	38.39	128.93	54.74	113.20	58.46	17.40	5~15	
	10/5/95	Flight system	1	4.00	4.01	30	29.91	37.43	125.28	54.05	~	~	~	5~15	no nucleation
	2/5/96	Flight system	0	4.00	4.03	30	29.88	40.08	136.07	56.68	119.94	63.26	15.02	5~15	
6	10/5/95	Flight system	-1	2.00	2.02	30	35.98	38.63	145.48	58.62	~	~	~	20~40	no nucleation
	10/5/95	Flight system	1	2.00	2.07	30	36.32	37.94	142.24	58.11	~	~	~	20~40	no nucleation
	2/5/96	Flight system	0	2.00	2.04	30	41.13	38.57	157.30	61.42	107.53	46.11	57.64	20~40	

Table A-II. Measured parameters at a/g=-1, a/g = +1, and Space Flight.

	Page 2 of 2														
Run#	Date of	Flight	Gravi	Heat Flux (W/cm^2)		Subcool,oF		Tbulk	Sys. Press	Tsat	T*wall	T*sup	t* time	100pps	
	Experiment	system	a/g	Nom.	Actual	Nom	Actual	°C	kPa	°C	°C	°C	sec	On-Off	
7	10/5/95	Flight system	-1	8.00	7.35	20	21.11	38.53	108.57	50.26	~	~	~	0~5	
	10/5/95	Flight system	1	8.00	8.15	20	21.10	37.81	108.31	49.53	80.32	30.79	1.00	0~5	
	2/5/96	Flight system	0	8.00	7.60	20	19.78	38.60	108.50	49.59	80.82	31.23	0.51	0~5	not explosive
8	10/5/95	Flight system	-1	4.00	3.85	20	19.51	38.41	108.11	49.25	111.15	61.90	16.80	5~15	
	10/5/95	Flight system	1	4.00	4.03	20	19.94	37.38	104.56	48.46	~	~	~	5~15	no nucleation
	2/5/96	Flight system	0	4.00	4.05	20	19.85	38.35	107.76	49.38	109.59	60.21	11.50	5~15	
9	10/5/95	Flight system	-1	2.00	2.02	20	6.84	38.48	108.18	42.28	~	~	~	20~40	no nucleation
	10/5/95	Flight system	1	2.00	2.06	20	19.84	37.96	106.38	48.99	~	~	~	20~40	no nucleation
	2/5/96	Flight system	0	2.00	2.04	20	19.89	39.14	110.66	50.19	109.95	59.76	62.39	20~40	

Table A-II. Continued.

RUN #	Time, sec	Peaks	Maximum Acceleration value			Noise
			x	y	z	
1		no	47	25	51	24
2		no	47	50	77	24
3	70.5	yes	47	25	152	24
3	70.8	yes	24	0	152	24
4		no	47	50	77	24
5	15.9	yes	148	50	0	24
5	16	yes	148	25	25	24
5	16.3	yes	147	25	26	24
5	42.7	yes	47	25	127	24
6		no	47	75	51	24
7		no	50	50	77	24
8	7.9	yes	0	25	178	24
8	8.1	yes	47	50	152	24
8	8.4	yes	47	50	178	24
8	8.7	yes	0	25	153	24
8	9	yes	0	50	177	24
8	9.3	yes	47	50	152	24
8	9.5	yes	0	50	127	24
8	9.9	yes	23	0	152	24
8	34.5	yes	47	0	152	24
8	79.9	yes	0	25	152	24
9	14.9	yes	0	25	127	24
9	15.2	yes	47	0	152	24
9	15.5	yes	0	0	152	24

Notes: (1) Accelerometer units are given as micro-g's.

(2) Heating in each run begins at t = 10 sec.

Table A-III. Summary of relatively larger acceleration excursions during PBE-IIB in STS-72 Flight.

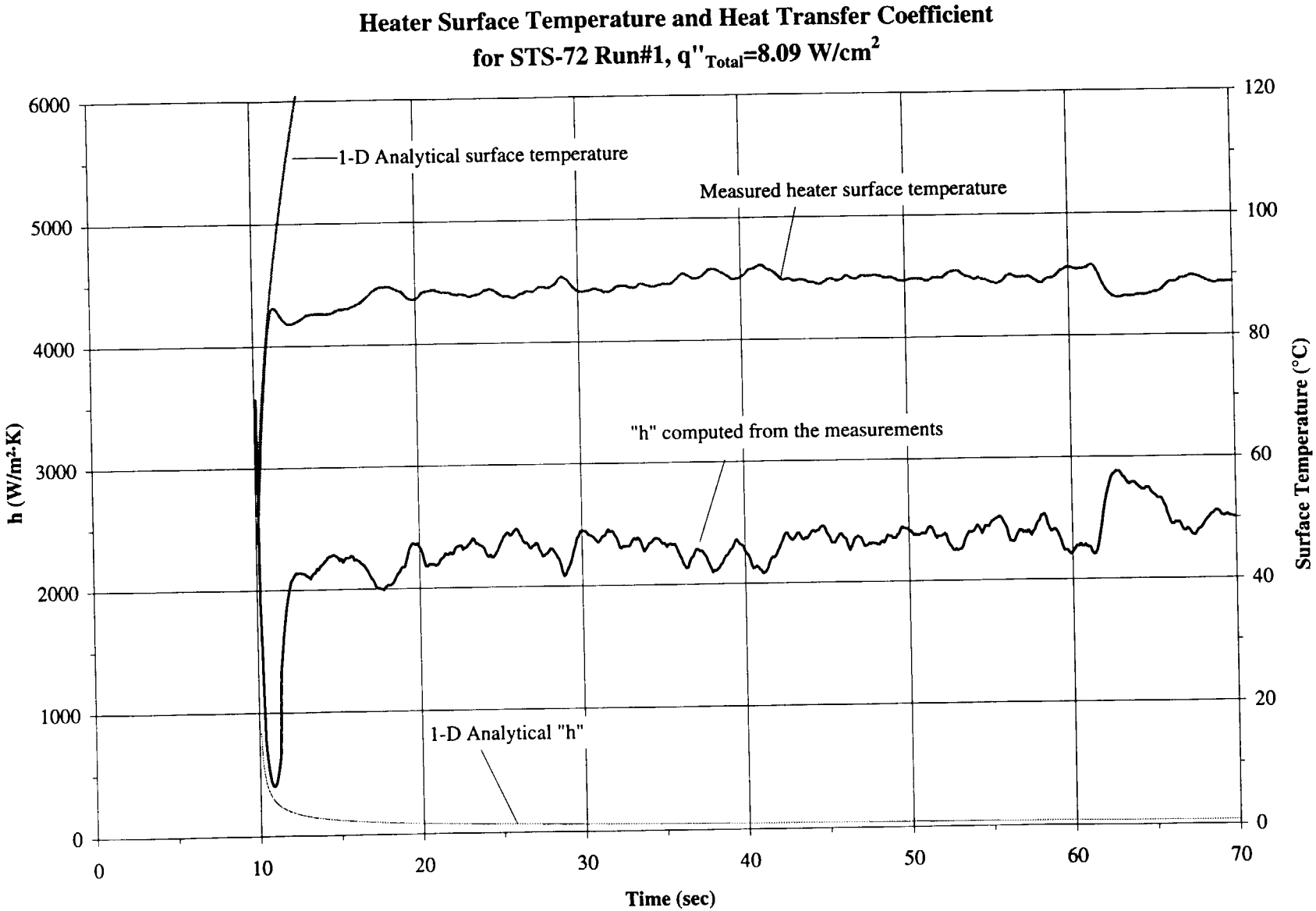

Figure A-1a. Mean heater surface temperature and derived heat transfer coefficient. PBE-IIB (STS-72). Run No. 1.

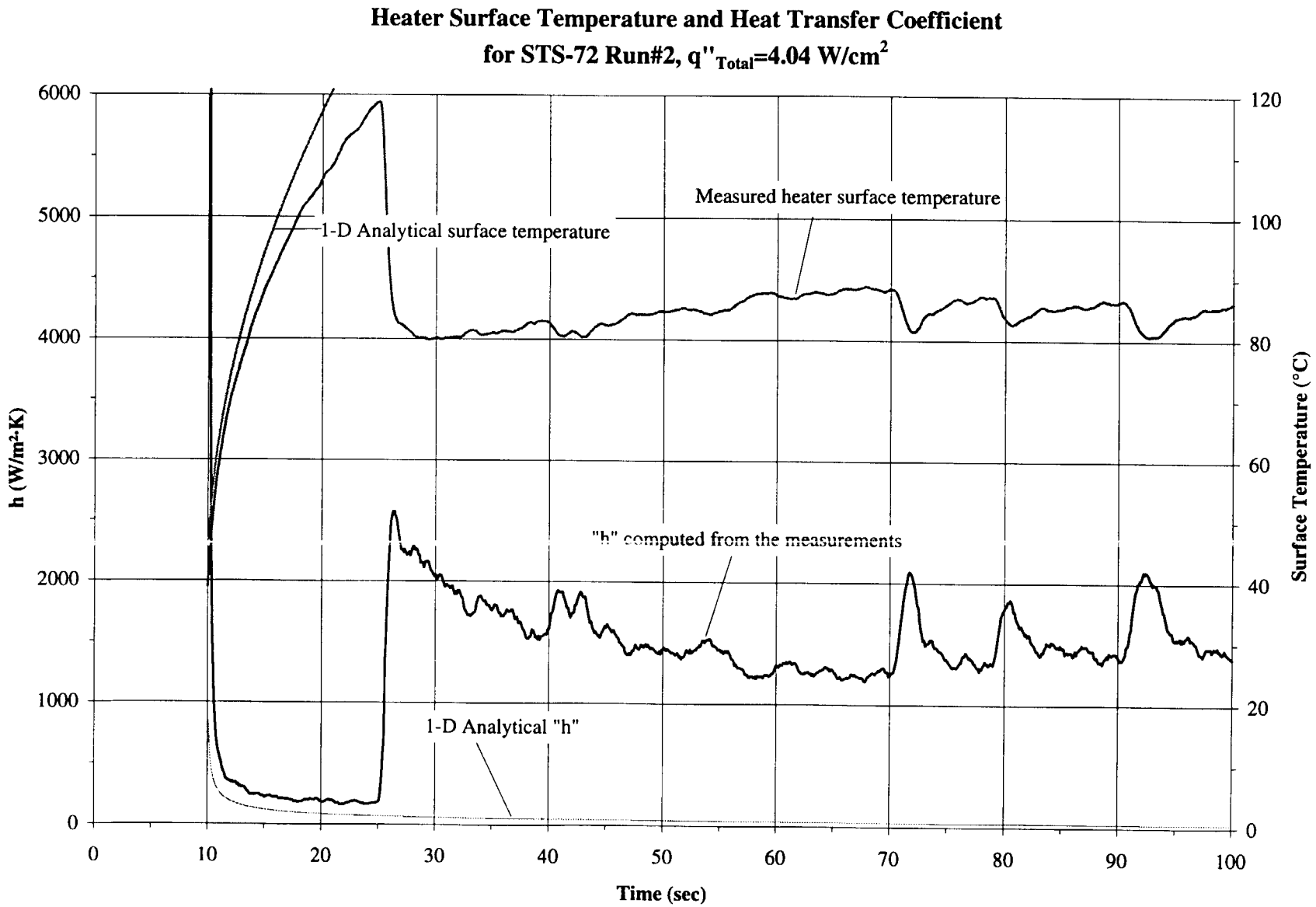

Figure A-1b. Mean heater surface temperature and derived heat transfer coefficient. PBE-IIB (STS-72). Run No. 2.

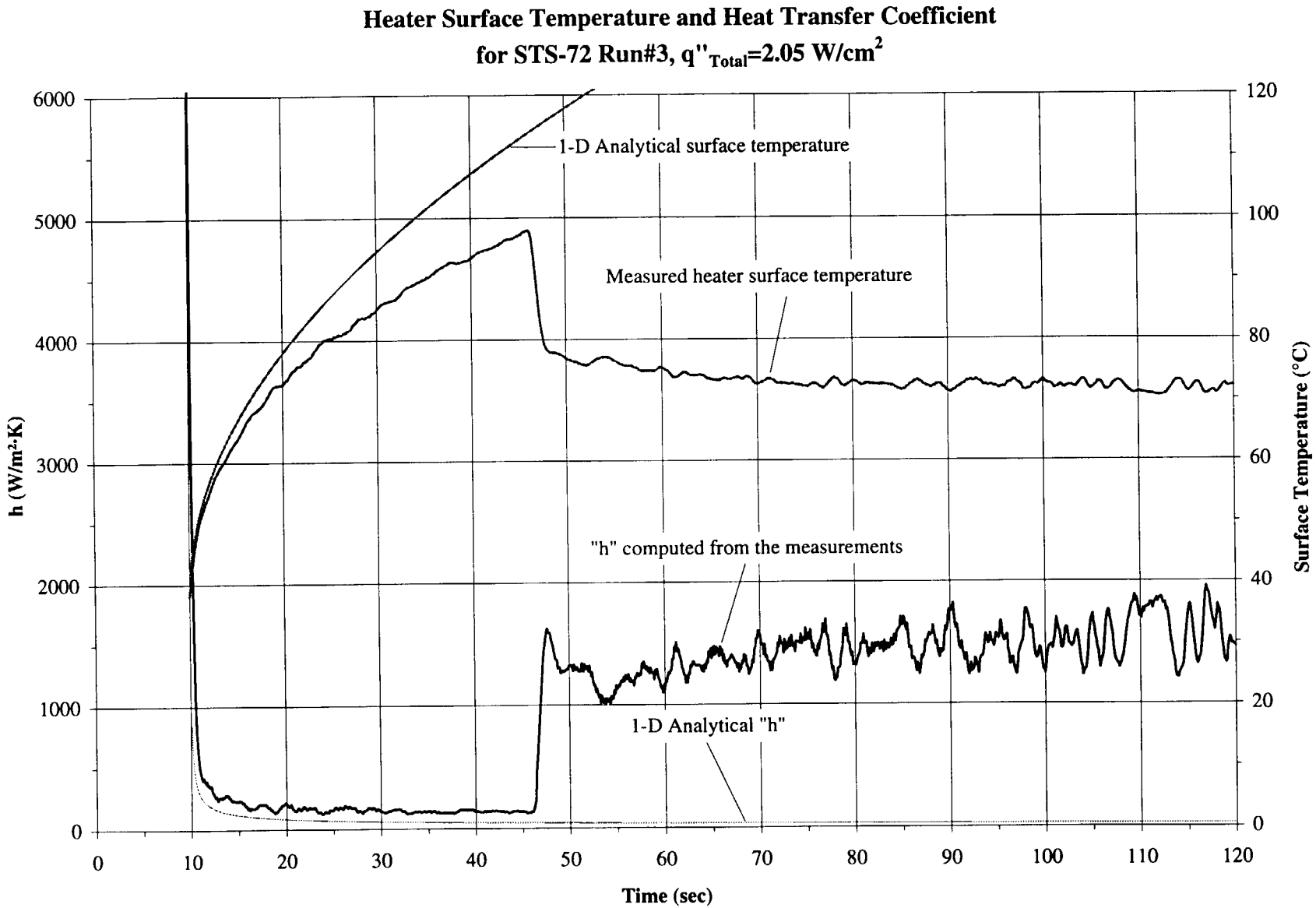

Figure A-1c. Mean heater surface temperature and derived heat transfer coefficient. PBE-IIB (STS-72). Run No. 3.

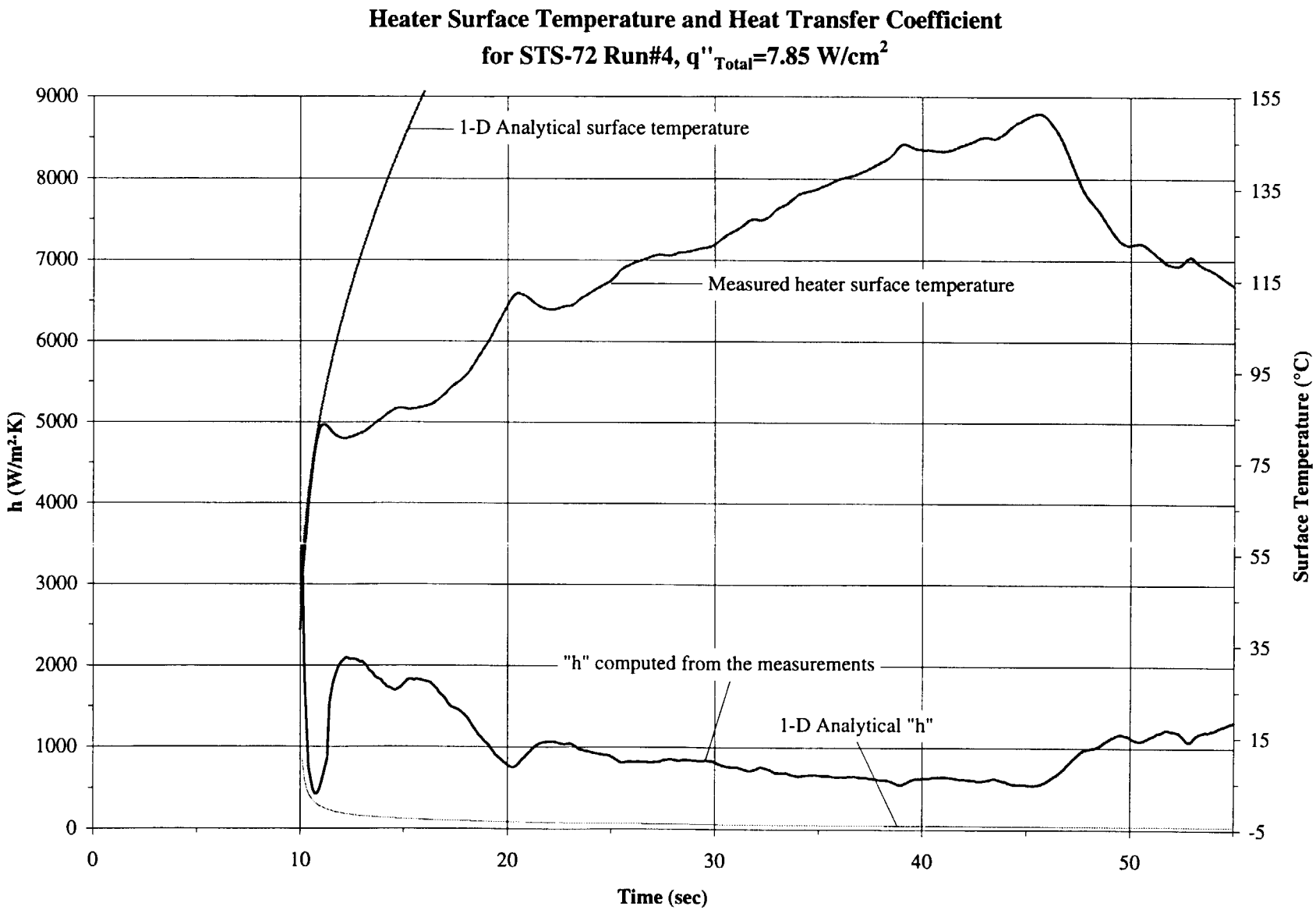

Figure A-1d. Mean heater surface temperature and derived heat transfer coefficient. PBE-IIB (STS-72). Run No. 4.

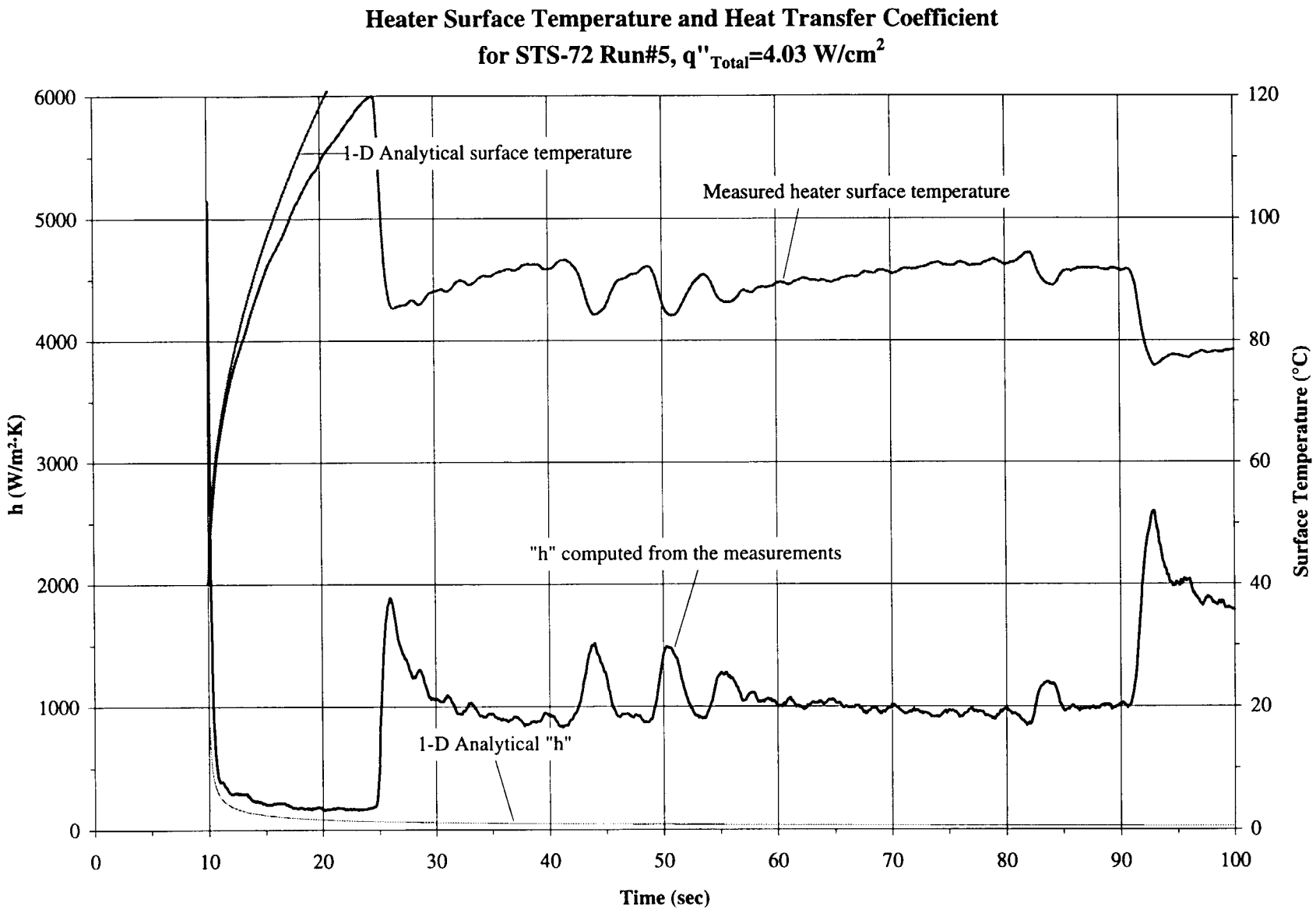

Figure A-1e. Mean heater surface temperature and derived heat transfer coefficient. PBE-IIB (STS-72). Run No. 5.

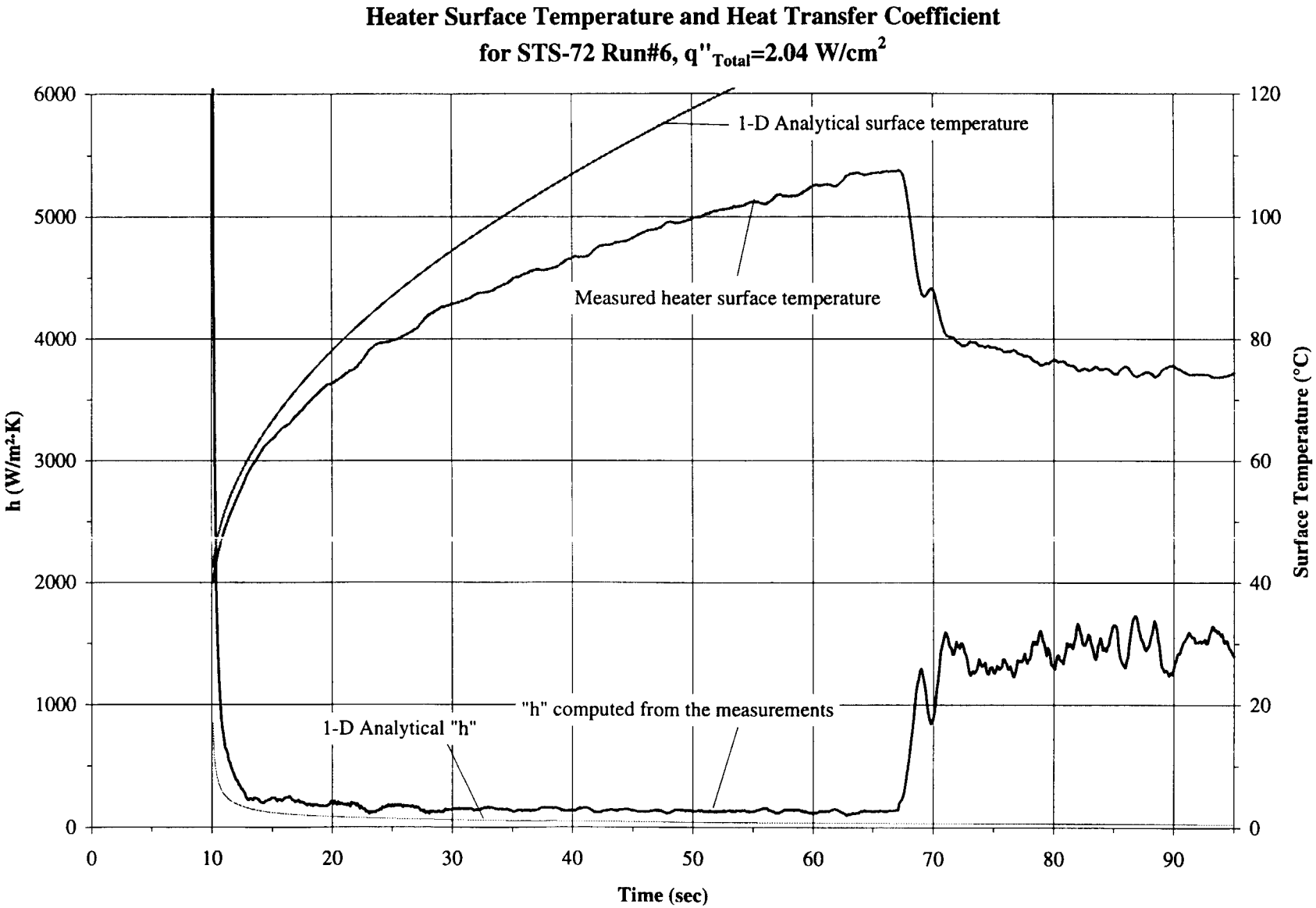

Figure A-1f. Mean heater surface temperature and derived heat transfer coefficient. PBE-IIB (STS-72). Run No. 6.

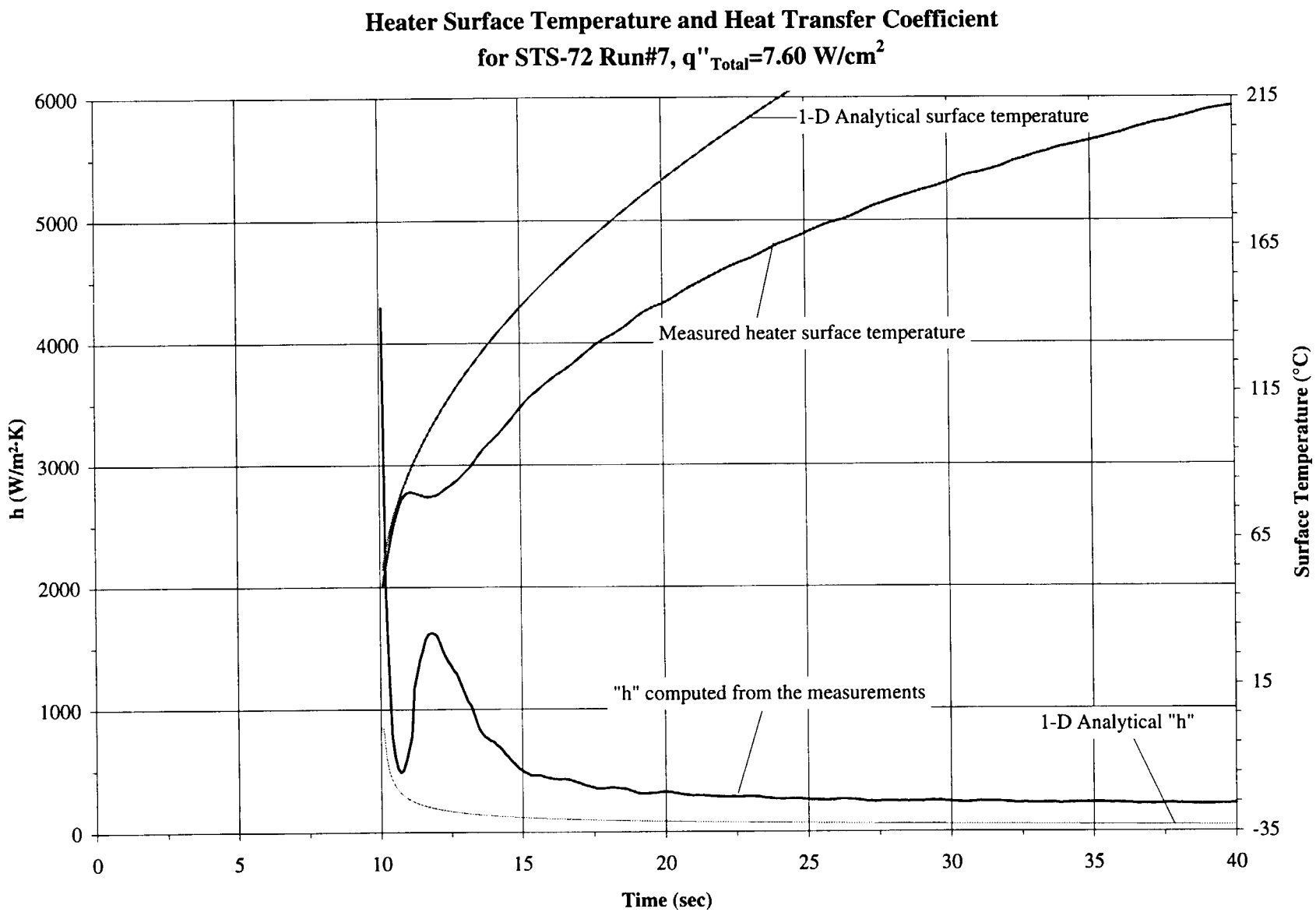

Figure A-1g. Mean heater surface temperature and derived heat transfer coefficient. PBE-IIB (STS-72). Run No. 7.

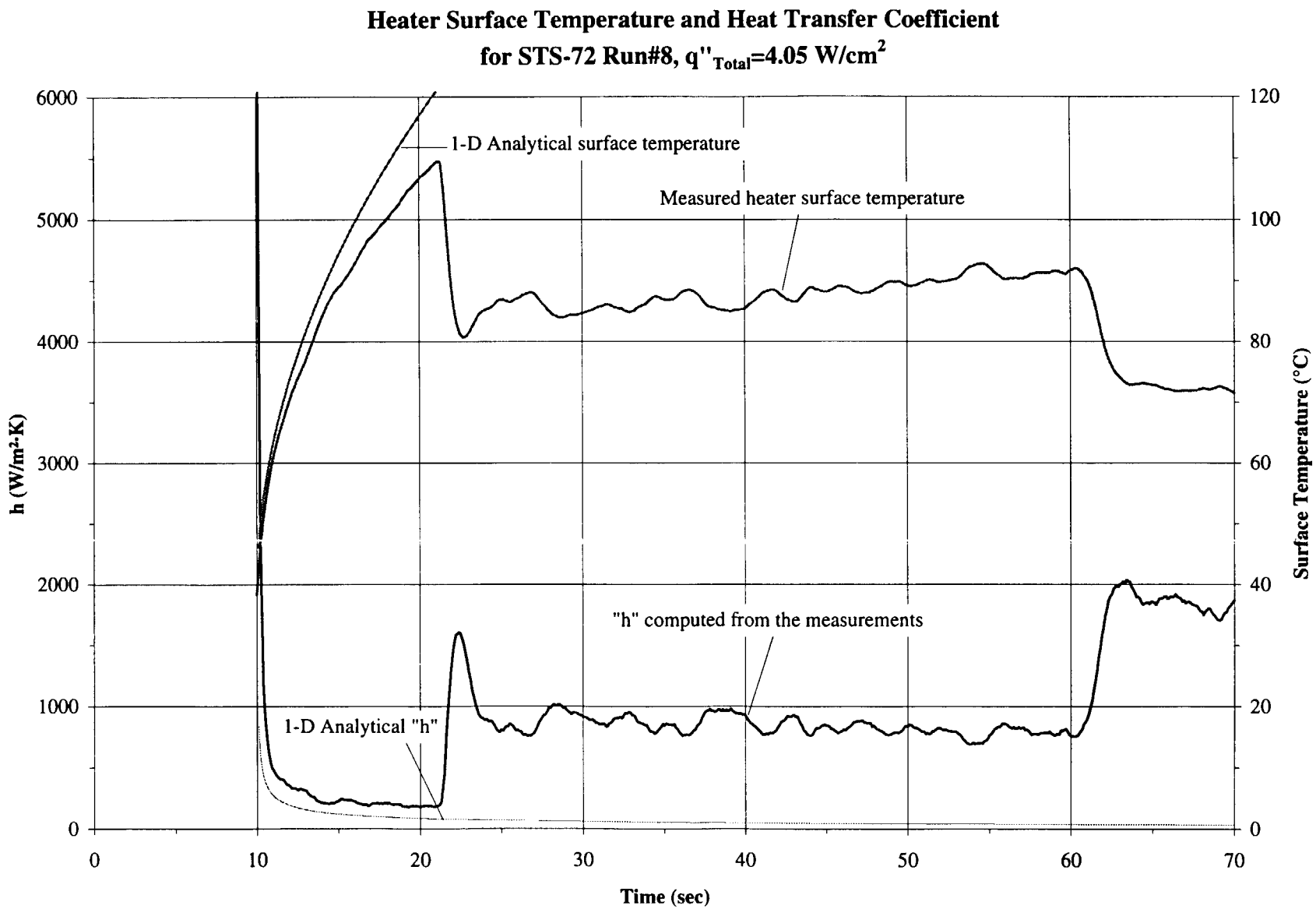

Figure A-1h. Mean heater surface temperature and derived heat transfer coefficient. PBE-IIB (STS-72). Run No. 8.

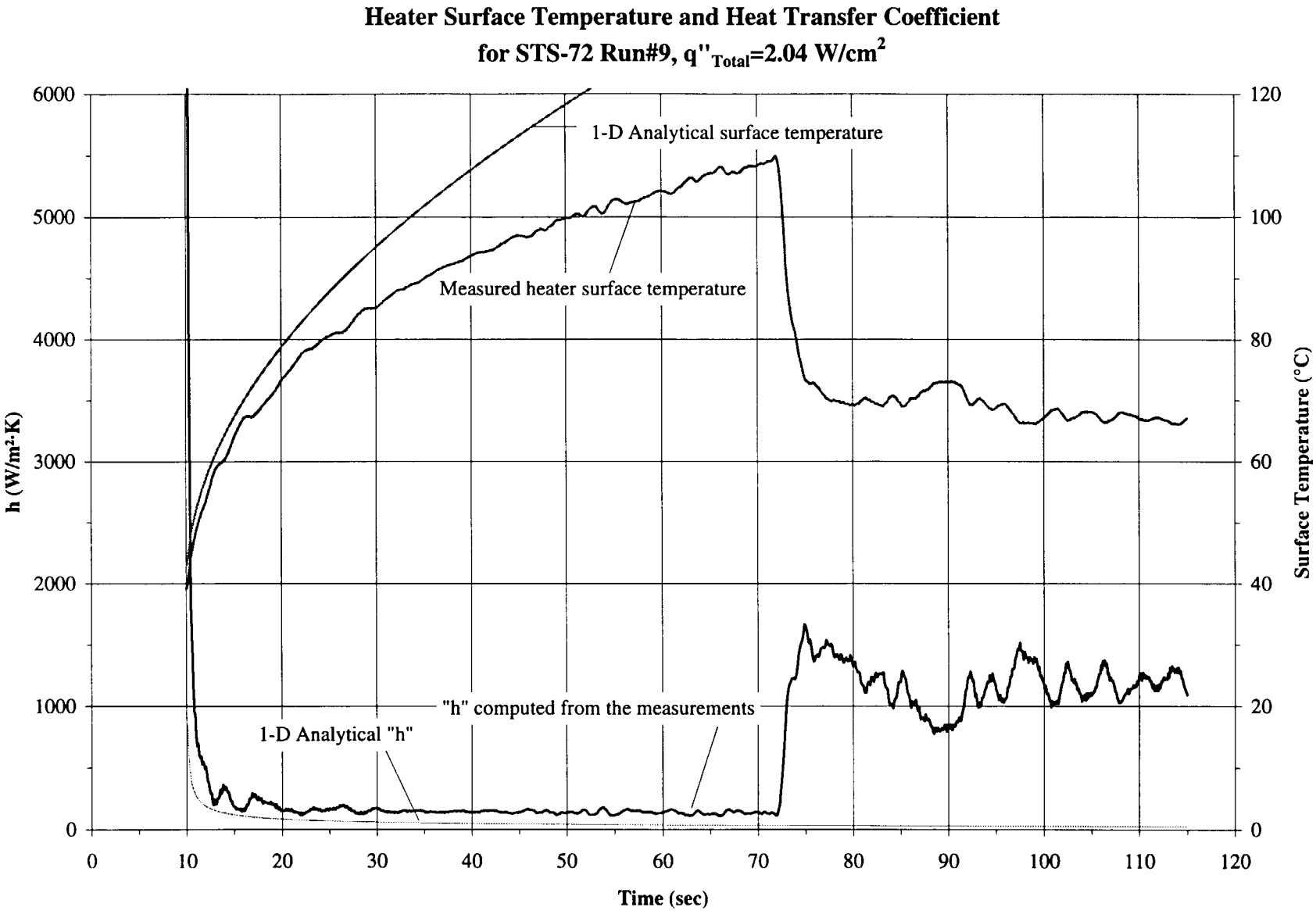

Figure A-1i. Mean heater surface temperature and derived heat transfer coefficient. PBE-IIB (STS-72). Run No. 9.

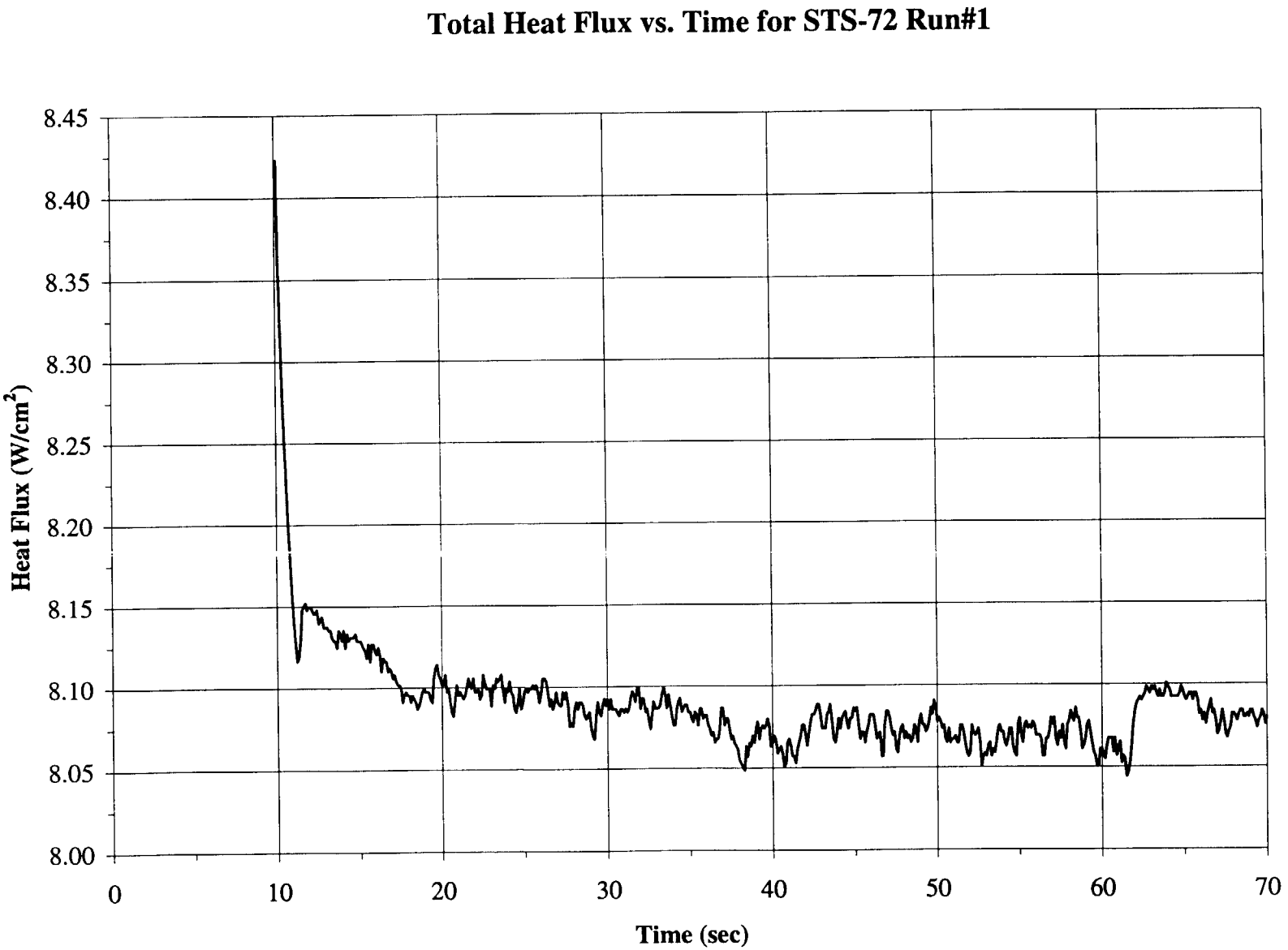

Figure A-2a. Heat flux input. PBE-IIB (STS-72). Run No. 1.

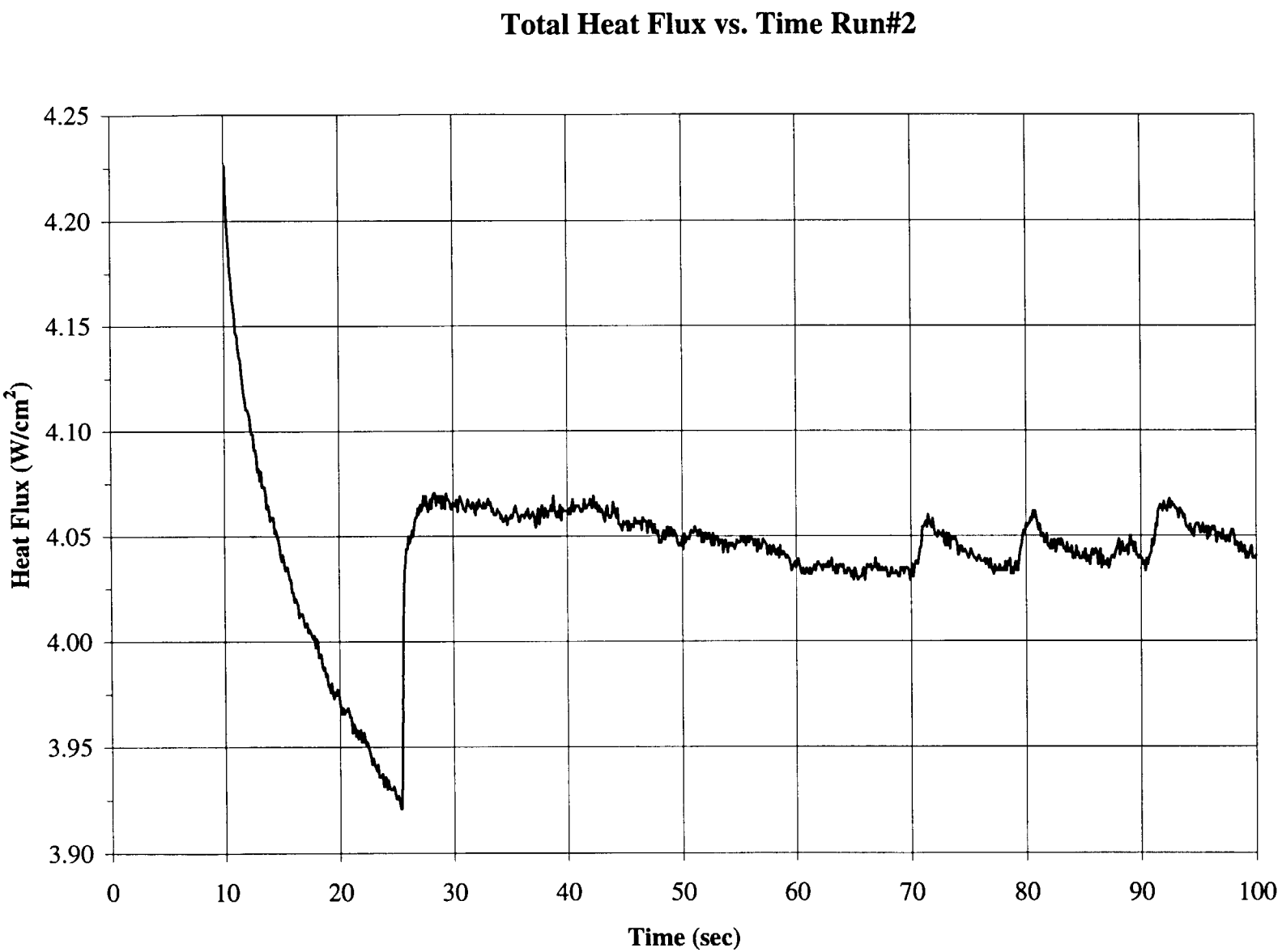

Figure A-2b. Heat flux input. PBE-IIB (STS-72). Run No. 2.

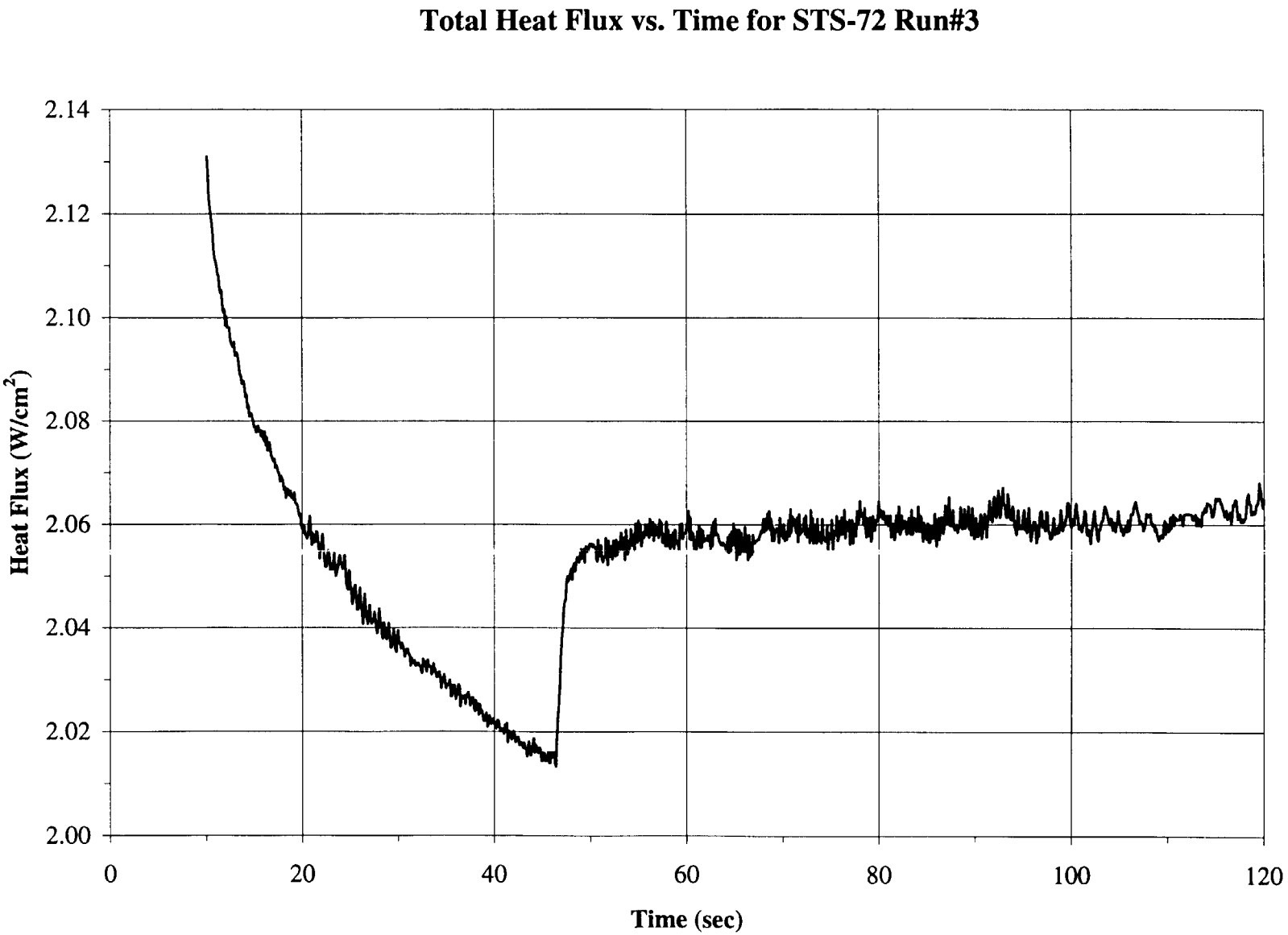

Figure A-2c. Heat flux input. PBE-IIB (STS-72). Run No. 3.

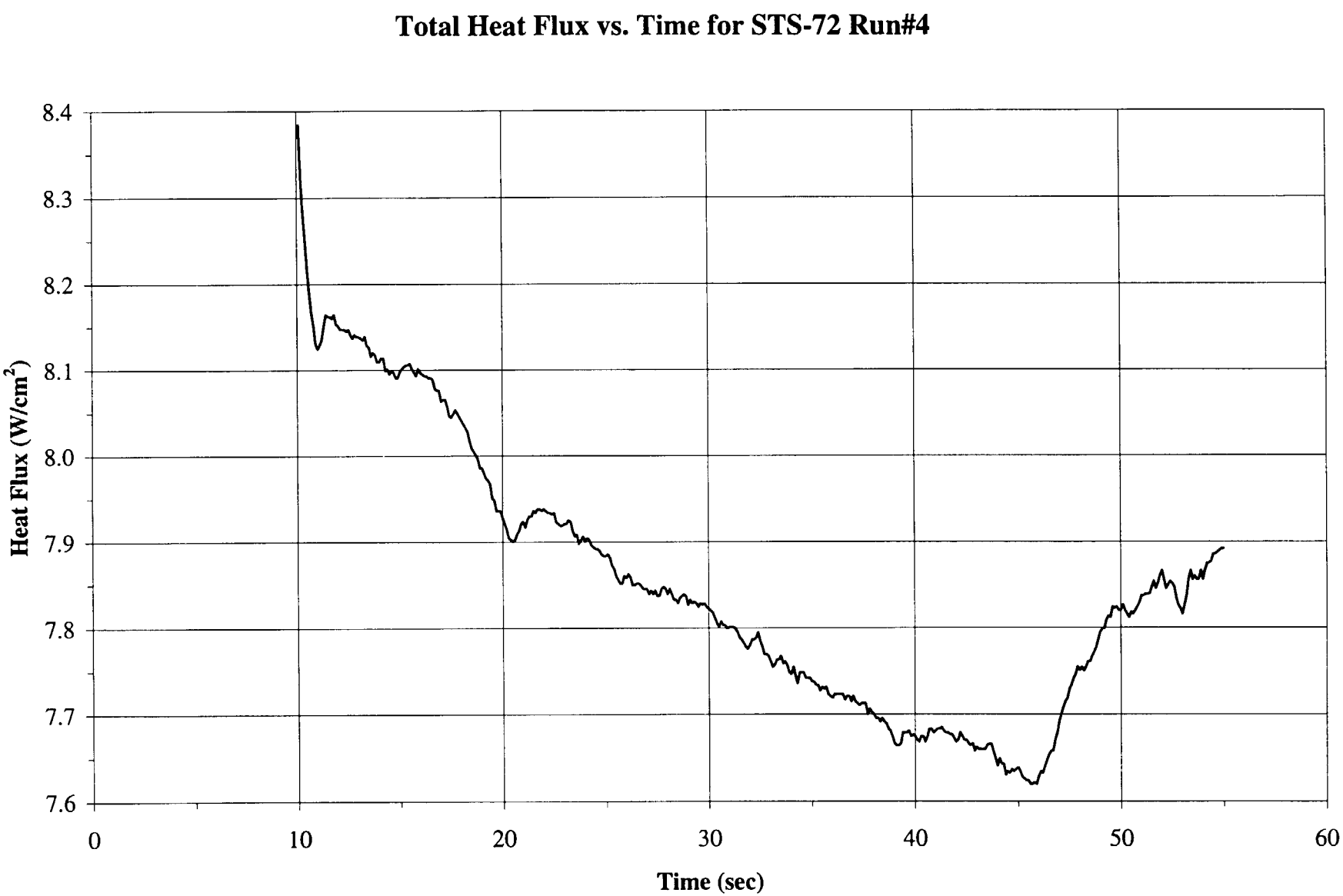

Figure A-2d. Heat flux input. PBE-IIB (STS-72). Run No. 4.

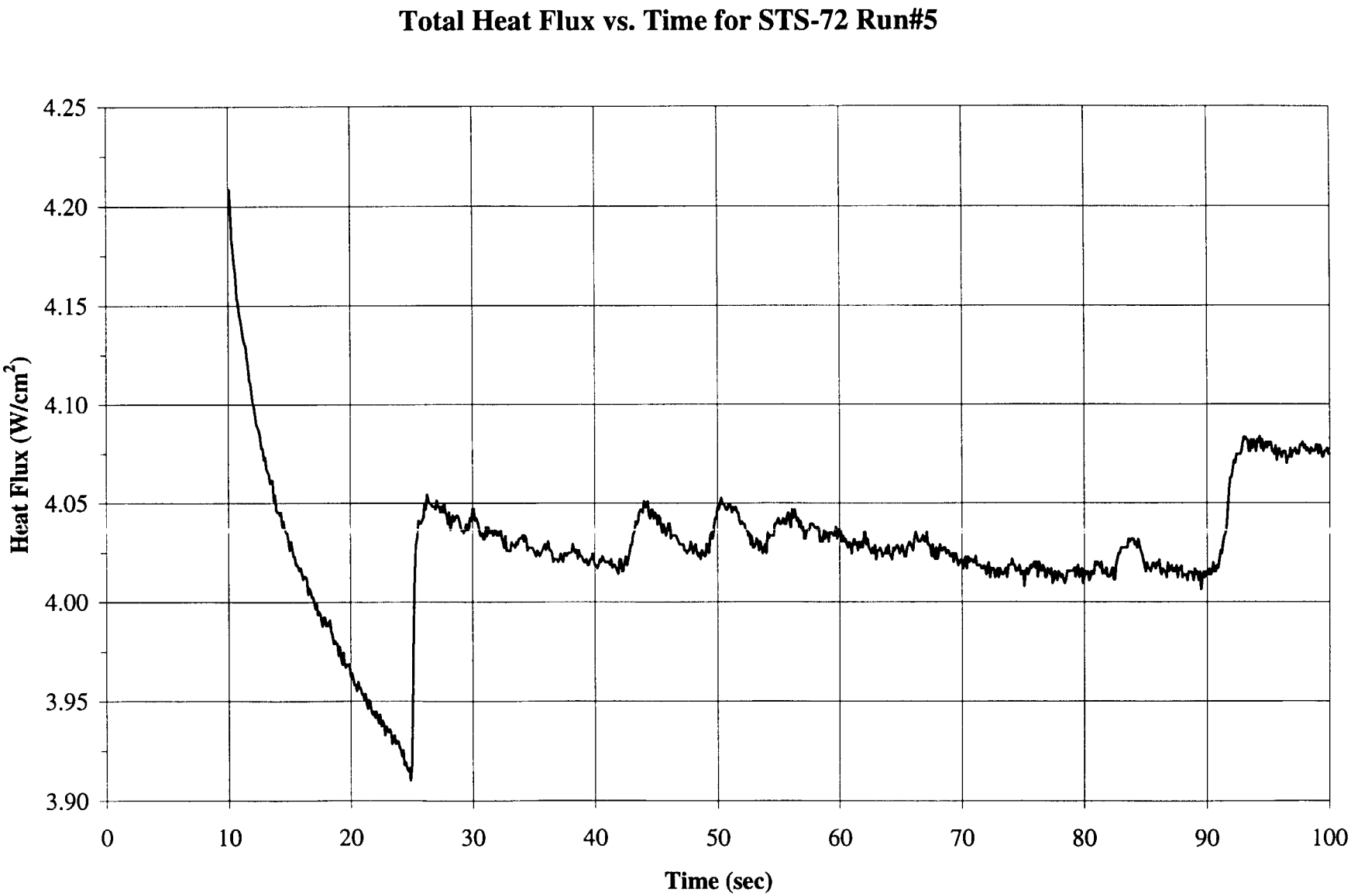

Figure A-2e. Heat flux input. PBE-IIB (STS-72). Run No. 5.

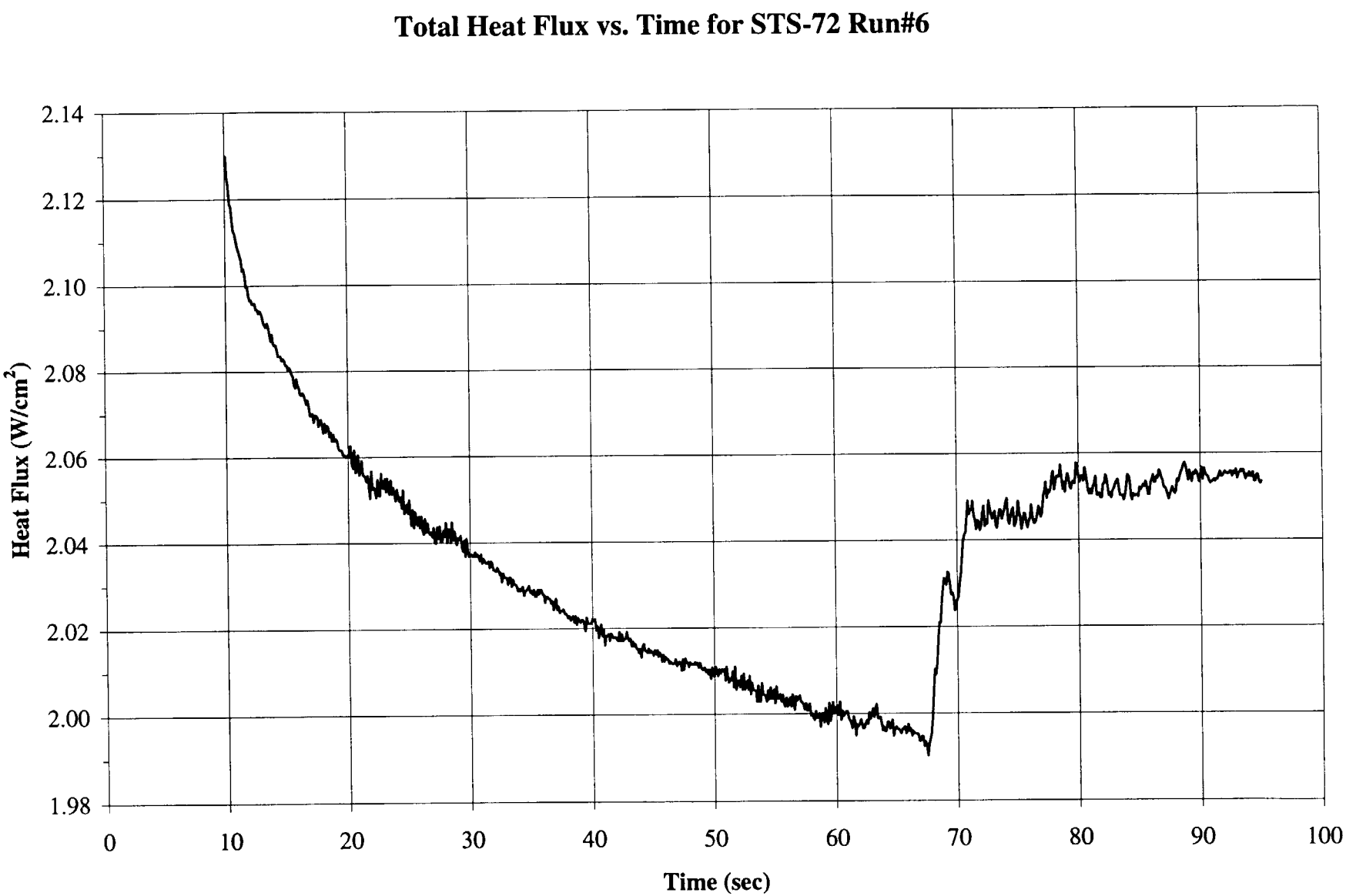

Figure A-2f. Heat flux input. PBE-IIB (STS-72). Run No. 6.

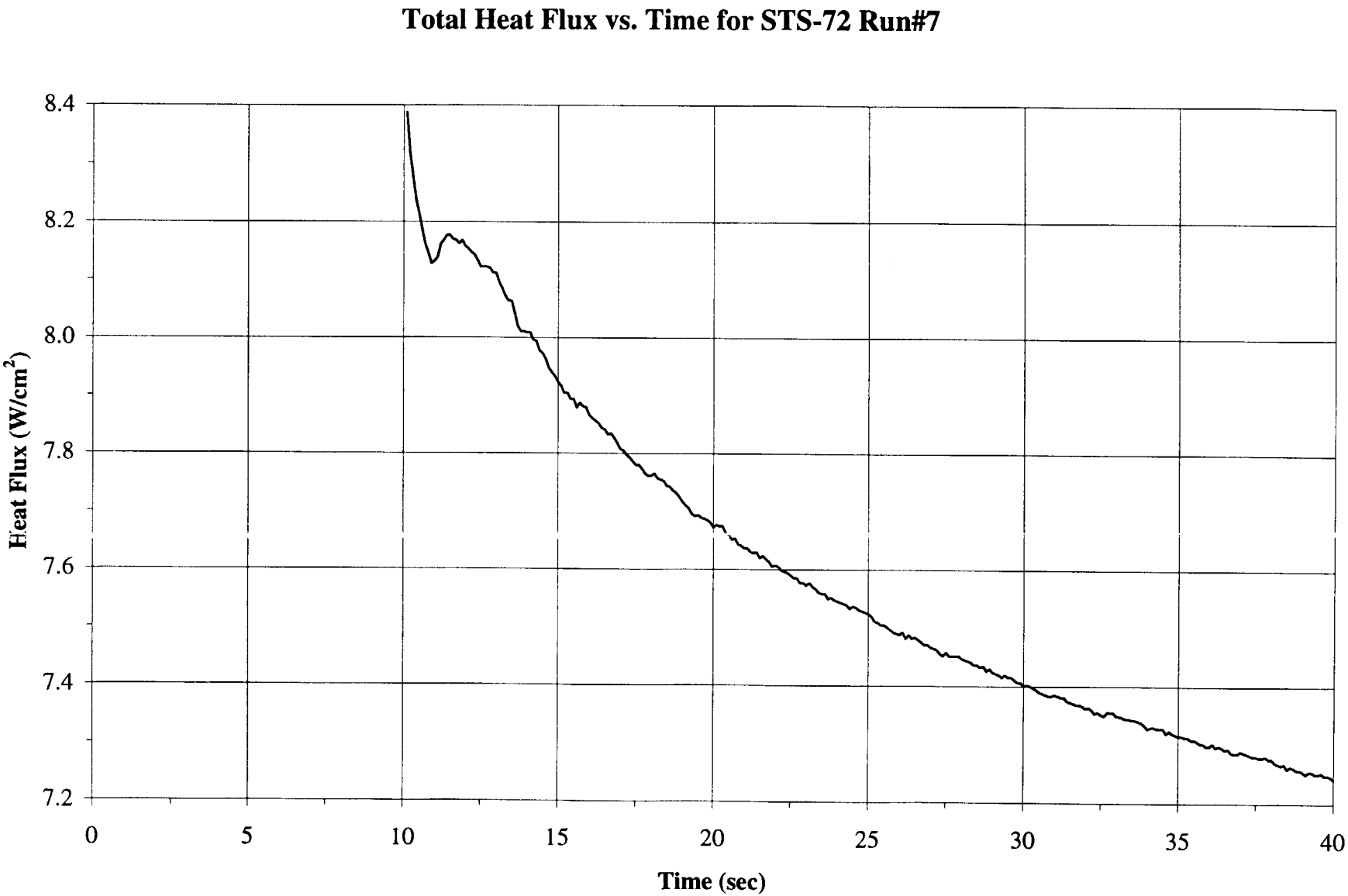

Figure A-2g. Heat flux input. PBE-IIB (STS-72). Run No. 7.

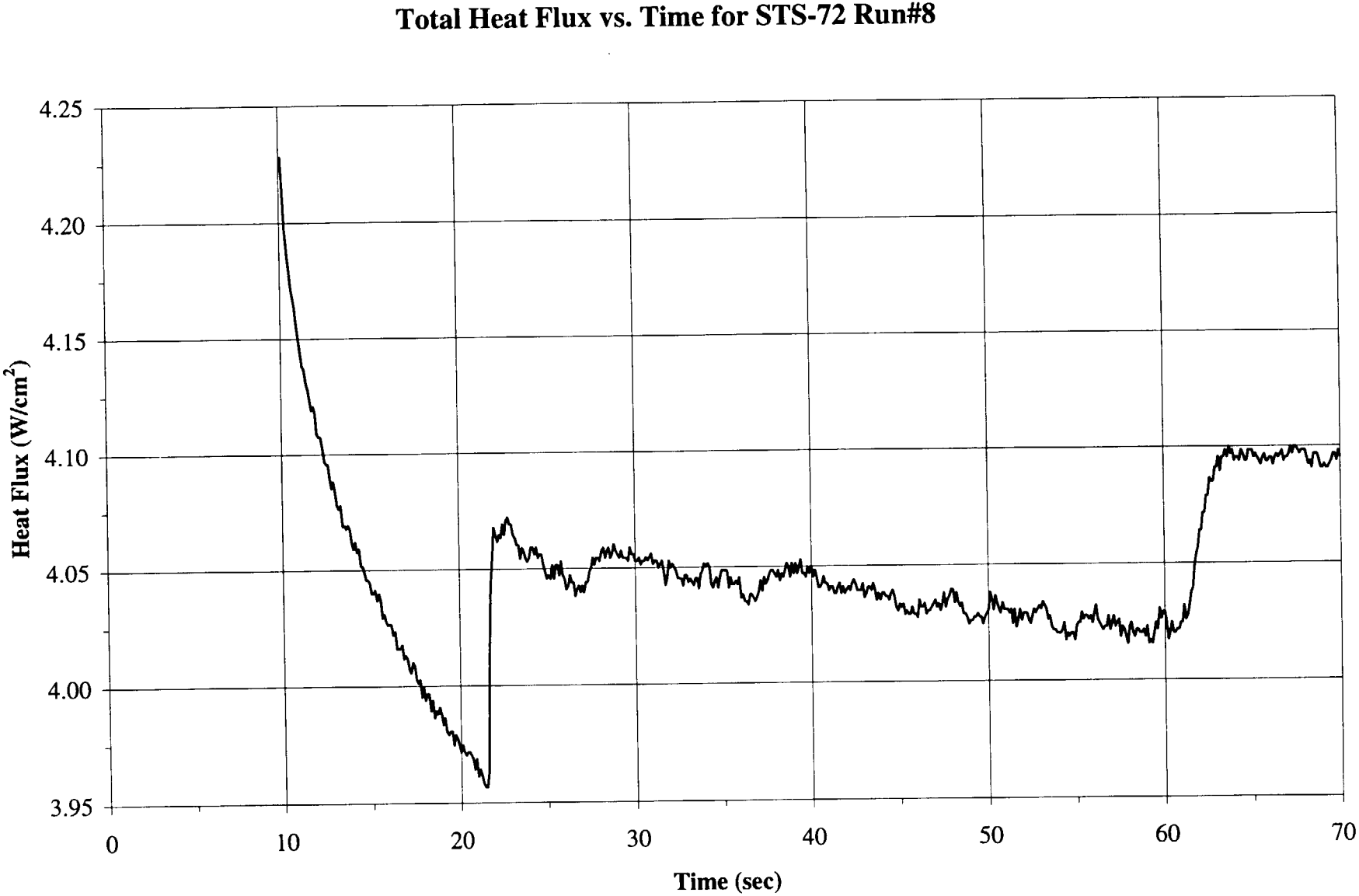

Figure A-2h. Heat flux input. PBE-IIB (STS-72). Run No. 8.

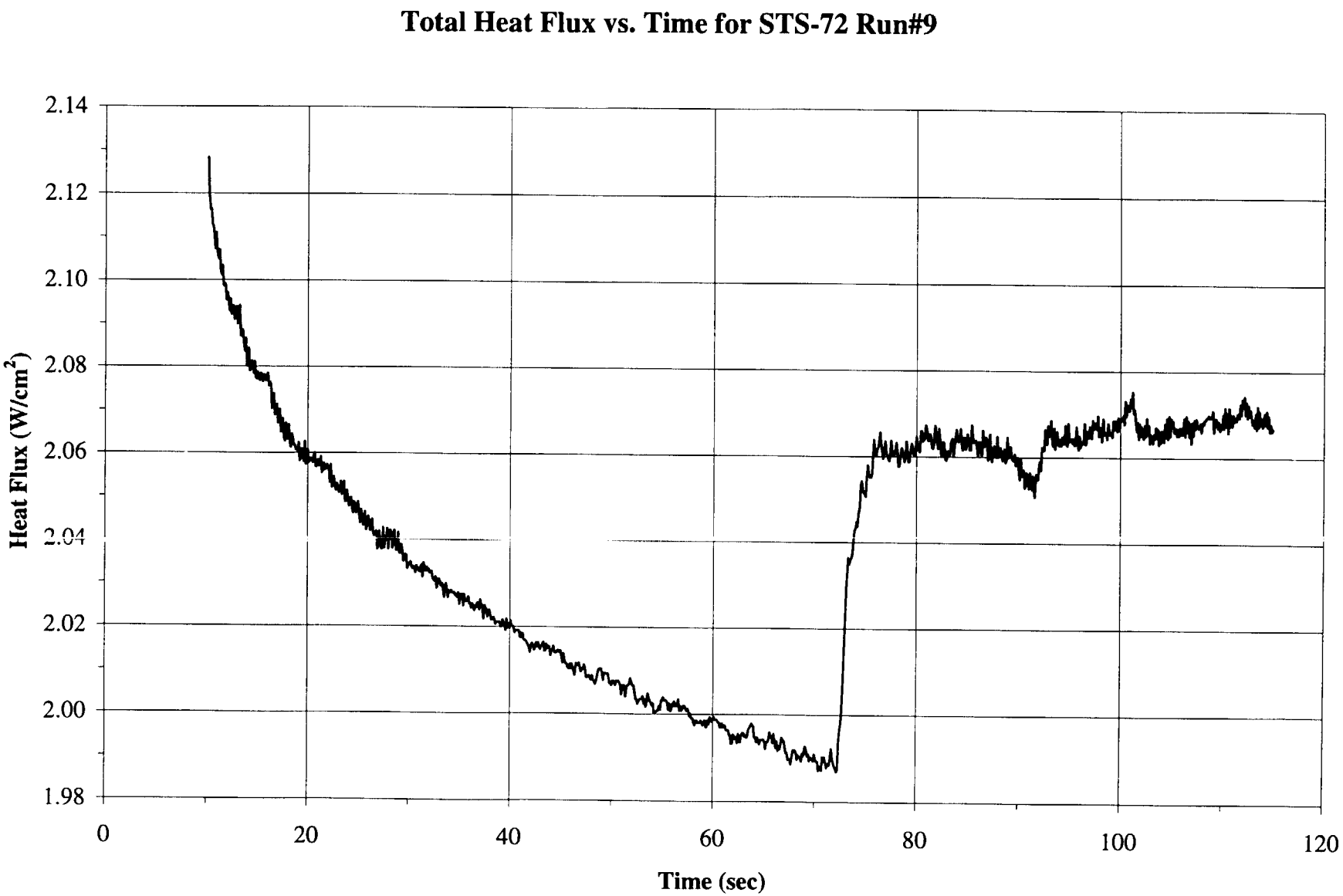

Figure A-2i. Heat flux input. PBE-IIB (STS-72). Run No. 9.

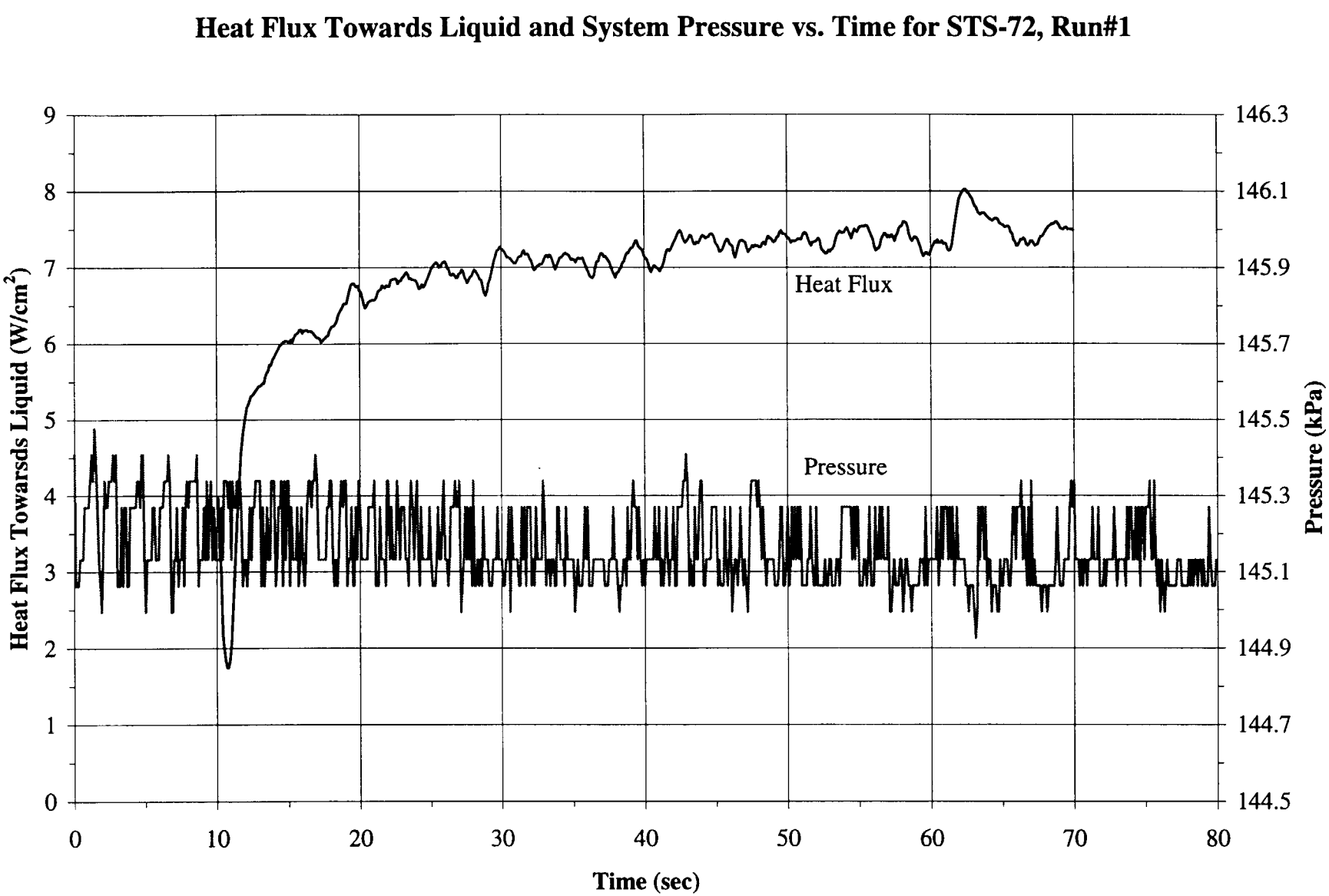

Figure A-3a. System pressure and fluid side mean heat flux. PBE-IIB (STS-72). Run No. 1.

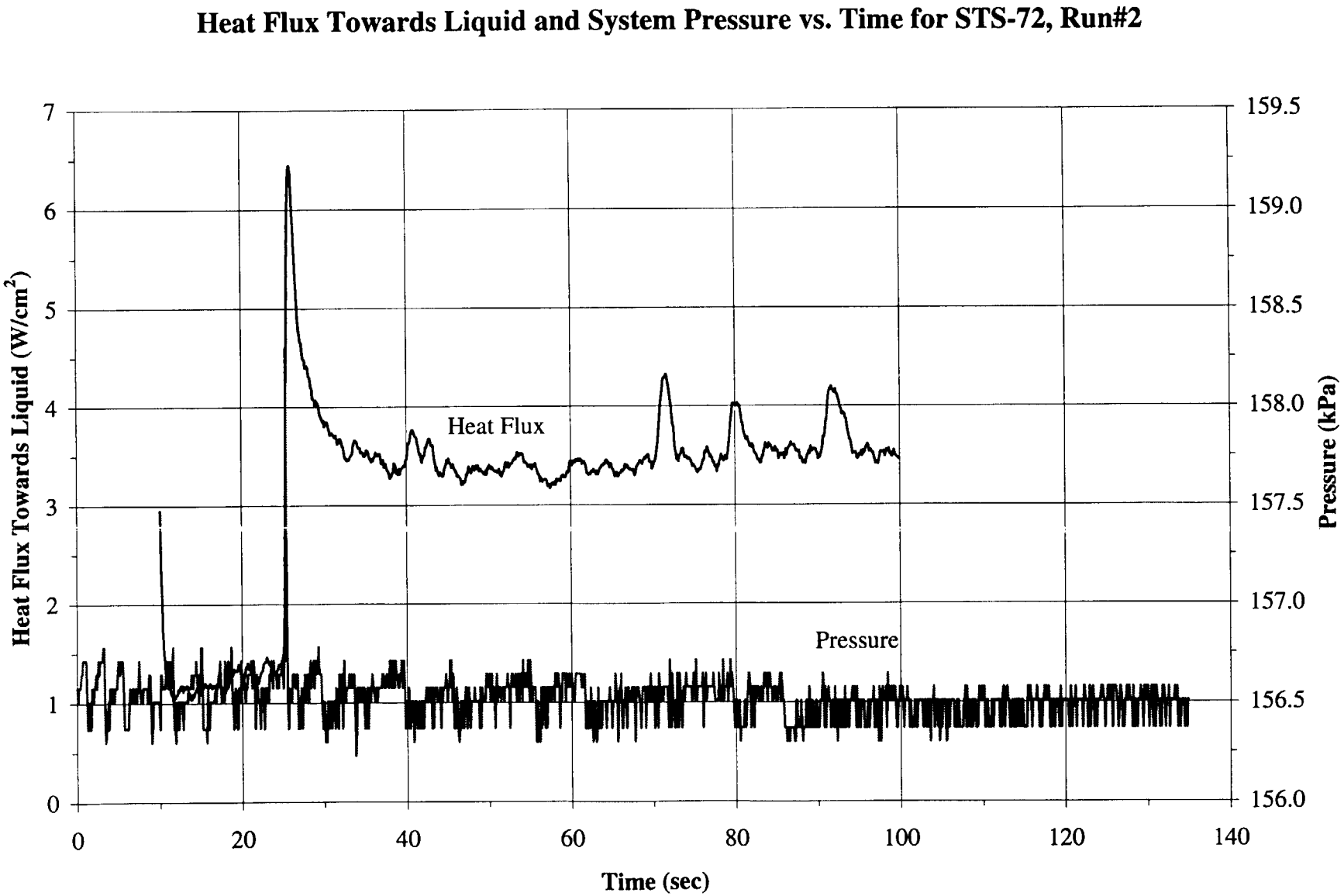

Figure A-3b. System pressure and fluid side mean heat flux. PBE-IIB (STS-72). Run No. 2.

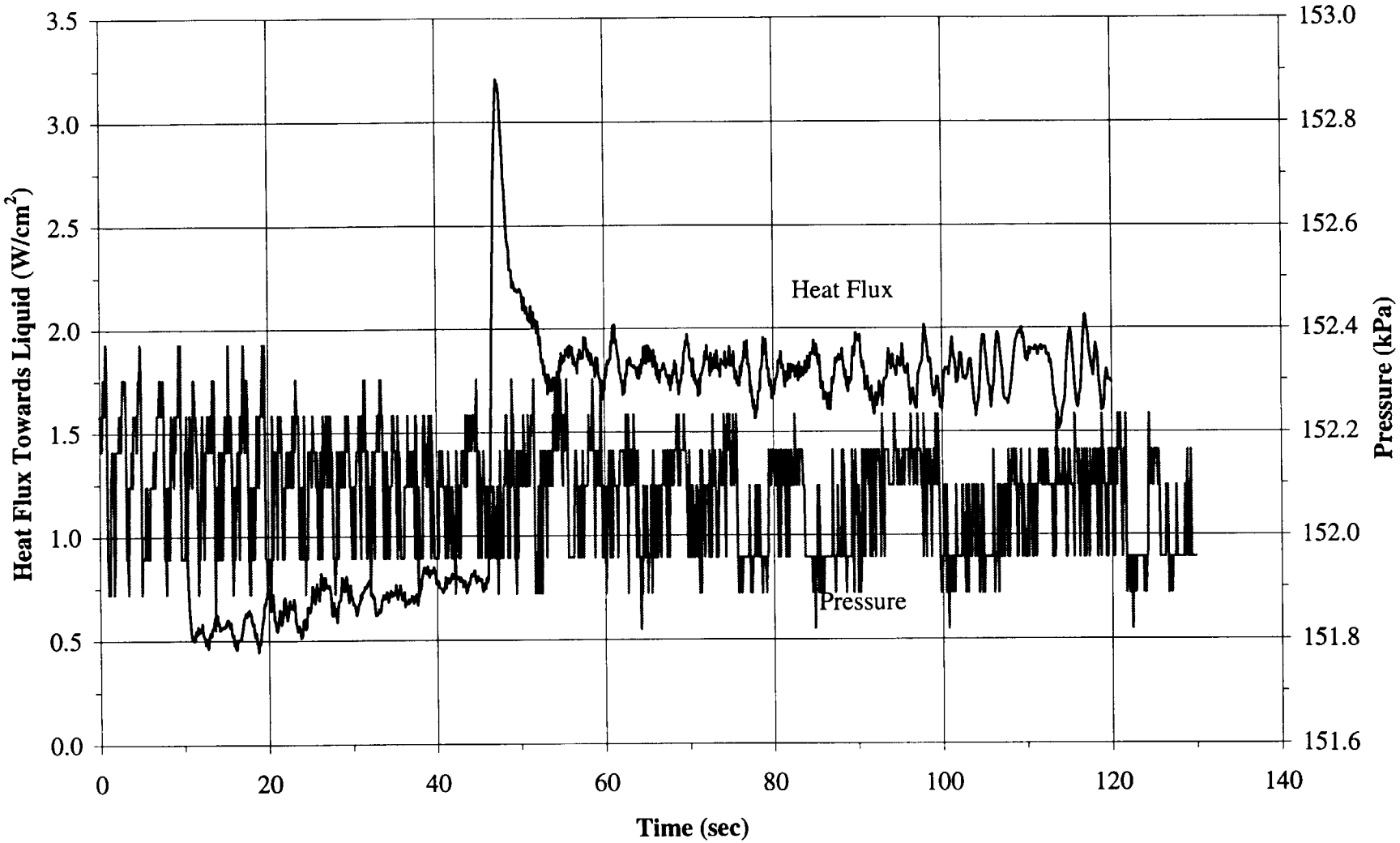

Figure A-3c. System pressure and fluid side mean heat flux. PBE-IIB (STS-72). Run No. 3.

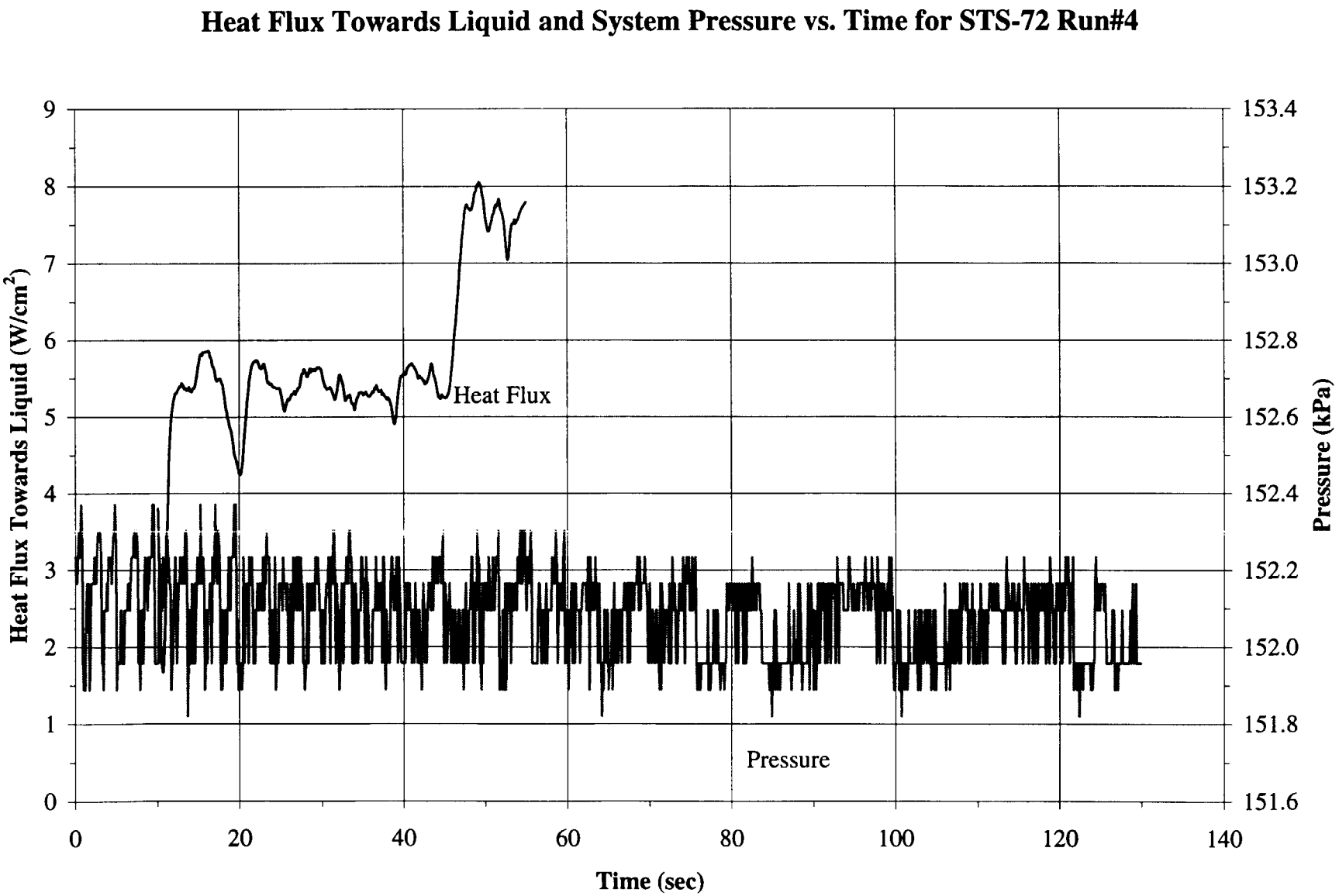

Figure A-3d. System pressure and fluid side mean heat flux. PBE-IIB (STS-72). Run No. 4.

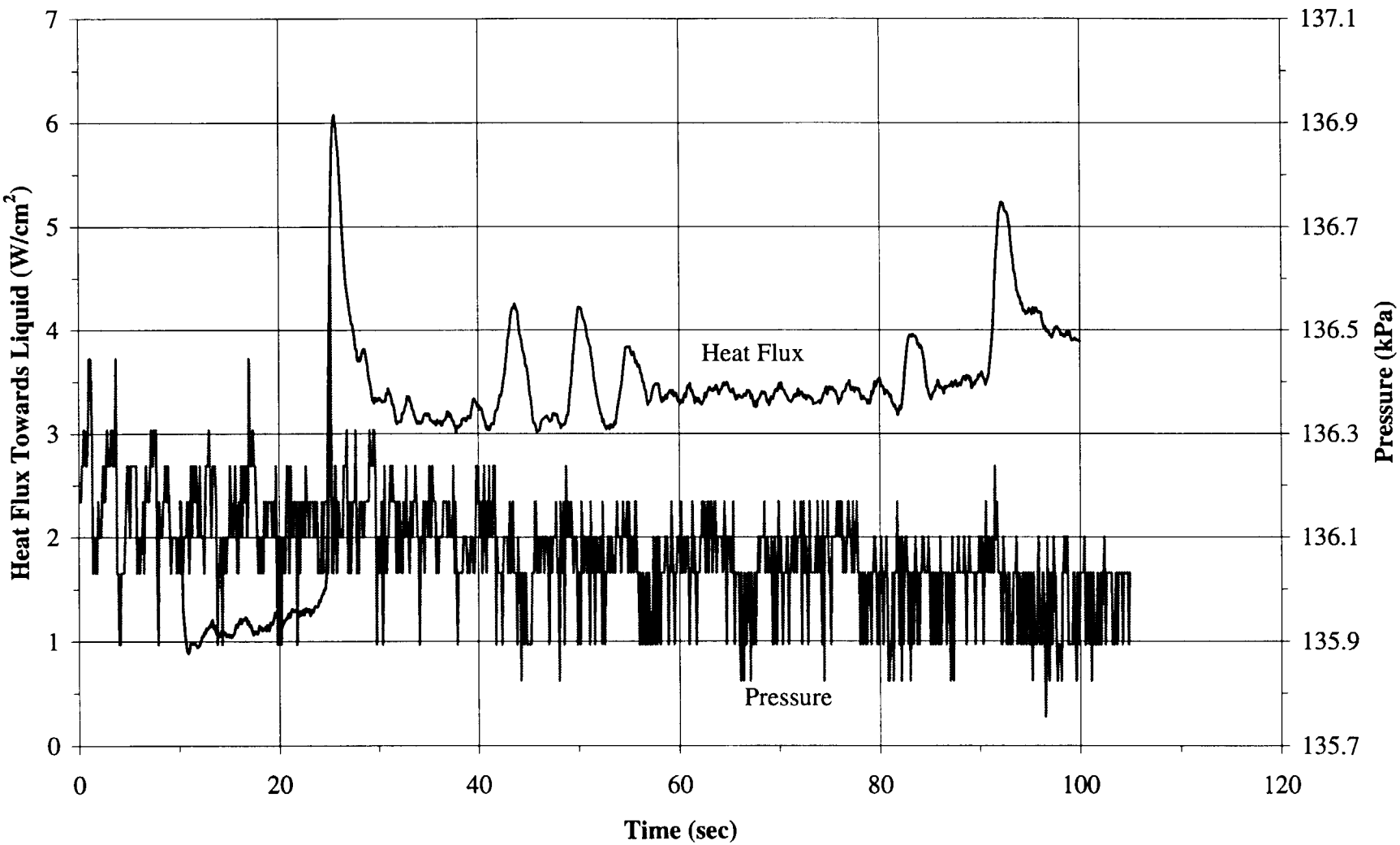

Figure A-3e. System pressure and fluid side mean heat flux. PBE-IIB (STS-72). Run No. 5.

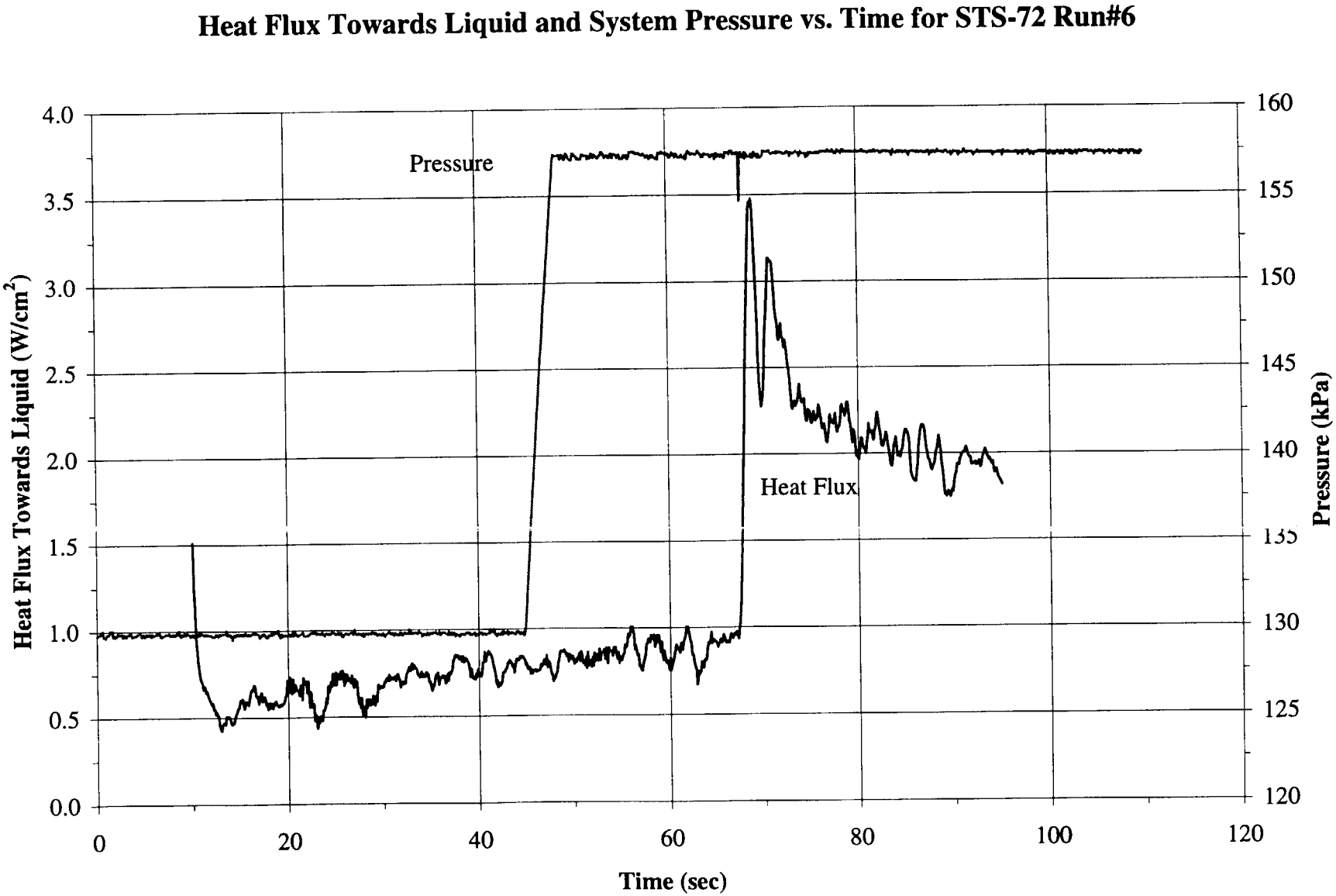

Figure A-3f. System pressure and fluid side mean heat flux. PBE-IIB (STS-72). Run No. 6.

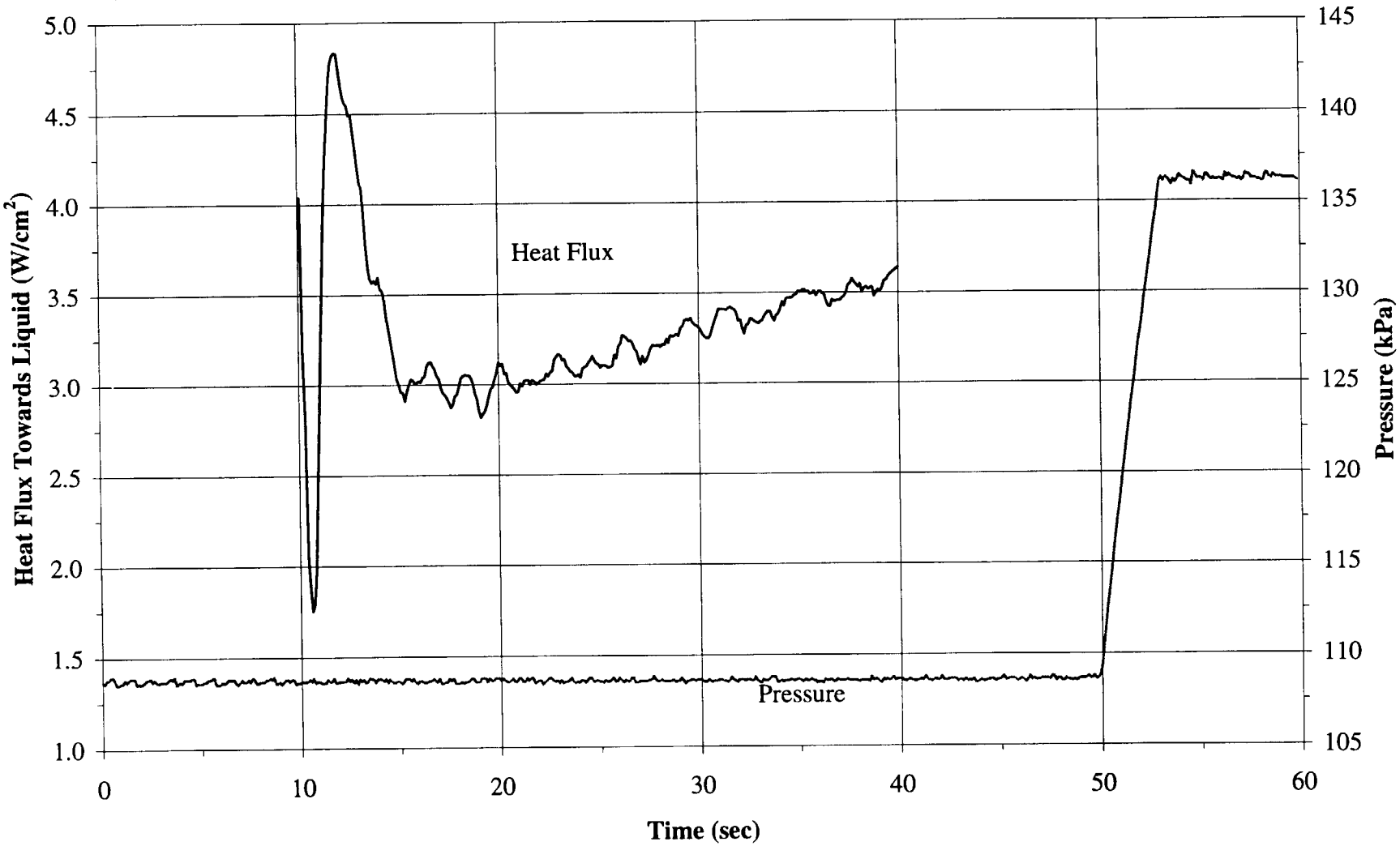

Figure A-3g. System pressure and fluid side mean heat flux. PBE-IIB (STS-72). Run No. 7.

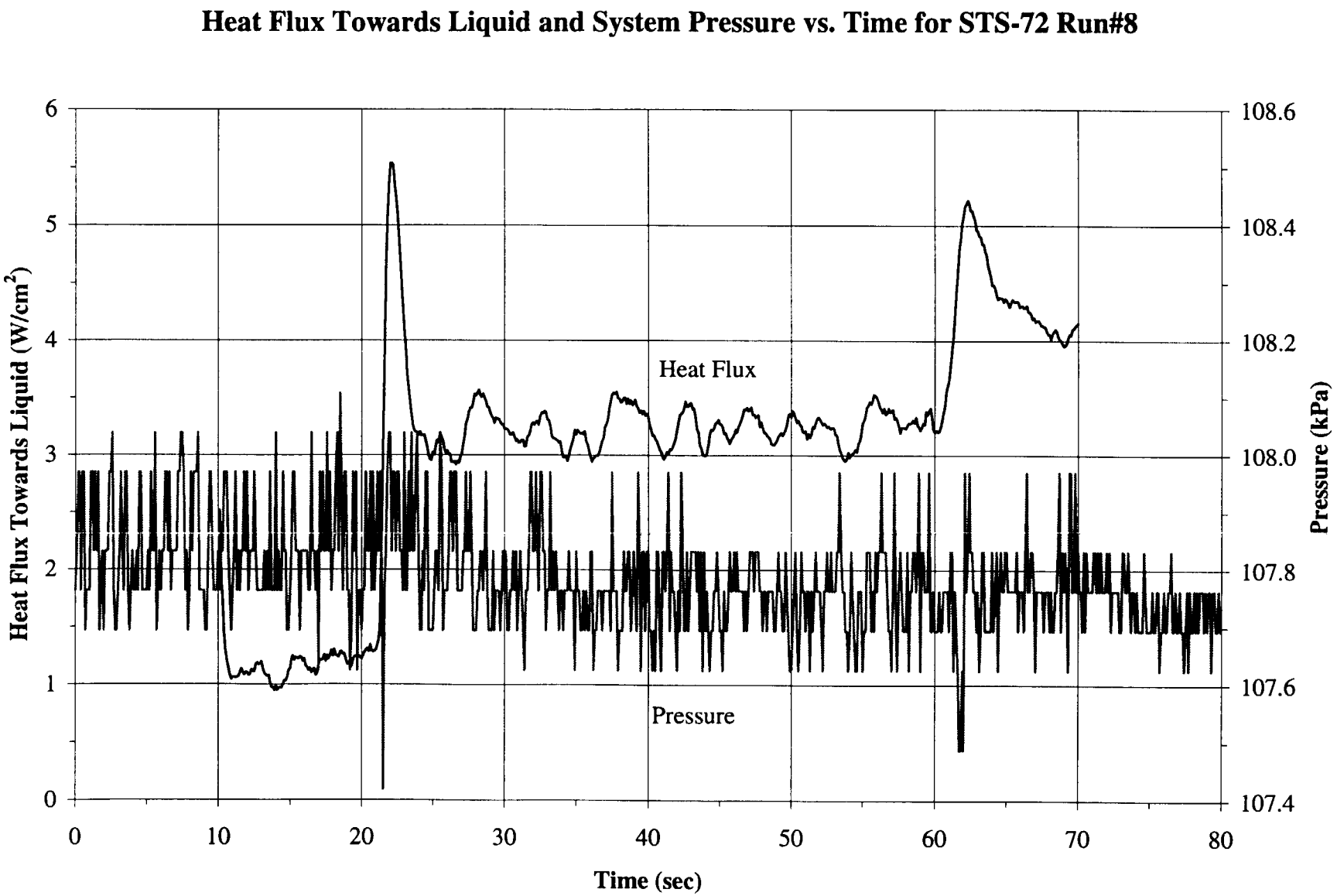

Figure A-3h. System pressure and fluid side mean heat flux. PBE-IIB (STS-72). Run No. 8.

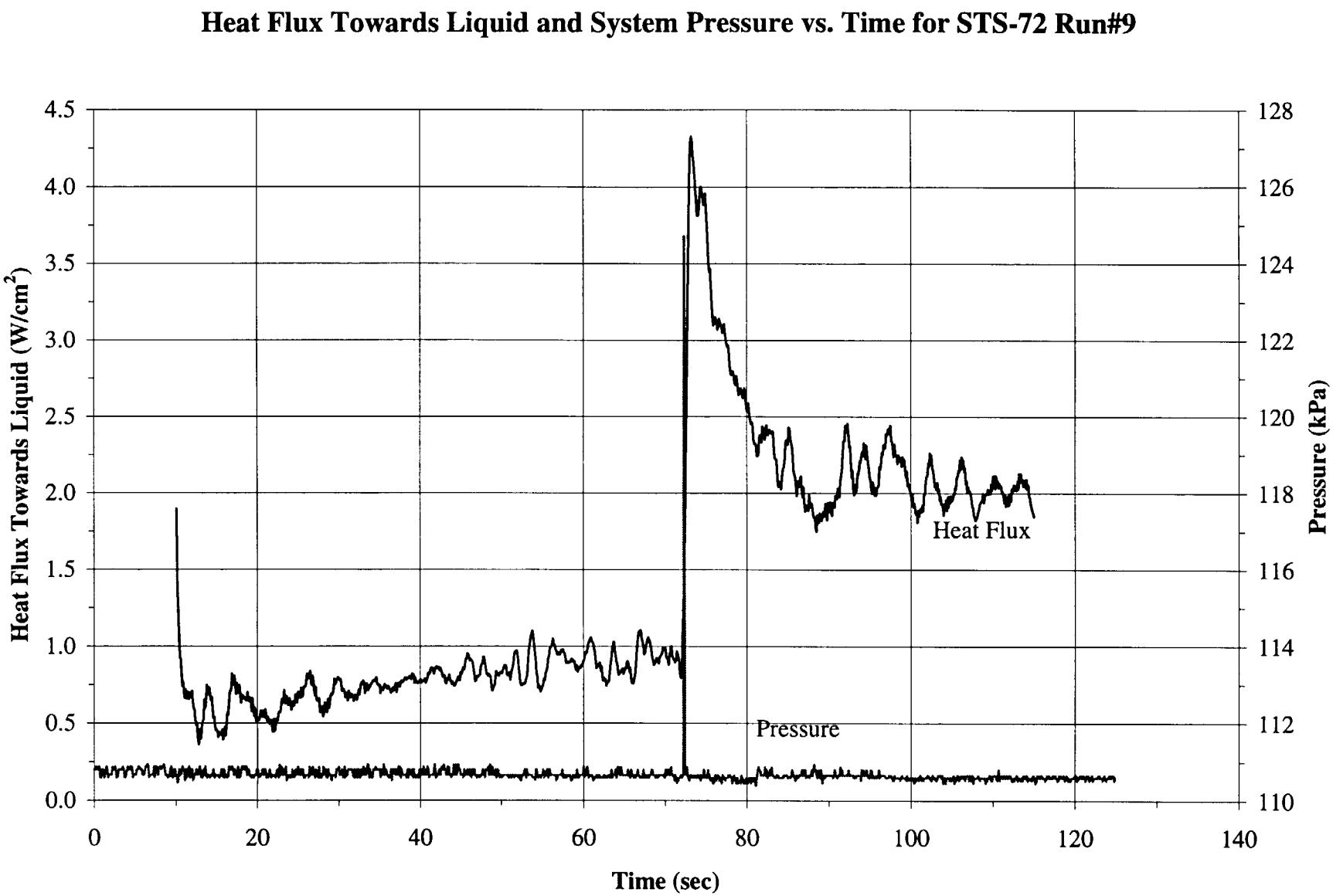

Figure A-3i. System pressure and fluid side mean heat flux. PBE-IIB (STS-72). Run No. 9.

A. Mean Heater Surface Temperature

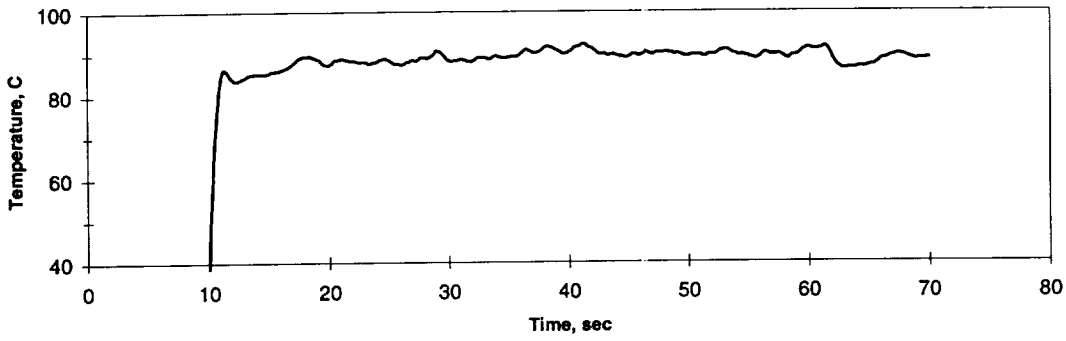

B. Local Fluid Temperatures

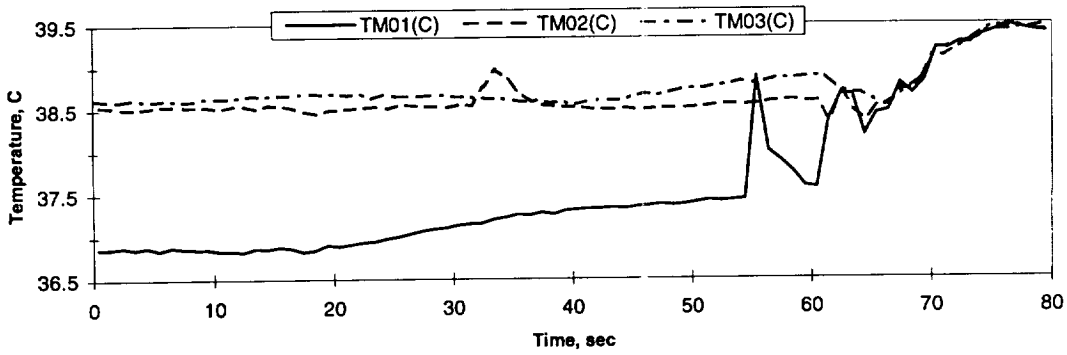

C. Far Field Bulk Temperatures

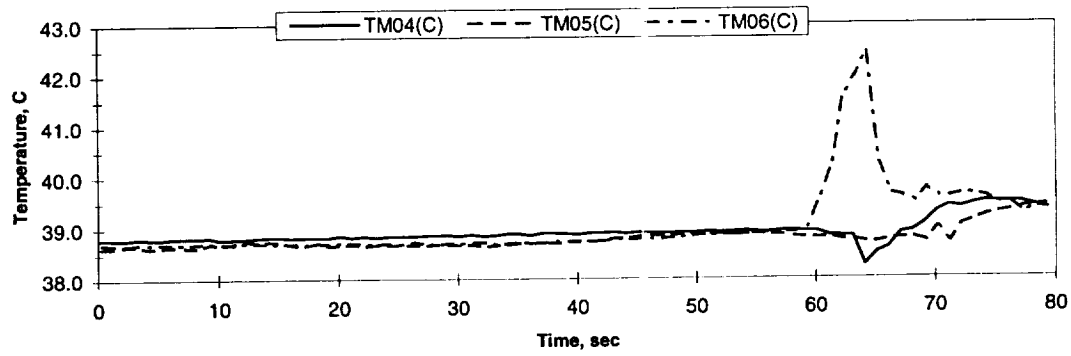

FIGURE: Measured Fluid Temperatures **STS-72 Run #1**

Heat Flux	Subcooling (F)	Heater Power On/Off	100 FPS On/Off	Stirrer Start	Repress Start	Total Time
8	40	10-70 sec.	10-15 sec.	60 sec.	--------	80 Sec

Figure A-4a. Measured fluid temperatures near primary heater and far field bulk liquid. PBE-IIB (STS-72). Run No. 1.

A. Mean Heater Surface Temperature

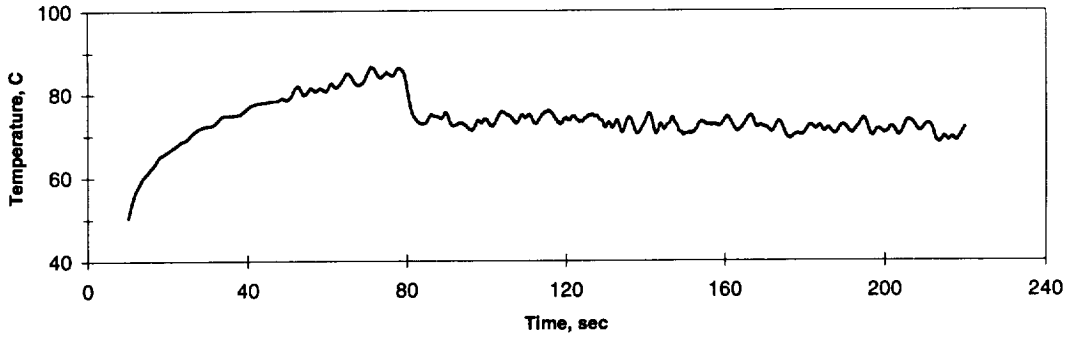

B. Local Fluid Temperatures

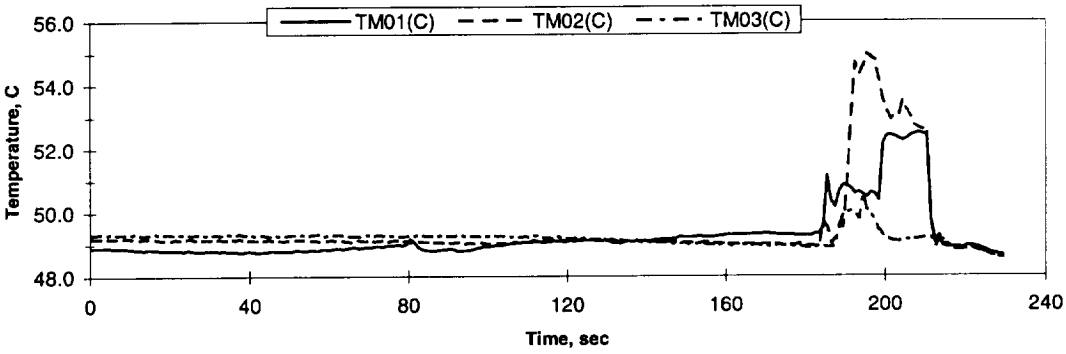

C. Far Field Bulk Temperatures

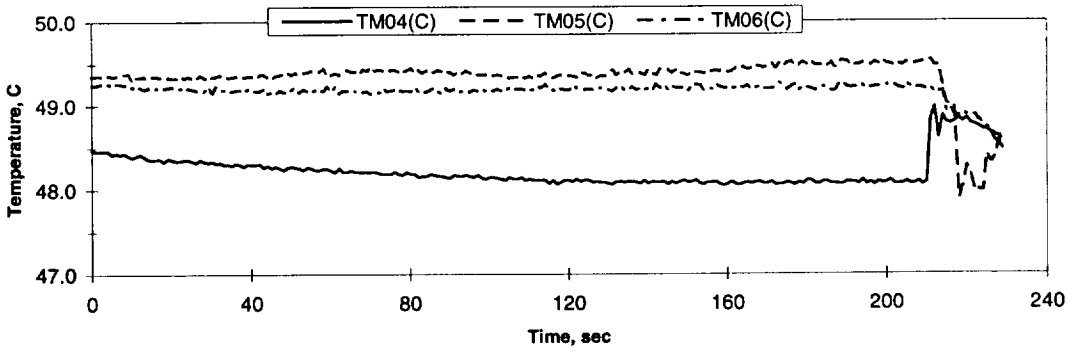

FIGURE: Measured Fluid Temperatures **STS-77 Run #2**

Heat Flux	Subcooling (F)	Heater Power On/Off	100 FPS On/Off	Stirrer Start	Repress Start	Total Time
1	20	10-220 sec.	----------	210 Sec.	--------	230 Sec

Figure A-4b. Measured fluid temperatures near primary heater and far field bulk liquid. PBE-IIB (STS-72). Run No. 2.

A. Mean Heater Surface Temperature

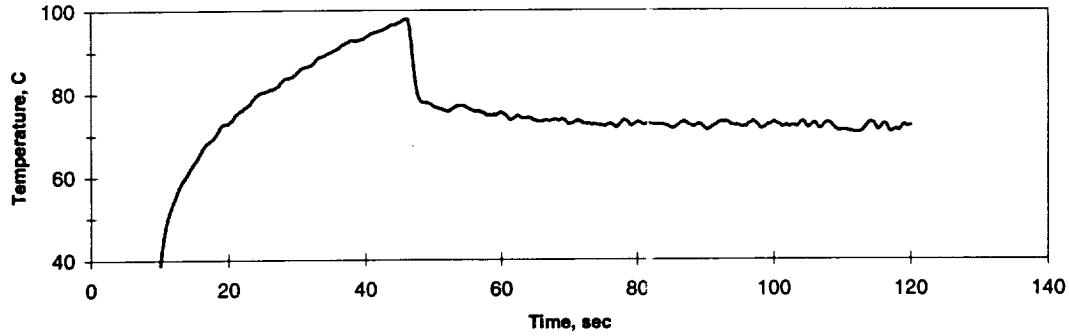

B. Local Fluid Temperatures

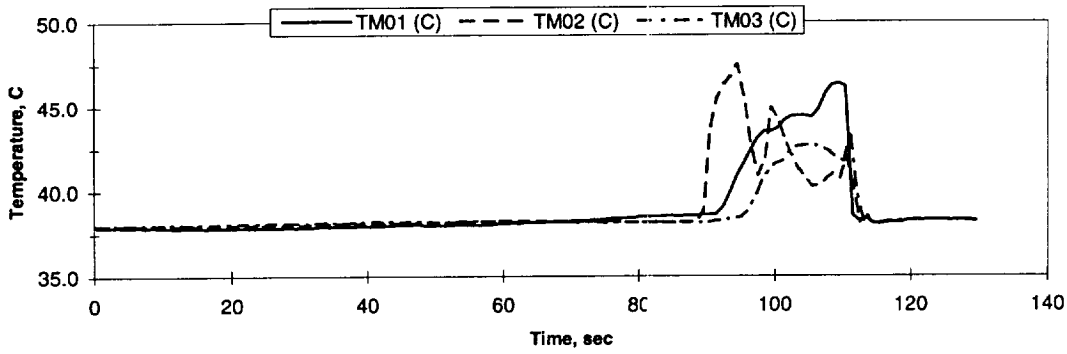

C. Far Field Bulk Temperatures

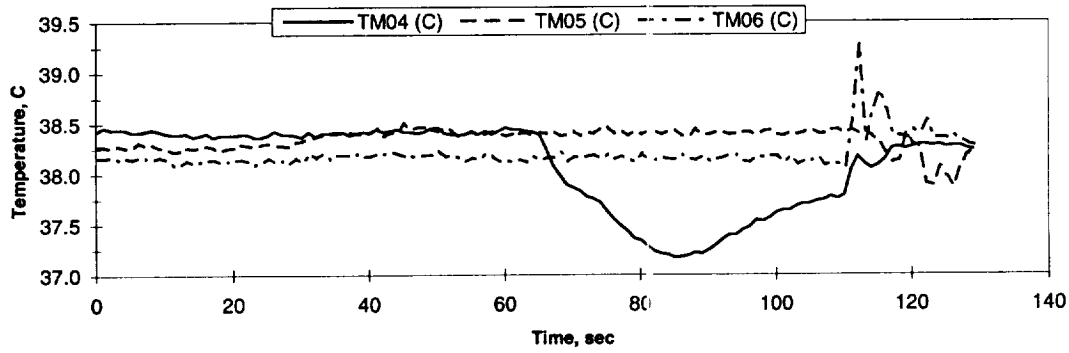

FIGURE: Measured Fluid Temperatures **STS-72 Run #3**

Heat Flux	Subcooling (F)	Heater Power On/Off	100 FPS On/Off	Stirrer Start	Repress Start	Total Time
2	40	10-120 sec.	30-50 sec.	110	--------	130 Sec

Figure A-4c. Measured fluid temperatures near primary heater and far field bulk liquid. PBE-IIB (STS-72). Run No. 3.

A. Mean Heater Surface Temperature

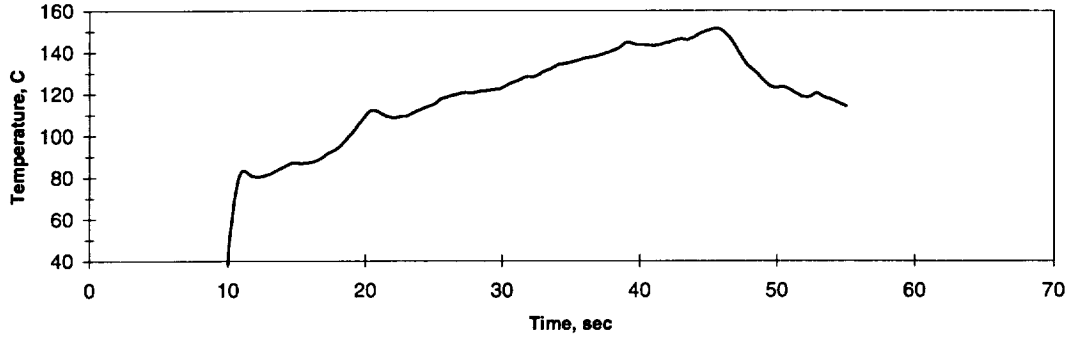

B. Local Fluid Temperatures

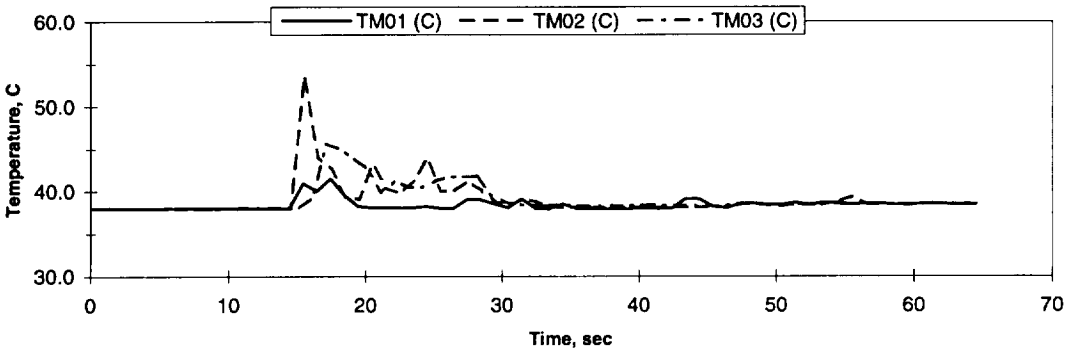

C. Far Field Bulk Temperatures

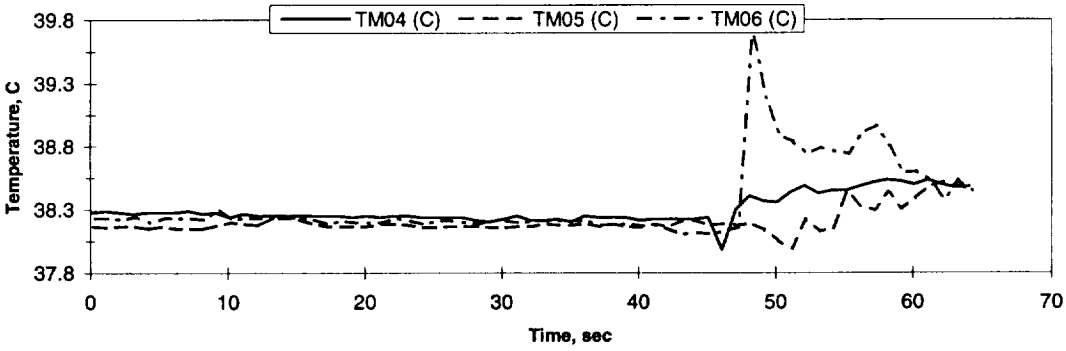

FIGURE: Measured Fluid Temperatures **STS-72 Run #4**

Heat Flux	Subcooling (F)	Heater Power On/Off	100 FPS On/Off	Stirrer Start	Repress Start	Total Time
8	30	10-55 sec.	10-15 sec.	45	--------	65 Sec

Figure A-4d. Measured fluid temperatures near primary heater and far field bulk liquid. PBE-IIB (STS-72). Run No. 4.

A. Mean Heater Surface Temperature

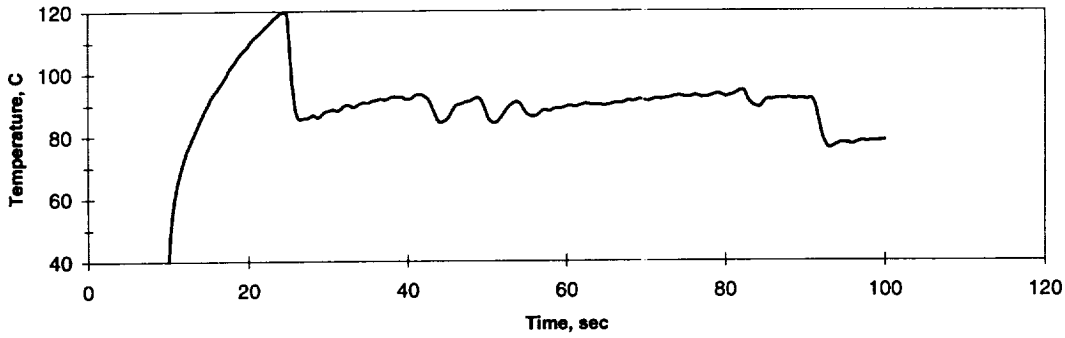

B. Local Fluid Temperatures

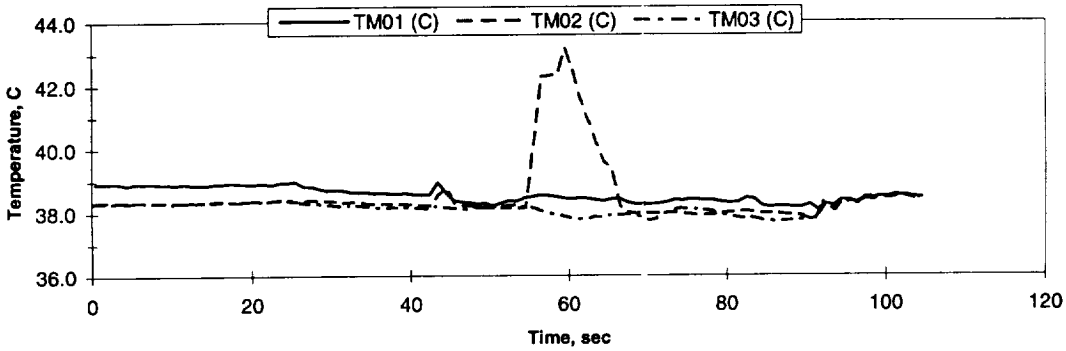

C. Far Field Bulk Temperatures

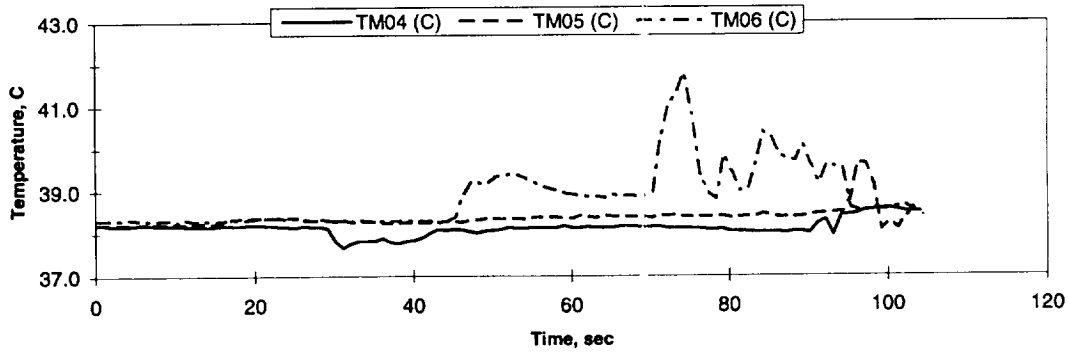

FIGURE: Measured Fluid Temperatures **STS-72 Run #5**

Heat Flux	Subcooling (F)	Heater Power On/Off	100 FPS On/Off	Stirrer Start	Repress Start	Total Time
4	30	10-100 sec.	15-25 sec.	90	--------	105 Sec

Figure A-4e. Measured fluid temperatures near primary heater and far field bulk liquid. PBE-IIB (STS-72). Run No. 5.

A. Mean Heater Surface Temperature

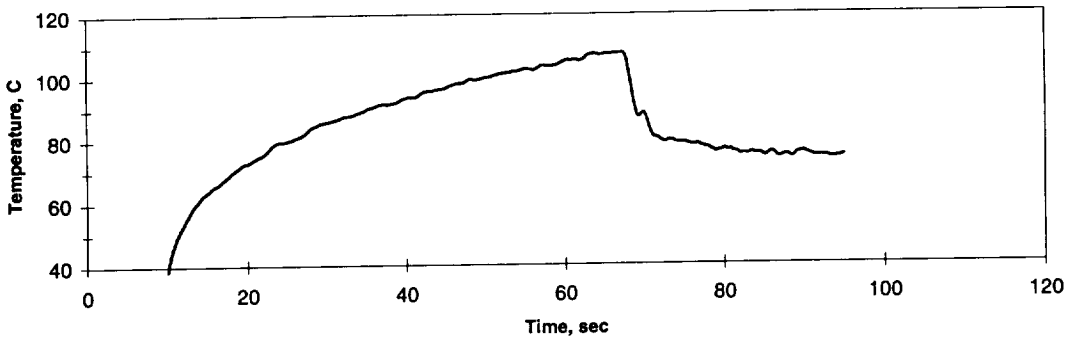

B. Local Fluid Temperatures

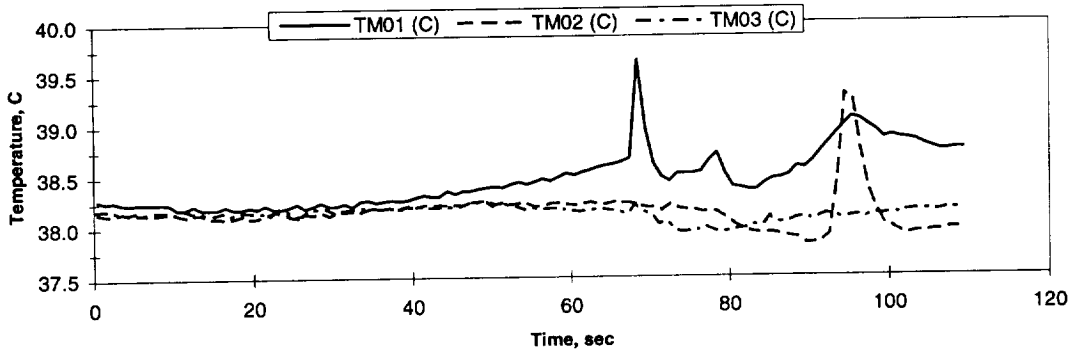

C. Far Field Bulk Temperatures

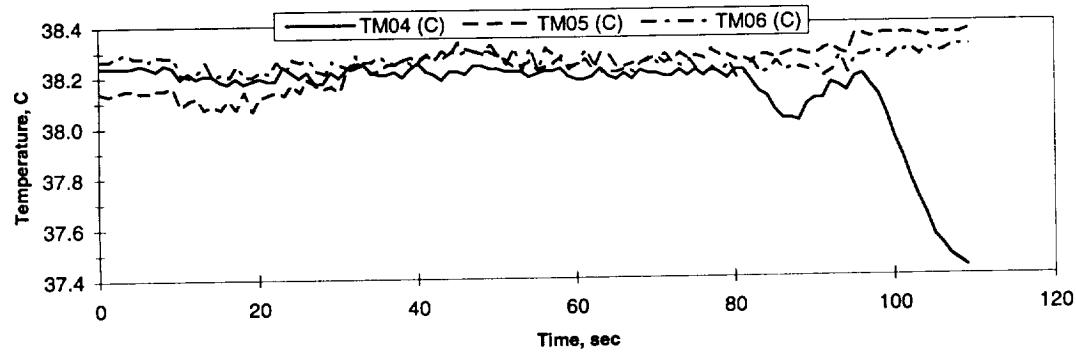

FIGURE: Measured Fluid Temperatures **STS-72 Run #6**

Heat Flux	Subcooling (F)	Heater Power On/Off	100 FPS On/Off	Stirrer Start	Repress Start	Total Time
2	30	10-95 sec.	30-50 sec.	---------	--------	110 Sec

Figure A-4f. Measured fluid temperatures near primary heater and far field bulk liquid. PBE-IIB (STS-72). Run No. 6.

A. Mean Heater Surface Temperature

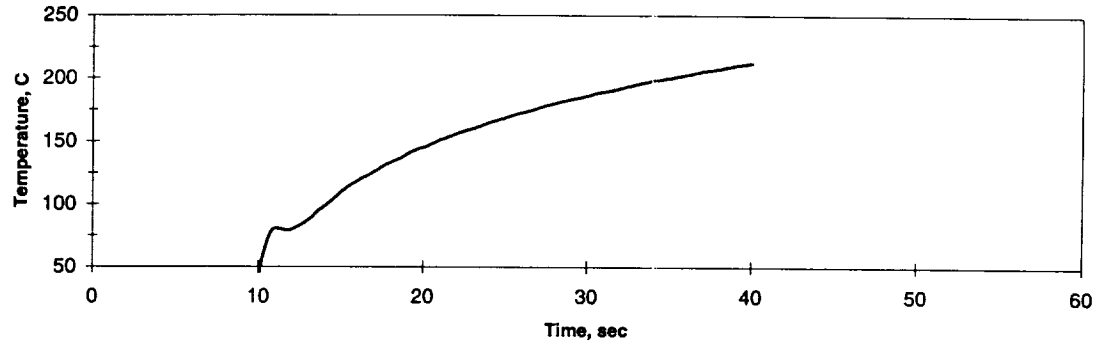

B. Local Fluid Temperatures

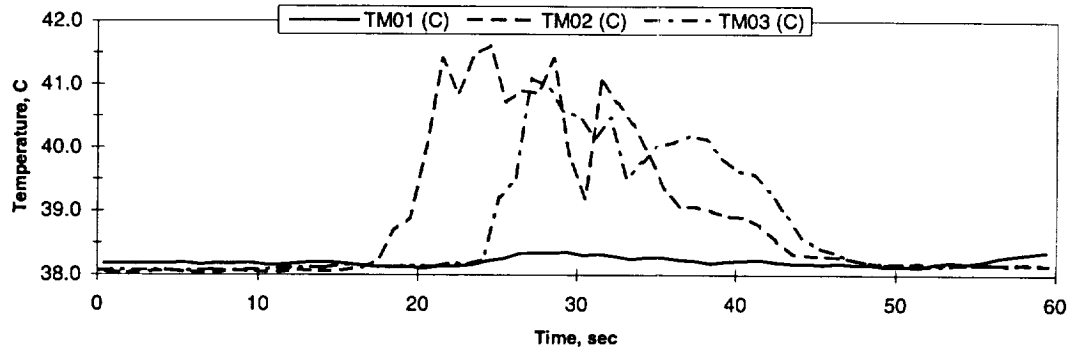

C. Far Field Bulk Temperatures

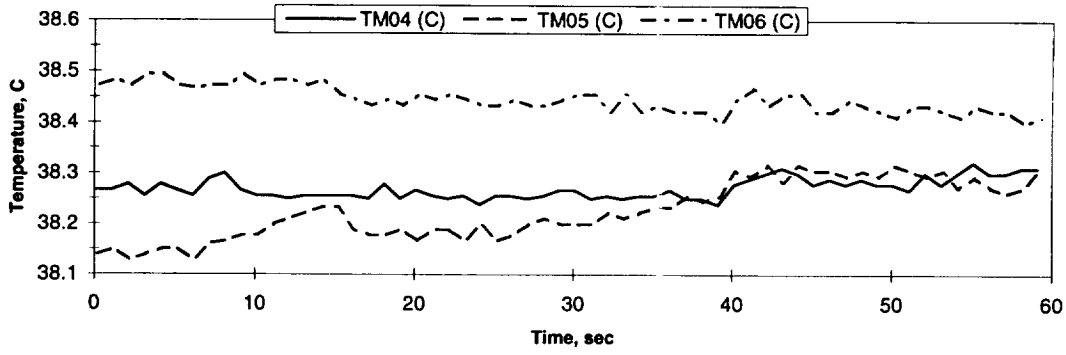

FIGURE: Measured Fluid Temperatures **STS-72 Run #7**

Heat Flux	Subcooling (F)	Heater Power On/Off	100 FPS On/Off	Stirrer Start	Repress Start	Total Time
8	20	10-40 sec.	10-15 sec.	---------	45	55 Sec

Figure A-4g. Measured fluid temperatures near primary heater and far field bulk liquid. PBE-IIB (STS-72). Run No. 7.

A. Mean Heater Surface Temperature

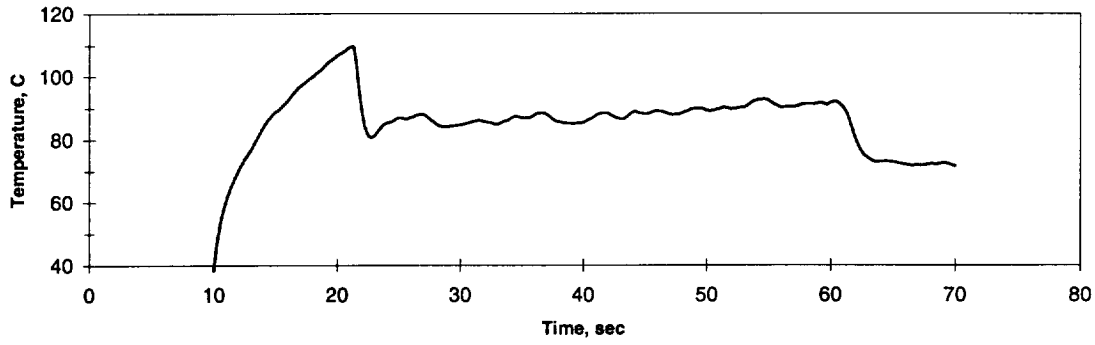

B. Local Fluid Temperatures

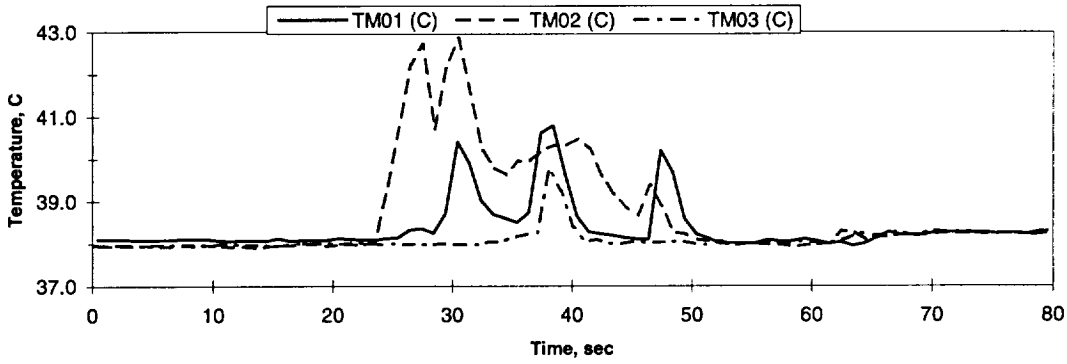

C. Far Field Bulk Temperatures

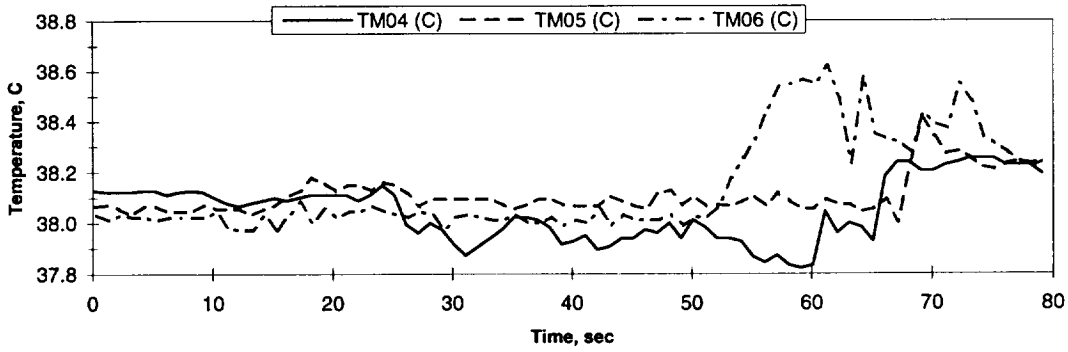

FIGURE: Measured Fluid Temperatures **STS-72 Run #8**

Heat Flux	Subcooling (F)	Heater Power On/Off	100 FPS On/Off	Stirrer Start	Repress Start	Total Time
4	20	10-70 sec.	15-25 sec.	60	--------	80 Sec

Figure A-4h. Measured fluid temperatures near primary heater and far field bulk liquid. PBE-IIB (STS-72). Run No. 8.

A. Mean Heater Surface Temperature

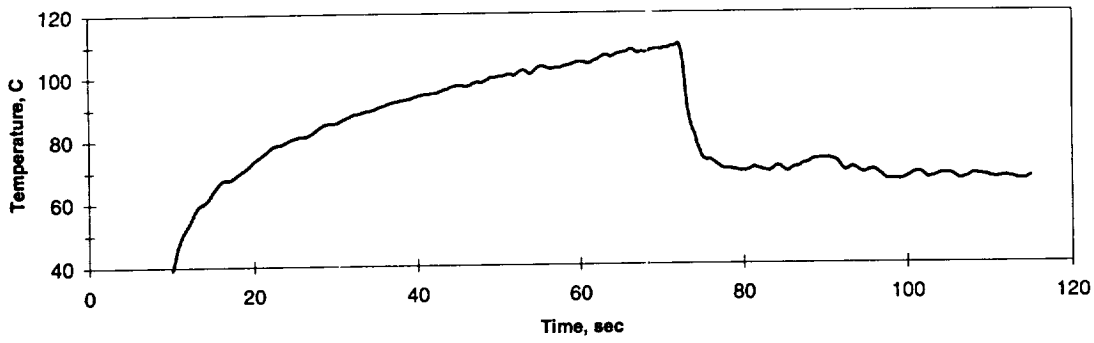

B. Local Fluid Temperatures

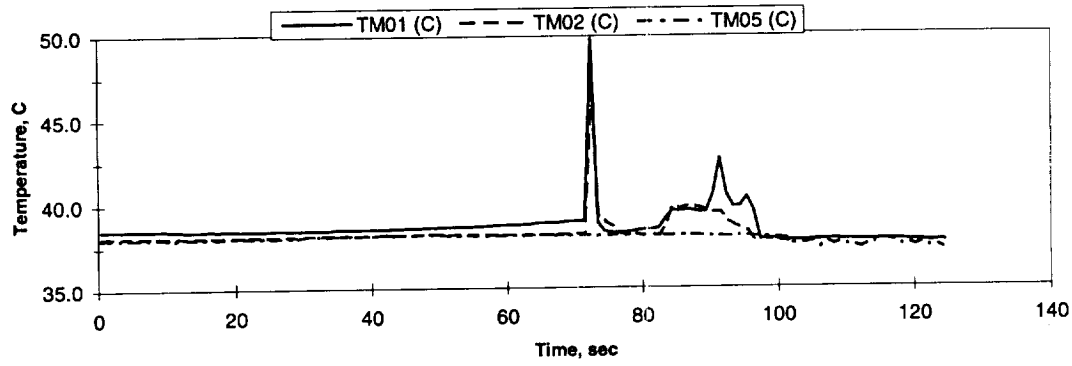

C. Far Field Bulk Temperatures

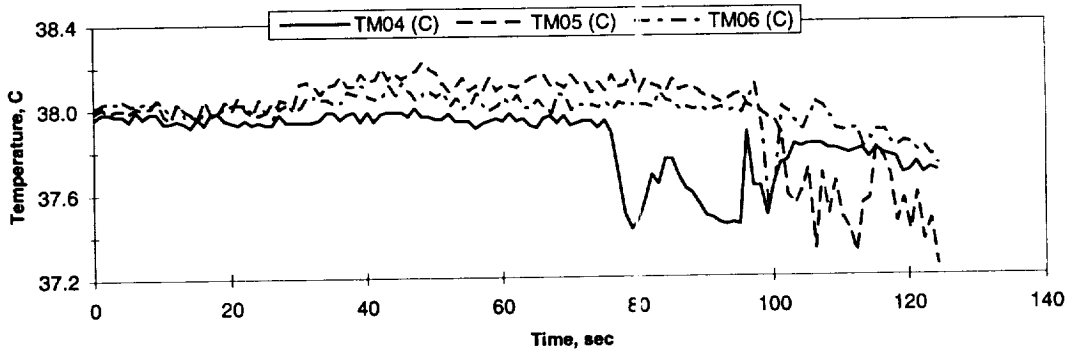

FIGURE: Measured Fluid Temperatures **STS-72 Run #9**

Heat Flux	Subcooling (F)	Heater Power On/Off	100 FPS On/Off	Stirrer Start	Repress Start	Total Time
2	20	10-115 sec.	30-50 sec.	95	--------	125 Sec

Figure A-4i. Measured fluid temperatures near primary heater and far field bulk liquid. PBE-IIB (STS-72). Run No. 9.

A. Mean Heater Surface Temperature

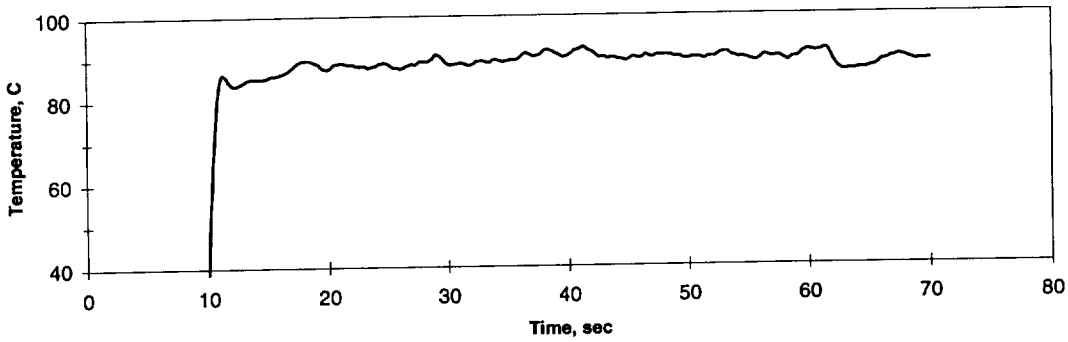

D.

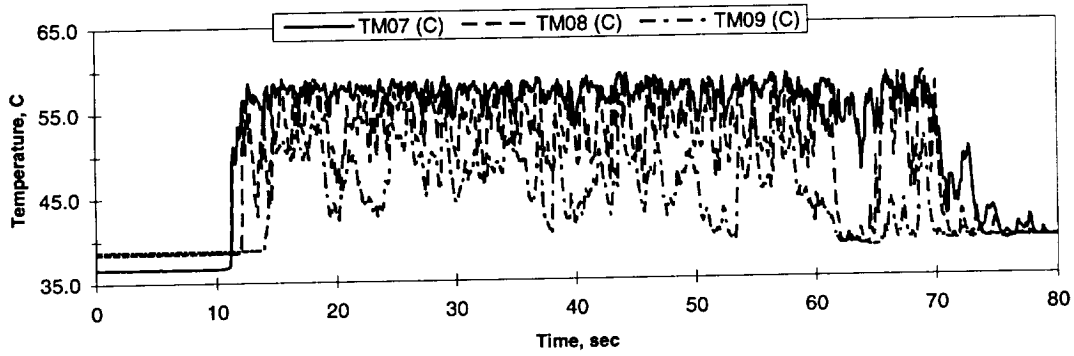

E.

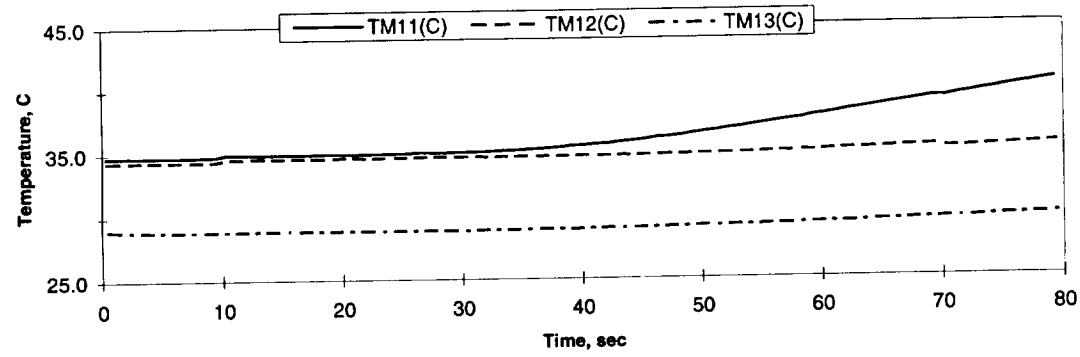

FIGURE: Measured Heater-Underside Temperatures **STS-72 Run #1**

Heat Flux	Subcooling (F)	Heater Power On/Off	100 FPS On/Off	Stirrer Start	Repress Start	Total Time
8	40	10-70 sec.	10-15 sec.	60 sec.	--------	80 Sec

Figure A-5a. Measured fluid temperatures near secondary heater and heater underside. PBE-IIB (STS-72). Run No. 1.

A. Mean Heater Surface Temperature

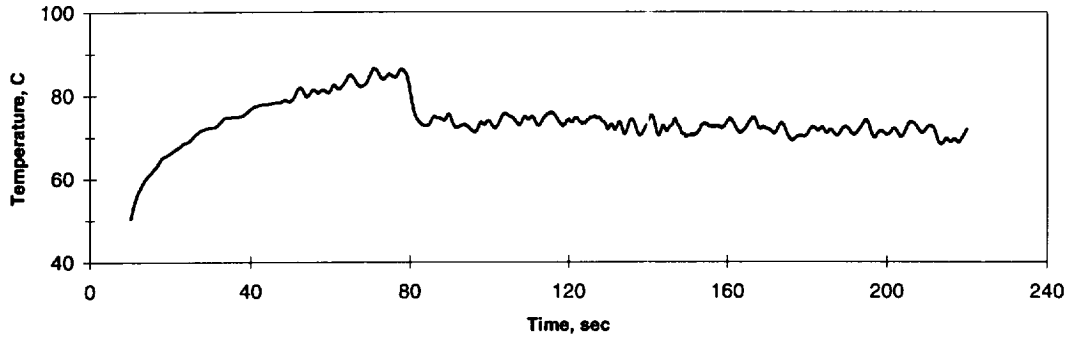

D.

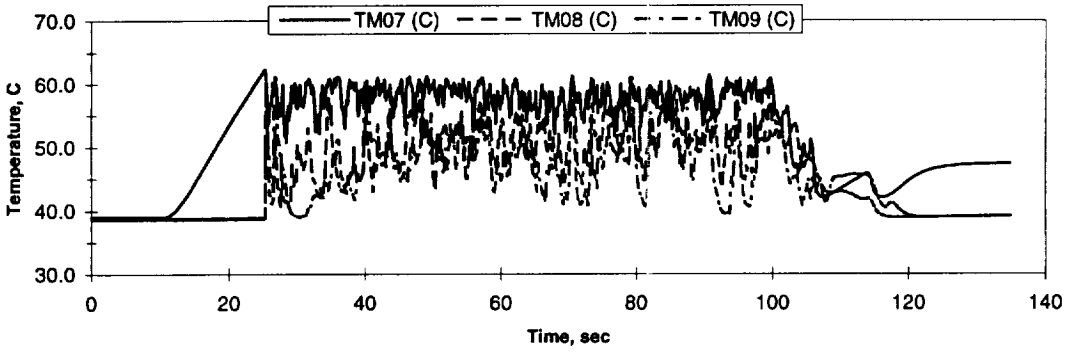

E.

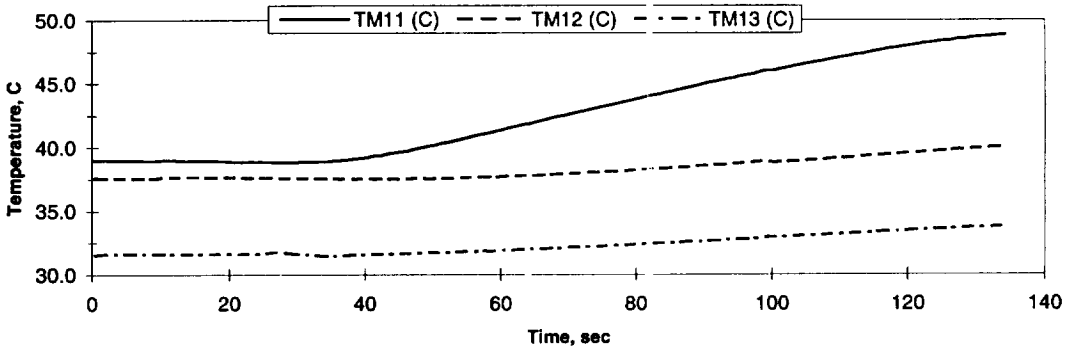

FIGURE: Measured Heater-Underside Temperatures **STS-72 Run #2**

Heat Flux	Subcooling (F)	Heater Power On/Off	100 FPS On/Off	Stirrer Start	Repress Start	Total Time
4	40	10-100 sec.	5-25 sec.	-------	--------	135 Sec

Figure A-5b. Measured fluid temperatures near secondary heater and heater underside. PBE-IIB (STS-72). Run No. 2.

A. Mean Heater Surface Temperature

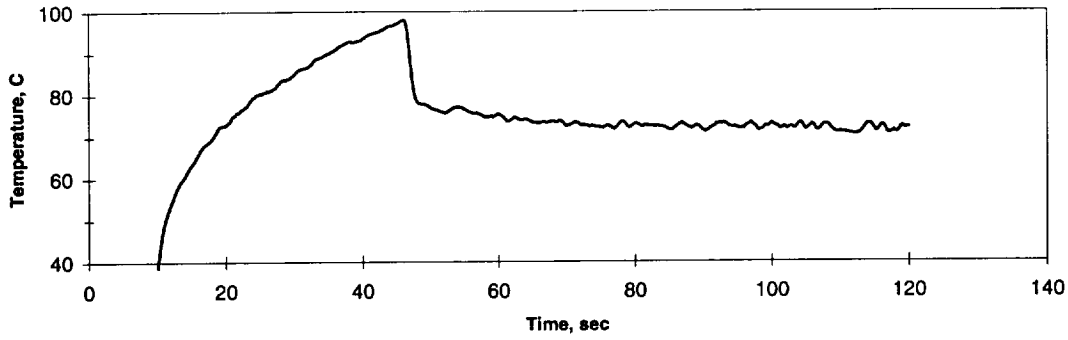

D.

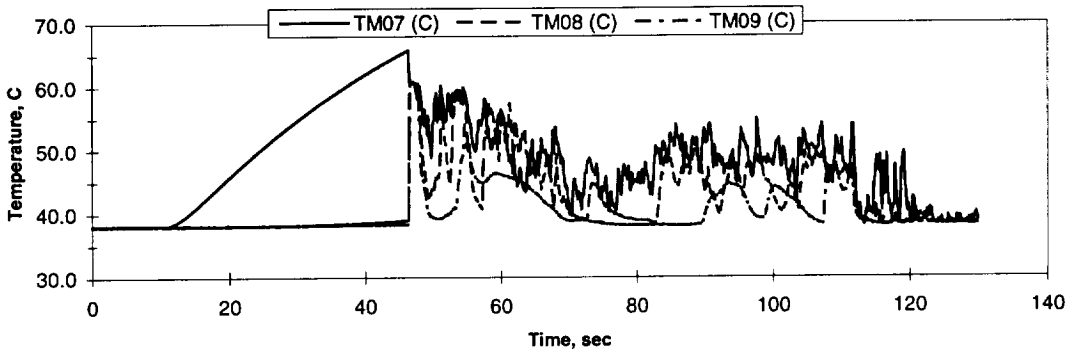

E.

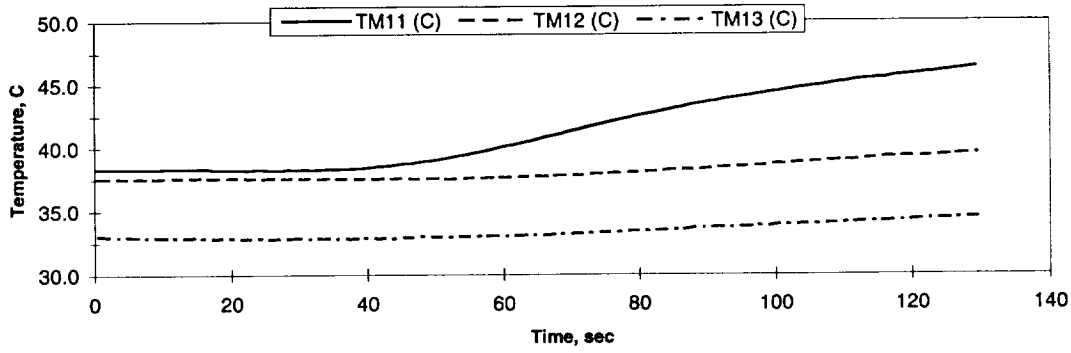

FIGURE: Measured Heater-Underside Temperatures **STS-72 Run #3**

Heat Flux	Subcooling (F)	Heater Power On/Off	100 FPS On/Off	Stirrer Start	Repress Start	Total Time
2	40	10-120 sec.	30-50 sec.	110	--------	130 Sec

Figure A-5c. Measured fluid temperatures near secondary heater and heater underside. PBE-IIB (STS-72). Run No. 3.

A. Mean Heater Surface Temperature

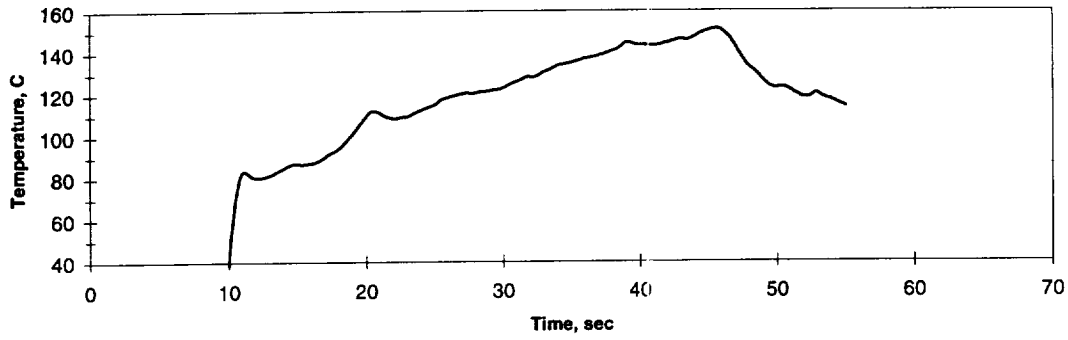

D.

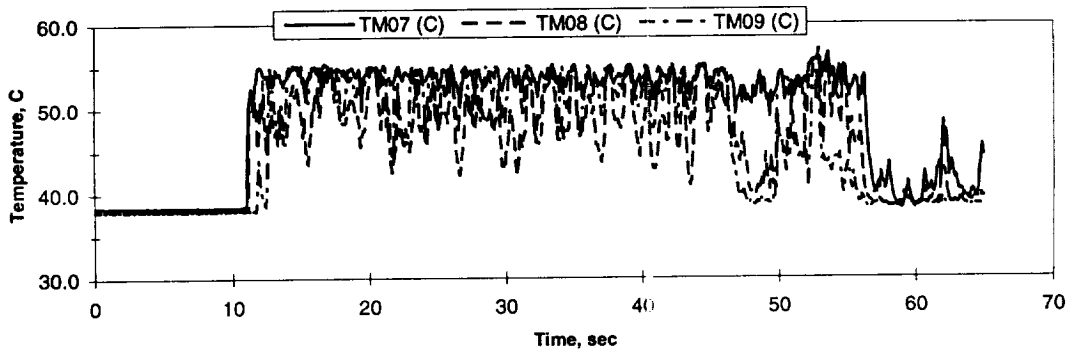

E.

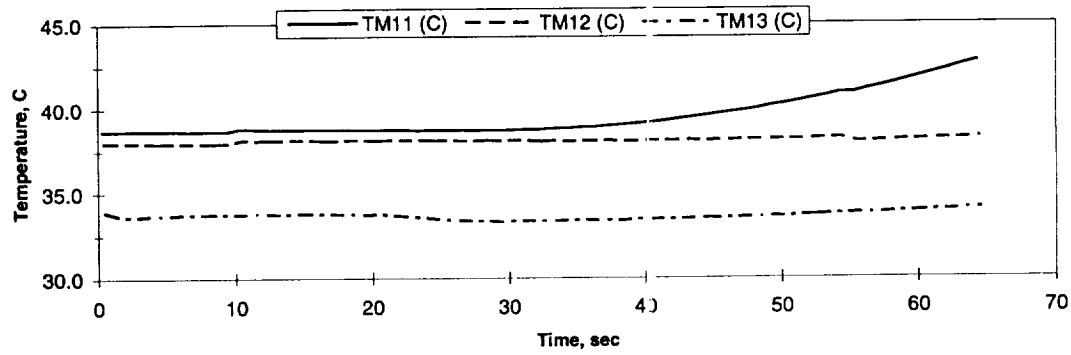

FIGURE: Measured Heater-Underside Temperatures **STS-72 Run #4**

Heat Flux	Subcooling (F)	Heater Power On/Off	100 FPS On/Off	Stirrer Start	Repress Start	Total Time
8	30	10-55 sec.	10-15 sec.	45	--------	65 Sec

Figure A-5d. Measured fluid temperatures near secondary heater and heater underside. PBE-IIB (STS-72). Run No. 4.

A. Mean Heater Surface Temperature

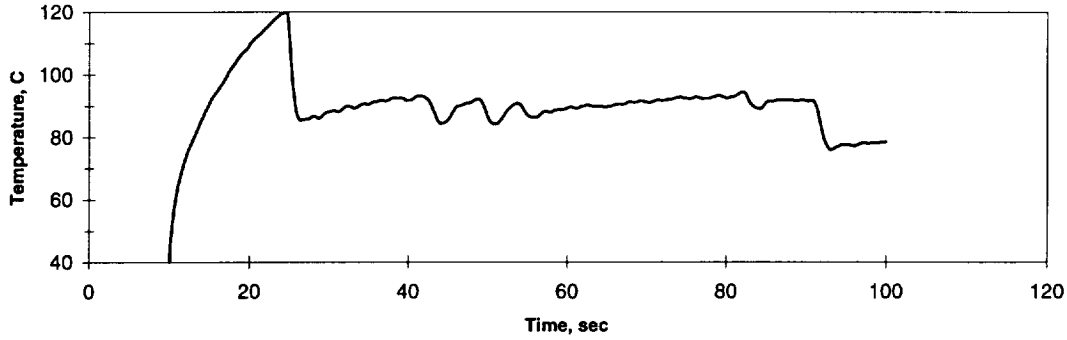

D.

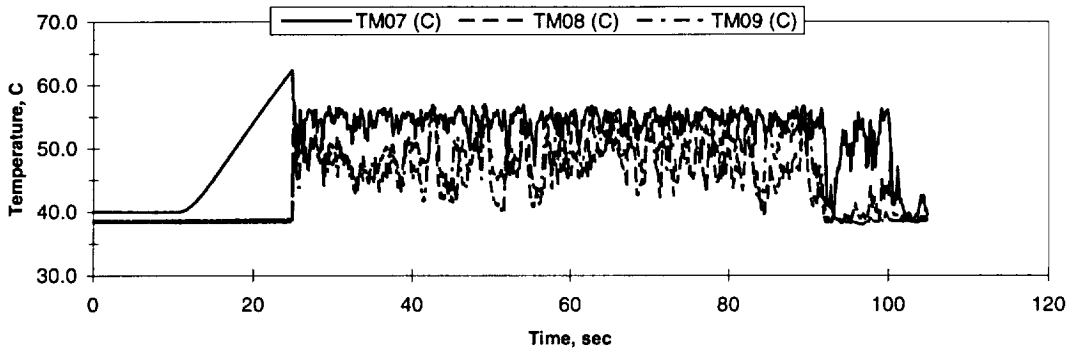

E.

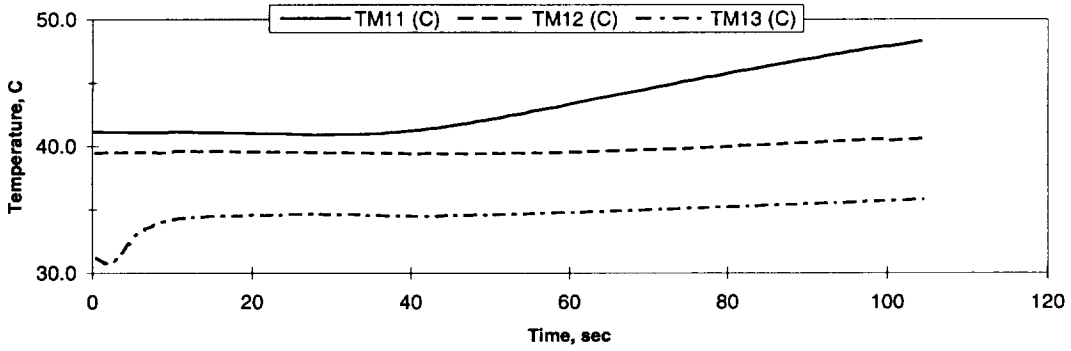

FIGURE: Measured Heater-Underside Temperatures **STS-72 Run #5**

Heat Flux	Subcooling (F)	Heater Power On/Off	100 FPS On/Off	Stirrer Start	Repress Start	Total Time
4	30	10-100 sec.	15-25 sec.	90	--------	105 Sec

Figure A-5e. Measured fluid temperatures near secondary heater and heater underside. PBE-IIB (STS-72). Run No. 5.

A. Mean Heater Surface Temperature

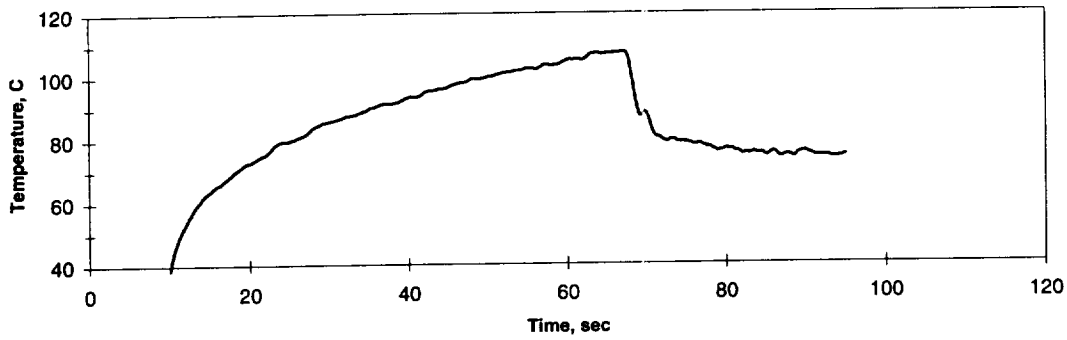

D.

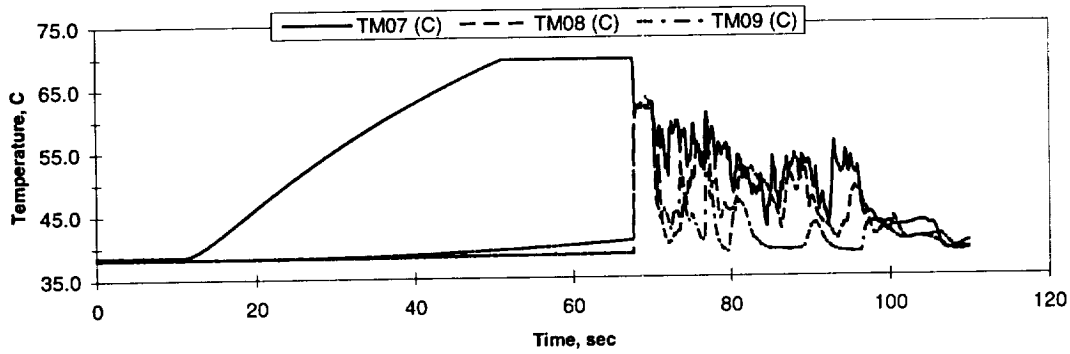

E.

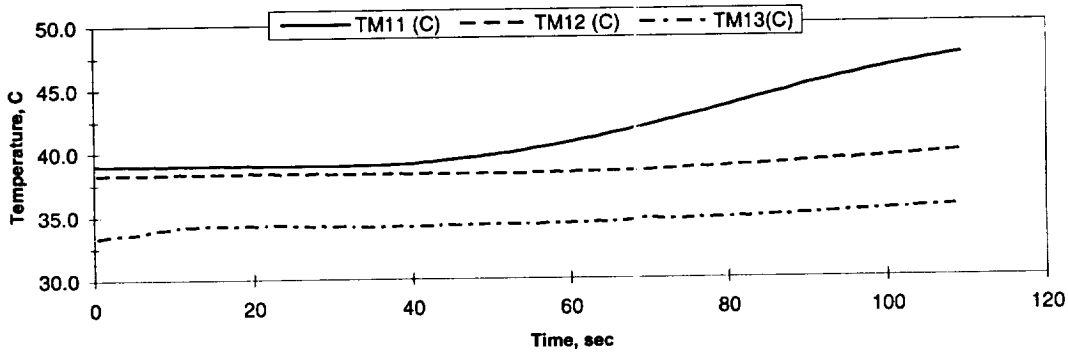

FIGURE: Measured Heater-Underside Temperatures **STS-72 Run #6**

Heat Flux	Subcooling (F)	Heater Power On/Off	100 FPS On/Off	Stirrer Start	Repress Start	Total Time
2	30	10-95 sec.	30-50 sec.	---------	--------	110 Sec

Figure A-5f. Measured fluid temperatures near secondary heater and heater underside. PBE-IIB (STS-72). Run No. 6.

A. Mean Heater Surface Temperature

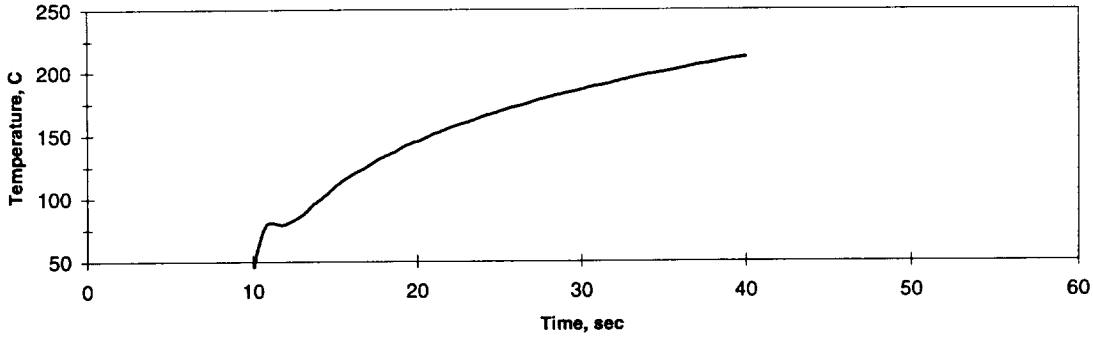

D.

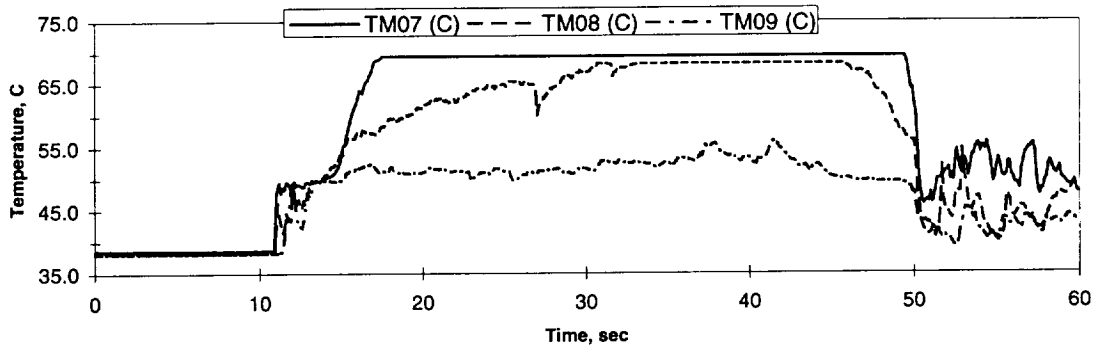

E.

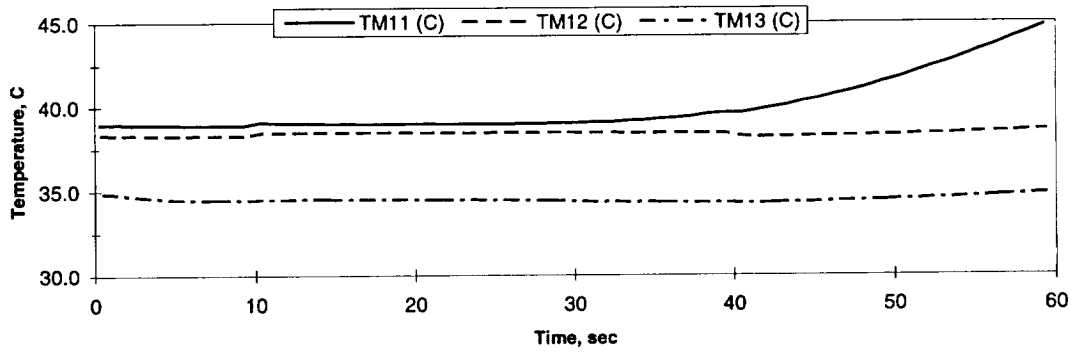

FIGURE: Measured Heater-Underside Temperatures **STS-72 Run #7**

Heat Flux	Subcooling (F)	Heater Power On/Off	100 FPS On/Off	Stirrer Start	Repress Start	Total Time
8	20	10-40 sec.	10-15 sec.	---------	45	55 Sec

Figure A-5g. Measured fluid temperatures near secondary heater and heater underside. PBE-IIB (STS-72). Run No. 7.

A. Mean Heater Surface Temperature

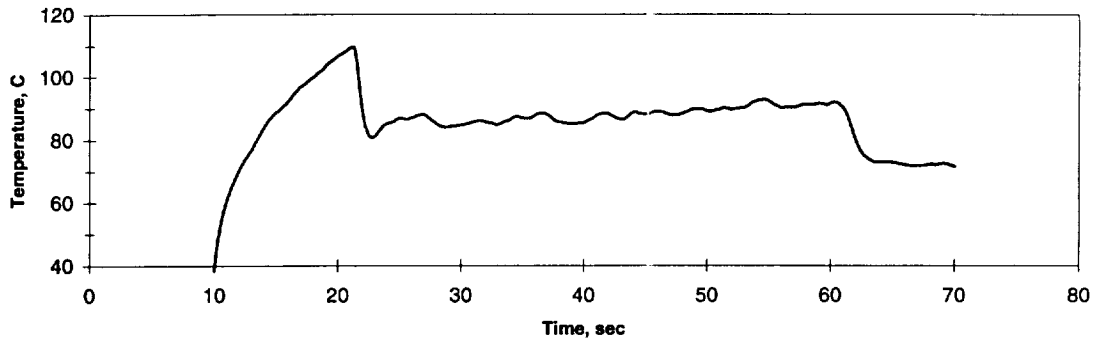

D.

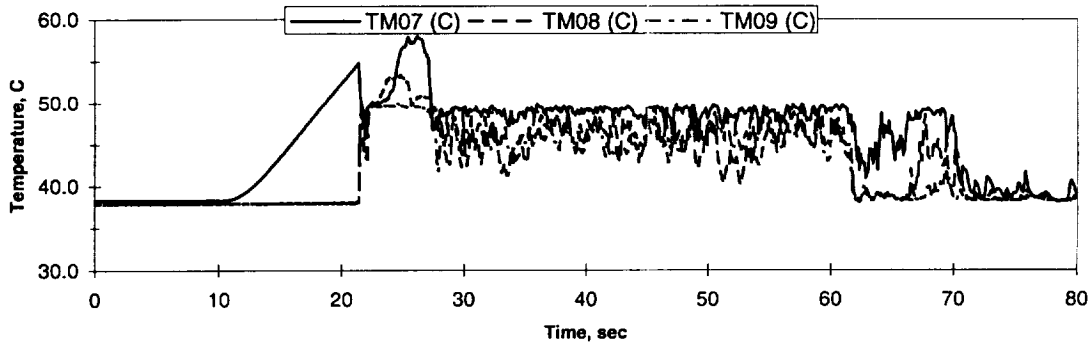

E.

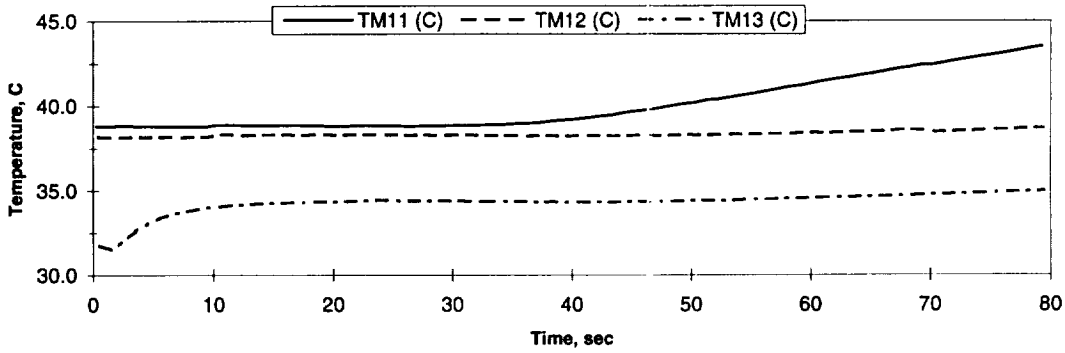

FIGURE: Measured Heater-Underside Temperatures **STS-72 Run #8**

Heat Flux	Subcooling (F)	Heater Power On/Off	100 FPS On/Off	Stirrer Start	Repress Start	Total Time
4	20	10-70 sec.	15-25 sec.	60	--------	80 Sec

Figure A-5h. Measured fluid temperatures near secondary heater and heater underside. PBE-IIB (STS-72). Run No. 8.

A. Mean Heater Surface Temperature

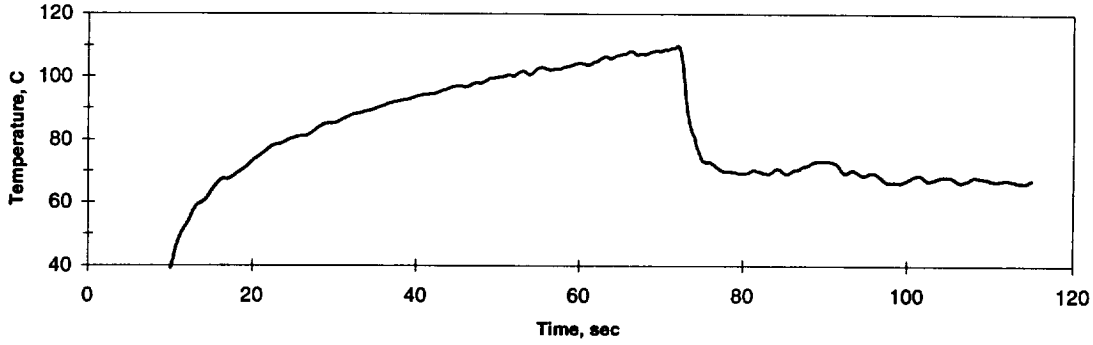

D.

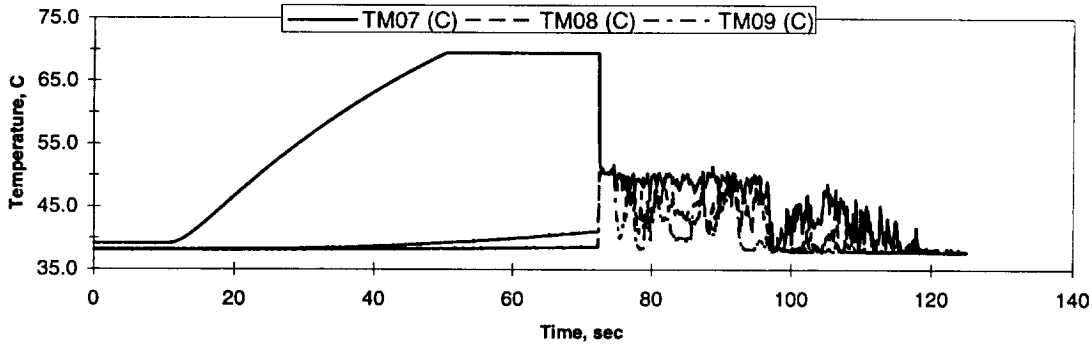

E.

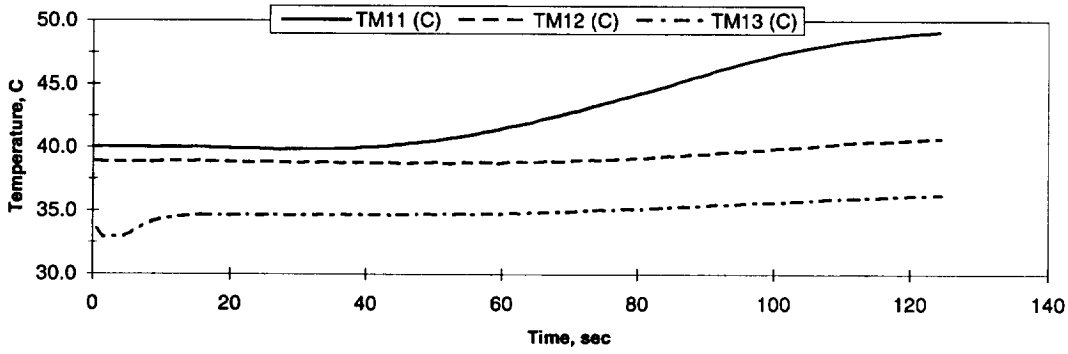

FIGURE: Measured Heater-Underside Temperatures **STS-72 Run #9**

Heat Flux	Subcooling (F)	Heater Power On/Off	100 FPS On/Off	Stirrer Start	Repress Start	Total Time
2	20	10-115 sec.	30-50 sec.	95	--------	125 Sec

Figure A-5i. Measured fluid temperatures near secondary heater and heater underside. PBE-IIB (STS-72). Run No. 9.

STS-72 **Run #1**

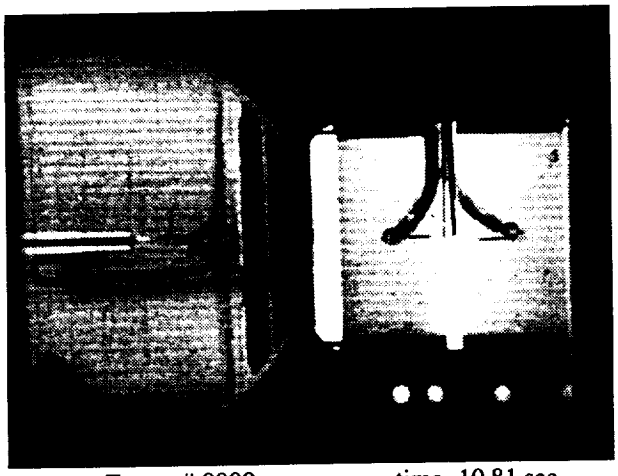

Frame # 0000 time=10.81 sec

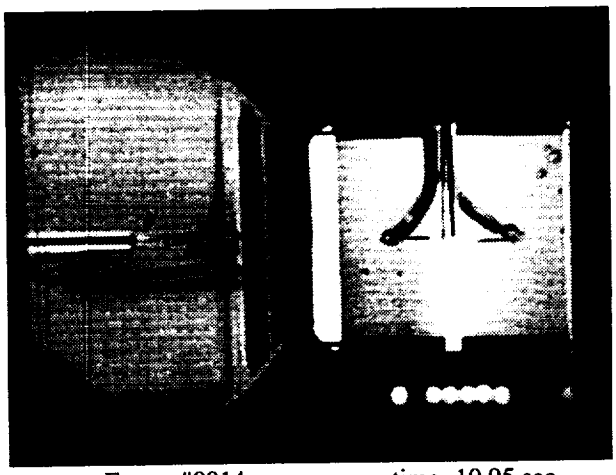

Frame #0014 time=10.95 sec

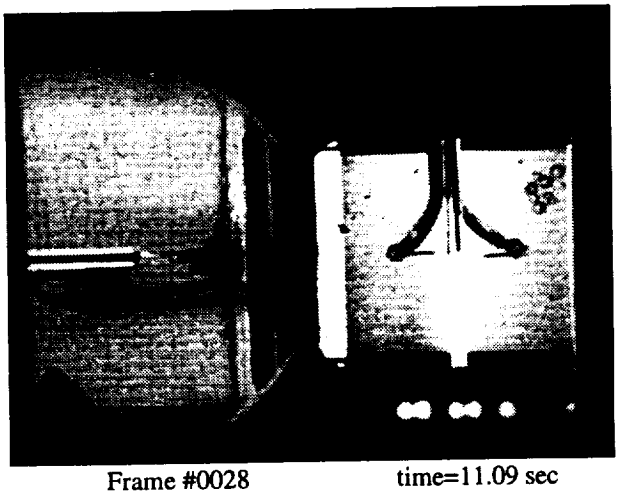

Frame #0028 time=11.09 sec

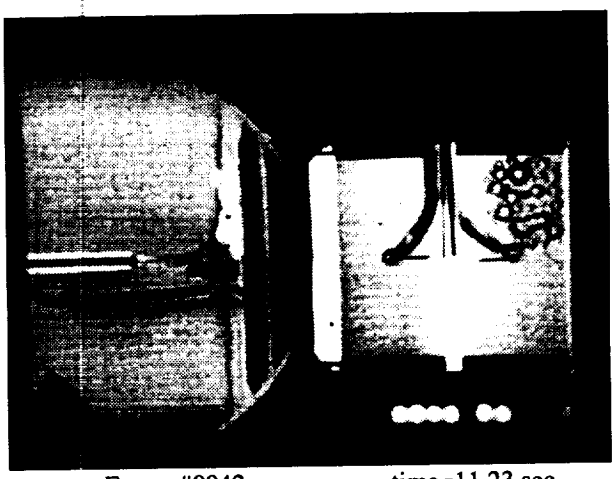

Frame #0042 time=11.23 sec

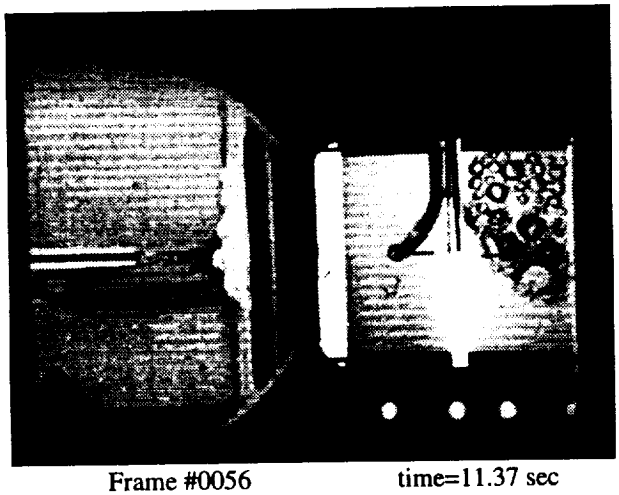

Frame #0056 time=11.37 sec

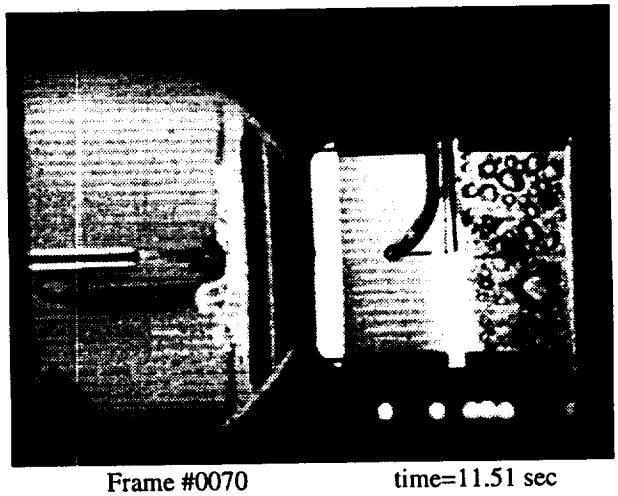

Frame #0070 time=11.51 sec

Figure A-6a. Selected Photographic Images. PBE-IIB (STS-72). Run No. 1.

STS-72 **Run #1**

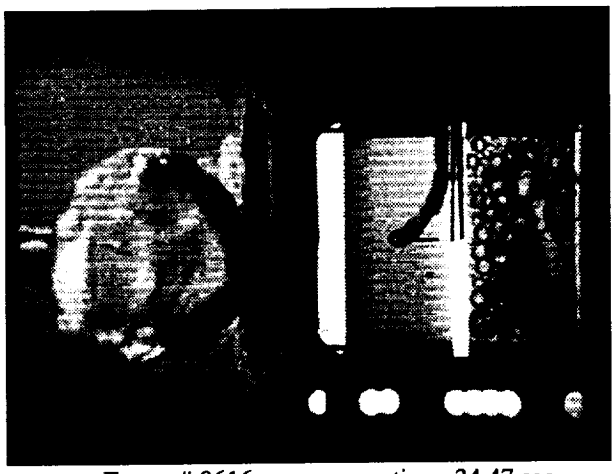

Frame # 0616 time=34.47 sec

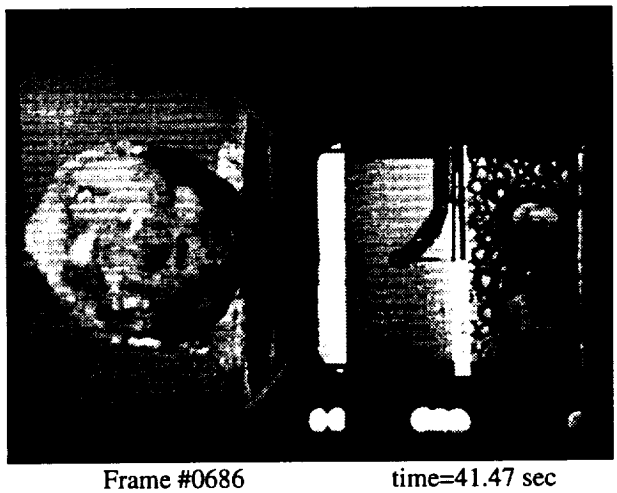

Frame #0686 time=41.47 sec

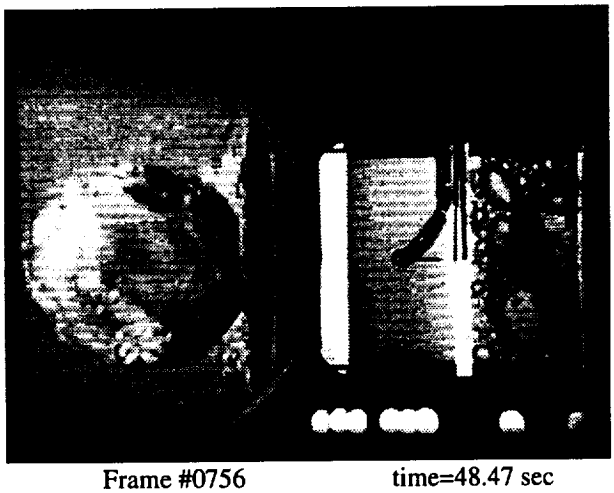

Frame #0756 time=48.47 sec

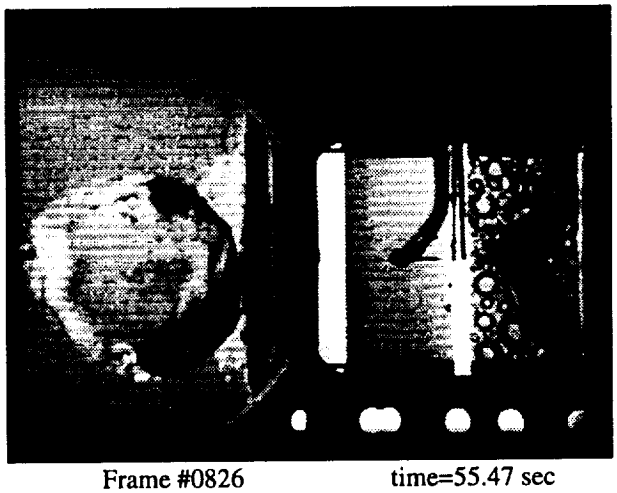

Frame #0826 time=55.47 sec

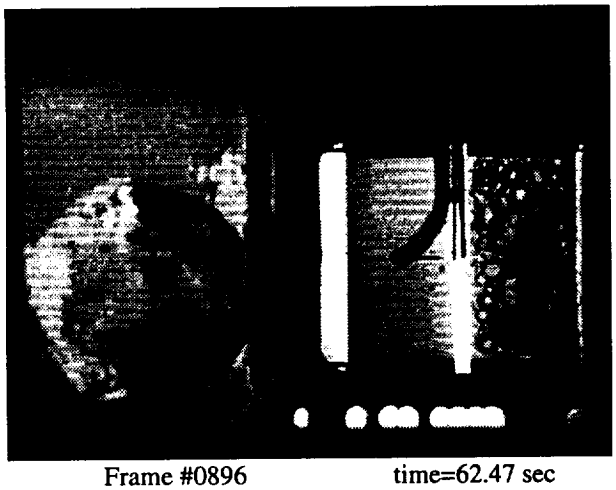

Frame #0896 time=62.47 sec

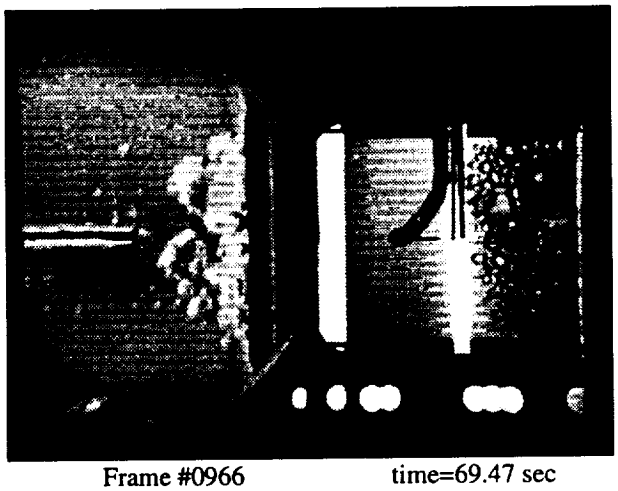

Frame #0966 time=69.47 sec

Figure A-6a. Continued.

STS-72 **Run #2**

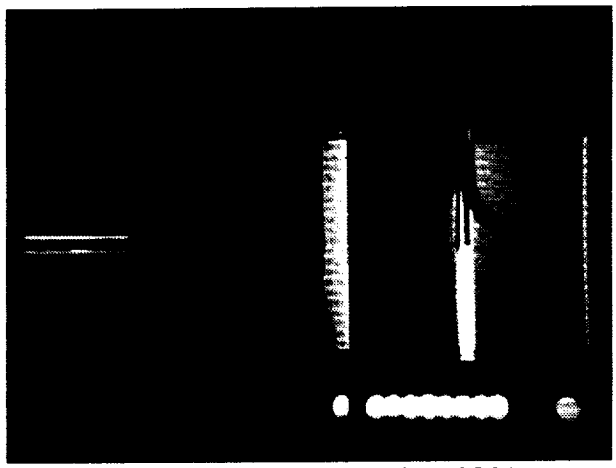

Frame # 0000 time=25.34 sec

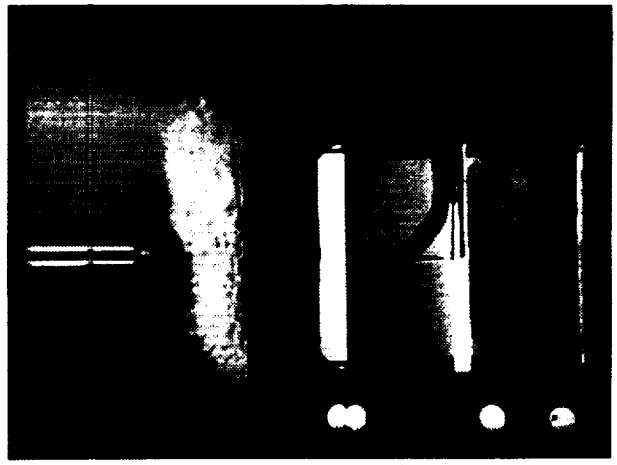

Frame #0001 time=25.44 sec

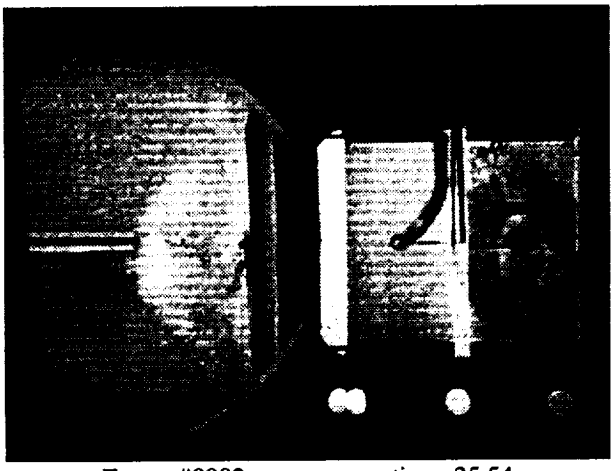

Frame #0002 time=25.54 sec

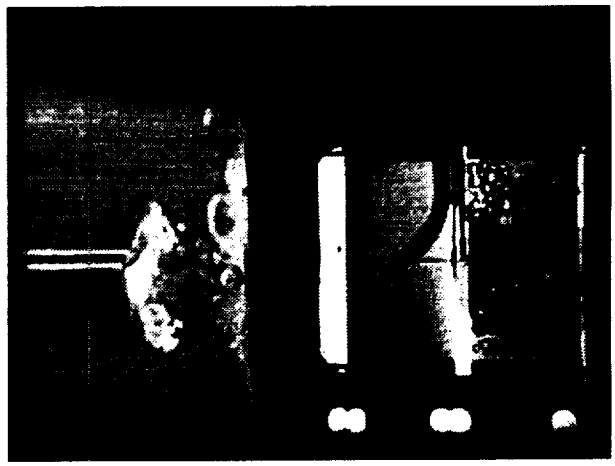

Frame #0003 time=25.64 sec

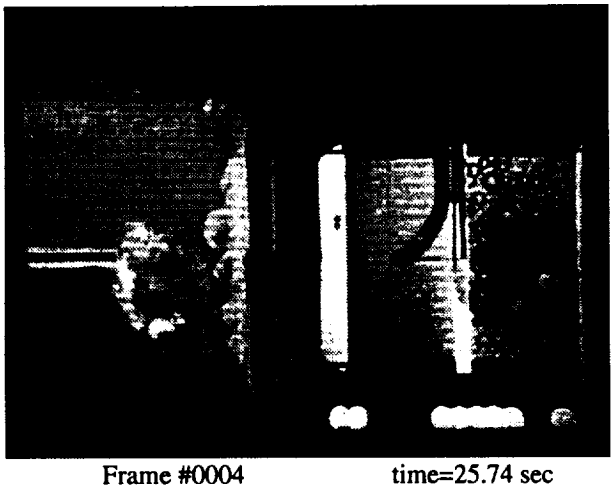

Frame #0004 time=25.74 sec

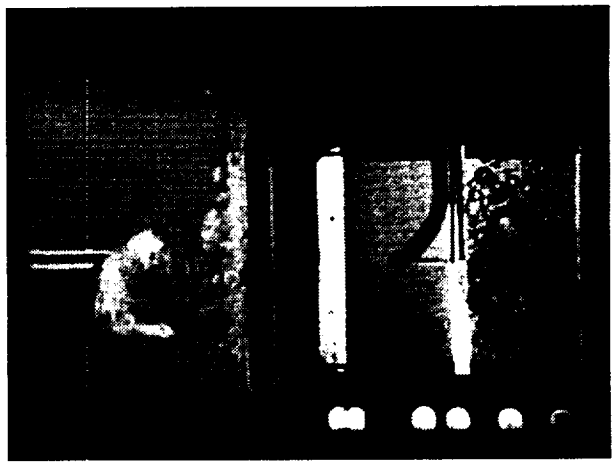

Frame #0005 time=25.84 sec

Figure A-6b. Selected Photographic Images. PBE-IIB (STS-72). Run No. 2.

STS-72 **Run #2**

Frame # 0020 time=38.26 sec

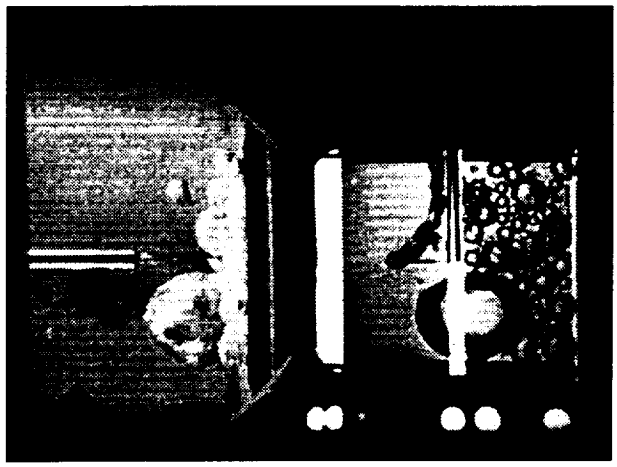

Frame #0160 time=52.26 sec

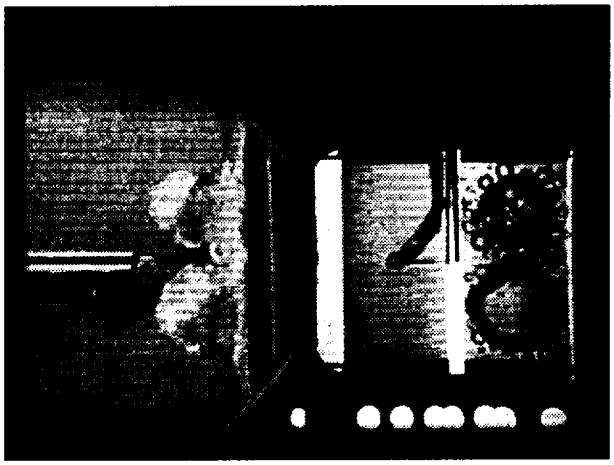

Frame #0300 time=66.26 sec

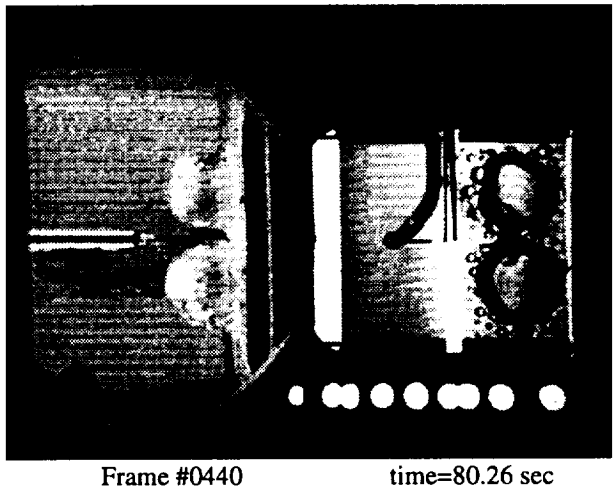

Frame #0440 time=80.26 sec

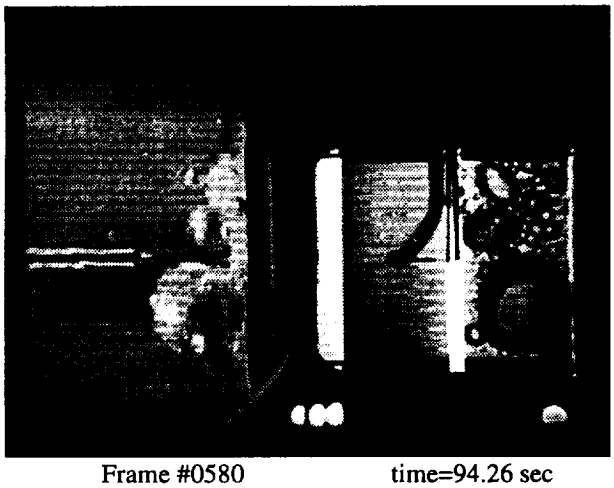

Frame #0580 time=94.26 sec

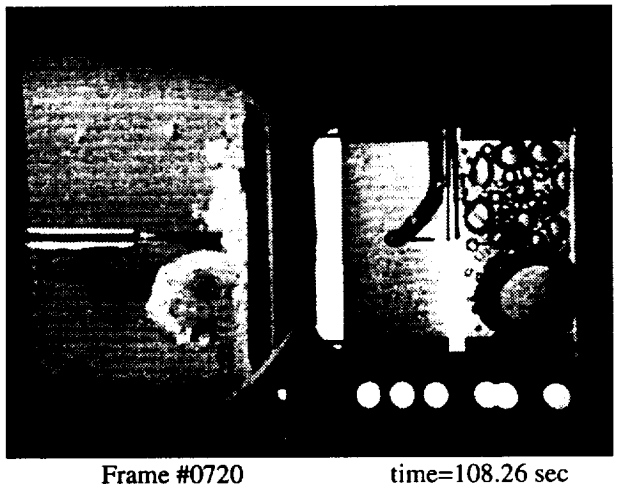

Frame #0720 time=108.26 sec

Figure A-6b. Continued.

STS-72 **Run #3**

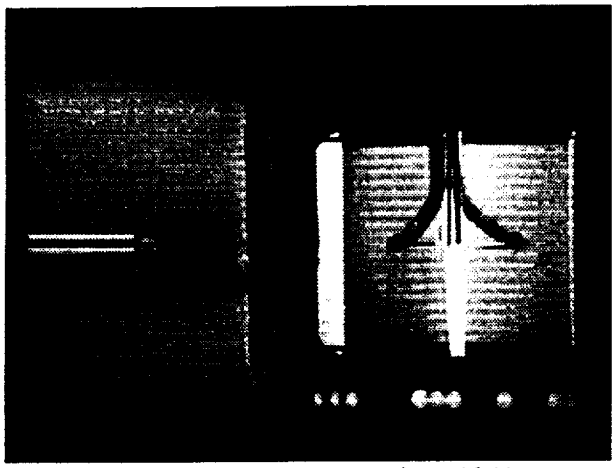

Frame # 0000 time=46.41 sec

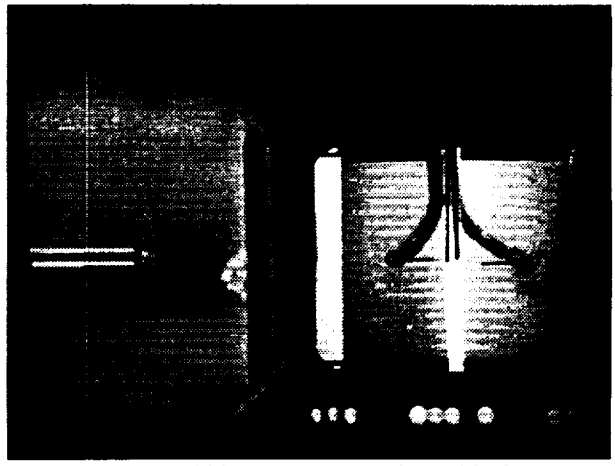

Frame #0001 time=46.42 sec

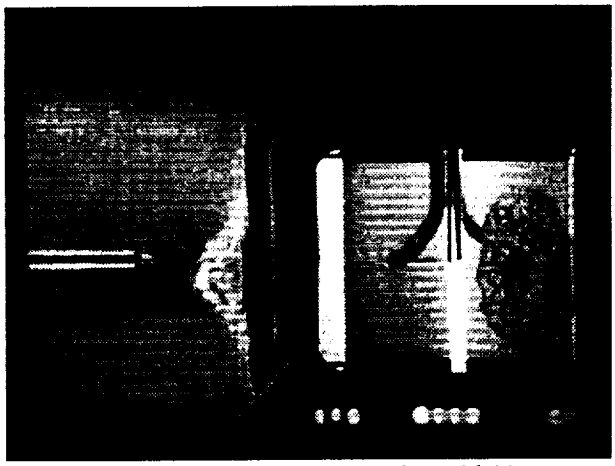

Frame #0003 time=46.44 sec

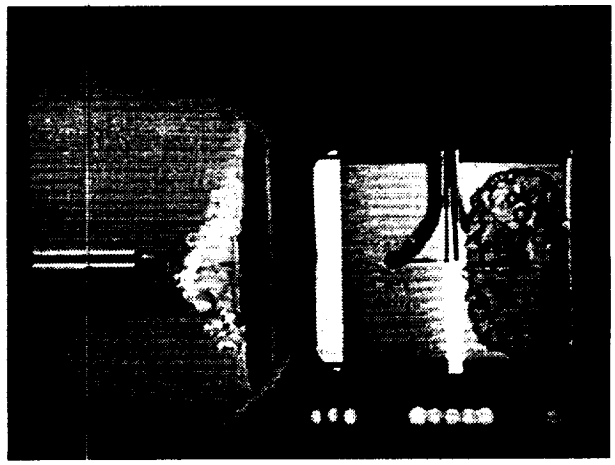

Frame #0005 time=46.46 sec

Frame #0007 time=46.48 sec

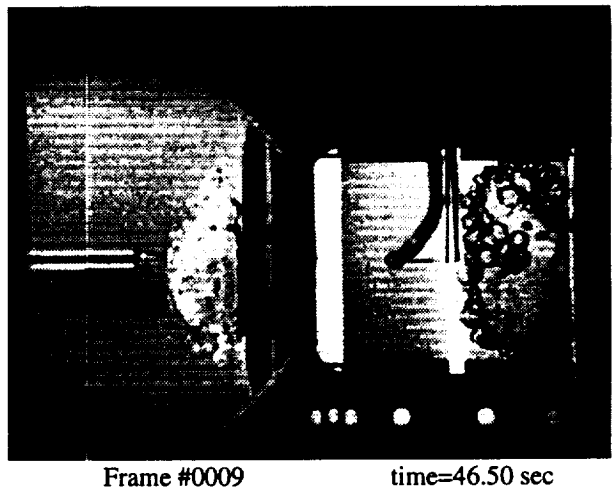

Frame #0009 time=46.50 sec

Figure A-6c. Selected Photographic Images. PBE-IIB (STS-72). Run No. 3.

STS-72 **Run #3**

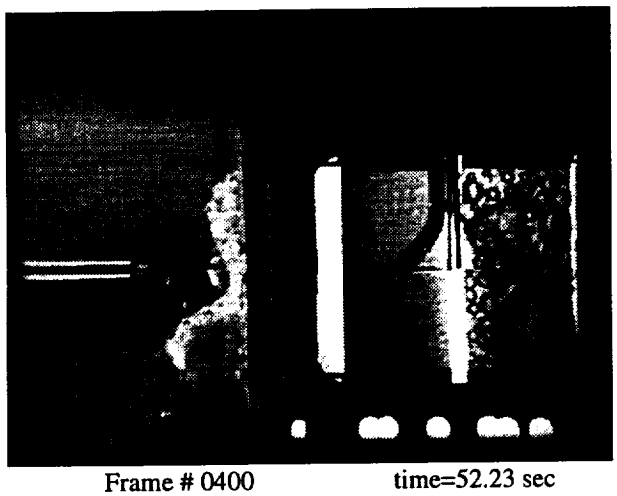

Frame # 0400 time=52.23 sec

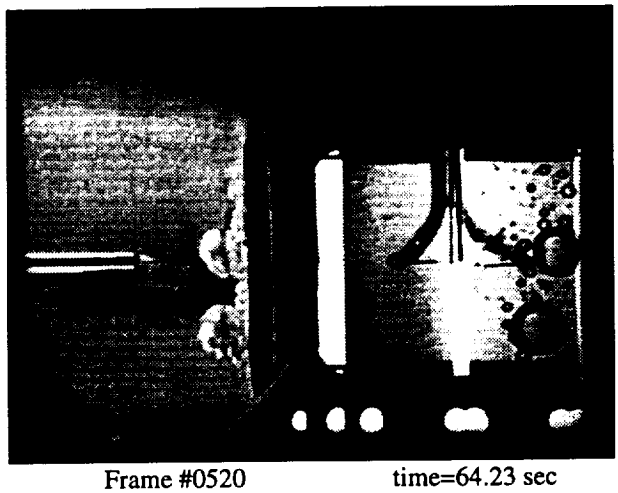

Frame #0520 time=64.23 sec

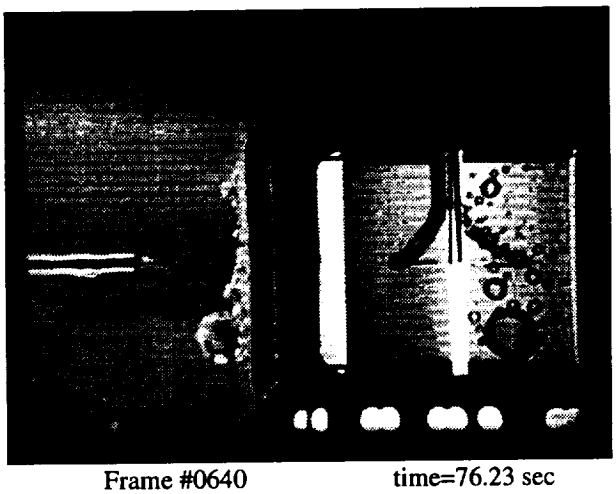

Frame #0640 time=76.23 sec

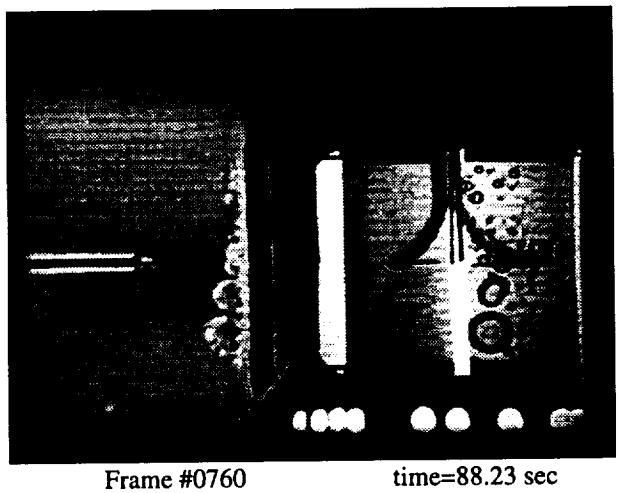

Frame #0760 time=88.23 sec

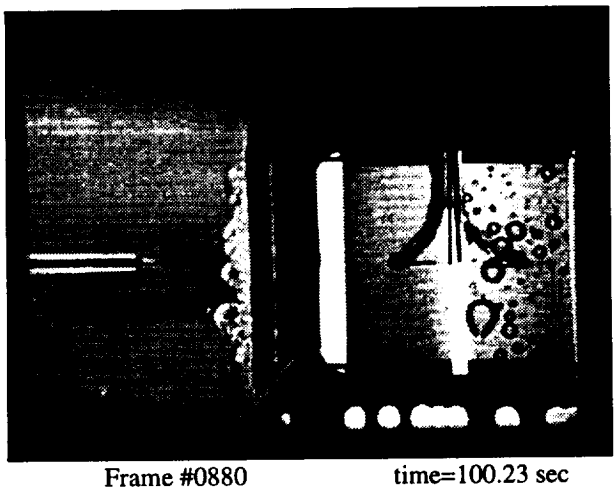

Frame #0880 time=100.23 sec

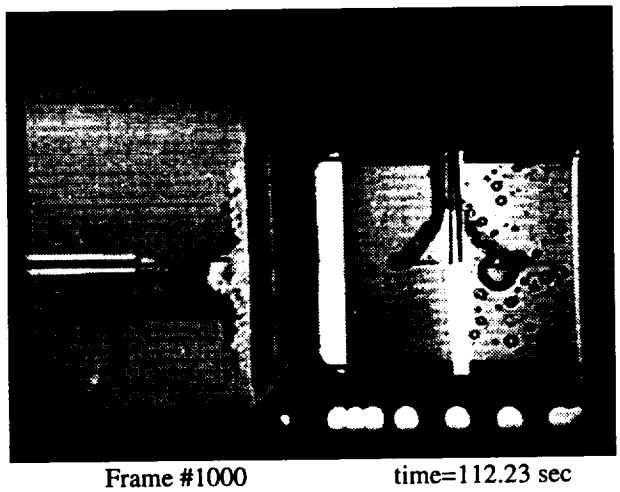

Frame #1000 time=112.23 sec

Figure A-6c. Continued.

STS-72 **Run #4**

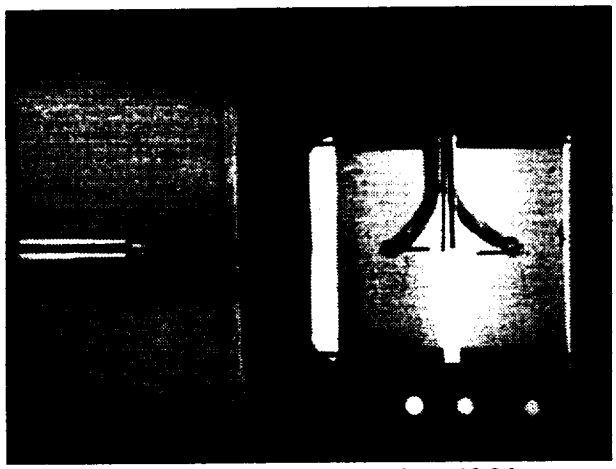

Frame # 0000 time=10.36 sec

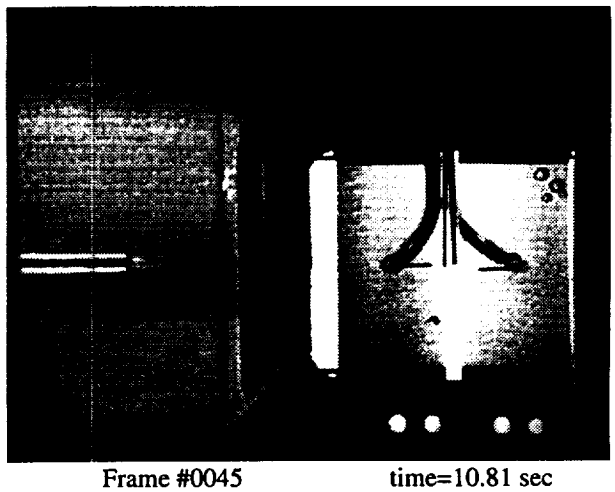

Frame #0045 time=10.81 sec

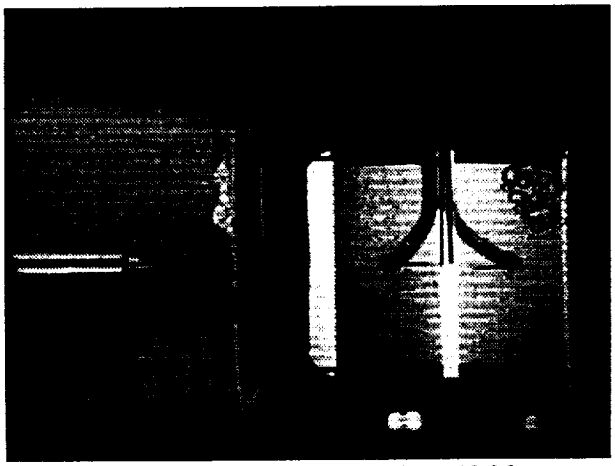

Frame #0060 time=10.96 sec

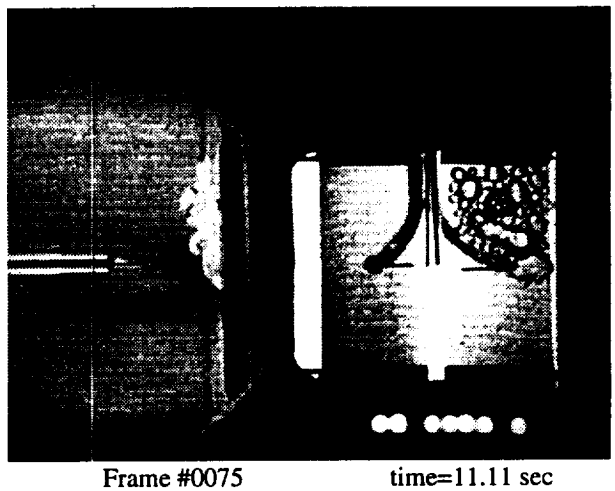

Frame #0075 time=11.11 sec

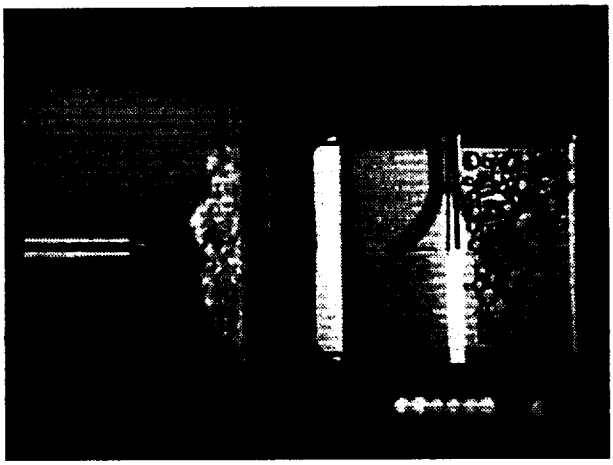

Frame #0090 time=11.26 sec

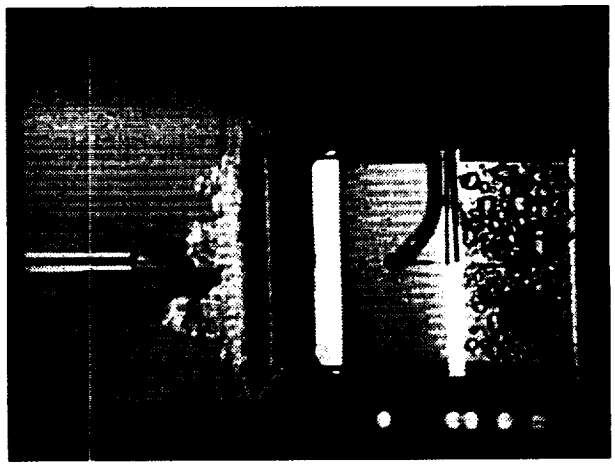

Frame #0105 time=11.41 sec

Figure A-6d. Selected Photographic Images. PBE-IIB (STS-72). Run No. 4.

STS-72 Run #4

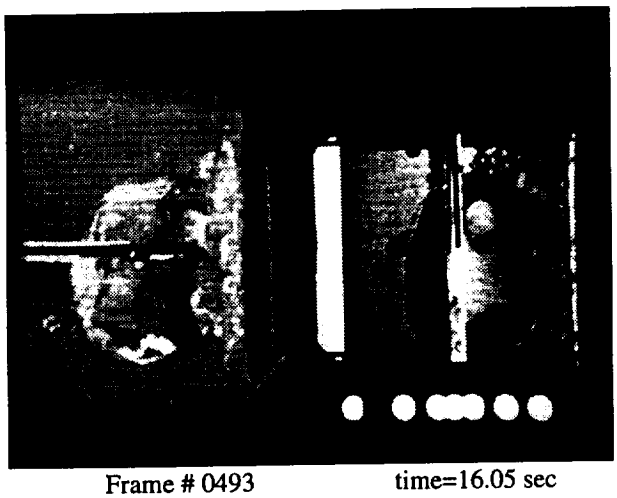

Frame # 0493 time=16.05 sec

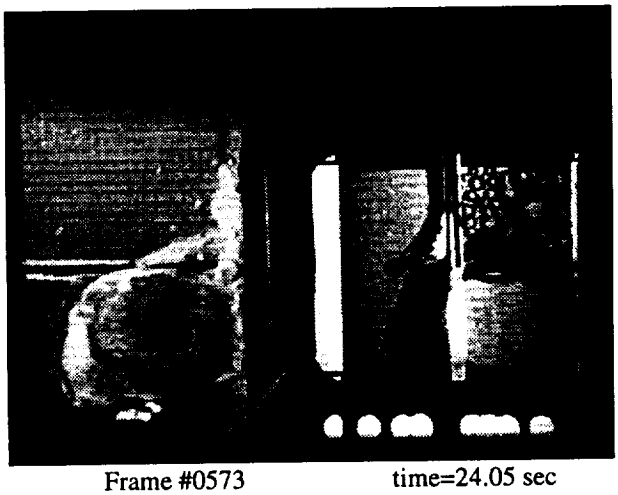

Frame #0573 time=24.05 sec

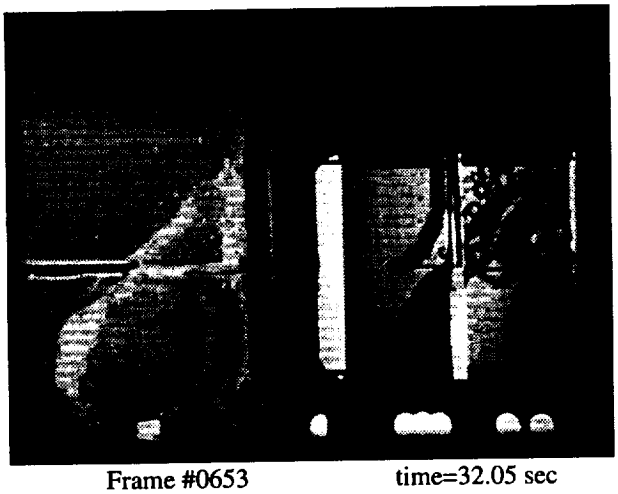

Frame #0653 time=32.05 sec

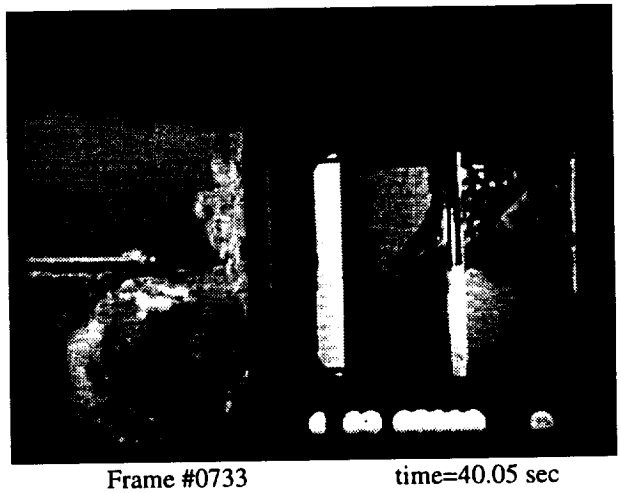

Frame #0733 time=40.05 sec

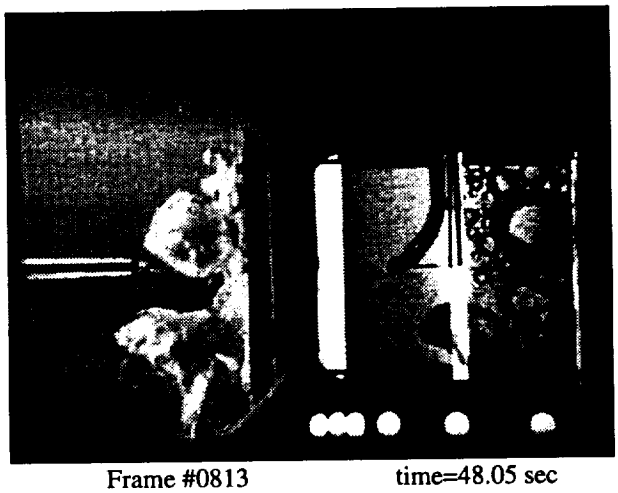

Frame #0813 time=48.05 sec

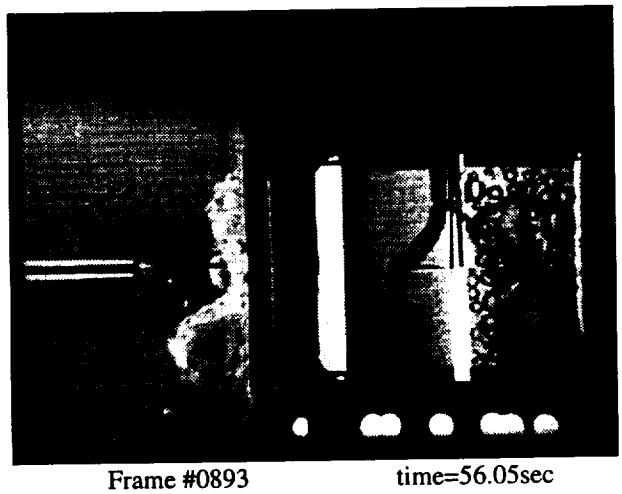

Frame #0893 time=56.05sec

Figure A-6d. Continued.

STS-72 **Run #5**

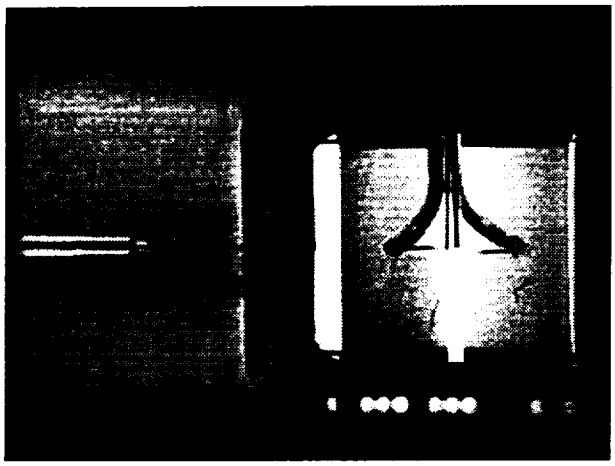

Frame # 0000 time=25.01 sec

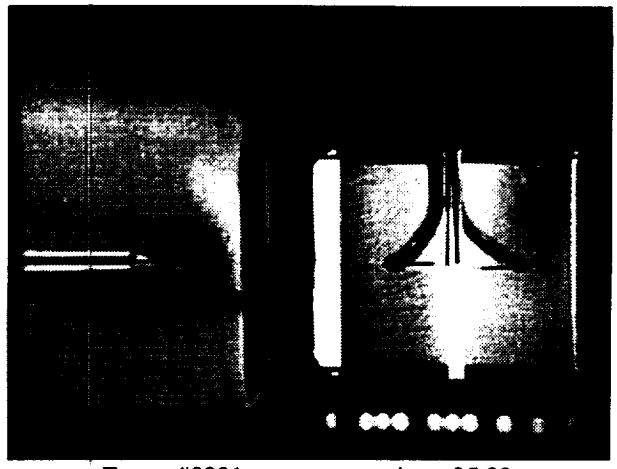

Frame #0001 time=25.02 sec

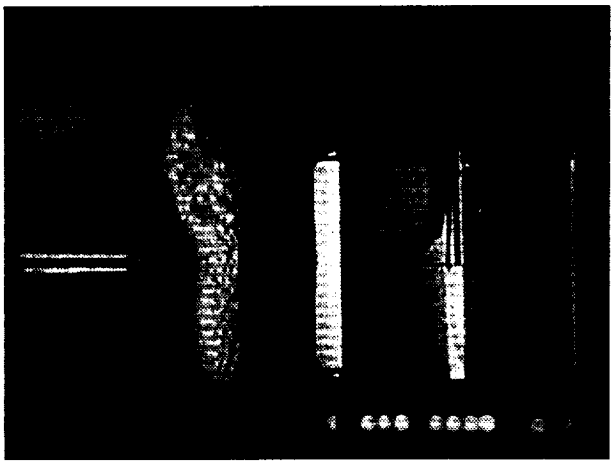

Frame #0002 time=25.03 sec

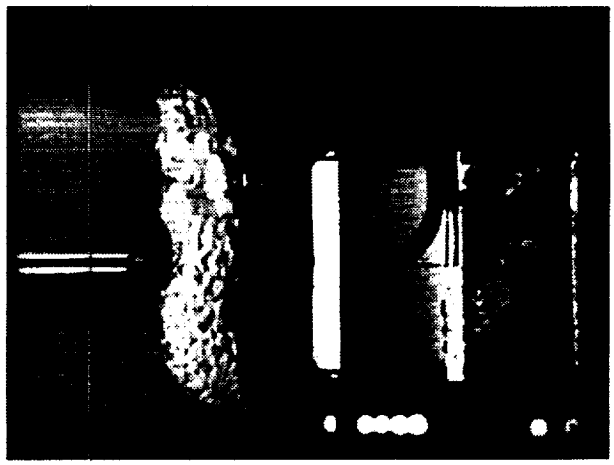

Frame #0004 time=25.05 sec

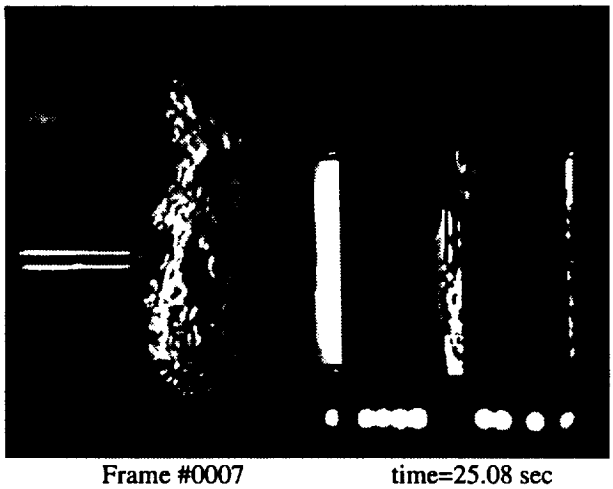

Frame #0007 time=25.08 sec

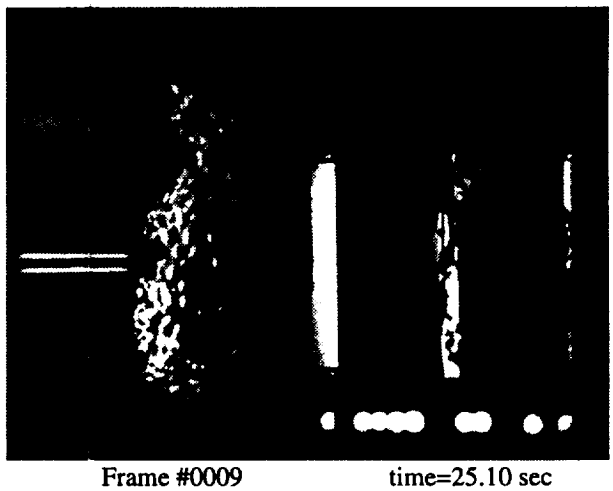

Frame #0009 time=25.10 sec

Figure A-6e. Selected Photographic Images. PBE-IIB (STS-72). Run No. 5.

STS-72 **Run #5**

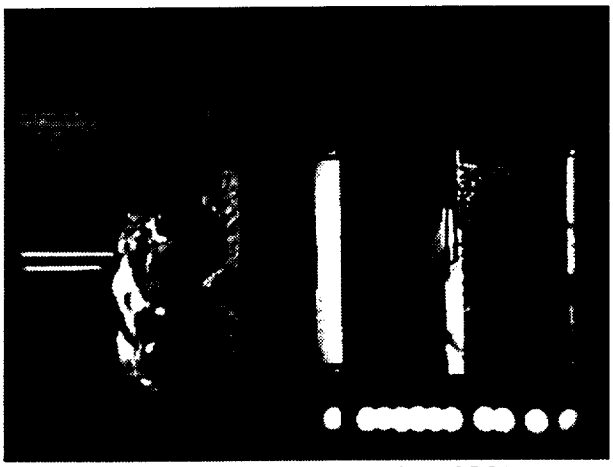

Frame # 0021 time=25.31 sec

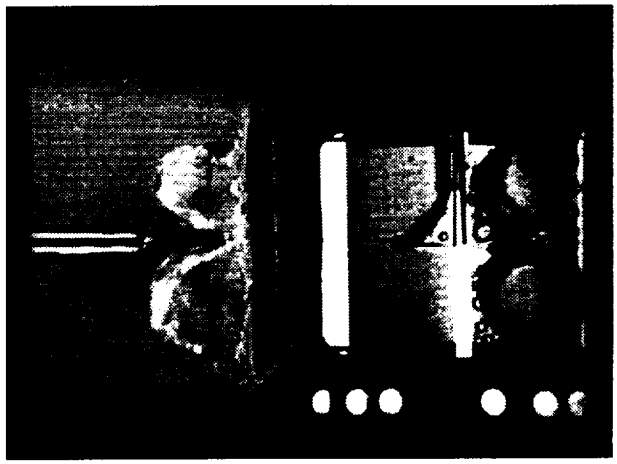

Frame #0141 time=37.07 sec

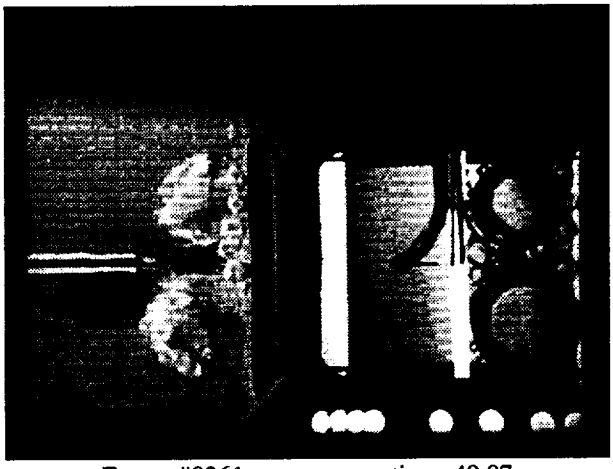

Frame #0261 time=49.07 sec

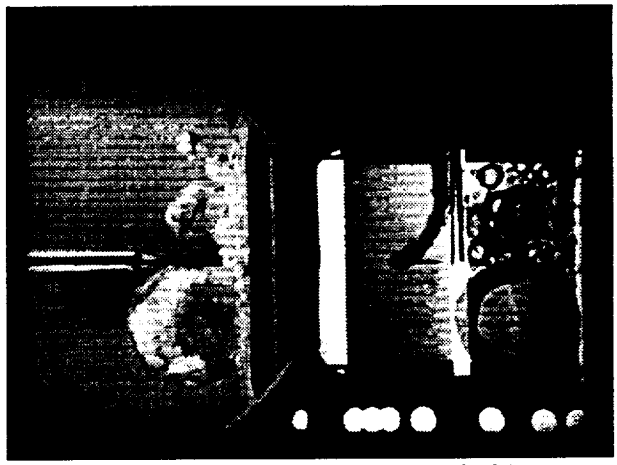

Frame #0381 time=61.07 sec

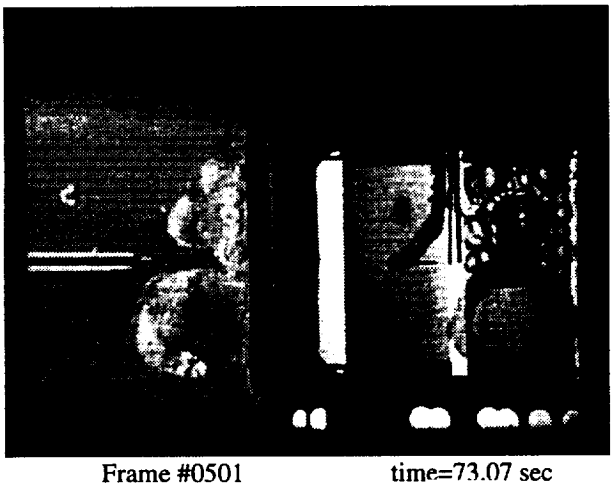

Frame #0501 time=73.07 sec

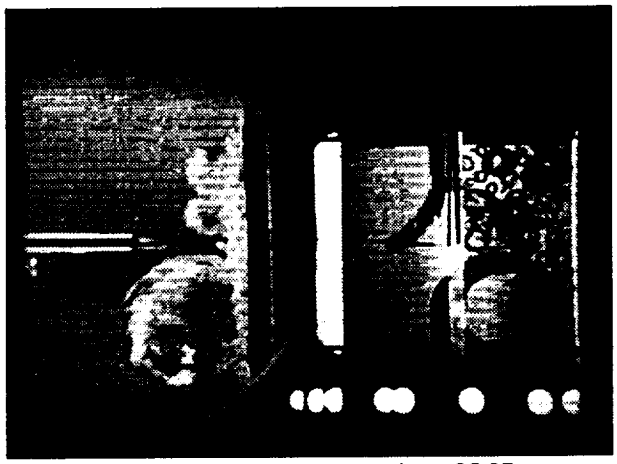

Frame #0621 time=85.07 sec

Figure A-6e. Continued.

STS-72 **Run #6**

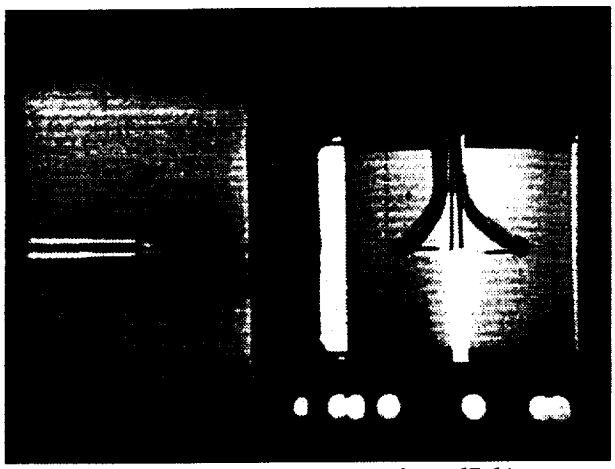

Frame # 0000 time=67.64 sec

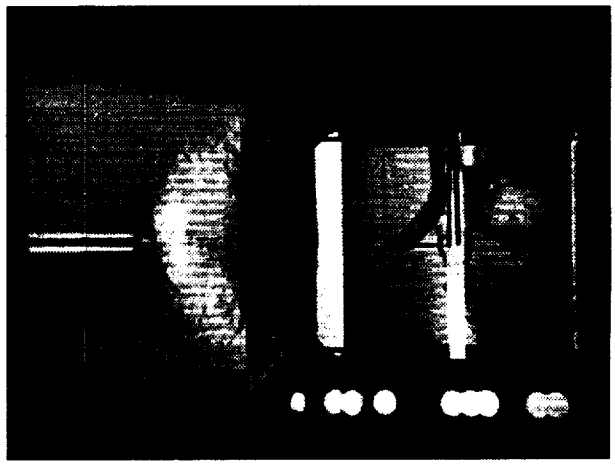

Frame #0001 time=67.74 sec

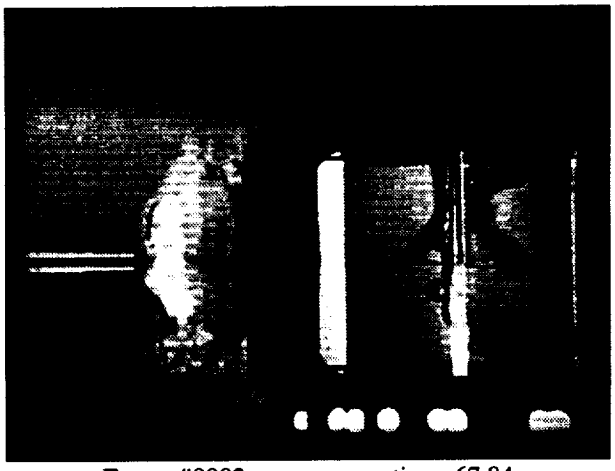

Frame #0002 time=67.84 sec

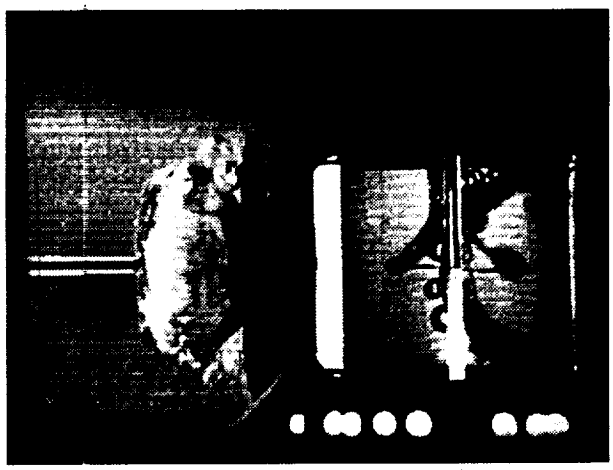

Frame #0003 time=67.94 sec

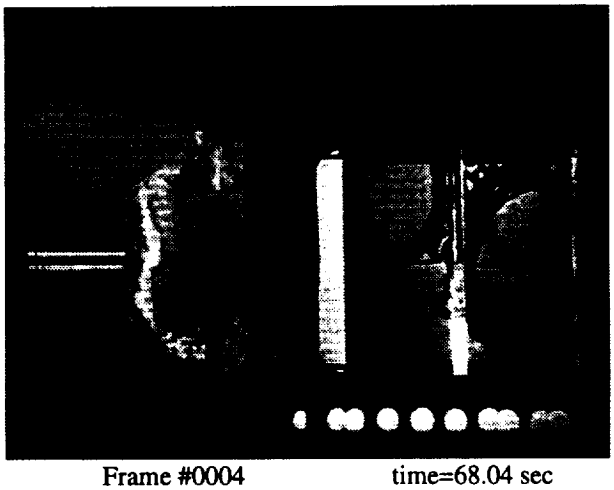

Frame #0004 time=68.04 sec

Frame #0005 time=68.14 sec

Figure A-6f. Selected Photographic Images. PBE-IIB (STS-72). Run No. 6.

STS-72 **Run #6**

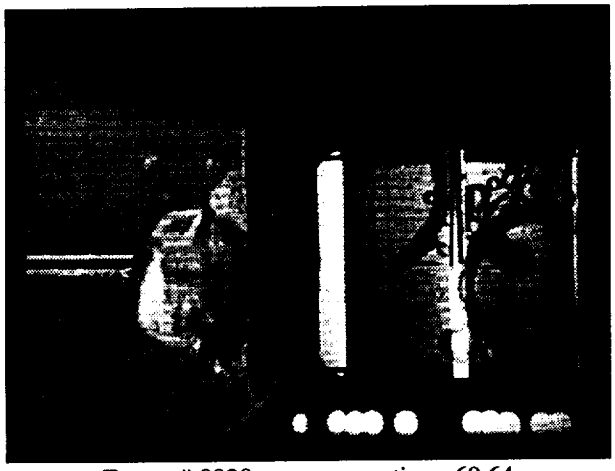

Frame # 0020 time=69.64 sec

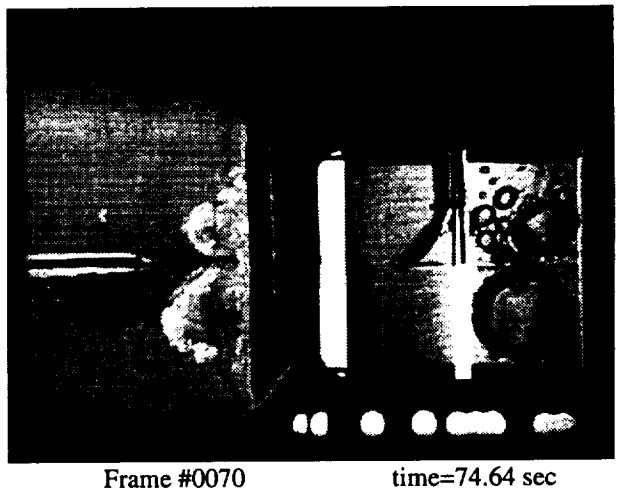

Frame #0070 time=74.64 sec

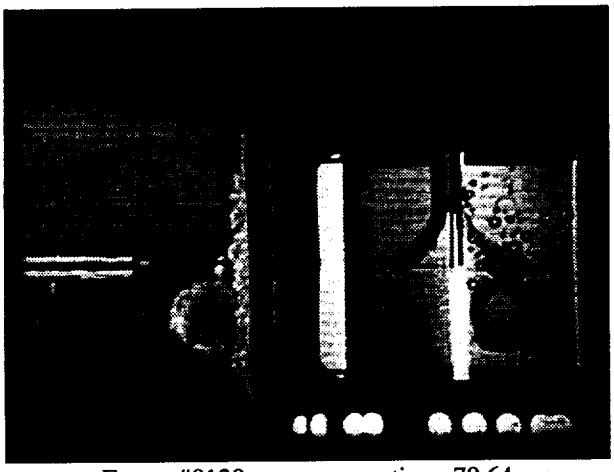

Frame #0120 time=79.64 sec

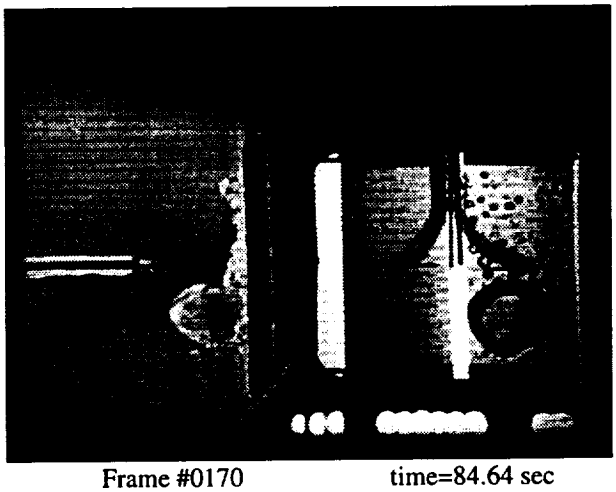

Frame #0170 time=84.64 sec

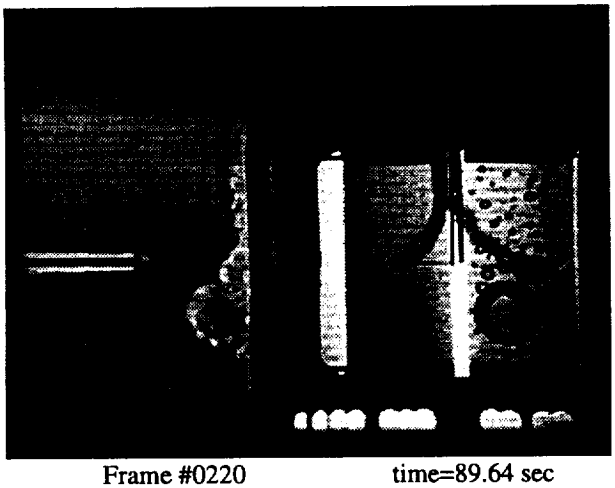

Frame #0220 time=89.64 sec

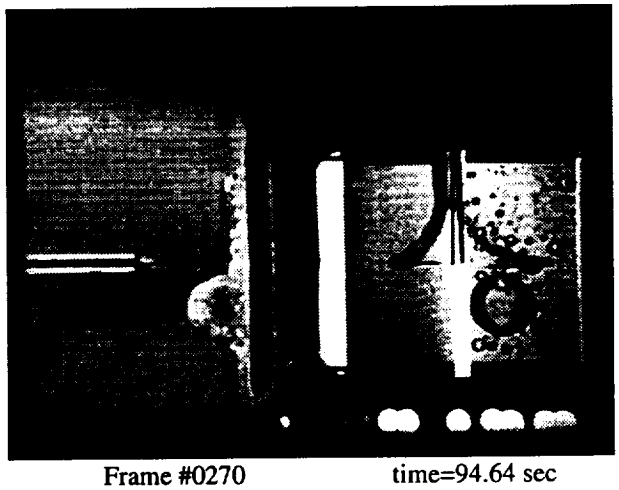

Frame #0270 time=94.64 sec

Figure A-6f. Continued.

STS-72 **Run #7**

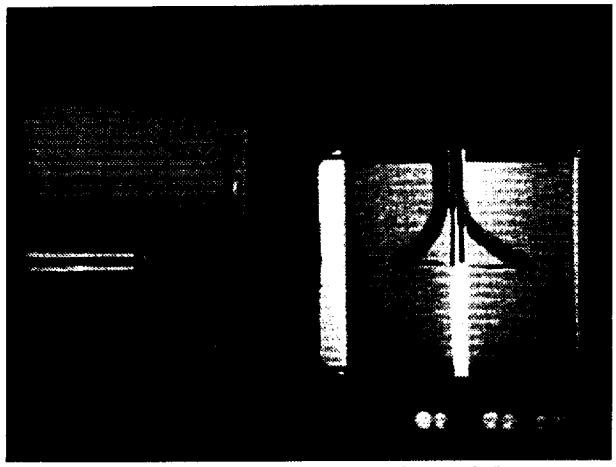

Frame # 0000 time=10.51 sec

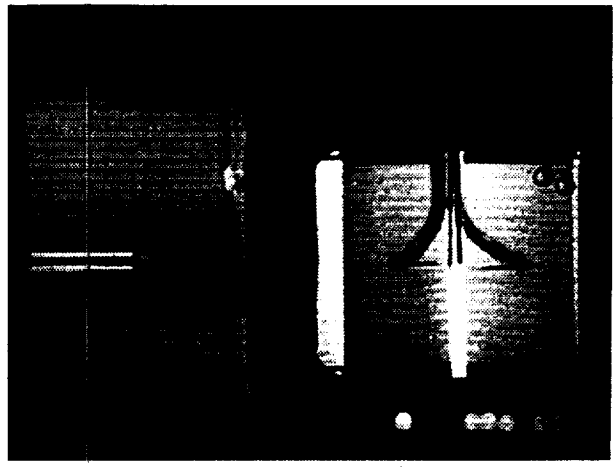

Frame #0020 time=10.71 sec

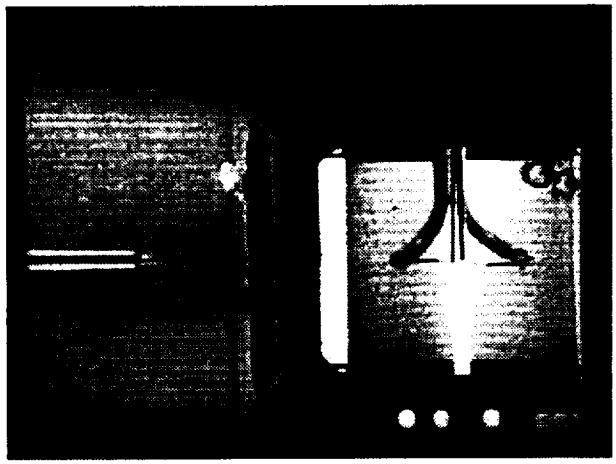

Frame #0030 time=10.81 sec

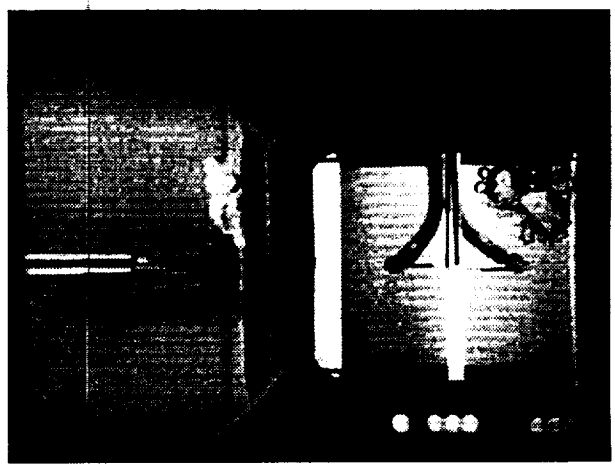

Frame #0040 time=10.91 sec

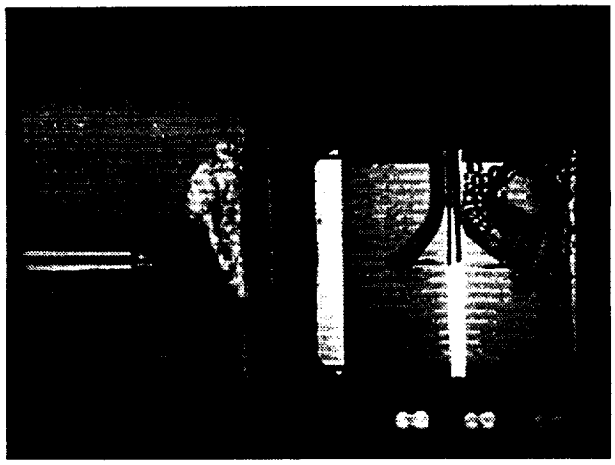

Frame #0050 time=11.01 sec

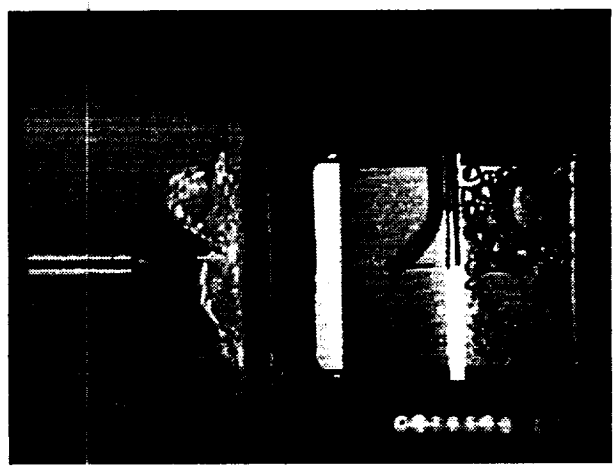

Frame #0060 time=11.11 sec

Figure A-6g. Selected Photographic Images. PBE-IIB (STS-72). Run No. 7.

STS-72 **Run #7**

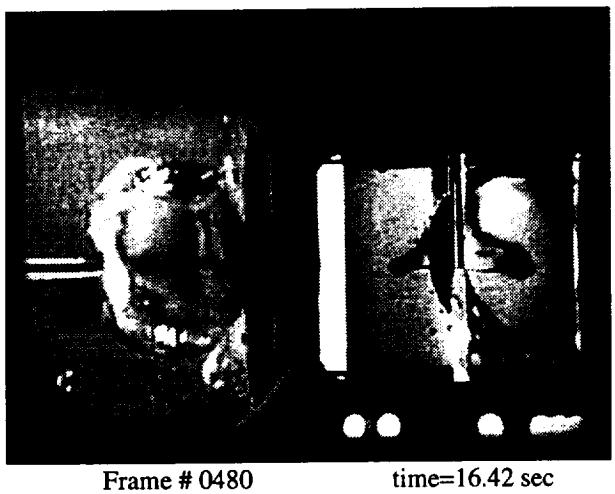

Frame # 0480 time=16.42 sec

Frame #0520 time=20.42 sec

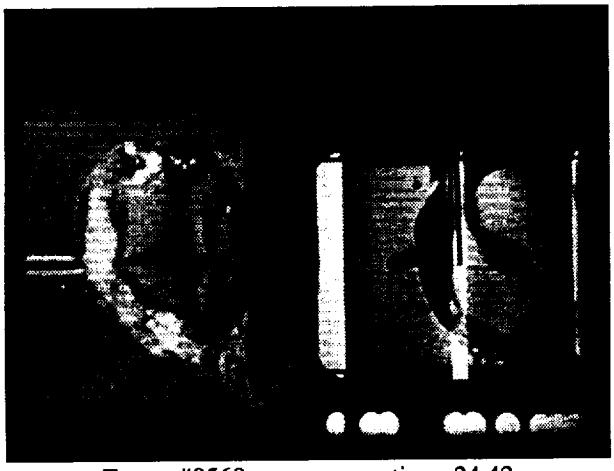

Frame #0560 time=24.42 sec

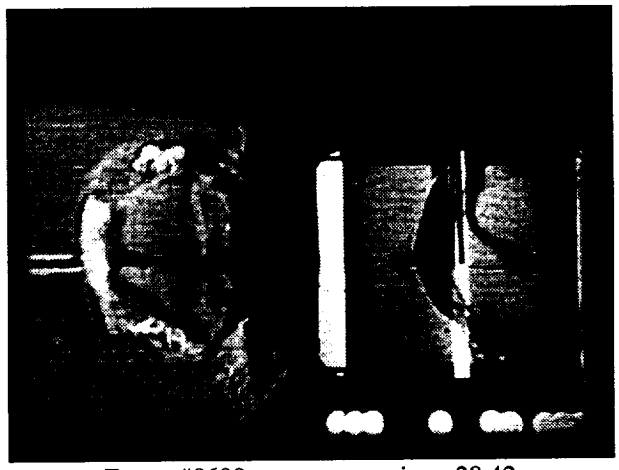

Frame #0600 time=28.42 sec

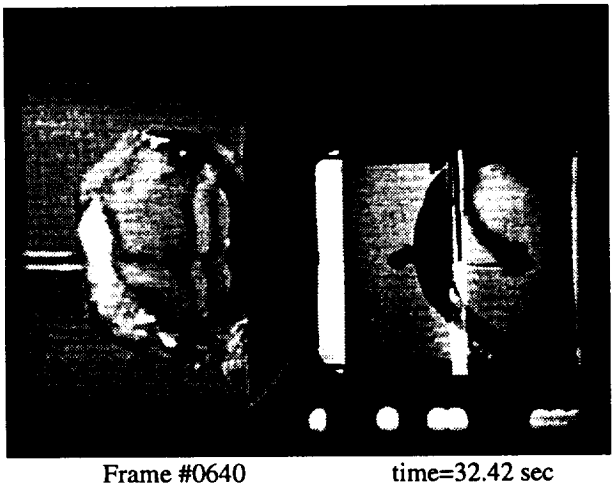

Frame #0640 time=32.42 sec

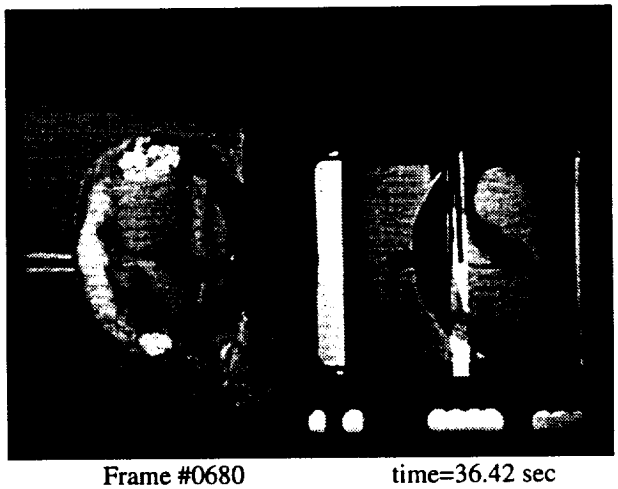

Frame #0680 time=36.42 sec

Figure A-6g. Continued.

STS-72 **Run #8**

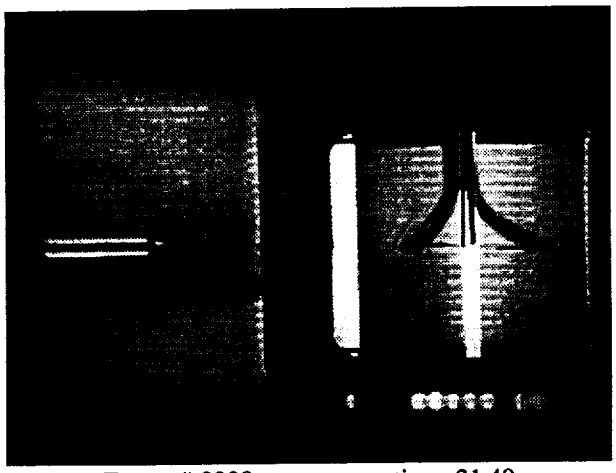

Frame # 0000 time=21.49 sec

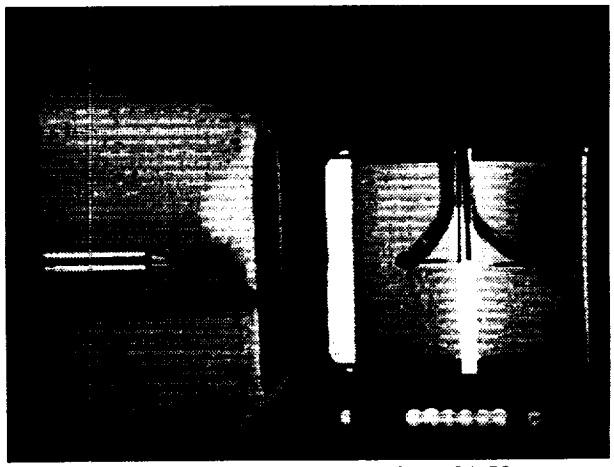

Frame #0001 time=21.50 sec

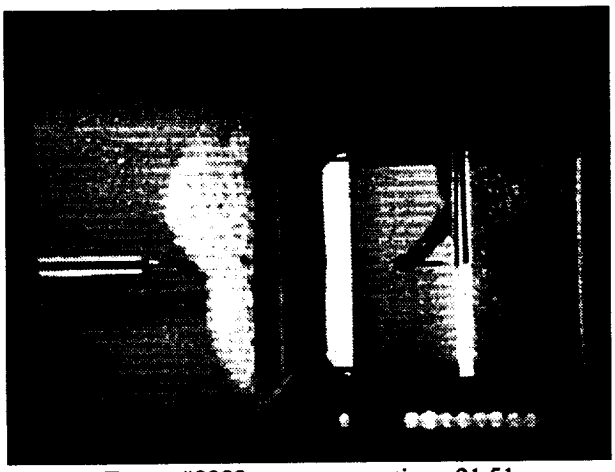

Frame #0002 time=21.51 sec

Frame #0003 time=21.52 sec

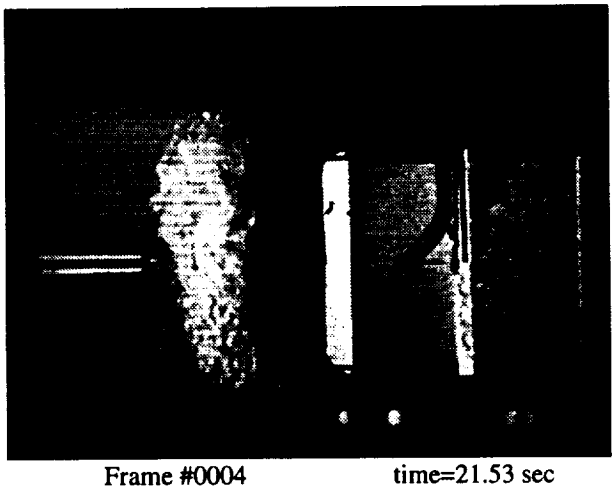

Frame #0004 time=21.53 sec

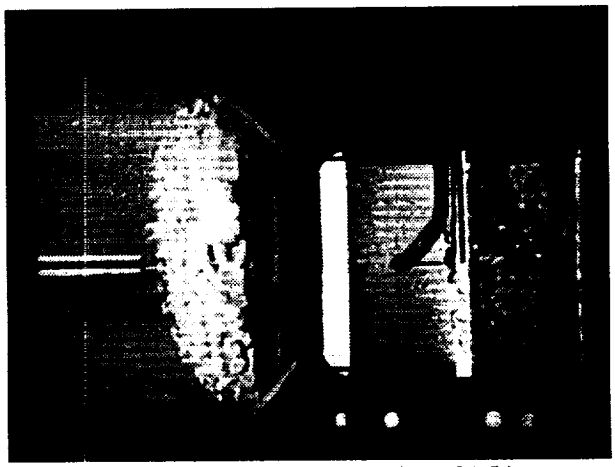

Frame #0005 time=21.54 sec

Figure A-6h. Selected Photographic Images. PBE-IIB (STS-72). Run No. 8.

STS-72 **Run #8**

Frame # 0380 time=26.13 sec

Frame #0440 time=32.13 sec

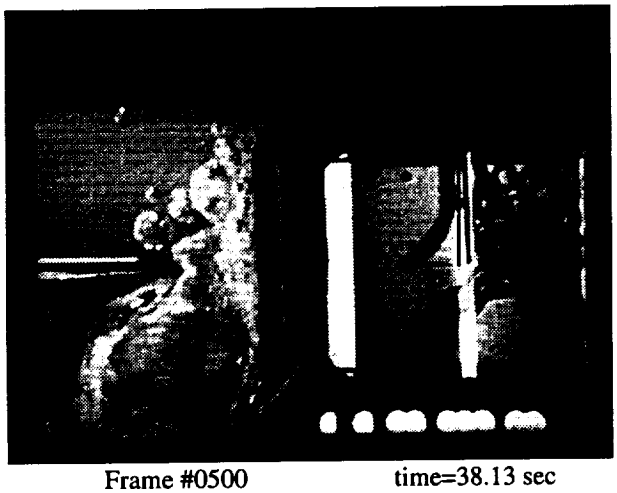

Frame #0500 time=38.13 sec

Frame #0560 time=44.13 sec

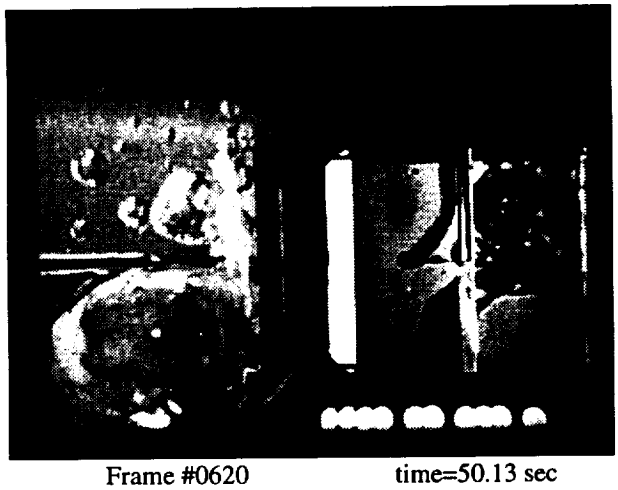

Frame #0620 time=50.13 sec

Frame #0680 time=56.13 sec

Figure A-6h. Continued.

STS-72 **Run #9**

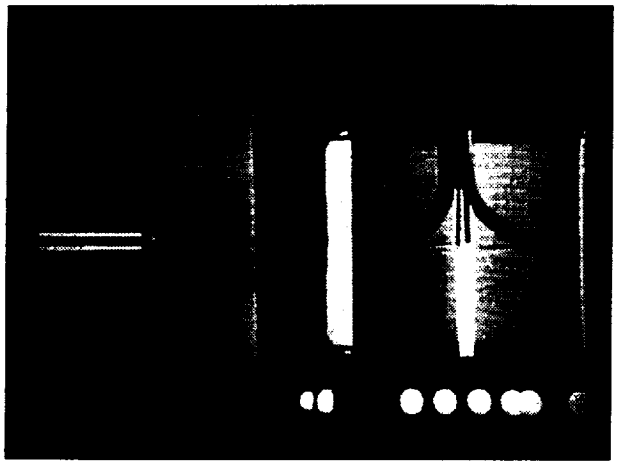

Frame # 0000 time=72.29 sec

Frame #0001 time=72.39 sec

Frame #0002 time=72.49 sec

Frame #0003 time=72.59 sec

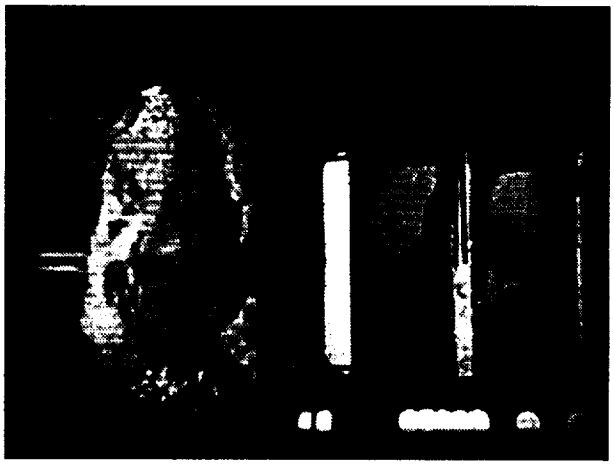

Frame #0004 time=72.69 sec

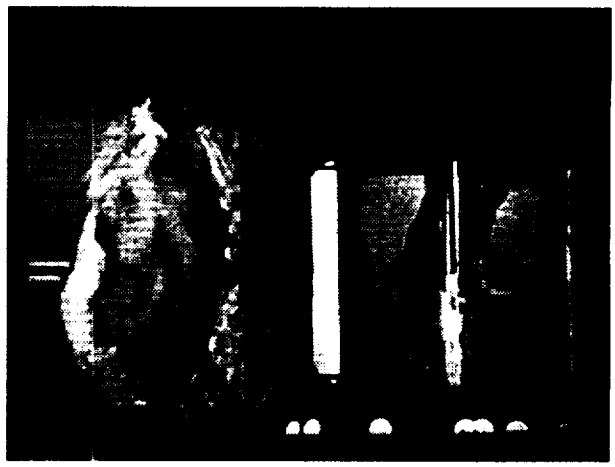

Frame #0005 time=72.79 sec

Figure A-6i. Selected Photographic Images. PBE-IIB (STS-72). Run No. 9.

STS-72 Run #9

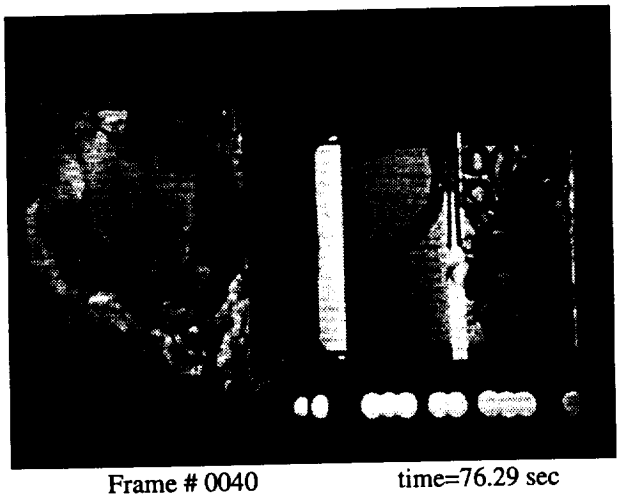

Frame # 0040 time=76.29 sec

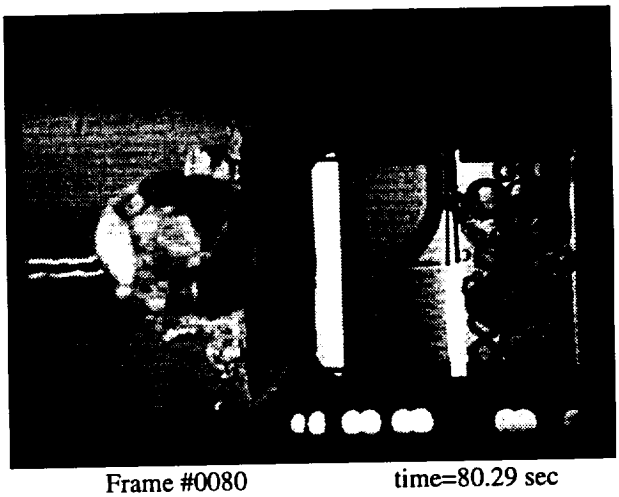

Frame #0080 time=80.29 sec

Frame #0120 time=84.29 sec

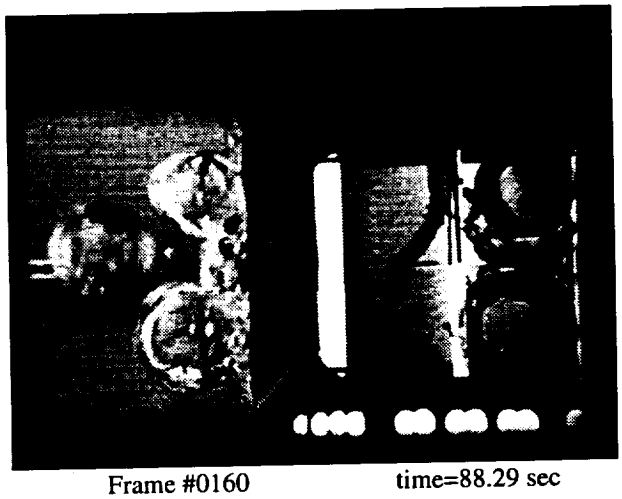

Frame #0160 time=88.29 sec

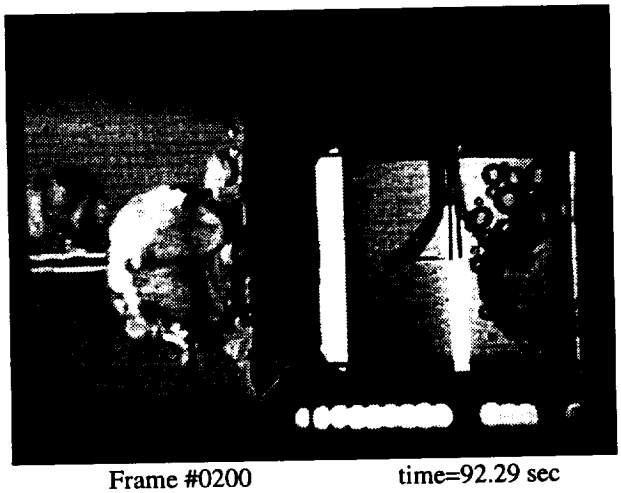

Frame #0200 time=92.29 sec

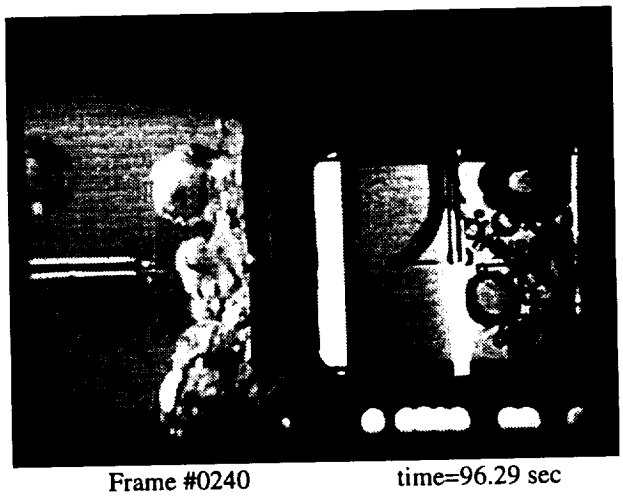

Frame #0240 time=96.29 sec

Figure A-6i. Continued.

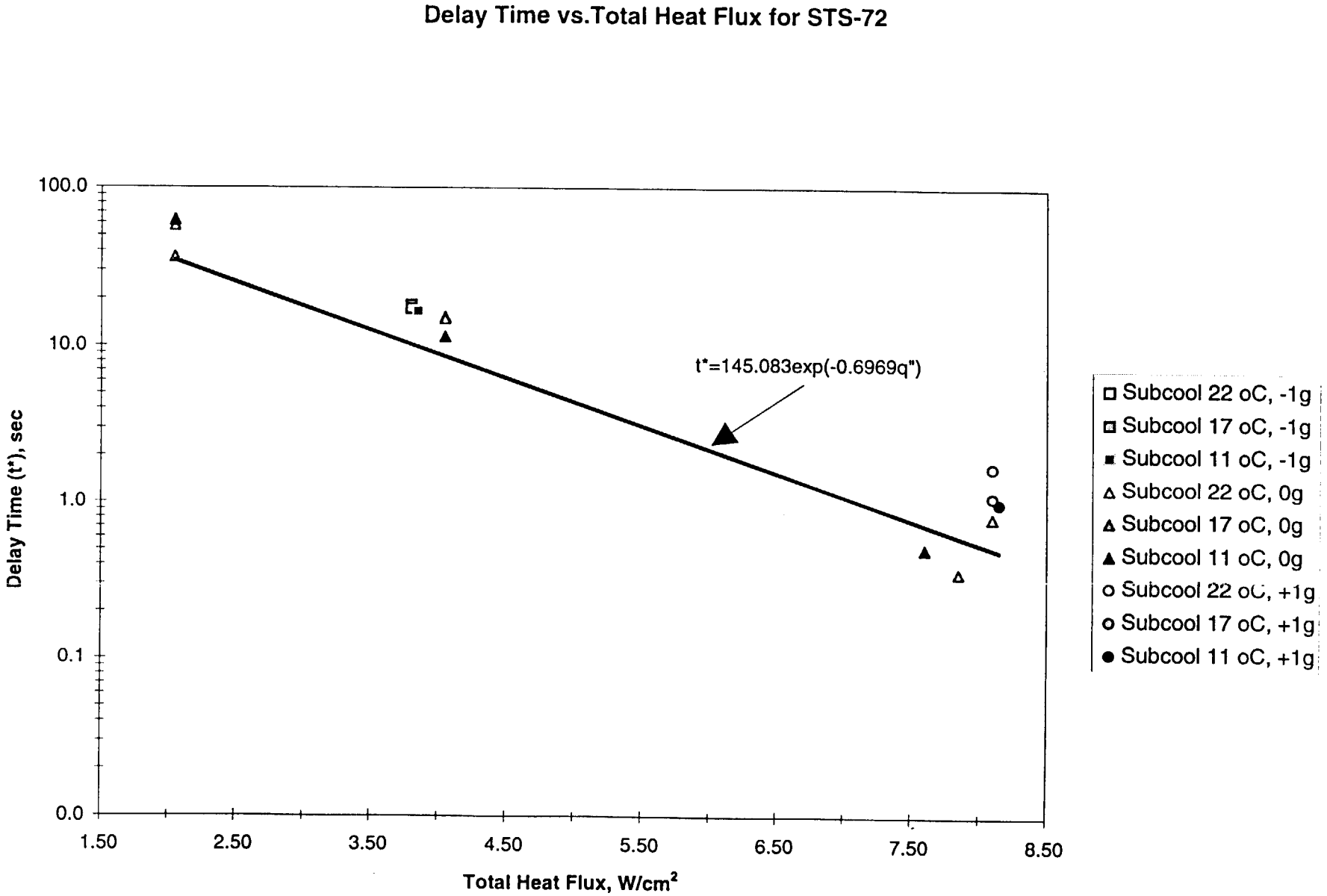

Figure A-7. Nucleation Delay Time. Comparisons with ground testing and drop tower correlation. PBE-IIB (STS-72).

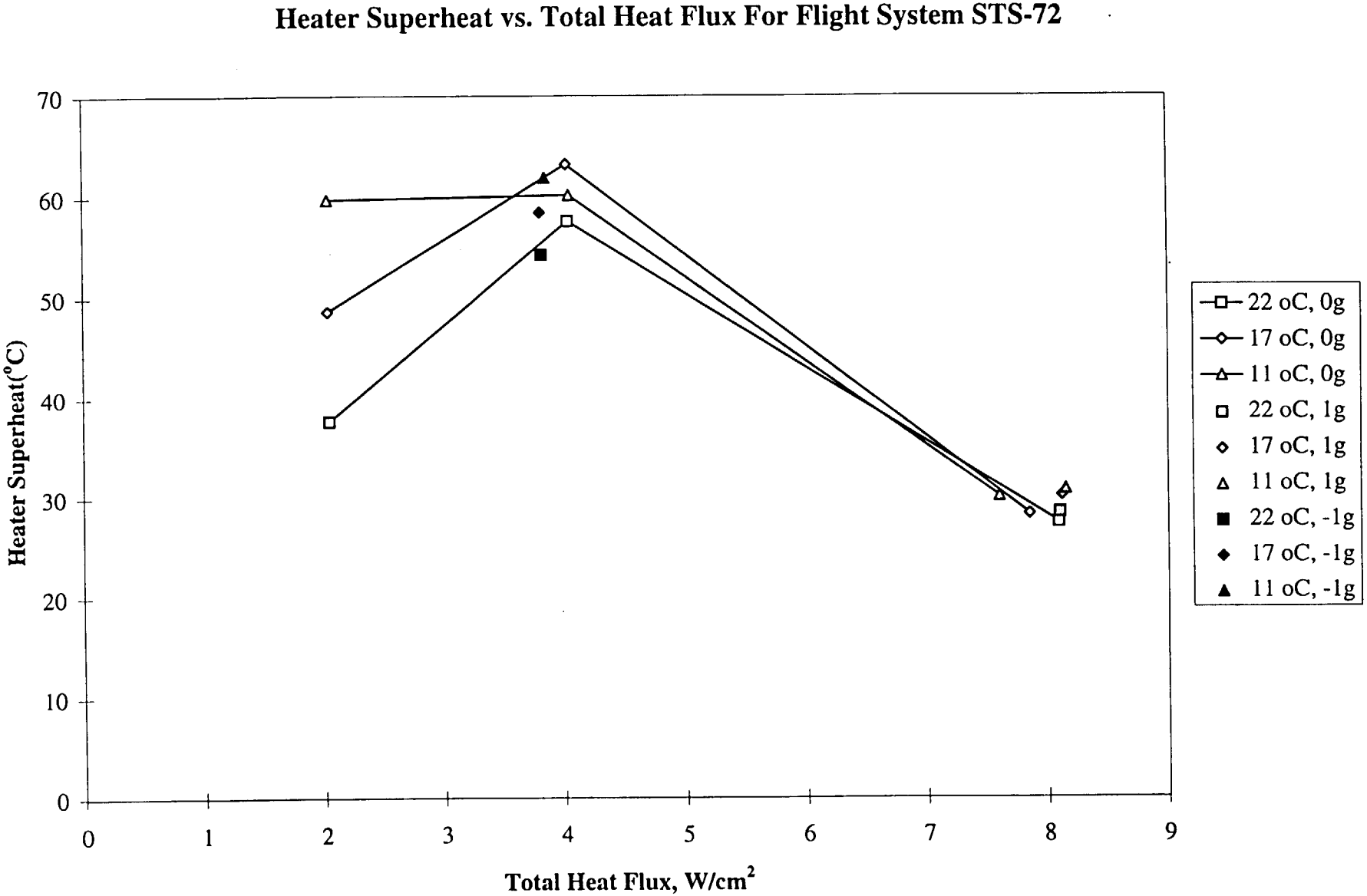

Figure A-8. Mean heater surface nucleation superheat. Comparisons with ground testing. PBE-IIB (STS-72).

STS-72 - Dry spot calculation

Run #	10 FPS	100FPS	Nucleation	Range	Rate	otal # fram	Analysis of frames	Notes	ata Storag
1	15 to 70	10 to 15	10.81	35 to 45	10 fps	100	100		OD6-B
2	25 to 100	15 to 25	25.44	30 to 50	10 fps	200	200		OD6-B
				65 to 95	10 fps	300	300		
3	50 to 120	30 to 50	46.41	80 to 110	10 fps	300	300		OD6-B
4	15 to 55	10 to 15	10.36	30 to 40	10 fps	100	100		OD6-B
5	25 to 100	15 to 25	25.02	40 to 60	10 fps	200	200		OD6-B
				80 to 85	10 fps	50	50		
6	50 to 95	30 to 50	67.64	nuc to 80	10 fps	124	124		OD6-B
7	15 to 40	10 to 15	10.51						
8	25 to 70	15 to 25	21.50	nuc to 33	both	430	115		OD6-B
				50 to 60	10 fps	100	100		
9	50 to 115	30 to 50	72.39	nuc to 95	10 fps	230	230		OD6-B

NOTE: All times are relative to zero. Heater power is activated at 10 seconds.

Table A-IV. Index for heater surface dry fraction measurements and computation of microgravity nucleate boiling heat transfer coefficients. PBE-IIB (STS-72).

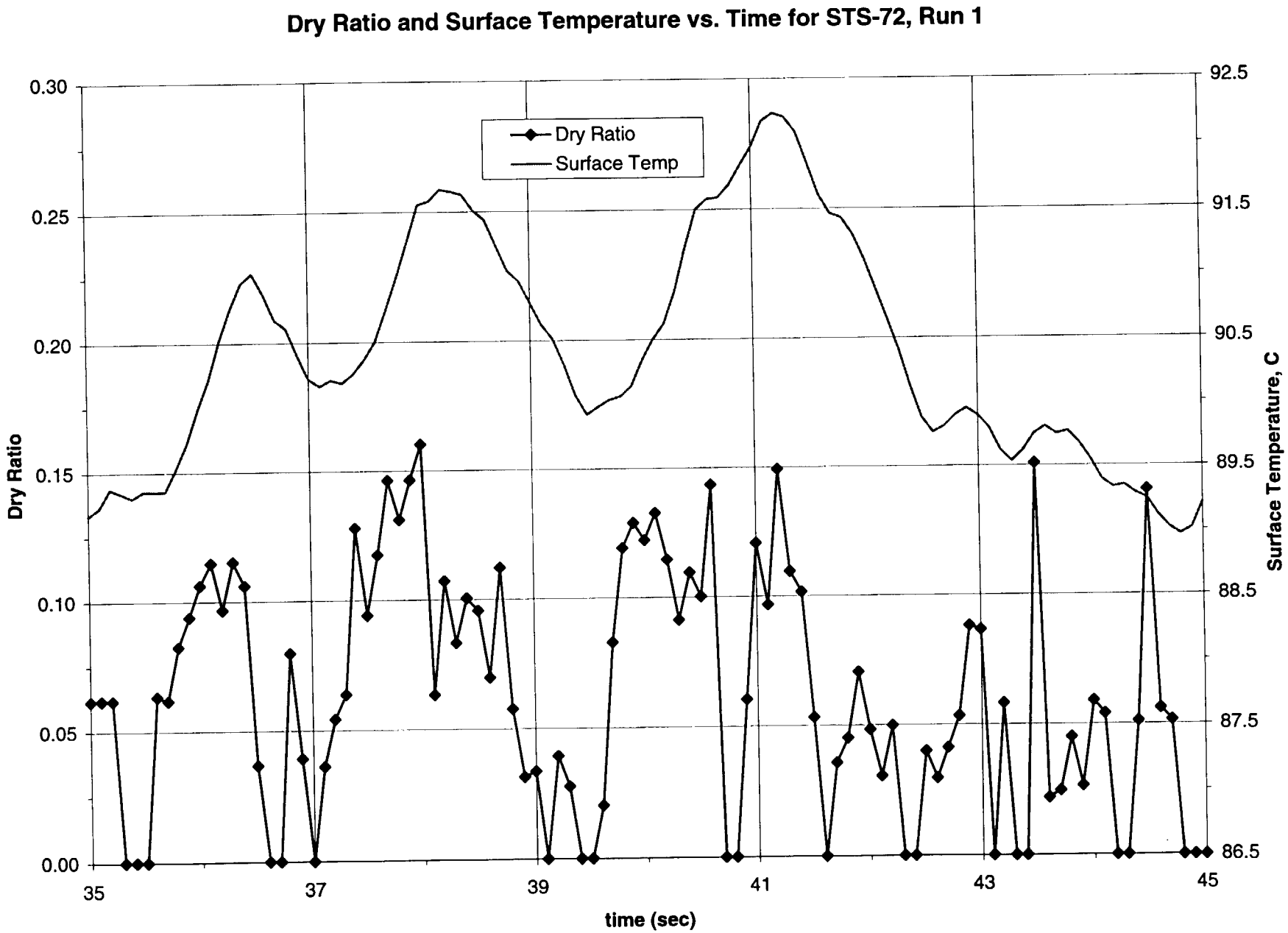

Figure A-10a-1-i. Heater surface dry fraction and mean temperature. PBE-IIB (STS-72). Run No. 1. Time interval: 35.0 - 45.0 seconds.

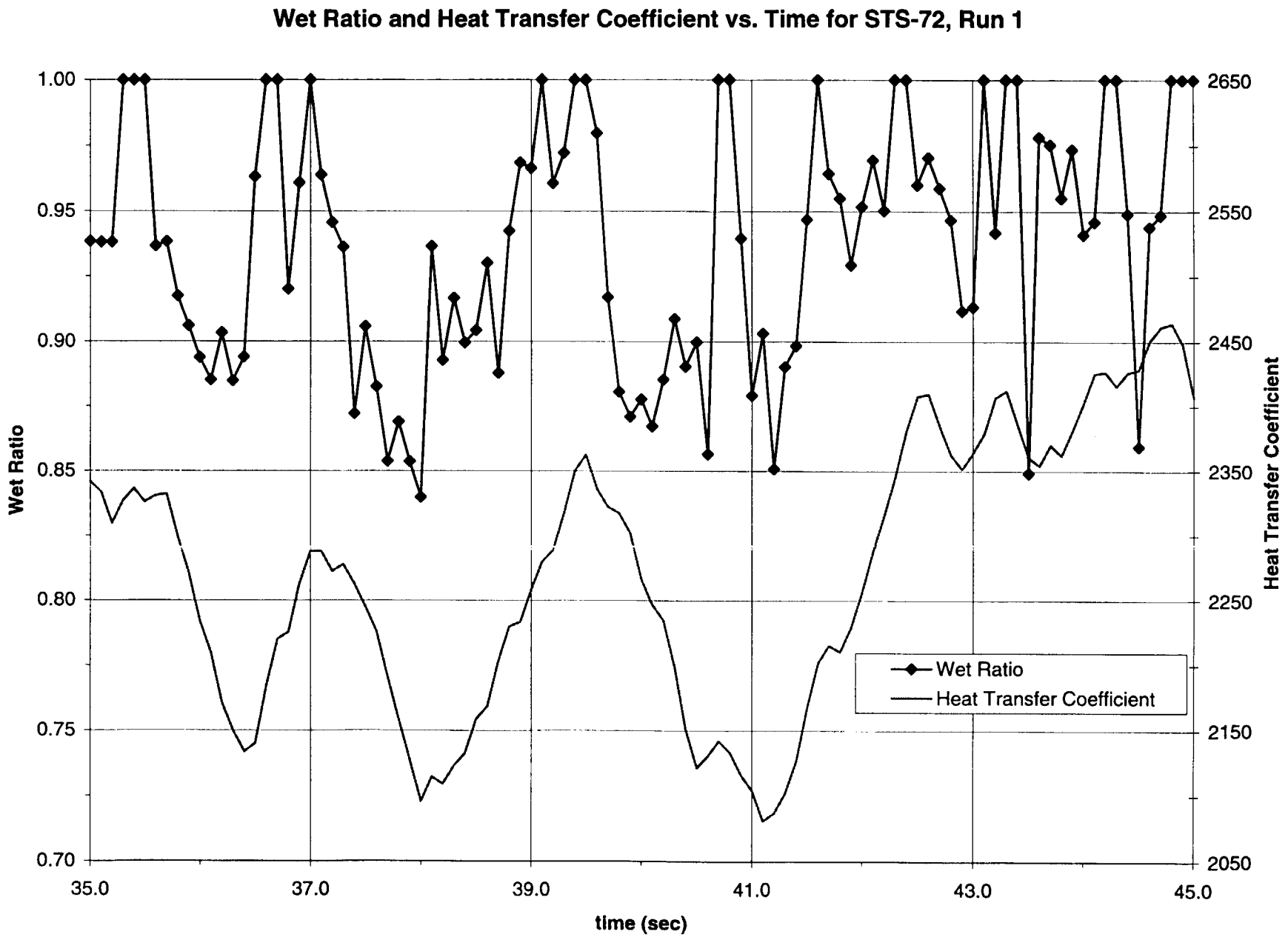

Figure A-10a-1-ii. Heater surface wet fraction and mean heat transfer coefficients. PBE-IIB (STS-72). Run No. 1. Time interval: 35.0 - 45.0 seconds.

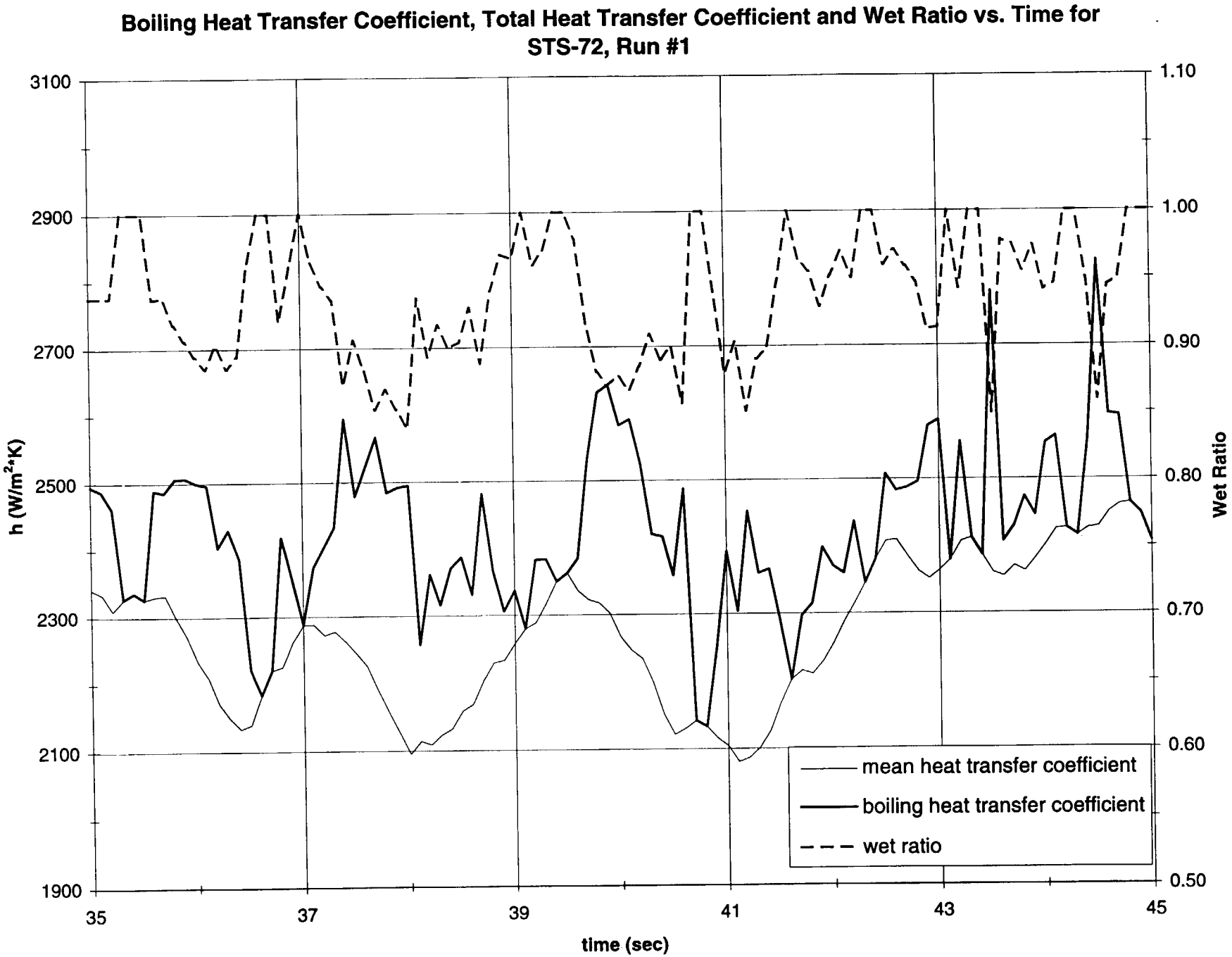

Figure A-10a-1-iii. Development of microgravity boiling heat transfer coefficient. PBE-IIB (STS-72). Run No. 1. Time interval: 35.0 - 45.0 seconds.

STS-72 Run #1

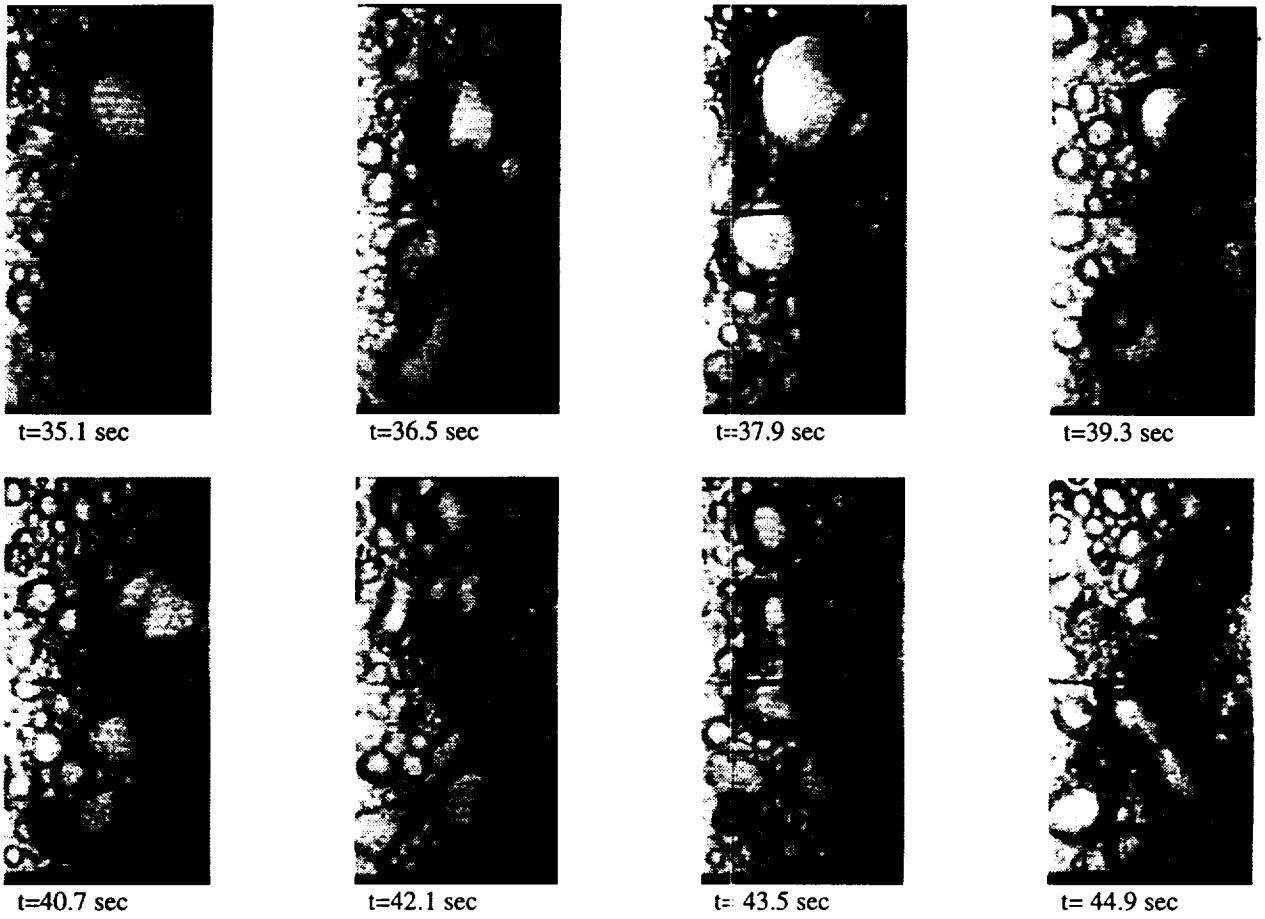

Figure A-10a-1-iv. Sample images showing dryout/rewetting. PBE-IIB (STS-72). Run No. 1. Time interval: 35.0 - 45.0.

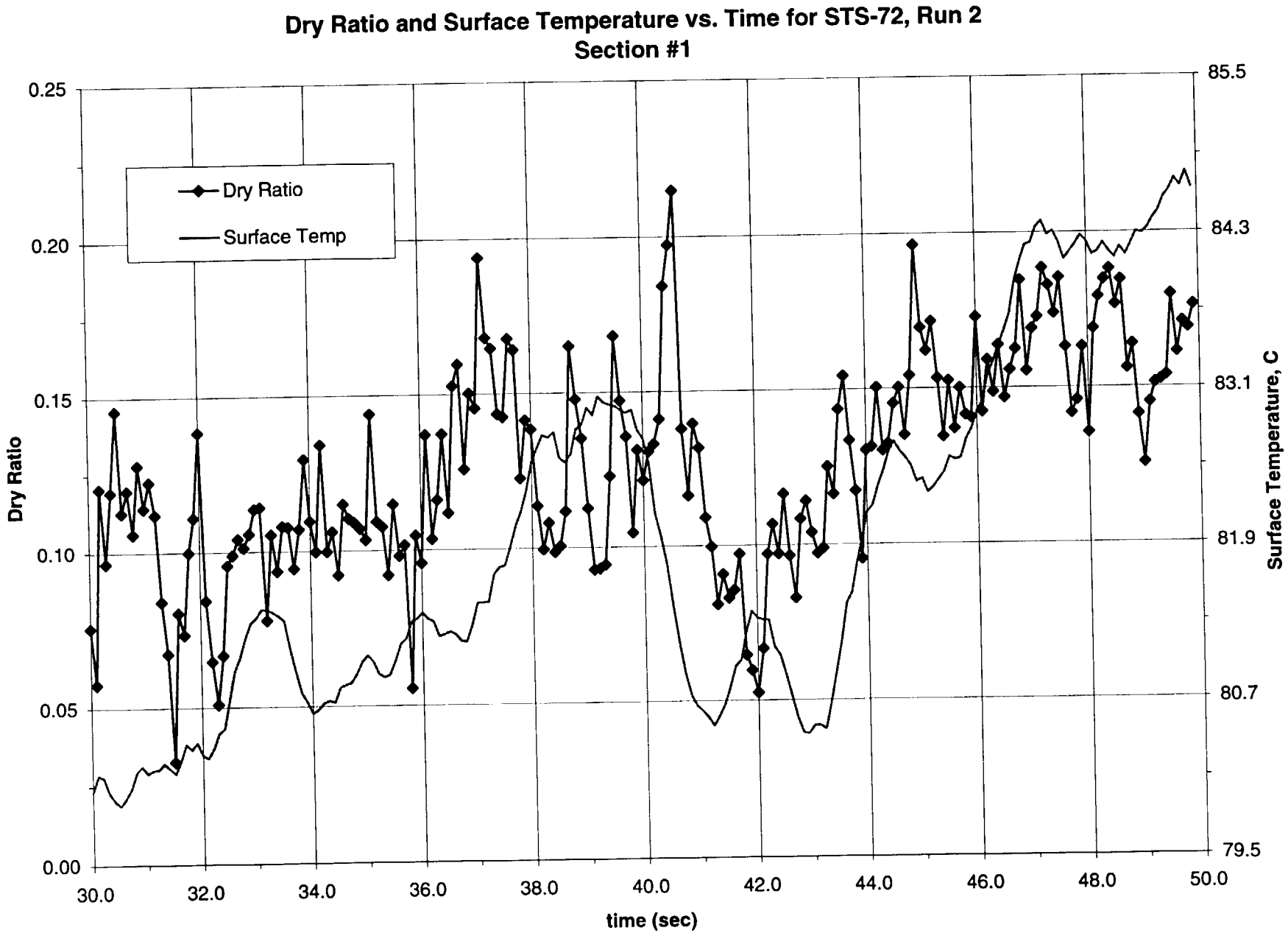

Figure A-10b-1-i. Heater surface dry fraction and mean temperature. PBE-IIB (STS-72). Run No. 2. Time interval: 30.0 - 50.0 seconds.

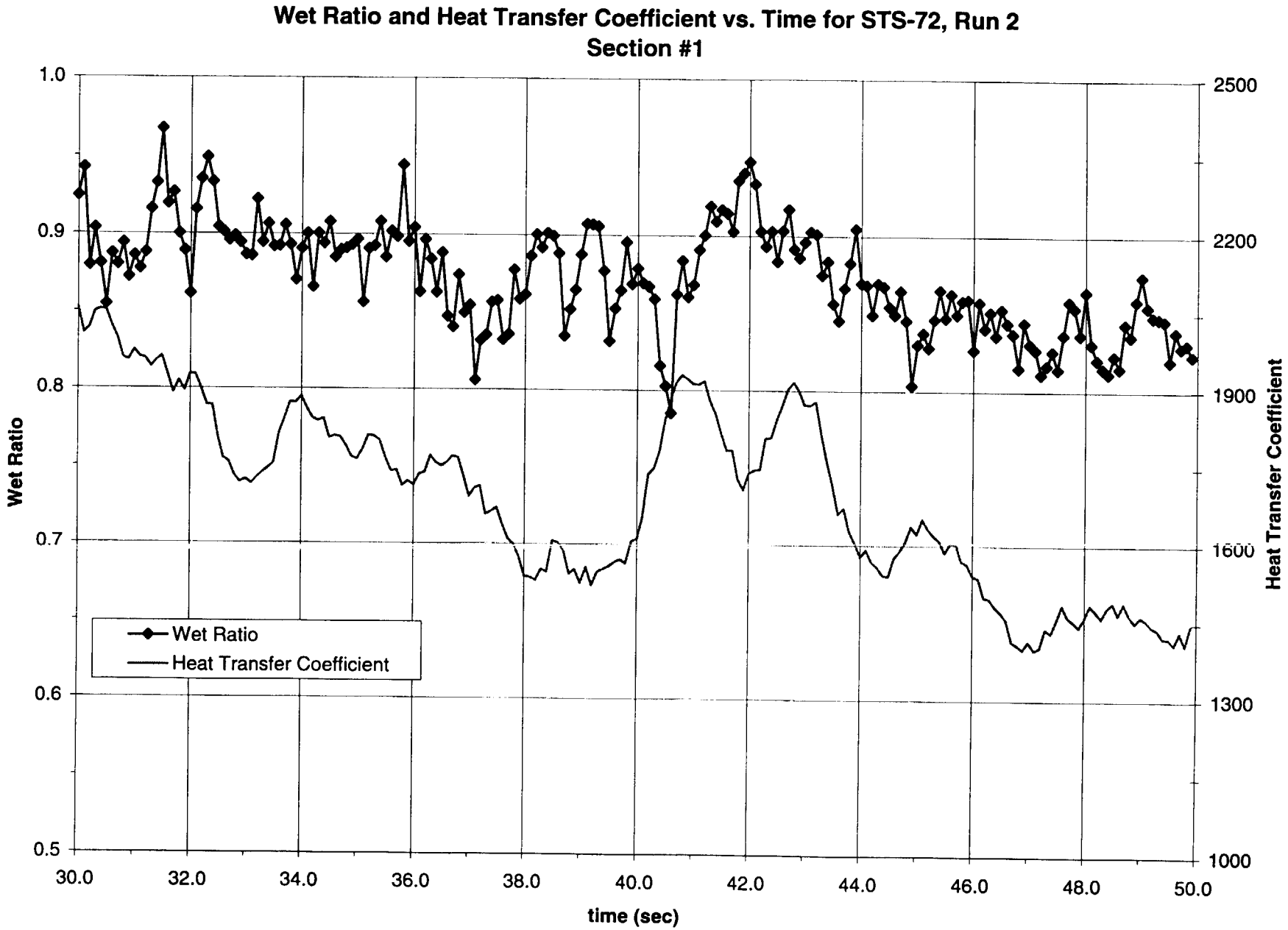

Figure A-10b-1-ii. Heater surface wet fraction and mean heat transfer coefficients. PBE-IIB (STS-72). Run No. 2. Time interval: 30.0 - 50.0 seconds.

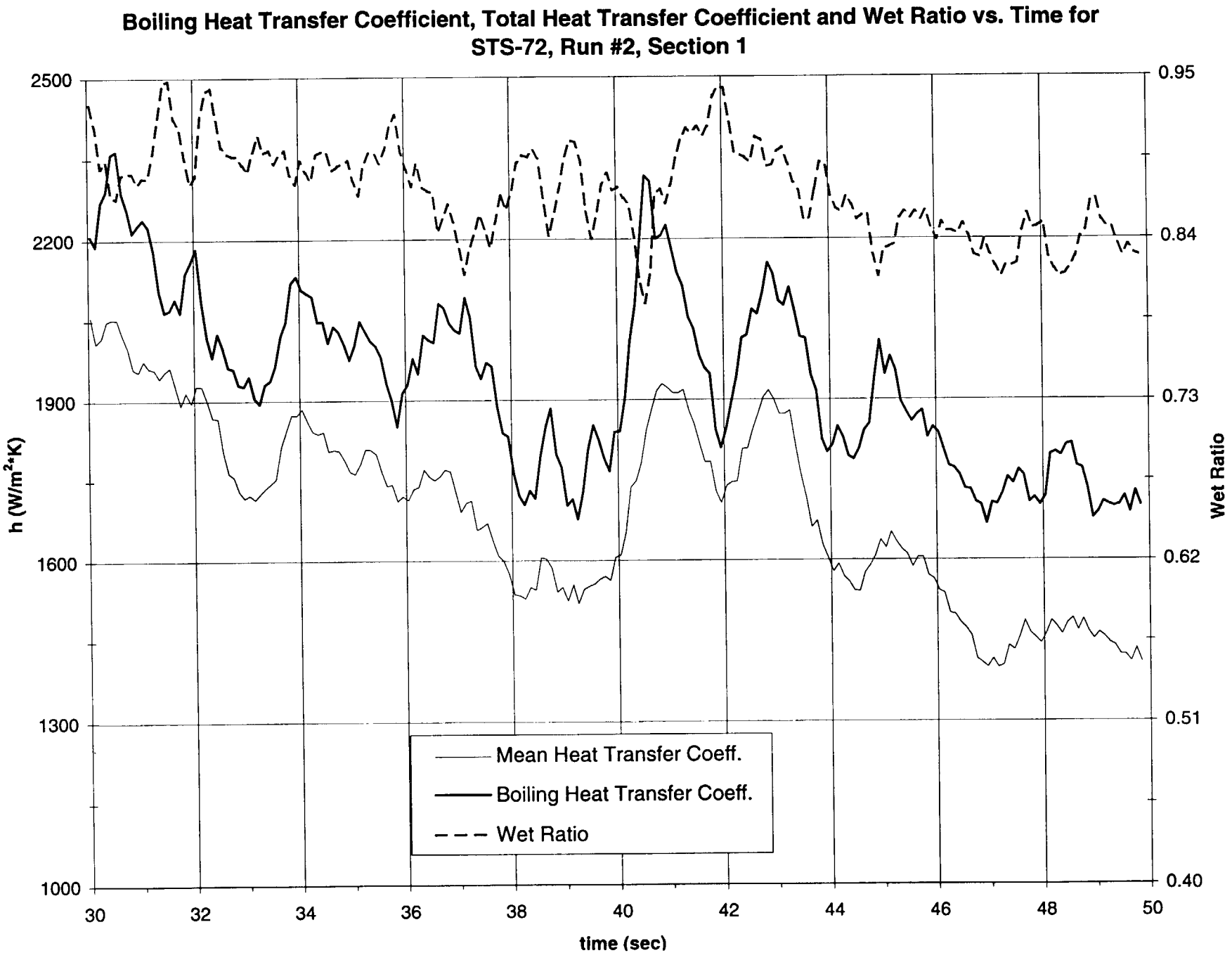

Figure A-10b-1-iii. Development of microgravity boiling heat transfer coefficient. PBE-IIB (STS-72). Run No. 2. Time interval: 30.0 - 50.0 seconds.

STS-72 Run #2, Section #1

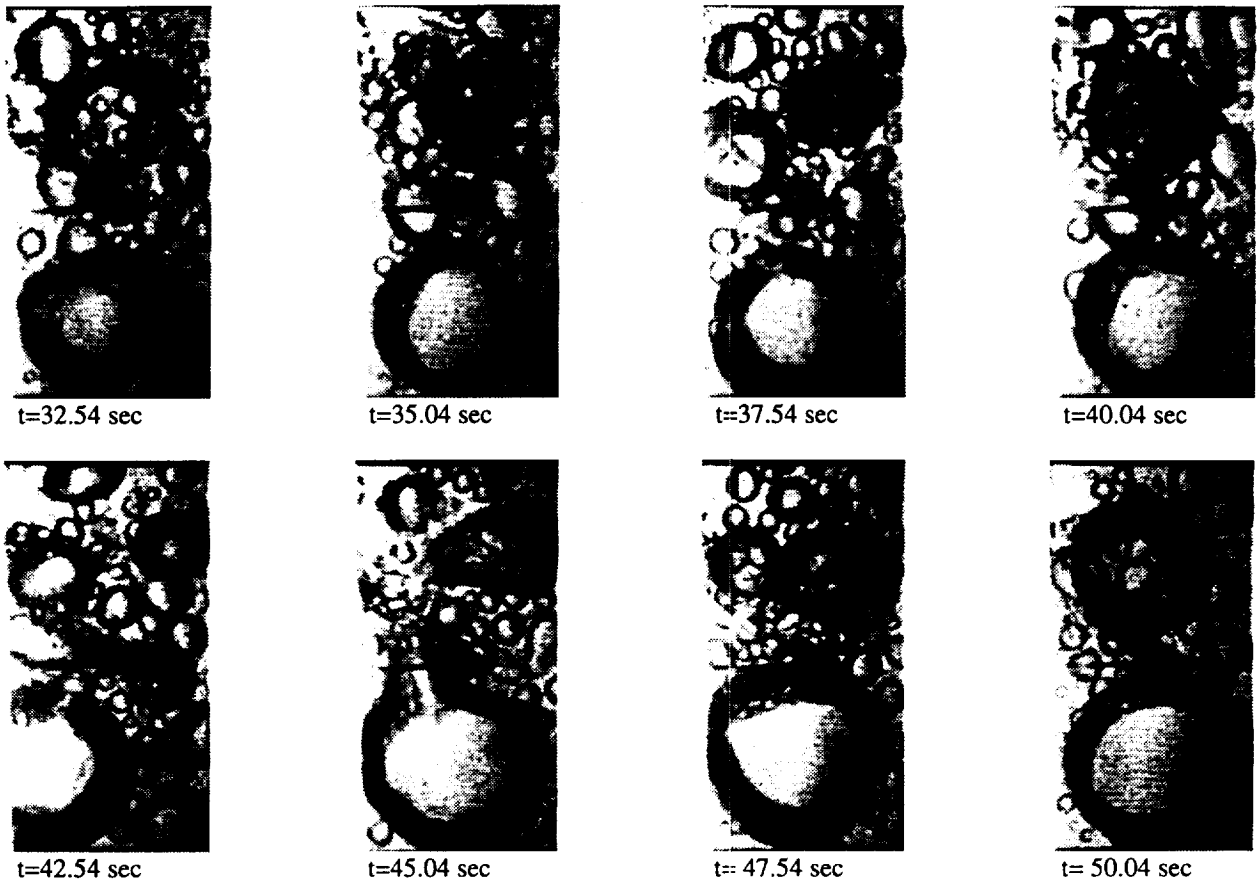

Figure A-10b-1-iv. Sample images showing dryout/rewetting. PBE-IIB (STS-72). Run No. 2. Time interval: 30.0 - 50.0 seconds.

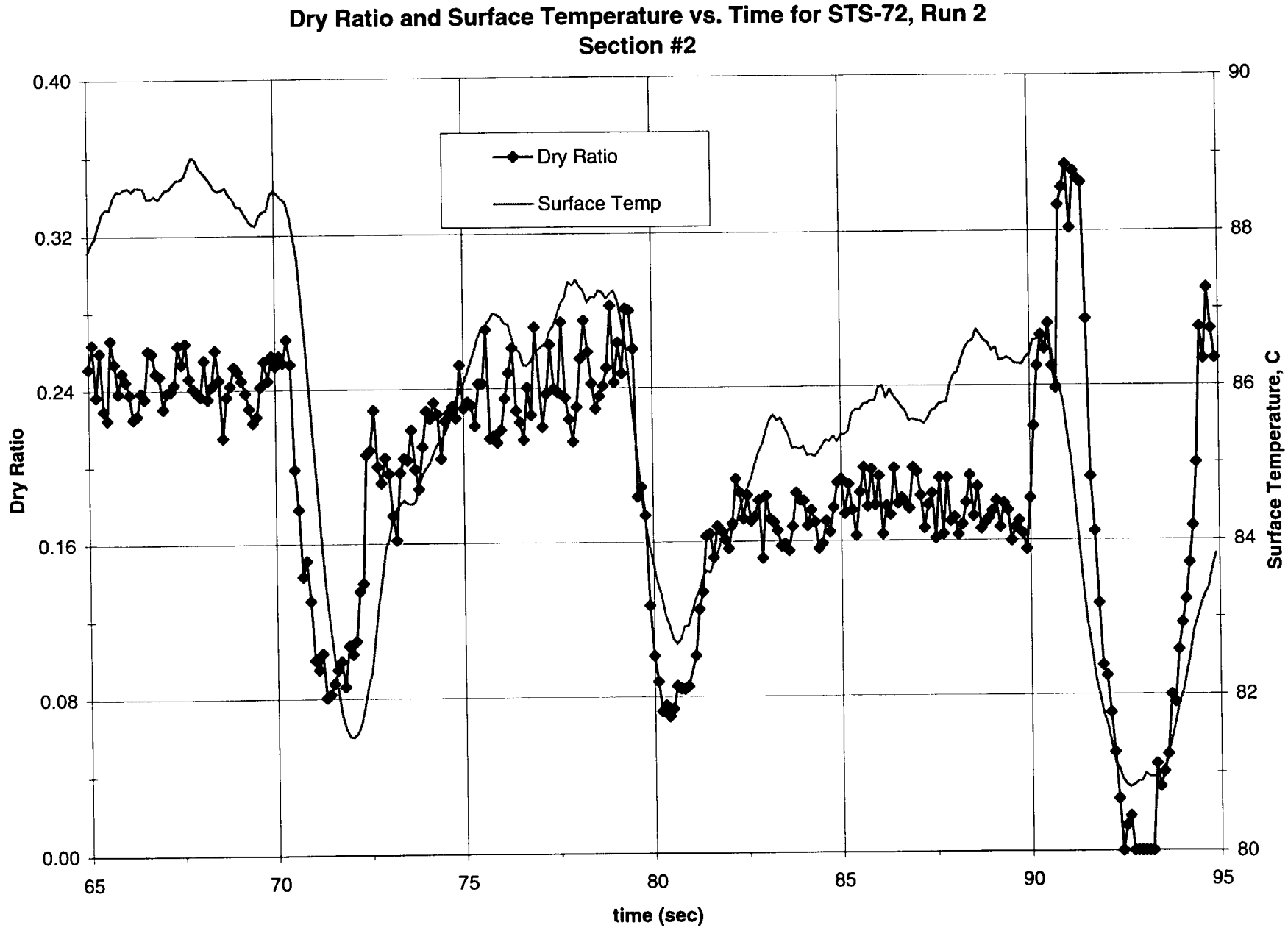

Figure A-10b-2-i. Heater surface dry fraction and mean temperature. PBE-IIB (STS-72). Run No. 2. Time interval: 65 - 95 seconds.

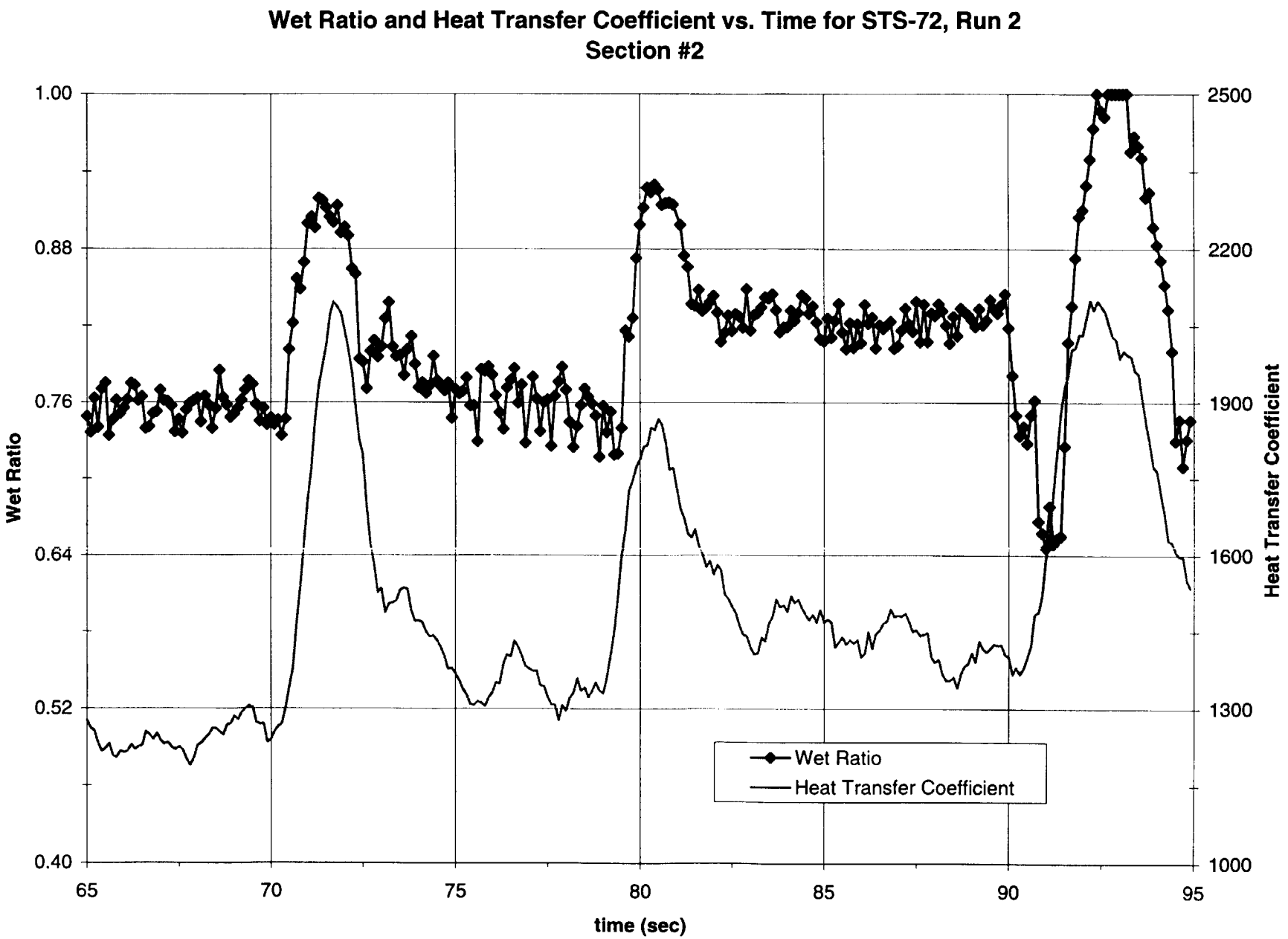

Figure A-10b-2-ii. Heater surface wet fraction and mean heat transfer coefficients. PBE-IIB (STS-72). Run No. 2. Time interval: 65 - 95 seconds.

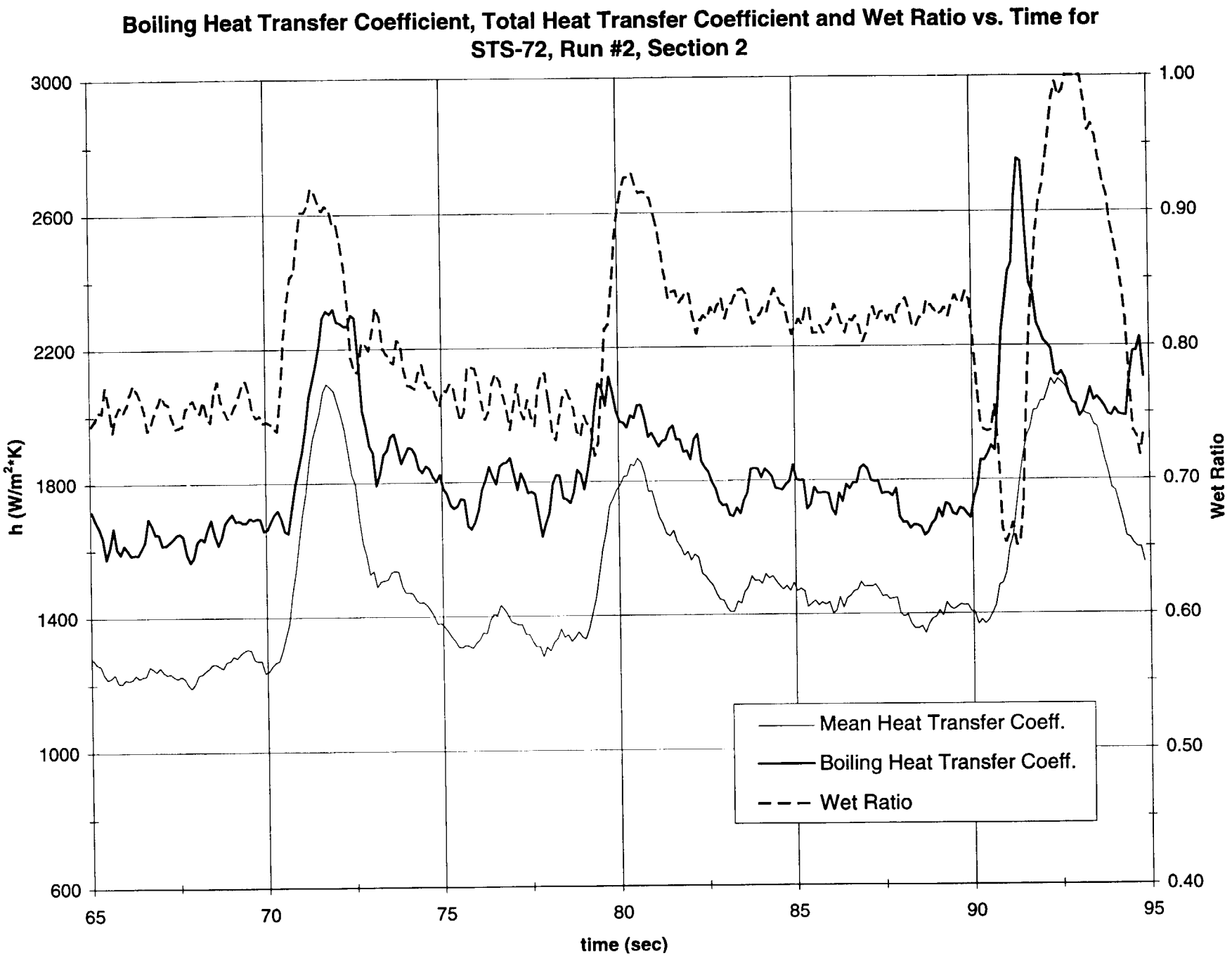

Figure A-10b-2-iii. Development of microgravity boiling heat transfer coefficient. PBE-IIB (STS-72). Run No. 2. Time interval: 65 - 95 seconds.

STS-72 Run #2, Section #2

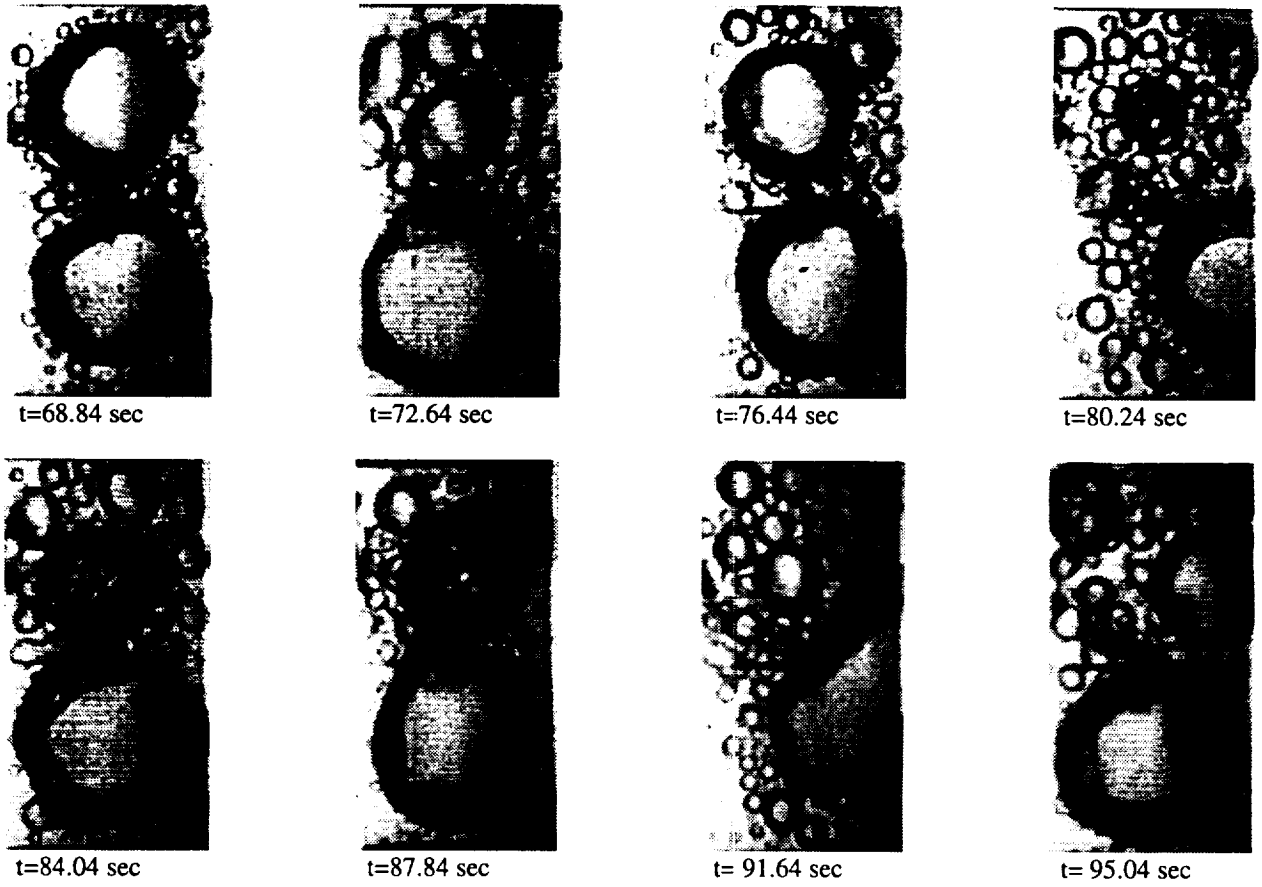

Figure A-10b-2-iv. Sample images showing dryout/rewetting. PBE-IIB (STS-72). Run No. 2. Time interval: 65 - 95 seconds.

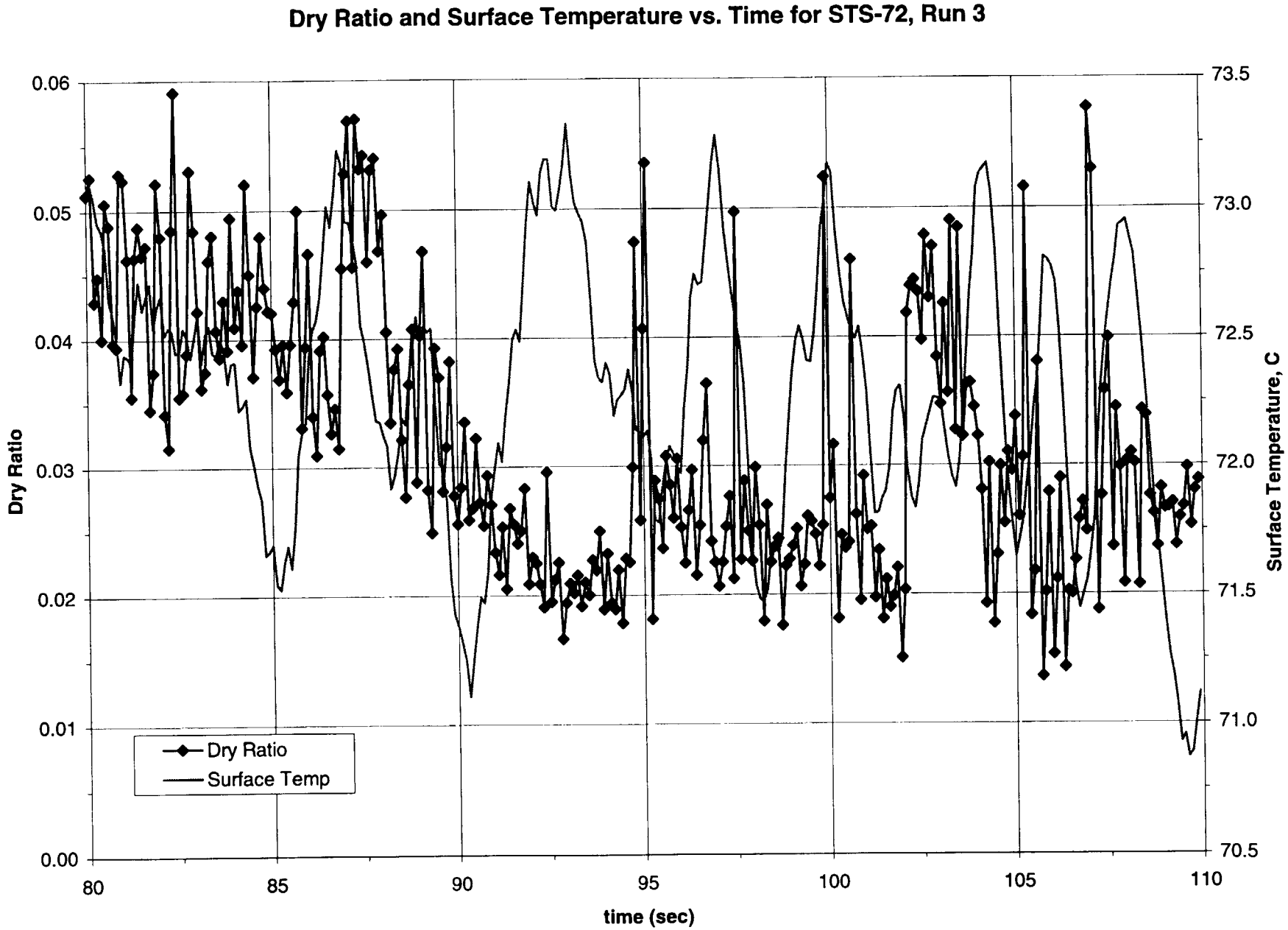

Figure A-10c-1-i. Heater surface dry fraction and mean temperature. PBE-IIB (STS-72). Run No. 3. Time interval: 80 - 110 seconds.

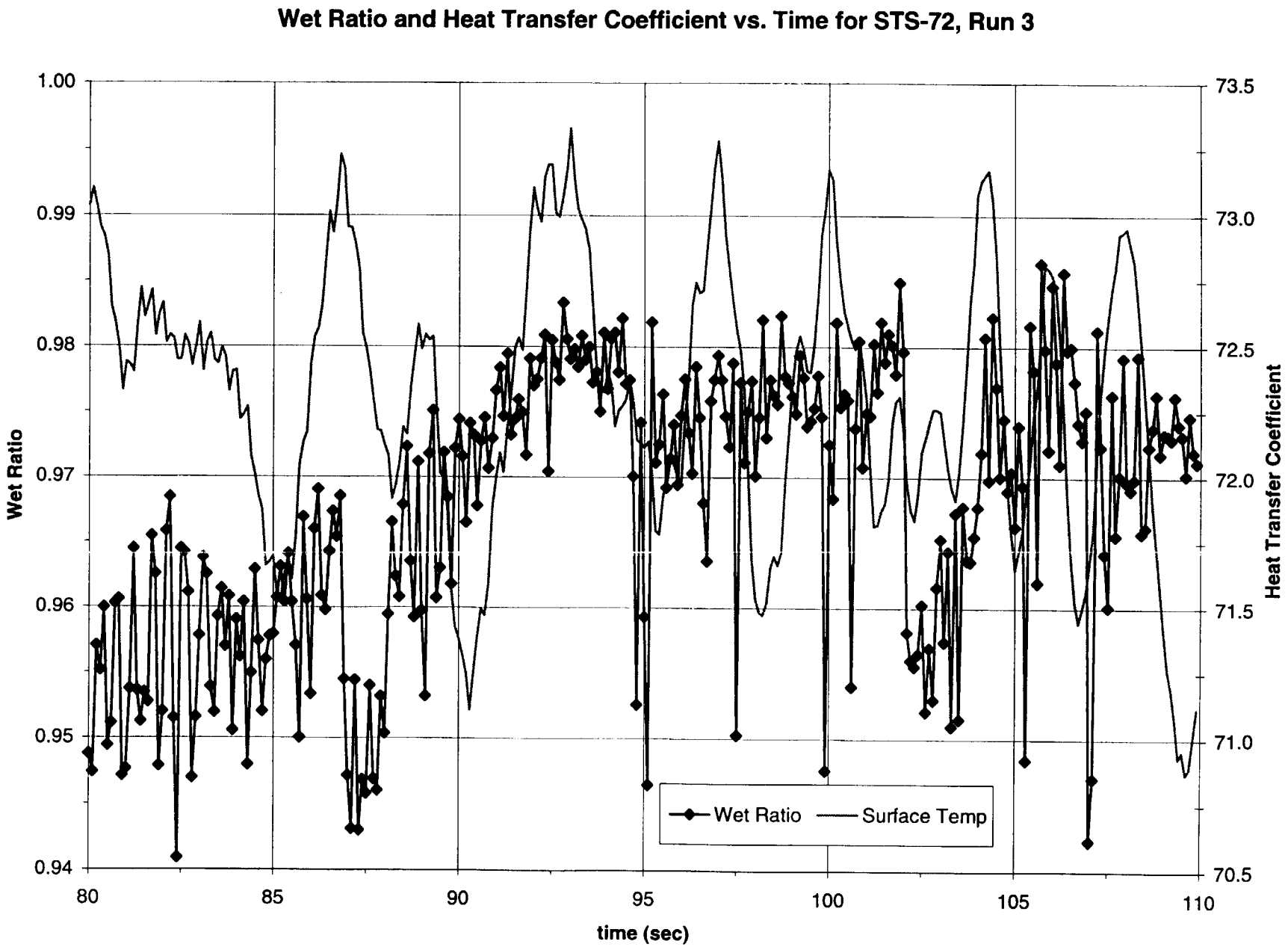

Figure A-10c-1-ii. Heater surface wet fraction and mean heat transfer coefficients. PBE-IIB (STS-72). Run No. 3. Time interval: 80 - 110 seconds.

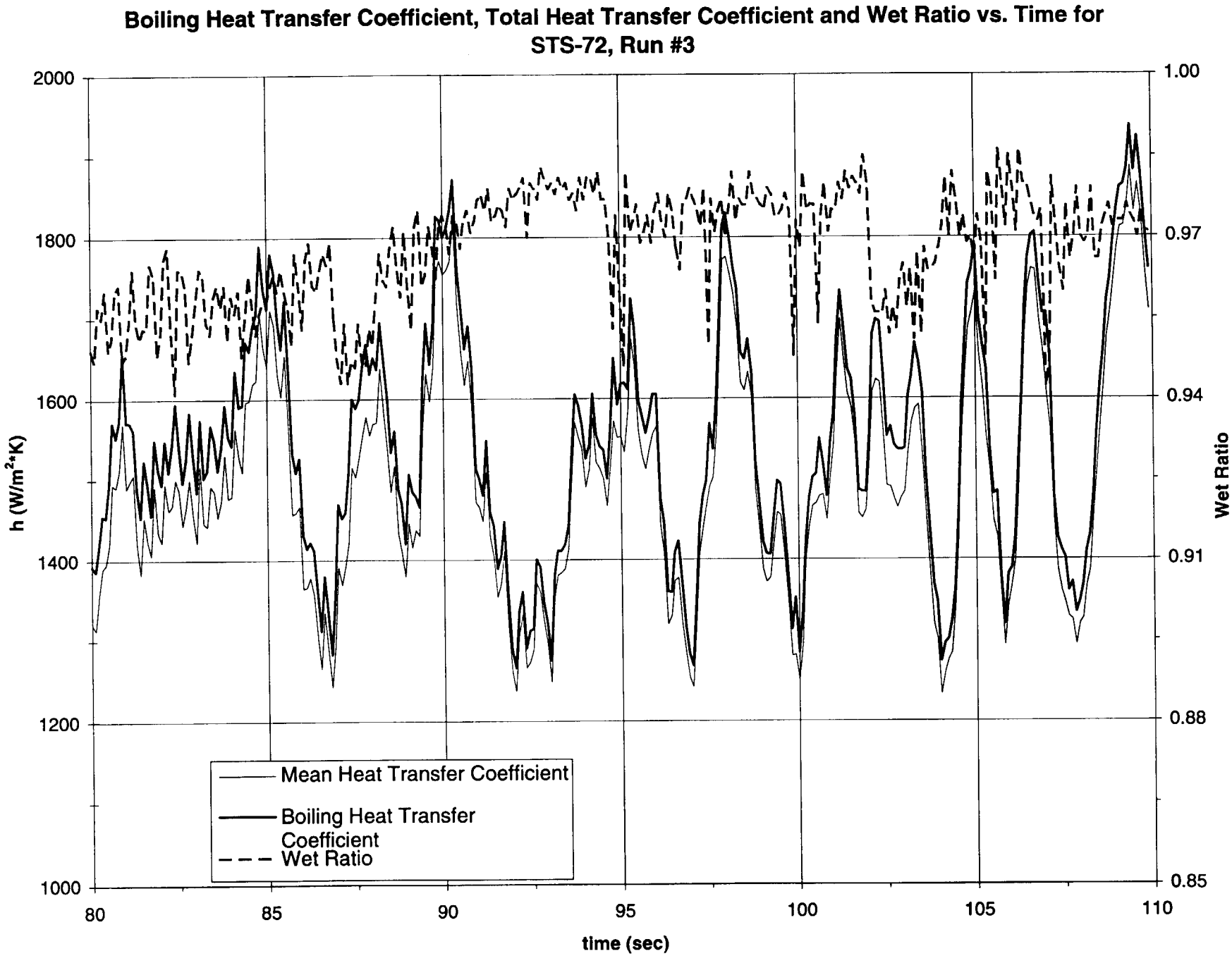

Figure A-10c-1-iii. Development of microgravity boiling heat transfer coefficient. PBE-IIB (STS-72). Run No. 3. Time interval: 80 - 110 seconds.

STS-72 Run #3

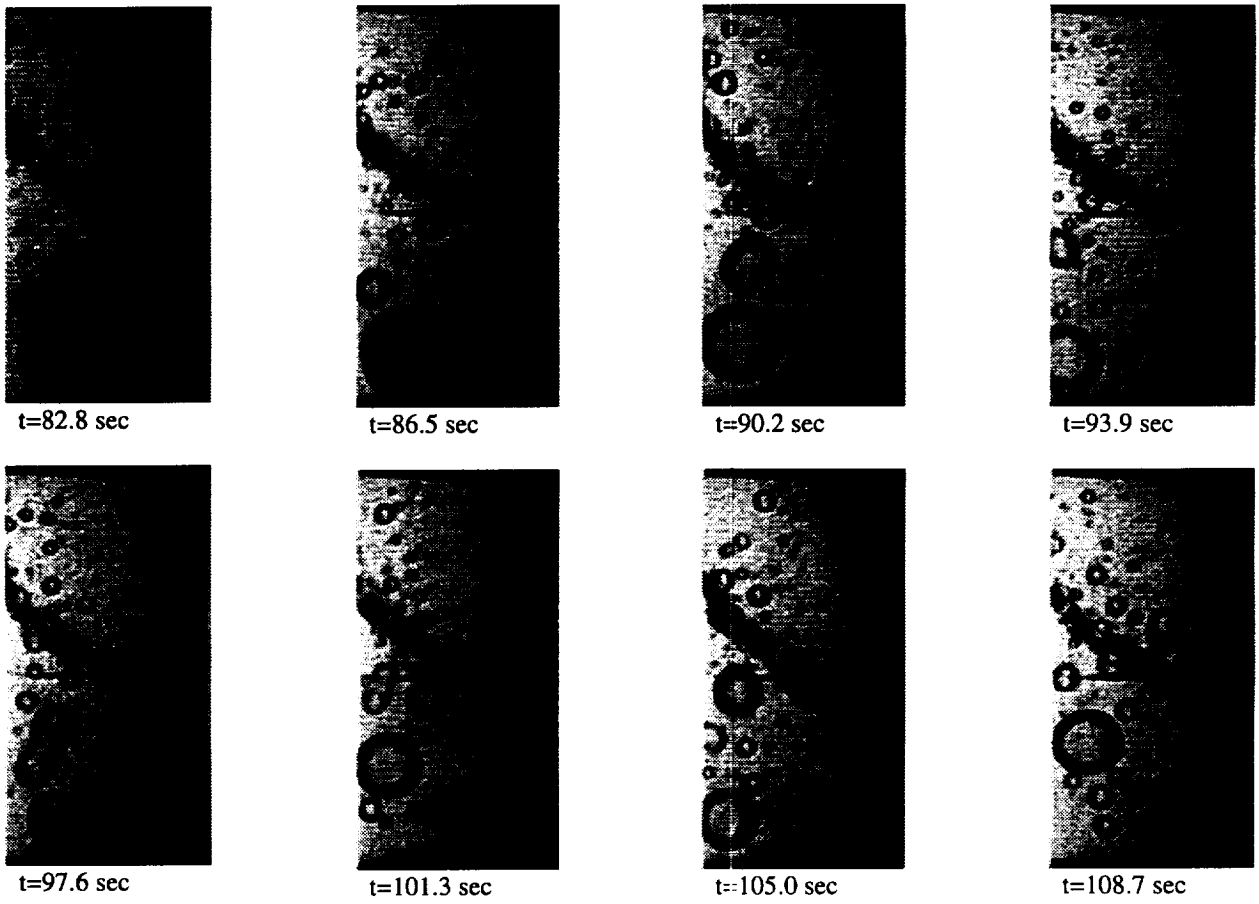

Figure A-10c-1-iv. Sample images showing dryout/rewetting. PBE-IIB (STS-72). Run No. 3. Time interval: 80 - 110 seconds.

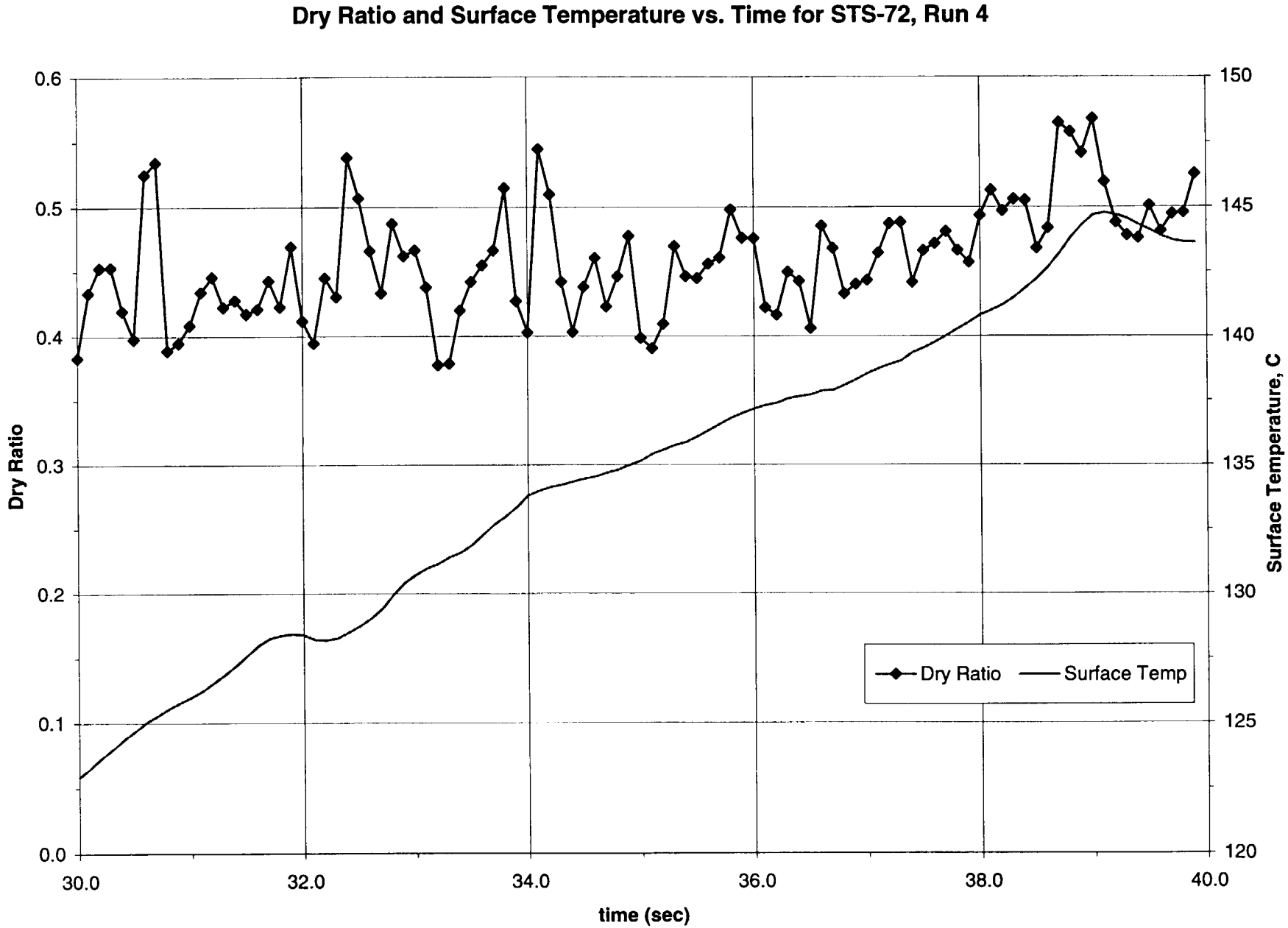

Figure A-10d-1-i. Heater surface dry fraction and mean temperature. PBE-IIB (STS-72). Run. No. 4. Time interval: 30 - 40 seconds.

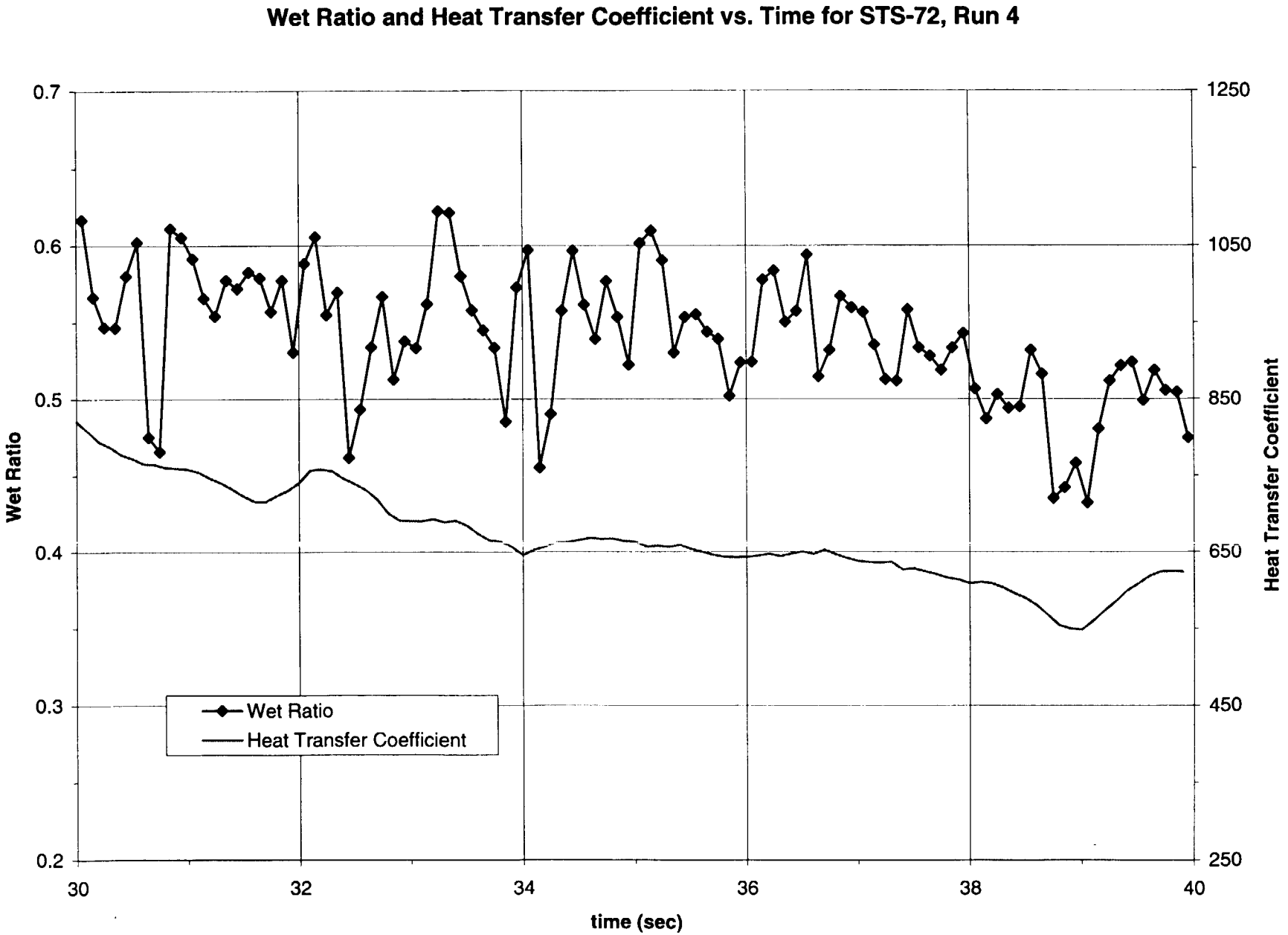

Figure A-10d-1-ii. Heater surface wet fraction and mean heat transfer coefficients. PBE-IIB (STS-72). Run No. 4. Time interval: 30 - 40 seconds.

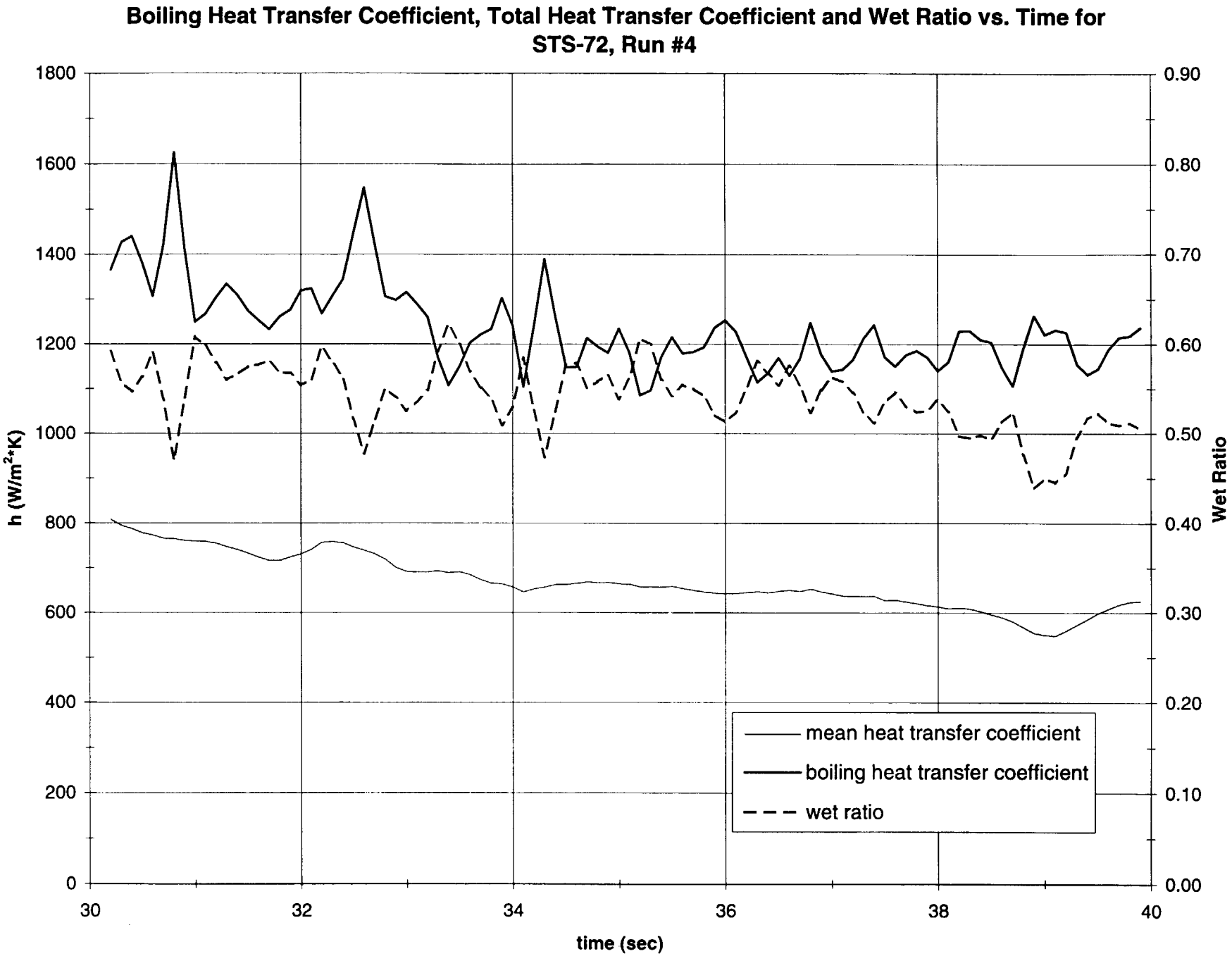

Figure A-10d-1-iii. Development of microgravity boiling heat transfer coefficient. PBE-IIB (STS-72). Run No. 4. Time interval: 30 - 40 seconds.

STS-72 Run #4

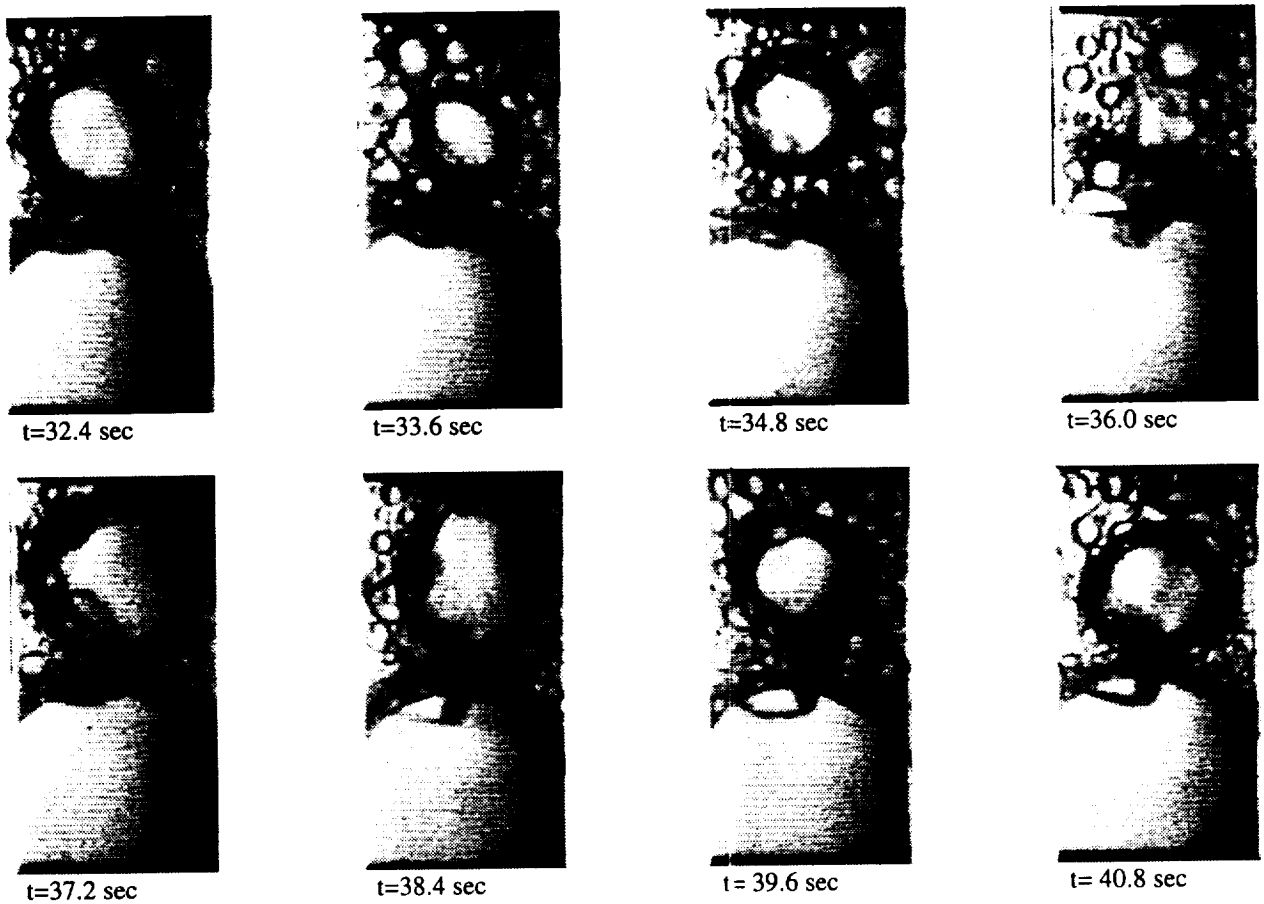

Figure A-10d-1-iv. Sample images showing dryout/rewetting. PBE-IIB (STS-72). Run No. 4. Time interval: 30 - 40 seconds.

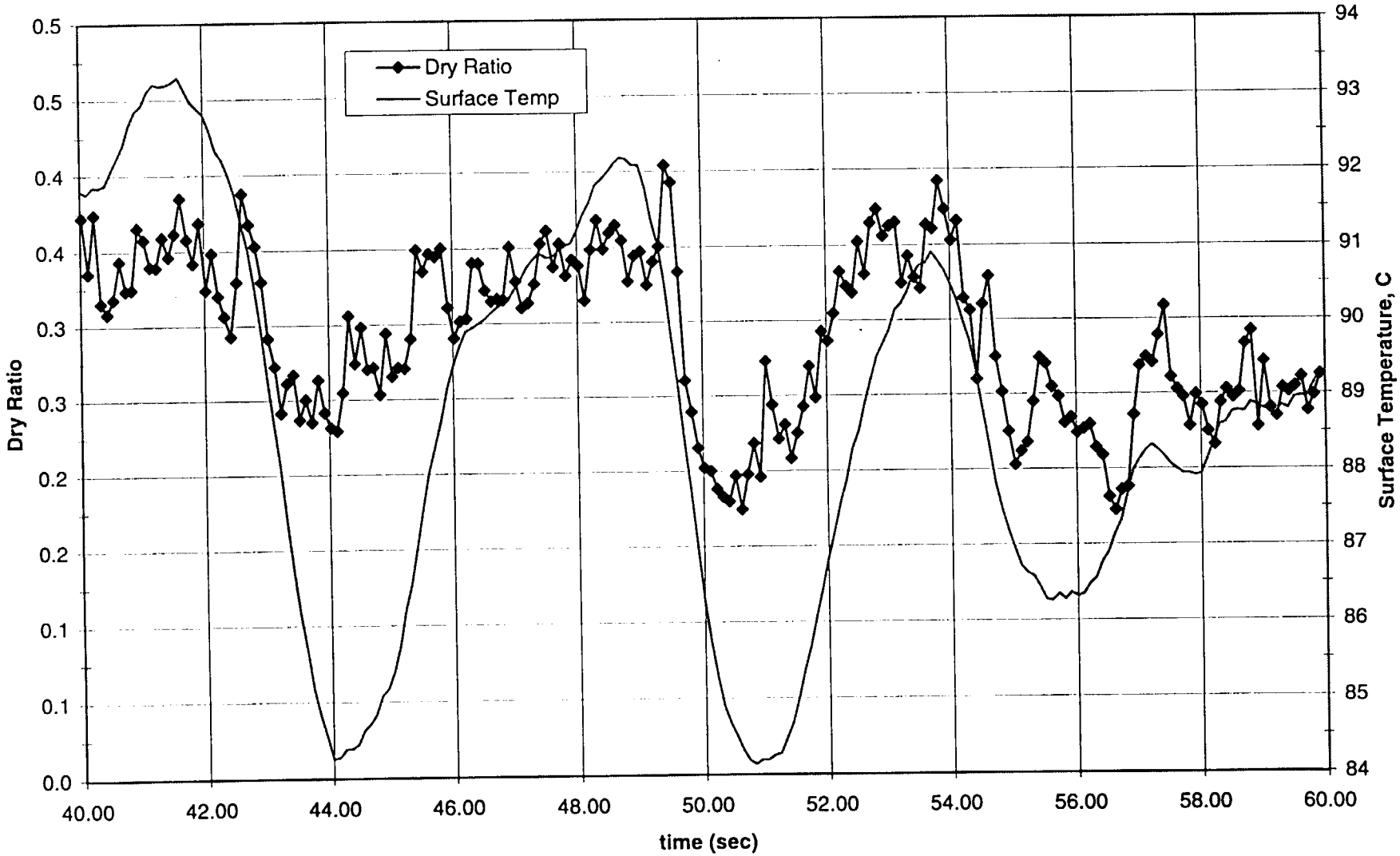

Figure A-10e-1-i. Heater surface dry fraction and mean temperature. PBE-IIB (STS-72). Run No. 5. Time interval: 40 - 60 seconds.

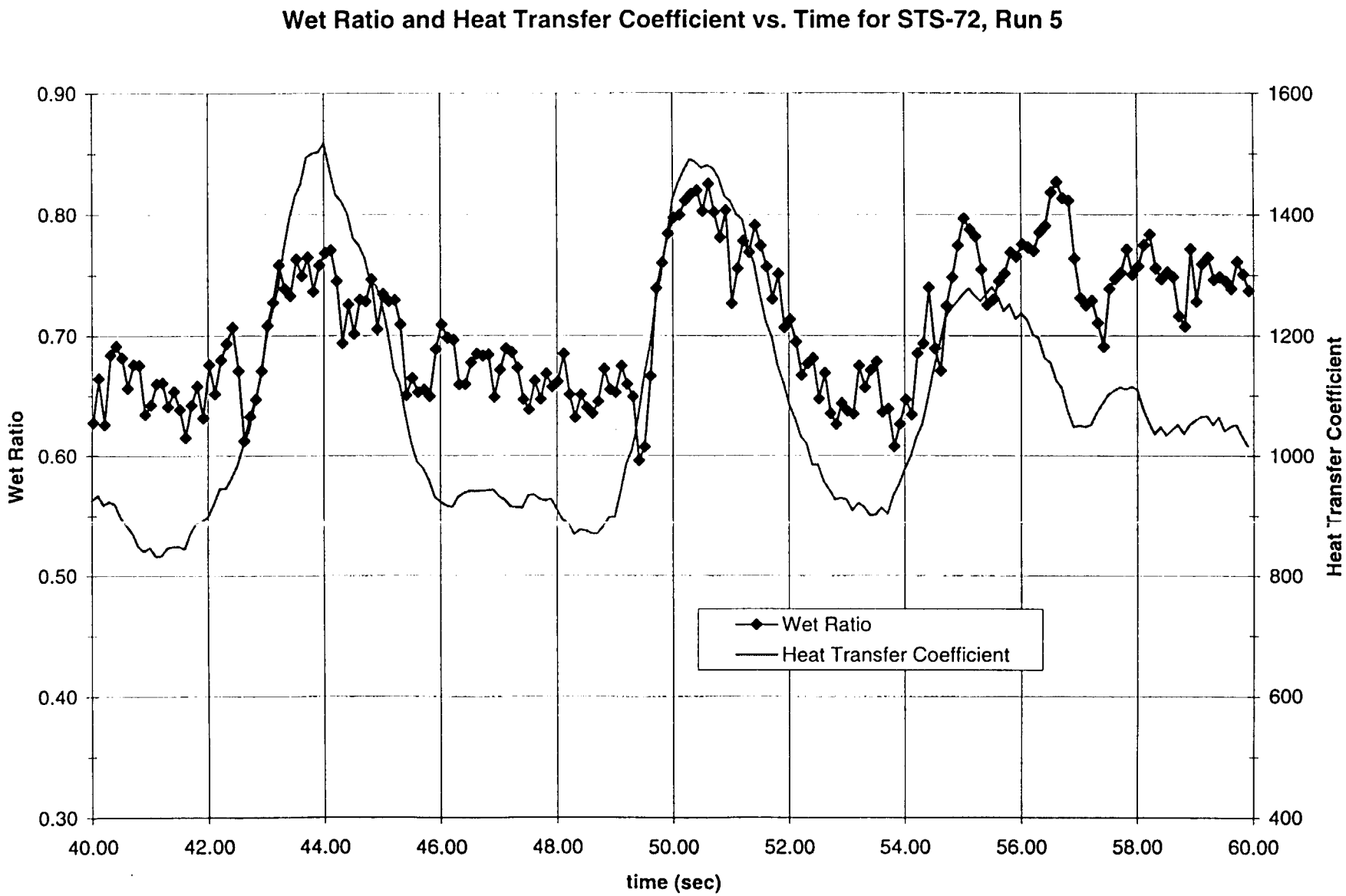

Figure A-10e-1-ii. Heat surface wet fraction and mean heat transfer coefficients. PBE-IIB (STS-72). Run No. 5. Time interval: 40 - 60 seconds.

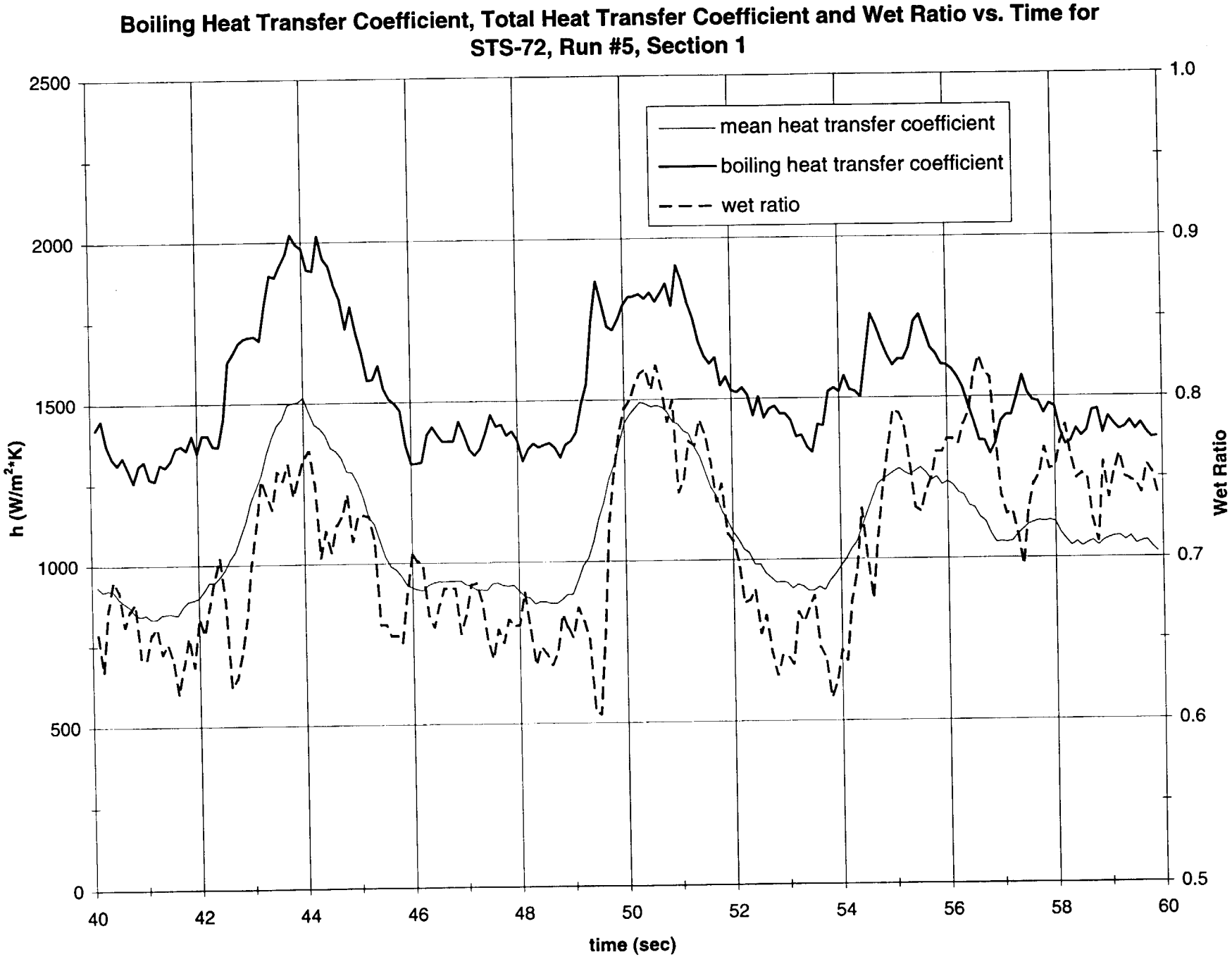

Figure A-10e-1-iii. Development of microgravity boiling heat transfer coefficient. PBE-IIB (STS-72). Run No. 5. Time interval: 40 - 60 seconds.

STS-72 Run #5, Section 1

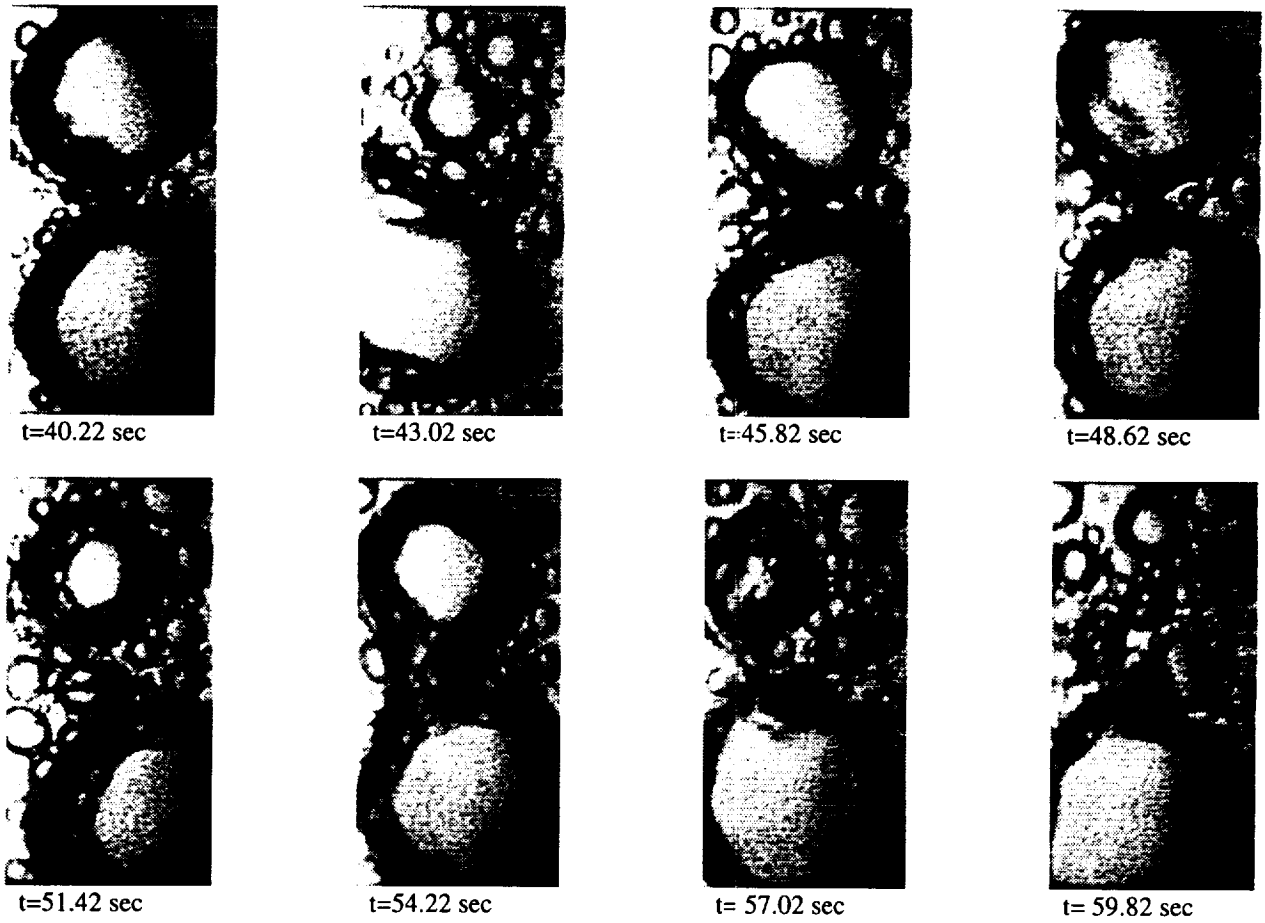

Figure A-10e-1-iv. Sample images showing dryout/rewetting. PBE-IIB (STS-72). Run No. 5. Time Interval: 40 - 60 seconds.

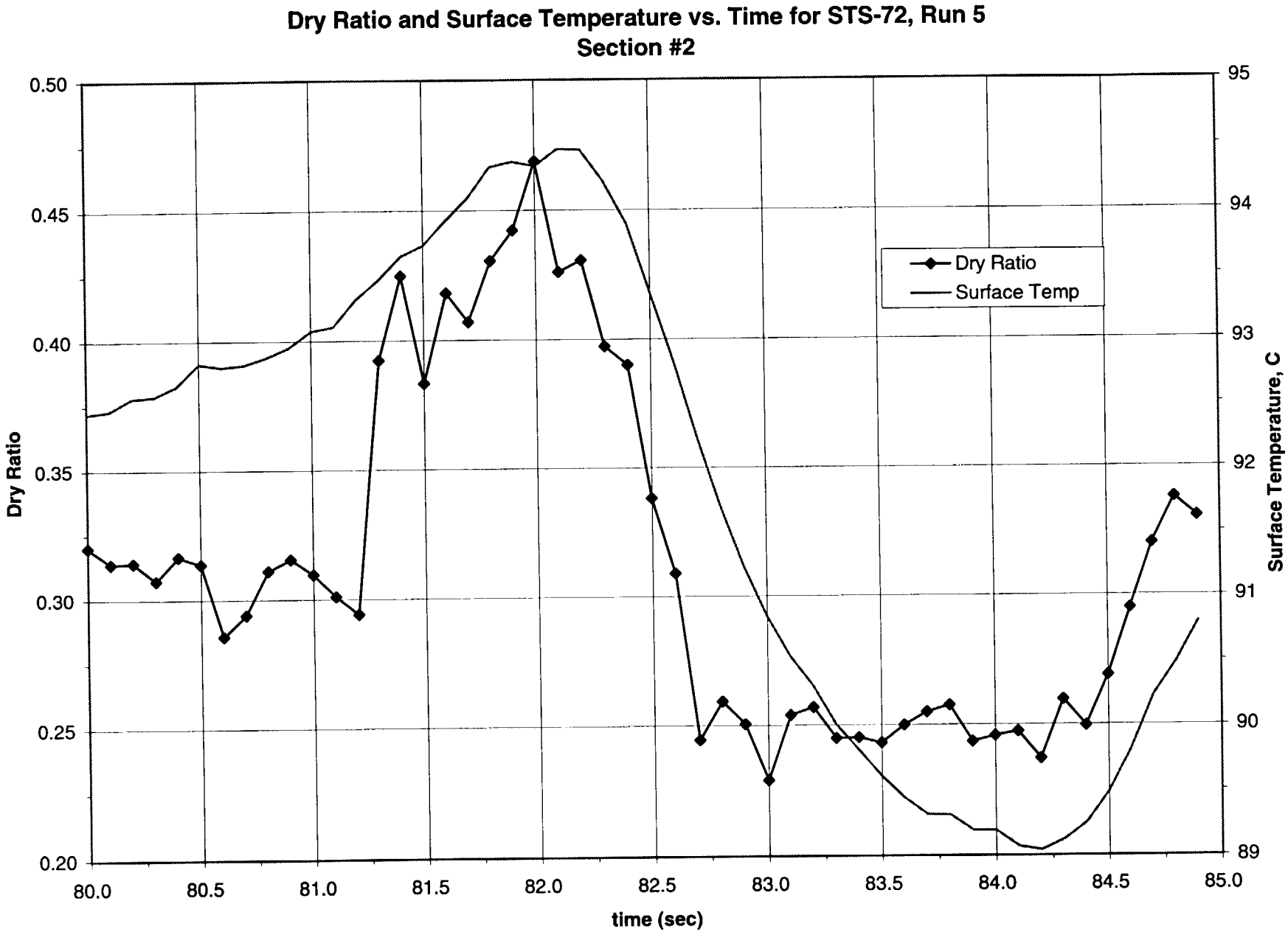

Figure A-10-e-2-i. Heater surface dry fraction and mean temperature. PBE-IIB (STS-72). Run No. 5. Time interval: 80 - 85 seconds.

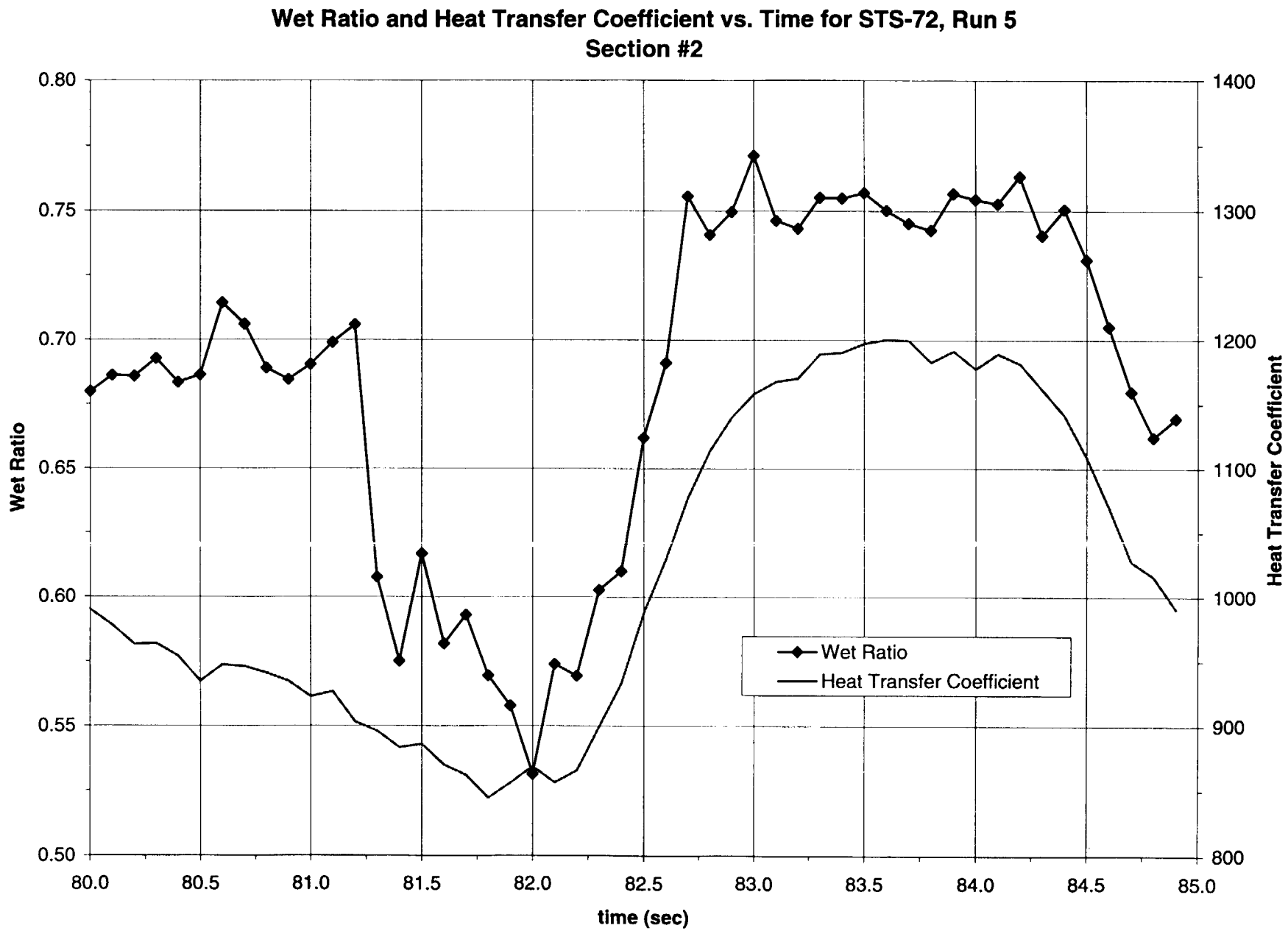

Figure A-10e-2-ii. Heater surface wet fraction and mean heat transfer coefficients. PBE-IIB (STS-72). Run No. 5. Time interval: 80 - 85 seconds.

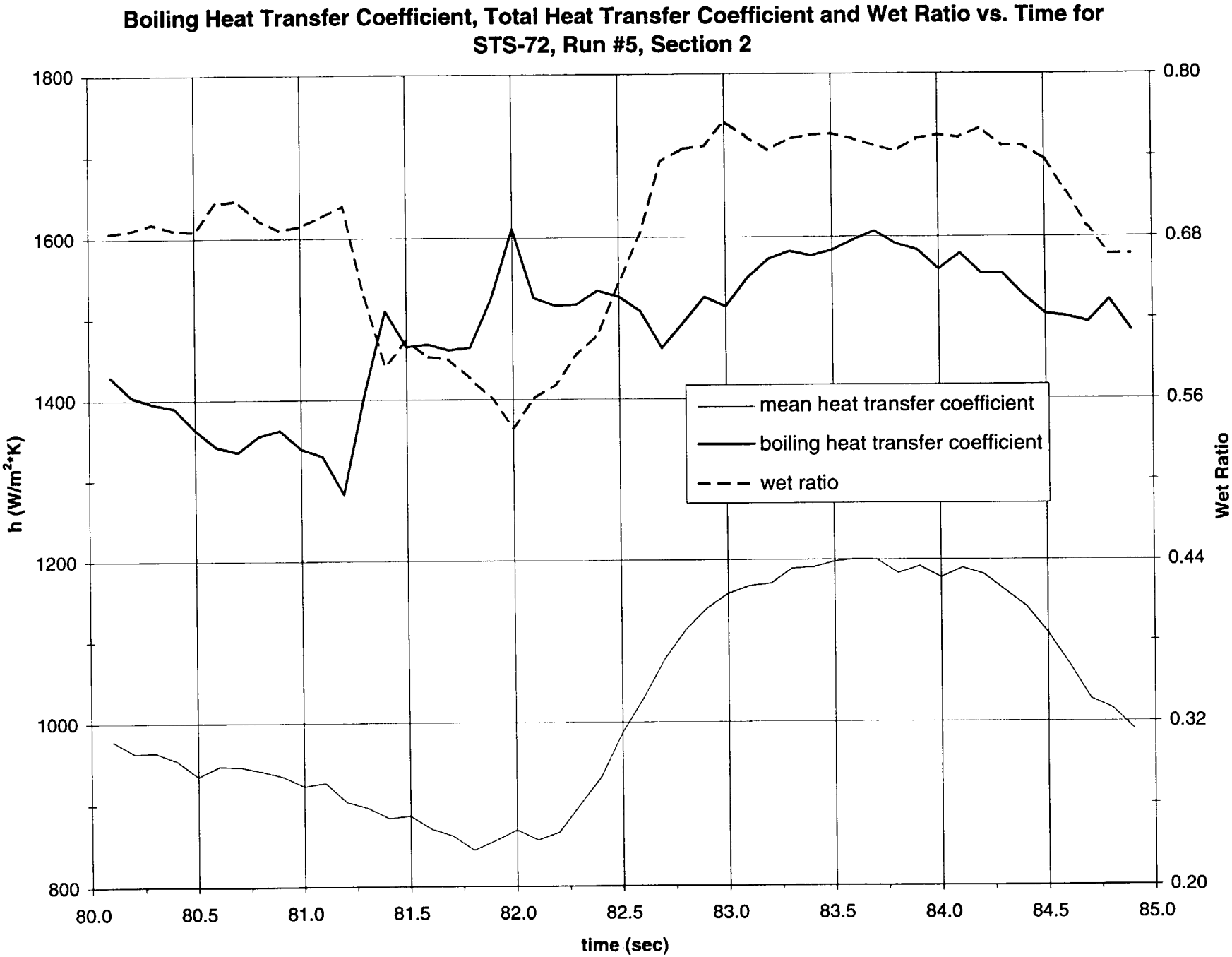

Figure A-10e-2-iii. Development of microgravity boiling heat transfer coefficient. PBE-IIB (STS-72). Run No. 5. Time interval: 80 - 85 seconds.

STS-72 Run #5, Section 2

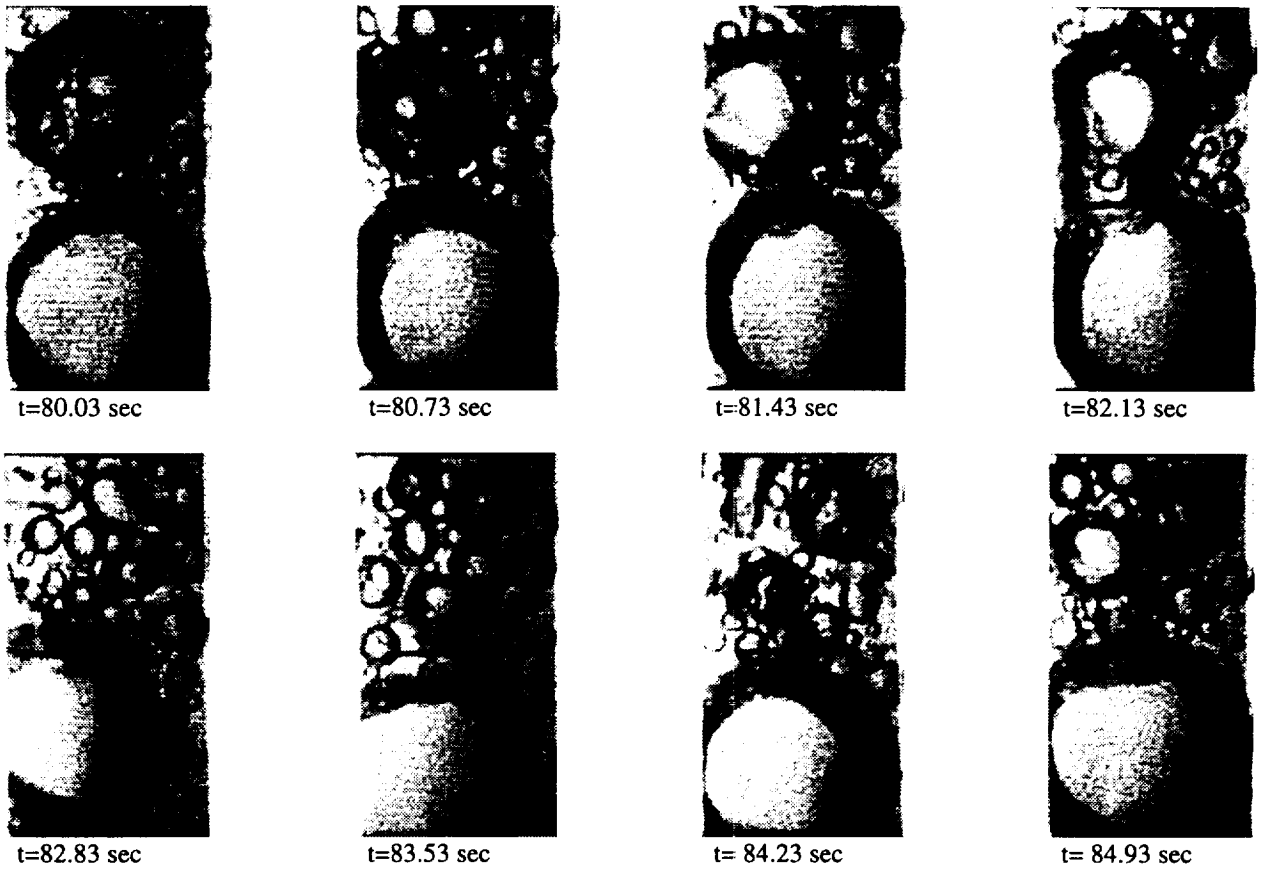

Figure A-10e-2-iv. Sample images showing dryout/rewetting. PBE-IIB (STS-72). Run No. 5. Time interval: 80 - 85 seconds.

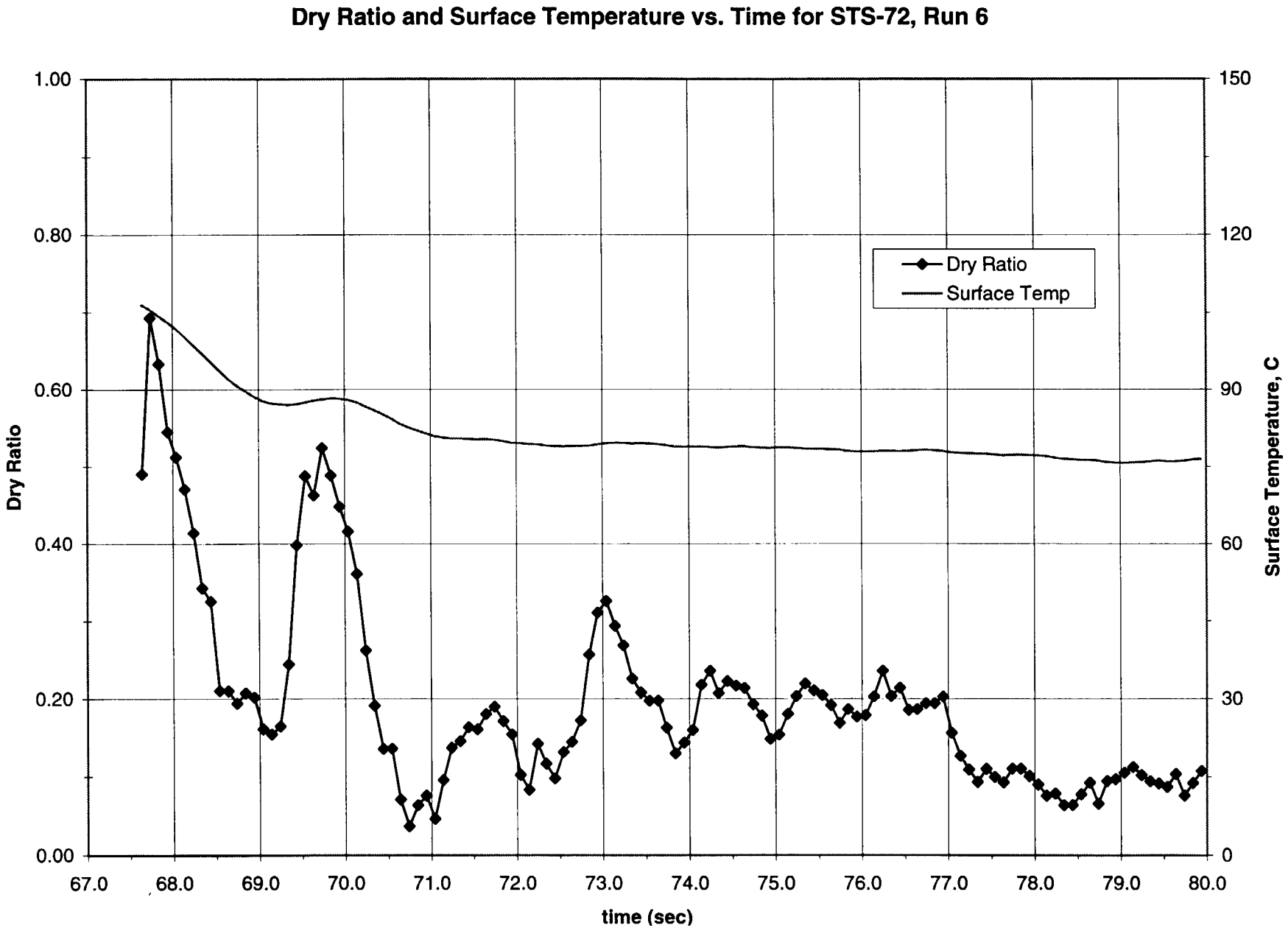

Figure A-10f-1-i. Heater surface dry fraction and mean temperature. PBE-IIB (STS-72). Run No. 6. Time interval: 67.5 - 80 seconds.

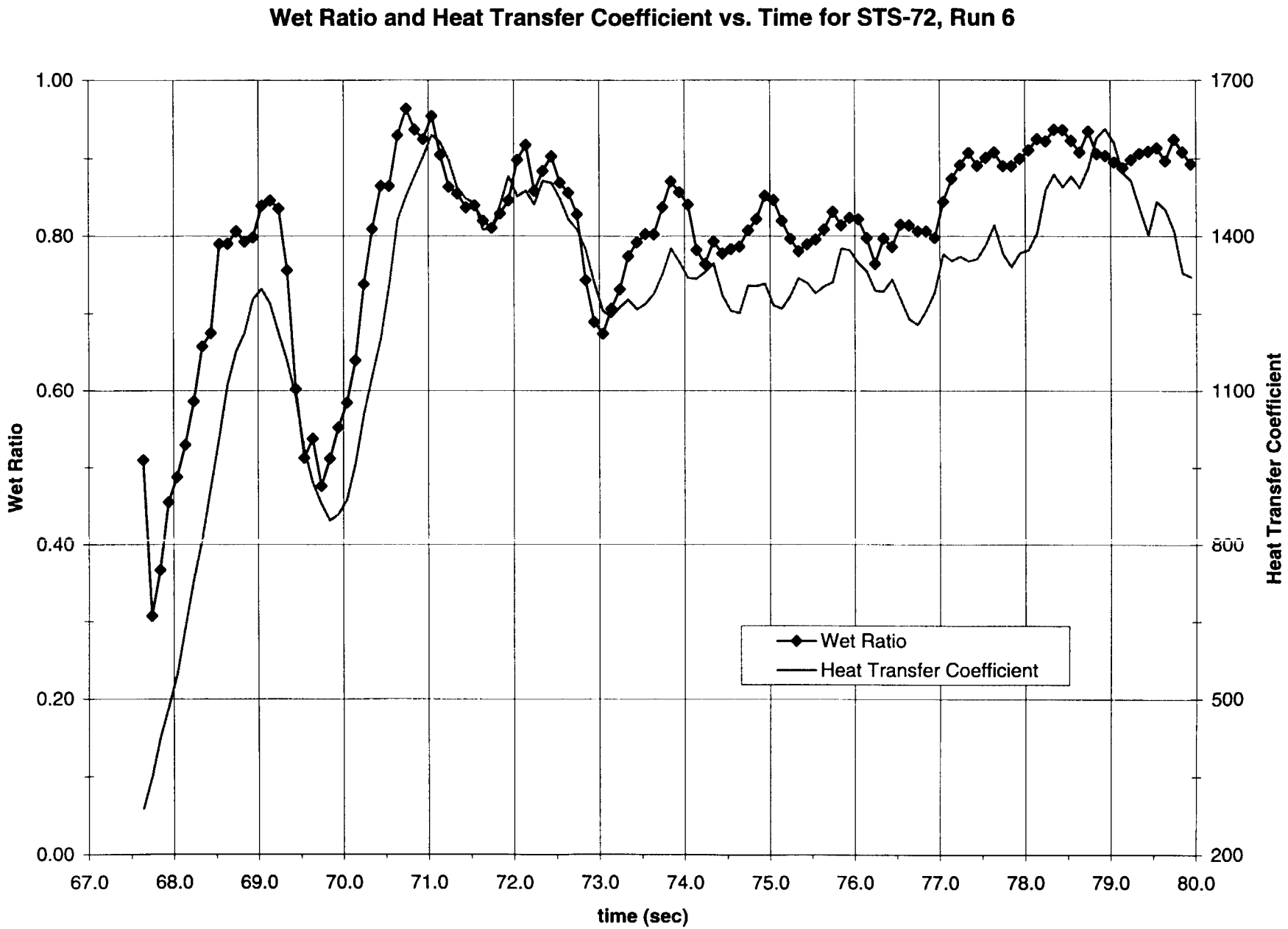

Figure A-10f-1-ii. Heater surface wet fraction and mean heat transfer coefficients. PBE-IIB (STS-72). Run No. 6. Time interval: 67.5 - 80 seconds.

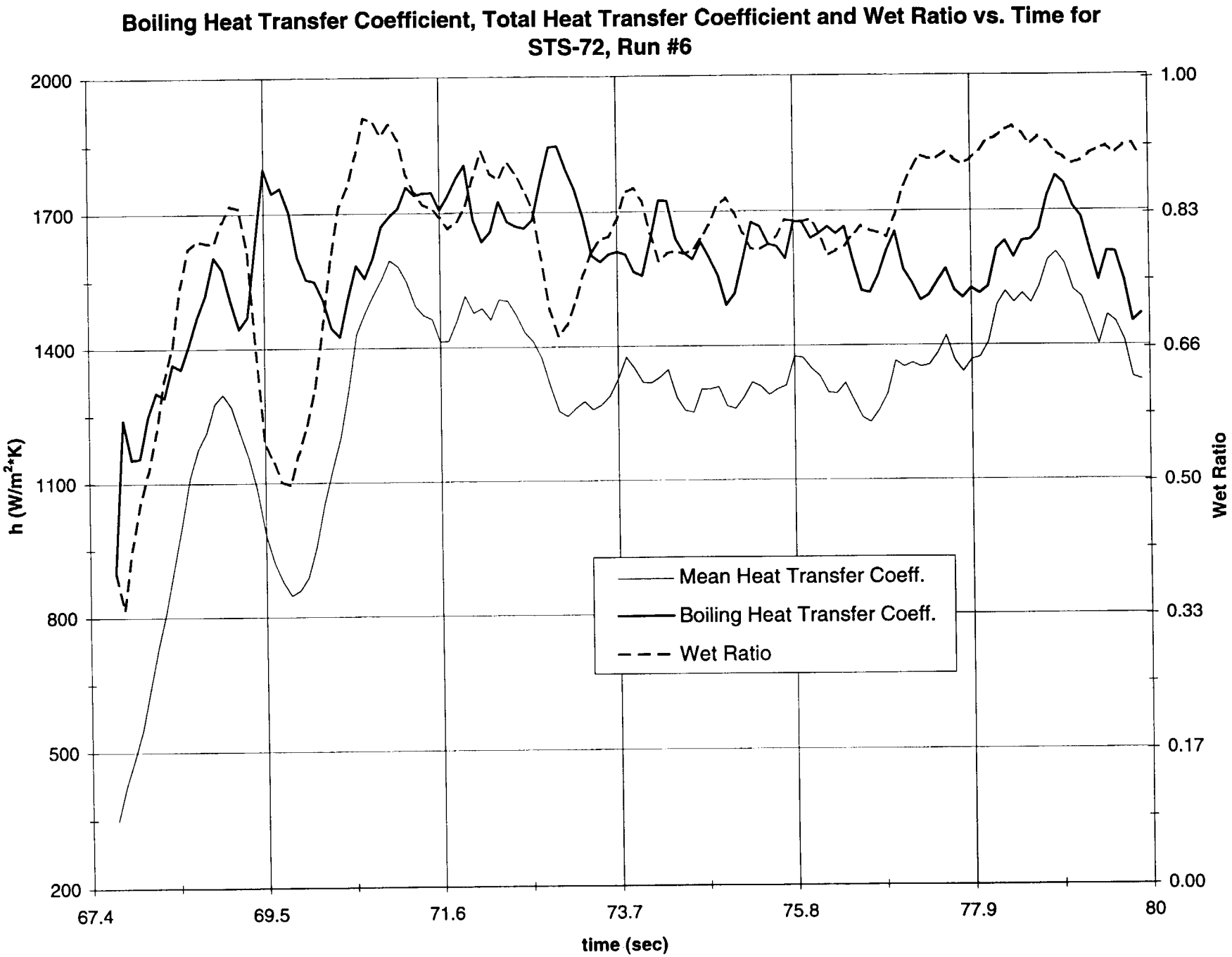

Figure A-10f-1-iii. Development of microgravity boiling heat transfer coefficient. PBE-IIB (STS-72). Run No. 6. Time interval: 67.5 - 80 seconds.

STS-72 Run #6

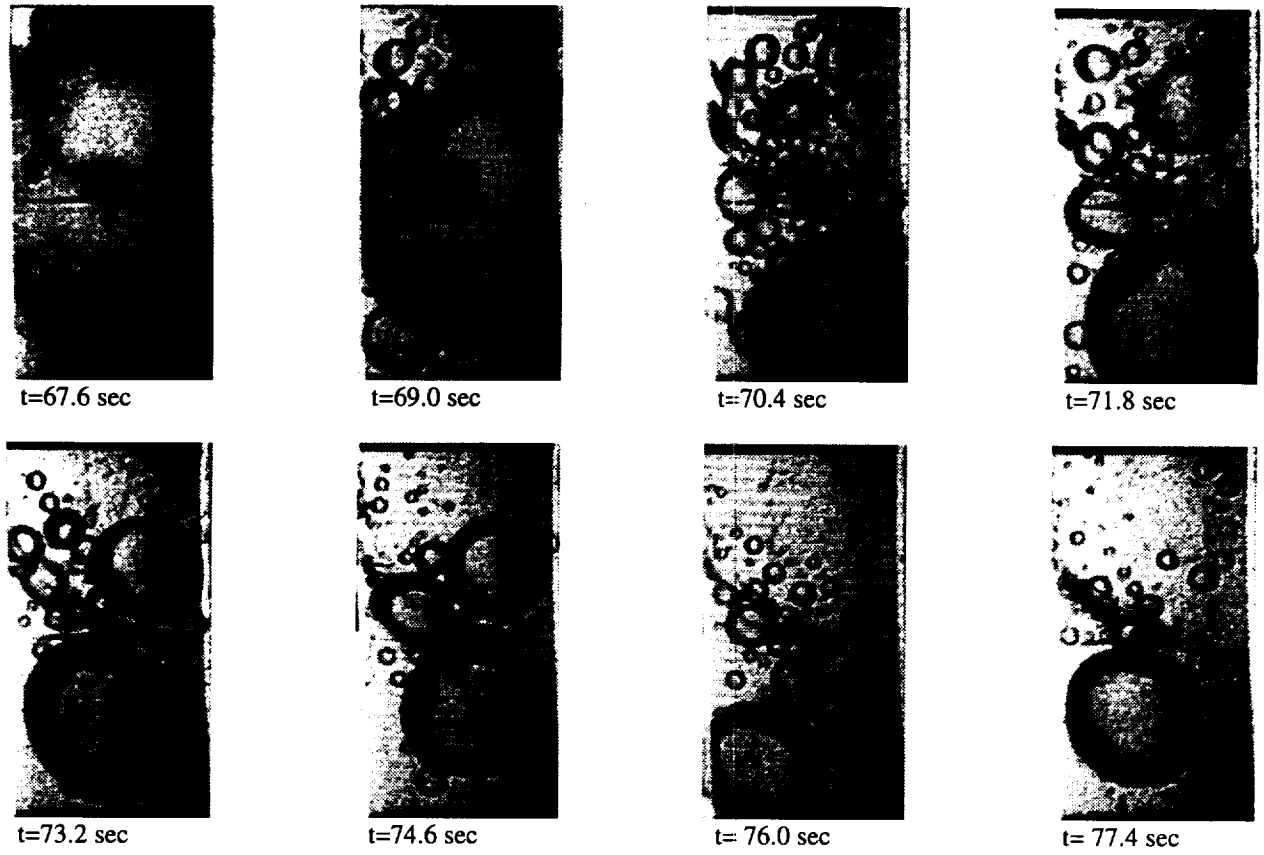

Figure A-10f-1-iv. Sample images showing dryout/rewetting. PBE-IIB (STS-72). Run No. 6. Time interval: 67.5 - 80 seconds.

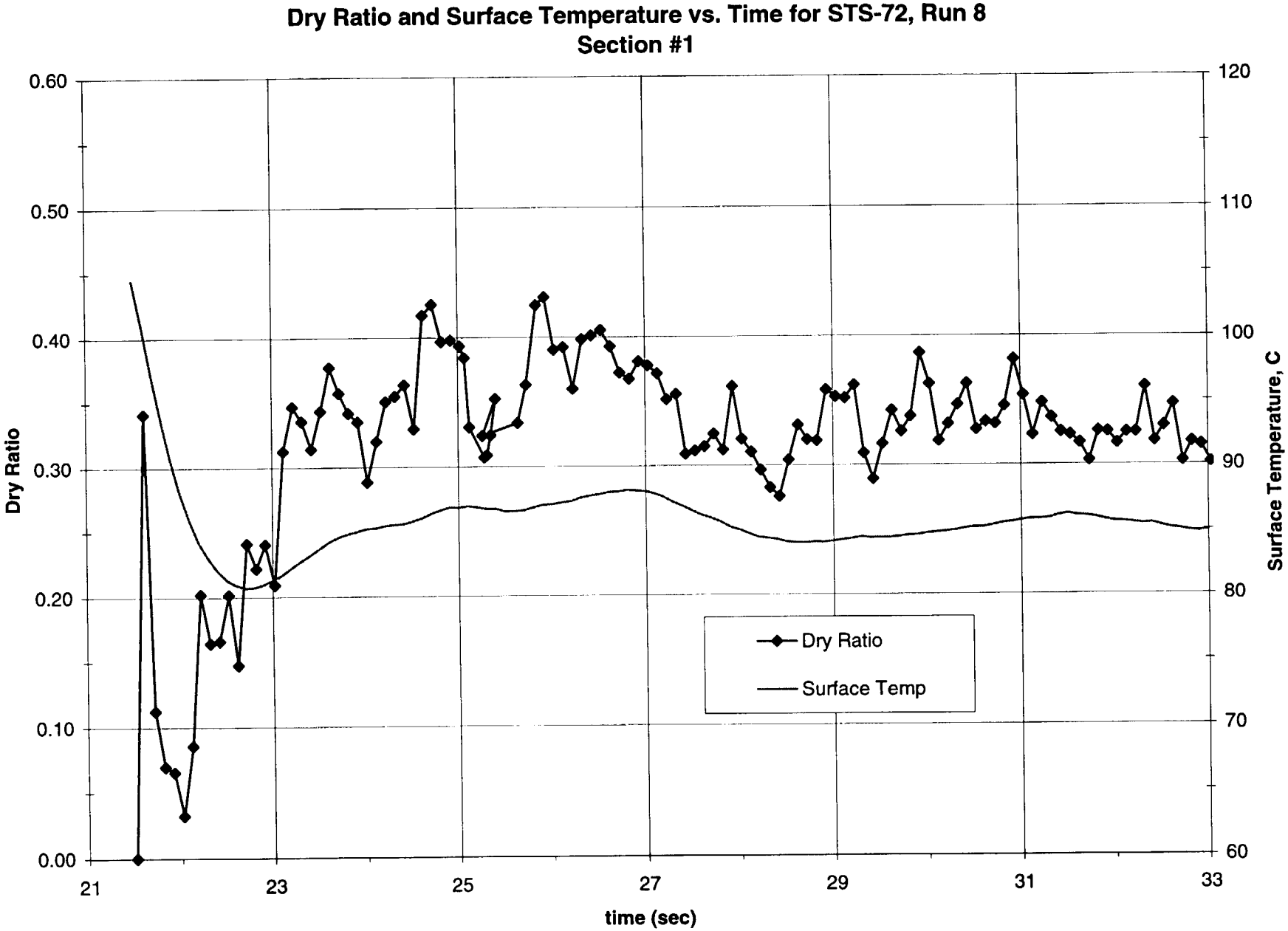

Figure A-10-h-1-i. Heater surface dry fraction and mean temperature. PBE-IIB (STS-72). Run No. 8. Time interval: 21 - 33 seconds.

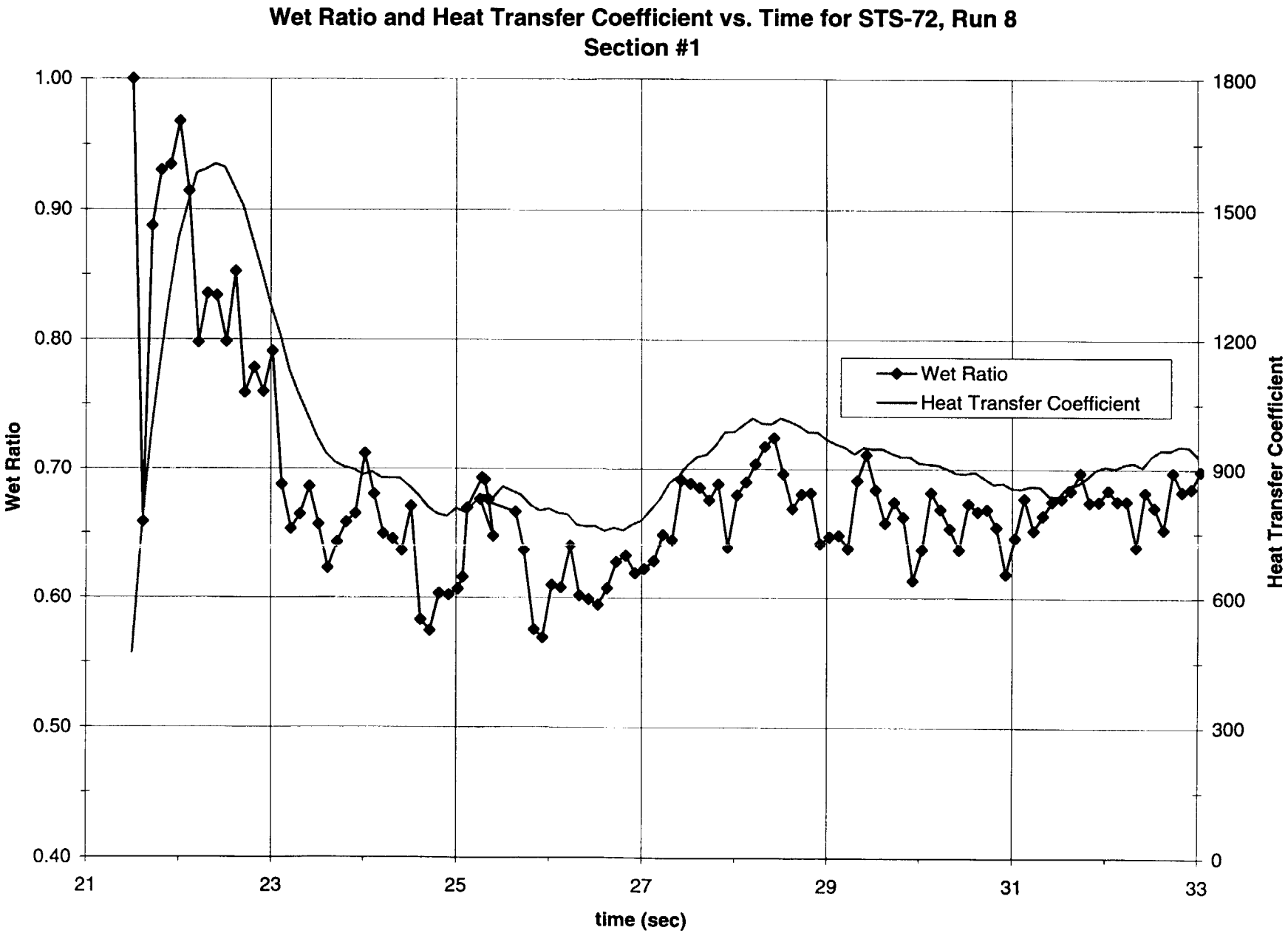

Figure A-10h-1-ii. Heater surface wet fraction and mean heat transfer coefficients. PBE-IIB (STS-72). Run No. 8. Time interval: 21 - 33 seconds.

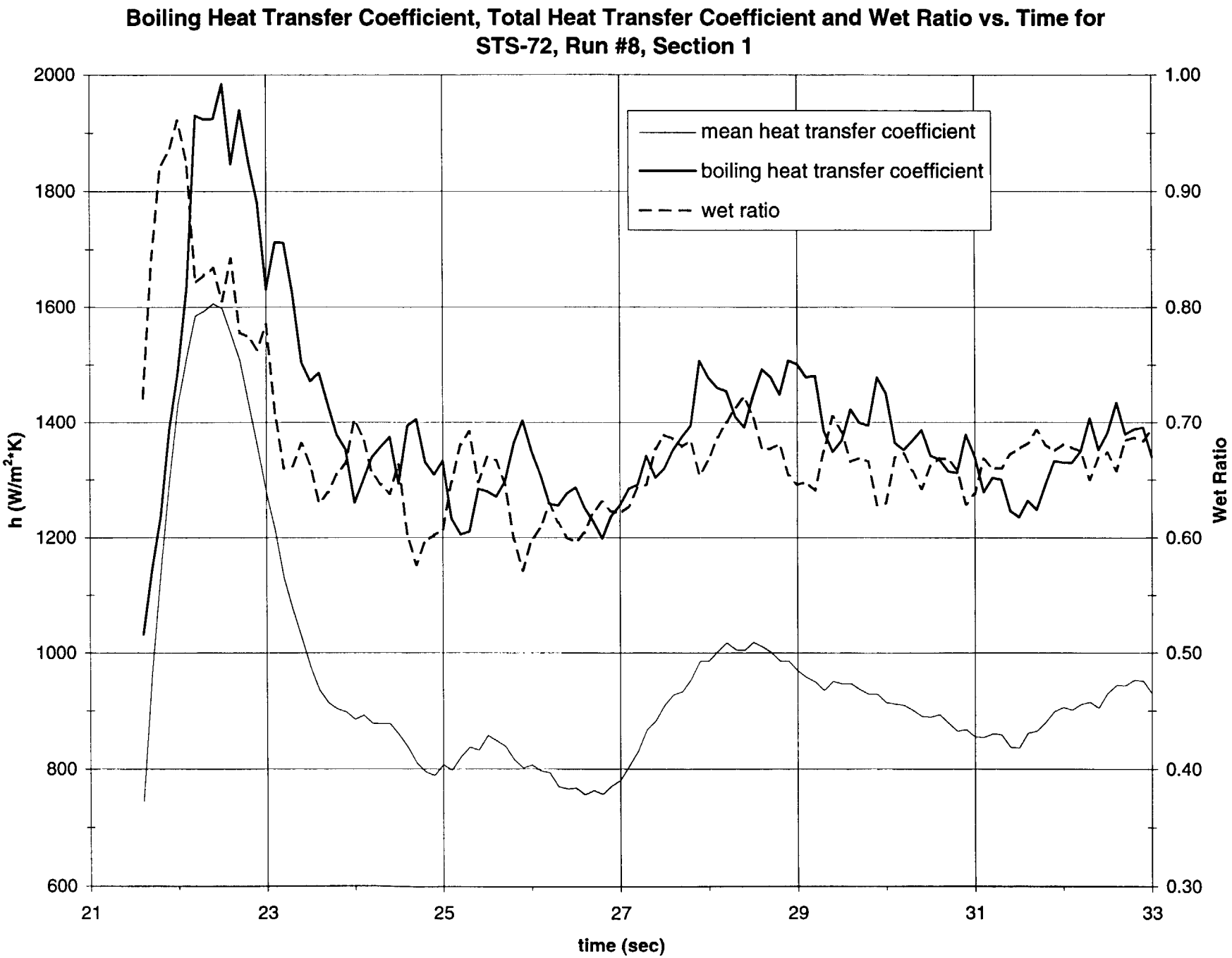

Figure A-10h-1-iii. Development of microgravity boiling heat transfer coefficient. PBE-IIB (STS-72). Run No. 8. Time interval: 21 - 33 seconds.

STS-72 Run #8, Section #1

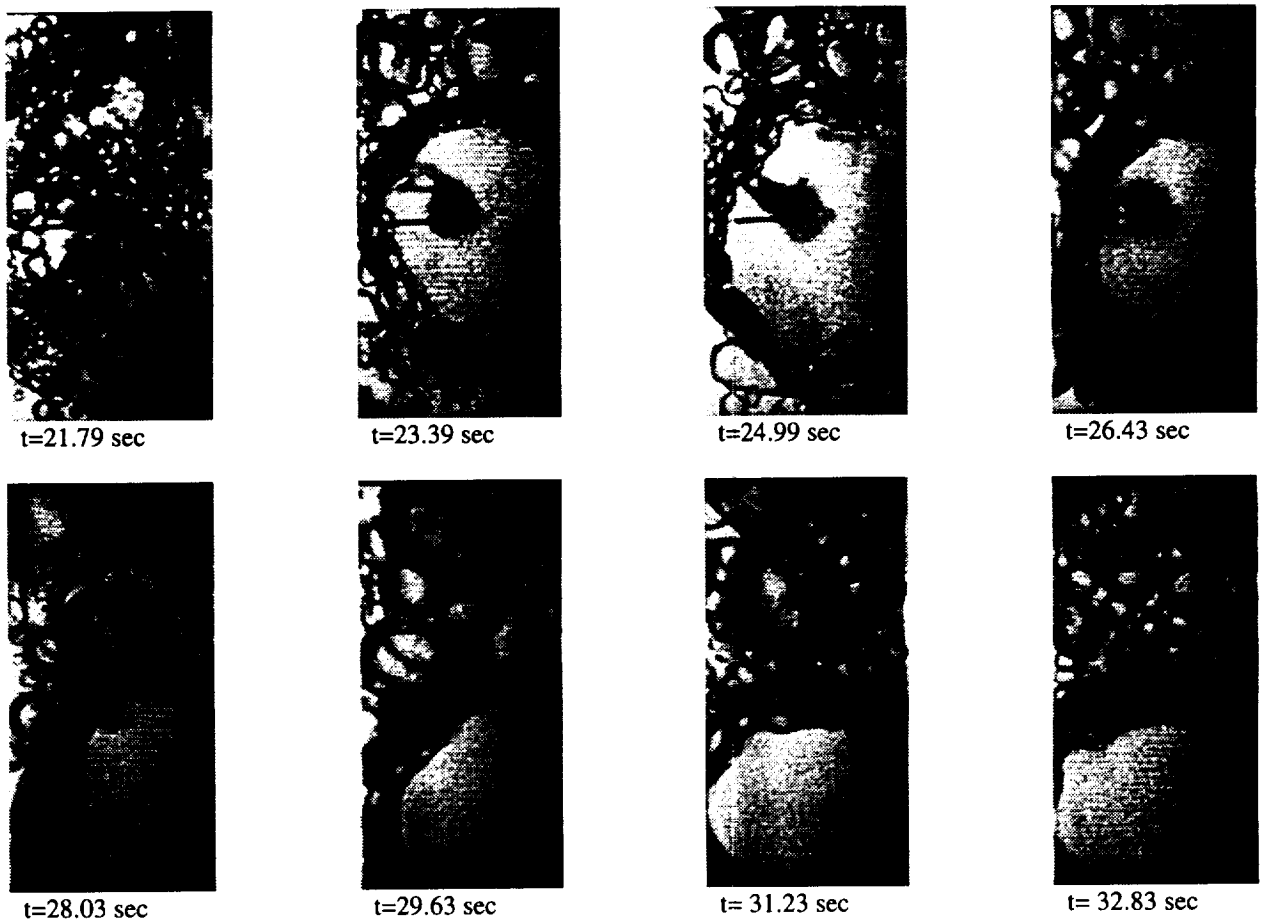

Figure A-10h-1-iv. Sample images showing dryout/rewetting. PBE-IIB (STS-72). Run No. 8. Time interval: 21 - 33 seconds.

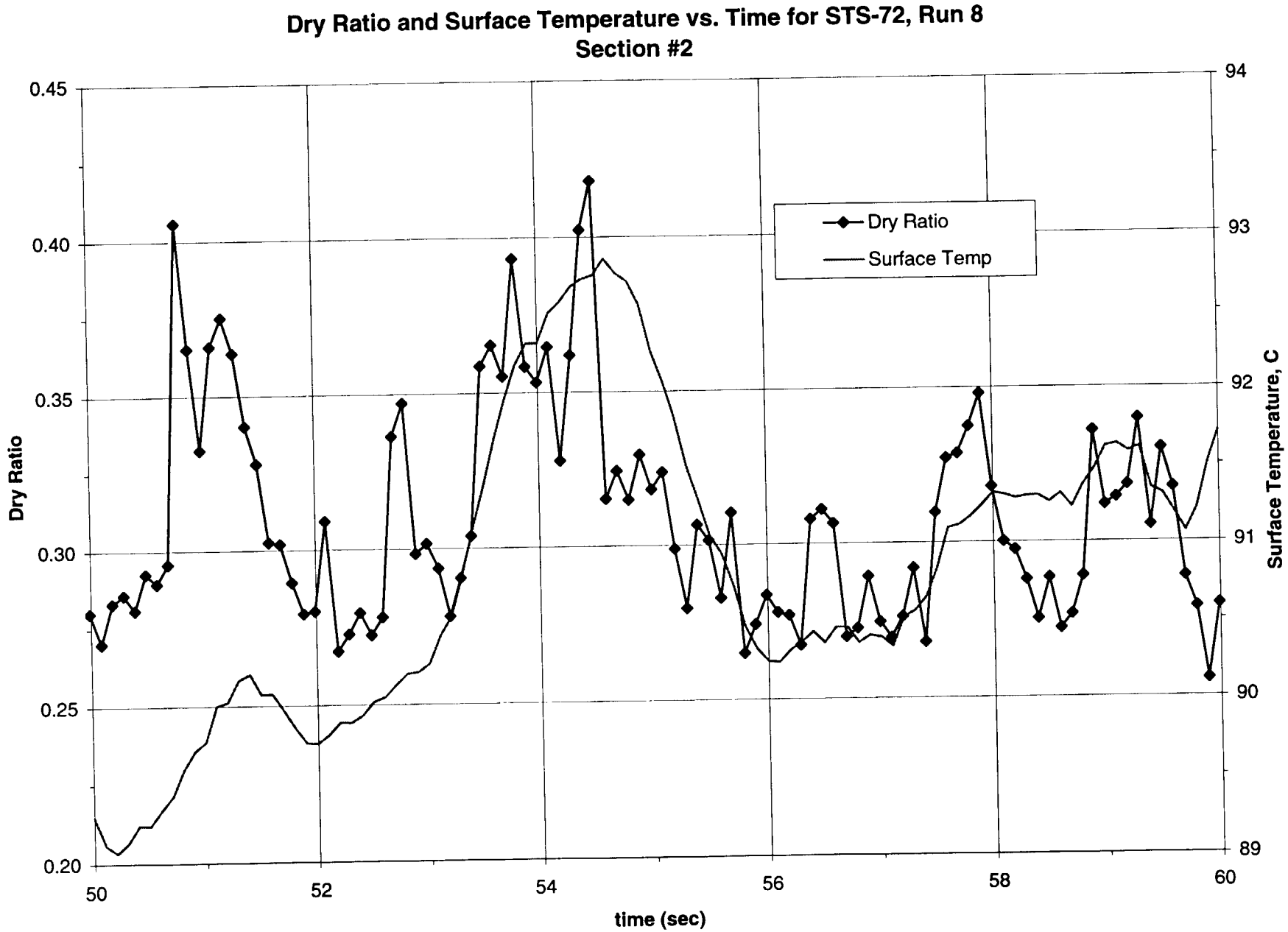

Figure A-10h-2-i. Heater surface dry fraction and mean temperature. PBE-IIB (STS-72). Run No. 8. Time interval: 50 - 60 seconds.

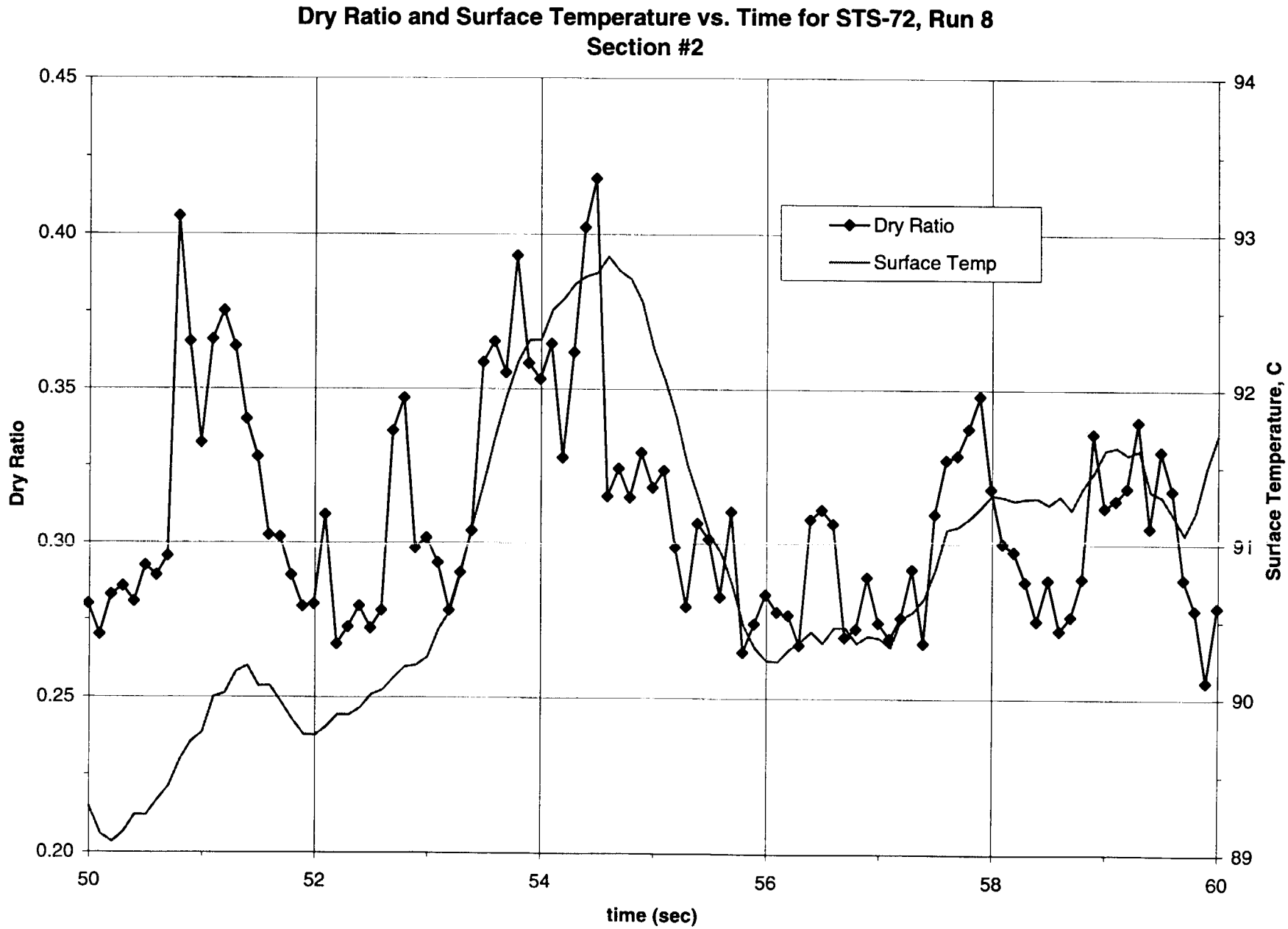

Figure A-10h-2-ii. Heater surface wet fraction and mean heat transfer coefficients. PBE-IIB (STS-72). Run No. 8. Time interval: 50 - 60 seconds.

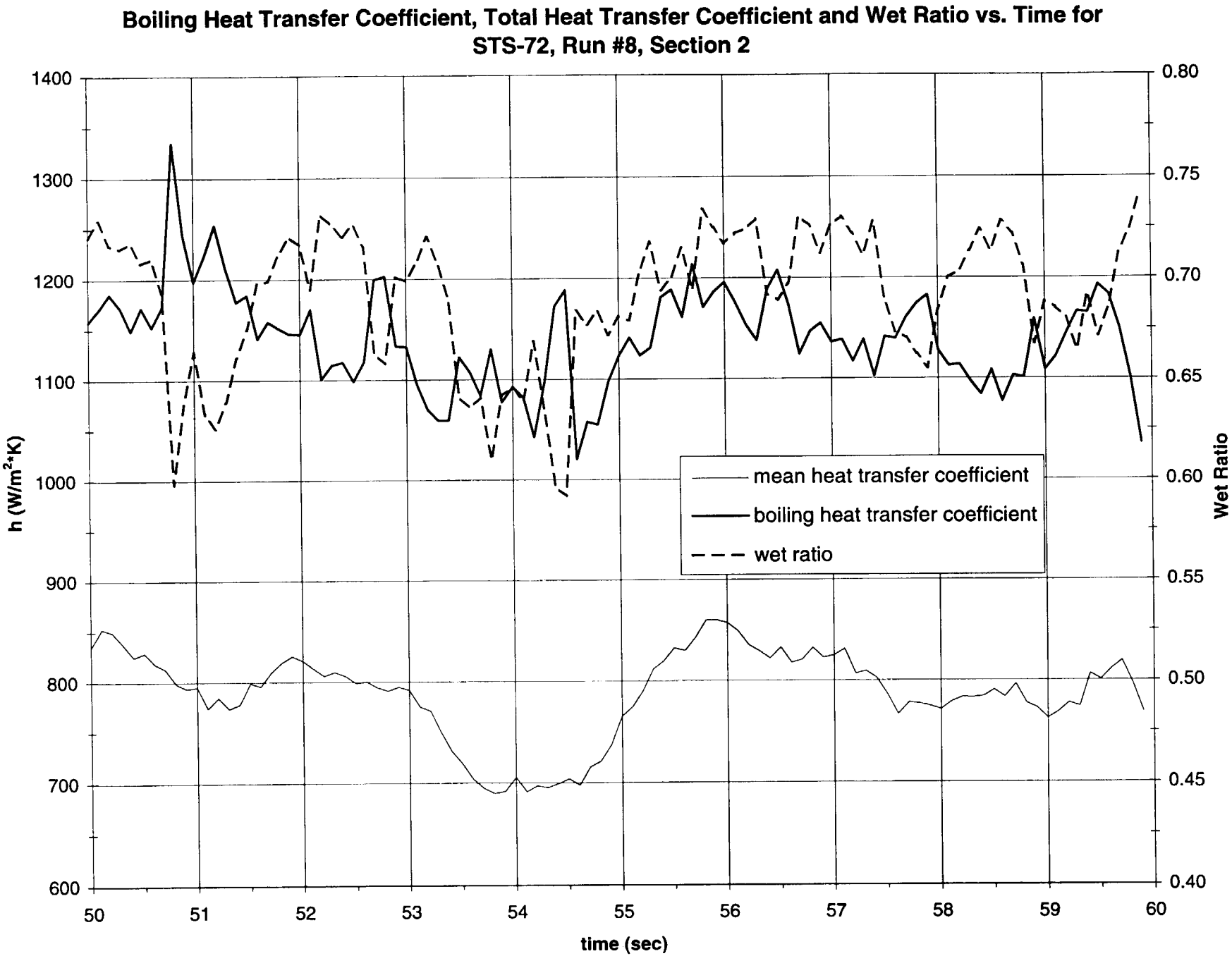

Figure A-10h-2-iii. Development of microgravity boiling heat transfer coefficient. PBE-IIB (STS-72). Run No. 8. Time interval: 50 - 60 seconds.

STS-72 Run #8, Section #2

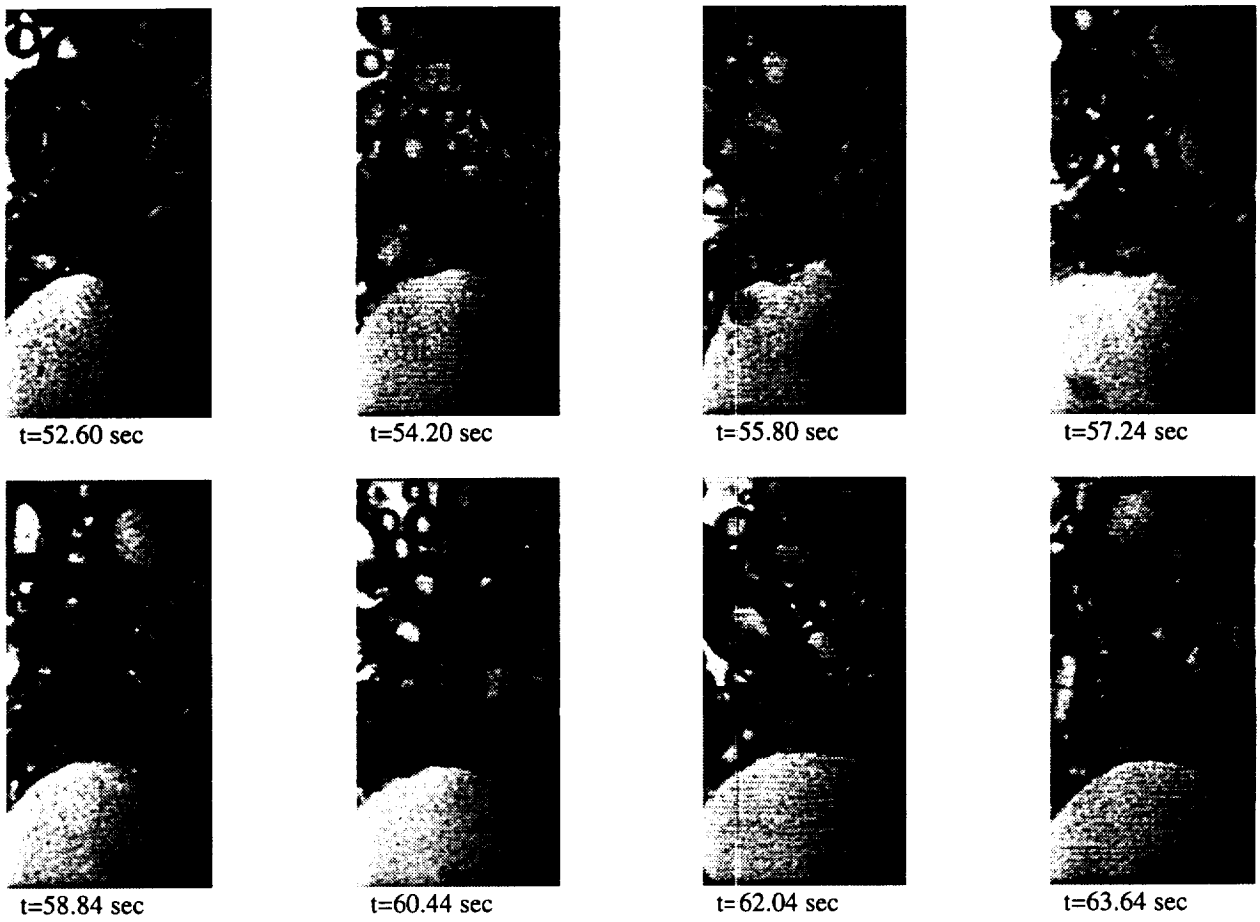

Figure A-10h-2-iv. Sample images showing dryout/rewetting. PBE-IIB (STS-72). Run No. 8. Time interval: 50 - 60 seconds.

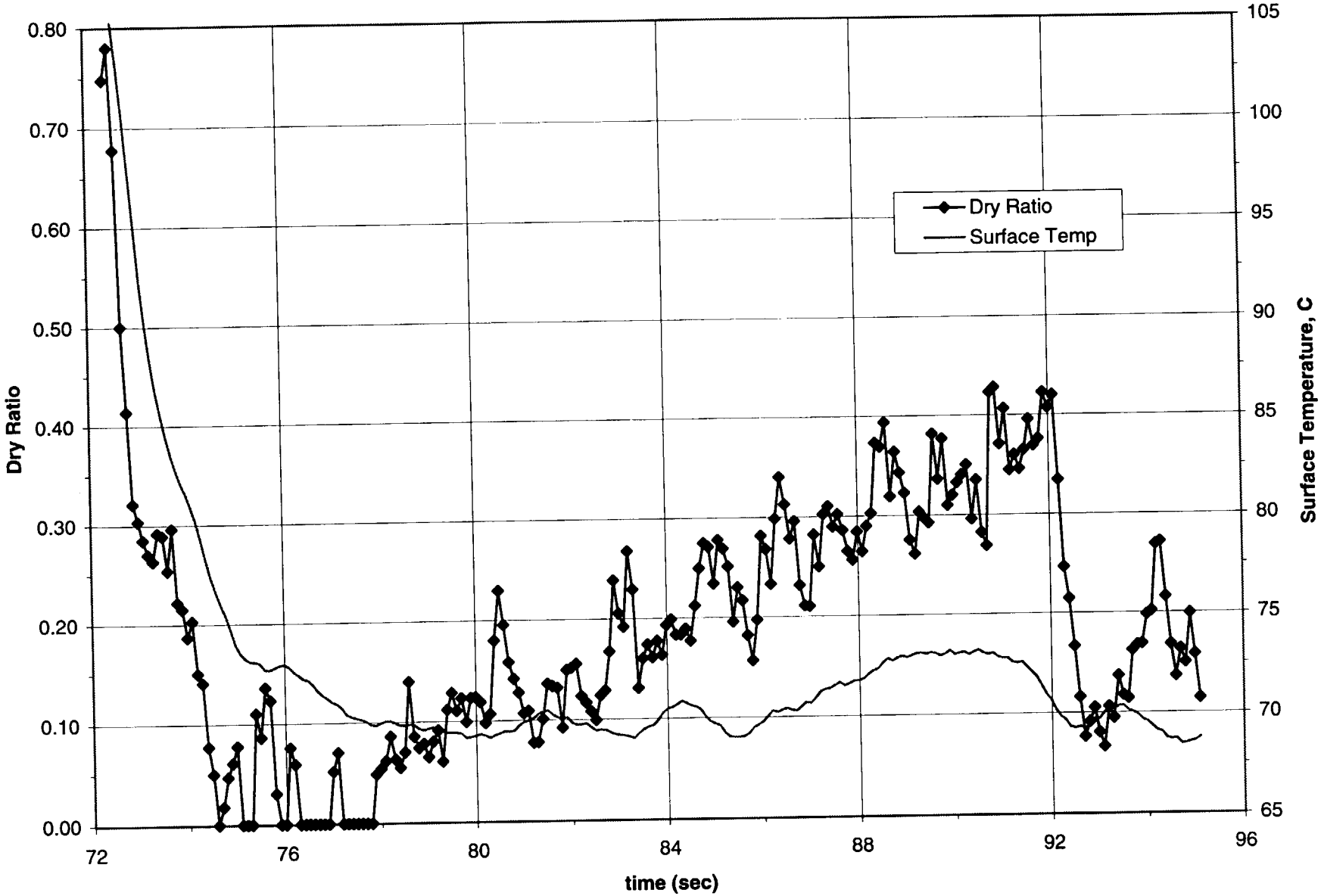

Figure A-10i-1-i. Heater surface dry fraction and mean temperature. PBE-IIB (STS-72). Run No. 9. Time interval: 72 - 95 seconds.

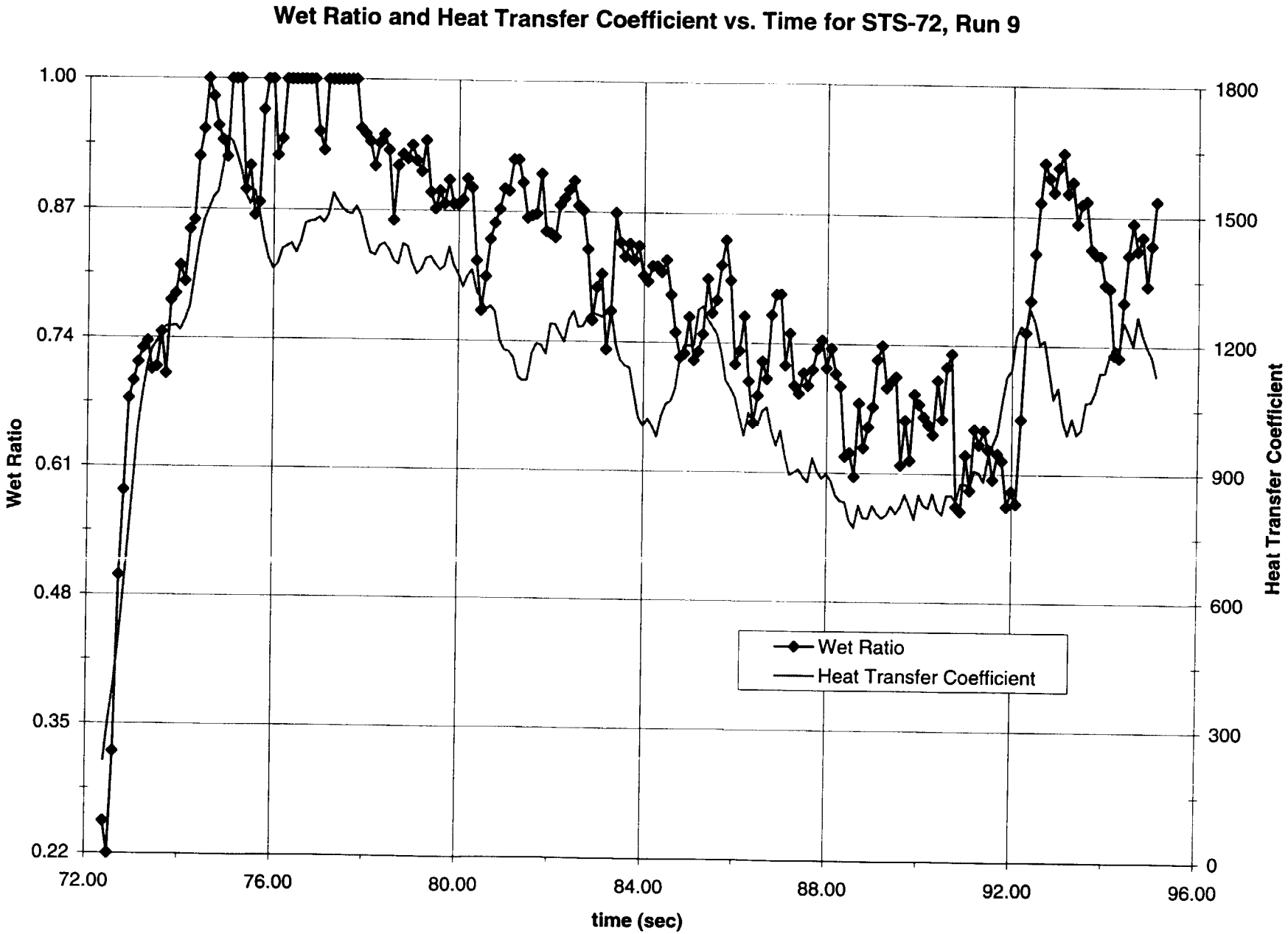

Figure A-10i-1-ii. Heater surface wet fraction and mean heat transfer coefficients. PBE-IIB (STS-72). Run No. 9. Time interval: 72 - 95 seconds.

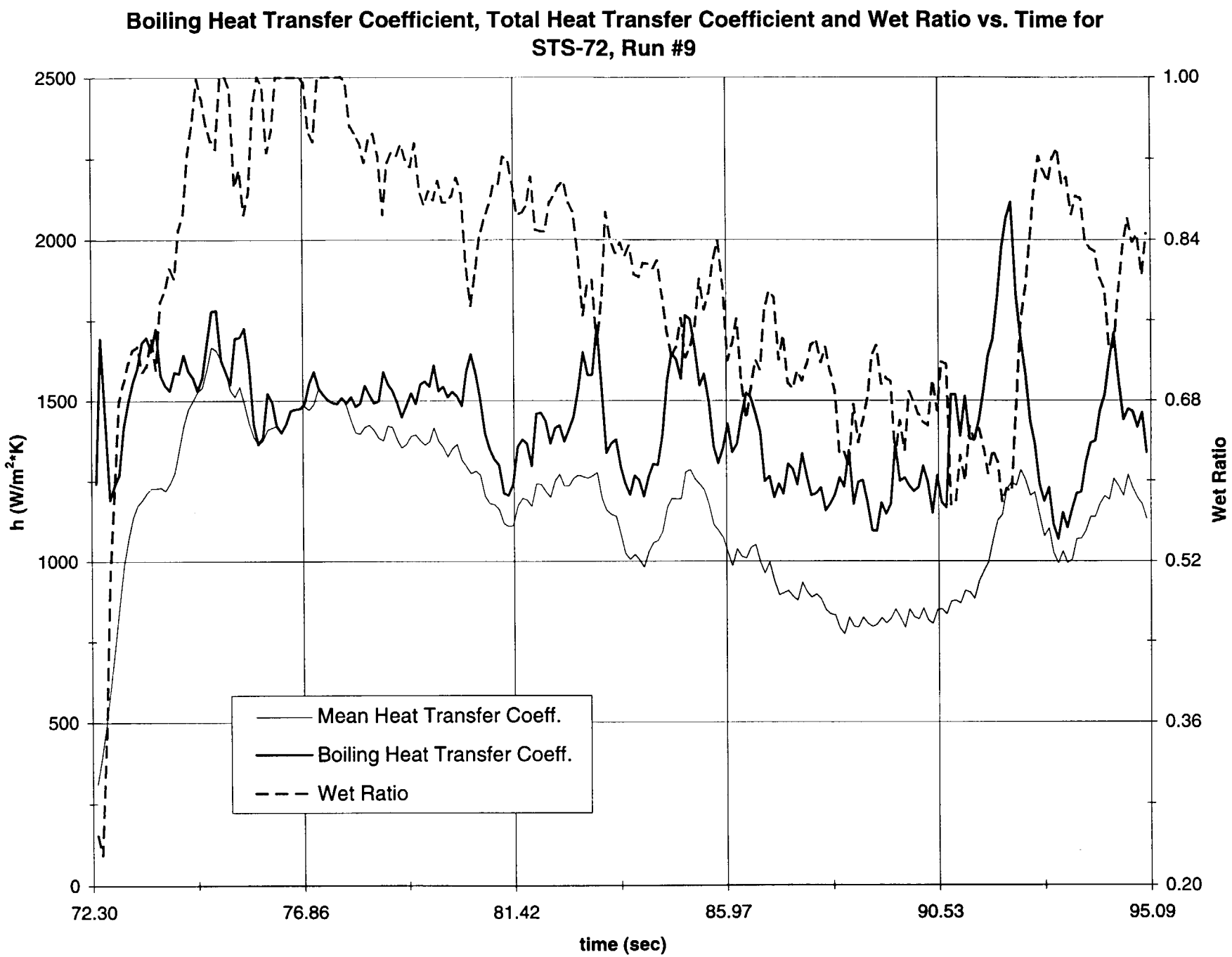

Figure A-10i-1-iii. Development of microgravity boiling heat transfer coefficient. PBE-IIB (STS-72). Run No. 9. Time interval: 72 - 95 seconds.

STS-72 Run #9

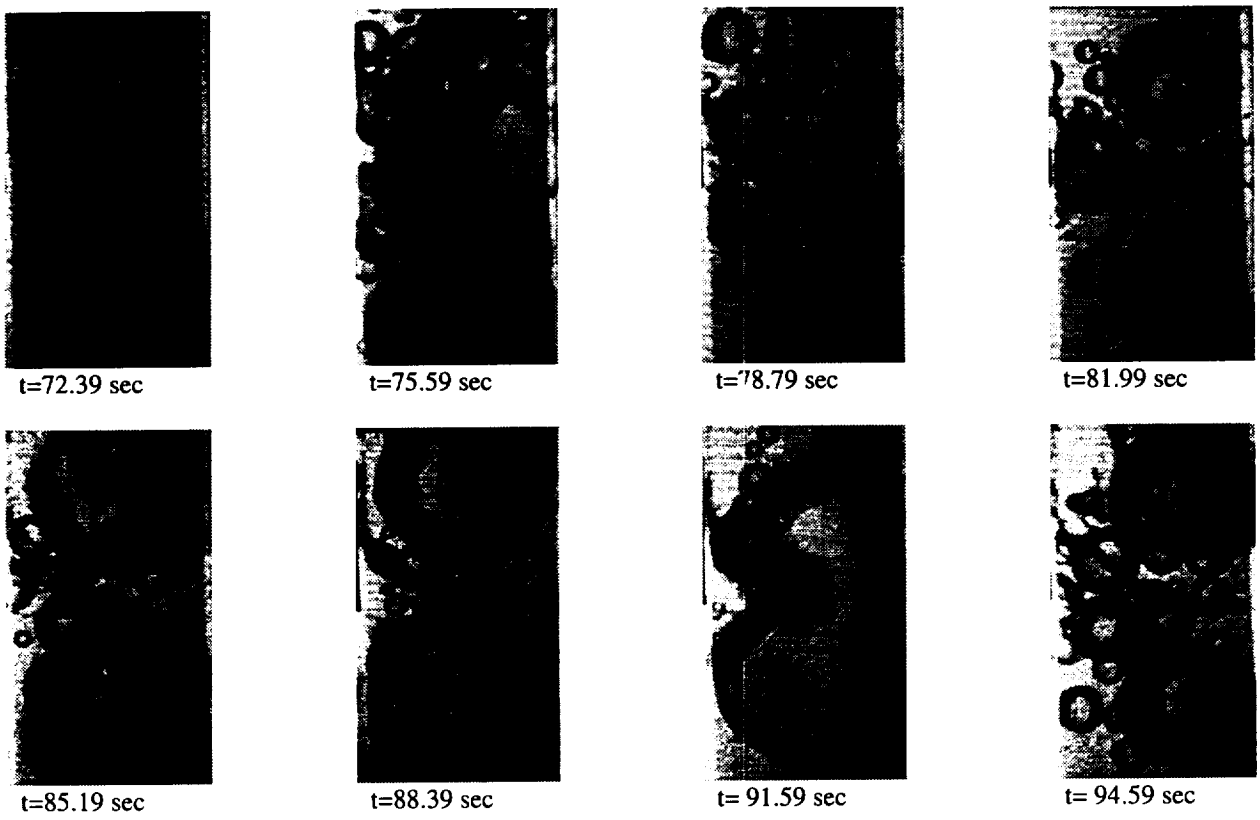

Figure A-10i-1-iv. Sample images showing dryout/rewetting. PBE-IIB (STS-72). Run No. 9. Time interval: 72 - 95 seconds.

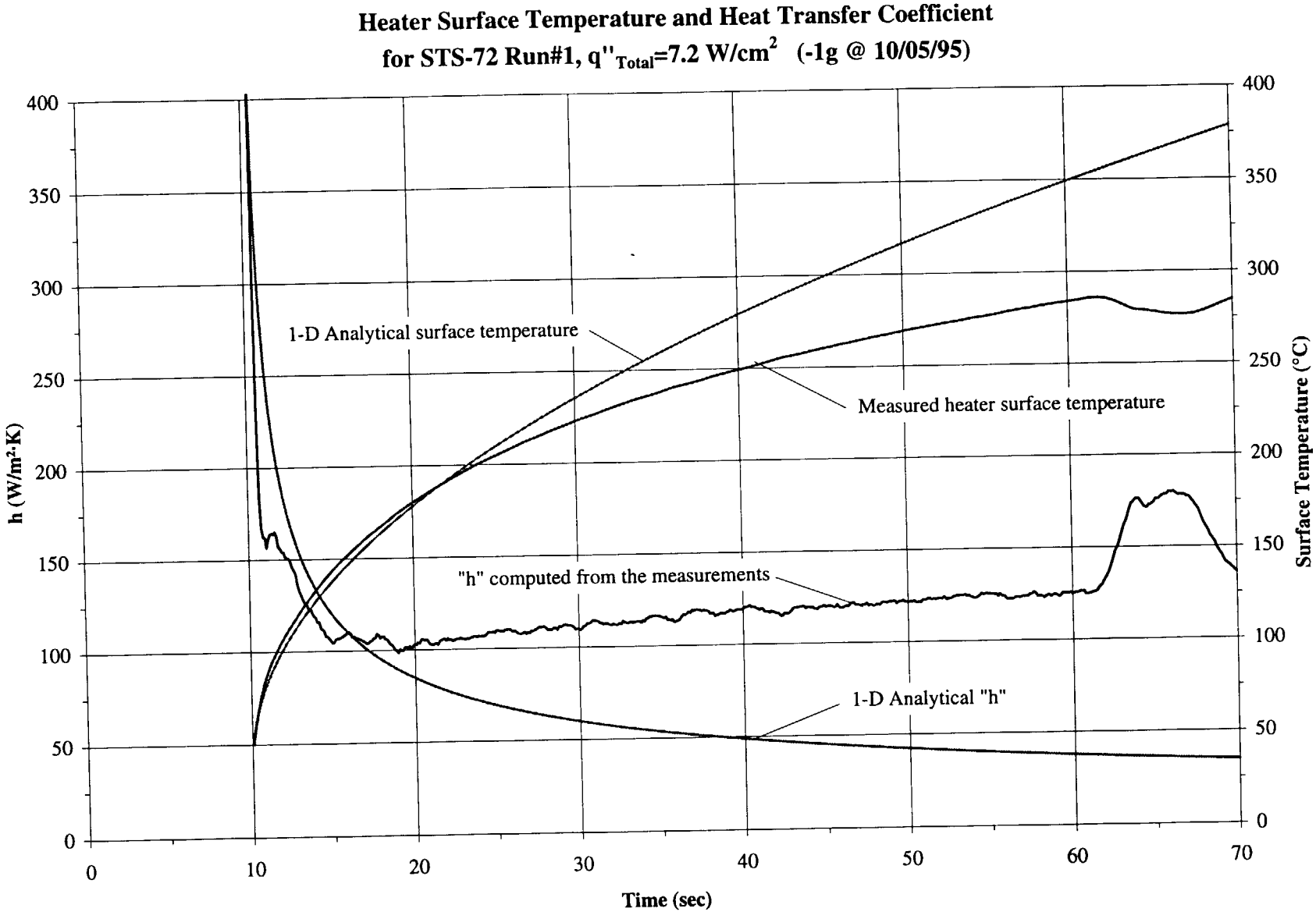

Figure A-11a. a/g = -1 Preflight test. Mean heater surface temperature and derived heat transfer coefficient. PBE-IIB (STS-72). Run No. 1.

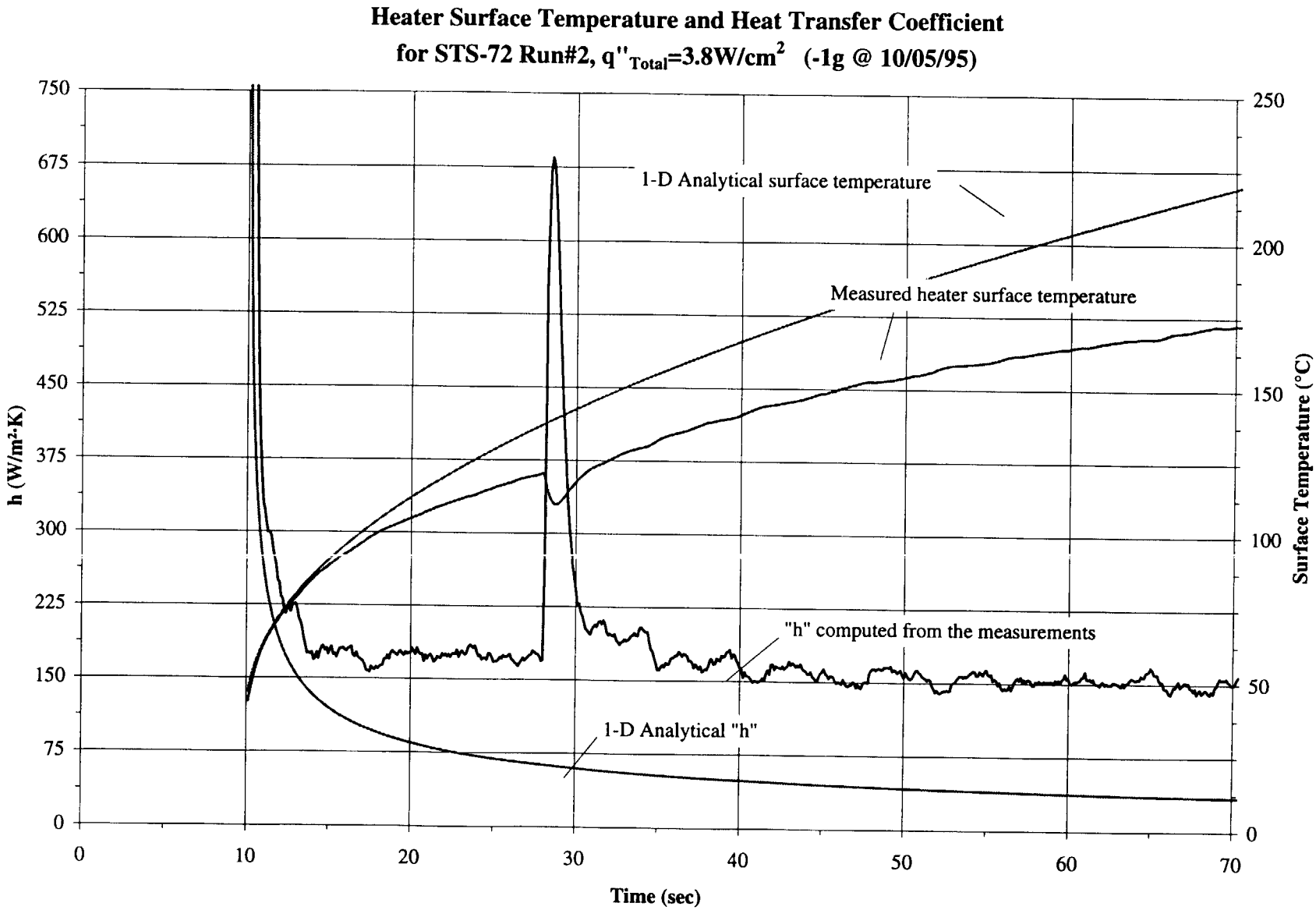

Figure A-11b. a/g = -1 Preflight test. Mean heater surface temperature and derived heat transfer coefficient. PBE-IIB (STS-72). Run No. 2.

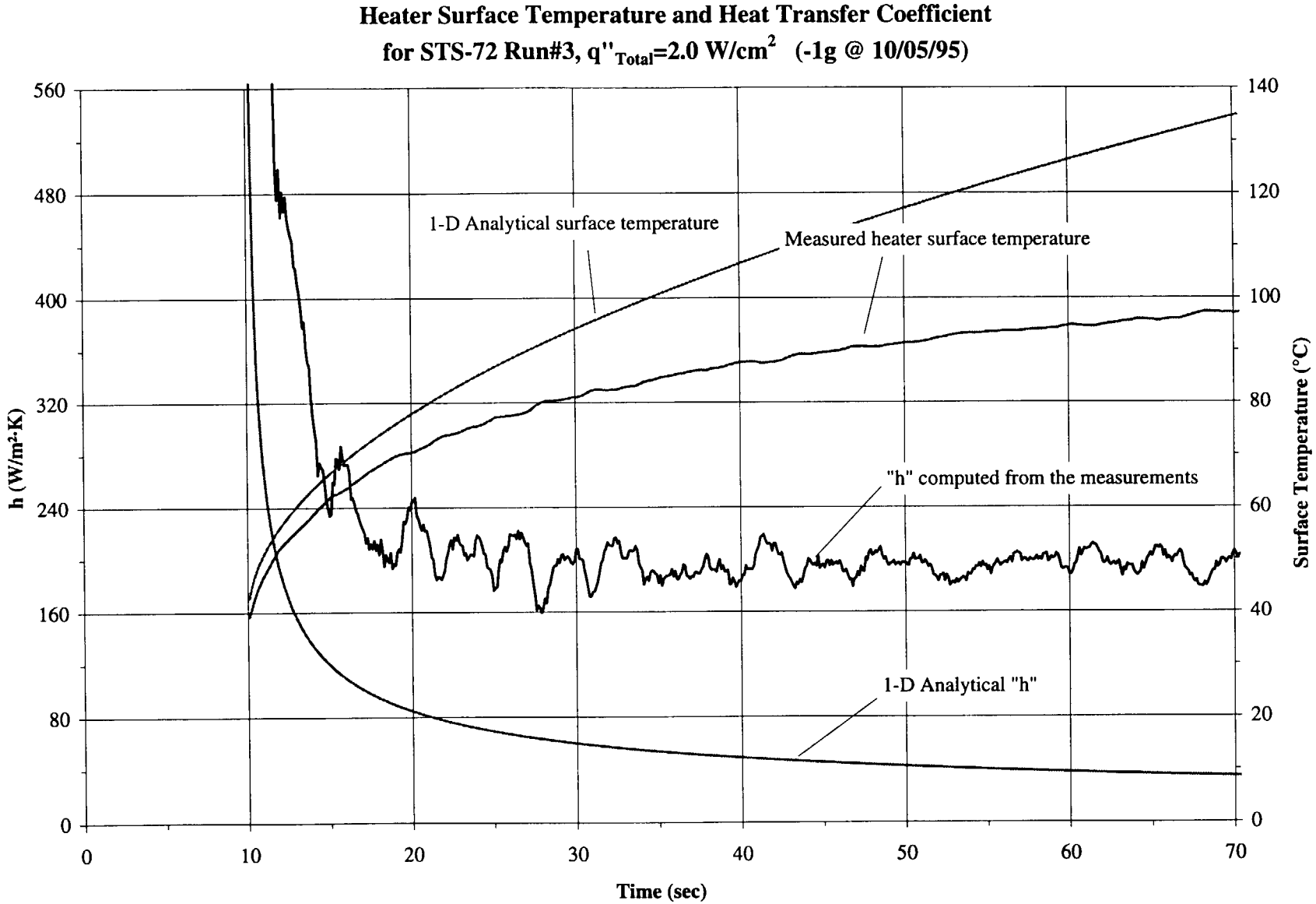

Figure A-11c. a/g = -1 Preflight test. Mean heater surface temperature and derived heat transfer coefficient. PBE-IIB (STS-72). Run No. 3.

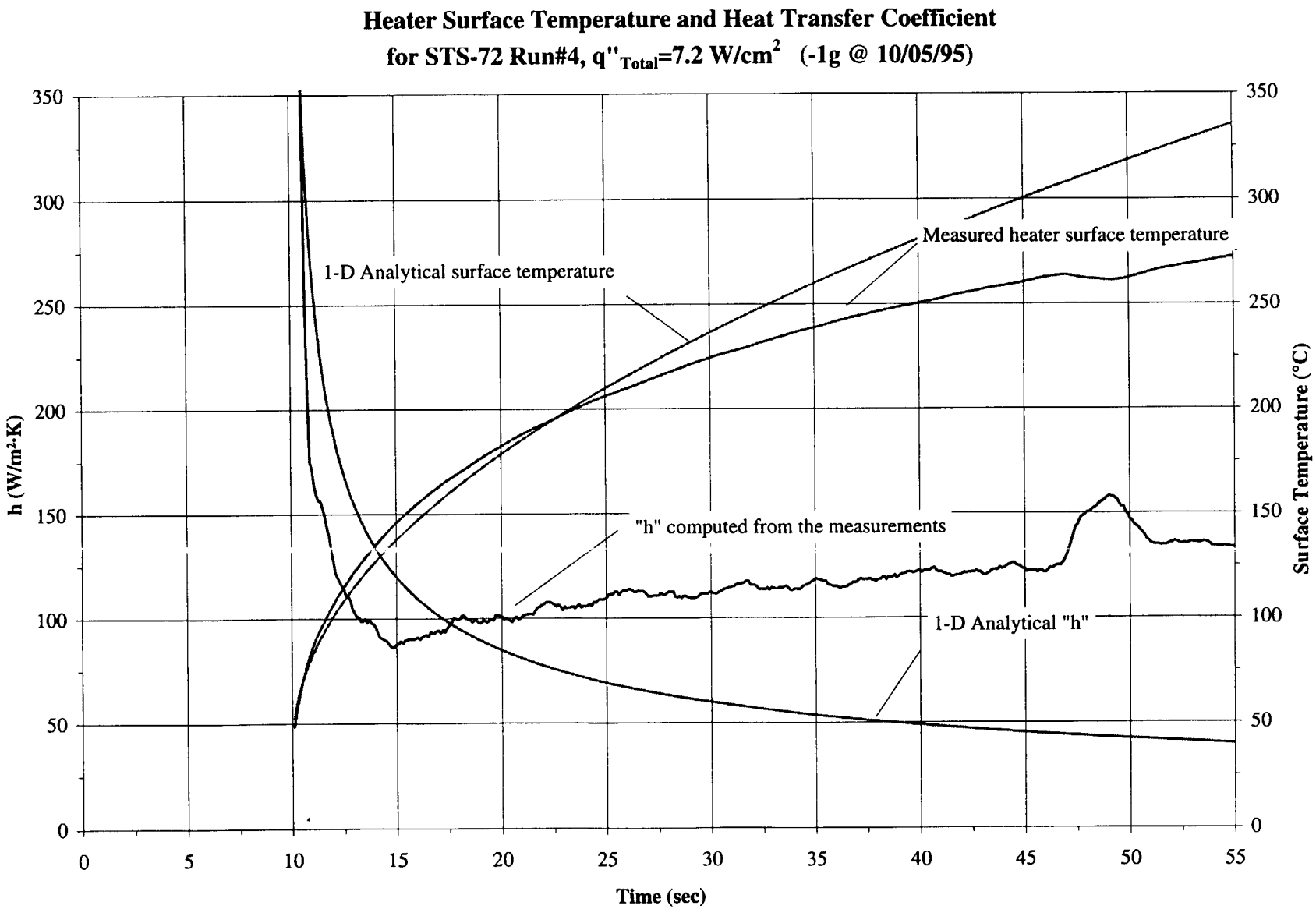

Figure A-11d. a/g = -1 Preflight test. Mean heater surface temperature and derived heat transfer coefficient. PBE-IIB (STS-72). Run No. 4.

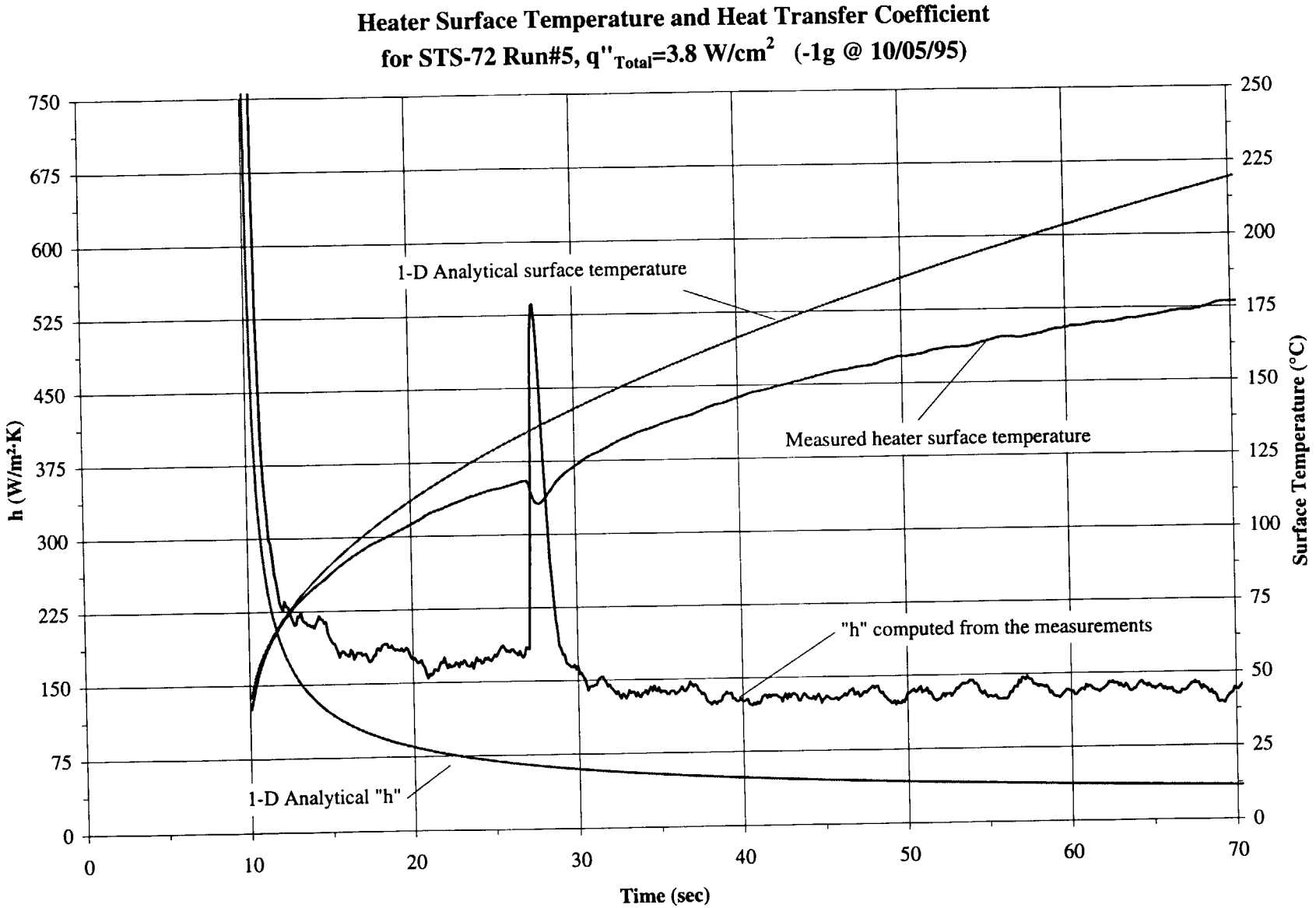

Figure A-11e. a/g = -1 Preflight test. Mean heater surface temperature and derived heat transfer coefficient. PBE-IIB (STS-72). Run No. 5.

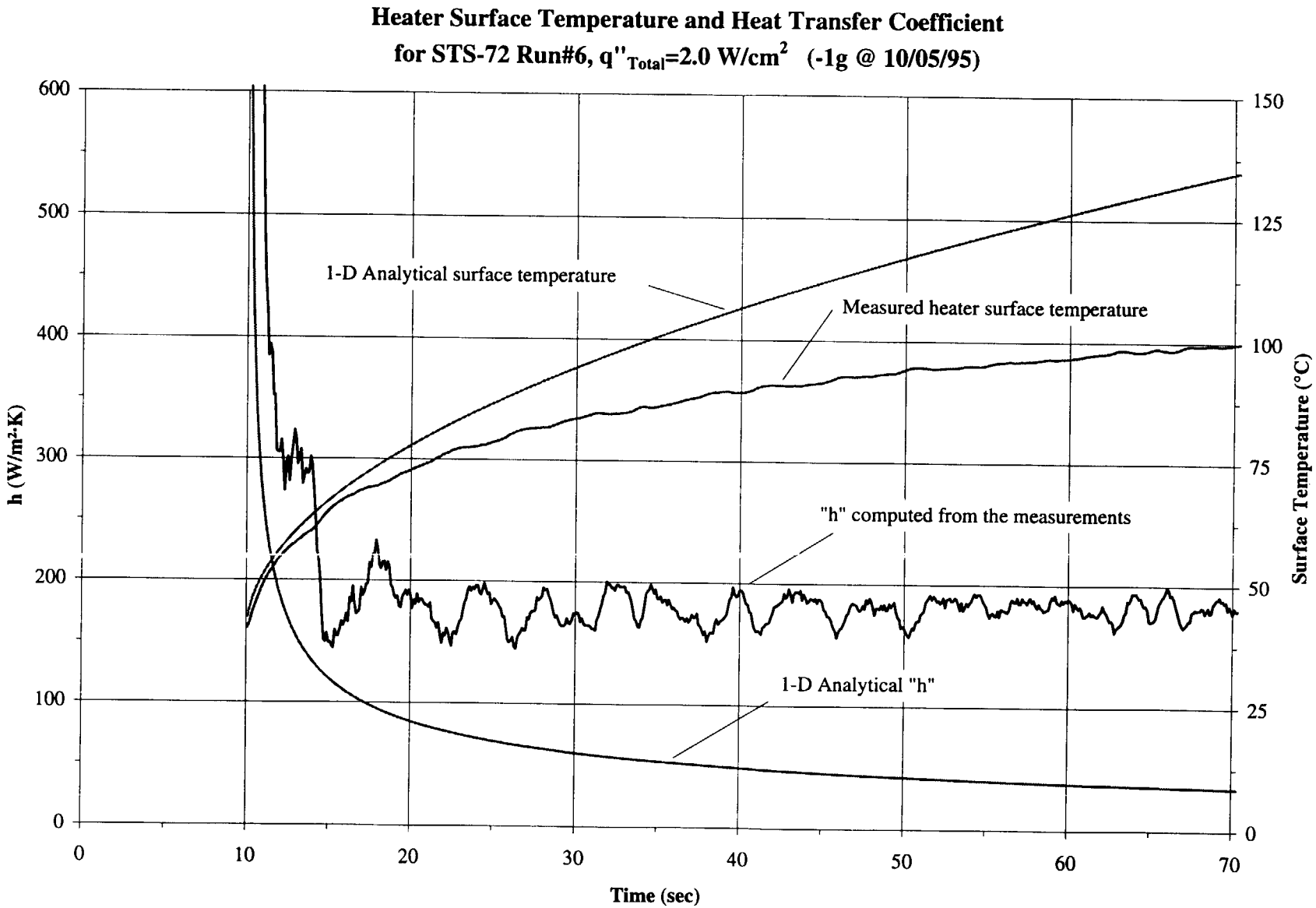

Figure A-11f. a/g = -1 Preflight test. Mean heater surface temperature and derived heat transfer coefficient. PBE-IIB (STS-72). Run No. 6.

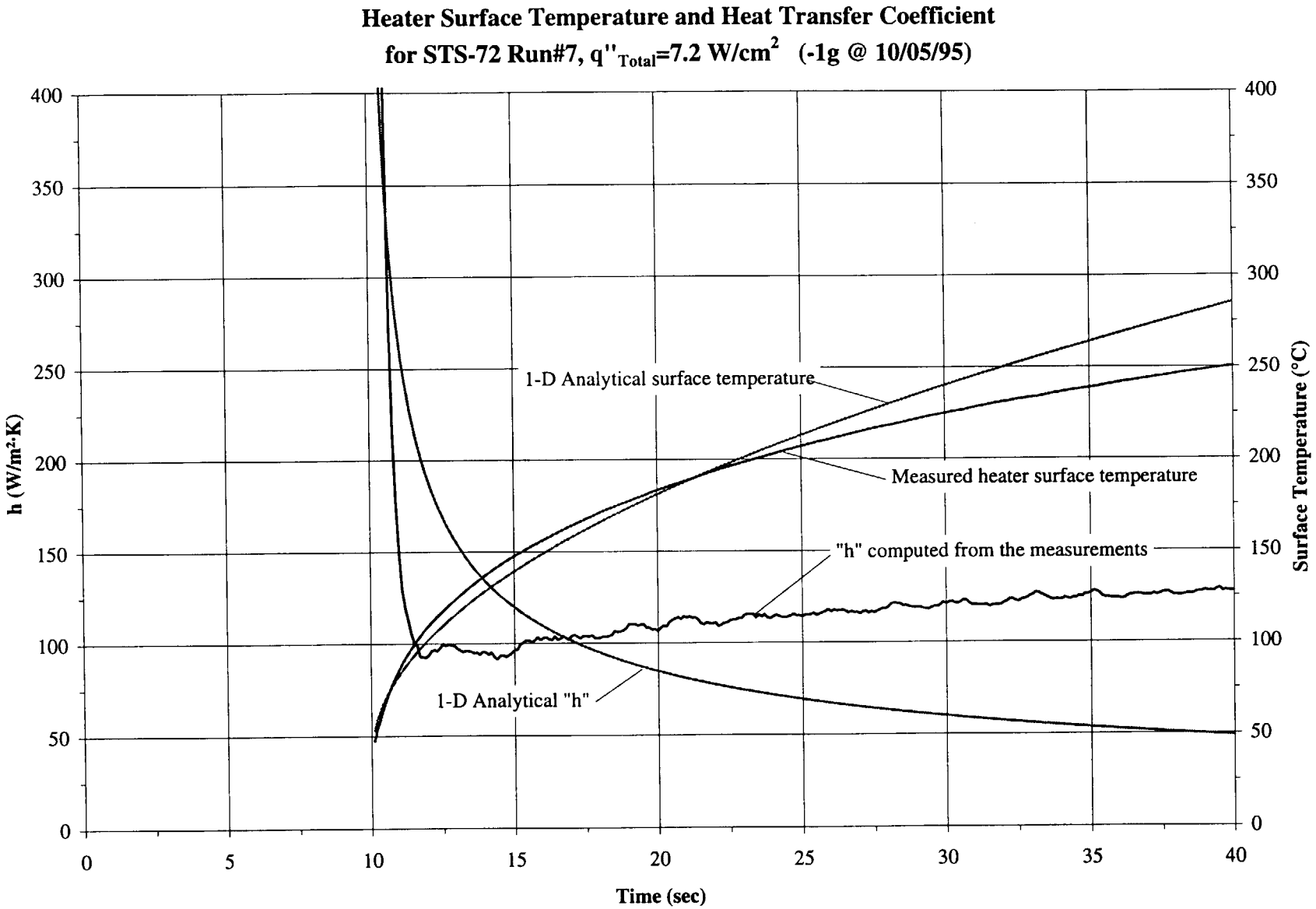

Figure A-11g. a/g = -1 Preflight test. Mean heater surface temperature and derived heat transfer coefficient. PBE-IIB (STS-72). Run No. 7.

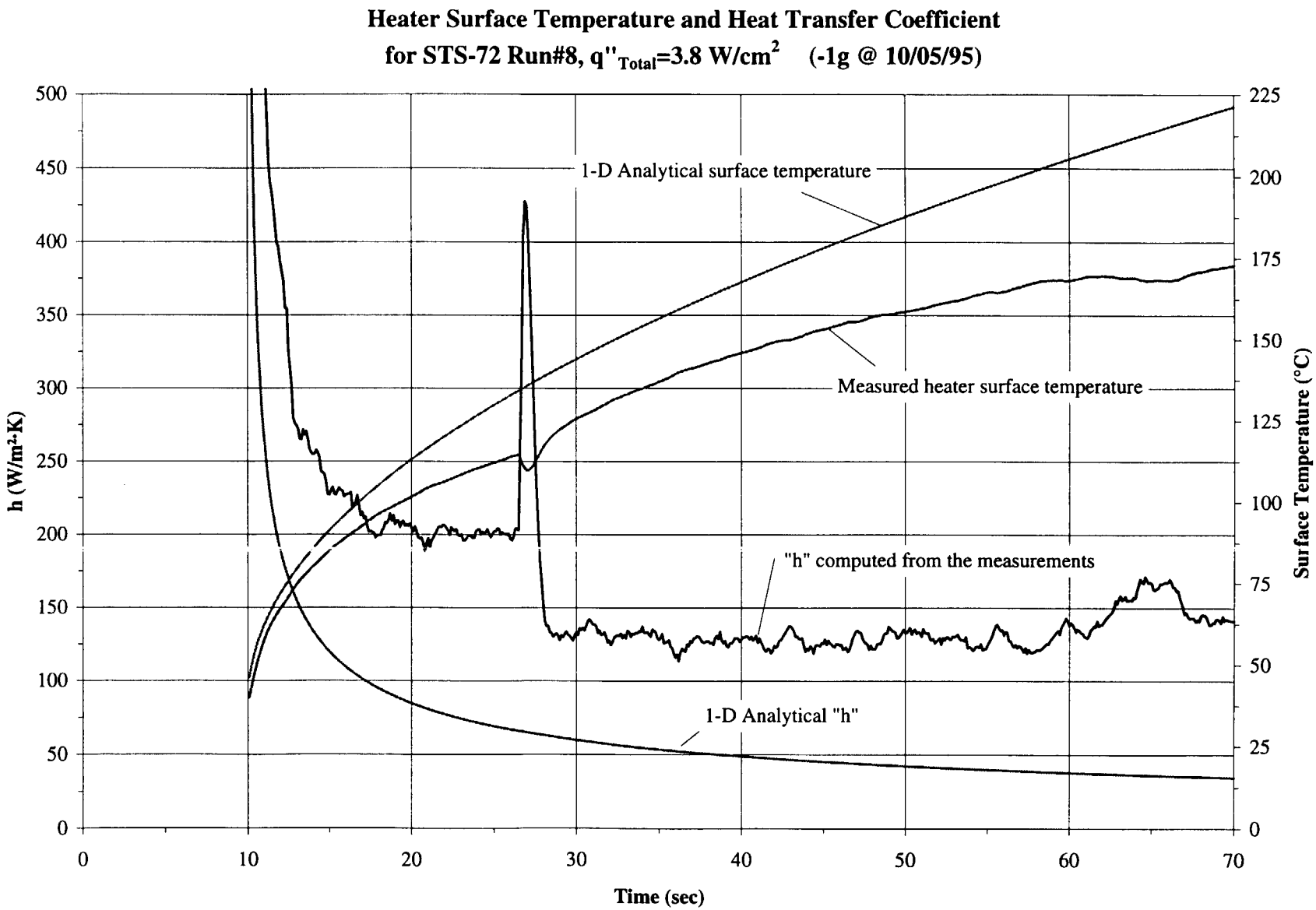

Figure A-11h. a/g = -1 Preflight test. Mean heater surface temperature and derived heat transfer coefficient. PBE-IIB (STS-72). Run No. 8.

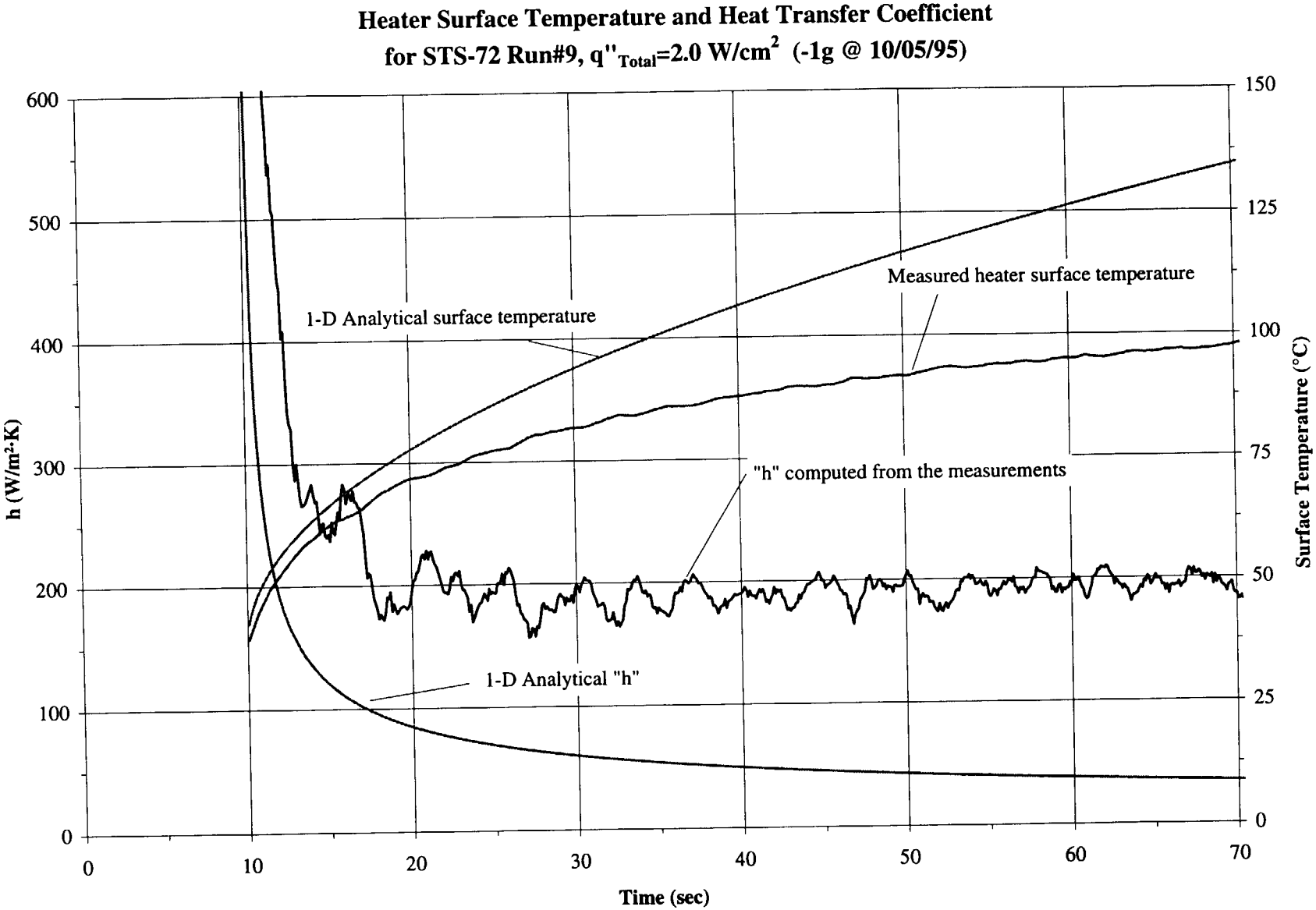

Figure A-11i. a/g = -1 Preflight test. Mean heater surface temperature and derived heat transfer coefficient. PBE-IIB (STS-72). Run No. 9.

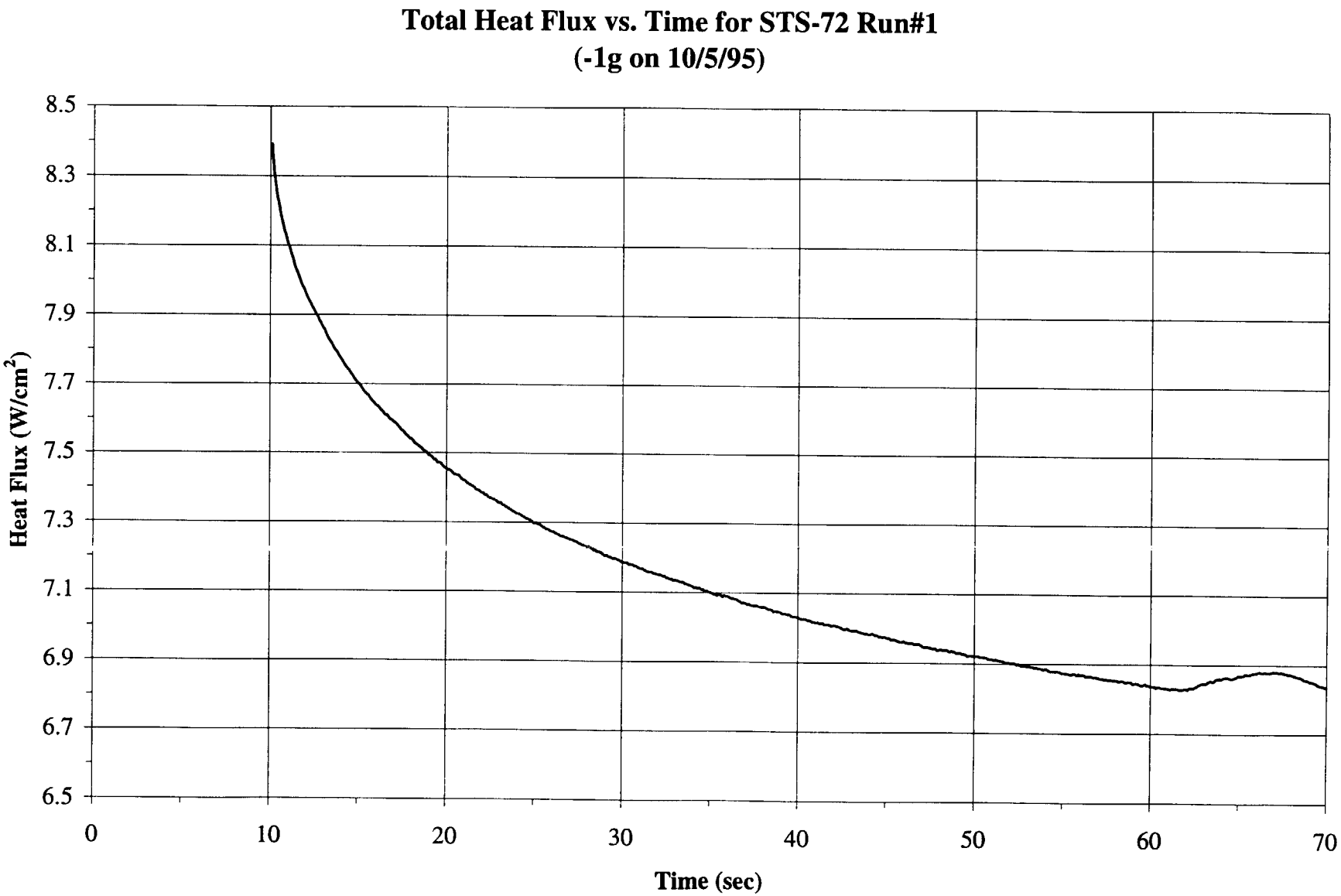

Figure A-12a. a/g = -1 Preflight test. Heat flux input. PBE-IIB (STS-72). Run No. 1.

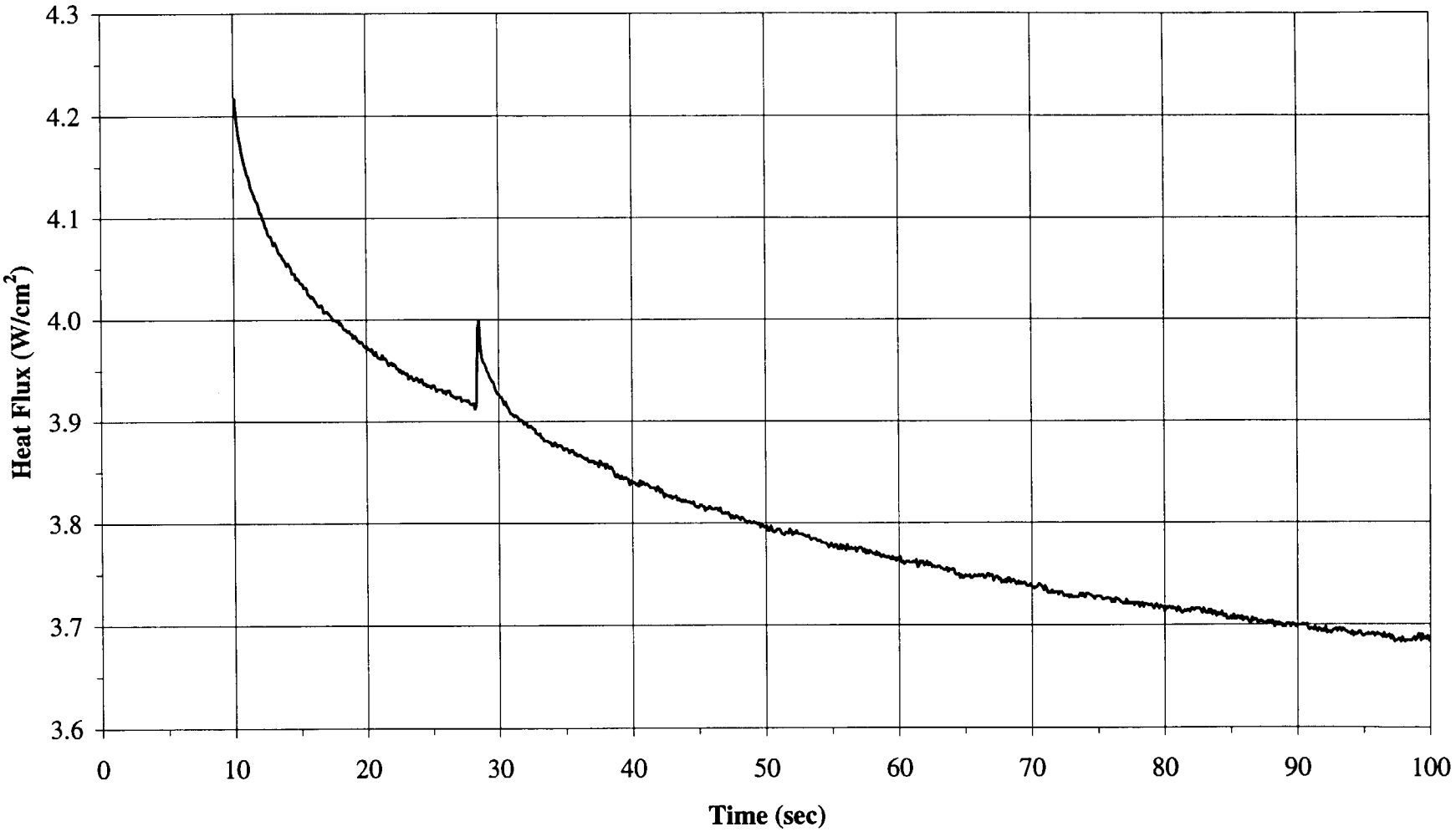

Figure A-12b. a/g = -1 Preflight test. Heat flux input. PBE-IIB (STS-72). Run No. 2.

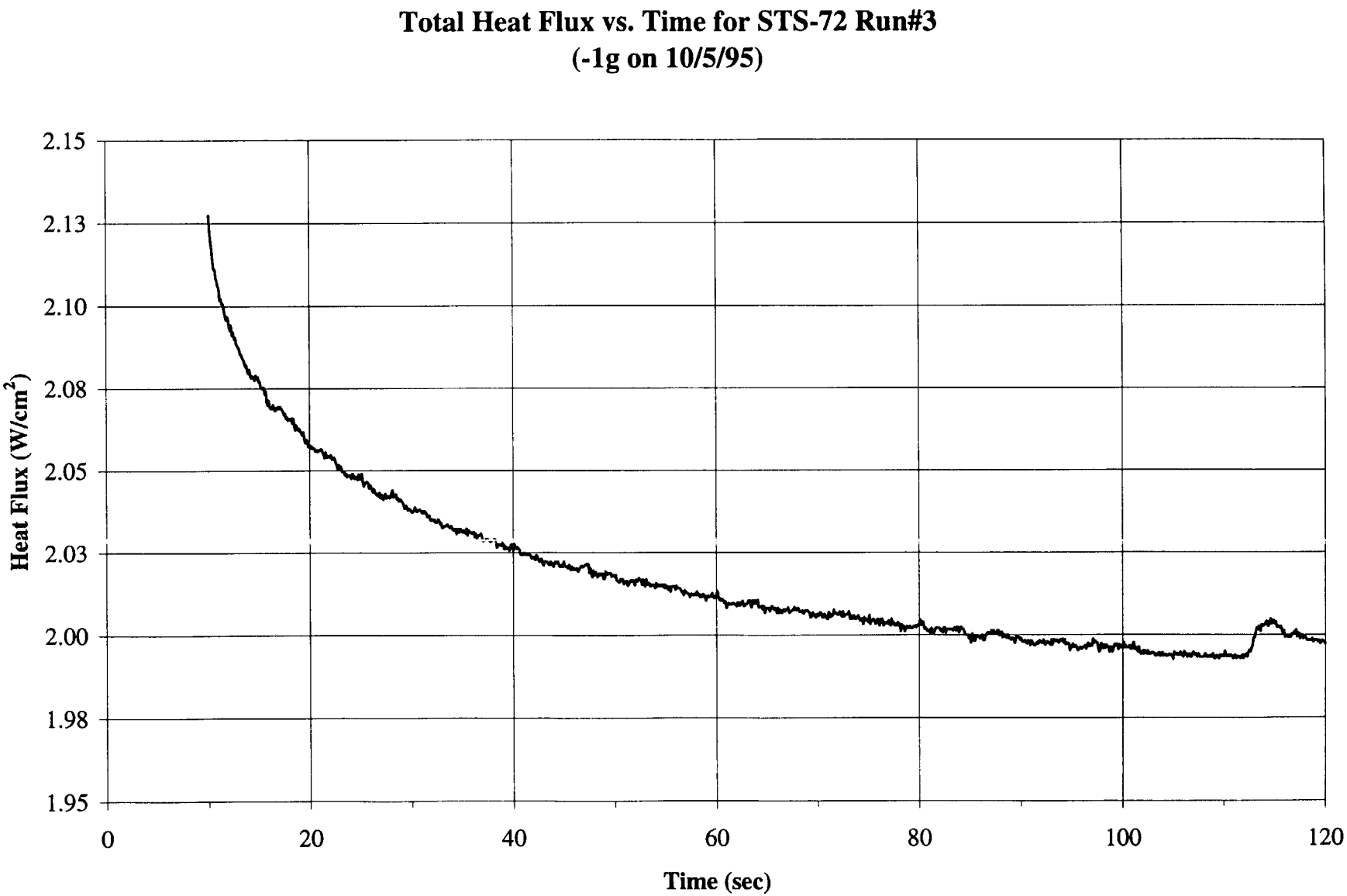

Figure A-12c. a/g = -1 Preflight test. Heat flux input. PBE-IIB (STS-72). Run No. 3.

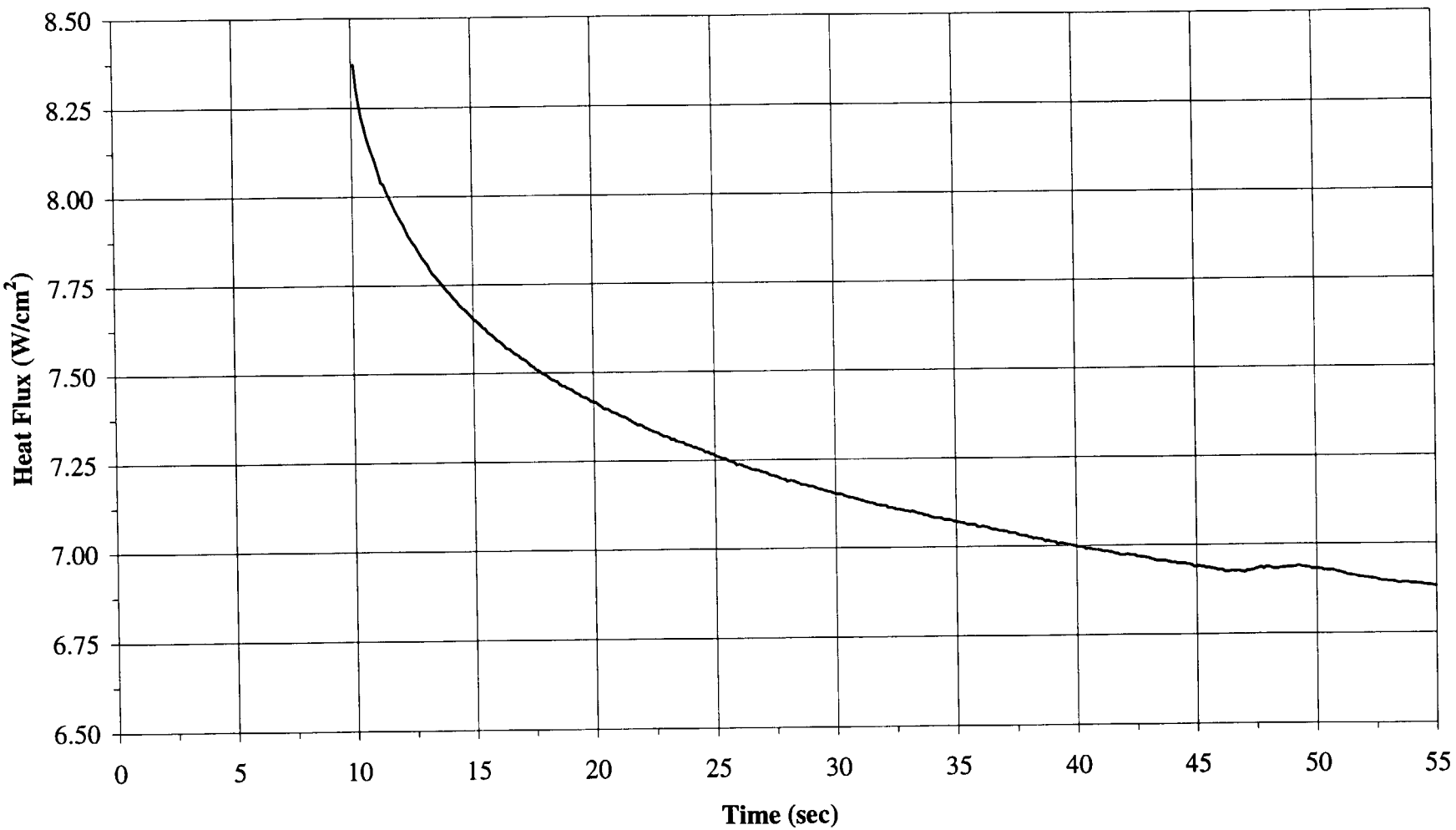

Figure A-12d. a/g = -1 Preflight test. Heat flux input. PBE-IIB (STS-72). Run No. 4.

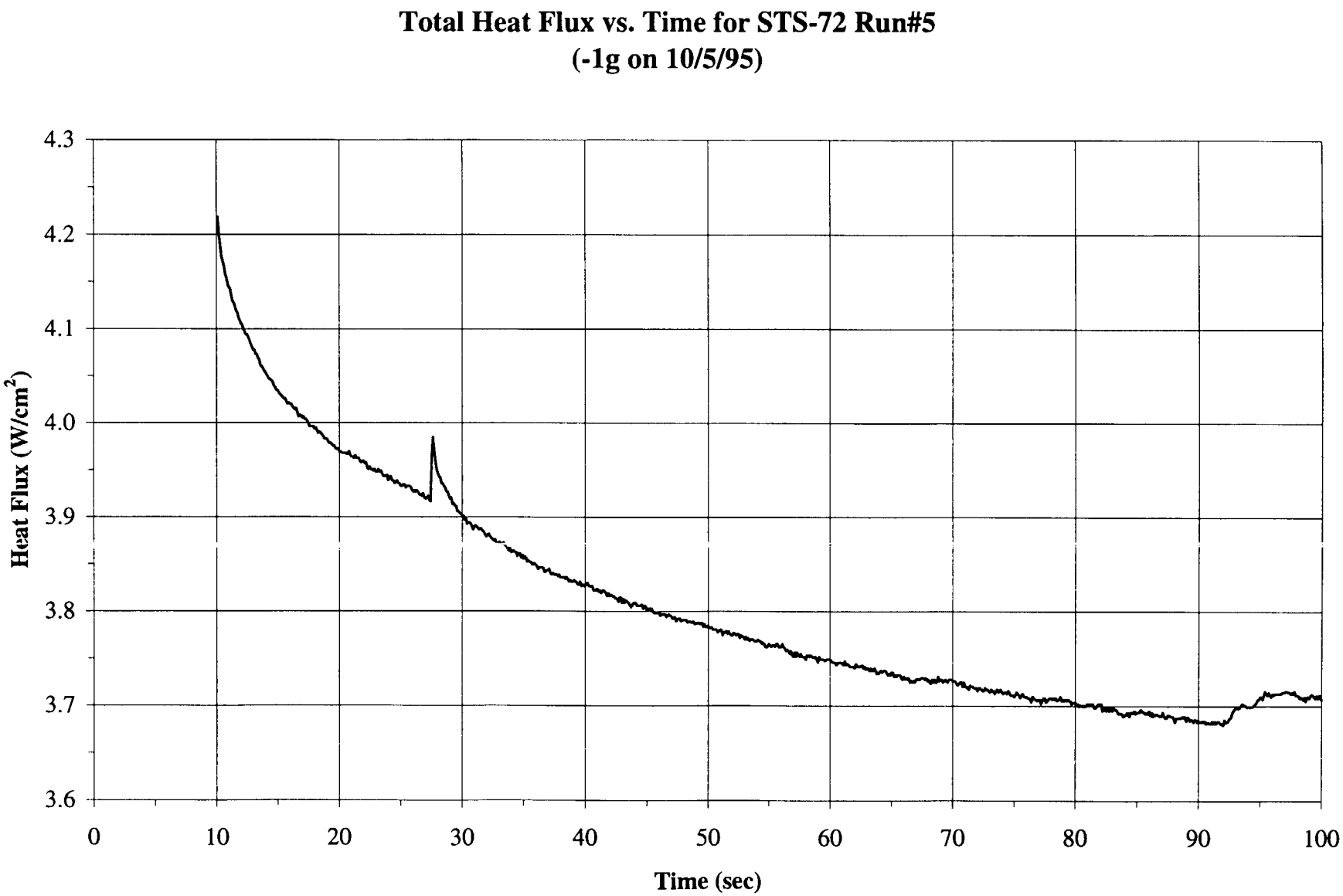

Figure A-12e. a/g = -1 Preflight test. Heat flux input. PBE-IIB (STS-72). Run No. 5.

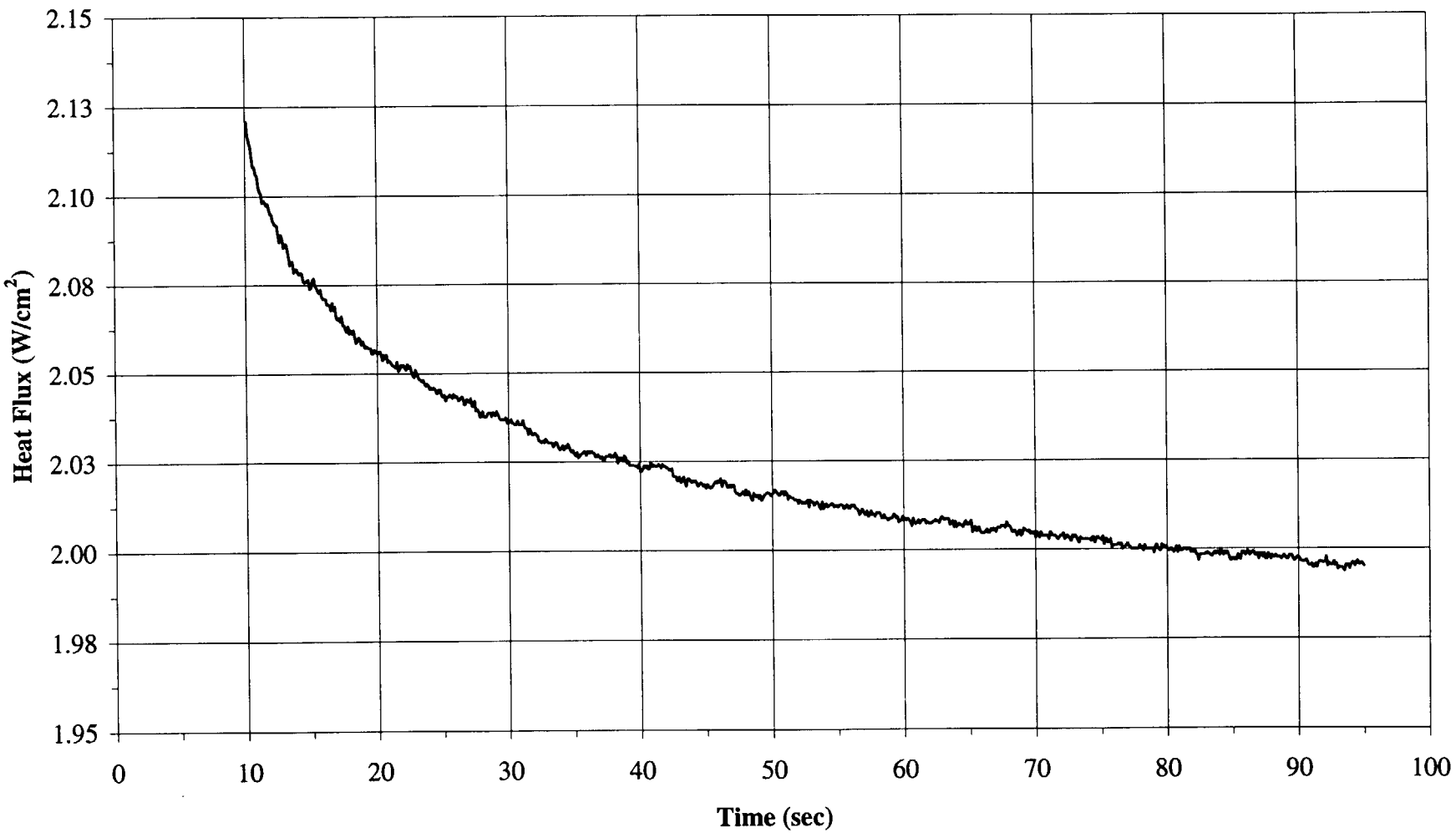

Figure A-12f. a/g = -1 Preflight test. Heat flux input. PBE-IIB (STS-72). Run No. 6.

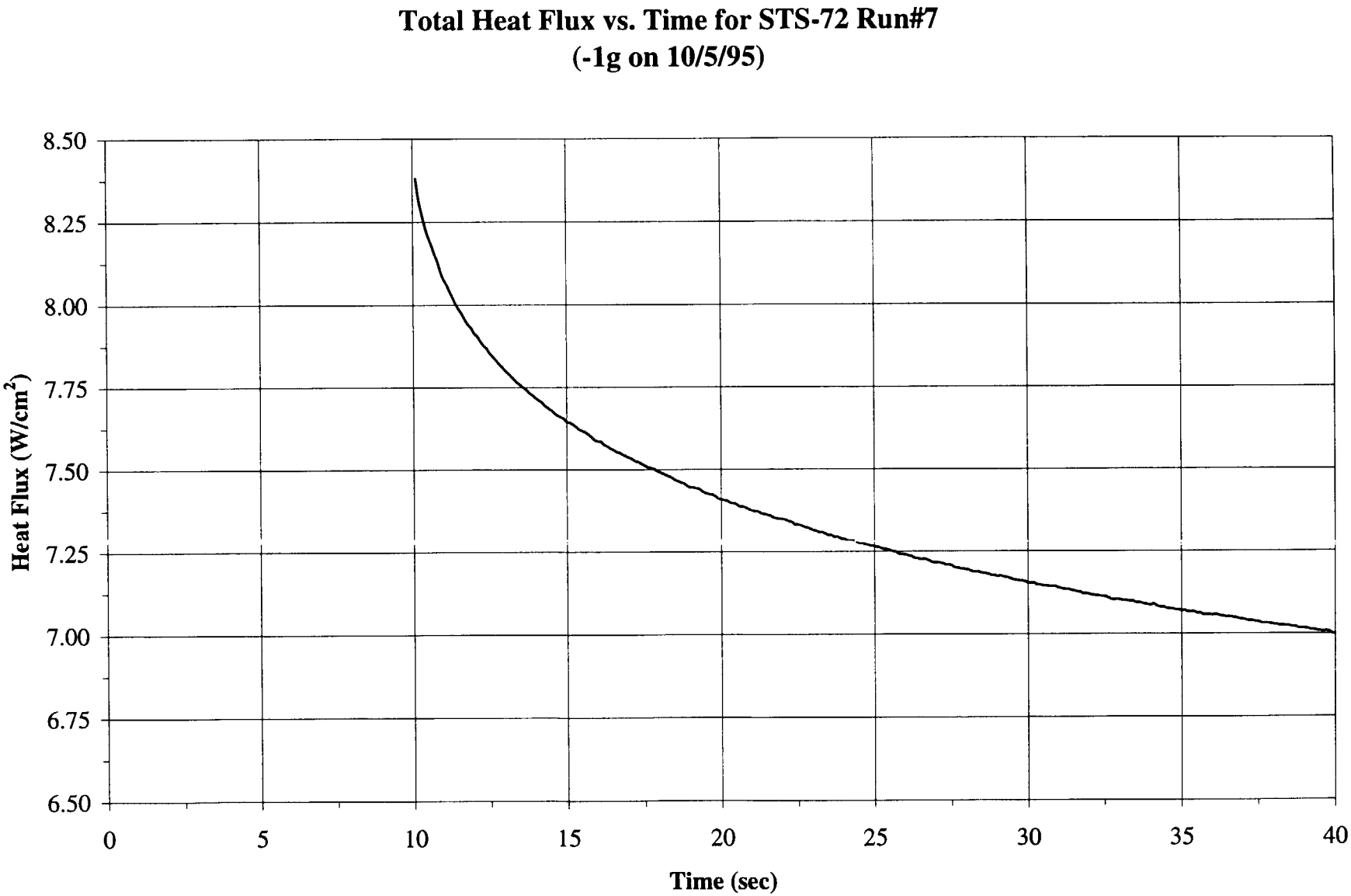

Figure A-12g. a/g = -1 Preflight test. Heat flux input. PBE-IIB (STS-72). Run No. 7.

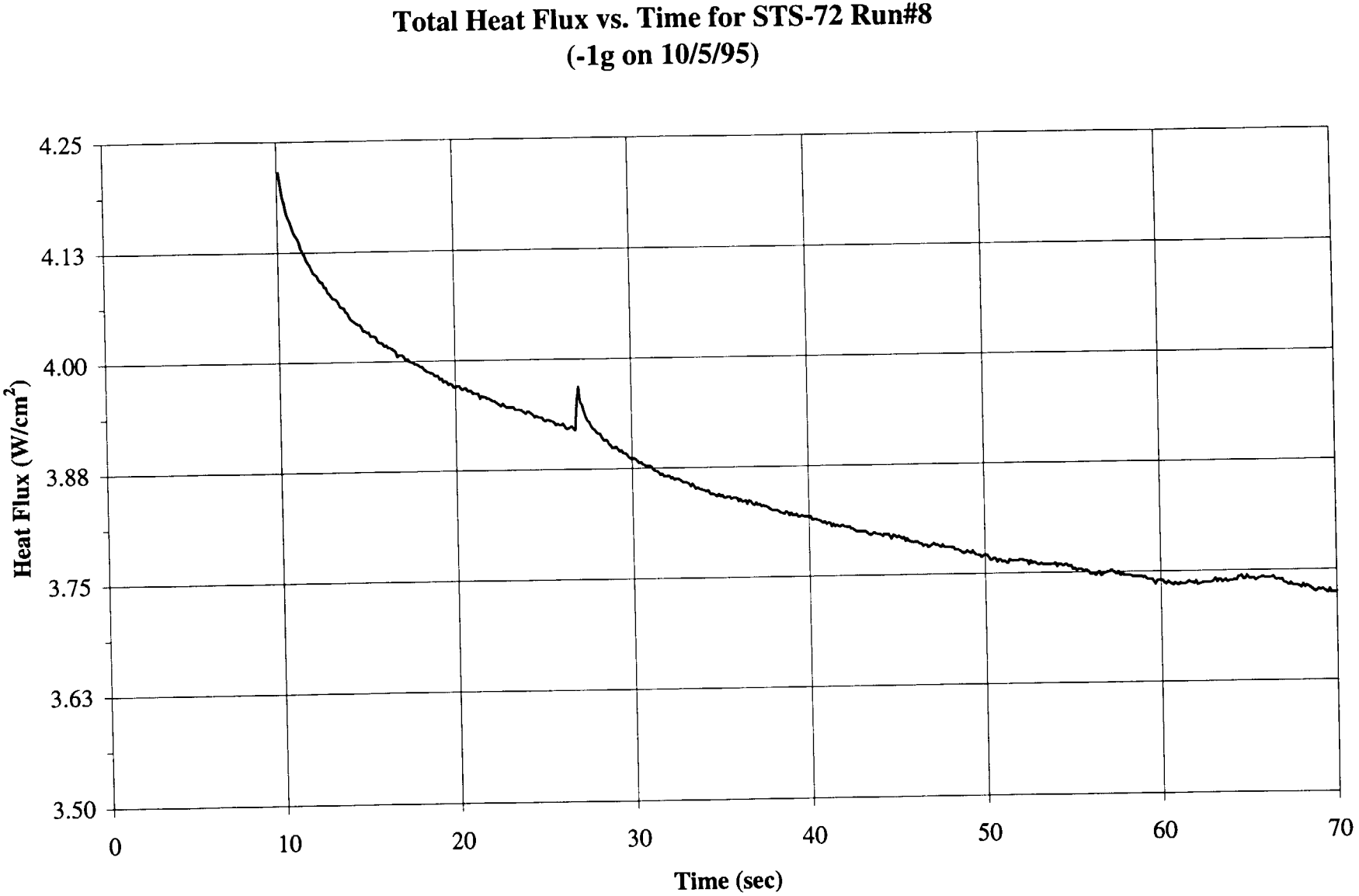

Figure A-12h. a/g = -1 Preflight test. Heat flux input. PBE-IIB (STS-72). Run No. 8.

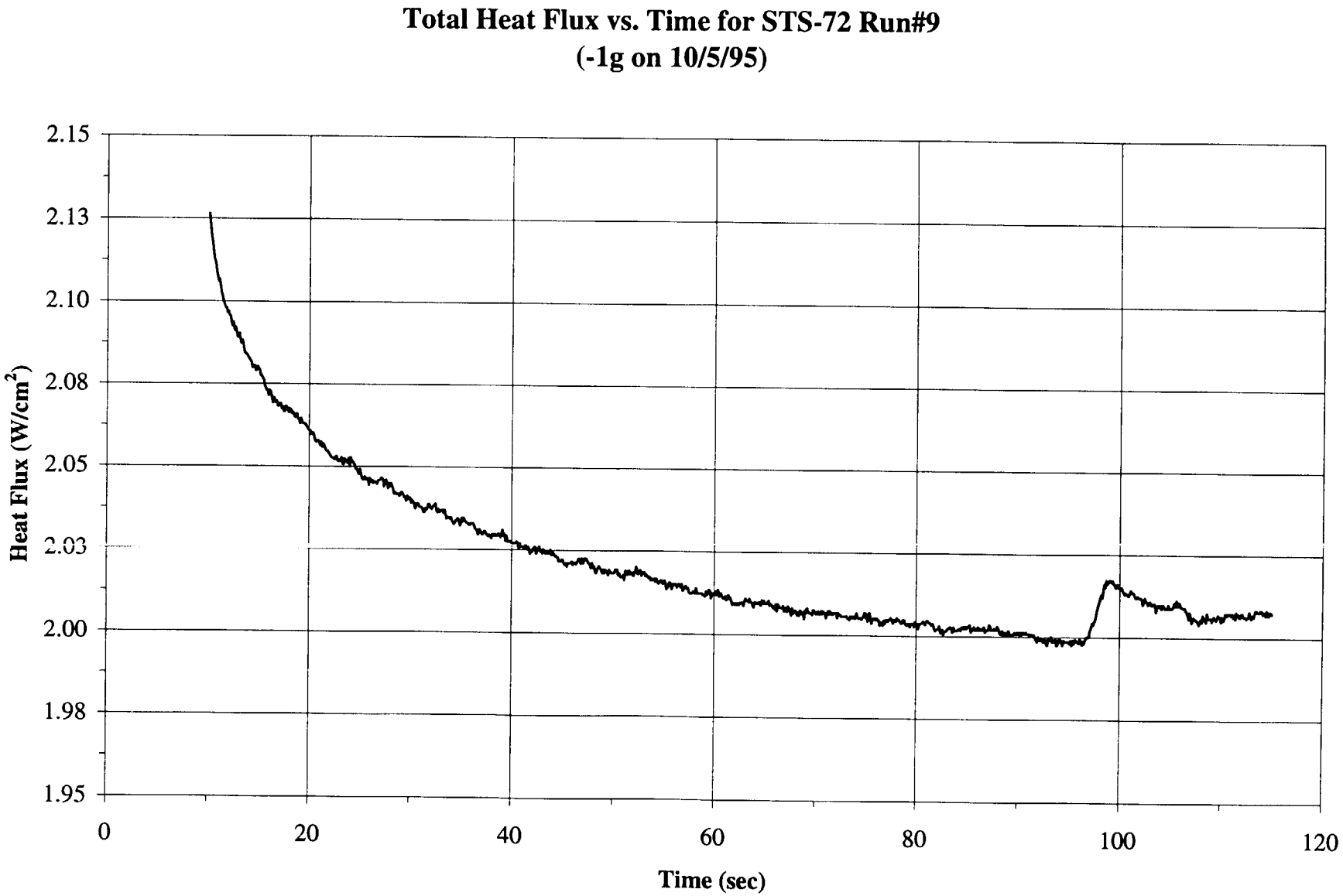

Figure A-12i. a/g = -1 Preflight test. Heat flux input. PBE-IIB (STS-72). Run No. 9.

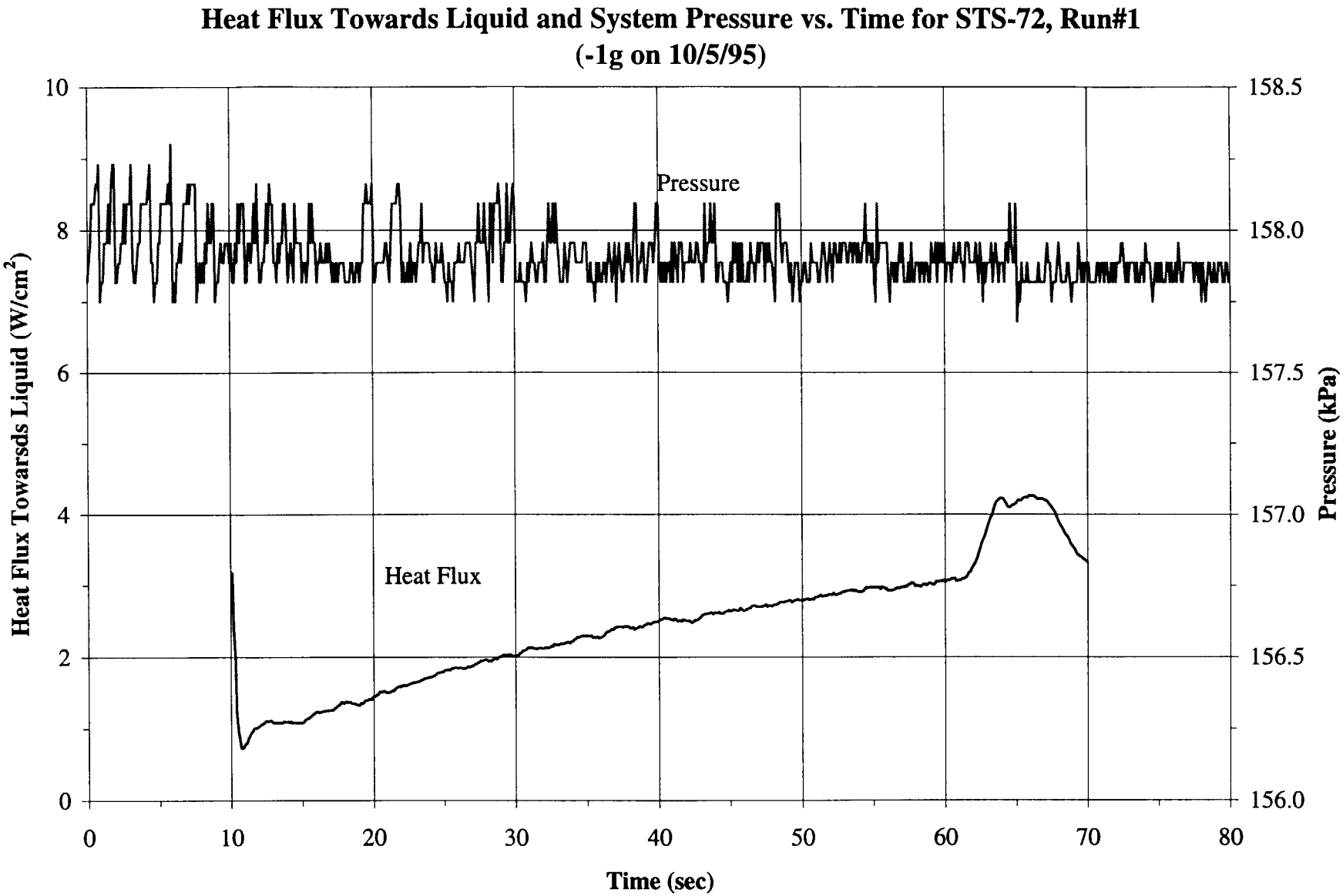

Figure A-13a. a/g = -1 Preflight test. System pressure and heat flux into fluid. PBE-IIB (STS-72). Run No. 1.

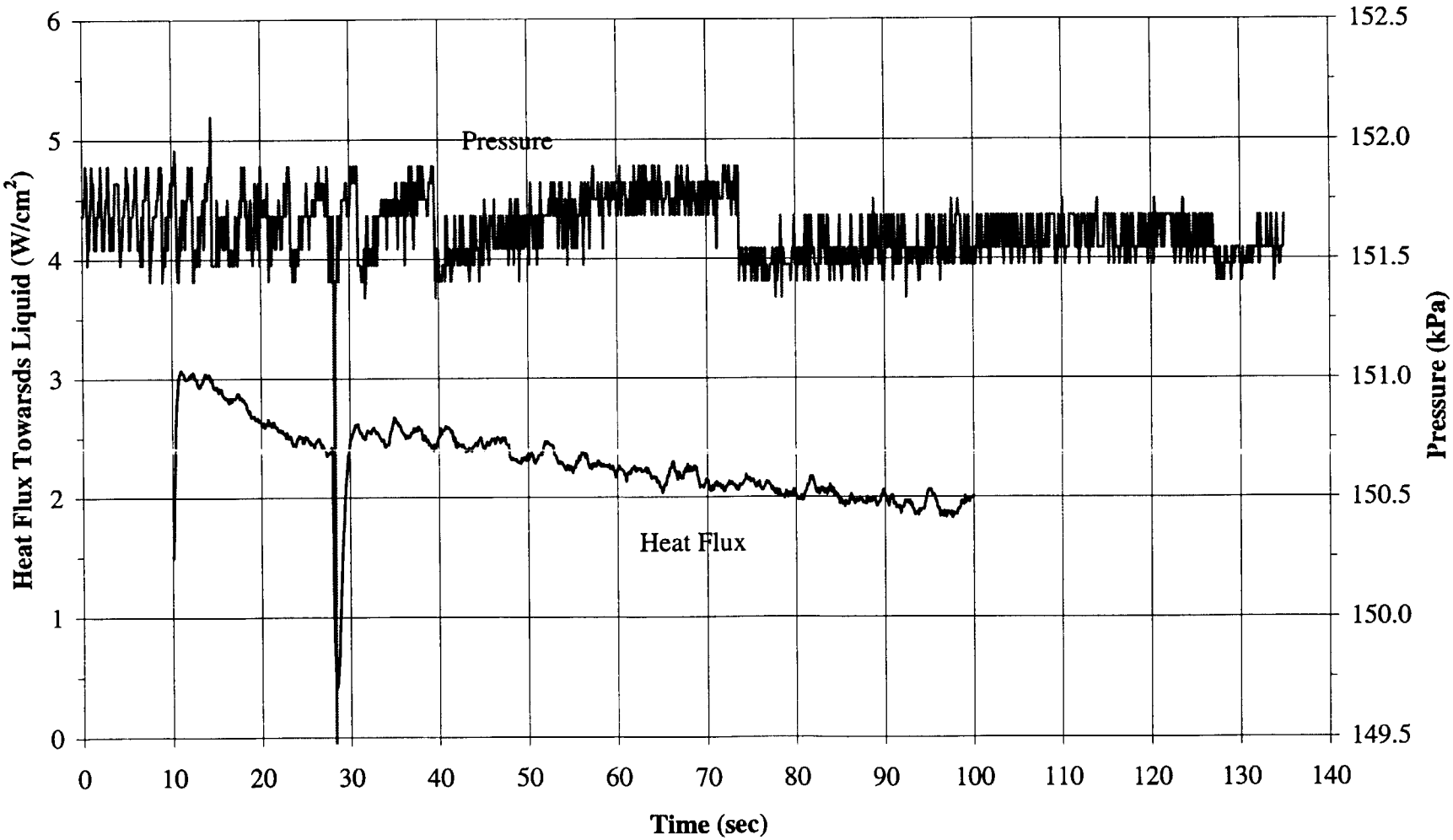

Figure A-13b. a/g = -1 Preflight test. System pressure and heat flux into fluid. PBE-IIB (STS-72). Run No. 2.

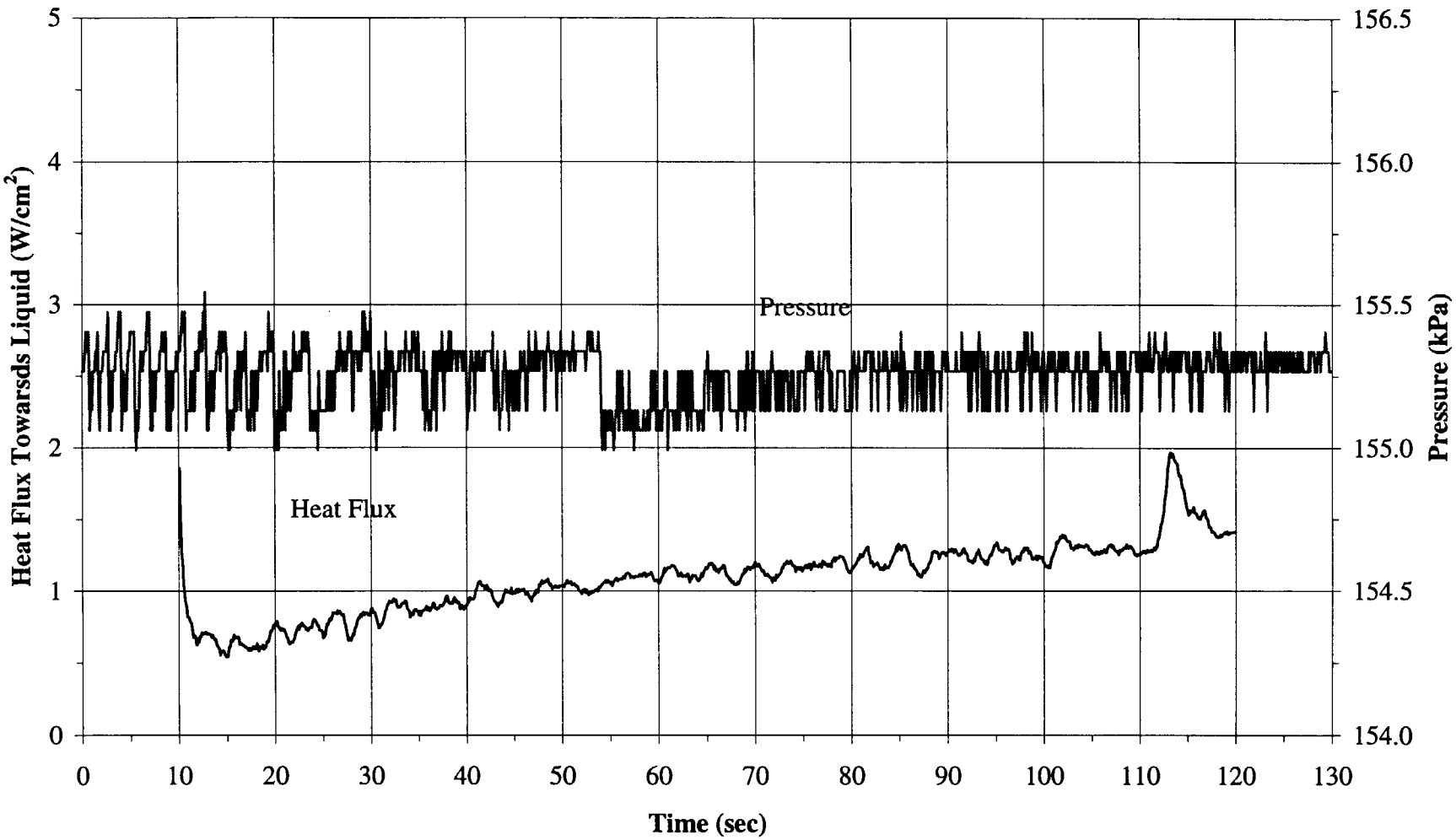

Figure A-13c. a/g = -1 Preflight test. System pressure and heat flux into fluid. PBE-IIB (STS-72). Run No. 3.

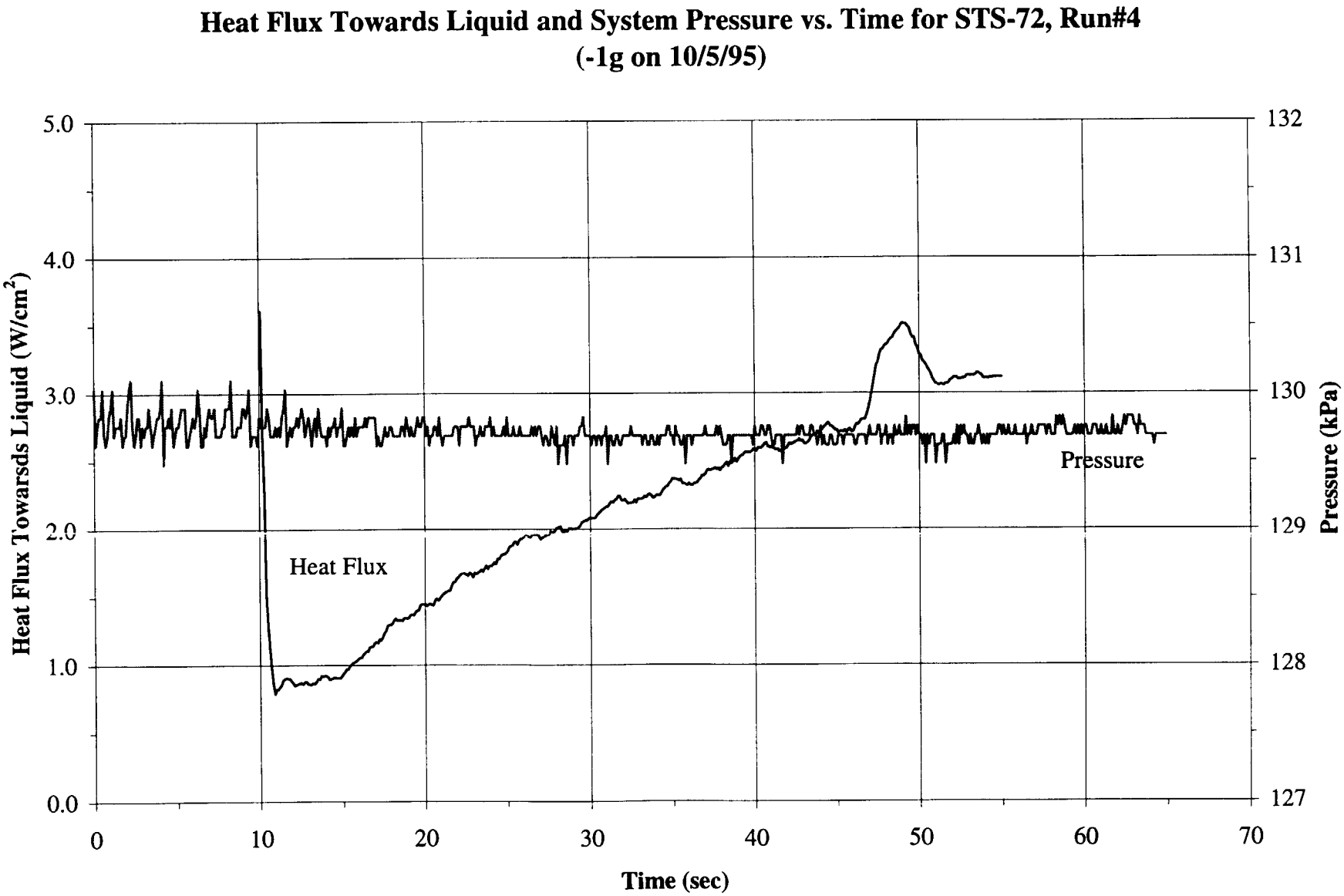

Figure A-13d. a/g = -1 Preflight test. System pressure and heat flux into fluid. PBE-IIB (STS-72). Run No. 4.

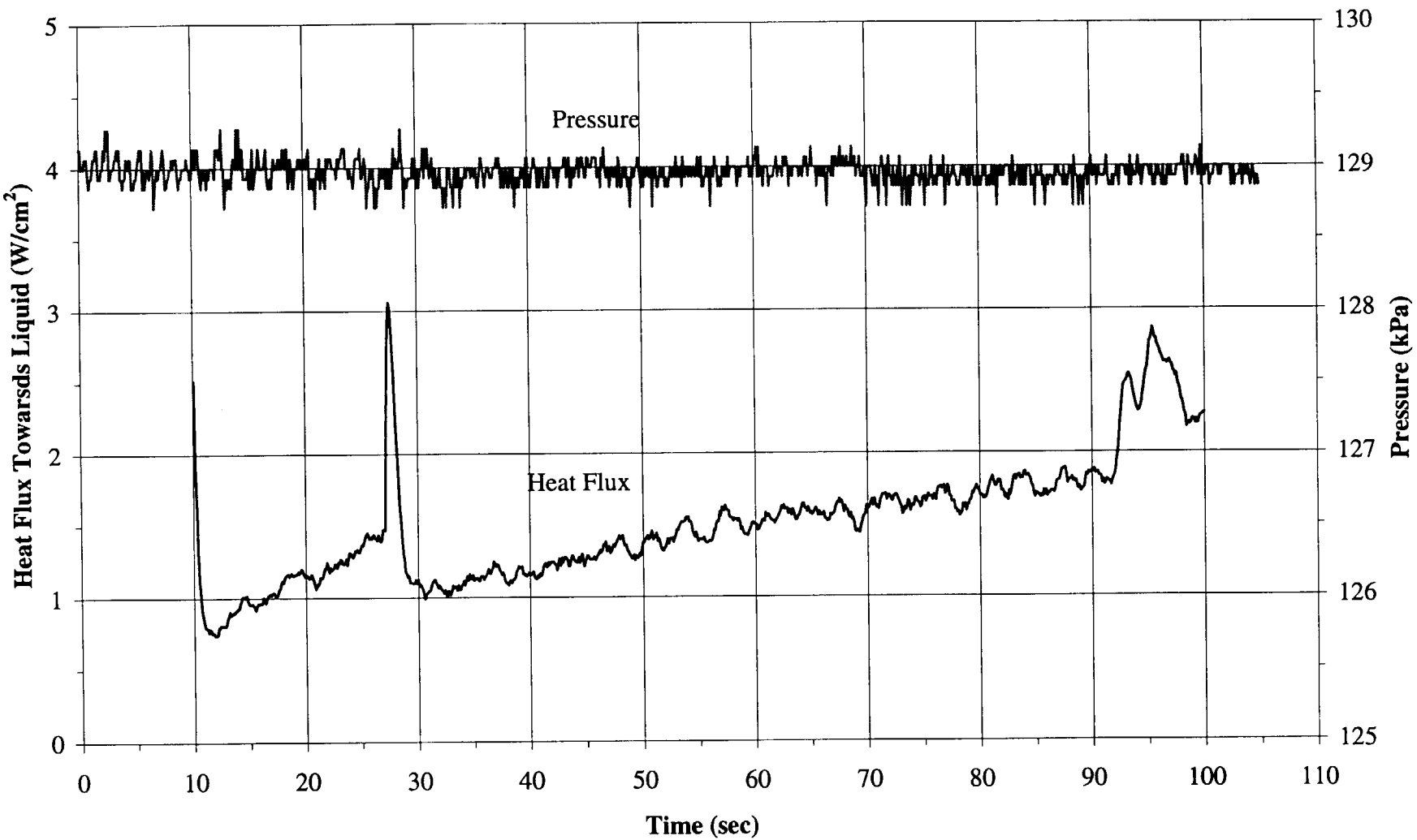

Figure A-13e. a/g = -1 Preflight test. System pressure and heat flux into fluid. PBE-IIB (STS-72). Run No. 5.

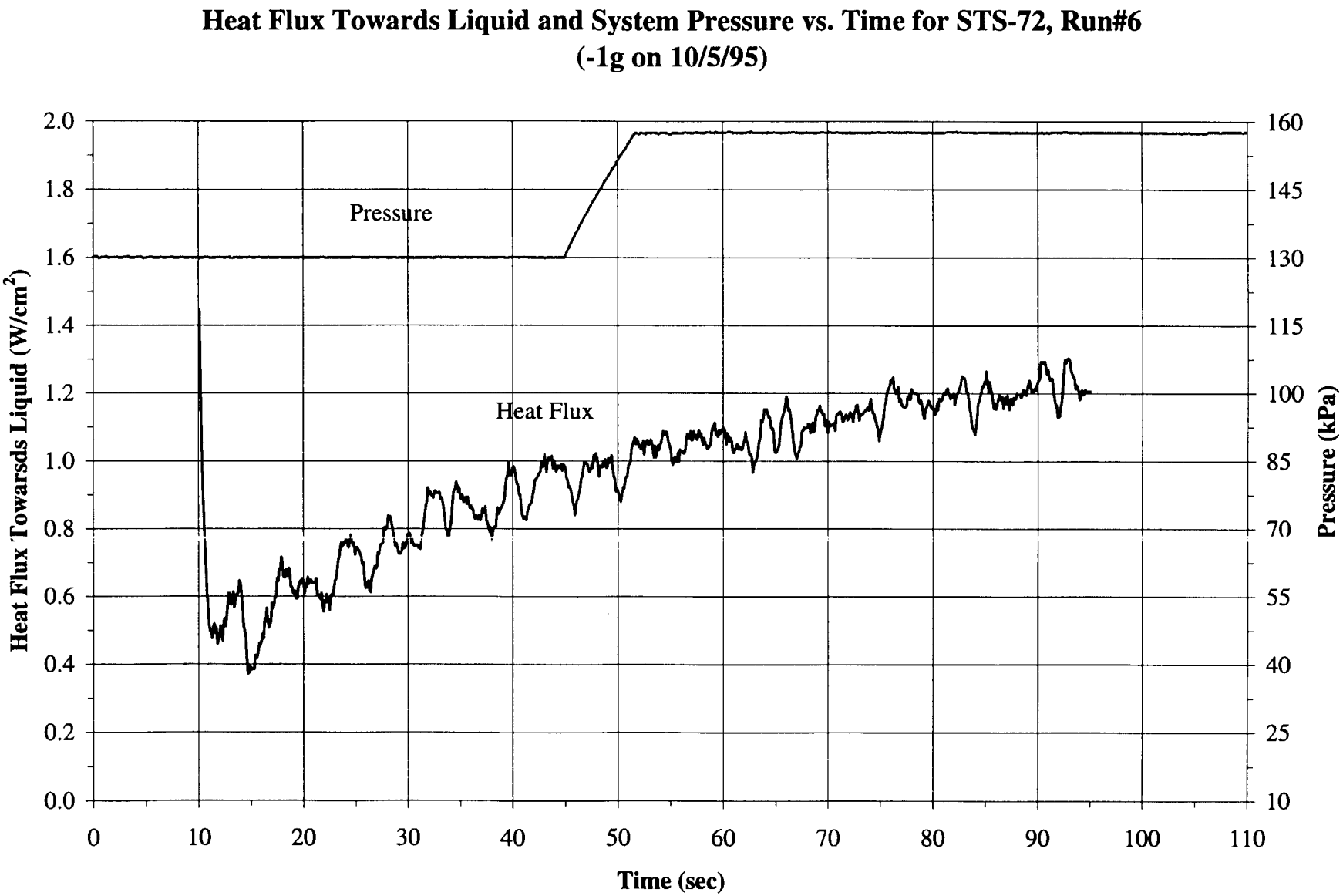

Figure A-13f. a/g = -1 Preflight test. System pressure and heat flux into fluid. PBE-IIB (STS-72). Run No. 6.

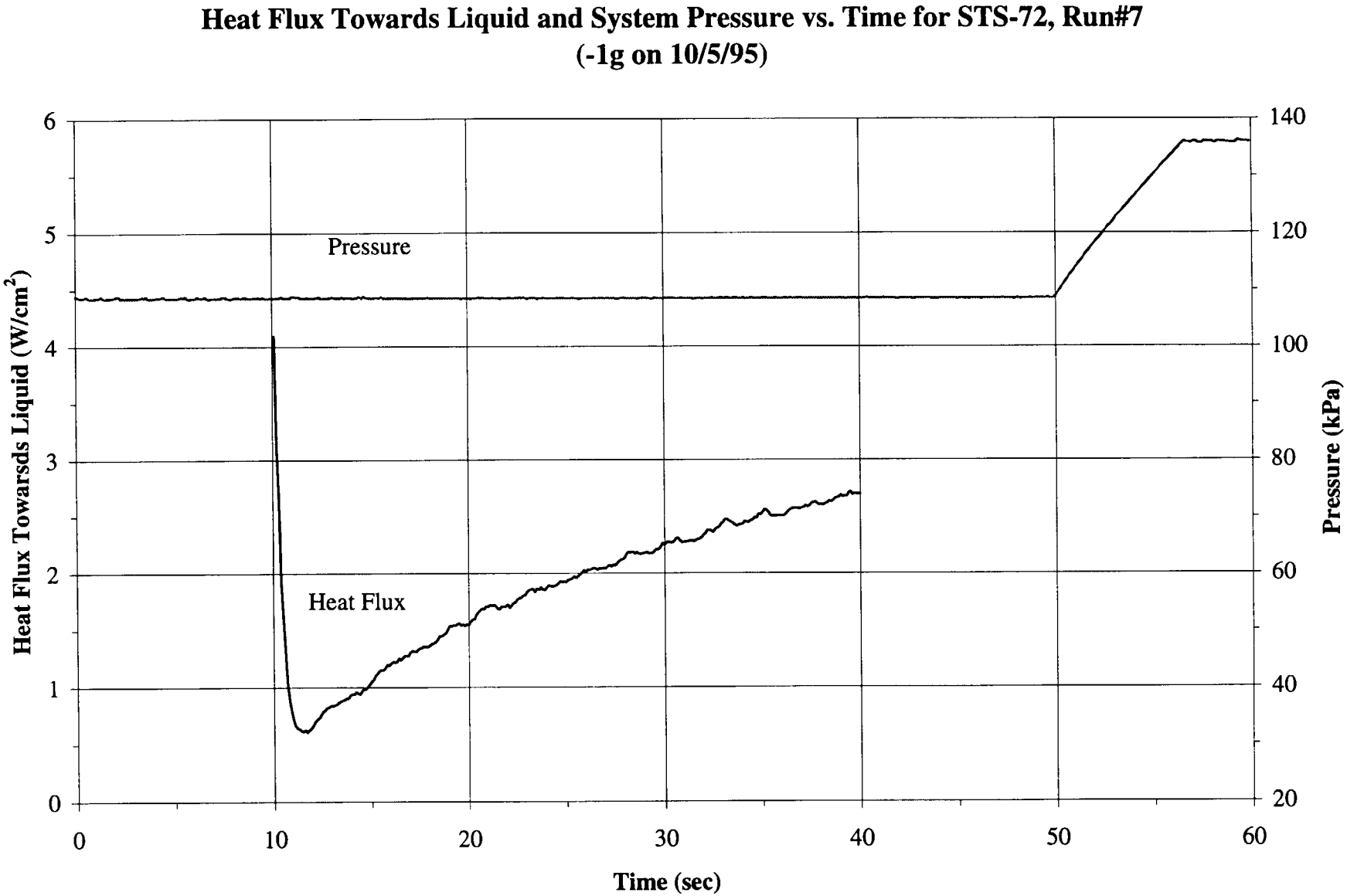

Figure A-13g. a/g = -1 Preflight test. System pressure and heat flux into fluid. PBE-IIB (STS-72). Run No. 7.

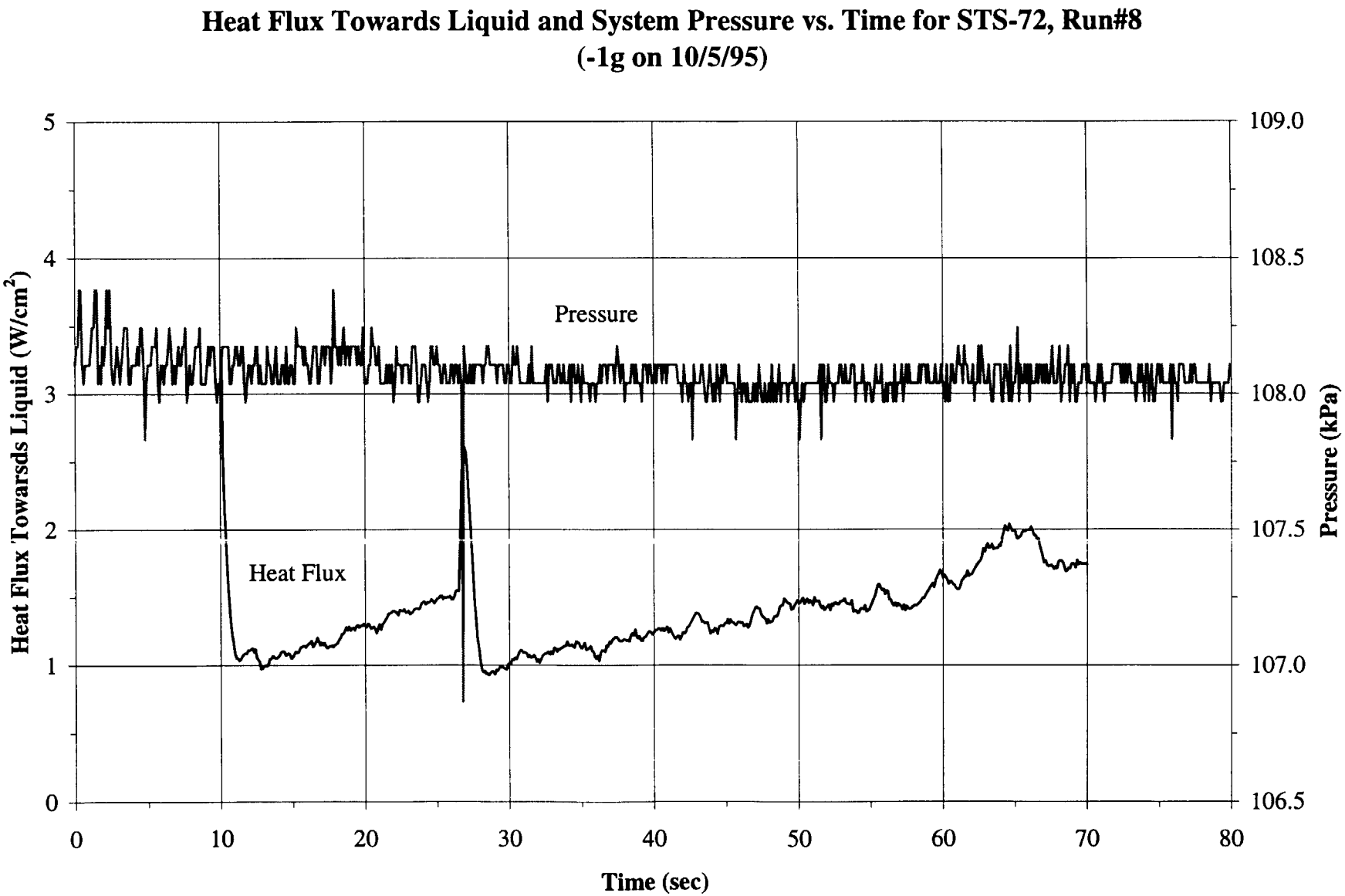

Figure A-13h. a/g = -1 Preflight test. System pressure and heat flux into fluid. PBE-IIB (STS-72). Run No. 8.

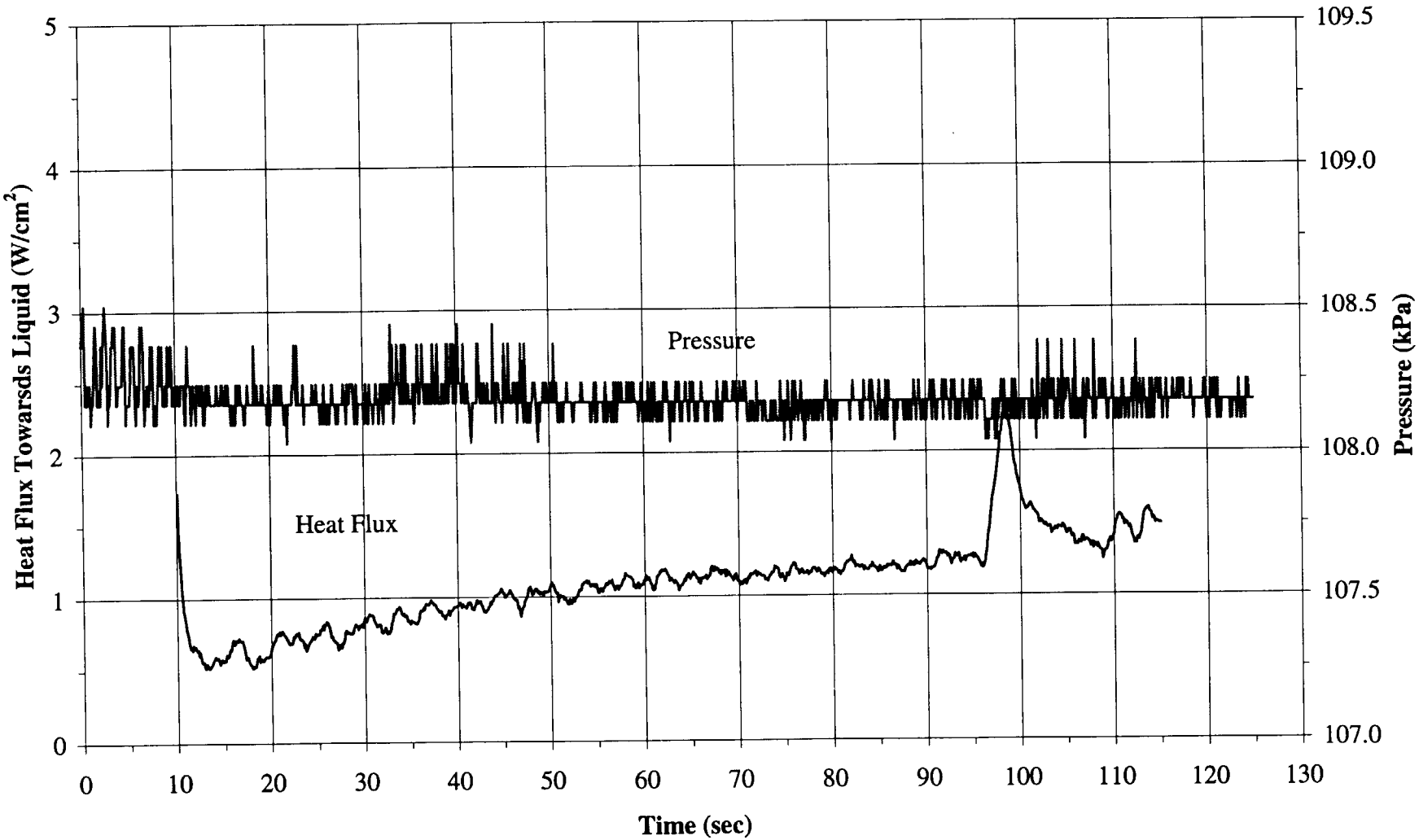

Figure A-13i. a/g = -1 Preflight test. System pressure and heat flux into fluid. PBE-IIB (STS-72). Run No. 9.

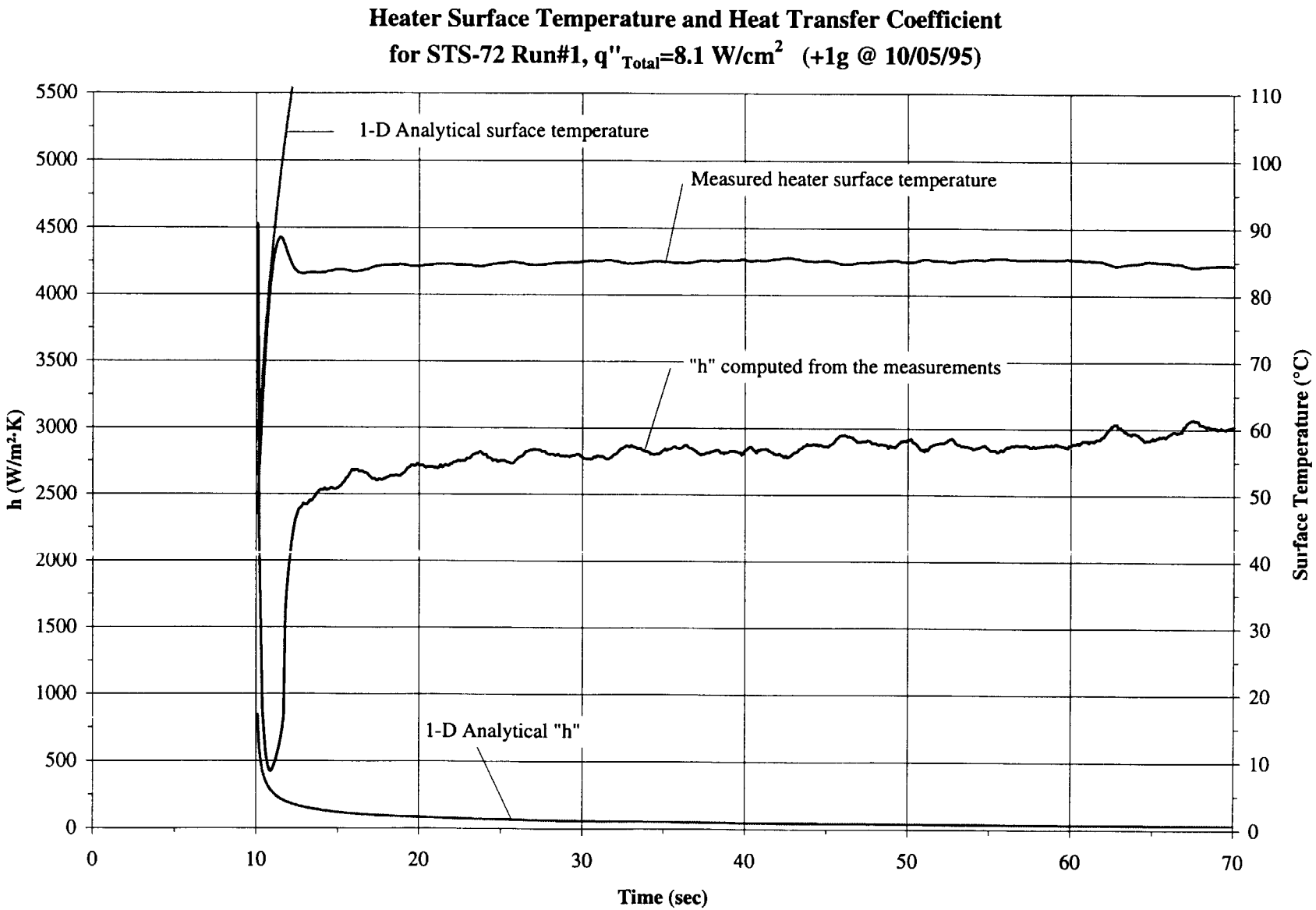

Figure A-14a. a/g = + 1 Preflight test. Mean heater surface temperature and derived heat transfer coefficient. PBE-IIB (STS-72). Run No. 1.

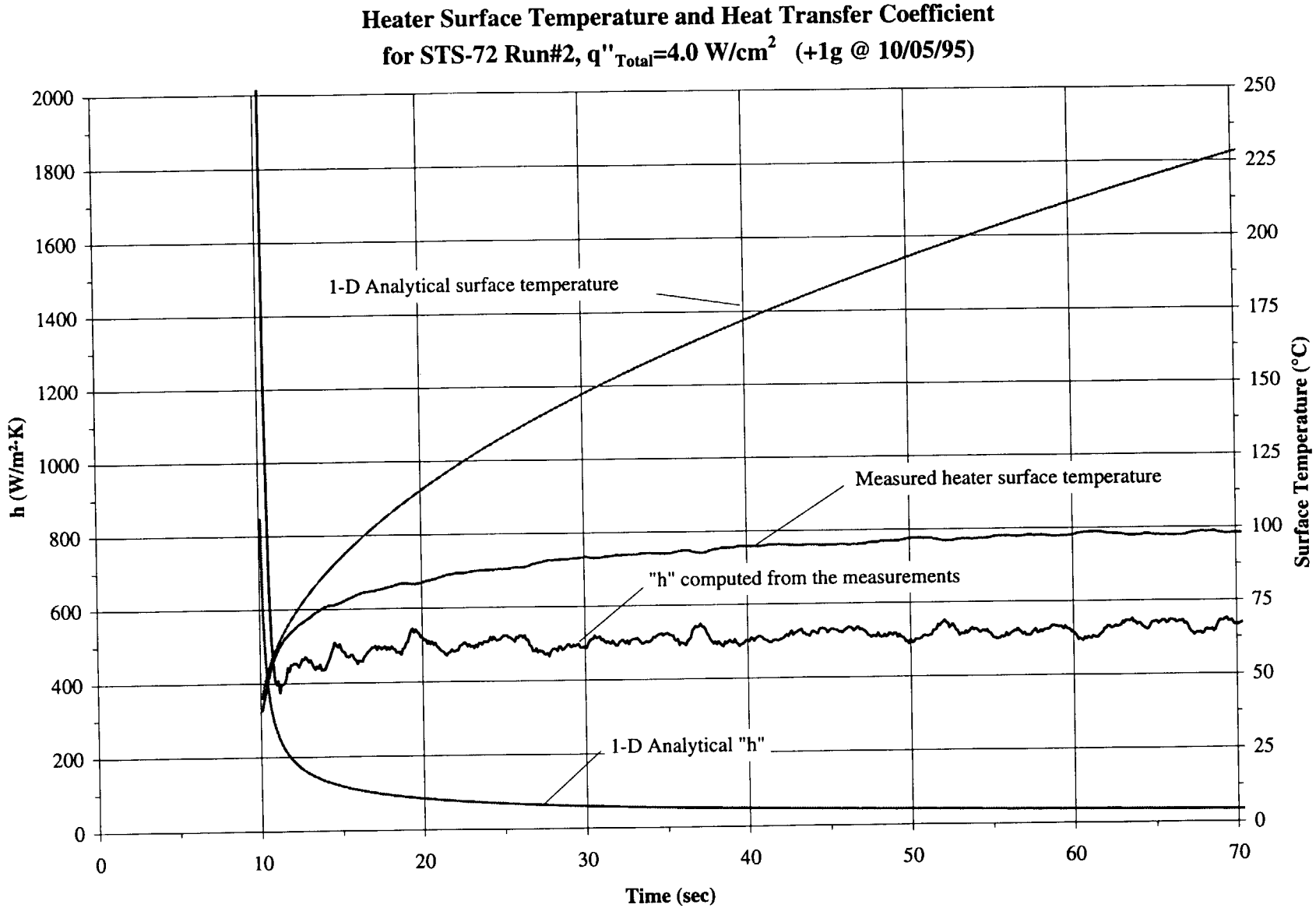

Figure A-14b. a/g = + 1 Preflight test. Mean heater surface temperature and derived heat transfer coefficient. PBE-IIB (STS-72). Run No. 2.

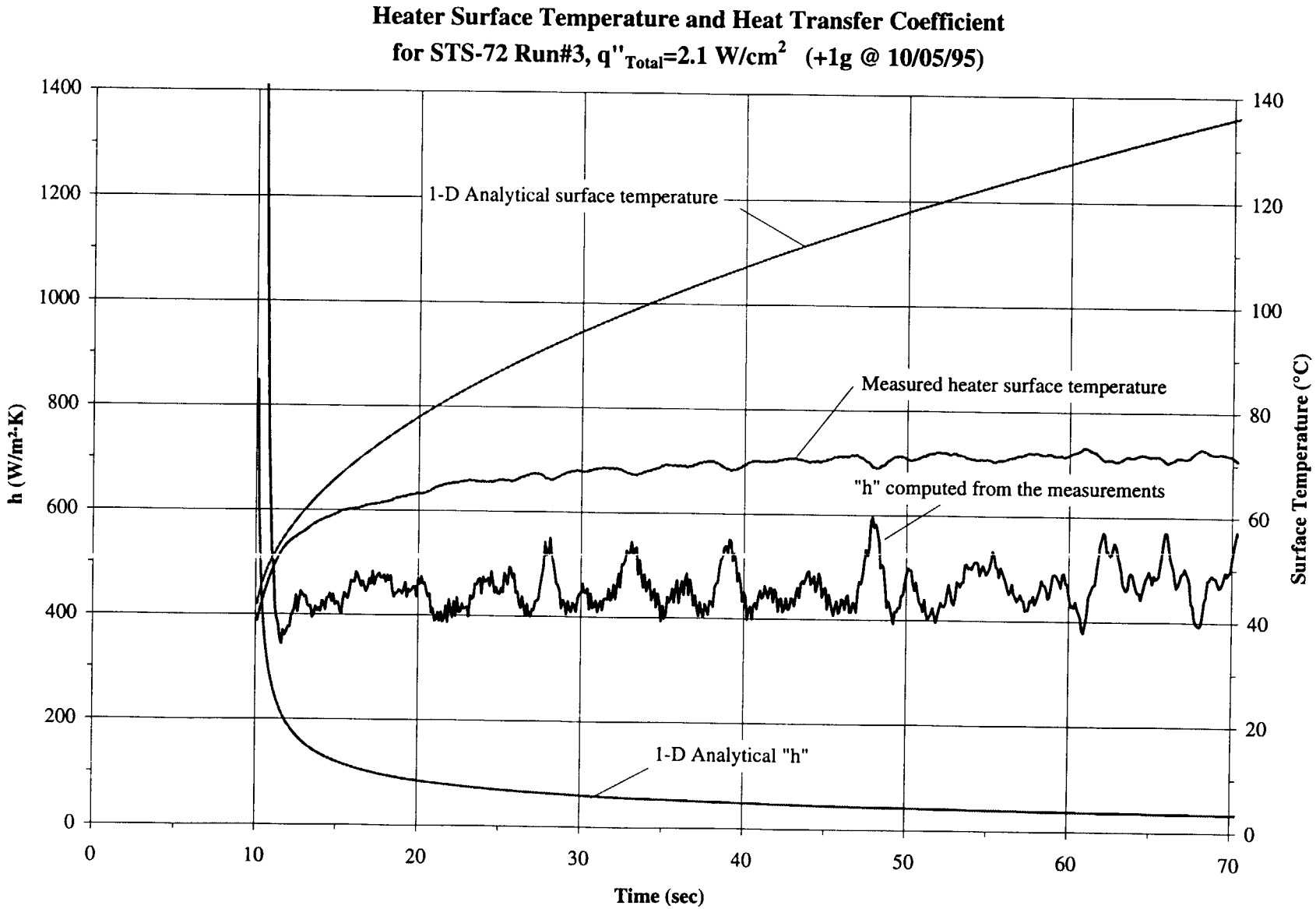

Figure A-14c. a/g = + 1 Preflight test. Mean heater surface temperature and derived heat transfer coefficient. PBE-IIB (STS-72). Run No. 3.

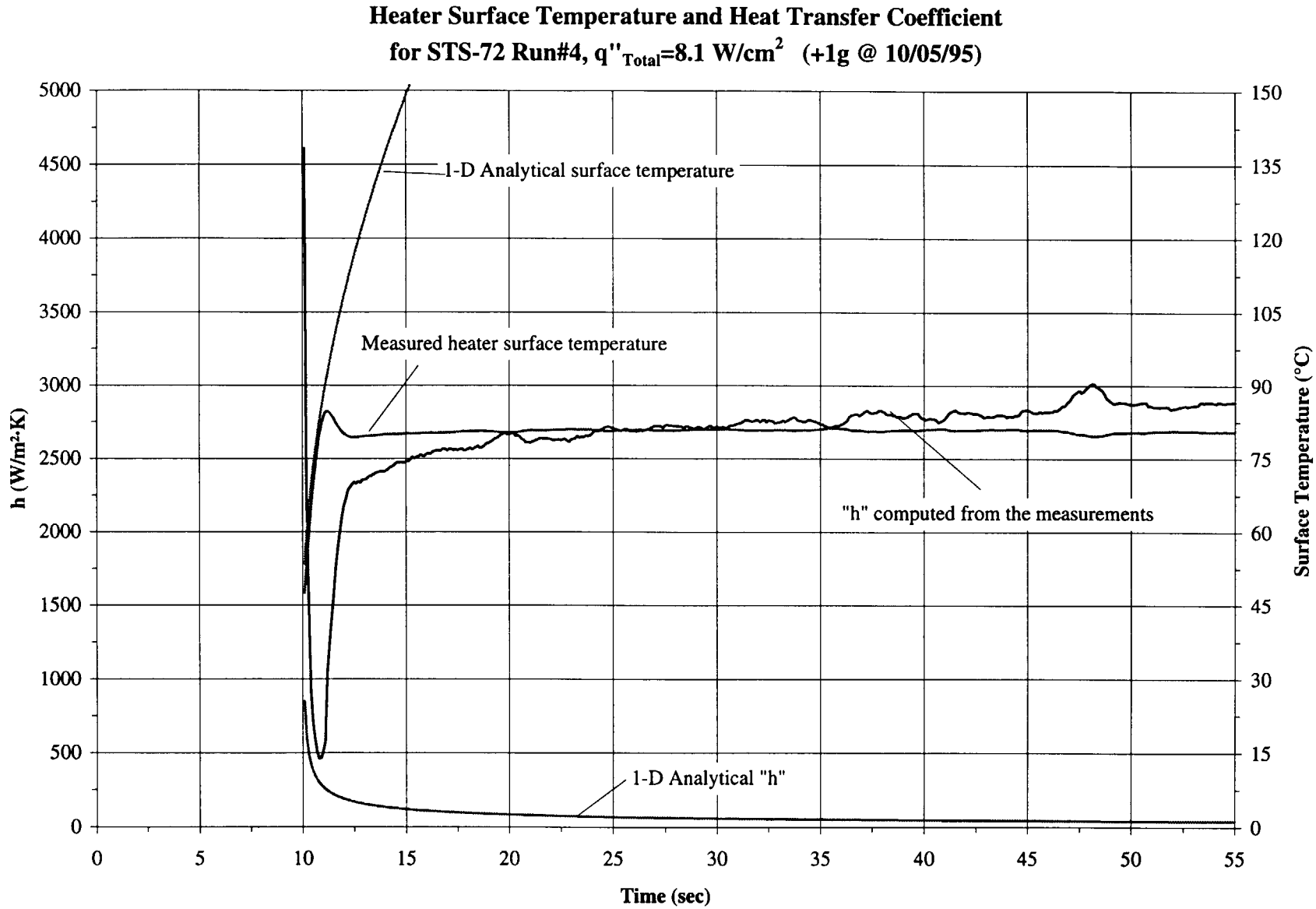

Figure A-14d. a/g = + 1 Preflight test. Mean heater surface temperature and derived heat transfer coefficient. PBE-IIB (STS-72). Run No. 4.

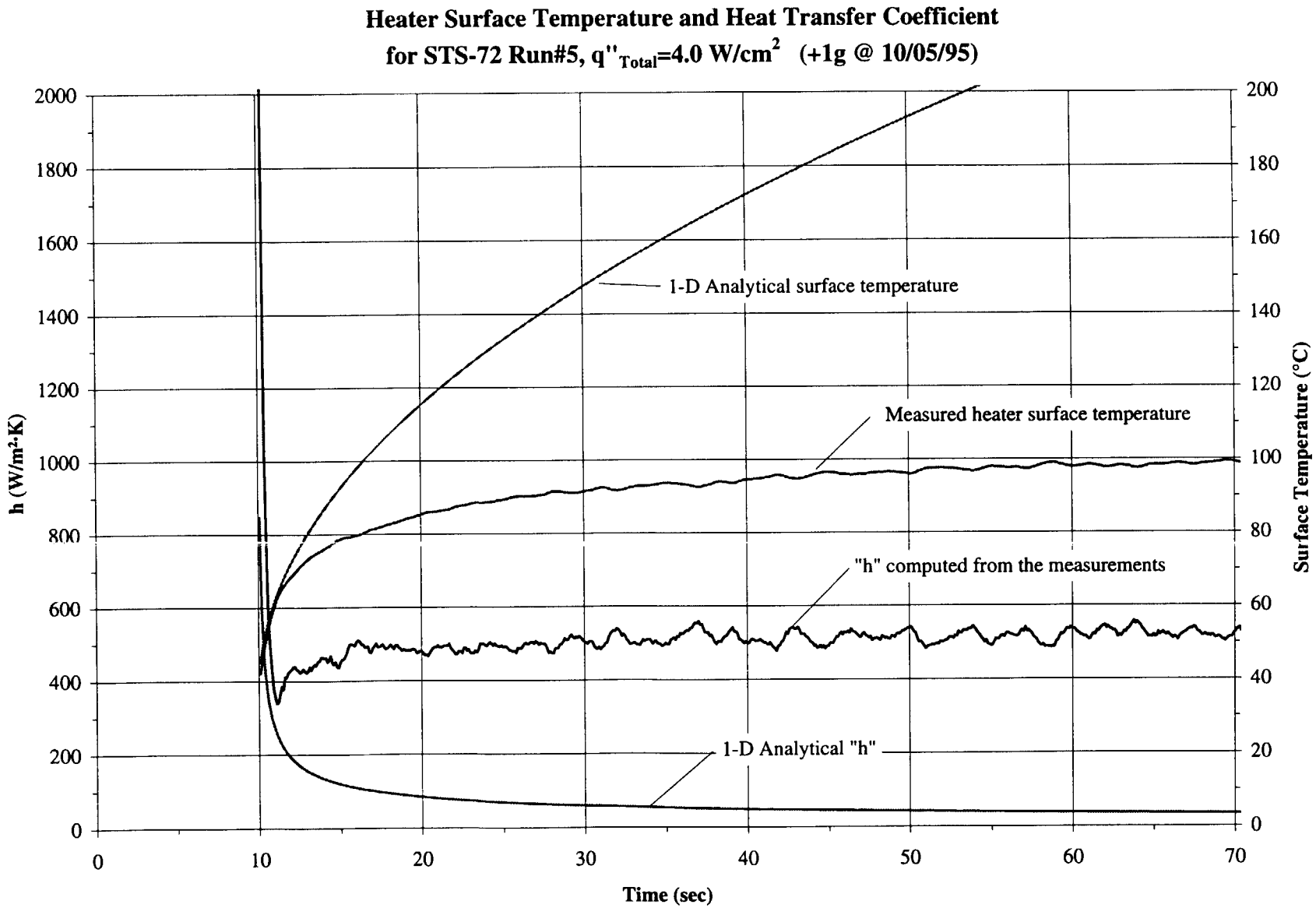

Figure A-14e. a/g = + 1 Preflight test. Mean heater surface temperature and derived heat transfer coefficient. PBE-IIB (STS-72). Run No. 5.

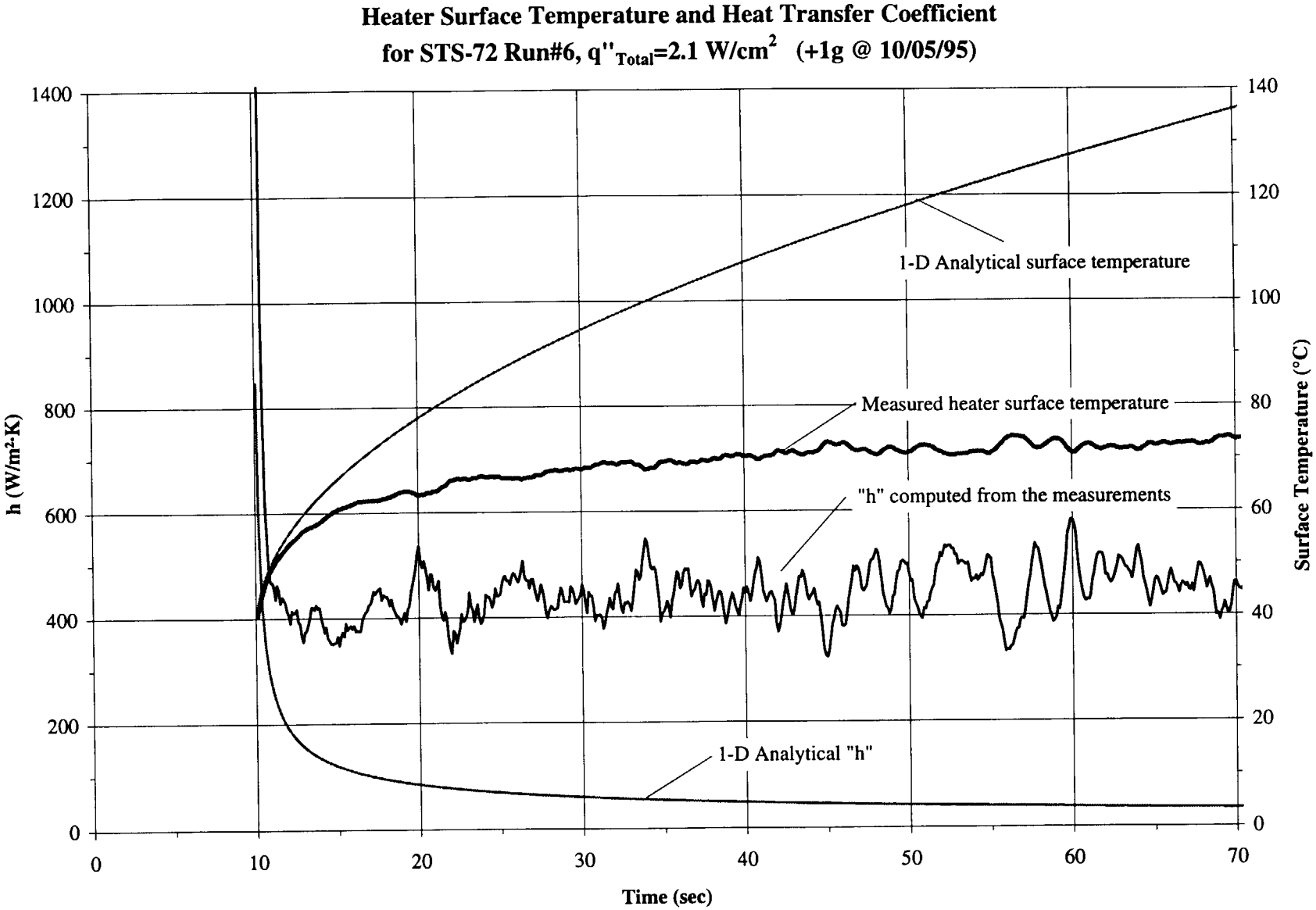

Figure A-14f. a/g = + 1 Preflight test. Mean heater surface temperature and derived heat transfer coefficient. PBE-IIB (STS-72). Run No. 6.

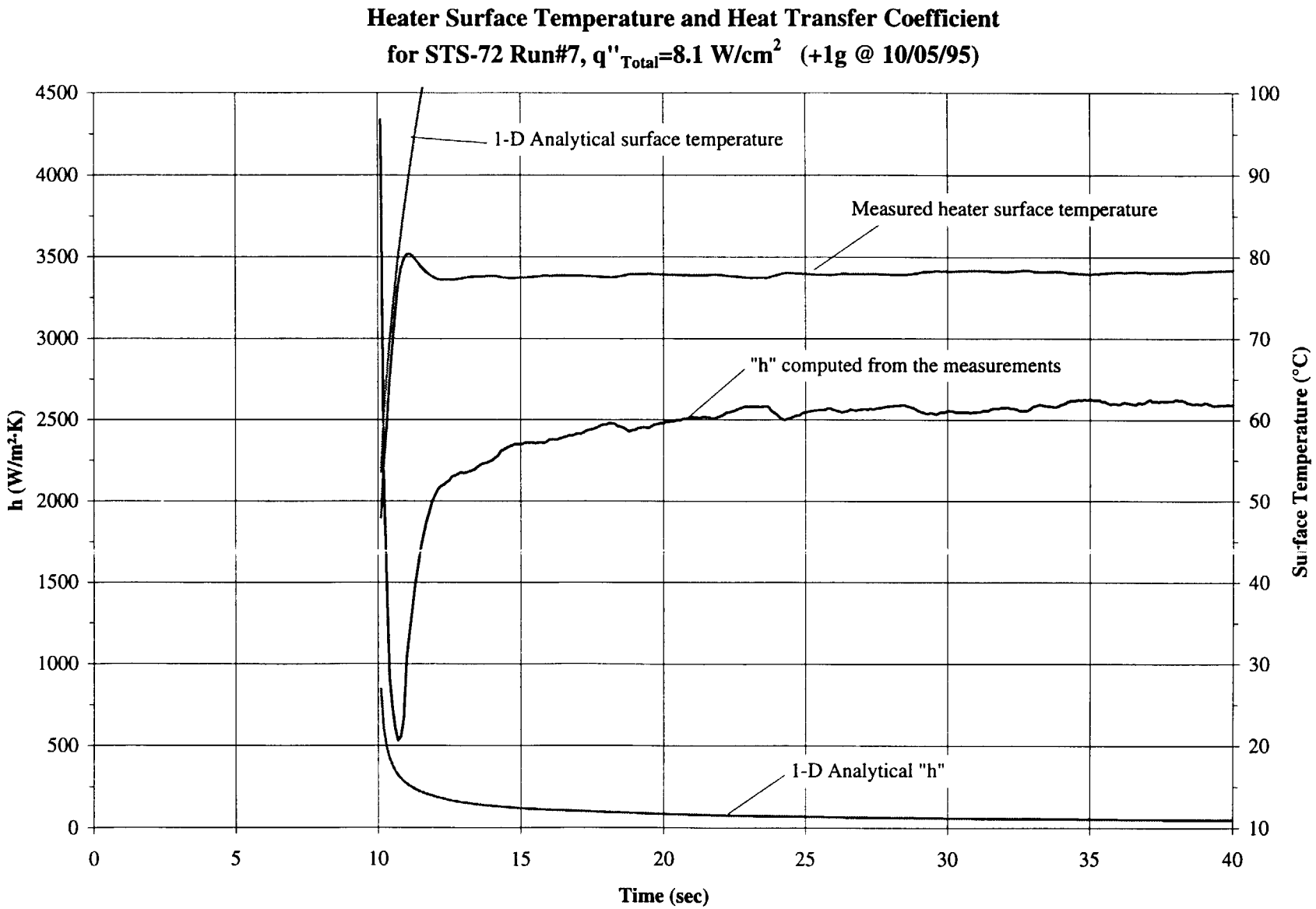

Figure A-14g. a/g = + 1 Preflight test. Mean heater surface temperature and derived heat transfer coefficient. PBE-IIB (STS-72). Run No. 7.

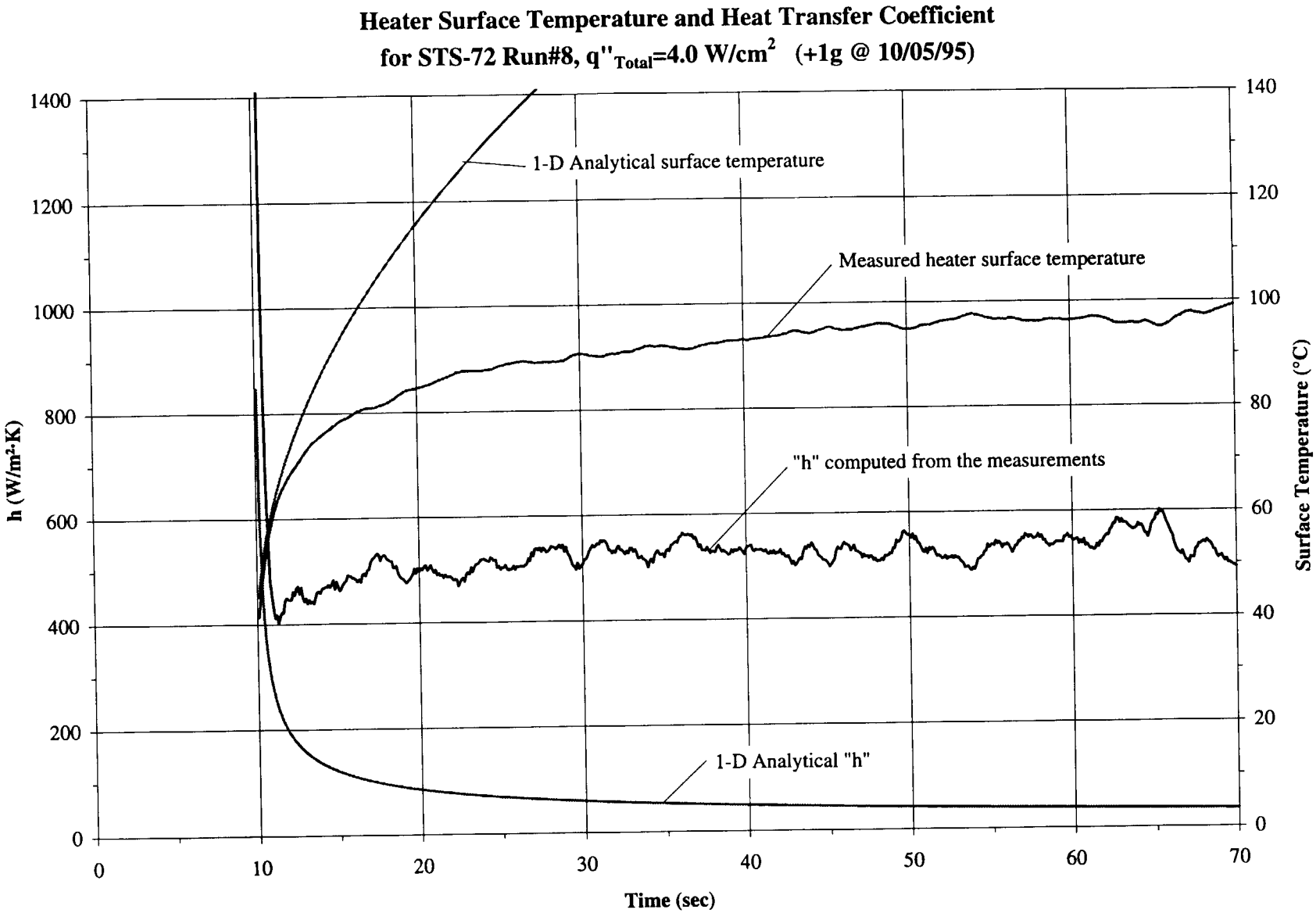

Figure A-14h. a/g = + 1 Preflight test. Mean heater surface temperature and derived heat transfer coefficient. PBE-IIB (STS-72). Run No. 8.

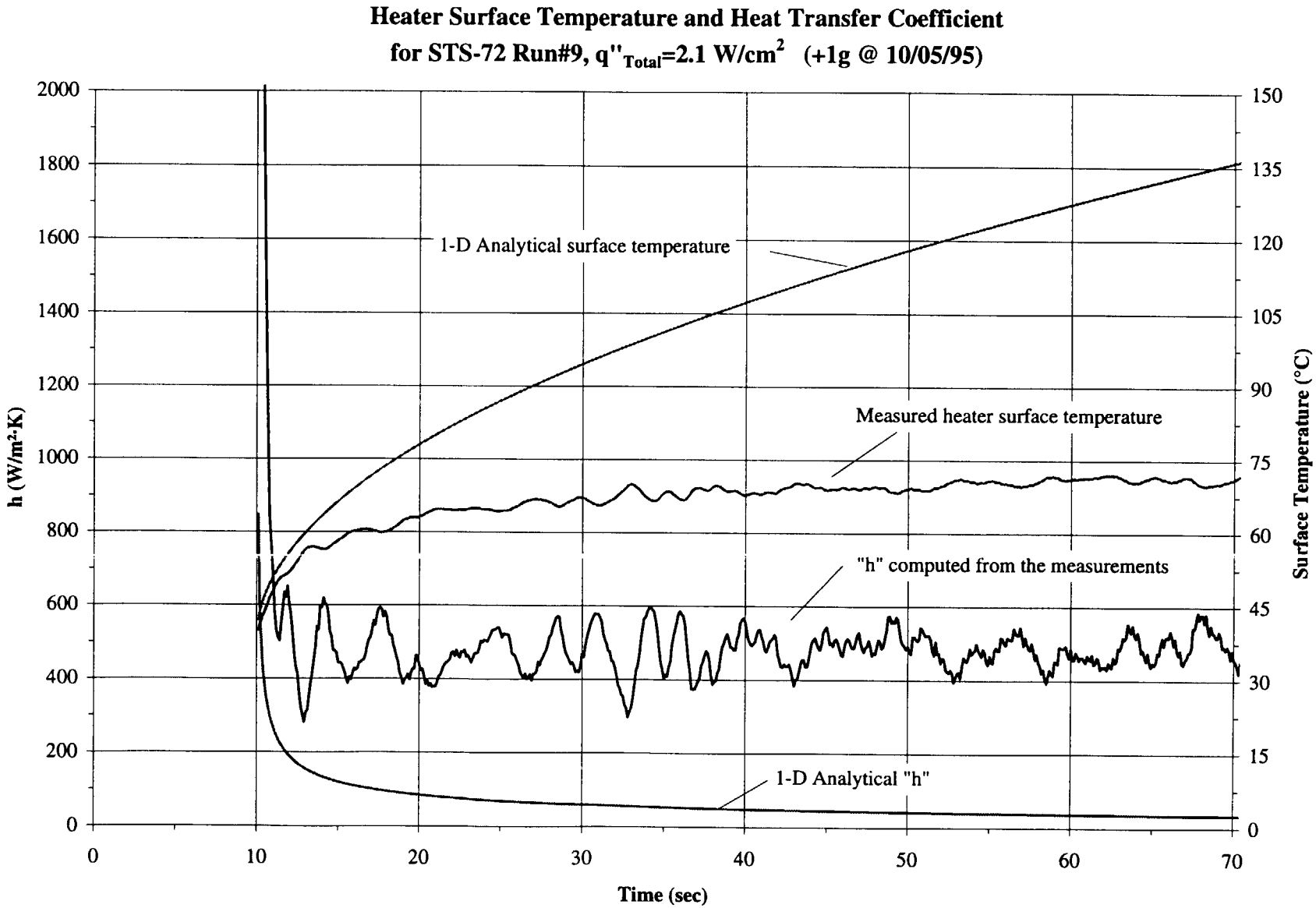

Figure A-14i. a/g = + 1 Preflight test. Mean heater surface temperature and derived heat transfer coefficient. PBE-IIB (STS-72). Run No. 9.

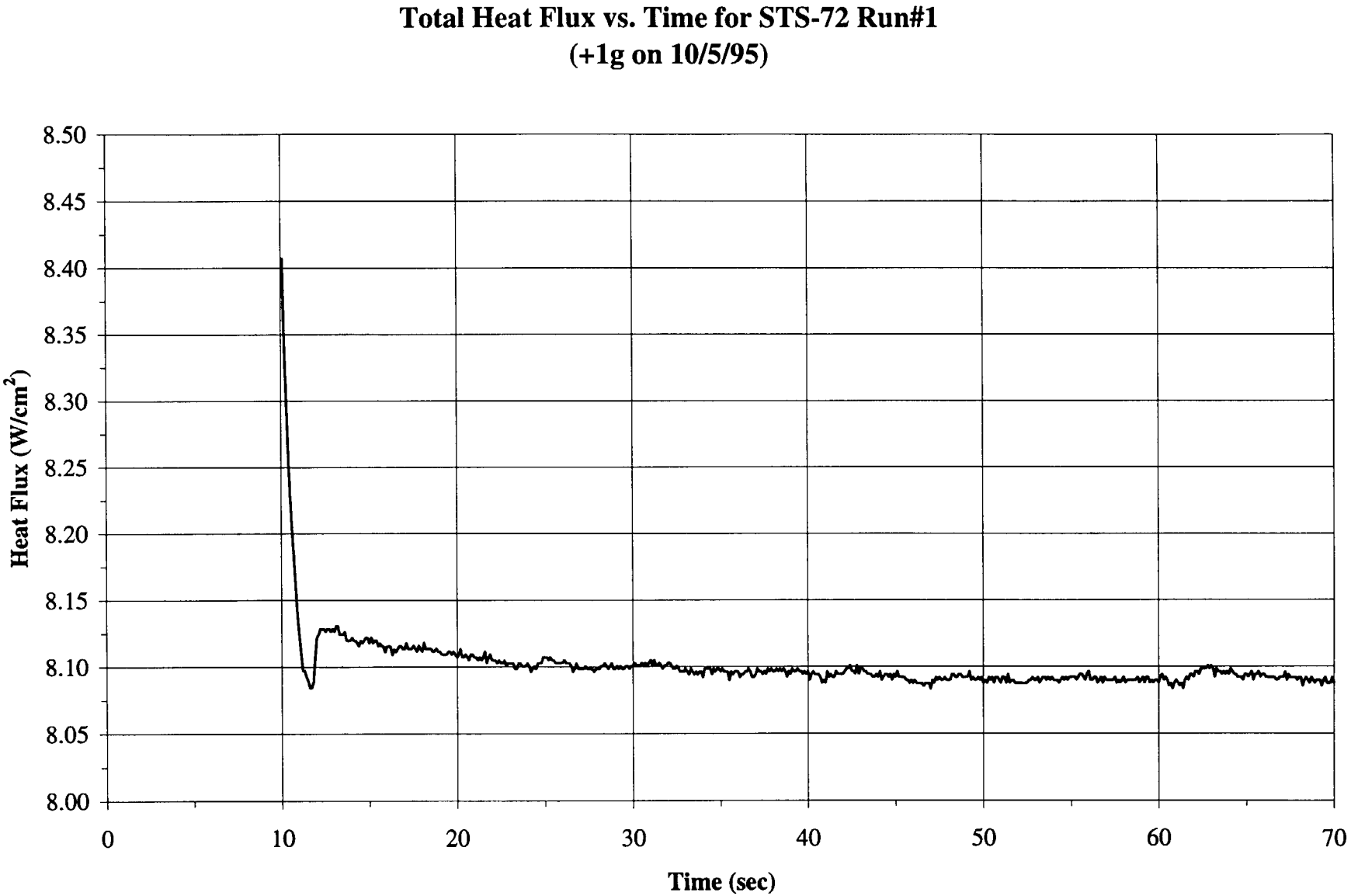

Figure A-15a. a/g = + 1 Preflight test. Heat flux input. PBE-IIB (STS-72). Run No. 1.

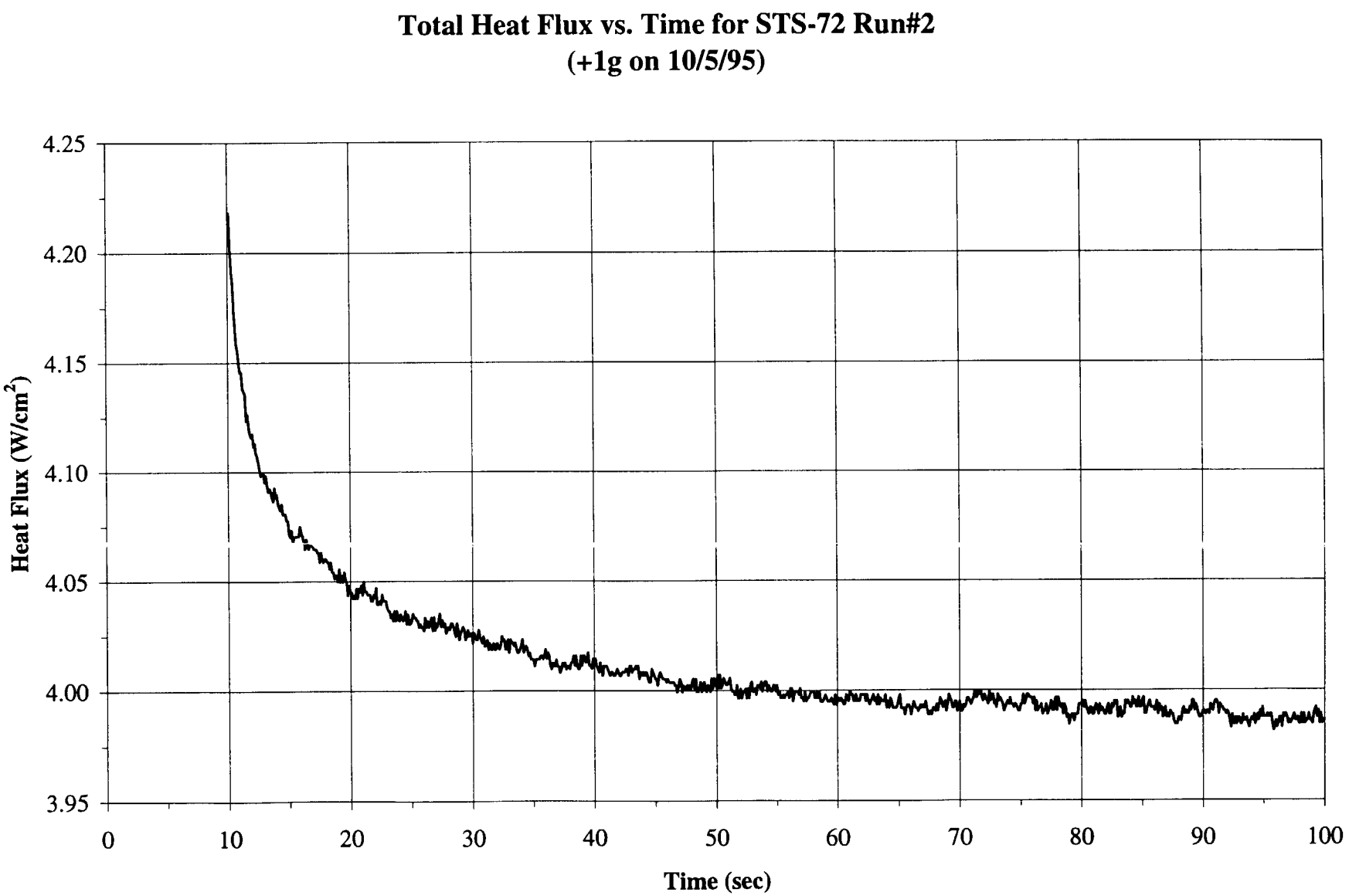

Figure A-15b. a/g = + 1 Preflight test. Heat flux input. PBE-IIB (STS-72). Run No. 2.

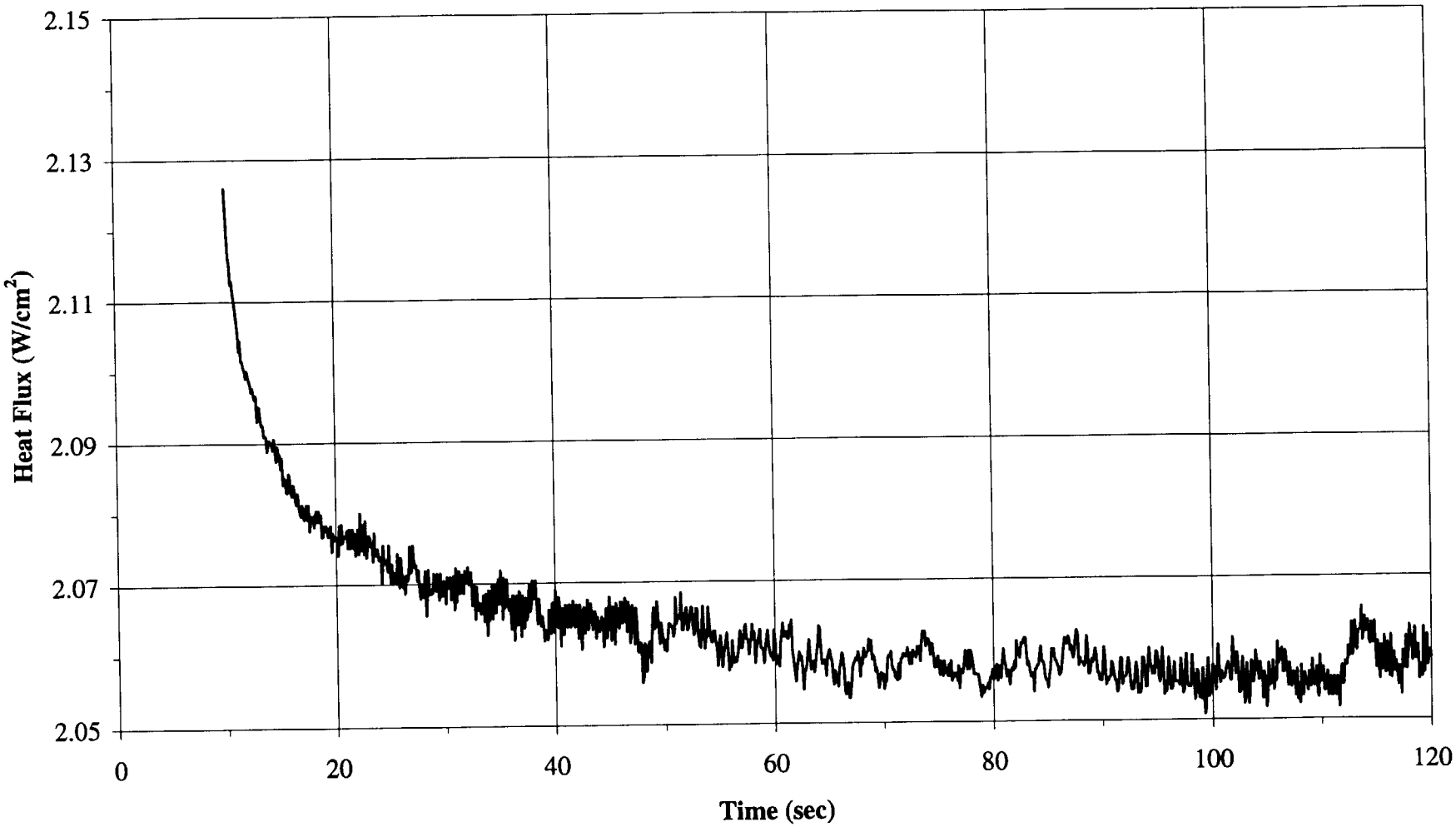

Figure A-15c. a/g = + 1 Preflight test. Heat flux input. PBE-IIB (STS-72). Run No. 3.

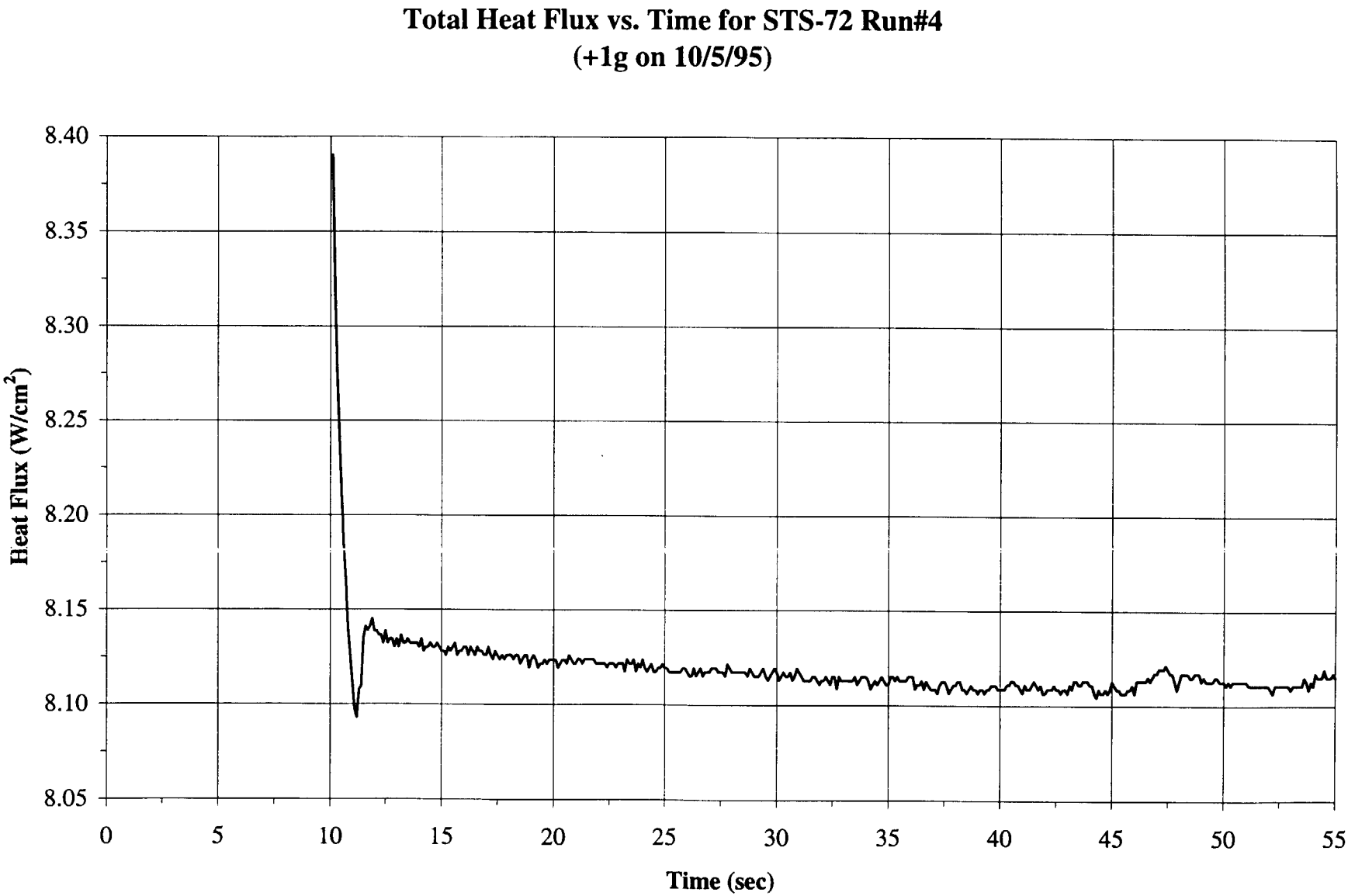

Figure A-15d. a/g = + 1 Preflight test. Heat flux input. PBE-IIB (STS-72). Run No. 4.

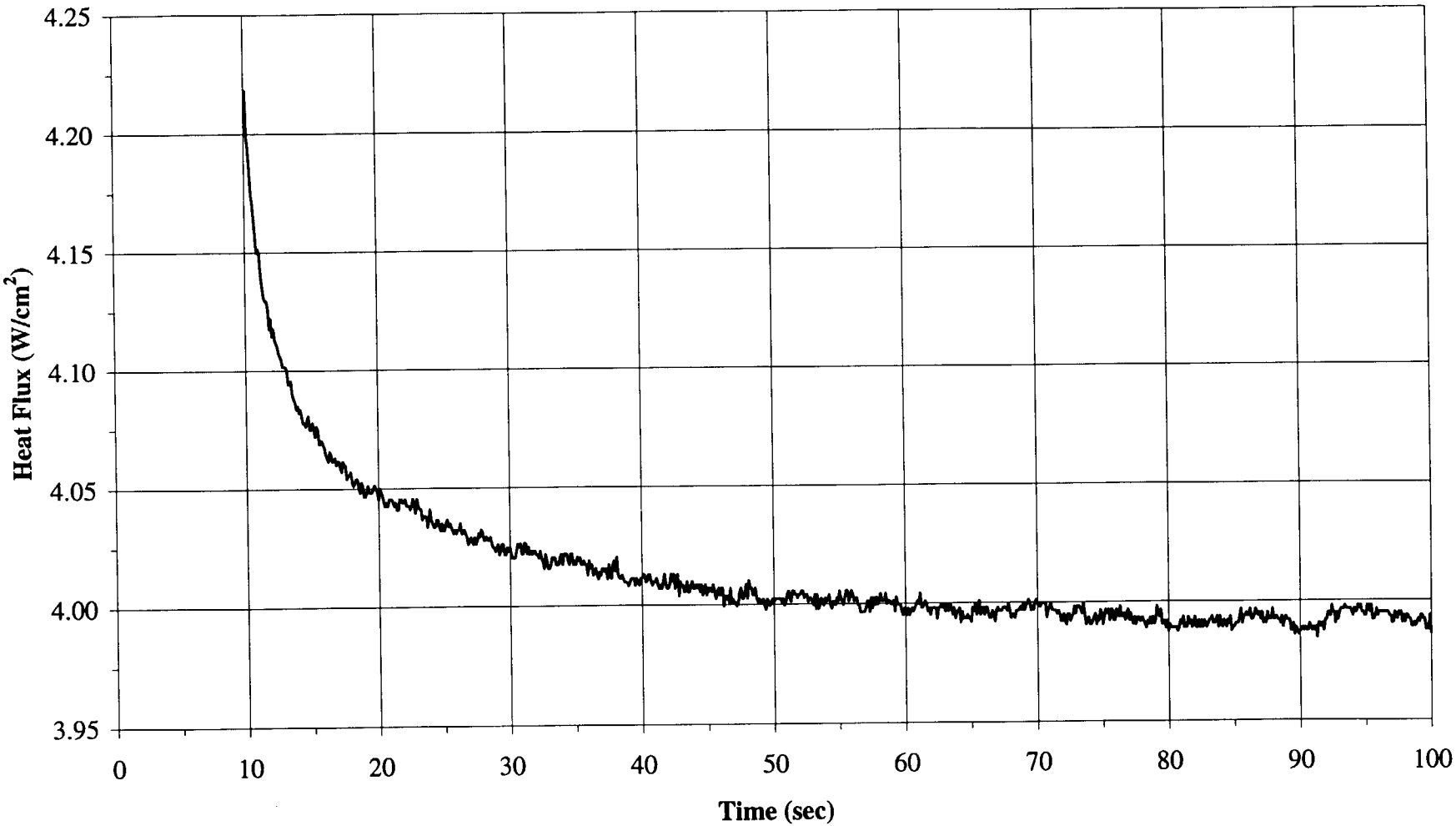

Figure A-15e. a/g = + 1 Preflight test. Heat flux input. PBE-IIB (STS-72). Run No. 5.

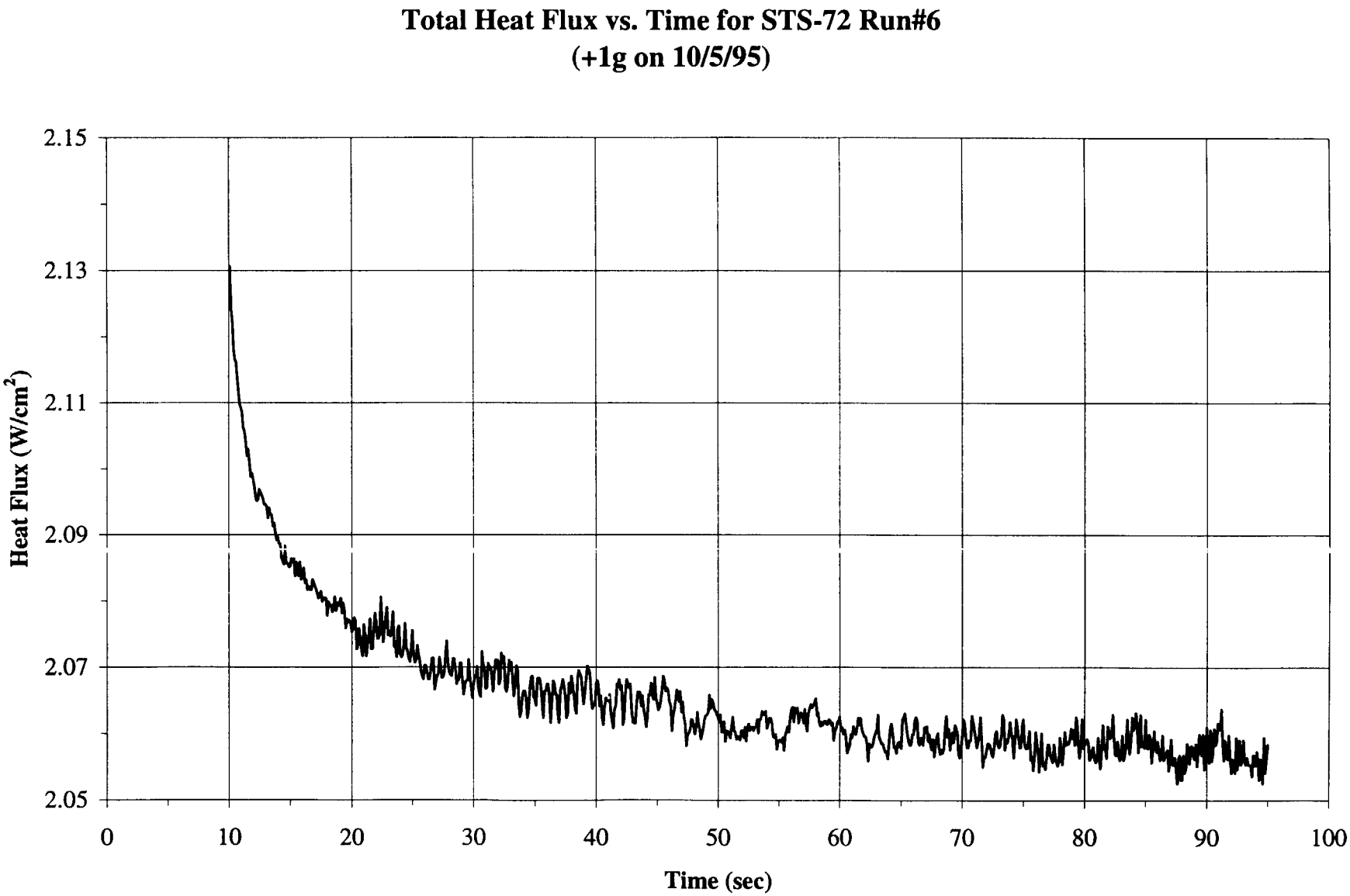

Figure A-15f. a/g = + 1 Preflight test. Heat flux input. PBE-IIB (STS-72). Run No. 6.

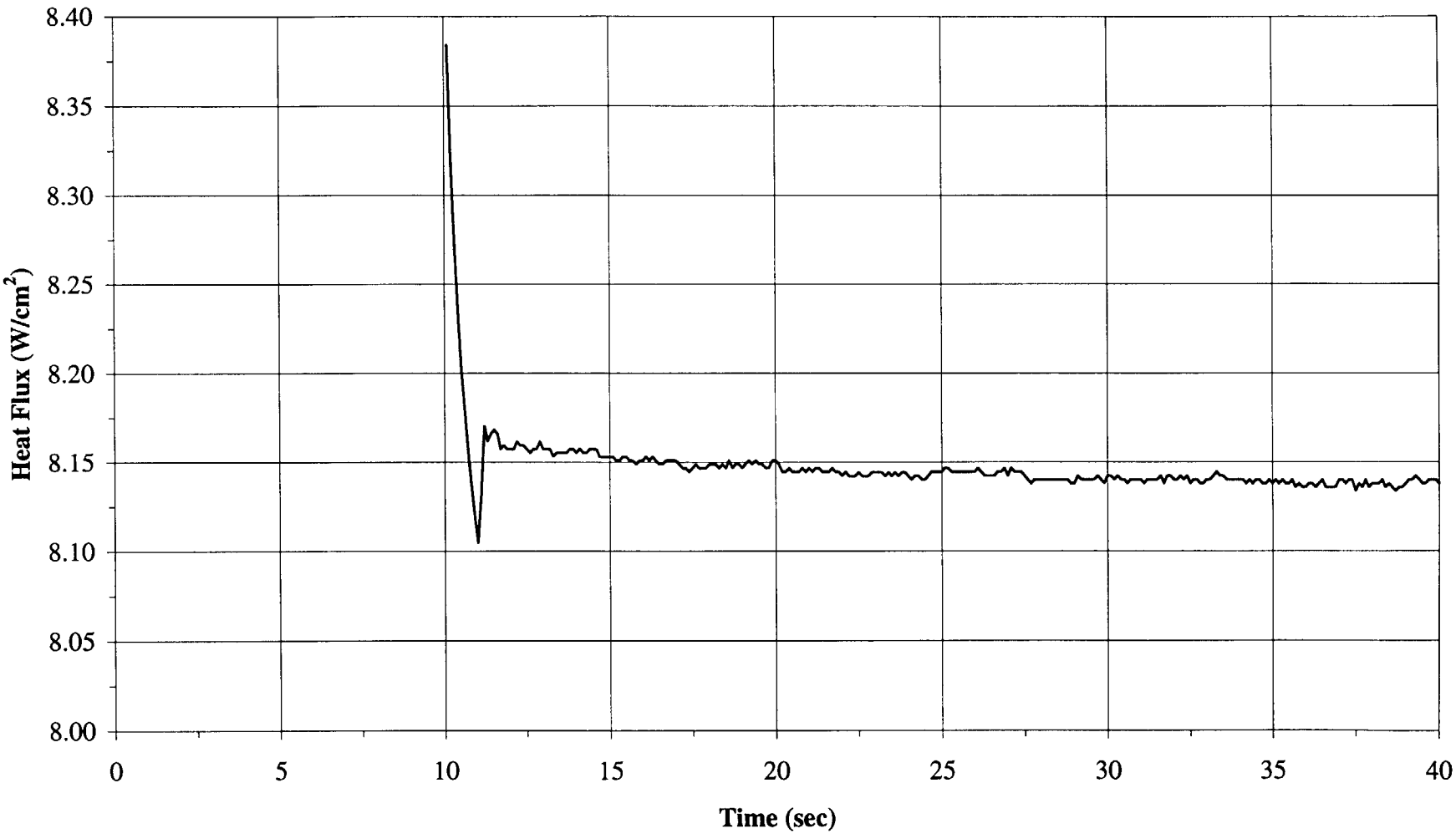

Figure A-15g. a/g = + 1 Preflight test. Heat flux input. PBE-IIB (STS-72). Run No. 7.

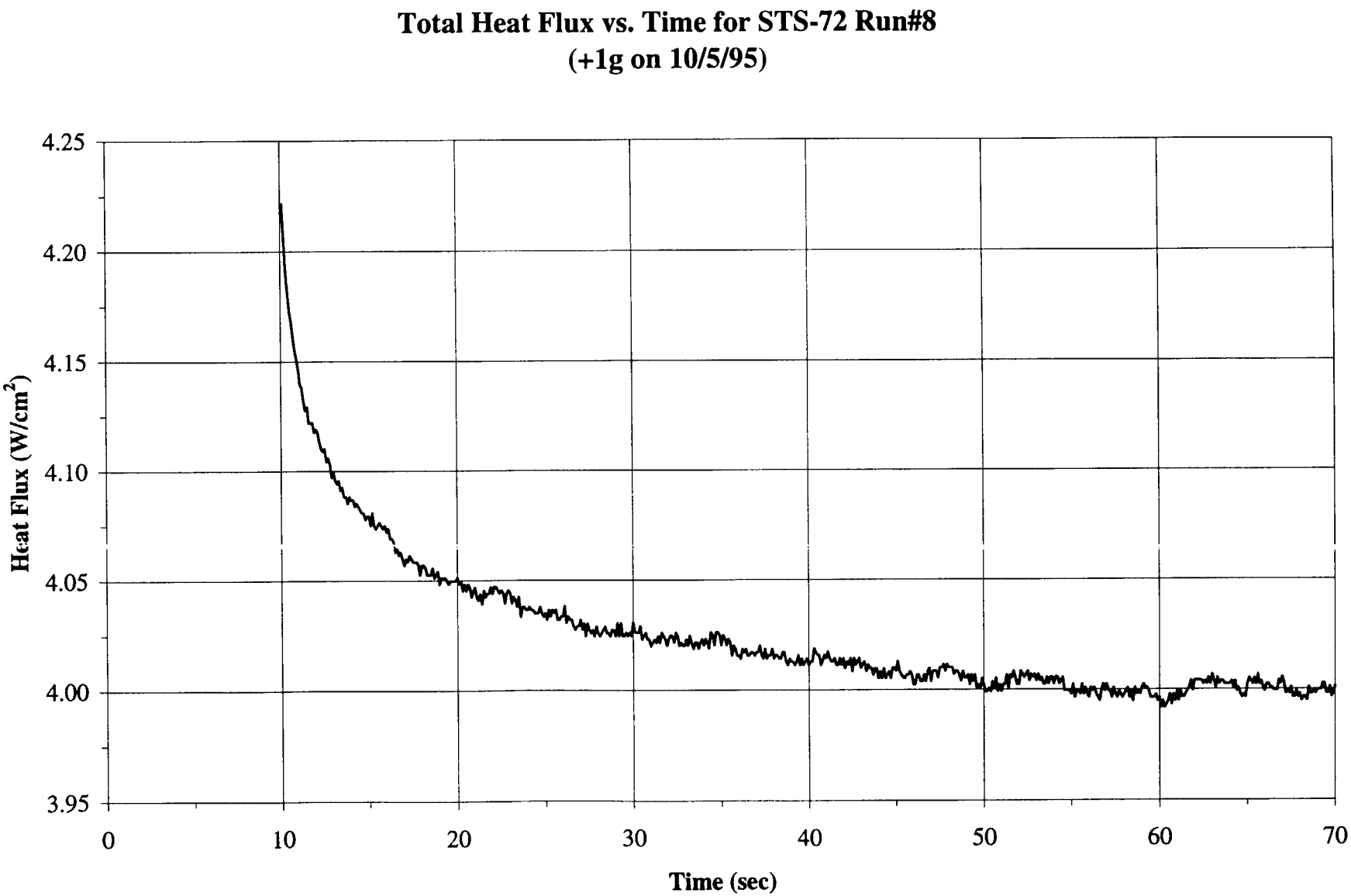

Figure A-15h. a/g = + 1 Preflight test. Heat flux input. PBE-IIB (STS-72). Run No. 8.

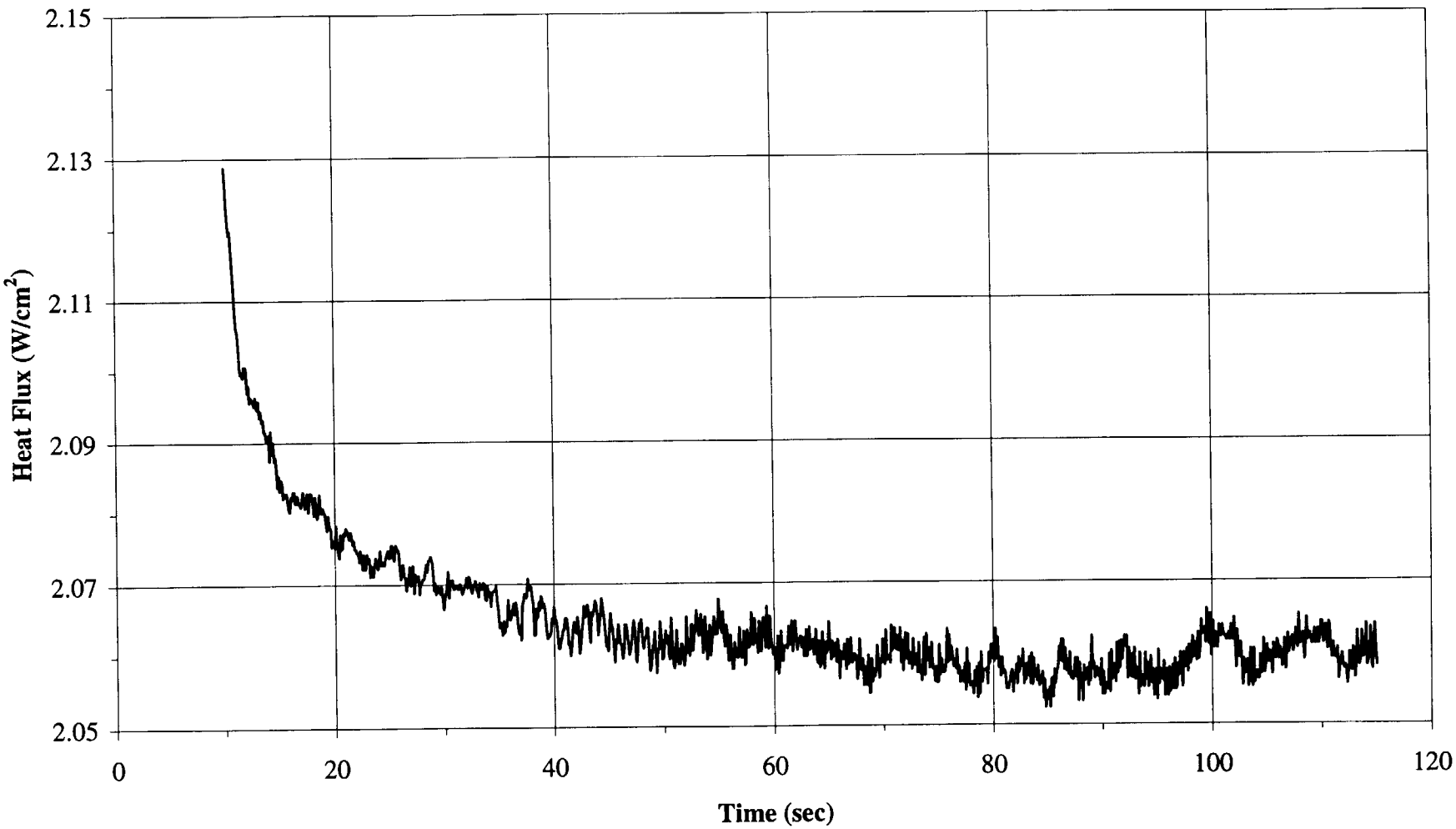

Figure A-15i. a/g = + 1 Preflight test. Heat flux input. PBE-IIB (STS-72). Run No. 9.

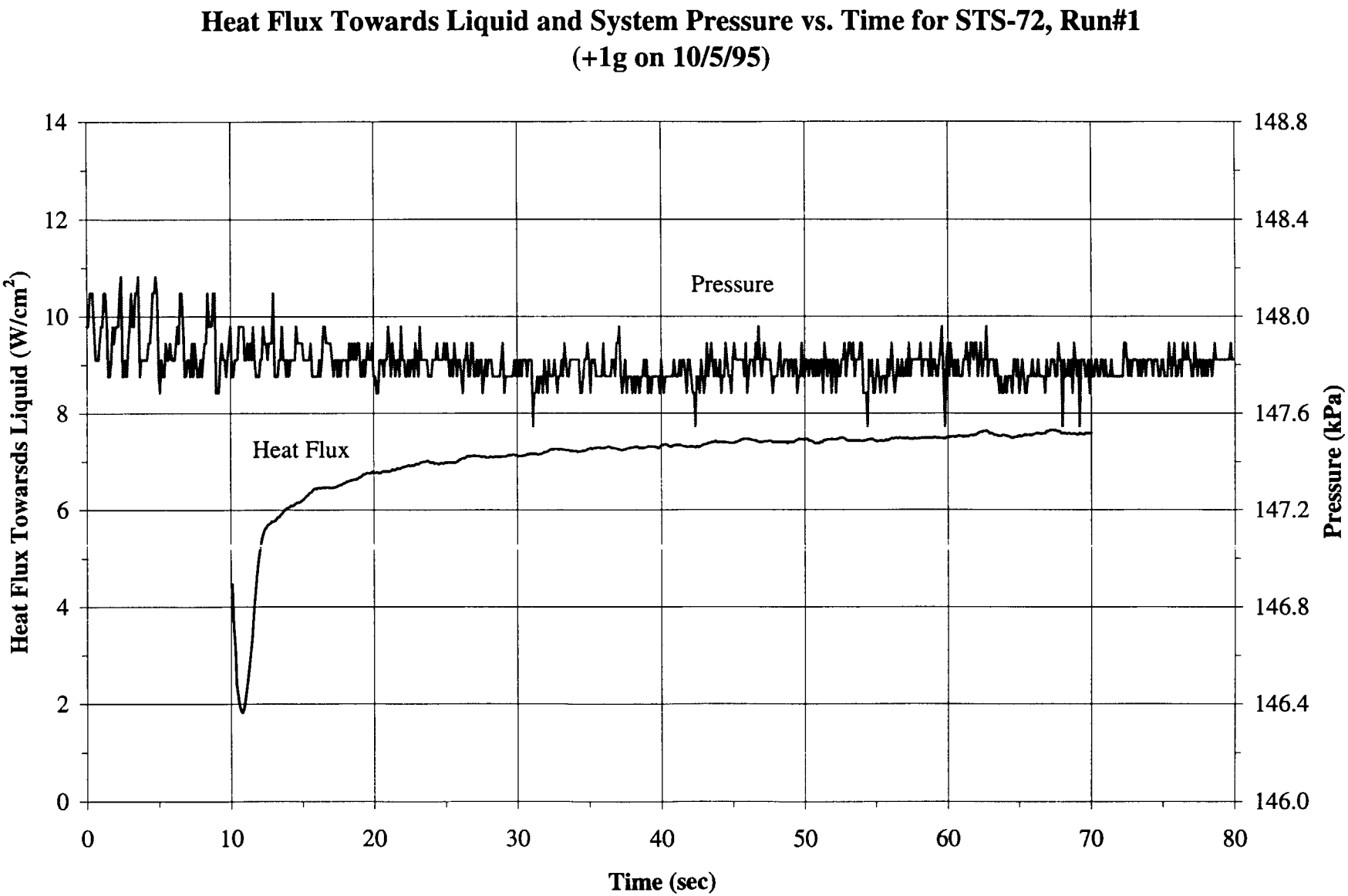

Figure A-16a. a/g = 1 Preflight test. System pressure and heat flux into fluid. PBE-(STS-72). Run No. 1.

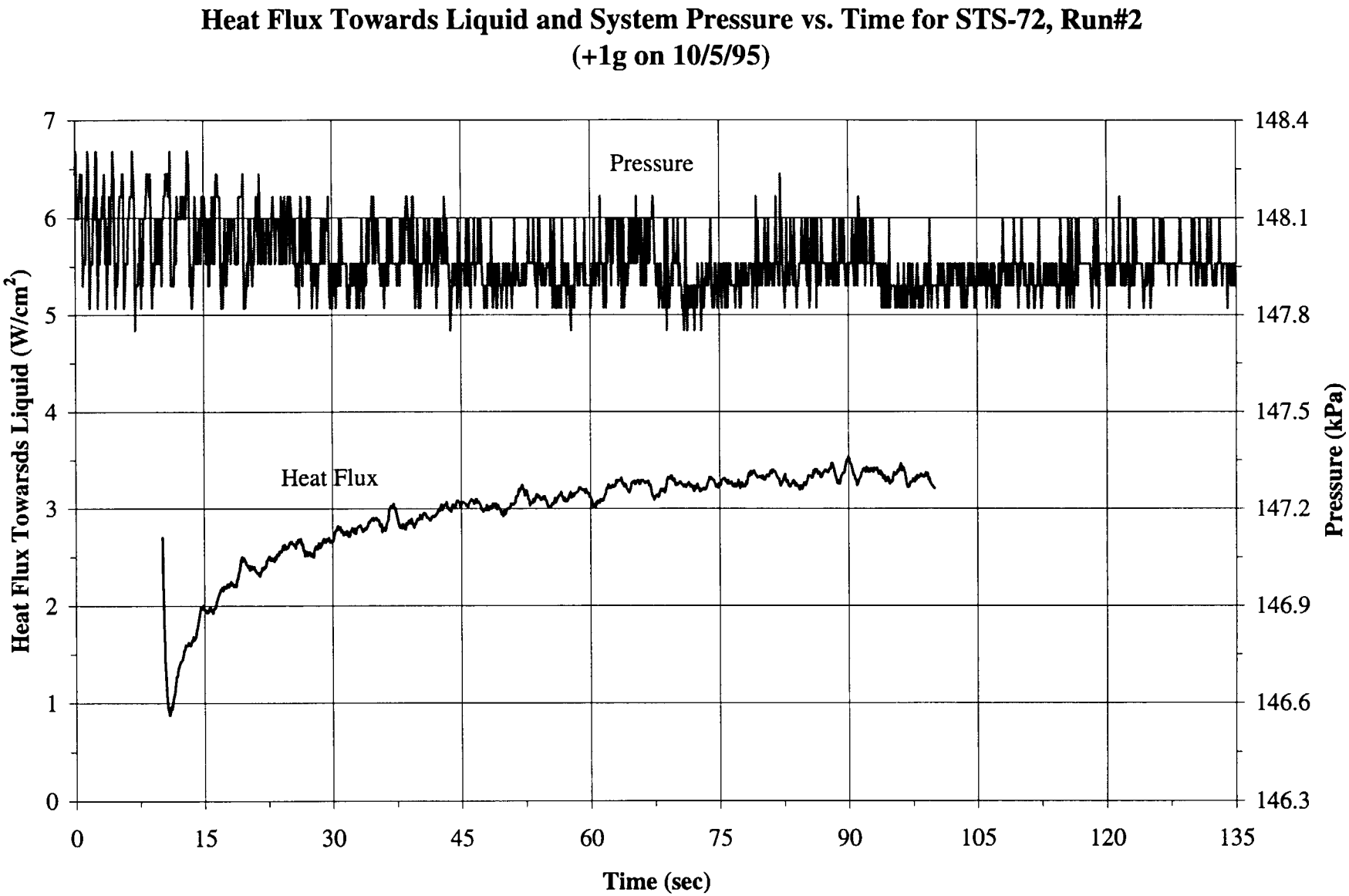

Figure A-16b. a/g = 1 Preflight test. System pressure and heat flux into fluid. PBE-(STS-72). Run No. 2.

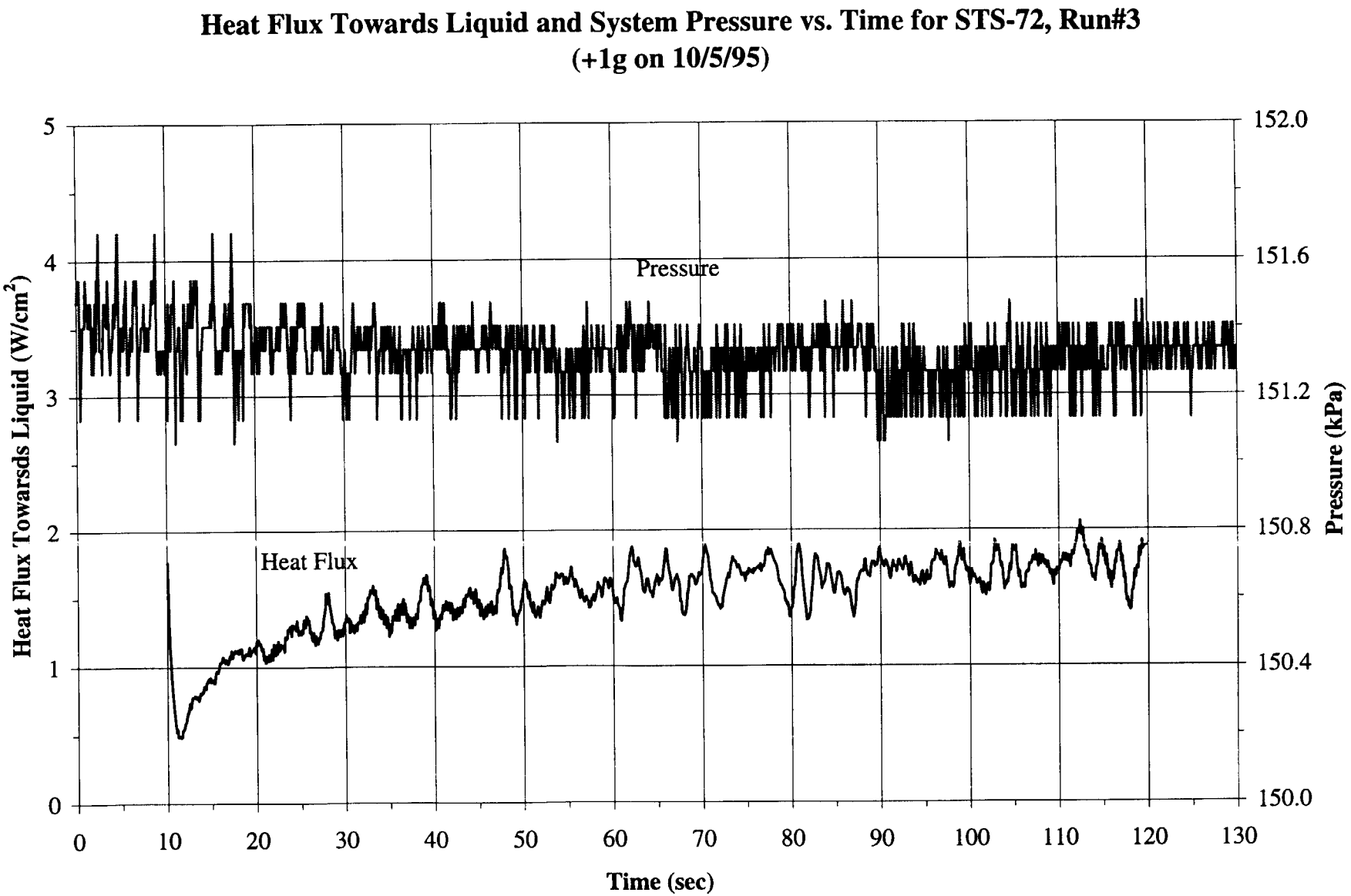

Figure A-16c. a/g = 1 Preflight test. System pressure and heat flux into fluid. PBE-(STS-72). Run No. 3.

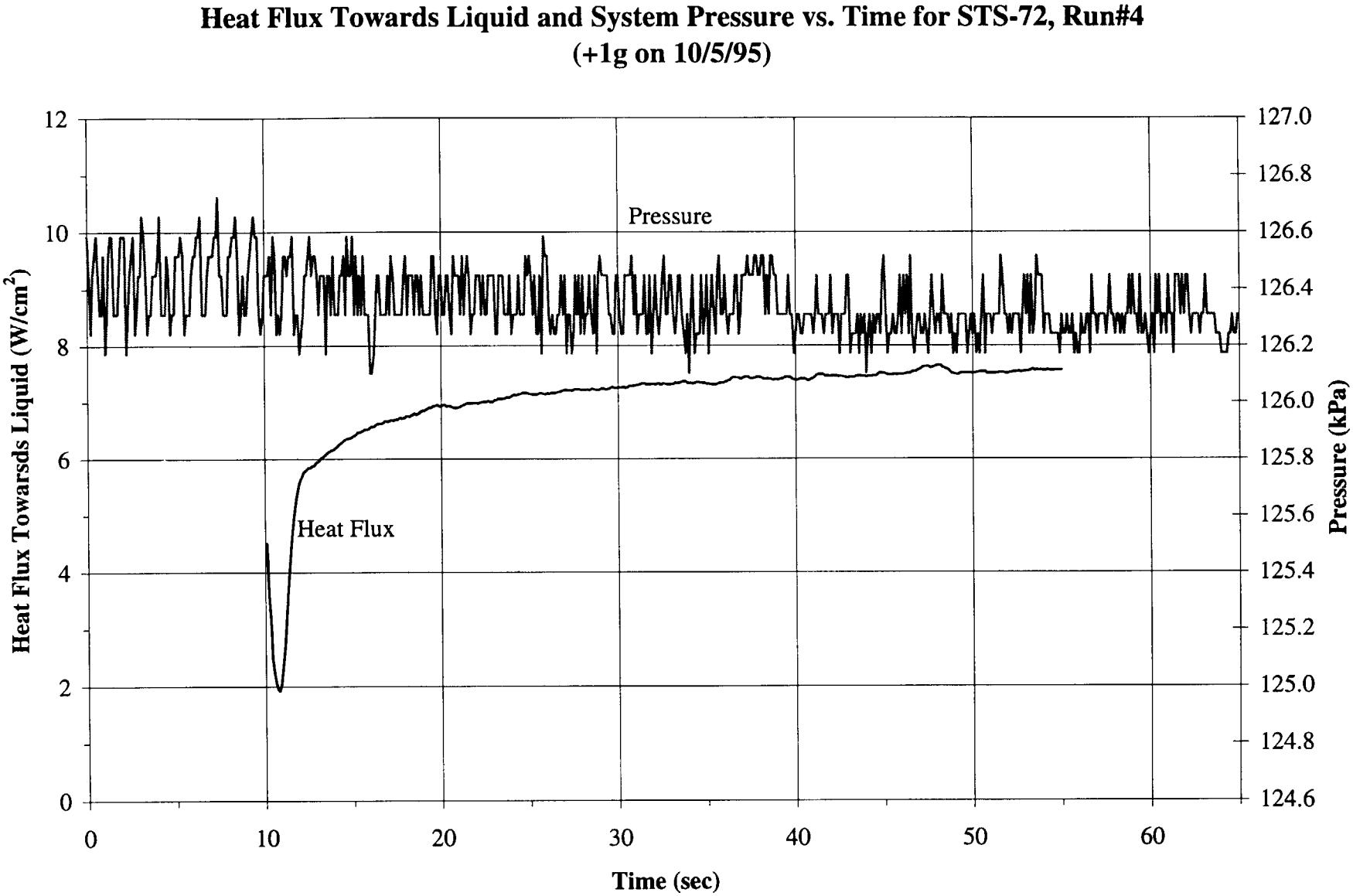

Figure A-16d. a/g = 1 Preflight test. System pressure and heat flux into fluid. PBE-(STS-72). Run No. 4.

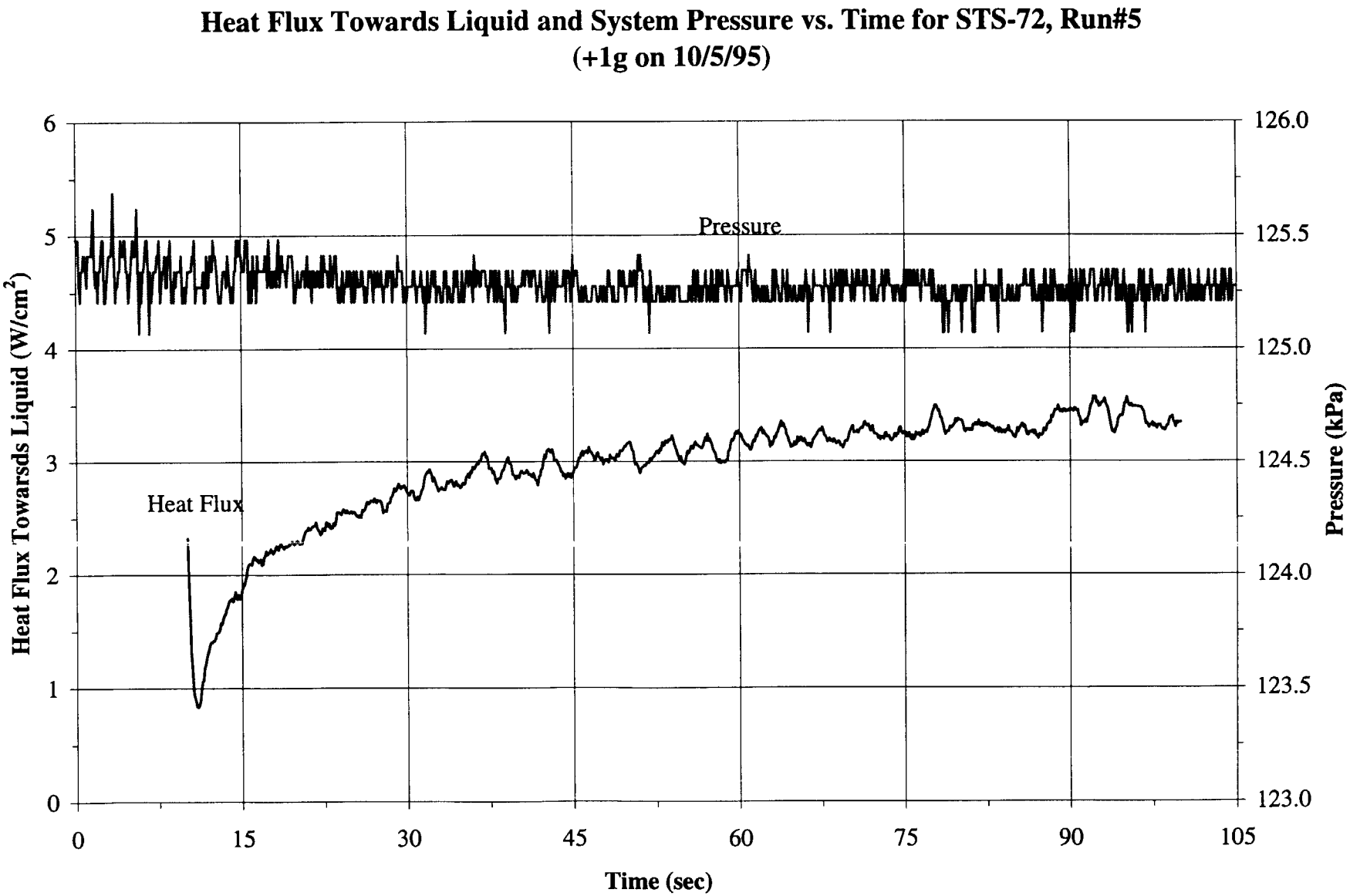

Figure A-16e. a/g = 1 Preflight test. System pressure and heat flux into fluid. PBE-(STS-72). Run No. 5.

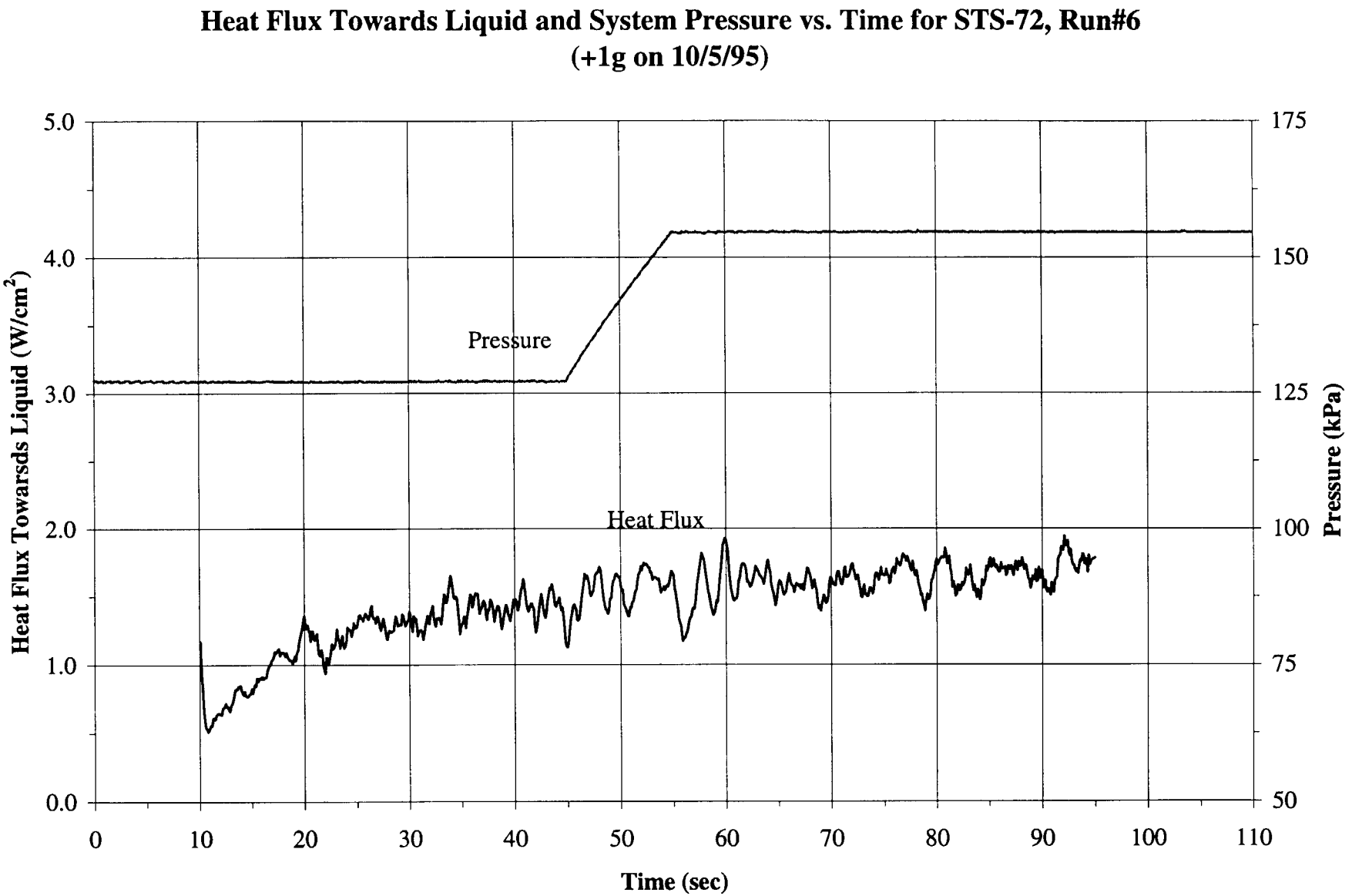

Figure A-16f. a/g = 1 Preflight test. System pressure and heat flux into fluid. PBE-(STS-72). Run No. 6.

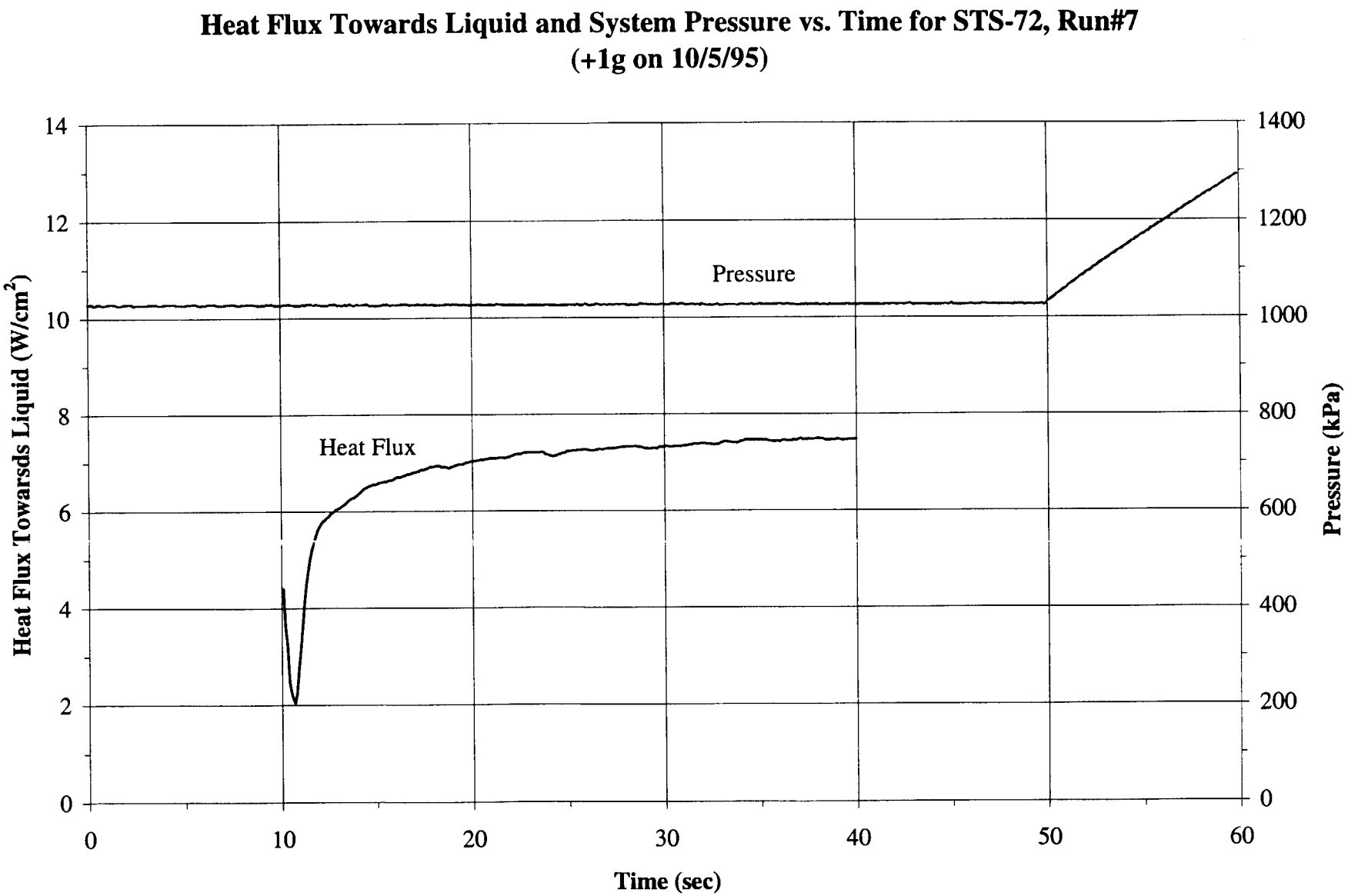

Figure A-16g. a/g = 1 Preflight test. System pressure and heat flux into fluid. PBE-(STS-72). Run No. 7.

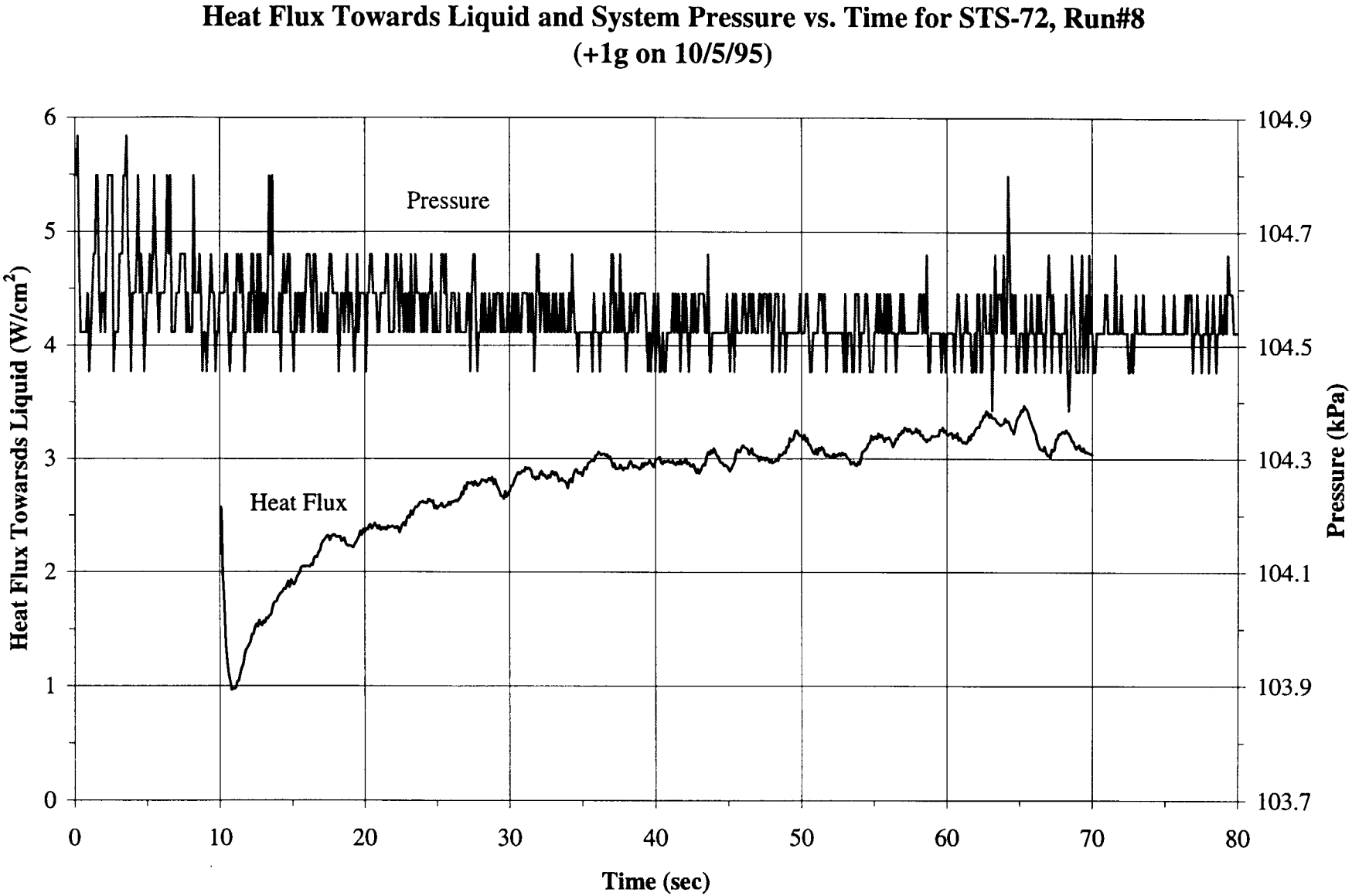

Figure A-16h. a/g = 1 Preflight test. System pressure and heat flux into fluid. PBE-(STS-72). Run No. 8.

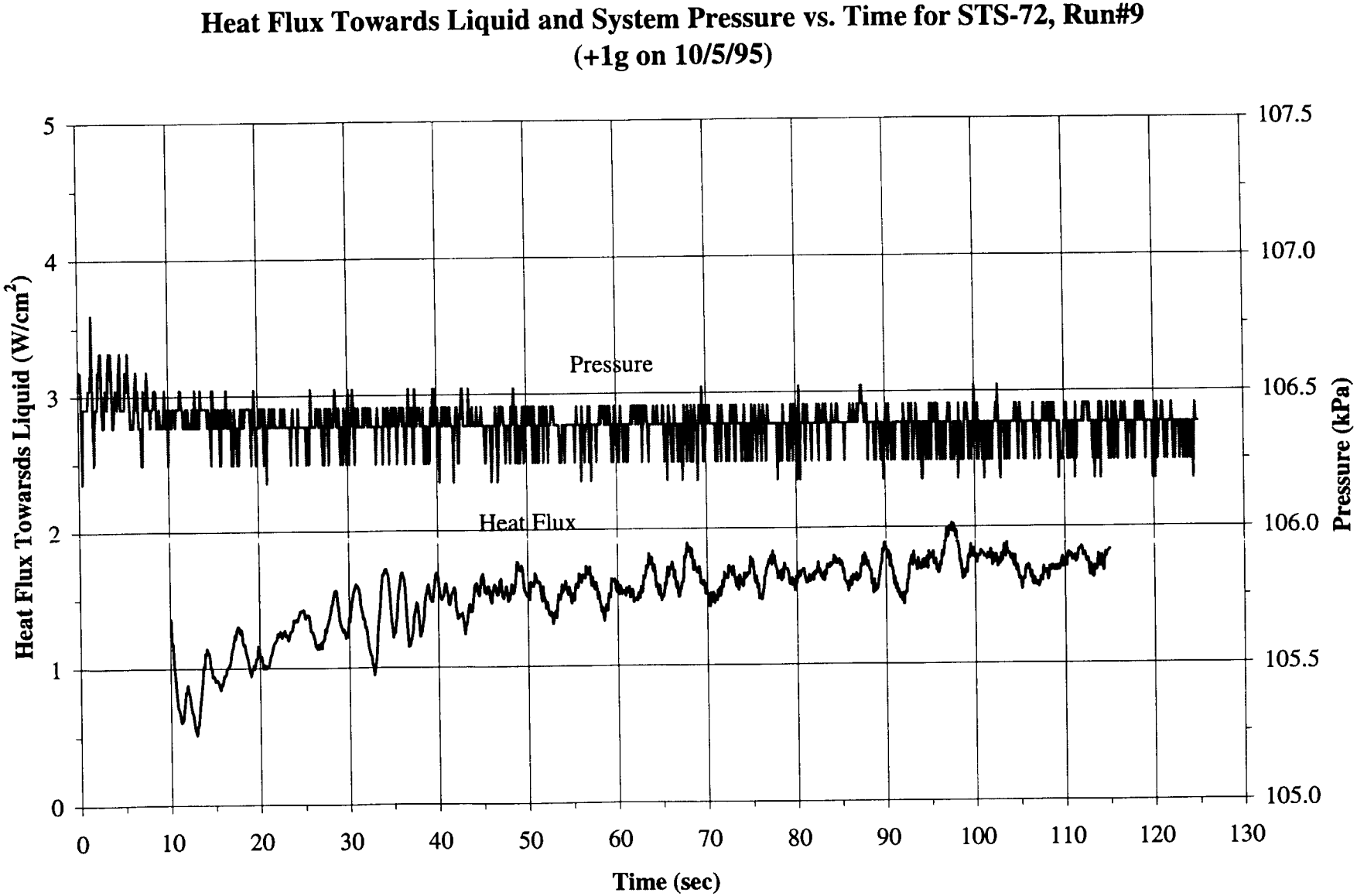

Figure A-16i. a/g = 1 Preflight test. System pressure and heat flux into fluid. PBE-(STS-72). Run No. 9.

Appendix B, PBE-IIA (STS-77). Experimental Results

PBE Flight-System Matrix (STS-77)

RUN #	HEAT FLUX W/CM^2	SUBCOOLING (^{0}F)	HEATER POWER ON/OFF (SEC)	10 FPS ON/OFF (SEC)	STIRRER START (SEC)	REPRESS. START (SEC)	TOTAL TEST TIME (SEC)
1	2	20	10-180	25-190	170	-	190
2	1	20	10-220	50-230	210	-	230
3	0.5	20	10-250	70-260	240	-	260
4	2	5	10-170	30-180	160	-	180
5	1	5	10-210	60-220	200	-	220
6	0.5	5	10-250	80-260	240	-	260
7	2	0.5	10-110	30-140	-	120	140
8	1	0.5	10-210	60-240	-	220	240
9	0.5	0.5	10-250	80-280	-	260	280

Table B-I. Test matrix for PBE-IIA on STS-77. (Flight Hardware)

NASA test Matrix for Pool boiling

a/g -1 experiment based on date 3/19/96
a/g+1 experiment based on date 3/19/96
a/g 0 experiment based on date 5/19/96 STS-77
a/g -1 experiment based on date 7/18/96
a/g+1 experiment based on date 7/18/96

Run#	Date of Experiment	Flight system	Gravi a/g	Heat Flux (W/cm^2) Nom.	Actual	Subcool,°F Nom	Actual	Tbulk °C	Sys. Press kPa	Tsat °C	T°wall °C	T°sup °C	t° time sec	10fps On-Off	Remarks
1	3/19/96	Flight system	-1	2.00	1.95	20	19.79	49.73	154.03	60.73	117.10	56.37	141.40	25-190	
	3/19/96	Flight system	+1	2.00	2.00	20	19.86	47.48	143.96	58.51	~	~	~	25-190	no nucleation
	5/19/96	Flight system	0	2.00	2.01	20	19.85	47.21	142.79	58.24	94.53	36.29	23.80	25-190	
	7/18/96	Flight system	-1	2.00	1.94	20	19.84	50.03	155.55	61.05	113.08	52.03	79.80	25-190	
	7/18/96	Flight system	+1	2.00	2.00	20	19.84	47.64	144.65	58.66	~	~	~	25-190	no nucleation
2	3/19/96	Flight system	-1	1.00	1.00	20	19.88	49.57	153.48	60.61	~	~	~	50-230	no nucleation
	3/19/96	Flight system	+1	1.00	1.00	20	19.84	48.20	147.13	59.22	~	~	~	50-230	no nucleation
	5/19/96	Flight system	0	1.00	1.00	20	19.81	49.67	153.82	60.68	86.00	25.32	68.30	50-230	
	7/18/96	Flight system	-1	1.00	1.00	20	19.90	49.47	153.06	60.52	~	~	~	50-230	no nucleation
	7/18/96	Flight system	+1	1.00	1.01	20	19.89	48.15	147.07	59.20	~	~	~	50-230	no nucleation
3	3/19/96	Flight system	-1	0.50	0.51	20	19.88	49.97	155.34	61.01	~	~	~	70-260	no nucleation
	3/19/96	Flight system	+1	0.50	0.51	20	19.83	48.27	147.48	59.29	~	~	~	70-260	no nucleation
	5/19/96	Flight system	0	0.50	0.51	20	19.85	48.69	149.41	59.72	~	~	~	70-260	no nucleation
	7/18/96	Flight system	-1	0.50	0.51	20	19.90	50.14	156.24	61.20	~	~	~	70-260	no nucleation
	7/18/96	Flight system	+1	0.50	0.51	20	19.86	48.39	148.03	59.42	~	~	~	70-260	no nucleation
4	3/19/96	Flight system	-1	2.00	1.94	5	4.81	49.33	117.35	52.00	114.54	62.54	93.70	30-180	
	3/19/96	Flight system	+1	2.00	2.00	5	4.85	47.98	112.45	50.68	~	~	~	30-180	no nucleation
	5/19/96	Flight system	0	2.00	2.02	5	4.80	48.91	115.76	51.58	96.76	45.18	23.60	30-180	
	7/18/96	Flight system	-1	2.00	1.94	5	4.85	49.37	117.56	52.06	110.25	58.19	70.80	30-180	
	7/18/96	Flight system	+1	2.00	2.01	5	4.87	47.96	112.38	50.66	~	~	~	30-180	no nucleation

Table B-II. Measured parameters at a/g = -1, a/g = +1, and Space Flight.

	Page 2 of 2														
Run#	Date of Experiment	Flight system	Gravi a/g	Heat Flux (W/cm^2) Nom.	Actual	Subcool,°F Nom	Actual	Tbulk °C	Sys. Press kPa	Tsat °C	T°wall °C	T°sup °C	t° time sec	10fps On-Off	Remarks
5	3/19/96	Flight system	-1	1.00	1.00	5	4.86	49.28	117.28	51.98	~	~	~	60-220	no nucleation
	3/19/96	Flight system	+1	1.00	1.01	5	4.80	48.03	112.52	50.70	~	~	~	60-220	no nucleation
	5/19/96	Flight system	0	1.00	1.01	5	4.82	48.97	116.04	51.65	86.29	34.64	79.60	60-220	
	7/18/96	Flight system	-1	1.00	1.00	5	4.86	48.99	116.18	51.69	~	~	~	60-220	no nucleation
	7/18/96	Flight system	+1	1.00	1.01	5	4.91	48.03	112.73	50.76	~	~	~	60-220	no nucleation
6	3/19/96	Flight system	-1	0.50	0.51	5	4.81	49.42	117.69	52.09	~	~	~	80-260	no nucleation
	3/19/96	Flight system	+1	0.50	0.51	5	4.85	48.01	112.52	50.70	~	~	~	80-260	no nucleation
	5/19/96	Flight system	0	0.50	0.51	5	4.81	49.00	116.11	51.67	75.56	23.89	190.50	80-260	
	7/18/96	Flight system	-1	0.50	0.51	5	4.85	49.51	118.11	52.20	~	~	~	80-260	no nucleation
	7/18/96	Flight system	+1	0.50	0.51	5	4.80	48.18	113.07	50.85	~	~	~	80-260	no nucleation
7	3/19/96	Flight system	-1	2.00	1.96	0.5	0.34	49.29	108.11	49.48	111.70	62.22	81.10	30-140	
	3/19/96	Flight system	+1	2.00	2.01	0.5	0.32	47.79	102.87	47.97	~	~	~	30-140	no nucleation
	5/19/96	Flight system	0	2.00	1.99	0.5	0.30	48.86	106.52	49.03	108.47	59.44	39.20	30-140	
	7/18/96	Flight system	-1	2.00	1.97	0.5	0.29	49.34	108.18	49.50	~	~	~	30-140	no nucleation
	7/18/96	Flight system	+1	2.00	2.01	0.5	0.30	47.91	103.21	48.07	~	~	~	30-140	no nucleation
8	3/19/96	Flight system	-1	1.00	1.00	0.5	0.38	49.13	107.63	49.34	~	~	~	60-240	no nucleation
	3/19/96	Flight system	+1	1.00	1.01	0.5	0.33	47.91	103.28	48.09	~	~	~	60-240	no nucleation
	5/19/96	Flight system	0	1.00	1.00	0.5	0.32	49.06	107.28	49.24	84.84	35.60	66.30	60-240	
	7/18/96	Flight system	-1	1.00	1.00	0.5	0.35	48.86	106.59	49.05	~	~	~	60-240	no nucleation
	7/18/96	Flight system	+1	1.00	1.01	0.5	0.30	47.81	102.87	47.97	~	~	~	60-240	no nucleation
9	3/19/96	Flight system	-1	0.50	0.51	0.5	0.36	49.30	108.18	49.50	~	~	~	80-280	no nucleation
	3/19/96	Flight system	+1	0.50	0.51	0.5	0.35	47.89	103.28	48.09	~	~	~	80-280	no nucleation
	5/19/96	Flight system	0	0.50	0.51	0.5	0.36	49.08	107.42	49.28	73.18	23.90	215.20	80-280	
	7/18/96	Flight system	-1	0.50	0.51	0.5	0.39	49.46	108.80	49.67	~	~	~	80-280	no nucleation
	7/18/96	Flight system	+1	0.50	0.51	0.5	0.32	47.83	103.01	48.01	~	~	~	80-280	no nucleation

Table B-II. Continued.

RUN #	Time, sec	Peaks	Maximum Acceleration value			Noise
			x	y	z	
1	105.0	yes	6	31	100	24
1	110.2	yes	6	119	24	24
1	110.4	yes	18	119	24	24
1	115.0	yes	18	106	27	24
1	115.1	yes	18	131	1	24
1	115.2	yes	6	106	1	24
1	115.3	yes	18	106	1	24
1	140.4	yes	166	156	75	24
1	140.5	yes	240	181	50	24
1	140.6	yes	18	156	77	24
1	140.7	yes	56	181	128	24
1	140.9	yes	166	19	50	24
1	141.0	yes	166	94	75	24
1	141.3	yes	117	19	100	24
1	183.3	yes	18	69	103	24
1	183.4	yes	43	19	103	24
2	111.9	yes	50	117	26	24
3	70.5	yes	47	25	152	24
3	70.8	yes	24	0	152	24
4		no	47	50	77	24
5	15.9	yes	148	50	0	24
5	16.0	yes	148	25	25	24
5	16.3	yes	147	25	26	24
5	42.7	yes	47	25	127	24
6		no	47	75	51	24
7		no	50	50	77	24
8	7.9	yes	0	25	178	24
8	8.1	yes	47	50	152	24
8	8.4	yes	47	50	178	24
8	8.7	yes	0	25	153	24
8	9.0	yes	0	50	177	24
8	9.3	yes	47	50	152	24
8	9.5	yes	0	50	127	24
8	9.9	yes	23	0	152	24
8	34.5	yes	47	0	152	24
8	79.9	yes	0	25	152	24
9	14.9	yes	0	25	127	24
9	15.2	yes	47	0	152	24
9	15.5	yes	0	0	152	24

Notes: (1) Accelerometer units are given as micro-g's.
(2) Heating in each run begins at t = 10 sec.

Table B-III. Summary of relatively larger acceleration excursions during PBE-IIA in STS-77 Flight.

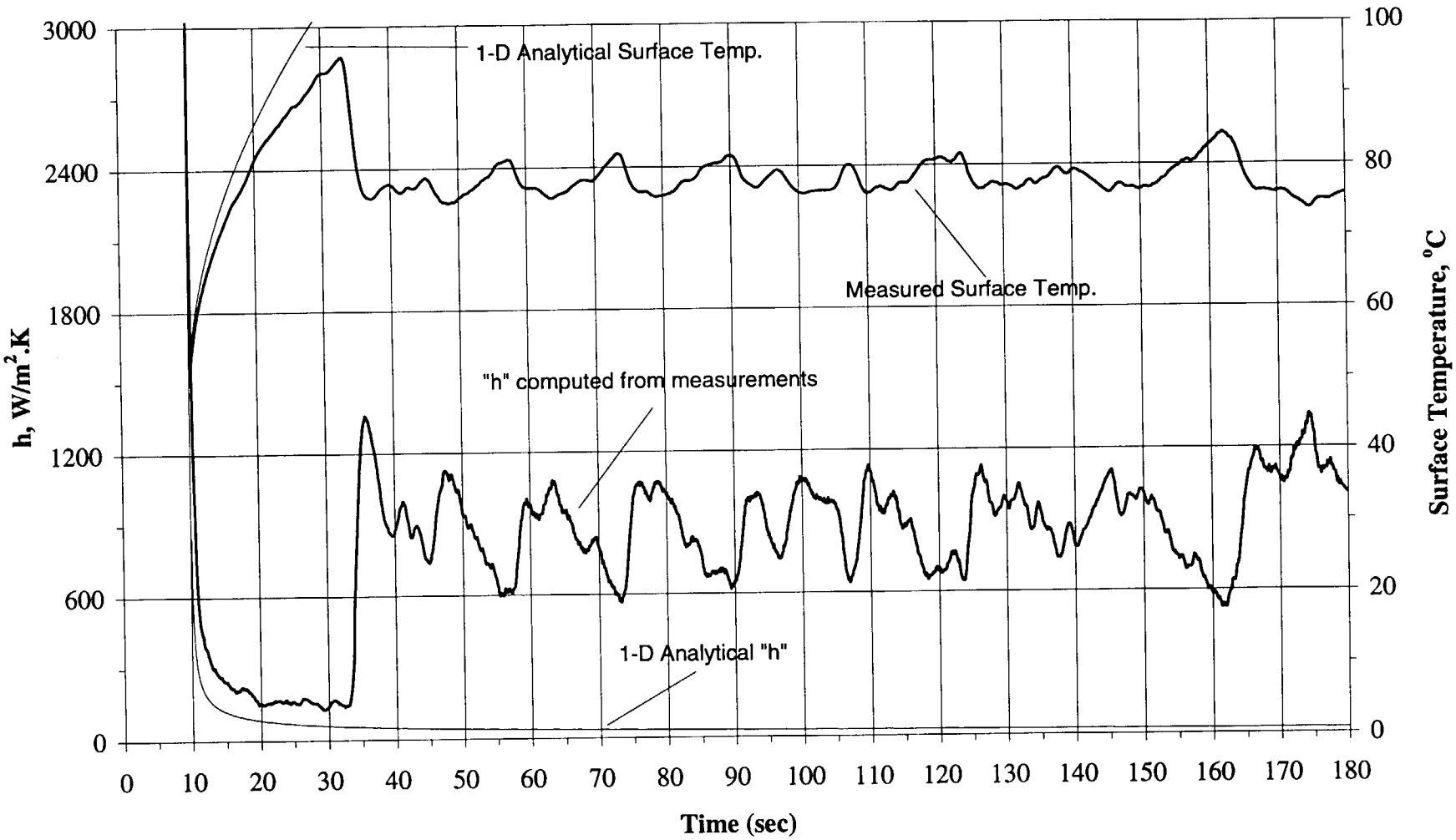

Figure B-1a. Mean heater surface temperature and derived heat transfer coefficient. PBE-IIA (STS-77). Run No. 1.

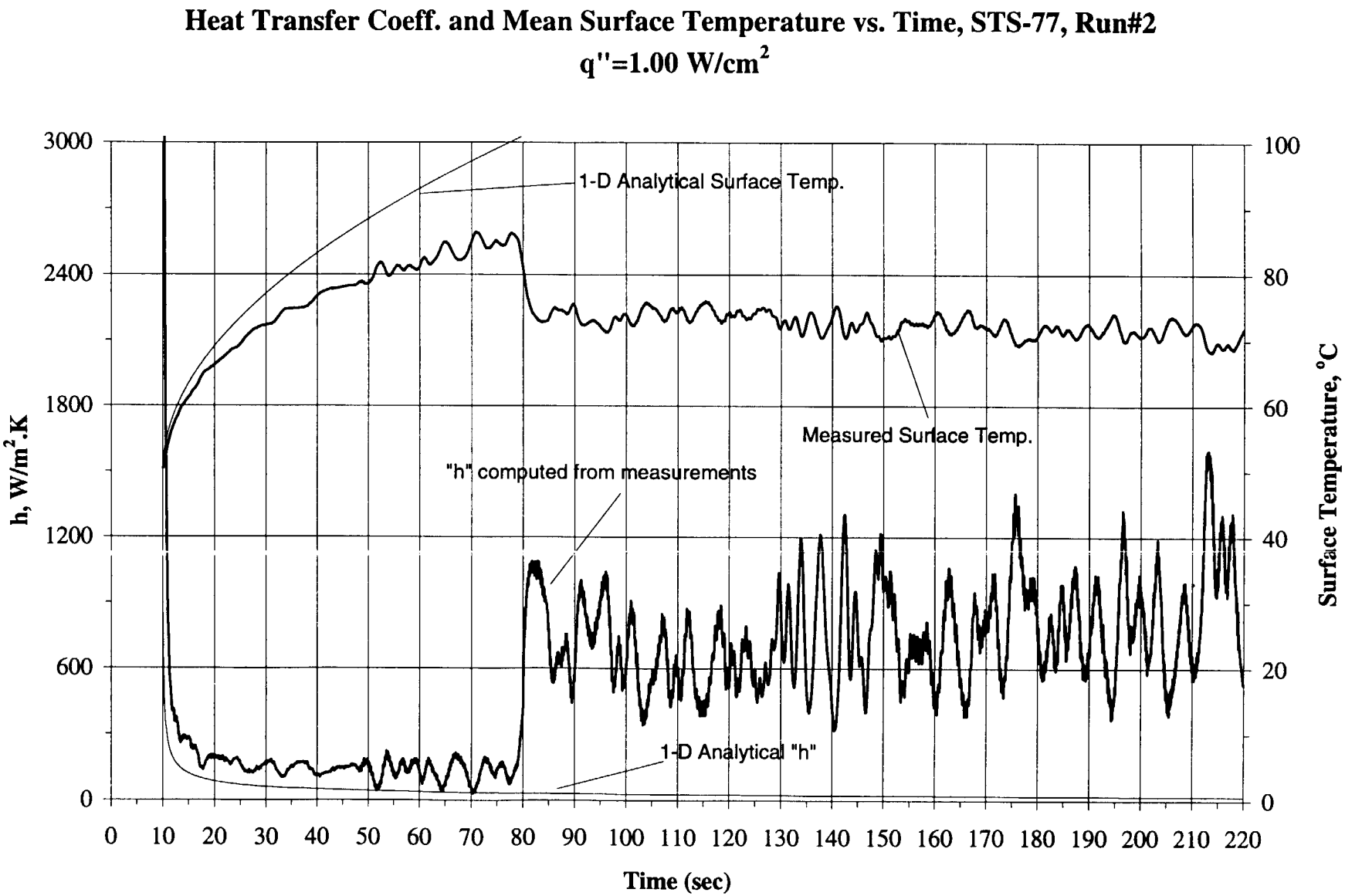

Figure B-1b. Mean heater surface temperature and derived heat transfer coefficient. PBE-IIA (STS-77). Run No. 2.

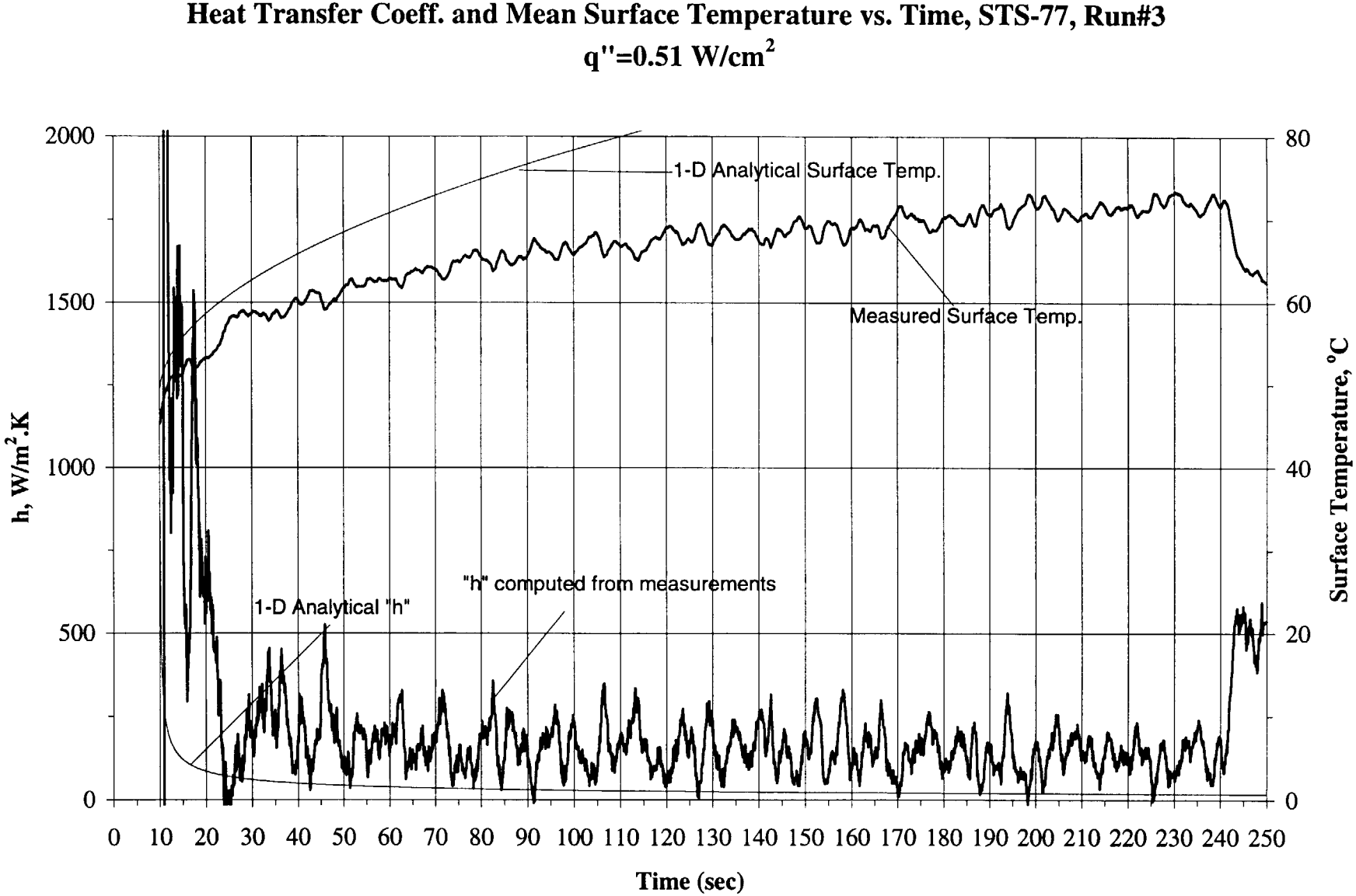

Figure B-1c. Mean heater surface temperature and derived heat transfer coefficient. PBE-IIA (STS-77). Run No. 3.

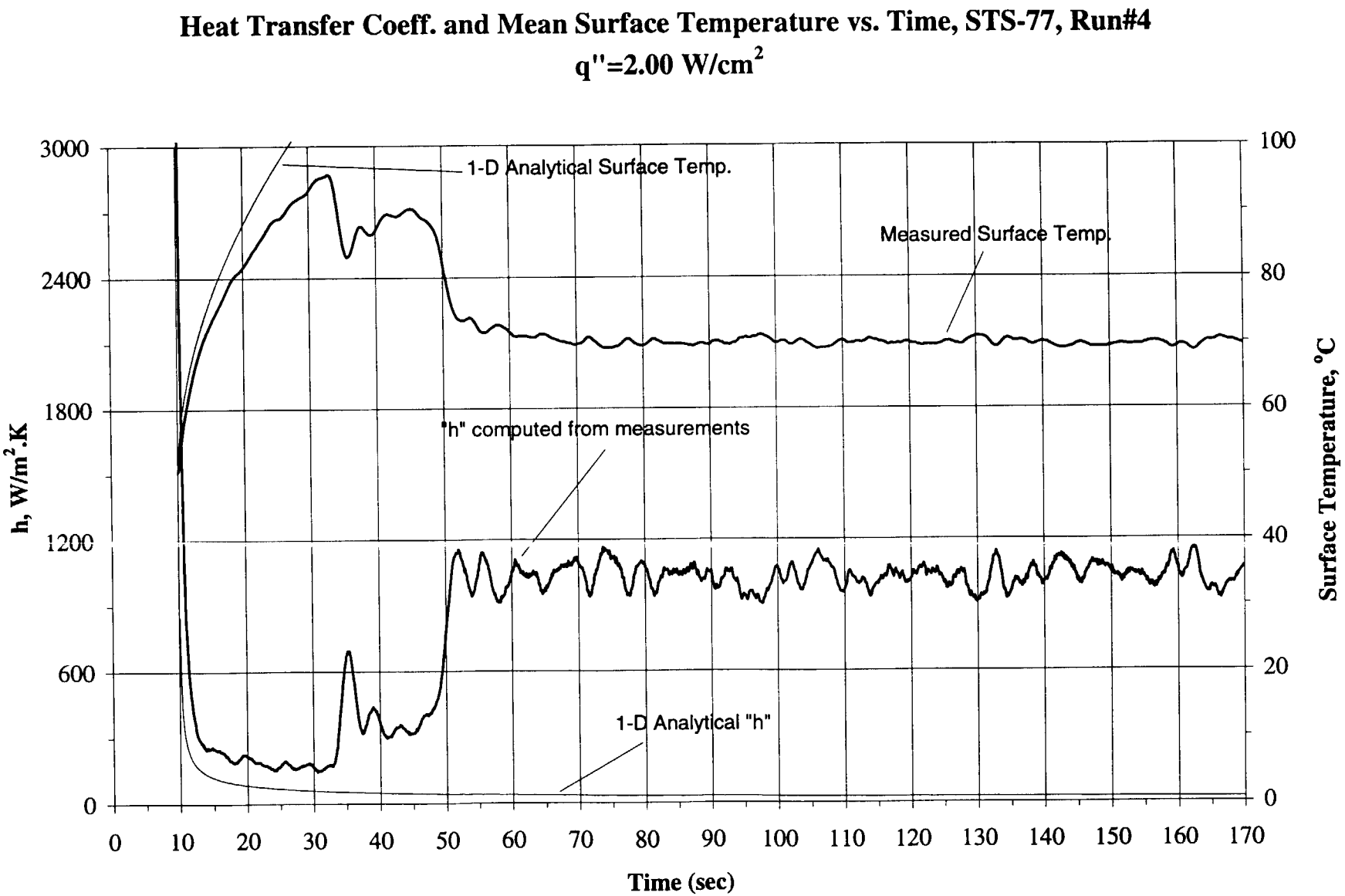

Figure B-1d. Mean heater surface temperature and derived heat transfer coefficient. PBE-IIA (STS-77). Run No. 4.

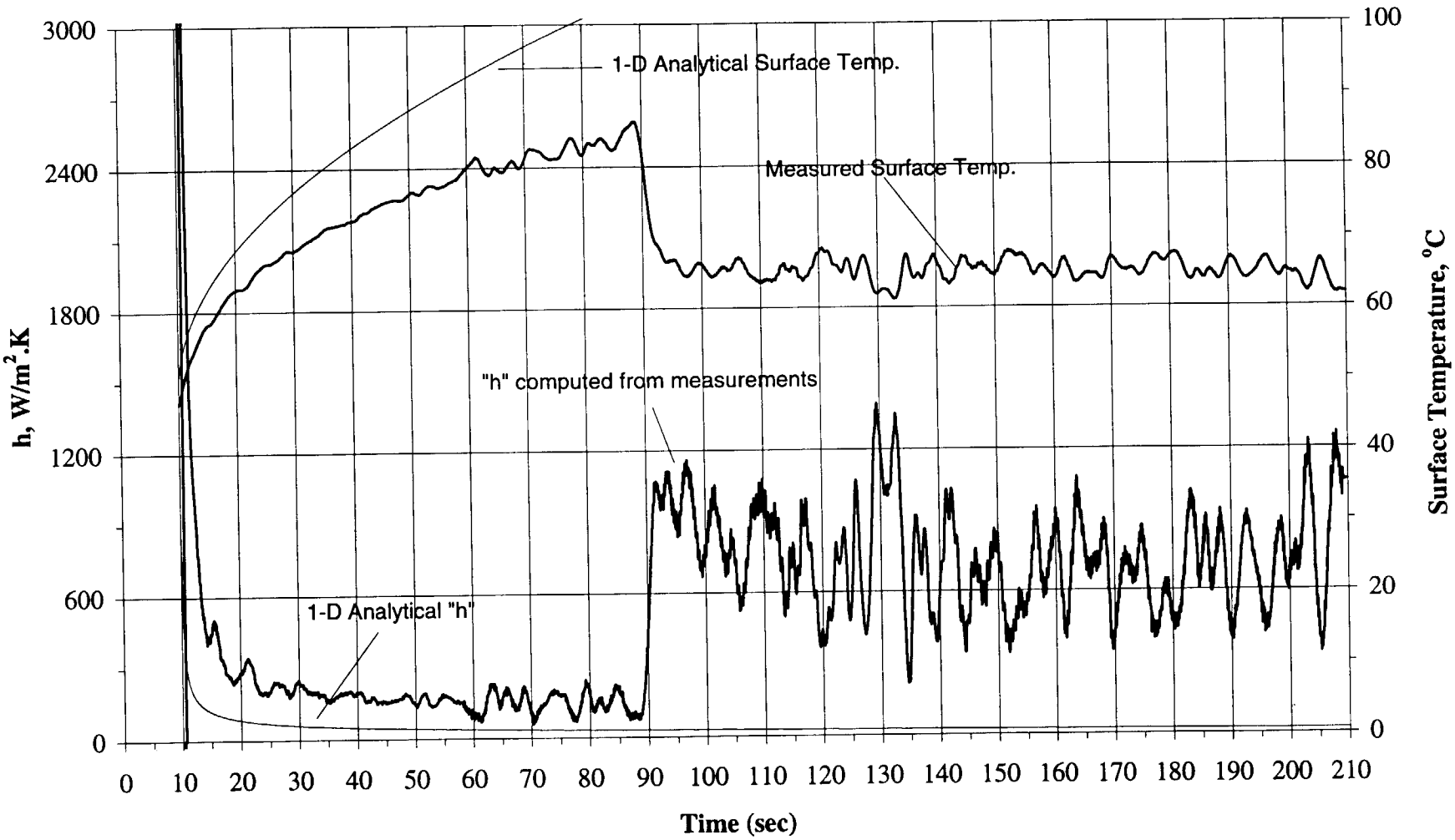

Figure B-1e. Mean heater surface temperature and derived heat transfer coefficient. PBE-IIA (STS-77). Run No. 5.

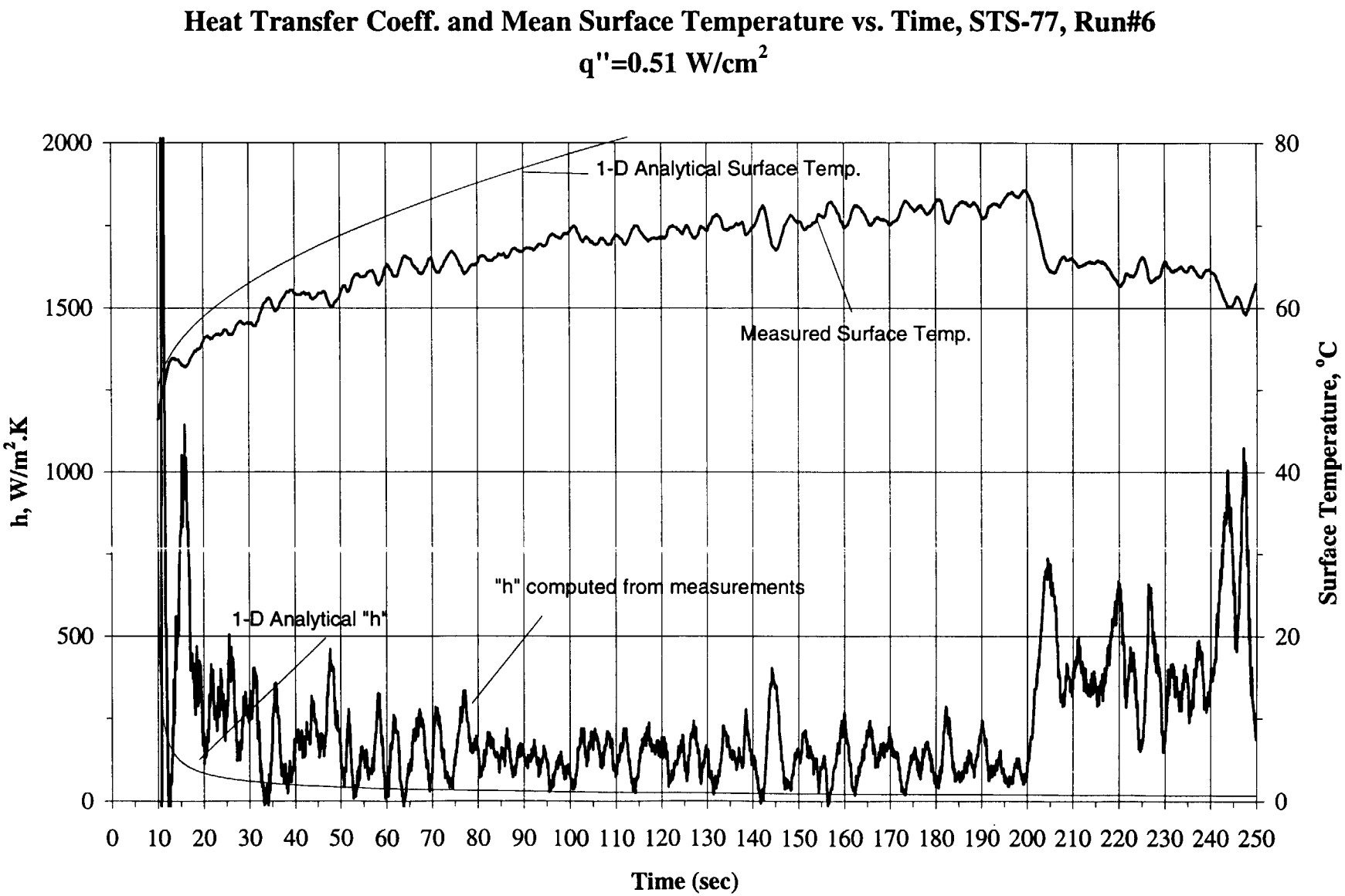

Figure B-1f. Mean heater surface temperature and derived heat transfer coefficient. PBE-IIA (STS-77). Run No. 6.

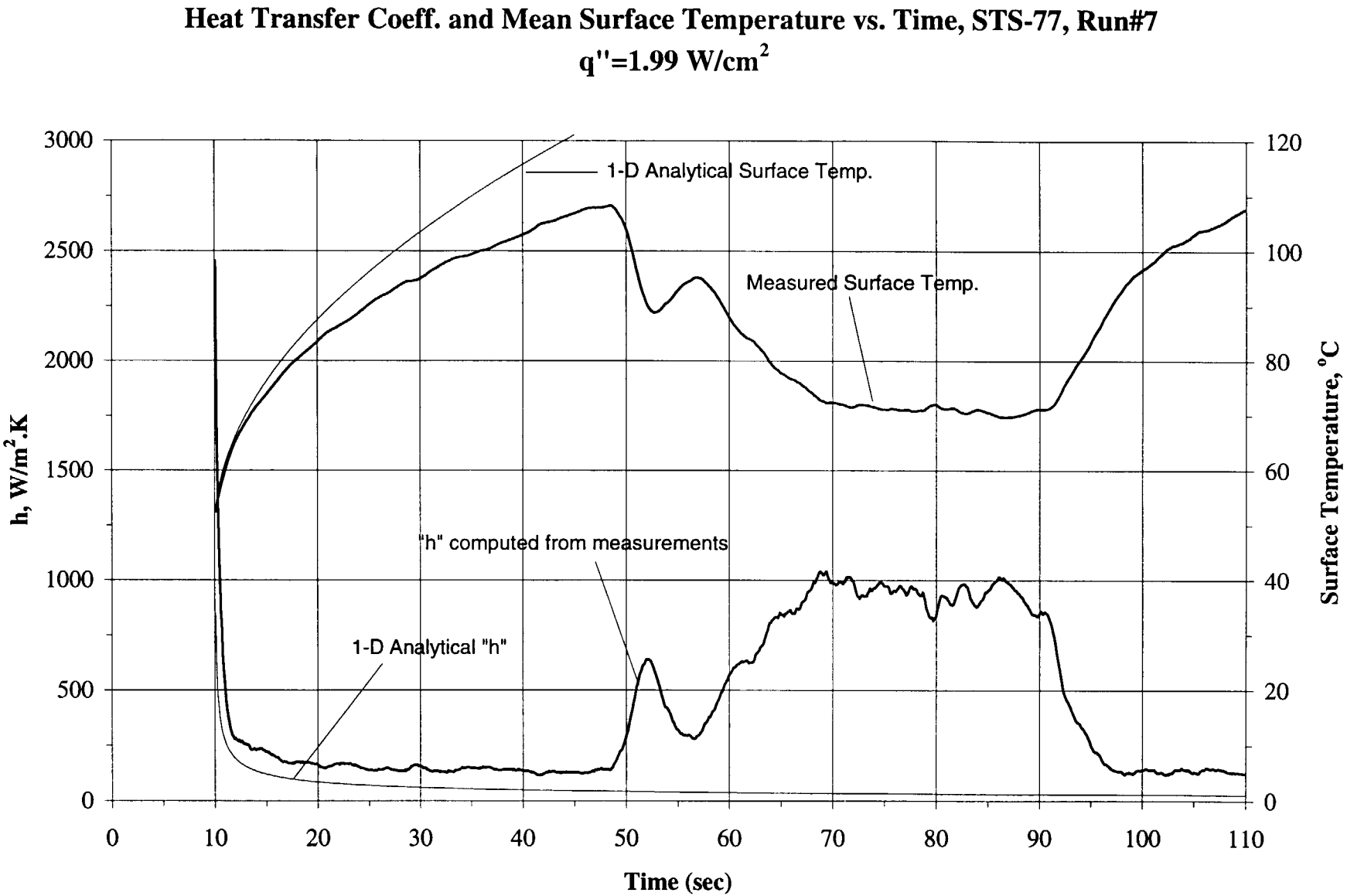

Figure B-1g. Mean heater surface temperature and derived heat transfer coefficient. PBE-IIA (STS-77). Run No. 7.

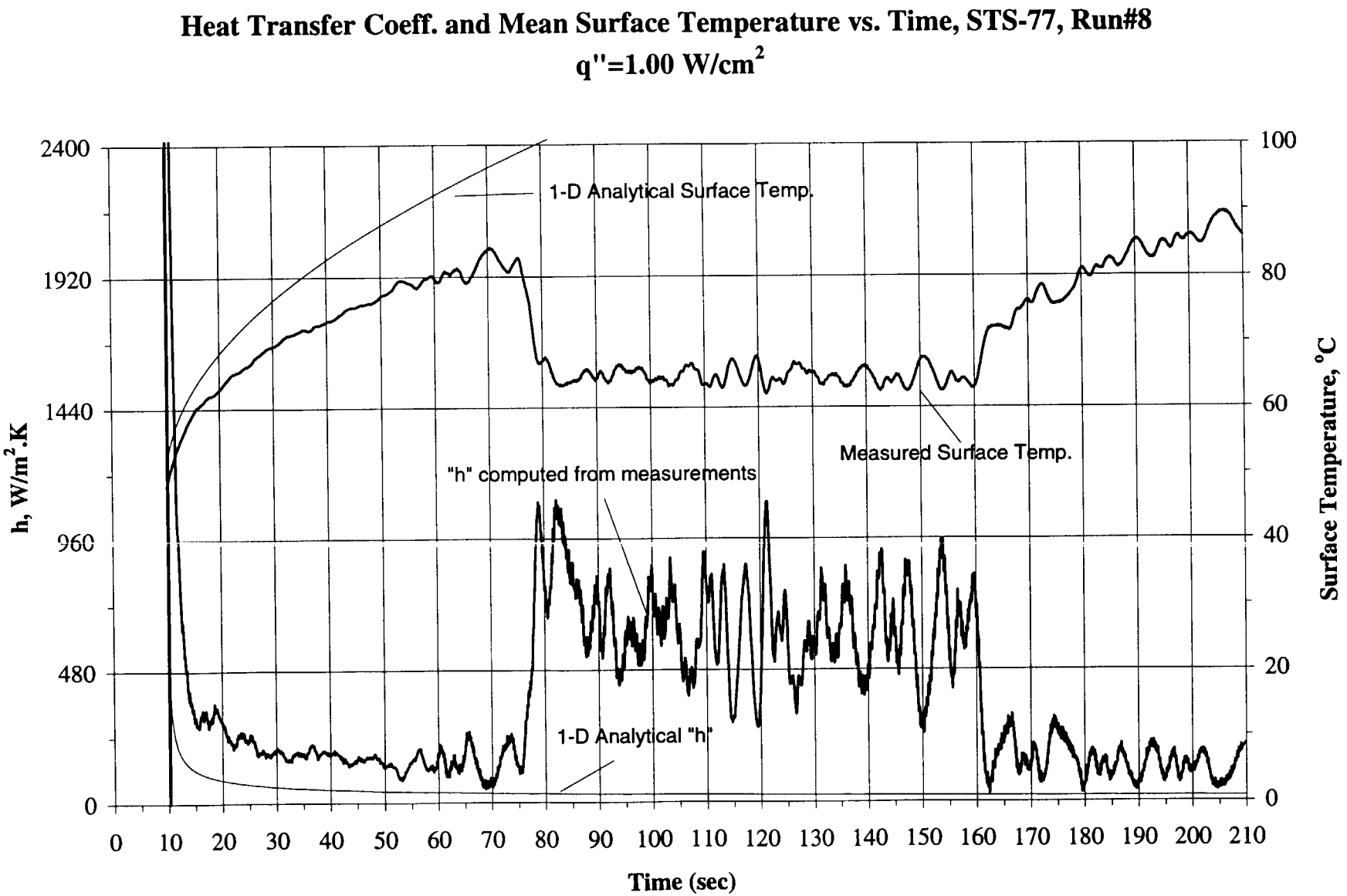

Figure B-1h. Mean heater surface temperature and derived heat transfer coefficient. PBE-IIA (STS-77). Run No. 8.

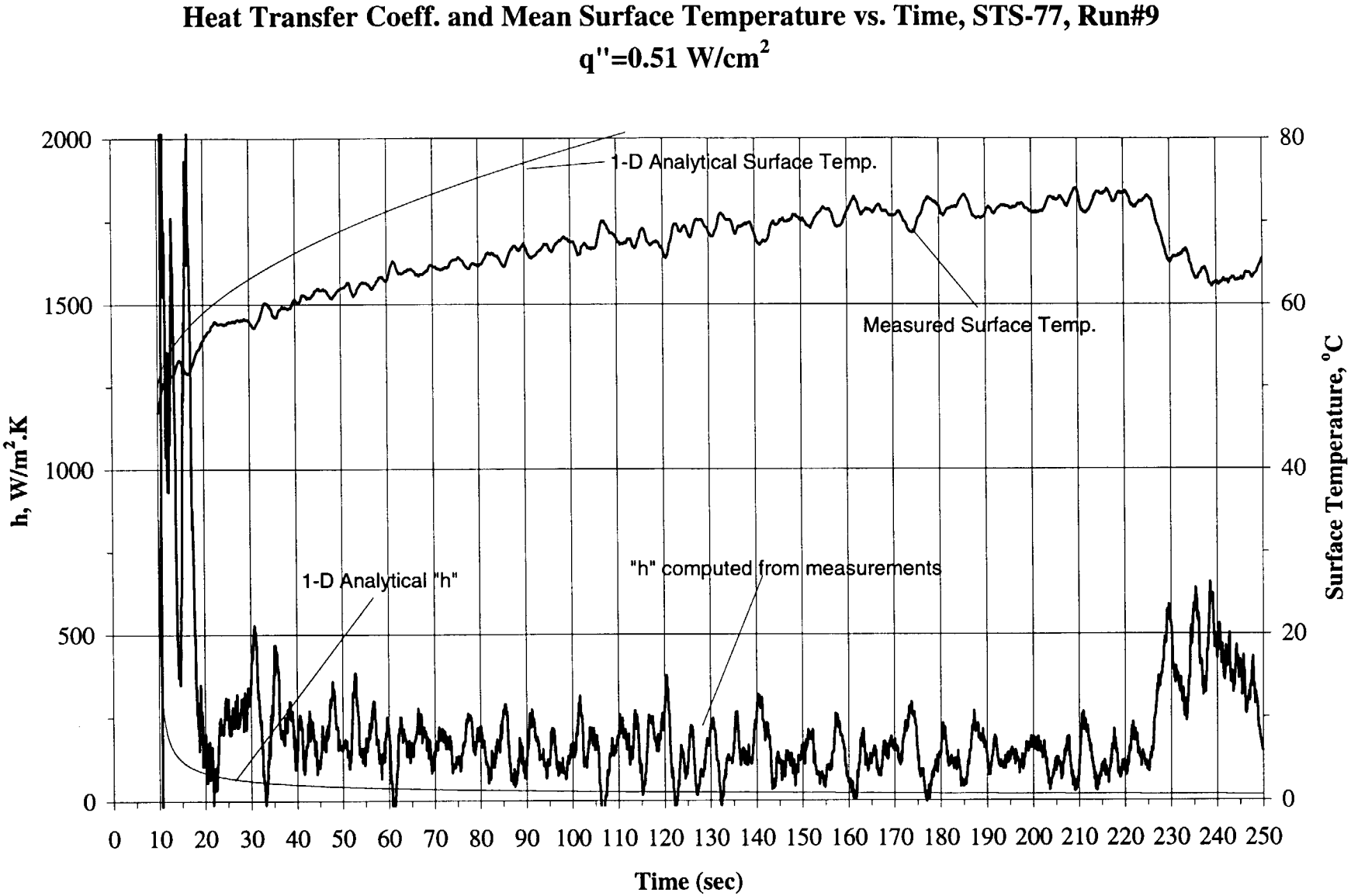

Figure B-1i. Mean heater surface temperature and derived heat transfer coefficient. PBE-IIA (STS-77). Run No. 9.

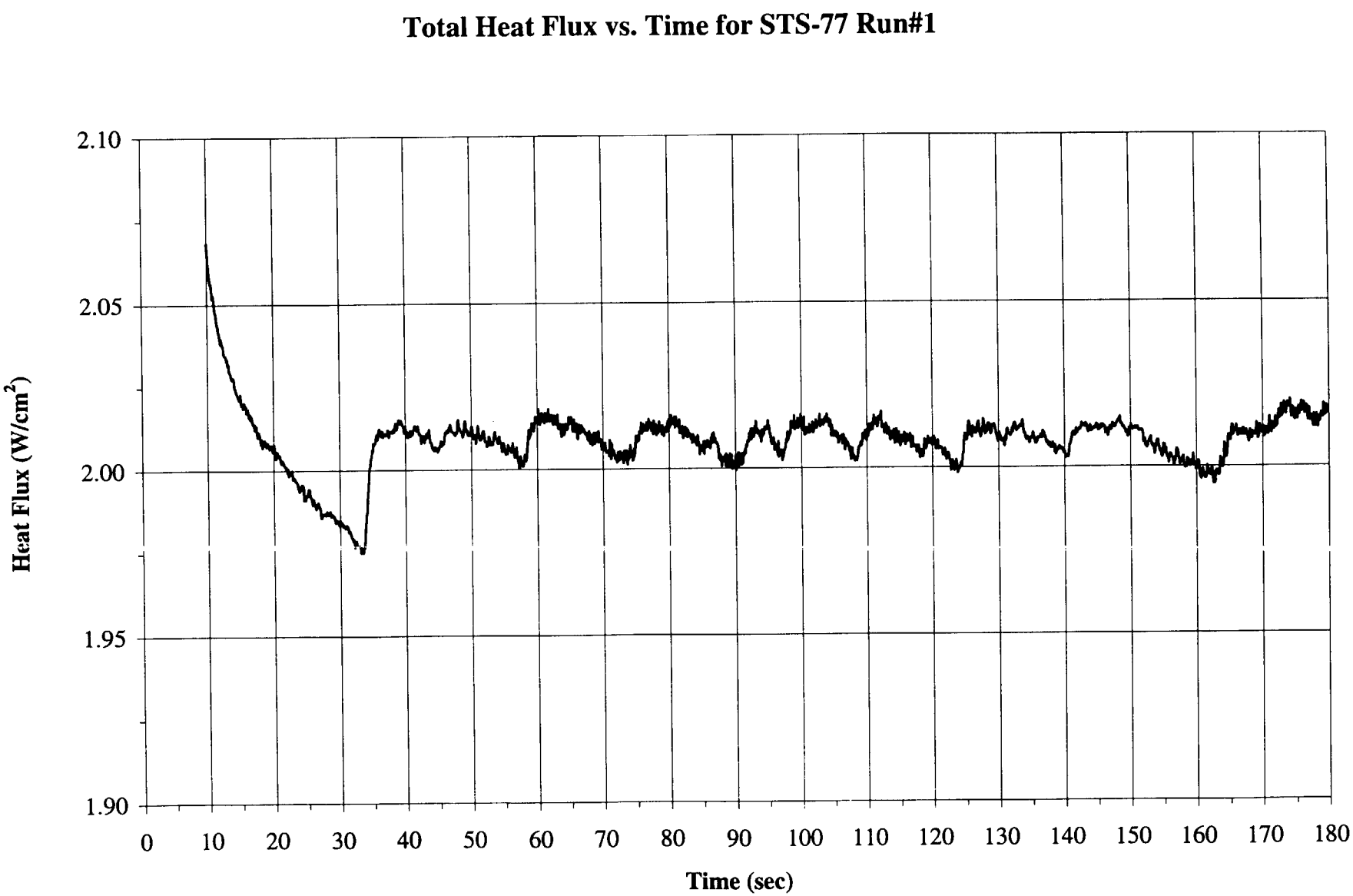

Figure B-2a. Heater flux input. PBE-IIA (STS-77). Run No. 1.

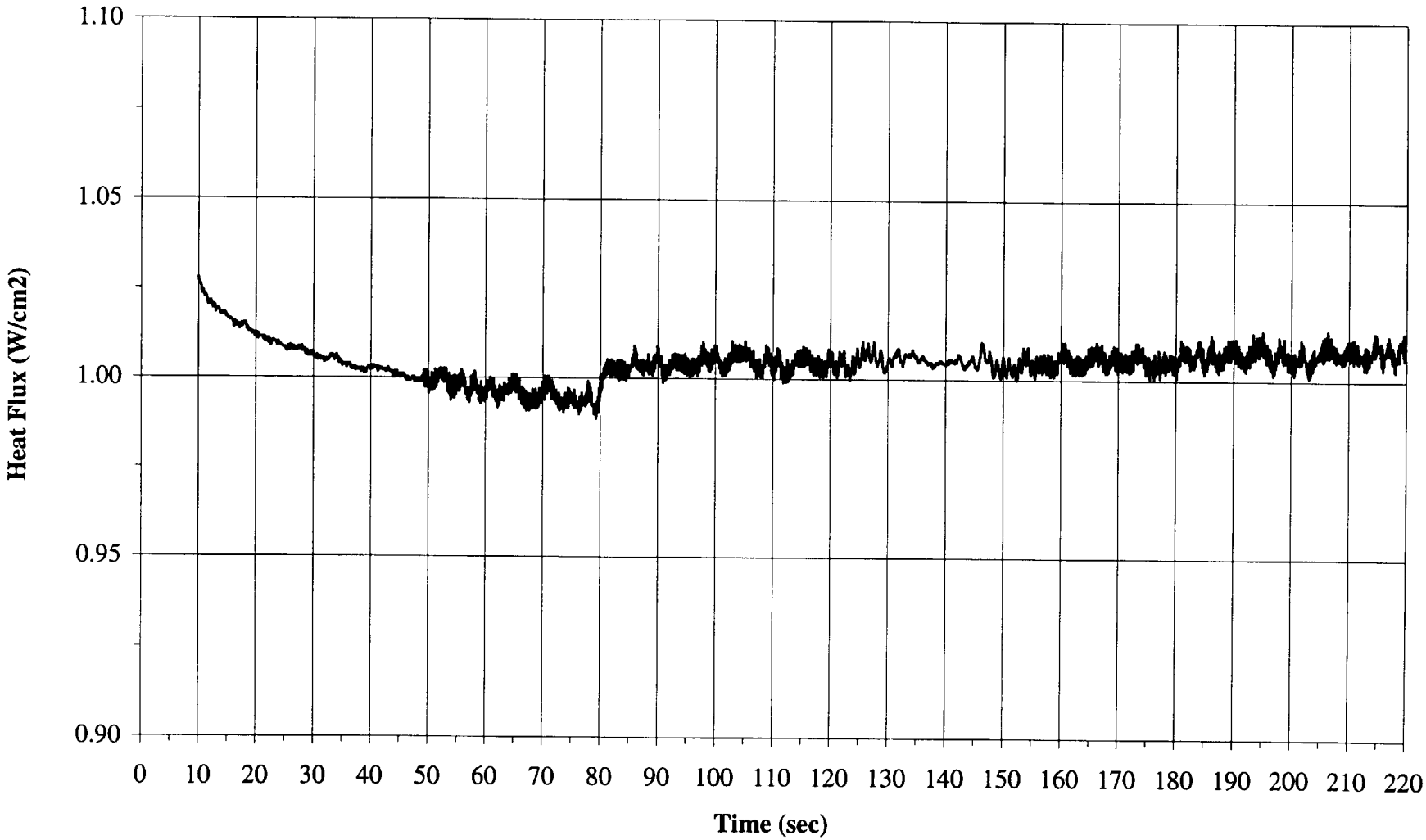

Figure B-2b. Heater flux input. PBE-IIA (STS-77). Run No. 2.

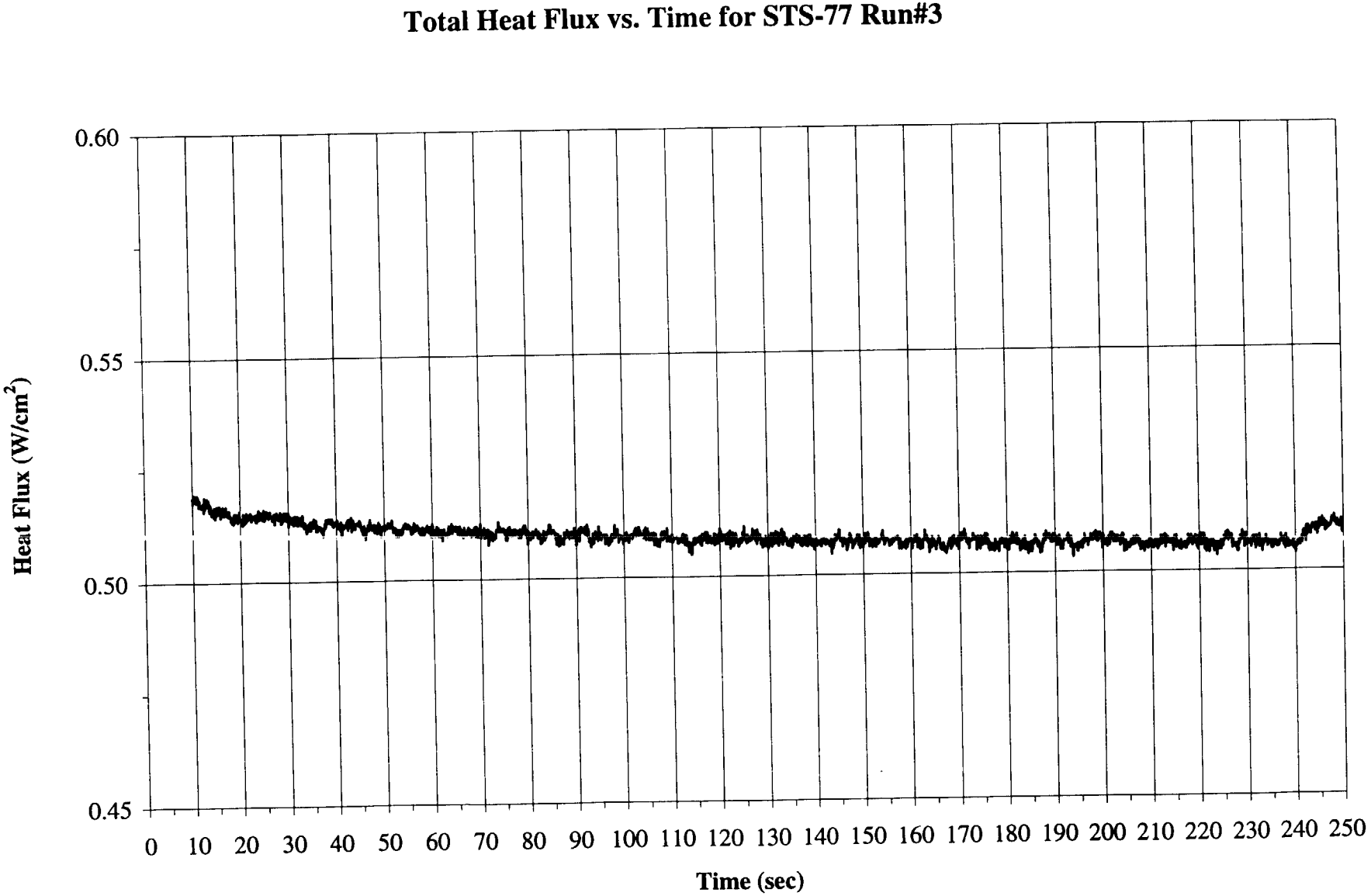

Figure B-2c. Heater flux input. PBE-IIA (STS-77). Run No. 3.

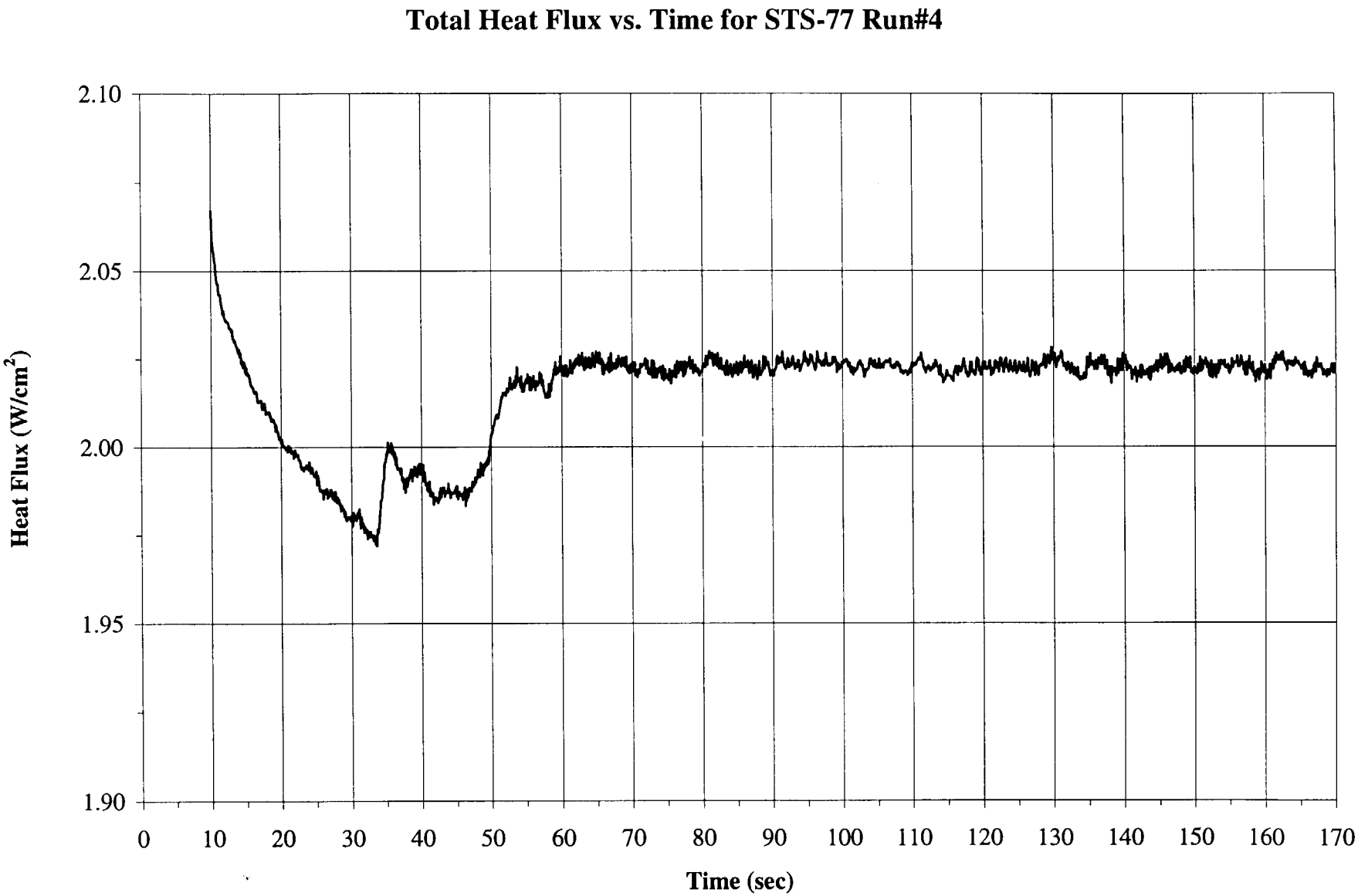

Figure B-2d. Heater flux input. PBE-IIA (STS-77). Run No. 4.

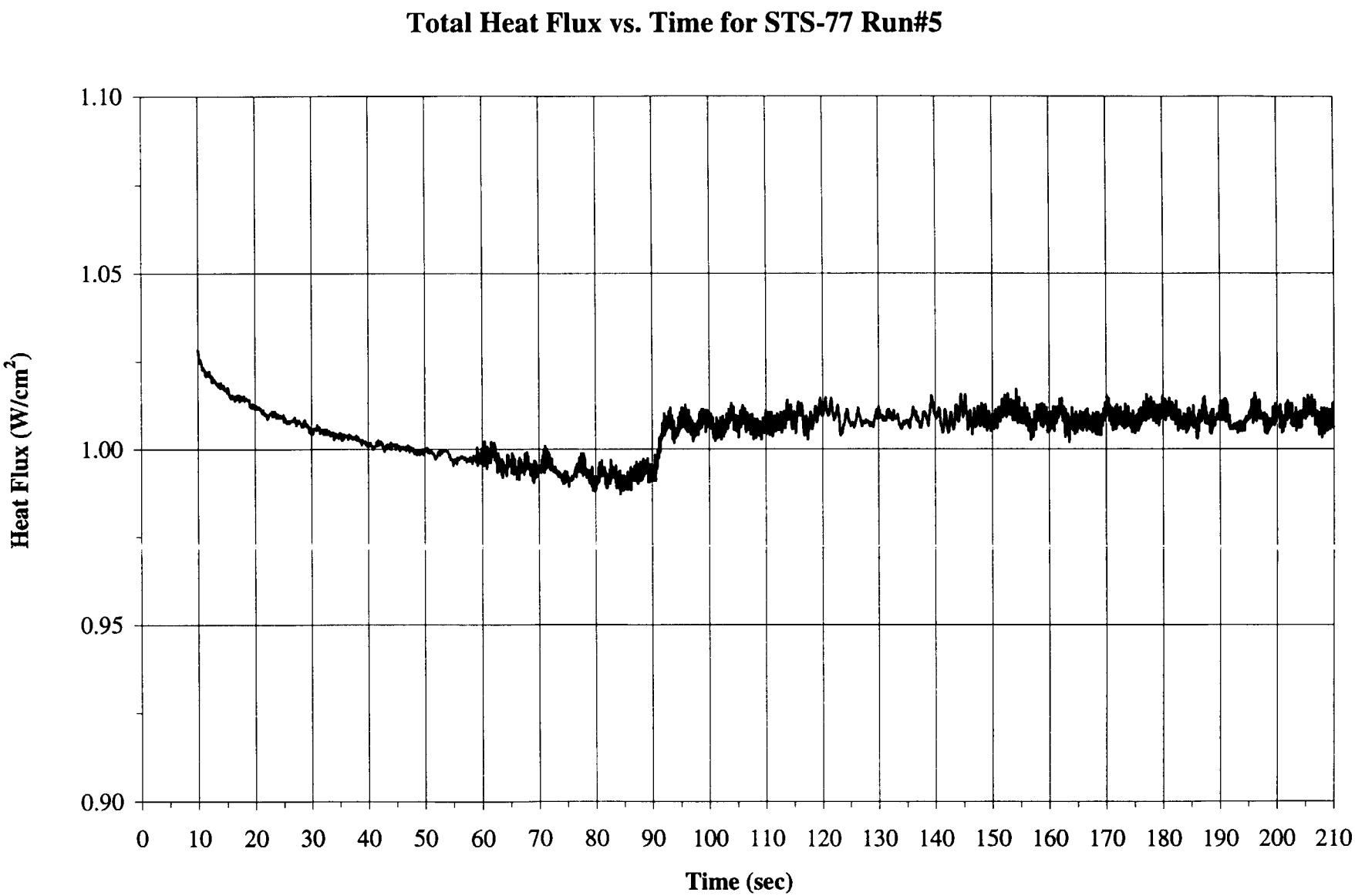

Figure B-2e. Heater flux input. PBE-IIA (STS-77). Run No. 5.

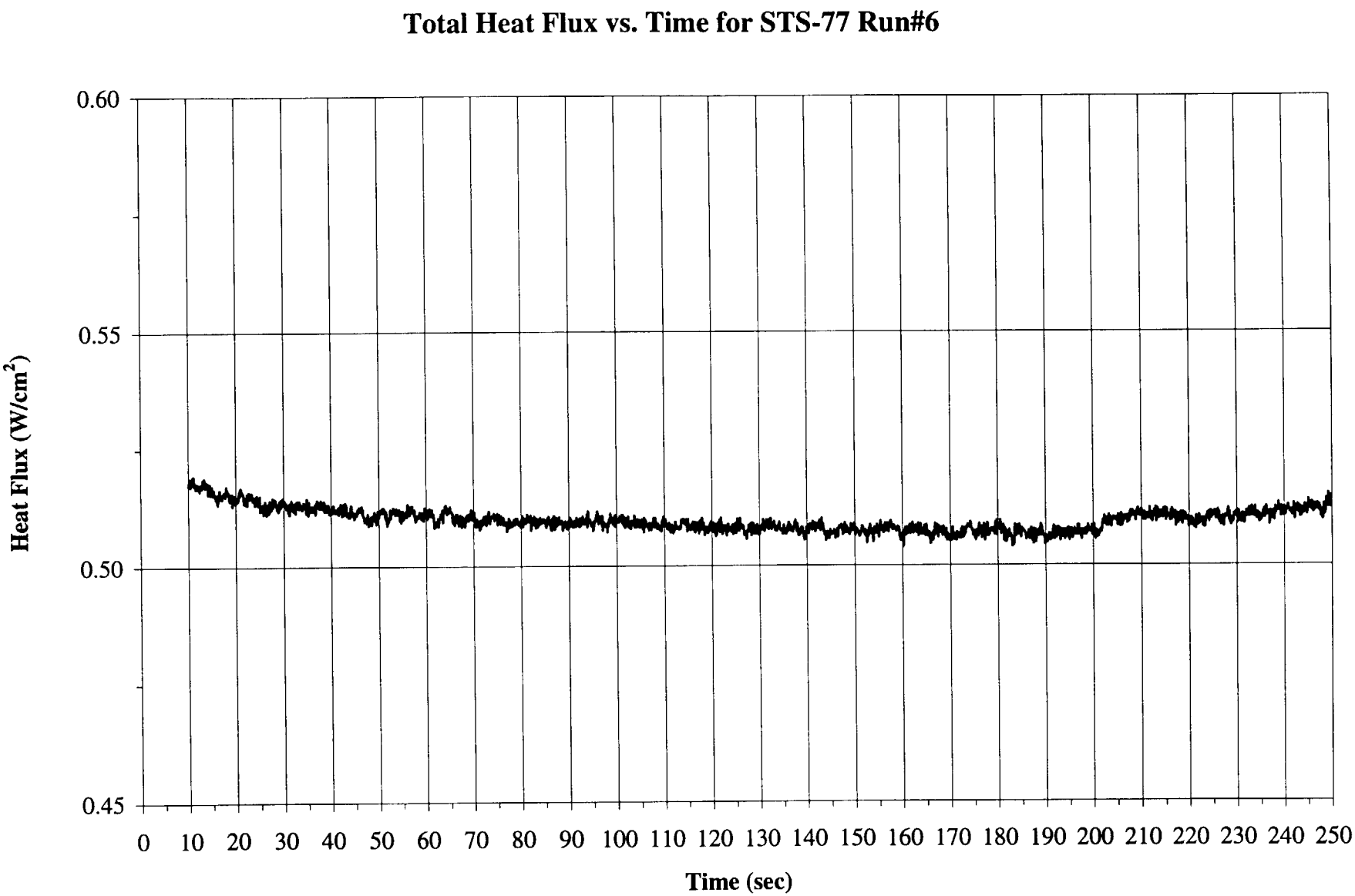

Figure B-2f. Heater flux input. PBE-IIA (STS-77). Run No. 6.

Figure B-2g. Heater flux input. PBE-IIA (STS-77). Run No. 7.

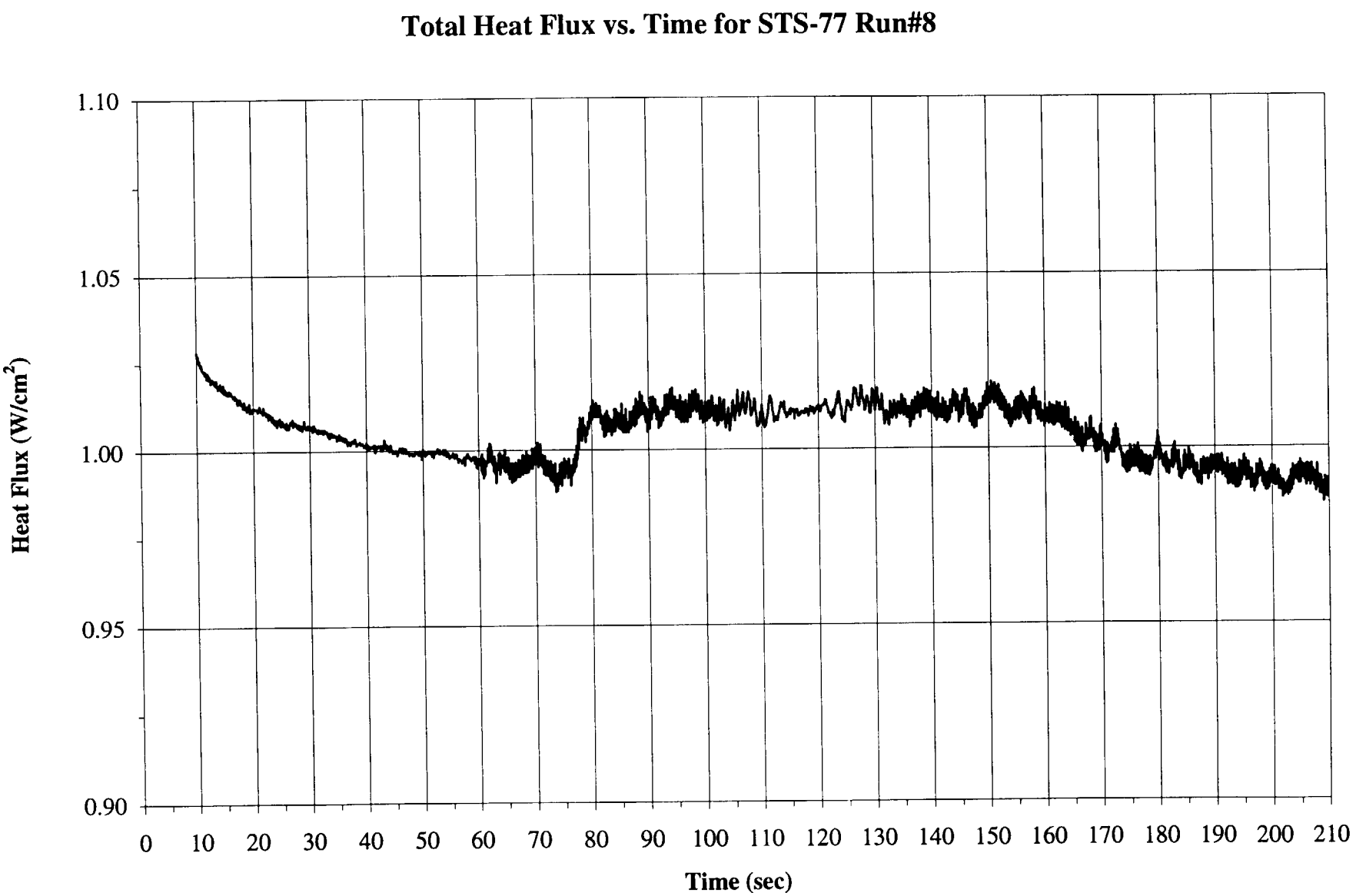

Figure B-2h. Heater flux input. PBE-IIA (STS-77). Run No. 8.

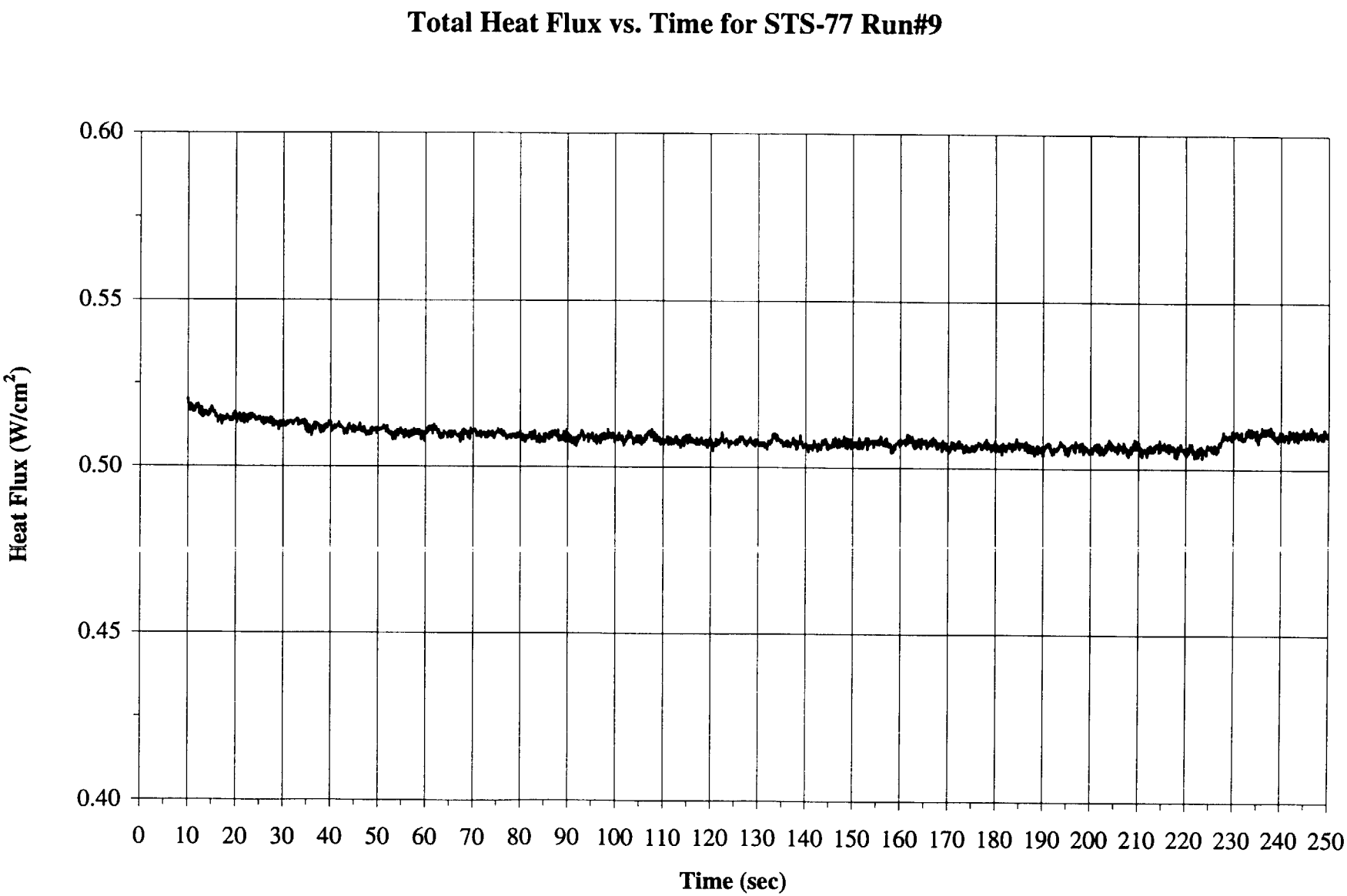

Figure B-2i. Heater flux input. PBE-IIA (STS-77). Run No. 9.

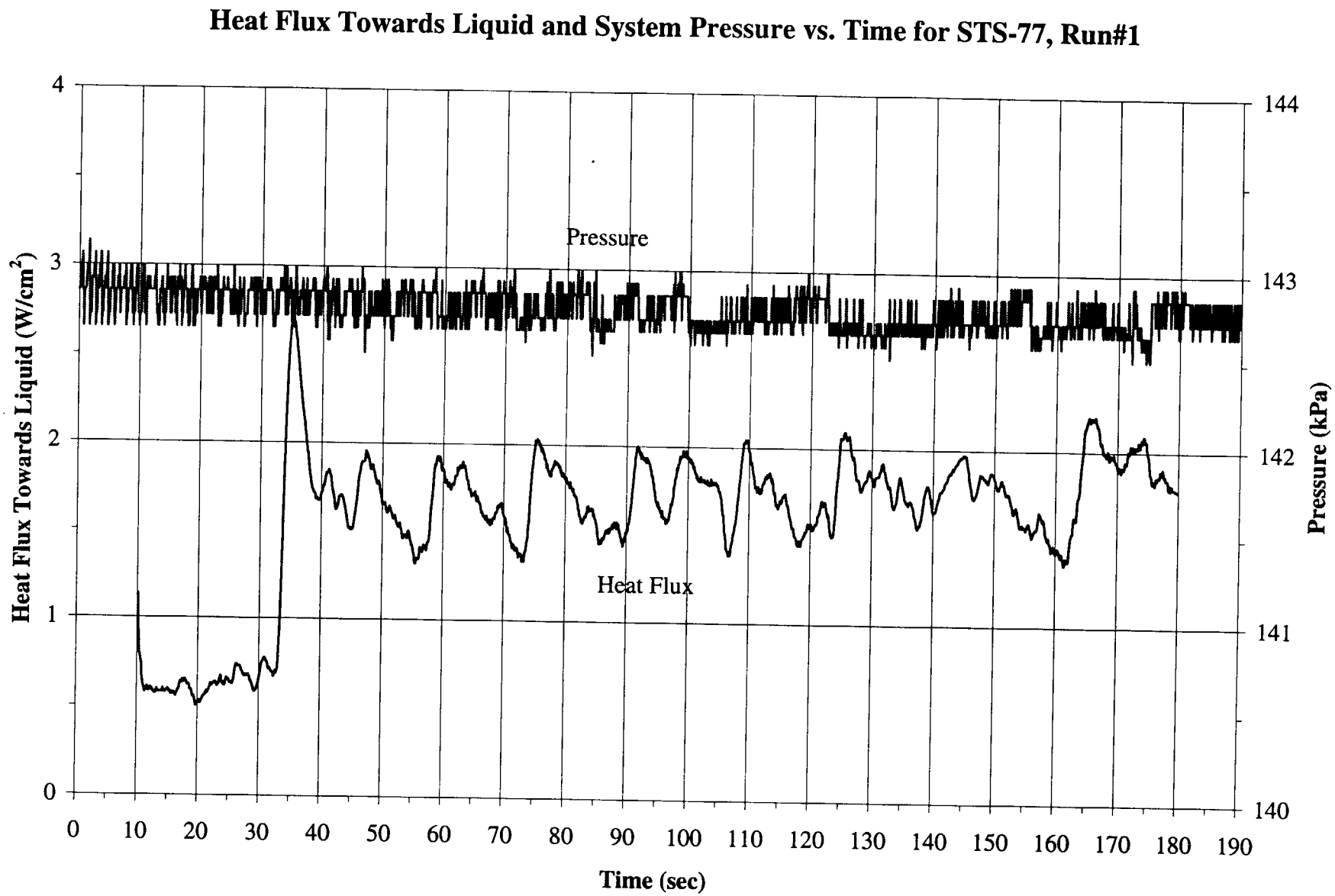

Figure B-3a. System pressure and fluid side mean heat flux. PBE-IIA (STS-77). Run No. 1.

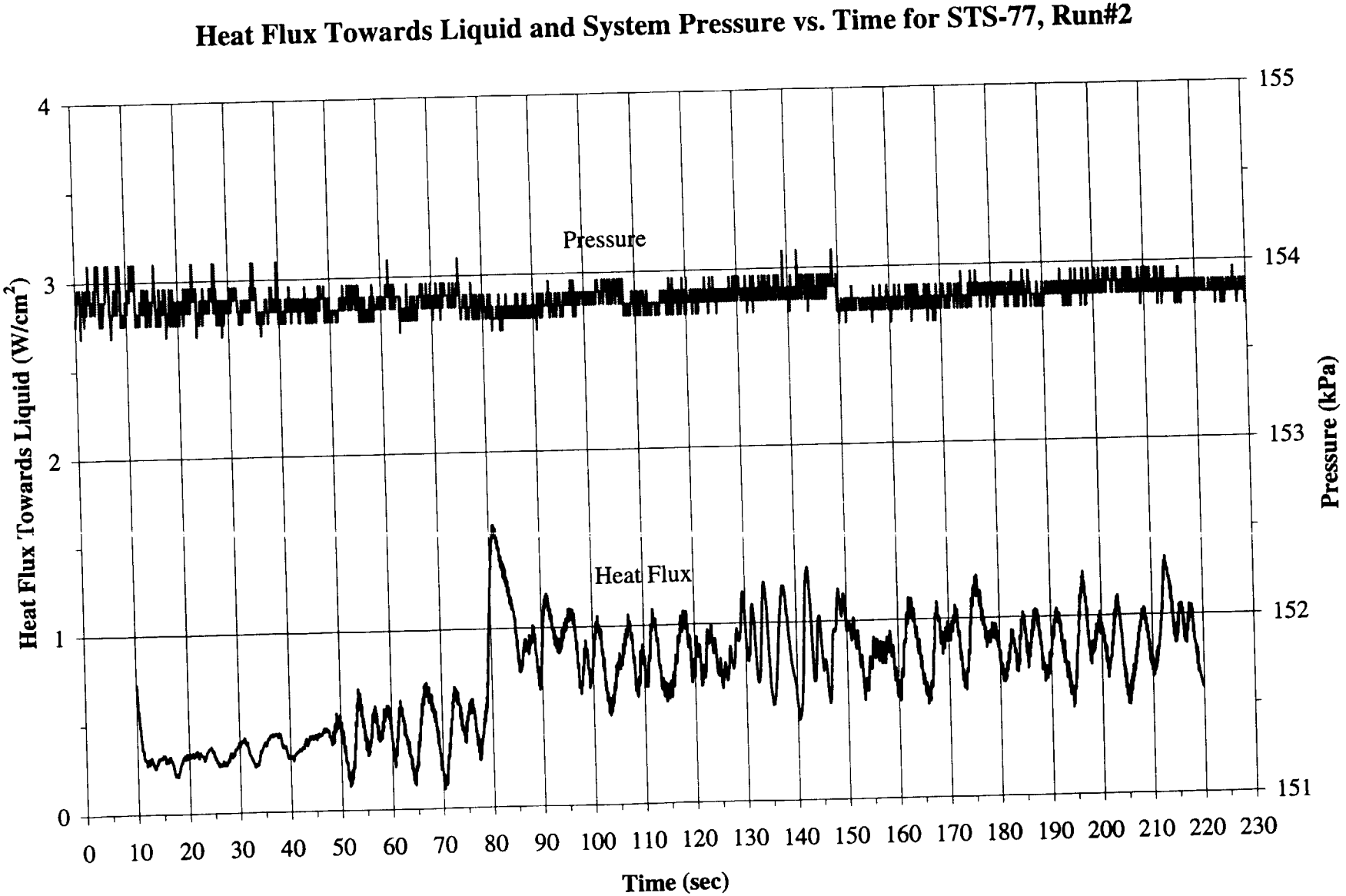

Figure B-3b. System pressure and fluid side mean heat flux. PBE-IIA (STS-77). Run No. 2.

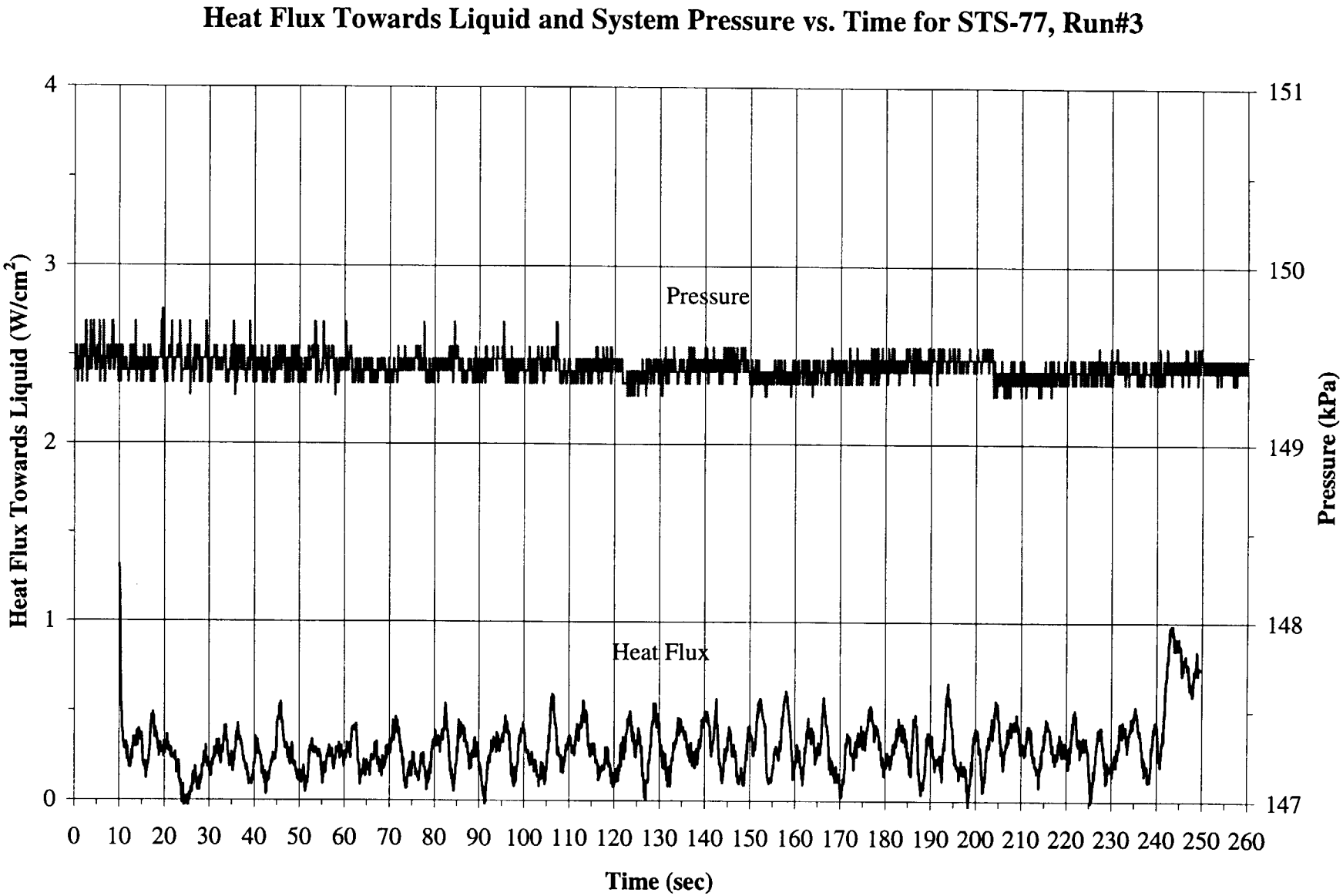

Figure B-3c. System pressure and fluid side mean heat flux. PBE-IIA (STS-77). Run No. 3.

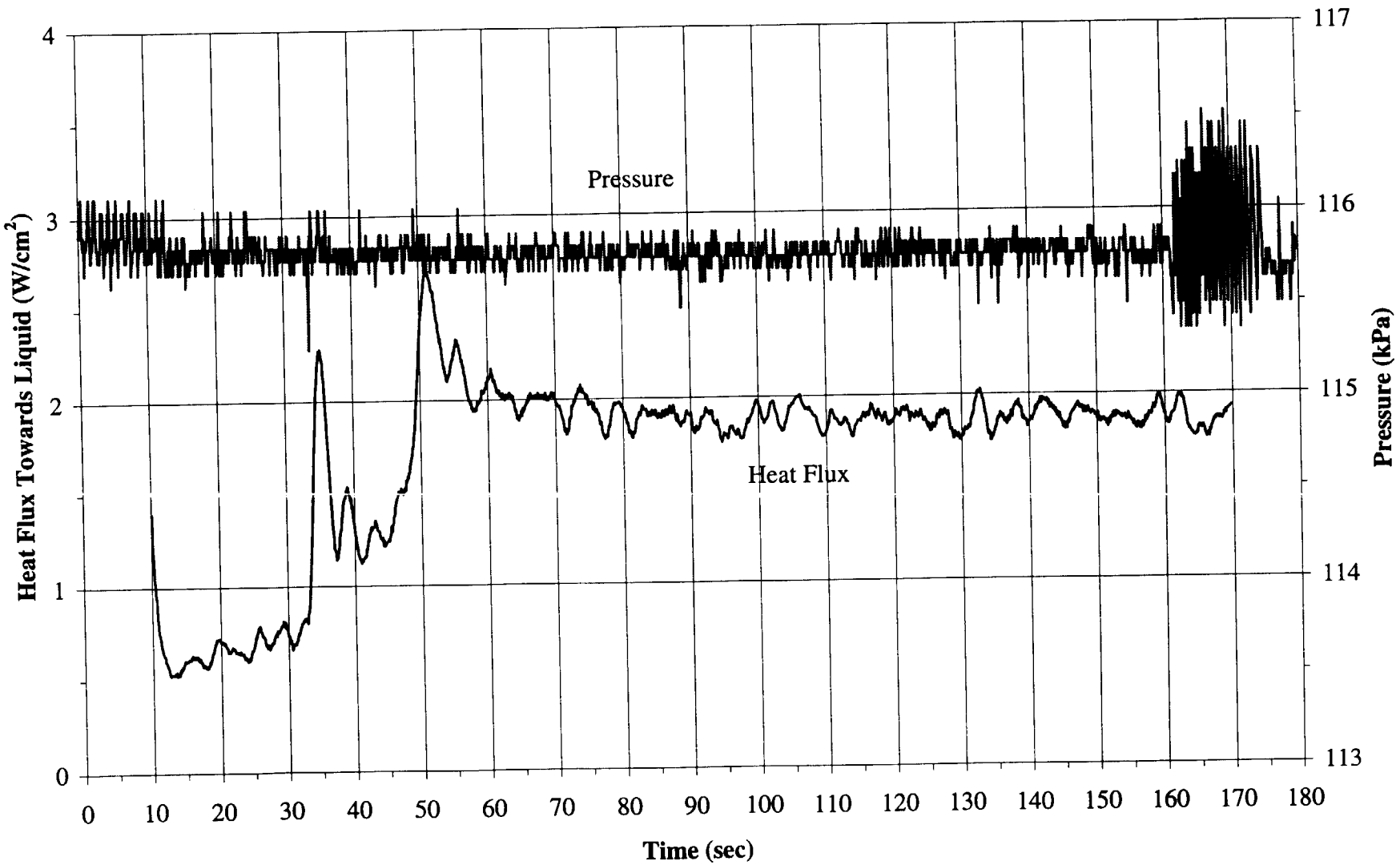

Figure B-3d. System pressure and fluid side mean heat flux. PBE-IIA (STS-77). Run No. 4.

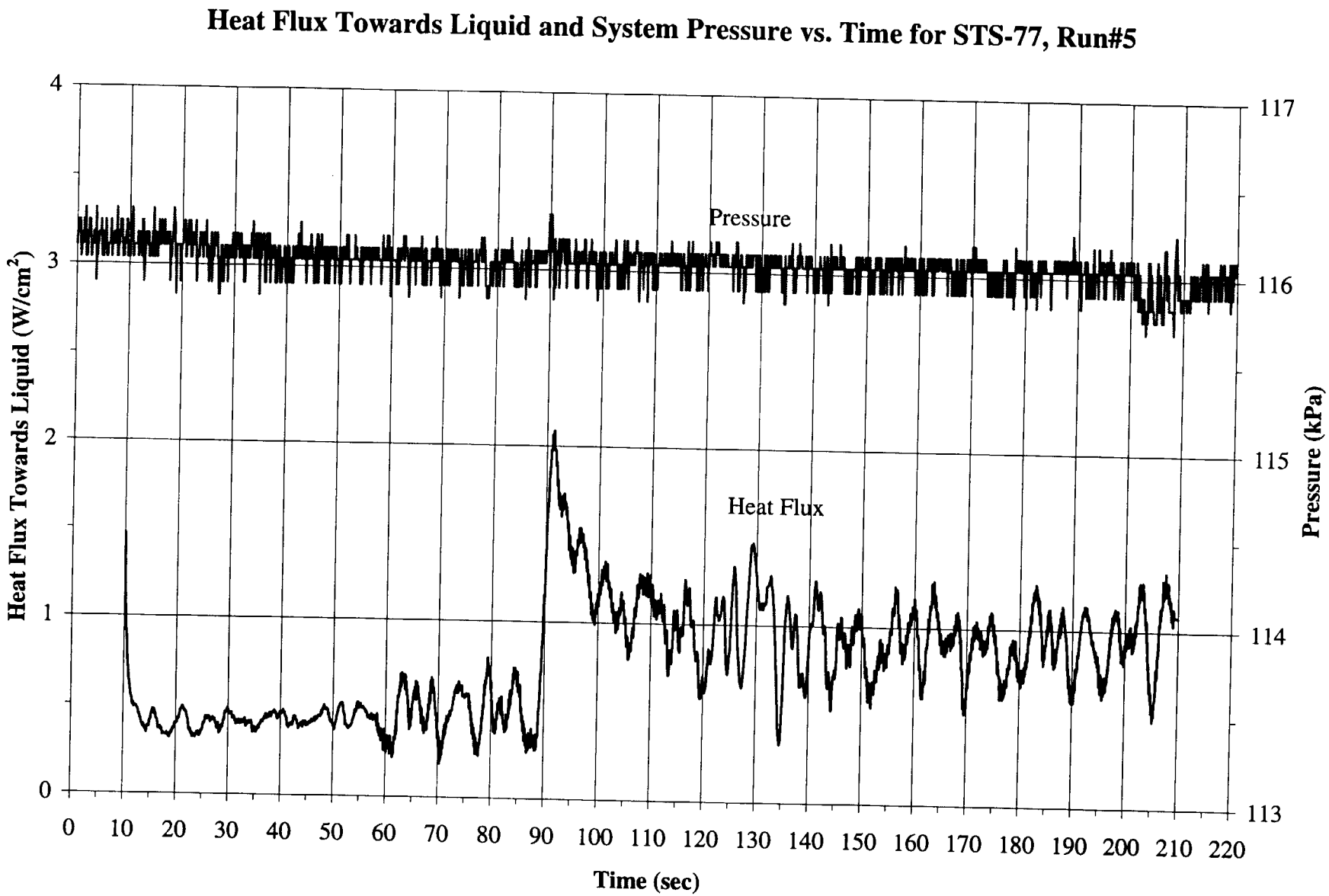

Figure B-3e. System pressure and fluid side mean heat flux. PBE-IIA (STS-77). Run No. 5.

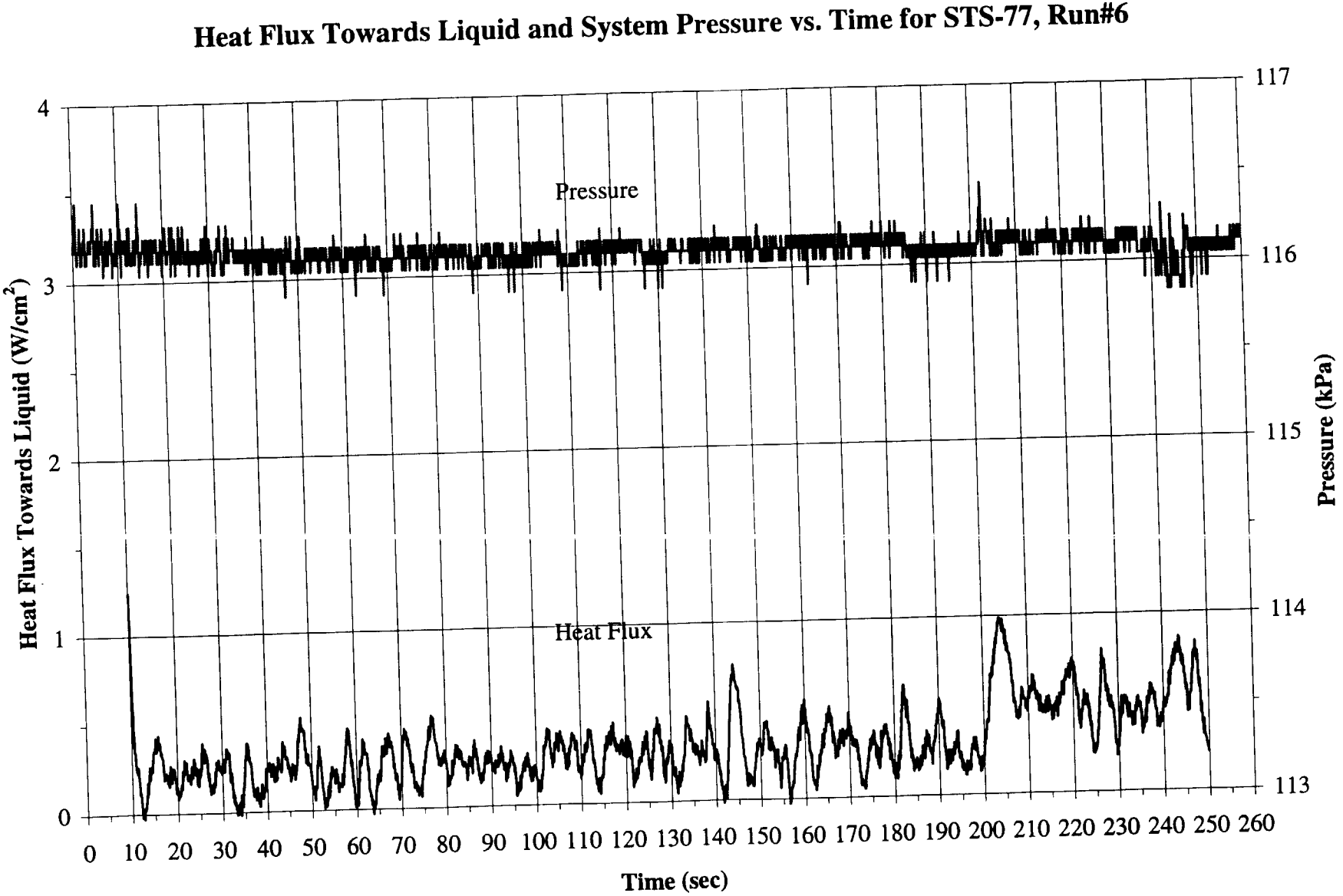

Figure B-3f. System pressure and fluid side mean heat flux. PBE-IIA (STS-77). Run No. 6.

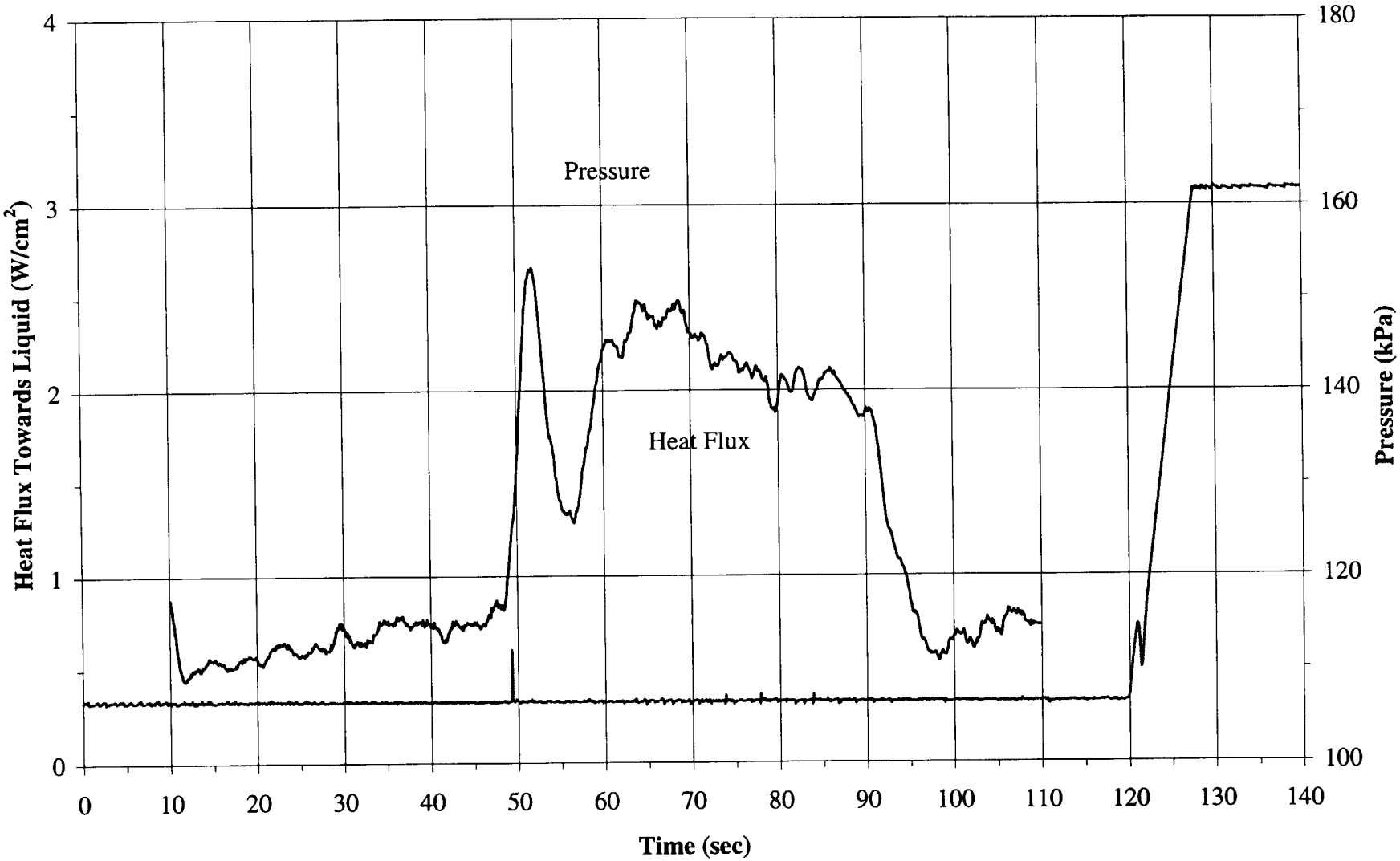

Figure B-3g. System pressure and fluid side mean heat flux. PBE-IIA (STS-77). Run No. 7.

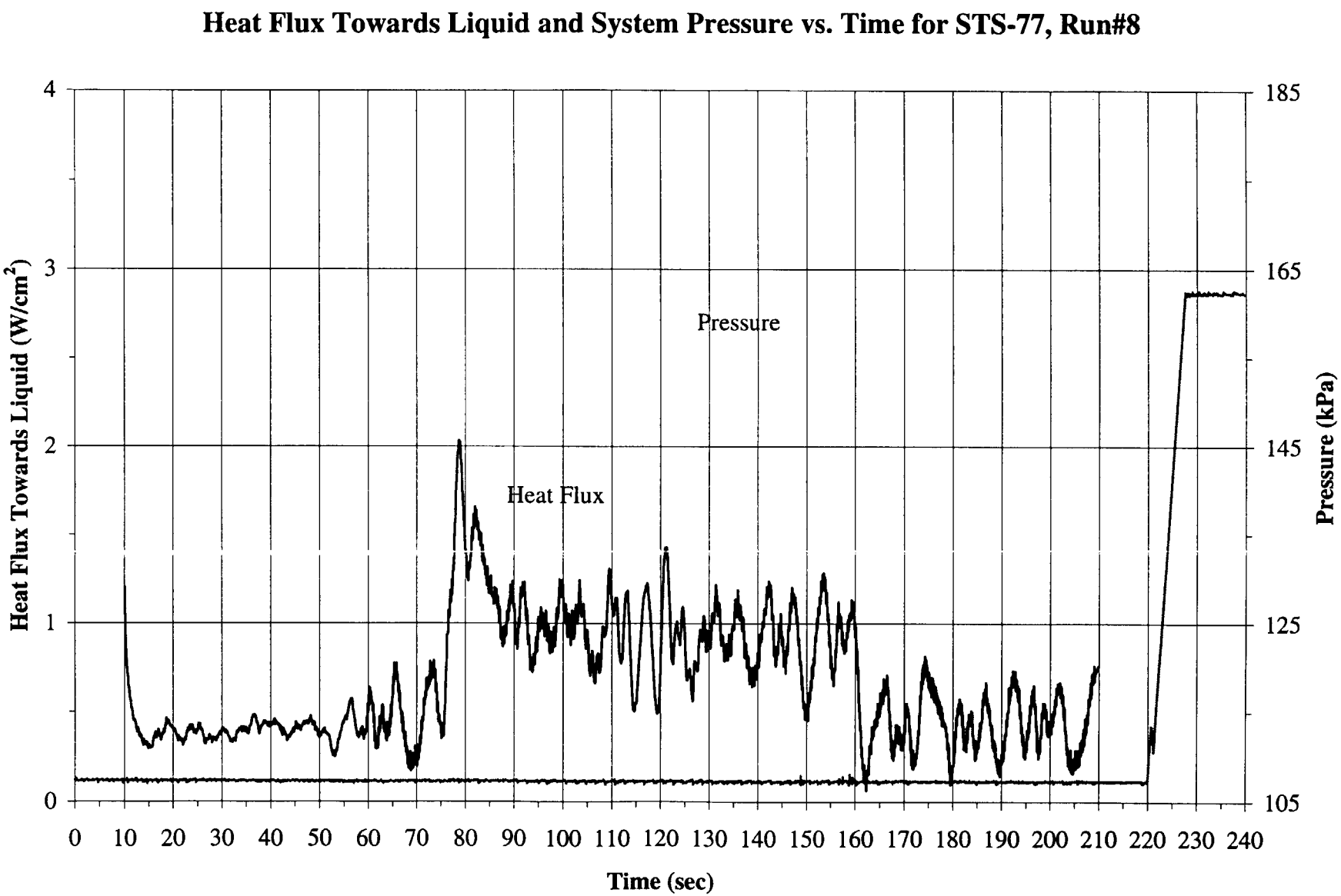

Figure B-3h. System pressure and fluid side mean heat flux. PBE-IIA (STS-77). Run No. 8.

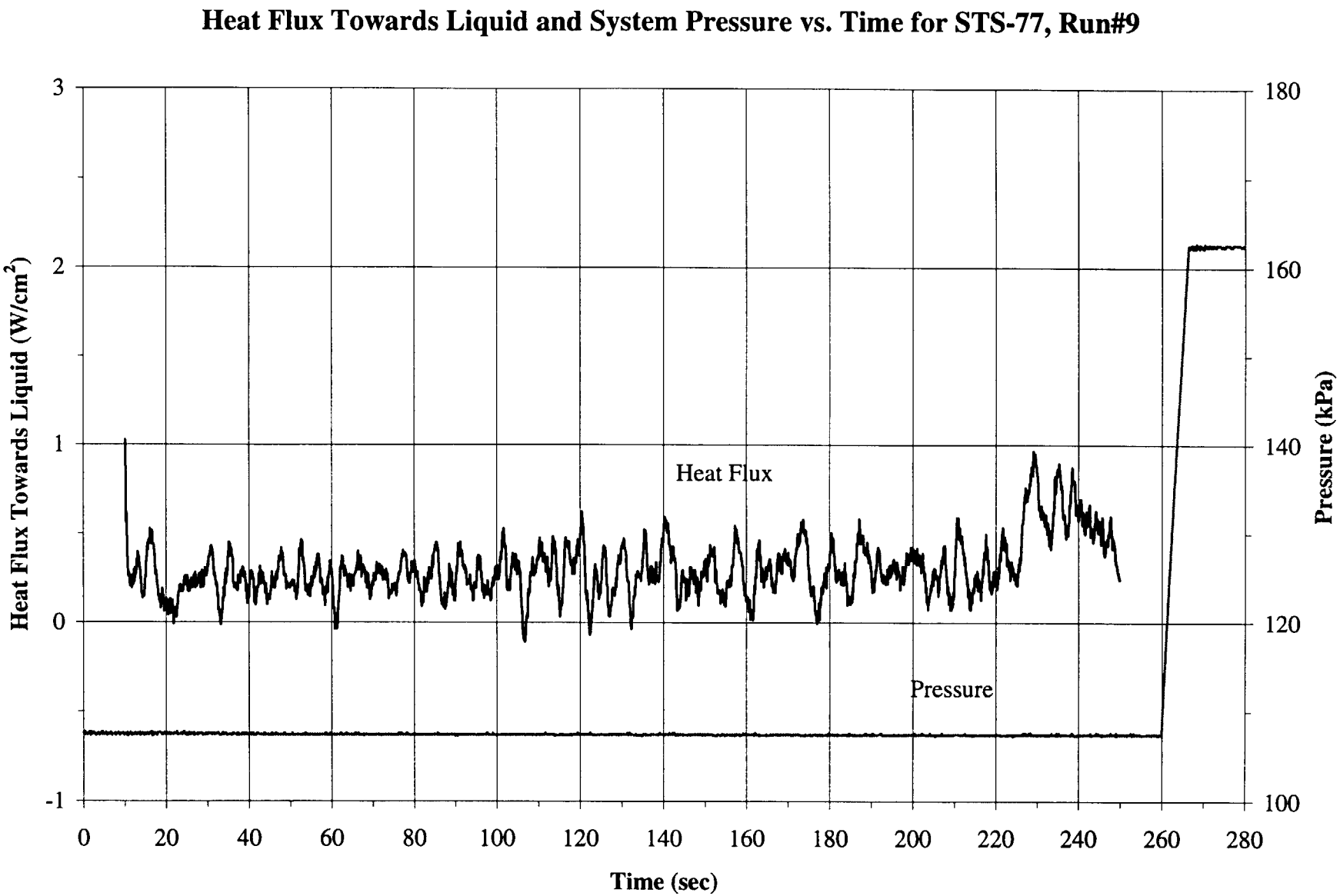

Figure B-3i. System pressure and fluid side mean heat flux. PBE-IIA (STS-77). Run No. 9.

A. Mean Heater Surface Temperature

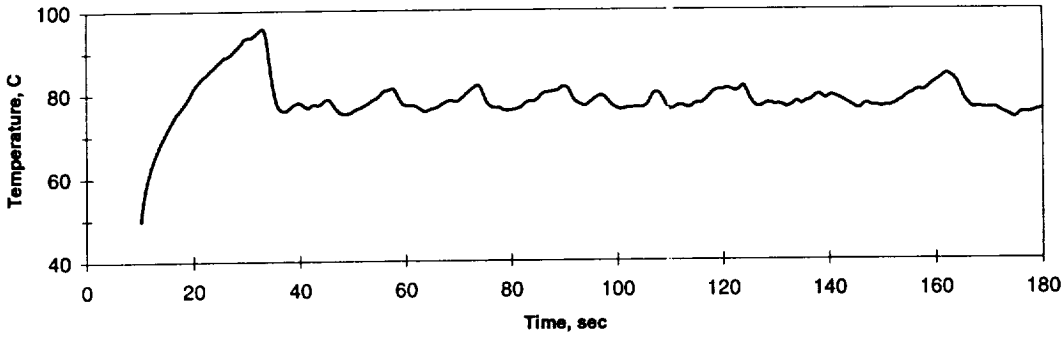

B. Local Fluid Temperatures

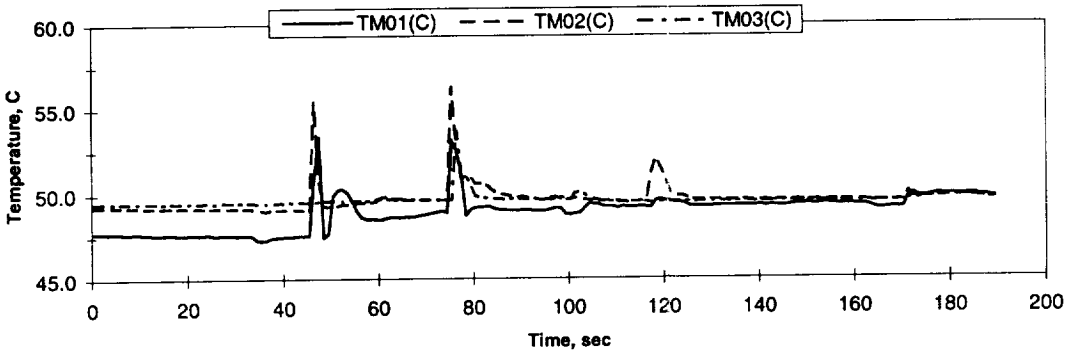

C. Far Field Temperatures

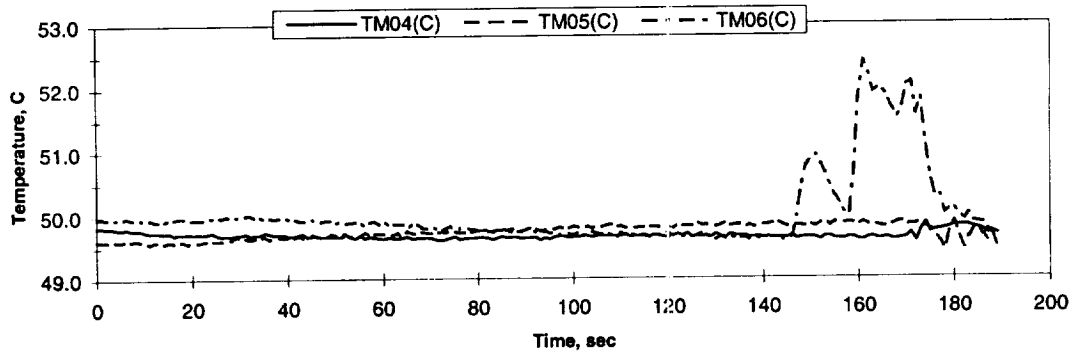

FIGURE: Measured Fluid Temperatures **STS-77 Run #1**

Heat Flux	Subcooling (F)	Heater Power On/Off	10 FPS On/Off	Stirrer Start	Repress Start	Total Time
2	20	10-180 sec.	25-190 sec.	170 sec.	----------	190 sec

Figure B-4a. Measured fluid temperatures near primary heater and far field bulk liquid. PBE-IIA (STS-77). Run No. 1.

A. Mean Heater Surface Temperature

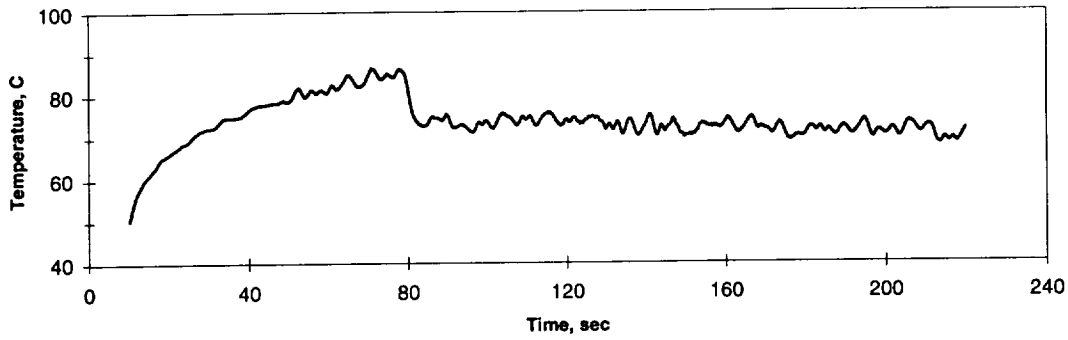

B. Local Fluid Temperatures

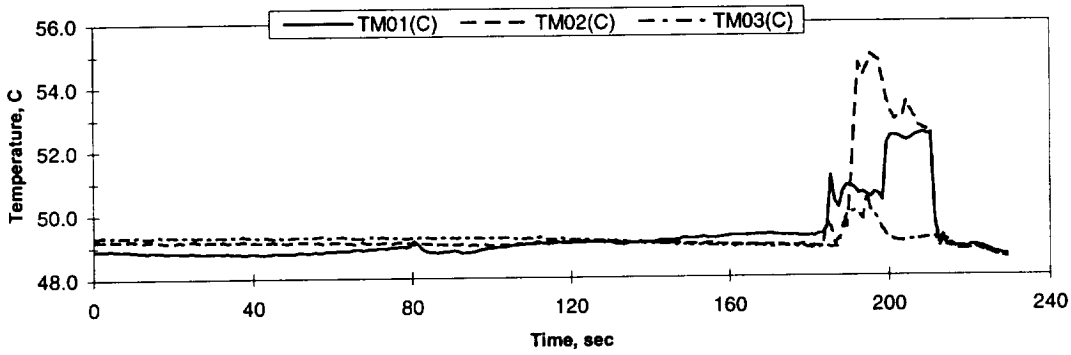

C. Far Field Temperatures

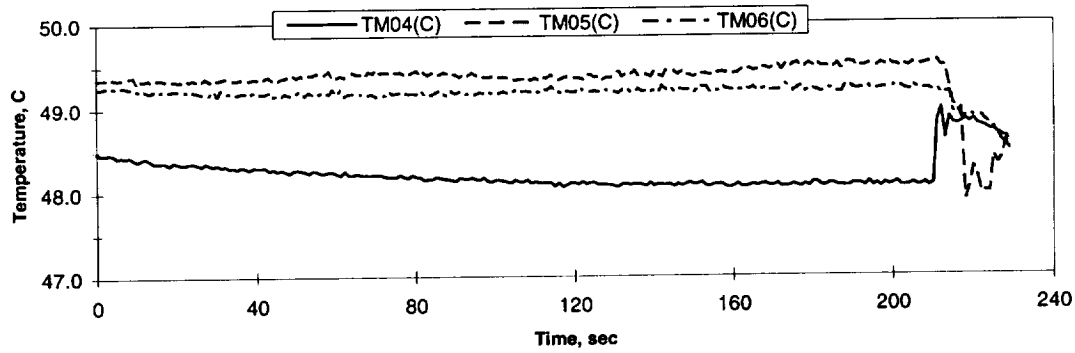

FIGURE: Measured Fluid Temperatures **STS-77 Run #2**

Heat Flux	Subcooling (F)	Heater Power On/Off	10 FPS On/Off	Stirrer Start	Repress Start	Total Time
1	20	10-220 sec.	50-230 sec.	210 sec.	--------	230 sec.

Figure B-4b. Measured fluid temperatures near primary heater and far field bulk liquid. PBE-IIA (STS-77). Run No. 2.

A. Mean Heater Surface Temperature

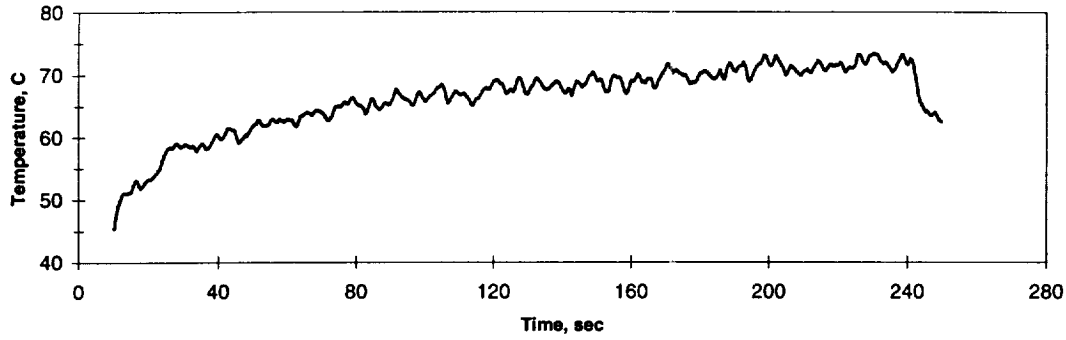

B. Local Fluid Temperatures

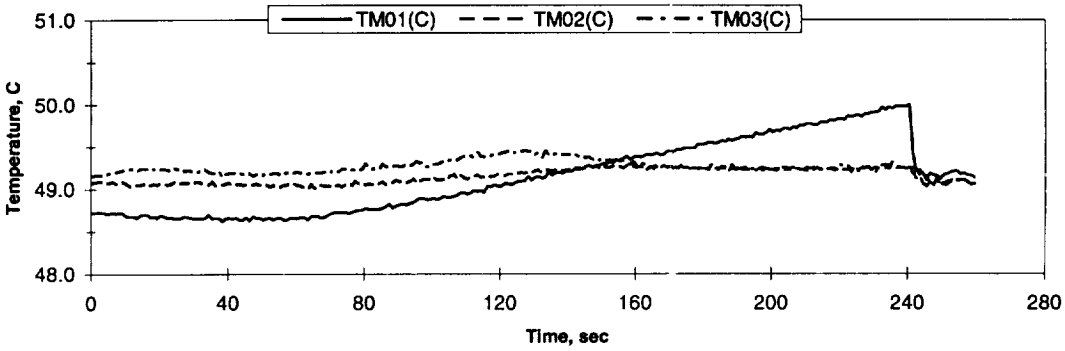

C. Far Field Temperatures

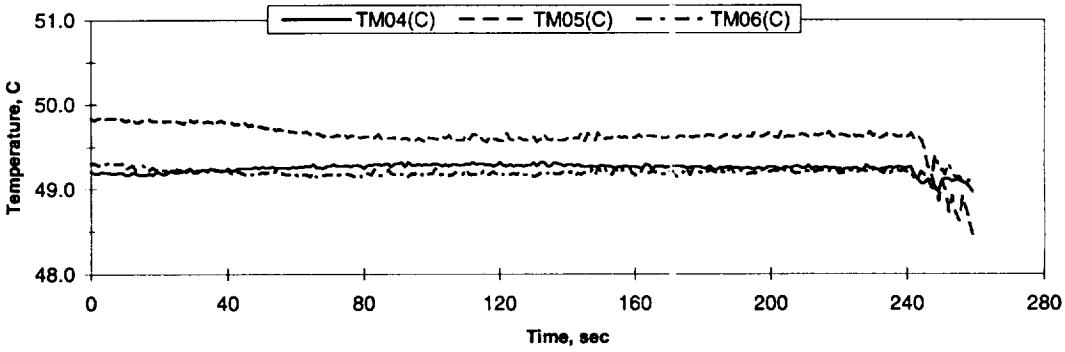

FIGURE: Measured Fluid Temperatures **STS-77 Run #3**

Heat Flux	Subcooling (F)	Heater Power On/Off	10 FPS On/Off	Stirrer Start	Repress Start	Total Time
0.5	20	10-250 sec.	70-260 sec.	240 sec.	--------	260 sec.

Figure B-4c. Measured fluid temperatures near primary heater and far field bulk liquid. PBE-IIA (STS-77). Run No. 3.

A. Mean Heater Surface Temperature

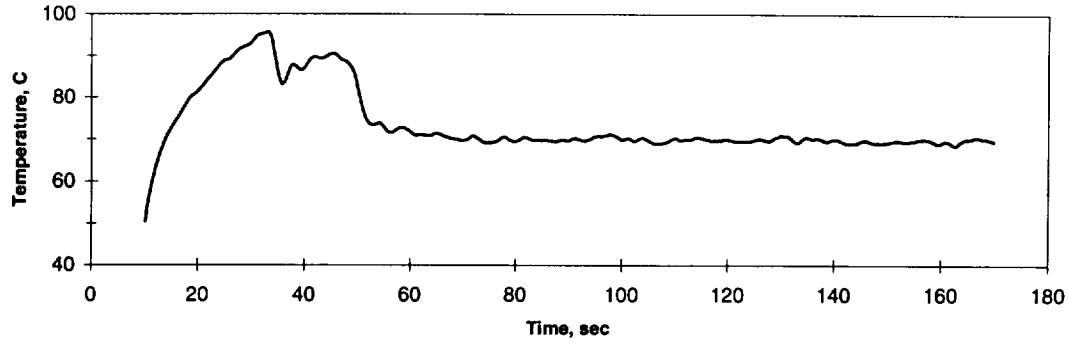

B. Local Fluid Temperatures

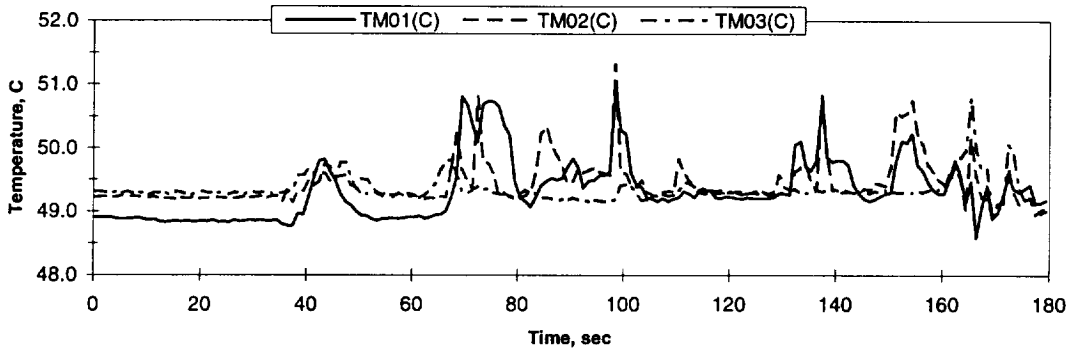

C. Far Field Temperatures

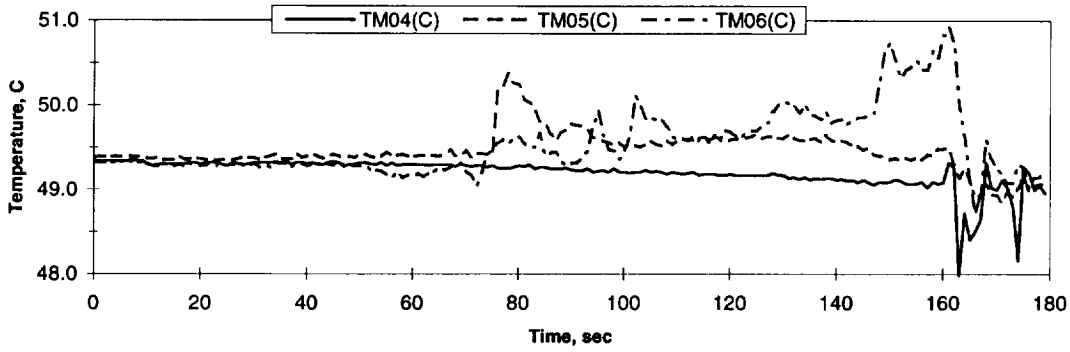

FIGURE: Measured Fluid Temperatures **STS-77 Run #4**

Heat Flux	Subcooling (F)	Heater Power On/Off	10 FPS On/Off	Stirrer Start	Repress Start	Total Time
2	5	10-170 sec.	30-180 sec.	160 sec.	--------	180 sec

Figure B-4d. Measured fluid temperatures near primary heater and far field bulk liquid. PBE-IIA (STS-77). Run No. 4.

A. Mean Heater Surface Temperature

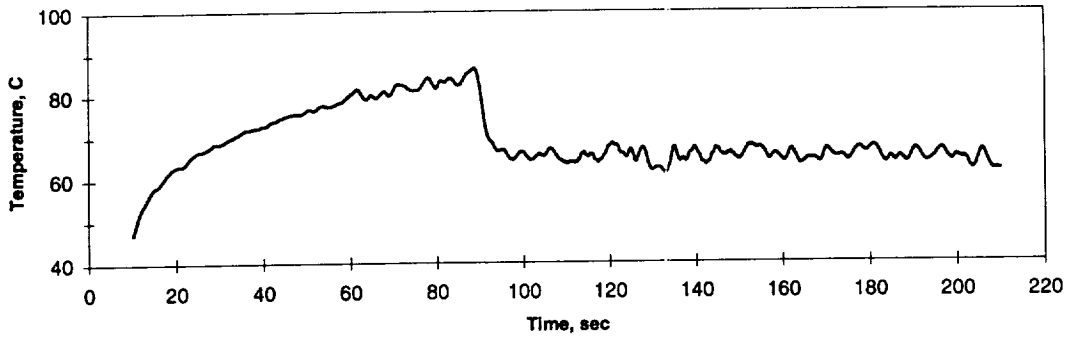

B. Local Fluid Temperatures

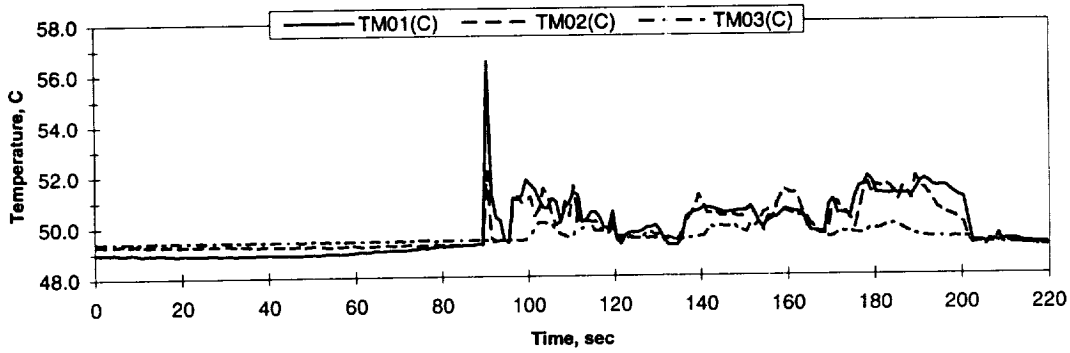

C. Far Field Temperatures

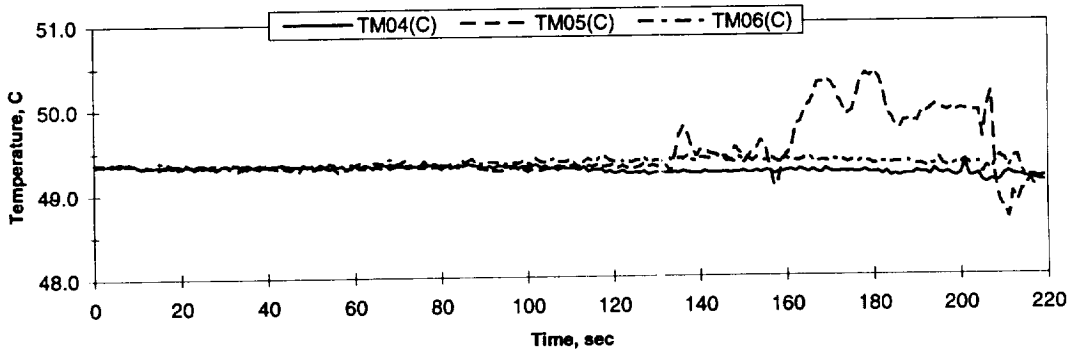

FIGURE: Measured Fluid Temperatures **STS-77 Run #5**

Heat Flux	Subcooling (F)	Heater Power On/Off	10 FPS On/Off	Stirrer Start	Repress Start	Total Time
1	5	10-210 sec.	60-220 sec.	200 sec.	--------	220 sec.

Figure B-4e. Measured fluid temperatures near primary heater and far field bulk liquid. PBE-IIA (STS-77). Run No. 5.

A. Mean Heater Surface Temperature

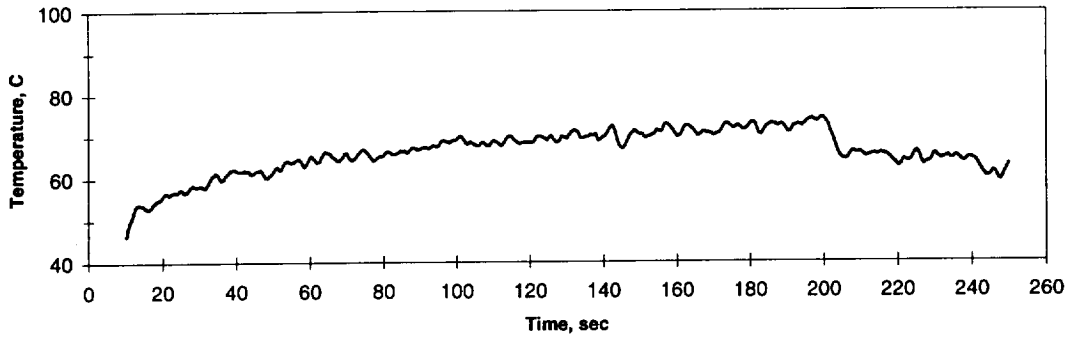

B. Local Fluid Temperatures

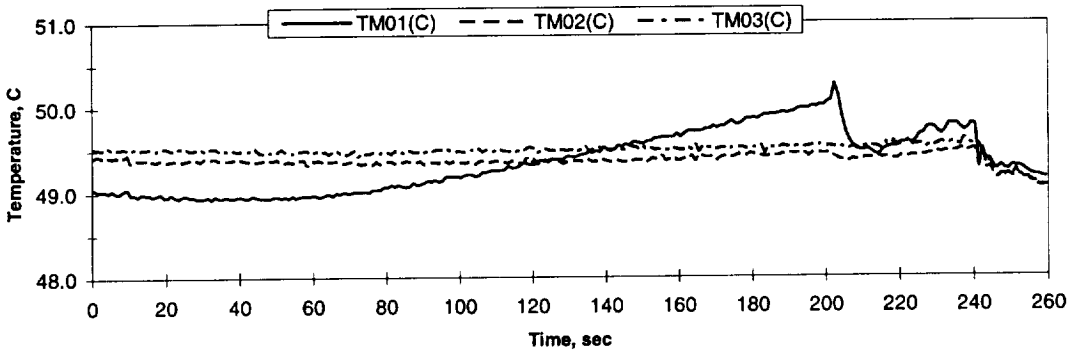

C. Far Field Temperatures

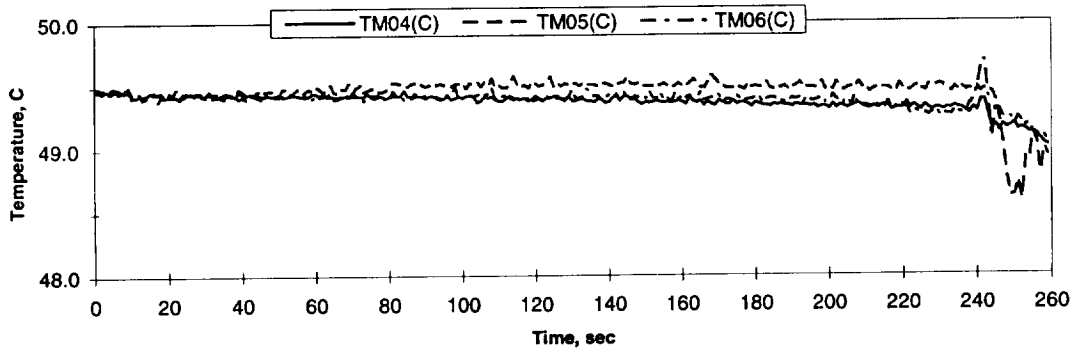

FIGURE: Measured Fluid Temperatures **STS-77 Run #6**

Heat Flux	Subcooling (F)	Heater Power On/Off	10 FPS On/Off	Stirrer Start	Repress Start	Total Time
0.5	5	10-250 sec.	80-260 sec.	240 sec.	--------	260 sec.

Figure B-4f. Measured fluid temperatures near primary heater and far field bulk liquid. PBE-IIA (STS-77). Run No. 6.

A. Mean Heater Surface Temperature

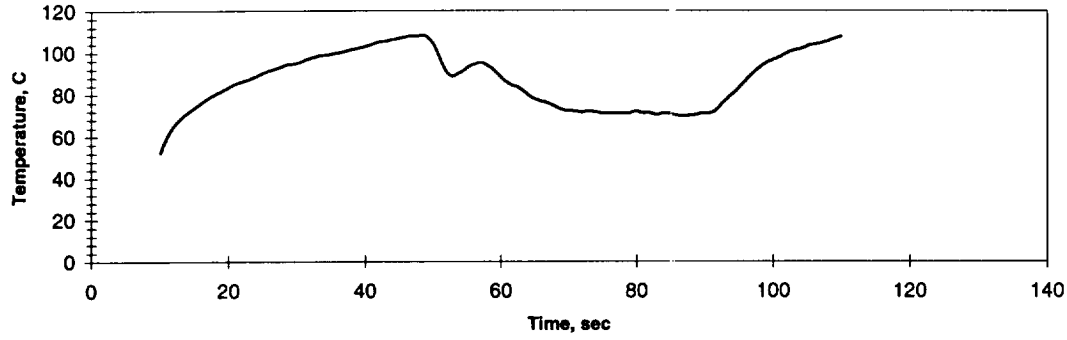

B. Local Fluid Temperatures

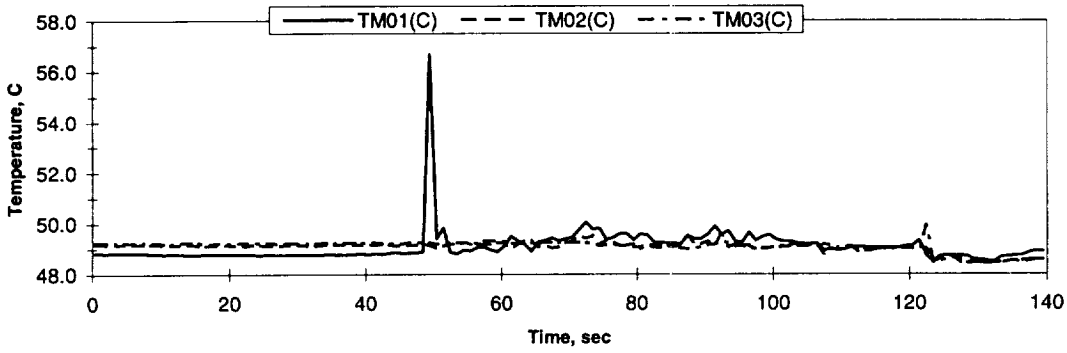

C. Far Field Temperatures

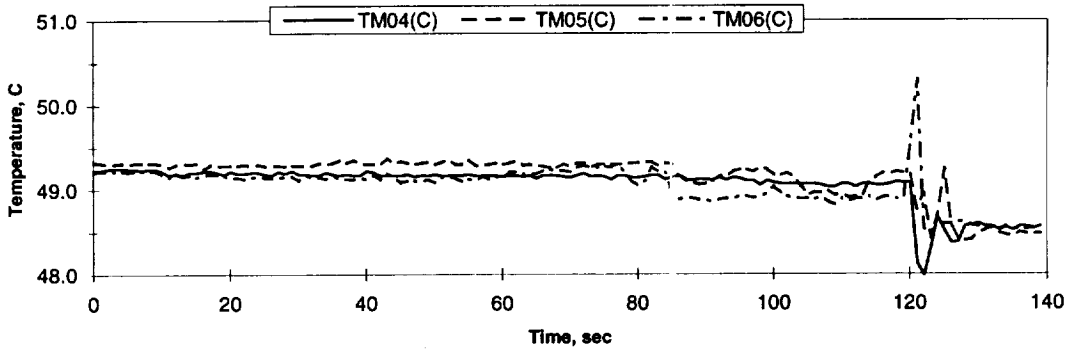

FIGURE: Measured Fluid Temperatures **STS-77 Run #7**

Heat Flux	Subcooling (F)	Heater Power On/Off	10 FPS On/Off	Stirrer Start	Repress Start	Total Time
2	0.5	10-110 sec.	30-140 sec.	---------	120 sec.	140 sec.

Figure B-4g. Measured fluid temperatures near primary heater and far field bulk liquid. PBE-IIA (STS-77). Run No. 7.

A. Mean Heater Surface Temperature

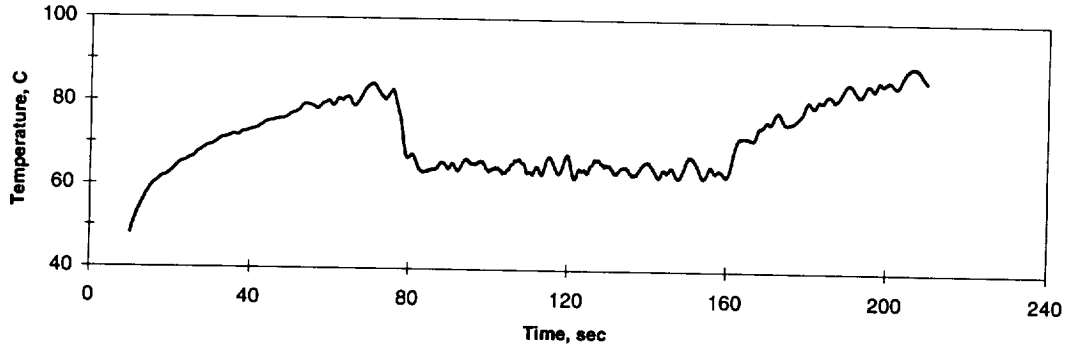

B. Local Fluid Temperatures

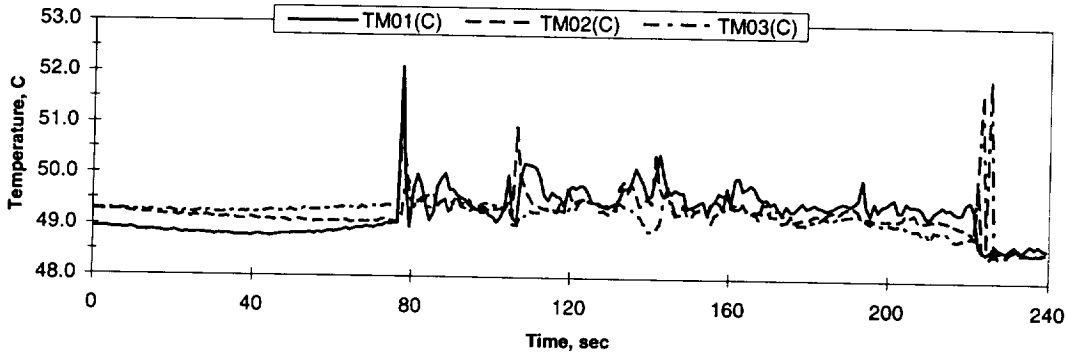

C. Far Field Temperatures

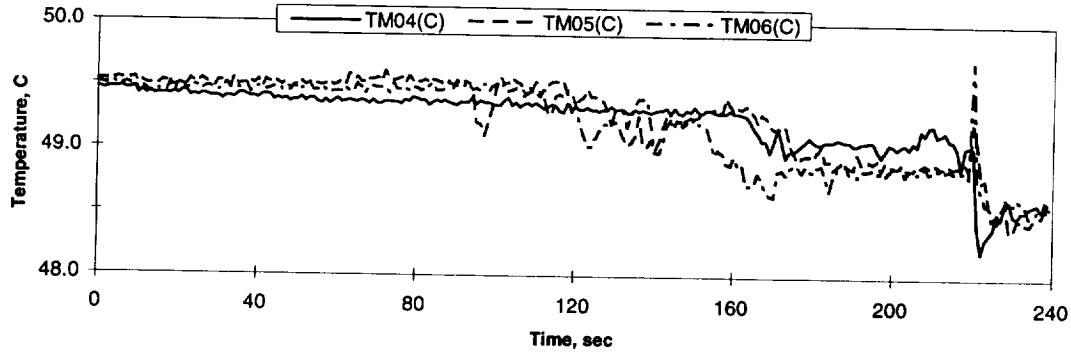

FIGURE: Measured Fluid Temperatures **STS-77 Run #8**

Heat Flux	Subcooling (F)	Heater Power On/Off	10 FPS On/Off	Stirrer Start	Repress Start	Total Time
1	0.5	10-210 sec.	60-240 sec.	----------	220 sec.	240 sec.

Figure B-4h. Measured fluid temperatures near primary heater and far field bulk liquid. PBE-IIA (STS-77). Run No. 8.

A. Mean Heater Surface Temperature

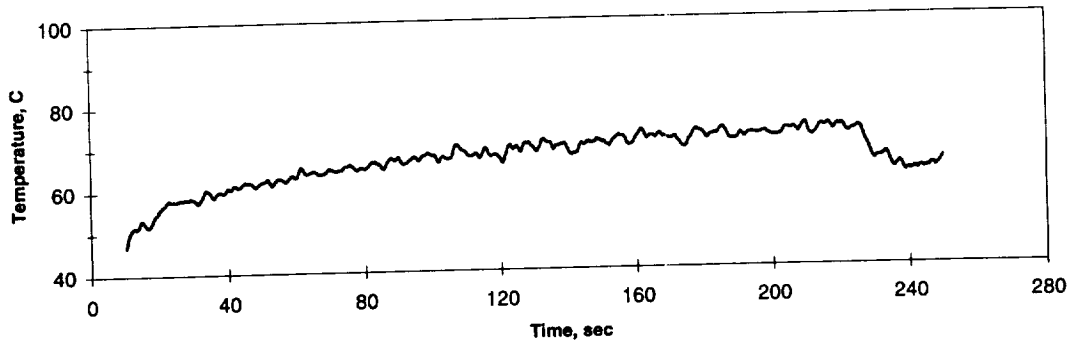

B. Local Fluid Temperatures

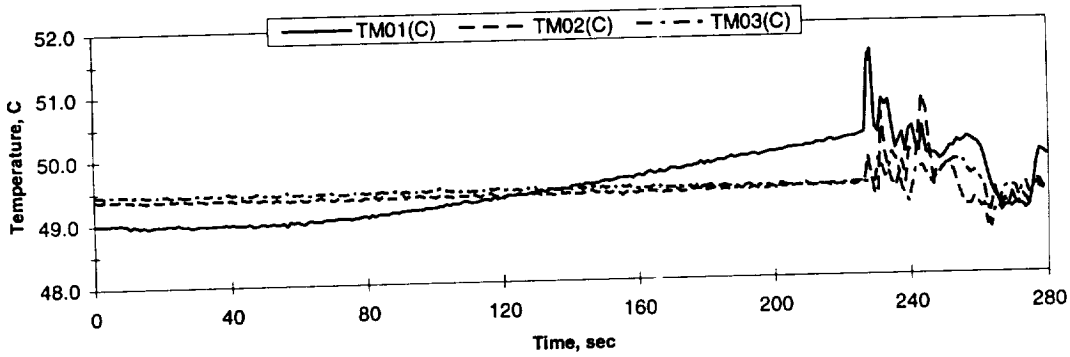

C. Far Field Temperatures

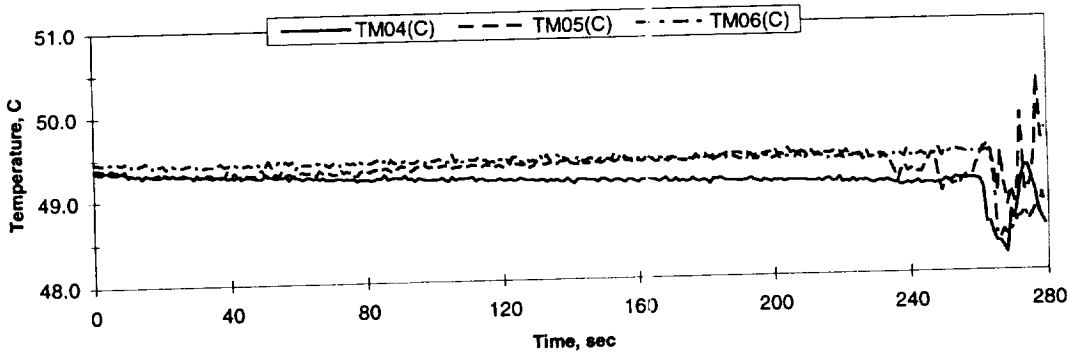

FIGURE: Measured Fluid Temperatures **STS-77 Run #9**

Heat Flux	Subcooling (F)	Heater Power On/Off	10 FPS On/Off	Stirrer Start	Repress Start	Total Time
0.5	0.5	10-250 sec.	80-280 sec.	----------	260 sec.	280 sec.

Figure B-4i. Measured fluid temperatures near primary heater and far field bulk liquid. PBE-IIA (STS-77). Run No. 9.

A. Mean Heater Surface Temperature

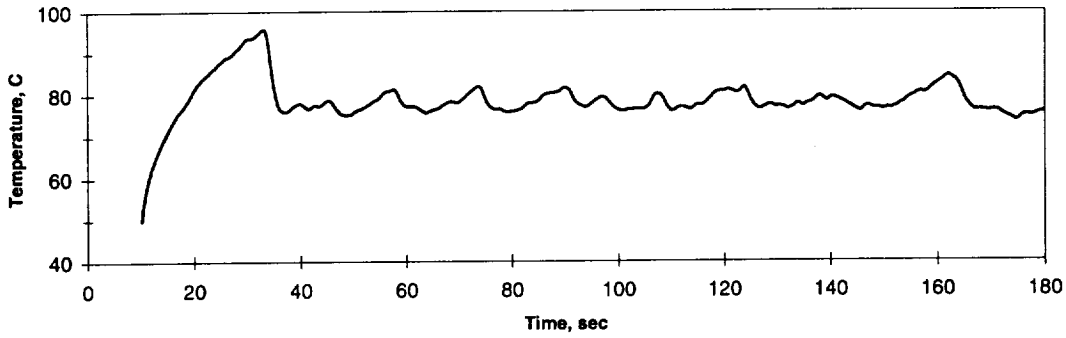

D.

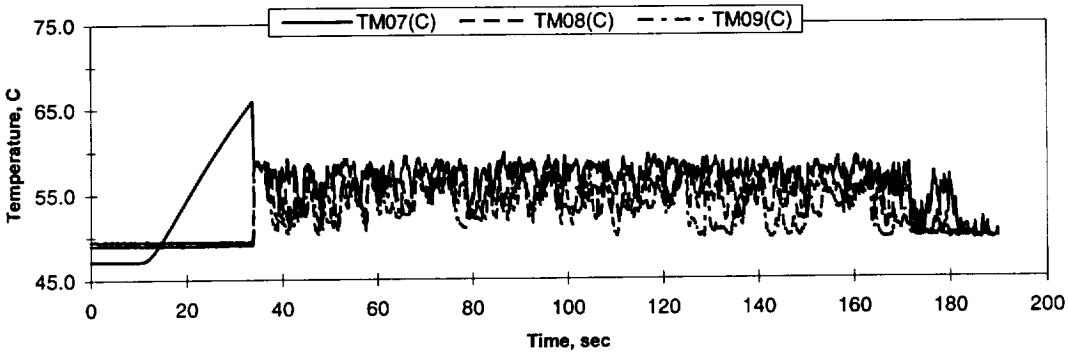

E.

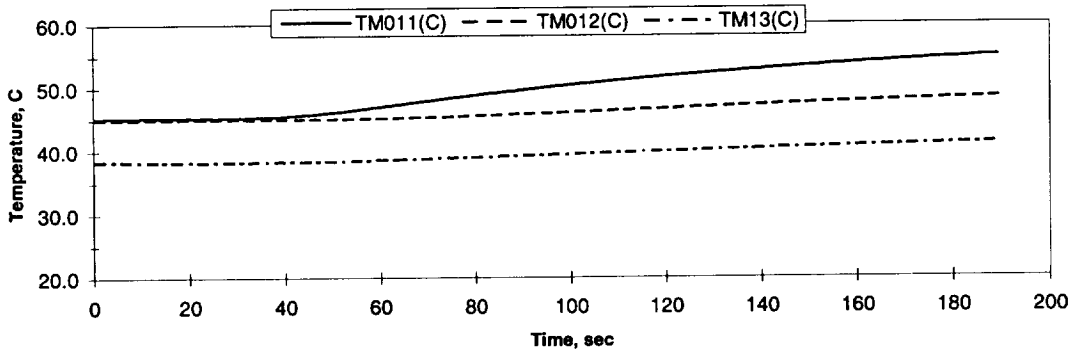

FIGURE: Measured Heater-Underside Temperatures **STS-77 Run #1**

Heat Flux	Subcooling (F)	Heater Power On/Off	10 FPS On/Off	Stirrer Start	Repress Start	Total Time
2	20	10-180 sec.	25-190 sec.	170 sec.	--------	190 sec.

Figure B-5a. Measured fluid temperatures near secondary heater and heater underside. PBE-IIA (STS-77). Run No. 1.

A. Mean Heater Surface Temperature

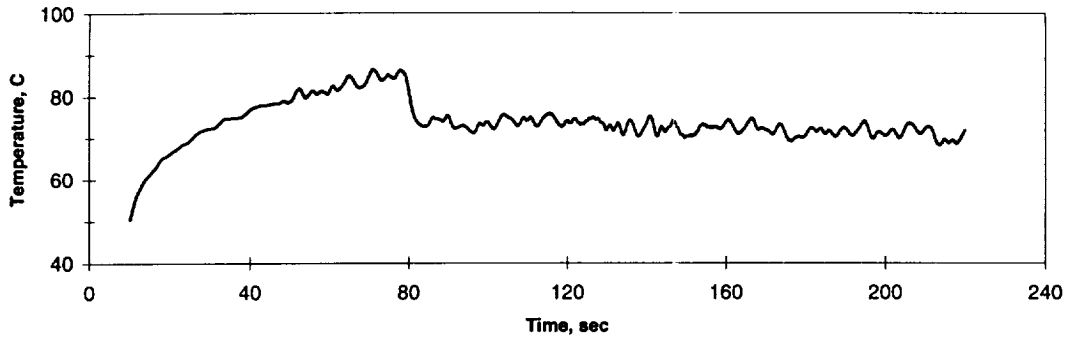

D.

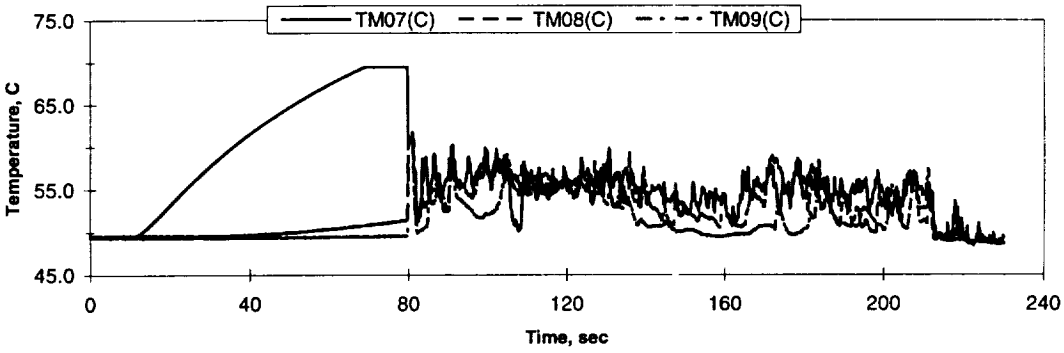

E.

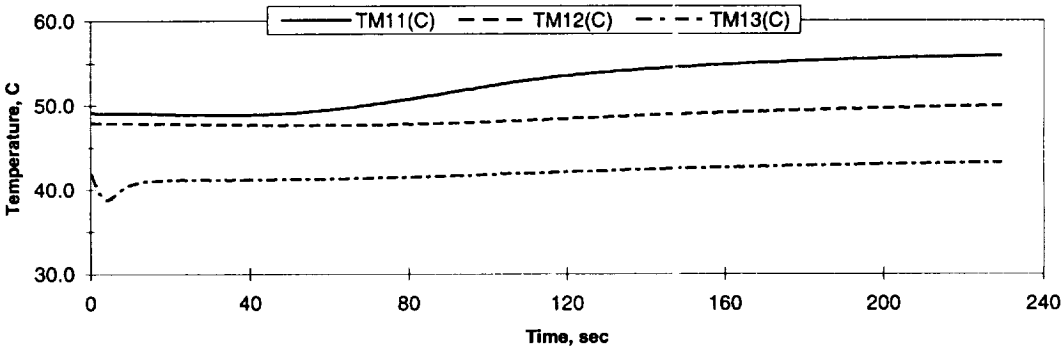

FIGURE: Measured Heater-Underside Temperatures **STS-77 Run #2**

Heat Flux	Subcooling (F)	Heater Power On/Off	10 FPS On/Off	Stirrer Start	Repress Start	Total Time
1	20	10-220 sec.	50-230 sec.	210 sec.	--------	230 sec

Figure B-5b. Measured fluid temperatures near secondary heater and heater underside. PBE-IIA (STS-77). Run No. 2.

A. Mean Heater Surface Temperature

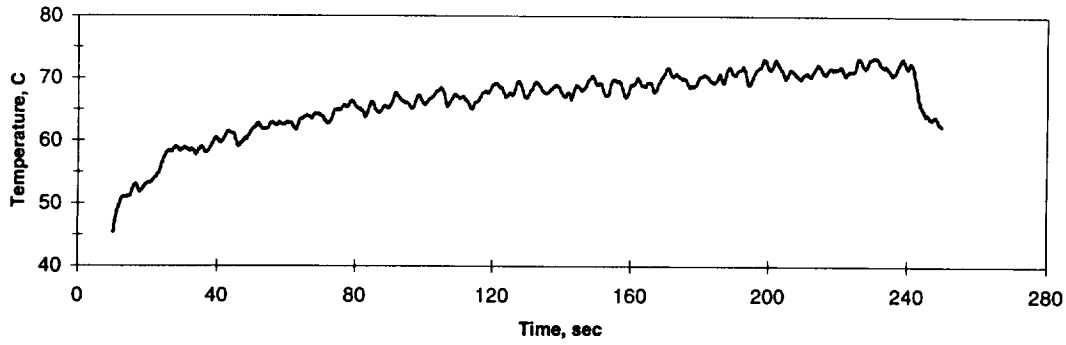

D.

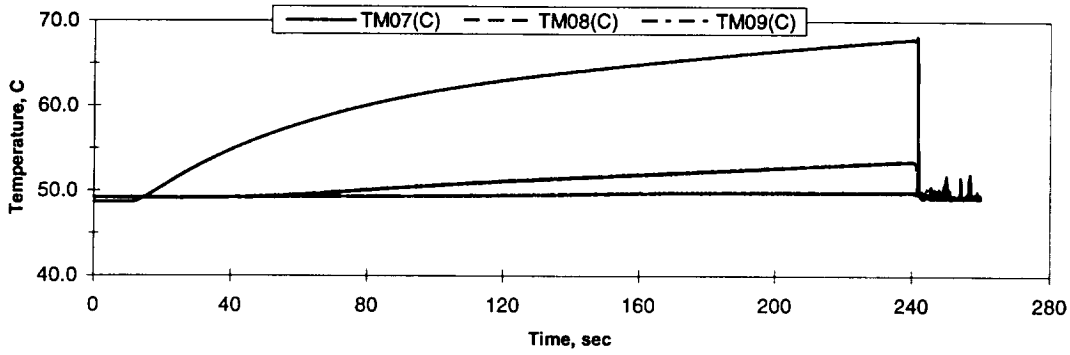

E.

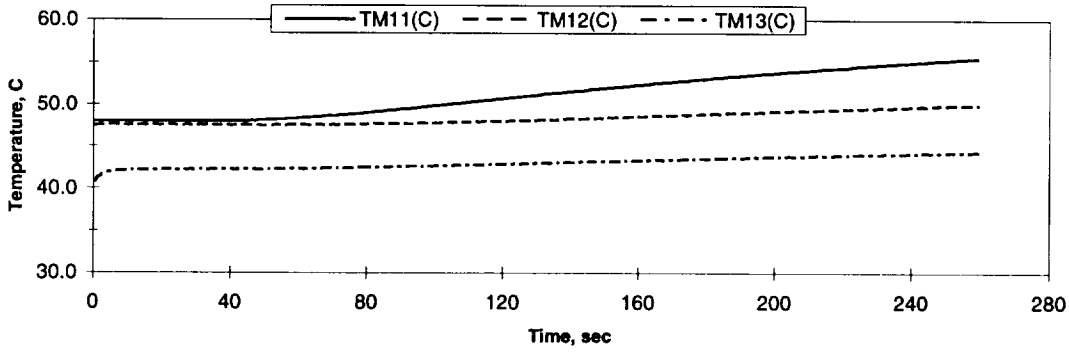

FIGURE: Measured Heater-Underside Temperatures **STS-77 Run #3**

Heat Flux	Subcooling (F)	Heater Power On/Off	10 FPS On/Off	Stirrer Start	Repress Start	Total Time
0.5	20	10-250 sec.	70-260 sec.	240 sec.	--------	260 sec.

Figure B-5c. Measured fluid temperatures near secondary heater and heater underside. PBE-IIA (STS-77). Run No. 3.

A. Mean Heater Surface Temperature

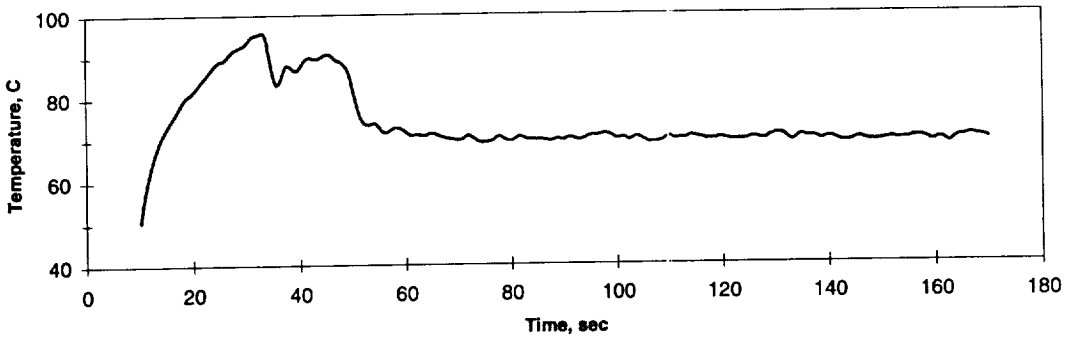

D.

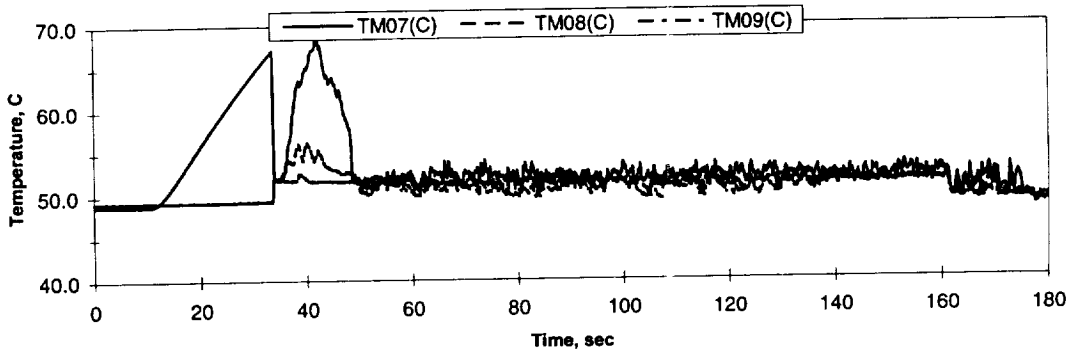

E.

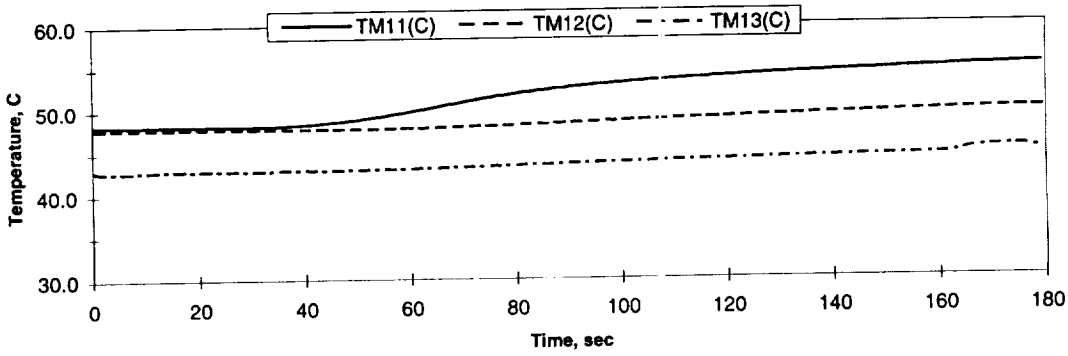

FIGURE: Measured Heater-Underside Temperatures **STS-77 Run #4**

Heat Flux	Subcooling (F)	Heater Power On/Off	10 FPS On/Off	Stirrer Start	Repress Start	Total Time
2	5	10-170 sec.	30-180 sec.	160 sec.	--------	180 sec.

Figure B-5d. Measured fluid temperatures near secondary heater and heater underside. PBE-IIA (STS-77). Run No. 4.

A. Mean Heater Surface Temperature

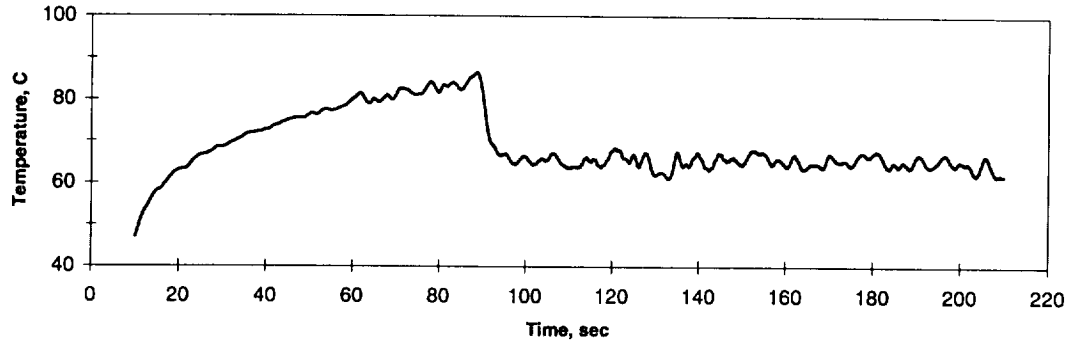

D.

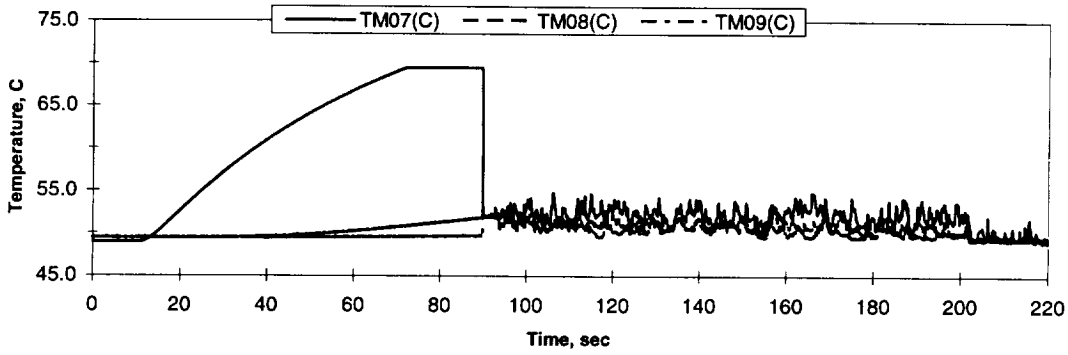

E.

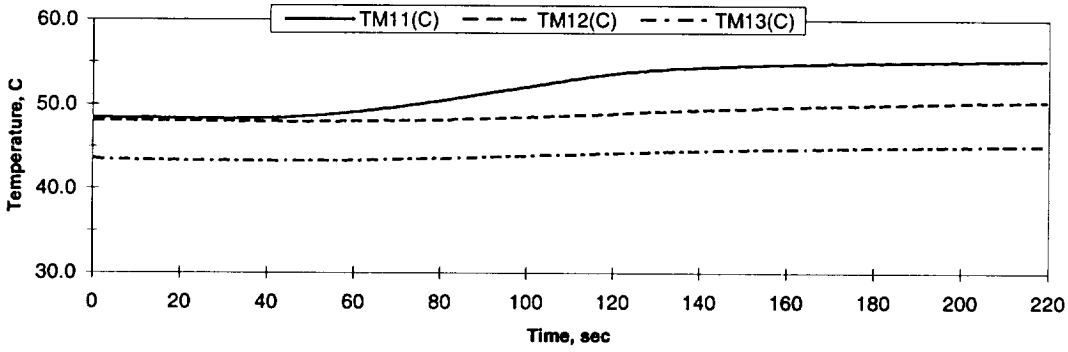

FIGURE: Measured Heater-Underside Temperatures **STS-77 Run #5**

Heat Flux	Subcooling (F)	Heater Power On/Off	10 FPS On/Off	Stirrer Start	Repress Start	Total Time
1	5	10-210 sec.	60-220 sec.	200 sec.	--------	220 sec.

Figure B-5e. Measured fluid temperatures near secondary heater and heater underside. PBE-IIA (STS-77). Run No. 5.

A. Mean Heater Surface Temperature

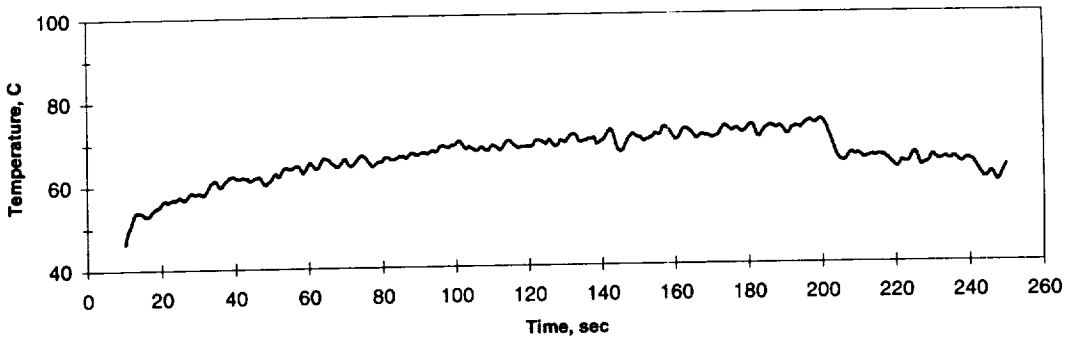

D.

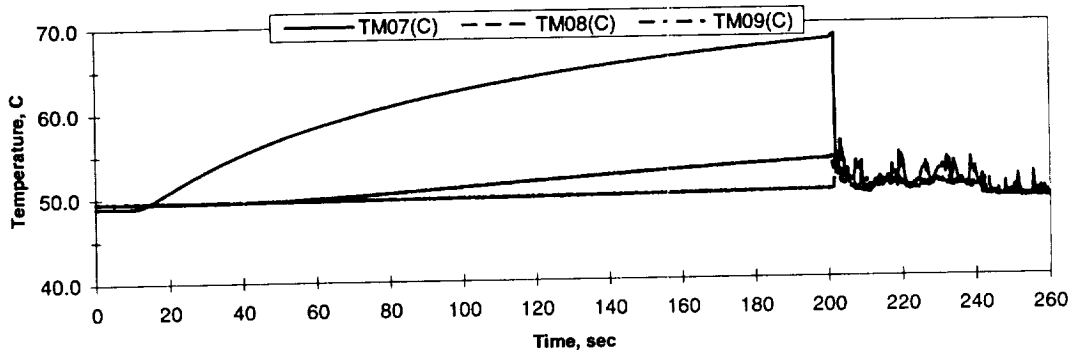

E.

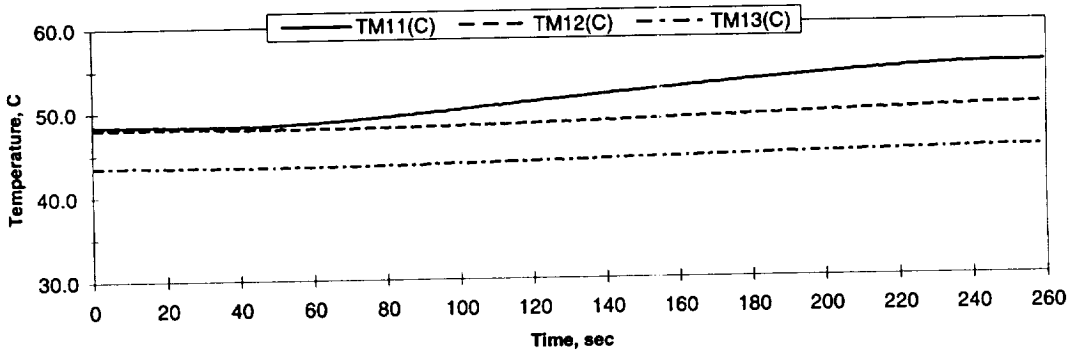

FIGURE: Measured Heater-Underside Temperatures **STS-77 Run #6**

Heat Flux	Subcooling (F)	Heater Power On/Off	10 FPS On/Off	Stirrer Start	Repress Start	Total Time
0.5	5	10-250 sec.	80-260 sec.	240 sec.	--------	260 sec.

Figure B-5f. Measured fluid temperatures near secondary heater and heater underside. PBE-IIA (STS-77). Run No. 6.

A. Mean Heater Surface Temperature

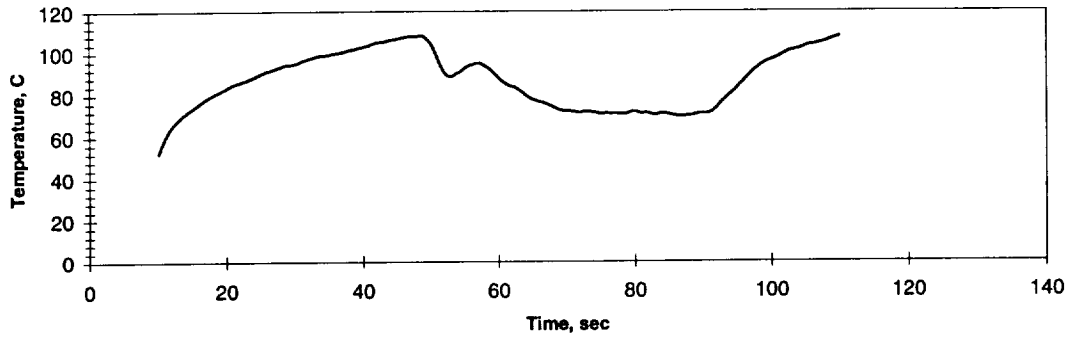

D.

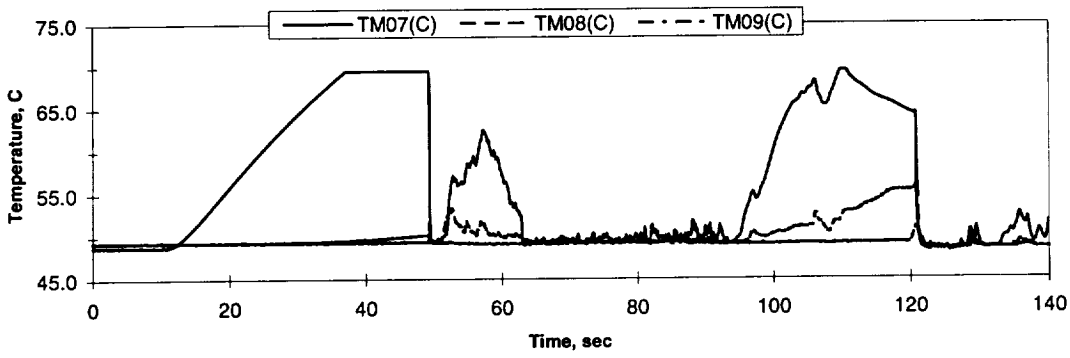

E.

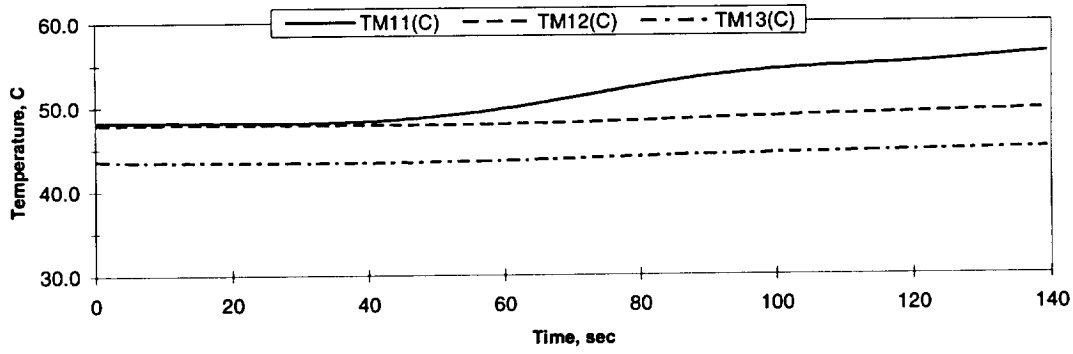

FIGURE: Measured Heater-Underside Temperatures **STS-77 Run #7**

Heat Flux	Subcooling (F)	Heater Power On/Off	10 FPS On/Off	Stirrer Start	Repress Start	Total Time
2	0.5	10-110 sec.	30-140 sec.	---------	120 sec.	140 sec.

Figure B-5g. Measured fluid temperatures near secondary heater and heater underside. PBE-IIA (STS-77). Run No. 7.

A. Mean Heater Surface Temperature

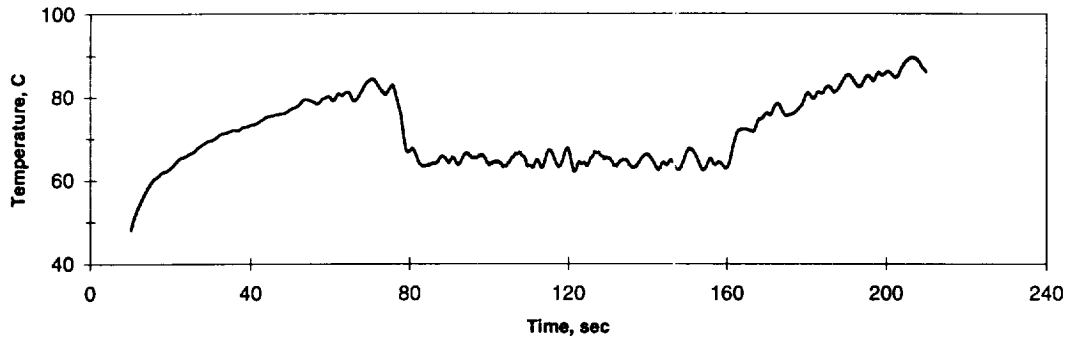

D.

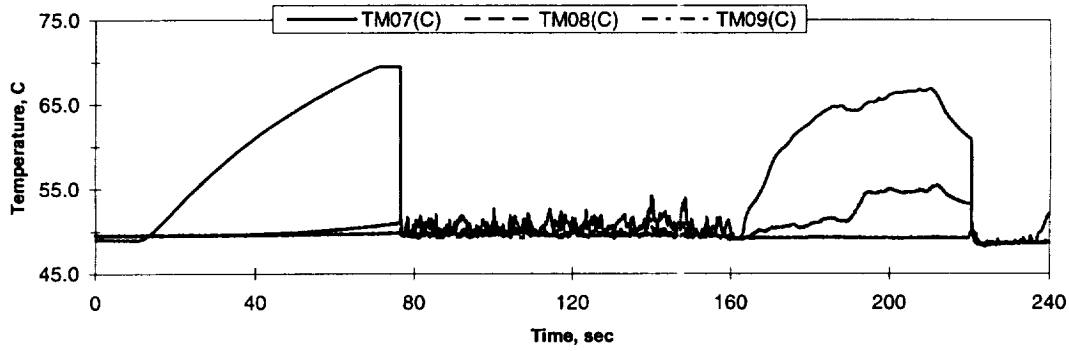

E.

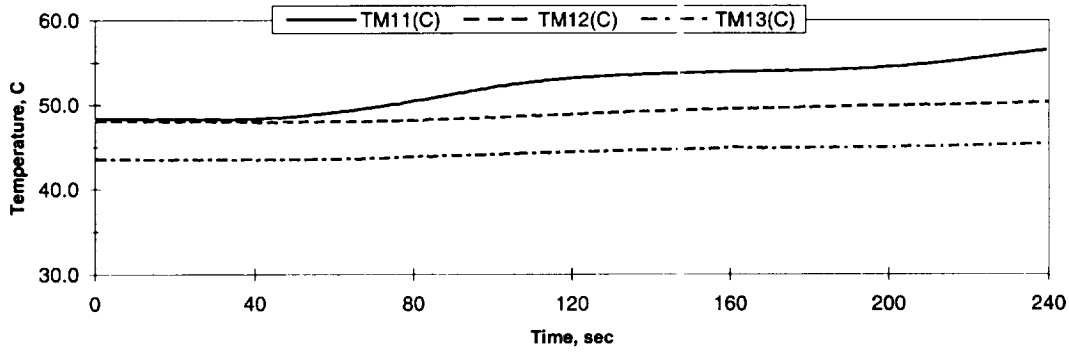

FIGURE: Measured Heater-Underside Temperatures **STS-77 Run #8**

Heat Flux	Subcooling (F)	Heater Power On/Off	10 FPS On/Off	Stirrer Start	Repress Start	Total Time
1	0.5	10-210 sec.	60-240 sec.	----------	220 sec.	240 sec.

Figure B-5h. Measured fluid temperatures near secondary heater and heater underside. PBE-IIA (STS-77). Run No. 8.

A. Mean Heater Surface Temperature

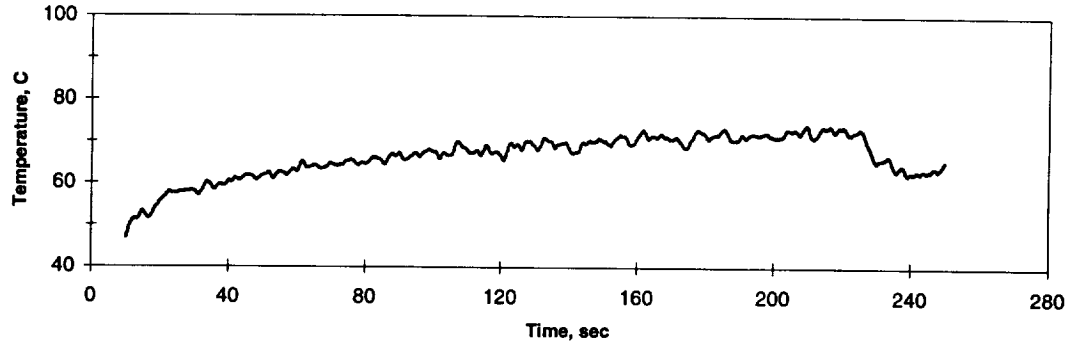

D.

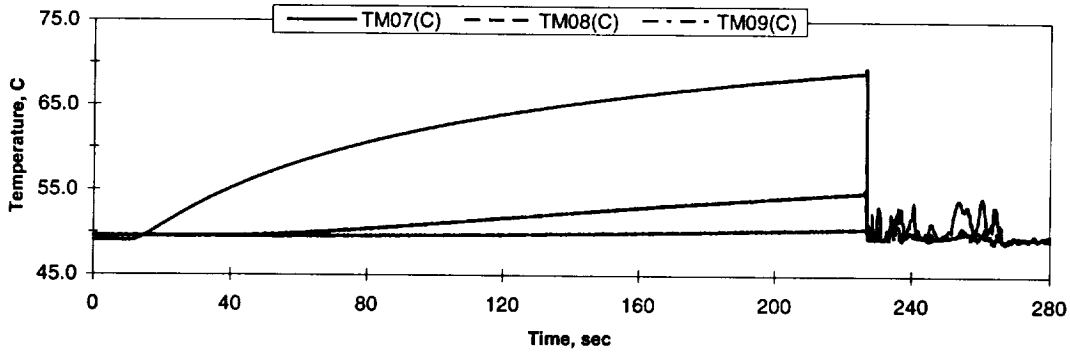

E.

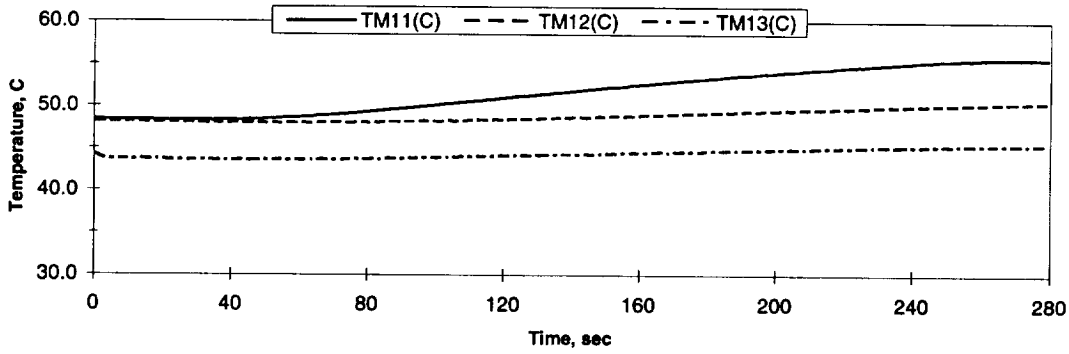

FIGURE: Measured Heater-Underside Temperatures **STS-77 Run #9**

Heat Flux	Subcooling (F)	Heater Power On/Off	10 FPS On/Off	Stirrer Start	Repress Start	Total Time
0.5	0.5	10-250 sec.	80-280 sec.	----------	260 sec.	280 sec.

Figure B-5i. Measured fluid temperatures near secondary heater and heater underside. PBE-IIA (STS-77). Run No. 9.

STS-77 Run #1

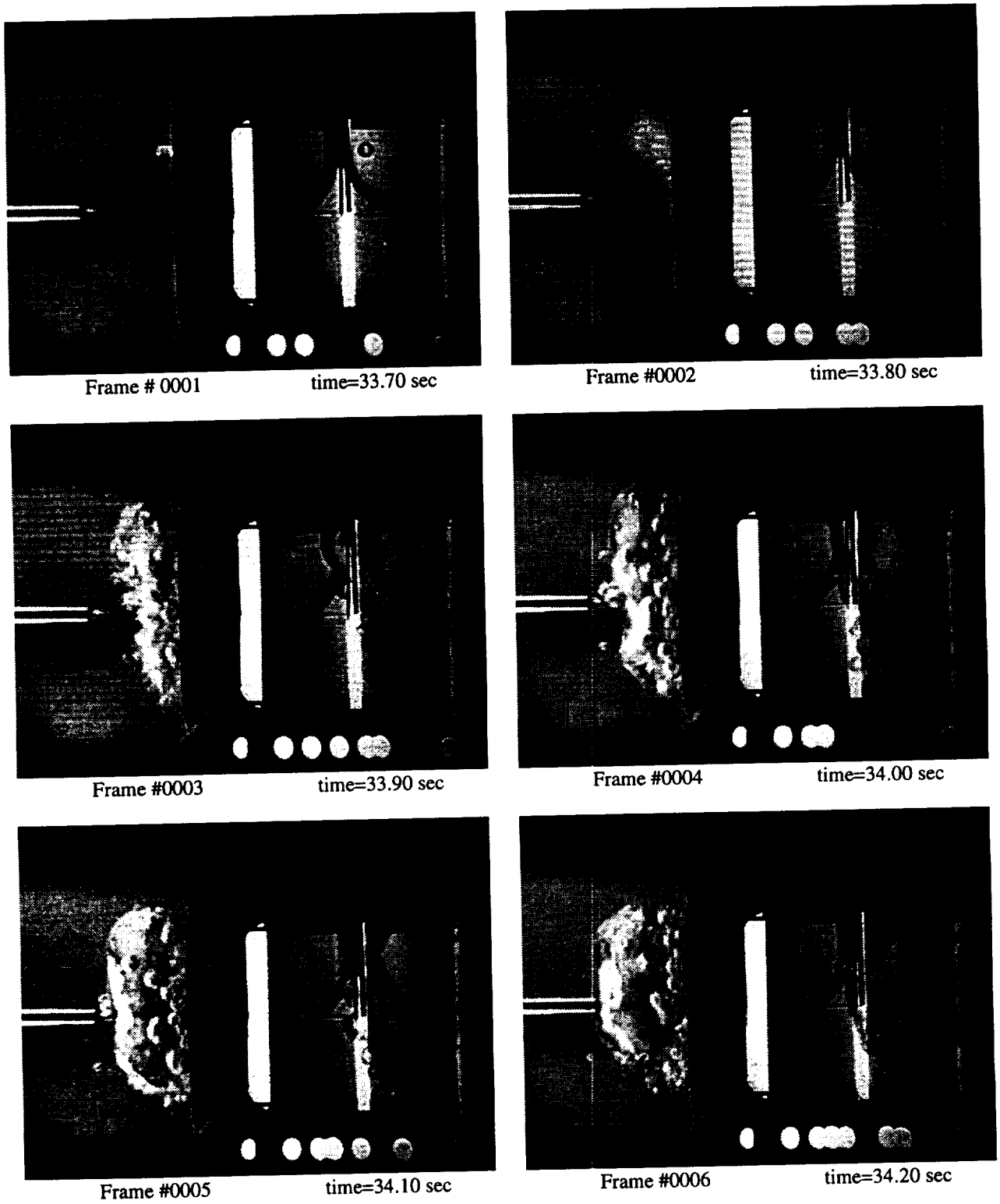

Figure B-6a. Selected Photographic Images. PBE-IIA (STS-77). Run No. 1.

STS-77 **Run #1**

Frame # 0013 time=35.10 sec

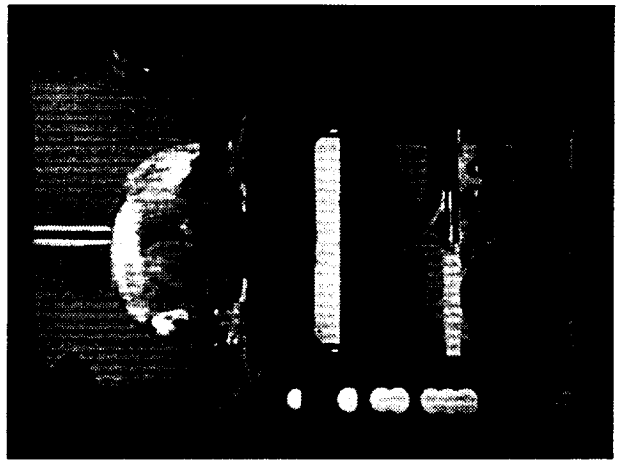

Frame #0253 time=59.10 sec

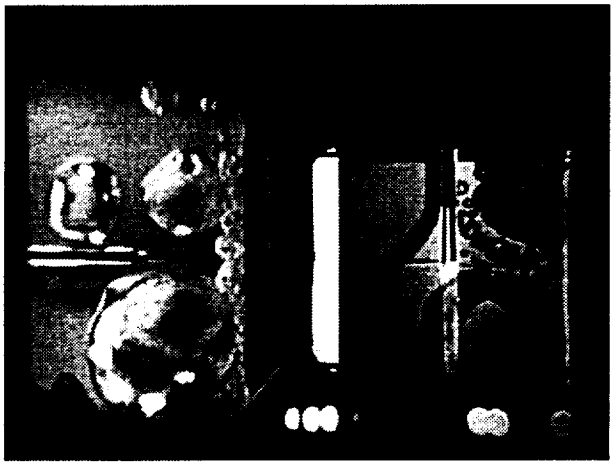

Frame #0493 time=83.10 sec

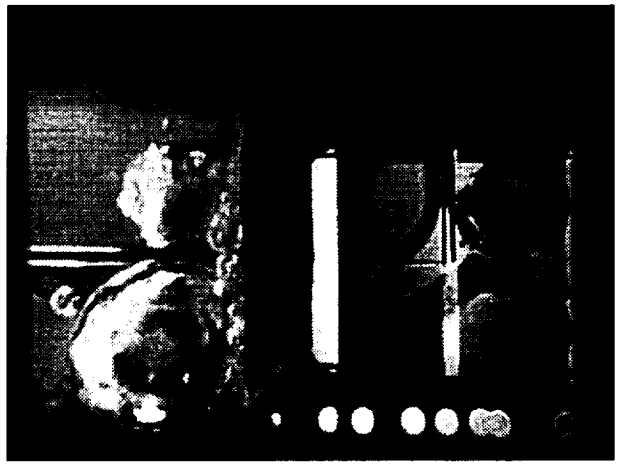

Frame #0733 time=107.1 sec

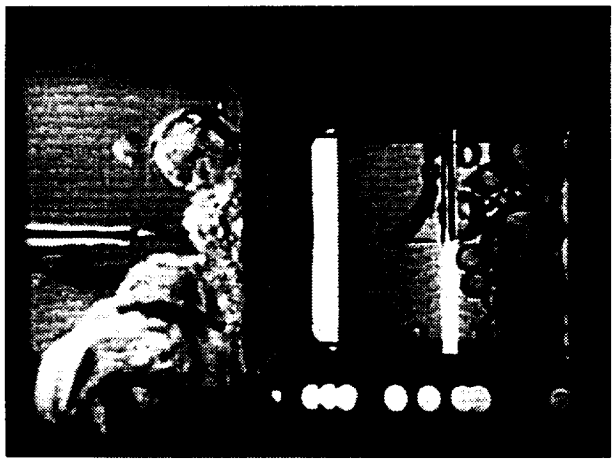

Frame #0973 time=131.10 sec

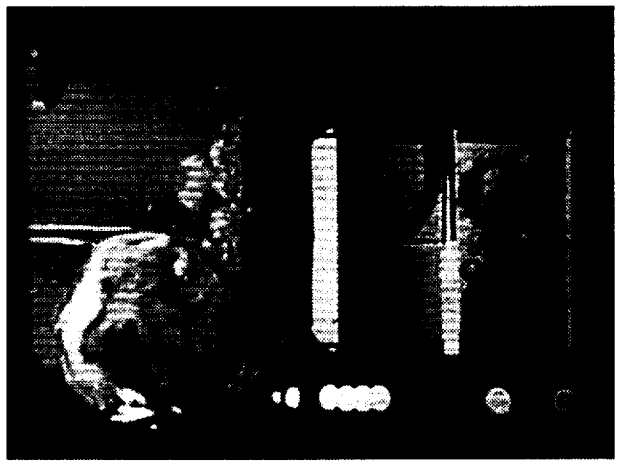

Frame #1213 time=155.10 sec

Figure B-6a. Continued.

STS-77 **Run #2**

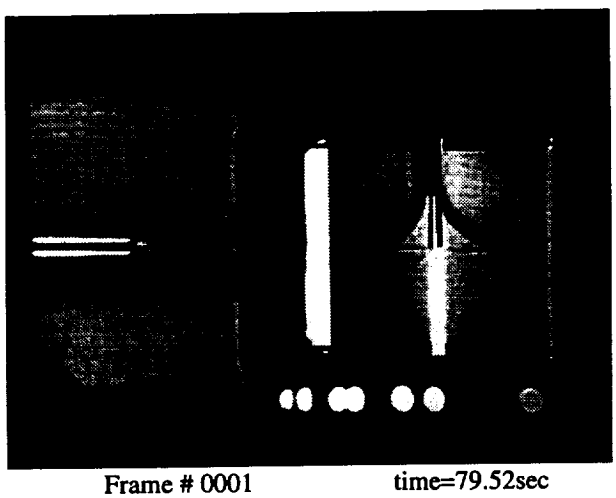

Frame # 0001 time=79.52sec

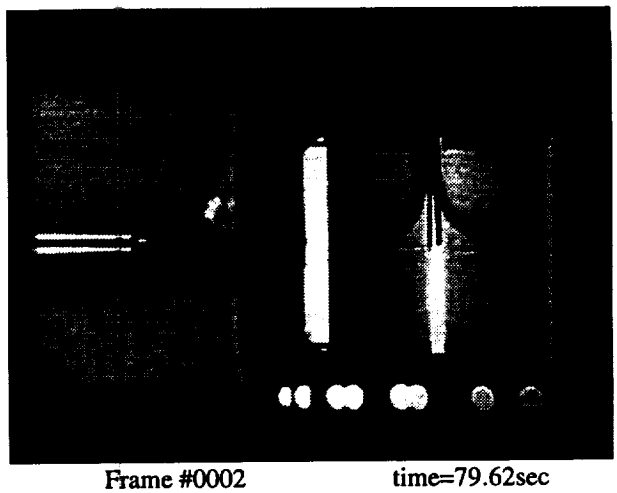

Frame #0002 time=79.62sec

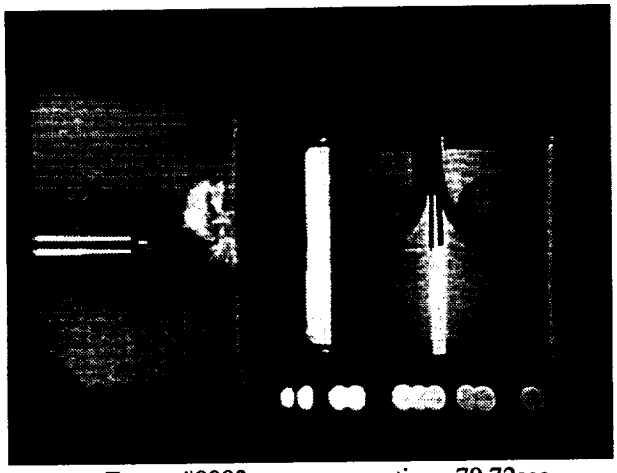

Frame #0003 time=79.72sec

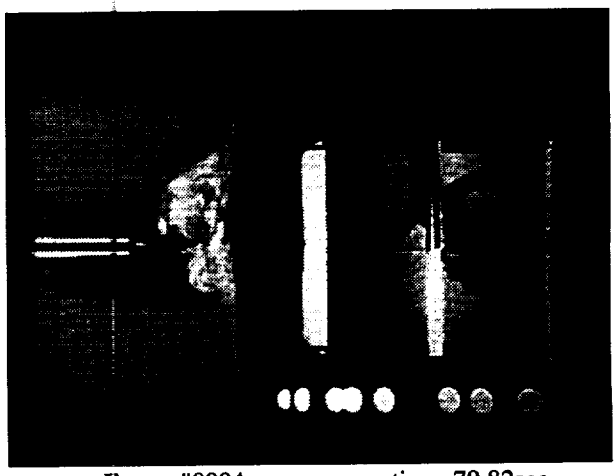

Frame #0004 time=79.82sec

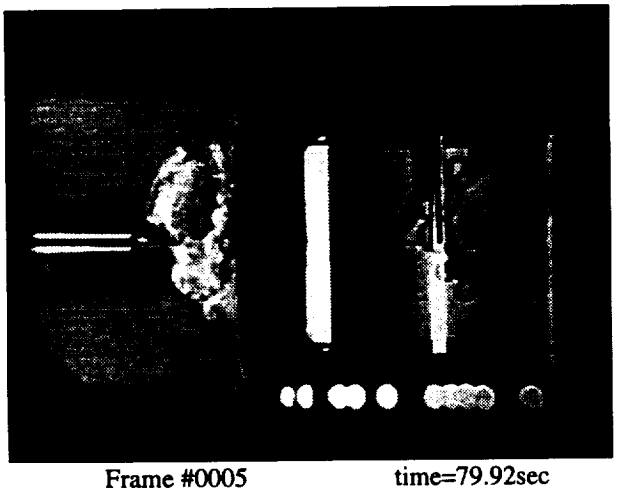

Frame #0005 time=79.92sec

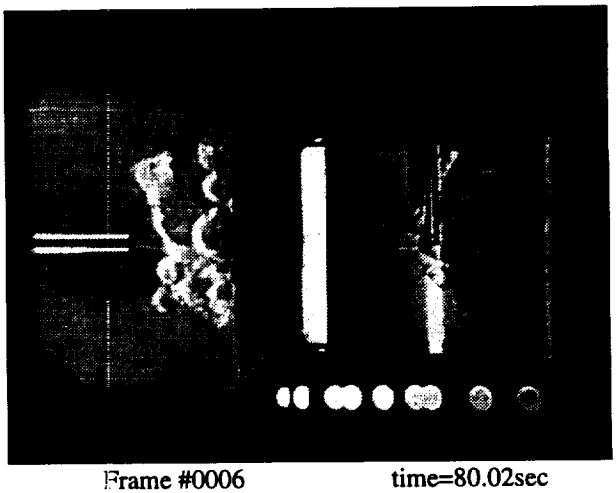

Frame #0006 time=80.02sec

Figure B-6b. Selected Photographic Images. PBE-IIA (STS-77). Run No. 2.

STS-77 **Run #2**

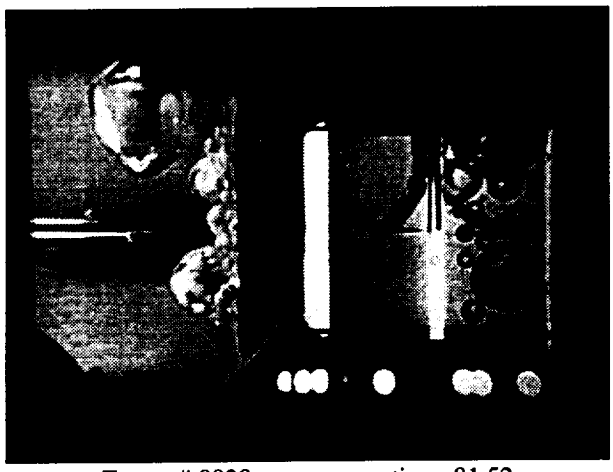

Frame # 0030 time=81.52sec

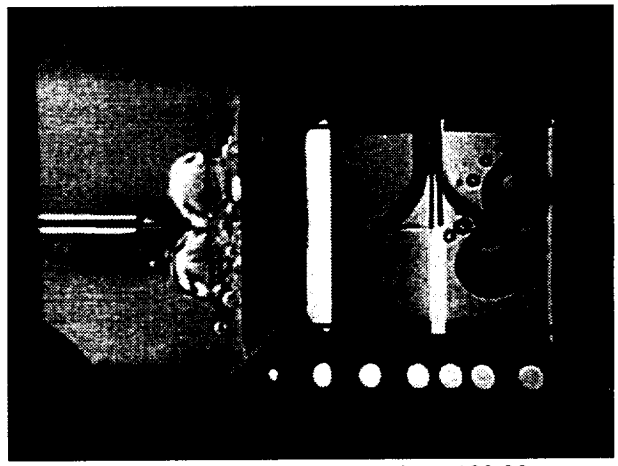

Frame #00248 time=103.32sec

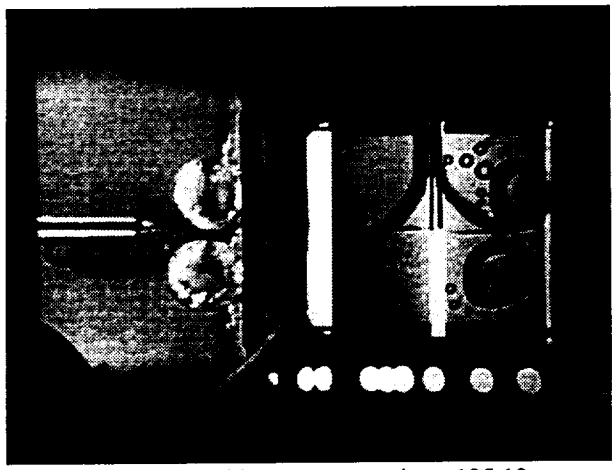

Frame #0466 time=125.12sec

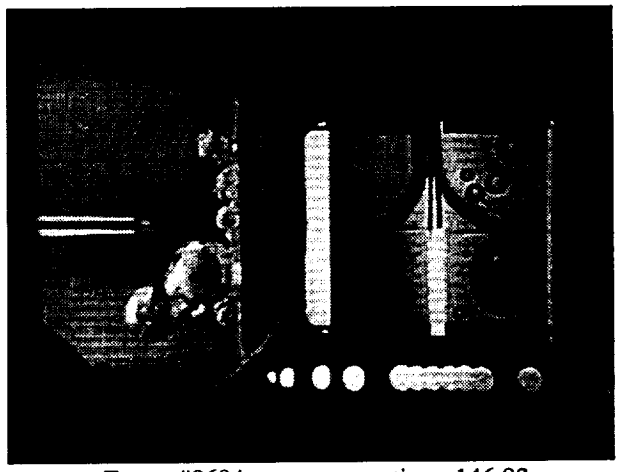

Frame #0684 time=146.92sec

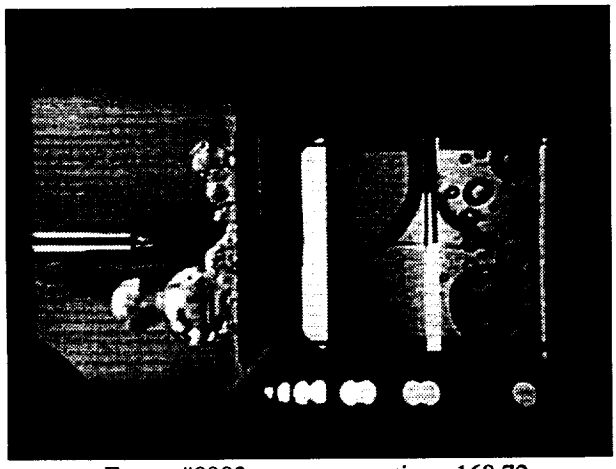

Frame #0902 time=168.72sec

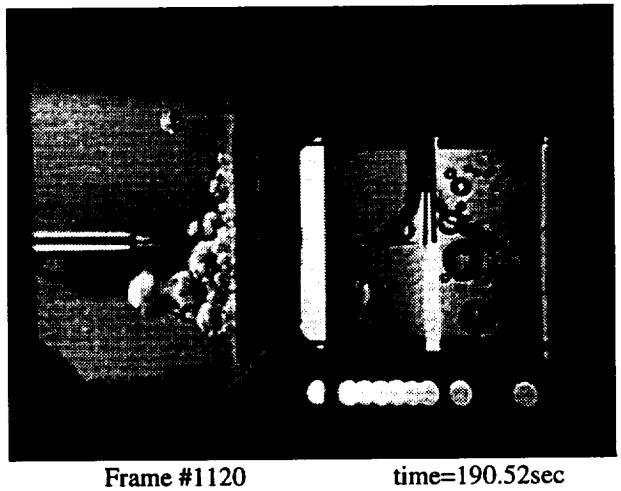

Frame #1120 time=190.52sec

Figure B-6b. Continued.

Figure B-6c. No boiling. PBE-IIA (STS-77). Run No. 3.

STS-77 Run #4

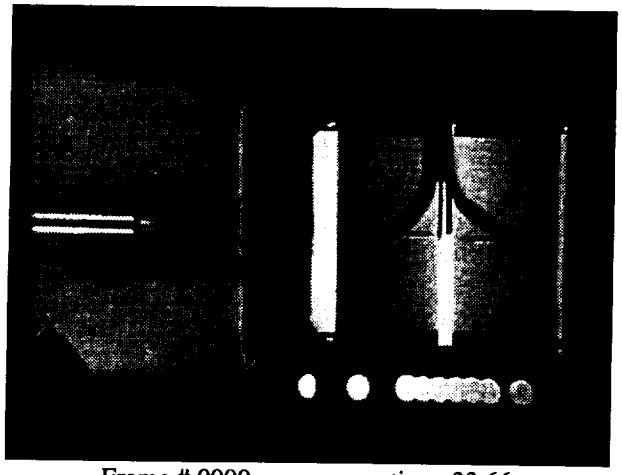

Frame # 0000 time=33.66sec

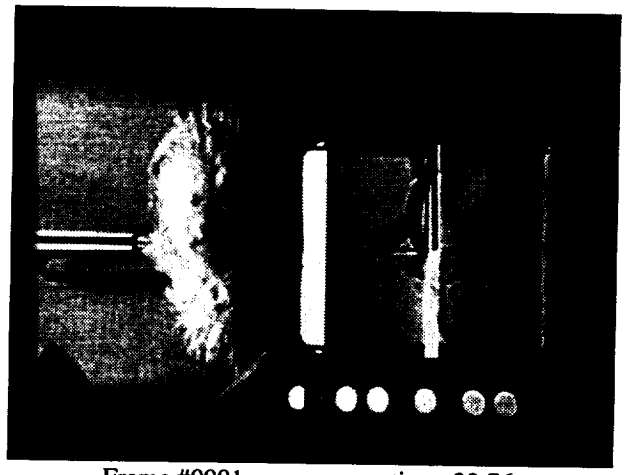

Frame #0001 time=33.76sec

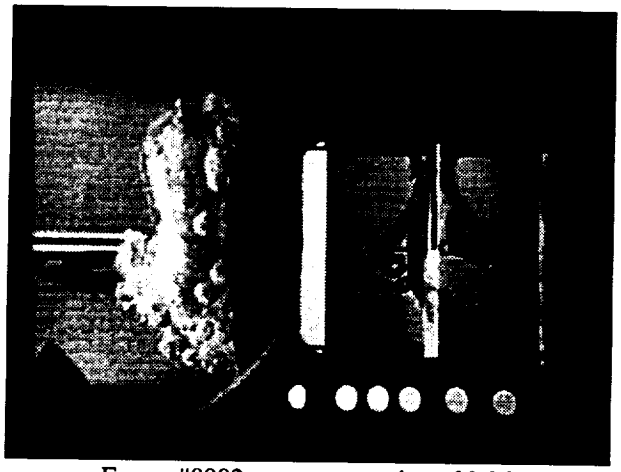

Frame #0002 time=33.86sec

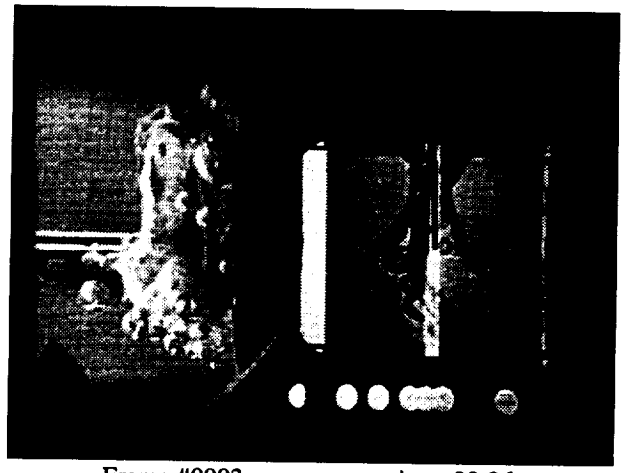

Frame #0003 time=33.96sec

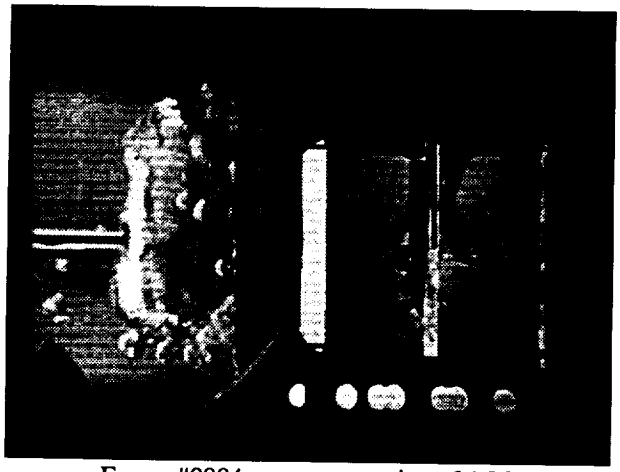

Frame #0004 time=34.06sec

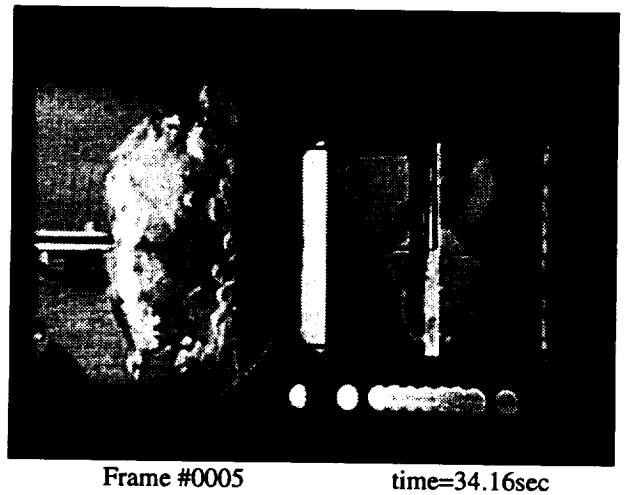

Frame #0005 time=34.16sec

Figure B-6d. Selected Photographic Images. PBE-IIA (STS-77). Run No. 4.

STS-77 Run #4

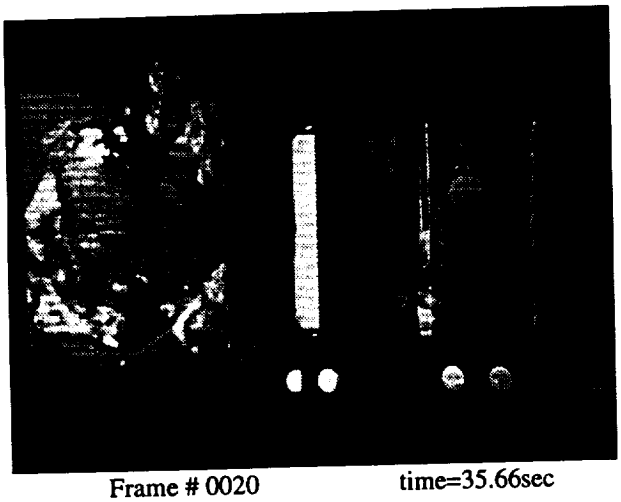

Frame # 0020 time=35.66sec

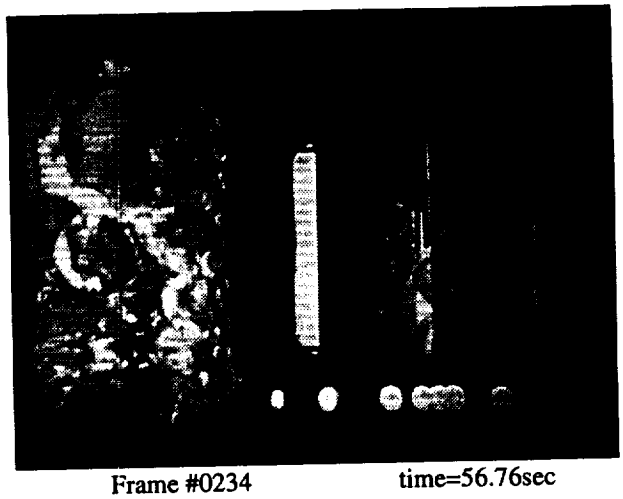

Frame #0234 time=56.76sec

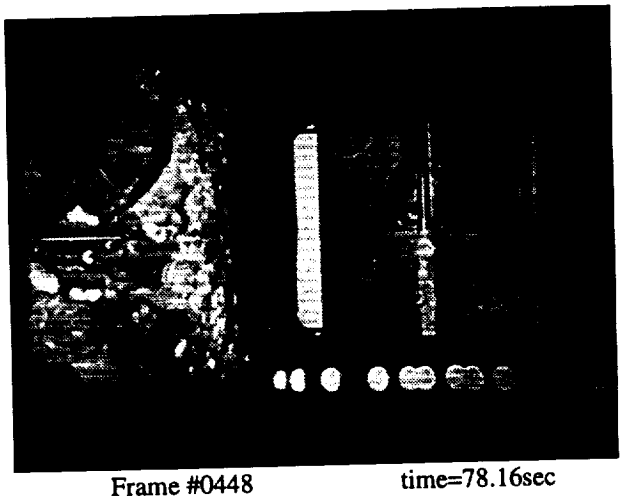

Frame #0448 time=78.16sec

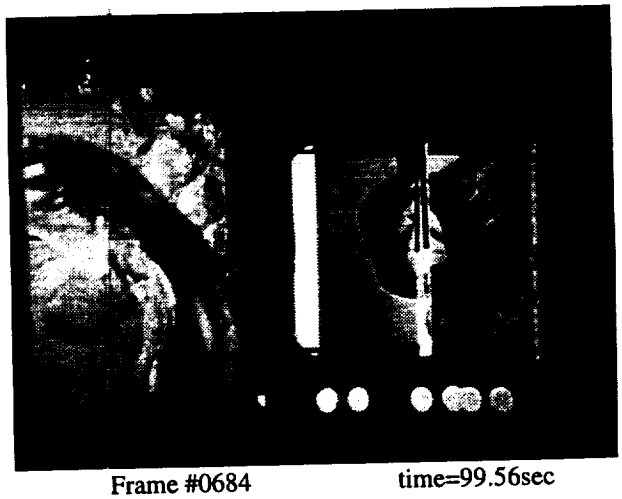

Frame #0684 time=99.56sec

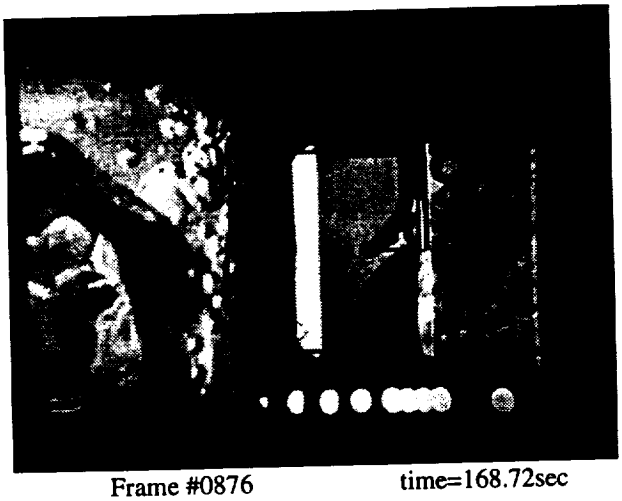

Frame #0876 time=168.72sec

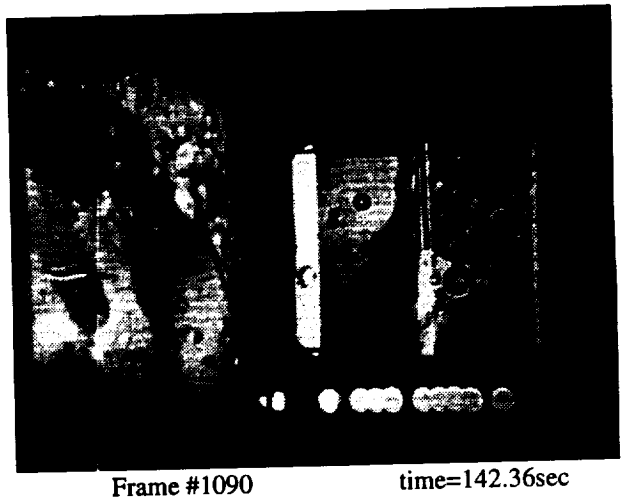

Frame #1090 time=142.36sec

Figure B-6d. Continued.

STS-77 **Run #5**

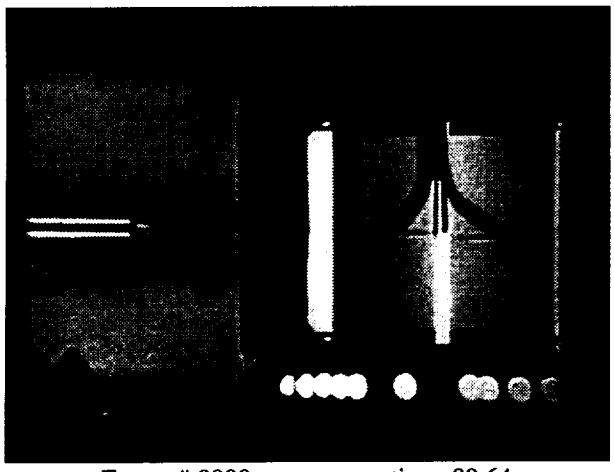

Frame # 0000 time=89.64sec

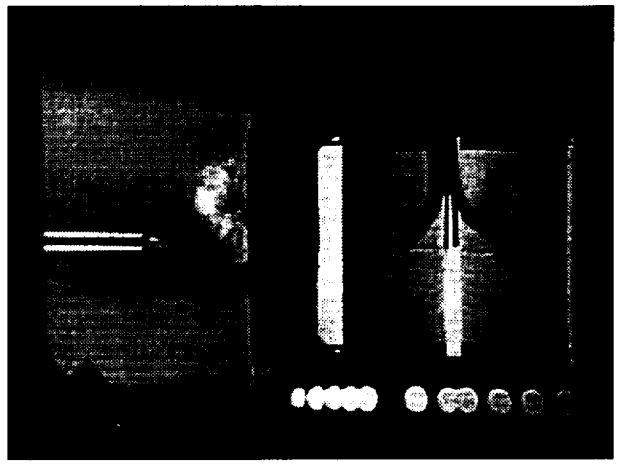

Frame #0001 time=89.74sec

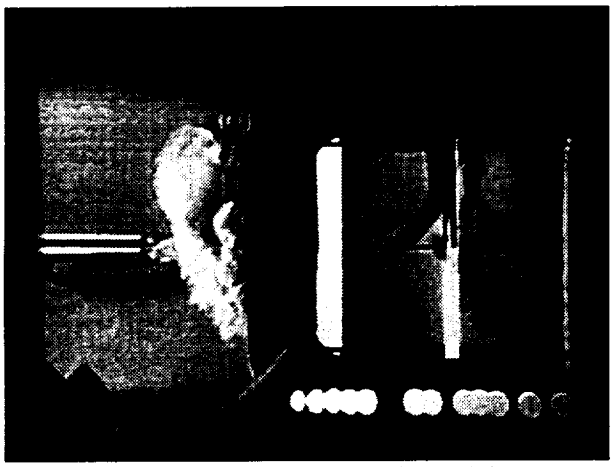

Frame #0002 time=89.84sec

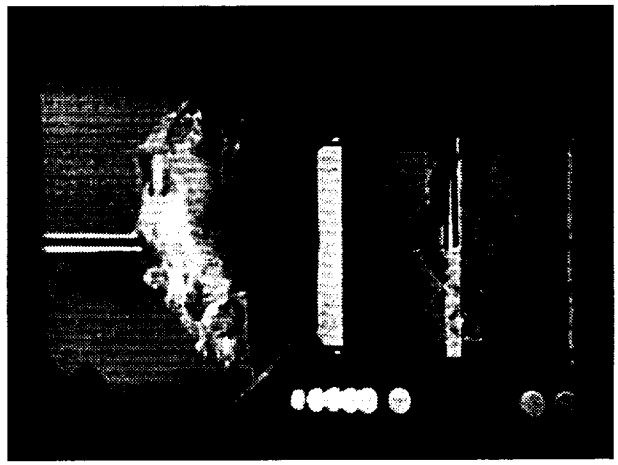

Frame #0003 time=89.94sec

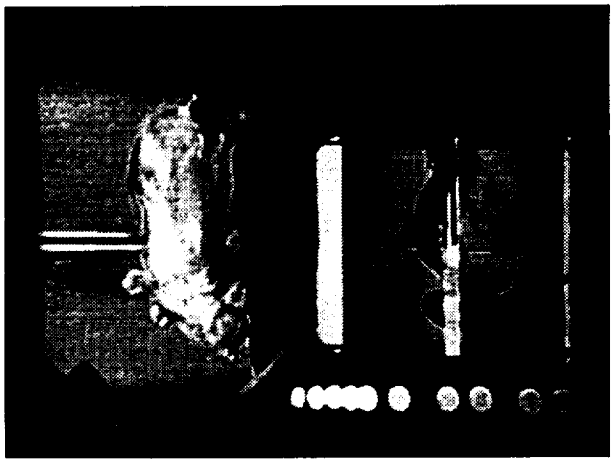

Frame #0004 time=90.04sec

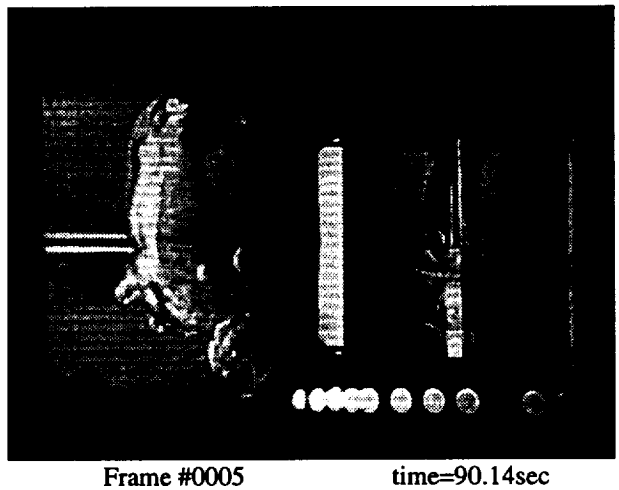

Frame #0005 time=90.14sec

Figure B-6e. Selected Photographic Images. PBE-IIA (STS-77). Run No. 5.

STS-77 Run #5

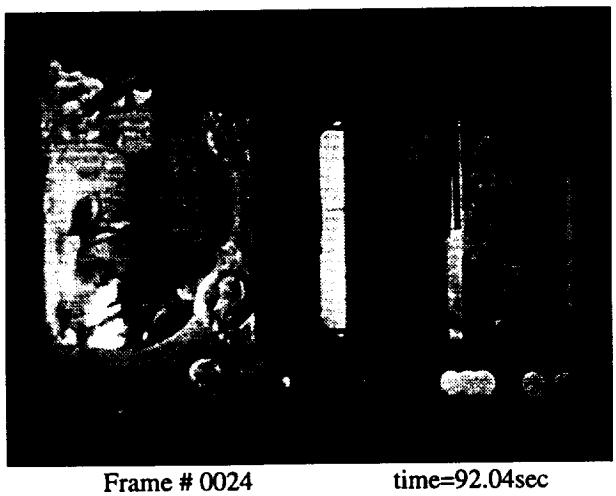

Frame # 0024 time=92.04sec

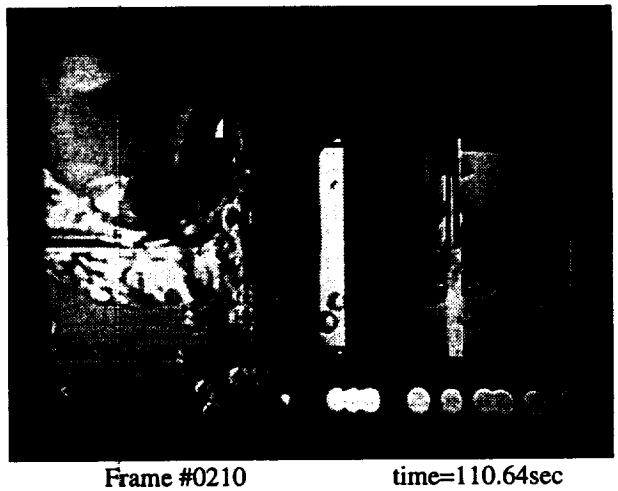

Frame #0210 time=110.64sec

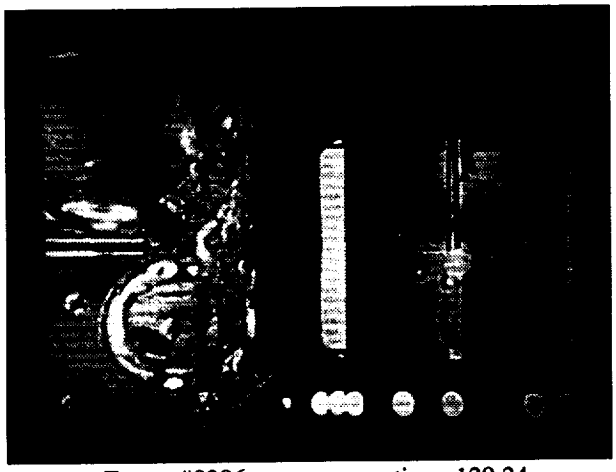

Frame #0396 time=129.24sec

Frame #0582 time=147.84sec

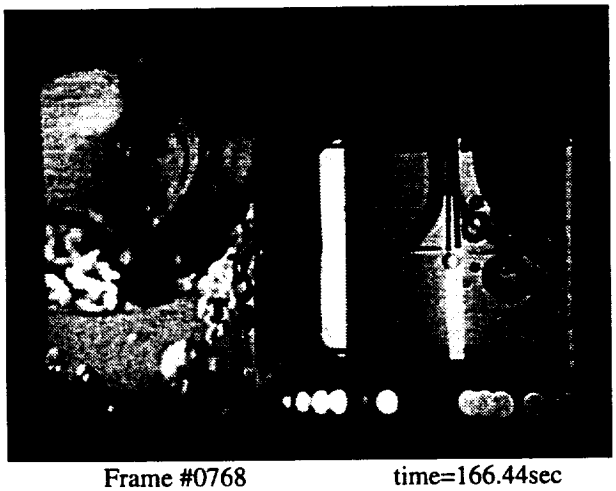

Frame #0768 time=166.44sec

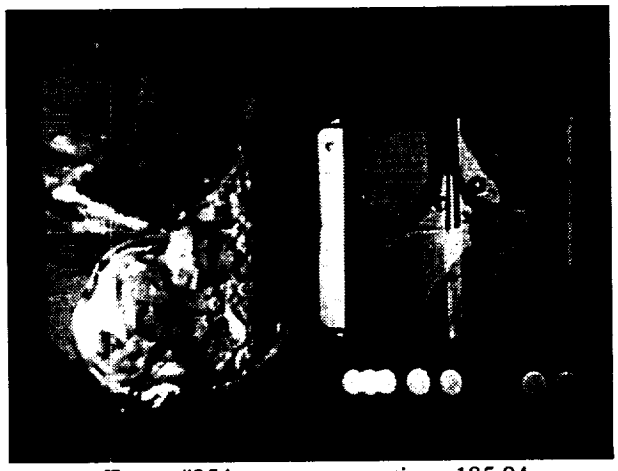

Frame #954 time=185.04sec

Figure B-6e. Continued.

STS-77 **Run #6**

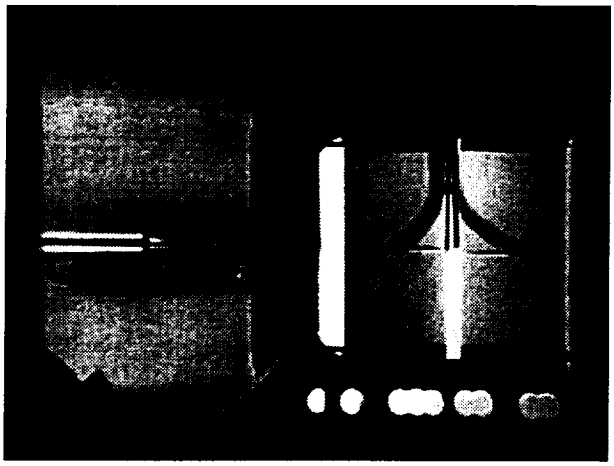

Frame # 0001 time=200.50sec

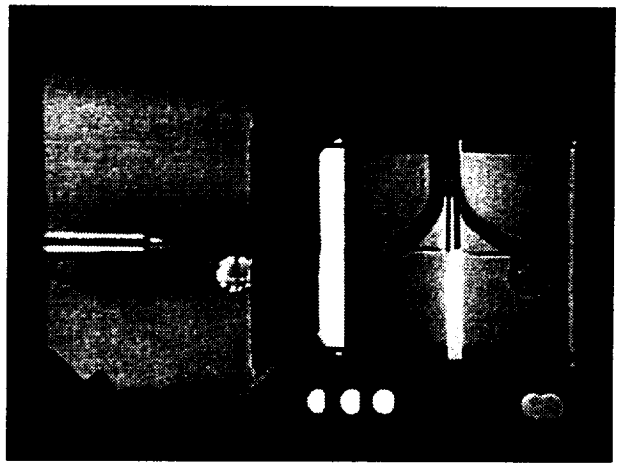

Frame #0002 time=200.60sec

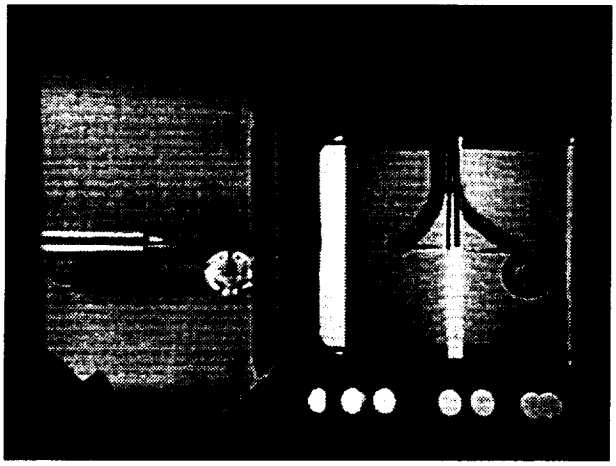

Frame #0003 time=200.70sec

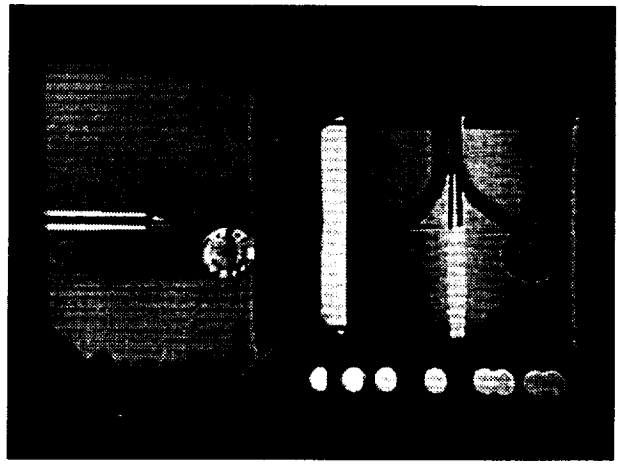

Frame #0004 time=200.80sec

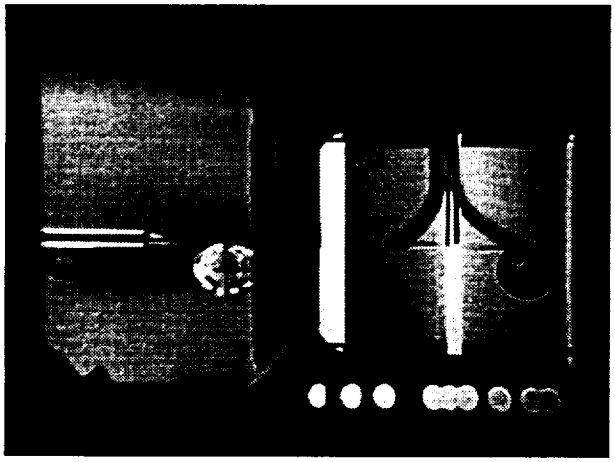

Frame #0005 time=200.90sec

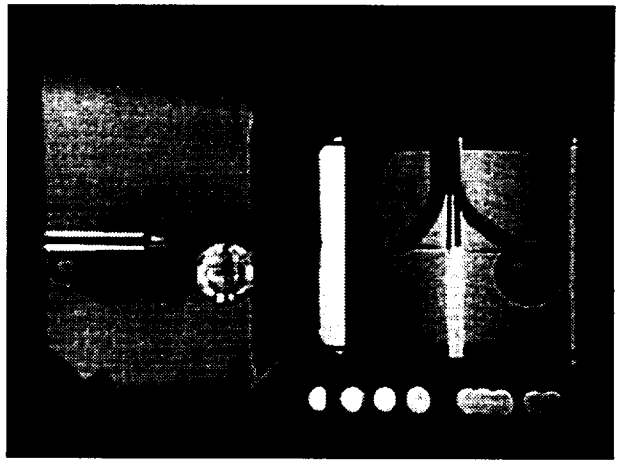

Frame #0006 time=201.00sec

Figure B-6f. Selected Photographic Images. PBE-IIA (STS-77). Run No. 6.

STS-77 Run #6

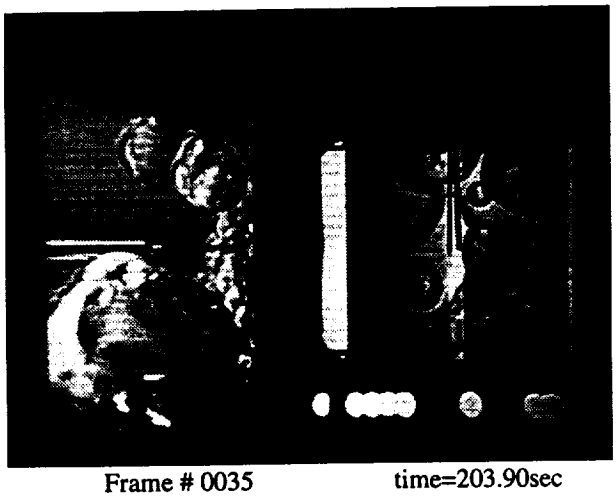

Frame # 0035 time=203.90sec

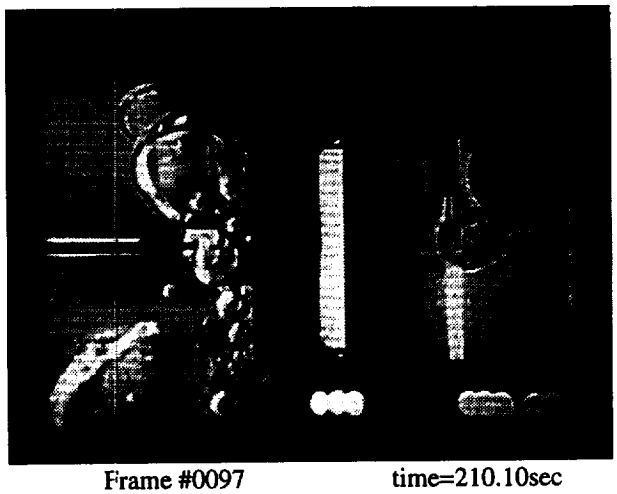

Frame #0097 time=210.10sec

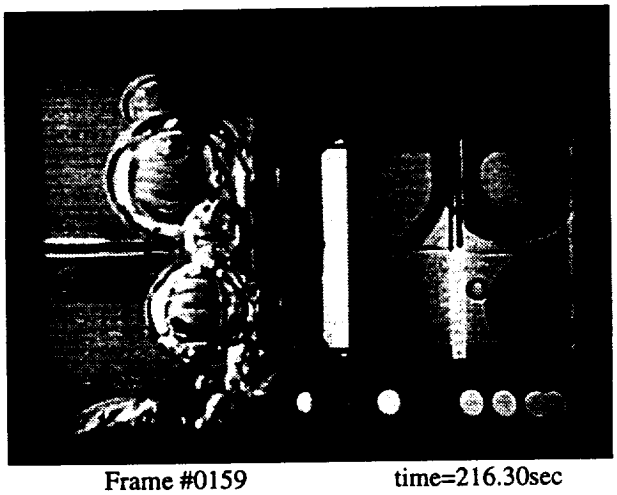

Frame #0159 time=216.30sec

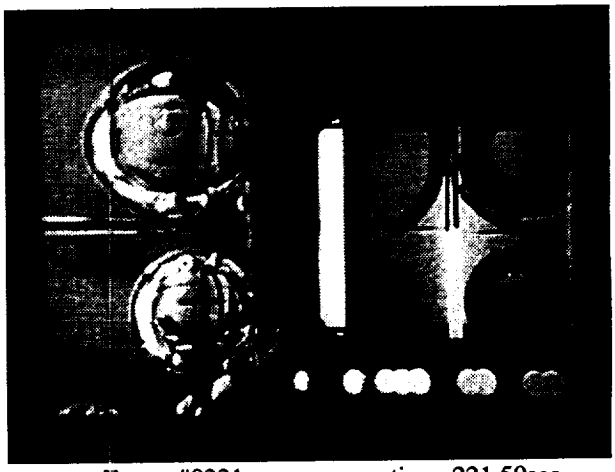

Frame #0221 time=221.50sec

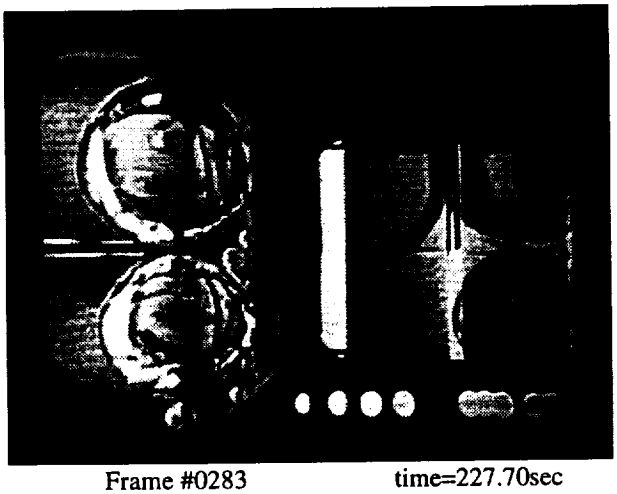

Frame #0283 time=227.70sec

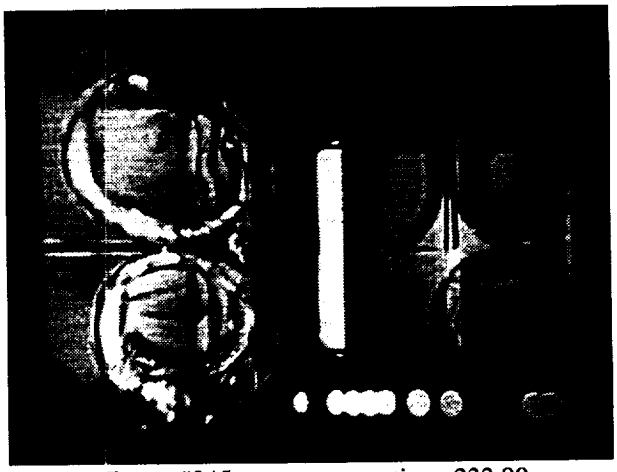

Frame #345 time=233.90sec

Figure B-6f. Continued.

STS-77 Run #7

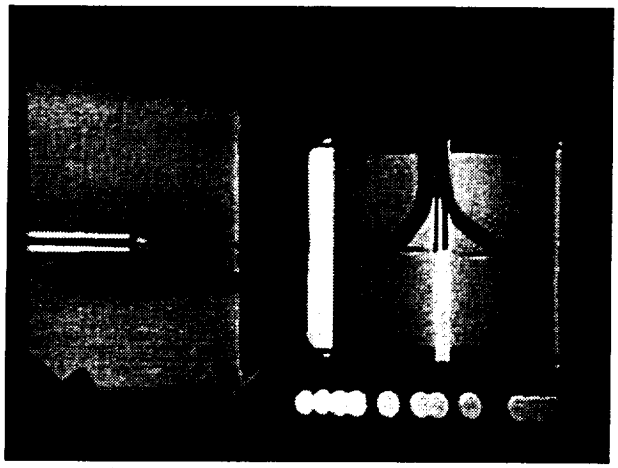

Frame # 0000 time=49.28sec

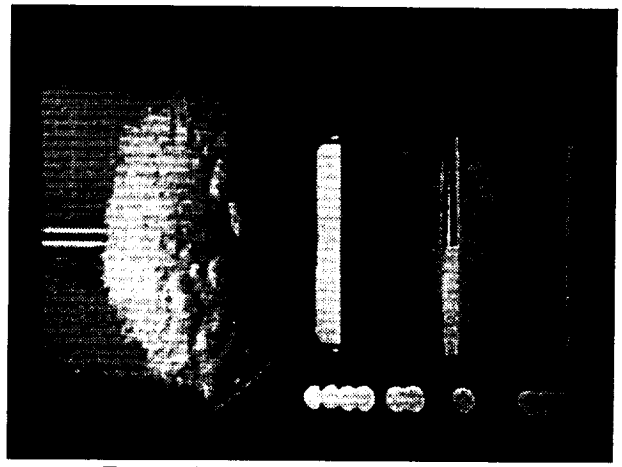

Frame #0001 time=49.38sec

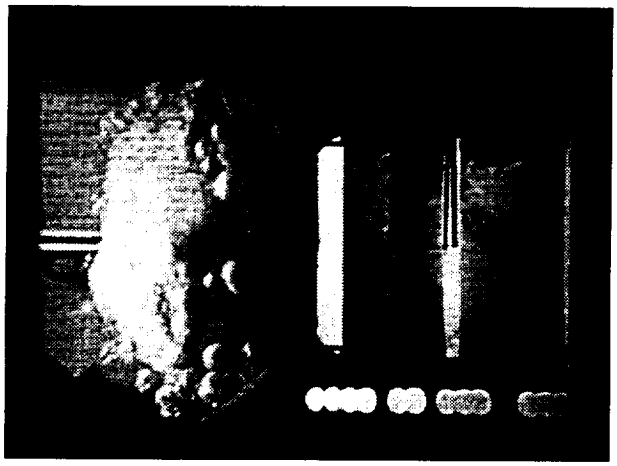

Frame #0002 time=49.48sec

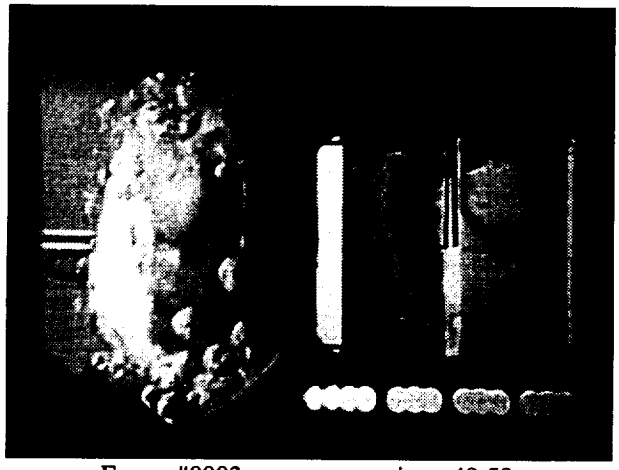

Frame #0003 time=49.58sec

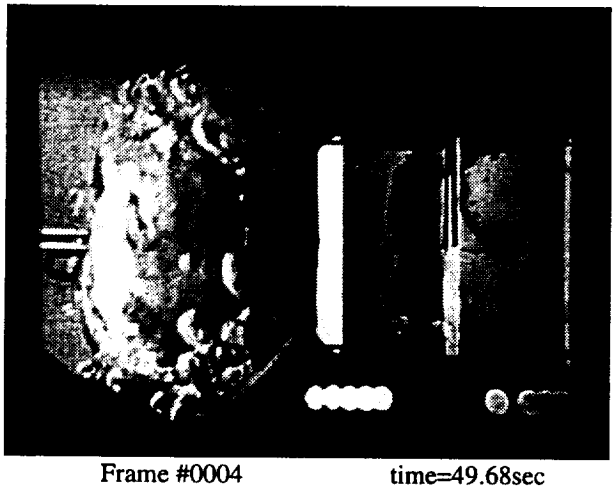

Frame #0004 time=49.68sec

Frame #0005 time=49.78sec

Figure B-6g. Selected Photographic Images. PBE-IIA (STS-77). Run No. 7.

STS-77 Run #7

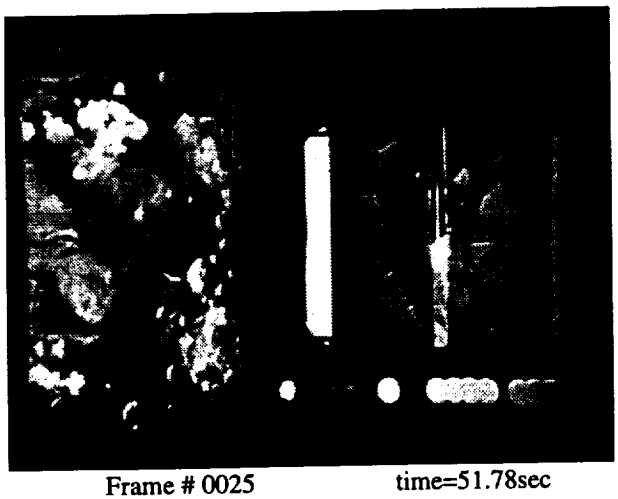

Frame # 0025 time=51.78sec

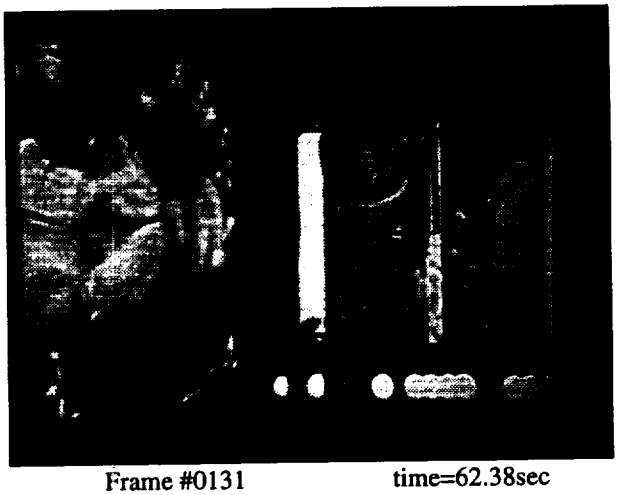

Frame #0131 time=62.38sec

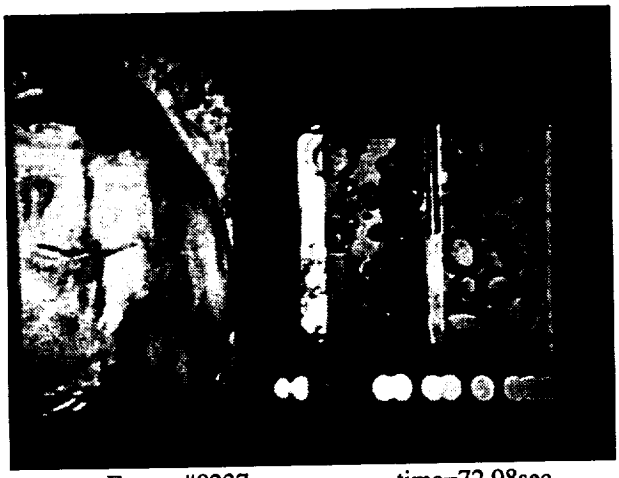

Frame #0237 time=72.98sec

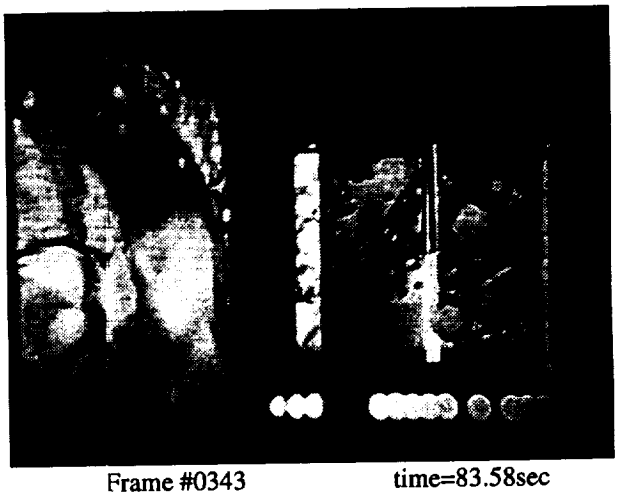

Frame #0343 time=83.58sec

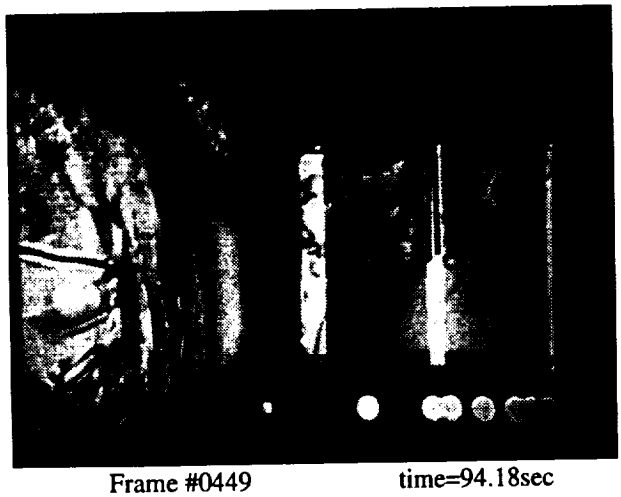

Frame #0449 time=94.18sec

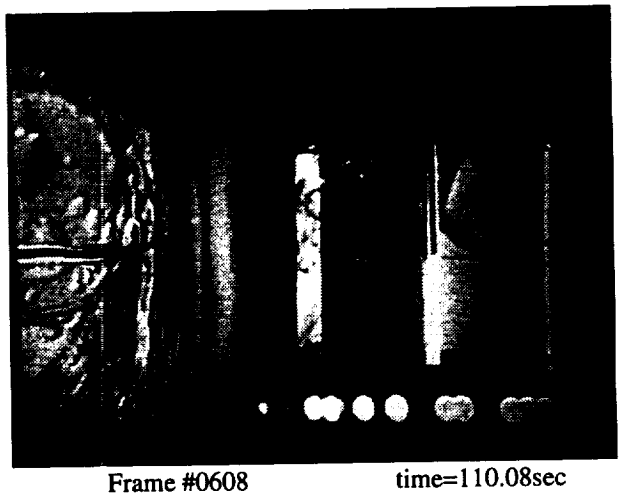

Frame #0608 time=110.08sec

Figure B-6g. Continued.

STS-77 **Run #8**

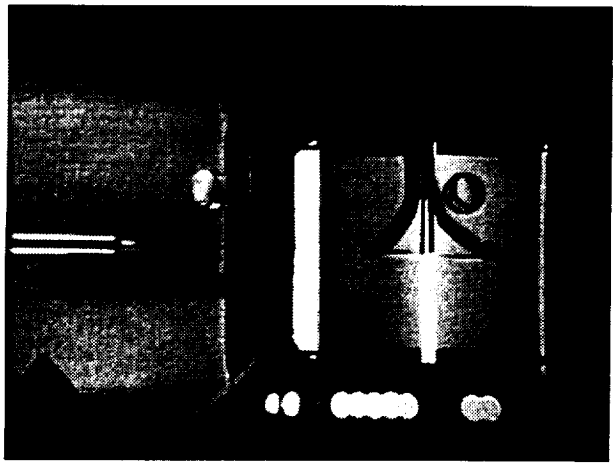

Frame # 0001 time=76.40sec

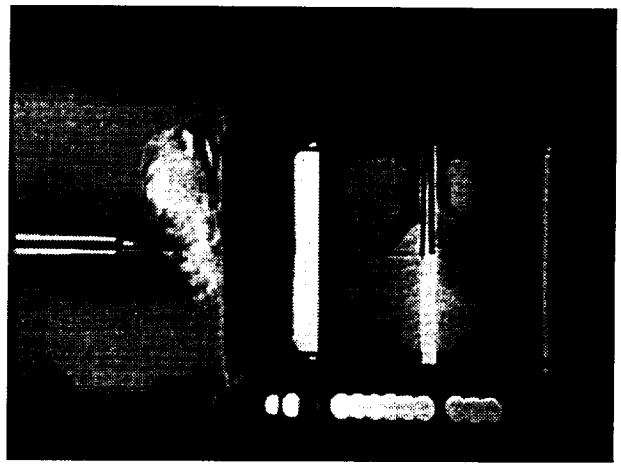

Frame #0002 time=76.50sec

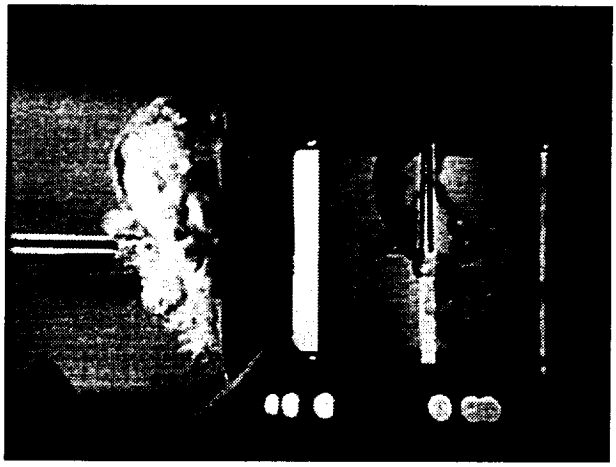

Frame #0003 time=76.60sec

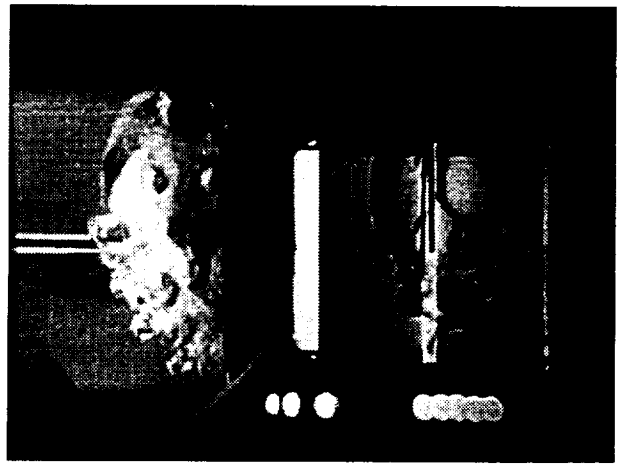

Frame #0004 time=76.70sec

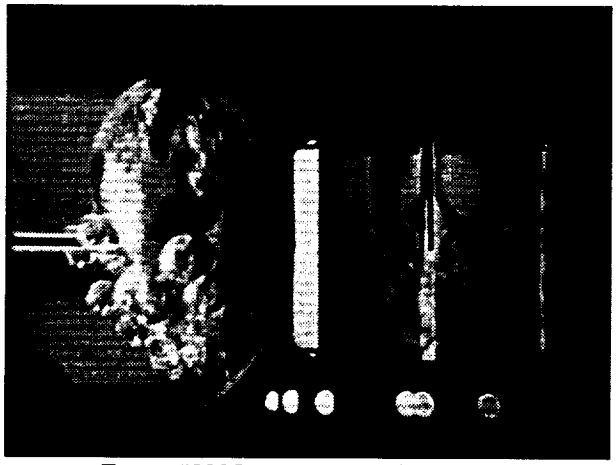

Frame #0005 time=76.80sec

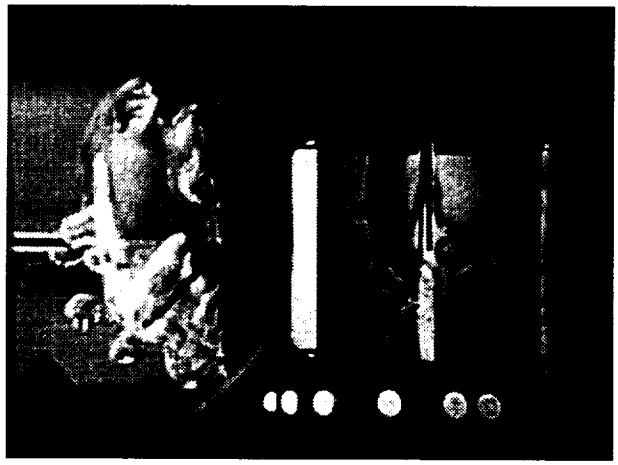

Frame #0006 time=76.90sec

Figure B-6h. Selected Photographic Images. PBE-IIA (STS-77). Run No. 8.

STS-77 **Run #8**

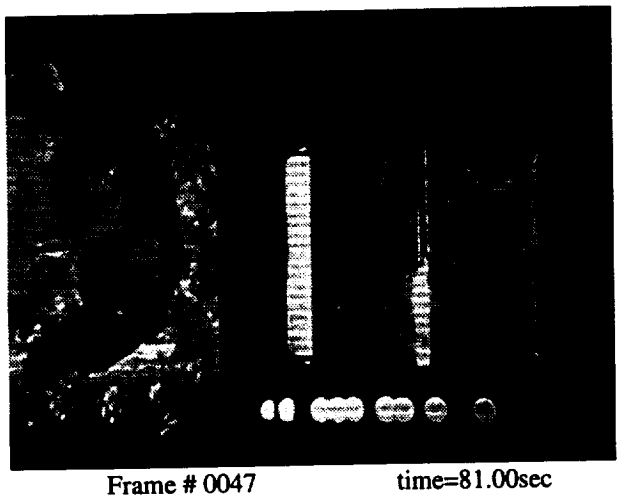

Frame # 0047 time=81.00sec

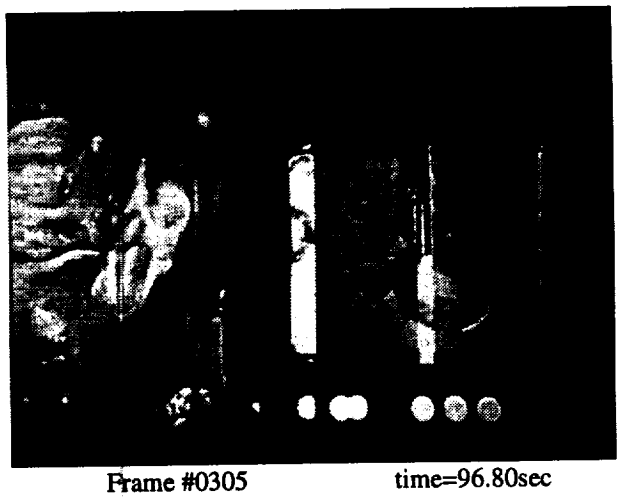

Frame #0305 time=96.80sec

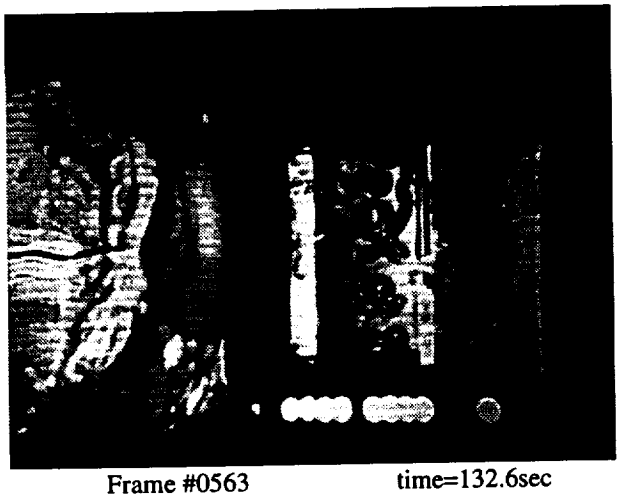

Frame #0563 time=132.6sec

Frame #0821 time=158.40sec

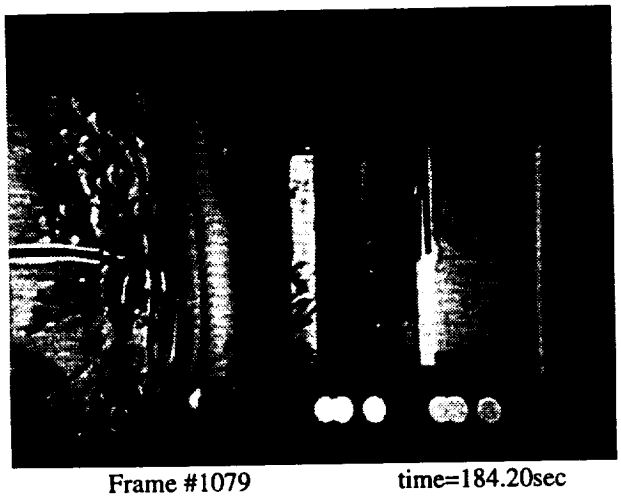

Frame #1079 time=184.20sec

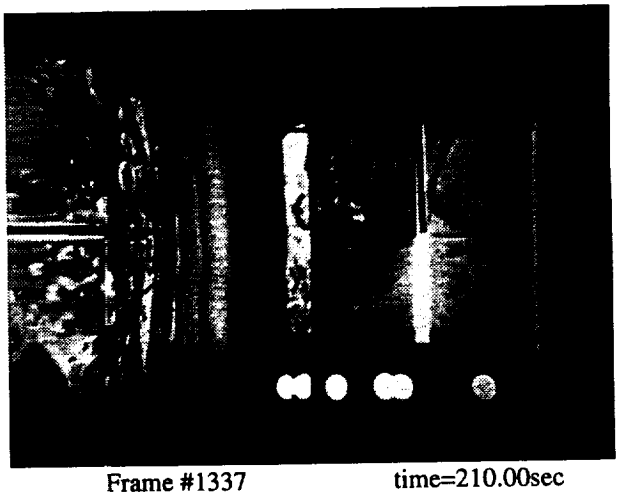

Frame #1337 time=210.00sec

Figure B-6h. Continued.

STS-77 Run #9

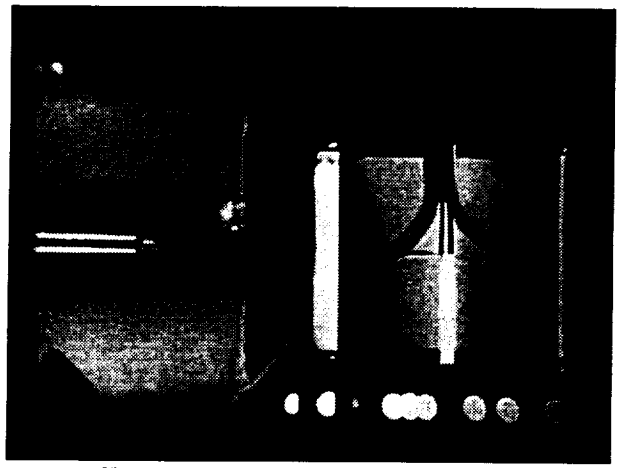

Frame # 0001 time=226.16sec

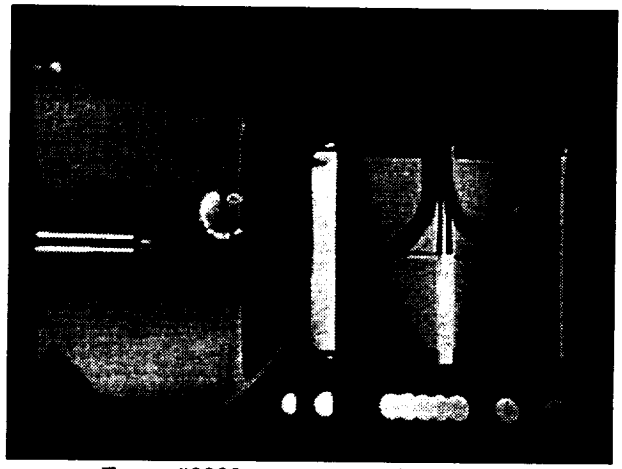

Frame #0002 time=226.26sec

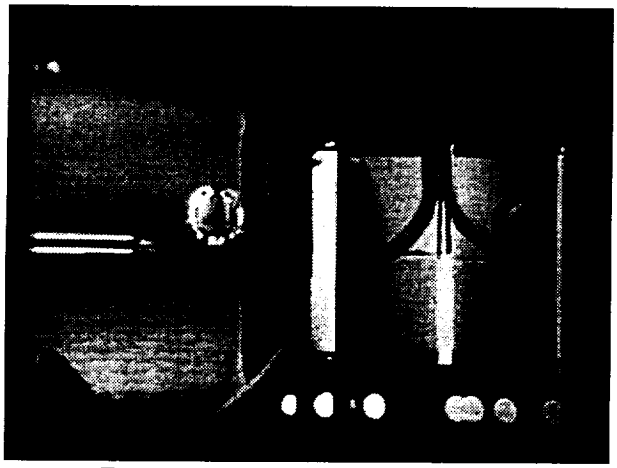

Frame #0003 time=226.36sec

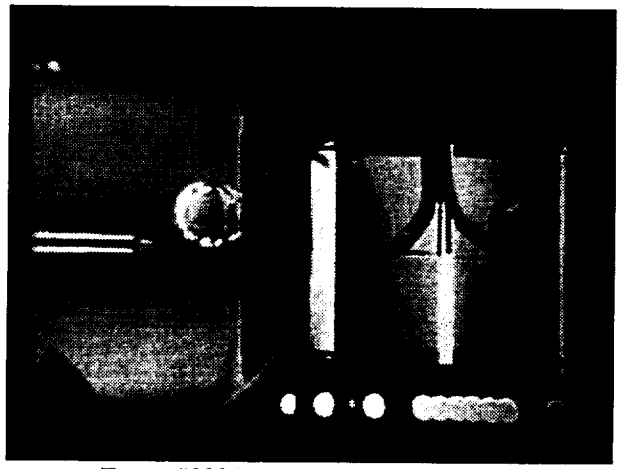

Frame #0004 time=226.46sec

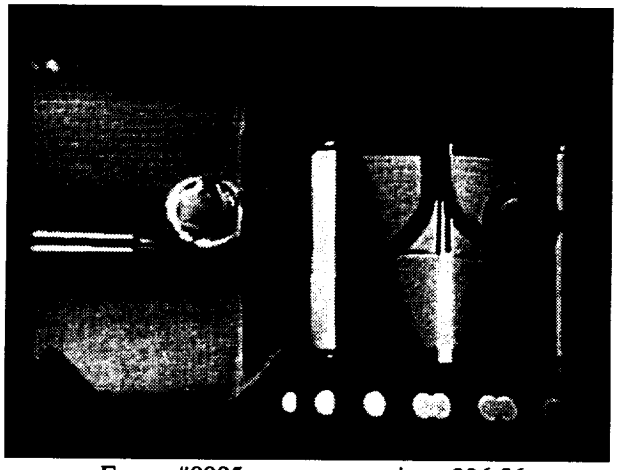

Frame #0005 time=226.56sec

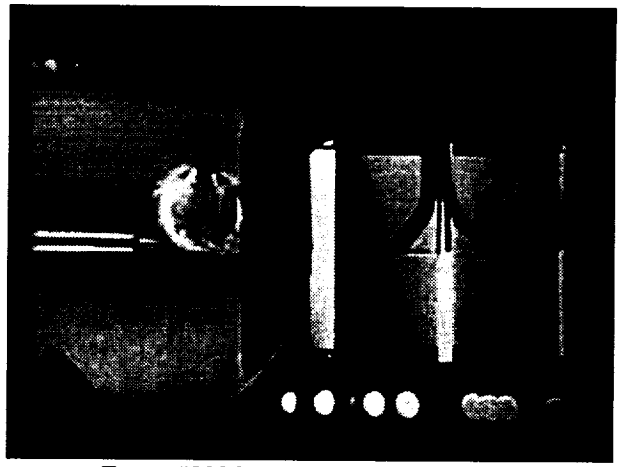

Frame #0006 time=226.66sec

Figure B-6i. Selected Photographic Images. PBE-IIA (STS-77). Run No. 9.

STS-77 Run #9

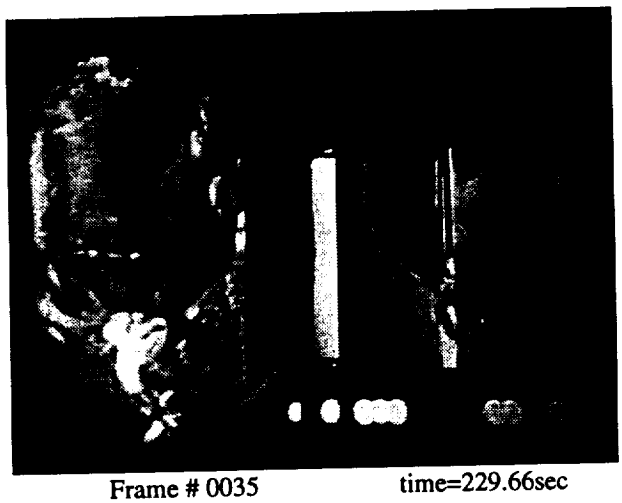

Frame # 0035 time=229.66sec

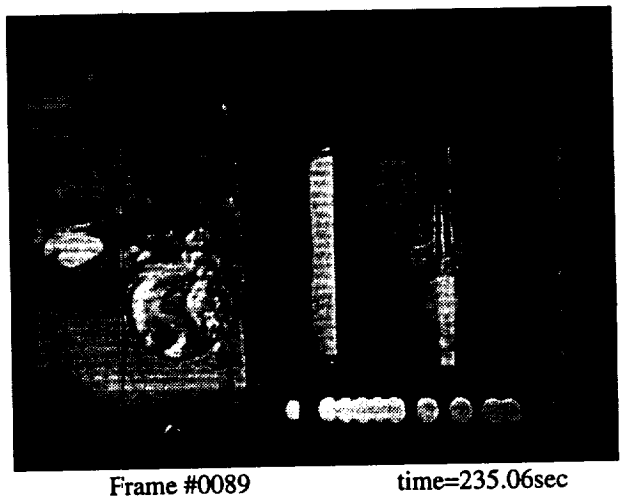

Frame #0089 time=235.06sec

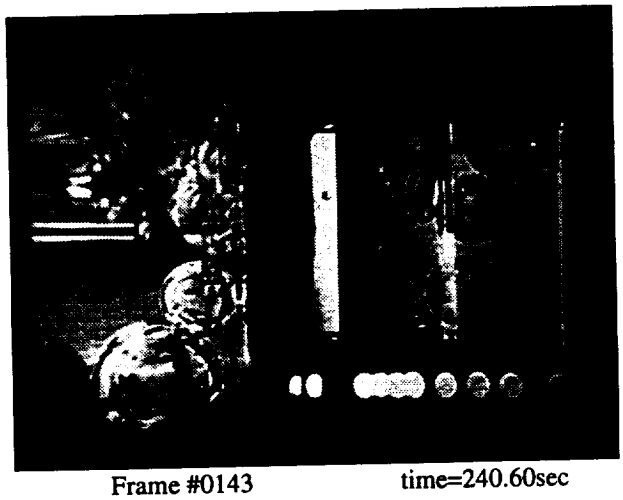

Frame #0143 time=240.60sec

Frame #0197 time=245.86sec

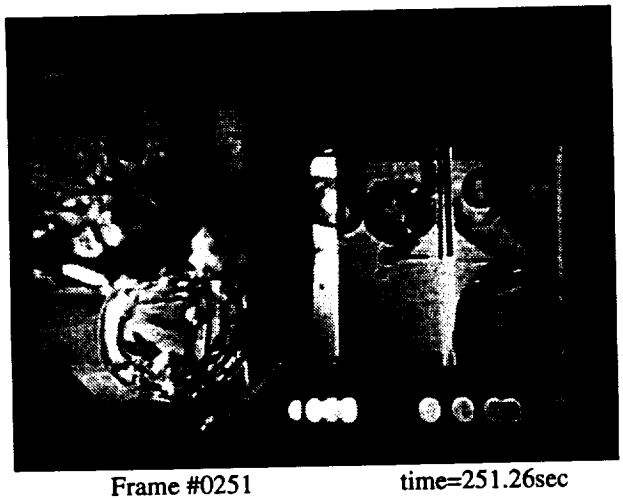

Frame #0251 time=251.26sec

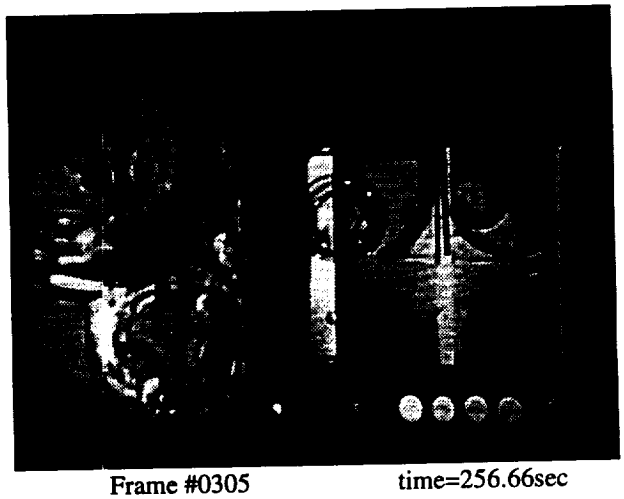

Frame #0305 time=256.66sec

Figure B-6i. Continue.

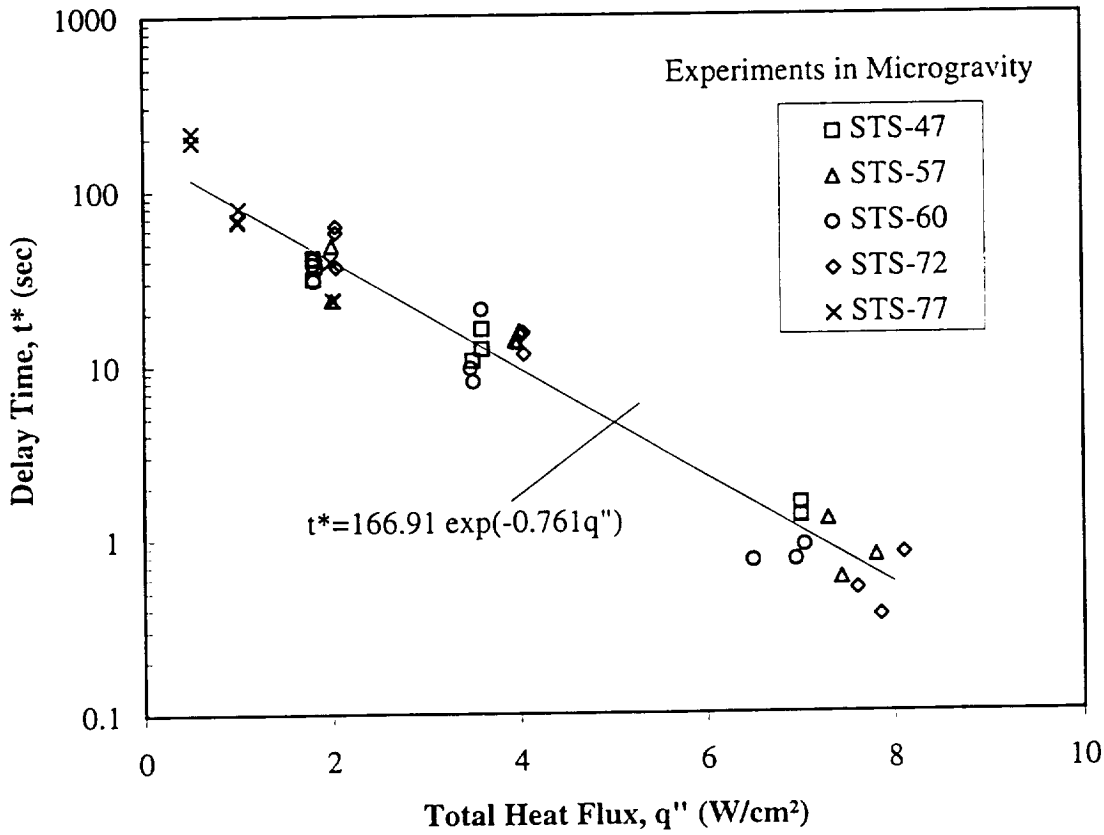

Figure B-7. Nucleation Delay Time. Comparison between Five (5) PBE space experiments and the best-fit correlation.

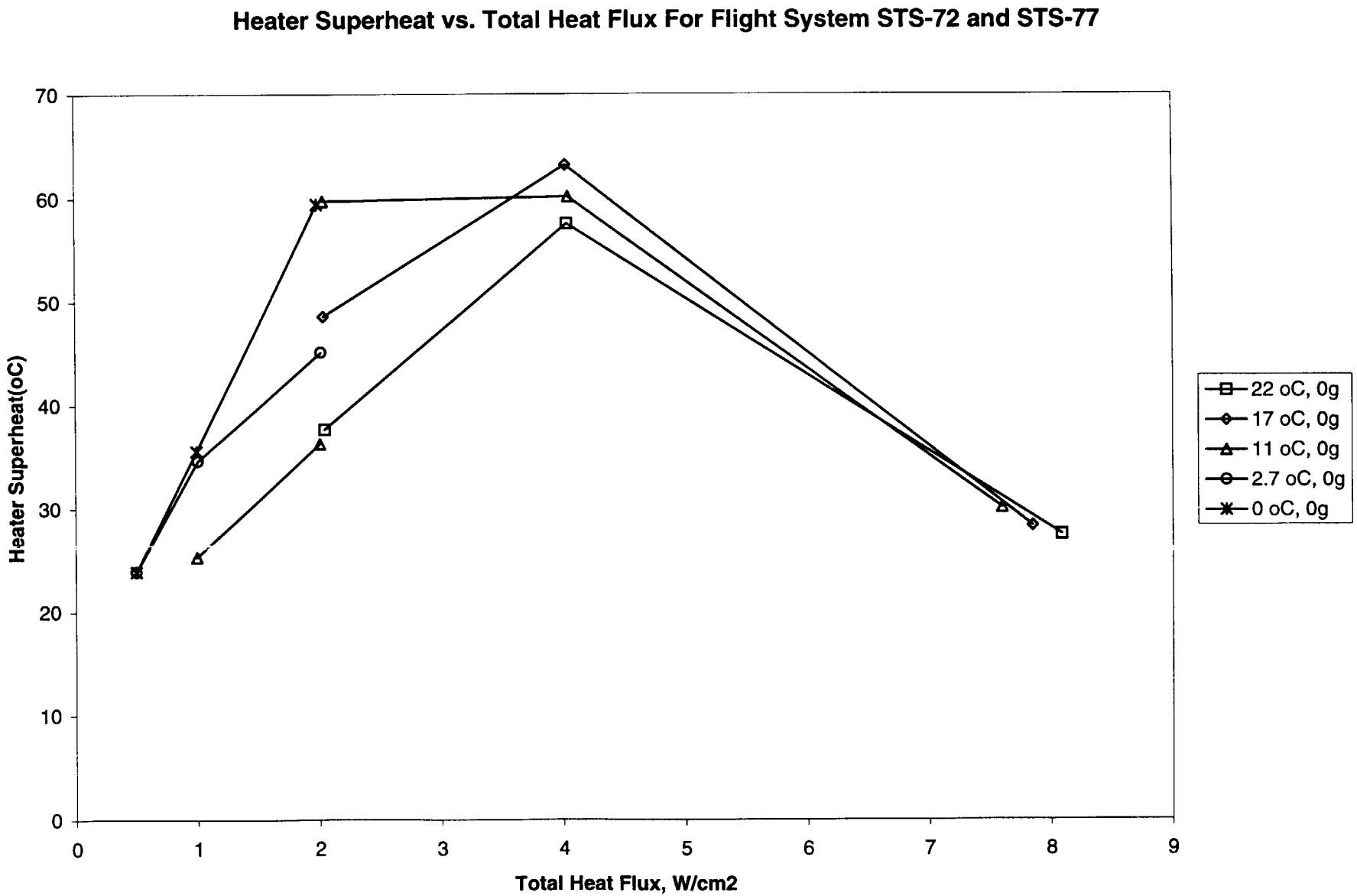

Figure B-8. Mean heater surface nucleation superheat. Comparison between PBE-IIB (STS-72) and PBE-IIA (STS-77).

STS-77 - Dry spot calculation

Run #	10 FPS	Nucleation	Range	Rate	Total # frames	Analysis of frames	Notes	Data Storage
1	0 to 170	23.80	40 to 90	10 fps	500	500		OD9-A
			110 to 130		200	200		OD9-A
			150 to 170		200	200		OD9-A
2	0 to 210	69.60	120 to 160	10 fps	400	400		OD9-A
			170 to 190		200	200		OD9-A
3	0 to 240	~	~	10 fps	~	~	no nuc.	~
4	0 to 160	23.60	~	10 fps	~	~	negligible dry area	~
5	0 to 200	79.60	110 to 140	10 fps	300	300		OD9-A
			160 to 180	10 fps	200	200		OD9-A,B
6	0 to 240	190.50	210 to 240	10 fps	300	300		OD9-B
7	0 to 100	39.20	55 to 70	10 fps	150	150		OD9-B
			70 to 95	10 fps	250	250		OD9-B
8	0 to 200	66.30	90 to 140	10 fps	500	500		OD9-B
9	0 to 240	216.20	227 to 250	10 fps	230	230		OD9-B

Table B-IV. Index for heater surface dry fraction measurements and computation of microgravity nucleate boiling heat transfer coefficients. PBE-IIA (STS-77).

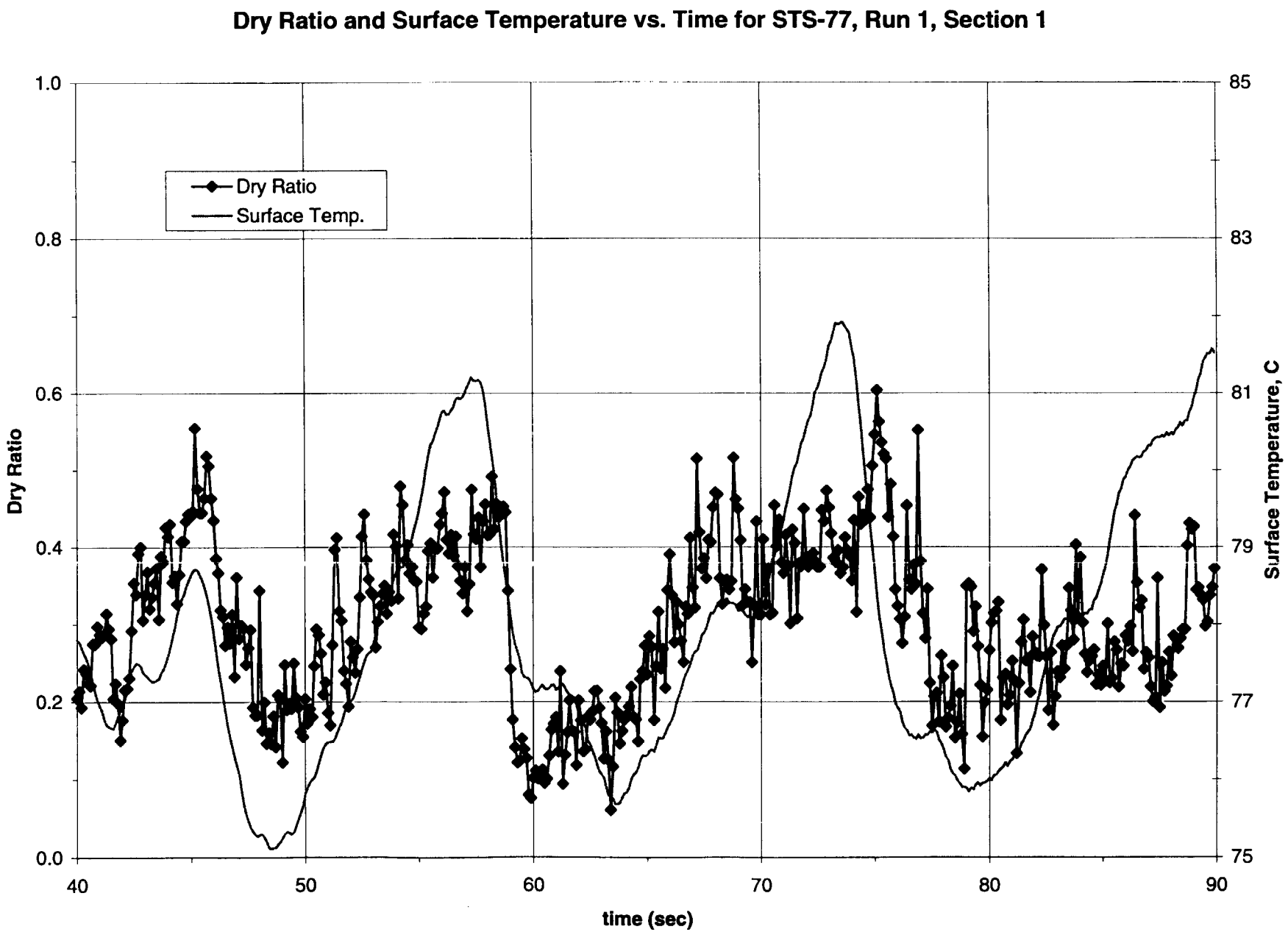

Figure B-10a-1-i. Heater surface dry fraction and mean temperature. PBE-IIA (STS-77). Run No. 1. Time interval: 40 - 90 seconds.

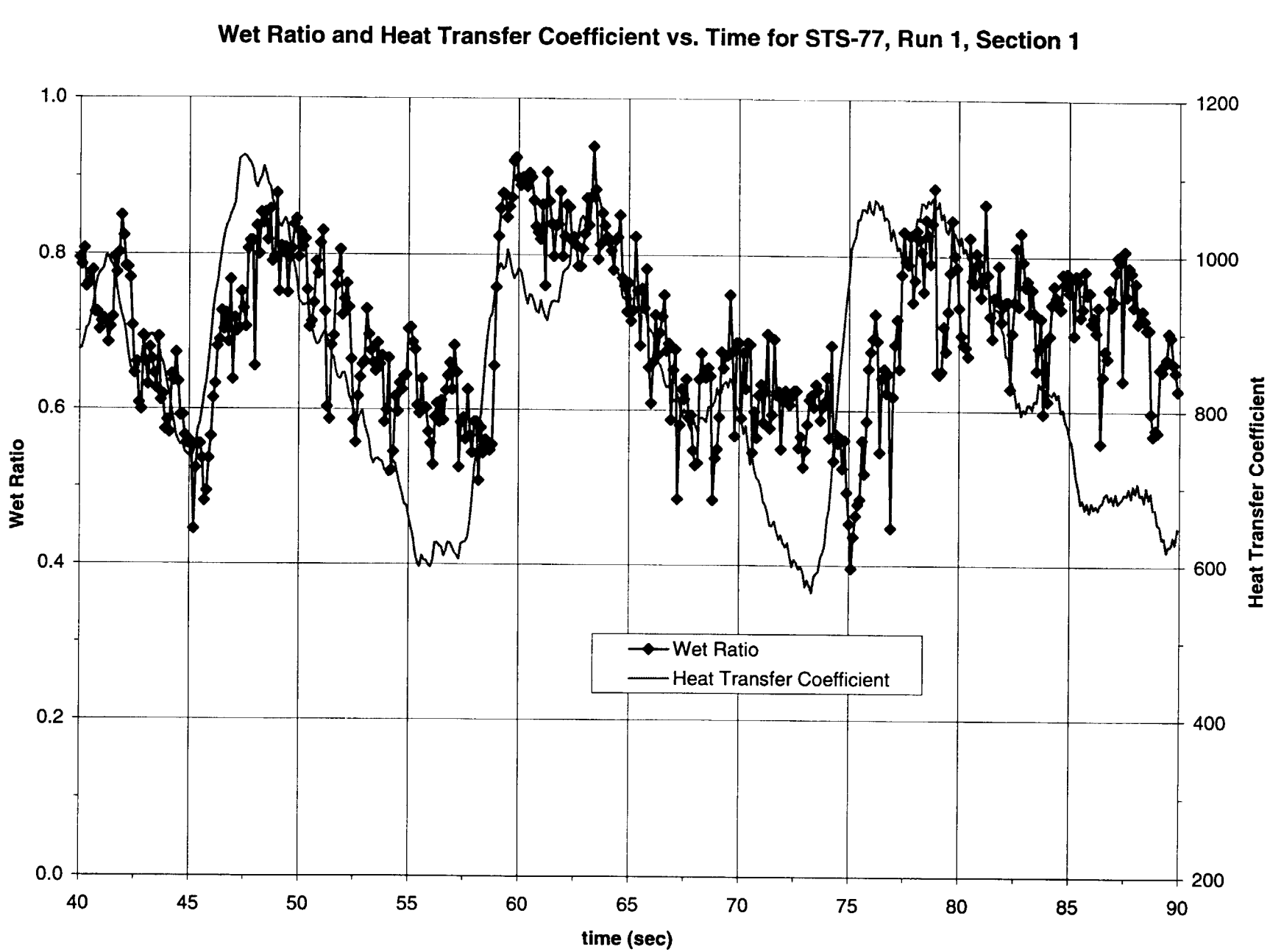

Figure B-10a-1-ii. Heater surface wet fraction and mean heat transfer coefficients. PBE-IIA (STS-77). Run No. 1. Time interval: 40 - 90 seconds.

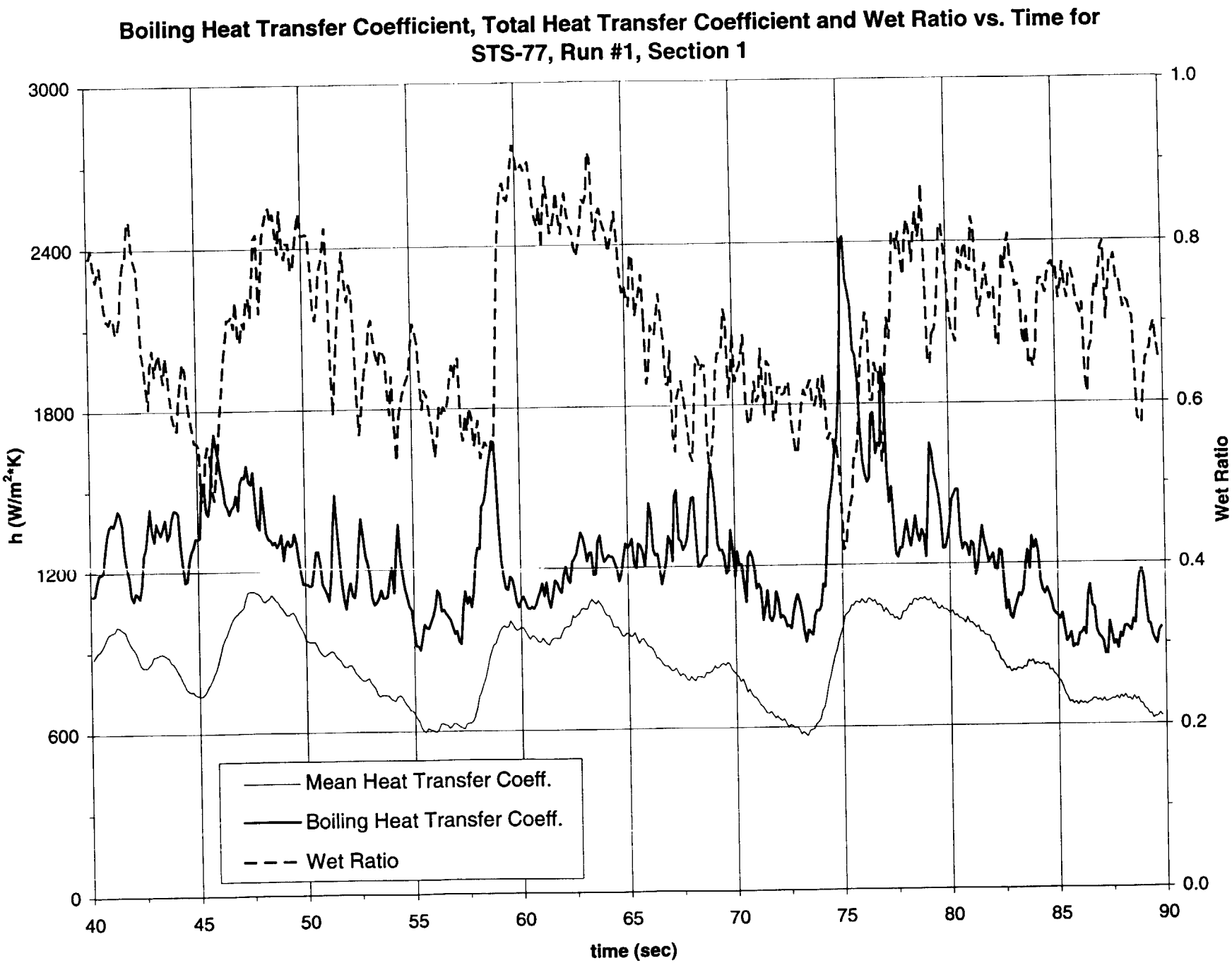

Figure B-10a-1-iii. Development of microgravity boiling heat transfer coefficient. PBE-IIA (STS-77). Run No. 1. Time interval: 40 - 90 seconds.

STS-77 Run #1, Section #1

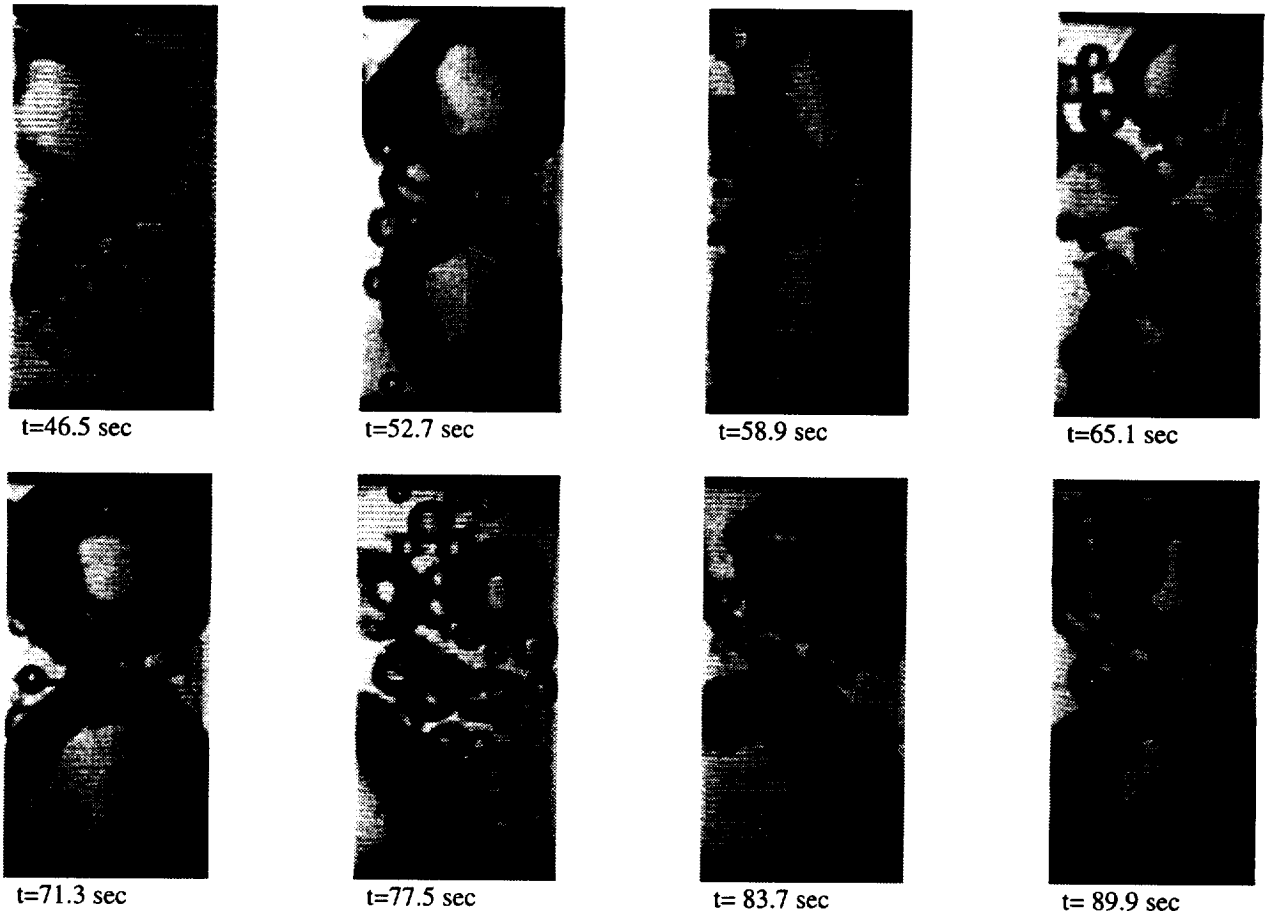

Figure B-10a-1-iv. Sample images showing dryout/rewetting. PBE-IIA (STS-77). Run No. 1. Time interval: 40 - 90 seconds.

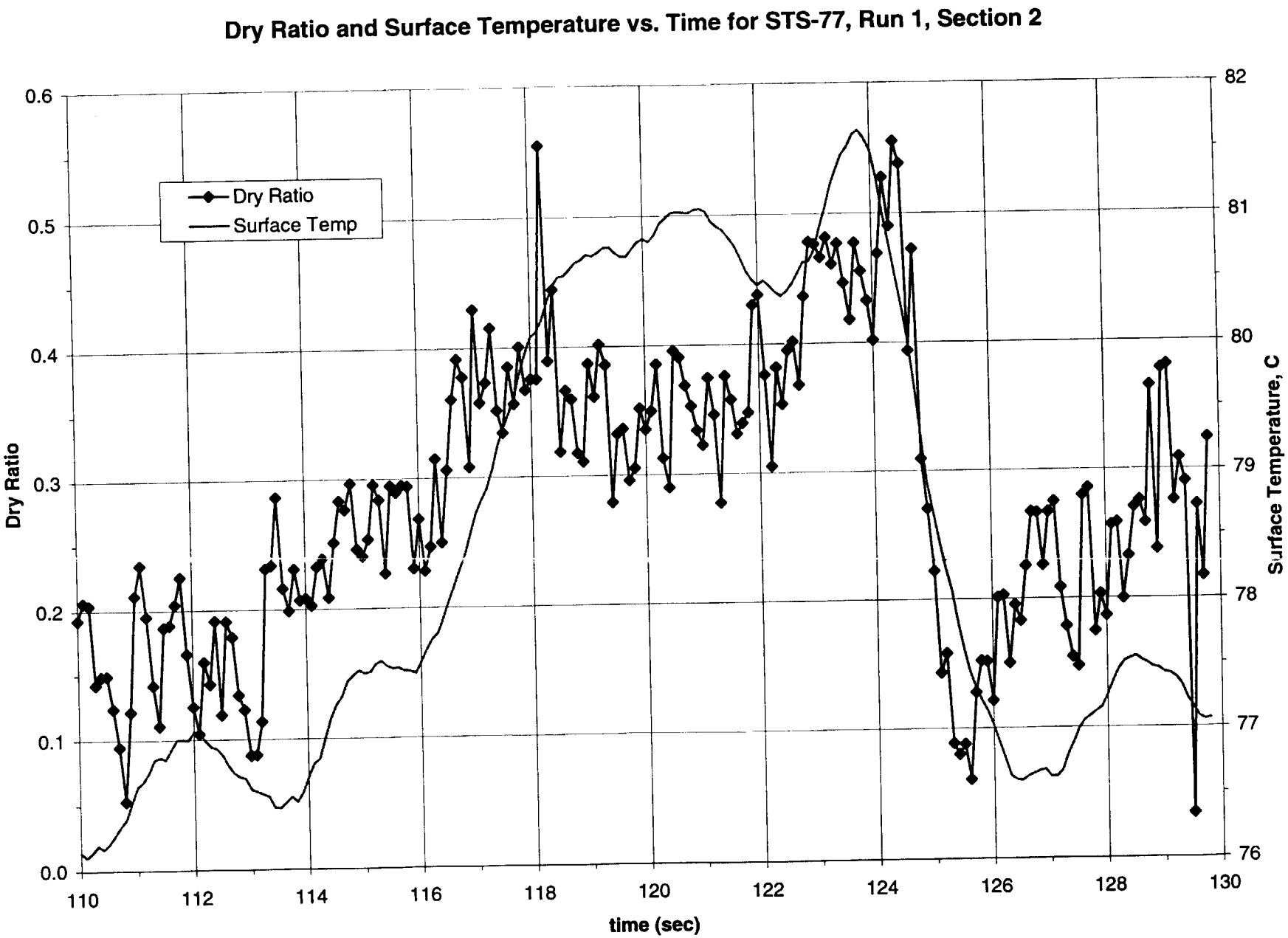

Figure B-10a-2-i. Heater surface dry fraction and mean temperature. PBE-IIA (STS-77). Run No. 1. Time interval: 110 - 130 seconds.

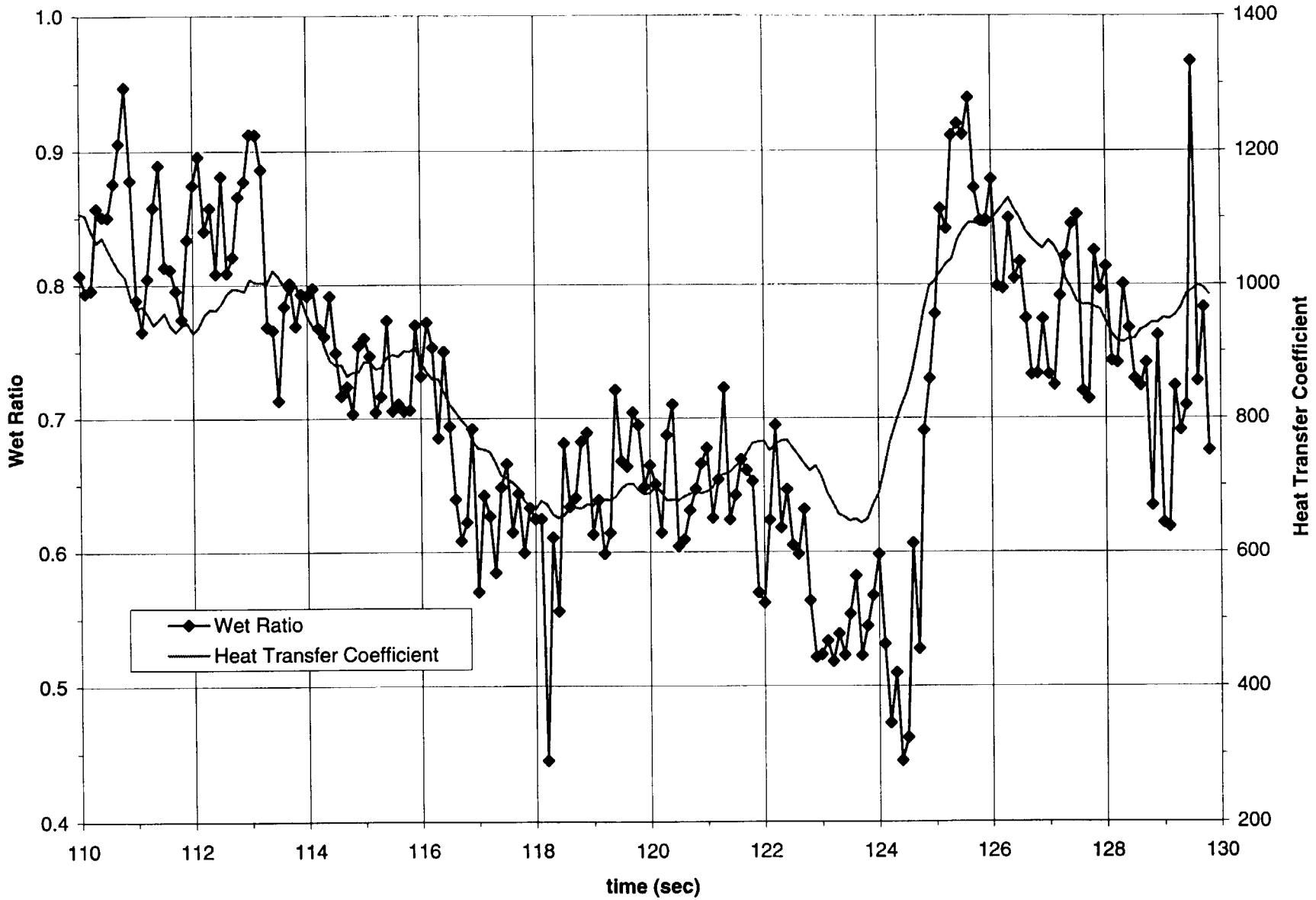

Figure B-10a-2-ii. Heater surface wet fraction and mean heat transfer coefficients. PBE-IIA (STS-77). Run No. 1. Time interval: 110 - 130 seconds.

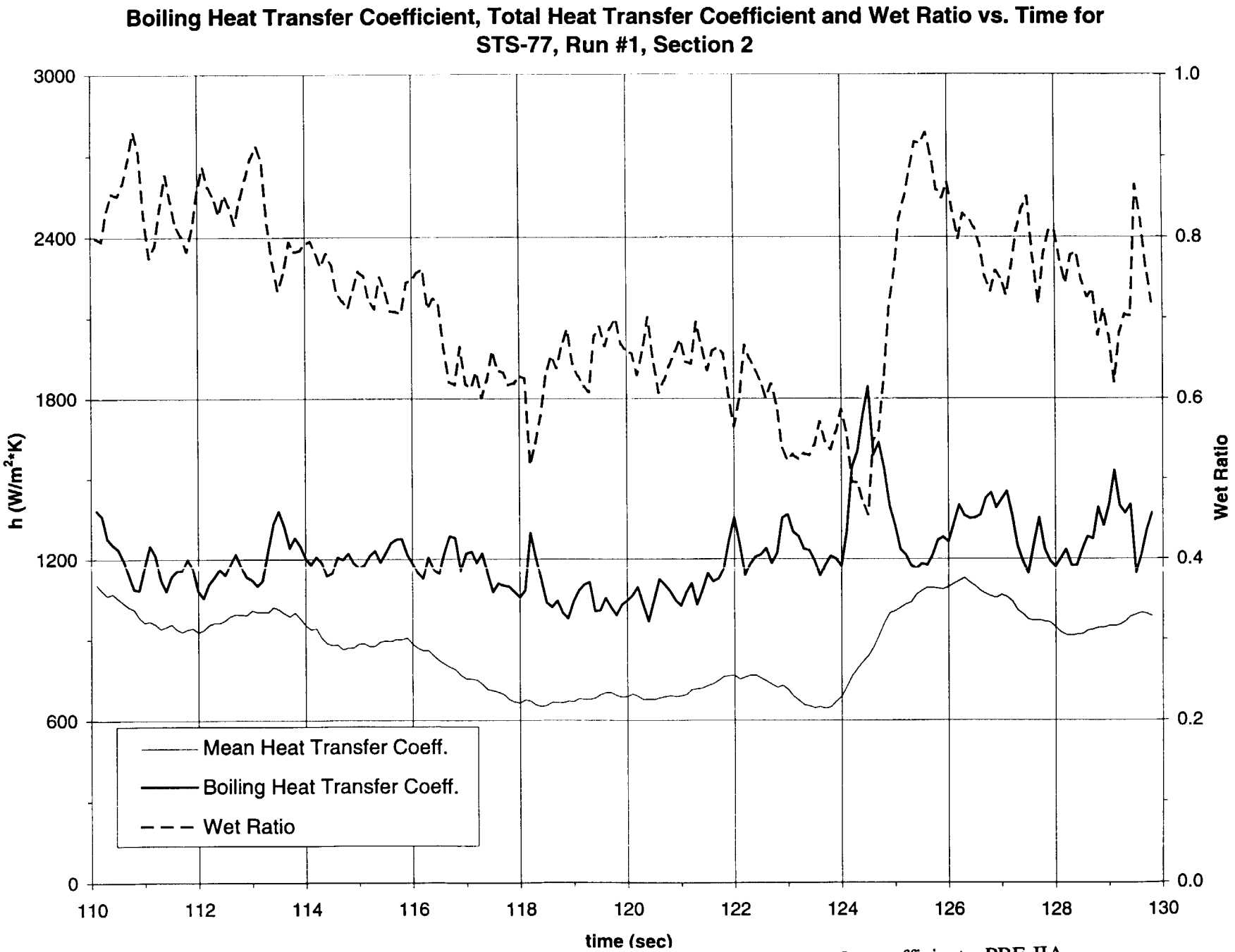

Figure B-10a-2-iii. Development of microgravity boiling heat transfer coefficient. PBE-IIA (STS-77) Run No. 1. Time interval: 110 - 130 seconds.

STS-77 Run #1, Section #2

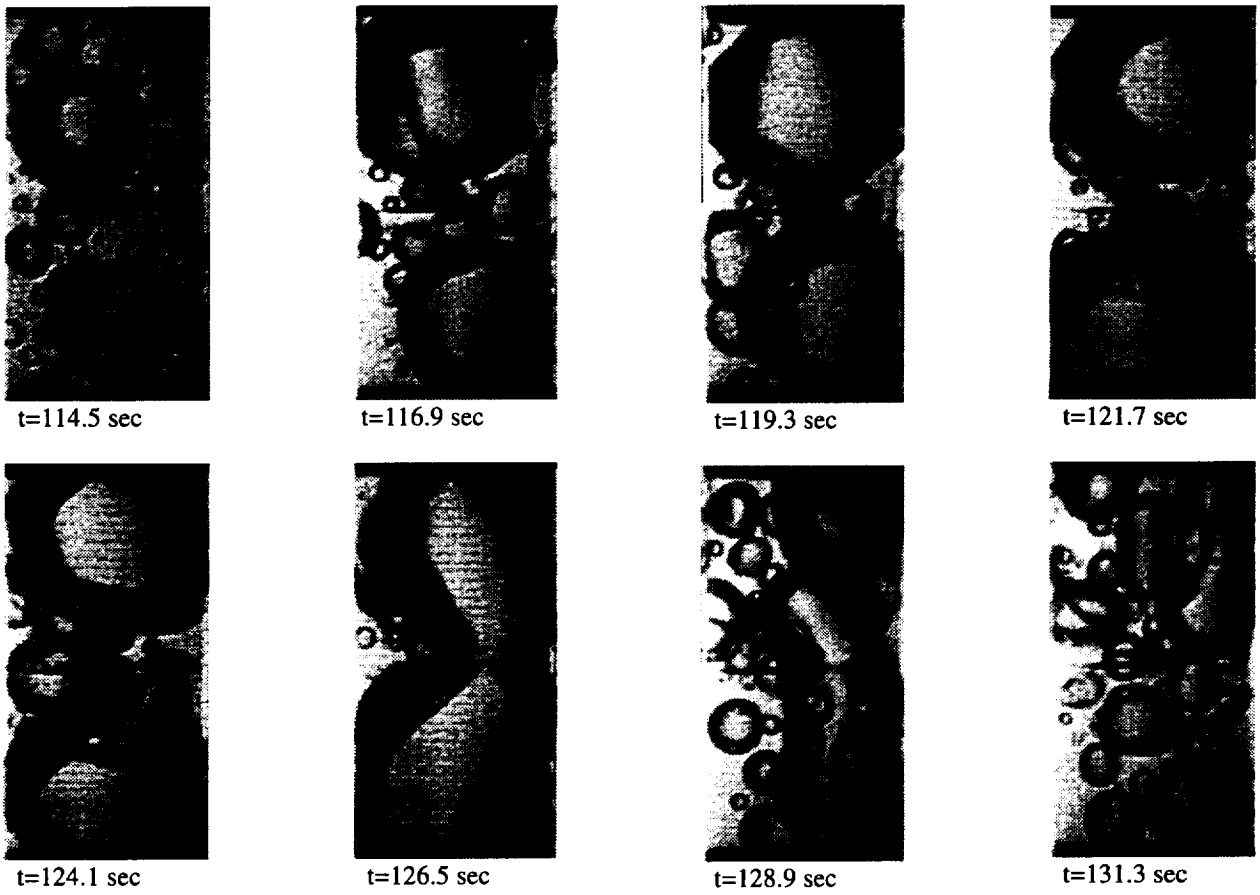

Figure B-10a-2-iv. Sample images showing dryout/rewetting. PBE-IIA (STS-77). Run No. 1. Time interval: 110 - 130 seconds.

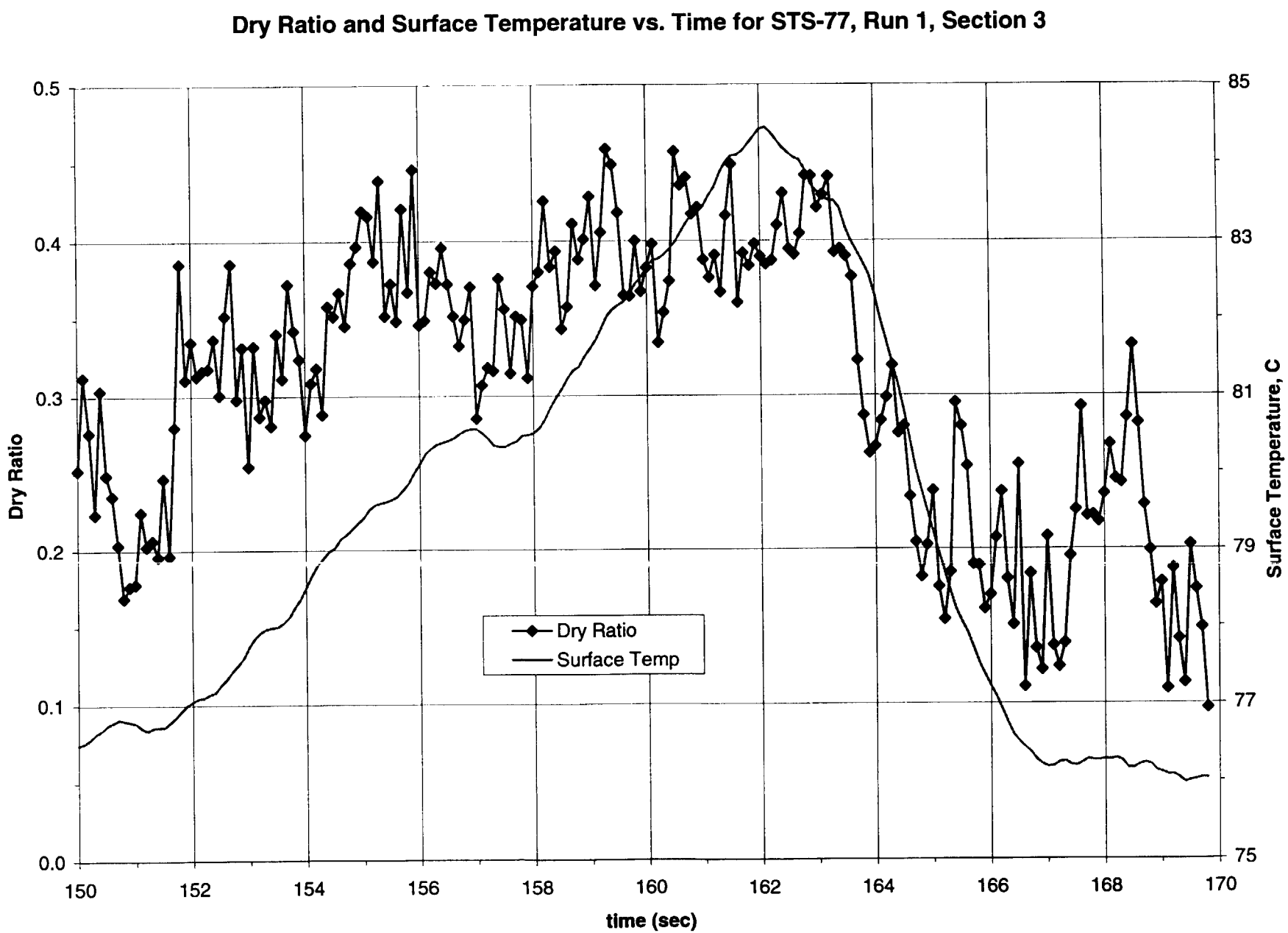

Figure B-10a-3-i. Heater surface dry fraction and mean temperature. PBE-IIA (STS-77). Run No. 1. Time interval: 150 - 170 seconds.

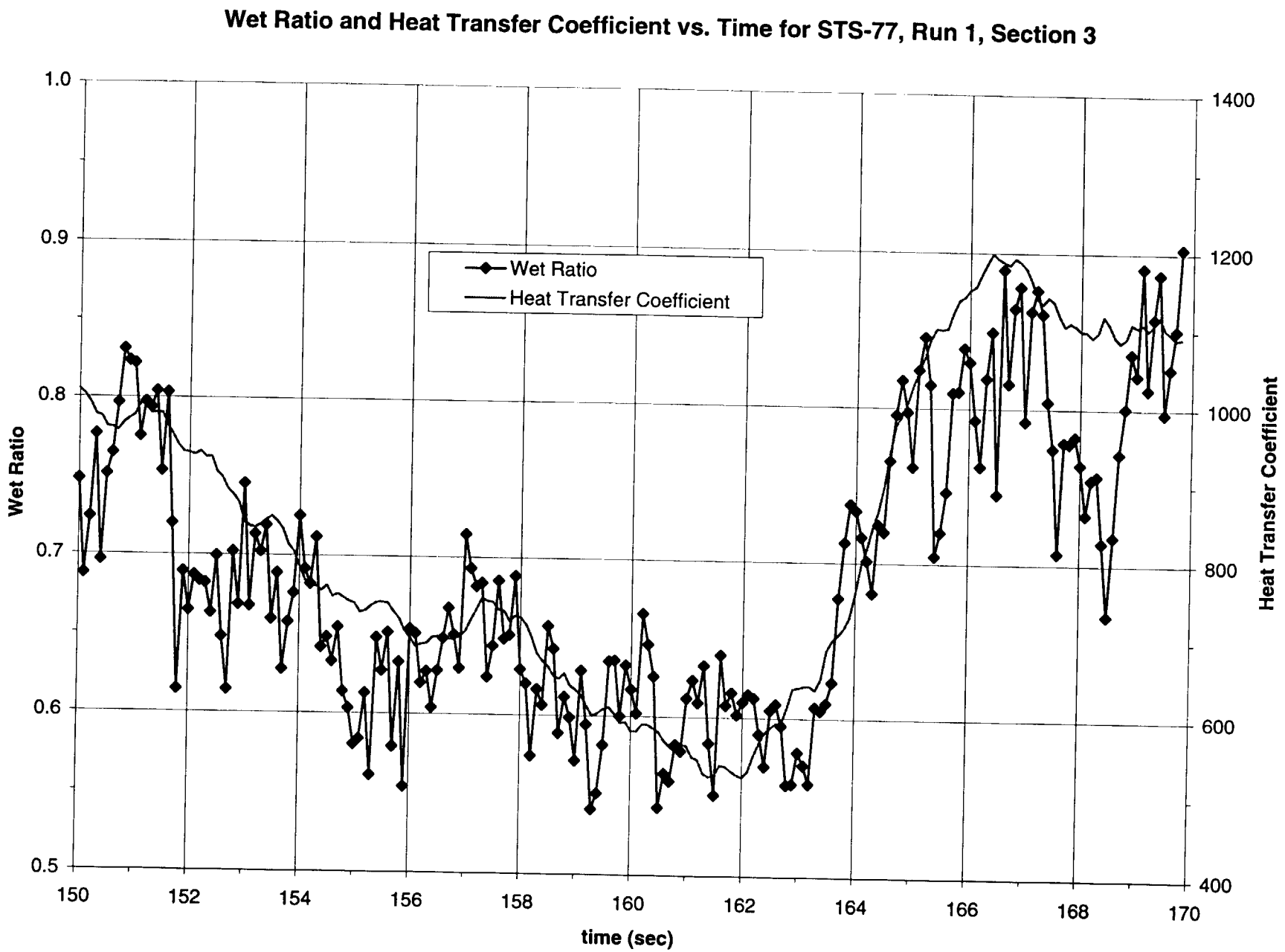

Figure B-10a-3-ii. Heater surface wet fraction and mean heat transfer coefficients. PBE-IIA (STS-77). Run No. 1. Time interval: 150 - 170 seconds.

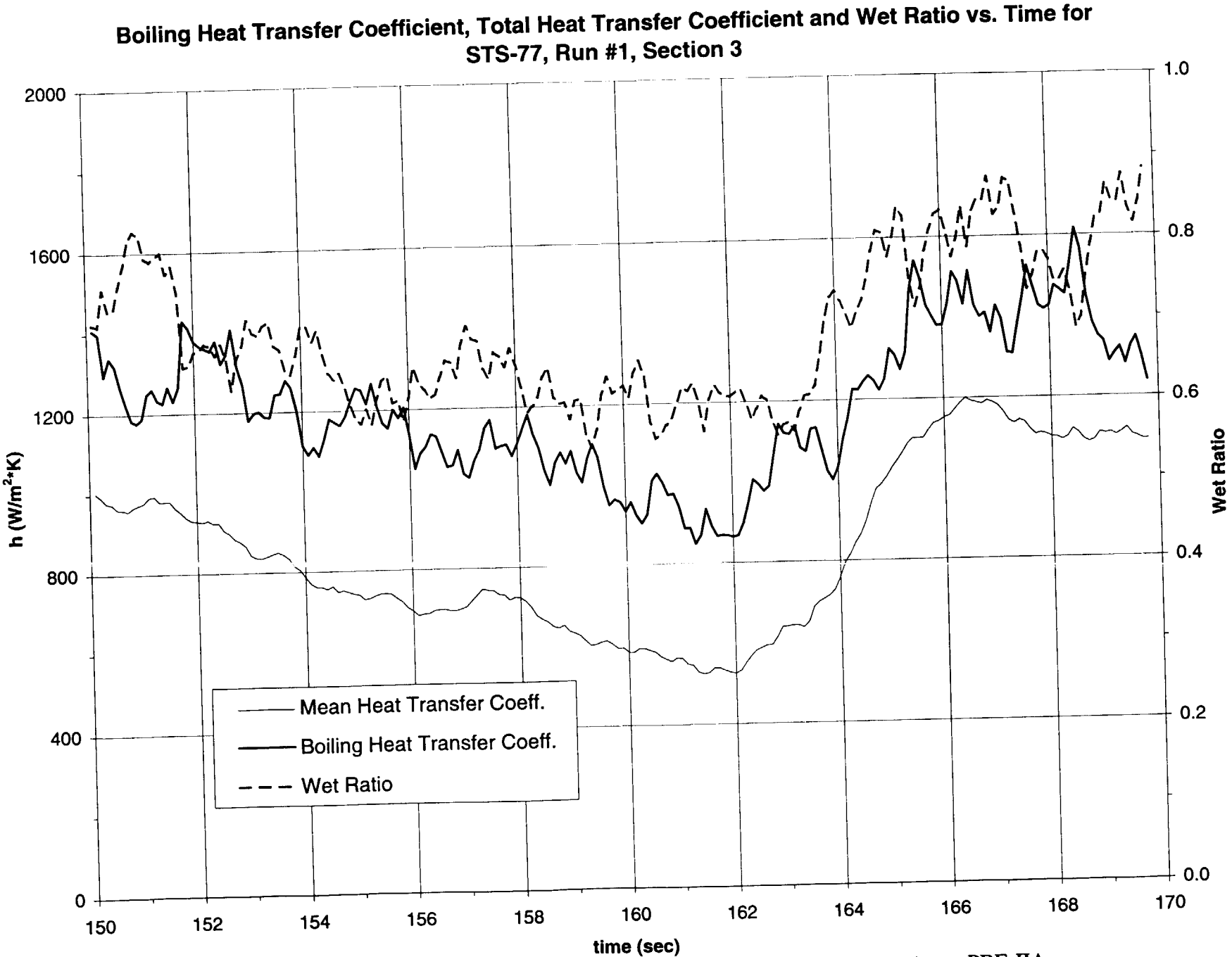

Figure B-10a-3-iii. Development of microgravity boiling heat transfer coefficient. PBE-IIA (STS-77). Run No. 1. Time interval: 150 - 170 seconds.

STS-77 Run #1, Section #3

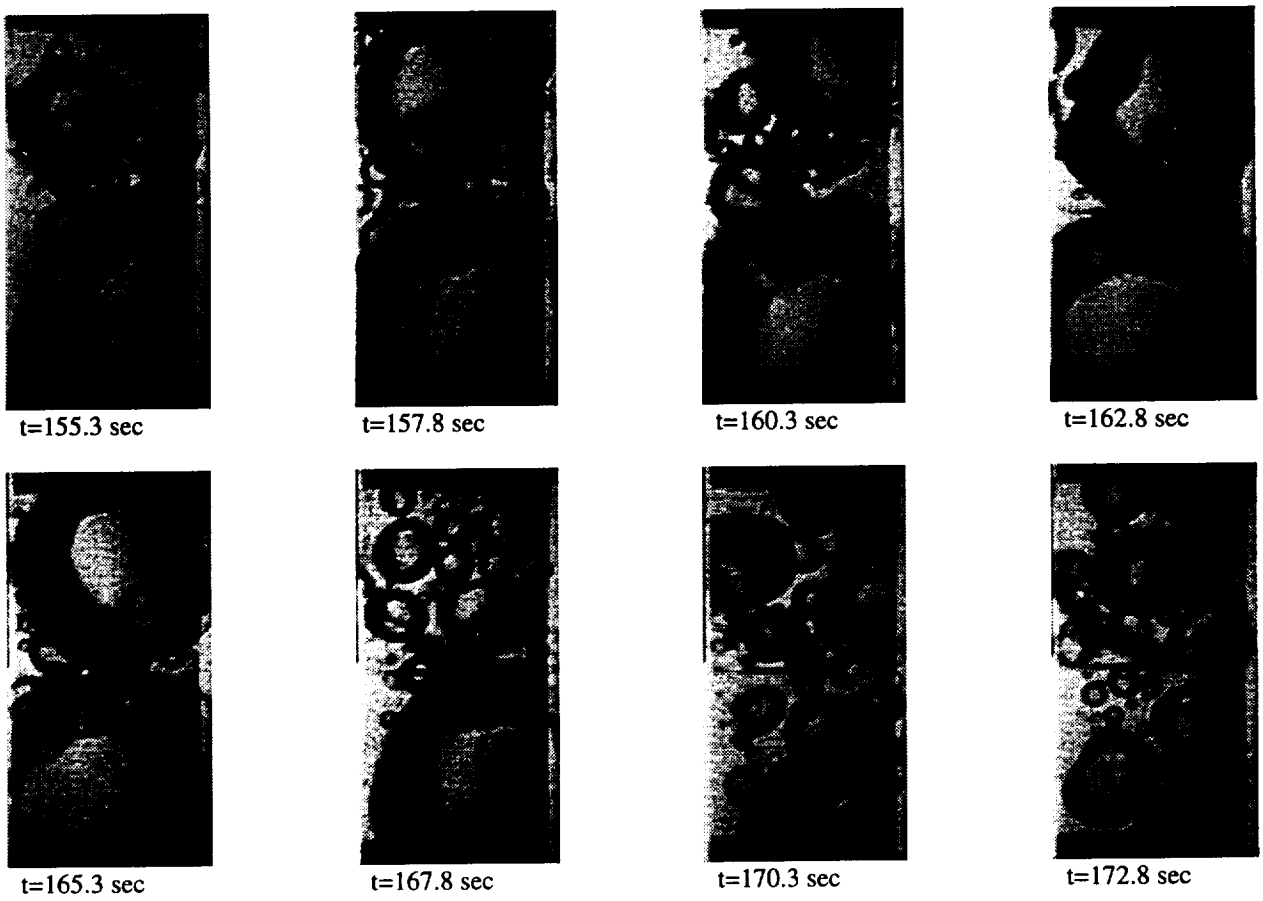

Figure B-10a-3-iv. Sample images showing dryout/rewetting. PBE-IIA (STS-77). Run No. 1. Time interval: 150 - 170 seconds.

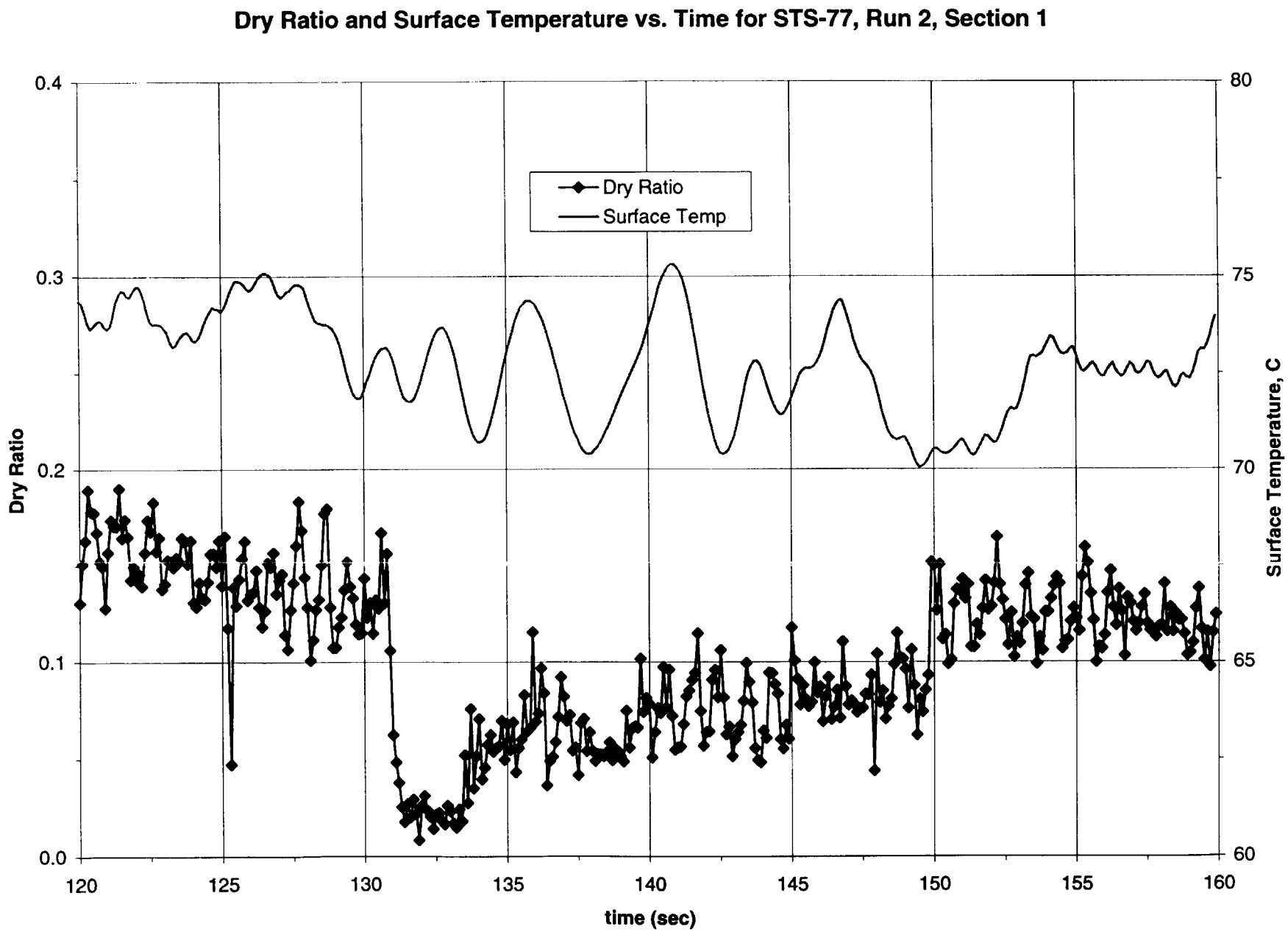

Figure B-10b-1-i. Heater surface dry fraction and mean temperature. PBE-IIA (STS-77). Run No. 2. Time interval: 120 - 160 seconds.

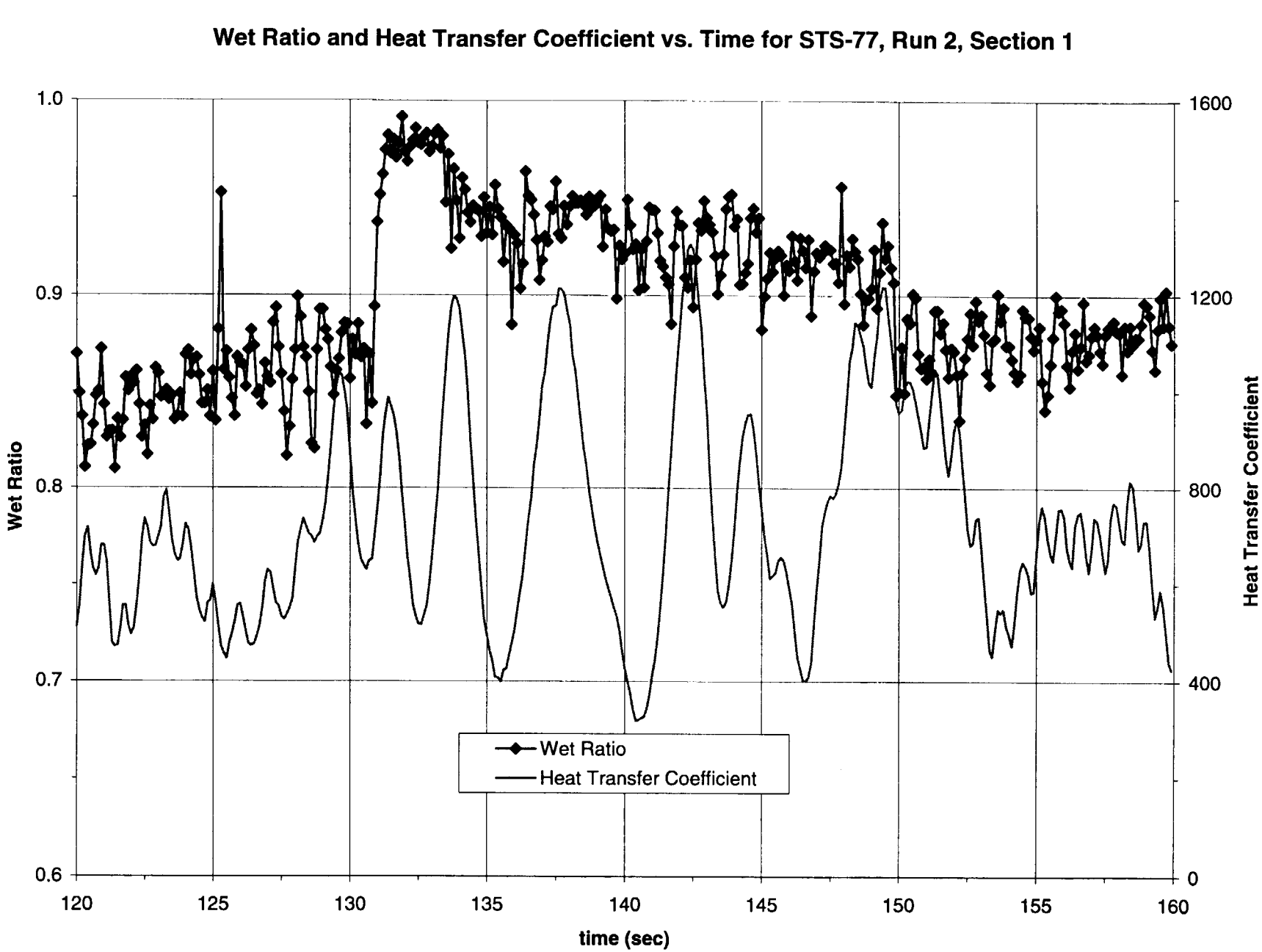

Figure B-10b-1-ii. Heater surface wet fraction and mean heat transfer coefficients. PBE-IIA (STS-77). Run No. 2. Time interval: 120 - 160 seconds.

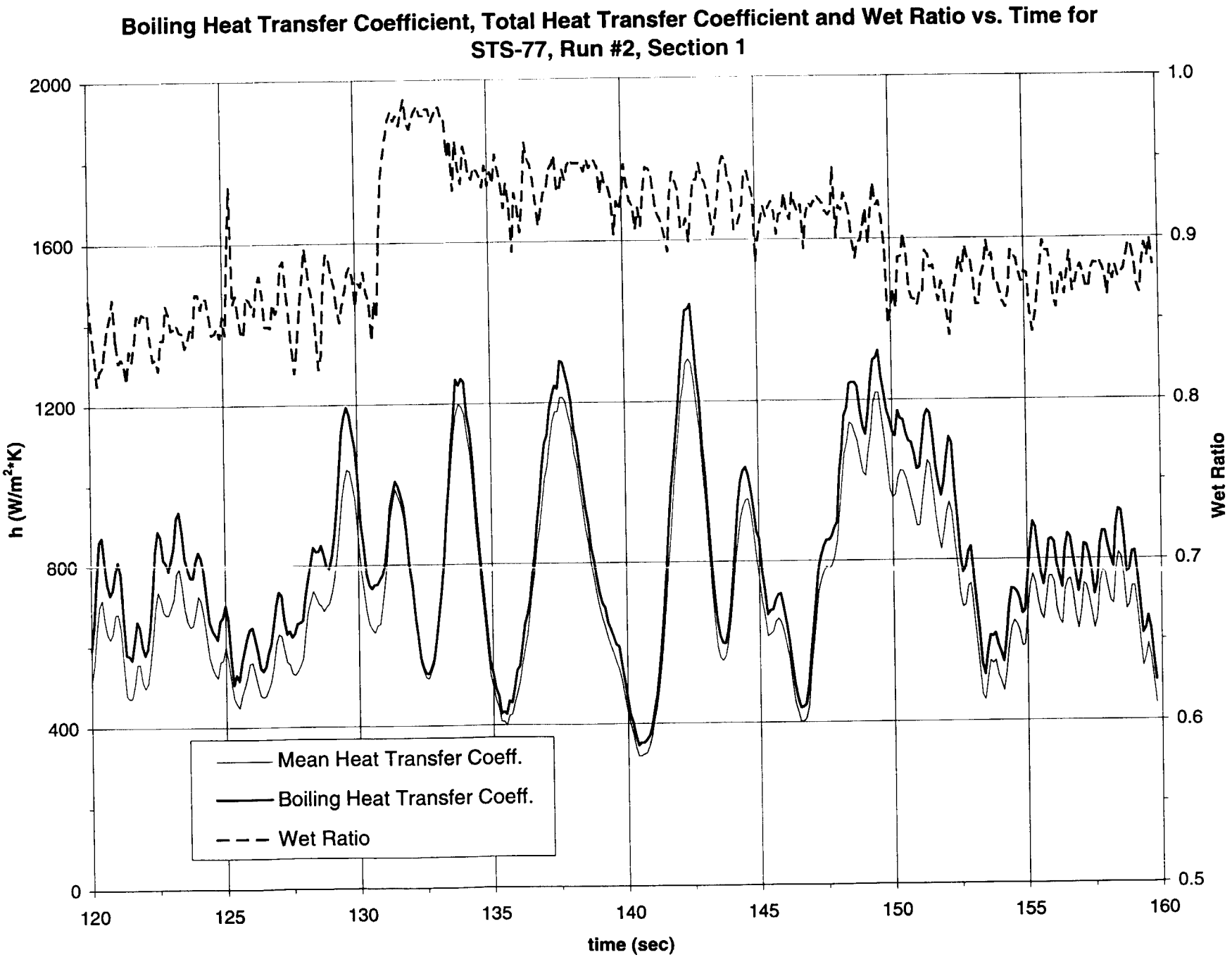

Figure B-10b-1-iii. Development of microgravity boiling heat transfer coefficient. PBE-IIA (STS-77). Run No. 2. Time interval: 120 - 160 seconds.

STS-77 Run #2, Section #1

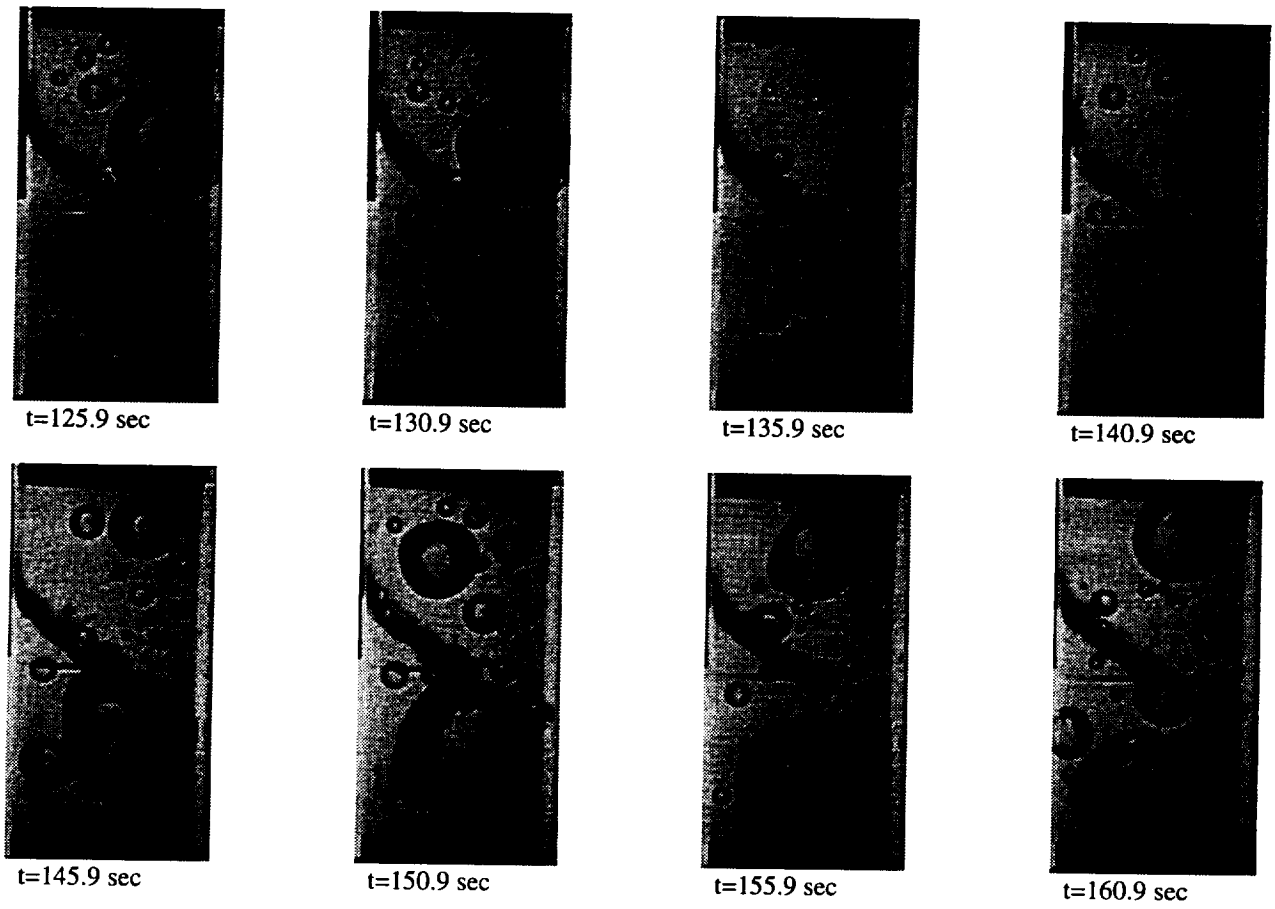

Figure B-10b-1-iv. Sample images showing dryout/rewetting. PBE-IIA (STS-77). Run No. 2. Time interval: 120 - 160 seconds.

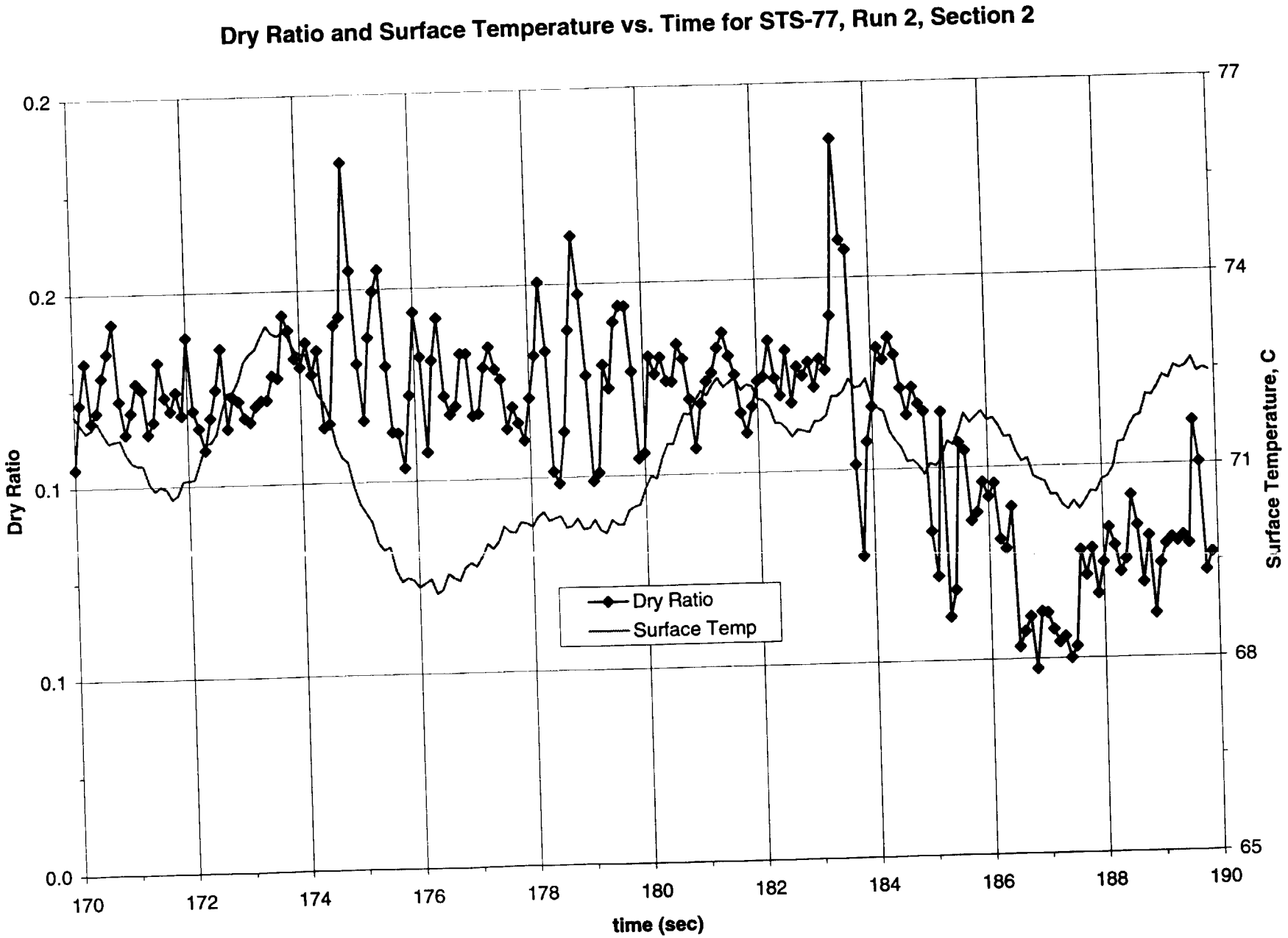

Figure B-10b-2-i. Heater surface dry fraction and mean temperature. PBE-IIA (STS-77). Run No. 2. Time interval: 170 - 190 seconds.

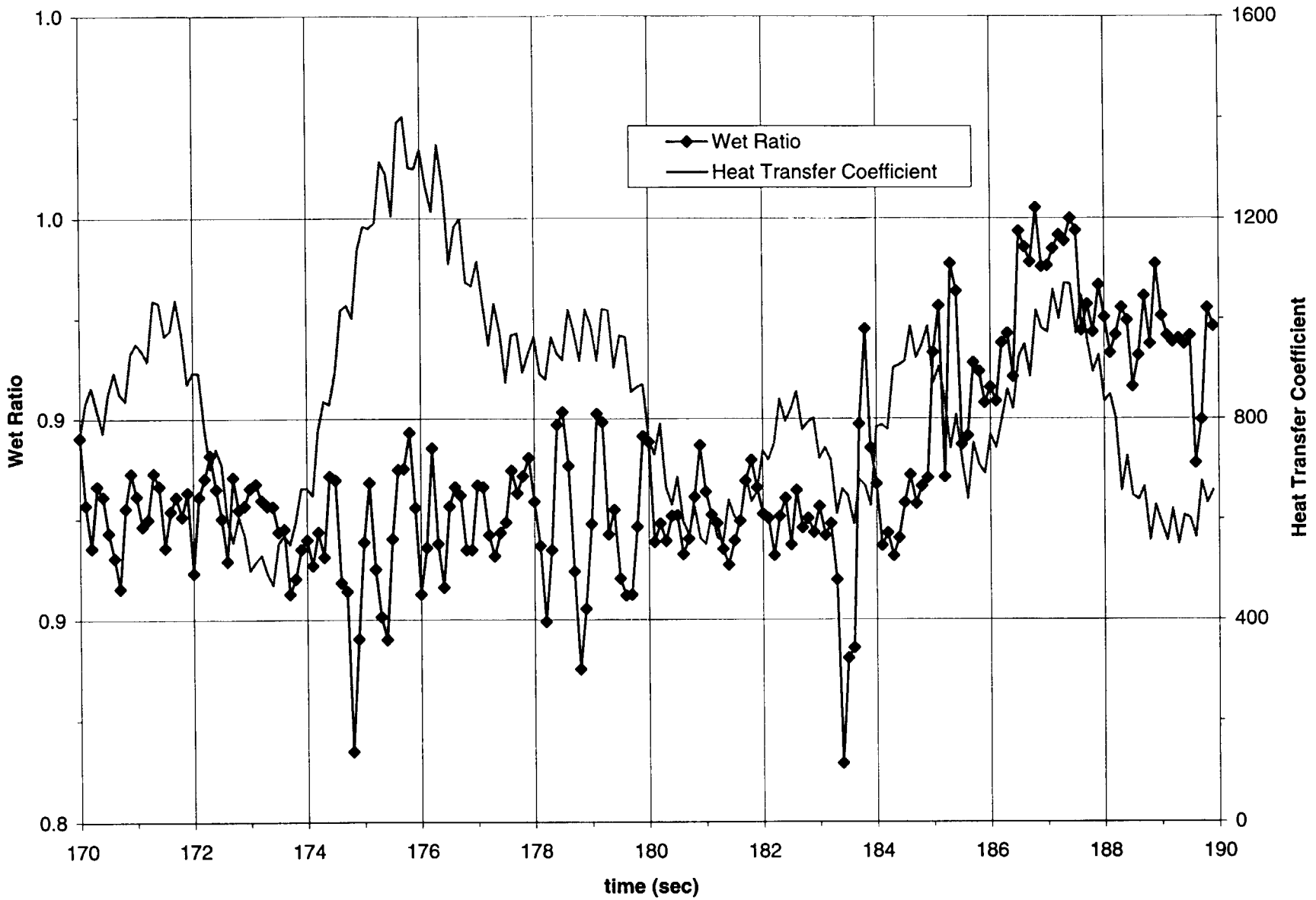

Figure B-10b-2-ii. Heater surface wet fraction and mean heat transfer coefficients. PBE-IIA (STS-77). Run No. 2. Time interval: 170 - 190 seconds.

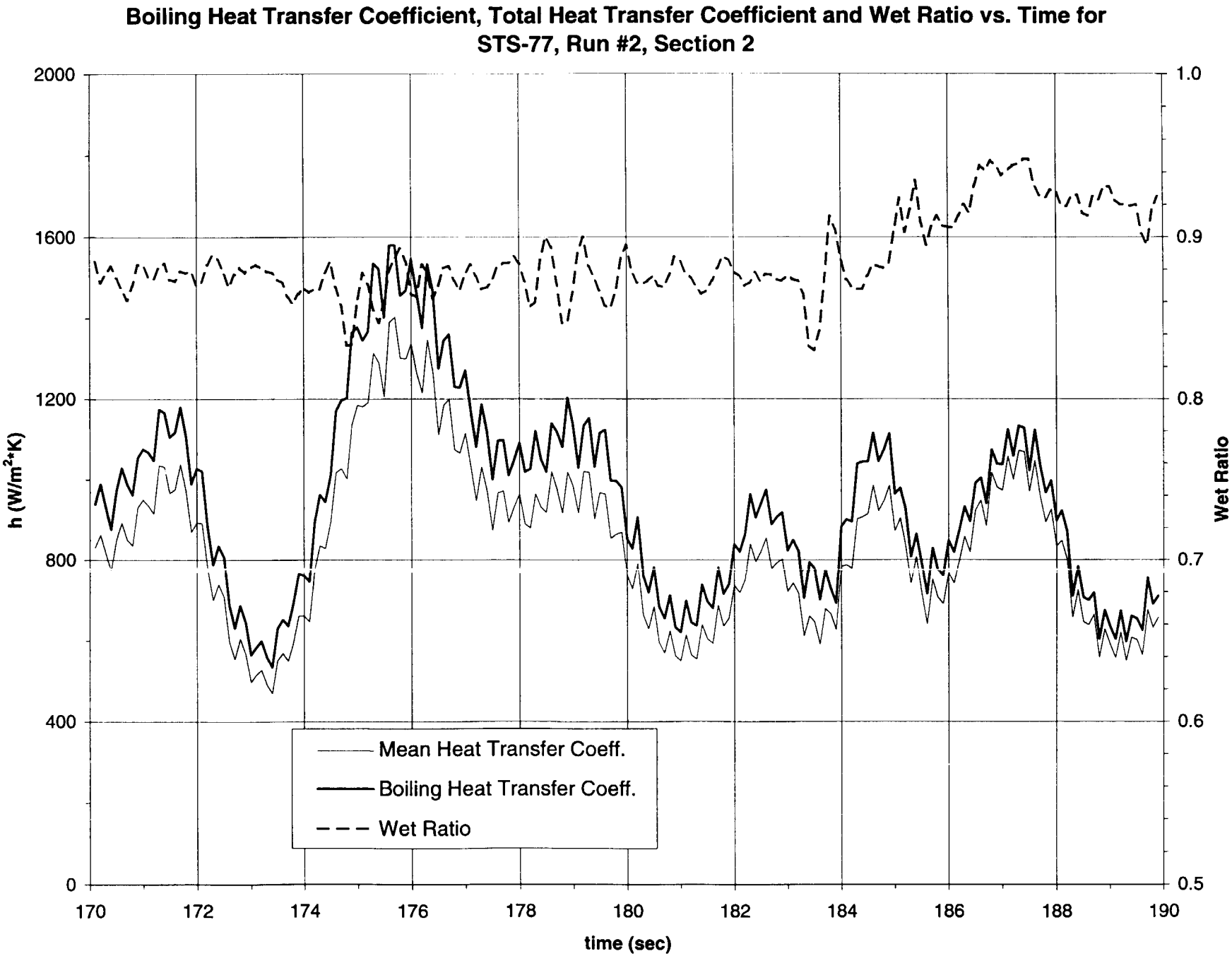

Figure B-10b-2-iii. Development of microgravity boiling heat transfer coefficient. PBE-IIA (STS-77). Run No. 2. Time interval: 170 - 190 seconds.

STS-77 Run #2, Section #2

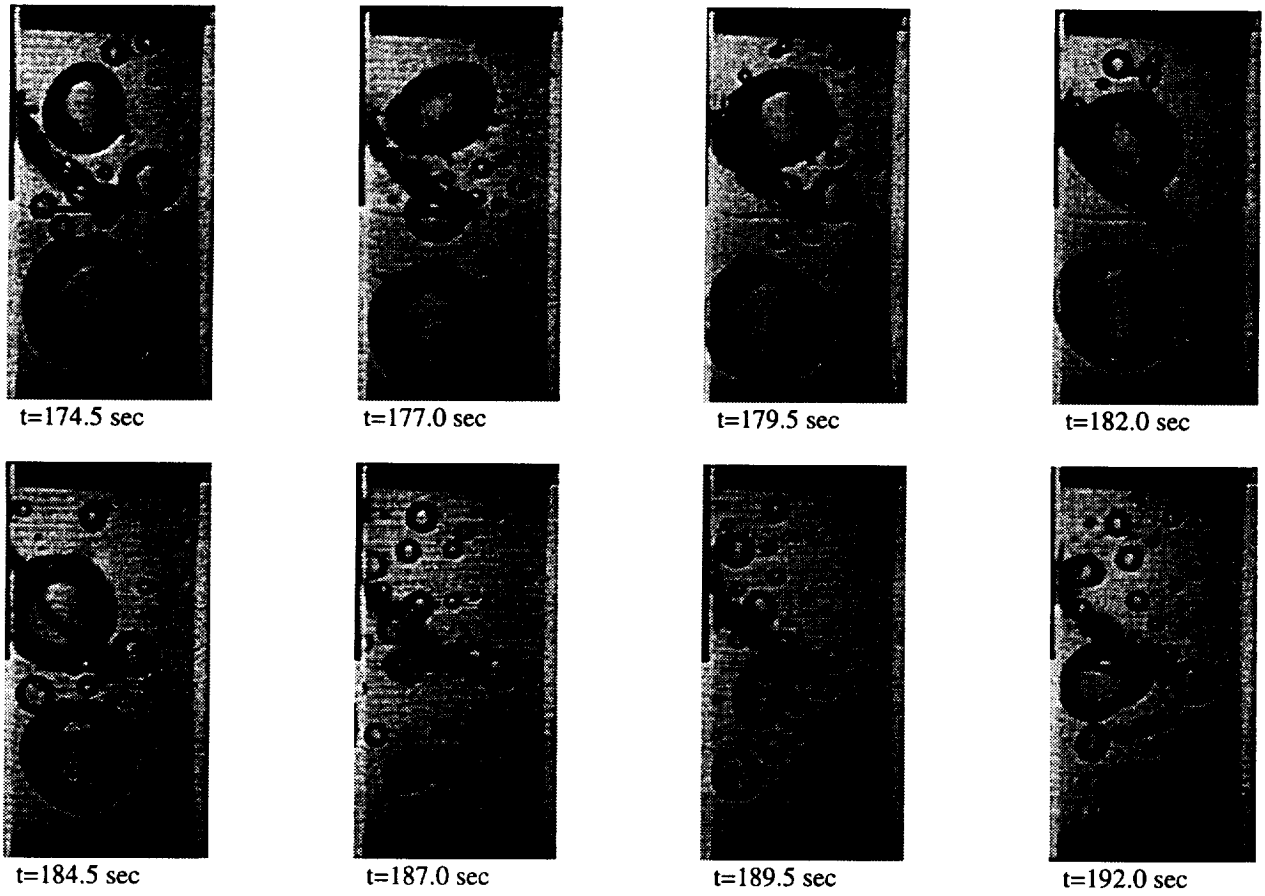

Figure B-10b-2-iv. Sample images showing dryout/rewetting. PBE-IIA (STS-77). Run No. 2. Time interval: 170 - 190 seconds.

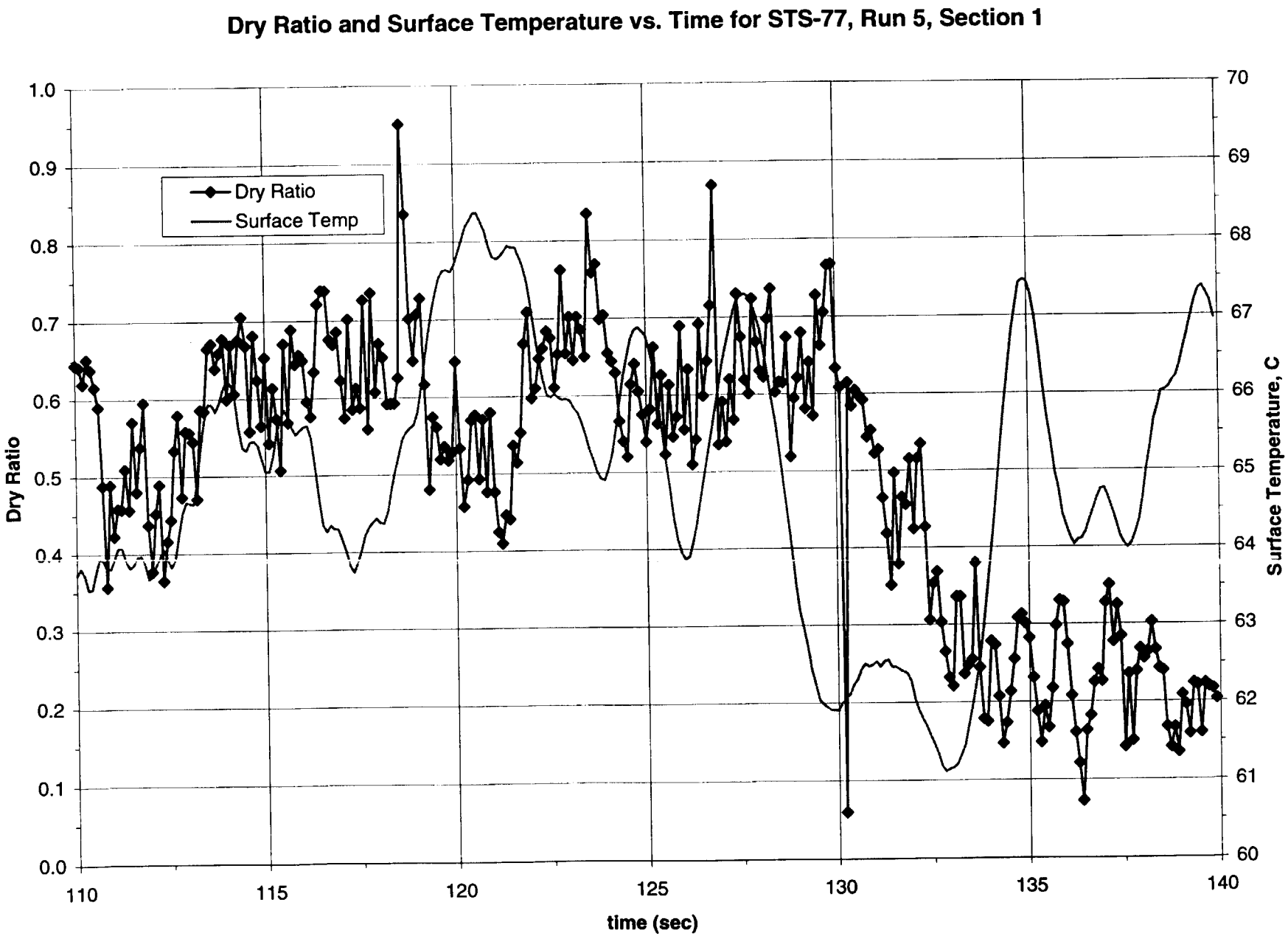

Figure B-10e-1-i. Heater surface dry fraction and mean temperature. PBE-IIA (STS-77). Run No. 5. Time interval: 110 - 140 seconds.

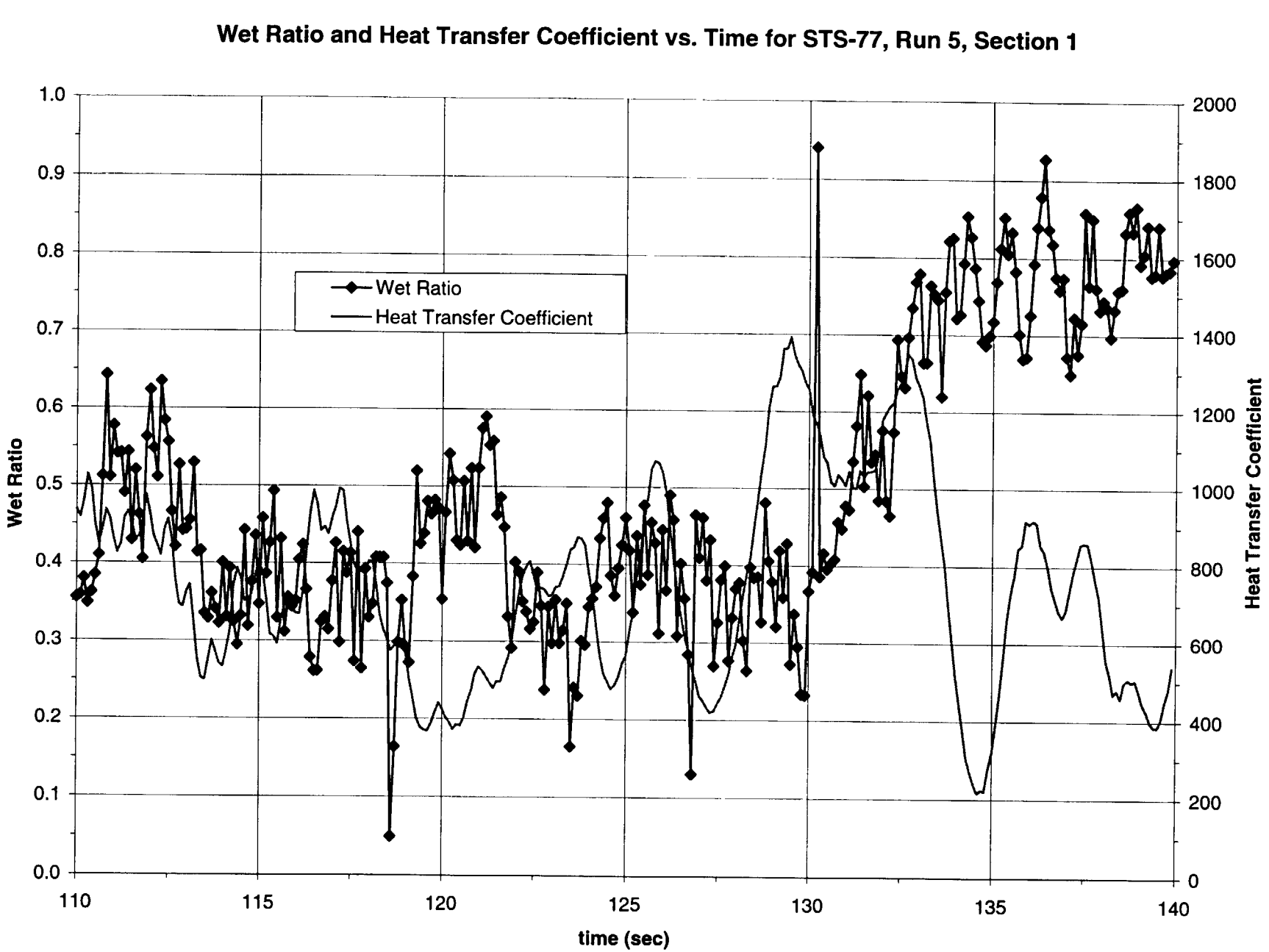

Figure B-10e-1-ii. Heater surface wet fraction and mean heat transfer coefficients. PBE-IIA (STS-77). Run No. 5. Time interval: 110 - 140 seconds.

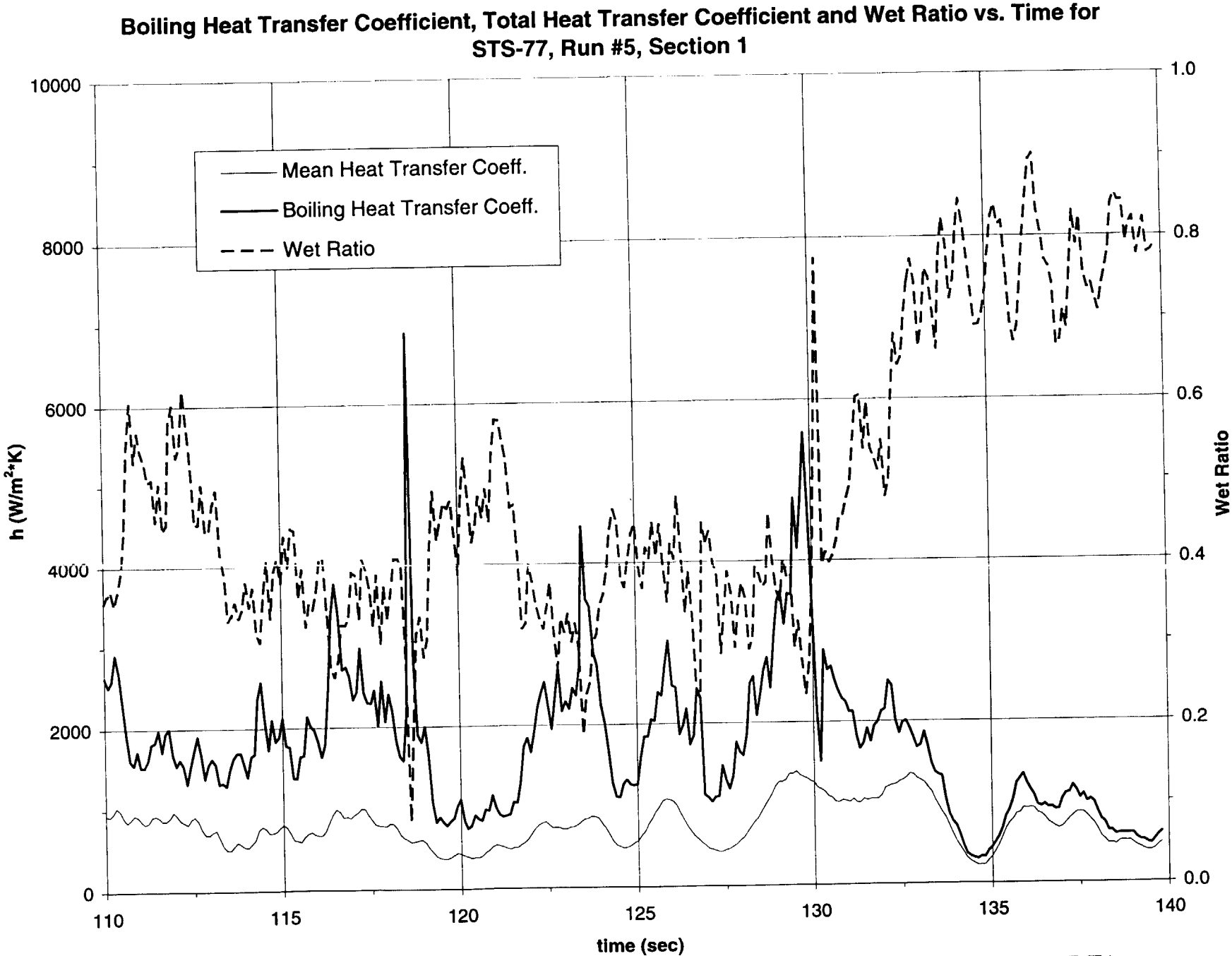

Figure B-10e-1-iii. Development of microgravity boiling heat transfer coefficient. PBE-IIA (STS-77). Run No. 5. Time interval: 110 - 140 seconds.

STS-77 Run #5, Section #1

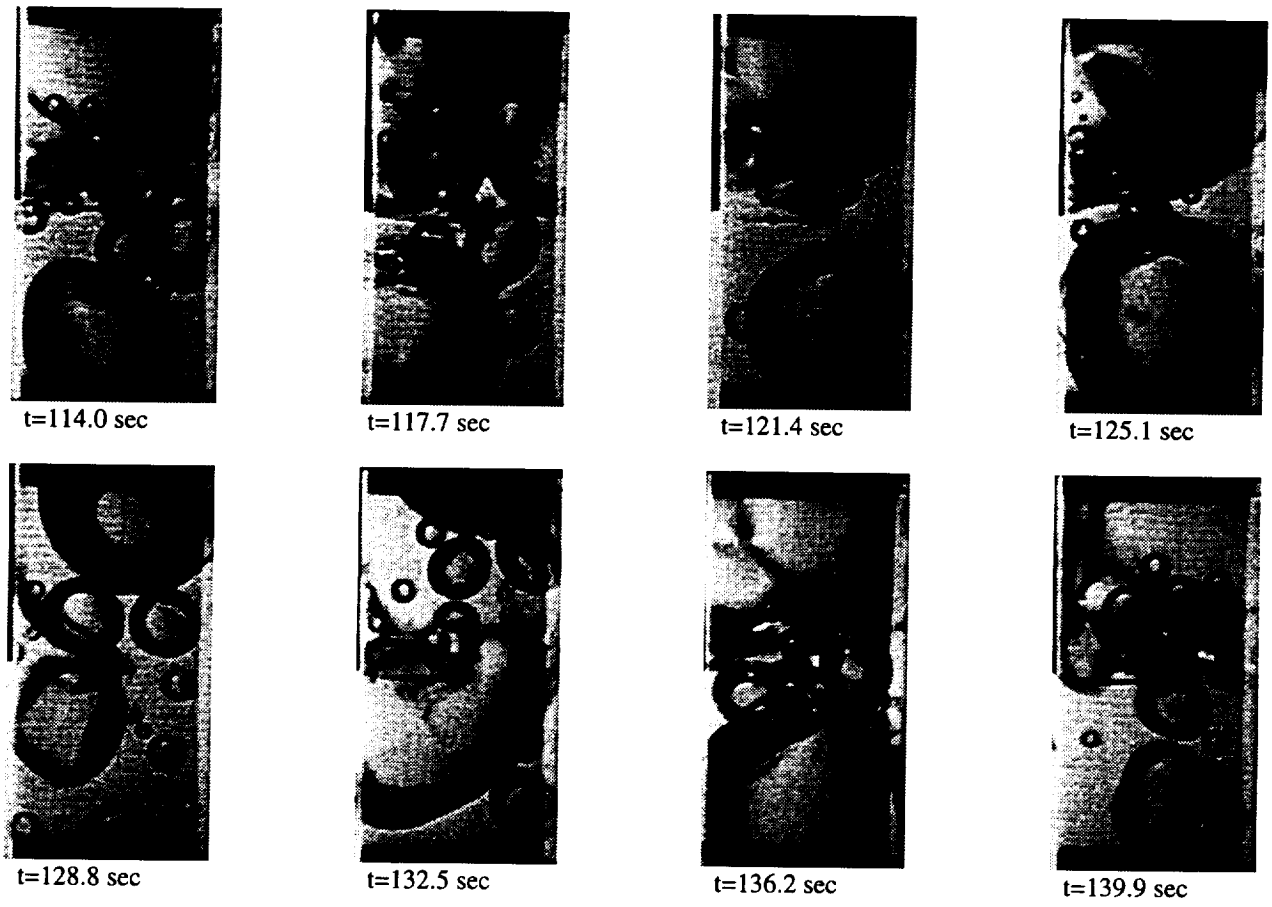

Figure B-10e-1-iv. Sample images showing dryout/rewetting. PBE-IIA (STS-77). Run No. 5. Time interval: 110 - 140 seconds.

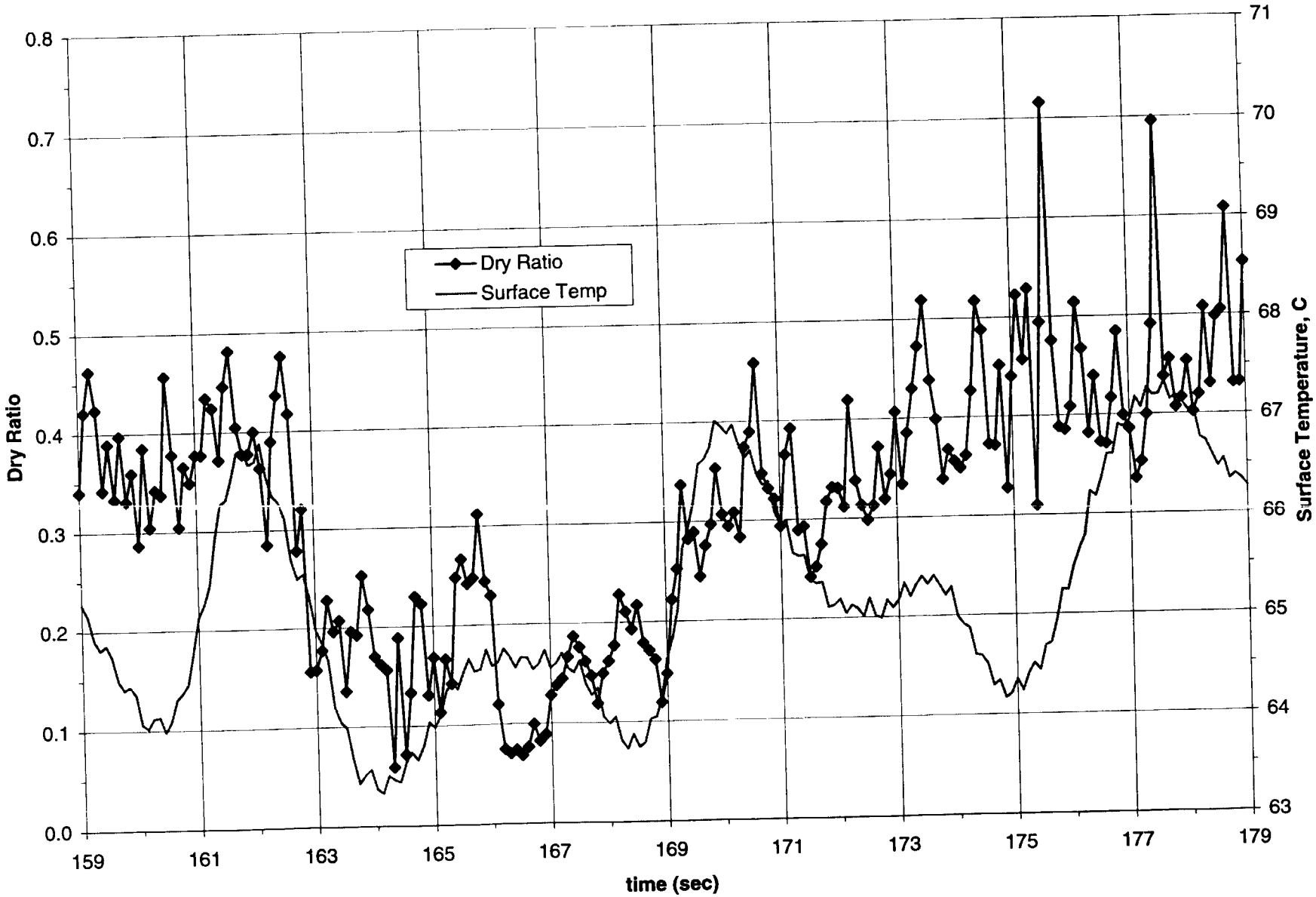

Figure B-10e-2-i. Heater surface dry fraction and mean temperature. PBE-IIA (STS-77). Run No. 5. Time interval: 159-179 seconds.

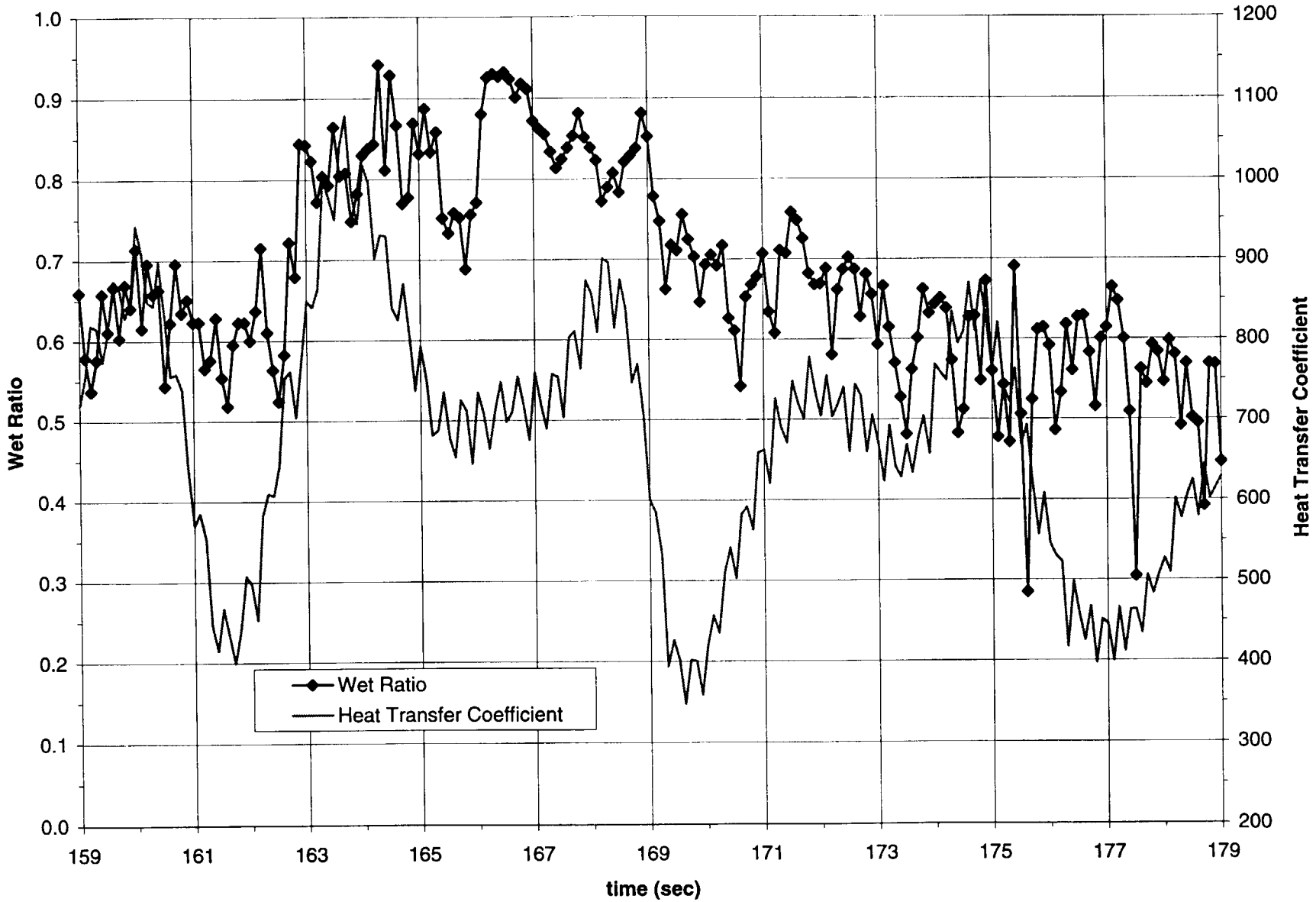

Figure B-10e-2-ii. Heater surface wet fraction and mean heat transfer coefficients. PBE-IIA (STS-77). Run No. 5. Time interval: 159-179 seconds.

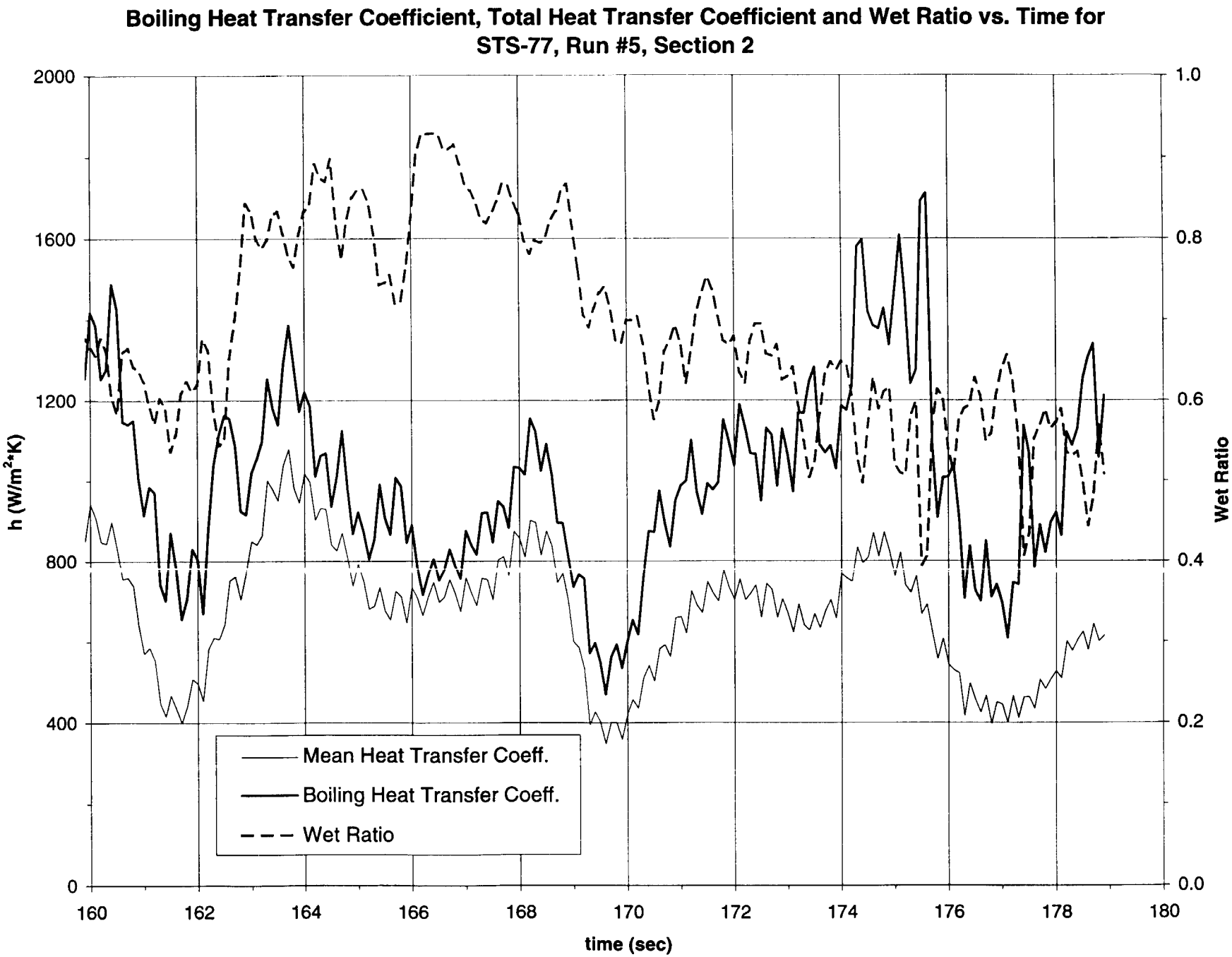

Figure B-10e-2-iii. Development of microgravity boiling heat transfer coefficient. PBE-IIA (STS-77). Run No. 5. Time interval: 159-179 seconds.

STS-77 Run #5, Section #2

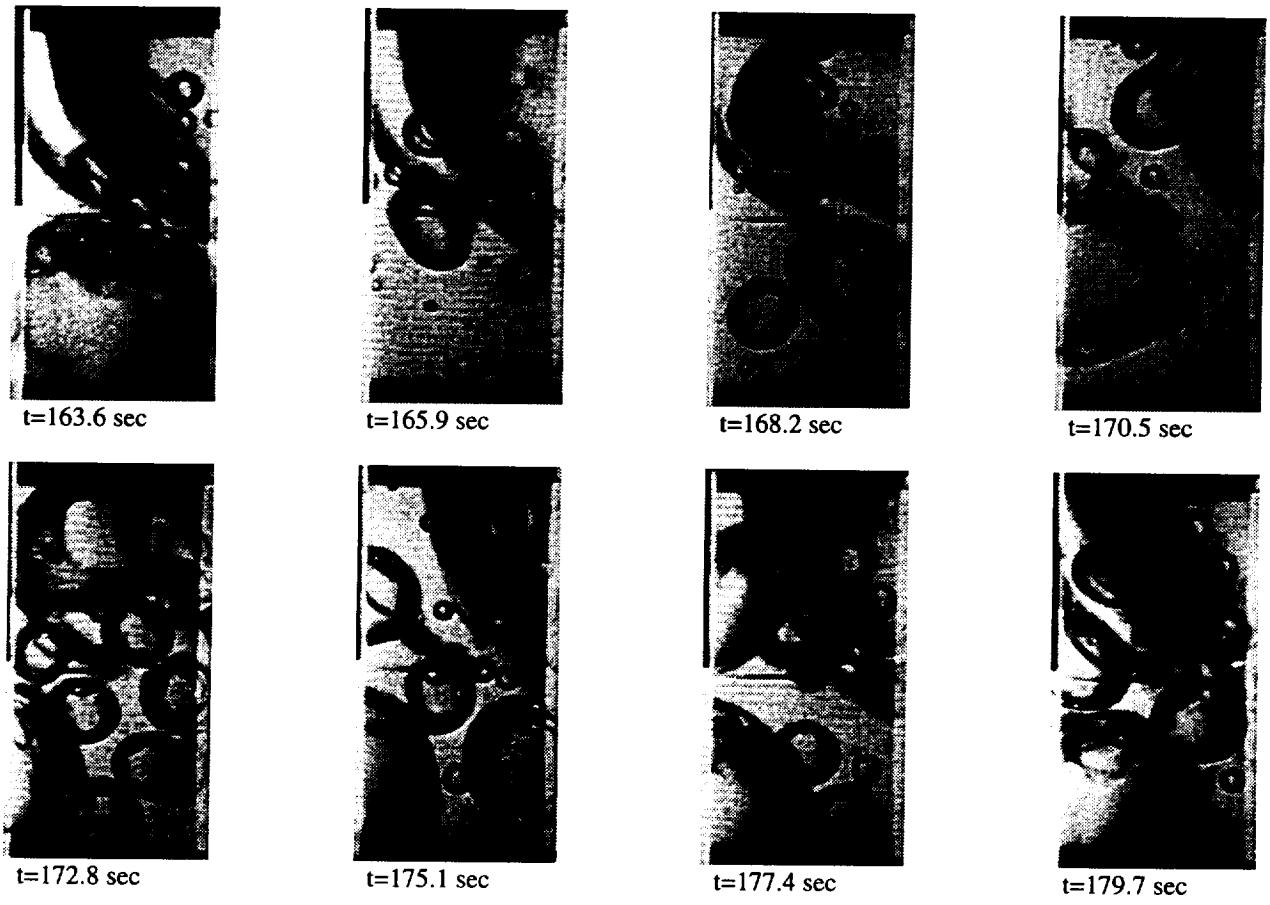

Figure B-10e-2-iv. Sample images showing dryout/rewetting. PBE-IIA (STS-77). Run No. 5. Time interval: 159-179 seconds.

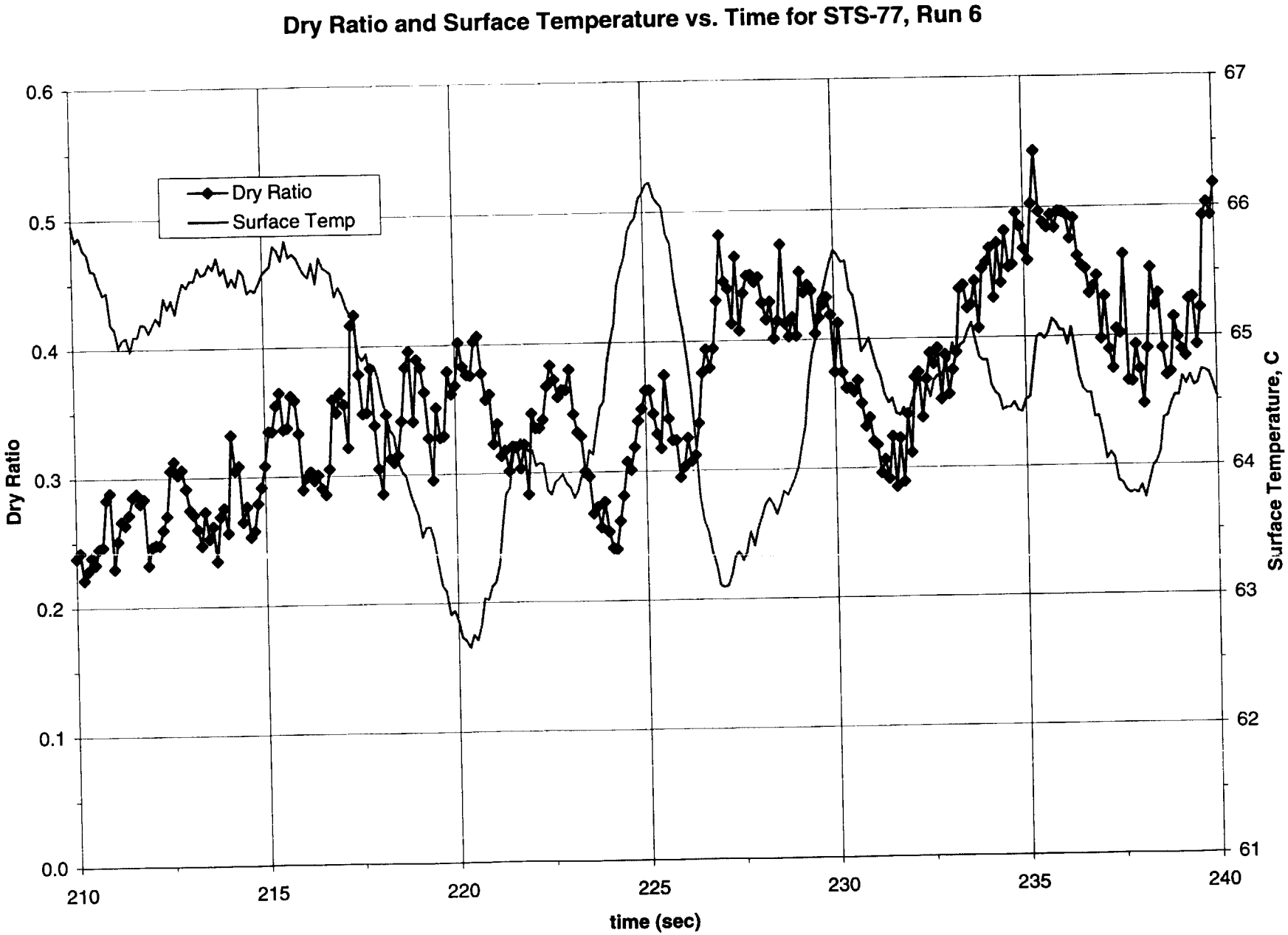

Figure B-10f-1-i. Heater surface dry fraction and mean temperature. PBE-IIA (STS-77). Run No. 6. Time interval: 210-240 seconds.

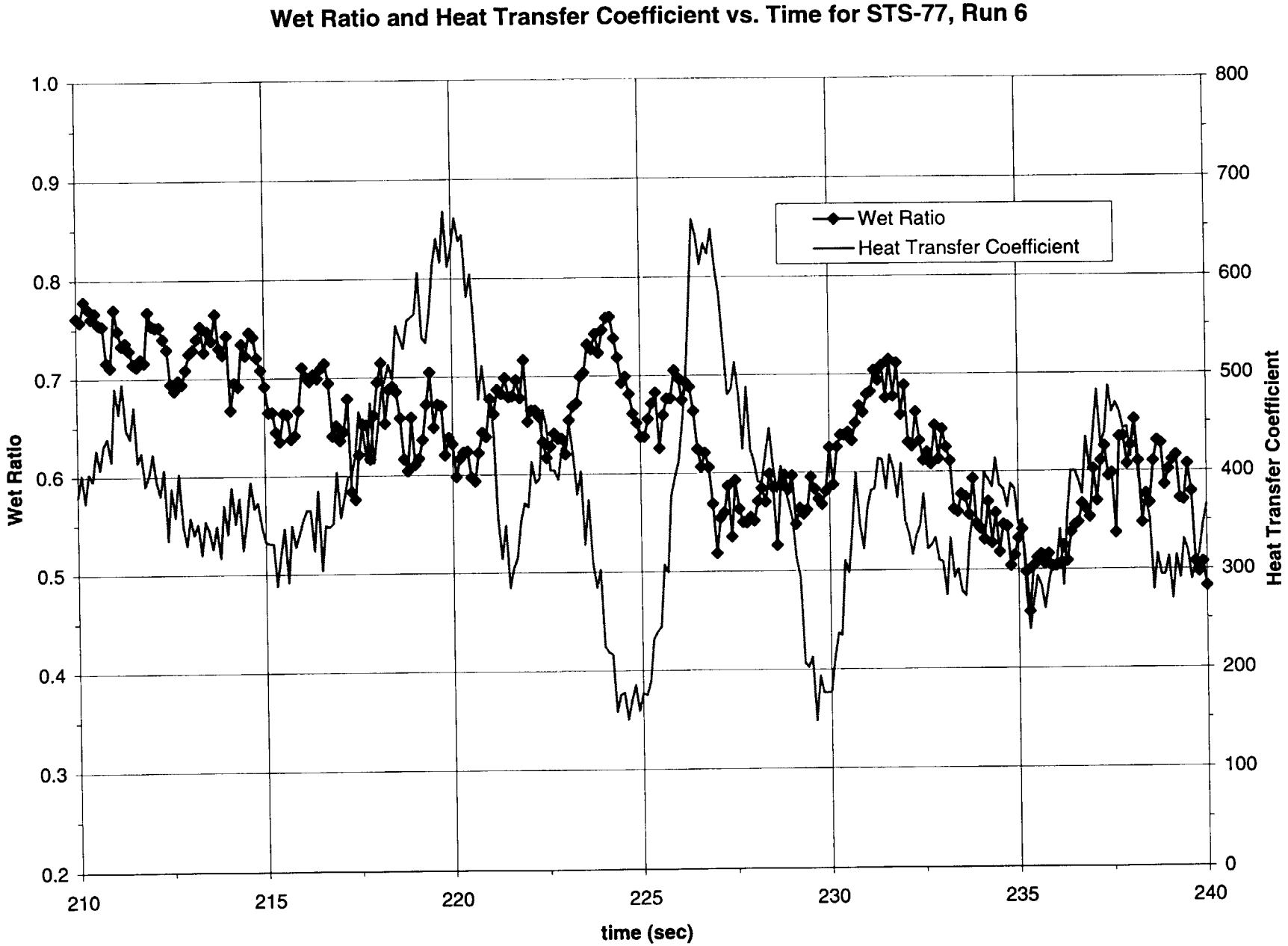

Figure B-10f-1-ii. Heater surface wet fraction and mean heat transfer coefficients. PBE-IIA (STS-77). Run No. 6. Time interval: 210-240 seconds.

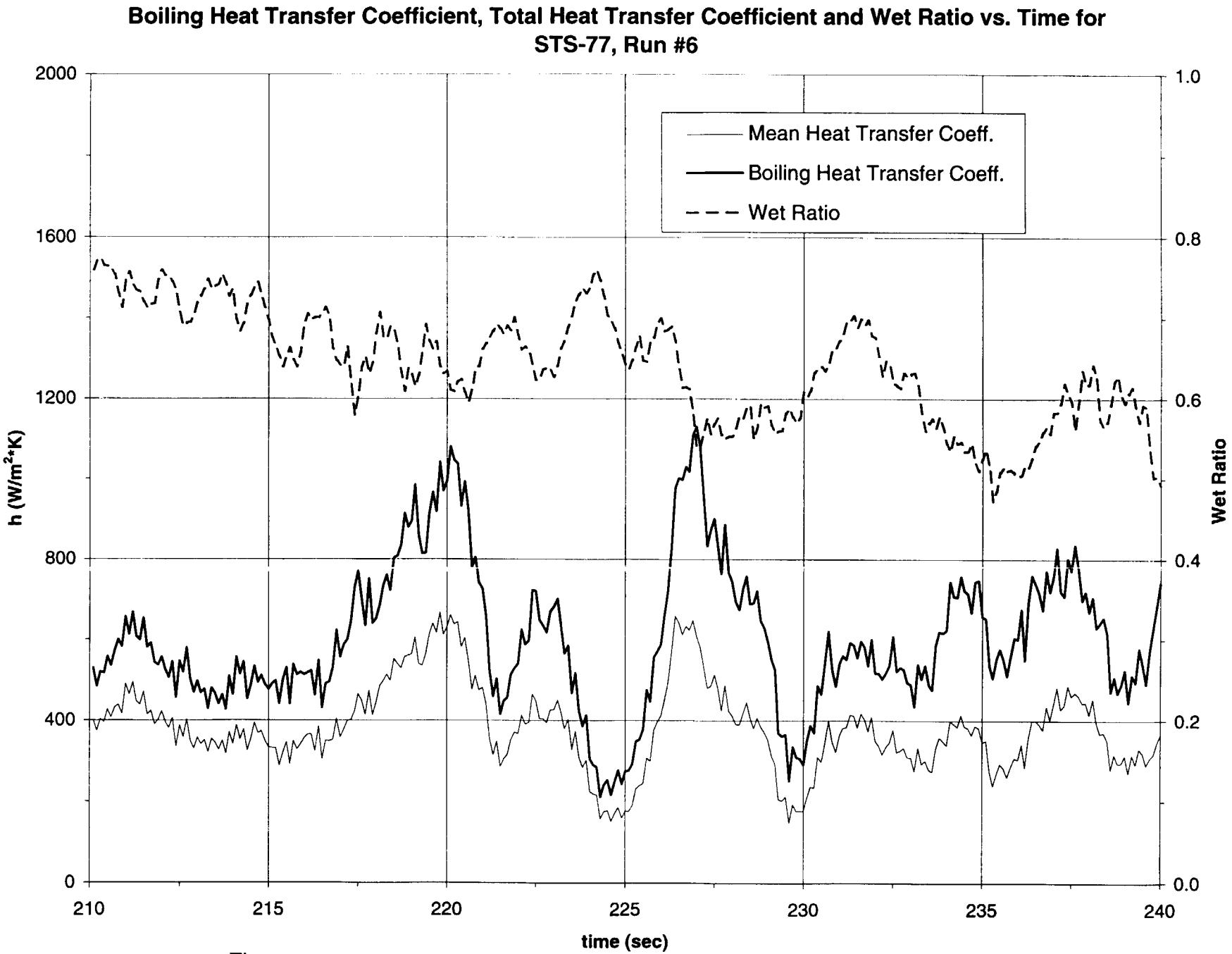

Figure B-10f-1-iii. Development of microgravity boiling heat transfer coefficient. PBE-IIA (STS-77) Run No. 6. Time interval: 210-240 seconds

STS-77 Run #6

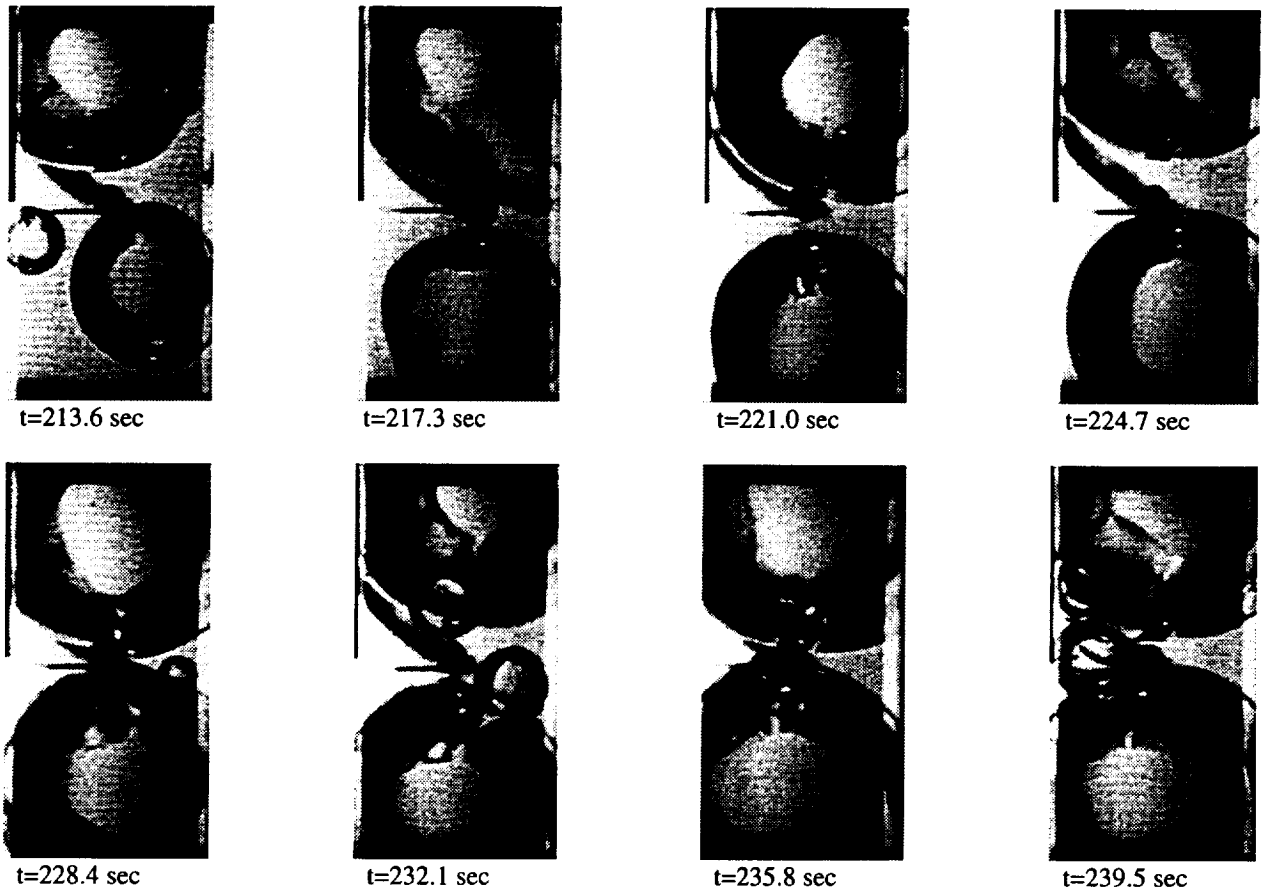

Figure B-10f-1-iv. Sample images showing dryout/rewetting. PBE-IIA (STS-77). Run No. 6. Time interval: 210-240 seconds.

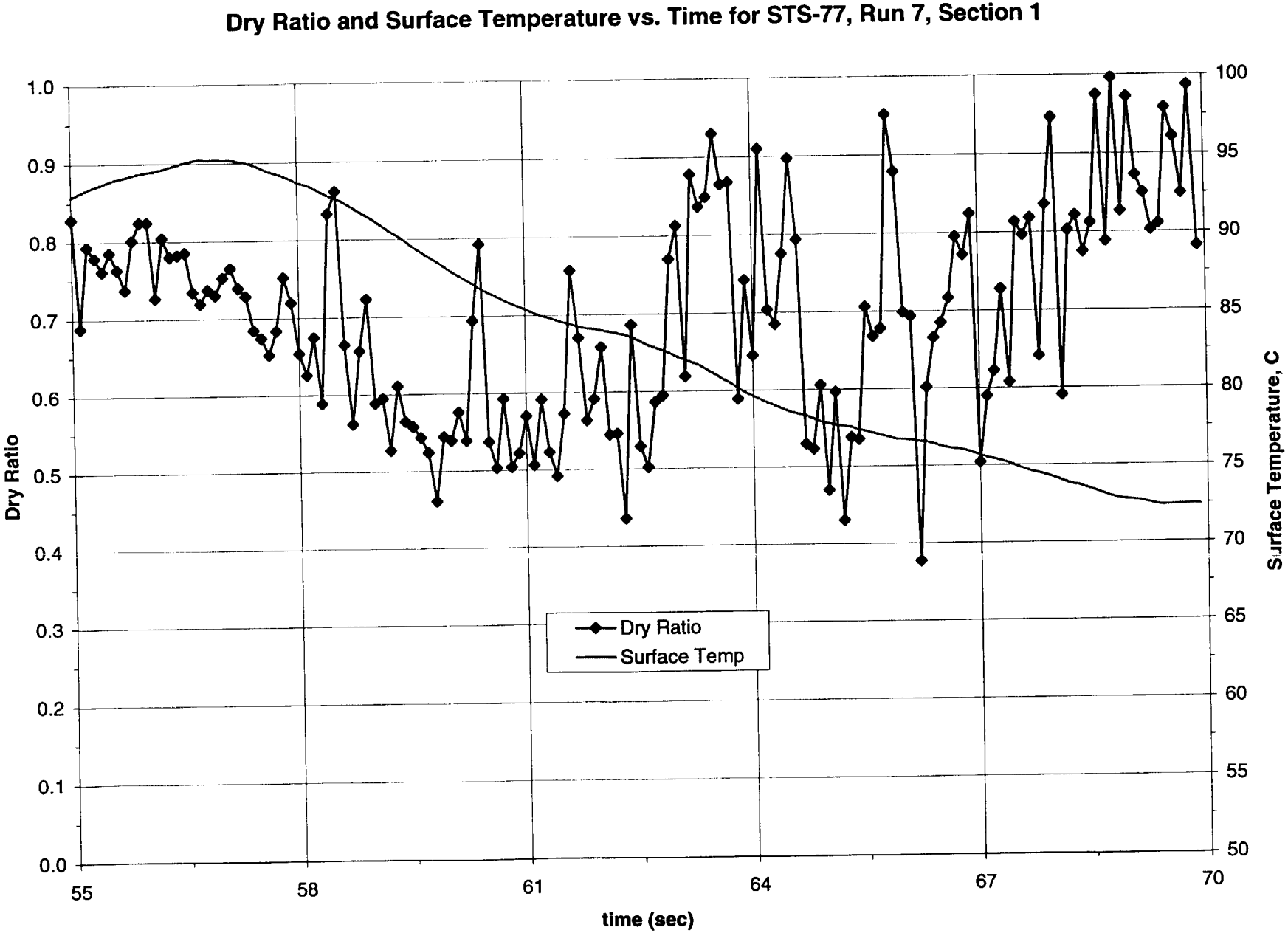

Figure B-10g-1-i. Heater surface dry fraction and mean temperature. PBE-IIA (STS-77). Run No. 7. Time interval: 55 - 70 seconds.

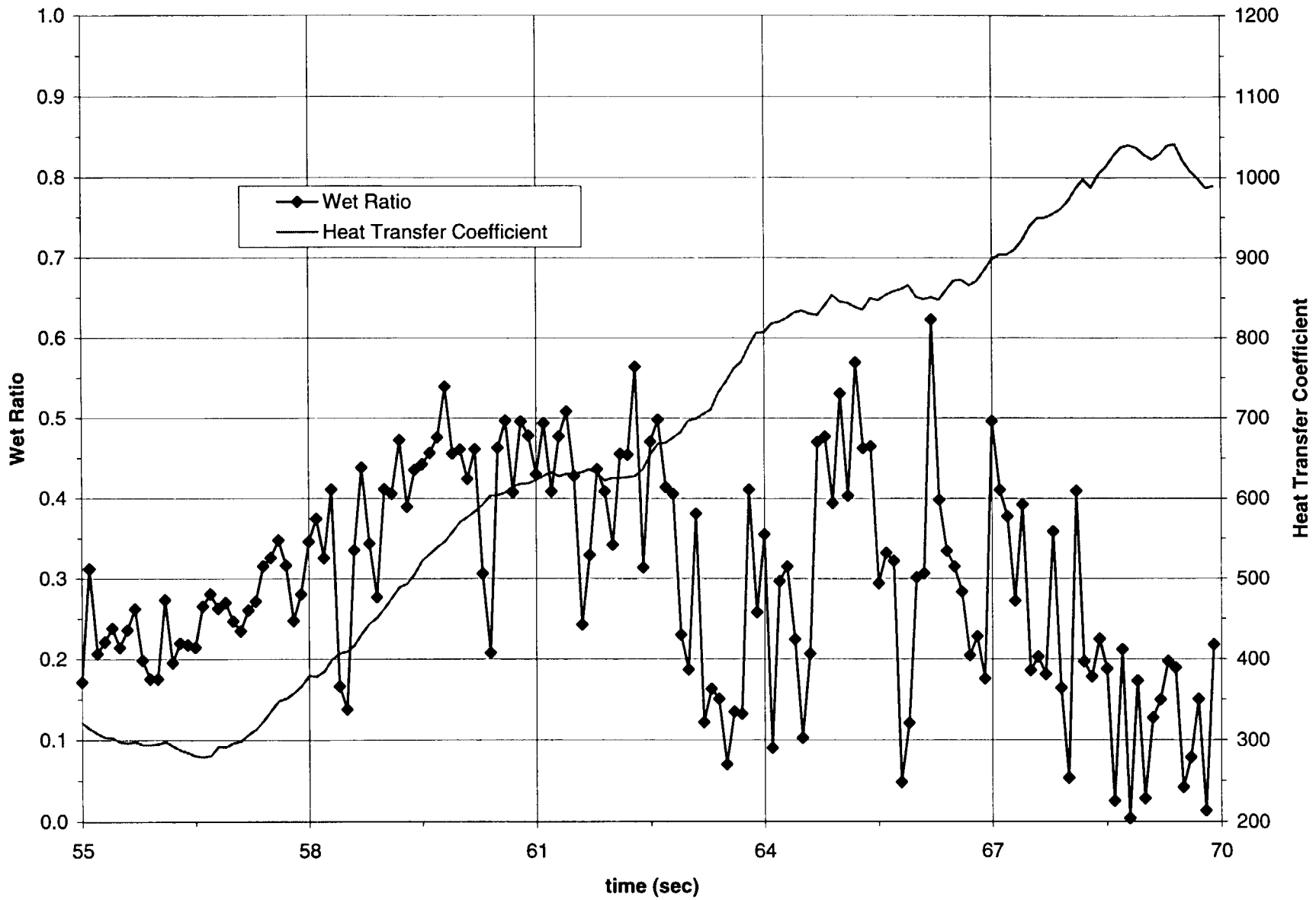

Figure B-10g-1-ii. Heater surface wet fraction and mean heat transfer coefficients. PBE-IIA (STS-77). Run No. 7. Time interval: 55 - 70 seconds.

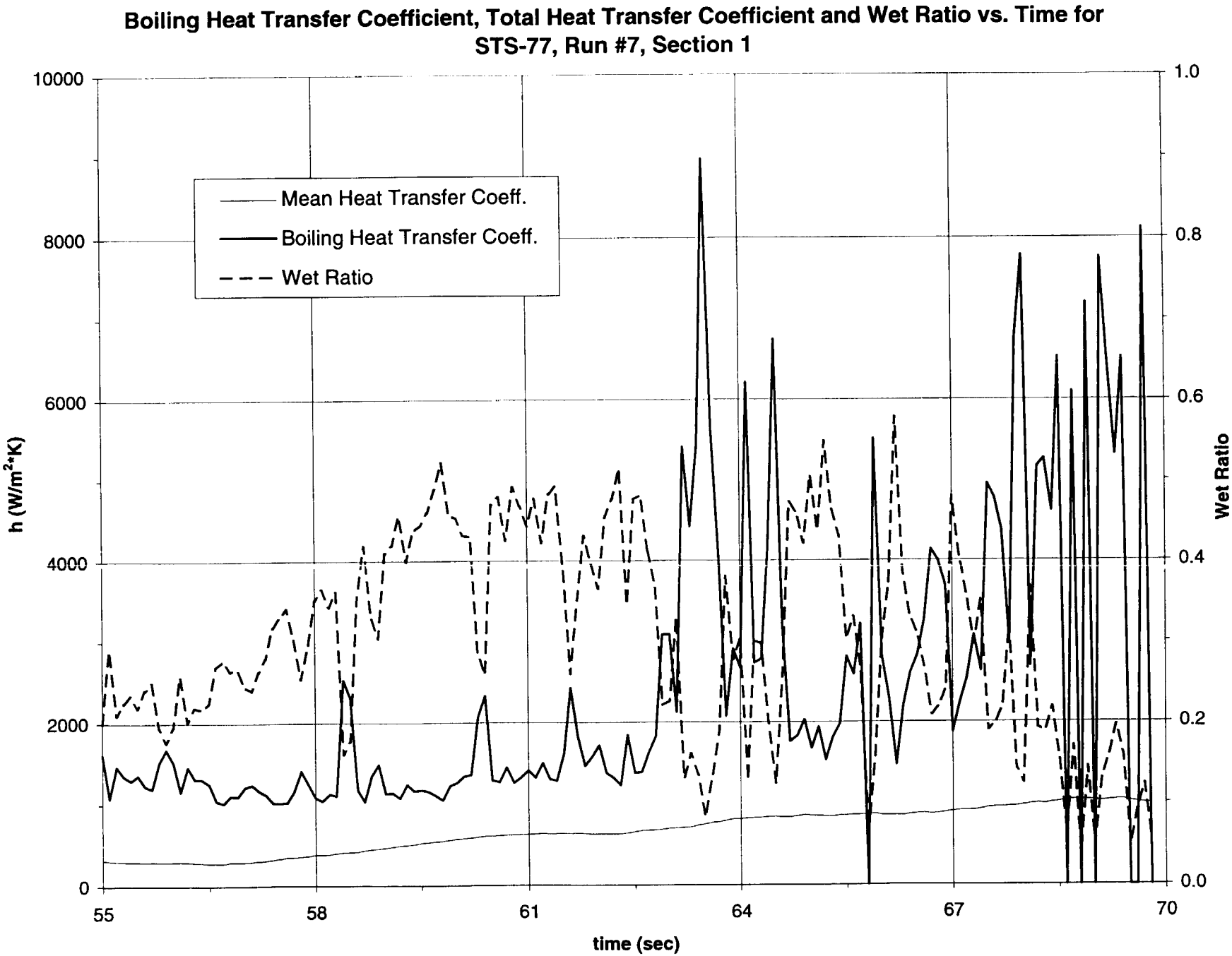

Figure B-10g-1-iii. Development of microgravity boiling heat transfer coefficient. PBE-IIA (STS-77). Run No. 7. Time interval: 55 - 70 seconds.

STS-77 Run #7, Section #1

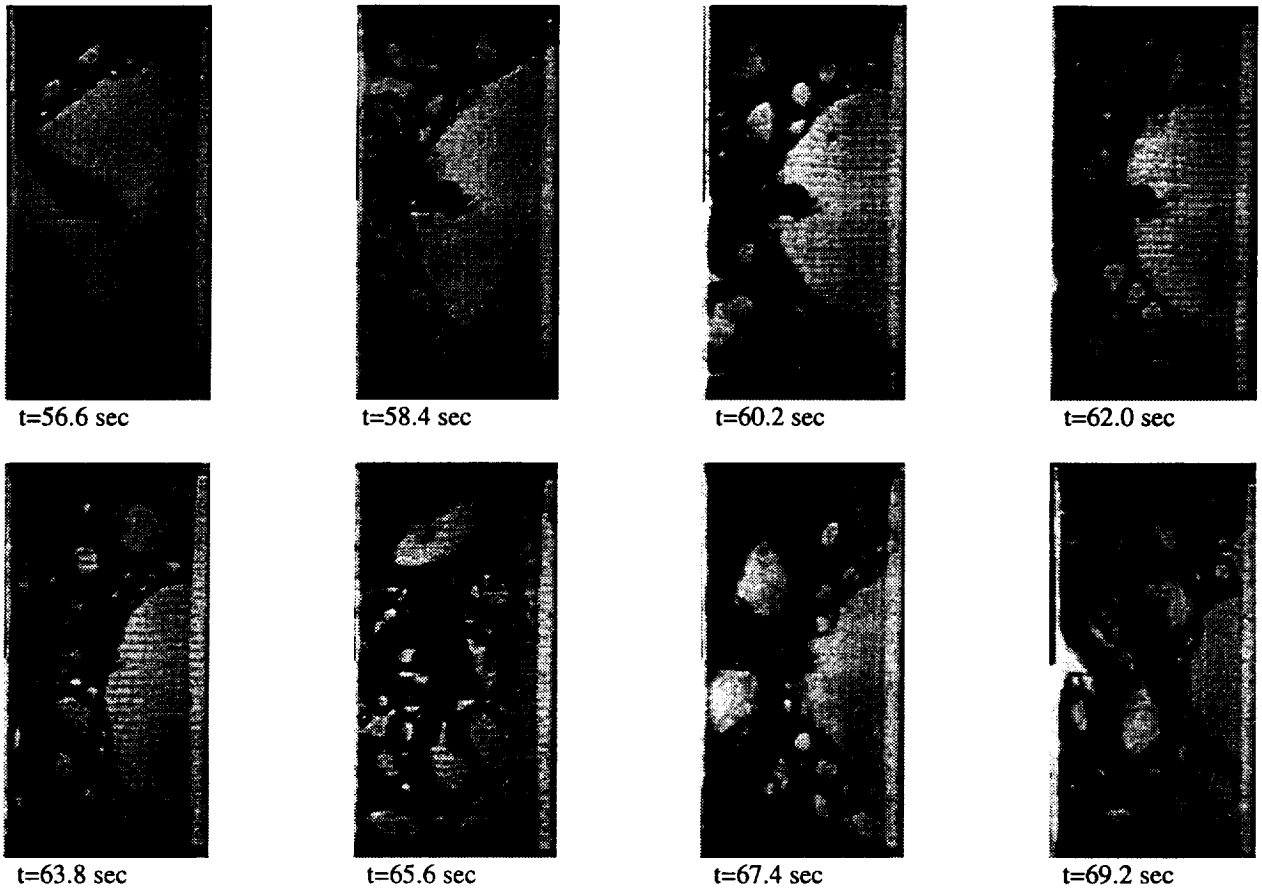

Figure B-10g-1-iv. Sample images showing dryout/rewetting. PBE-IIA (STS-77). Run No. 7. Time interval: 55 - 70 seconds.

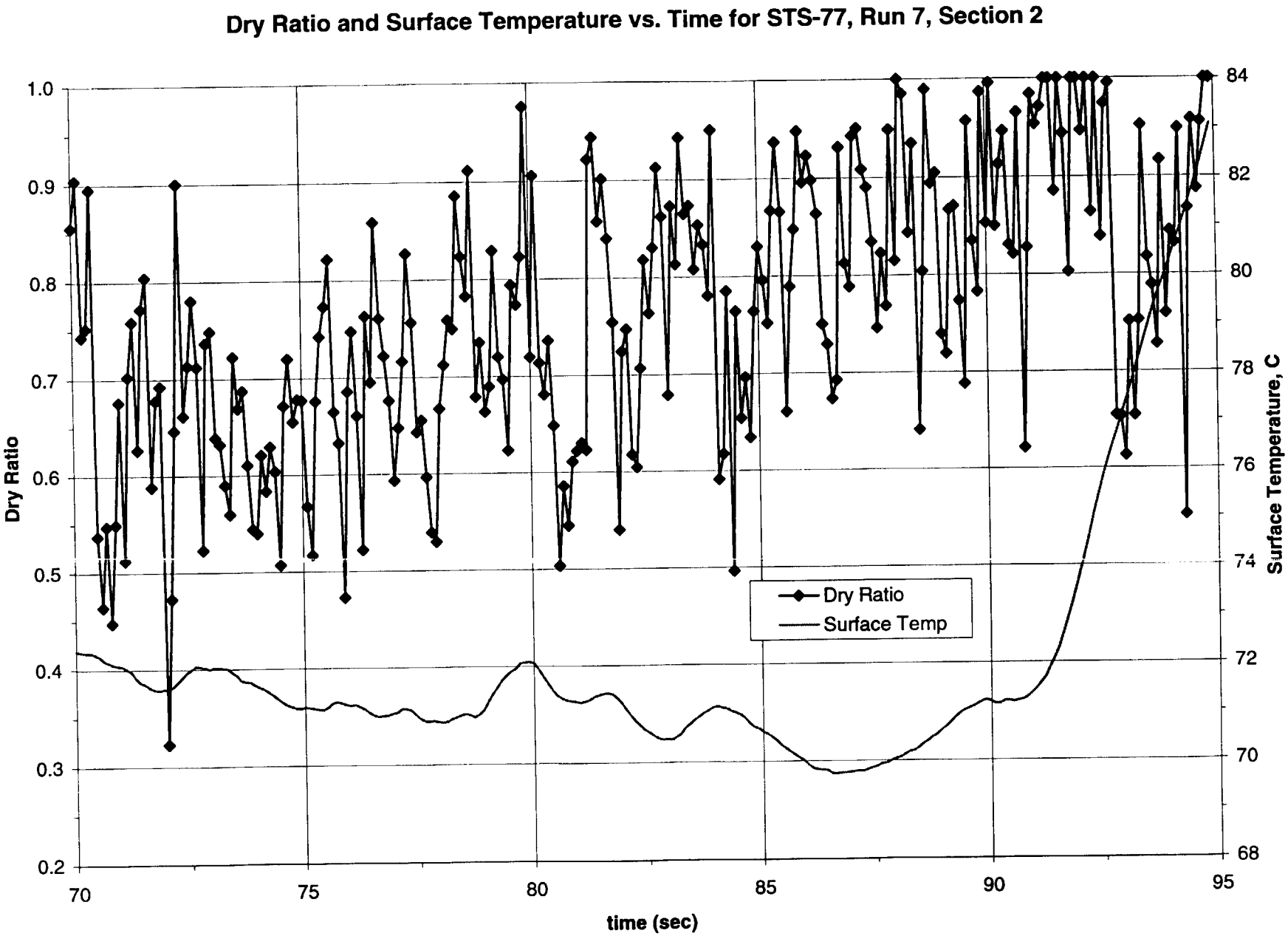

Figure B-10g-2-i. Heater surface dry fraction and mean temperature. PBE-IIA (STS-77). Run No. 7. Time interval: 70 - 95 seconds.

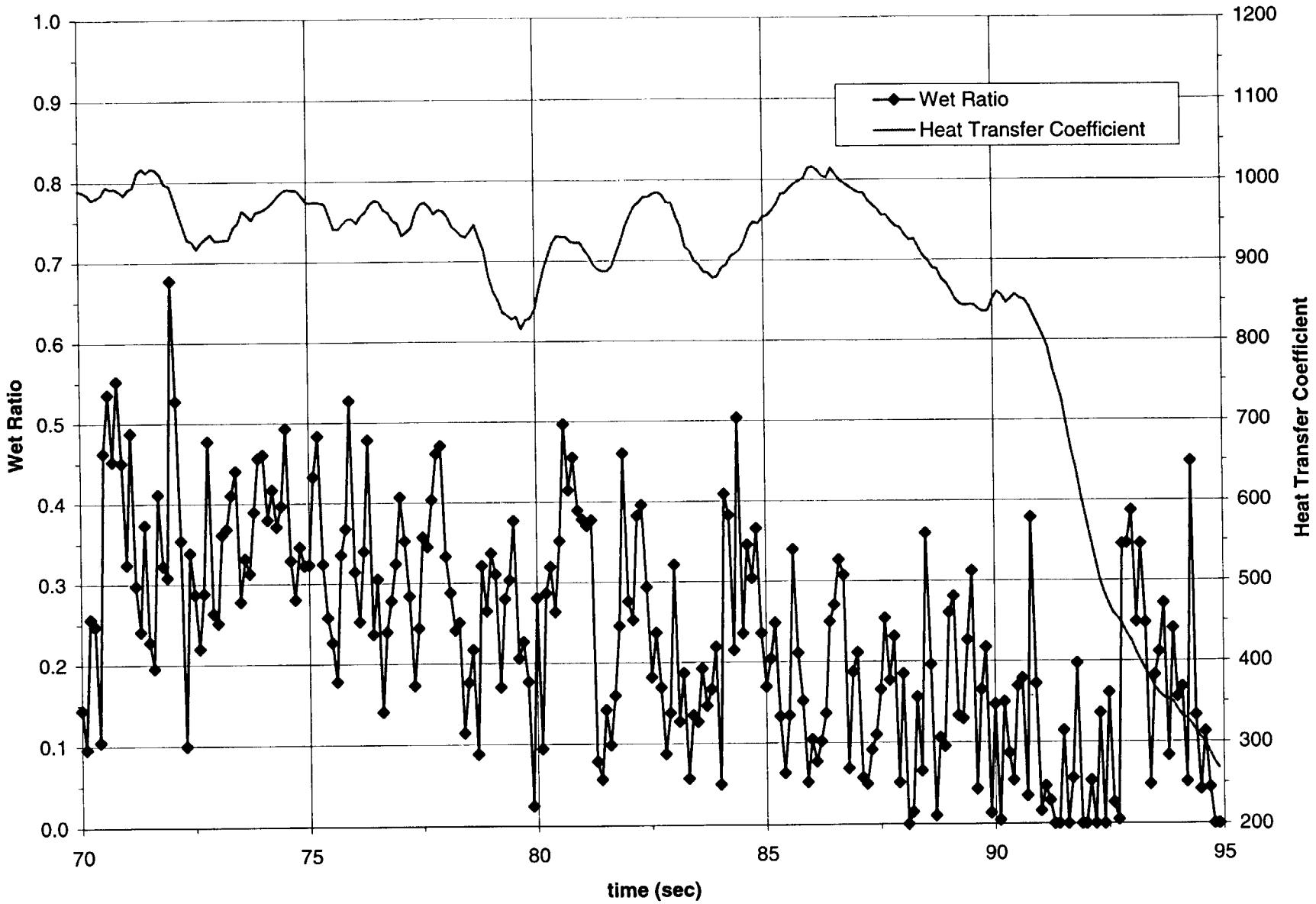

Figure B-10g-2-ii. Heater surface wet fraction and mean heat transfer coefficients. PBE-IIA (STS-77). Run No. 7. Time interval: 70 - 95 seconds.

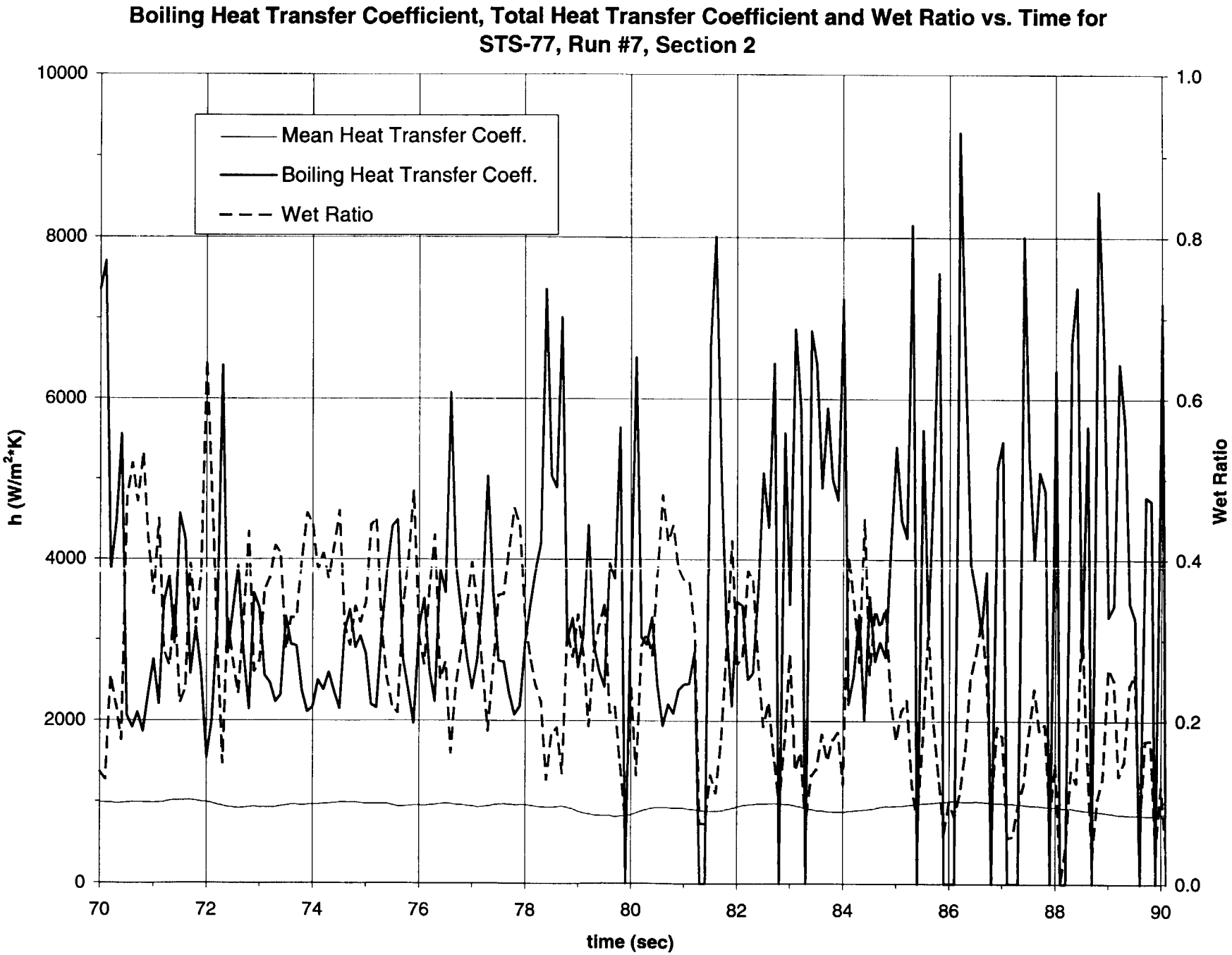

Figure B-10g-2-iii. Development of microgravity boiling heat transfer coefficient. PBE-IIA (STS-77) Run No. 7. Time interval: 70 - 95 seconds.

STS-77 Run #7, Section #2

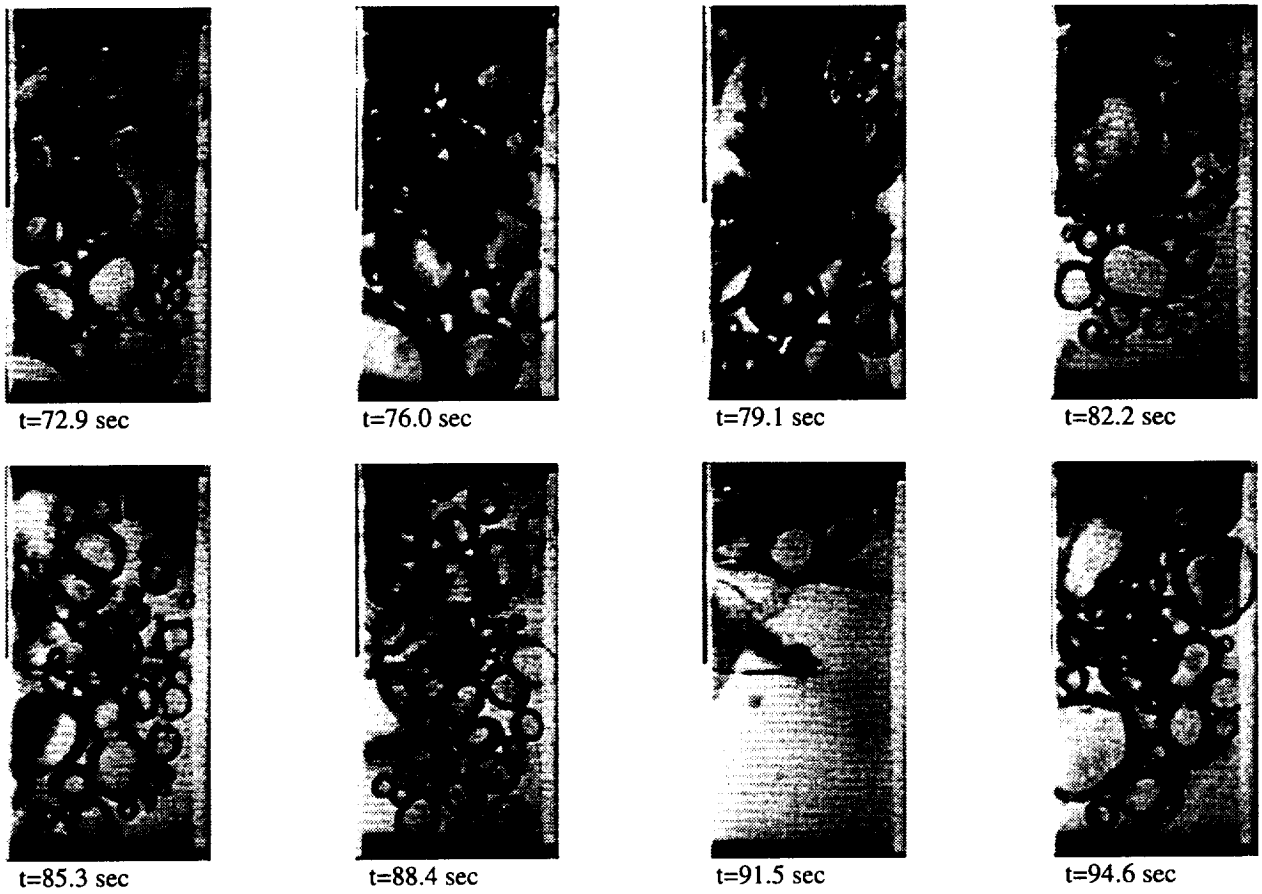

Figure B-10g-2-iv. Sample images showing dryout/rewetting. PBE-IIA (STS-77). Run No. 7. Time interval: 70 - 95 seconds.

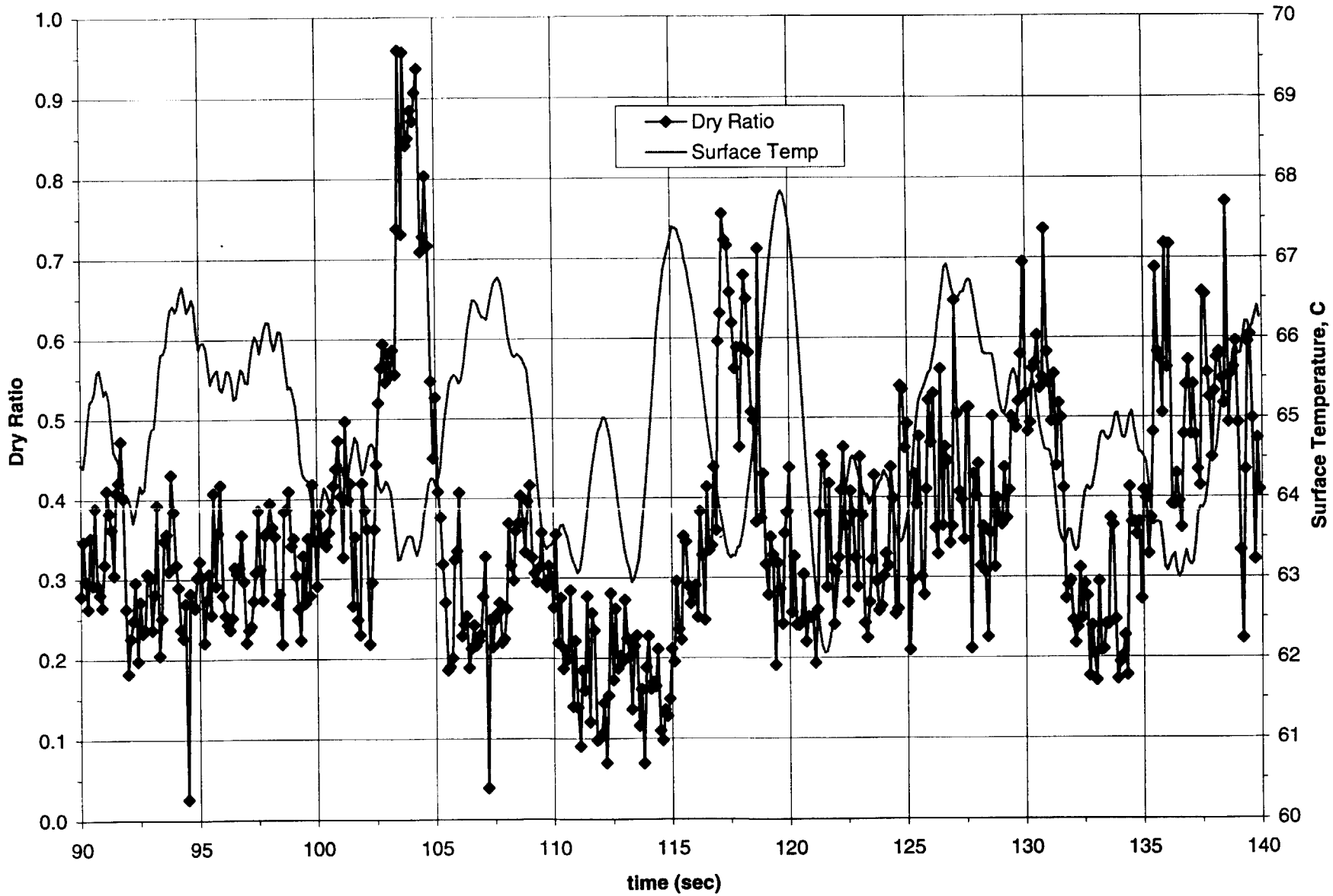

Figure B-10h-1-i. Heater surface dry fraction and mean temperature. PBE-IIA (STS-77). Run No. 8. Time interval: 90 - 140 seconds.

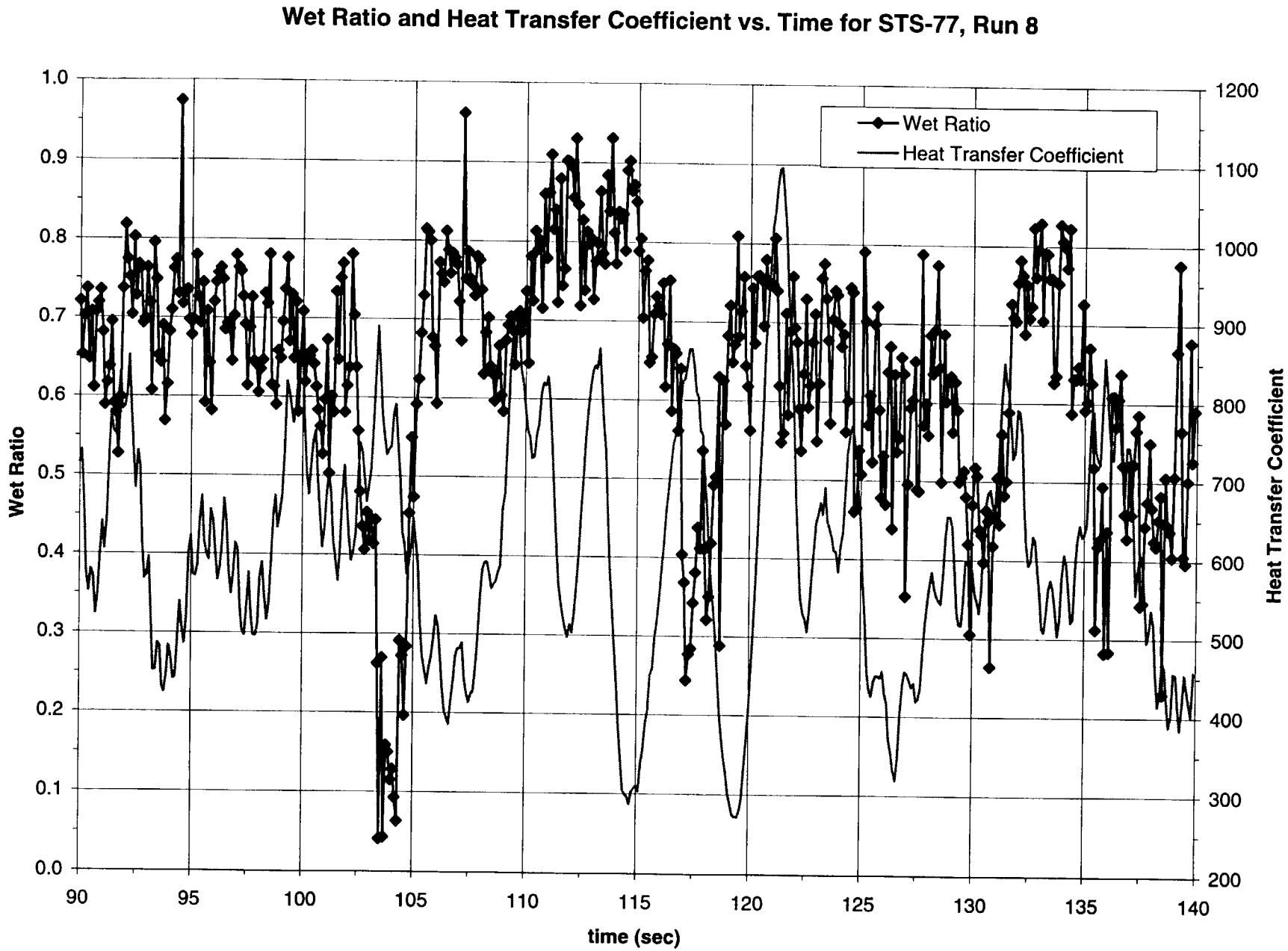

Figure B-10h-1-ii. Heater surface wet fraction and mean heat transfer coefficients. PBE-IIA (STS-77). Run No. 8. Time interval: 90 - 140 seconds.

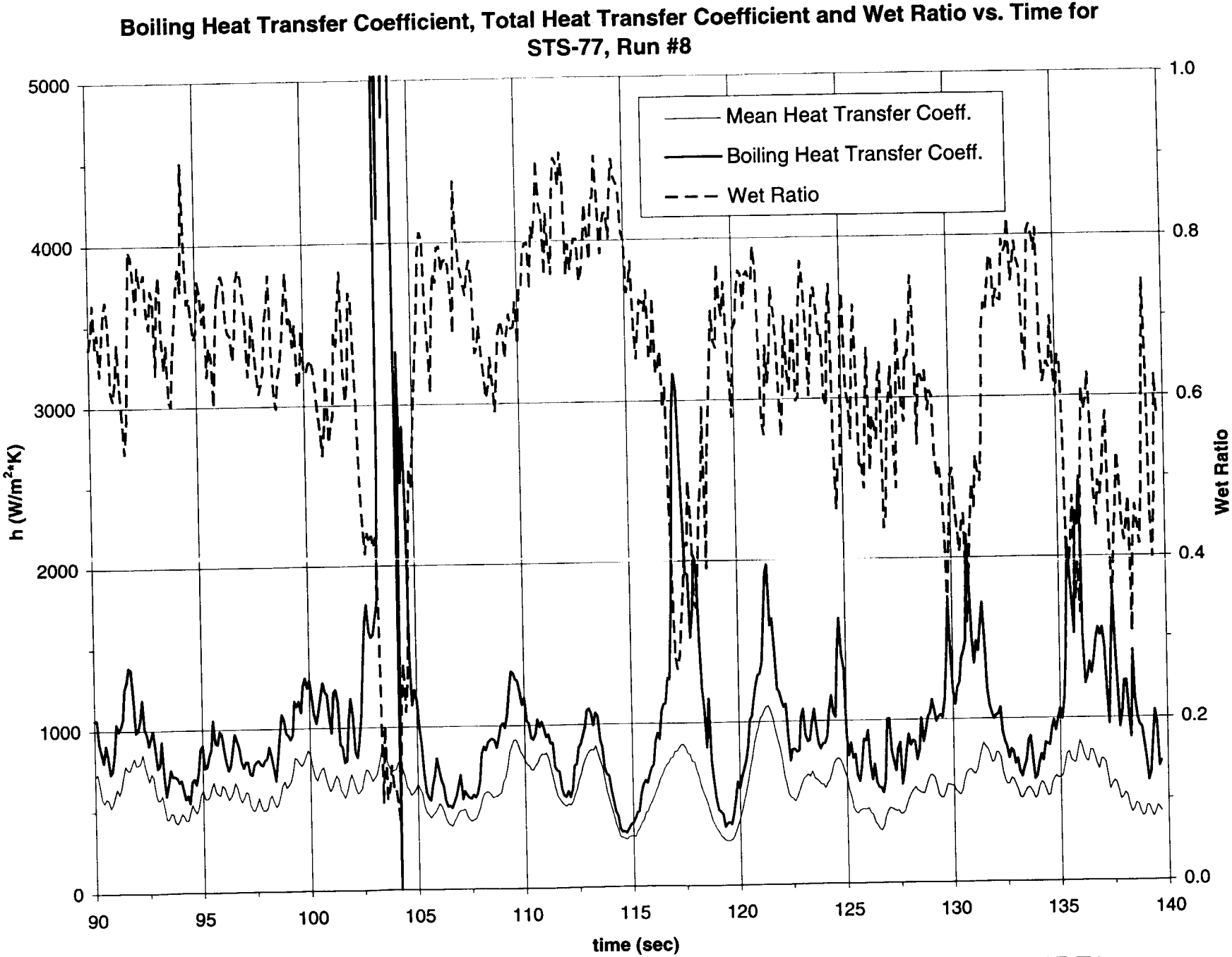

Figure B-10h-1-iii. Development of microgravity boiling heat transfer coefficient. PBE-IIA (STS-77). Run No. 8. Time interval: 90 - 140 seconds.

STS-77 Run #8

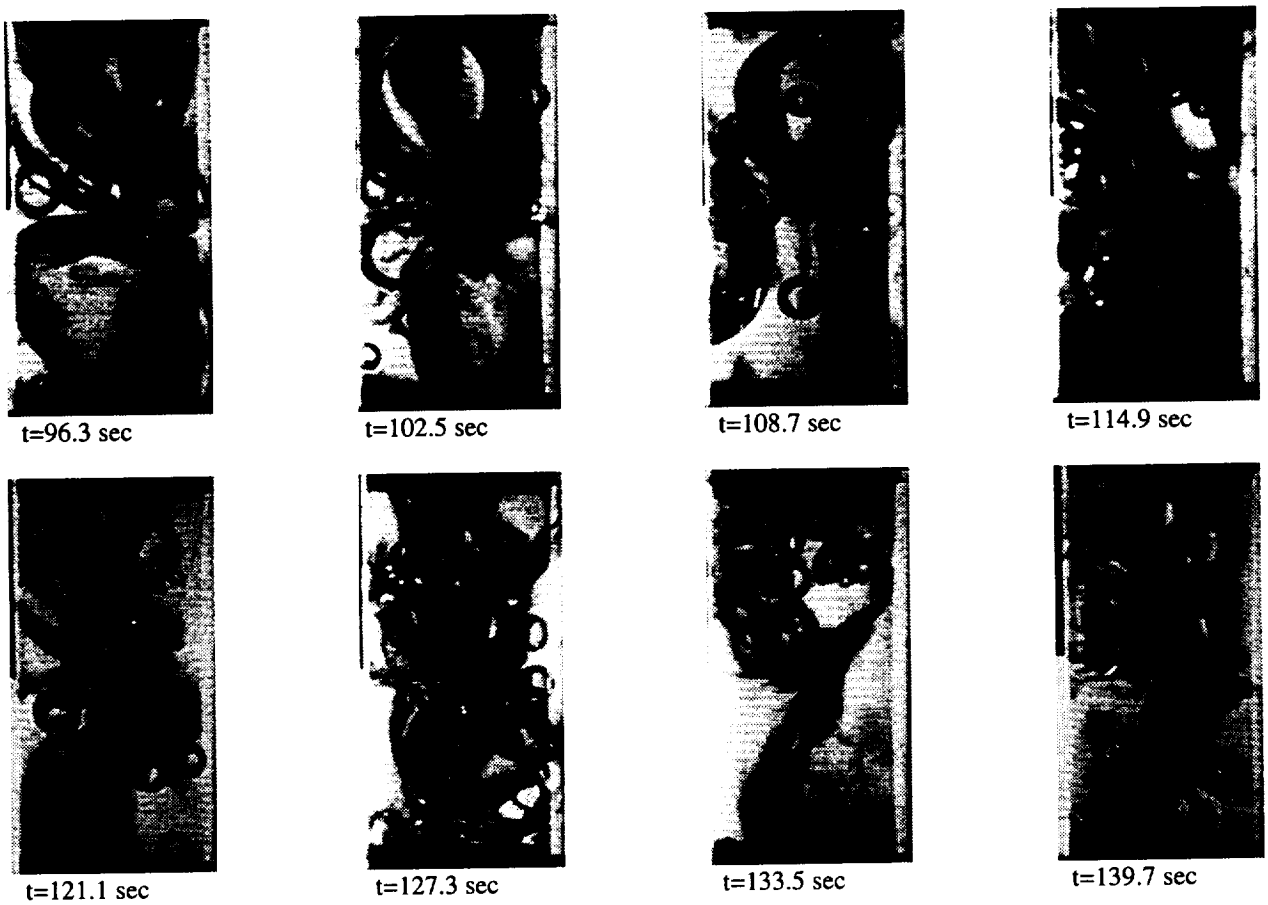

Figure B-10h-1-iv. Sample images showing dryout/rewetting. PBE-IIA (STS-77). Run No. 8. Time interval: 90 - 140 seconds.

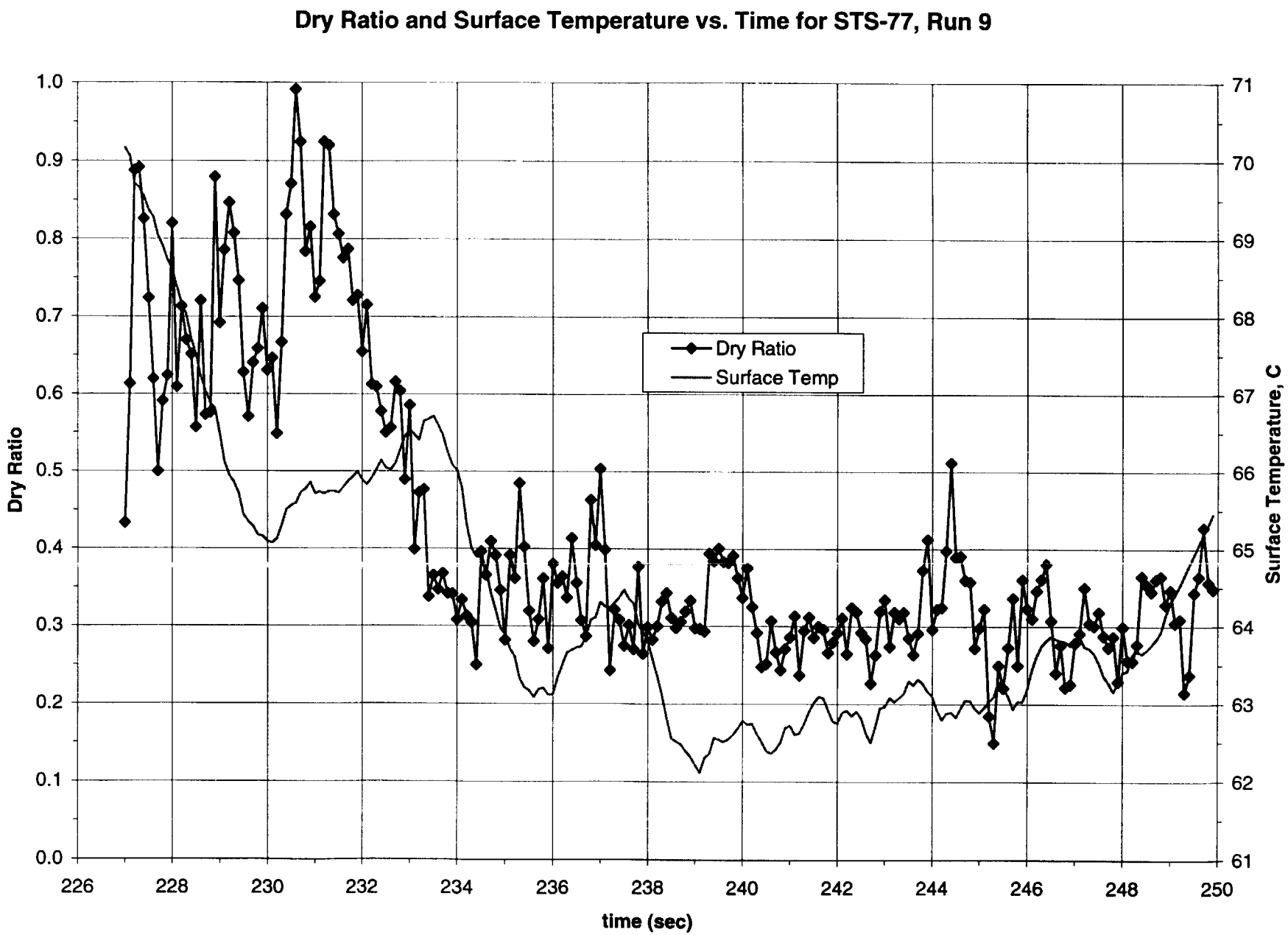

Figure B-10i-1-i. Heater surface dry fraction and mean temperature. PBE-IIA (STS-77). Run No. 9. Time interval: 226 - 250 seconds.

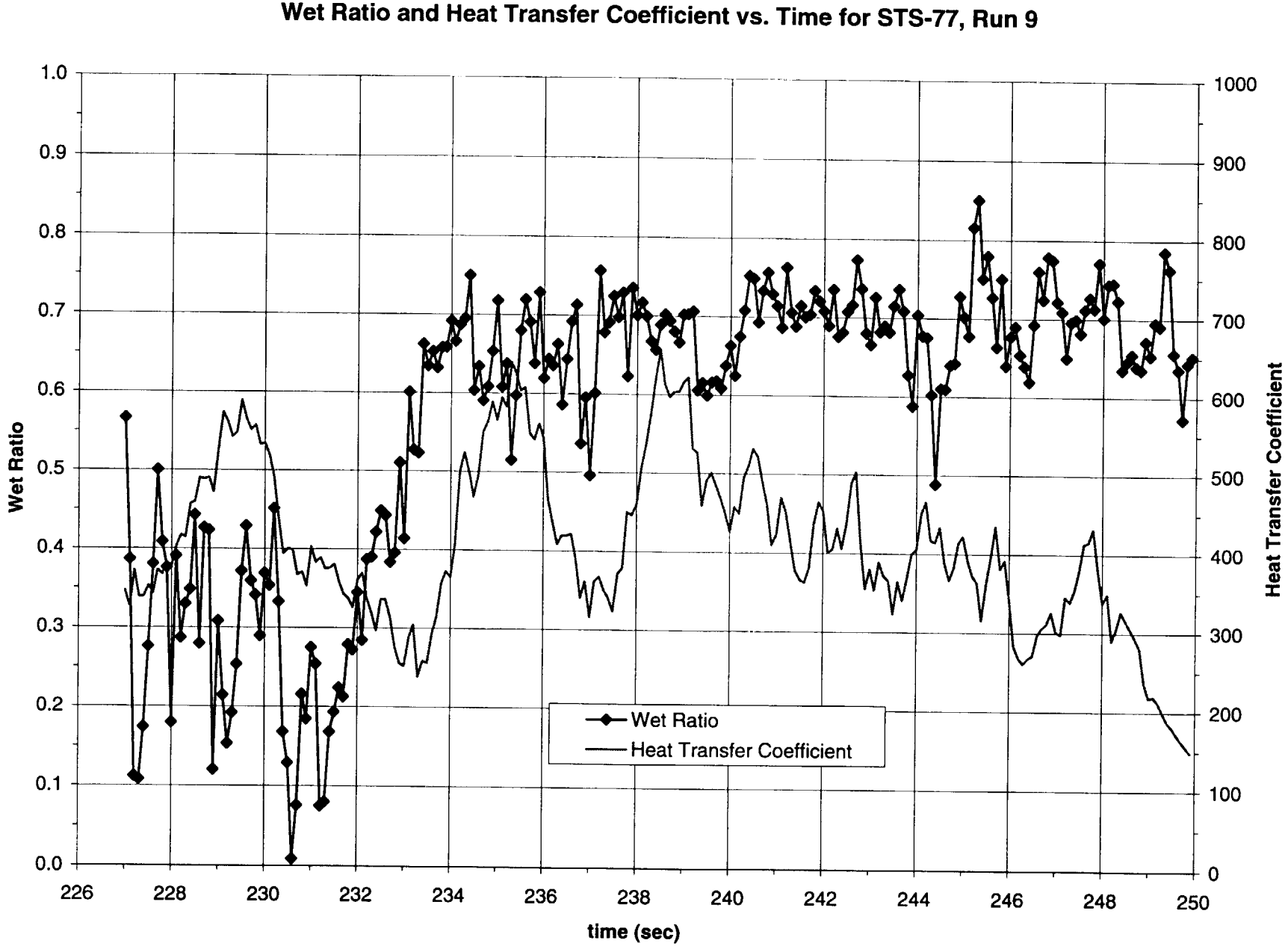

Figure B-10i-1-ii. Heater surface wet fraction and mean heat transfer coefficients. PBE-IIA (STS-77). Run No. 9. Time interval: 226 - 250 seconds.

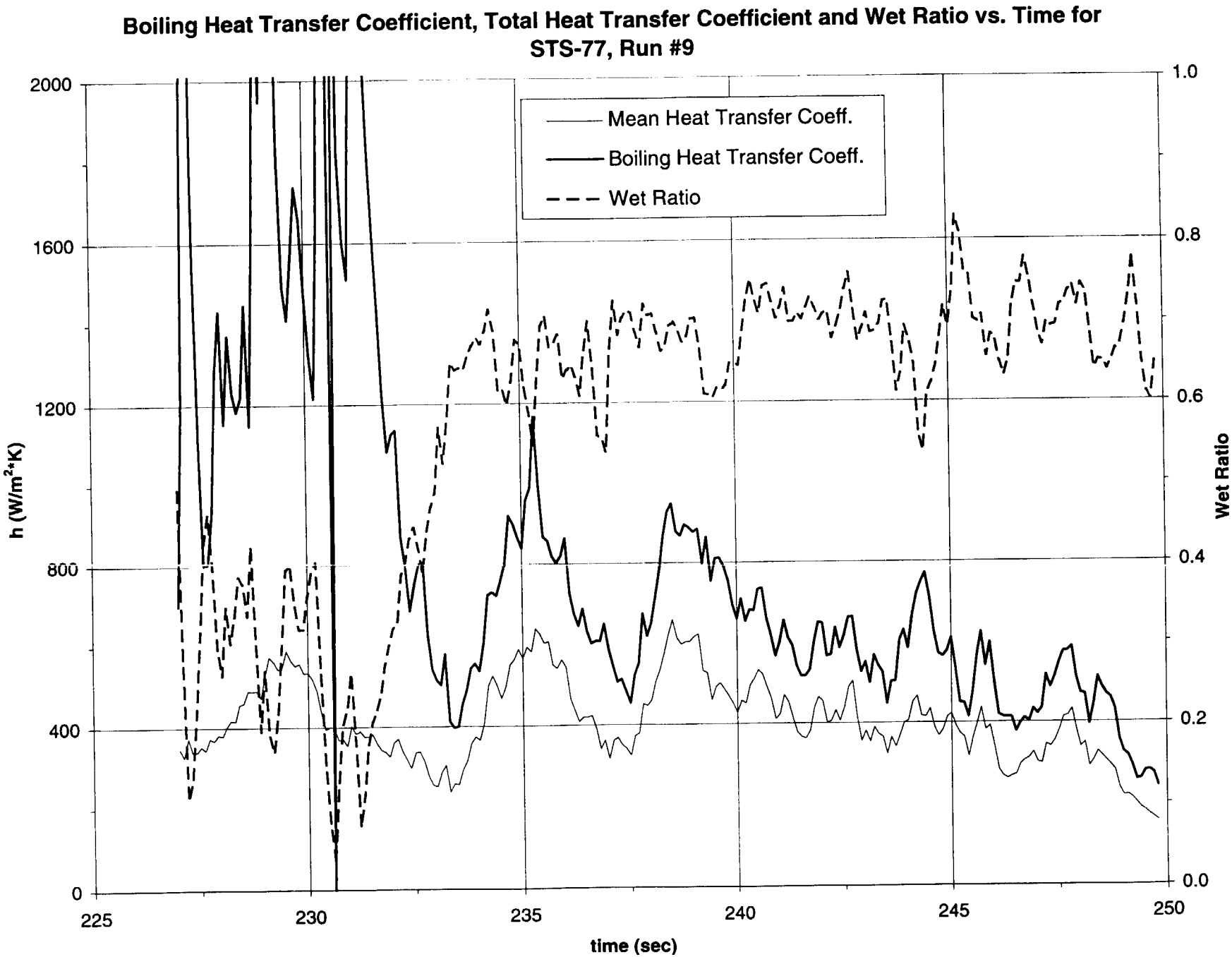

Figure B-10i-1-iii. Development of microgravity boiling heat transfer coefficient. PBE-IIA (STS-77) Run No. 9. Time interval: 226 - 250 seconds.

STS-77 Run #9

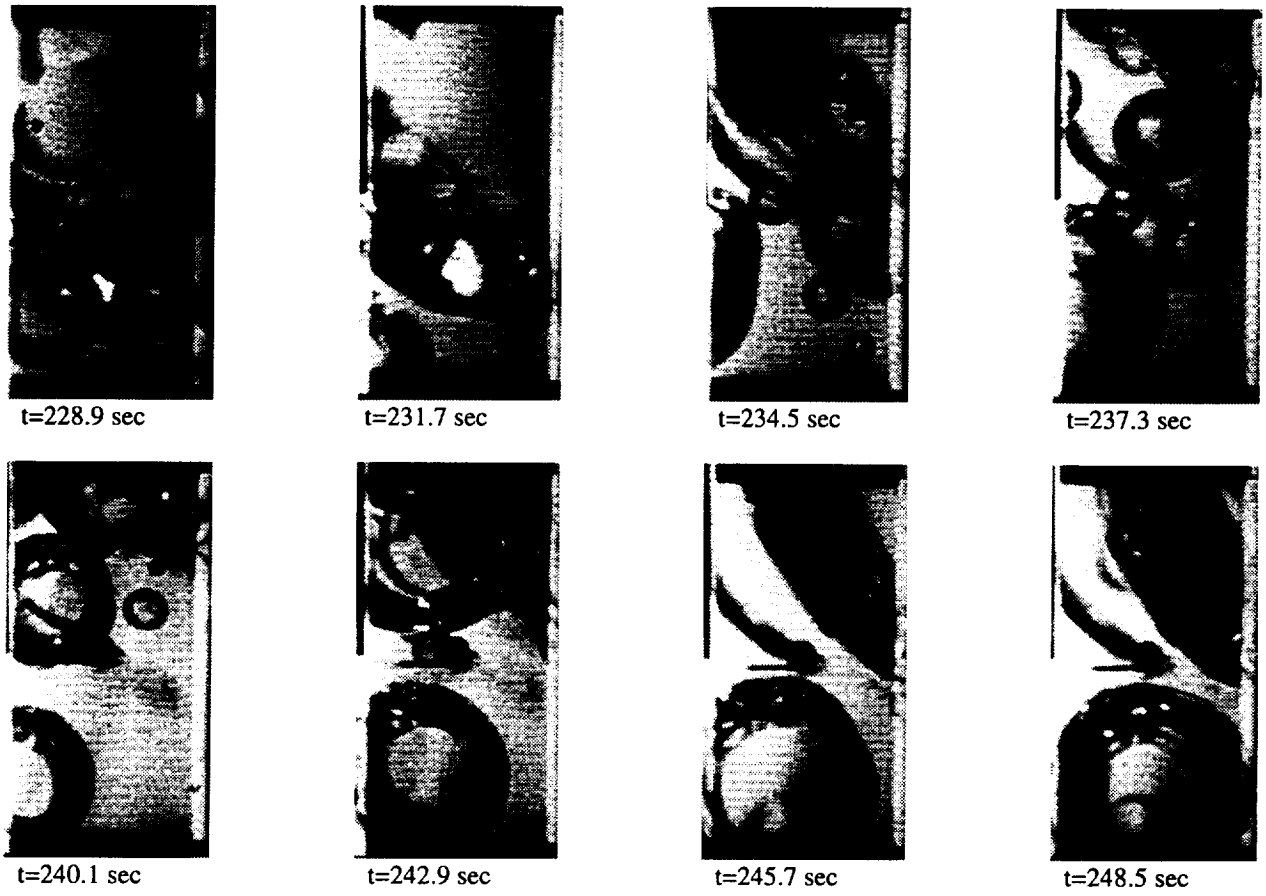

Figure B-10i-1-iv. Sample images showing dryout/rewetting. PBE-IIA (STS-77). Run No. 9. Time interval: 226 - 250 seconds.

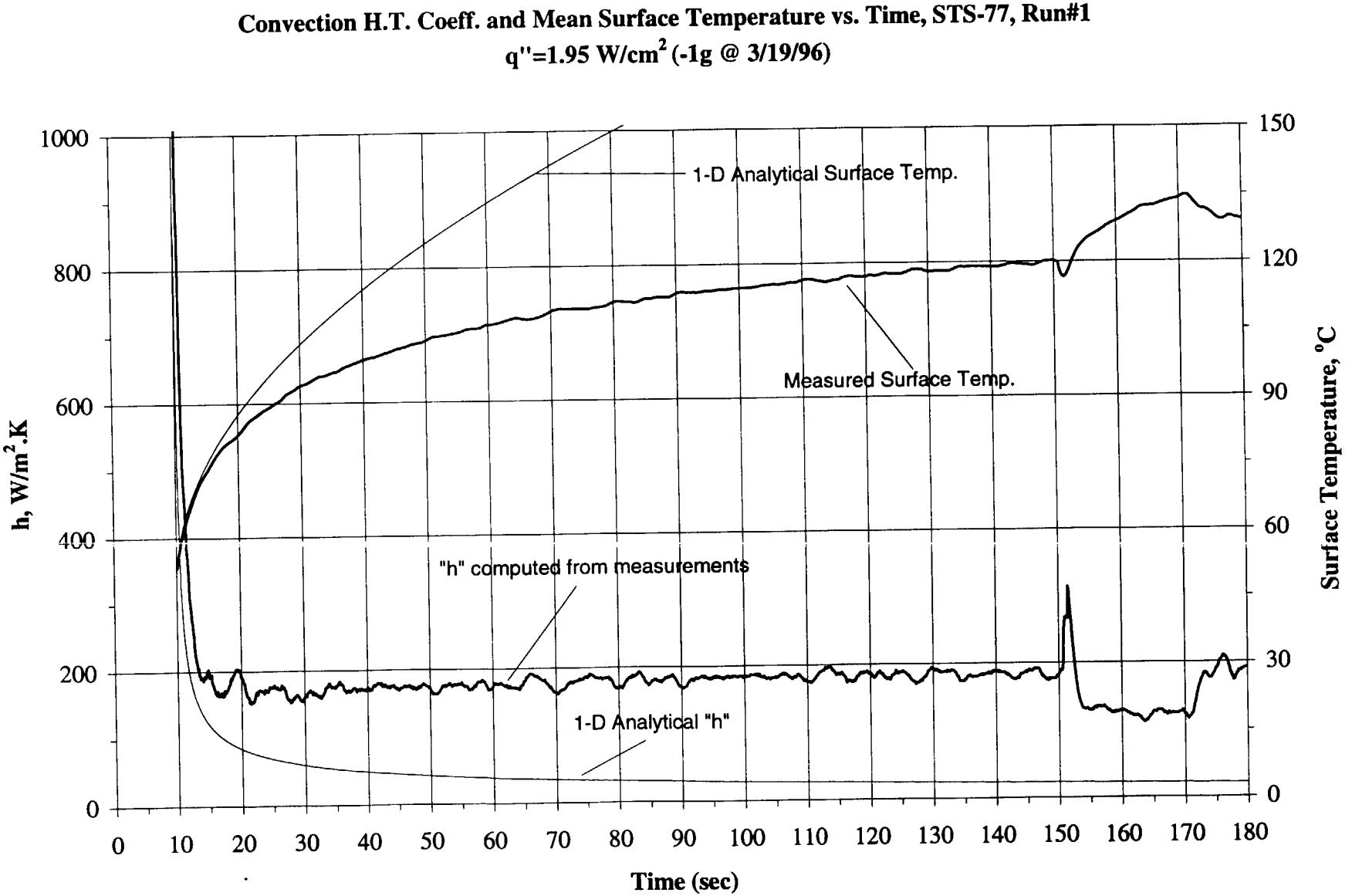

Figure B-11a. a/g = -1 Preflight test. Mean heater surface temperature and derived heat transfer coefficient. PBE-IIA (STS-77). Run No. 1.

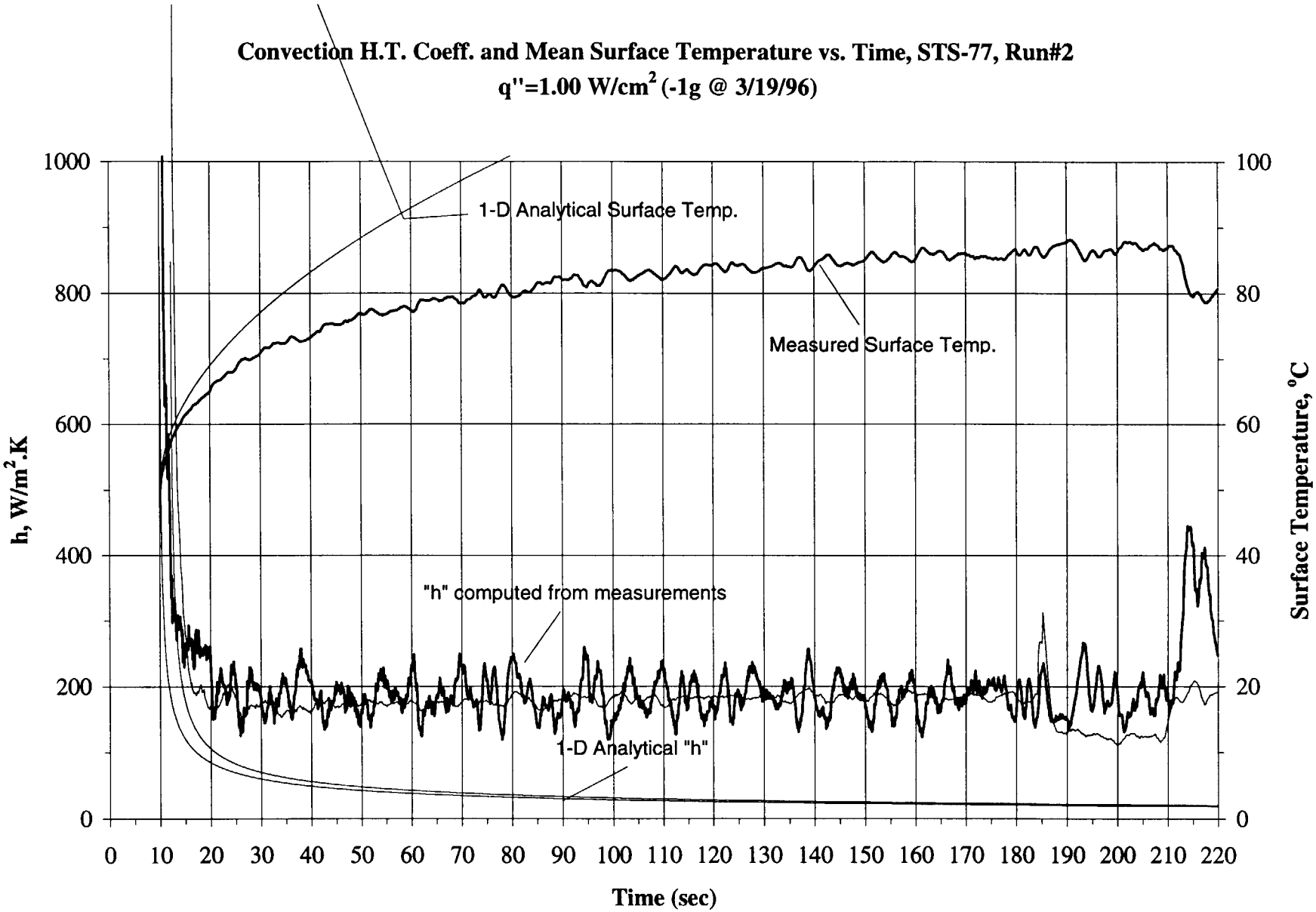

Figure B-11b. a/g = -1 Preflight test. Mean heater surface temperature and derived heat transfer coefficient. PBE-IIA (STS-77). Run No. 2.

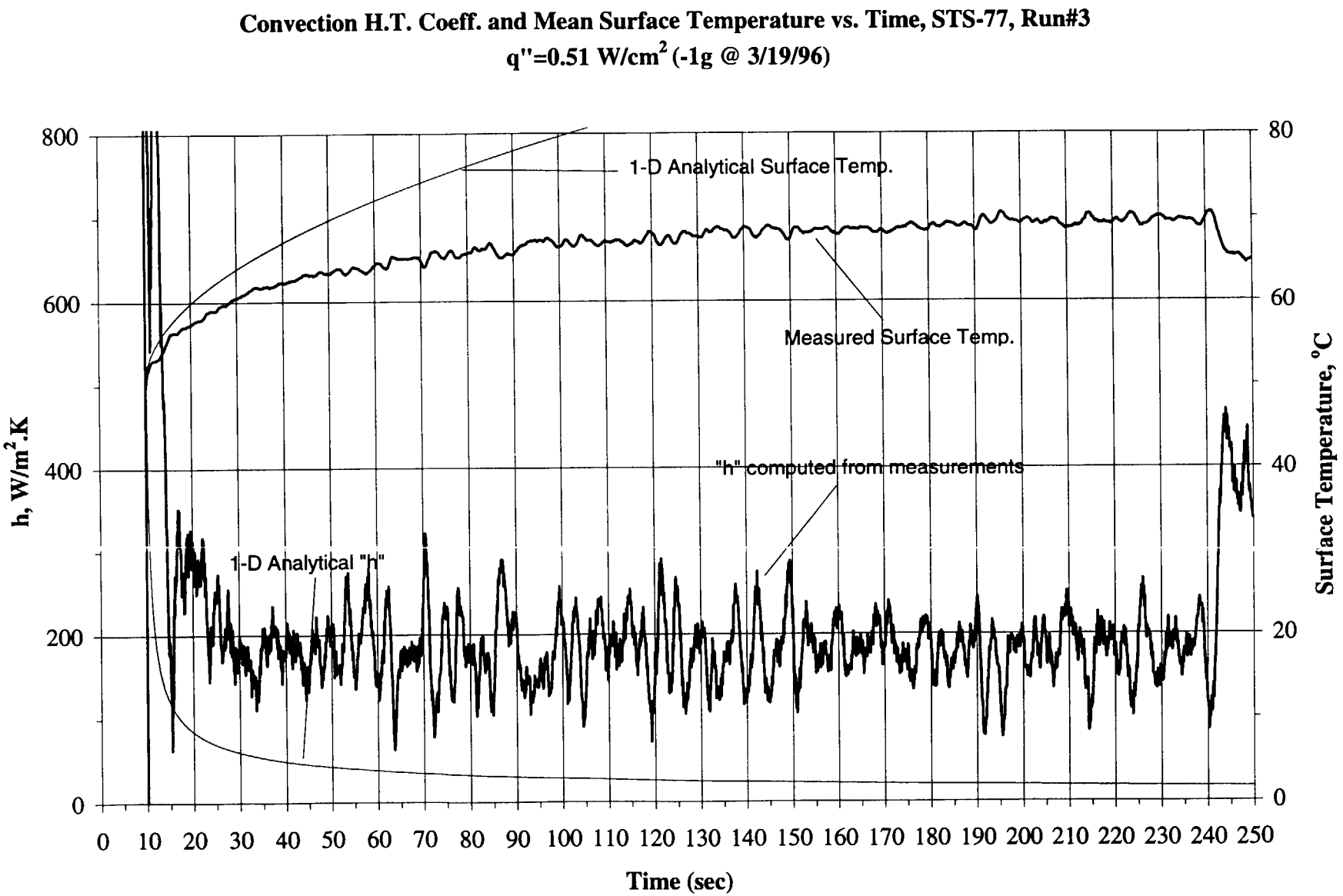

Figure B-11c. a/g = -1 Preflight test. Mean heater surface temperature and derived heat transfer coefficient. PBE-IIA (STS-77). Run No. 3.

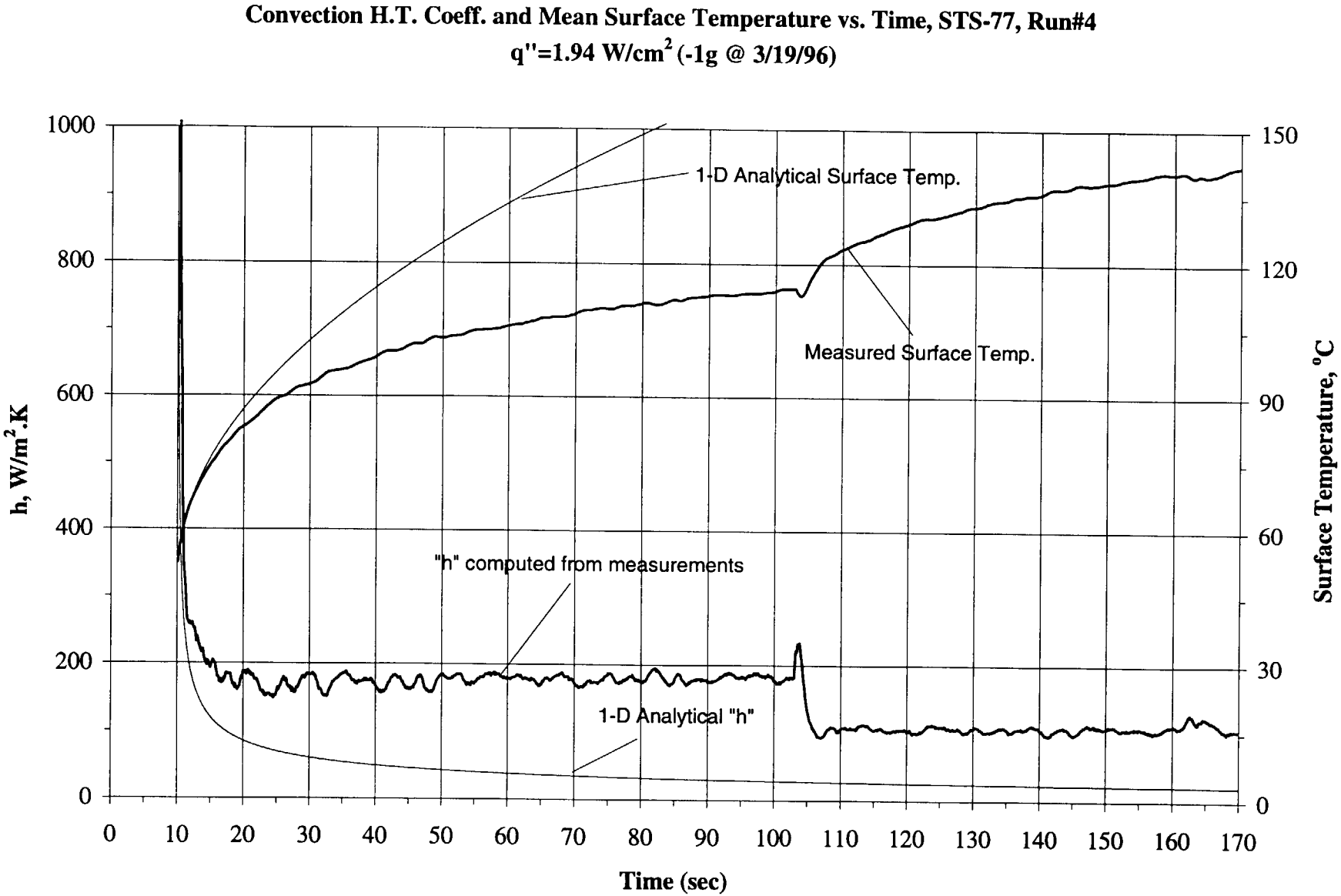

Figure B-11d. a/g = -1 Preflight test. Mean heater surface temperature and derived heat transfer coefficient. PBE-IIA (STS-77). Run No. 4.

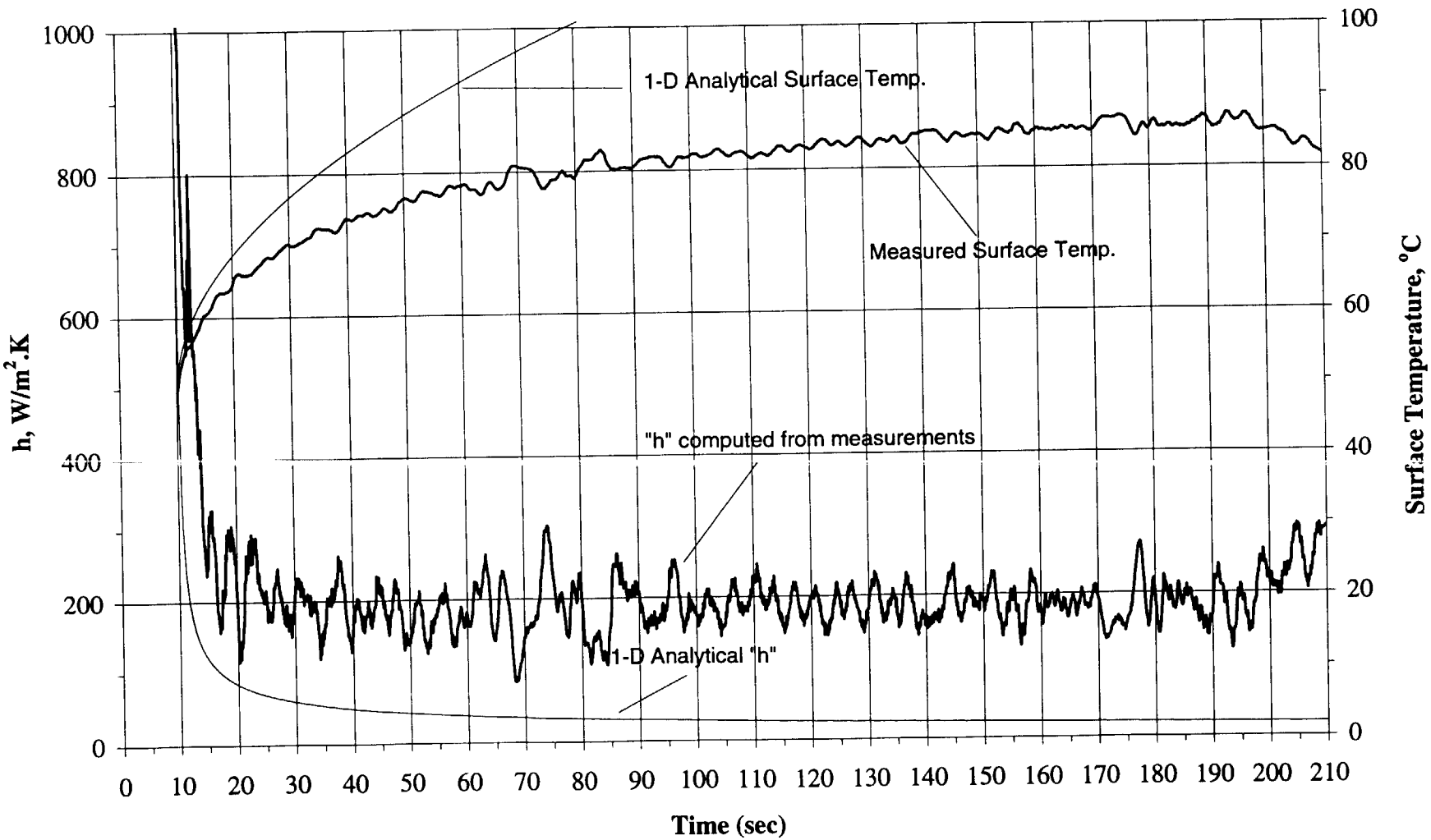

Figure B-11e. a/g = -1 Preflight test. Mean heater surface temperature and derived heat transfer coefficient. PBE-IIA (STS-77). Run No. 5.

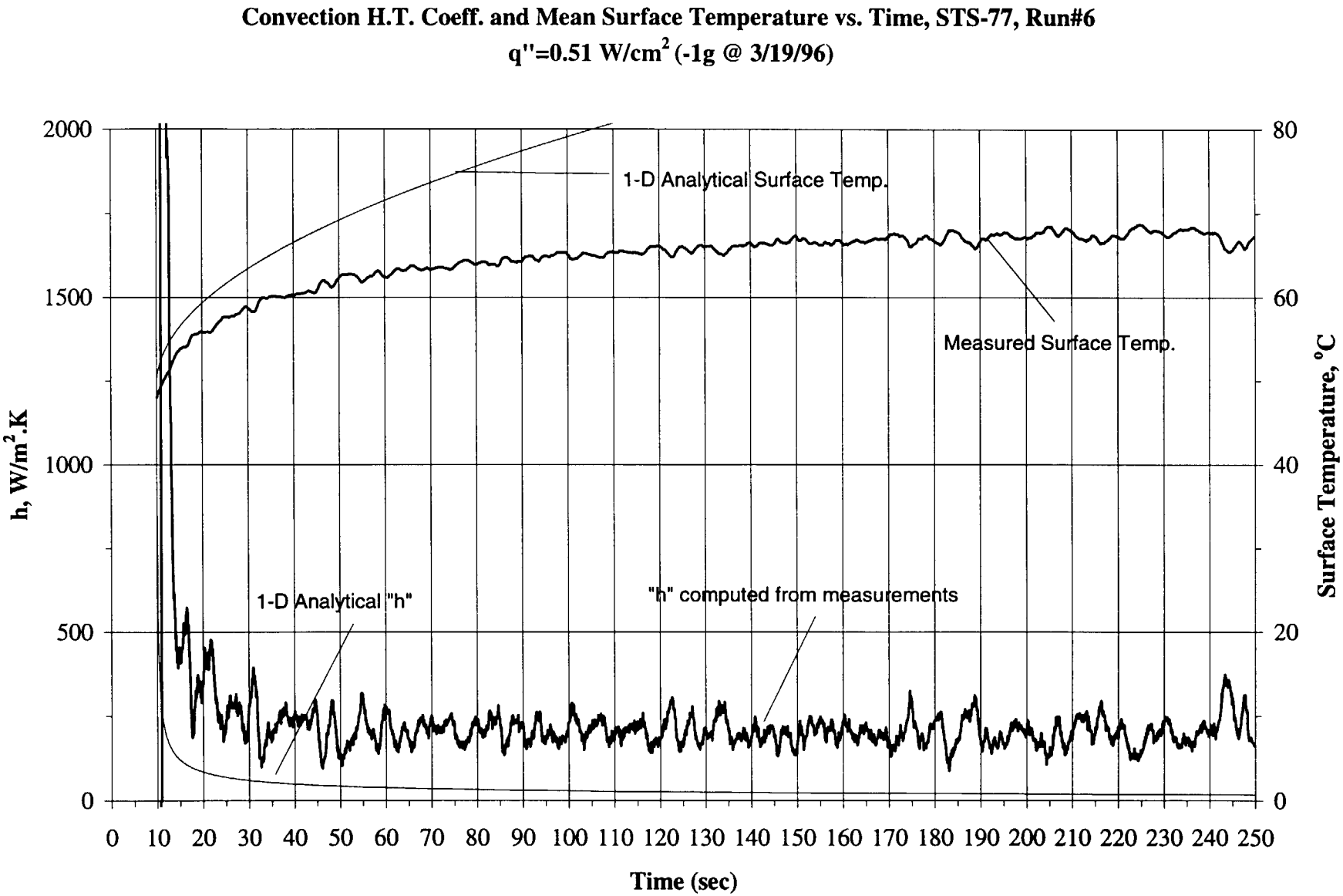

Figure B-11f. a/g = -1 Preflight test. Mean heater surface temperature and derived heat transfer coefficient. PBE-IIA (STS-77). Run No. 6.

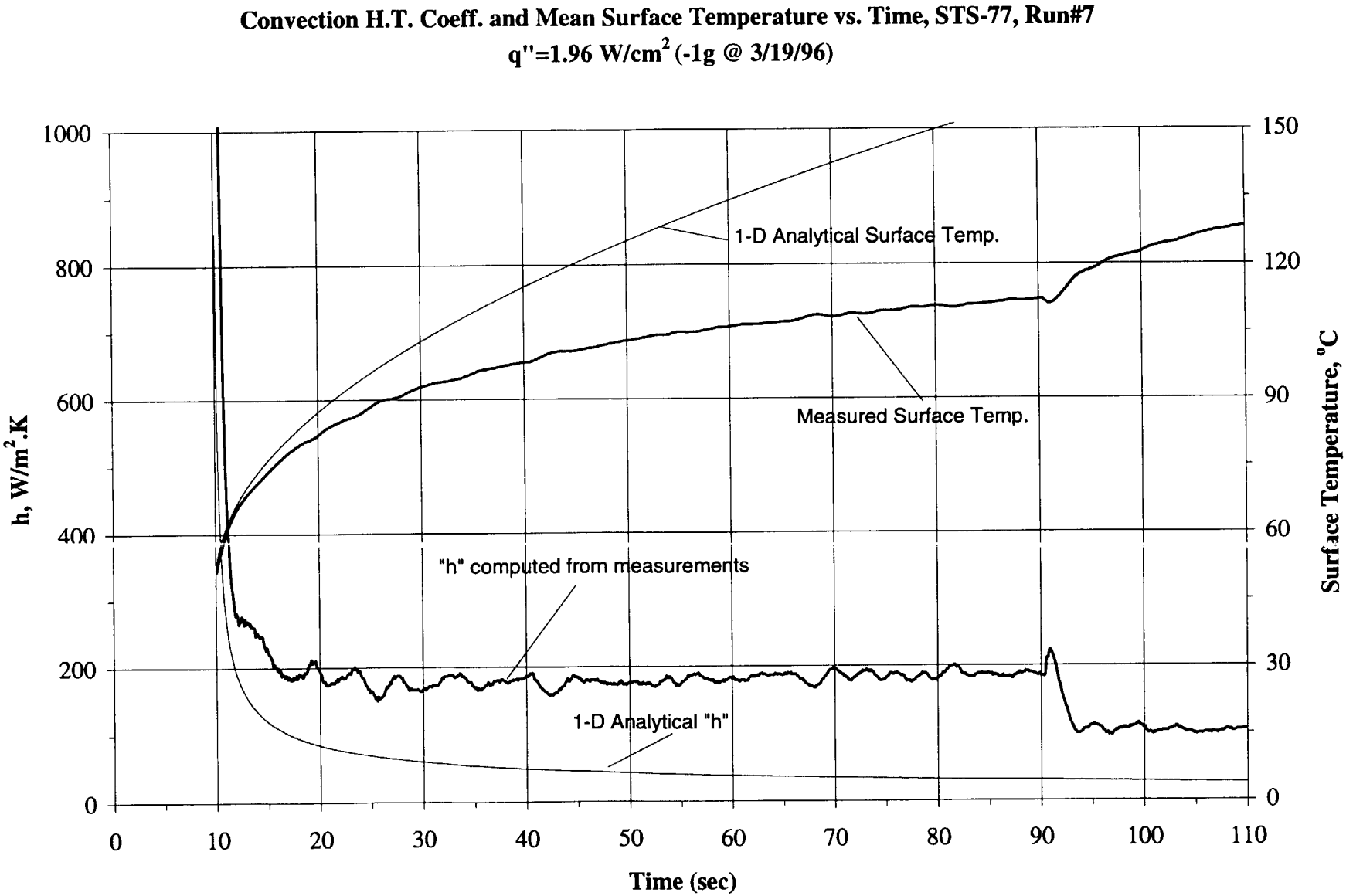

Figure B-11g. a/g = -1 Preflight test. Mean heater surface temperature and derived heat transfer coefficient. PBE-IIA (STS-77). Run No. 7.

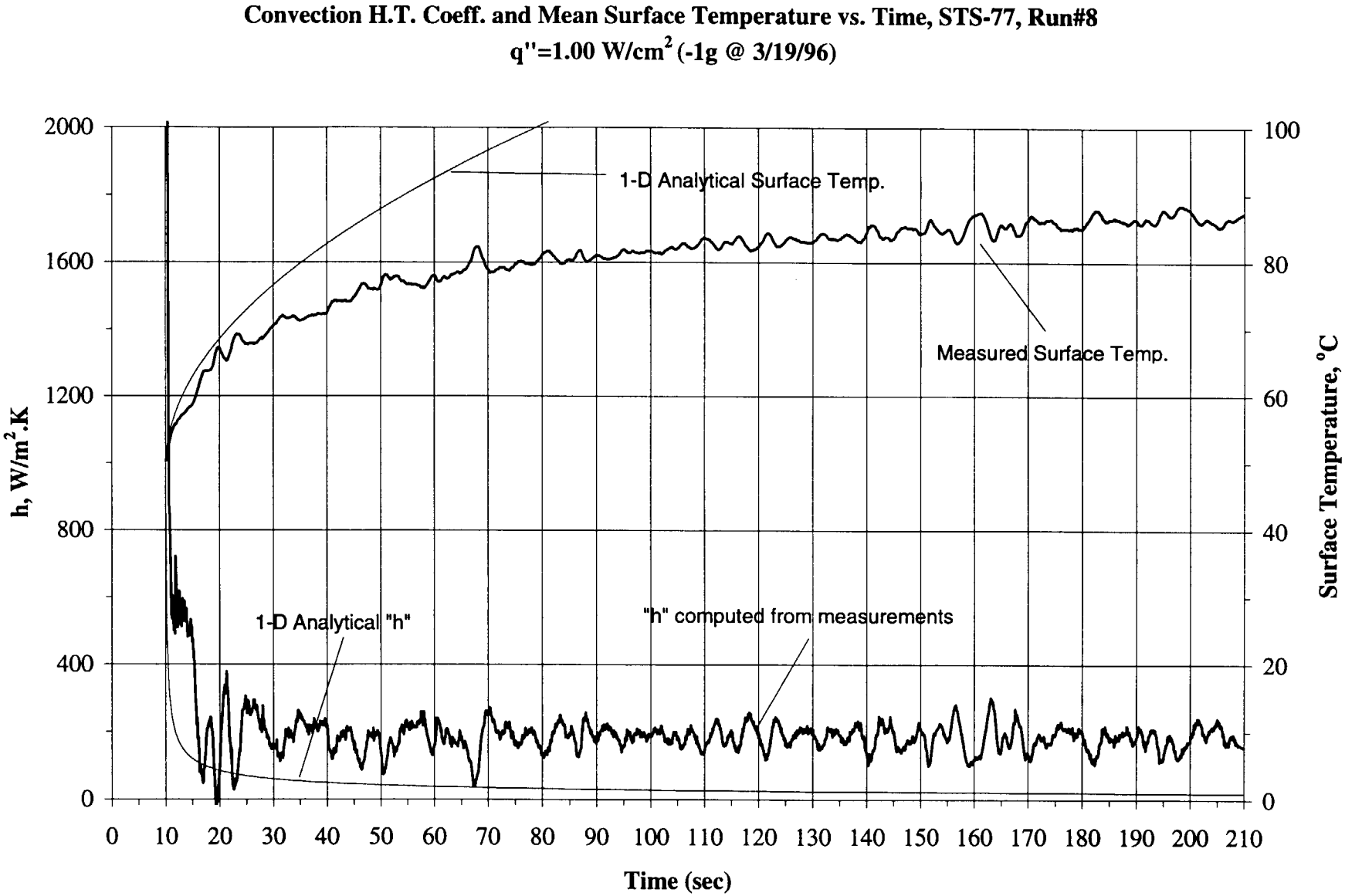

Figure B-11h. a/g = -1 Preflight test. Mean heater surface temperature and derived heat transfer coefficient. PBE-IIA (STS-77). Run No. 8.

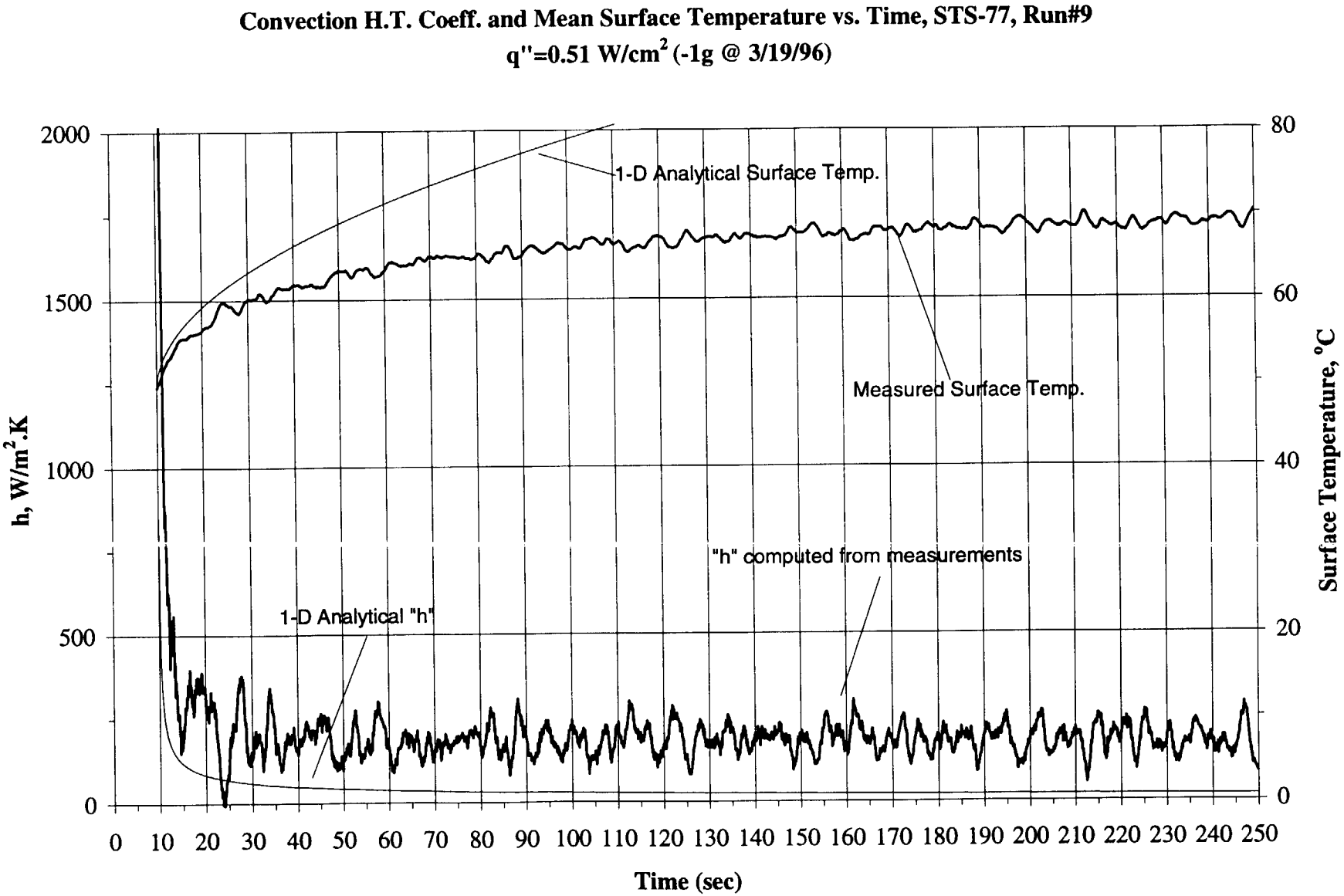

Figure B-11i. a/g = -1 Preflight test. Mean heater surface temperature and derived heat transfer coefficient. PBE-IIA (STS-77). Run No. 9.

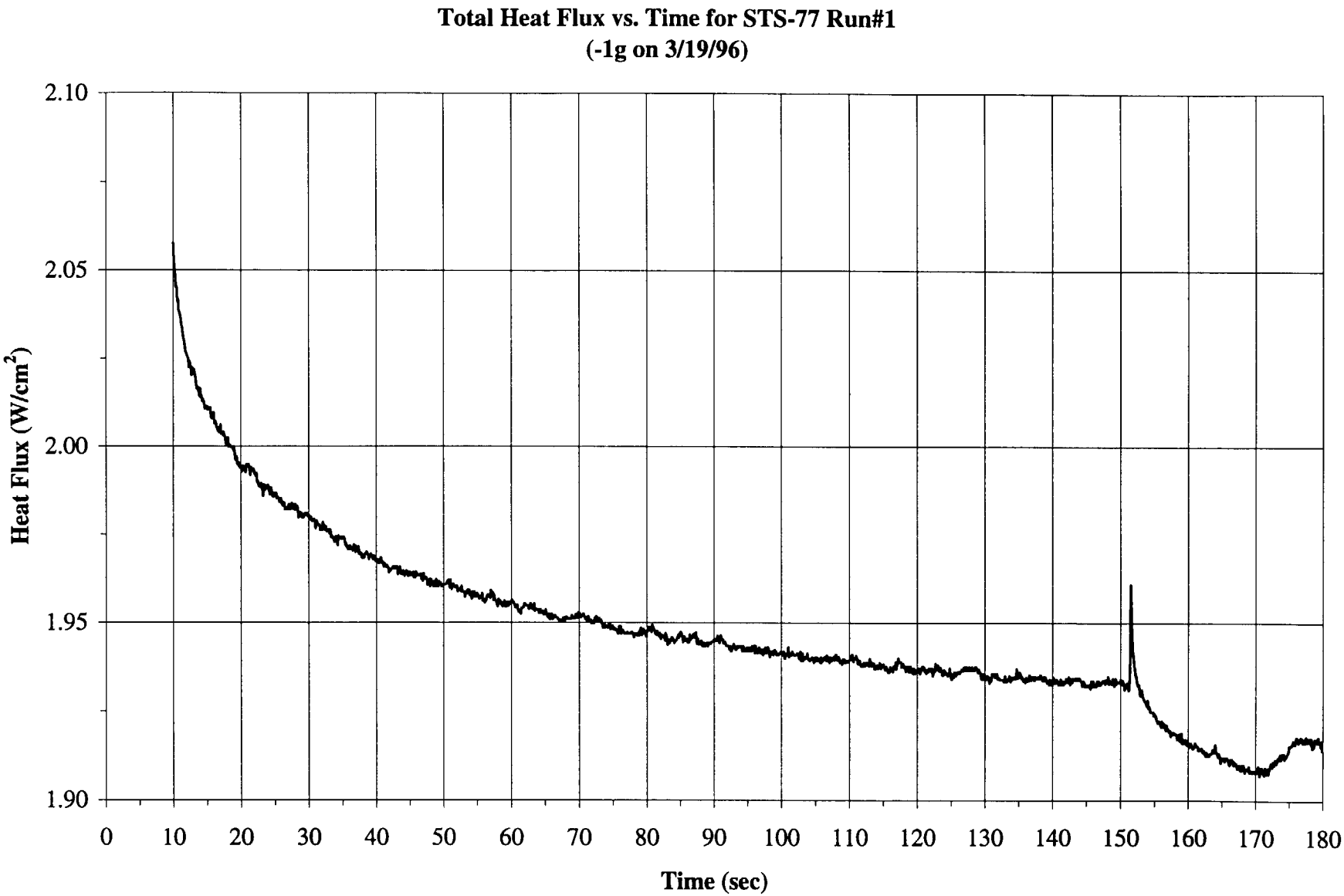

Figure B-12a. a/g = -1 Preflight test. Heat flux input. PBE-IIA (STS-77). Run No. 1.

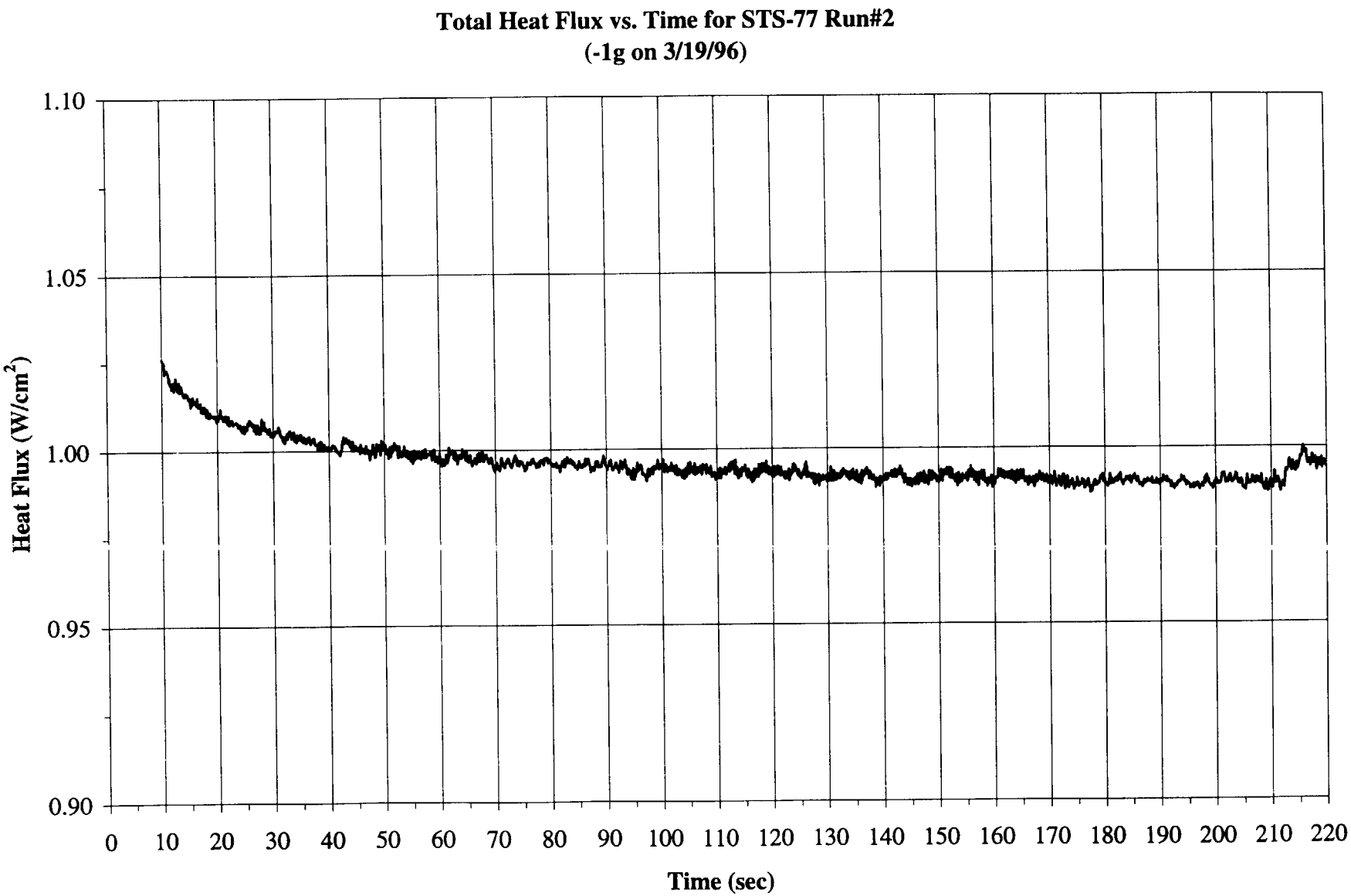

Figure B-12b. a/g = -1 Preflight test. Heat flux input. PBE-IIA (STS-77). Run No. 2.

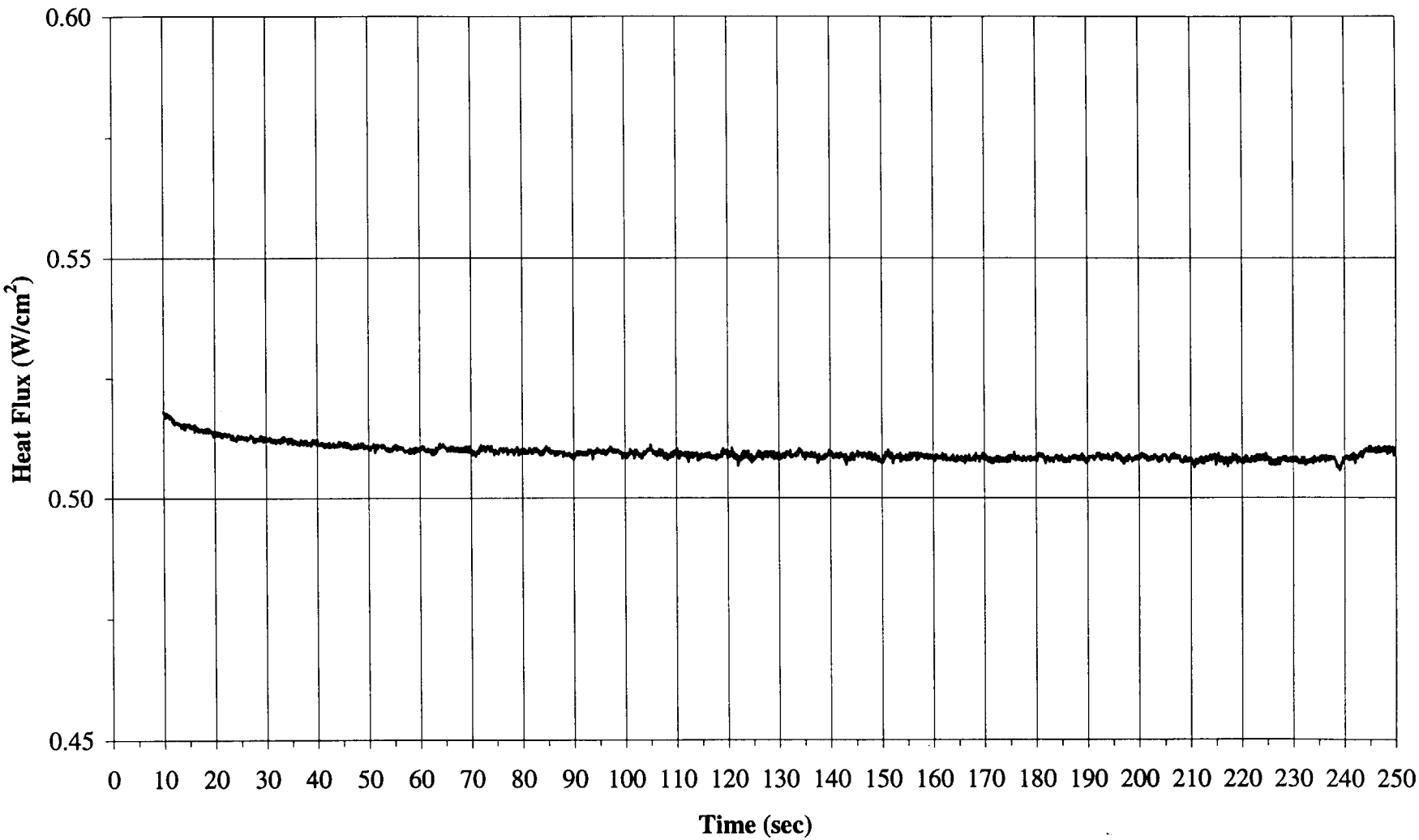

Figure B-12c. a/g = -1 Preflight test. Heat flux input. PBE-IIA (STS-77). Run No. 3.

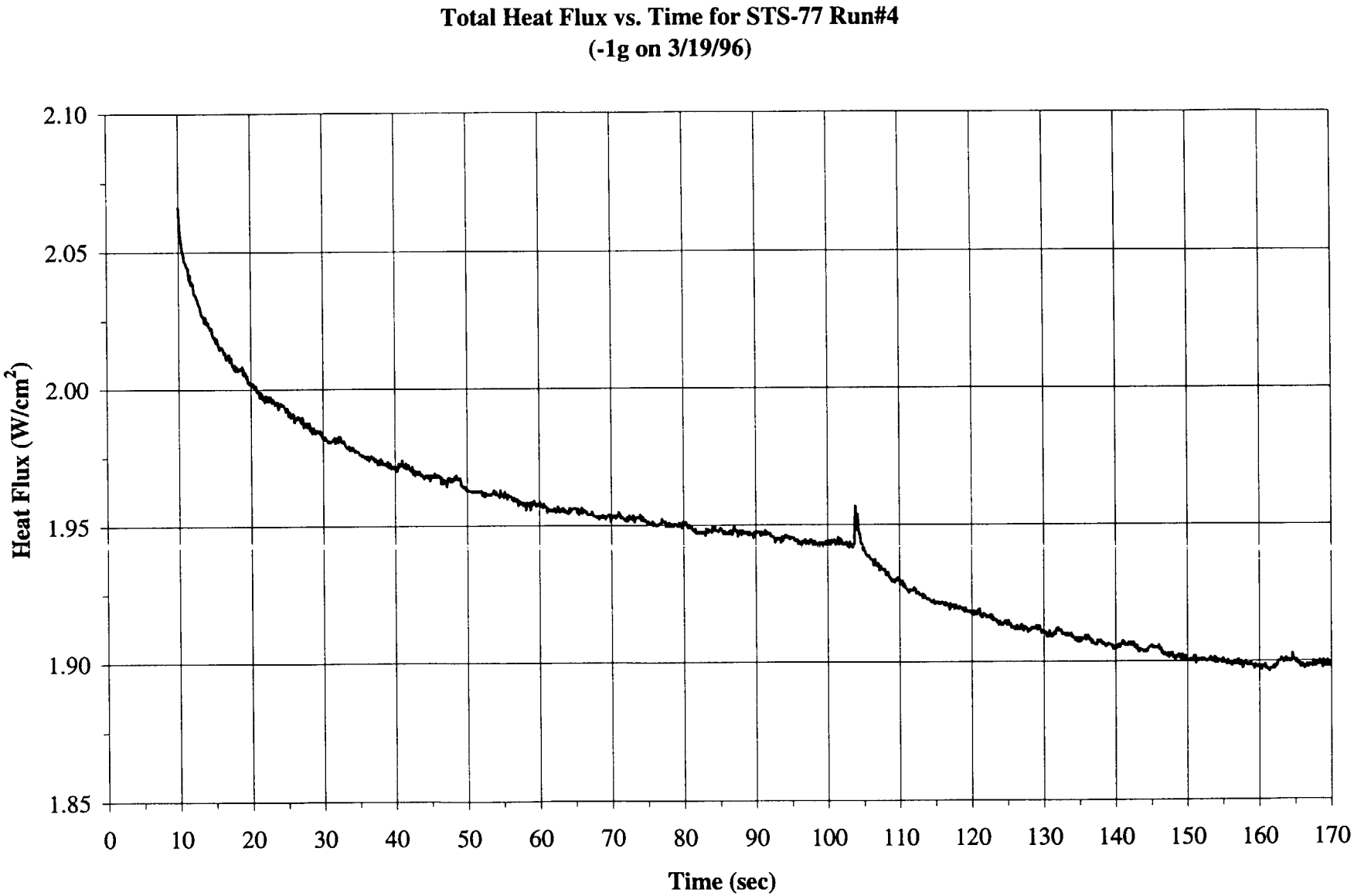

Figure B-12d. a/g = -1 Preflight test. Heat flux input. PBE-IIA (STS-77). Run No. 4.

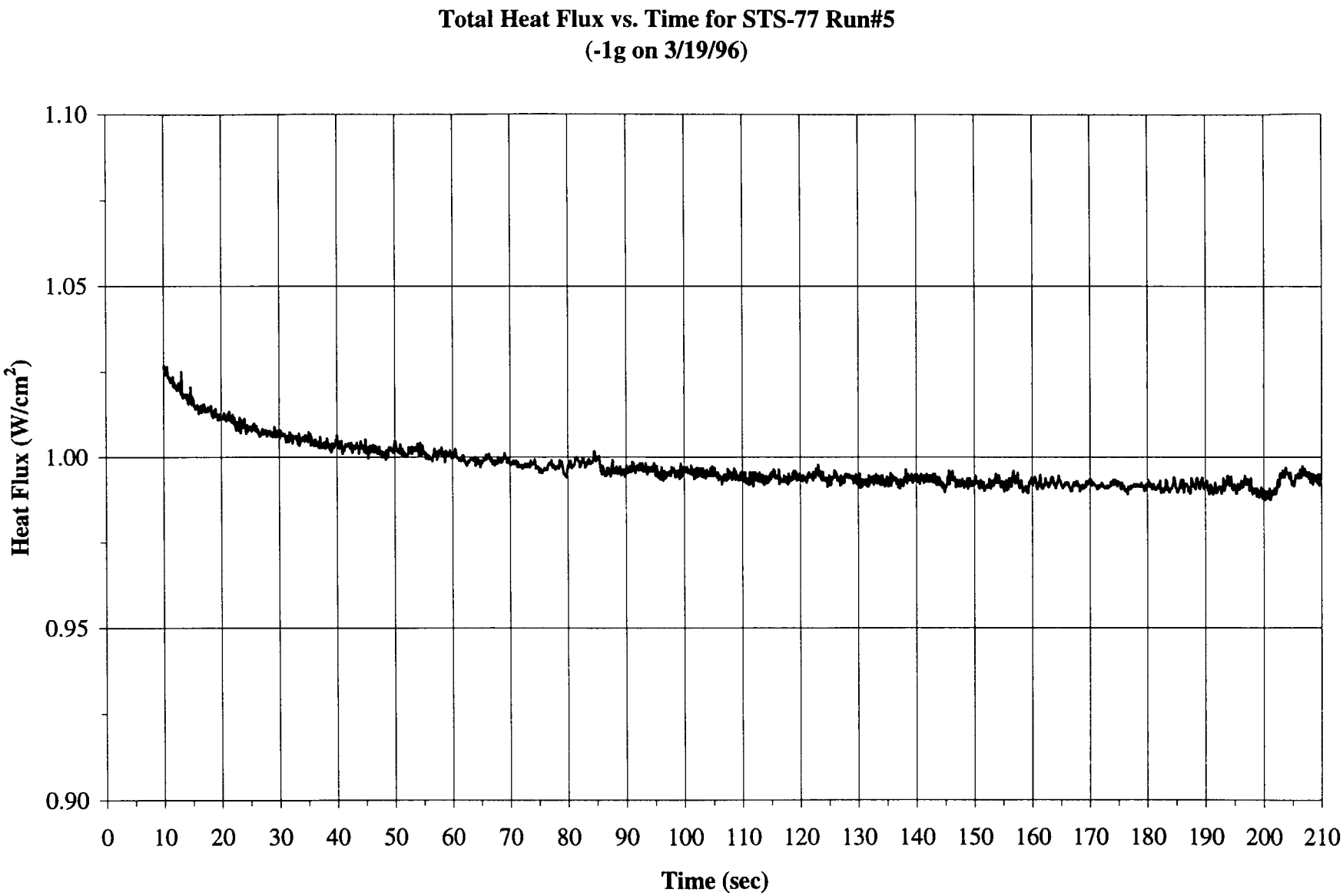

Figure B-12e. a/g = -1 Preflight test. Heat flux input. PBE-IIA (STS-77). Run No. 5.

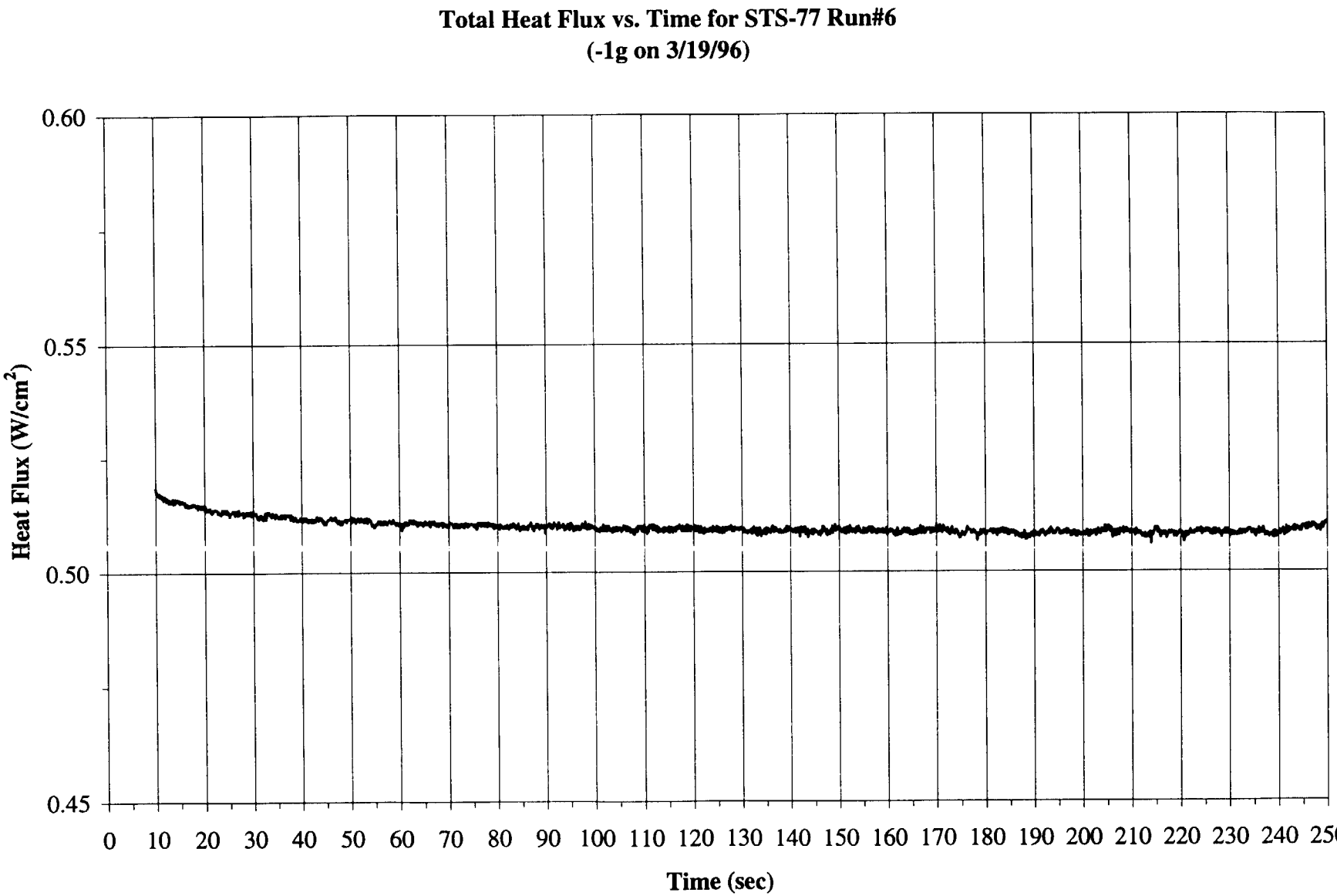

Figure B-12f. a/g = -1 Preflight test. Heat flux input. PBE-IIA (STS-77). Run No. 6.

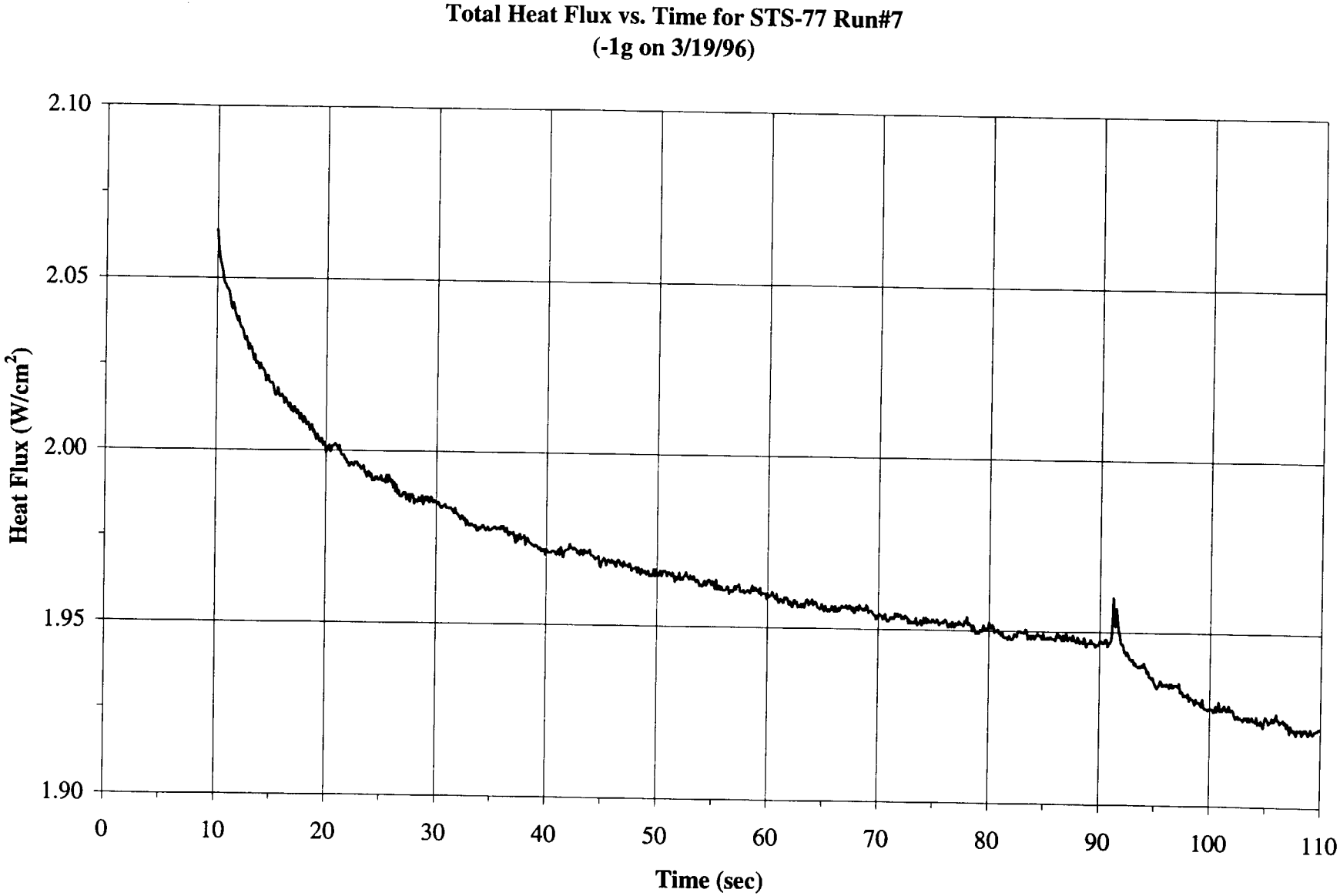

Figure B-12g. a/g = -1 Preflight test. Heat flux input. PBE-IIA (STS-77). Run No.7.

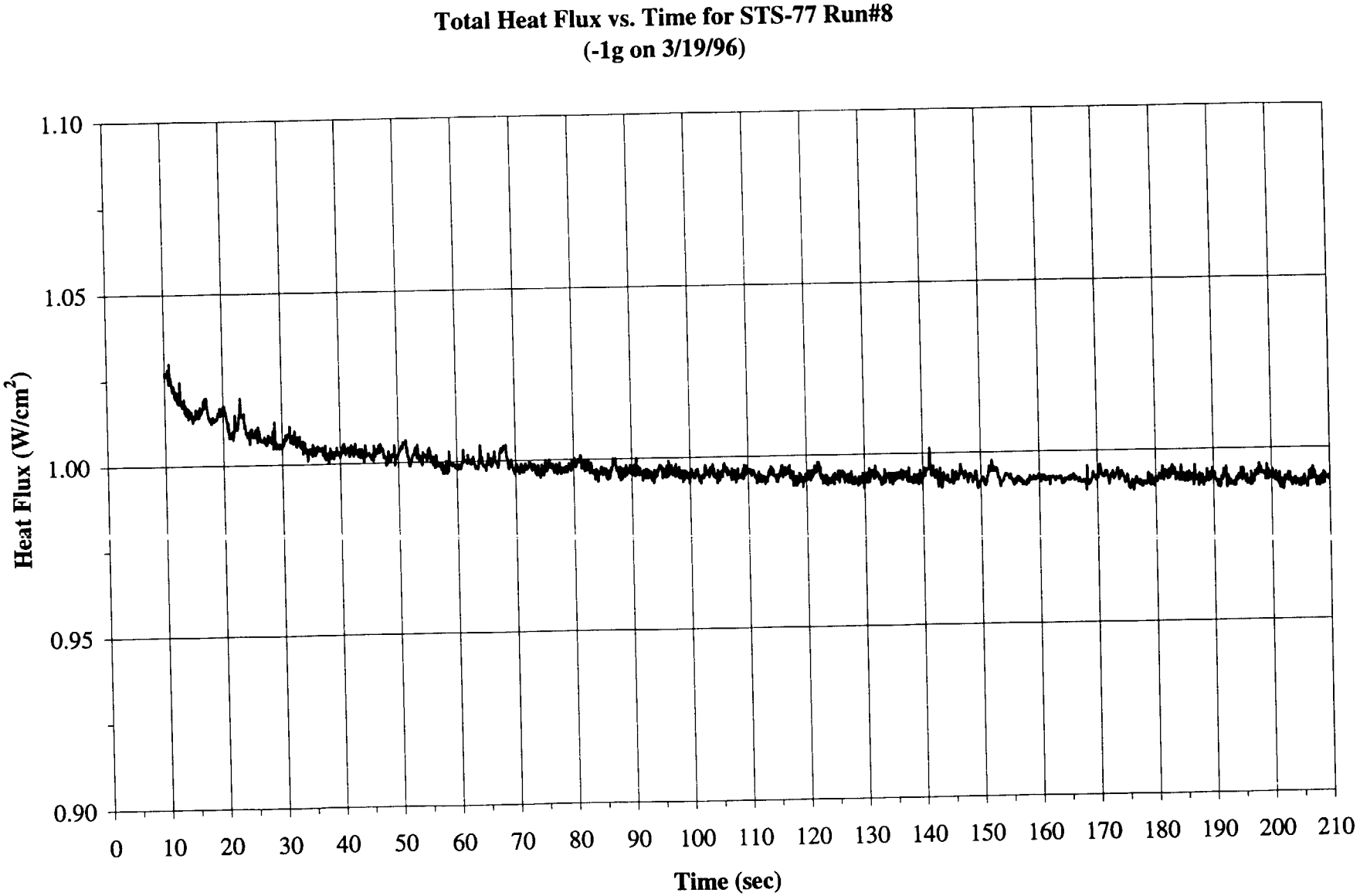

Figure B-12h. a/g = -1 Preflight test. Heat flux input. PBE-IIA (STS-77). Run No. 8.

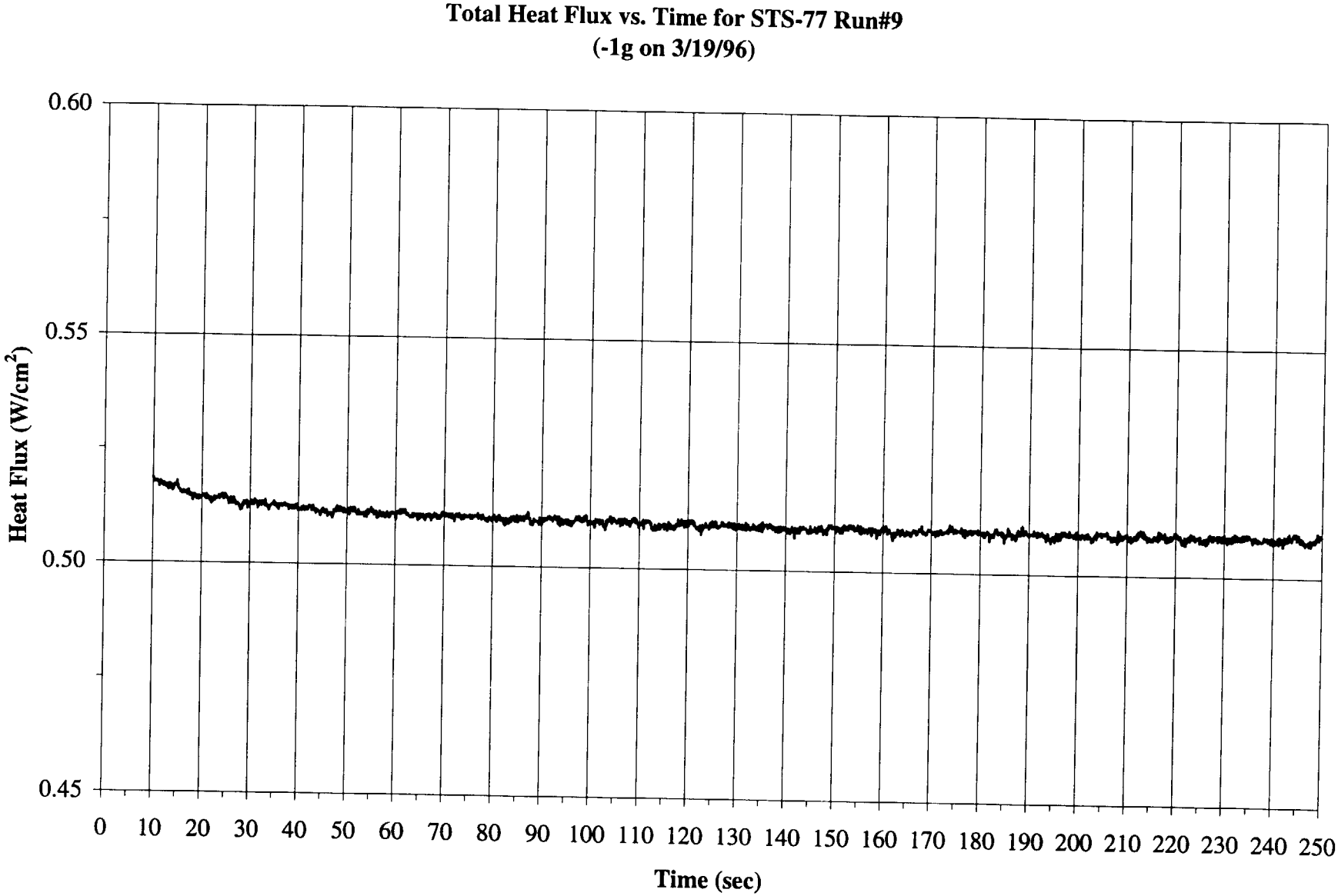

Figure B-12i. a/g = -1 Preflight test. Heat flux input. PBE-IIA (STS-77). Run No. 9.

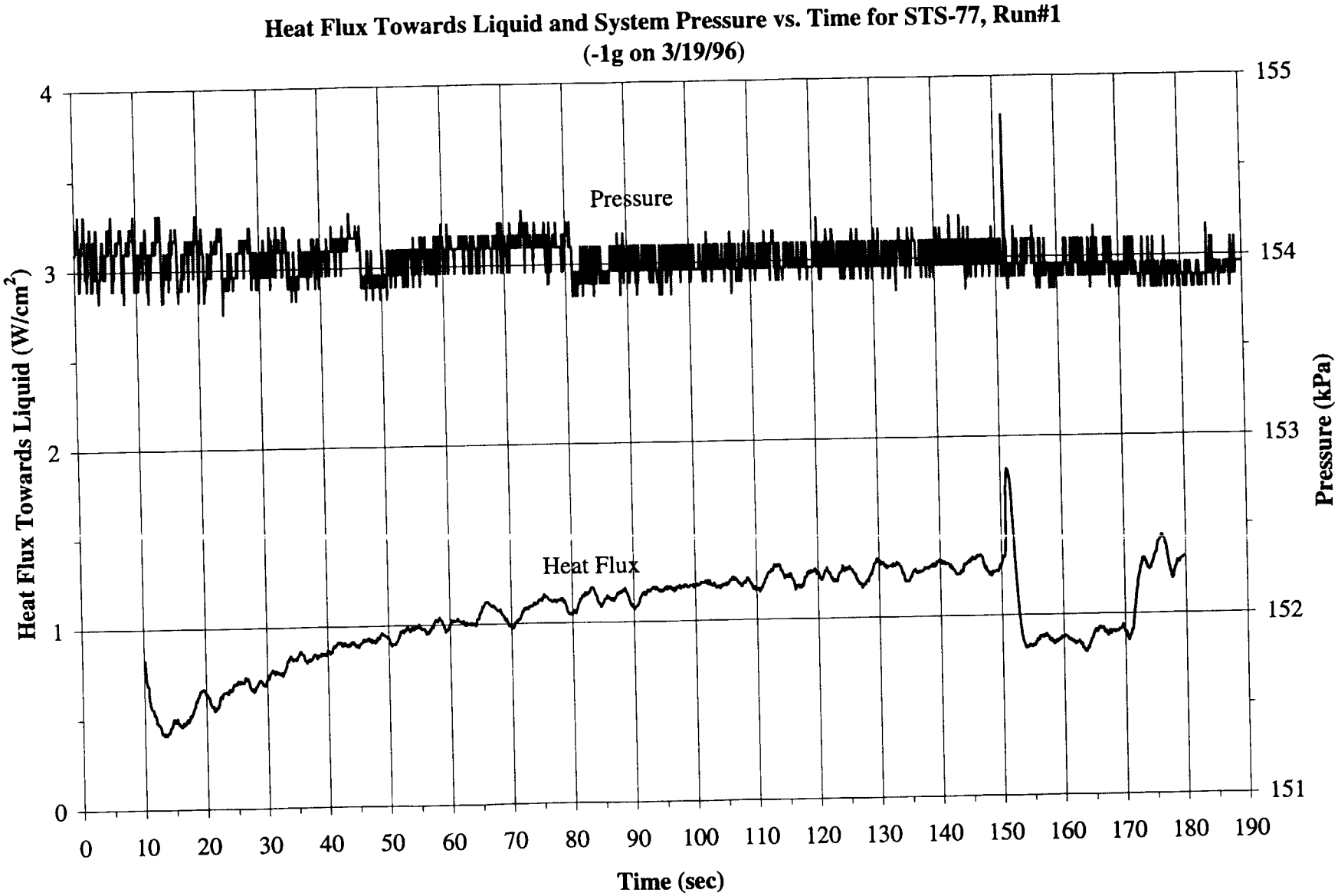

Figure B-13a. a/g = -1 Preflight test. System pressure and heat flux into fluid. PBE-IIA (STS-77). Run No. 1.

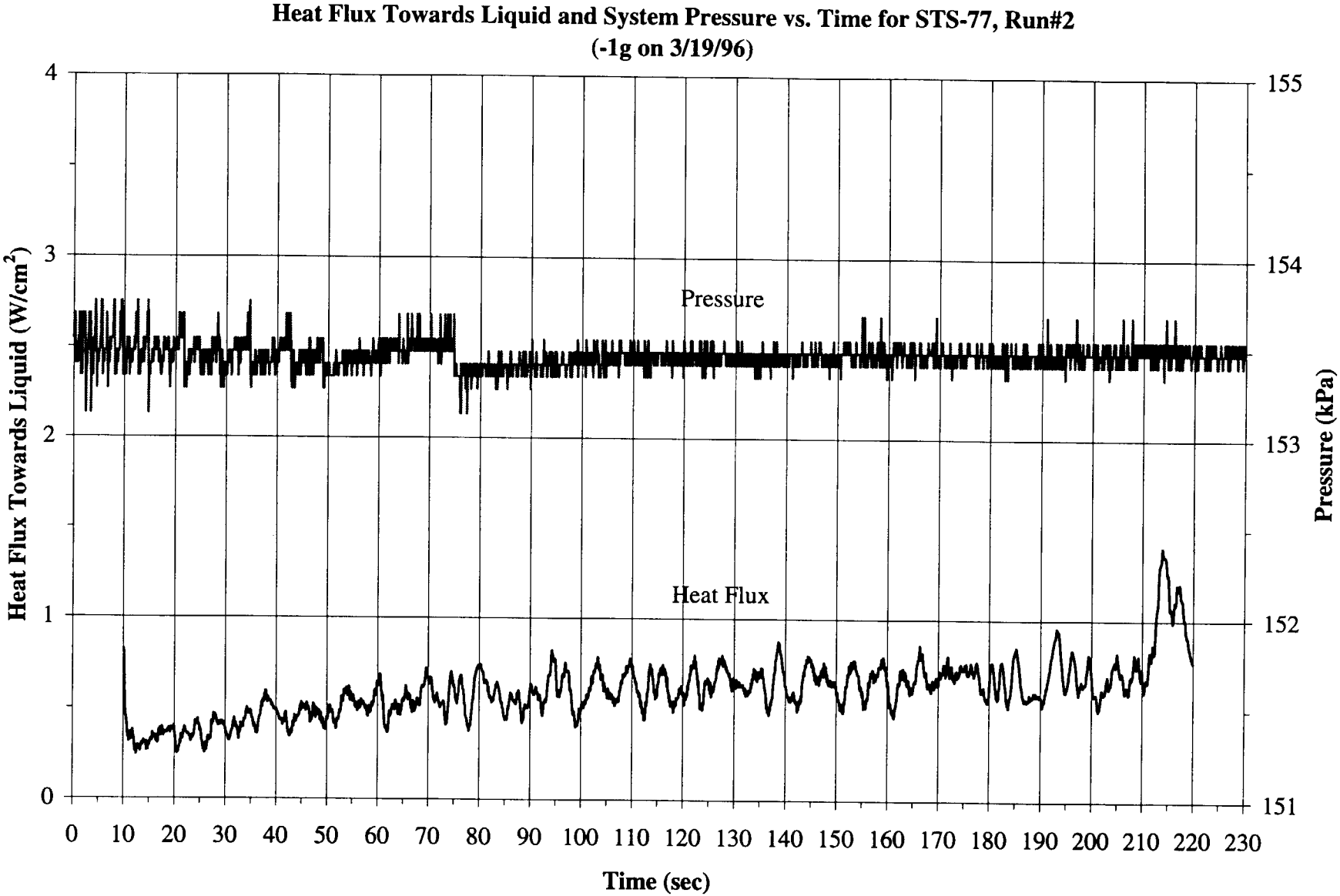

Figure B-13b. a/g = -1 Preflight test. System pressure and heat flux into fluid. PBE-IIA (STS-77). Run No. 2.

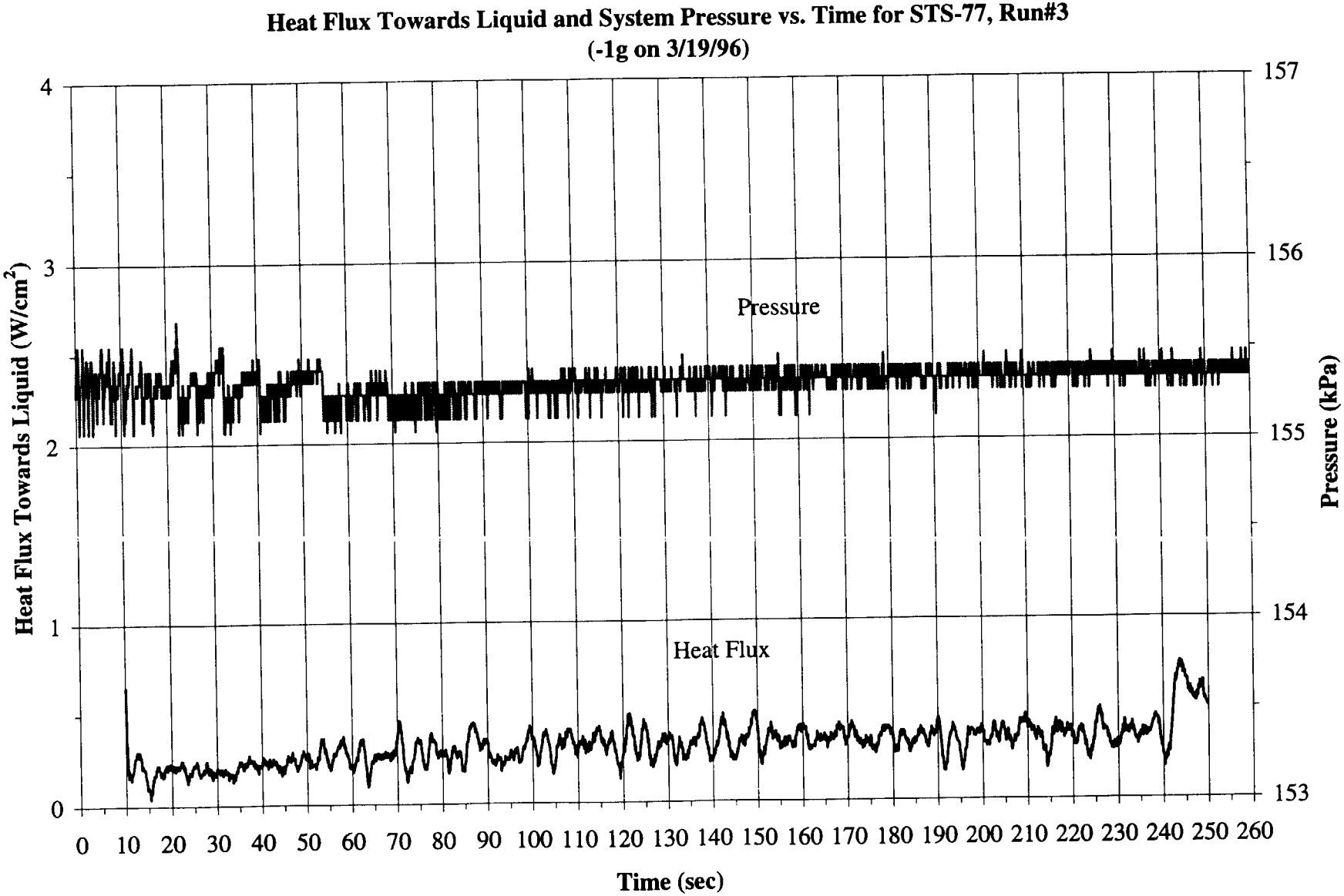

Figure B-13c. a/g = -1 Preflight test. System pressure and heat flux into fluid. PBE-IIA (STS-77). Run No. 3.

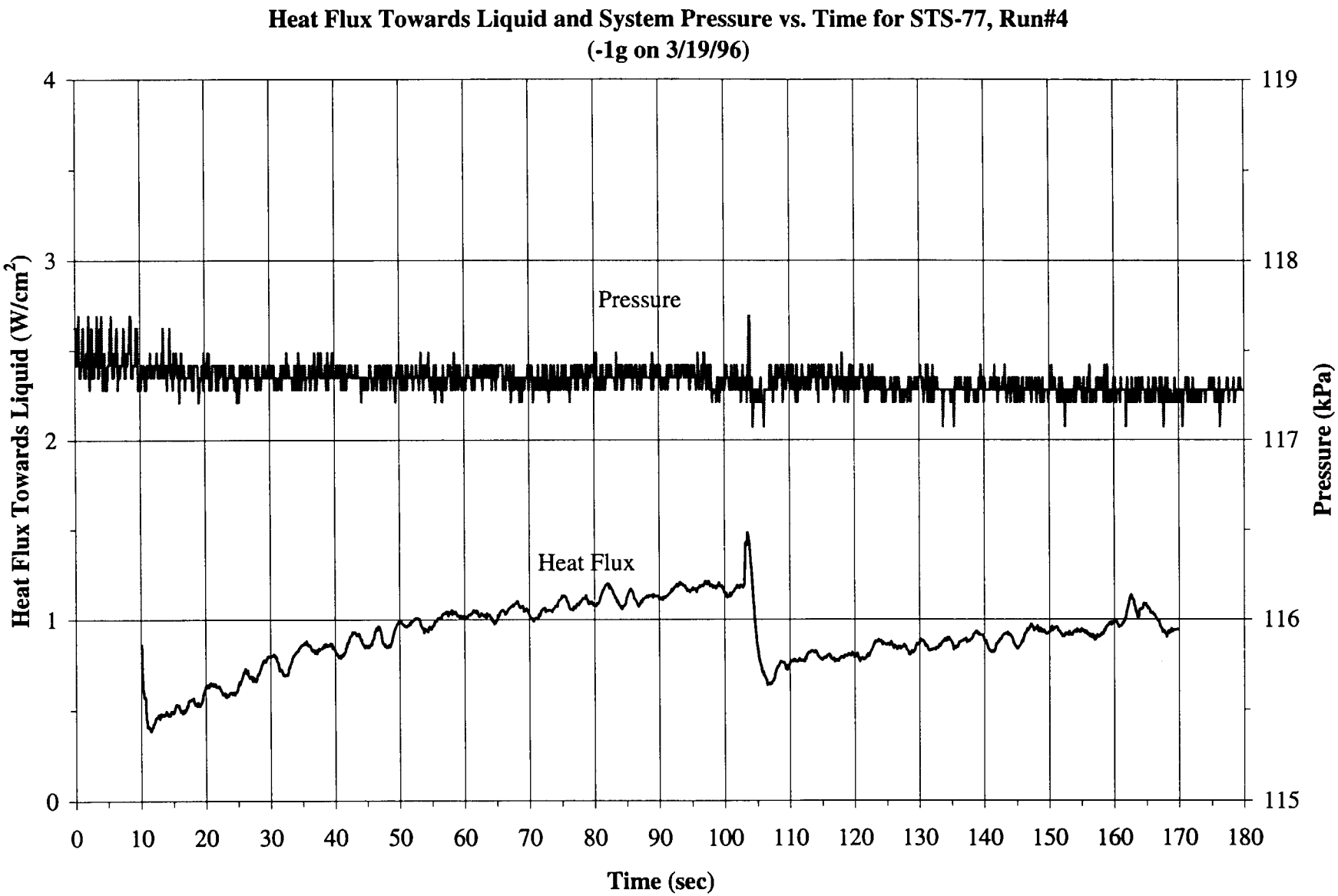

Figure B-13d. a/g = -1 Preflight test. System pressure and heat flux into fluid. PBE-IIA (STS-77). Run No. 4.

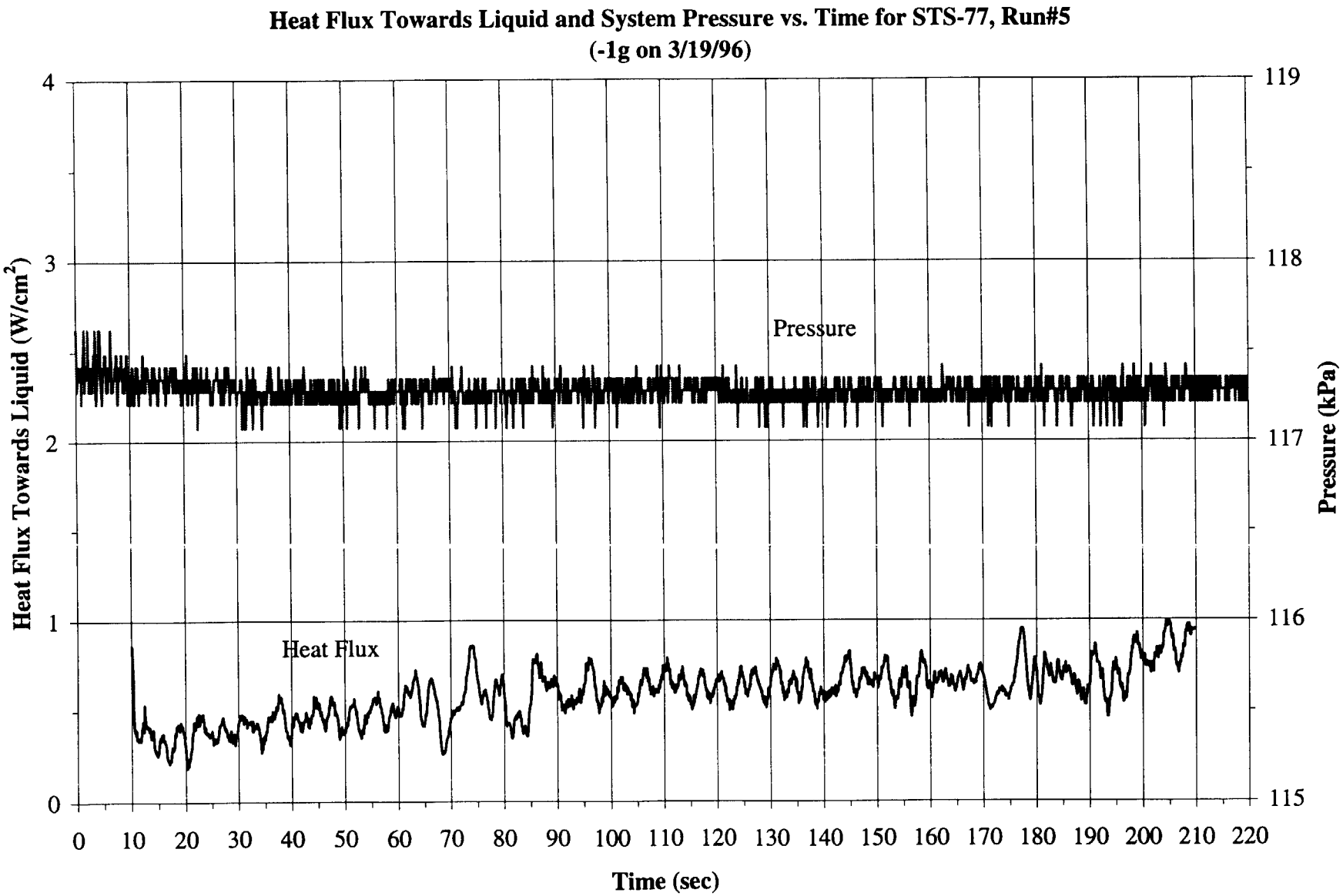

Figure B-13e. a/g = -1 Preflight test. System pressure and heat flux into fluid. PBE-IIA (STS-77). Run No. 5.

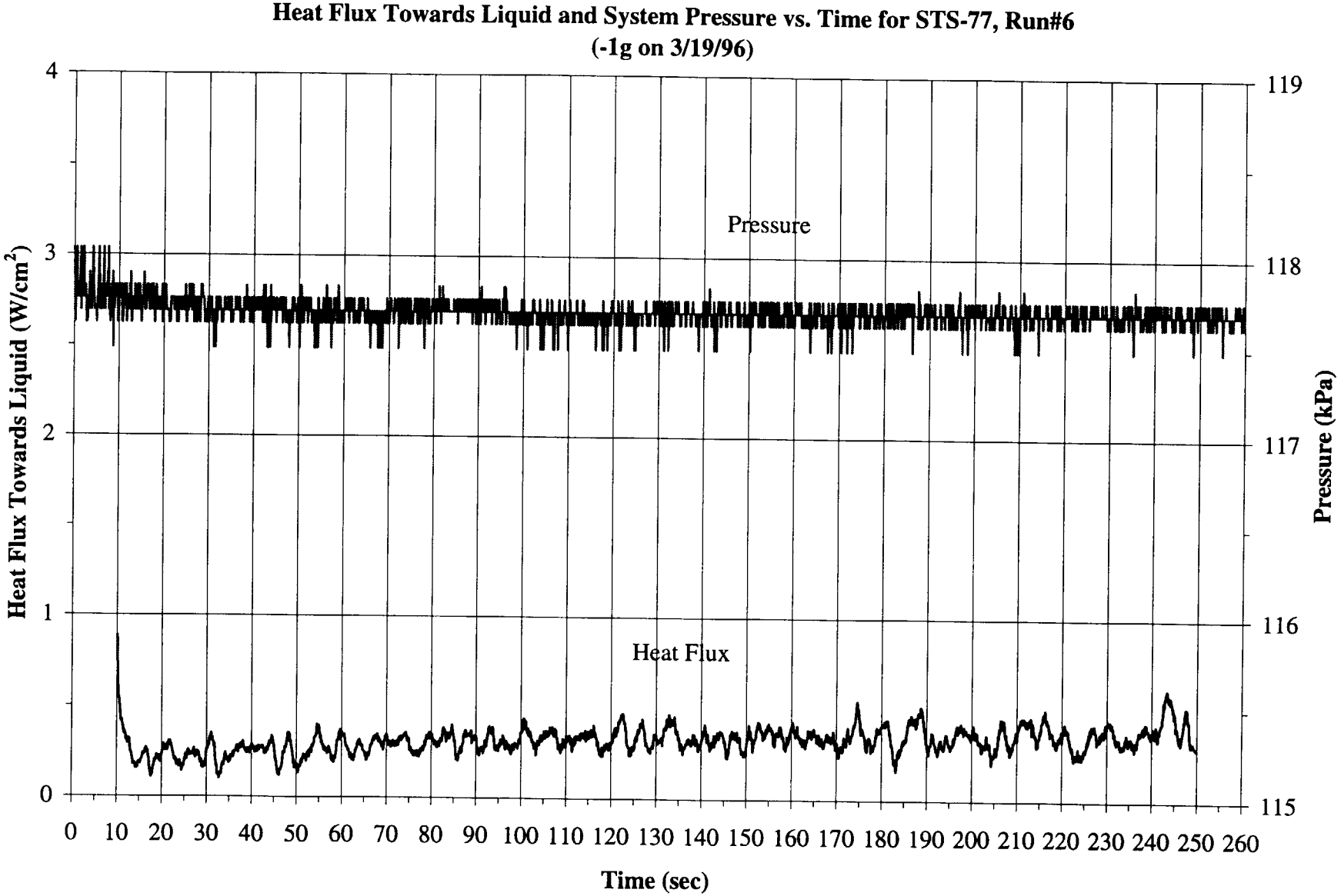

Figure B-13f. a/g = -1 Preflight test. System pressure and heat flux into fluid. PBE-IIA (STS-77). Run No. 6.

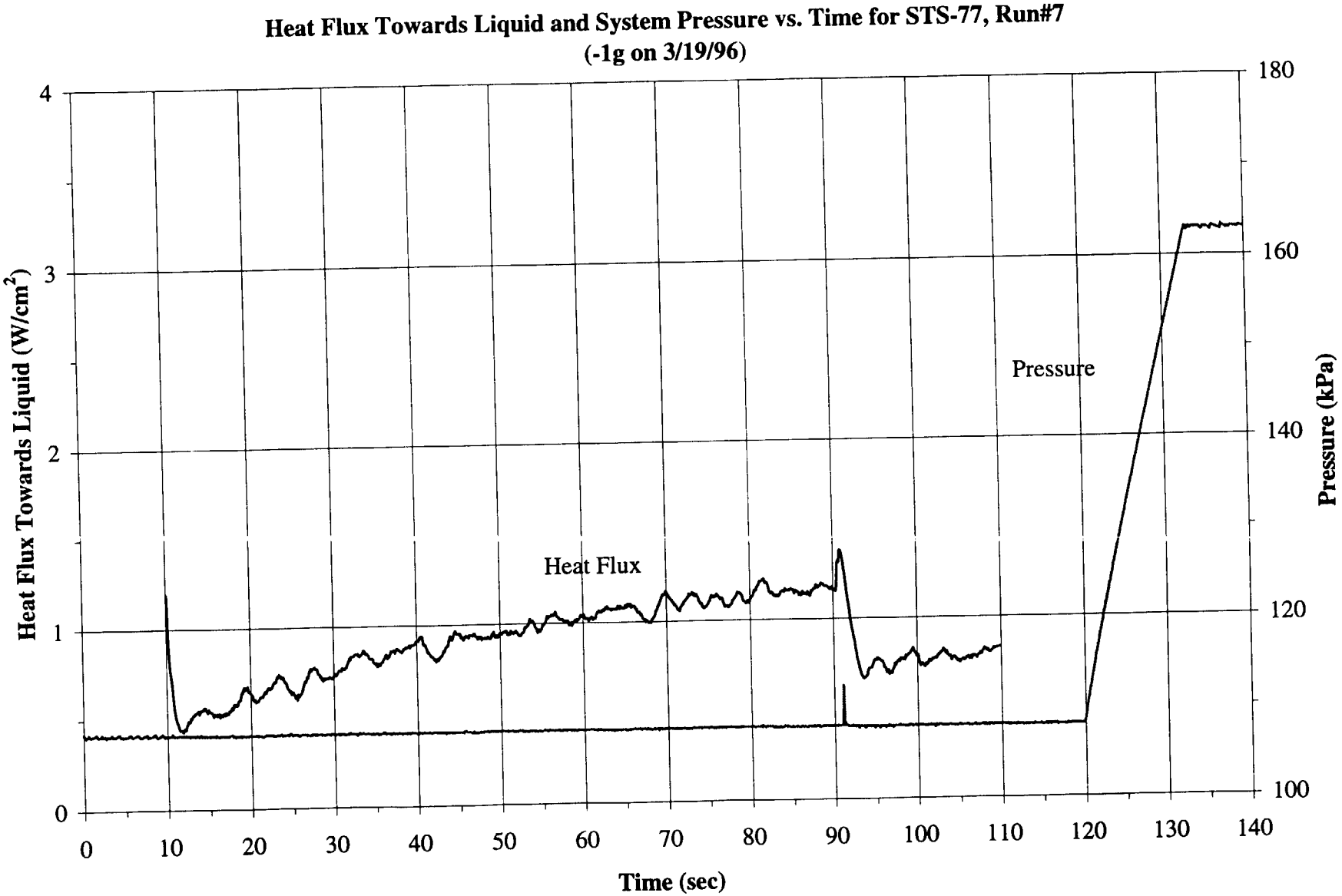

Figure B-13g. a/g = -1 Preflight test. System pressure and heat flux into fluid. PBE-IIA (STS-77). Run No. 7.

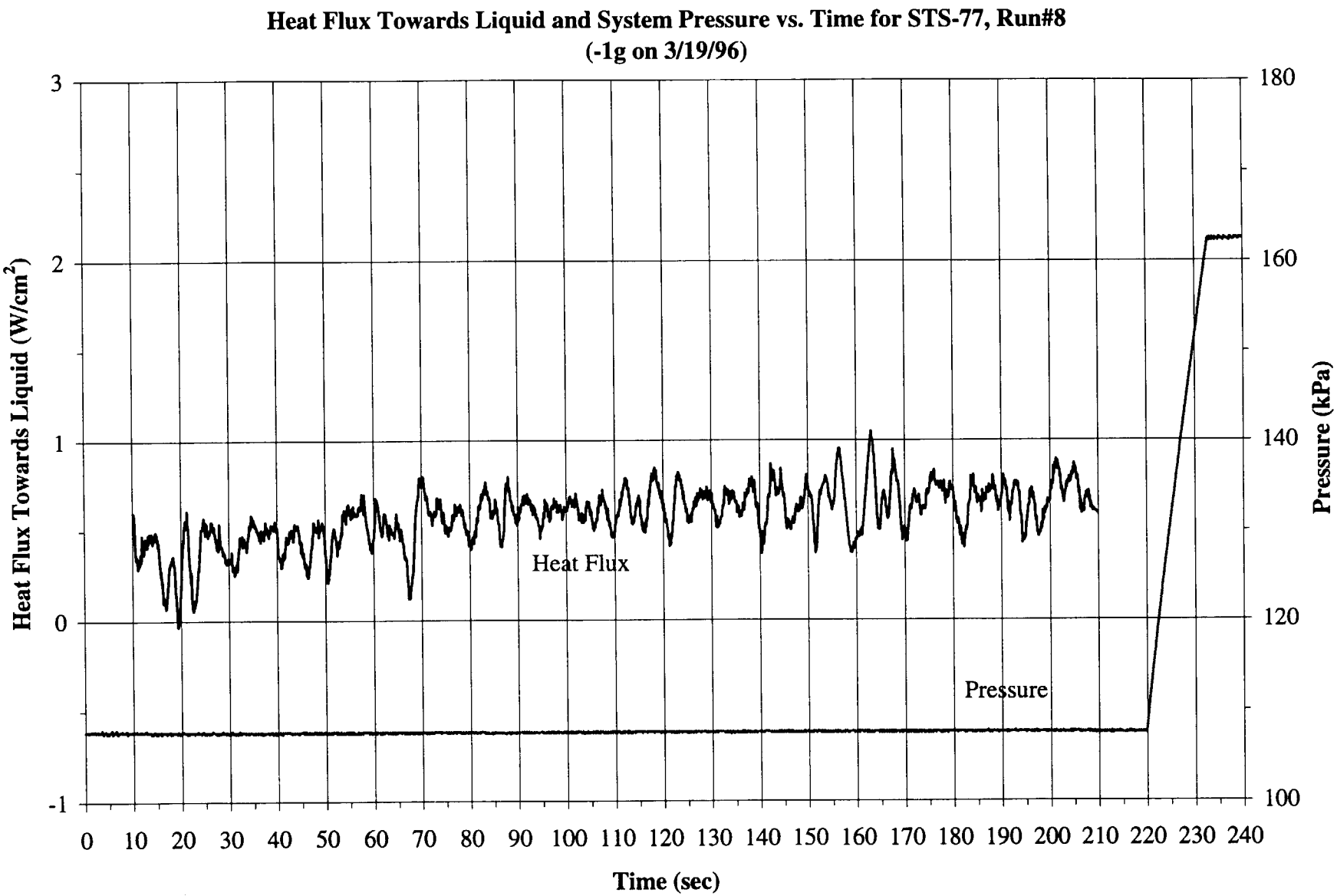

Figure B-13h. a/g = -1 Preflight test. System pressure and heat flux into fluid. PBE-IIA (STS-77). Run No. 8.

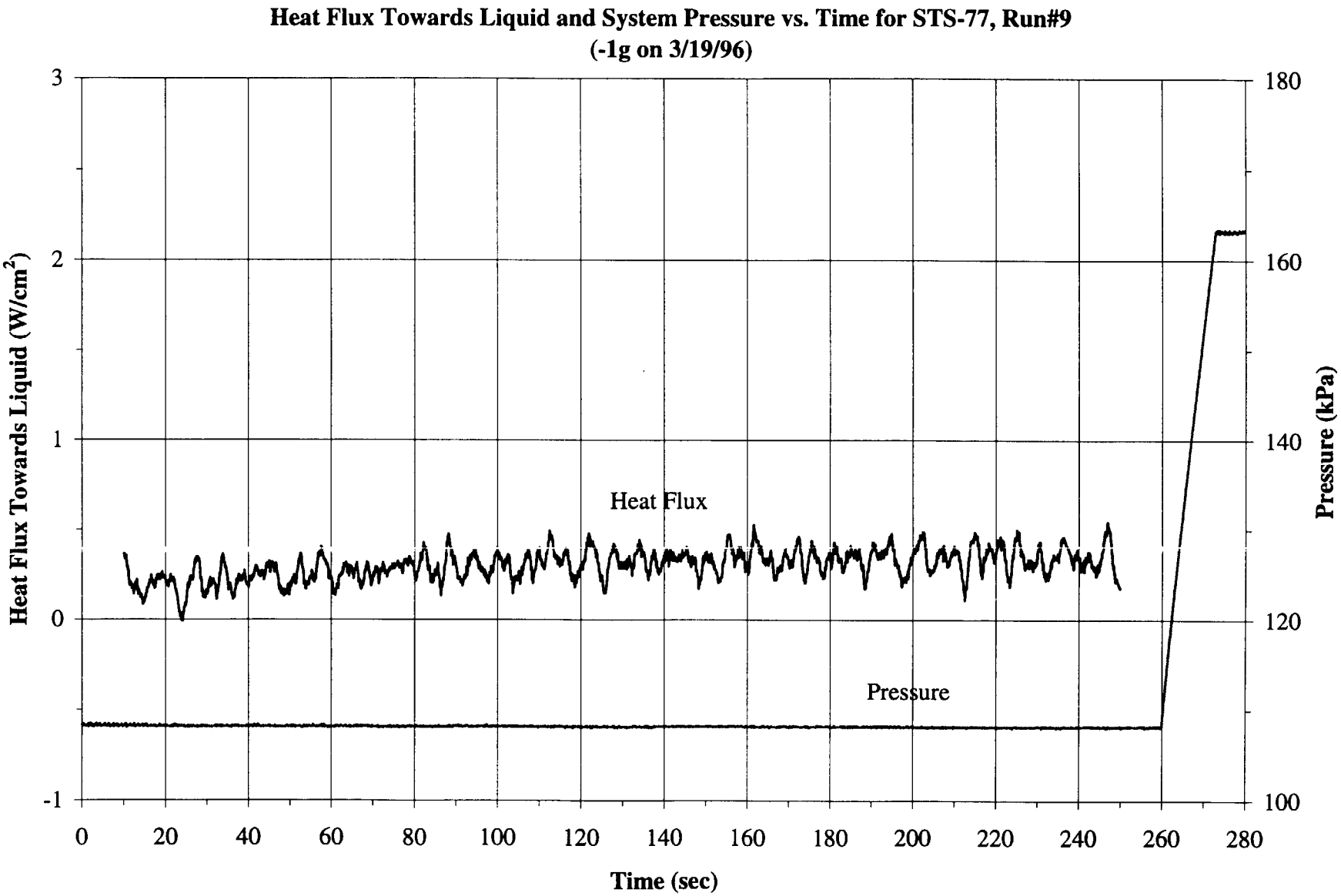

Figure B-13i. a/g = -1 Preflight test. System pressure and heat flux into fluid. PBE-IIA (STS-77). Run No. 9.

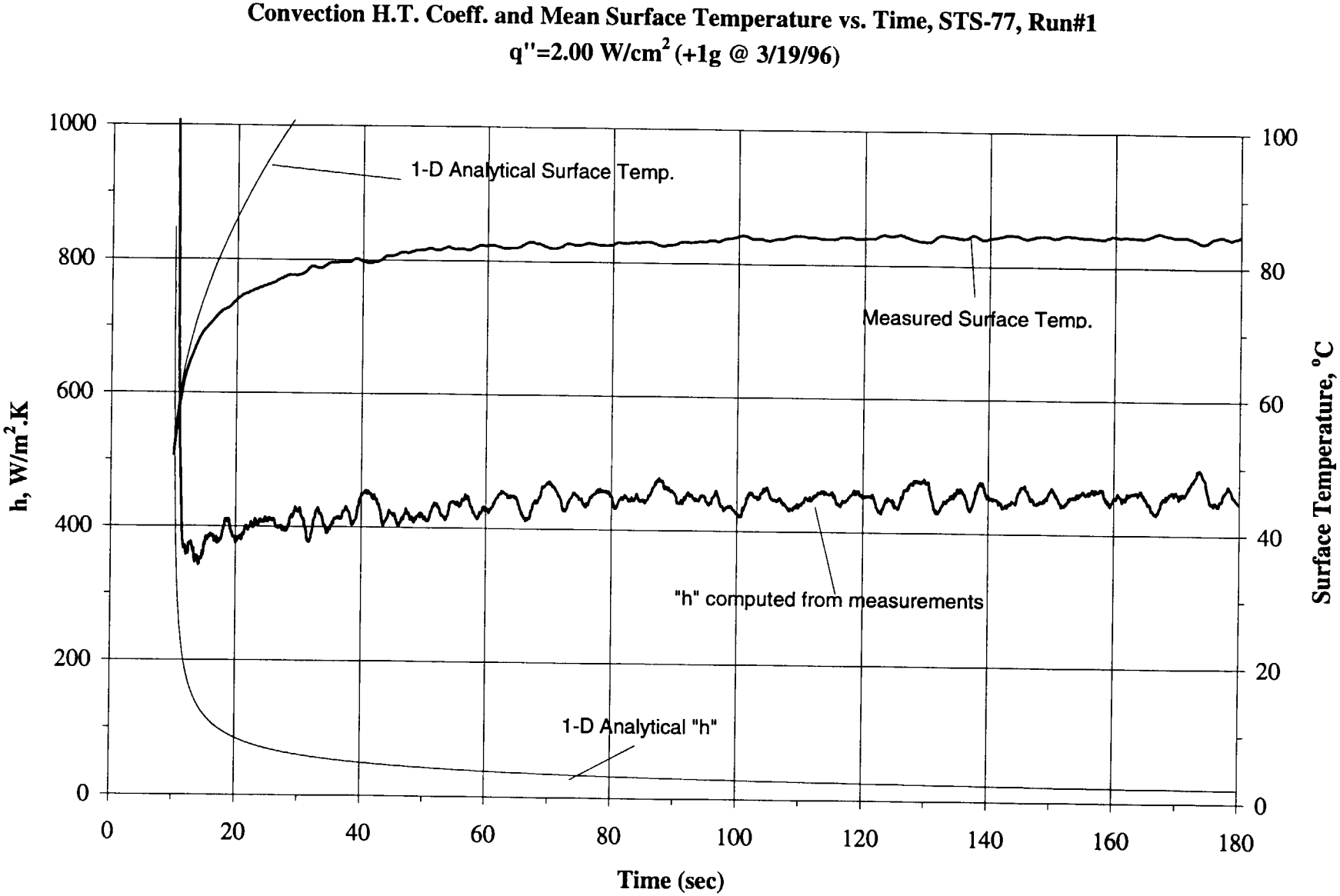

Figure B-14a. a/g = +1 Preflight test. Mean heater surface temperature and derived heat transfer coefficient. PBE-IIA (STS-77). Run No. 1.

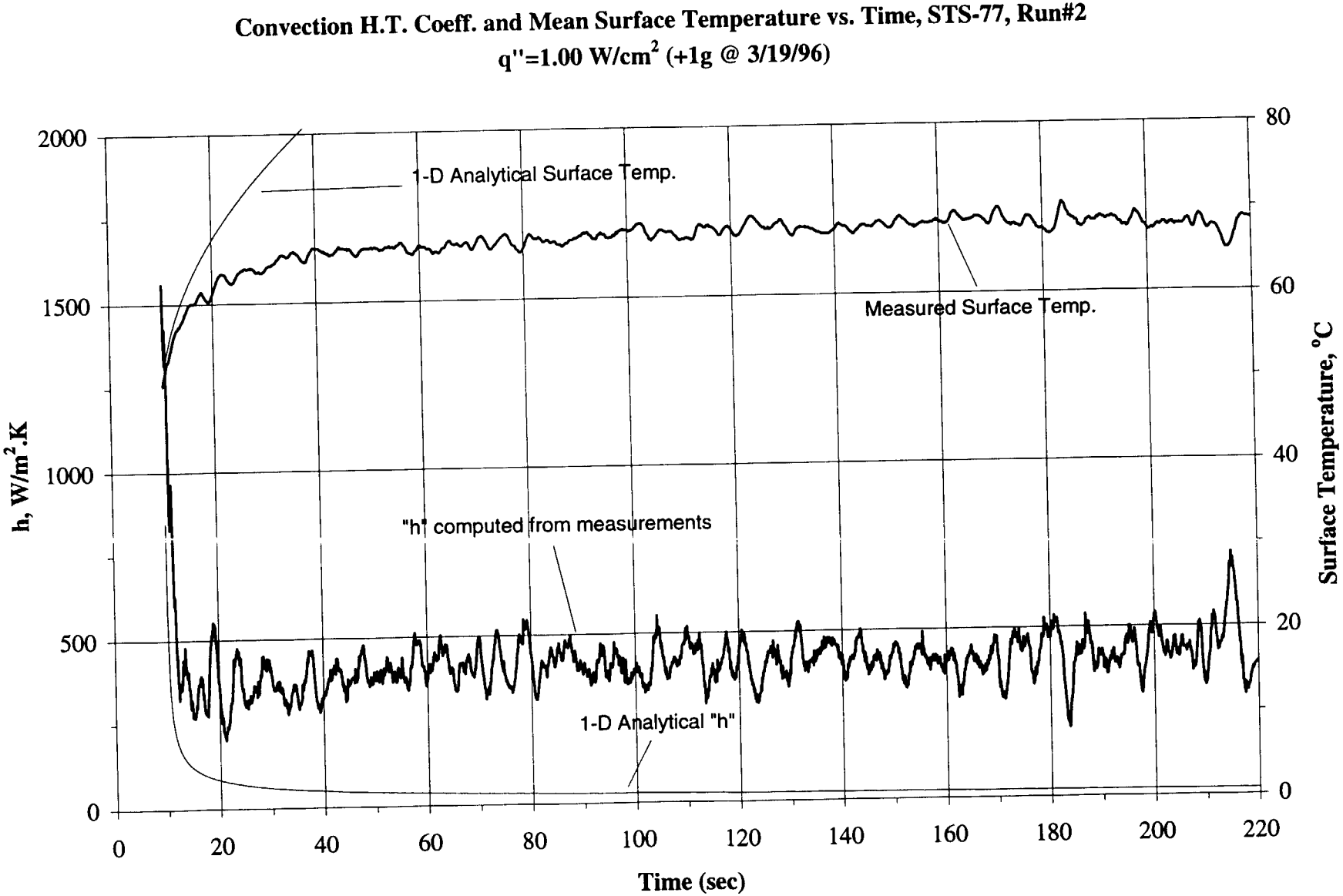

Figure B-14b. a/g = +1 Preflight test. Mean heater surface temperature and derived heat transfer coefficient. PBE-IIA (STS-77). Run No. 2.

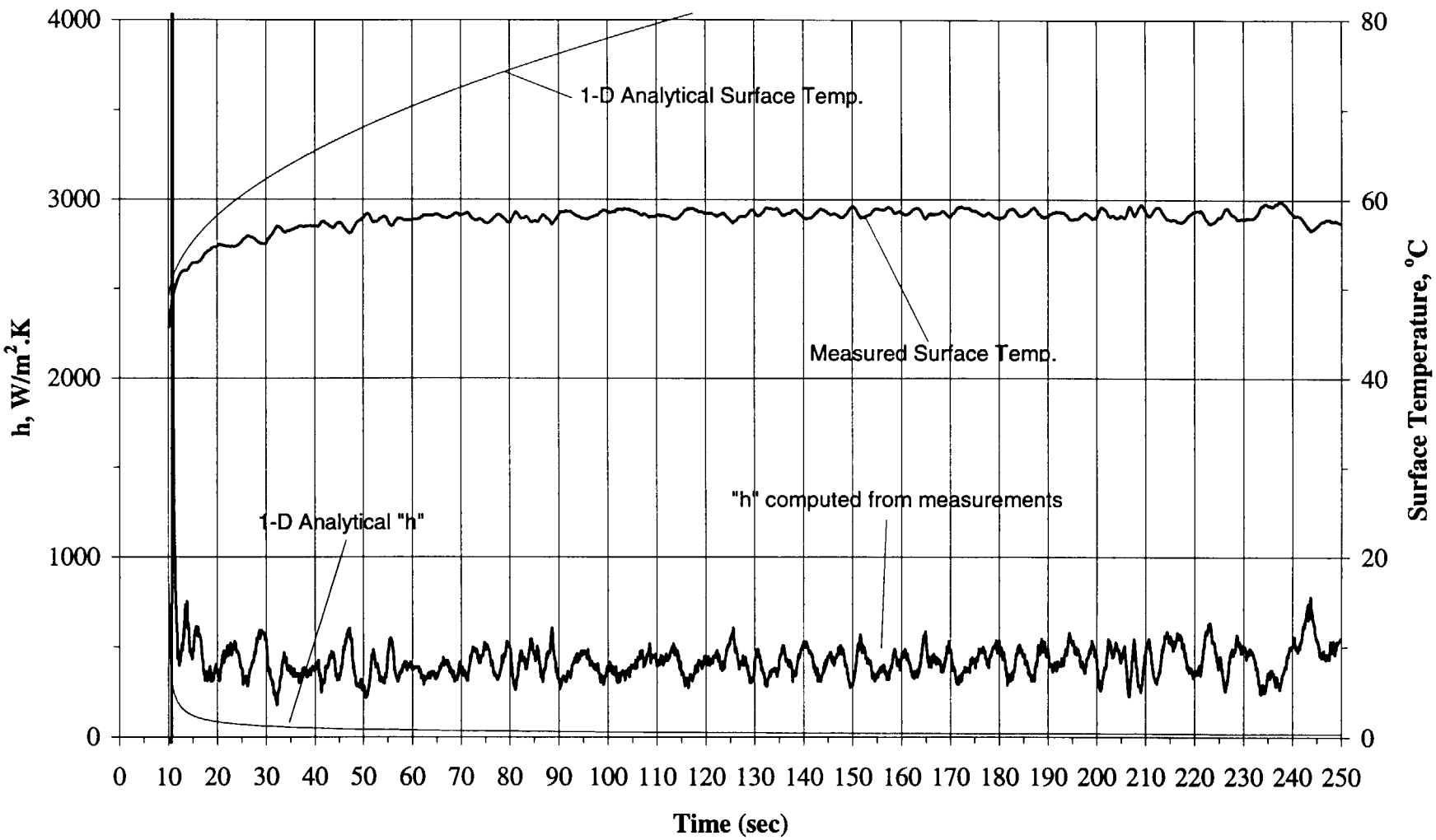

Figure B-14c. a/g = +1 Preflight test. Mean heater surface temperature and derived heat transfer coefficient. PBE-IIA (STS-77). Run No. 3.

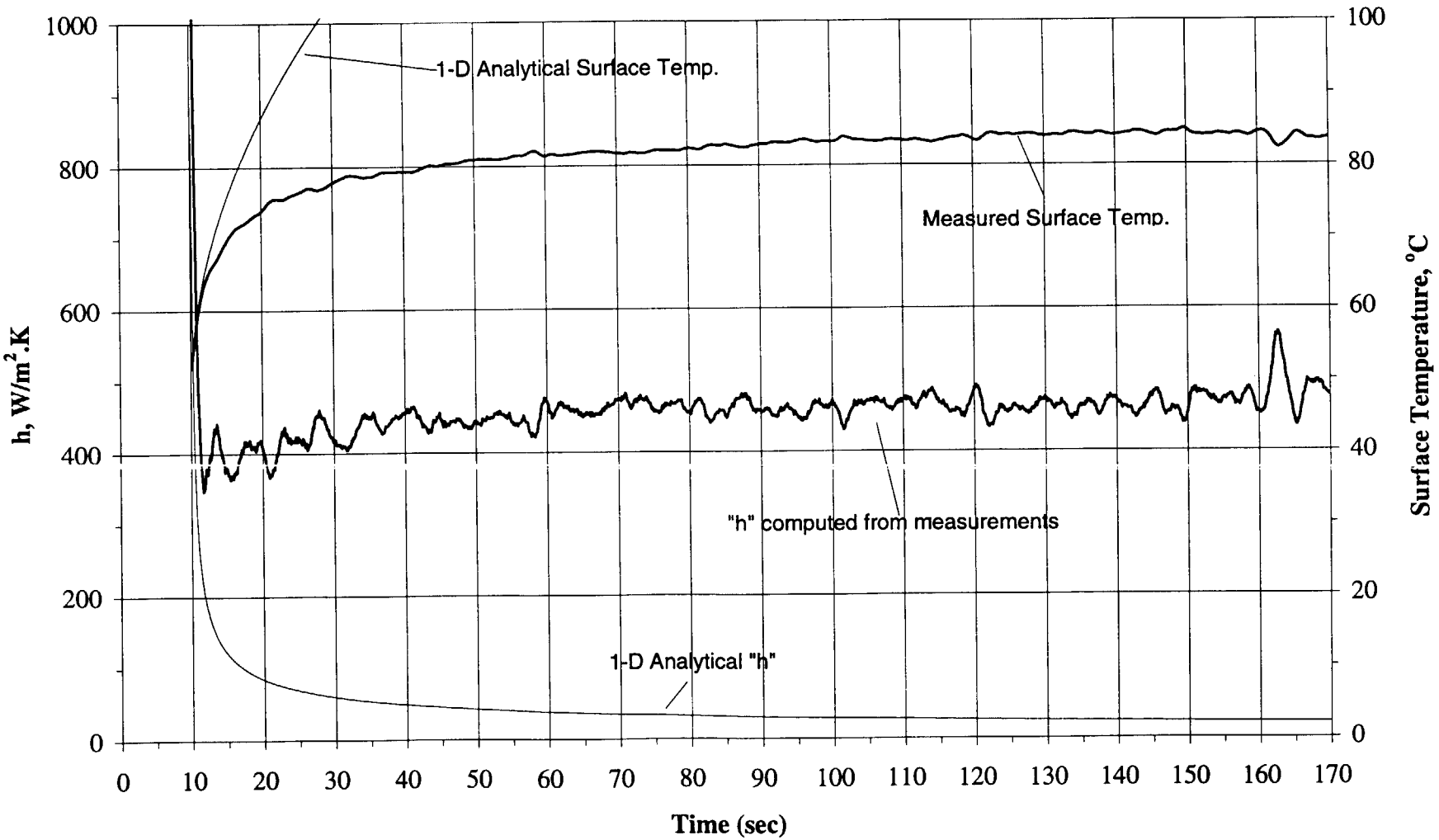

Figure B-14d. a/g = +1 Preflight test. Mean heater surface temperature and derived heat transfer coefficient. PBE-IIA (STS-77). Run No. 4.

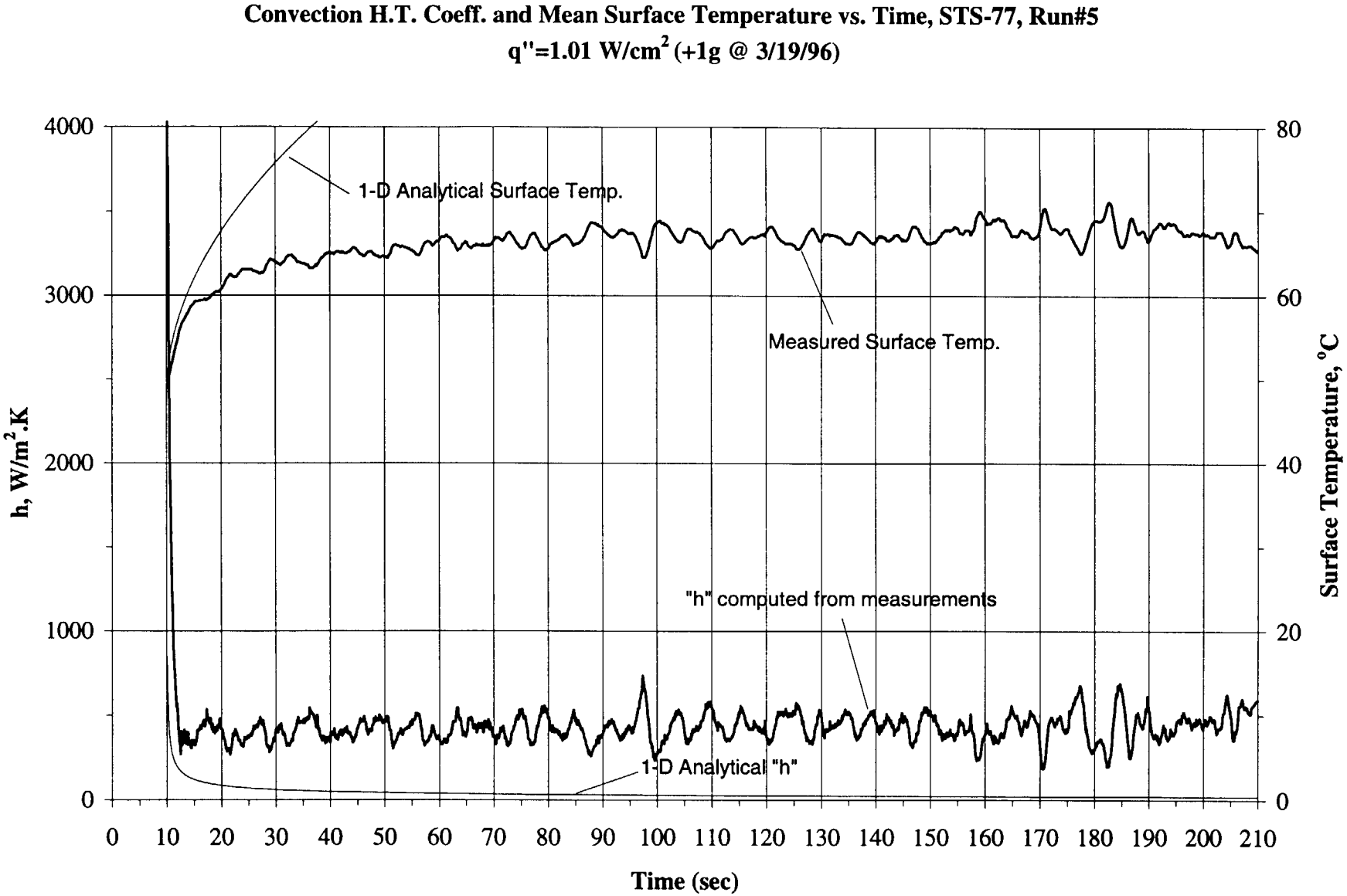

Figure B-14e. a/g = +1 Preflight test. Mean heater surface temperature and derived heat transfer coefficient. PBE-IIA (STS-77). Run No. 5.

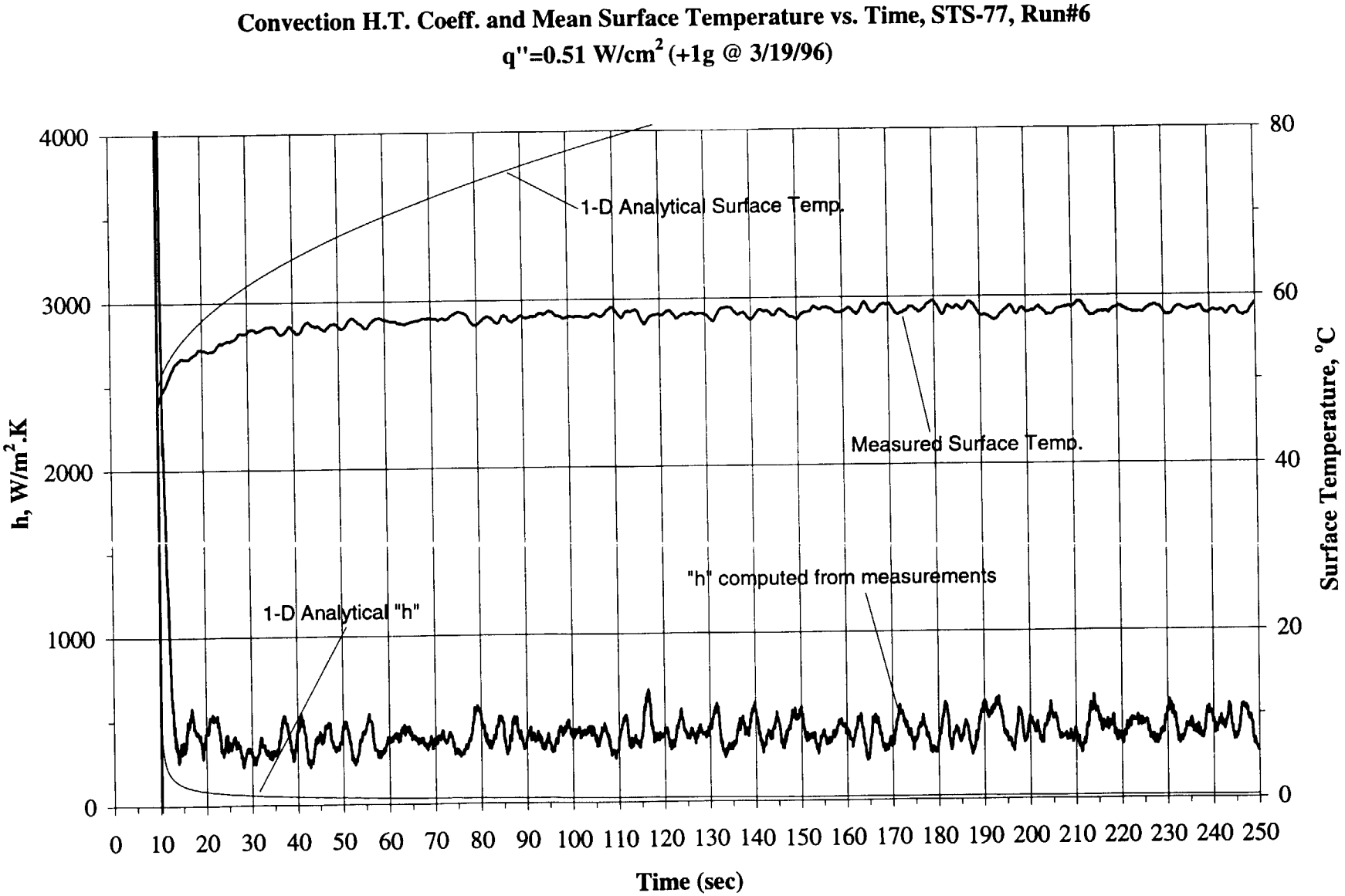

Figure B-14f. a/g = +1 Preflight test. Mean heater surface temperature and derived heat transfer coefficient. PBE-IIA (STS-77). Run No. 6.

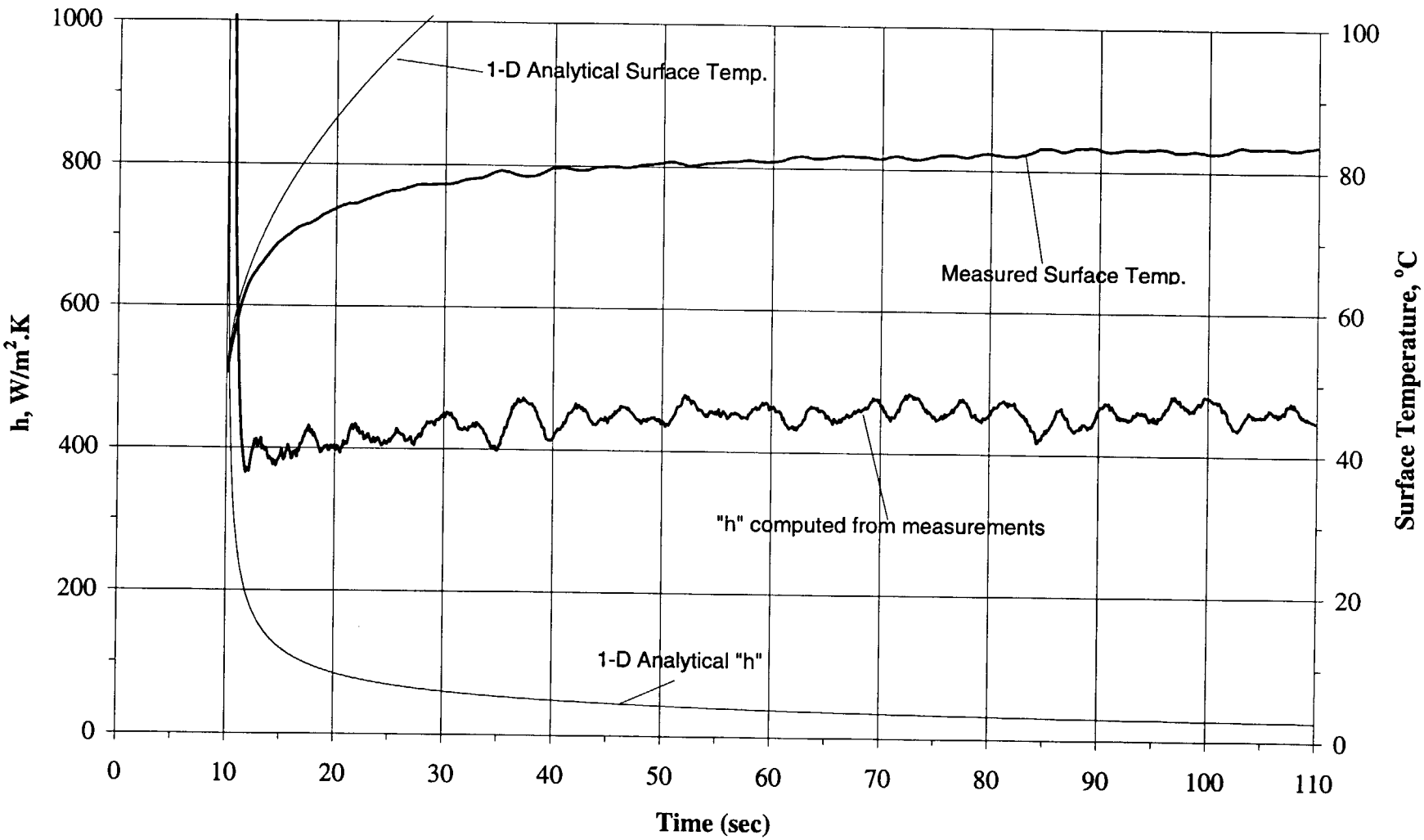

Figure B-14g. a/g = +1 Preflight test. Mean heater surface temperature and derived heat transfer coefficient. PBE-IIA (STS-77). Run No. 7.

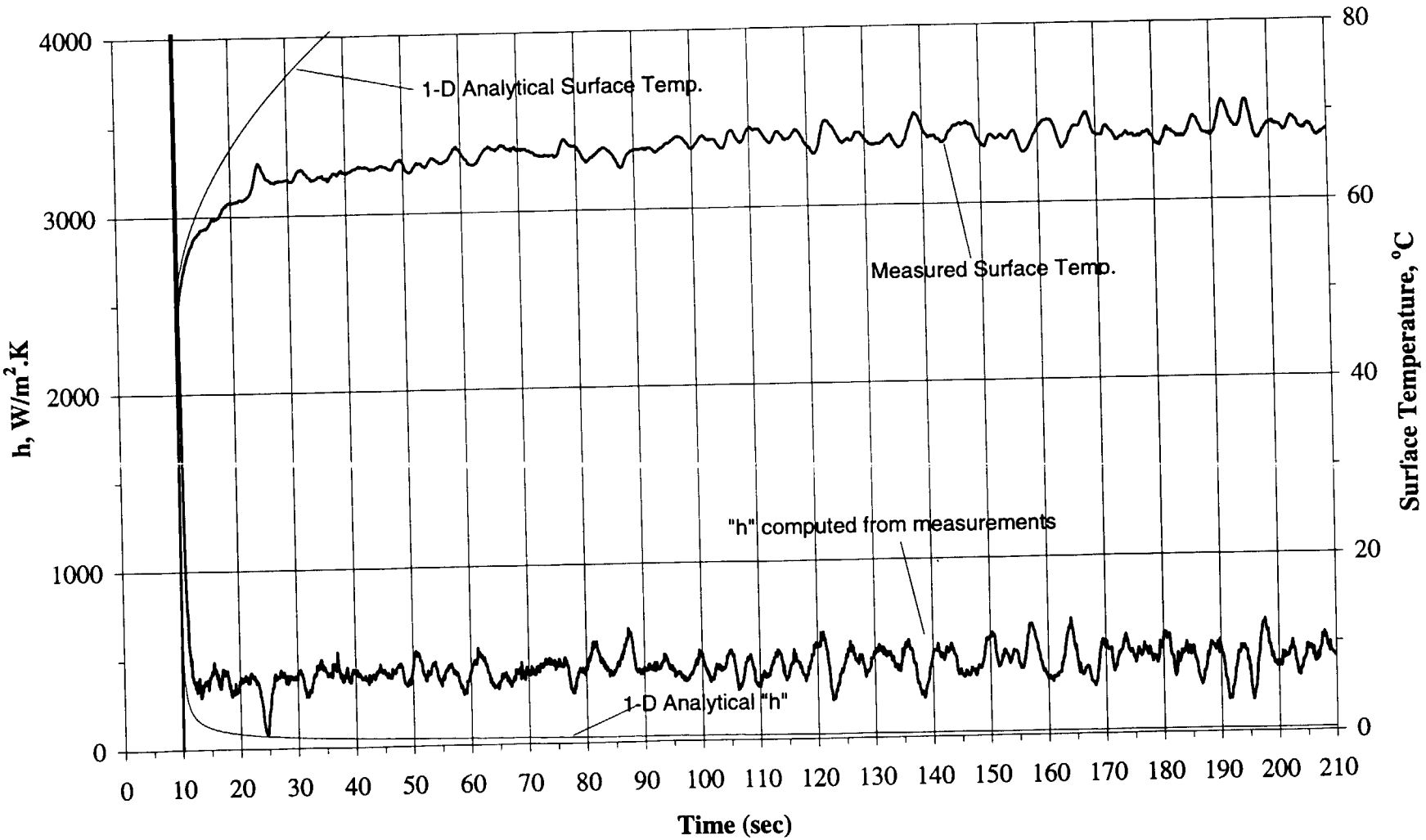

Figure B-14h. a/g = +1 Preflight test. Mean heater surface temperature and derived heat transfer coefficient. PBE-IIA (STS-77). Run No. 8.

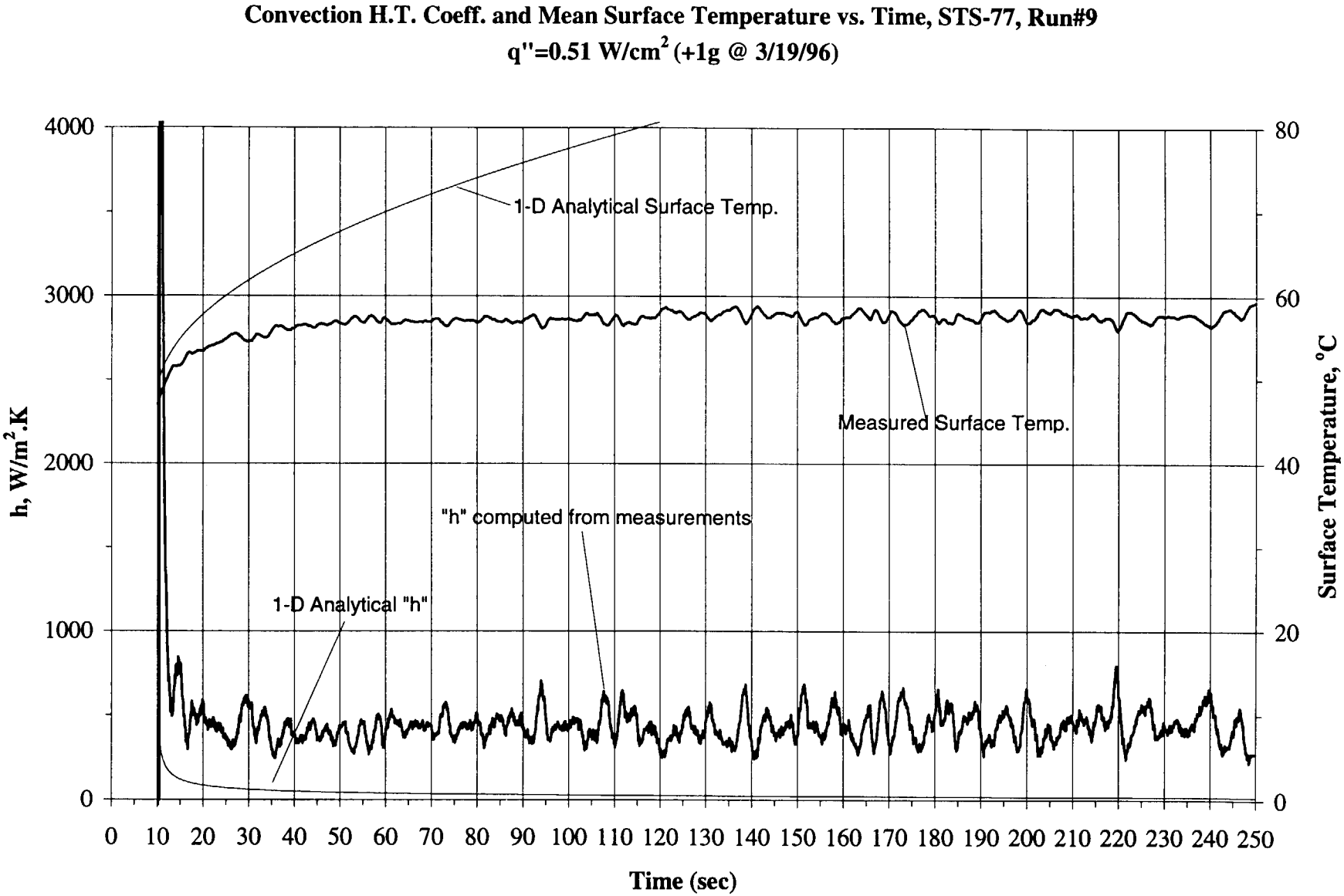

Figure B-14i. a/g = +1 Preflight test. Mean heater surface temperature and derived heat transfer coefficient. PBE-IIA (STS-77). Run No. 9.

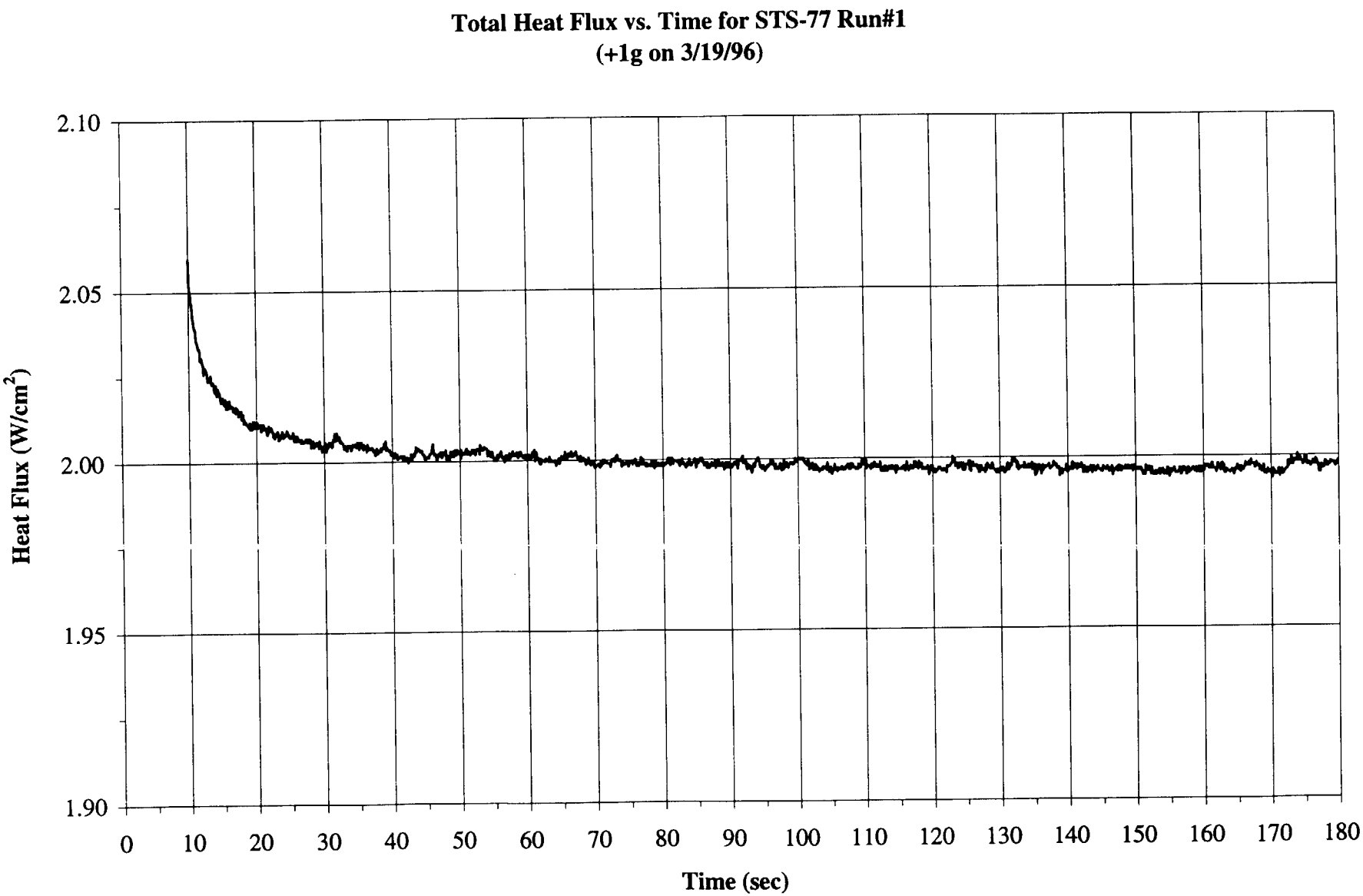

Figure B-15a. a/g = +1 Preflight test. Heat flux input. PBE-IIA (STS-77). Run No. 1.

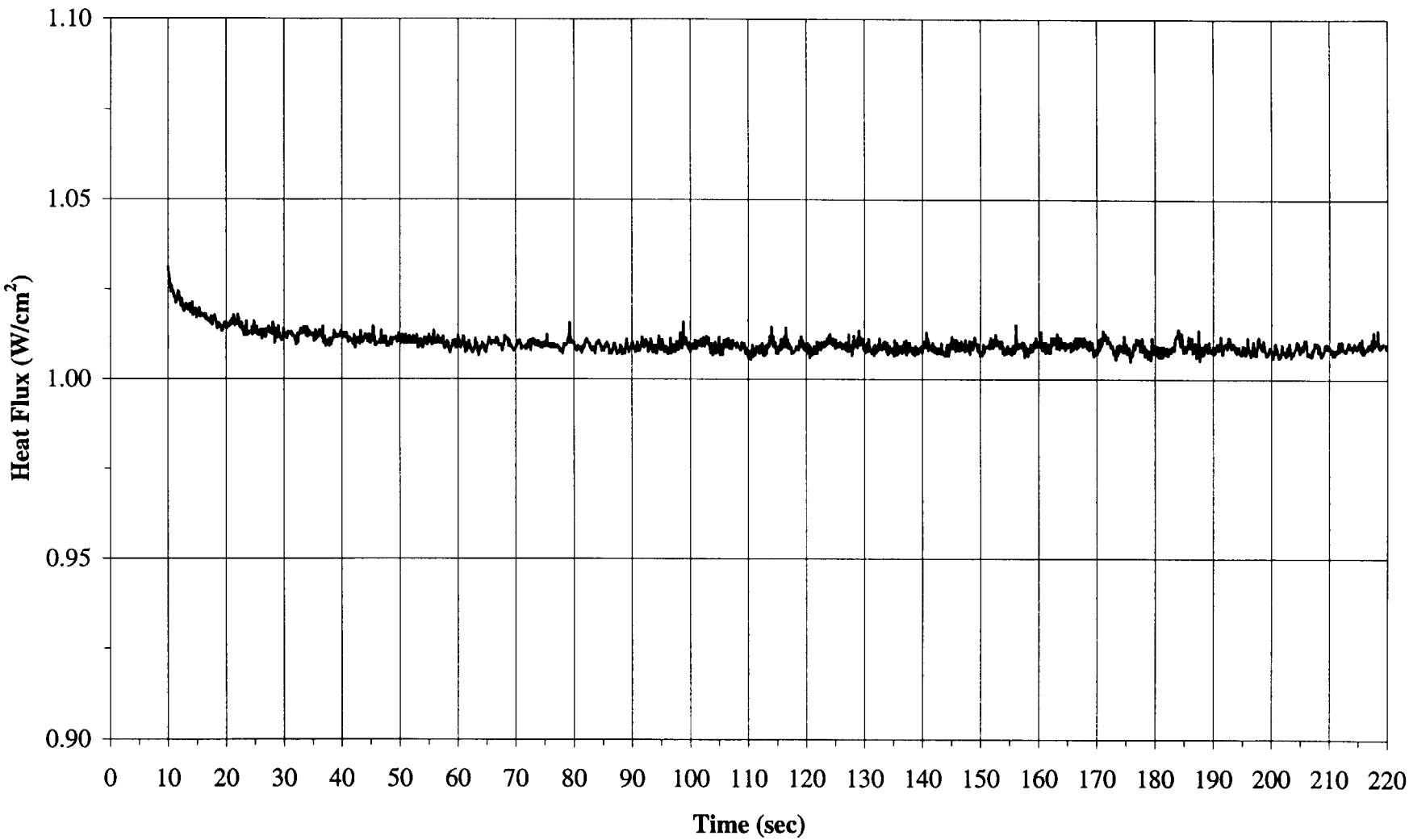

Figure B-15b. a/g = +1 Preflight test. Heat flux input. PBE-IIA (STS-77). Run No. 2.

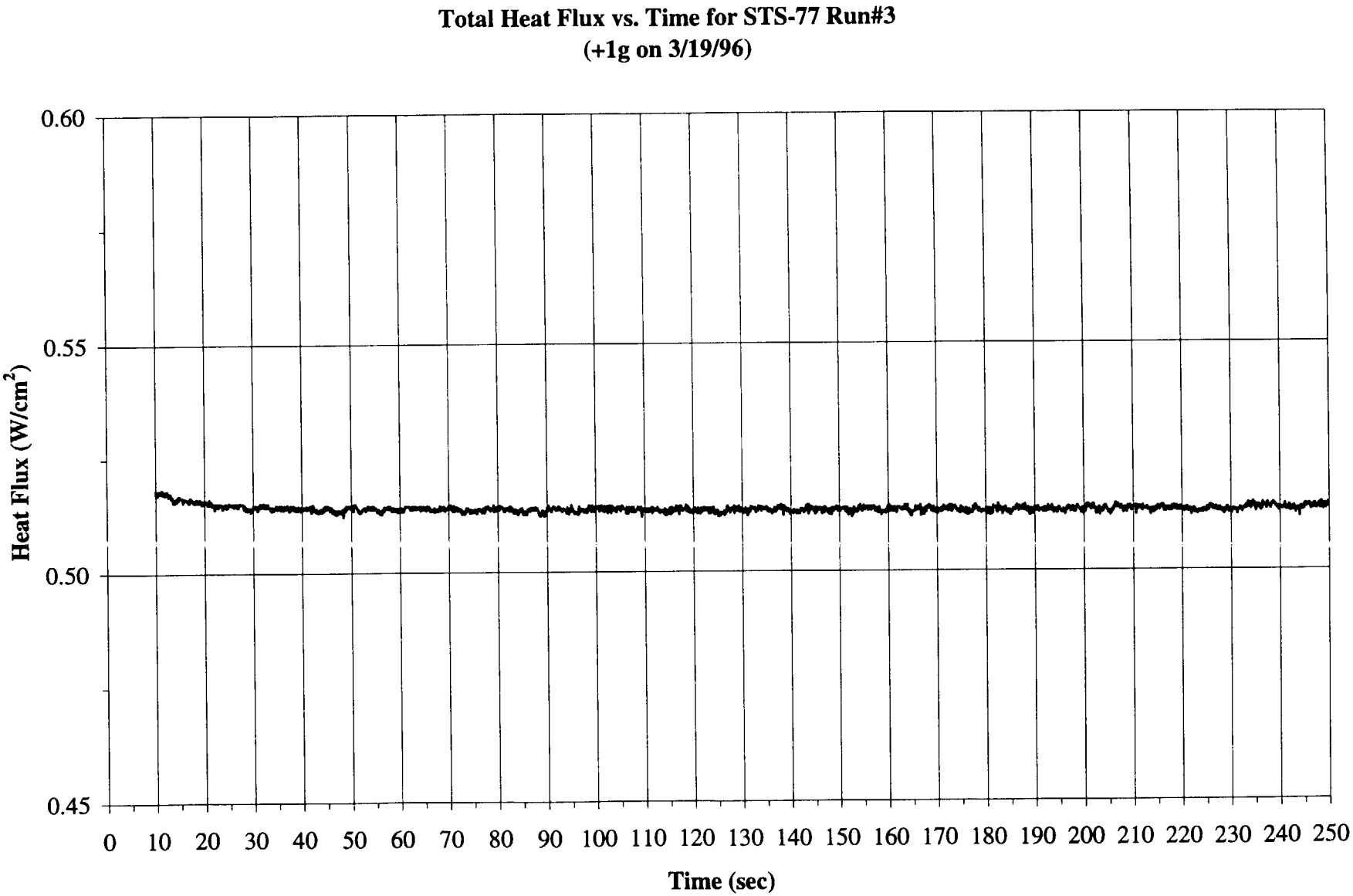

Figure B-15c. a/g = +1 Preflight test. Heat flux input. PBE-IIA (STS-77). Run No. 3.

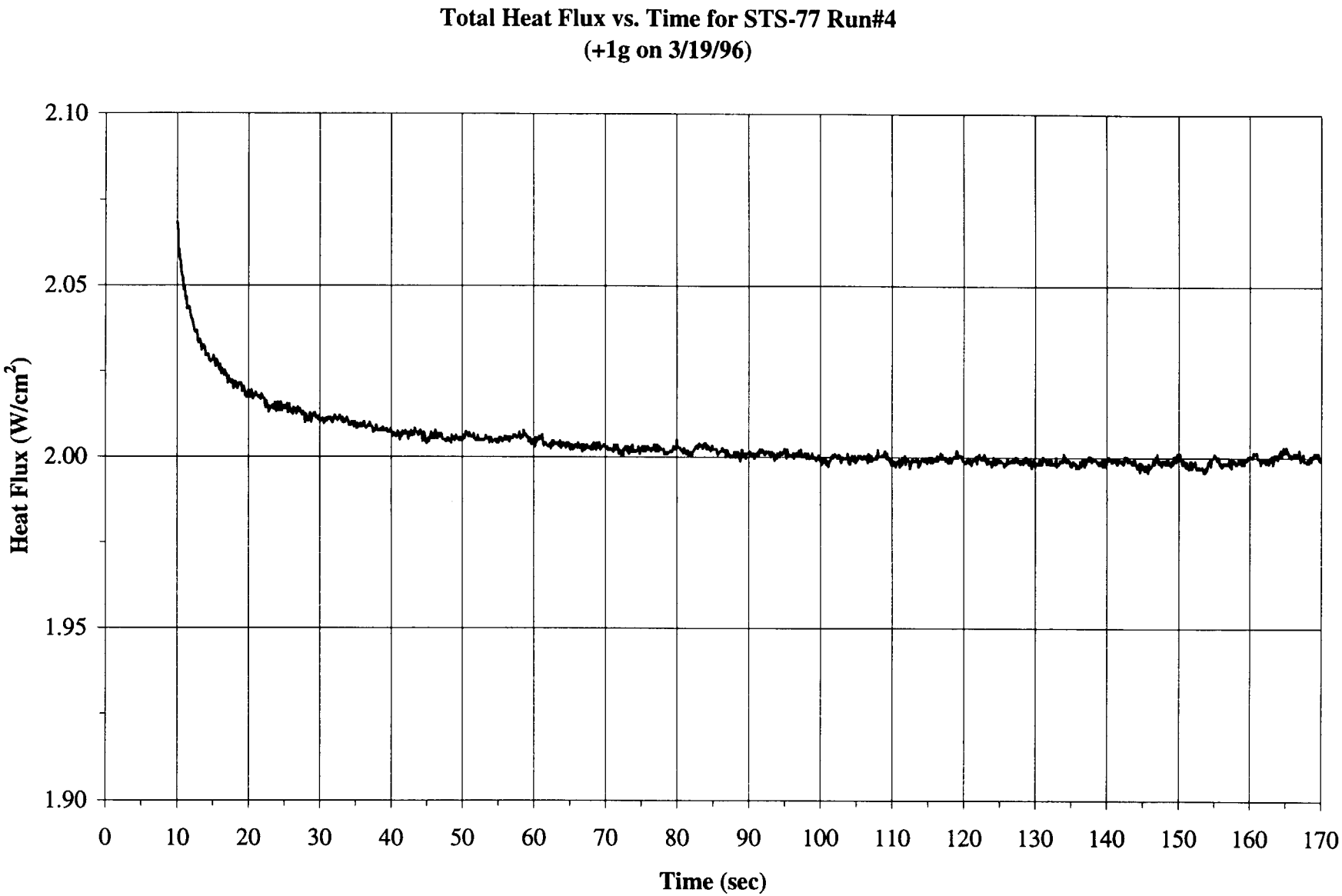

Figure B-15d. a/g = +1 Preflight test. Heat flux input. PBE-IIA (STS-77). Run No. 4.

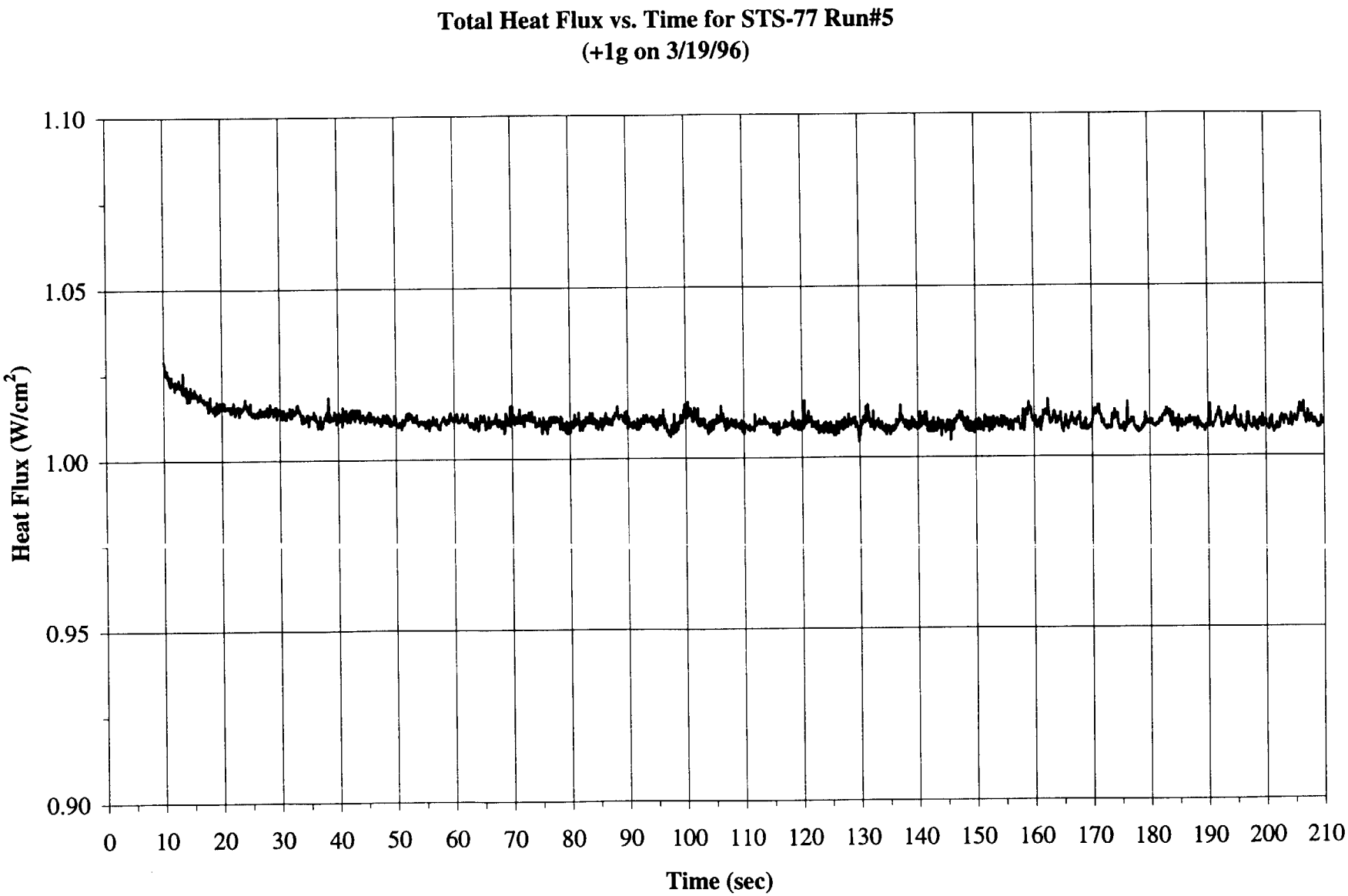

Figure B-15e. a/g = +1 Preflight test. Heat flux input. PBE-IIA (STS-77). Run No. 5.

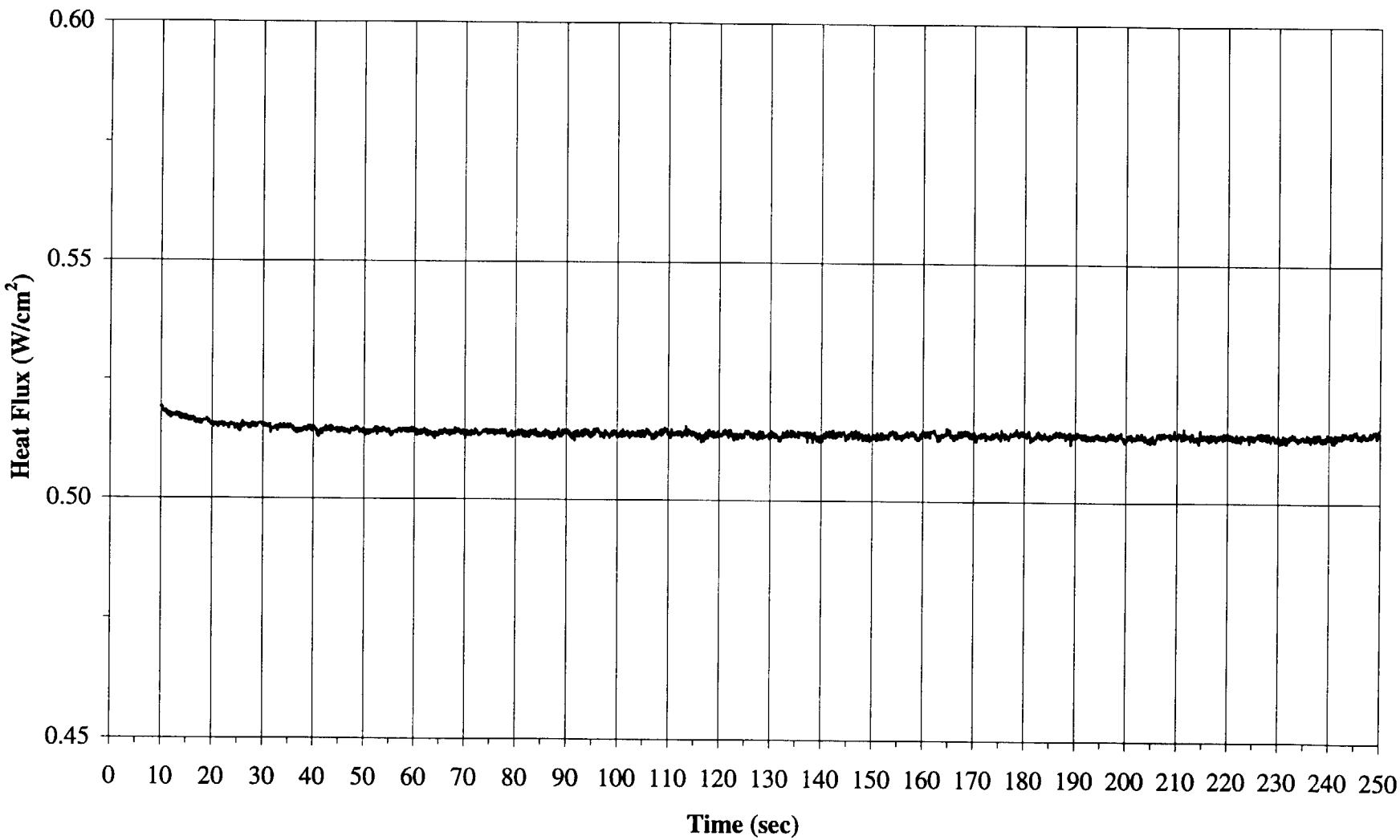

Figure B-15f. a/g = +1 Preflight test. Heat flux input. PBE-IIA (STS-77). Run No. 6.

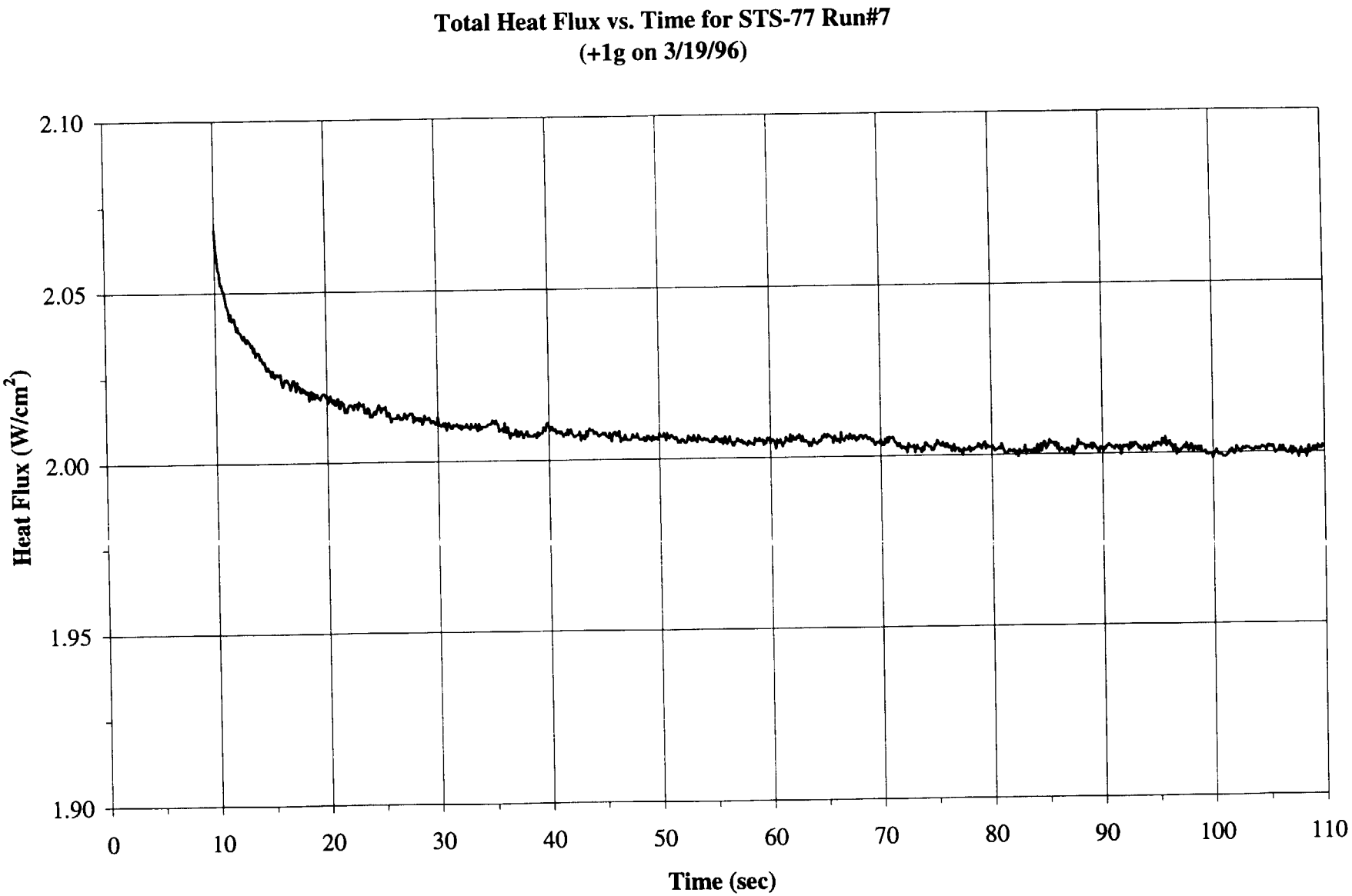

Figure B-15g. a/g = +1 Preflight test. Heat flux input. PBE-IIA (STS-77). Run No. 7.

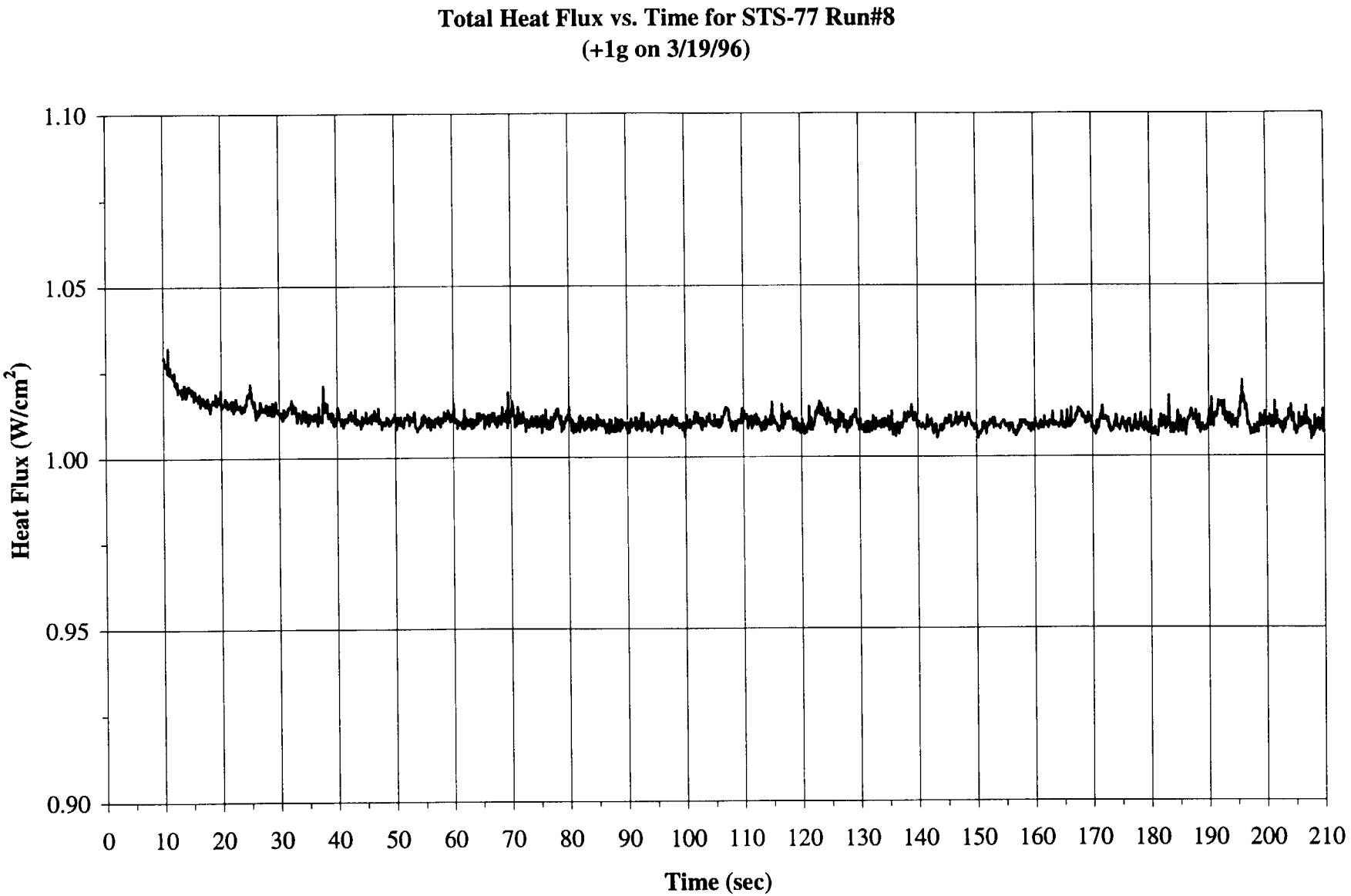

Figure B-15h. a/g = +1 Preflight test. Heat flux input. PBE-IIA (STS-77). Run No. 8.

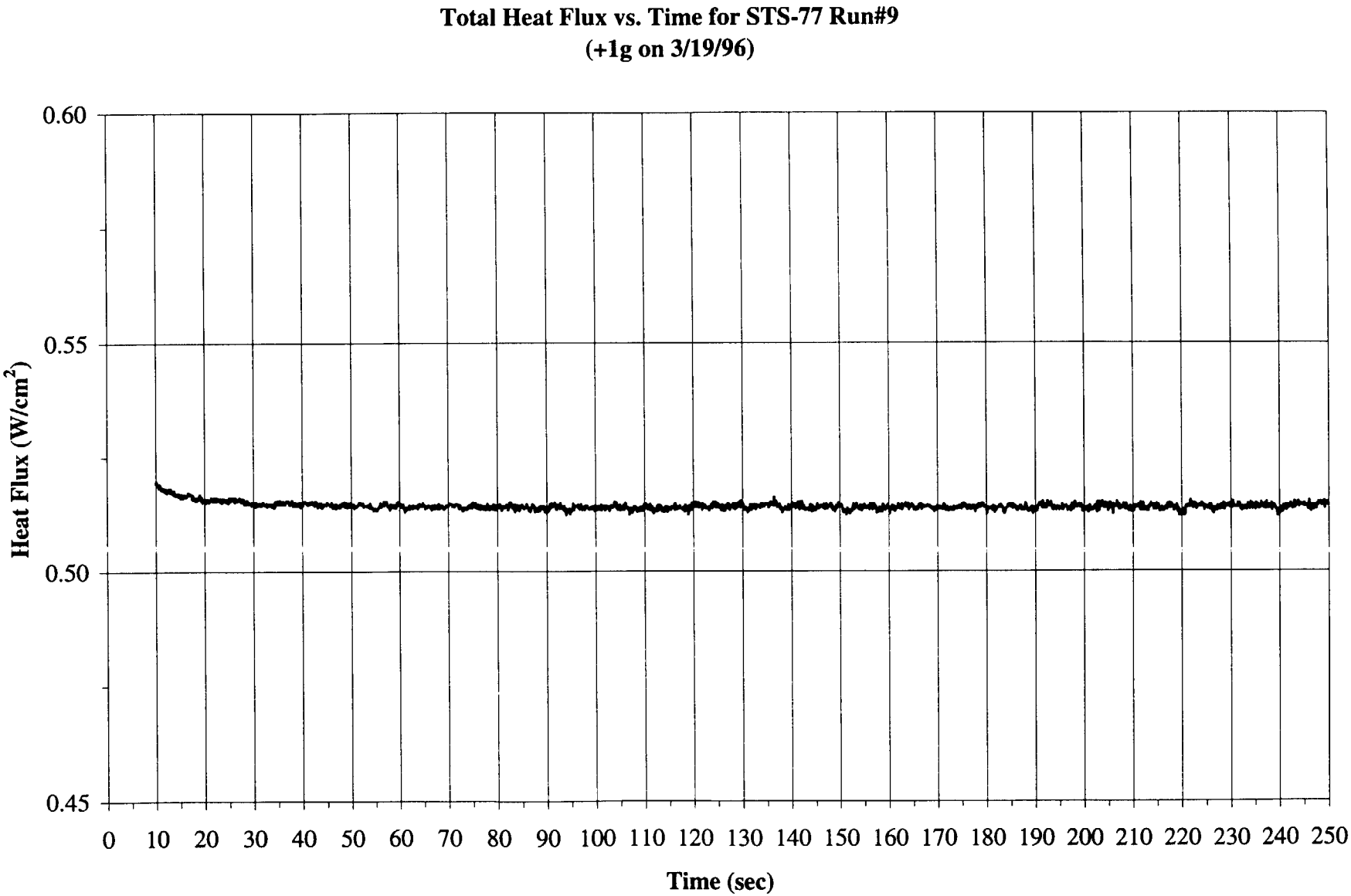

Figure B-15i. a/g = +1 Preflight test. Heat flux input. PBE-IIA (STS-77). Run No. 9.

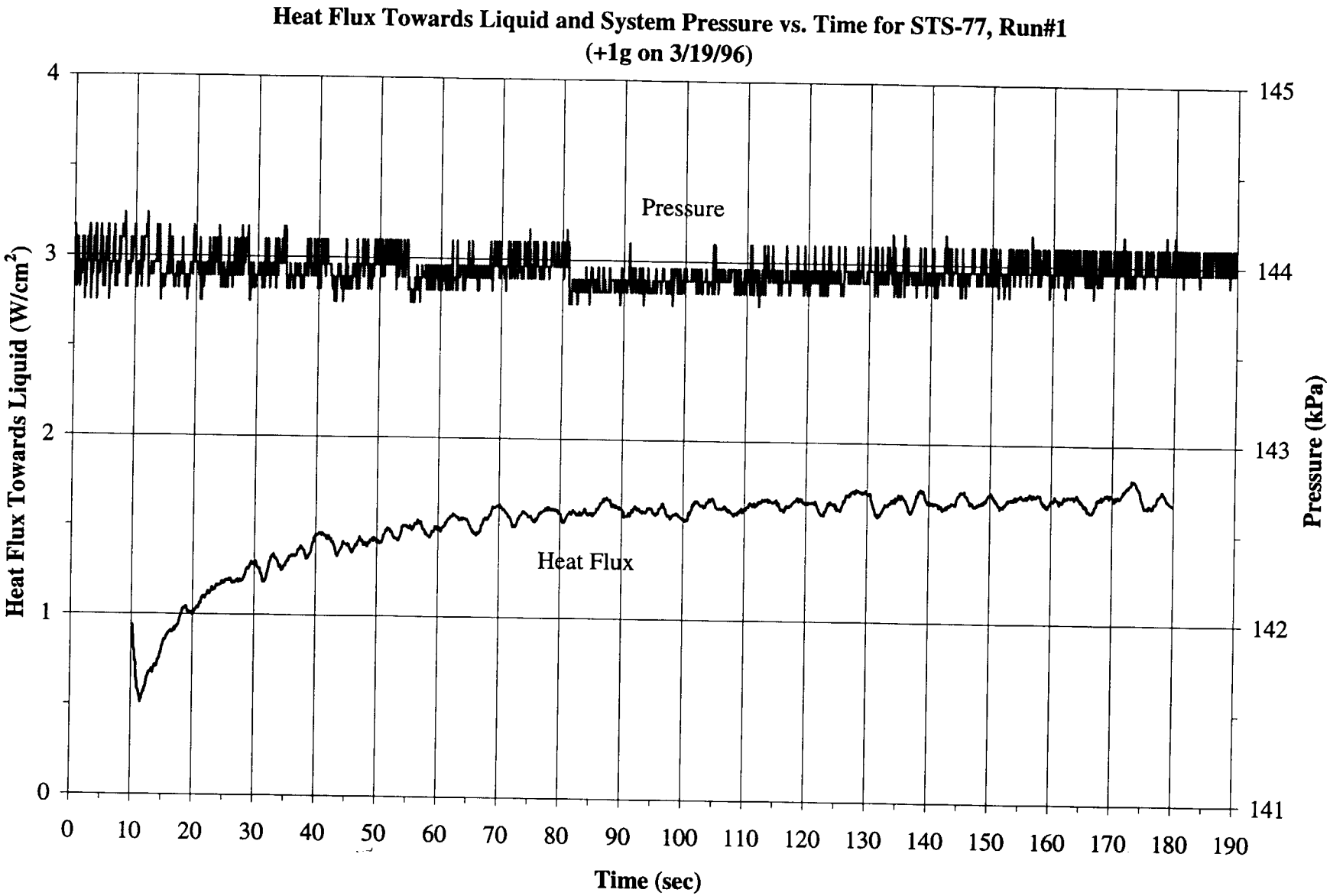

Figure B-16a. a/g = +1 Preflight test. System pressure and heat flux into fluid. PBE-IIA (STS-77). Run No. 1.

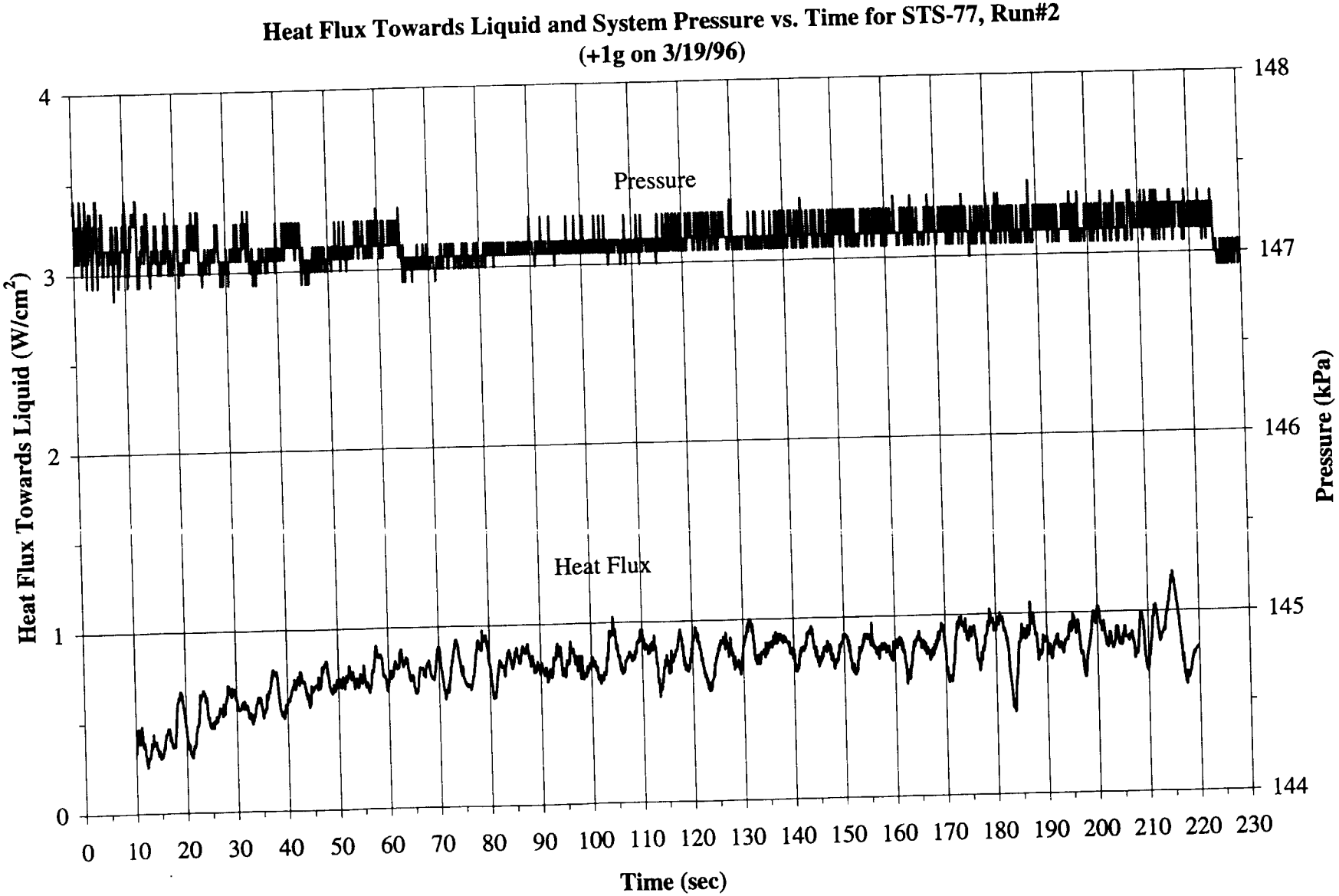

Figure B-16b. a/g = +1 Preflight test. System pressure and heat flux into fluid. PBE-IIA (STS-77). Run No. 2.

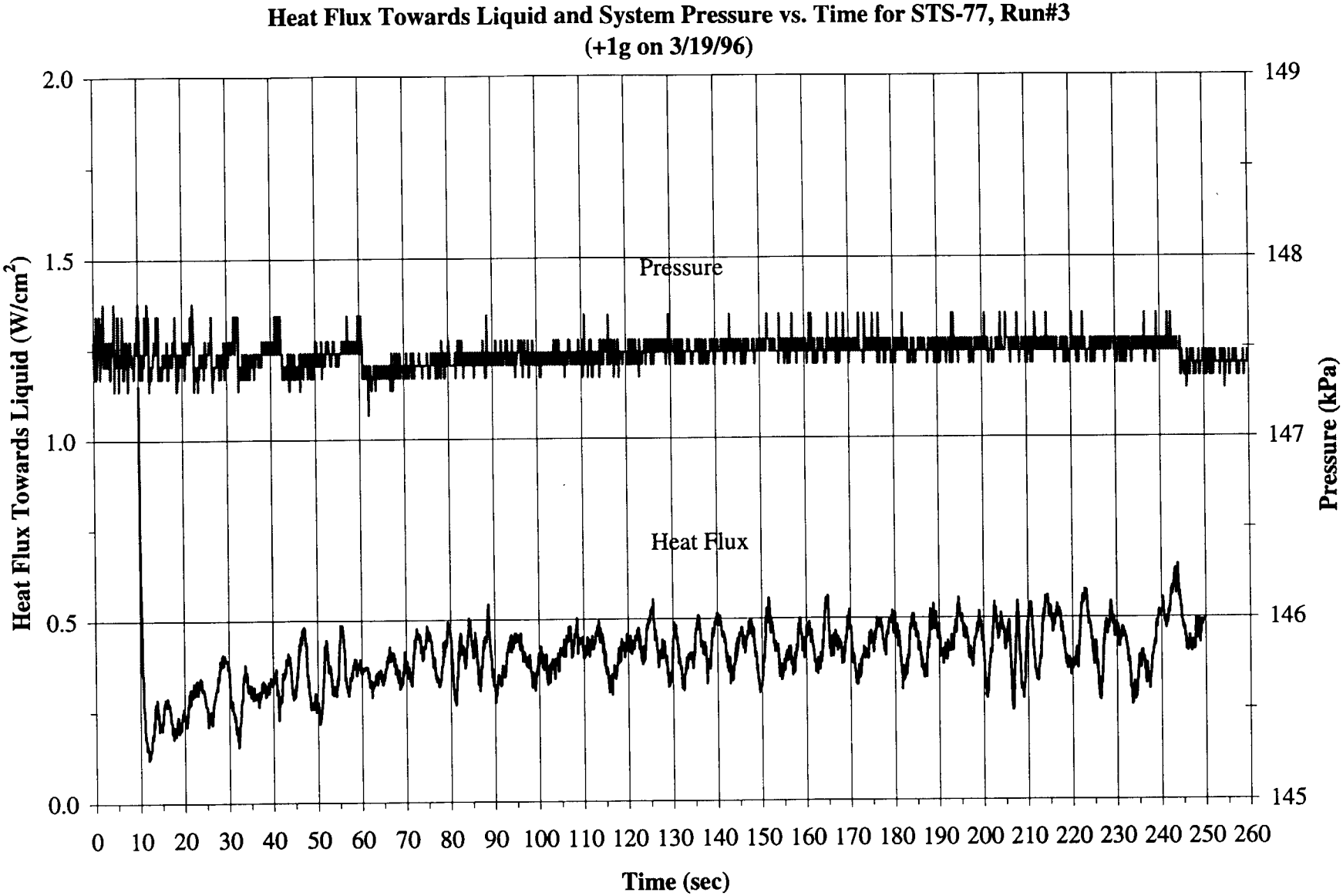

Figure B-16c. a/g = +1 Preflight test. System pressure and heat flux into fluid. PBE-IIA (STS-77). Run No. 3.

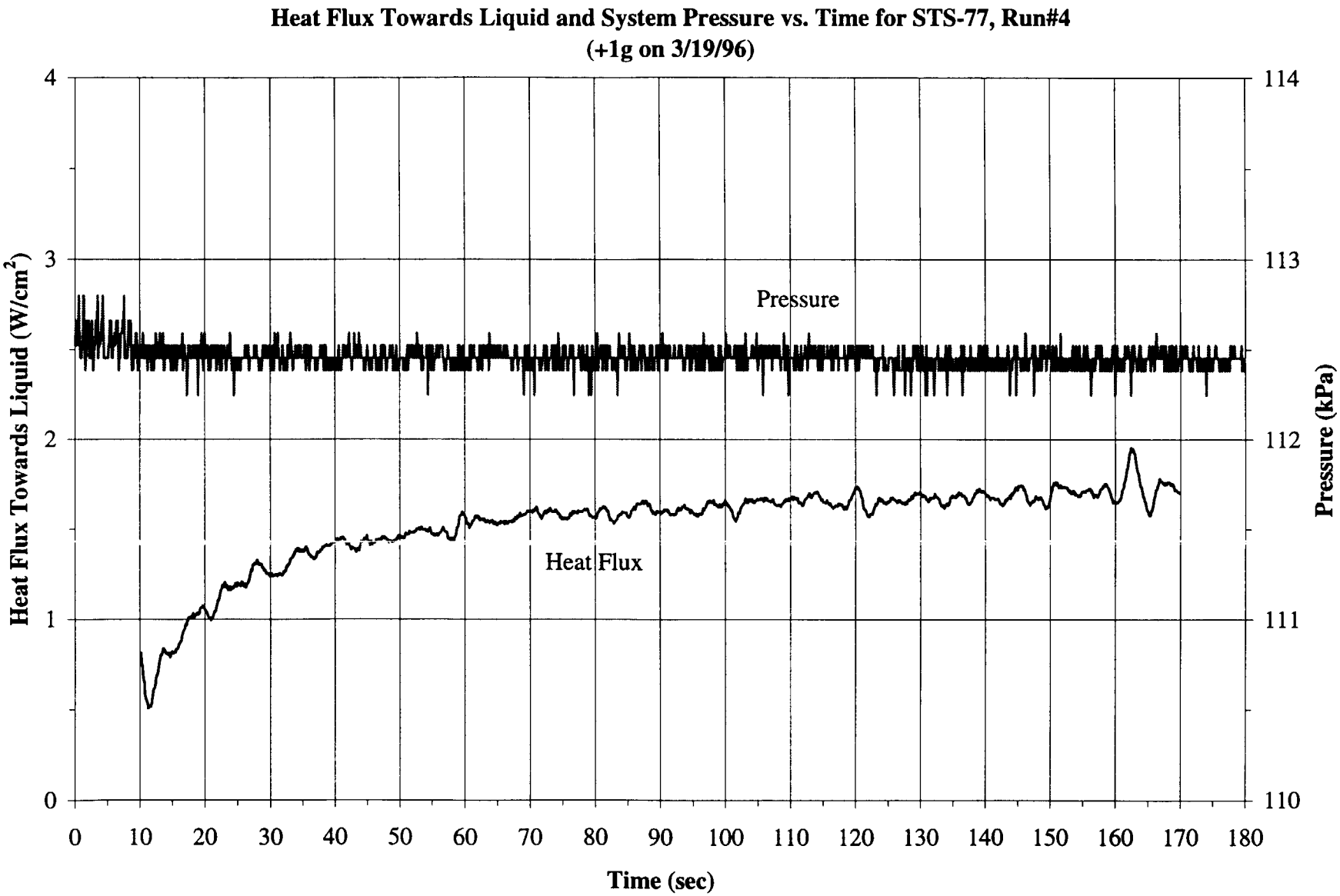

Figure B-16d. a/g = +1 Preflight test. System pressure and heat flux into fluid. PBE-IIA (STS-77). Run No. 4.

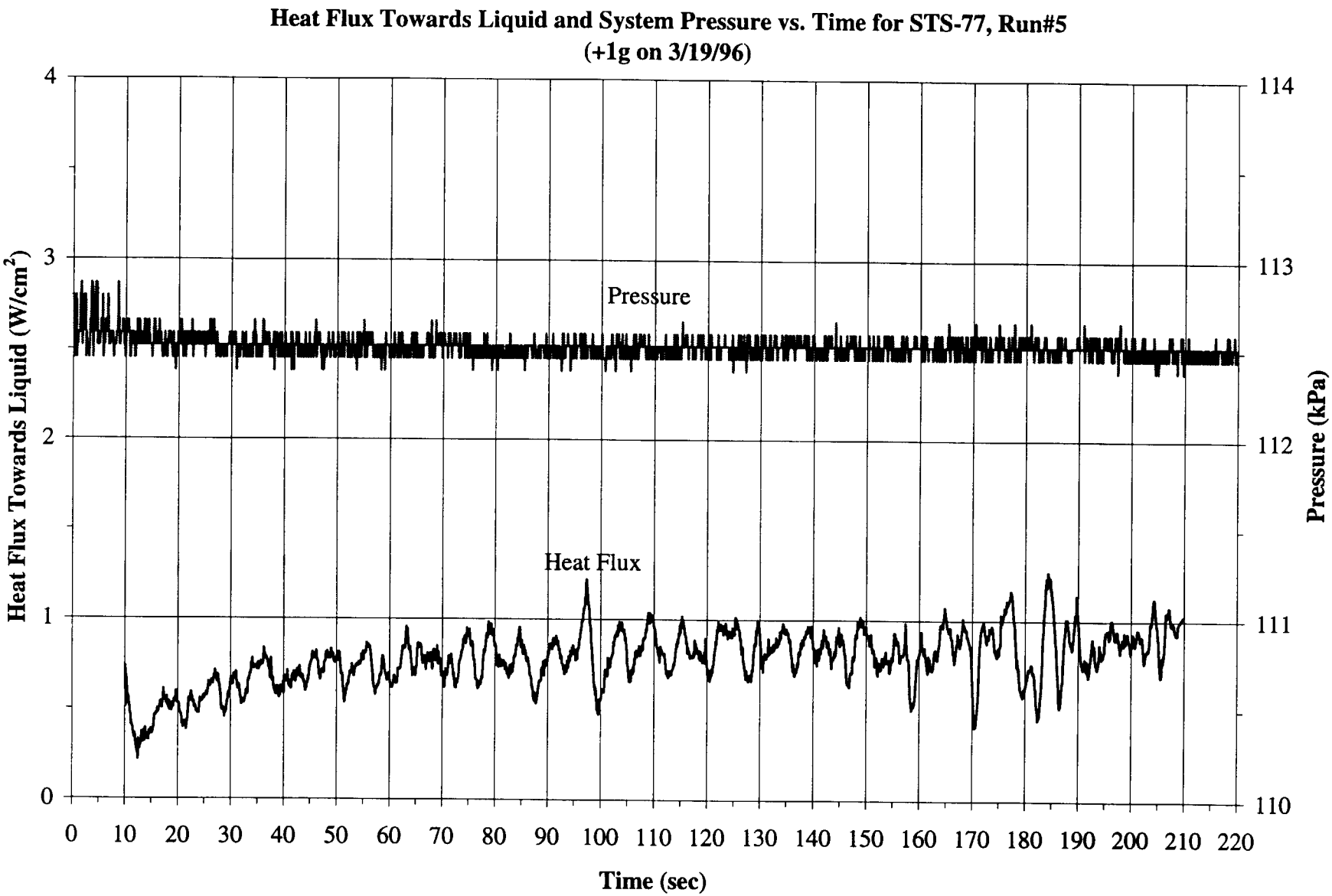

Figure B-16e. a/g = +1 Preflight test. System pressure and heat flux into fluid. PBE-IIA (STS-77). Run No. 5.

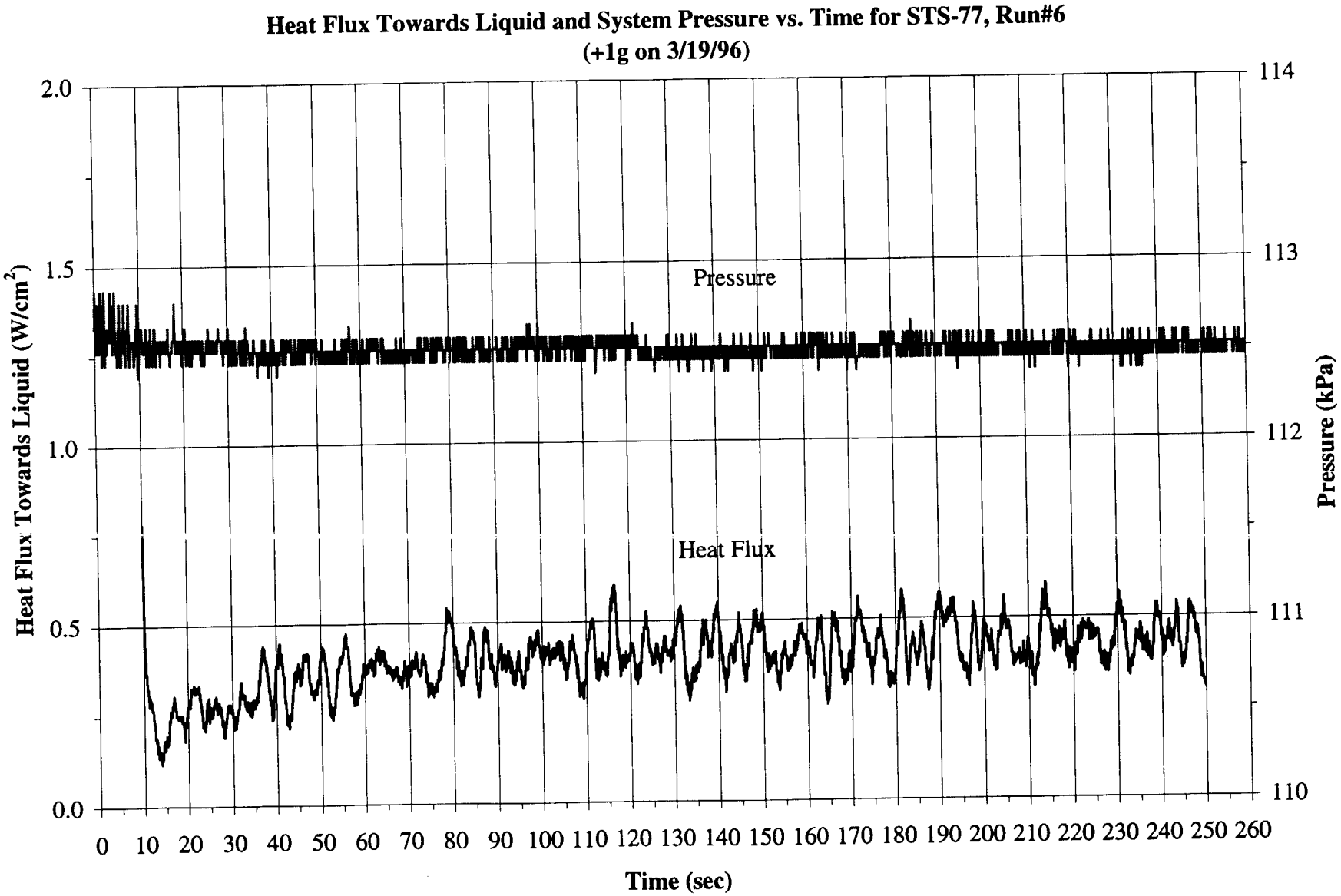

Figure B-16f. a/g = +1 Preflight test. System pressure and heat flux into fluid. PBE-IIA (STS-77). Run No. 6.

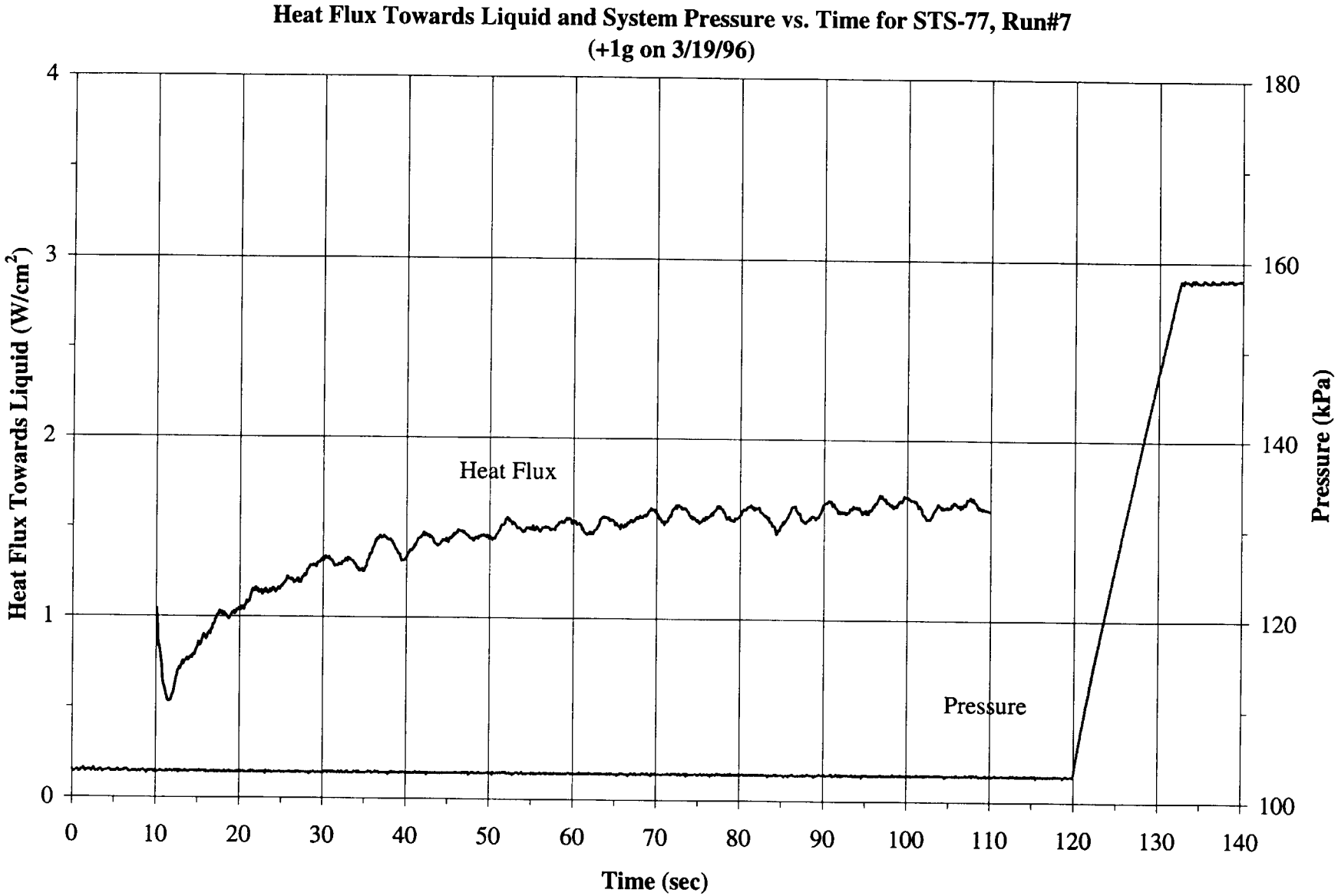

Figure B-16g. a/g = +1 Preflight test. System pressure and heat flux into fluid. PBE-IIA (STS-77). Run No. 7.

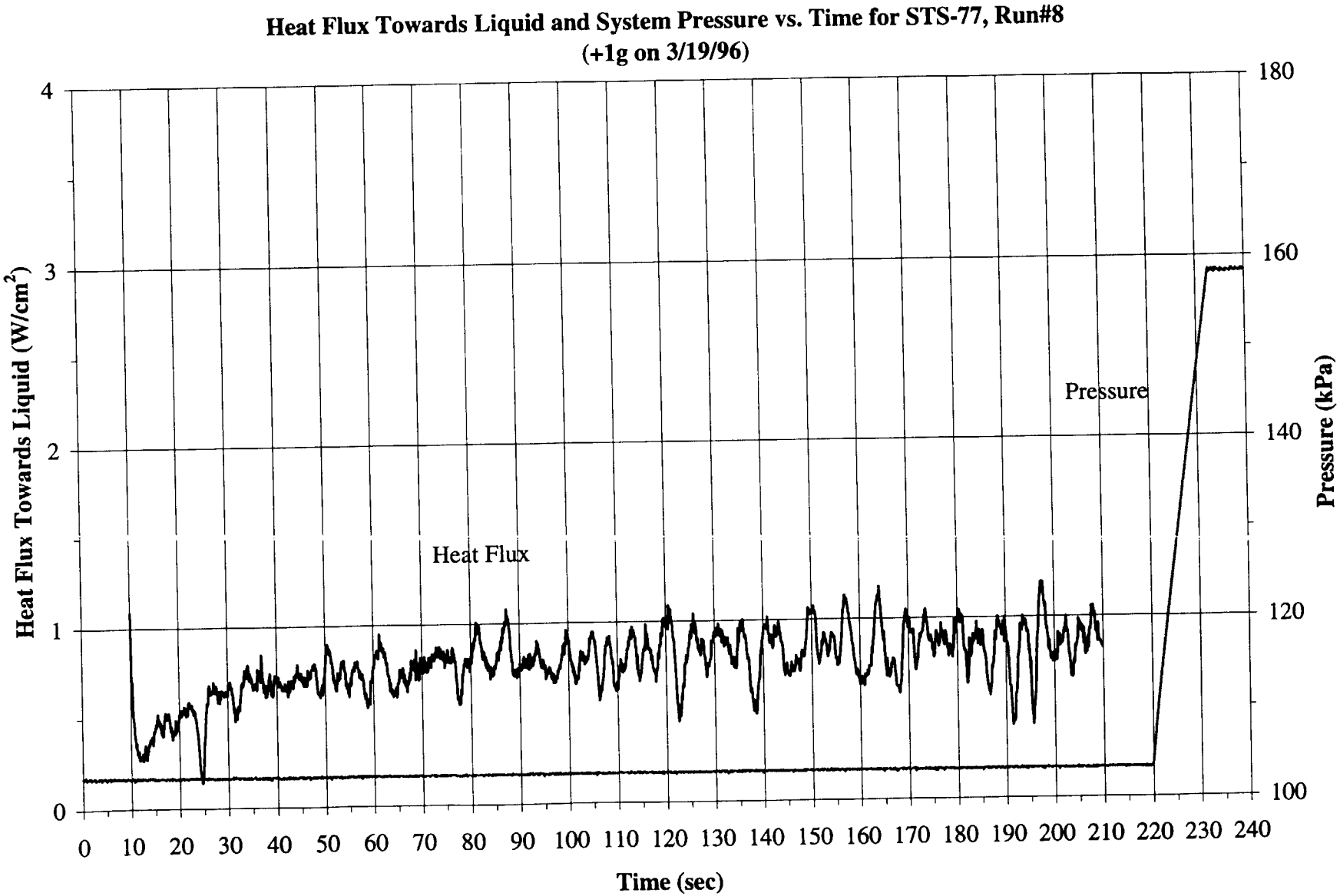

Figure B-16h. a/g = +1 Preflight test. System pressure and heat flux into fluid. PBE-IIA (STS-77). Run No. 8.

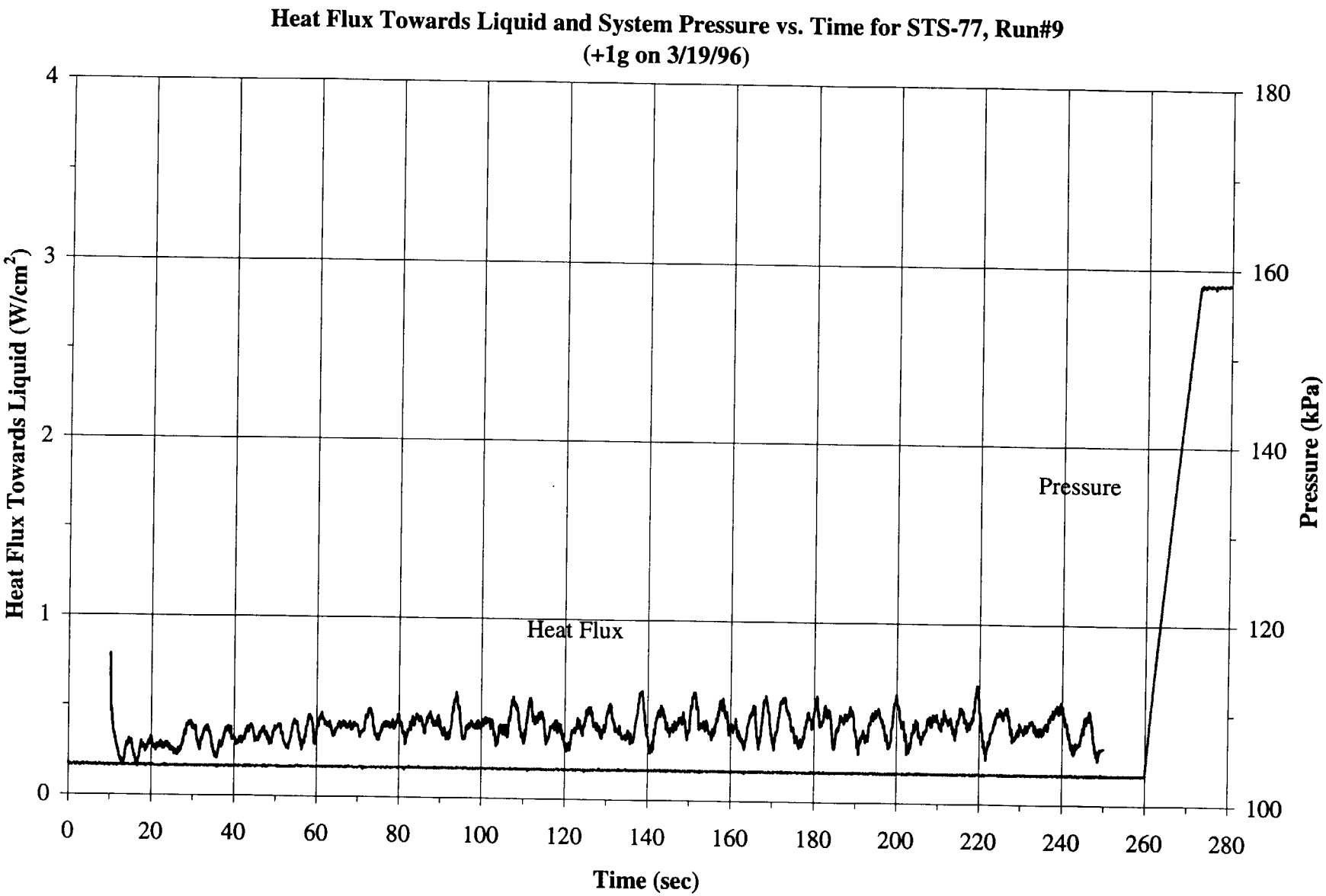

Figure B-16i. a/g = +1 Preflight test. System pressure and heat flux into fluid. PBE-IIA (STS-77). Run No. 9.

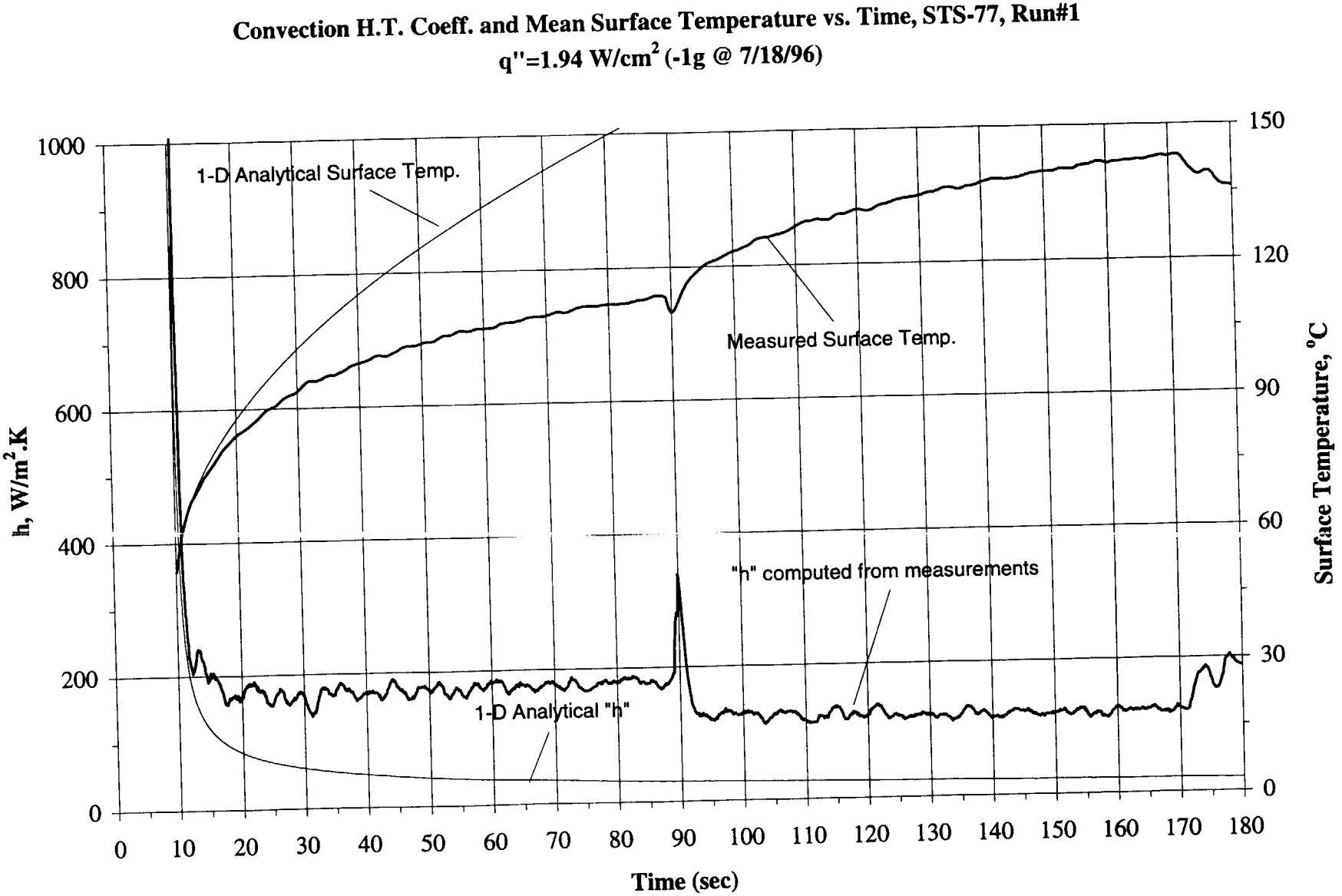

Figure B-17a. a/g = -1 Postflight test. Mean heater surface temperature and derived heat transfer coefficient. PBE-IIA (STS-77). Run No. 1.

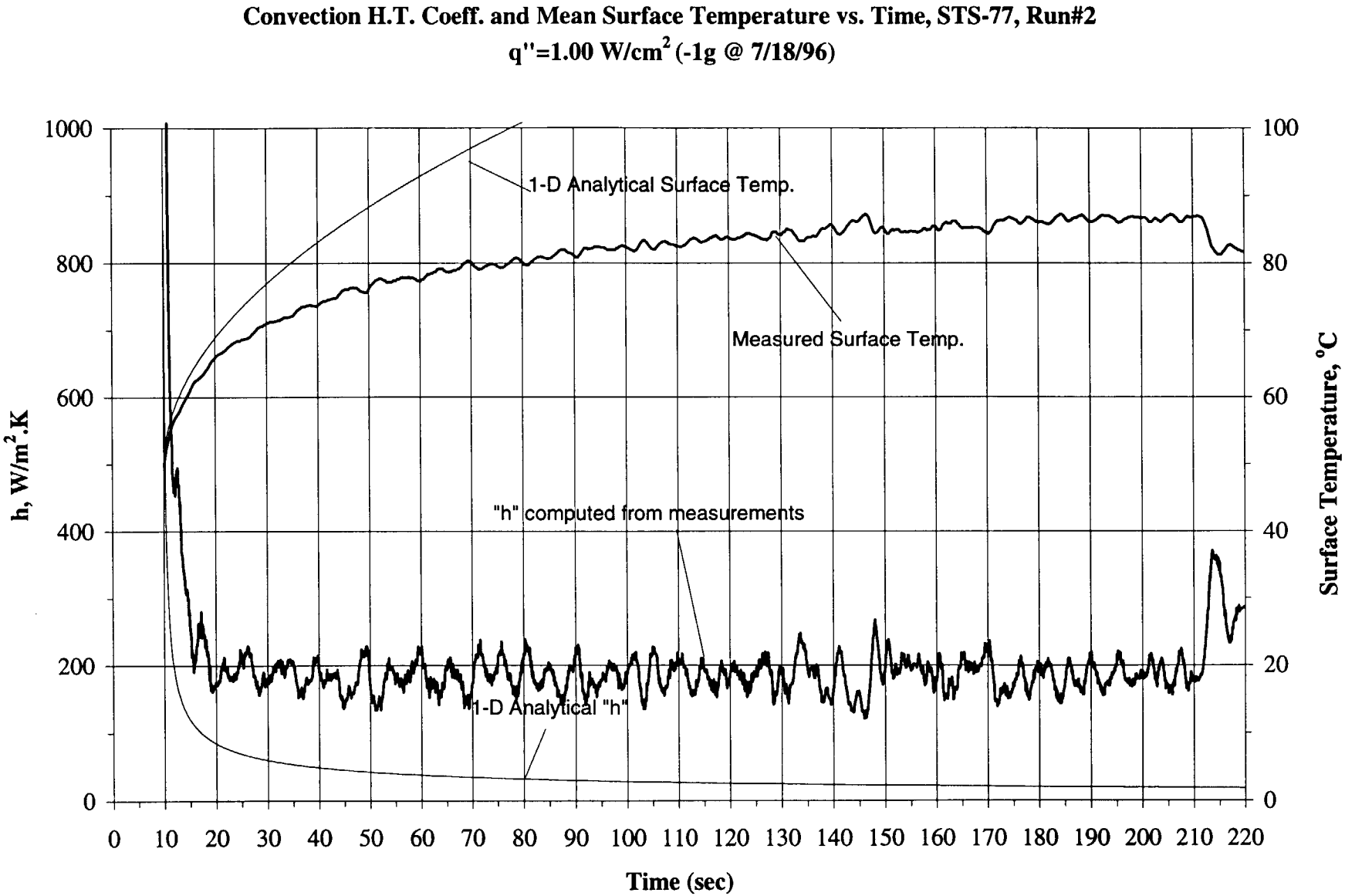

Figure B-17b. a/g = -1 Postflight test. Mean heater surface temperature and derived heat transfer coefficient. PBE-IIA (STS-77). Run No. 2.

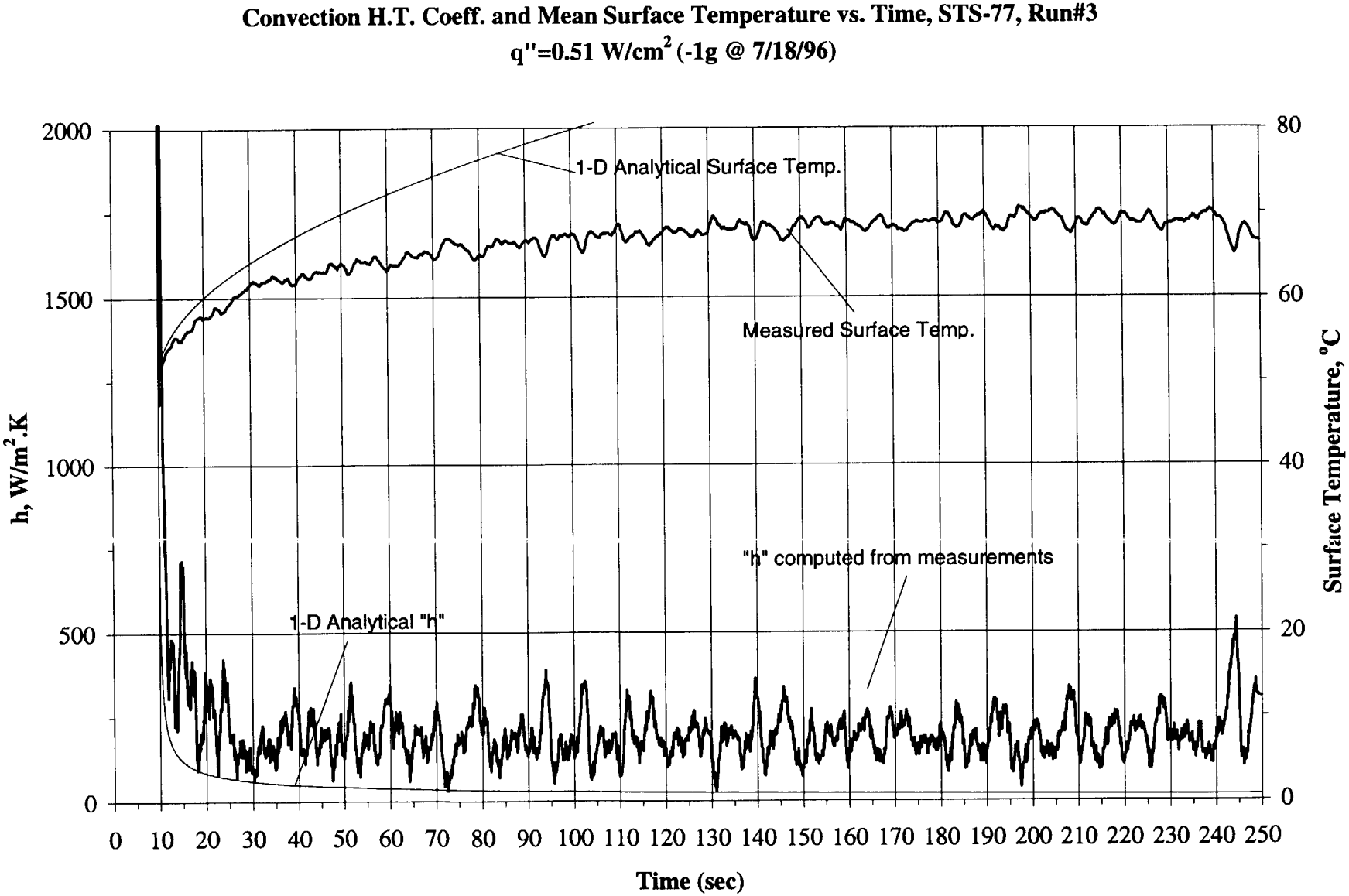

Figure B-17c. a/g = -1 Postflight test. Mean heater surface temperature and derived heat transfer coefficient. PBE-IIA (STS-77). Run No. 3.

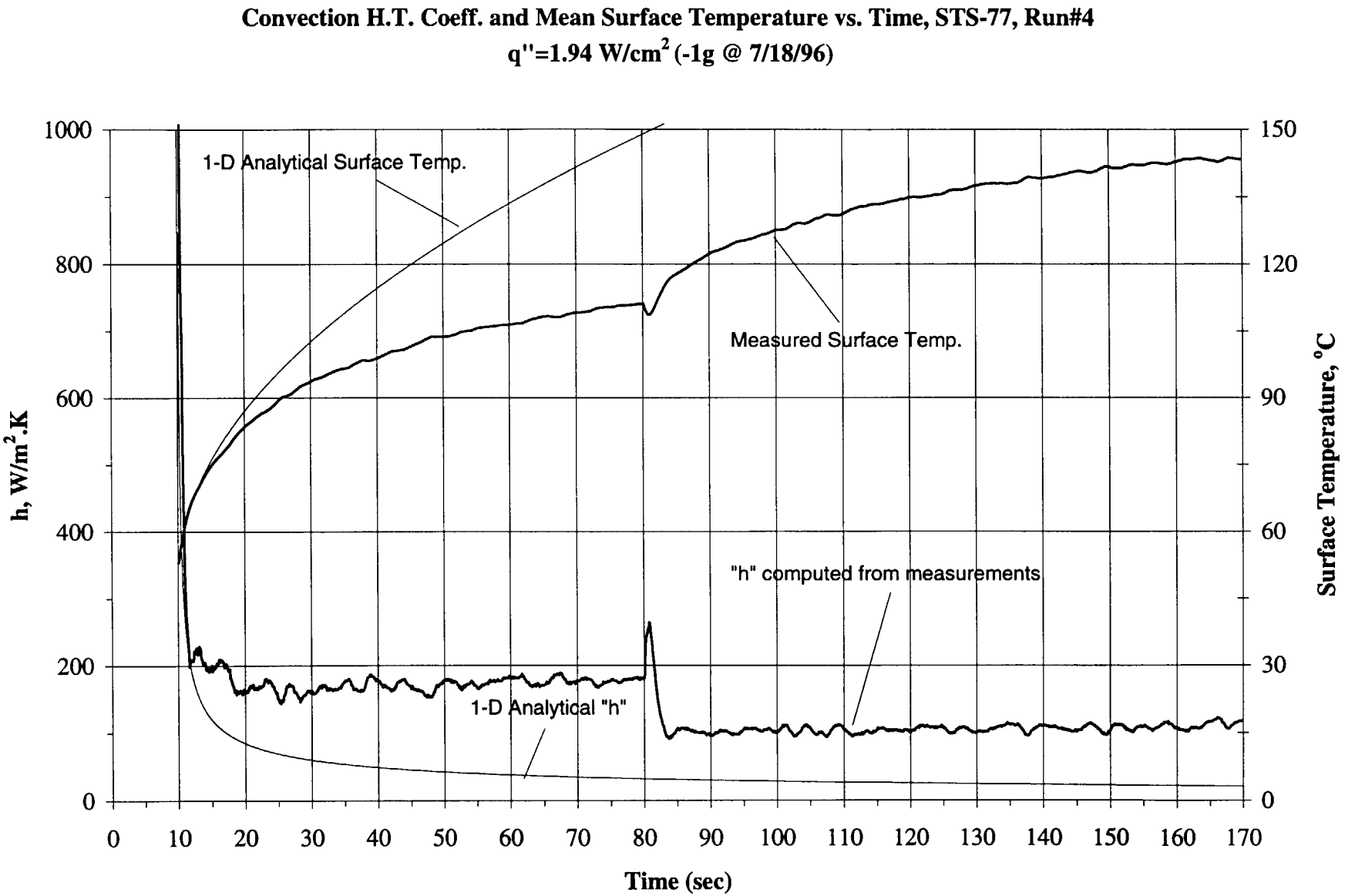

Figure B-17d. a/g = -1 Postflight test. Mean heater surface temperature and derived heat transfer coefficient. PBE-IIA (STS-77). Run No. 4.

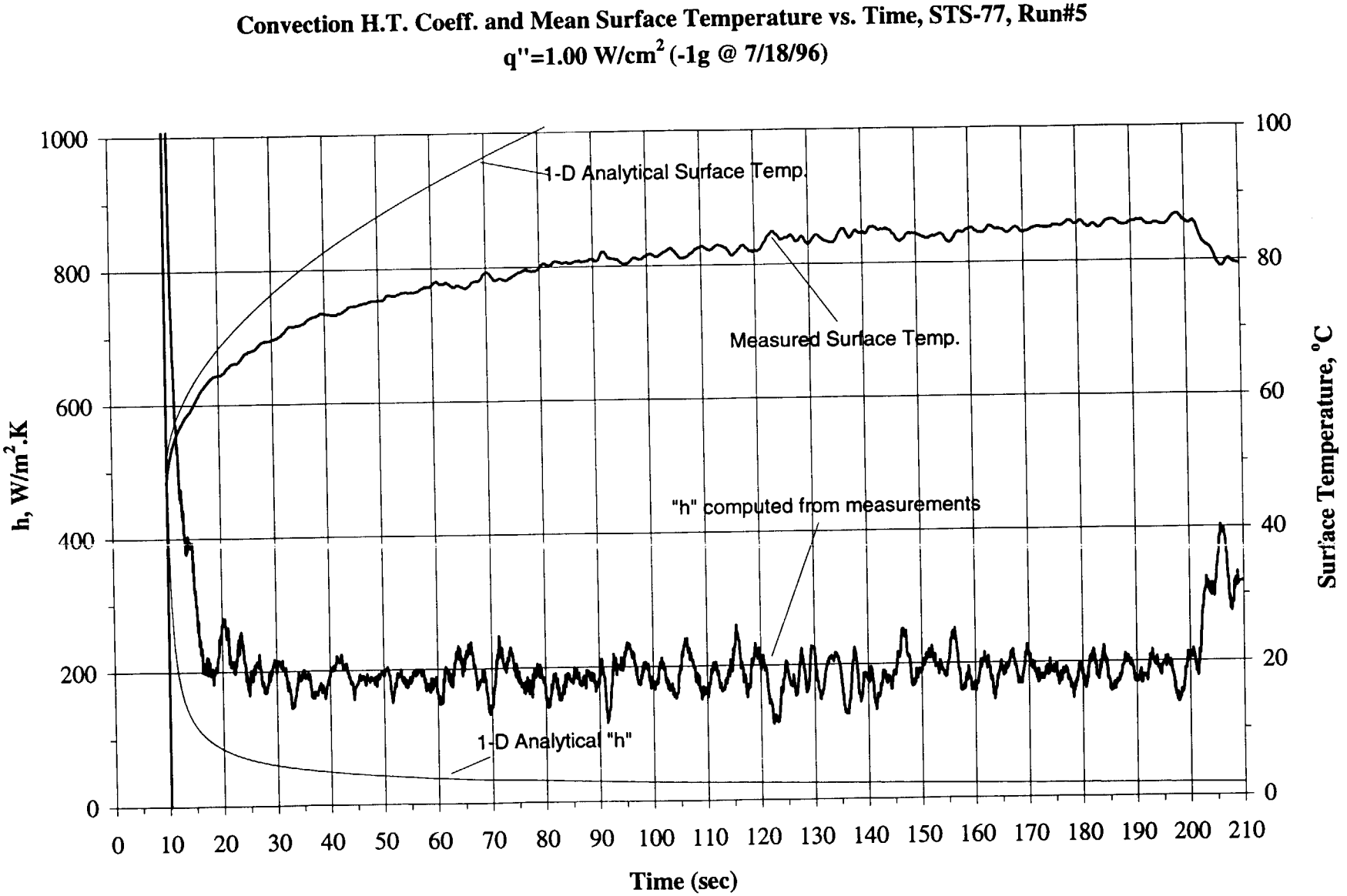

Figure B-17e. a/g = -1 Postflight test. Mean heater surface temperature and derived heat transfer coefficient. PBE-IIA (STS-77). Run No. 5.

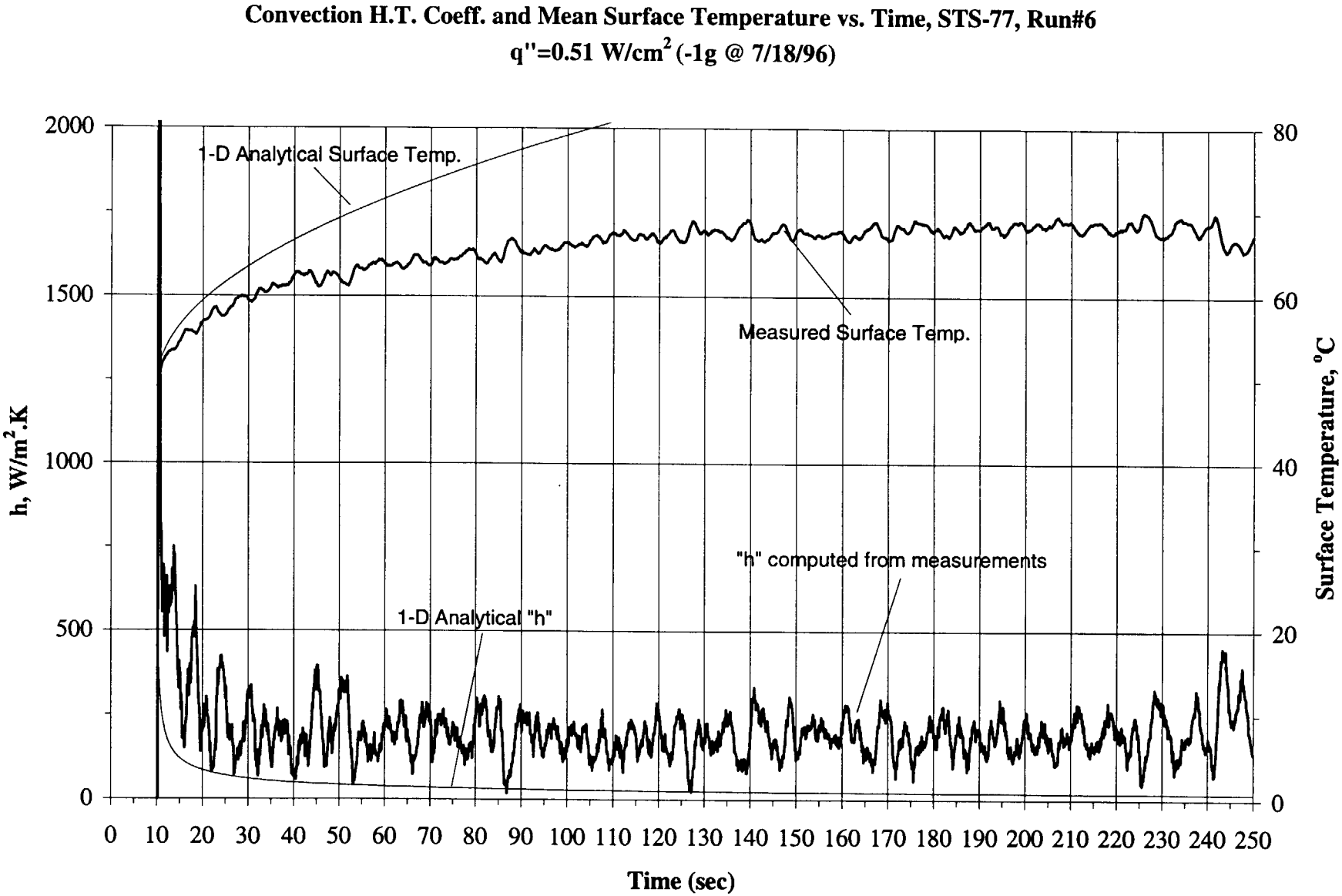

Figure B-17f. a/g = -1 Postflight test. Mean heater surface temperature and derived heat transfer coefficient. PBE-IIA (STS-77). Run No. 6.

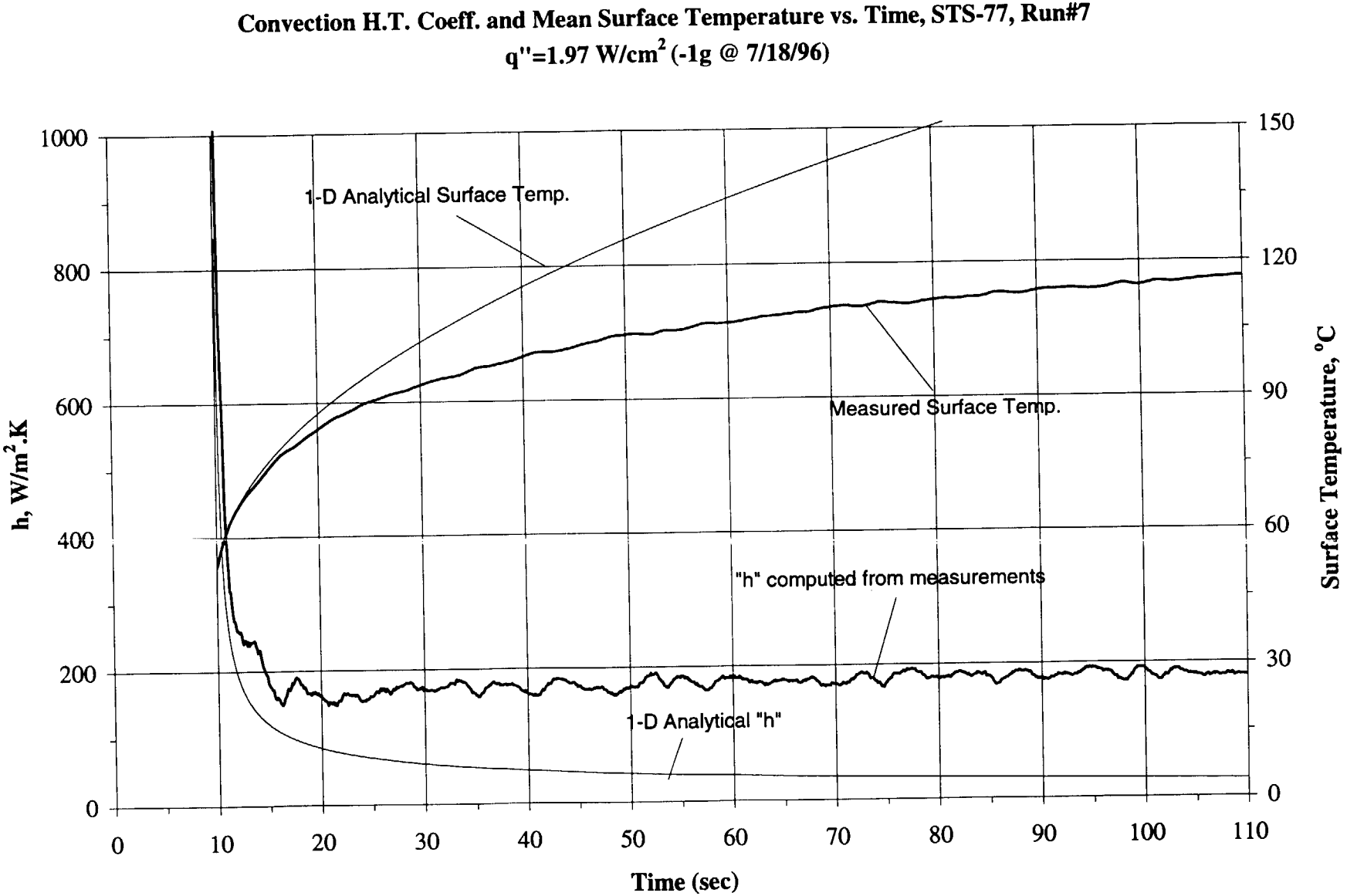

Figure B-17g. a/g = -1 Postflight test. Mean heater surface temperature and derived heat transfer coefficient. PBE-IIA (STS-77). Run No. 7.

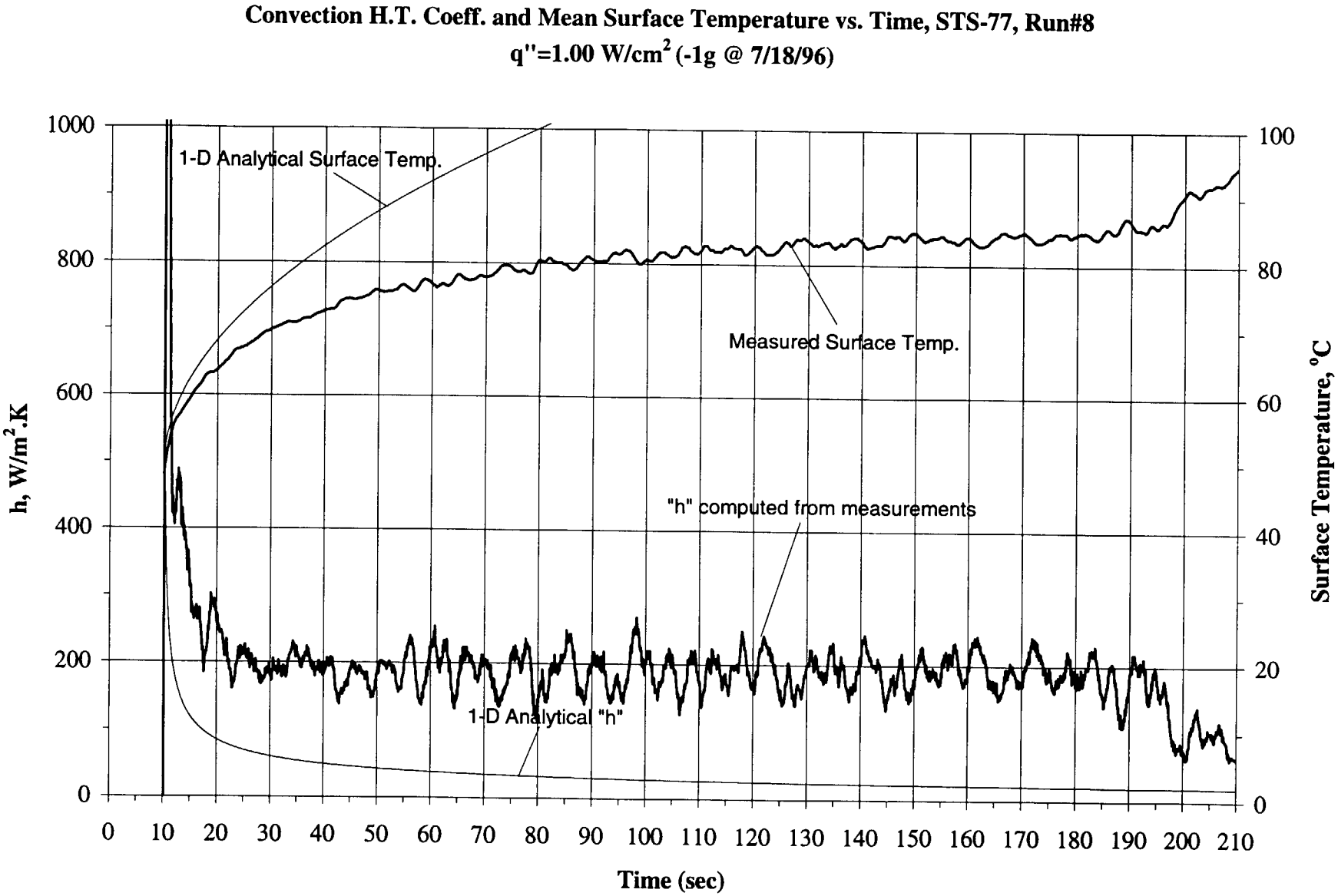

Figure B-17h. a/g = -1 Postflight test. Mean heater surface temperature and derived heat transfer coefficient. PBE-IIA (STS-77). Run No. 8.

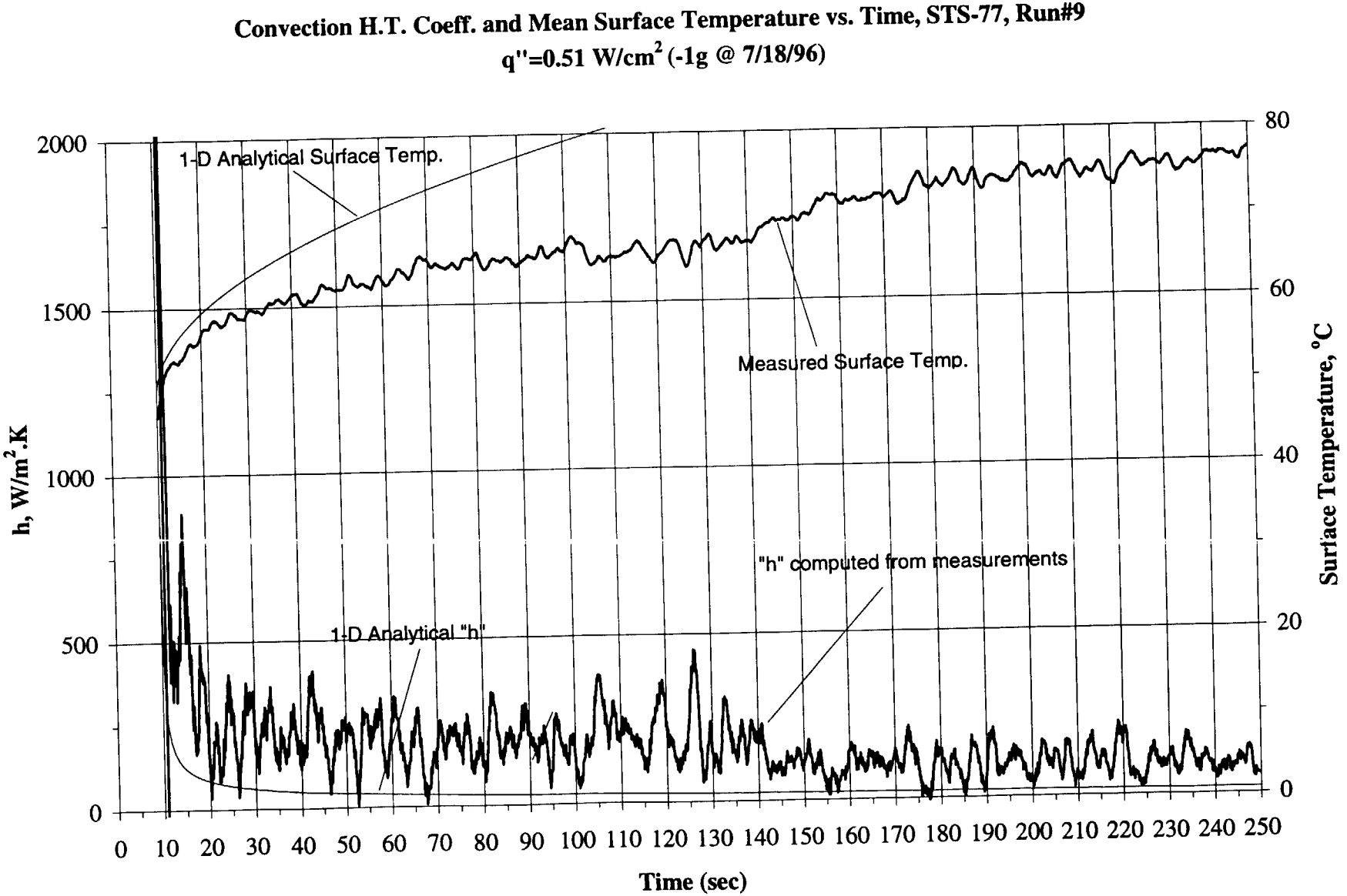

Figure B-17i. a/g = -+1 Postflight test. Mean heater surface temperature and derived heat transfer coefficient. PBE-IIA (STS-77). Run No. 9.

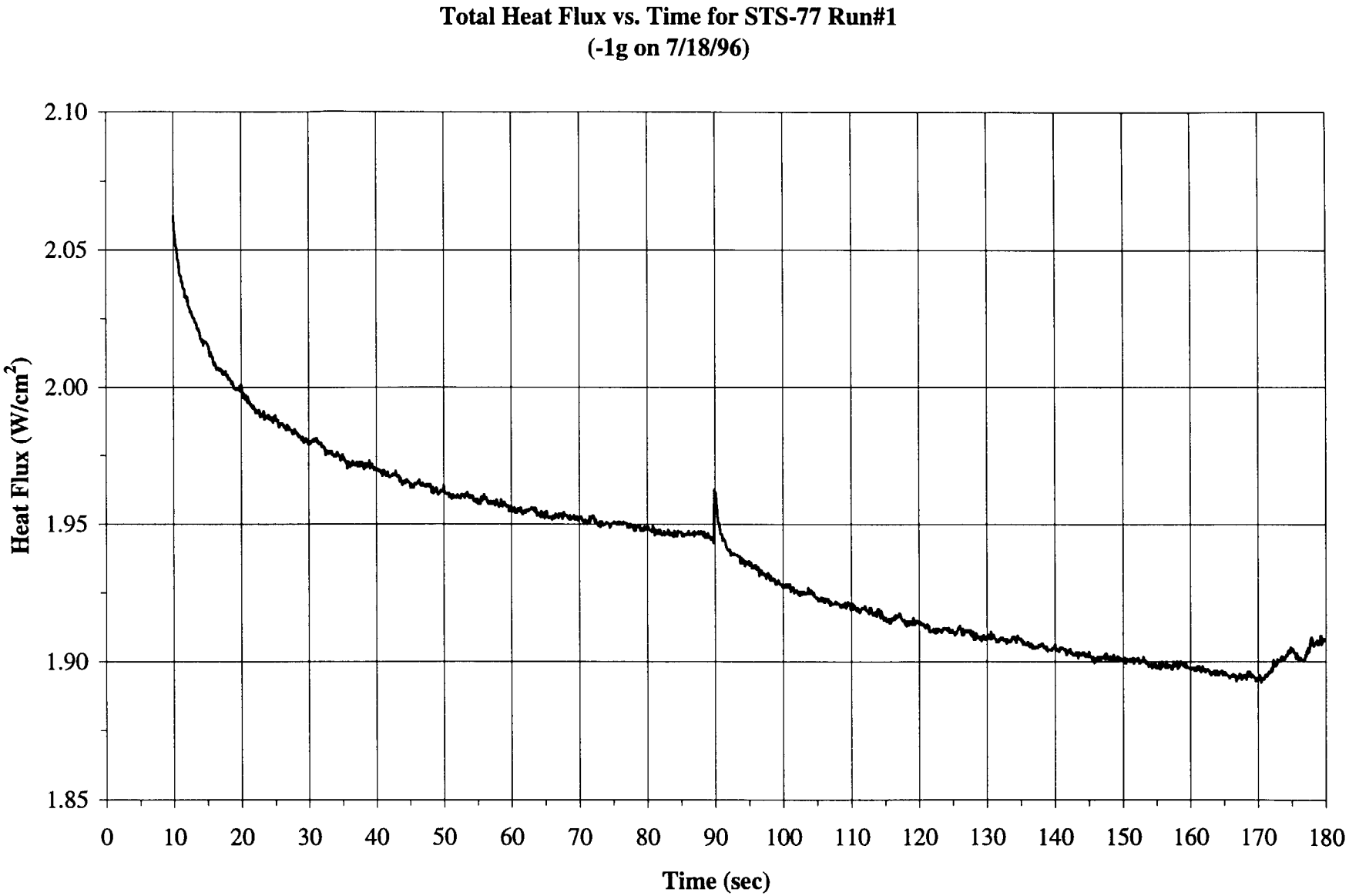

Figure B-18a. a/g = - 1 Postflight test. Heat flux input. PBE-IIA (STS-77). Run No. 1.

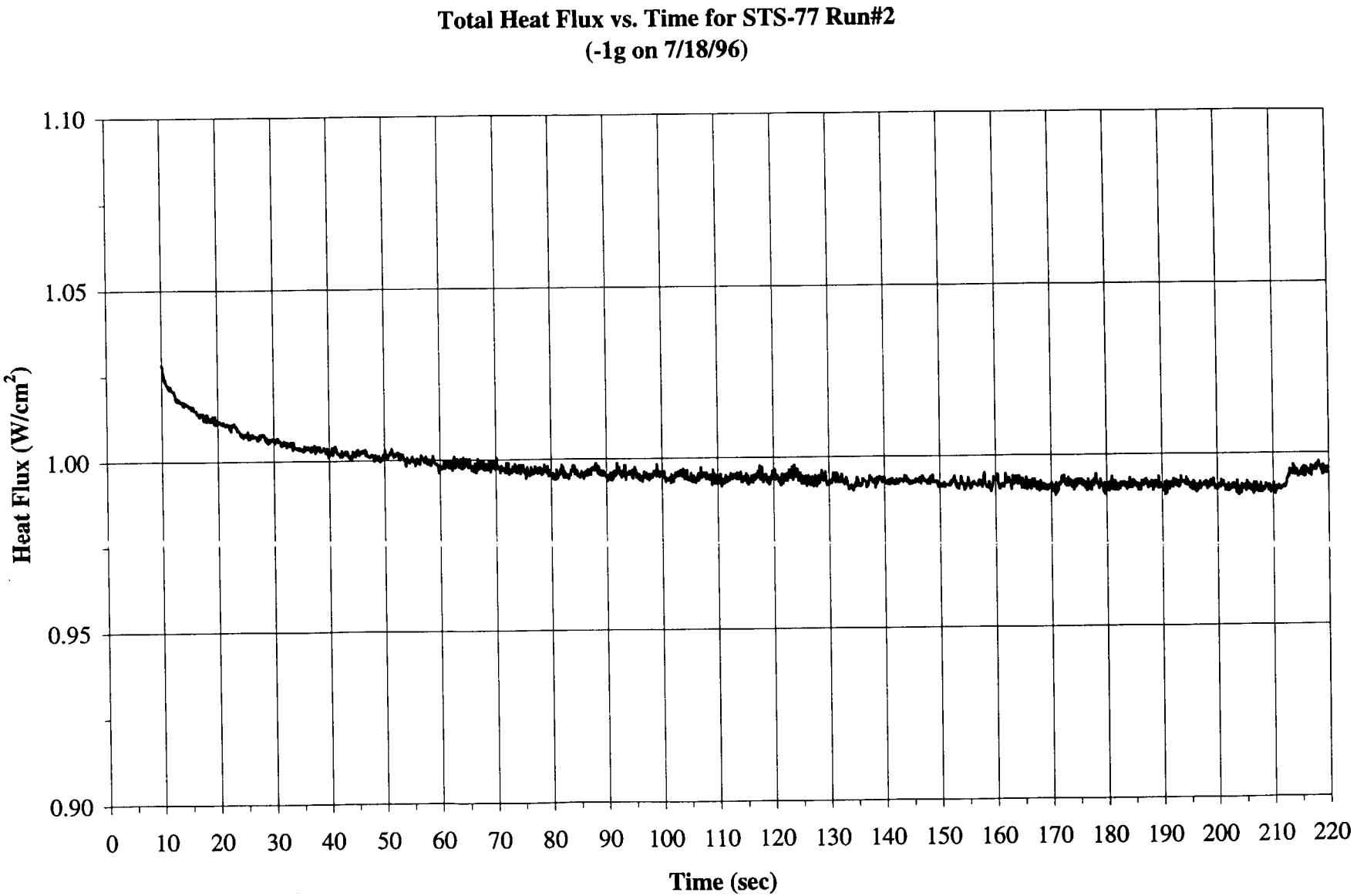

Figure B-18b. a/g = - 1 Postflight test. Heat flux input. PBE-IIA (STS-77). Run No. 2.

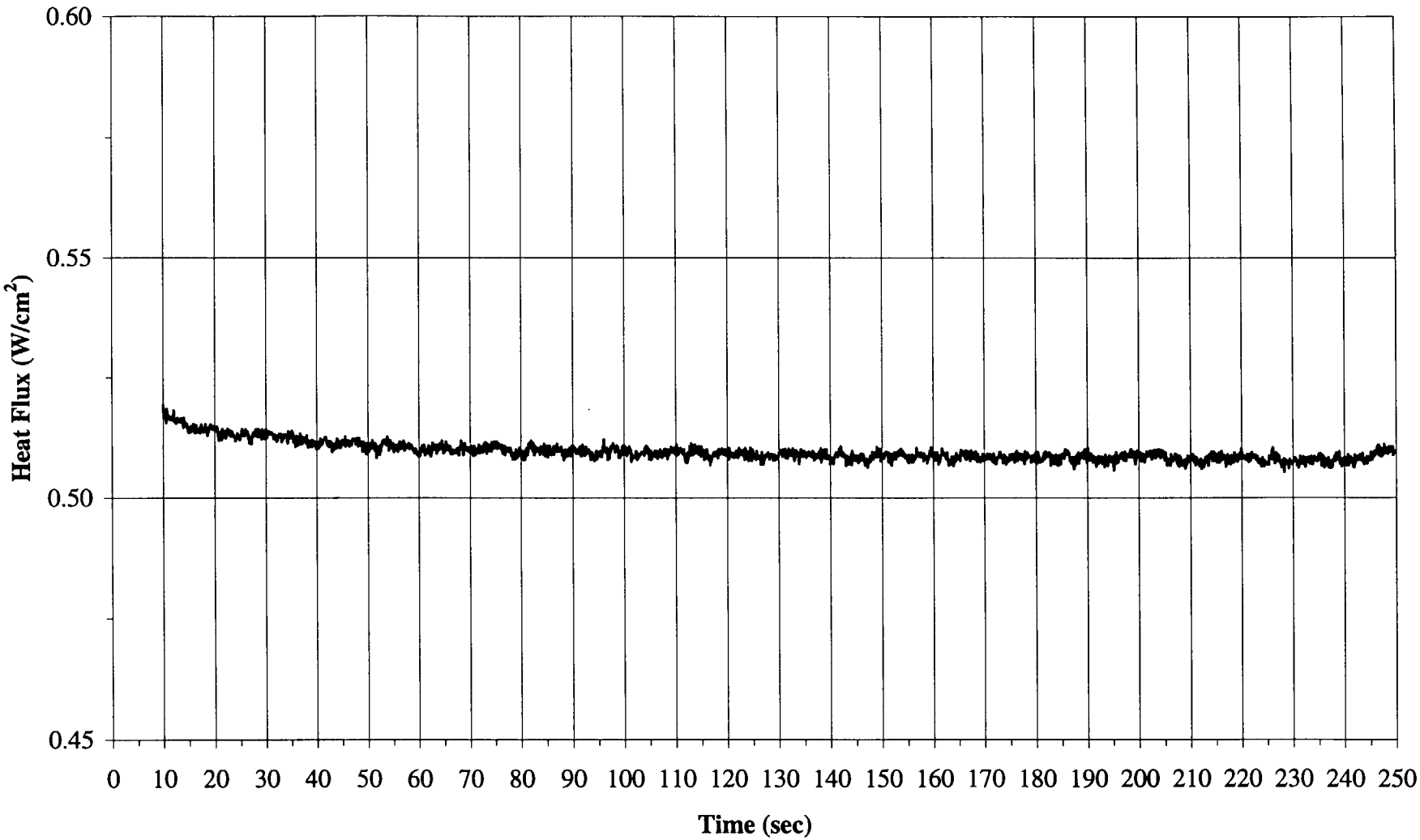

Figure B-18c. a/g = - 1 Postflight test. Heat flux input. PBE-IIA (STS-77). Run No. 3.

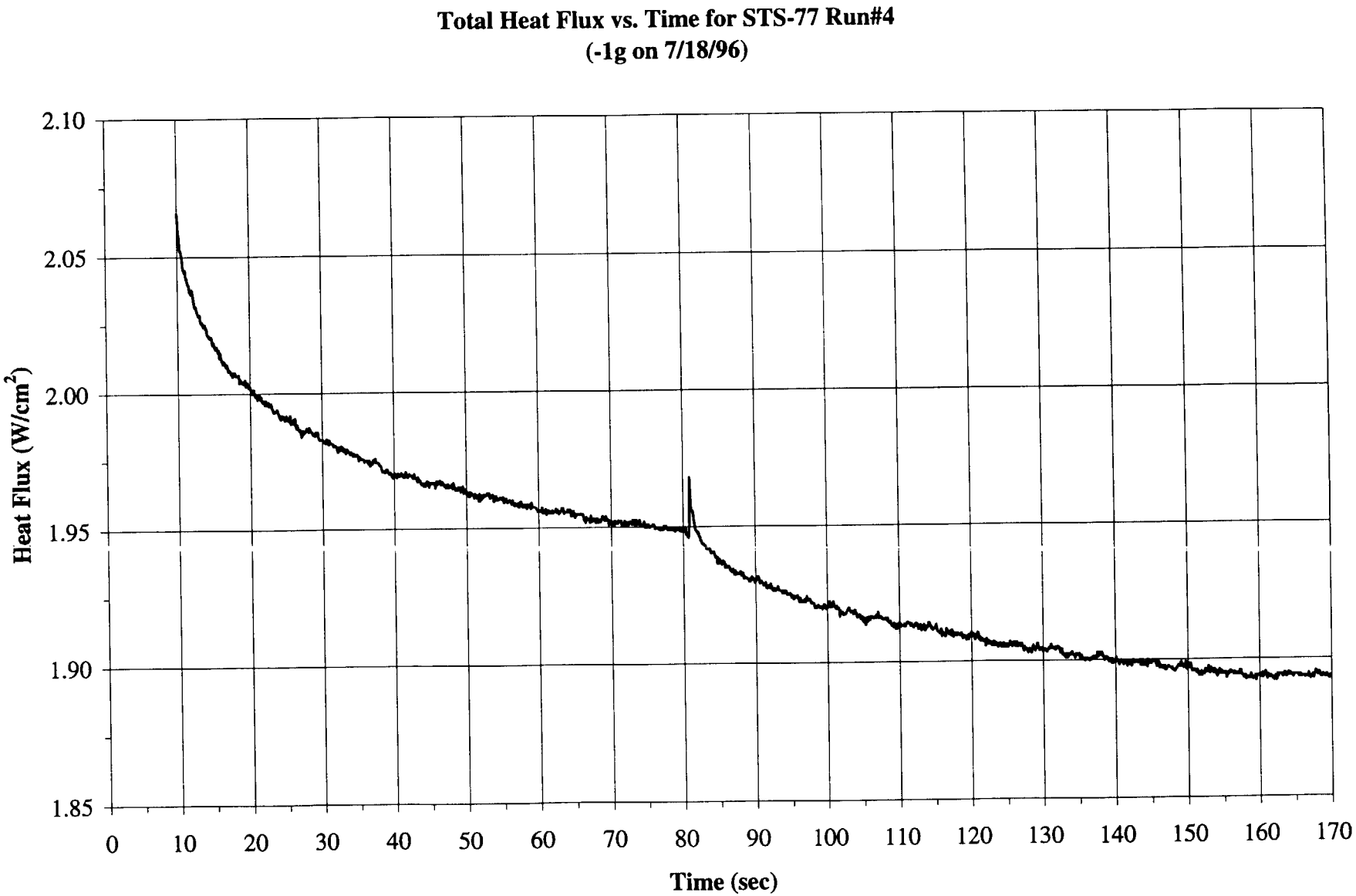

Figure B-18d. a/g = - 1 Postflight test. Heat flux input. PBE-IIA (STS-77). Run No. 4.

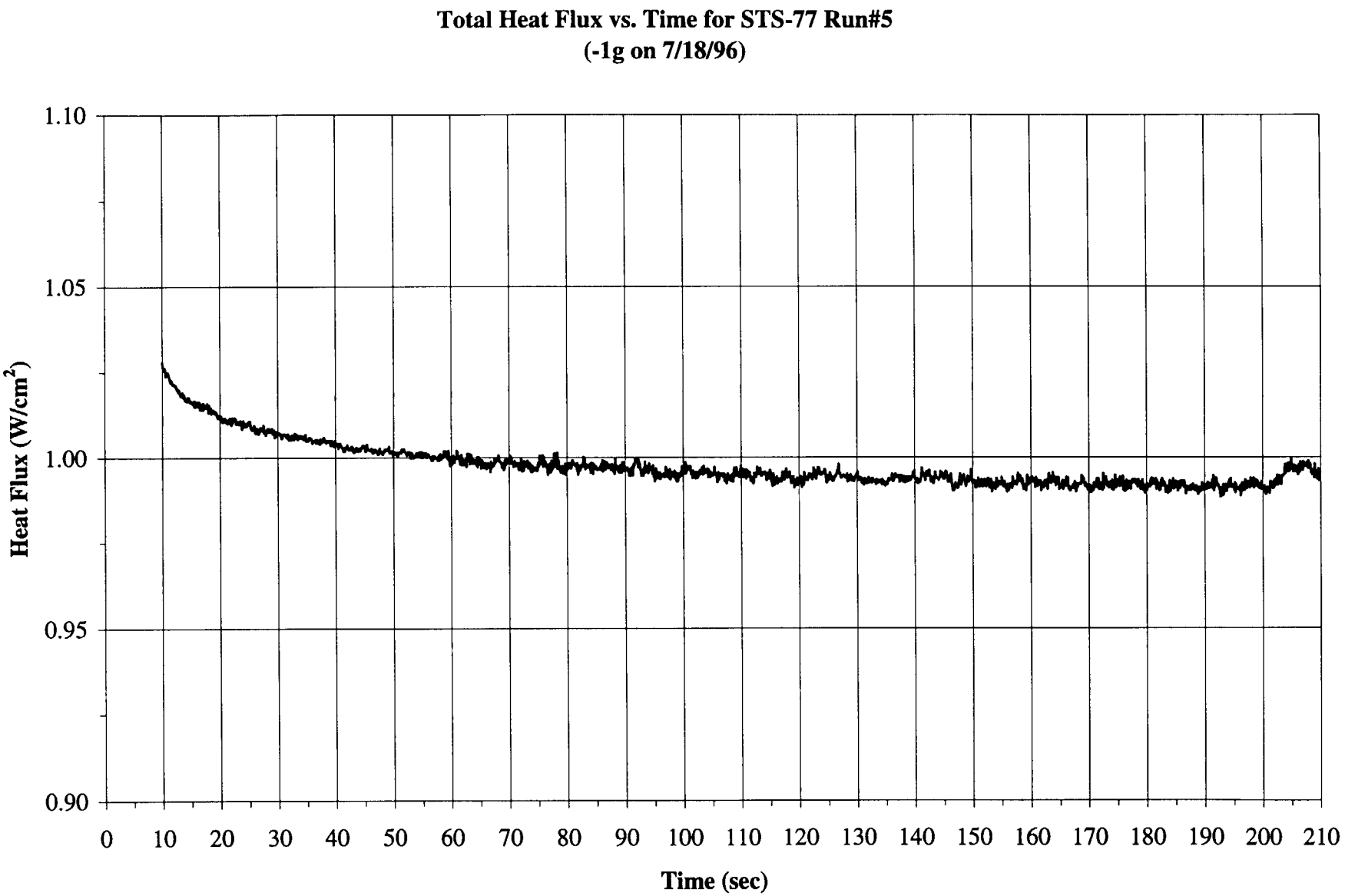

Figure B-18e. a/g = - 1 Postflight test. Heat flux input. PBE-IIA (STS-77). Run No. 5.

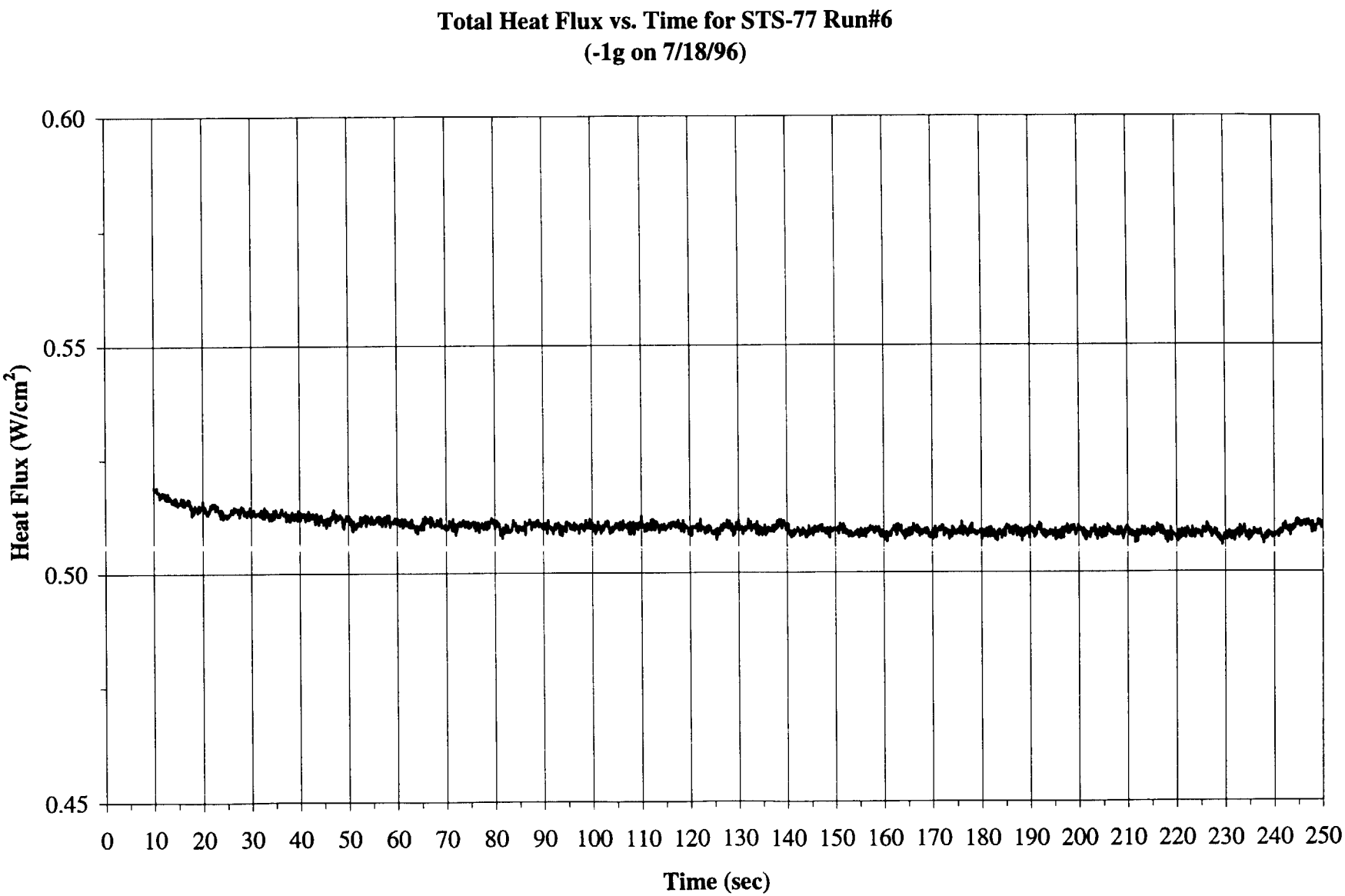

Figure B-18f. a/g = - 1 Postflight test. Heat flux input. PBE-IIA (STS-77). Run No. 6.

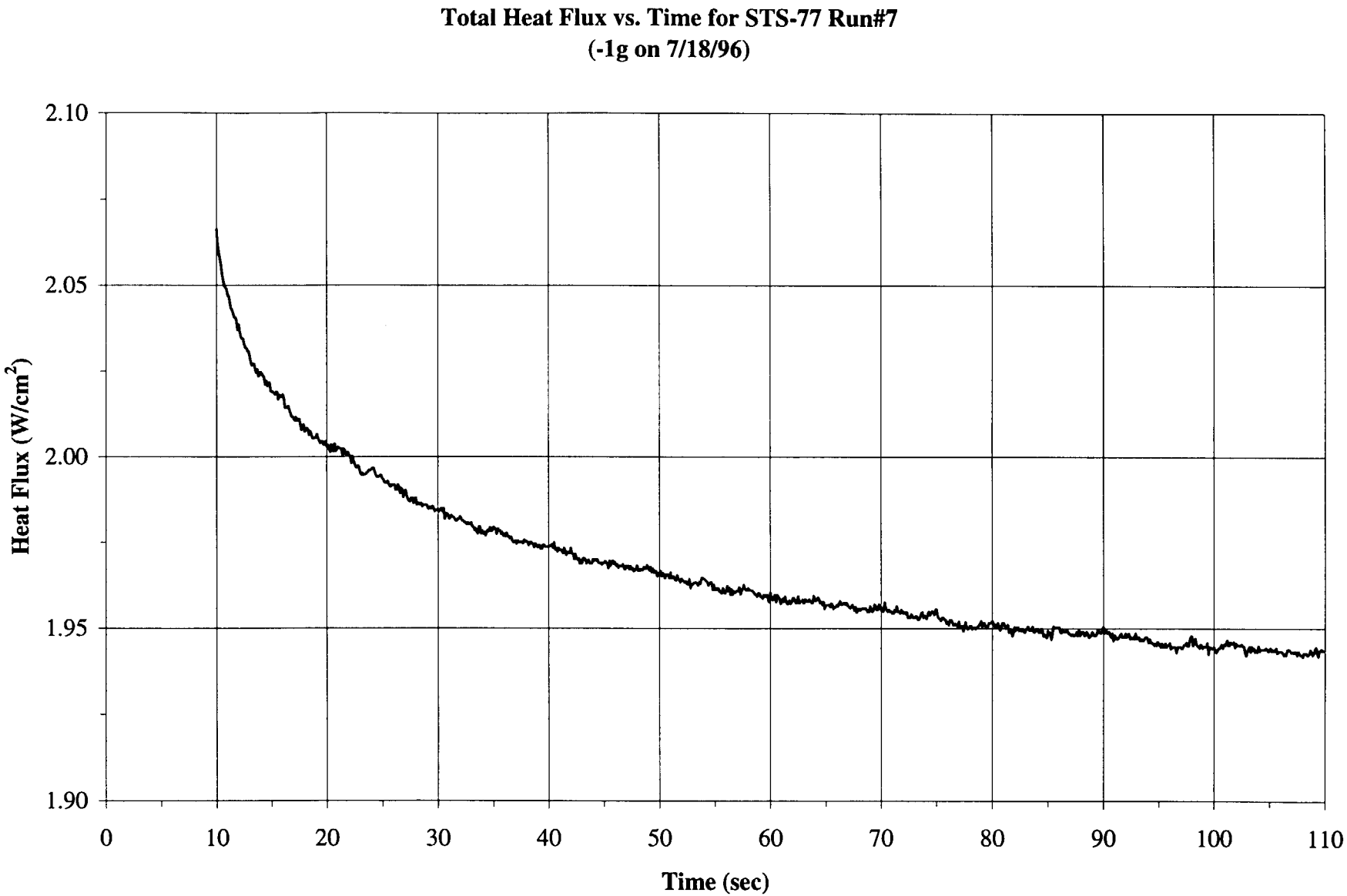

Figure B-18g. a/g = - 1 Postflight test. Heat flux input. PBE-IIA (STS-77). Run No. 7.

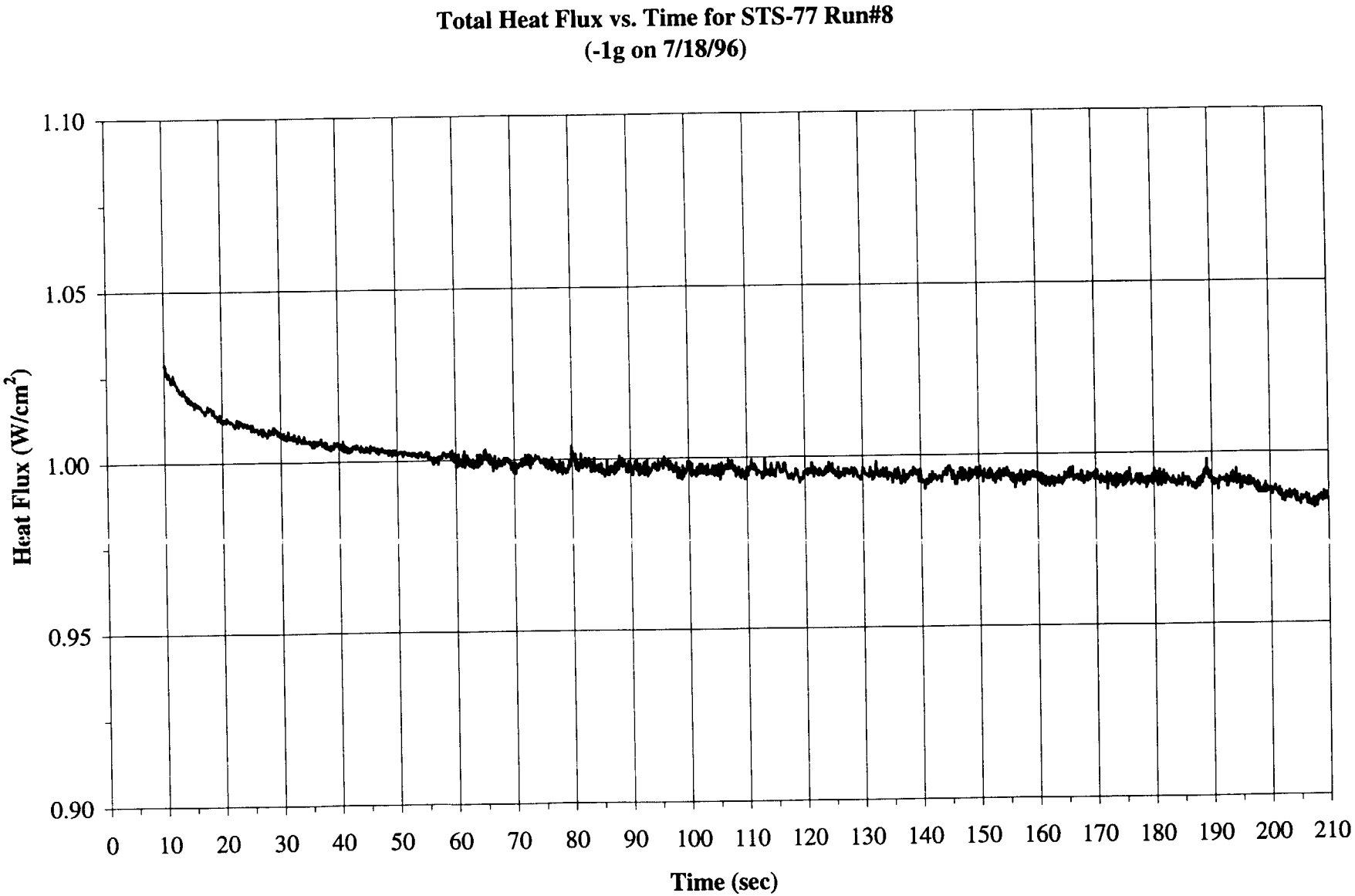

Figure B-18h. a/g = - 1 Postflight test. Heat flux input. PBE-IIA (STS-77). Run No. 8.

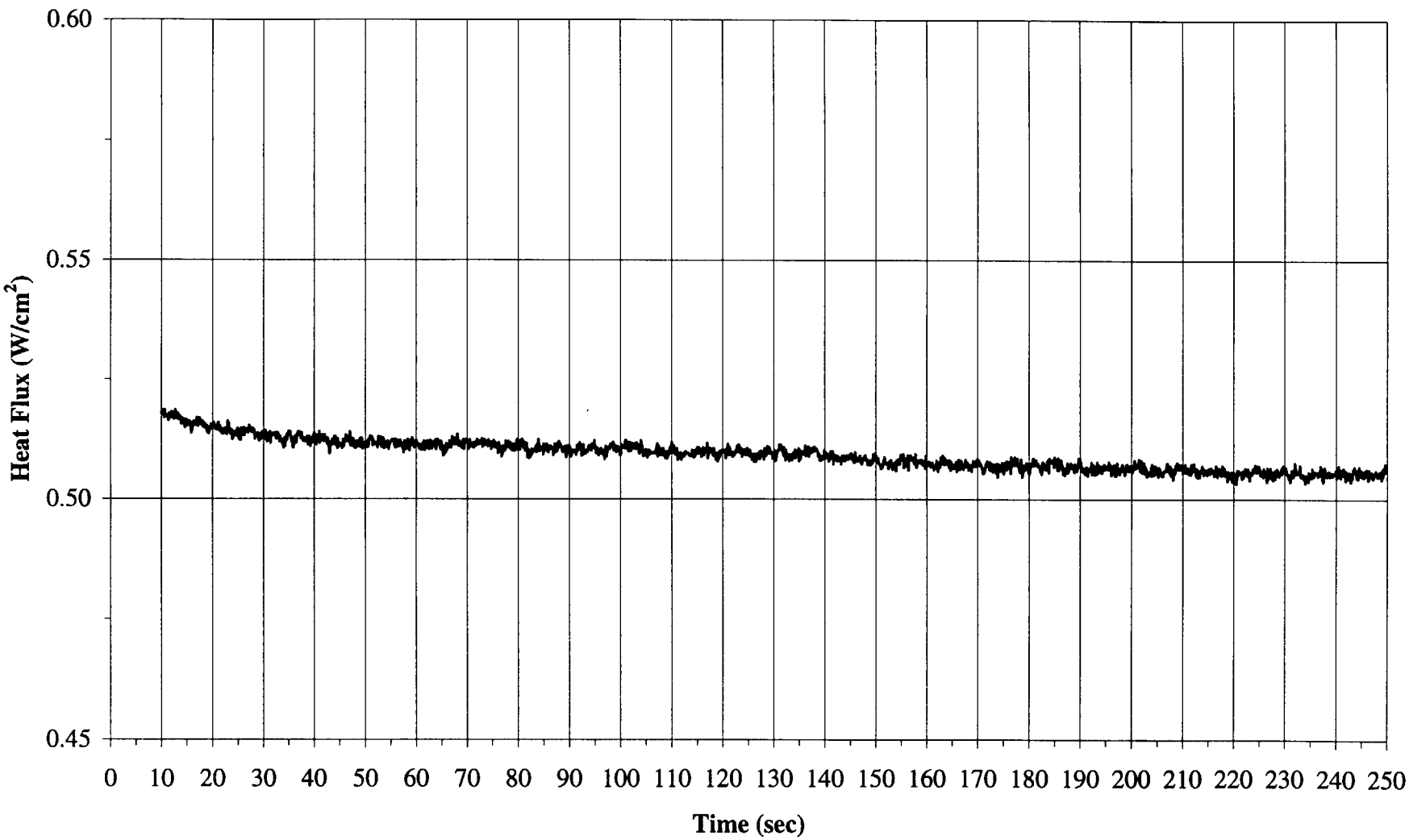

Figure B-18i. a/g = - 1 Postflight test. Heat flux input. PBE-IIA (STS-77). Run No. 9.

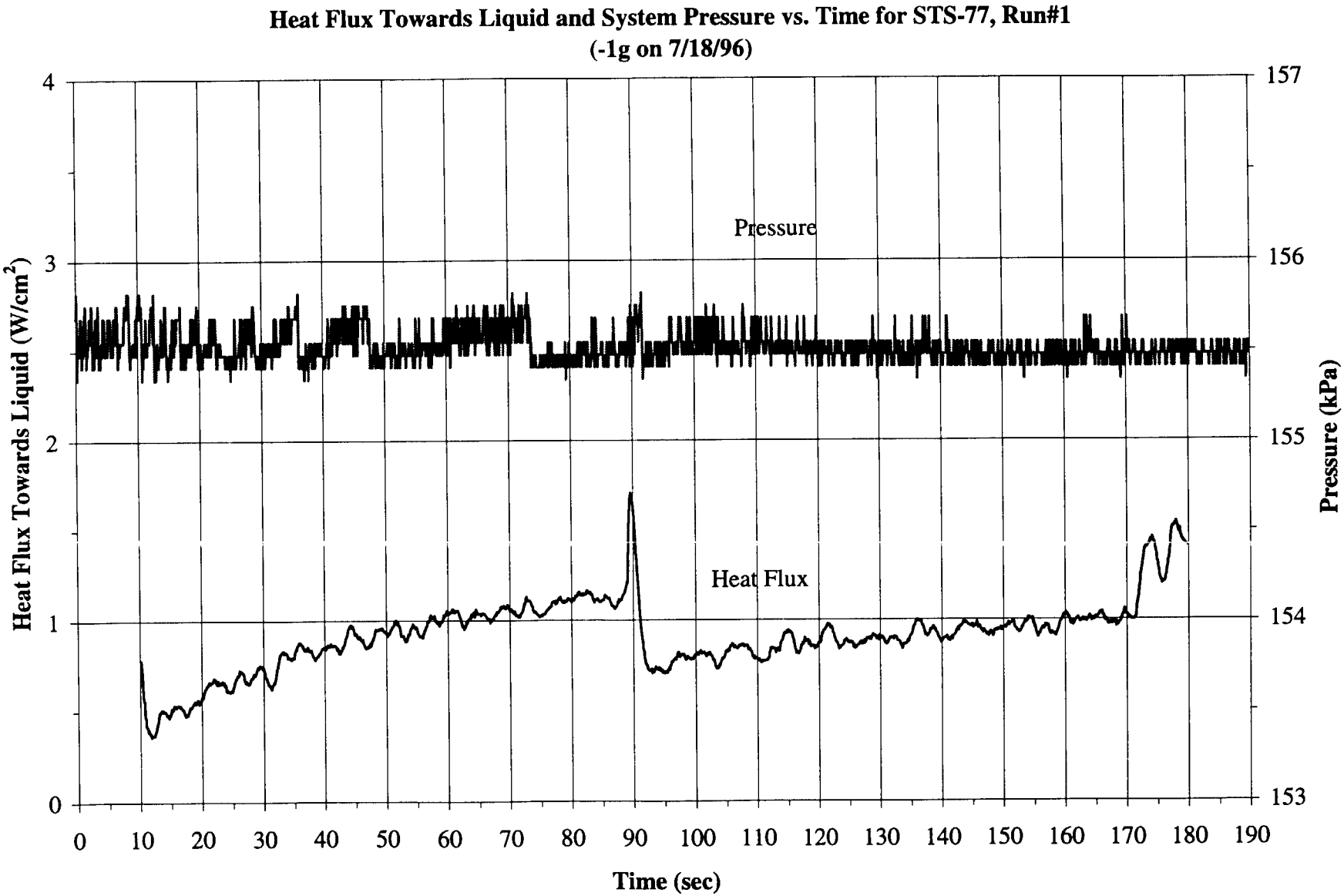

Figure B-19a. a/g = -1 Postflight test. System pressure and heat flux into fluid. PBE-IIA (STS-77). Run No. 1.

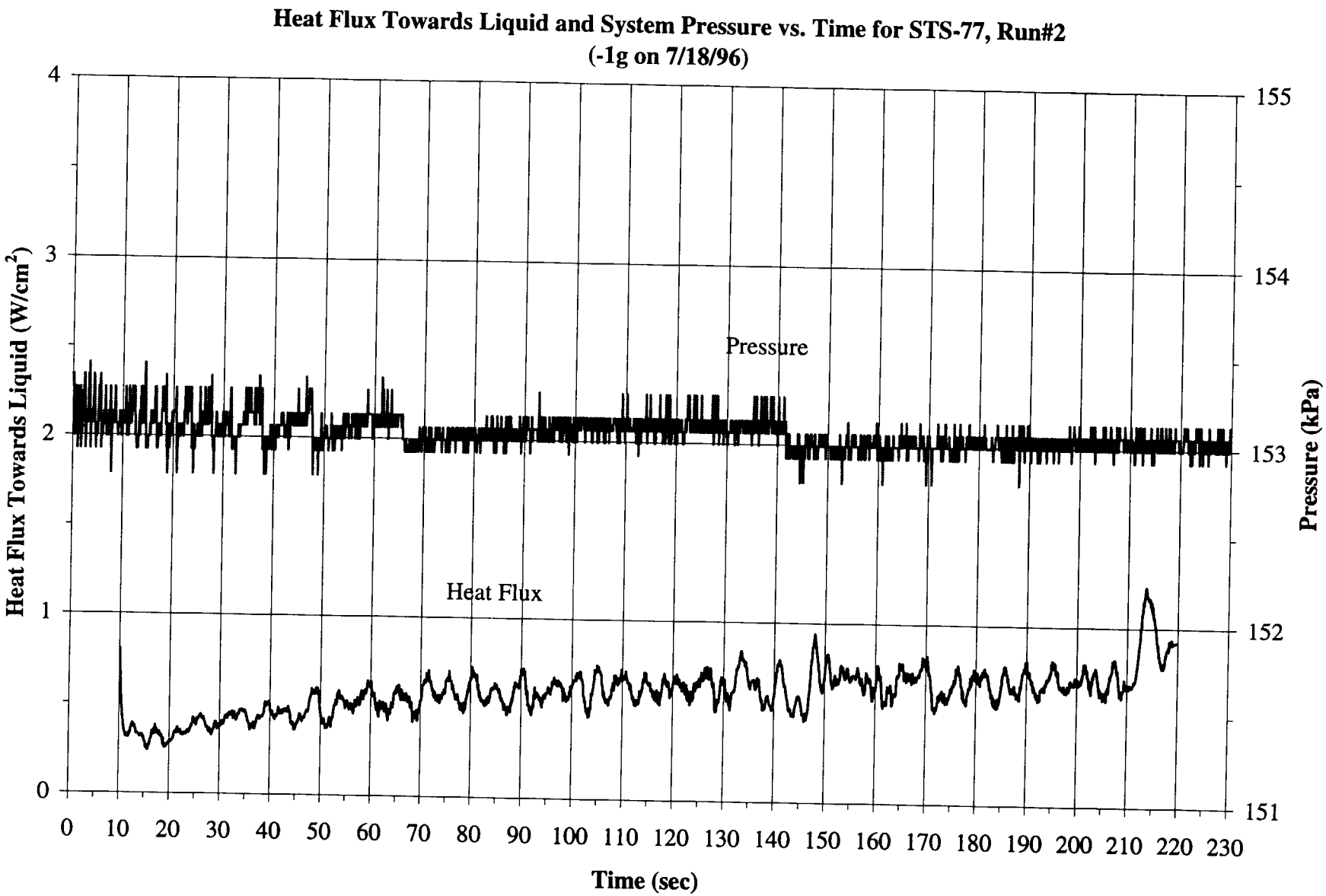

Figure B-19b. a/g = -1 Postflight test. System pressure and heat flux into fluid. PBE-IIA (STS-77). Run No. 2.

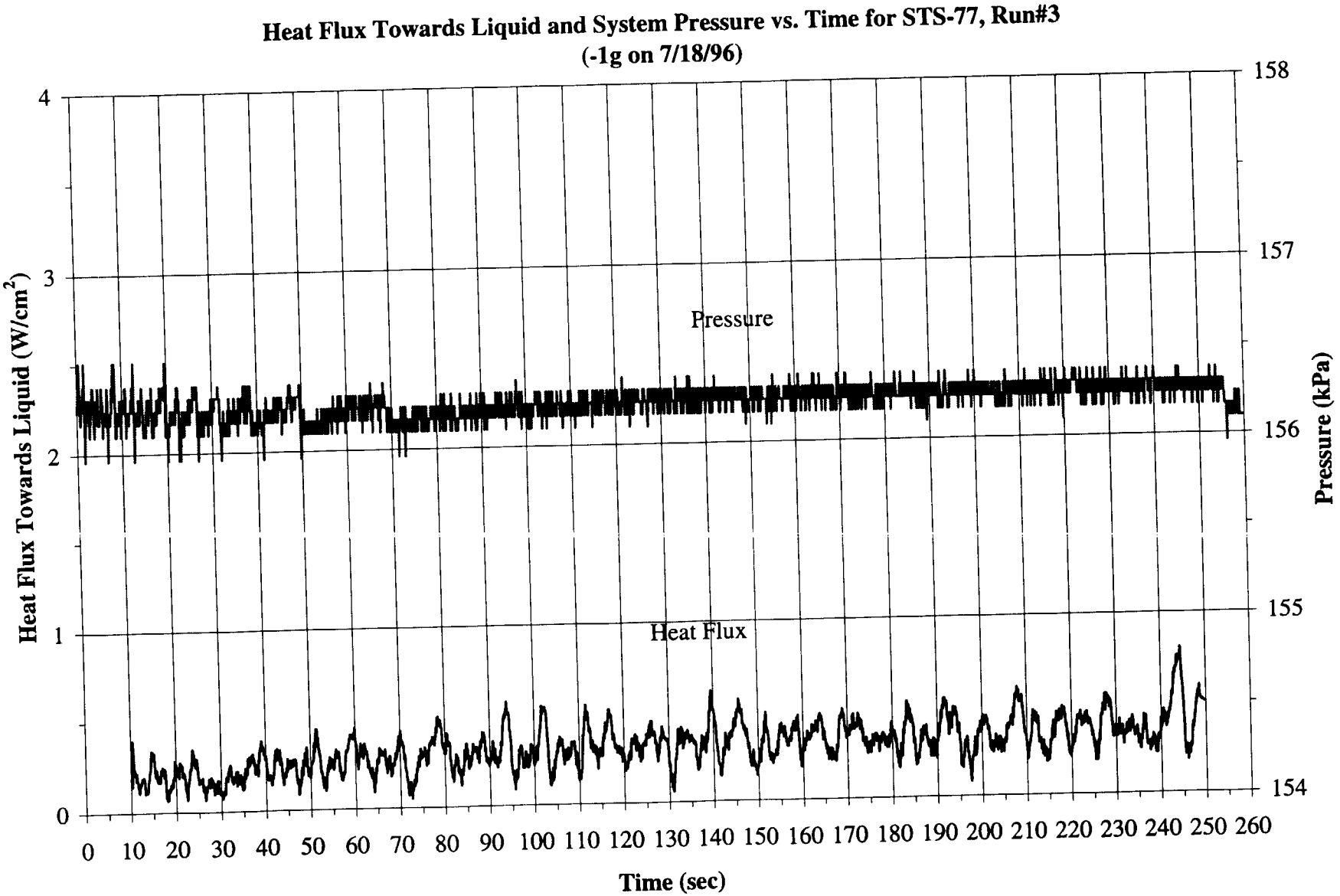

Figure B-19c. a/g = -1 Postflight test. System pressure and heat flux into fluid. PBE-IIA (STS-77). Run No. 3.

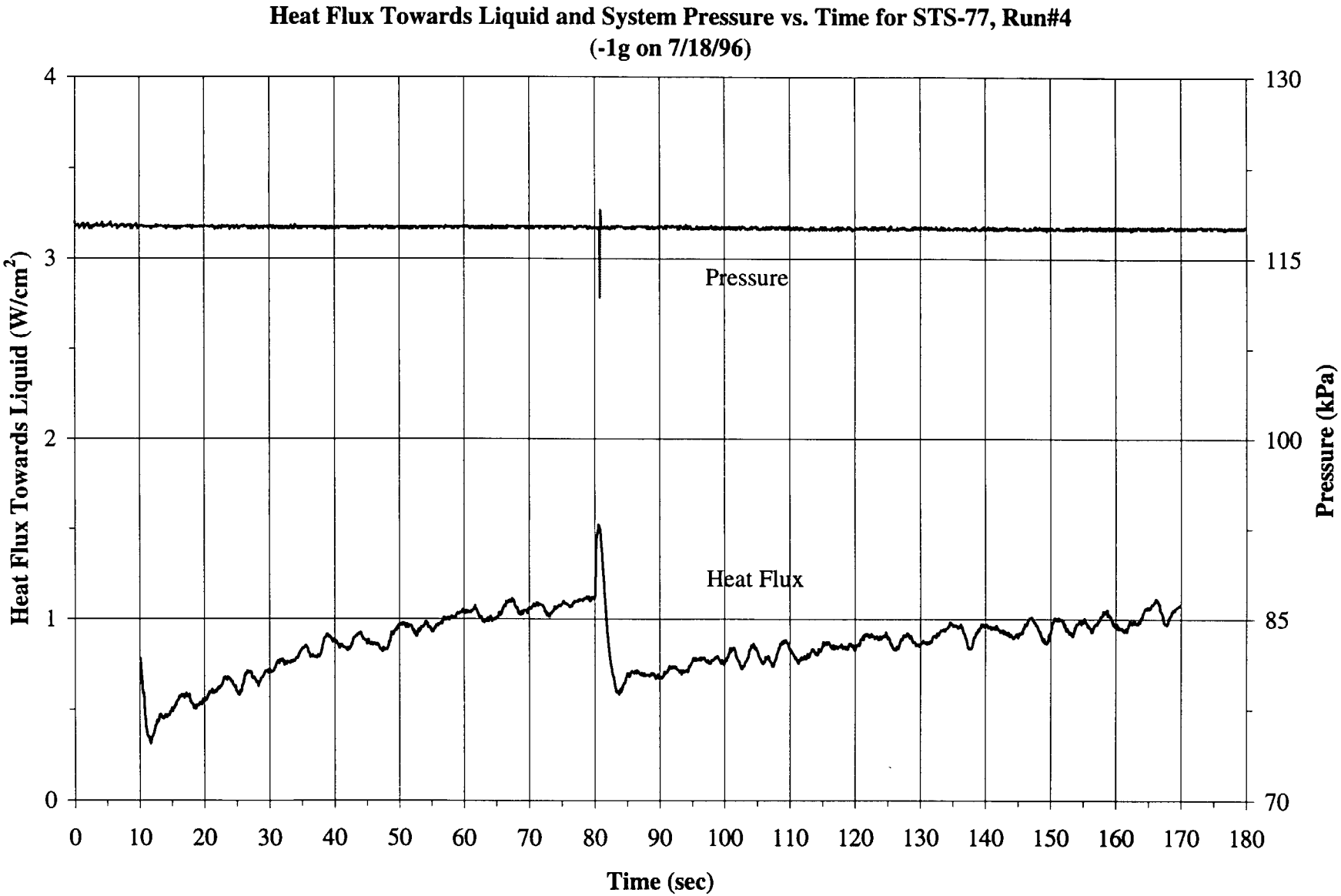

Figure B-19d. a/g = -1 Postflight test. System pressure and heat flux into fluid. PBE-IIA (STS-77). Run No. 4.

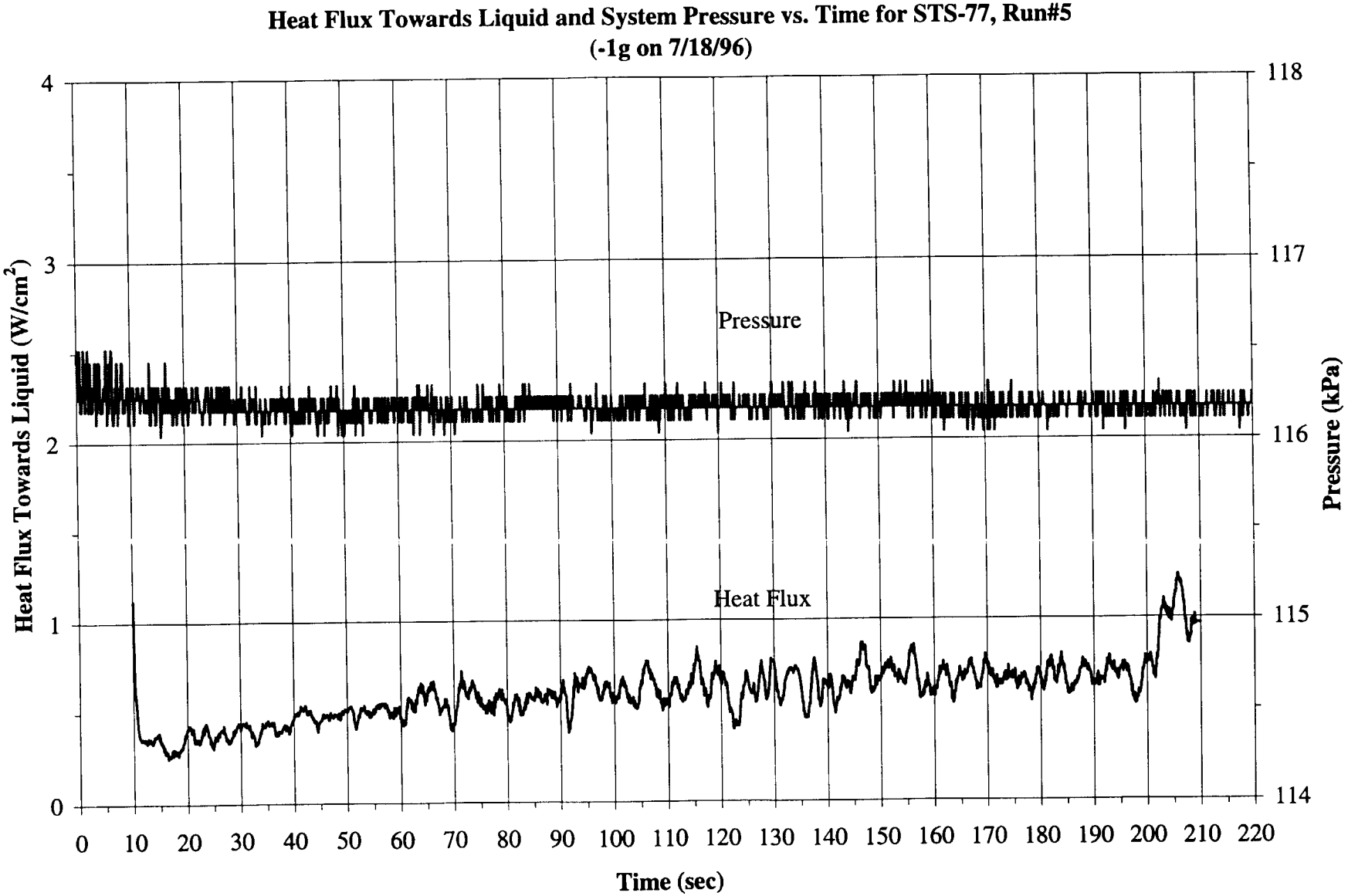

Figure B-19e. a/g = -1 Postflight test. System pressure and heat flux into fluid. PBE-IIA (STS-77). Run No. 5.

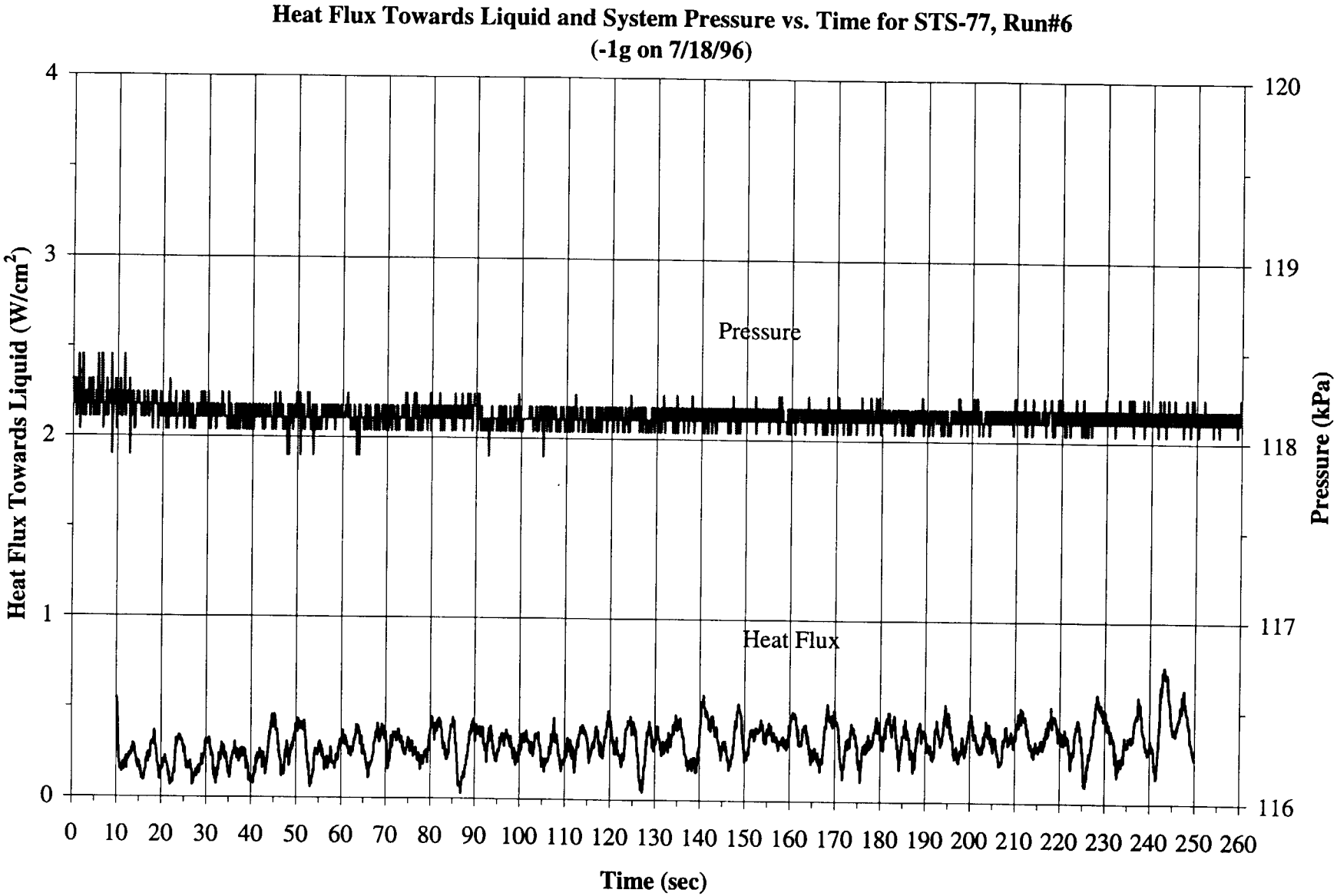

Figure B-19f. a/g = -1 Postflight test. System pressure and heat flux into fluid. PBE-IIA (STS-77). Run No. 6.

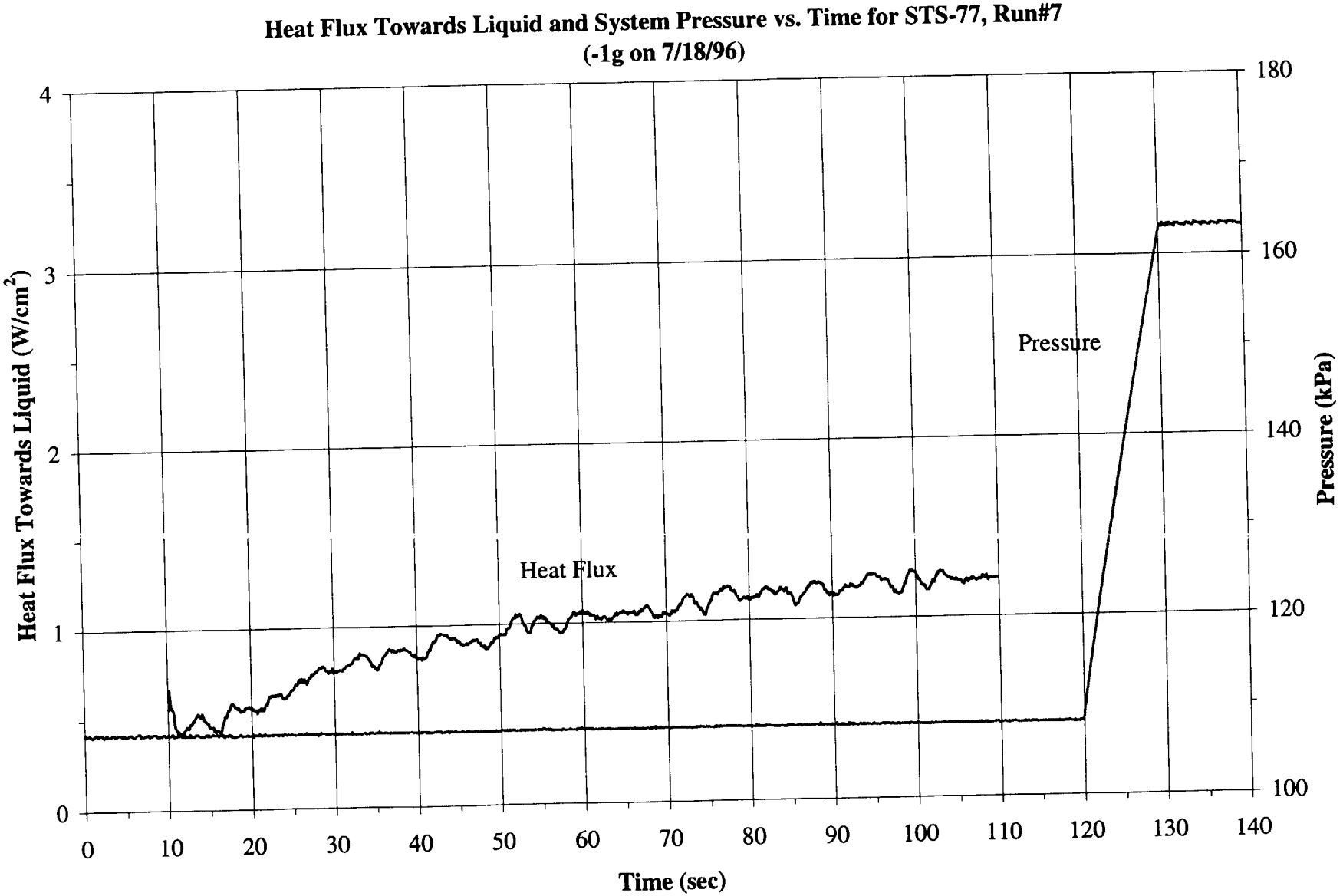

Figure B-19g. a/g = -1 Postflight test. System pressure and heat flux into fluid. PBE-IIA (STS-77). Run No. 7.

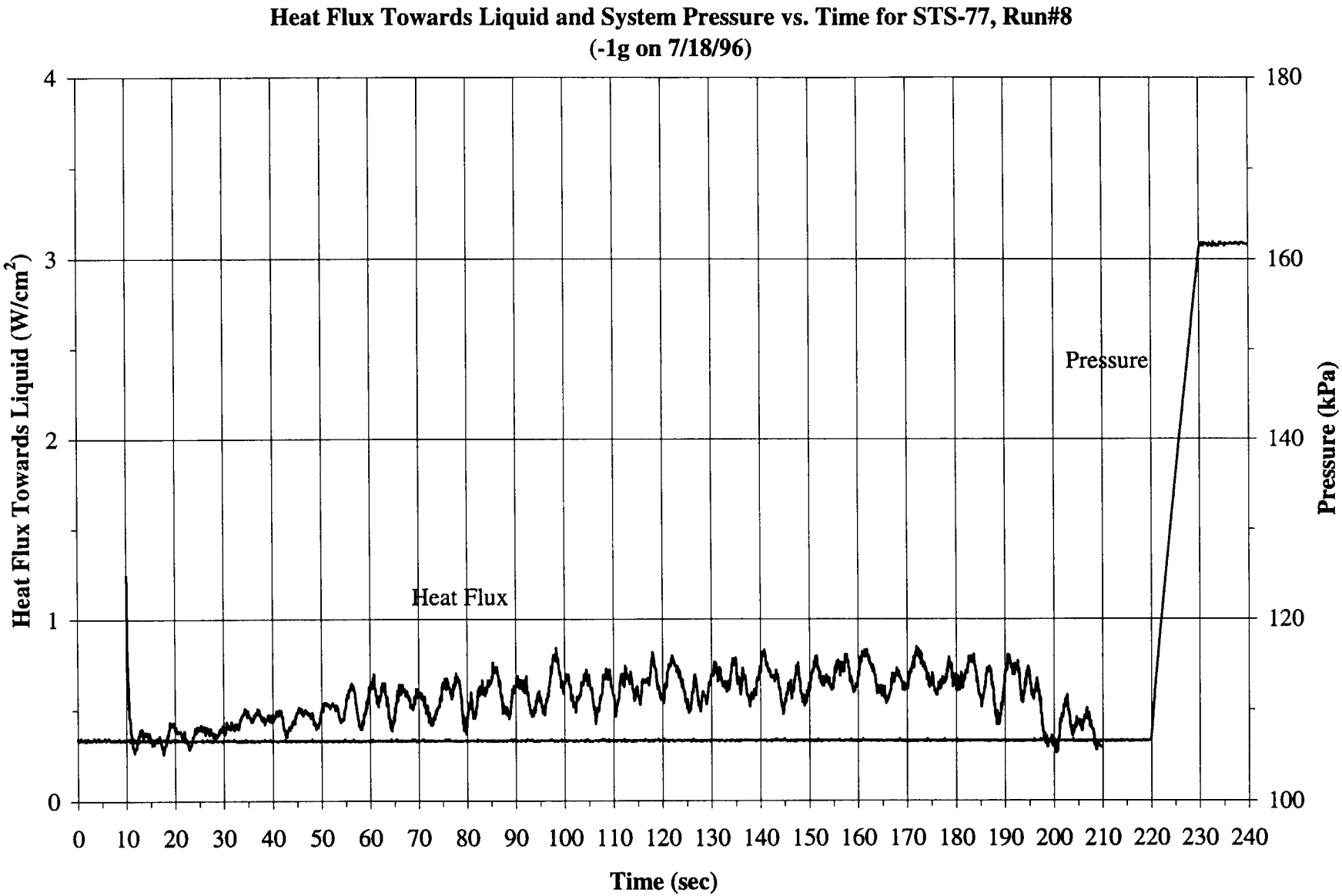

Figure B-19h. a/g = -1 Postflight test. System pressure and heat flux into fluid. PBE-IIA (STS-77). Run No. 8.

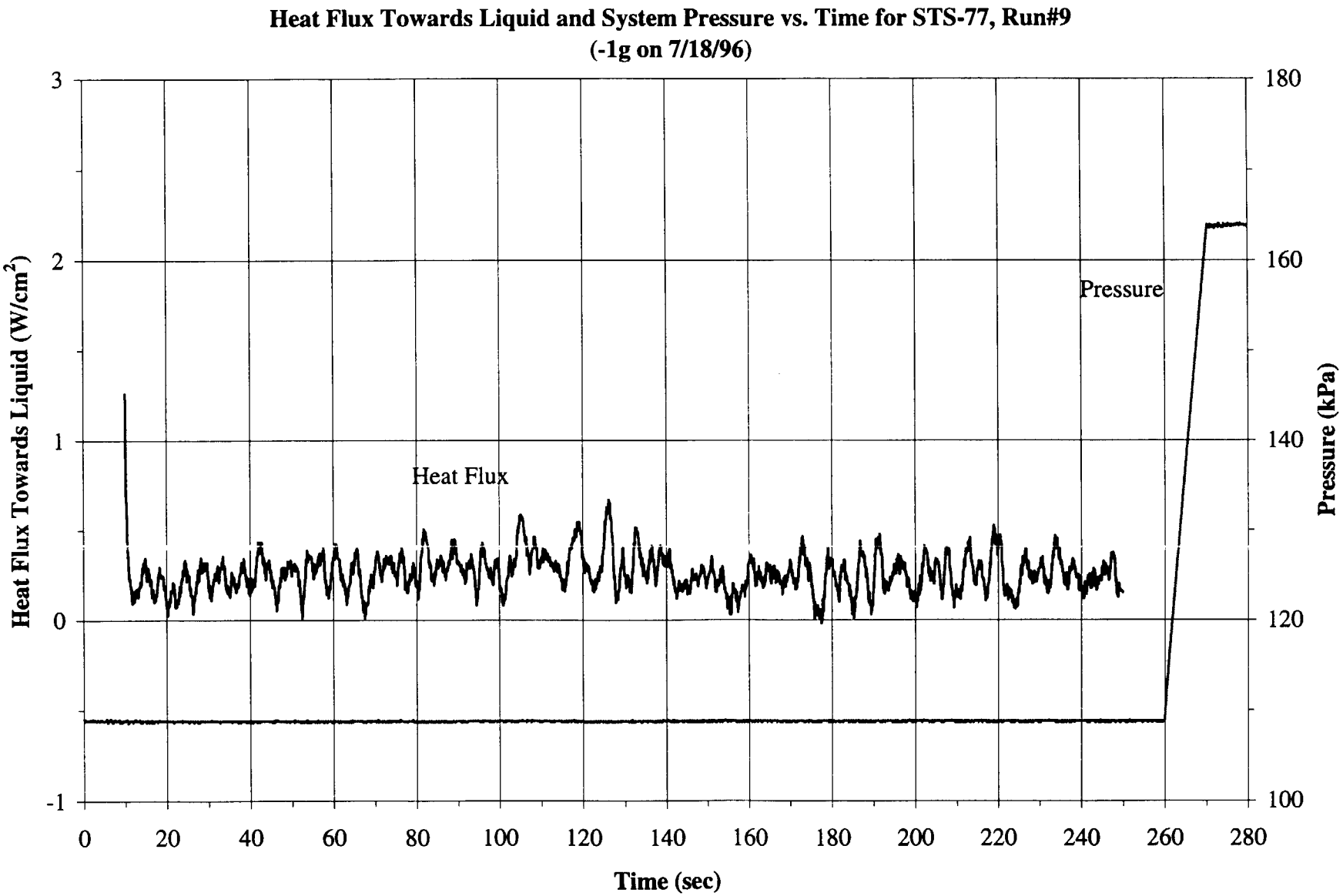

Figure B-19i. a/g = -1 Postflight test. System pressure and heat flux into fluid. PBE-IIA (STS-77). Run No. 9.

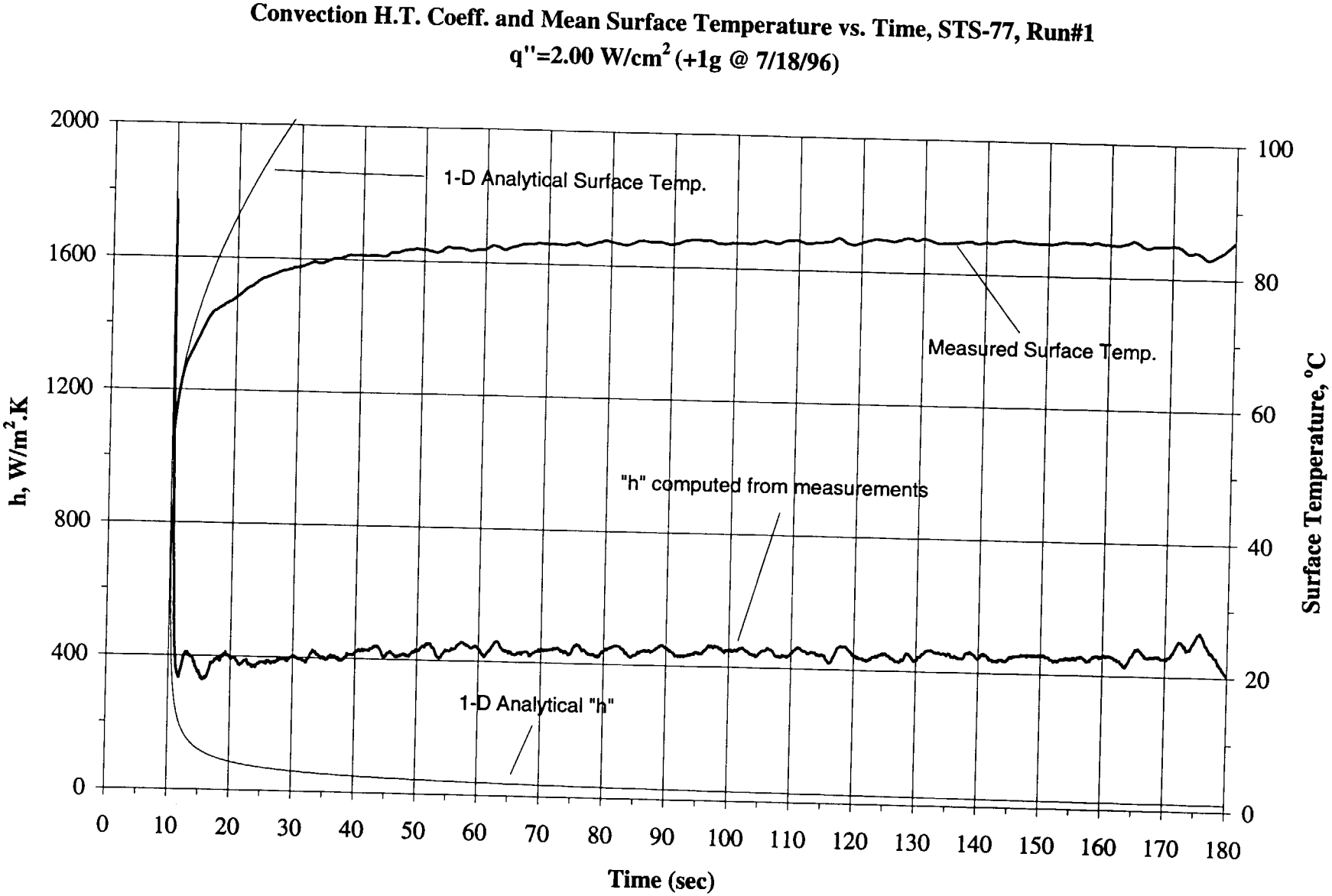

Figure B-20a. a/g = +1 Postflight test. Mean heater surface temperature and derived heat transfer coefficient. PBE-IIA (STS-77). Run No. 1.

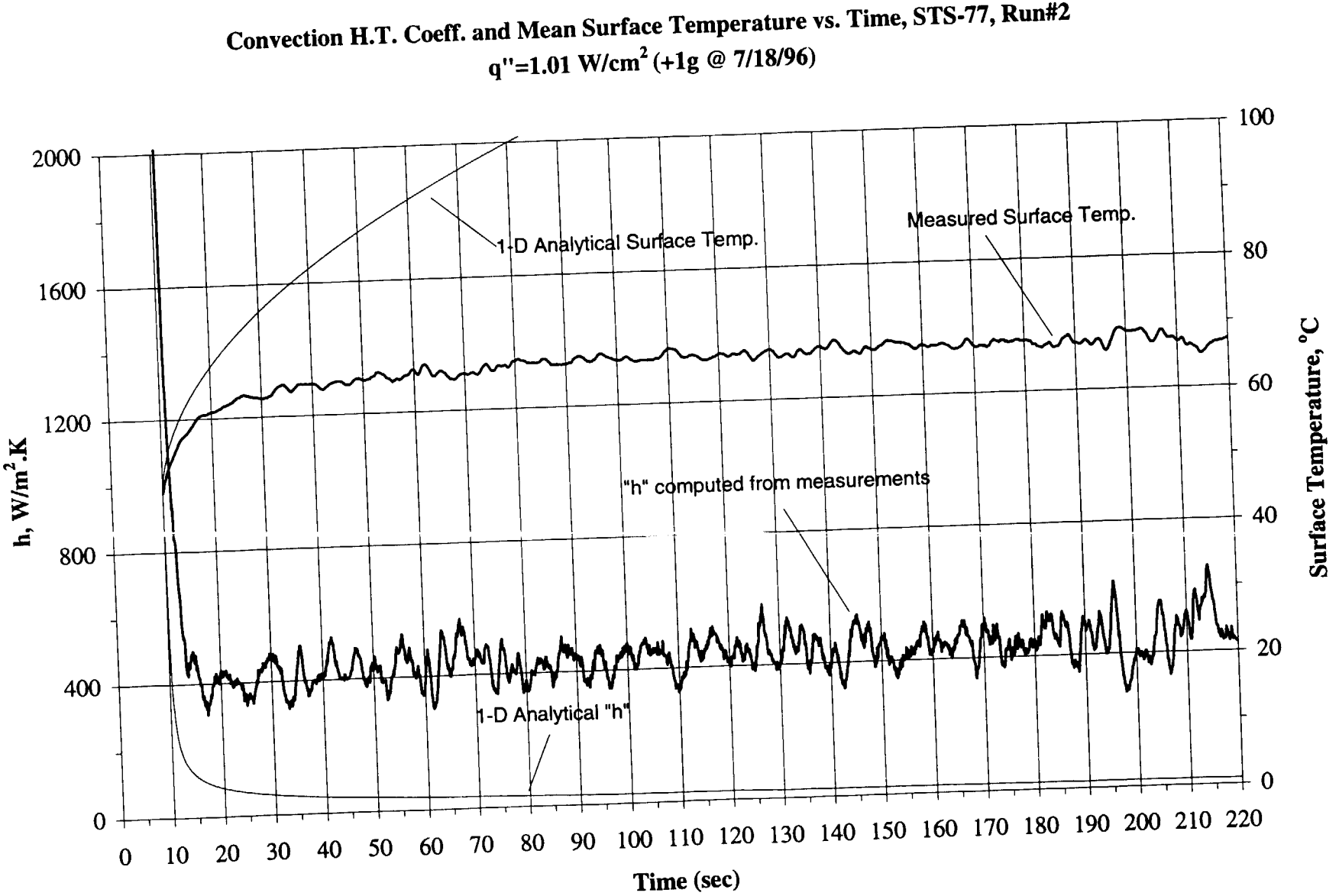

Figure B-20b. a/g = +1 Postflight test. Mean heater surface temperature and derived heat transfer coefficient. PBE-IIA (STS-77). Run No. 2.

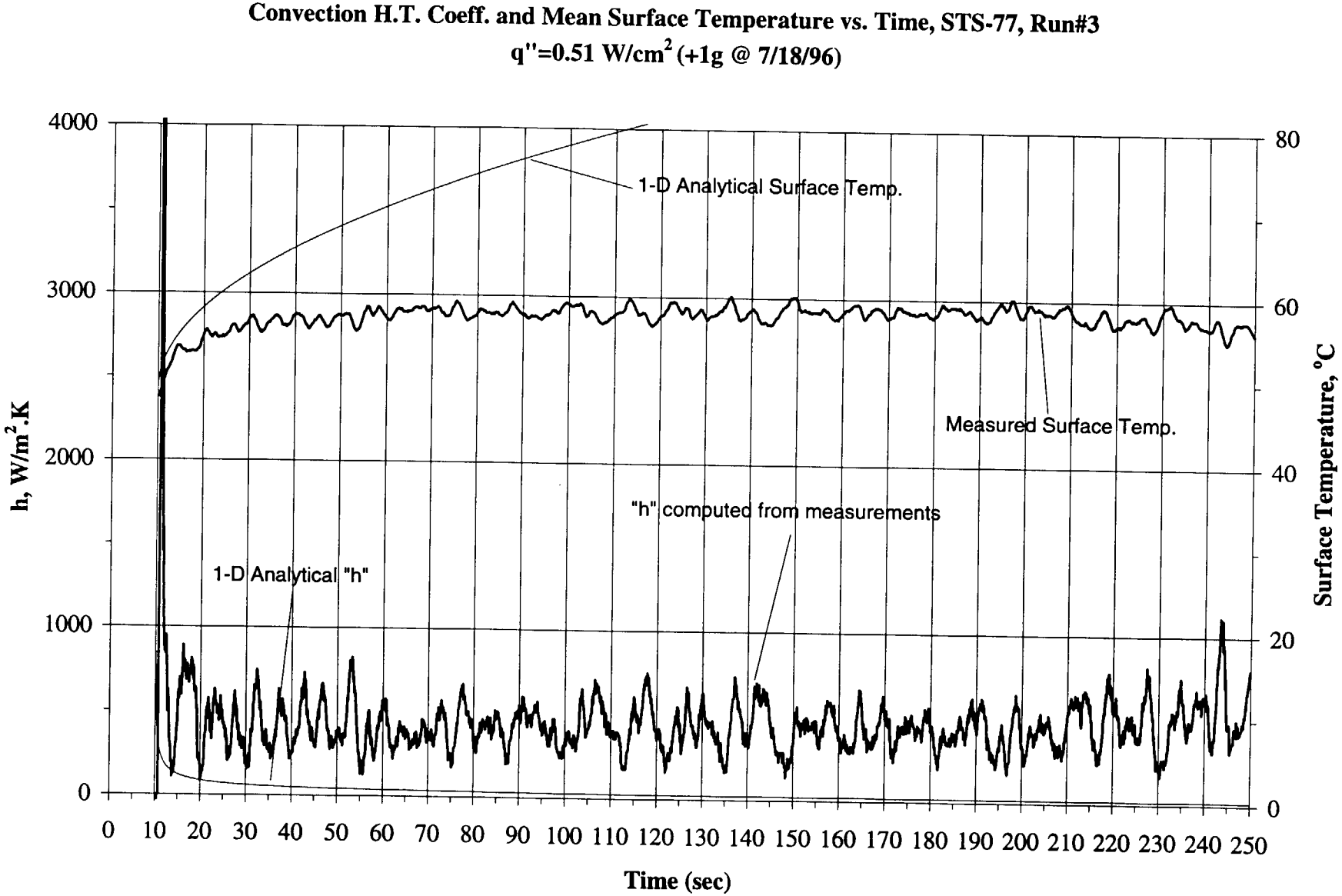

Figure B-20c. a/g = +1 Postflight test. Mean heater surface temperature and derived heat transfer coefficient. PBE-IIA (STS-77). Run No. 3.

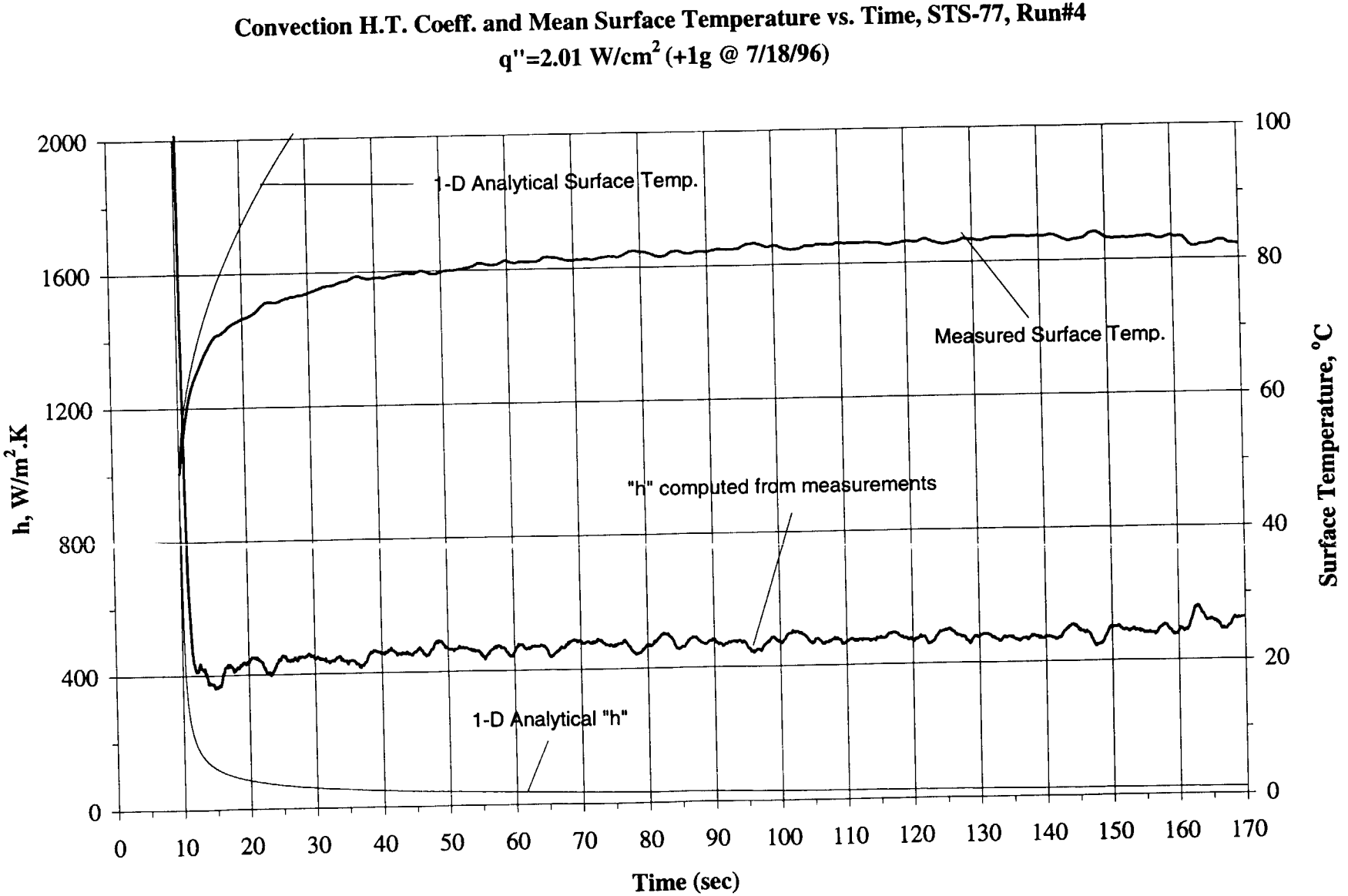

Figure B-20d. a/g = +1 Postflight test. Mean heater surface temperature and derived heat transfer coefficient. PBE-IIA (STS-77). Run No. 4.

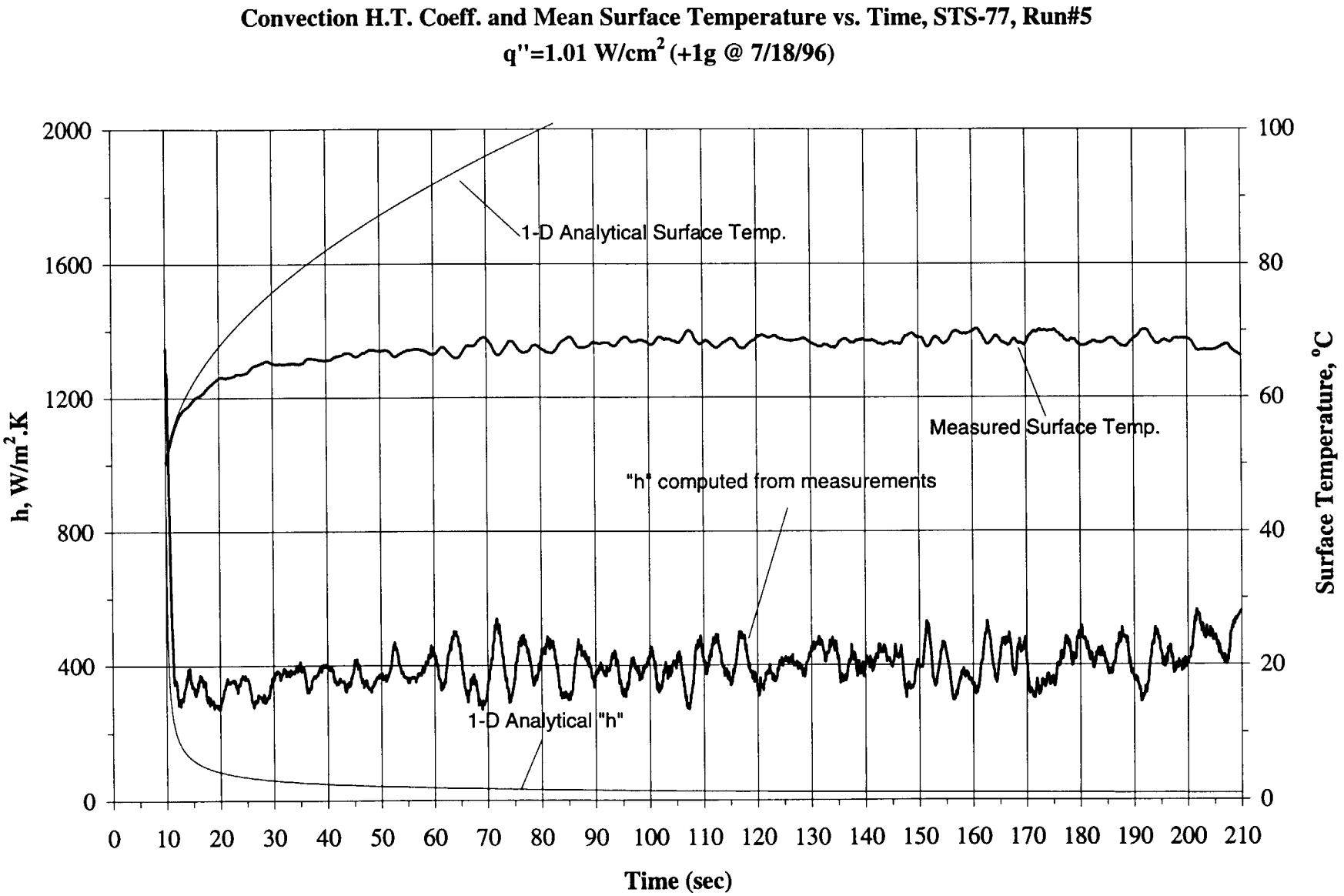

Figure B-20e. a/g = +1 Postflight test. Mean heater surface temperature and derived heat transfer coefficient. PBE-IIA (STS-77). Run No. 5.

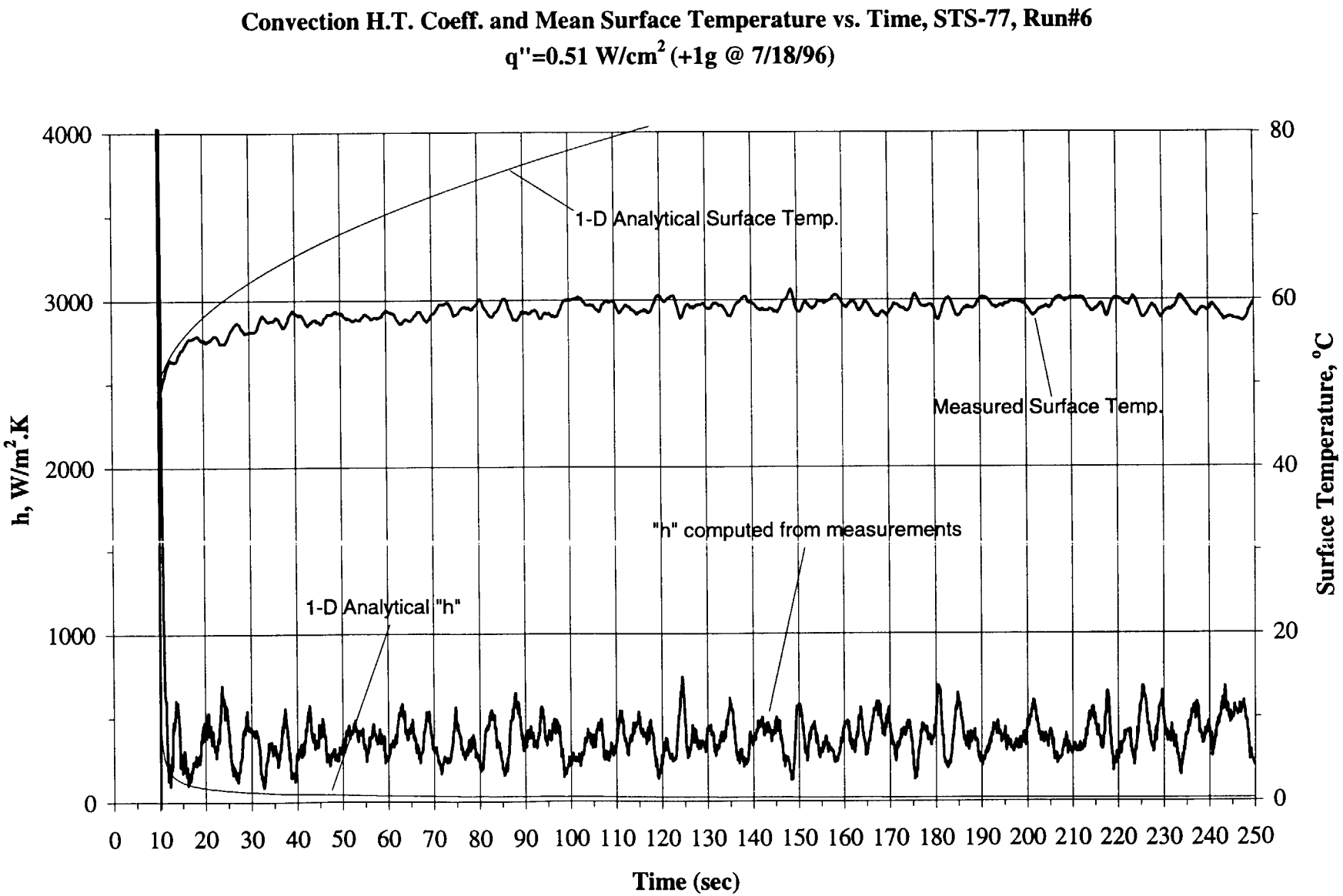

Figure B-20f. a/g = +1 Postflight test. Mean heater surface temperature and derived heat transfer coefficient. PBE-IIA (STS-77). Run No. 6.

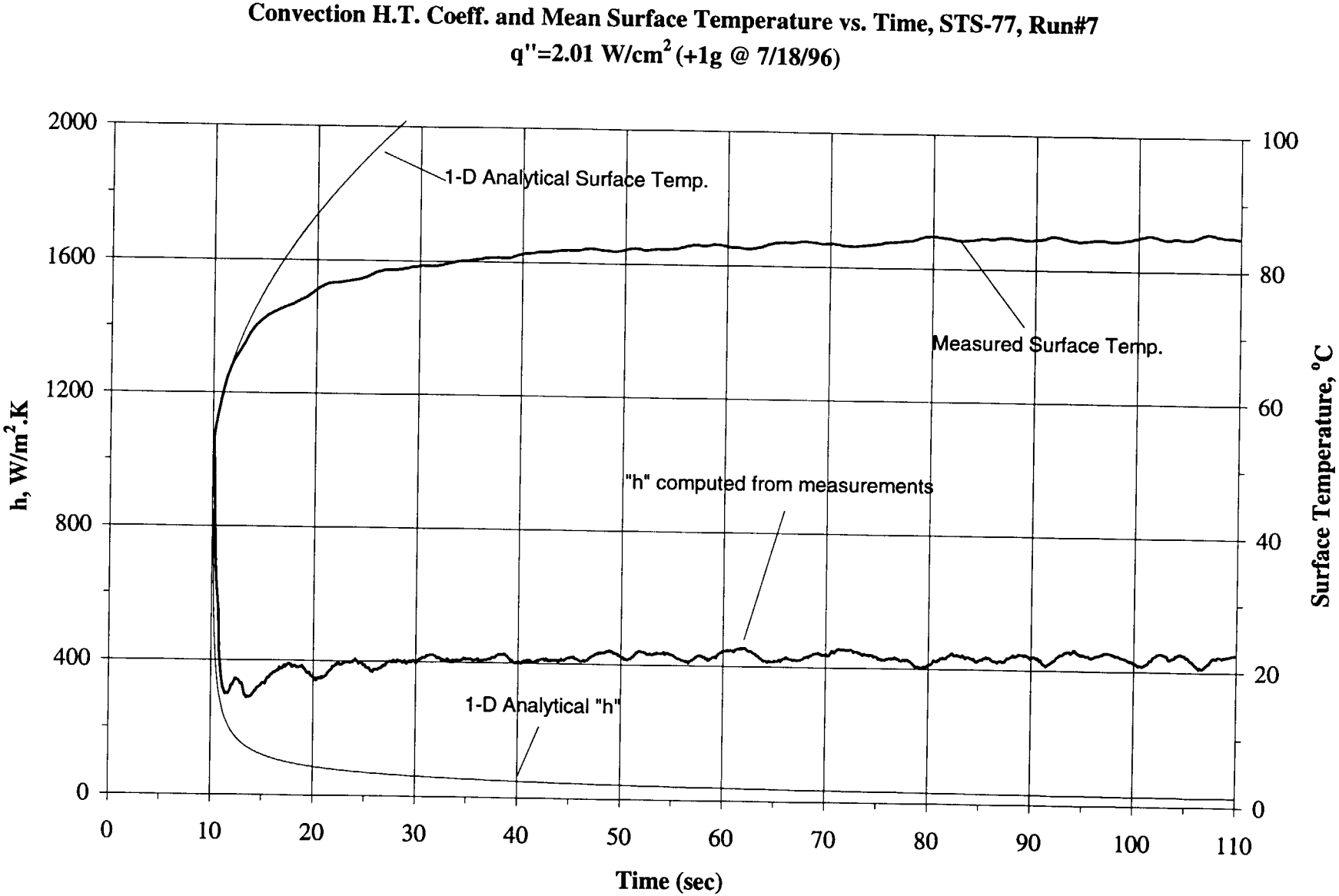

Figure B-20g. a/g = +1 Postflight test. Mean heater surface temperature and derived heat transfer coefficient. PBE-IIA (STS-77). Run No. 7.

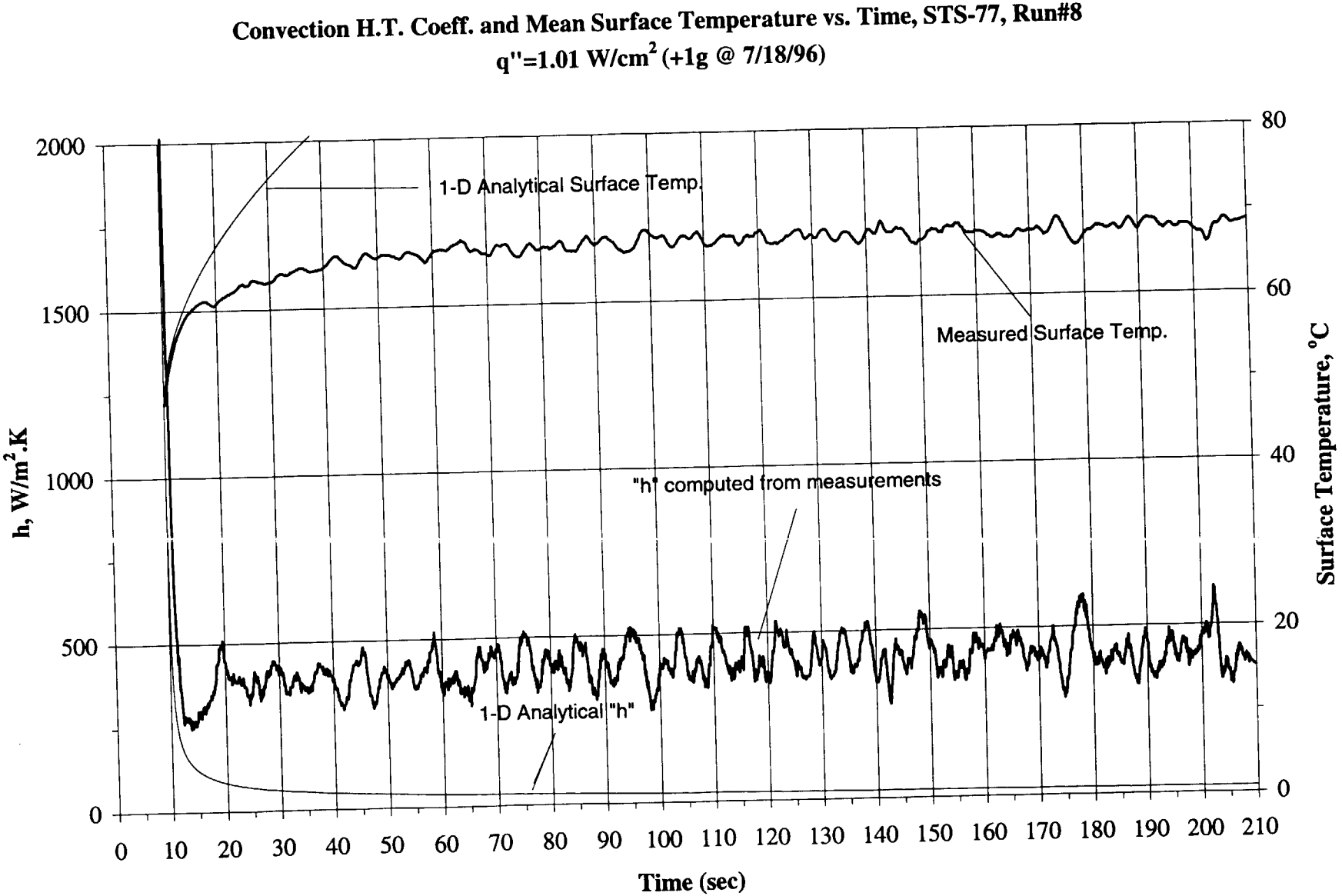

Figure B-20h. a/g = +1 Postflight test. Mean heater surface temperature and derived heat transfer coefficient. PBE-IIA (STS-77). Run No. 8.

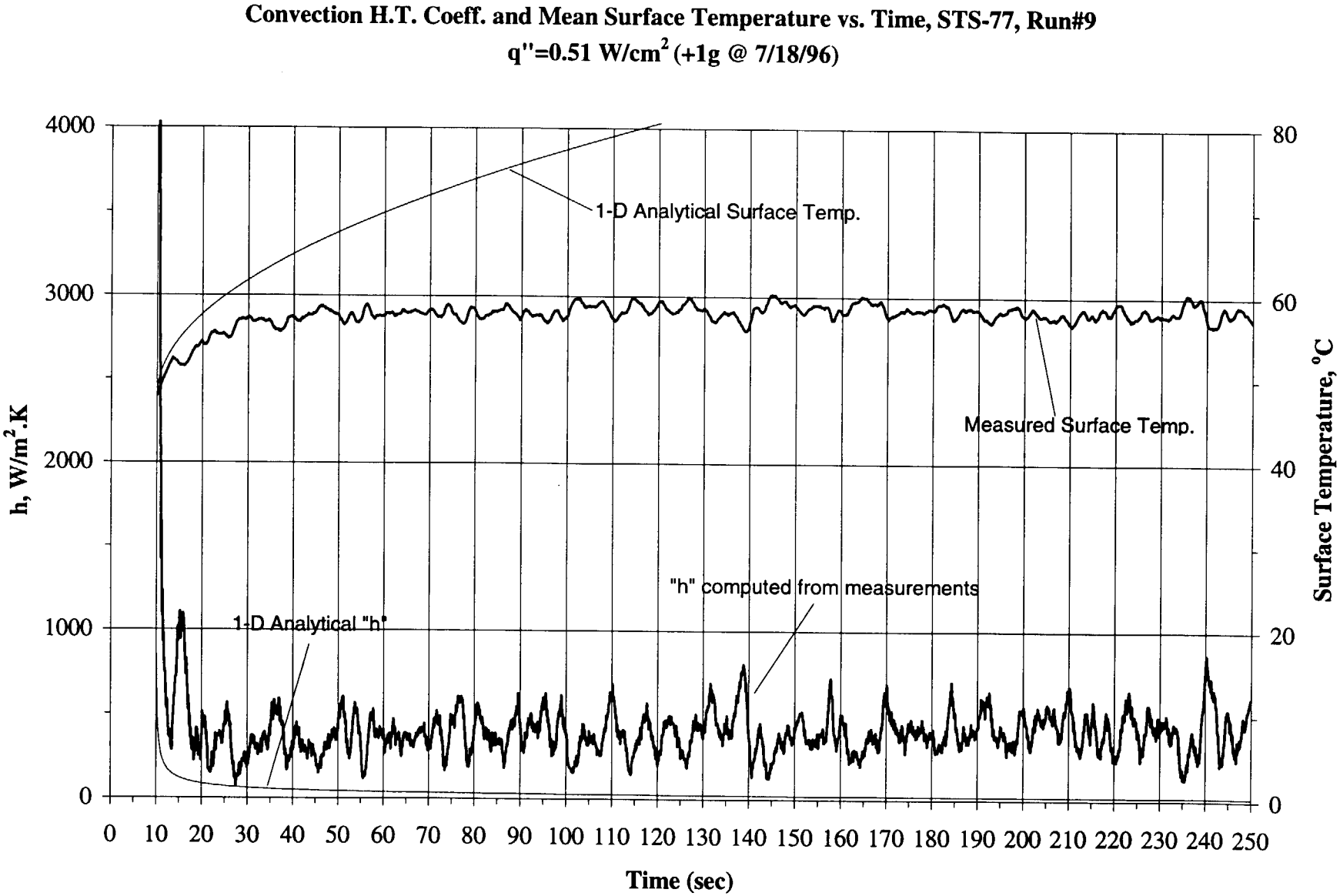

Figure B-20i. a/g = +1 Postflight test. Mean heater surface temperature and derived heat transfer coefficient. PBE-IIA (STS-77). Run No. 9.

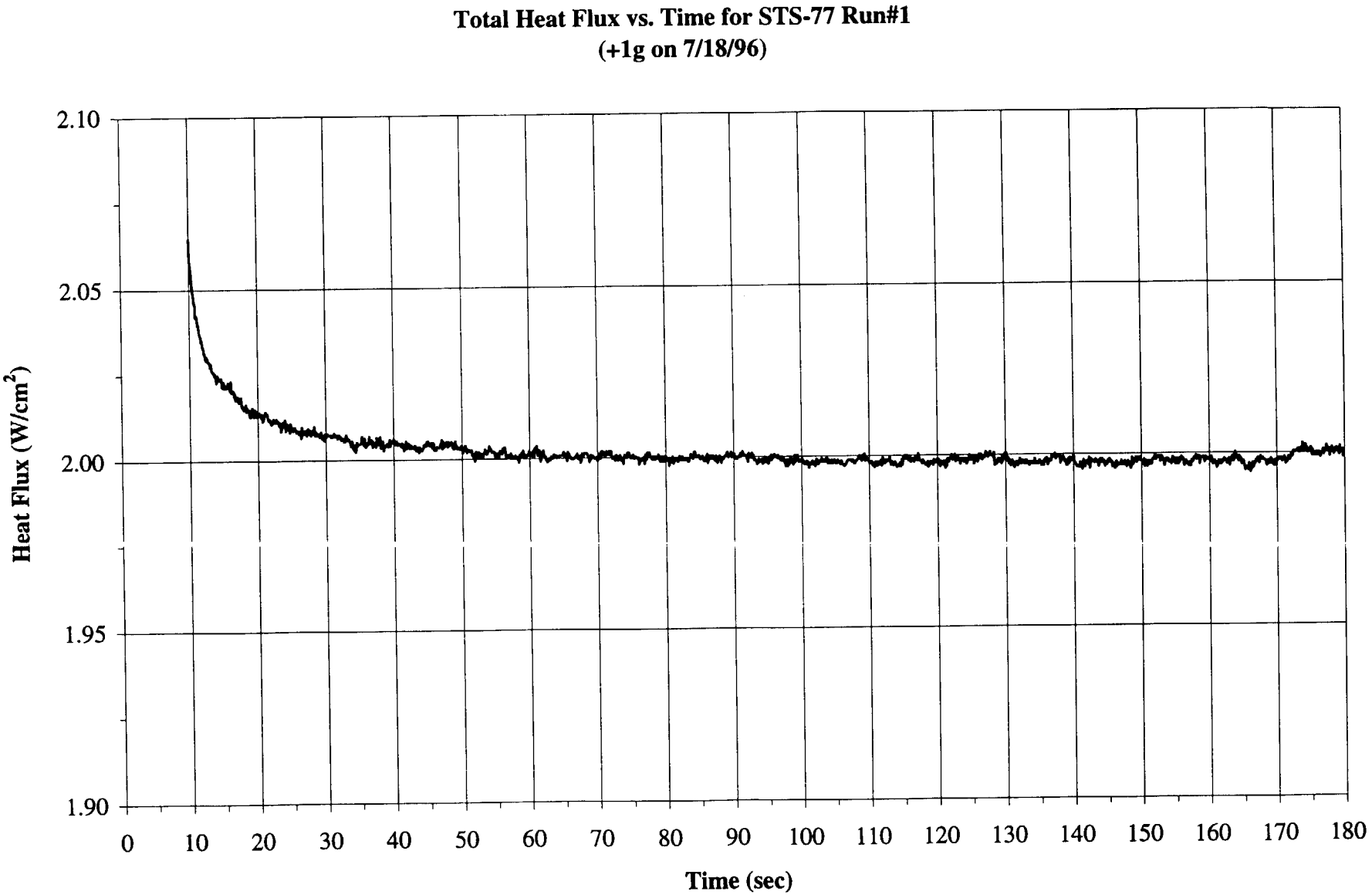

Figure B-21a. a/g = +1 Postflight test. Heat flux input. PBE-IIA (STS-77). Run No. 1.

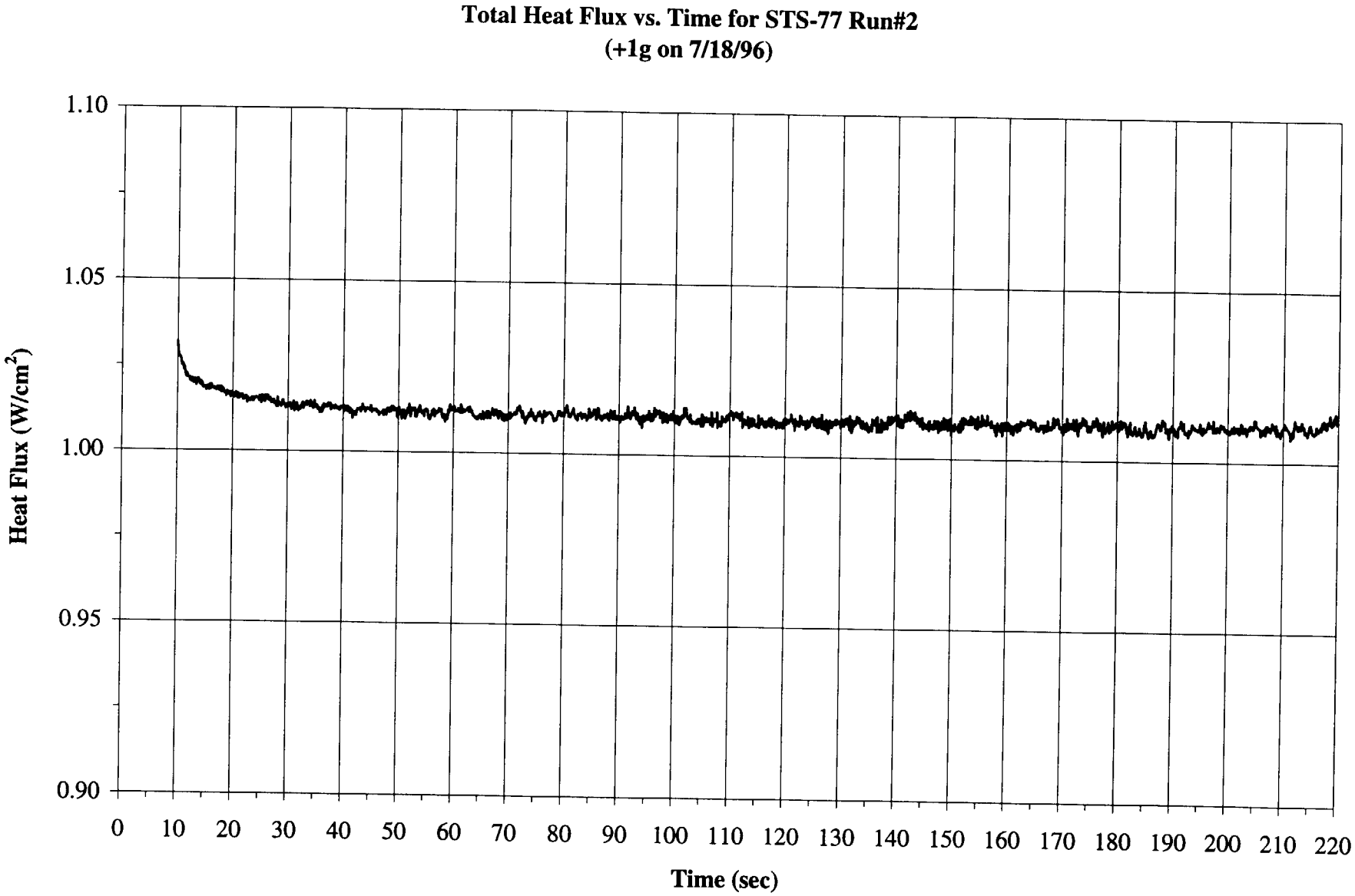

Figure B-21b. a/g = +1 Postflight test. Heat flux input. PBE-IIA (STS-77). Run No. 2.

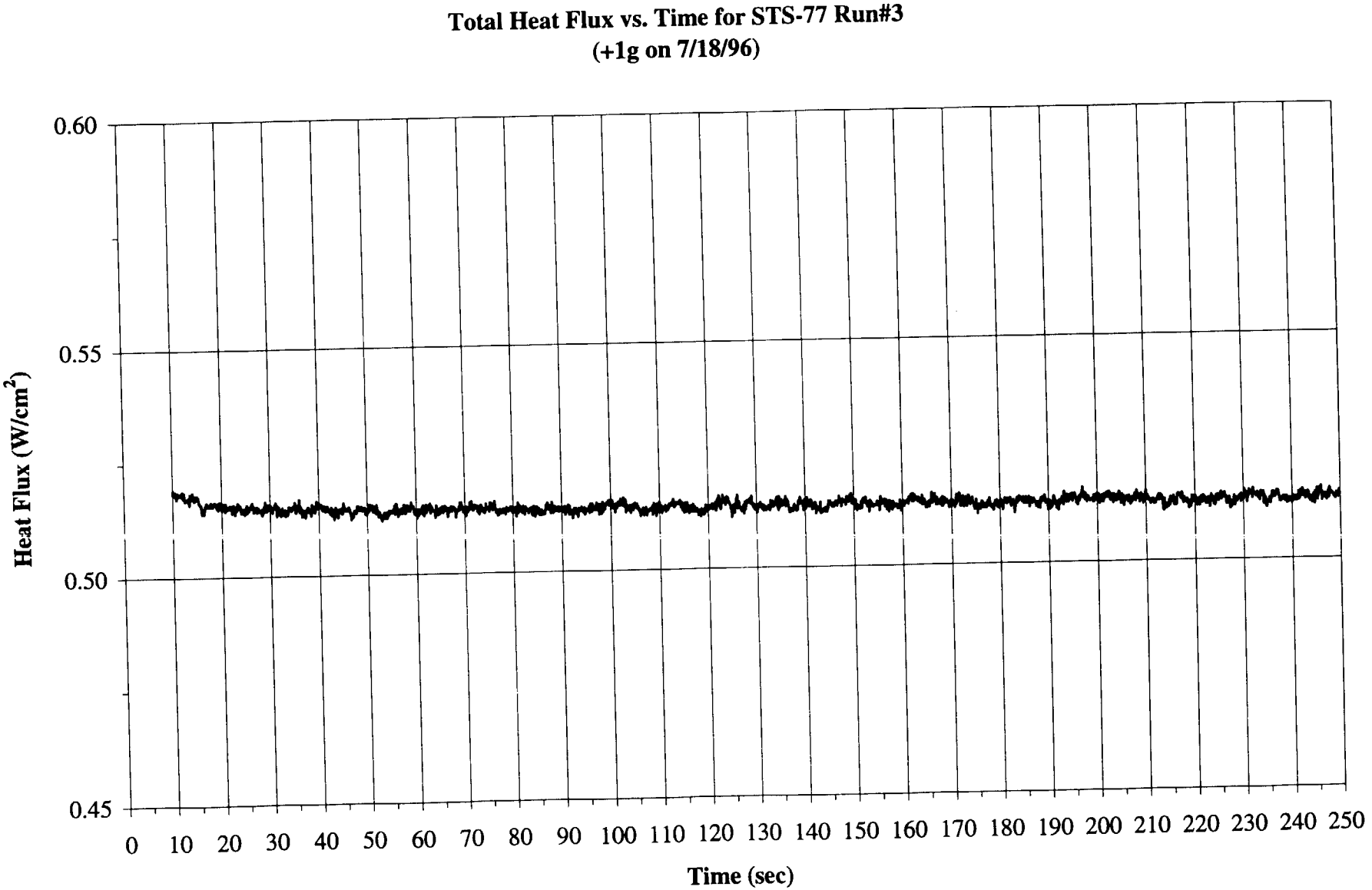

Figure B-21c. a/g = +1 Postflight test. Heat flux input. PBE-IIA (STS-77). Run No. 3.

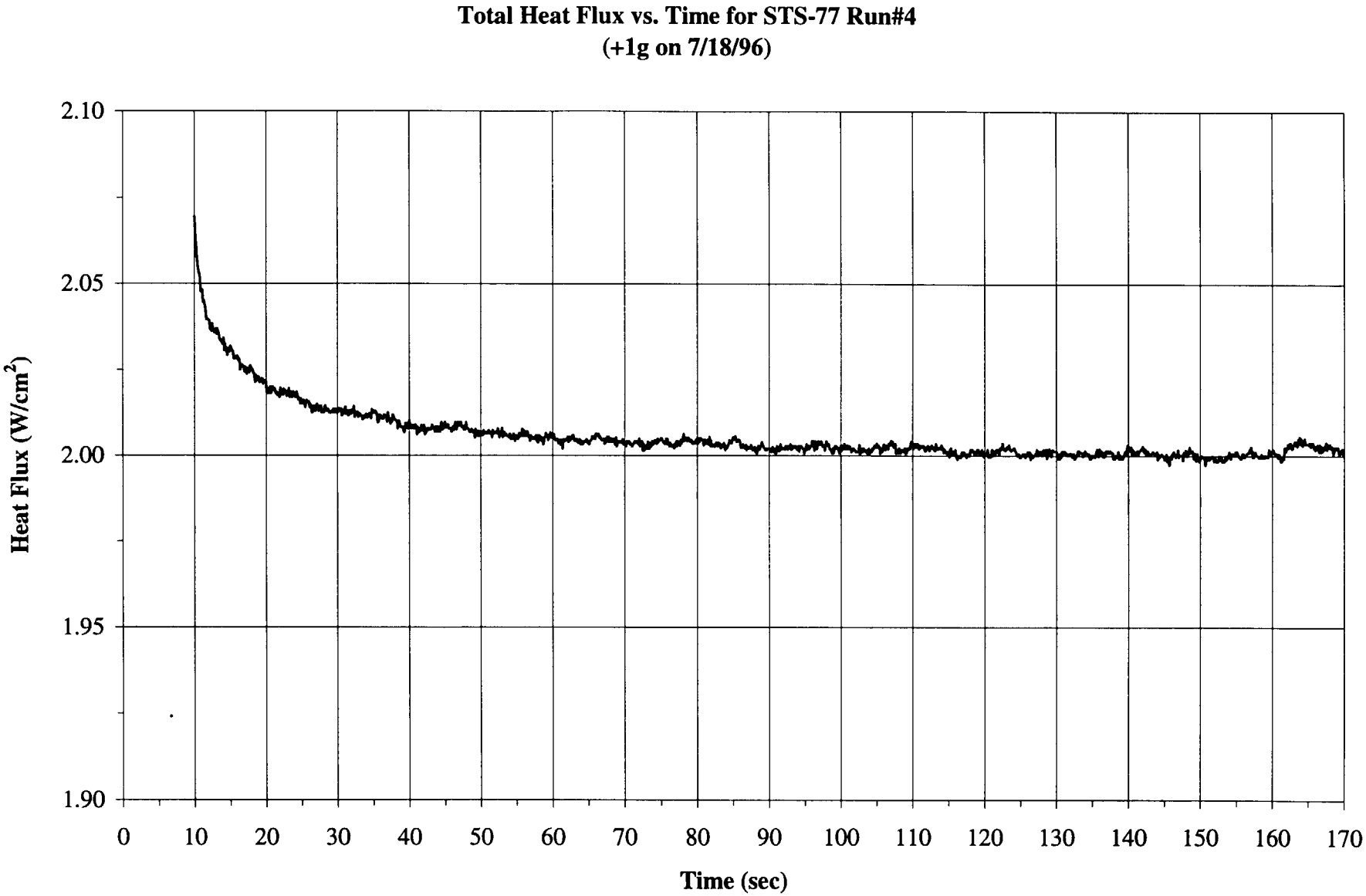

Figure B-21d. a/g = +1 Postflight test. Heat flux input. PBE-IIA (STS-77). Run No. 4.

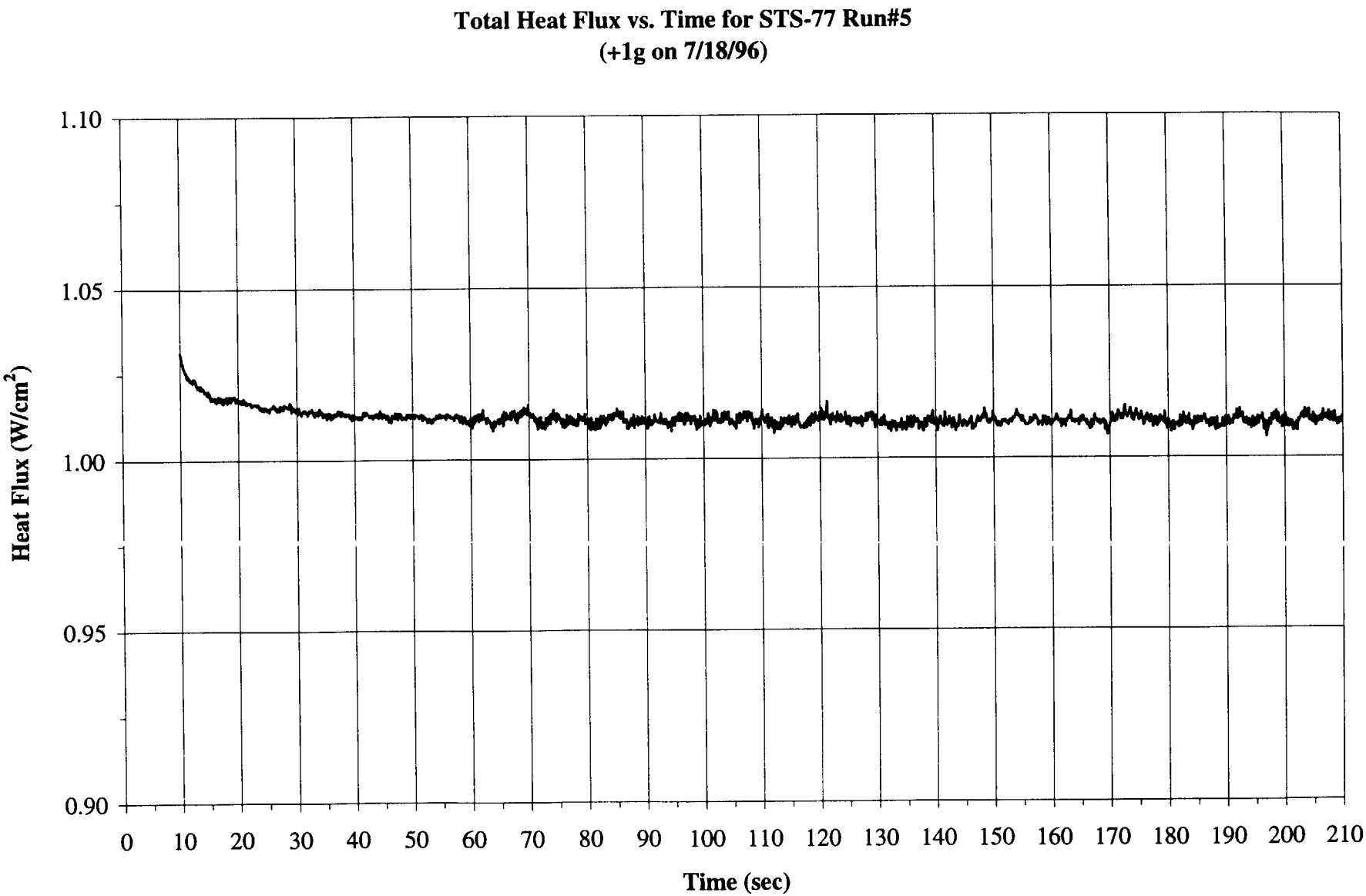

Figure B-21e. a/g = +1 Postflight test. Heat flux input. PBE-IIA (STS-77). Run No. 5.

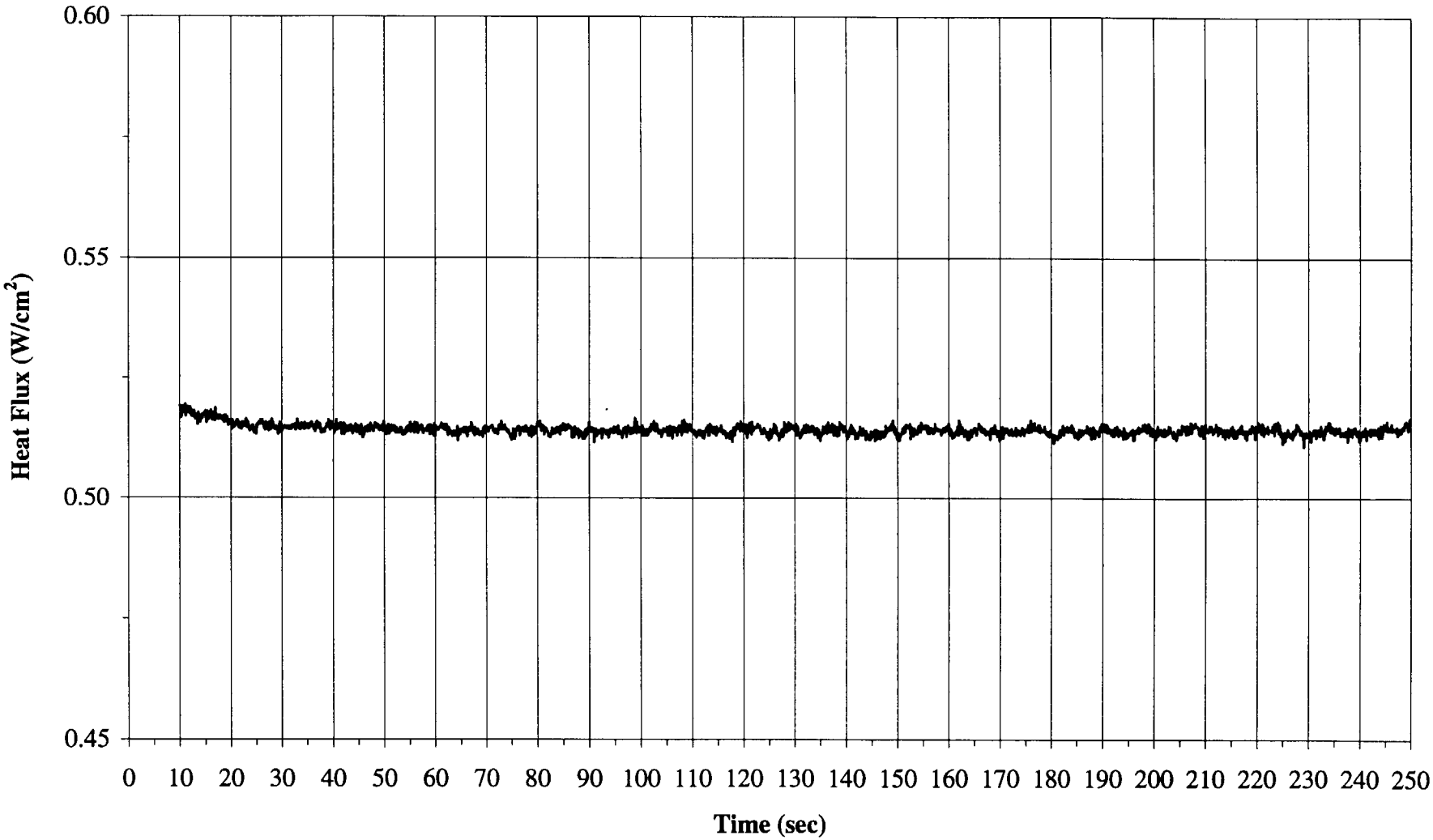

Figure B-21f. a/g = +1 Postflight test. Heat flux input. PBE-IIA (STS-77). Run No. 6.

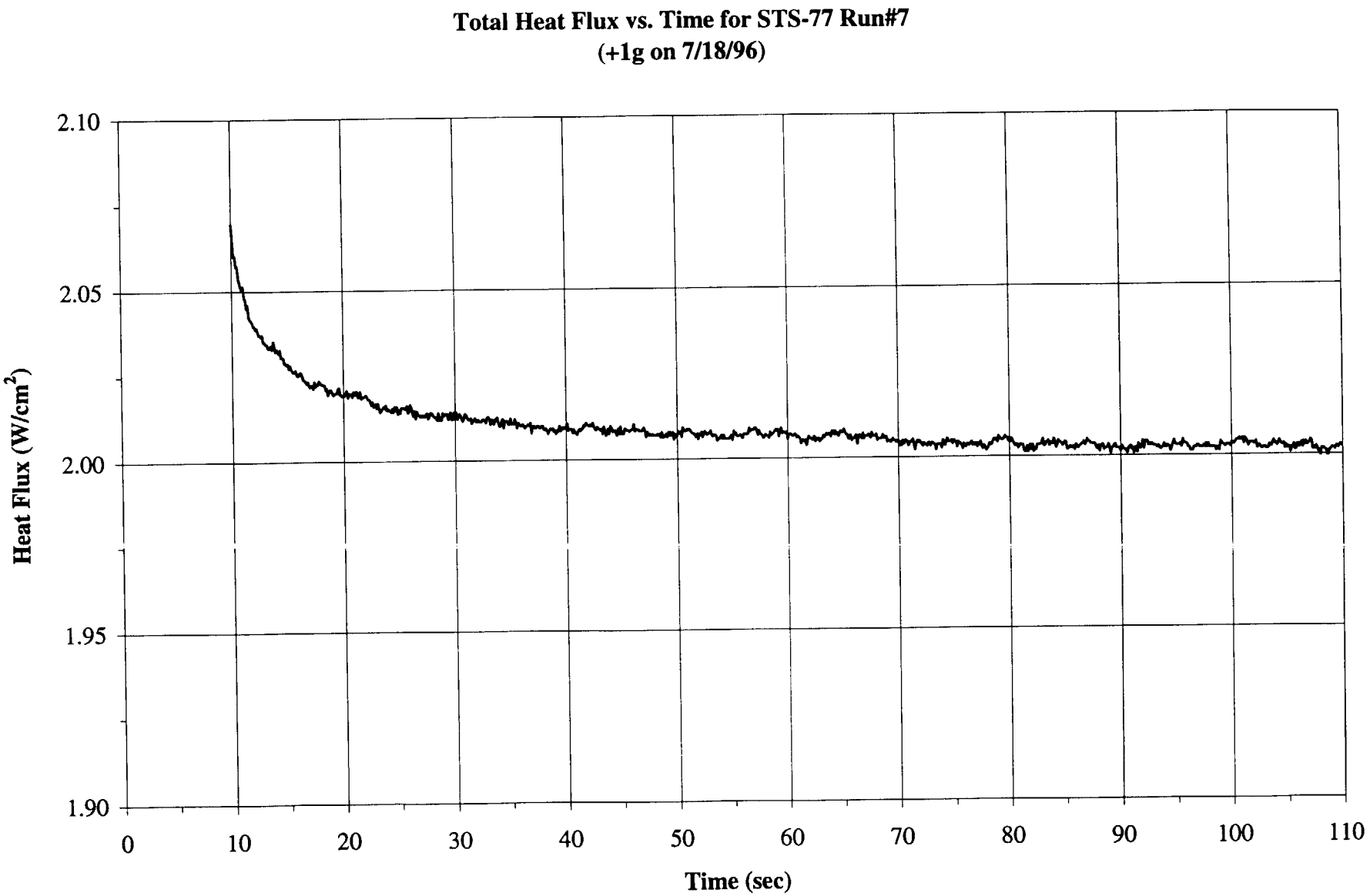

Figure B-21g. a/g = +1 Postflight test. Heat flux input. PBE-IIA (STS-77). Run No. 7.

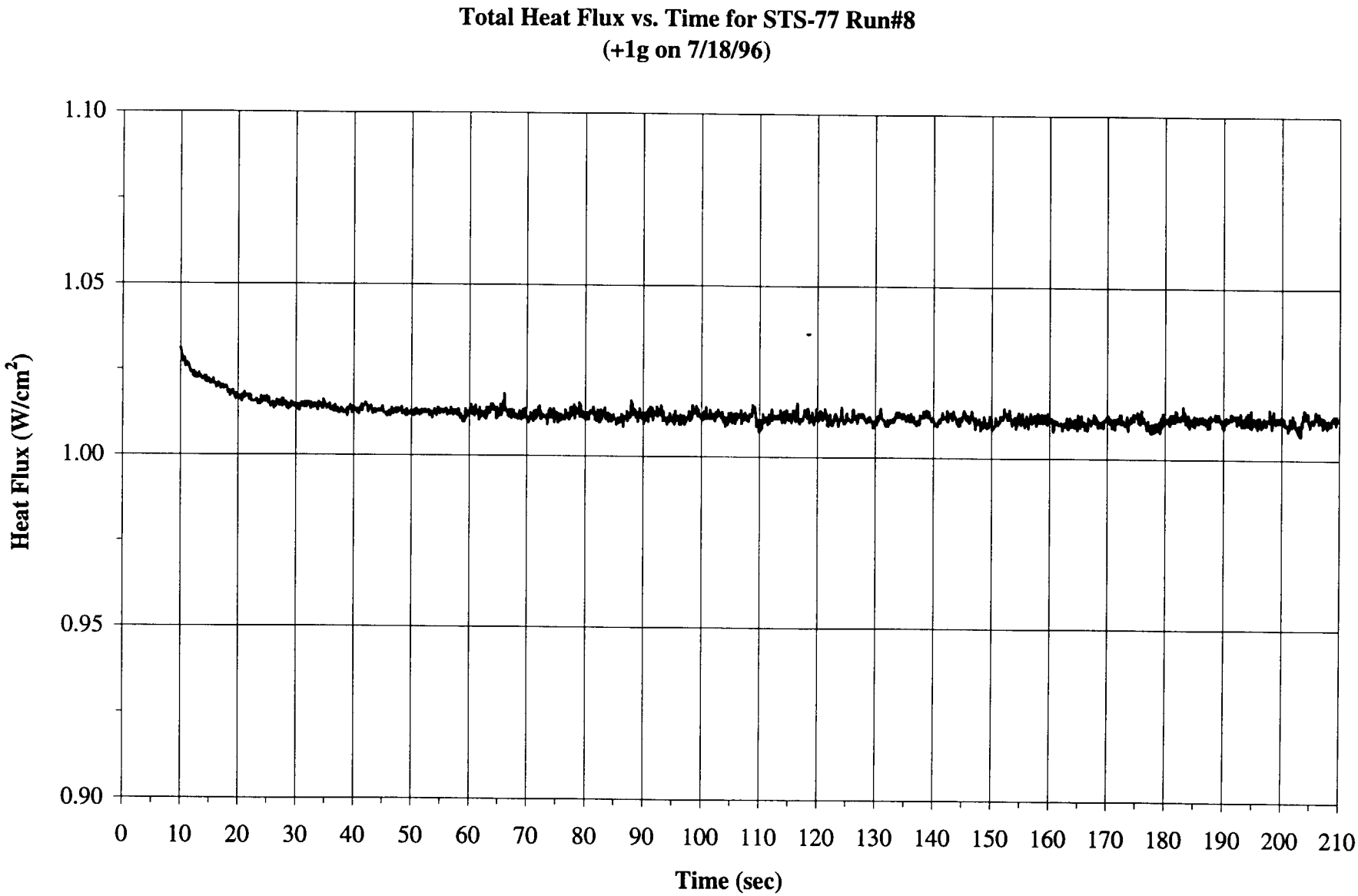

Figure B-21h. a/g = +1 Postflight test. Heat flux input. PBE-IIA (STS-77). Run No. 8.

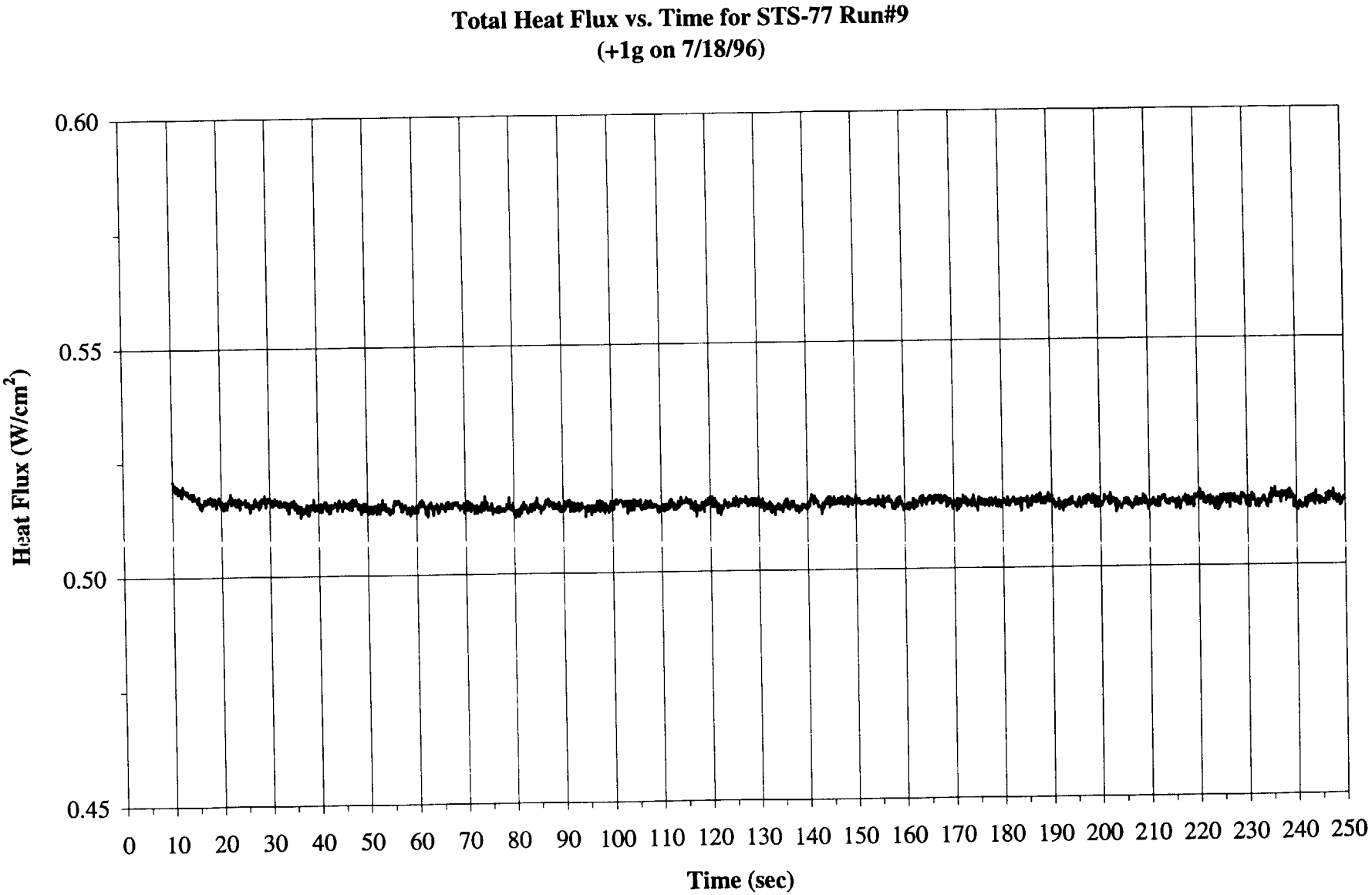

Figure B-21i. a/g = +1 Postflight test. Heat flux input. PBE-IIA (STS-77). Run No. 9.

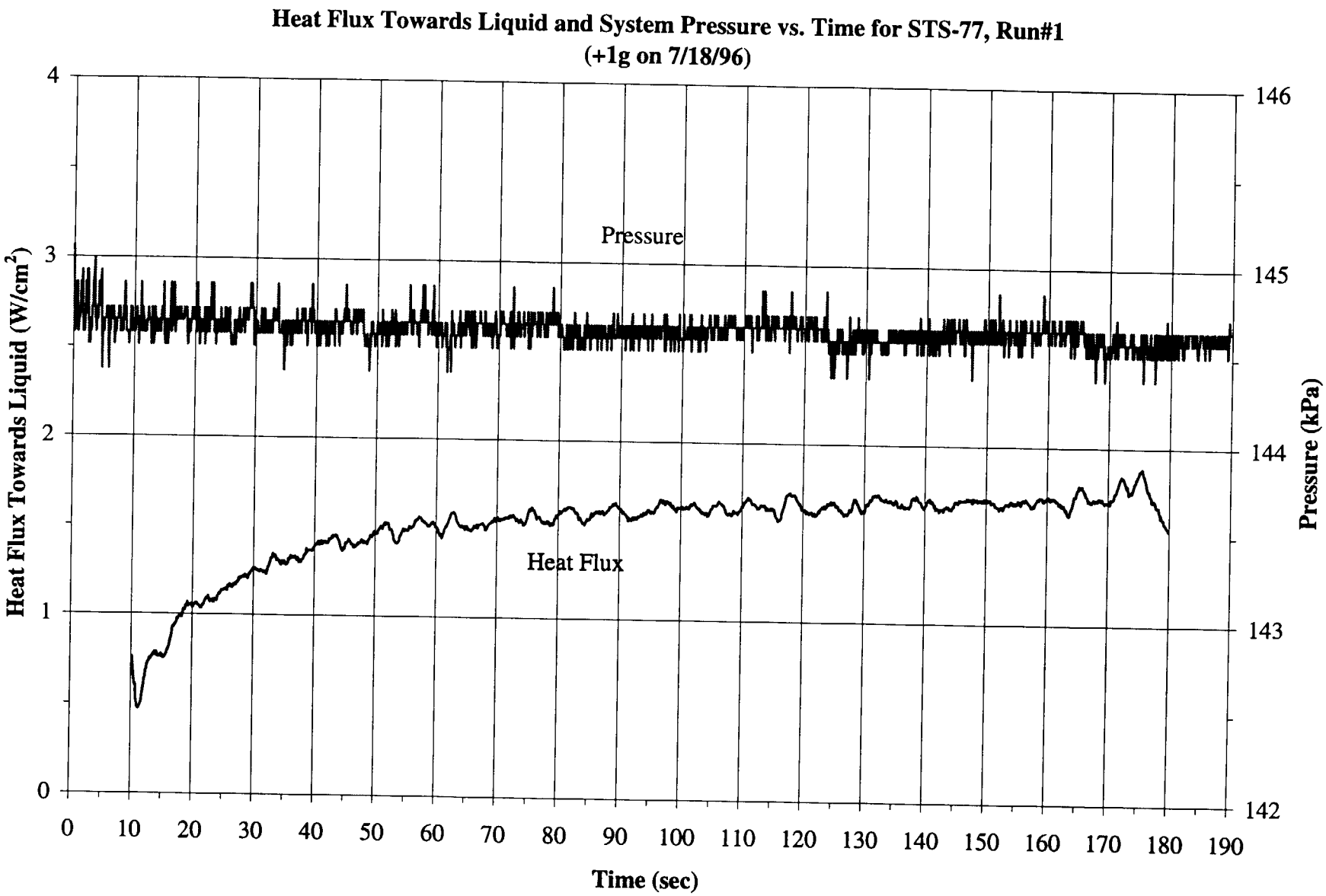

Figure B-22a. a/g = +1 Postflight test. System pressure and heat flux into fluid. PBE-IIA (STS-77). Run No. 1.

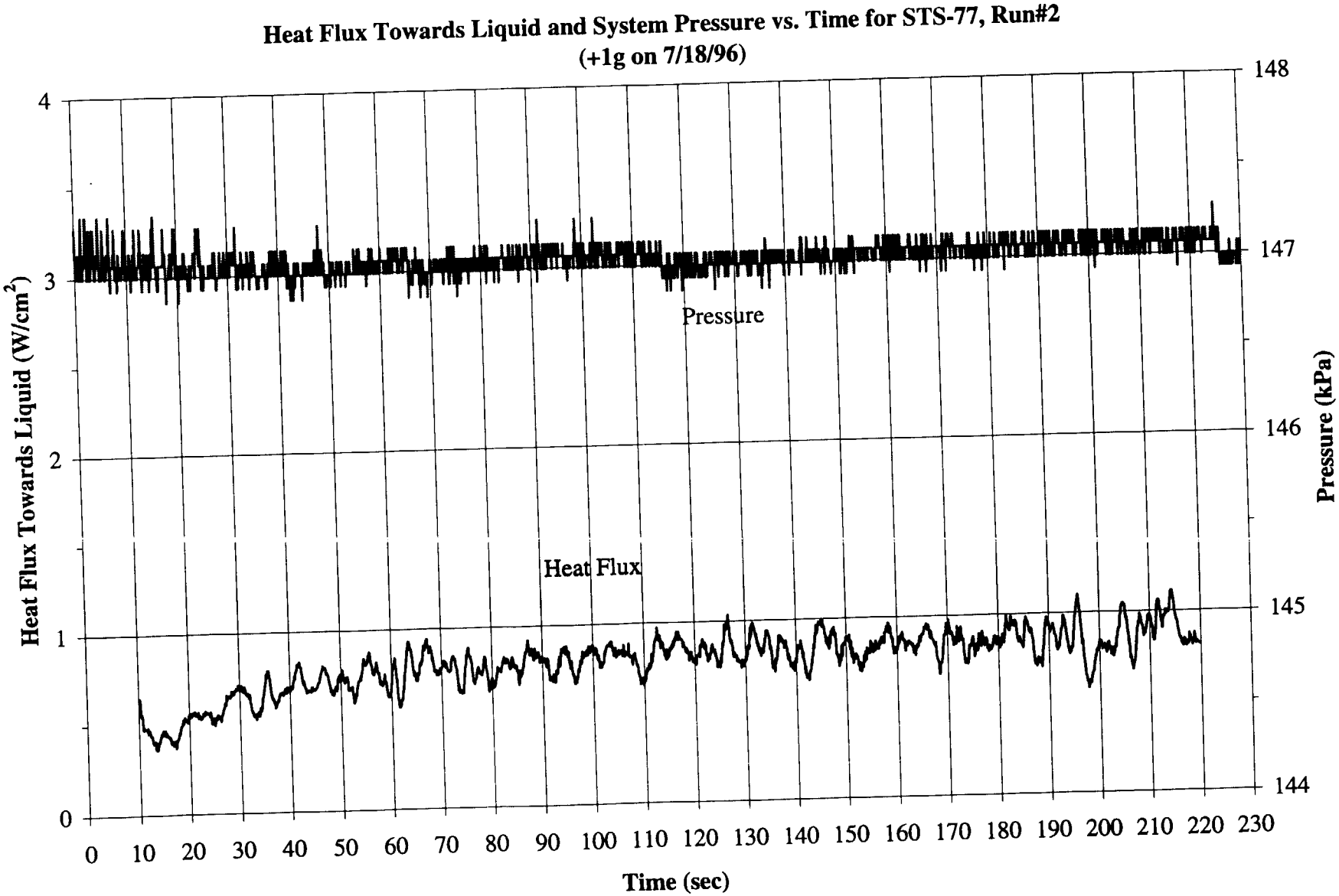

Figure B-22b. a/g = +1 Postflight test. System pressure and heat flux into fluid. PBE-IIA (STS-77). Run No. 2.

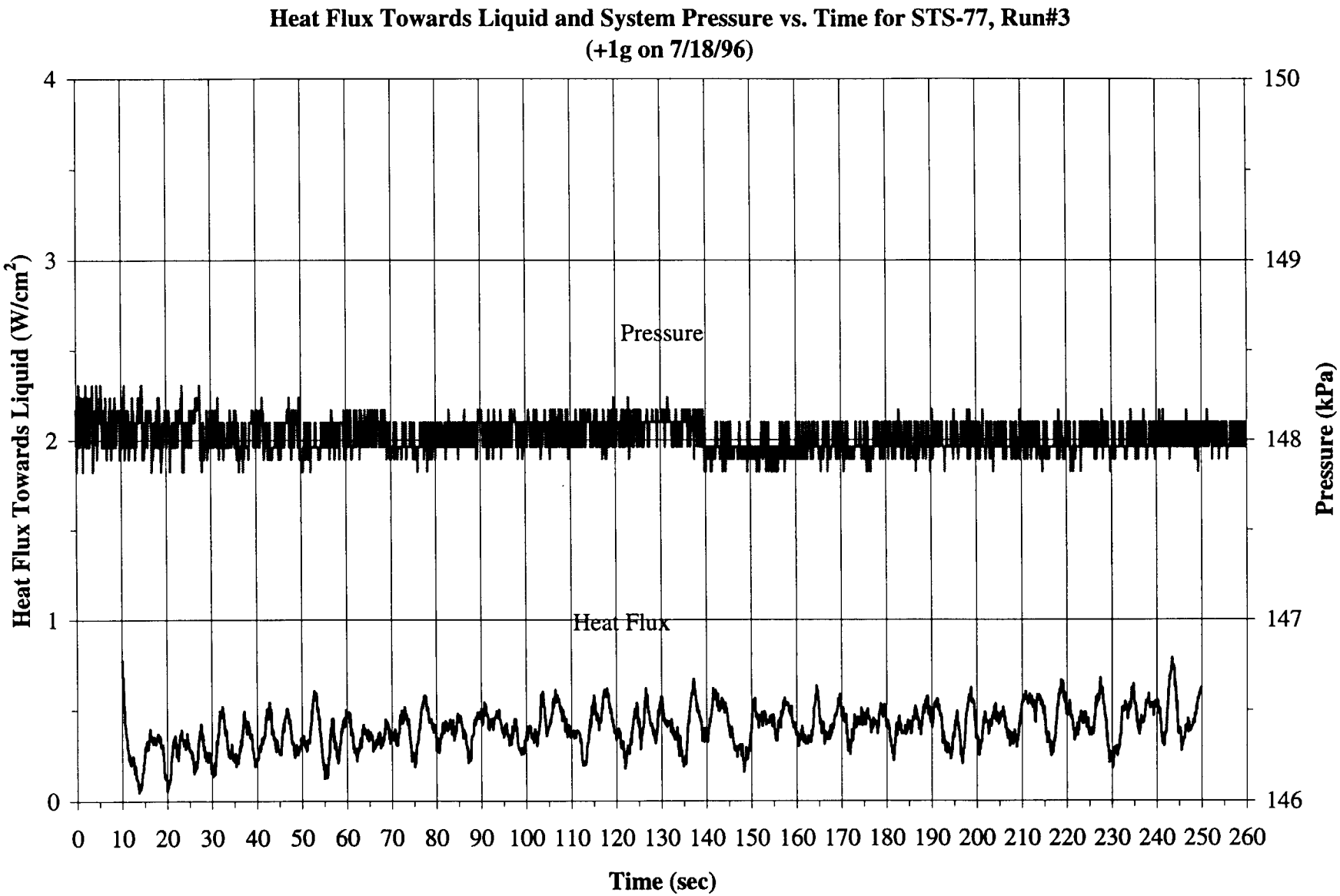

Figure B-22c. a/g = +1 Postflight test. System pressure and heat flux into fluid. PBE-IIA (STS-77). Run No. 3.

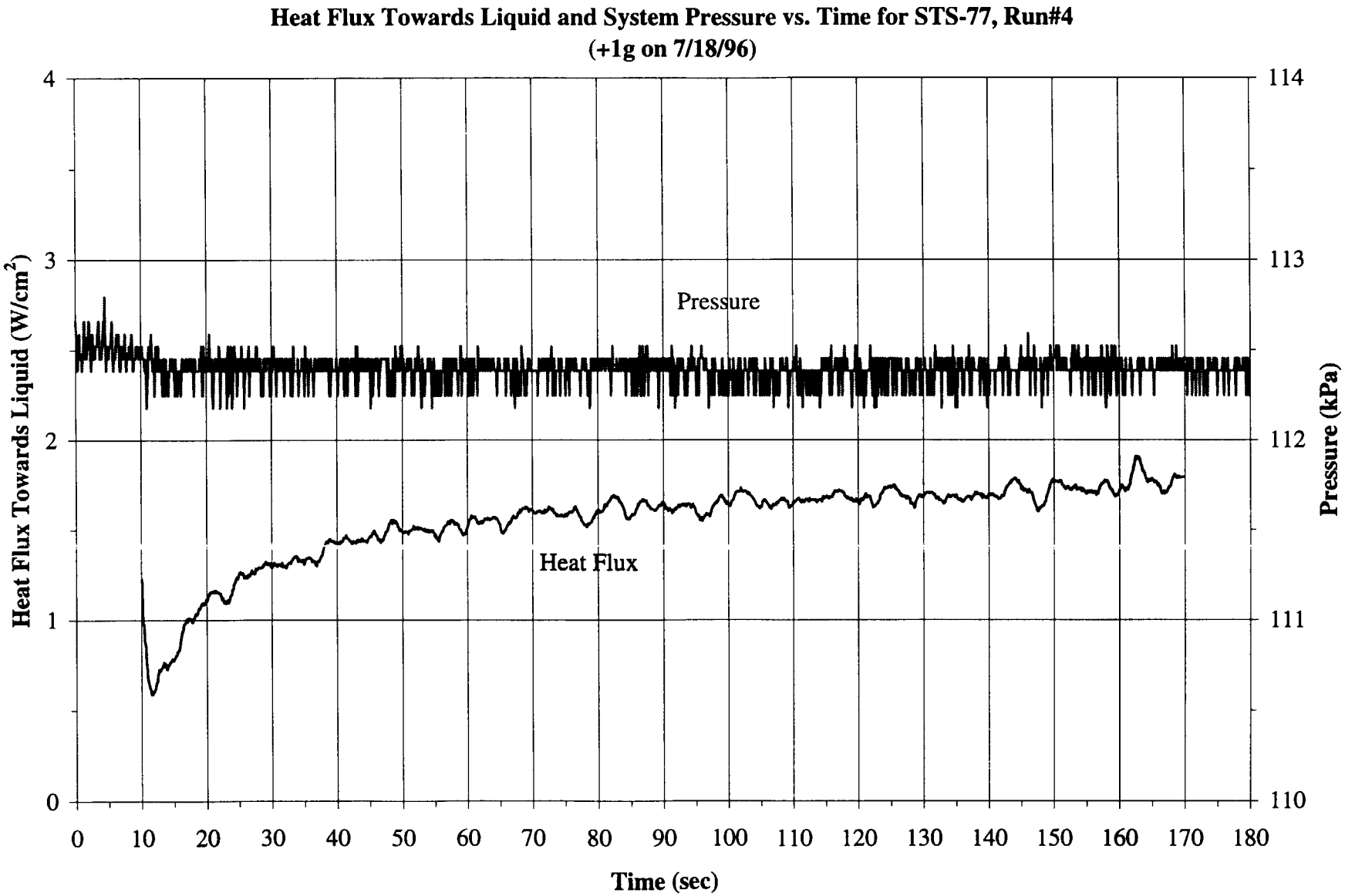

Figure B-22d. a/g = +1 Postflight test. System pressure and heat flux into fluid. PBE-IIA (STS-77). Run No. 4.

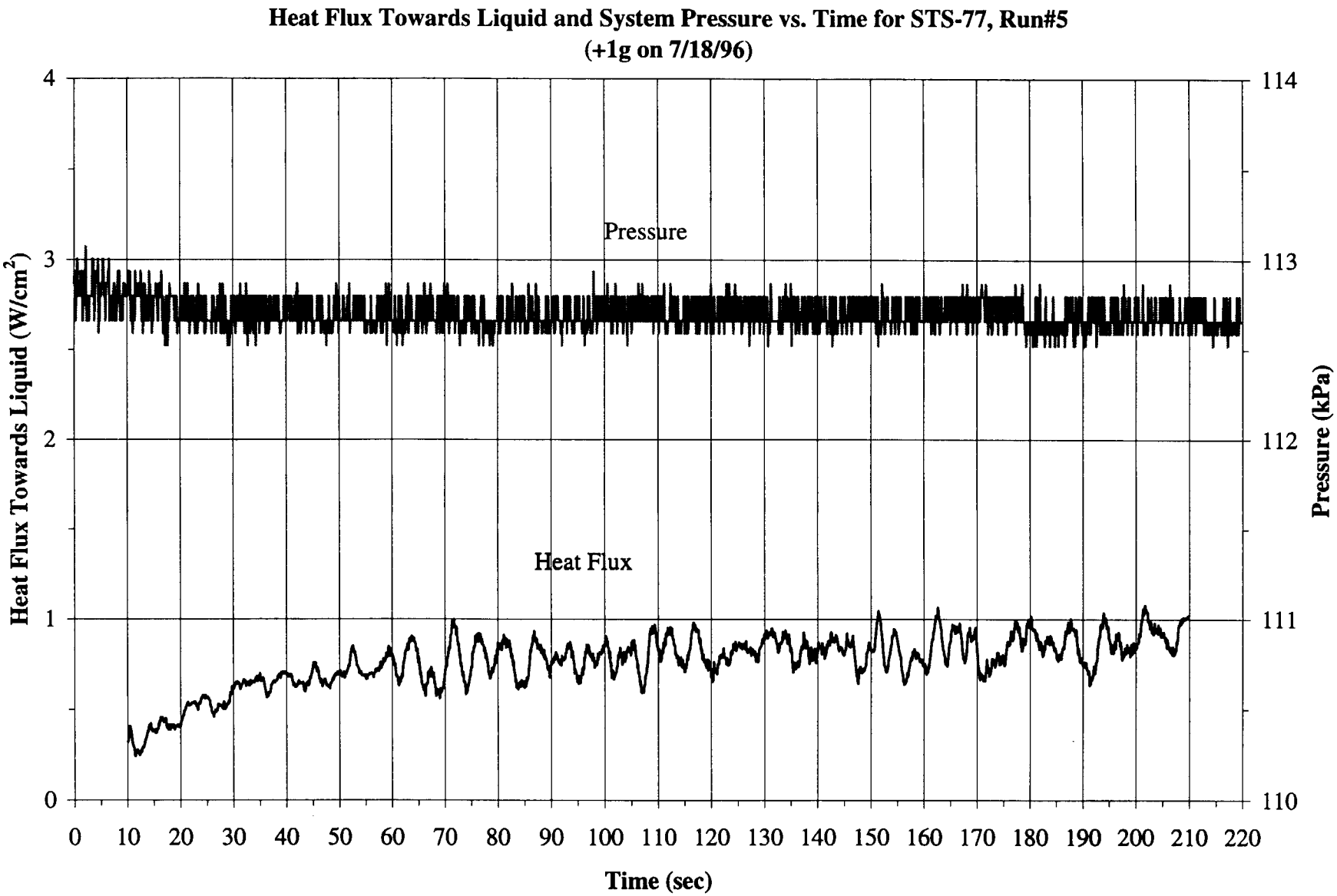

Figure B-22e. a/g = +1 Postflight test. System pressure and heat flux into fluid. PBE-IIA (STS-77). Run No. 5.

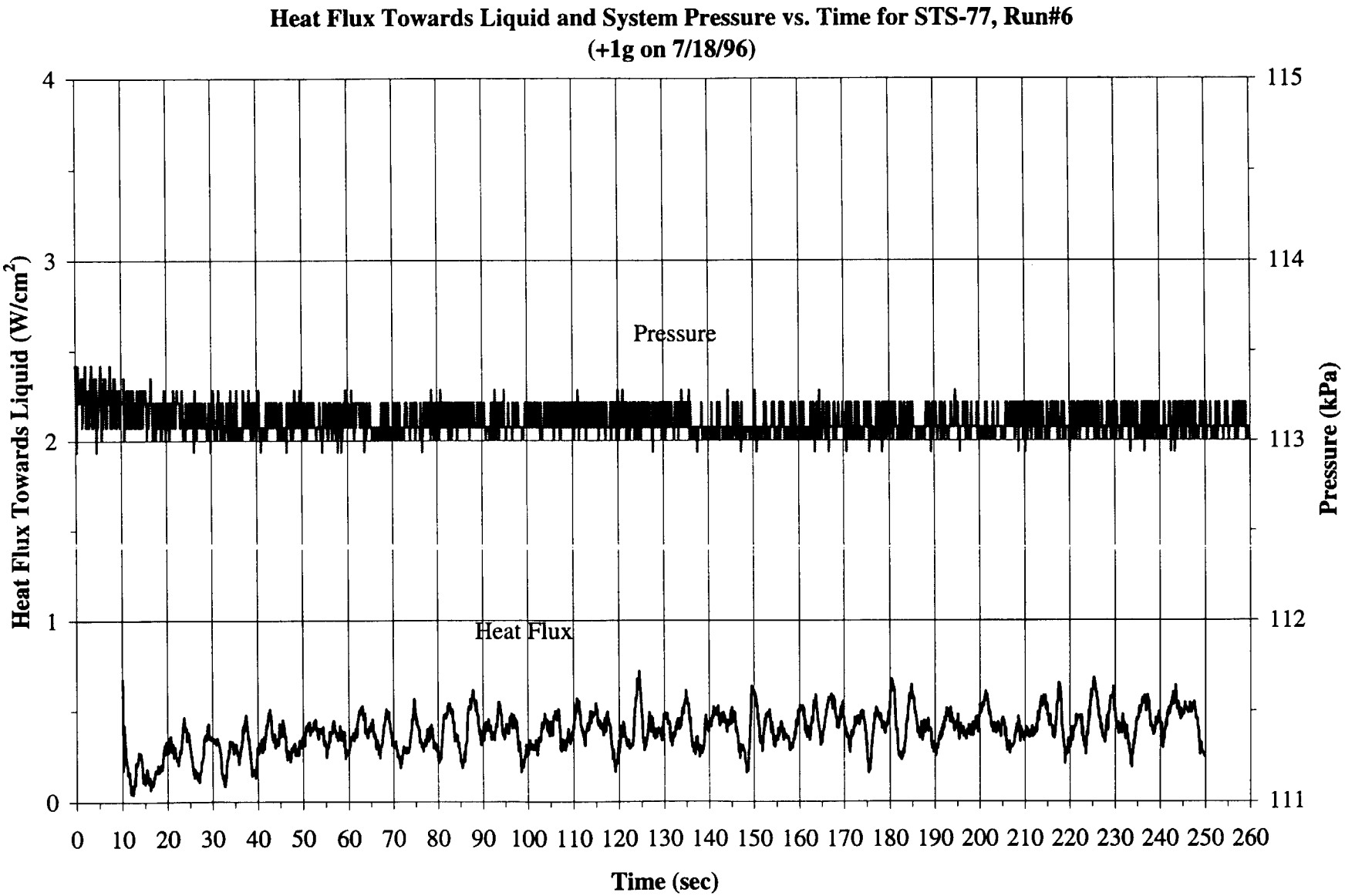

Figure B-22f. a/g = +1 Postflight test. System pressure and heat flux into fluid. PBE-IIA (STS-77). Run No. 6.

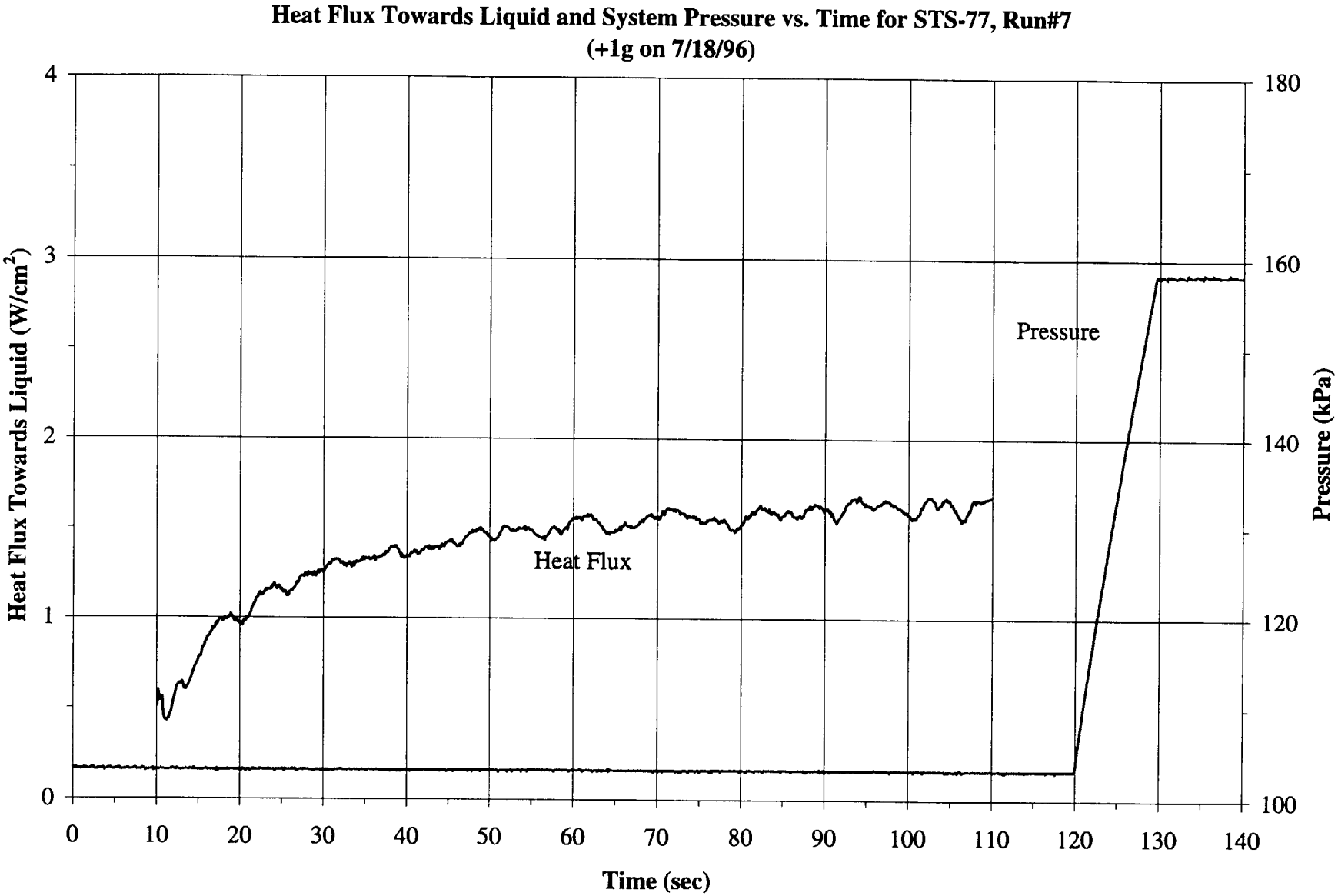

Figure B-22g. a/g = +1 Postflight test. System pressure and heat flux into fluid. PBE-IIA (STS-77). Run No. 7.

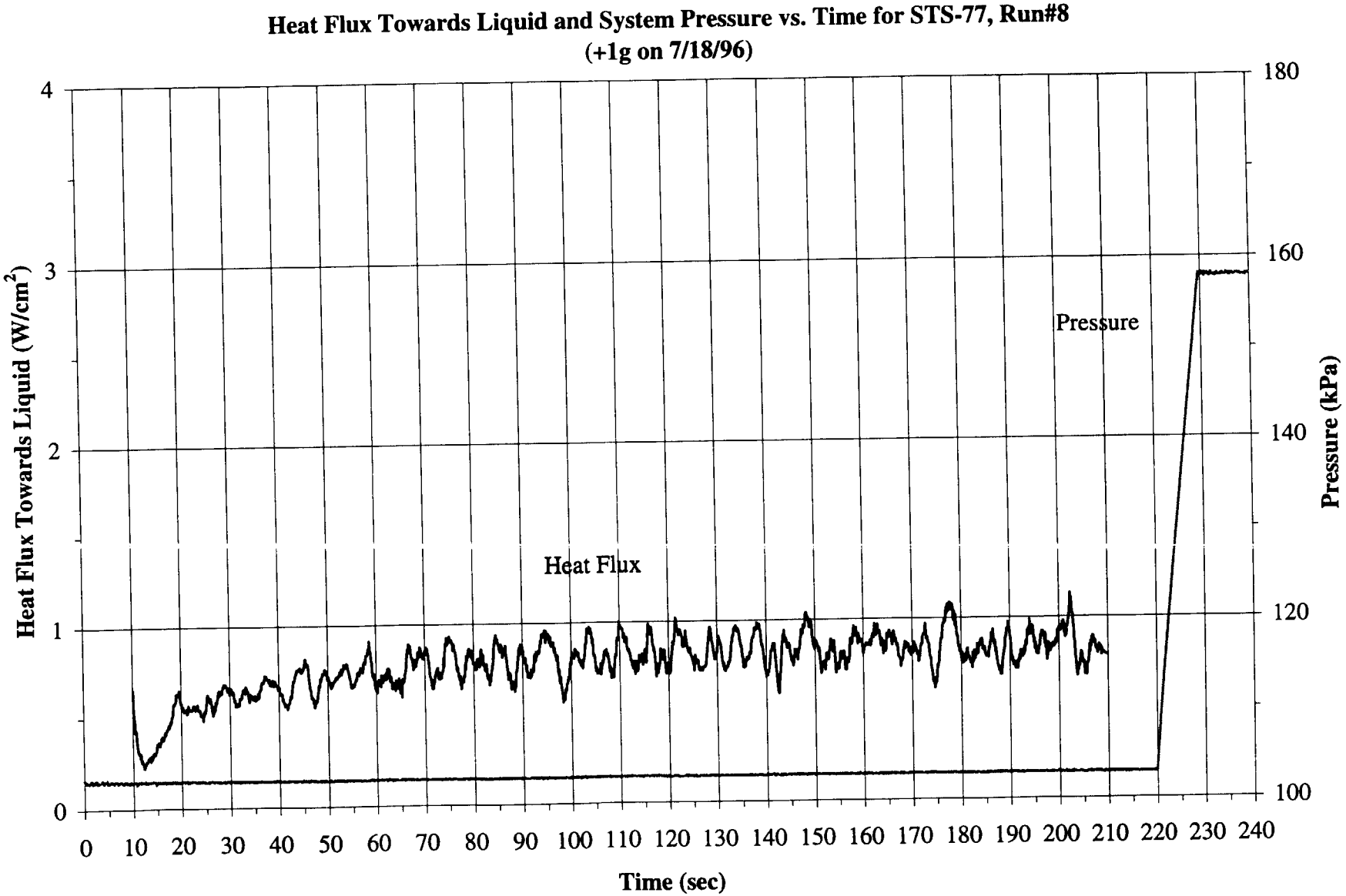

Figure B-22h. a/g = +1 Postflight test. System pressure and heat flux into fluid. PBE-IIA (STS-77). Run No. 8.

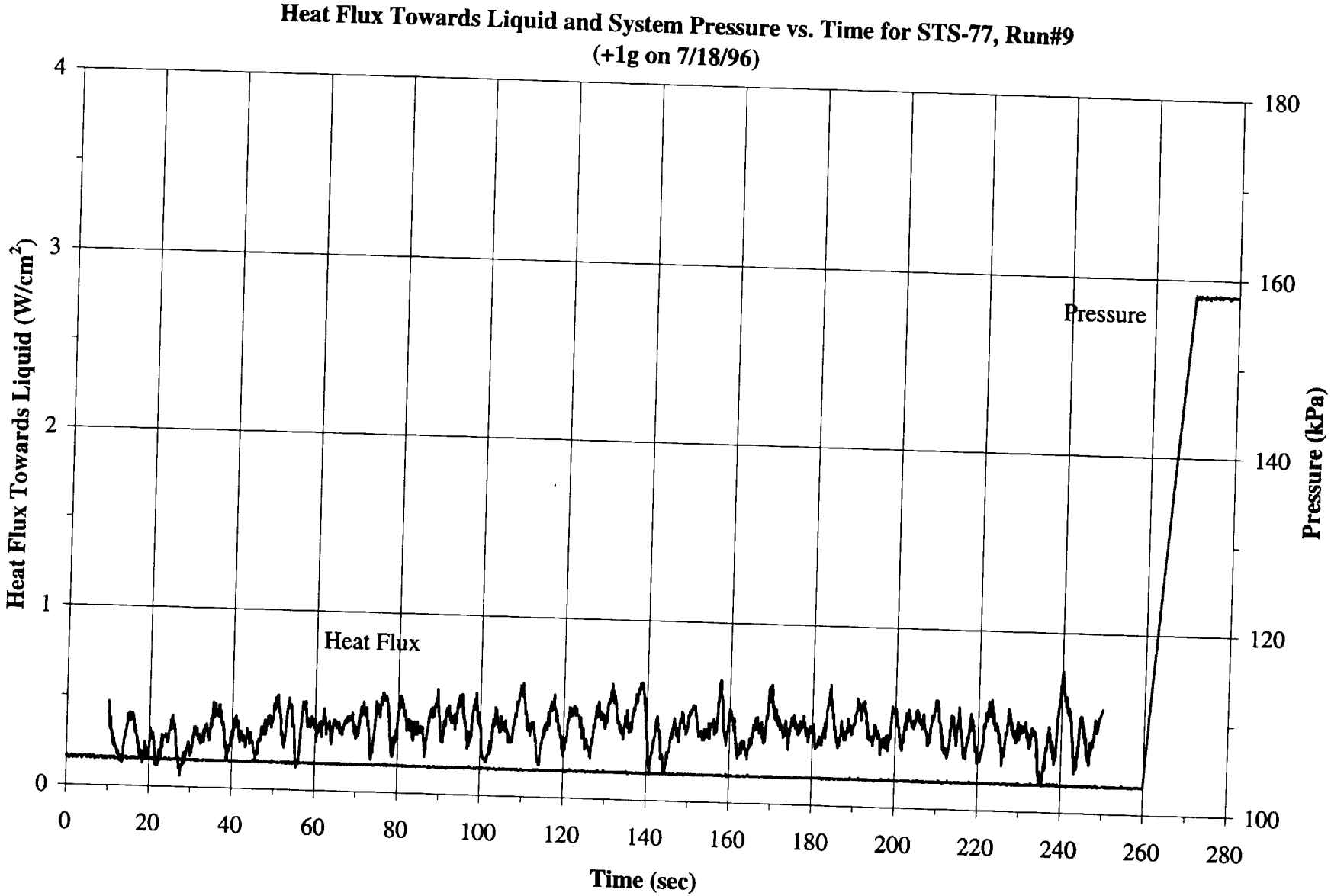

Figure B-22i. a/g = +1 Postflight test. System pressure and heat flux into fluid. PBE-IIA (STS-77). Run No. 9.

REPORT DOCUMENTATION PAGE

Form Approved
OMB No. 0704-0188

1. AGENCY USE ONLY (*Leave blank*)	2. REPORT DATE	3. REPORT TYPE AND DATES COVERED
	June 1998	Final Contractor Report

4. TITLE AND SUBTITLE

Dryout and Rewetting in the Pool Boiling Experiment Flown on STS-72 (PBE-II B) and STS-77 (PBE-II A)

5. FUNDING NUMBERS

WU–963–25–0B–00
NAG3–1684

6. AUTHOR(S)

Herman Merte, Jr., Ho Sung Lee, and Robert B. Keller

7. PERFORMING ORGANIZATION NAME(S) AND ADDRESS(ES)

University of Michigan
College of Engineering
Department of Mechanical Engineering
Ann Arbor, Michigan 48109-2125

8. PERFORMING ORGANIZATION REPORT NUMBER

E–11185

9. SPONSORING/MONITORING AGENCY NAME(S) AND ADDRESS(ES)

National Aeronautics and Space Administration
Lewis Research Center
Cleveland, Ohio 44135–3191

10. SPONSORING/MONITORING AGENCY REPORT NUMBER

NASA CR—1998-207410
UM-MEAM-98-01

11. SUPPLEMENTARY NOTES

Project Manager, Francis Chiaramonte, Microgravity Science Division, NASA Lewis Research Center, organization code 6712, (216) 433–8040.

12a. DISTRIBUTION/AVAILABILITY STATEMENT

Unclassified - Unlimited
Subject Category: 34 Distribution: Nonstandard

This publication is available from the NASA Center for AeroSpace Information, (301) 621–0390.

12b. DISTRIBUTION CODE

13. ABSTRACT (*Maximum 200 words*)

Experiments were conducted in the microgravity of space in which a pool of liquid (R-113), initially at a precisely defined pressure and temperature, is subjected to a step imposed heat flux from a semi-transparent thin-film heater forming part of one wall of the container such that boiling is initiated and maintained for a defined period of time at a constant pressure level. A total of nine tests were conducted at three levels of heat flux and three levels of subcooling in each of the two space experiments in a GAS canister on the STS-77, -72, respectively. Three (3) modes of propagation of boiling across the heater surface and subsequent vapor bubble growths were observed, in addition to the two (2) modes observed in the previous microgravity pool boiling space flights on STS-47, -57, and -60. Of particular interest were the extremely dynamic or "explosive" growths, which were determined to be the consequence of the large increase in the liquid-vapor interface area associated with the appearance of a corrugated or rough interface. Predictions of circumstances for its onset have been carried out. Assumptions were necessary regarding the character of disturbances necessary for the instabilities to grow. Also, a new vapor bubble phenomena was observed in which small vapor bubbles migrated toward a larger bubble, eventually coalescing with this larger bubble. The heat transfer was enhanced approximately 30% as a result of these migrating bubbles, which is believed to be a vapor bubble manifestation of Marangoni convection and/or molecular momentum effects, sometimes referred to as vapor recoil. The circumstances of heat flux and liquid subcooling necessary to produce heater surface dryout for an initially stagnant liquid subjected to an imposed heat flux have been more closely identified.

14. SUBJECT TERMS

Boiling; Heat flux; Reduced gravity; Buoyancy; Pool boiling; Microgravity applications; Space Shuttle missions 72 and 77; Get Away Special canister

15. NUMBER OF PAGES

538

16. PRICE CODE

A23

17. SECURITY CLASSIFICATION OF REPORT	18. SECURITY CLASSIFICATION OF THIS PAGE	19. SECURITY CLASSIFICATION OF ABSTRACT	20. LIMITATION OF ABSTRACT
Unclassified	Unclassified	Unclassified	